WIND ENERGY ENGINEERING

A HANDBOOK FOR ONSHORE AND OFFSHORE WIND TURBINES

EDITED BY TREVOR M. LETCHER

SECOND EDITION

Wind Energy Engineering

A Handbook for Onshore and Offshore Wind Turbines

This page intentionally left blank

Wind Energy Engineering

A Handbook for Onshore and Offshore Wind Turbines

Second Edition

Edited by

Trevor M. Letcher
School of Chemistry, University of KwaZulu-Natal, Durban, South Africa

ACADEMIC PRESS
An imprint of Elsevier

Academic Press is an imprint of Elsevier
125 London Wall, London EC2Y 5AS, United Kingdom
525 B Street, Suite 1650, San Diego, CA 92101, United States
50 Hampshire Street, 5th Floor, Cambridge, MA 02139, United States
The Boulevard, Langford Lane, Kidlington, Oxford OX5 1GB, United Kingdom

ISBN: 978-0-323-99353-1

Publisher: Charlotte Cockle
Acquisitions Editor: Edward Payne
Editorial Project Manager: Franchezca A. Cabural
Production Project Manager: Surya Narayanan Jayachandran
Cover Designer: Mathew Limbert

Typeset by MPS Limited, Chennai, India

Contents

Section F
Economics of wind energy and certification issues

List of Contributors

Muhammad Aleem University of Surrey, Guildford, London, United Kingdom; Department of Civil and Environmental Engineering, University of Surrey, Guildford, London, United Kingdom

Antonio Alonso-Cepeda Renewable Energy Research Institute and DIEEAC-ETSII-AB, Universidad de Castilla-La Mancha, Albacete, Castilla-La Mancha, Spain

Sadra Amani Department of Sustainability, Civil and Environmental Engineering, University of Surrey, Guildford, London, United Kingdom

Francesco Avallone Faculty of Aerospace Engineering, FPT Department, Wind Energy Section, Aeroacoustics Research Group, Delft University of Technology, Delft, The Netherlands

AbuBakr S. Bahaj Energy & Climate Change Divisions, & Sustainable Energy Research Group, Faculty of Engineering and the Environment, University of Southampton, Southampton, United Kingdom

Wes Baker Electric Power Research Institute (EPRI), Palo Alto, CA, United States

Charles J. Barnhart Institute for Energy Studies, Western Washington University, Bellinghamm, WA, United States

Sukanta Basu Faculty of Civil Engineering and Geosciences, Delft University of Technology, Delft, the Netherlands

S. Bhattacharya Department of Civil Engineering, University of Surrey, Surrey, United Kingdom

Subhamoy Bhattacharya University of Surrey, Guildford, London, United Kingdom; OWF-PRA, London, United Kingdom; Department of Geomechanics, University of Surrey, United Kingdom; Department of Sustainability, Civil and Environmental Engineering, University of Surrey, Guildford, London, United Kingdom; Renew Risk (OWF-PRA Limited), London, United Kingdom; Department of Civil and Environmental Engineering, University of Surrey, Guildford, London, United Kingdom; University of Surrey, Guildford, London, United Kingdom

B Bhowmik UCD Centre for Mechanics, Dynamical Systems and Risk Laboratory, School of Mechanical and Materials Engineering, University College Dublin, Dublin, Ireland

Alessandro Bianchini Department of Industrial Engineering, Università degli Studi di Firenze, Firenze, Italy

Surya Biswal Department of Civil and Environmental Engineering, University of Surrey, Guildford, London, United Kingdom; Department of Sustainability, Civil and Environmental Engineering, University of Surrey, Guildford, London, United Kingdom

Michael Carbajales-Dale Environmental Engineering and Earth Sciences, Clemson University, Clemson, SC, United States

Liang Cui Department of Sustainability, Civil and Environmental Engineering, University of Surrey, Guildford, London, United Kingdom

Kaoshan Dai Department of Civil Engineering, Sichuan University, Chengdu, Sichuan, P. R. China; MOE Key Lab of Deep Underground Science and Engineering, Sichuan University, Chengdu, Sichuan, P. R. China; State Key Lab of Hydraulics and Mountain River Engineering, Sichuan University, Chengdu, Sichuan, P. R. China; Institution of Disaster Management and Reconstruct, Sichuan University, Chengdu, Sichuan, P. R. China

Hasan Emre Demirci Izmir Katip Celebi University, Izmir, Turkey

Cian Desmond Gavin and Doherty Geosolutions Ltd., Dublin, Ireland

Yilser Devrim Department of Energy Systems Engineering, Atilim University, Ankara, Turkey

Beatrice Dower MVGLA, Comrie, Perthshire, United Kingdom

Ergin Erdem Department of Engineering, Robert Morris University, Moon Township, PA, United States

Serkan Eryilmaz Department of Industrial Engineering, Atilim University, Ankara, Turkey

Jianhao Fang School of Mechanical Engineering, Zhejiang University, Hangzhou, P. R. China

B Ghosh QUANT Group, Department of Civil, Structural and Environmental Engineering, Trinity College Dublin, Dublin, Ireland

Bidisha Ghosh School of Civil, Structural and Environmental Engineering, Trinity College Dublin, Dublin, Ireland

Emilio Gómez-Lázaro Renewable Energy Research Institute and DIEEAC-ETSII-AB, Universidad de Castilla-La Mancha, Albacete, Castilla-La Mancha, Spain

JM González-Sopeña QUANT Group, Department of Civil, Structural and Environmental Engineering, Trinity College Dublin, Dublin, Ireland

Luca Greco CNR-INM INstitute of Marine Engineering, Rome, Italy

Marc van Grieken MVGLA, Comrie, Perthshire, United Kingdom

Peiyang Guo Department of Electrical and Electronic Engineering, the University of Hong Kong, Hong Kong, P. R. China

Sumanta Haldar School of Infrastructure, Indian Institute of Technology Bhubaneswar, Odisha, India

Anca Daniela Hansen DTU Wind and Energy Systems, Technical University of Denmark, Roskilde, Denmark

Martin Otto Lavér Hansen DTU Wind and Energy Systems, Technical University of Denmark, Lyngby, Denmark

Yi Hong Zhejiang University, P.R. China

Andrés Honrubia-Escribano Renewable Energy Research Institute and DIEEAC-ETSII-AB, Universidad de Castilla-La Mancha, Albacete, Castilla-La Mancha, Spain

Weifei Hu State Key Laboratory of Fluid Power and Mechatronic Systems, Zhejiang University, Hangzhou, P. R. China; Engineering Research Center for Design Engineering and Digital Twin of Zhejiang Province, Hangzhou, P. R. China; School of Mechanical Engineering, Zhejiang University, Hangzhou, P. R. China

Zhenhua Huang Department of Mechanical and Energy Engineering, University of North Texas, Denton, TX, United States

Vesna Jaksic Civil Structural and Environmental Engineering Department, Munster Technological University, Cork, Ireland

Saleh Jalbi Department of Sustainability, Civil and Environmental Engineering, University of Surrey, Guildford, London, United Kingdom

Maria James School of Infrastructure, Indian Institute of Technology Bhubaneswar, Odisha, India

Patrick A.B. James Energy & Climate Change Divisions, & Sustainable Energy Research Group, Faculty of Engineering and the Environment, University of Southampton, Southampton, United Kingdom

Sachin Jindal Department of Civil and Environmental Engineering, University of Surrey, Guildford, London, United Kingdom

Alexander Kalmikov Massachusetts Institute of Technology, Cambridge, MA, United States

Madjid Karimirad School of Natural and Built Environment, Queen's University Belfast, Belfast, United Kingdom

Jacqueline Lam Department of Electrical and Electronic Engineering, the University of Hong Kong, Hong Kong, P. R. China; Energy Policy Research Group, the University of Cambridge, Cambridge, United Kingdom

Trevor M. Letcher School of Chemistry, University of KwaZulu-Natal, Durban, South Africa

Victor O.K. Li Department of Electrical and Electronic Engineering, the University of Hong Kong, Hong Kong, P. R. China; Energy Policy Research Group, the University of Cambridge, Cambridge, United Kingdom

Junwei Liu Qingdao University of Technology, P.R. China

Zhenyu Liu State Key Laboratory of Fluid Power and Mechatronic Systems, Zhejiang University, Hangzhou, P. R. China; Engineering Research Center for Design Engineering and Digital Twin of Zhejiang Province, Hangzhou, P. R. China; School of Mechanical Engineering, Zhejiang University, Hangzhou, P. R. China

Domenico Lombardi Department of Geotechnical Engineering, The University of Manchester, United Kingdom

Susana Lopez-Querol University College London, London, United Kingdom

Xi Lu School of Environment and State Key Joint Laboratory of Environment S imulation and Pollution Control, Tsinghua University, Beijing, P. R. China

Lovemore Machiridza Buckinghamshire, United Kingdom

Abdollah Malekjafarian School of Civil Engineering, University College Dublin, Dublin, Ireland

Michael B. McElroy Harvard John A. Paulson School of Engineering and Applied Sciences, Department of Earth and Planetary Sciences, Harvard University, Cambridge, MA, United States

Jorge Mendoza University of Surrey, Guildford, London, United Kingdom

P Mucchielli UCD Centre for Mechanics, Dynamical Systems and Risk Laboratory, School of Mechanical and Materials Engineering, University College Dublin, Dublin, Ireland

Gavin M. Mudd Environmental Engineering, Monash University, Clayton, VIC, Australia

Eduard Muljadi Department of Electrical and Computer Engineering, Samuel Ginn College of Engineering, Auburn University, Auburn, AL, United States

Jimmy Murphy School of Civil Engineering, University College Cork, Cork, Ireland

George Nikitas Department of Geomechanics, University of Surrey, United Kingdom

Michael O'Byrne School of Civil, Structural and Environmental Engineering, Trinity College Dublin, Dublin, Ireland

Ryan O'Connor EDF Renewables North America, Denver, CO, United States

Deirdre O'Donnell Centre for Mechanics, Dynamical Systems and Risk Laboratory, School of Mechanical and Materials Engineering, University College Dublin, Dublin, Ireland

V. Pakrashi UCD Centre for Mechanics, Dynamical Systems and Risk Laboratory, School of Mechanical and Materials Engineering, University College Dublin, Dublin, Ireland; Centre for Mechanics, Dynamical Systems and Risk Laboratory, School of Mechanical and Materials Engineering, University College Dublin, Dublin, Ireland

Vikram Pakrashi School of Mechanical and Materials Engineering, University College Dublin, Dublin, Ireland

Athul Prabhakaran Department of Structural Engineering, University of California, San Diego, CA, United States

Ganga Prakhya Sir Robert McAlpine, London, United Kingdom

Luke J. Prendergast Department of Civil Engineering, Faculty of Engineering, University of Nottingham, Nottingham, United Kingdom

Magdi Ragheb Department of Engineering, University of Illinois at Urbana-Champaign, Urbana, IL, United States

Daniele Ragni Faculty of Aerospace Engineering, FPT Department, Wind Energy Section, Aeroacoustics Research Group, Delft University of Technology, Delft, The Netherlands

Haroon Rashid Department of Civil Engineering, Indian Institute of Technology Bombay, Mumbai, Maharashtra, India

Kieran Ruane Civil Structural and Environmental Engineering Department, Munster Technological University, Cork, Ireland

Rajib Sarkar Department of Civil Engineering, IIT (ISM) Dhanbad, Dhanbad, Jharkhand, India

Franck Schoefs Institut Universitaire Mer et Littoral, Nantes University, Nantes, France

Masoud Shadlou Department of Sustainability, Civil and Environmental Engineering, University of Surrey, Guildford, London, United Kingdom

Shawn Sheng National Renewable Energy Laboratory, Golden, CO, United States

Jing Shi College of Engineering and Applied Science, University of Cincinnati, Cincinnati, OH, United States

Gohar Shoukat Centre for Mechanics, Dynamical Systems and Risk Laboratory, School of Mechanical and Materials Engineering, University College Dublin, Dublin, Ireland

Jianrong Tan State Key Laboratory of Fluid Power and Mechatronic Systems, Zhejiang University, Hangzhou, P. R. China; Engineering Research Center for Design Engineering and Digital Twin of Zhejiang Province, Hangzhou, P. R. China; School of Mechanical Engineering, Zhejiang University, Hangzhou, P. R. China

Claudio Testa CNR-INM INstitute of Marine Engineering, Rome, Italy

Ramon Varghese School of Mechanical and Materials Engineering, University College Dublin, Dublin, Ireland; Centre for Mechanics, Dynamical Systems and Risk Laboratory, School of Mechanical and Materials Engineering, University College Dublin, Dublin, Ireland

Raquel Villena-Ruiz Renewable Energy Research Institute and DIEEAC-ETSII-AB, Universidad de Castilla-La Mancha, Albacete, Castilla-La Mancha, Spain

Lizhong Wang Zhejiang University, P.R. China

Shanshan Wang Department of Electrical and Electronic Engineering, the University of Hong Kong, Hong Kong, P. R. China

Ying Wang Department of Intelligent Construction and Management, Nanjing Tech University, Nanjing, Jiangsu Province, P. R. China

Zhehan Weng Environmental Engineering, Monash University, Clayton, VIC, Australia

Christopher Simon Wright School of Civil Engineering, University College Cork, Cork, Ireland; Gavin and Doherty Geosolutions Ltd., Dublin, Ireland

Danyang Zhu Department of Electrical and Electronic Engineering, the University of Hong Kong, Hong Kong, P. R. China

This page intentionally left blank

Preface

Wind Energy Engineering, 1st Edition (2016) was an outcome of our earlier book, *Future Energy, Improved, Sustainable and Clean Options for Our Planet, 2nd Edition* (Elsevier 2014). It was felt that the wind turbine industry was developing so rapidly that it was now necessary to compile a collection of wind energy−related topics into one volume. In the intervening years since the first edition, there has been an exponential growth in wind turbine deployment and the industry had grown from 154 GW in 2016 to 837 GW by the end of 2021. This growth is the raison d'etre for our updated second edition. Our volume has also grown from 26 chapters to this edition of 35 chapters.

The use of renewable energy sources, such as wind and sun, for electricity generation is becoming commonplace in our society as we move away from fossil fuels to more sustainable forms of energy, free from carbon dioxide production. The move cannot come quickly enough as each month we hear that the previous month was the hottest month since records began and that CO_2 levels are increasing every year and have now passed the 421-ppm level, as measured at Mauna Loa in Hawaii (June 11, 2022); it was 400 ppm in 2016. The CO_2 concentration has increased by more than 50% since preindustrial times when the concentration was 280 ppm and had been at that level for thousands of years.

Our book gives an overall view of wind energy with a special focus on technical issues surrounding wind turbines. The 35 chapters are divided into the following six sections: Introduction; Wind Resource and Wind Energy Worldwide; Wind Turbine Technology; Storing Energy; Environmental Impacts of Wind Energy; Economics of Wind Energy; and Certification Issues. In more detail, the book includes chapters in the following areas:

- scientific aspects (basic theory of wind energy, global potential for producing electricity from wind);
- wind energy in China to give a flavor of developments in a leading wind energy country;
- the history of wind power;
- engineering aspects which include the design of different types of wind turbines, basic technologies and problems, and reliability of wind turbines;
- small-scale turbines and the storing of excess electricity;
- environmental aspects including life-cycle investigation, landscape, and safety issues; and
- economics of wind power generation.

It is hoped that the book will act as a springboard for new developments and perhaps lead to synergistic advances by linking ideas from different chapters. Another way that this book can help in expanding and developing the wind industry is through contact between readers and authors and to this effect e-mail addresses of the authors have been included.

This volume is unique in the genre of books of related interests in that each chapter of *Wind Energy Engineering* has been written by an expert scientist or engineer, working in the field. Authors have been chosen for their expertise in their respective fields and come from 15 countries: Australia, Belgium, China, Denmark, Germany, Hong Kong, India, Ireland, Italy, The Netherlands, South Africa, Spain, Turkey, United Kingdom, and the United States. Most of the authors come from developed countries as most of the research and development in this relatively new field is based in these countries. However, we look forward to the future when new approaches to wind energy, focusing on local conditions in emerging countries, are developed by scientists and engineers working in those countries. Perhaps this new book will aid in this endeavor.

The chapters in this book can be considered as snapshots, taken in 2022, of the state of this rapidly developing industry. *Wind Energy Engineering* goes hand in hand with two other books we have recently published: *Climate Change: Observed Impacts on Planet Earth, 3rd Edition* (Elsevier 2021) and *Storing Energy: With Special Reference to Renewable Energy Sources, 2nd Edition* (Elsevier, 2022).

For consistency and to appeal to an international audience, the International System of Units and Quantities is reflected in the book with the use of the Système International d'Unités (SI) throughout. Other units such as Imperial units are written in parenthesis. The index notation is used to remove any ambiguities; for example, billion and trillion

are written as 10^9 and 10^{12}, respectively. To avoid further ambiguities where possible, the concept of quantity calculus is used. It is based on the equation: physical quantity = number × unit. To give an example: power = 200 W and hence, 200 = power/W. This is of particular importance in the headings of tables and the labeling of graph axes.

A vital concern related to the development and use of renewable and sustainable forms of energy, such as wind, is the question of what can be done when it appears that politicians misunderstand or ignore and corporations overlook the realities of climate change and the importance of renewable energy sources. The solution lies in sound scientific data and education. As educators, we believe that only a sustained grassroots movement to educate citizens, politicians, and corporate leaders of the world has any hope of success. Our book is part of this aim. It gives an insight into the subject which we hope readers will consider and discuss. The book is written, not only for students, teachers, professors, and researchers into renewable energy, but for politicians, government decision-makers, captains of industry, corporate leaders, journalists, editors, and all other interested people.

I wish to thank all 88 authors and coauthors for their cooperation, help, and especially, for writing their chapters. It has been a pleasure working with each and every one of the authors. I also wish to thank the staff of Elsevier, and especially Franchezca Cabural, for their professionalism and help in producing this well-presented volume.

Trevor M. Letcher

Section A

Introduction

This page intentionally left blank

Chapter 1

Why wind energy

Trevor M. Letcher
School of Chemistry, University of KwaZulu-Natal, Durban, South Africa

1.1 Introduction

Wind Energy Engineering: a handbook for onshore and offshore wind turbines, 2nd edition is aimed at giving an overview and an insight into most aspects of wind energy. The industry is rapidly reaching a mature stage and it was felt that the time had come, since the publication of the first edition in 2017, to take stock of the wide-ranging topics linked to the generation of electricity from wind. These topics include: a historical background; the reasons for the interest in wind energy; the fundamental science behind the industry; engineering aspects of building wind turbines, generating electricity, and coupling to the grid, environmental issues; economics; and the future prospects of the industry. Having all these disparate topics in one volume of 37 chapters gives the reader a chance to know the subject and for the specialist, a chance to delve deeper. The latter will be rewarded with copious references to the latest work for further study. This book is an outcome of earlier books we published, entitled *Future Energy: Improved, Sustainable and Clean Options for Our Planet* (Elsevier, 2008, 2014 and 2020), where only one chapter was devoted to wind energy [1].

1.2 Climate change and the growth of the wind turbine industry

Today, with the shadow of global warming and climate change looming over us, there is a need for the energy industry to urgently find energy sources free of carbon dioxide pollution. Energy-related carbon dioxide (CO_2) emissions are the trigger for global warming. These emissions come from electricity production, transport in all its forms, cement and steel making, fertilizer production, and industry in general, to mention a few. It is this anthropogenically derived carbon dioxide that causes an initial global temperature rise which in turn increases the amount of water vapor in the air as a result of evaporation from warmer seas, which leads to a further increase in global temperature. It has been estimated that water vapor contributes 70% to the overall global warming effect with carbon dioxide contributing only 30%. However, it is the concentration of carbon dioxide in the atmosphere that must be reduced if we are to make any headway in our attempt to contain the rising global temperature and the resulting climate change.

The fight against climate change must become an important feature in energy policy-making, but the implications are daunting. The emission goals pledged by countries under the United Nations Framework Convention on Climate Change are laudable but it is still not enough to reach the level of keeping global warming to just 2°C above the preindustrial level by 2035. The outcome of COP26 in Glasgow in November 2021, further highlighted the difficulty in getting a global consensus on tackling global warming. The temperature rise of 2°C was first mooted in 1996 by the environment ministers of the European Council who declared that "global average temperatures should not exceed 2 degrees above the preindustrial level." It took until 2010, when the Cancun Agreement was signed, that the 2°C was enshrined in an international climate policy agreement to "hold the increase in global average temperature below 2°C above preindustrial levels."

The spotlight is on the renewable energy industry to find energy sources free of carbon dioxide pollution. The other options are to reduce our consumption of energy and consequently our standard of living or to capture CO_2 and bury it in caverns or under the sea (capture and storage, CCS). For many reasons, including our natural reticence toward lowering our standard of living, the cost of CCS, the increasing rise in the population of the world, and the aspirations of all to a life with available electricity, it is unlikely that these two options will prevail. To put the problem in perspective, world energy production (this includes transport, electricity, heating, and industrial) reached 173,340 TW in 2019,

Wind Energy Engineering. DOI: https://doi.org/10.1016/B978-0-323-99353-1.00025-6

TABLE 1.1 World Energy consumption, from different forms of energy, in 2019 and 2010 [2].

	2019	2010
	Energy/Terawatt-hours	
Solar	1793	88
Wind	3540	903
Hydro	10,455	8953
Nuclear	6923	7219
Natural gas	39,292	31,606
Oil	53,620	48,050
Coal	43,849	41,999
Biomass	11,111	11,666

upto 12% from 2010 [2]. In 2020, wind energy contributed only 6% of the total. The breakdown of the forms of energy contributing to the total energy consumption in 2019, before COVID, is given in Table 1.1.

Despite dire warnings, there seems to be little international governmental control in reducing fossil fuels. Fossil fuels still account for 79% (coal 25%, oil 31%, and gas 23%) of the world's energy production (Table 1.1). The fossil fuel figure for 2019, is marginally less than the figure for 2010 which was 80% (coal 27.6%, oil 31.6%, and gas 20.8%), so little change has taken place. A small positive sign on the horizon was that over the nine years from 2010, the energy production by renewable forms of energy did grow significantly, albeit from a low base. Hydroelectricity is still the main renewable energy form accounting for 6% of global energy production while wind and solar photovoltaics continued their rapid growth but accounted for around only 3% of global energy production. In 2019, nonfossil sources, including nuclear energy and biomass, accounted for 13.5% of world energy production. Nuclear energy contributed 4% to the global energy production [2].

The figures in Table 1.1 refer to the total global energy production. This energy from these sources (largely fossil fuel, as we have seen above) is used not only to make electricity but to power most forms of transport and turn the wheels of industry. All these activities contribute to increasing the carbon dioxide concentration in the atmosphere. The relative contributions of CO_2 in the atmosphere, in 2020 in the US [3] are given as follows:

- Petroleum 45% (mostly burnt in supplying energy for transport 77% and 16% for industry),
- Gas 36% (largely used to make electricity 38% and in industry 32%),
- Coal 19% (largely used for making electricity).

These CO_2 contributions can be further broken down into [3]:

- Transport 36% (uses 97% petroleum),
- Industry 29% (uses petrol 25%, gas 41% and electricity 28%),
- Residential 20% (uses 64% electricity, 29%gas) and,
- Commercial 16% (70% electricity and 24% gas).

In this book, we will focus our attention on electricity generation from wind energy. In *Future Energy* [1] on page 7, we reported that the production of electricity worldwide in 2016, was responsible for 28% of the global greenhouse gases (GHGs, mainly CO_2 and CH_4). Fossil fuel was responsible for producing 66% of global electricity (coal 40%, gas 22% and oil 4%) (see Table 1.1 of reference) [1]. Wind and solar energy are at the forefront of the drive to significantly reduce the GHGs to meet the 2°C limit. In 2020, wind turbines produced 743 GW of electricity [4] (it was 433 GW in 2015—see reference) [1] and are now slightly below solar photovoltaic in capacity (773 GW in 2020) [5], but this is still a mere drop in the ocean. In 2020, wind and solar energy produced nearly 9% of the global supply of electricity [6]. This represents a significant increase from 5% in 2015 [6]. However, there is much work to be done. Unfortunately, coal is still a significant energy source for generating electricity. The main countries using coal to produce electricity are China, the USA, India, and Australia. In 2020, coal produced 57% of China's electricity (reduced from 72% in 2005) [7] and 19% of the USA's electricity (reduced from 40% in 2012) [8]. Indonesia, Australia, and

Russia are the largest exporters of coal (455, 393, and 217 Mt, respectively) [9]. The main importers of coal in 2020 are China (17.3% of the total global coal imports) Japan (16.8%), India (916.7%), and South Korea (10%) [10].

With well-developed wind and other renewable energy industries, we should not need to consider fracking, exploiting tar sands for oil and gas, or any other environmentally unfriendly fossil fuel mining; we should be working toward a situation where our huge fossil fuel reserves in all its forms are left in the ground. In reality, this will only come about when wind energy and other renewable forms of energy become cheaper and more convenient to use than fossil fuel. With mass production and bigger and more efficient wind turbines, this could become a reality.

Wind and solar photovoltaic power have shown strong growth in recent years; a hopeful sign that global efforts to reduce greenhouse gas emissions is taking off. To illustrate I quote reference [11], "In 2010, solar and wind combined made up only 1.7% of global electricity generation. By 2020, it had climbed to 8.7%—far higher than what had previously been predicted by mainstream energy models. For example, in 2012 the International Energy Agency expected that global solar energy generation would reach 550 TW-h in 2030, but that number was exceeded by 2018."

Wind power, a total of 743 GW in 2020 [12] is growing exponentially. Global wind power expanded by 93 GW in 2020 alone. In spite of this increase, global solar voltaic power has now passed wind power in magnitude and stands at 773 GW [13]. Solar voltaic power is also growing exponentially and in 2020 it increased by 138 GW [13].

The reasons for the exponential growth in both wind and solar voltaic power are due to falling costs and economies of scale; moreover, social attitudes play an important part. This is particularly true for solar voltaic power with neighbors copying neighbors in a socially contagious drive to show green credentials and perhaps also, to reduce the cost of household electricity. Over the past 10 years, the cost of solar photovoltaic electricity has fallen to 85% [11] and over the same time period the costs of both onshore and offshore wind electricity have been cut by about half [11]. Both of these renewable sources are now cost-competitive with fossil fuel electricity [11]. Government support has also played its part in the growth of renewable energy with tax credits, subsidies, competitive auctions, and feed-in-tariffs. In spite of the lukewarm response at COP26 in Glasgow in November 2021, hundreds of countries worldwide have pledged to increase renewable energy and according to reference [11] "more than 600 cities worldwide have 100% renewable energy targets"

1.3 Background

The extraction of kinetic energy from wind and its conversion to useful types of energy is a process that has been used for centuries. It is believed that the first windmills were invented 2000 years ago by the Persians and also by the Chinese and were used to grind corn as well as to lift water. Later, the Dutch developed windmills to drain their land in the fourteenth century and, by the nineteenth century, millions of small windmills were installed in the USA and throughout the world for pumping water (from boreholes) for stock and farm home water needs. The nineteenth century also saw the development of small wind machines (0.2−3 kW producing 32 V, direct current) in rural areas of America to operate appliances. These early developments came to an end when the 1936 Rural Electrification Administration in the US was created and grid electricity was supplied to most rural communities. The generation of grid electricity, using wind turbines, has its origins in the USA in the 1970s. Its development was initiated by the need to replace energy derived from fossil fuels with renewable forms of energy. Of all the renewable forms of energy (wind, solar, geothermal, ocean, and hydroelectric), wind and solar have shown significant positive growth. Over the past 16 years, wind energy capacity has increased from 48 to 743 GW [14] and solar PV from 2.6 to 773 GW [15]. These figures reflect the maximum possible power available and not what was actually delivered.

Wind energy is really a secondary level form of energy, reliant on the sun's uneven heating of the earth's surface, thus creating temperature differentials that create density and pressure differences in the air. The disparity in heating is often a result of the different heat capacities of the material (for example, soil and water) being heated by the sun. This is seen in the daily land and sea breezes in every coastal region. The different reflective nature of the rocks, soil and vegetation, snow and water also play a part. The direction of the wind is partly determined by the rotation of the earth (trade winds) and the topography of the land with winds channeled between mountains and hills with valleys acting as conduits. Taking these issues into account, the tops of hills and mountains, gaps in mountain ranges, and coastal areas are often the best places to harness onshore wind power (see Chapters 3 and 4).

The extraction of wind energy by turbine blades is based on the same principle that gives airplane wings their lift. The wind causes a pocket of low-pressure air on the downside of the blade. This causes the blade to move toward the low pressure causing the rotor to turn. This is known as the *lift*. The force of this lift is much stronger than the force of the wind against the front side of the blade. This is called the *drag*. A combination of lift and drag causes the rotor to spin. This turns the generator and makes electricity. The power generated by a wind turbine is proportional to the cube

of the wind velocity. ($P = av^3$, where P is power, a is a constant, and v is the wind velocity.). Also, the power generated is proportional to the area swept out by the blades making the power a function of the square of blade length ($P = br^2$, where b is a constant and r is the length of the blade), so the bigger the blade the more power can be extracted——hence the drive to make larger and larger wind turbines (see Chapters 3, 4, 8 and 11). Another issue with the placing of wind farms is that the wind offshore is stronger and more constant (daily with land and sea breezes) than it is onshore. Furthermore, most cities are situated in coastal regions and this could mean a reduction in electricity transmission costs if wind farms are situated offshore and near the customer base. These issues make it very likely that the future of wind energy lies in offshore wind farms, even though offshore wind farms cost more to establish than onshore wind farms.

The rapid development of wind turbine technology has been due to the ingenuity of skillful engineers and material scientists. The first serious wind turbines developed for electricity production in the 1970s were rated at about 500 kW; today 8 MW and 10 MW turbines are being erected with plans to design 20 MW turbines. A typical, modern 3 MW wind turbine can produce enough electricity to power 1000 American homes. The largest wind turbine today is the Chinese MySE 16.0−242 model, designed by MingYang Smart Energy; it is rated at 15 MW [16] and has a rotor diameter of 242 m. Seventy of those turbines are equivalent to a typical I GW power station. One of the reasons for the high structure is that the winds are more stable and faster the higher the turbine is from the ground or the sea. The offshore turbines tend to be larger than the onshore turbines. The limit to the size of wind turbines being manufactured and commissioned is at present determined by: the problems in transporting the large blades and pillar components (long, large blades on transport carriers have difficulty in maneuvering round bends in roads and also cannot pass under most motorway bridges); the mechanic strength of the glass fiber blades; the size of the cranes required to erect the turbines; and the cost. A solution to some of these problems is to build the blades and pillars offshore. A similar situation exists for oil rigs.

In spite of wind energy producing only 6% of the world's electricity in 2020 (increased from 4% in 2016), some countries have embraced this technology more than others [17]. In the European Union, wind energy contributes 9% of the electricity production whereas in North America this figure is only 4%. The application of wind energy in producing electricity is fast becoming a major contribution to the energy mix of many countries in Europe. In 2020, wind contributed 16.4% of the electricity in the EU, with the UK producing 24.8% of electricity from wind farms, with over 11% coming from offshore wind farms. In 2020 in Denmark, wind turbines contribute 56% of all electrical production from its 5 GW installed turbine capacity [18]. Denmark has over 6000 wind turbines of which 630 are offshore [19]. It was reported in the news [20] that in Portugal, for four days in 2016, all the electricity used was from renewable sources, and 22% of this came from wind energy. The global capacity of wind energy was 743 GW in 2020 [21] and is largely made up of wind turbines in China (288 GW), the USA (122 GW), Germany 63 GW, India (39 GW), and Spain 27 GW [22]. If the current rate of growth continues, wind energy could supply one-third of all global electricity production by 2030 [22].

1.4 Advantages of wind energy

There are many advantages to using wind turbines to generate electricity and these advantages have been the driving force behind their rapid development.

- *Provision for a clean source of energy*: The almost pollution-free nature of wind energy is one of the compelling reasons for its development. It delivers electricity without producing carbon dioxide. The relatively small amount of greenhouse gas emissions associated with wind turbines are produced in the manufacture and transport of the turbines and blades. It is also free of particulates which are a major problem with coal-fired power stations. Particulates have been blamed for the rise of asthma and possibly Alzheimer's disease in our society so any reduction in these fine particles floating in the atmosphere is a major health advantage. Another atmospheric pollutant that comes with coal or oil-fired power stations is sulfur dioxide, formed from the burning of sulfur impurities. It is this SO_2 that is largely responsible for acid rain and also climate change. Replacing fossil fuel power stations with wind energy and other renewable energy can rid the planet of this dangerous pollutant.

  It is estimated that a 1 MW wind turbine offsets 2360 t (2600 US tons) of CO_2 [23].

- *Sustainability*: Whenever the sun shines and the wind blows, energy can be harnessed and sent to the grid. This makes wind a sustainable source of energy and another good reason to invest in wind farms. Furthermore, with the advent of climate change and global warming (the air molecules are moving faster), there is more energy in the atmosphere and we can expect stronger winds in the future.

- *Location*: Wind turbines can be erected almost anywhere, for example, on existing farms. Very often good windy sites are not in competition with urban development or another land usage; such areas include the tops of mountains or gullies between hills.
- *Compatibility with other land uses*: Wind turbines can be erected on pastureland with little disturbance to the animals and the general farming activities. Other areas such as near landfills sites, the sides of motorways, and major roads, where urban development is unlikely to take place, are ideal locations to consider for wind farms.
- *Reduction of costly transport costs of electricity from far-away power stations*: Transporting alternating current electricity at great distances is expensive because of the cost of the cables and pylons and also because of the loss of power due to the electrical resistance of the cables.
- *National security*: The wind is a free source of energy. Being independent of foreign sources of fuel (e.g., fossil fuel and indeed of electricity) is a great advantage. It means no price hikes over which we have no control and no embargoes on importing fuel or even electricity from foreign countries.
- *Conservation of water*: Traditional power stations using coal, oil, gas or nuclear fuel all use large volumes of water. Wind farms use almost no water. In September 2012, Civil Society Institute of the US published a report, "The Hidden Costs of Electricity: Comparing the Hidden Costs of Power Generation Fuels," and their conclusions were: nuclear uses 2660−4180 L/(MW h) (700−1100 gallons/MW h) in closed-loop systems; Coal uses 1750−2280 L/(MW h) (500−600 gal/MW h) in closed-loop; Biomass uses 152 000−380 000 L/(MW h) (40 000−100 000 gal/MWh) for irrigating crops to burn; Solar uses 855−1976 L/(MW h) (225−520 gal/MW h) (washing photovoltaic panels); and wind uses 170−320 L/(MW h) (45−85 gal/MW h) [24].
- *Reduction of destructive mining*: The pumping of oil and gas (especially from ocean beds) and the mining of coal or uranium all have serious environmental impacts on the sea or land. Wind farms are relatively benign in this respect and farming and other activities can take place around the turbines as the real action is over a hundred meters above the ground or sea. See [25] for the environmental issues with coal mining in Australia.
- *Short commissioning time*: Wind farms can be commissioned over a relatively short time; and two or three years from conception to electricity production is not impossible. This can be compared to the many decades it takes to design, build and commission a nuclear power station [previously 16 and now 27]. The fast rate of growth of the wind energy industry over the past 50 years could well be due to the speed at which wind farms can be commissioned.
- *Cost-effectiveness*: Over the past decade, the cost of turbines has decreased significantly as a result of improved designs and mass production, so today the cost of producing electricity from wind farms is now very competitive with fossil fuel-derived electricity [26]. Together, with the drop in investment costs, there has been a significant increase in the efficiency of turbines through increased hub height and larger rotor blade diameter. The overall cost of wind energy is linked to the energy used in turbine manufacture. Wind energy is capital intensive with 75% of the total cost of energy related to the upfront costs of the manufacturing the turbines foundations, electrical equipment, and grid connections [27]. It has been estimated that the energy used in the production of a turbine is recouped in the seven months of operation and when one considers that the lifespan of a turbine is over 30 years and the energy and financial gains are significant [28].
- *Creation of jobs and local resources*: The wind turbine industry is a rapidly growing industry and employs thousands of workers in the manufacturing processes, transport of turbines, erection of turbines, and in servicing working turbines. Wind Energy projects can be of great help in developing local resources, labor, capital, and even materials. In 2016, the US Energy Department analyzed the future of wind energy and quantified the environmental, social, and economic benefits coming from the wind industry. The industry in the USA currently supports more than 50,000 jobs in services such as manufacturing, installation, and maintenance. Wind energy has become part of the country's clean energy mix. It suggested that by 2050, more than 600,000 wind-related jobs could be supported by the industry [29].
- *Source of income for farmers, ranchers and foresters, and grid operators*:

Land for onshore wind farms is leased to electricity supply companies, making a tidy profit for the landowners who can carry on the normal activity on the land with little interference from the turbines. Lease times of between 25 and 50 years are common. The UK Government has suggested that for a 2.5 M turbine, costing £3.3×10^6, the payback time was between 1 and 5 years, allowing plenty of time for a good return on the investment [30,31].

- *Rapid Instigation of power*: National grids supply a steady level of electricity (the base load) to meet the needs of a country. If, for some reason, the supply of electricity needs to be suddenly increased, it is not always possible as it can take days to start up a new power station. If the wind is blowing or if the wind energy has been stored then the supply can take just minutes to feed into the National grid.

- *Diversification of power supply*: With our total reliance on electricity, it is well worth diversifying our energy sources so that we are not reliant on one type of energy, be it fossil fuel (which is at the mercy of foreign governments which can raise prices suddenly as was done in the 1970s), nuclear (again we are at the mercy of countries supplying uranium), or solar (the sun does not always shine).
- *Stability of cost of electricity*: Once the wind farm is in place the cost of the electricity to customers should be stable. It is not a function of the price of imported fuels [31].
- *International Cooperation*: It has been found that in many instances there is a clear relationship between a manufacturer's success in its home country market and its eventual success in the global wind power market. Lewis and Wiser recently wrote, "Government policies that support a sizable, stable market for wind power, in conjunction with policies that specifically provide incentives for wind power technology to be manufactured locally, are most likely to result in the establishment of an internationally competitive wind industry" [32]. This comment written 10 years ago could well have been written even today and illustrates the importance and success of international cooperation.

1.5 Challenges facing the wind turbine industry

There are of course a number of challenges associated with harnessing the power of the wind.

- *The Intermittency of wind*: Wind is unpredictable and this is perhaps the most important of all the problems associated with electricity production from wind farms. The wind may not be blowing when the electricity from a wind farm is required. Furthermore, when the wind is blowing and electricity is being produced, it is possible that the energy is not required. The solution is to store the electricity when it is not required and use the stored electricity in times of need. This can be done in a number of ways: batteries, pumped water storage, pumped air or methane into caverns, and even driving trains uphills [33].
- *Good sites are often in remote locations*: The best windy sites are often in hilly, mountainous regions away from urban areas. This does mean that the electricity produced onshore has to be transported along expensive high voltage cables to reach customers.
- *Noise pollution*: The noise from a rotating wind turbine falls off exponentially with distance from the tower, and at 500 m the sound level is less than 35 dB which is not substantial when the normal conversation is rated at 60 dB [34].
- *Esthetics*: While some people deplore the sight of wind turbines, others look upon them as pleasing and useful structures. Over the past century, we have got used to massive pylons marching across our countryside, carrying high voltage lines. Surely wind turbines are better looking than that! There have been thoughts of painting wind turbines to fit in with the landscape (see Chapter 31).
- *Turbine blades can damage wildlife*: There is much evidence that birds and bats are being killed by the turning blades of wind turbines. However, the impact on these populations is negligible compared to the large number of bird deaths caused by household cats, car windscreens, or sparrow hawks, it is reported that collisions with turbine blades result in 33,000 bird deaths while cats are responsible for 100 to 200 million each year in the US. It has been reported that the modern huge-bladed slow-turning turbines are responsible for far fewer bird deaths than the faster-turning turbines [35,36].
- *Safety*: The major safety hazard associated with turbines, once they are in place, is the possibility of a blade coming adrift, which could cause serious harm to people or animals nearby. Furthermore, a buckled blade could cause a collapse of the tower and that too could cause serious damage. Wind turbines should be erected away from human habitation.
- *Frequency of light and shadows*: It has been reported that the frequency and strobe effect of turning blades could affect the human brain. Wind turbines produce a shadow flicker by the interruption of sunlight by the turbine blades. Research work has shown this flicker can cause epilepsy in certain patients [37]. It was found that the proportion of patients affected by viewing wind turbines, expressed as a distance in multiples of the hub height of the turbine, showed that seizure risk does not decrease significantly until the distance exceeds 100 times the hub height. The results show that the flash frequency is the critical factor and should be kept to a maximum of three per second, i.e., sixty revolutions per minute for a three-bladed turbine. Furthermore, on wind farms, the shadows cast by one turbine on another should not be viewable by the public if the cumulative flash rate exceeds three per second. If possible, turbine blades should not be reflective [37]. Wind turbines are designed to operate over a given range of wind speeds and this is usually between 4 and 15 m/s (between 10 and 40 miles per hour). The speed of the rotating blade

can be controlled and slow rotating turbines could be made turbines less of a problem for epilepsy sufferers and for other problems that are a danger to birds and bats.

- *New and unfamiliar technology*: Wind turbines and their accompanying generators can be considered new technology and are often unfamiliar to most general engineers. This can be a problem if a turbine malfunctions in a rural area. The infrastructure and training of staff to support and maintain turbines must accompany the commissioning of new turbines. However, it is reported that wind turbines require less maintenance than many other electricity-producing equipments [38].
- *Shortage of the Rare Earth Element, Neodymium, needed to Manufacture Turbine Magnets*: Modern turbines require special permanent magnets and these are made from an alloy that contains the rare earth element neodymium (Nd). A 3 MW turbine needs a 2.7 kg magnet made from neodymium, iron, and boron (NdFeB). These are permanent magnets and are very much stronger than iron magnets. It is necessary to have such strong magnets in order to generate electricity at the slow speeds that wind turbines operate at. It is a case of "the stronger the magnet the more the electrons move." The supply of neodymium and other rare Earth metals has been dominated by China but this is slowly changing with the reopening of mines in the US.
- *Initial Cost*: The initial cost of setting up a wind farm is perhaps the most serious drawback. It is for this reason that many governments throughout the world still offer subsidies. This is however outweighed by the rewards over the lifetime of the turbine, both financially and environmentally (see Chapter 25) [39]. In the USA, most of the commercial-scale turbines installed today are 2 MW in size and cost roughly $3−$4 million installed [40].

1.6 The potential of wind energy worldwide

The potential for wind energy is enormous, especially in developing countries. This is particularly true in rural communities which are not yet linked to grid electricity. For these regions, it is an economically viable alternative to diesel engines and even coal-fired power stations [41]. Developing countries with their often, obsolete energy supply structures should be investing in this new and proven energy industry which is fast reaching market maturity. In many cases, it would save on buying fuel from other countries, and instead they could enjoy the luxury of free fuel in the form of wind. One issue we must not overlook is the linking of wind turbine farms and national grids. This has been part of the success story of the wind industry. The next major advancement could well be more effective energy storage for times when the wind is blowing and electricity is not required.

Even in developed and industrialized countries, wind is becoming a major player. To put it in perspective, on Sunday at about 2 pm on 15 May, in 2016, over 95% of Germany's electricity was supplied by renewable energy (36% by wind, 45.2% by solar energy, and the rest by hydro and biomass) [42]. That could not have been envisaged 40 years ago. The Norwegian island of Samsø is showing the way for rural communities. It has a population of 4000 and is totally dependent on wind energy for all its electricity. The 21 wind turbines, most of which are part-owned by the islanders, supply the island with almost 30×10^6 kWh of energy and on top of that 80 $\times 10^6$ kWh is sold to the national grid. In 2020 in Denmark, 48% of the electricity produced was from wind power [43]. This stems from a decision in 1985 to abandon nuclear power and invest in renewable energy. This initiated the beginning of the Danish domination of turbine manufacturers in Europe. For many developed countries, the incentive to invest heavily in wind energy has been dictated by the need to reduce CO_2 emissions. However, today, with the competitive price of wind energy [26], the rising cost of fossil fuel exploration, and the political drive to close coal-fired power stations, the future looks very bright for the wind turbine industry.

References

[1] Letcher TM. In: Letcher TM, editor. Future Energy: Improved, Sustainable and Clean Options for Our Planet. 3rd ed. London: Elsevier; 2020.
[2] https://ourworldindata.org/energy-production-consumption.
[3] https://www.eia.gov/energyexplained/energy-and-the-environment/where-greenhouse-gases-come-from.php.
[4] https://gwec.net/global-wind-report-2021.
[5] https://www.iea.org/reports/renewables-2021/executive-summary.
[6] https://ember-climate.org/commentary/2021/07/08/top-15-wind-and-solar-power-countries-in-2020/#:~:text = Ember's%20recent%20Global%20Electricity.TWh)%20of%20the%20world%20electricity.
[7] https://www.cnbc.com/2021/04/29/climate-china-has-no-other-choice-but-to-rely-on-coal-power-for-now.html.
[8] https://www.eia.gov/energyexplained/electricity/electricity-in-the-us.php#:~:text = Coal%20was%20the%20third%2Dlargest.in%202020%E2%80%94about%2019%25.
[9] https://www.statista.com/statistics/270952/global-hard-coal-exports-2009.

[10] https://www.worldstopexports.com/coal-imports-by-country/.
[11] https://www.wri.org/insights/growth-renewable-energy-sector-explained.
[12] https://gwec.net/global-wind-report-2021/#:~:text = 2020%20was%20the%20best%20year,achieves%20net%20zero%20by%202050.
[13] https://www.statista.com/statistics/280220/global-cumulative-installed-solar-pv-capacity/#:~:text = Global%20cumulative%20solar%20photovoltaic%20capacity,installed%20in%20that%20same%20year.
[14] https://gwec.net/global-wind-report-2021/#:~:text = Today%2C%20there%20is%20now%20743.carbon%20emissions%20of%20South%20America.
[15] https://www.iea.org/reports/renewables-2020/solar-pv.
[16] https://www.nesfircroft.com/blog/2021/12/the-biggest-wind-turbines-in-the-world#:~:text = MingYang%20Smart%20Energy%2C%20a%20Chinese.%2Dsquare%2Dmeter%20swept%20area.
[17] https://yearbook.enerdata.net/renewables/wind-solar-share-electricity-production.html.
[18] https://www.statista.com/statistics/990723/number-of-active-wind-power-turbines-in-denmark/#:~:text = Wind%20power%20production&text = In%202019%2C%2016.1%20terawatt%20hours,945%20gigawatt%20hours%20were%20produced.
[19] https://www.statista.com/statistics/990723/number-of-active-wind-power-turbines-in-denmark/.
[20] https://www.theguardian.com/environment/2016/may/18/portugal-runs-for-four-days-straight-on-renewable-energy-alone?CMP = share_btn_fb.
[21] https://yearbook.enerdata.net/renewables/wind-solar-share-electricity-production.html.
[22] https://www.nsenergybusiness.com/features/top-countries-wind-energy-capacity.
[23] https://yaleclimateconnections.org/2021/06/whats-the-carbon-footprint-of-a-wind-turbine/.
[24] Keith G, Jackson S, Napoleon A, Comings T, Ramey JA, Synapse Report, 12 September 2012. Cambridge, MA. <http://www.synapse-energy.com>.
[25] http://www.ewea.org/wind-energy-basics/faq/.
[26] http://www.eia.gov/forecasts/aeo/assumptions/pdf/table_8.2.pdf.
[27] The Economics of Wind Energy, by the European Wind Energy, editor S Krohn; March 2009. <http://www.ewea.org/fileadmin/files/library/publications/./Economics_of_Wind_Energy.p>.
[28] Duggy A, Rogers M, Ayompe L. Renewable energy and energy efficiency: assessment of projects and policies. Chichester: Wiley Blackwell; 2015.
[29] http://energy.gov/eere/articles/wind-energy-supporting-600000-jobs-2050.
[30] https://www.wind-watch.org/documents/five-questions-to-ask-before-signing-a-wind-energy-lease/.
[31] http://www.local.gov.uk/home/-/journal_content/56/10180/3510194/ARTICLE.
[32] Lewis JI, Wise RH. Fostering a renewable energy technology industry. Energy Policy 2007;35(3):1844−2857.
[33] Storing energy: with special reference to renewable energy sources. ed. T. M. Letcher, New York: Elsevier, 25 chapters, 565 pp., ISBN: 978-0-128-03440-8; 2016.
[34] http://ramblingsdc.net/wtnoise.html.
[35] https://www1.eere.energy.gov/wind/pdfs/birds_and_bats_fact_sheet.pdf.
[36] http://savetheeaglesinternational.org/new/us-windfarms-kill-10-20-times-more-than-previously-thought.html.
[37] Harding G, Harding P, Wilkins A. Wind turbines, flicker, photosensitive epilepsy. Epilepsea 2008;49:1095−8.
[38] http://www.windmeasurementinternational.com/wind-turbines/om-turbines.php.
[39] https://www.renewablesfirst.co.uk/windpower/windpower-learning-centre/how-much-does-a-farm-wind-turbine-small-wind-farm-turbine-cost/.
[40] http://www.windustry.org/how_much_do_wind_turbines_cost.
[41] http://www.altenergy.org/Glossary/intro.html.
[42] http://www.sciencealert.com/last-sunday-95-percent-of-germany-s-energy-was-provided-.
[43] https://www.iea.org/countries/denmark.

Chapter 2

History of harnessing wind power

Magdi Ragheb
Department of Engineering, University of Illinois at Urbana-Champaign, Urbana, IL, United States

> There is nothing new under the sun but there are lots of old things we do not know.
>
> Ambrose Bierce, USA journalist, satirist

2.1 Introduction

President Abraham Lincoln, in the "Discoveries and Inventions" 1860 lecture, *New York Times*, November 22, 1936, is quoted as:

> Of all the forces of nature, I should think the wind contains the largest amount of motive power ... Take any given space of the Earth's surface, for instance, Illinois, and all the power exerted by all the men, beasts, running water and steam over and upon it shall not equal the 100th part of what is exerted by the blowing of the wind over and upon the same place. And yet it has not, so far in the world's history, become properly valued as motive power. It is applied extensively and advantageously to sail vessels in navigation. Add to this a few windmills and pumps and you have about all. As yet the wind is an untamed, unharnessed force, and quite possibly one of the greatest discoveries hereafter to be made will be the taming and harnessing of it.

Wind power has been used since early history by mariners for sailing boats on rivers and lakes and then ships at sea. Since the early recorded history, it has been used by successive cultures and civilizations. It is a fascinating field of study and captivates the interest of passionate creative and romantic people. Its future success depends on setting its footing on solid and realistic science, engineering and economics; and avoiding unrealistic dreams of perpetual motion machines and unrealistic romanticism. Compared with modern machines powered by fossil fuels, wind machines depend on the wind as a fuel. Unfortunately, the wind is intermittent, unreliable, unsteady, and unpredictable and in some places on Earth, it does not even blow at all. Yet, the advantage of the wind as a source of energy is that it is not just renewable, but infinite in magnitude originating in the Sun's fusion energy that is trapped in the Earth's atmosphere.

Windmills and water-driven mills were the only power generators for over 1200 years predating the 18th century's Industrial Revolution. They existed in antiquity in Egypt, Persia, Mesopotamia, and China. In the 7th century BCE, king Hammurabi of Babylon implemented a plan to irrigate the fertile plains of the Euphrates and Tigris Rivers using vertical-axis wind machines [1].

Wind energy conversion has been reinvented many times in human history and is undergoing a new process of reengineering as the leading mechanically based renewable energy source. It is challenging conventional energy sources into becoming a viable alternatives to them. As fossil fuels are experiencing localized as well as global availability problems and peaking in their production and concerns about pollution and greenhouse-gas emissions are getting highlighted, wind machines and generators are reclaiming with new materials, electronic controls, and advanced technology, an important share of the energy production field (Fig. 2.1).

The word "windmill" primarily refers to a wind-powered machine that grinds or mills grain such as wheat or corn and turns it into flour for bread making. This has been the most common function in addition to numerous other applications such as grinding of spices, lumber sawing, mines ventilation, iron and copper foundries power, gun-powder manufacturing, oil extraction from oil seeds, nuts and grains, converting old rags into paper, grinding colored powders into dyes, manufacturing snuff tobacco, and water pumping in Europe in the pre-Industrial Revolution era, and even lopping bee hives into towns under siege during warfare.

Wind Energy Engineering. DOI: https://doi.org/10.1016/B978-0-323-99353-1.00017-7

FIGURE 2.1 Modern wind turbines are replacing the iconic old American wind turbine technology on the American High Plains. *Photo: M. Ragheb.*

Holland has used windmills since CE 1350 to drain marshes and shallow lakes and turn them into productive agricultural land. They were coupled to an Archimedean screw, Egyptian noria, or Persian water wheel; all of them are early pump concepts that could elevate water to a height of 5 m. The noria's etymology comes from the Arabic: "Al Naoura" which literally means: "The wailing"; this is so-called because of the wailing sound it generates as it rotates. The "noria," is basically a water wheel that lifts water into an aqueduct carrying water to cities and fields using the flow energy of a water stream, similar to the modern hydraulic ram. It has a function similar to the chain pumps of which the "saqiya," literally "irrigator" in Arabic, which dates back to Babylonian (700 BCE) and Pharaonic (4000 BCE) times, is an example. Noria machines were in widespread use in the premedieval Islamic civilization before their evolution into the European windmills, and specimens are still in operation in some parts of the world today. Their introduction may have originated from Spain where Ibn Bassal (CE 1038−75) of Al Andalus (Andalusia) pioneered the use of a flywheel mechanism in the noria and saqiya to smooth out the delivery of power from the driving device to the driven machine [1].

Windmills were replaced by steam and internal combustion engines using fossil fuels ranging from coal to oil and natural gas as well as hydroelectric and nuclear energy. Nowadays wind turbines are primarily used in electrical power generation. The terminology "wind generators" becomes a more appropriate designation. Wind power has evolved from impulse or drag-driven heavy systems to light aerodynamic systems. The latter is not a modern concept, as it has been known to the ancient sailors and mariners and was applied to the development of sail windmills.

2.2 Wind machines in antiquity

Out of respect for the wind's capability of destructiveness in tornadoes, hurricanes, typhoons, and storms, legends arose that the winds were imprisoned underground within the Earth and were released at the whim of a beneficent or malevolent deity. In ancient Greece, the god Aeolus was the ruler of the winds. Many primitive people thought that the wind could be controlled by magic. Control over the wind resources was reserved for the Royals in some societies, and later for the clergy [1].

In early Christianity, it was thought that the wind was God breathing to punish or reward the Earthly mortals. Mariners for centuries had legends dealing with their fears and superstitions about the wind. As early as 4000 BCE, ancient Egyptian pottery depicts ships with square sails using the prevailing northerly wind to sail up the Nile River from north to the south against its current. During the ancient Egyptian Fifth Dynasty around 2500 BCE, sailing ships advanced enough to go to sea and made trading trips along the East Coast of Africa to the land of Bunt. A relief on the walls of the Deir Al Bahari Queen Hatshepsut's temple in Luxor, Egypt, shows the sailboats sent on a trading and exploration expedition around the East coast of Africa. They sailed through an ancient canal dug to connect the Nile River to the Red Sea (Fig. 2.2). By 150 BCE an account by Hero of Alexandria, Egypt in his *Spiritalia seu Pneumatica* describes a pneumatic application of a four-bladed wheel driven by the wind moving the piston of an air pump to blow the pipes of a musical organ with compressed air. A prayer wheel was used in Asia around CE 400 whose scoops caught the wind and rotated on a vertical shaft.

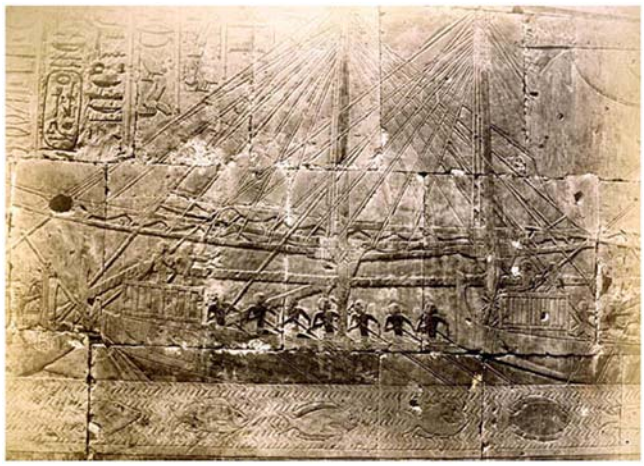

FIGURE 2.2 Relief of dual sail and rowing boats on the walls of the Deir Al Bahari's Queen Hatshepsut's temple in Luxor, Egypt, commemorating a trading expedition to the land of Bunt around the Eastern Coast of Africa.

FIGURE 2.3 Remaining vestiges of ancient vertical-axis windmills or "Panemones" at Seistan, near the border between Iran and Afghanistan. The rotors were made from cloth or bundles of reeds and wood.

2.3 Islamic civilization windmills

Around 200−100 BCE windmills with woven reed sails were used in the Middle Eastern region for grinding grain. The first documented invention of a real windmill occurred in the year CE 644 during the rule of the second Islamic Caliph: Omar Ibn Al Khattab. A subject of Persian heritage, who proposed to him that he is able to build one, was commissioned by the Caliph Omar Ibn Al Khattab to build a grain mill rotated by the wind.

The next written account comes from two Islamic geographers who tell of windmills built in the sandy and windy province of Seistan in present-day Iran around CE 947. The first application had to do with drifting sand dunes which could bury whole villages and cities. To control the sand drifts, the people of Seistan ingenuously enclosed the sand drift or dune in a structure of timber and thorny bushes higher than the dune. In the lower part, they opened a door for the wind to enter and blow away the upper levels of sand in a vortex or tornado carrying the sand to be deposited evenly on the surrounding fields [1].

The Islamic geographer Ali Al Massoudi wrote about Seistan in CE 947: "Wind turns mills which pump water from wells to irrigate the gardens. There is no place on Earth where people make more use of the wind." Another Islamic scholar, Al Qazwini in CE 1283, described how the people of Seistan used the wind to grind their wheat, as well as to control the drifting sand and to pump water. From that perspective, the region of Seistan can be considered the birthplace of the eastern vertical-axis windmill in Islamic times (Fig. 2.3).

The Syrian cosmographer Al Damashqi (The Damascan) in CE 1300 described these vertical-axis windmills in detail. They were erected in high places on top of hills, a mosque minaret or a tower in a castle. They were built as two-storied structures. The mill that turned and ground the grain into flour was in the upper story. The lower part contained the mill that was rotated by the blowing wind. The wheel turned one of two millstones in the upper section. Four slits existed in the walls of the first story with the outer part wider than the inner part. This formed ducts through which

the wind blew from any direction. The ducted wind hit a reel with 6−12 cloth-covered arms rotating it. The reel moved the millstone that ground the grain. Other vertical windmills were used around the same time period in Afghanistan. They were driven by the prevalent north wind. A series of shutters and shields controlled the wind inlet [1].

Used originally in Persia and Afghanistan, windmills spread throughout the Islamic World and the Far East grinding grain and pumping water. They were adapted to crushing sugarcane for the manufacture of molasses and the extraction of sugar in Egypt. Centuries later, in the West Indies and the Caribbean Region, the West Indians hired Egyptian millwrights to establish the first sugar plantations. As Genghis Khan invaded Persia in the 12th century, the millwrights were induced to travel to China where bamboo horizontal mills with sails of matting adapted from Chinese sailing boat designs became common in the open fields. Superstition apparently suppresses their use today.

2.4 Medieval European windmills

The concept of the windmill first spread to Europe through the Islamic culture established in Morocco, at that time period referred to as Andalusia, to contemporary Portugal and Spain, by traders and merchants (Fig. 2.4). Another entry was through the trade routes through Russia and Scandinavia. A third route is attributed to the returning crusaders to Europe from the Middle East. A fourth way was through the Islamic Sicily into Italy.

The historian Mabillon in CE 1105 writes that a convent in France was allowed to construct watermills and windmills. Windmills according to him were becoming common in Italy in the 12th century. Questions aroused about whether the tithes for them belonged to the clergy. The controversy was decided in favor of the Church by Pope Celestine III. Mabillon recounts a story about an abbey in Northamptonshire, England in CE 1143 that was in a wooded area that was denuded over a period of 189 years: "That in the whole neighborhood there was no house, wind or water mill built for which timber was not taken from this wood." As wood was depleted for windmills construction, coal was used as a replacement energy source as a harbinger of the steam engine and a source in the Industrial Revolution [1].

The first record of a windmill built in England was in Bury St. Edmunds in 1191. It was built in defiance of the then-vested authority and later destroyed by the Abbot. By the 14th century, the British monarchs watched the victories and defeats of their battling armies from the safety and high ground of the top of windmills scattered on the hills. A windmill was erected in Cologne, Germany in CE 1222. A windmill appeared in Siena Italy in CE 1237. Count Floris V in Holland granted the burghers of Haarlem the right to pay 6 shillings in tax for a windmill and 3 shillings for a horse mill in 1274.

In the 12−15th centuries, the construction of windmills spread throughout central Europe all the way to Scandinavia reaching Finland in CE 1400. Windmills became the prime power movers all over Europe for grinding grain, pumping water, paper making, pressing oil from oil seeds, and sawing wood for ships and home construction. The Dutch drainage mill was developed in Holland maintaining the land reclaimed from the sea, marshes, or shallow lakes. The

FIGURE 2.4 Los Molinos at Consuegra, 77 km (48 miles) south of Madrid on the plains of Castilla-La Mancha, Spain. Windmills were so common by the end of the 16th century that the author Miguel de Cervantes recounts windmills and the encounter of his hero Don Quixote with them in La Mancha; which originally was an Arabic word meaning "dry, waterless land." The wind flour mills were on the River Ebro and Don Quixote in his delusion mistook them as giants and charged them with his horse Rocinante and his squire Sancho Panza [1].

Cistercian monks in France had introduced such a type of windmill to drain the lakes of their region. Peat was being mined for the fuel needed by emerging cities, and this formed shallow lakes which grew in size over time and required systematic drainage by the 1300s. The first Dutch marsh mills were started in the 1400s. By the 1600s, there were 2000 of them operating to drain 0.8×10^6 ha (2 million acres) of land in Holland.

2.5 Aegean and Mediterranean windmills

The windmills on the island of Crete, the Aegean Islands as well as in Portugal and Spain were tower mills. The post mill which evolved into the tower mill was never observed in the Aegean area. Jib or triangular sails were typically used in the Iberian Peninsula and the Mediterranean. Their similarity to sailing ships is noticeable. They used 6−12 triangular cloth sails that were put up or down through roller reefing or by rolling them around the sail support. They were situated at the center of the mill or sheeted at mid-ship (Fig. 2.5).

The Aegean Islands windmills were small compared with the European windmills with a size of 4−12 m in diameter. The Dutch polder or scoop windmill measured about 29 m in diameter. They were placed four to twelve in a row. Being efficient and well suited to the local conditions, they survived long after their use as wind power usage declined elsewhere.

Polders are low-lying tracts of land-forming hydrological entities that are surrounded by dikes or embankments. These are usually land reclaimed from a body of water such as an ocean shore or a shallow lake. They exist usually below sea level at river deltas, coastal areas, and fenlands and require constant drainage by opening sluices at low tide, by windmills in the past and pumps at present. The city of New Orleans in the United States is considered a polder area, seriously affected by flooding from hurricanes.

The earliest windmill structures were developed in the Middle East at the time of the Islamic Civilization and spread along the Mediterranean coast and in Persia around CE 500−900. Windmill technology was partly transferred to Medieval Europe by the returning crusaders in the 12th century. It developed there as the horizontal-axis design with tall structures on which the sails turned at a right angle to the ground.

Vertical-axis windmills are still being built in different parts of the world by enterprising farmers for irrigation and drainage purposes. A conventional aerodynamic sail and a Chinese impulse sail vertical-axis designs were built and used. An early description of a Chinese windmill was around CE 1219 by Yeh Lu Chu Tshai, a Chinese statesperson. Vertical-axis windmills using drag or impulse rather than cloth sails were built in Nebraska, United States around 1898 (Fig. 2.6).

Vertical-axis windmills have the advantage of a simple design consisting of six or more sails that are set upright upon horizontal arms resting on a tower or in the open, and which are attached to a vertical shaft positioned at the center. The sails are set in a fixed position that is oblique to the direction in which the wind will hit them. Their operation is independent of the direction from which the wind blows. The disadvantage of the vertical-axis design is that it may not be self-starting, and only one or two of the sails would catch the wind at any given time. The part of the sail catching the wind must then expend energy moving the dead weight of the part that is not catching it unless a shield configuration is adopted. Thus vertical-axis windmills are considered less efficient than horizontal-axis windmills where the force of the blowing wind is evenly distributed on all sails [1].

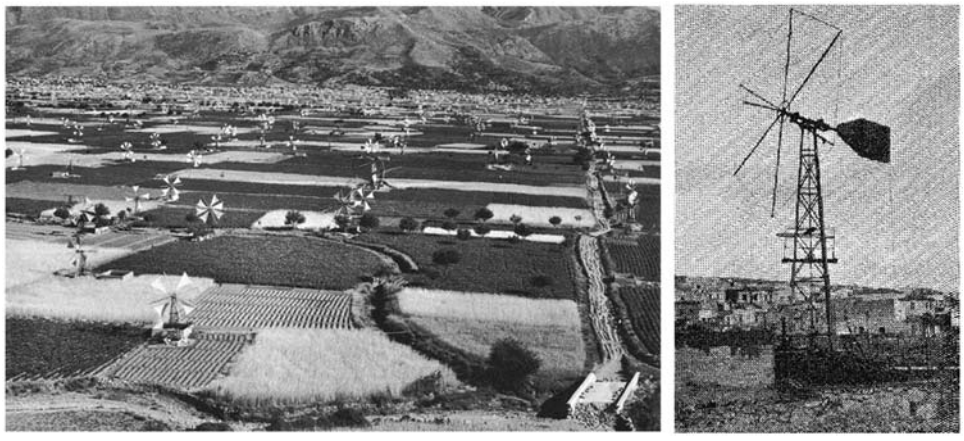

FIGURE 2.5 Sail water-pumping windmills harvesting the wind in large numbers on the island of Crete in the Mediterranean Sea.

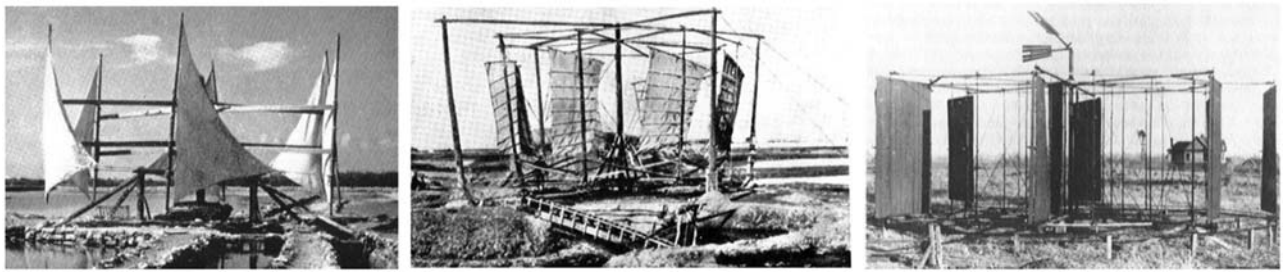

FIGURE 2.6 Conventional-sail vertical-axis wind irrigation turbine, using aerodynamic sails (*top*). Chinese-sail vertical-axis wind irrigation machine using impulse or drag sails (*center*). Merry-go-round drag-sails water-pumping mill at Lincoln, Nebraska, United States, 1898 (*bottom*).

FIGURE 2.7 Evolution of Dutch windmill designs: rotating cage post windmill with rotating lever wheel in the back and pegged wheel acted as a yaw mechanism to rotate the windmill to face the wind (*left*), tower design (Funenkade Olen windmill, Amsterdam, Holland) (*center*), and rotating-roof smock design for pumping drainage water (*right*).

2.6 Dutch and European windmills

European windmills were custom designed and built with the particular site and wind conditions taken into consideration. They were of primary importance in the life of rural Europe, grinding grain for flour and pumping water, so they were installed before other structures were erected in European villages. Being erected on high ground to catch the wind from all directions, they were major landmarks seen from long distances by travelers.

The horizontal-axis machines were considered to possess a higher efficiency than the vertical-axis types; hence they were widely adopted in Europe. The villagers personalized them and gave them individual names, much like boats today. The miller, doubling as a wind wright, commanded high authority, wealth, power, and respect in the village hierarchy. He usually charged the farmers a fraction of the grain being milled for his service. This was supplemented by the flour dust accumulated on different parts of the windmill that he collected as a bonus. Being the richest man in town made him prominent politically. The miller's profession was a hazardous one, particularly under stormy wind conditions. It required great skill and bodily strength climbing up the structure unfurling the sails for wind operation, or furling them to prevent the windmill arms from running away, damaging or destroying the windmill structure under wind gale conditions. With wooden windmills, the danger of fire was prominent through friction [1].

There evolved three types of European windmills (Fig. 2.7):

1. *Post design*: The post design refers to a massive upright post around which the entire body of the mill rotates in the direction of the blowing wind and was first described in CE 1270. The body of the mill supported the sails and the equipment. These designs were constructed out of wood. They used wood cogs and ring gears to transmit the rotor blades' rotation to a horizontal grindstone.

2. *Tower design*: This is also often referred to as the Dutch Mill. It was developed in the 14−15th centuries starting around 1390. The tower mill was installed on top of a tower of several stories. The construction material is brick with a wooden roof. It differs from the post mill in that instead of the whole windmill rotating around a central post, only its top or cap rotated to position or yawed the rotor blades to catch the wind. It formed an integral system for grain grinding and storage as well as the living quarters of the wind wright or wind smith and his family in the first story. The windmill needed continuous undivided attention while it was running, particularly under stormy conditions where the wind wright had to furl the sail on the blades and brake the mill to a stop. A runaway windmill is a hazardous situation that if uncontrolled, would disintegrate the whole structure launching flying debris into neighboring structures; a hazard that exists in modern wind turbines. The post and the tower windmills had to be yawed manually to face the wind using a large wheeled lever at the back of the windmill. A lateral fan was added later to automate the yaw orientation of the mill into the prevailing wind direction.
3. *Smock design*: The smock design differs from the tower windmill in the construction materials used. The smock design has a stone base with a wooden upper section that is framed with weatherboarding that is either tarred or painted. The name "smock" originates from the way these windmills' appearance looks like the linen smocks worn at the time in Holland and Europe [1].

2.7 The American windmill

This multiblade design appeared in Europe in the 17th century. Leupold Jacob from Leipzig in 1724 in a book: *Journal of Hydraulic Arts*, or in German: *Schauplatz der Wasser Künste*, introduced an eight-bladed self-regulating wind turbine that drove a single action piston water pump using a crankshaft and a tie rod. In an ingenious design, each blade was capable of pivoting around its own axis maintained by a spring system that is progressively extended in a high wind condition resulting in the rotor revolving in a gale no faster than in a moderate wind, avoiding the destructive situation of a runaway wind turbine (Fig. 2.8).

This design did not spread on the European continent, but rather on the American Great Plains. Starting in 1870, as a simple, economic, and a most successful design, it conquered the American continent and migrated back to Europe and the rest of the world where it was named: "The American Windmill." The most common windmill in America was built in the 19th century as a vertical steel structure topped with a rotating multibladed drag or impulse propeller that caught the wind. Its rotational motion is converted into linear motion that pumped water and stored it in a water tank for irrigation, cattle drinking, and water supply to steam locomotives.

The American Windmills were simple in construction and standardized in design. They could be easily dismantled and moved to other locations for reassembly. Their maintenance was simple amounting to the addition of lubrication oil to the geared components, with parts that are interchangeable and could be cannibalized from one machine to another.

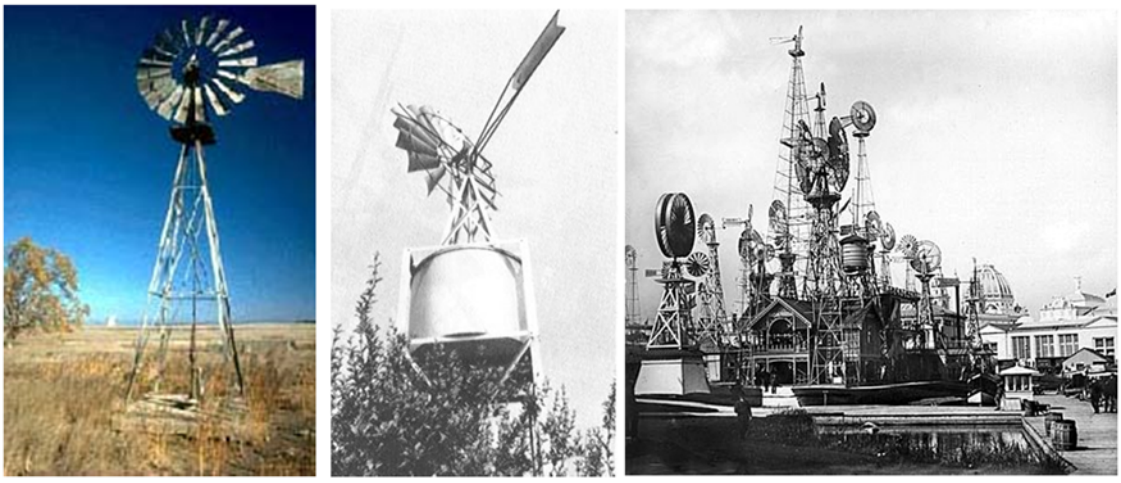

FIGURE 2.8 American water-pumping windmill used a ground water storage tank for cattle drinking (*left*). American water-pumping windmill with a tower water storage tank to feed gardens or steam locomotives. This is an example of a gravity pumped energy storage system (*center*). American Windmill versions competition at "The World Columbian Exposition," Chicago, USA in 1893, as a commemoration of Christopher Columbus arrival to the New World 100 years earlier (*right*).

The standardization led to the spread of the American Windmills in many altered versions in the American West as well as all over the world.

Early on, wooden slats were nailed to rims with tail rudders for an orientation toward the wind or yawing. Instead of using a rudder, some designs used weather vanes operating downwind from the tower. Speed control was provided by spring and weight mechanisms and by feathering the blades to reduce the thrust in high winds. Around 1870, galvanized steel blades replaced the wooden slats allowing high-speed operation that needed a reduction gearbox to operate the reciprocal water pump at its required low speed [1].

The Halladay design introduced in 1854 evolved into the Aermotor and Dempster designs that became operational in different parts of the world. Starting in 1850, about 6 million small turbines of 750 W (one Imperial horsepower) power or less were installed in the United States, primarily for water pumping for cattle and farm needs. Larger windmills with rotor diameters of up to 18 m diameter provided water for the steam boilers of the locomotives of the western railroads. This is really how the "American West was won": through the windmill and the steam locomotive.

2.8 Historical developments

The earliest horizontal-axis windmills possessed short sails, which were made later longer and more efficient in catching the kinetic energy from the wind. As the sails were elongated, the axle or wind shaft on which they rotated had to be emplaced higher off the ground on the windmill structure or buck. Irrespective of their design, some common features exist in windmills. For horizontal-axis windmills, the features are:

1. A means of catching the wind through sails, arms, or rotor blades rotating around an axle.
2. A yaw mechanism to turn the sails, arms, or blades so that they face the wind. Otherwise, as the wind direction shifts, the windmill would stall.
3. A gear system and interlocking equipment transmit the wind energy to the millstone, water pump, wood saw, or electrical generator that they are powering.

Vertical-axis windmills share the first and third features only since they catch the wind from all directions without the need to adjust them like in the case of horizontal-axis windmills. The use of sails on the European windmills added an element of aerodynamic lift leading to higher rotor efficiency through its increased speed. The evolutionary perfection process took 500 years leading to windmills that have the components and features of modern windmills.

Some windmills had aerodynamic brakes, spoilers, flaps, and leading edge airfoil sections that were precursors to the modern airplane wing. Features of modern airfoil rotor blades were incorporated through insight and trial and error: a nonlinear twist of the blades from their root to their tip, introducing a camber along the leading edge, emplacement of the blade spar at the quarter chord position at 25% of the way from the leading edge to the trailing edge, and designing the blade with its center of gravity at that same 1/4 chord position.

The simplest windmills sails are just cloth sails attached to the rotating arms or blades. Designs using multiple sails were used in the Mediterranean region such as at Alexandria, Egypt (Fig. 2.9). A design with small sails attached to multiple arms was used in Greece. With a small number of arms, large sails were used for Portuguese, Spanish, and French windmills. Some were equipped with bells at the end of their rotating arms, generating an audible alarm for stray cattle or humans.

FIGURE 2.9 Alexandria, Egypt's Moulins du Gabari (Al Qabbari), built on a hill overseeing the harbor of Alexandria, showing their furled sails.

Better structural strength was achieved with wooden frames covered with cloth in what became known as common sails. Initially, the cloth was only placed over the frames or entirely removed. Later, a method for reefing or furling the cloth was developed to control the sail area depending on the wind speed. The common sails were light in weight and powerful but they had to be stopped by the millwright furling the sail. Stopping the mill by an additional brake was needed. In many situations, the wind became stronger than the brake could handle. The mill then could run out of grain and its millstones would now run dry, generating a spark shower igniting fires. Runaway wind turbines could also lead to the vibration that would disintegrate the windmill wooden parts. In freezing weather, the cloth could become wet and frozen.

The wind wright had to skillfully ride out a storm much like a sailing ship's captain had to weather a storm at sea. One method to slow the sails in a high wind was to jam the grain into the millstones so that they act as a brake slowing down the sail rotation. A second method was to force the edge of the sail onto the wind. If the wind suddenly shifted, it could hit the windmill from behind with the sails and cause them to be blown off [1].

Combinations of wood and metal were used to prevent fires from the friction of similar components. Many cloth sails lasted for as long as 40−50 years. Interestingly, the sails were built with a counterclockwise rotation, a tradition that endures today in most wind turbines, with rare exceptions.

Modern wind generators have evolved from a drag or impulse system into an airfoil system similar to airplane propellers and wings. Wood and glass epoxy, fiberglass, aluminum, and graphite composite materials are now used in their construction.

2.9 Windmills applications

Barley- and rice-hulling windmills operated by hulling stones that were larger than the common millstones removing the thin outer cover of the grain kernel. They were grit stones with a few deep furrows with the grain flung out along them without being ground. Requiring heavier equipment and a stronger wind location than grinding mills, hulling mills were limited in number [1].

Different windmill applications required different specialized machinery. Oil mills pressed oil from oil seeds and nuts. Grinding mills ground spices. Sawmills sawed wood into planks for construction and shipbuilding. Irrigation and drainage mills reclaimed the low lands of Holland or the Netherlands from the sea by drying out marches and shallow lakes. Polder drainage windmill designs used a scoop wheel or noria, and other designs used an Archimedean screw or "tambour."

2.10 Discussion

At the beginning of the 20th century, the first modern windmills driving electrical generators were introduced in France by Darrieus and then spread worldwide. The steam engine and then the internal combustion engine replaced sails on ships and mills. Both were more efficient than windmills using fossil fuels as a source of energy rather than the wind [1].

It is recognized that renewable sources of energy are characterized by the use of a large labor supply providing job opportunities in high-population economies. Their implementation is rapid: it takes about 2 years in the United States for the implementation and production of wind parks projects since they only require local regulations, whereas other conventional energy sources such as coal and nuclear power stations require 10 years or more because they are bound by lengthy federal regulations [2−6].

A symbiotic coupling of wind technologies with other energy sources exists through sharing access to the electrical grid system. The two units 2309 MWe Boiling Water Reactors LaSalle nuclear power plant near Marseilles, Illinois, United States operated by Exelon Nuclear Corporation and the Grand Ridge Wind Farm operated by Invenergy LLC in the adjacent farmland near Ransom in Illinois, United States are jointly sited and connected to the same electrical grid system. The nuclear reactor and the wind turbines are both manufactured by the General Electric (GE) Company. The GE 1.5 MW SLE wind turbines have a hub height of 80 m and are net recipients of about 5 kW of electrical power from the grid on a standby basis, but then become net exporters of electricity into the electrical grid under favorable wind conditions (Fig. 2.10).

The world is embarking on a third industrial revolution: the Low Carbon Age; and wind power is being reinvented to help fill the need.

FIGURE 2.10 Symbiotic coupling of nuclear and wind technologies views during winter and summer. The two units 2309 MWe Boiling Water Reactors LaSalle nuclear power plant near Marseilles, Illinois, United States operated by Exelon Nuclear corporation and the Grand Ridge Wind Farm operated by Invenergy LLC in the adjacent farmland near Ransom in Illinois, United States. The nuclear reactor and the wind turbines are both manufactured by the General Electric Company [6].

References

[1] Johnson GJ. Wind energy systems. Englewood Cliffs, NJ: Prentice Hall; 1985.

[2] Ragheb M, Ragheb AM, Carriveau R. Wind turbines theory-the Betz equation and optimal rotor tip speed ratio fundamental and advanced topics in wind power. In: Carriveau R, editor. Fundamental and advanced topics in wind power. InTech; 2011. Available from: http://www.intechopen.com/articles/show/title/wind-turbines-theory-the-betzequation-and-optimal-rotor-tip-speed-ratio. ISBN: 978-953-307-508-2.

[3] Ragheb M. Coupling wind power as a renewable source to nuclear energy as a conventional energy option. In: Invited paper submitted for presentation at the Academy of Sciences for the Developing World—Arab Regional Office, TWAS-ARO, 7th annual meeting seminar: "Water, nuclear and renewable energies: challenges versus opportunities" conference, Center for Special Studies and Programs, CSSP, Bibliotheca Alexandrina, Alexandria, Egypt, December 28−29, 2011 <http://www.bibalex.org/CSSP/Presentations/Attachments/Coupling%20Wind%20Power%20as%20a%20Renewable%20Resource%20to%20Nuclear%20Energy%20as%20a%20Conventional%20Energy%20Option.pdf>.

[4] Kate Rogers K, Ragheb M. Symbiotic coupling of wind power and nuclear power generation. In: Proceedings of the 1st international nuclear and renewable energy conference (INREC10), Amman, Jordan, March 21−24, 2010.

[5] Weisensee P, Ragheb M. Integrated wind and solar qattara depression project with pumped storage as part of desertec. In: The role of engineering towards a better environment, RETBE'12, 9th international conference, Alexandria University, Faculty of Engineering, December 22−24, 2012.

[6] Ragheb M. Wind power systems: NPRE 475, Lecture Notes, <http://www.mragheb.com/NPRE%20475%20Wind%20Power%20Systems/index.htm>; 2016.

Section B

Wind resource and wind energy

This page intentionally left blank

Chapter 3

Wind power fundamentals

Alexander Kalmikov
Massachusetts Institute of Technology, Cambridge, MA, United States

3.1 Wind physics basics: what is wind and how wind is generated

Wind is atmospheric air in motion.[1] It is ubiquitous and one of the basic physical elements of our environment. Depending on the speed of the moving air, wind might feel light and ethereal, appearing silent and invisible to the naked eye. Or, it can be a strong and destructive force, loud and visible as a result of the heavy debris it carries along. The velocity of the air motion defines the strength of wind and is directly related to the amount of mechanical energy in the wind, that is—its **kinetic energy**. The original source of this energy, however, is solar radiation. The electromagnetic radiation from the sun unevenly heats the earth's surface, stronger in the tropics and weaker in the high latitudes. Also, as a result of a differential absorption of sunlight by soil, rock, water and vegetation, air in different regions warms up at a different rate. This uneven heating is converted through convective processes to air movement, which is adjusted by the rotation of the earth. The convective processes are disturbances of the hydrostatic balance whereby, otherwise stagnant, air masses are displaced and propelled in reaction to forces induced by changes in air density and buoyancy due to temperature differences. Air is pushed from high to low-pressure regions, balancing friction and inertial forces due to the rotation of the earth.

The patterns of differential earth surface heating, as well as other thermal processes such as evaporation, precipitation, clouds, shade and variations of surface radiation absorption, appear on different space and time scales. These are coupled with inertial forces due to earth rotation and flow momentum redistribution to drive a variety of wind generation processes, leading to the existence of a large variety of wind phenomena. These winds can be categorized based on their spatial scale and physical generation mechanisms.

3.2 Wind types: a brief overview of wind power meteorology

Wind systems span a wide range of spatial scales, from global circulation on the planetary scale, through synoptic scale weather systems, to mesoscale regional and microscale local winds. Table 3.1 lists the spatial scales of these broad wind type categories. Examples of planetary circulations are sustained zonal flows such as the jet stream, trade winds, and polar jets. Mesoscale winds include orographic and thermally induced circulations [1]. On the microscale wind systems include flow channeling by urban topography [2] as well as submesoscale convective wind storm phenomena, as an example.

A long list of various wind types can be assembled from scientific and colloquial names of different winds around the world. The associated physical phenomena enable a finer classification across the spatial scales. The forces of the generating physical mechanisms define geostrophic winds, thermal winds, and gradient winds. Katabatic and anabatic winds are local topographic winds generated by the cooling and heating of mountain slopes. Bora, Foehn, and Chinook are locale-specific names for strong downslope wind storms [3]. In Greenland, Piteraq is a downslope storm as strong as a hurricane, with sustained wind speeds of 70 m/s (160 miles/h). In coastal areas, sea breeze and land breeze mesoscale circulations occur with regular daily frequency. Convective storms generate strong transient winds, with downdrafts which can be particularly dangerous (and not very useful for wind power harvesting). Hurricanes and typhoons,

1. We focus on air motions with net total displacement, excluding fast small amplitude oscillatory motions due to adiabatic pressure fluctuations associated with propagation of sound waves.

Wind Energy Engineering. DOI: https://doi.org/10.1016/B978-0-323-99353-1.00007-4

TABLE 3.1 Spatial scales of wind systems and a sample of associated wind types.

Spatial scales	Wind types	Length scale
Planetary scale	Global circulation	10,000 km
Synoptic scale	Weather systems	1000 km
Mesoscale	Regional orographic or thermally induced circulations	10–100 km
Microscale	Local flow modulation, boundary layer turbulent gusts	100–1000 m

as well as smaller-scale tornadoes, are examples of very energetic and destructive rotational wind storms. A microscale version of these winds are gusts, dust devils, and microbursts. Nocturnal jets appear in regular cycles in regions where night-time cooling calms turbulence and reduces friction near the ground. Atmospheric waves driven by gravity and modulated by topography are common in mountainous places. Locale-specific regional wind names include Santa Anas, nor'easters and Etesian winds, to mention just a few.

Meteorology is the scientific field involved in the study and explanation of all these wind phenomena. It enables both a theoretical understanding and the practical forecasting capabilities of wind. Statistics of observed wind occurrences define wind climates in different regions. Mathematical and computer models are used for theoretical analysis, exploratory resource assessment, and operational forecasting of winds. Meteorology literature, focusing on wind power is available, in the form of introductory texts and reviews [4–7].

3.3 Fundamental equation of wind power: kinetic energy flux and wind power density

The fundamental equation of wind power answers the most basic quantitative question—*how much energy is in the wind*. First, we distinguish between concepts of *power* and *energy*. Power is the time rate of energy. Therefore, wind power quantifies how much energy can be generated by a wind turbine per unit time. Illustratively, we will show that the physical meaning of the power of the wind is also the rate of wind energy flow through an open window.

Wind energy depends on:

- amount of air (the volume of air in consideration)
- speed of air (the magnitude of its velocity)
- mass of air (related to its volume via density)

Wind power quantifies the amount of wind energy flowing through an area of interest per unit of time. In other words, wind power is the flux of wind energy through an area of interest. *Flux* is a fundamental concept in fluid mechanics, measuring the rate of flow of any quantity carried with the moving fluid, by definition normalized per unit area. For example, *mass flux* is the rate of mass flow through an area of interest divided by this area. *Volume flux* is the volume flowing through the area of interest per unit time and per unit area. Consider an area element A (Fig. 3.1) and flow of magnitude U through this area.[2] The volume of air flowing through this area during unit time dt is given by the volume of the cylinder with cross-section area A and length $U \cdot dt$, that is the volume $A \cdot U \cdot dt$. Therefore, the volume flow rate is $A \cdot U$, the volume flux is U. The mass flow rate is derived by multiplying the volume flow rate by the density of the flow ρ and is equal to the mass of that cylinder divided by unit time

$$\frac{dm}{dt} = \rho \cdot A \cdot U \tag{3.1}$$

Wind energy by definition is the energy content of airflow due to its motion. This type of energy is called **kinetic energy** and is a function of its mass and velocity, given by

$$KE = \tfrac{1}{2} \cdot m \cdot U^2 \tag{3.2}$$

2. Here we restrict the discussion to flow perpendicular to the area of interest. In general, flow is a vector quantify that can be oriented in any direction and only its component perpendicular to the area element is considered when quantifying the flux through that area.

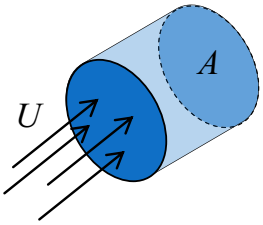

FIGURE 3.1 Schematics of airflow at velocity U through area A. The cylinder depicts the volume flowing in unit time dt through area A.

Wind power is the rate of kinetic energy flow. In derivation similar to the other flow rate quantities discussed above, the amount of kinetic energy flowing per unit of time through a given area is equal to the kinetic energy content of the cylinder, as shown in the following equation (Fig. 3.1).

$$P = \tfrac{1}{2} \cdot \frac{dm}{dt} \cdot U^2 \tag{3.3}$$

Here mass flow rate (3.1) was substituted for air mass in (3.2). The resultant equation for wind power is

$$P = \tfrac{1}{2} \cdot \rho \cdot A \cdot U^3 \tag{3.4}$$

This is a fundamental equation in wind power analysis. It exhibits a highly nonlinear cubic dependence on wind speed. For example, doubling the wind speed leads to an eightfold increase in its available power. This explains why ambient wind speed is the main factor in quantifying wind energy. In Eq. (3.4), the power of the wind is a linear function of air density and as a result of the limited range of air density variability, the density is of secondary importance. The power dependence on the area implies a nonlinear quadratic dependence on the radius of a wind turbine swept area, highlighting the advantages of longer wind turbine blades.

It is customary to normalize ambient wind power by dividing it by the area of interest; that is in terms of specific power flow. This leads to the definition of kinetic wind energy flux, known as **wind power density** (*WDP*). Similarly, to the definitions of flux and flow rate above, wind energy flux is wind energy flow rate per unit area, given by:

$$WPD \equiv \frac{P}{A} = \tfrac{1}{2} \cdot \rho \cdot U^3 \tag{3.5}$$

Wind power density is used to compare wind resources independent of wind turbine size and is the quantitative basis for the standard classification of wind resources at the National Renewable Energy Laboratory (NREL) of the United States. Mean wind power density has advantages over mean wind speed for comparing sites with different probability distribution skewness, because of the cubic nonlinear dependence of wind power on wind speed (see Fig. 11 in Ref. [8] and discussion therein). Further technical details of this classification system were originally introduced in reference [9]. Typical values of wind power classes with the corresponding power densities and mean wind speeds are presented in Table 3.2.

3.4 Wind power capture: efficiency in extracting wind power

In the previous section, we considered the total wind power content of ambient airflow. Fundamentally, not all this power is available for utilization. The efficiency in wind power extraction is quantified by the **Power Coefficient** (C_p) which is the ratio of power extracted by the turbine to the total power of the wind resource $C_p = P_T/P_{wind}$.

Turbine power capture, therefore, is given by

$$\mathrm{P}_T = \tfrac{1}{2} \cdot \rho \cdot A \cdot U^3 \cdot C_p \tag{3.6}$$

which is always smaller than P_{wind}. In fact, there exists a theoretical upper limit on the maximum extractable power fraction, known as the **Betz Limit**. According to Betz's theory [11] the maximum possible power coefficient $C_p = 16/27$, that is, 59% efficiency is the best a conventional wind turbine can do in extracting power from the wind. The reason why higher, for example, 100%, efficiency is not possible is due to the fluid mechanical nature of wind power, dependent on the continuous flow of air in motion. If, hypothetically speaking, 100% of kinetic energy was extracted, then the flow of air would be reduced to a complete stop and no velocity would remain available to sustain the flow through the energy extraction device, irrespective of the specific wind turbine technology used. The maximum extraction efficiency is achieved at the optimum balance of the largest wind slowdown that still maintains sufficiently fast flow past the turbine.

TABLE 3.2 Wind power classes measured at 50 m above ground according to NREL wind power density-based classification [10].

Wind power classification			
Wind power class	**Resource potential**	**Wind power density/W/m^2**	**Wind speed/m/s**
1	Poor	0–200	0.0–5.9
2	Marginal	200–300	5.9–6.7
3	Fair	300–400	6.7–7.4
4	Good	500–600	7.4–7.9
5	Excellent	500–600	7.9–8.4
6	Outstanding	600–800	8.4–9.3
7	Superb	>800	>9.3

Wind speed corresponding to each class is the mean wind speed based on the Rayleigh probability distribution of equivalent mean wind power density at 1500 m elevation above sea level.
Source: Data adopted from http://www.nrel.gov/gis/data/GIS_Data_Technology_Specific/United_States/Wind/50m/Colorado_Wind_50m.zip.

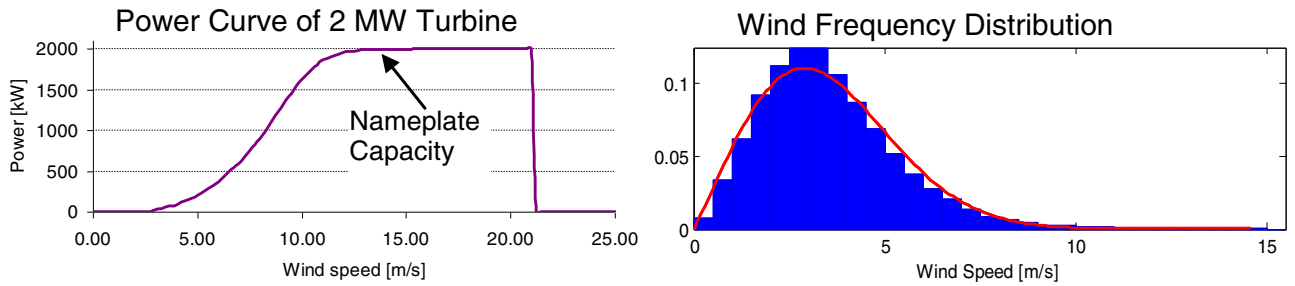

FIGURE 3.2 Typical wind turbine power curve (*left panel*) and the statistics of wind variability (*right panel*) given by a histogram and Weibull probability density fit.

(See references [12,13] for further technical details and a historic account of Betz limit derivations by contemporary researchers).

Another key metric of wind power efficiency is the **Capacity Factor** (*CF*) quantifying the fraction of the installed generating capacity that actually generates power.

$$CF = \frac{E_{actual}}{E_{ideal}} = \frac{time \cdot \overline{P}}{time \cdot P_N} = \frac{\overline{P}}{P_N} \tag{3.7}$$

The *CF* is the ratio of the actual generated energy to the energy which could potentially be generated by the system in consideration under ideal environmental conditions. Considering that energy is the product of its time rate, that is, the power with the elapsed time, this energy ratio is equal to the ratio of average power $\overline{P}$ to the nominal power of the system P_N. For a single wind turbine this nominal power is equal to its nameplate capacity, typically the maximum power it can generate under favorable wind conditions. Considering a typical power curve for a turbine (Fig. 3.2) this is the flat region for strong wind just below the cut-out wind speed.

Equivalently, *CF* can be regarded as the fraction of the year the turbine generator is operating at rated power (nominal capacity), that is, the ratio of the effective time relative to the total time, given as:

$$CF = \frac{E_{actual}}{E_{ideal}} = \frac{E_{actual}}{time \cdot P_N} = \frac{E_{actual}/P_N}{time} = \frac{time_{effective}}{time} \tag{3.8}$$

Therefore, total annual energy generation can be calculated by multiplying turbine (or wind plant) rated power P_N by the time length of one year and by *CF*.

$$E_{actual} = P_N \cdot time_{effective} = P_N \cdot time \cdot CF \tag{3.9}$$

A typical value of *CF* for an economically viable project is 30%, reaching about 50% in regions with a very good wind resources. The *CF* is based on both the characteristics of the turbine and the site—integrating the power curve with the wind resource frequency distribution (Fig. 3.2) produces the actual generation or the average power. This highlights the dependence of power production on wind variability and the importance of wind meteorology and climatology for wind power forecasting and resource assessment.

3.5 Conclusion

Wind power technology is based on the utilization of kinetic wind energy. This is the energy contained in air motion itself. Since this is a form of mechanical energy of a moving fluid, its quantification requires elements of fluid mechanics. We reviewed the concepts of kinetic energy flux and derived the fundamental equation of wind power—quantifying the rate of wind energy flow and the available power. Standard metrics of wind power resource and utilization efficiency were introduced. The nature of wind was discussed with a brief overview of wind power meteorology.

References

[1] Pielke Sr RA. Mesoscale meteorological modeling, Vol. 98. Academic Press; 2013.
[2] Kalmikov A, Uncovering MIT wind myths through micro-climatological CFD analysis, arXiv 2013; 1310.3538.
[3] Durran DR. Downslope winds. Encycl Atmos Sci 2003;644–50.
[4] Emeis S. Wind energy meteorology. Berlin, Heidelberg: Springer Berlin Heidelberg; 2013.
[5] Petersen EL, Mortensen NG, Landberg L, Højstrup J, Frank HP. Wind power meteorology. Part I: climate and turbulence. Wind Energy 1998;1:25–45.
[6] Petersen EL, Mortensen NG, Landberg L, Højstrup J, Frank HP. Wind power meteorology. Part II: siting and models. Wind Energy 1998;1:55–72.
[7] Banta RM, Pichugina YL, Kelley ND, Hardesty RM, Brewer WA. Wind energy meteorology: insight into wind properties in the turbine-rotor layer of the atmosphere from high-resolution doppler lidar. Bull Am Meteorol Soc 2013;94:883–902.
[8] Elliott DL, et al. *Wind energy resource assessment of the Caribbean and Central America*. No. PNL-6234. Richland, WA (United States): Pacific Northwest National Laboratory (PNNL); 1987. Available from: https://doi.org/10.2172/971424.
[9] Elliott DL, Barchet WR. Wind energy resources atlas. Volume 1. Northwest Region. United States: N.p; 1980. Available from: https://doi.org/10.2172/5319588.
[10] Available from: https://windexchange.energy.gov/maps-data/16.
[11] Betz A. The maximum of the theoretically possible exploitation of wind by means of a wind motor. Wind Eng 2013;37(4):441–6 Translation of: Das Maximum der theoretisch möglichen Ausnützung des Windes durch Windmotoren, Zeitschrift für das gesamte Turbinenwesen, Heft 26, 1920.
[12] van Kuik GAM. The Betz-Joukovsky limit: on the contributions to rotor aerodynamics by the British, German and Russian scientific schools. Wind Energy 2012;15:335–44.
[13] van Kuik GAM. The Lanchester-Betz-Joukovsky limit. Wind Energy 2007;10:289–91.

This page intentionally left blank

Chapter 4

Estimation of wind energy potential and prediction of wind power

Jing Shi[1] **and Ergin Erdem**[2]

[1]*College of Engineering and Applied Science, University of Cincinnati, Cincinnati, OH, United States,* [2]*Department of Engineering, Robert Morris University, Moon Township, PA, United States*

4.1 Introduction

Wind is one of the prominent renewable energy resources. The percentage of wind energy-based resources for electricity generation has been steadily growing. In 2019 Denmark produced approximately 47.2% of its electricity from wind-based resources [1]. There is a strong growth pattern in terms of the installed wind capacity. Even with the impact of COVID-19, the installed wind capacity reached the level of 743 GW in 2020, from 650 GW in 2019, representing an increase of 93 GW. Out of 93 GW, 86.9 GW of the capacity increase is associated with the onshore resources, where the remaining 6.1 GW is in the offshore locations. China has a total installed capacity of 288,320 MW, whereas the United States has 122,317 MW. Entire Europe has the total capacity of 218,912 MW [2]. The utilization rates of wind-based resources for generating electricity are different throughout various regions. In the United States, overall, 8.4% of the total electricity was obtained from wind-based resources, while the States of Iowa and Kansas produced 58% and 43% of the electricity from wind-based resources, respectively, in 2020 [3].

To assess the wind energy feasibility at a particular site, it is imperative to conduct a successful wind resource assessment and measuring program. To embark on such a study, it is important to develop a sound quality assurance plan and framework associated with each wind potential program. The measurement, equipment, and apparatus selection that have acceptable standards, data collection, and analysis schemes are important aspects to consider.

Usually, wind potential assessment programs consist of several important steps. They can be listed as preliminary area identification, area wind resource evaluation, and micro-siting (i.e., choosing the best location for the wind turbine within the wind potential assessment site) [4]. Those aspects are discussed in more detail in the following sections.

The first wind resource assessment program starts with wind atlases (i.e., wind resource maps) depicting the wind potential. The data obtained from the satellites are now being used extensively along with the data obtained from ground resources. To cite an instance, the Solar and Wind Energy Resource Assessment (SWERA) project for the United Nations Environment Programme is one of the extensive initiatives that have been formed for this purpose [5].

During recent decades, considerable effort has been spent on improving the accuracy and detailing the level of wind atlases. To improve the accuracy, extensive network of ground measurement units must be deployed. With the inclusion of the satellite and remotely obtained data, the accuracy and resolution of the atlases should significantly improve. As such, there is an ongoing effort initiated by the International Renewable Energy Agency to combine the publicly available Geographic Information System (GIS) data to obtain a comprehensive picture of the available wind resources. For this purpose, the Energy Sector Management Assistance Program allocated US$22.5 million for supporting the projects conducted over 12 different countries until the year 2018 [6]. However, it should be also kept in mind that there is a need for actual field work no matter how detailed and accurate the wind atlases are. The data should be validated for short, medium, and long-term time periods for tapping the whole potential of a wind site [7].

The outline of the chapter is as follows. In Section 4.2, we discuss the main principles associated with developing a successful wind assessment program. In Section 4.3, we outline the main aspects of a wind potential assessment program which involves instrumentation, data handling, preliminary analysis, and hind-sight analysis such as Measure-Correlate-Predict. In Section 4.4, the methods for obtaining the average wind power based on wind speed measurements

Wind Energy Engineering. DOI: https://doi.org/10.1016/B978-0-323-99353-1.00027-X

are described. In Section 4.5, we discuss the aspects associated with the wind assessment such as the scale of analysis (i.e., microscale, mesoscale, macroscale), the analytical models, and software that might be utilized for the siting purposes, for example, Wind Atlas Analysis and Application Program (WAsP), Computational Fluid Dynamics (CFD) based approaches, and the spatial exploration models. In Section 4.6, we provide additional considerations associated with wind resource assessment such as extreme wind speed analysis, rugged terrain analysis, wake of turbines, uncertainty analysis, and estimation of losses associated with electricity production. In Section 4.7, we summarize the analytical approaches associated with the forecasting of wind speed and wind power. In Section 4.8, we provide overall conclusive remarks.

4.2 Principles for successful development for a wind assessment program

A successful wind assessment program includes site identification, preliminary resource assessment, and micro-siting, according to New York State Energy Research and Development Authority [8], with wind atlases serving as a valuable tool for preliminary analysis. Apart from using wind atlases, there are additional steps that should be performed. These are identified as: (1) instantaneous wind speed measurement to estimate the wind potential; (2) interviewing stakeholders regarding the environmental impact of the wind turbines; (3) studying the meteorological information regarding the wind speed and the wind direction; (4) availability of land; (5) terrain features, that is, surveying the obstructions that might impede the wind flow [7].

In general, a preliminary resource assessment includes defined measurement plans where the key decisions on the tower placement, height, and instrumentation are given. Besides those decisions, the determination of whether adequate wind resources exist within the specified area, a comparison of different areas for distinguishing relative development potential, obtaining representative data for the estimation of economic viability and performance of wind turbines, and the screening of the potential of wind turbine installation sites are also important considerations [4].

Regarding micro-siting, the main aspects of decision-making involve conducting additional measurements for validating the data, conducting the necessary adjustments for the wind shear and the long-term wind climate, numerical flow modeling, and the corresponding uncertainty estimation. Moreover, in the micro-siting phase, small-scale variability of the wind resource over the terrain of interest is quantified to position one or more wind turbines to maximize overall energy output [8].

Wind atlases are starting point for a preliminary site-selection. However, it should be kept in mind that these maps give only a rough estimate and might differ from the actual wind speeds by $\pm 10\%$ to 15%. Since wind power is a function of the cube of the wind speed, the deviation between actual and estimated wind output could be further compounded; this might lead to differences of up to $\pm 20\%$ [9].

Usually, the classification of wind sites with respect to wind potential is on a 5-scale rating. According to this classification, class 5 is considered extremely suitable for a wind farm, whereas class 1 is deemed unfeasible. In that regard, Bennui et al. [10] use the GIS and employ a multiple decision criteria-based method to classify wind sites. The decision criteria are wind speed information, elevation, slope, highways and railways, built-up area, forest zone, and scenic area.

Researchers have developed comprehensive methods for assessing wind potential. To cite an instance, Lawan et al. [11] conduct a structured analysis and review of the steps for conducting the wind resource assessment program for Malaysia. They also discuss the prospects and challenges of using wind energy both in developing and developed countries. It is believed that developing countries, especially in Asia, have untapped potential for wind energy and they suggested that the government and private entities should work together, especially for harvesting wind energy in remote and rural areas. It is also pointed out that wind speed distribution, energy potential modeling, determining cut-in, cut-out and rated wind turbine velocities, wind speed profiling, and proper software selection are important aspects once the wind potential is properly assessed

Similarly, there are some analytical methods used for comparing wind potentials at different sites. Corbett et al. [12] develop a methodology based on the CFD approach for comparing 13 wind farm sites involving 74 mast pairs. The CFD-based approach should be fine-tuned with respect to the flow characteristics of the wind, using care, expertise, and engineering judgment, especially for complex terrain conditions. Additionally, wind assessment programs could play a pivotal role in shaping the decisions. For instance, Wang et al. [13] emphasize the importance of holistic approaches that would necessitate the integration challenges associated with the Chinese wind energy policies. To obtain the full potential of wind-based resources, it is vital to determine the predictability with successful forecasting models, and improve energy markets with the objectives of long-term development and pricing reforms. To enhance predictability and create effective markets, research and development on wind resource assessment programs are of

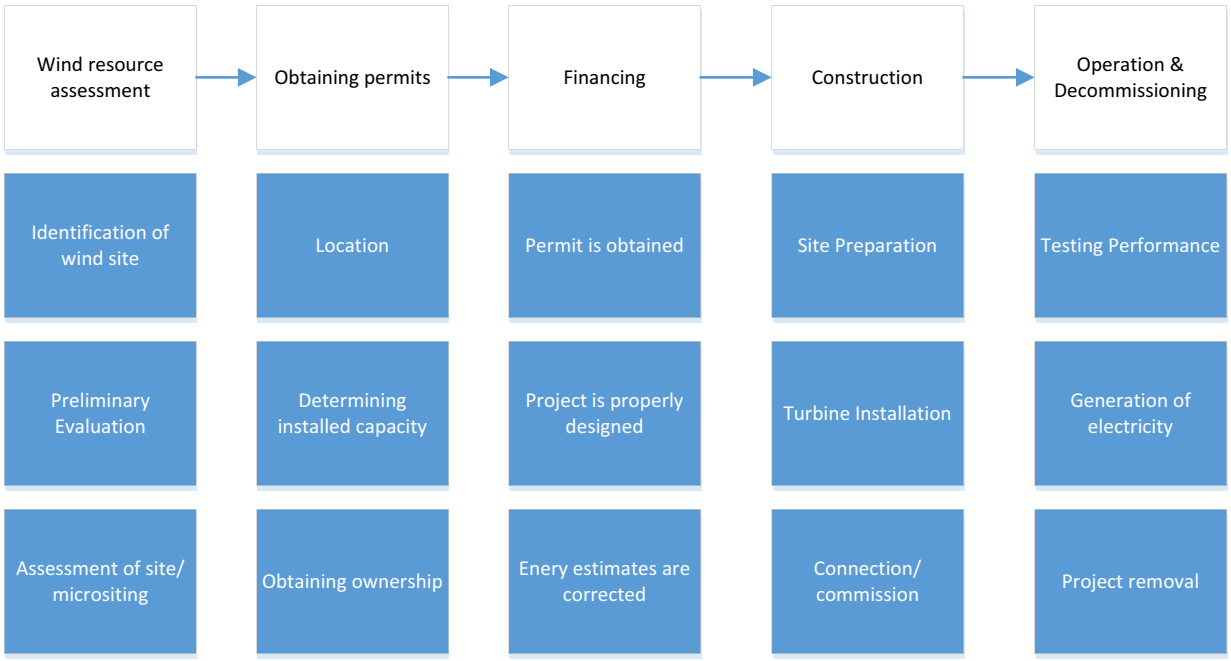

FIGURE 4.1 Stages of the wind energy project lifecycle [14].

paramount interest and these activities should be conducted transparently. The steps that should be conducted for realizing a successful wind energy system are given in Fig. 4.1.

4.3 Main aspects of a wind assessment program

One of the most important parameters in determining the electric power obtained from wind-based resources is wind speed. The general equation relating wind power to the swept area, wind speed, and density of air is [7];

$$P_w = \frac{1}{2}\rho A v^3 \tag{4.1}$$

where P_w is the wind power, ρ is the density of the air, and v is the wind speed. This represents the total energy obtained from the wind flow. In terms of generating electric energy, only a certain proportion of the kinetic energy of the wind can be converted. This relation can be expressed as follows:

$$P_e = \eta_e \eta_m C_p P_w \tag{4.2}$$

where P_e is the amount of electric power generated, η_e is the electric conversion efficiency of the wind turbine, η_m is the mechanical efficiency, and C_p is the power coefficient. The upper limit for the power coefficient (i.e., the proportion of the amount that can be extracted from the kinetic energy of the wind) is 59.3% regardless of the geometry of the wind turbine. Usually, the power coefficient of modern wind turbines is between 45% and 50% [15]. Fig. 4.2 is a typical power curve of a wind turbine that shows the relation between the generated wind power and the wind speed.

As illustrated in Fig. 4.2, at low wind speeds, there is not enough torque applied by the wind to generate electricity. The minimum wind speed at which electricity can be generated is called the cut-in speed, namely, the speed at which the rotor of the wind turbine begins turning. As described in Eqs. (4.1) and (4.2), the generated wind power increases with the cube power of the wind speed, up to a certain value which is called rated power. The rated output is usually obtained at the maximum speed that the rotor is allowed to turn. Usually, the wind turbine manufacturers place an upper limit on the speed that the blades are allowed to turn to increase the longevity of the blades by preventing and minimizing bird impacts, rain, erosion, etc. [16]. Typically, the tip of the blade of the rotor turns at a maximum speed of 120 m/s. Turning the blades faster could lead to problems. Beyond a certain speed, to prevent structural damages, the rotor is brought to a standstill by a brake. This particular wind speed is called the cut-out wind speed.

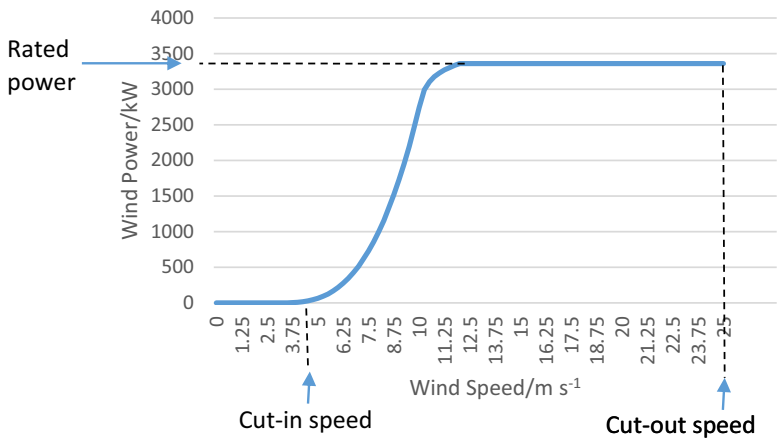

FIGURE 4.2 Power curve of a typical wind turbine.

To determine the potential of a wind-based resource to the fullest extent, identification and survey of the site are the most vital concern. For this purpose, proper instrumentation plays a crucial role. Wind power maps give only crude information regarding the specific information sites. To characterize the wind-related properties, and collect associated data, a sound data acquisition program with the following aspects should be taken into consideration [8]:

- Equipment procurement tailored according to program specifications
- Equipment calibration, frequency, method, and reporting requirements
- Monitoring station installation, verification, and checklists related to maintenance and operation
- Data collection and screening
- Data analysis guidelines that also include corresponding calculations
- Data validation methods and flagging criteria, the frequency of reporting, and associated format
- Internal audits for various aspects such as site installation, operation and maintenance, and data handling

Some consider placing remote sensing equipment for collecting the wind-related data. In a study conducted by Rodrigo et al. [17], the procedures for the testing and evaluation of the remote sensing equipment for the wind-related attributes are investigated. For this purpose, two terrains with different topologies (i.e., a flat and a complex terrain) are considered. An intercomparison between sound and light-based equipment (i.e., SODAR—Sound Detection and Ranging system and LIDAR—Light Detection and Ranging system) that can remotely sense the wind is made. The researchers use a single-point regression, ensemble-averaged profile analysis, and a performance matrix in the evaluation steps and discuss the principles associated with the remote sensing equipment for a wide variety of terrain conditions. The analysis is helpful for extending the scope of the wind energy potential assessment campaigns and measuring the corresponding wind attributes at certain heights without the need for installing anemometers at specified distances. It is concluded that although the remote sensing technologies using sound and light wave technologies show improvement, defining standards for testing and calibration is difficult for the complex terrain applications. It is also indicated that a multitude of prototype designs in terms of the uncertainty of the measurements with respect to various terrain conditions should be evaluated for remote sensing equipment to develop standards for generating bankable data.

For the wind turbines located offshore, other approaches are of interest. To cite an instance, Nicholls-Lee [18] discusses the possibility of instrumentation platforms that have mobility deployed for assessing wind potential offshore. The feasibility of a lightweight, floating platform for a repositionable meteorological measurement station is evaluated. Contrary to the traditional anemometers, LIDAR is adopted for capturing the wind speed and direction at specified heights. Such a platform could be a viable alternative to deploying costly masts to capture the offshore wind potential. Other researchers discuss the potential for utilizing the data captured by satellites for conducting wind resource assessments [19,20].

Aside from the wind speed, one of the most important wind attributes is the ambient air temperature. The air temperature is a dictating factor for the air density. As indicated in Eq. (4.3), wind power increases with the air density. The relation between the air temperature and the air density for humid air can be approximated using the ideal gas formula:

$$\rho_{humid\ air} = \frac{p_d}{R_d T} + \frac{p_v}{R_v T} \tag{4.3}$$

where $\rho_{humid\ air}$ is the density of humid air (kg/m^3), p_d is the partial pressure of the dry air (in Pascal), T is the temperature (in Kelvin), R_d is the specific gas constant for dry air [i.e., 287.058 J/(kg · K)], p_v is the partial pressure of the water vapor (in Pascal), and R_v is the specific gas constant for water vapor [i.e., 461.495 J/(kg · K)]. The temperature readings should be conducted several meters above the ground to minimize the effects of surface heating [7].

Another consideration is the determination of the distance between the measurement point and the potential location of wind turbines. It should be kept in mind that as the terrain becomes more complex due to the variability associated with the local wind characteristics, the maximum distance between the point of measurement and the potential location should decrease. As a rule of thumb, that distance should be 5−8 km for a relatively simple terrain, and 1−3 km for the regions where complex terrain conditions are present (e.g., steep geometrically complex ridgelines, coastal sites with varying distance from the shore or heavily forested areas) [8]. This necessitates the placement of a larger number of measurement towers for wind farms as compared to stand-alone turbines. Intuitively, the number of towers should be increased to analyze the perturbation of the more complex terrain on the wind flow. In that regard, the tower placement should be representative of the turbine locations. Nevertheless, to obtain a comprehensive picture and analyze the wind flow over an area more accurately, some towers should also be placed at the coordinates where less-than-ideal conditions exist [21].

For deciding the final location of turbines, a preliminary analysis needs to be conducted using software (e.g., WindPRO) based on the wind resource maps and terrain-based constraints. The siting of wind turbines at a location involves grouping turbines into clusters based on distance. For relatively flat terrains, the rule of thumb is to place the 10−12 turbines in one cluster, and for more complex terrains, place 5−7 wind turbines in one cluster. After forming the cluster, the median wind speed within the cluster is calculated based on the wind resource map, and the locations at which the median speed is observed are selected for the potential location for the measurement points and hence the construction of towers. Usually, two or three candidate locations are selected for a tower. Then, by visual examination, the final location of those towers (one for each cluster) is selected in such a way that those towers are sufficiently spread out [22].

Furthermore, consideration should be given to the extrapolation of data obtained from different wind sites. The following simple equation might be used for this purpose [8].

$$v_2 = v_1 \left(\frac{h_2}{h_1}\right)^{\alpha} \tag{4.4}$$

where v_1 is the known speed at measurement height h_1, v_2 denotes the wind speed at the height h_2 where the wind speed is extrapolated, and α is the wind shear exponent. Various factors affect the wind shear exponent, including vegetation cover, terrain, general climate, and even the time of the day. In the literature, α values ranging between 0 and 0.4 are reported [8].

Not only the new measurement facilities but also existing measurement units might be used for the wind resource assessment. For this purpose, existing towers, airport measurement units, and spatial extrapolation models might be used. Waewsak et al. [23] use a 120 m wind tower at the shoreline to analyze the monthly mean wind speeds and dominant wind directions. Using this data, they obtain a 20 m resolution microscale map, and estimate the annual energy productions, wake effects, and theoretical capacity factors. In a similar fashion, Kim and Kim [24] use the AMOS (Aerodrome Meteorological Observation System) wind data measured at Yeosu Airport to develop a wind resource map. Based on this map and by employing three cases with different designs for the wind turbine, a comparative economic analysis is conducted.

Generally, measure-correlate-predict can be defined as the collection of methods that are used for the estimation of long-term wind resources based on short-term data. The idea is about using the short-term campaign and correlating it with an overlapping but climatologically representative time series (i.e., 5 years, preferably 10 years) [25]. The larger the wind project becomes (in terms of installed capacity, power rating, or similar performance measures), the more important the accurate prediction of the wind resources. For smaller projects (i.e., for wind farms with less than 100 MW output), the length of time for recording measurements varies between 4−6 weeks [8]. However, for larger projects long-term measurements might be needed for capturing the differences due to the change of seasons, or factors associated with a complex terrain. The methods that have been used to extrapolate data for long-term performance began in the 1940s for single stations and gradually evolved into more complex methods. Those early methods usually use linear, nonlinear, and probabilistic transfer functions and could be applied to time series data as well as to frequency distributions of associated wind speeds [26].

4.4 Estimating wind power based on wind speed measurements

After the data acquisition and validation phase, the next step is to analyze the data for estimating the wind energy that would be produced over a certain period. As previously indicated, the wind speed varies over time and statistical

distributions might be employed for this case. Weibull distributions are usually employed for modeling wind speed distributions [27]. Based on this assumption, the following model can be used to estimate the wind power output. Following Eq. (4.5), the average wind power can be calculated as [28]:

$$P_{ave} = \zeta P_E \tag{4.5}$$

where P_{ave} is the average wind factor, ζ is the capacity factor, and P_E is the electricity power generated. To find the ζ value, the following integral should be evaluated:

$$\zeta = \frac{1}{V_R^3}\int_{v_c}^{v_R} v^3 f(v)dv + \int_{v_R}^{v_F} f(v)dv \tag{4.6}$$

where v_R is the wind speed at which the rated power is reached, v_C is the cut-in speed, v_F is the cut-out speed, $f(v)$ is the probability density function of the wind speed. Assuming that the Weibull distribution, which is one of the most widely used distribution for characterizing wind speed, is used, ζ can be calculated as:

$$\zeta = \left(\frac{v_c}{v_R}\right)^3 e^{-(v_c/c)^k} + 3\frac{\Gamma\left(\frac{3}{k}\right)}{k}\left(\frac{v_R}{c}\right)^3\left[\gamma\left(\left(\frac{v_R}{c}\right)^k, \frac{3}{k}\right) - \gamma\left(\left(\frac{v_c}{c}\right)^k, \frac{3}{k}\right)\right] - e^{(v_f/c)^k} \tag{4.7}$$

where $\left(\frac{v_R}{c}\right)$ is the normalized rated speed, Γ is the gamma function, γ is the incomplete gamma function, c is the Weibull scale parameter, and k is the shape parameter.

The Weibull scale parameter can be estimated from the following equation:

$$k = \left(\frac{\sigma}{\overline{x}}\right)^{-1.086} \tag{4.8}$$

$$\frac{c}{\overline{x}} = \left(0.568 + \frac{0.433}{k}\right)^{\frac{-1}{k}} \tag{4.9}$$

where σ is the standard deviation of the wind speed, and $\overline{x}$ is the average wind speed.

Various approaches have been used for determining the underlying distribution governing the wind speed equation. Zhou et al. [29] compare various distributions for modeling the wind speed distribution, and concluded that the maximum entropy-based functions proved to be a versatile tool. The authors conduct a comprehensive study on five North Dakota Sites and indicate that no distribution outperforms any others but Rayleigh-based distributions, in general, are inferior when compared to other distributions (e.g., maximum entropy-based, Weibull, Rayleigh, gamma, lognormal, and inverse Gaussian). Some researchers have used the bivariate distribution for modeling and characterizing wind attributes (i.e., direction and speed) simultaneously. Erdem et al. [30] provide a comparison for modeling the wind speed and direction using three different approaches (namely, angular-linear, Farlie-Gumbel-Morgenstern, and anisotropic lognormal approaches), in terms of the root mean square error and R^2 values. The Farlie-Gumbel-Morgenstern approach provides compatible results while the anisotropic normal distribution lags behind. Fractional distributions can also be used for modeling the wind speed distributions, such as the fractional Weibull distributions [31]. Some researchers have developed nontraditional methods for characterizing the wind speed distributions over a long period of time. For instance, Li and Shi [32] combine an averaging Bayesian model and Markov Chain Monte Carlo sampling methods and conclude that the combined approach provided comparative reliability and robustness in describing the long-term wind speed distributions for the selected wind sites.

4.5 Wind resource estimation project; scope and methods

In terms of the scope, wind resource assessment can be conducted at different levels (i.e., microscale, mesoscale, and macroscale). As the name implies, microscale wind resource assessment campaigns usually entail assessing the wind power for a smaller region such as the local/site coverage, mesoscale entails the national coverage, and macroscale usually focuses on estimating the wind potential on a global scale. The resolution of the wind power assessment program differs widely with respect to scale. In general, microscale entails a resolution of between 10 and 100 m, mesoscale entails the resolution of approximately 5 km, and mesoscale incorporates a resolution of approximately 50−200 km [33].

The estimates for global wind power vary depending on the assumptions and associated constraints. Most researchers evaluate the potential of both onshore and offshore wind. To gain access to the untapped potential associated with

the offshore platforms, newly constructed onshore wind projects have larger turbine dimensions and power, increased size of the wind farms, and increased water depth and distance to the shore to utilize the wind power more efficiently. As such, average turbine capacities for the newly constructed projects reach 6−7 MW as compared to the average of 3−4 MW for the existing onshore wind turbines [34]. Tong et al. [35] indicate that neglecting the transmission constraints, without the need for the excess annual energy generation and facilities for storing the energy, the wind, and power resources can meet at least 72% of the electricity demand, whereas in the United States, this number increases to 85%. The authors also indicate that adding the energy storage facilities, increasing the installed capacity in terms of the generating excess annual demand, and pooling the available resources of contiguous, multinational regions might help to increase the reliability of the power grid. However, the amount of improvement varies with respect to regions. To cite an instance, through macro energy model simulations, it is indicated that for smaller countries at higher latitudes with wind-heavy resources (more than 95% of the total mix), higher gains in reliability are achievable by regional aggregation.

The estimates for total wind potential vary considerably. Lu et al. [36] predict the global wind energy potential to be 840 000 TW h per year based on the Goddard Earth Observing System Data Assimilation System (GEOS-5 DAS) dataset. This dataset uses a weather/climate model incorporating inputs from a wide variety of observational sources (surface and sound measurements) and a suite of measurements and observations from a combination of airborne vehicles (e.g., aircraft and balloons), sea units (e.g., ships and buoys), and satellites. This creates fairly accurate high-resolution wind potential maps. It is indicated that 36% of the capacity factor is the breakeven point for satisfying the world demand for electricity power if those wind turbines are only located onshore. It is also stipulated that using the wind resources in the form of network of land-based 2.5 MW wind turbines located in nonforested, ice-free, and nonurban areas, it is possible to satisfy more than 40 times the total electricity demand worldwide, and 5 times the total energy consumption in all forms provided that they are operating at 20% of their rated capacity. For the contiguous United States, using the resources in the central plain states, it is possible to accommodate as much as 16 times the total current demand for electricity. Also, onshore wind farms have some growth potential, especially for Russia, Canada, the United Kingdom, and the United States.

Bosch et al. [37], by assuming the average capacity factor greater than 20% and array losses of 12.5%, indicate that the offshore sites have an estimated wind capacity of 329,600 TWh. The recent improvements and technological advances could enable tapping this potential further. However, another point raised is that out of 329,600 TWh of current potential, 64,800 TWh is associated with shallow water zone (0−40 m), 34,800 TWh at transitional waters zone (40−60 m), and 230,000 TWh remains at the deep-water zone (i.e., 60−1000 m). The associated costs of construction and operation rise with respect to the distance of the offshore wind turbine to the shore and the depth of the sea. For deep water, floating wind turbines might be a viable option. Currently, such research has been conducted, and floating wind farms have already been deployed on a commercial basis albeit on a limited scale. The prevalence of those platforms will help tap the potential of offshore regions where winds are stronger and steadier [38].

On the other hand, Hoogwijk and Graus [39] by employing a more constrained model, estimate that the global capacity for wind-based resources for generating electricity is 110 000 TW h/year. The theoretical potential involves natural and climatic factors, while geographical potential involves examining land use and land cover limitations. It is also indicated that market potential involves the demand for energy, competing technologies, and examining corresponding policies and measures.

As previously described, various models are employed for describing wind flow. These models, usually used for micro-siting decisions, can be divided into four categories: conceptual, experimental, statistical, and numerical [8]. As the name implies, conceptual models refer to the basic concepts and discuss how wind flow is affected by the terrain. Some researchers employ conceptual models to quantify the effects of offshore and coastal wind turbines on the ecology. To cite an instance, Wilson et al. [40] employ those models to evaluate the impact of offshore wind turbines and the associated infrastructure (e.g., substations and subsea cables, etc.) on the sea-life.

Experimental models usually involve creating physical models of terrains, and experimentally studying the actual flow. Experimental models are traditionally employed for testing wind turbine designs or validating analytical wind flow models [41,42]. Usually, those designs necessitate the use of wind tunnels or related equipment. Recently, other means have been developed. For example, Conan et al. [43] use the sand erosion model to detect and evaluate high wind speed areas for wind power estimation. This model is low cost, easy to build, and repeatable, and it can be used to estimate the wind characteristics such as the amplification factor and the fractional speed-up ratio.

Statistical models aim at finding the relation between various terrain characteristics (e.g., surface roughness, elevation, and slope exposure) and the wind power [8]. Shahab et al. [44] use parametric and nonparametric statistical approaches for determining the requirements associated with an energy storage system for providing the baseload for

wind farms. Forest et al. [45] employ the multiple kernel learning regression for assessing the wind performance over a complex terrain. Rather than the topographic indexes to obtain the regression equation, their method is based on the support vector regression method. One advantage of the approach is that the algorithm, based on the inclusion of additional data in a nonparametric fashion, actually learns.

Numerical models can be divided into four major groups. The first group is the mass-consistent models, which are formed by the group of equations based on the principle of mass conservation. Those models were developed in the 1970s and 1980s and have been used with success as approximation techniques even for complex terrains. The success is due to their simplicity and the applicability of the physical principles governing the equations [46]. The second generation of the models that are collectively known as the Jackson-Hunt-based approach incorporates the conservation of momentum as well as the conservation of mass by employing Navier−Stokes type of equations [47]. Over the years, the basic theoretical construction has been developed which has led to widely used software packages. Among them, WAsP is a popular choice for micro-siting decisions for wind turbines [48]. The Ms3DJH/3R models are used in conjunction with the mass-consistent models to study boundary layer flow over analytical two-dimensional hills with varying slopes [49]. Raptor Non-linear software is used for modeling the wind flow over steep terrain [50].

Among the Jackson-Hunt-based approach, the WAsP software has been enjoying popularity, especially in Europe. It was first developed by the Technical University of Denmark in 1987 and has been further enhanced over time to incorporate different models for the projection of horizontal and vertical extrapolation of data for application over different types of terrain [51]. Various modules for WAsP have also been developed, such as the functionality to estimate the effects of surface roughness changes and obstacles [8,52].

Recently, the third group of numerical models (i.e., CFD-based approaches) is also gaining popularity thanks to increasing computing power. These approaches are usually aimed at developing a steady-state independent solution for wind and turbulence fields, which can be used for wind power assessment for complex terrains [53]. CFD models make use of the equations based on Reynolds-averaged Navier−Stokes for motion [54]. The CFD-based models can also be used for regions where thermal instability exists [22]. CFD-based approaches on real-life problems have mixed success. While they have been verified in the experimental setting with 2-D and 3-D flow with the steep hills using wind tunnels, researchers report mixed results for wind power estimation for real-life cases [8,55−57].

The fourth group of numerical methods incorporates the mesoscale numerical weather prediction (MNWP) models. Those models are usually employed for weather forecasting, and can also incorporate energy and time. Such models can be used for modeling various atmospheric-related phenomena such as thermally driven mesoscale circulations, atmospheric stability, and buoyancy. Other wind-related characteristics such as pressure, humidity, and temperature can also be modeled. One of the shortcomings is that the computational resource requirements for these models are prohibitively high [14]. A general flowchart for the MNWP model is presented in Fig. 4.3.

Meanwhile, researchers have explored the feasibility of hybrid approaches. There are some applications that combine the MNWP models with the Jackson-Hunt-based models or the mass-consistent models such as the AWS Truepower's MesoMap, Risoe National Laboratory's Karlsruhe Atmospheric Mesoscale Model-WAsP, and Environment Canada's AnemoScope system [59−61].

In addition, spatial extrapolation models can be used for extrapolating the wind data obtained from one wind location to assess the potential at another wind site. Techniques based on statistics or artificial intelligence have been used for this purpose. For instance, Garcia-Rojo [62] employs a procedure based on the calculation of the joint probability distribution of the wind at a local station and a meteorological mast, and compares it with the estimation of a measure-predict-correlate model. Some researchers employ spatial extrapolation models for predicting the wind power in a vertical sense in such a way that the data obtained from a certain height is extrapolated to obtain an estimate for a different height. As an example, Durisic and Mikulovic [63] adopt wind data obtained at three different locations to form a synthetic model using the method of least squares. The proposed approach can also be used as a tool to refine the input for the WAsP model.

4.6 Further considerations for wind speed assessment

Wind turbines are designed to shut off to prevent damage beyond a threshold wind speed. In analyzing extreme winds, An and Pandey [64] compare four different approaches [i.e., Standard Gumbel, Modified Gumbel, Peaks-Over-Threshold (POT), and Method of Independent Storms (MIS)], and conclude that the MIS produces more reliable results as compared to other types of the methods, especially the POT method.

Terrain characteristics are also worth considering. Wind assessment becomes more difficult with increasing terrain complexity; traditional WAsP software works better for flatter terrains. A ruggedness index can be analogously defined

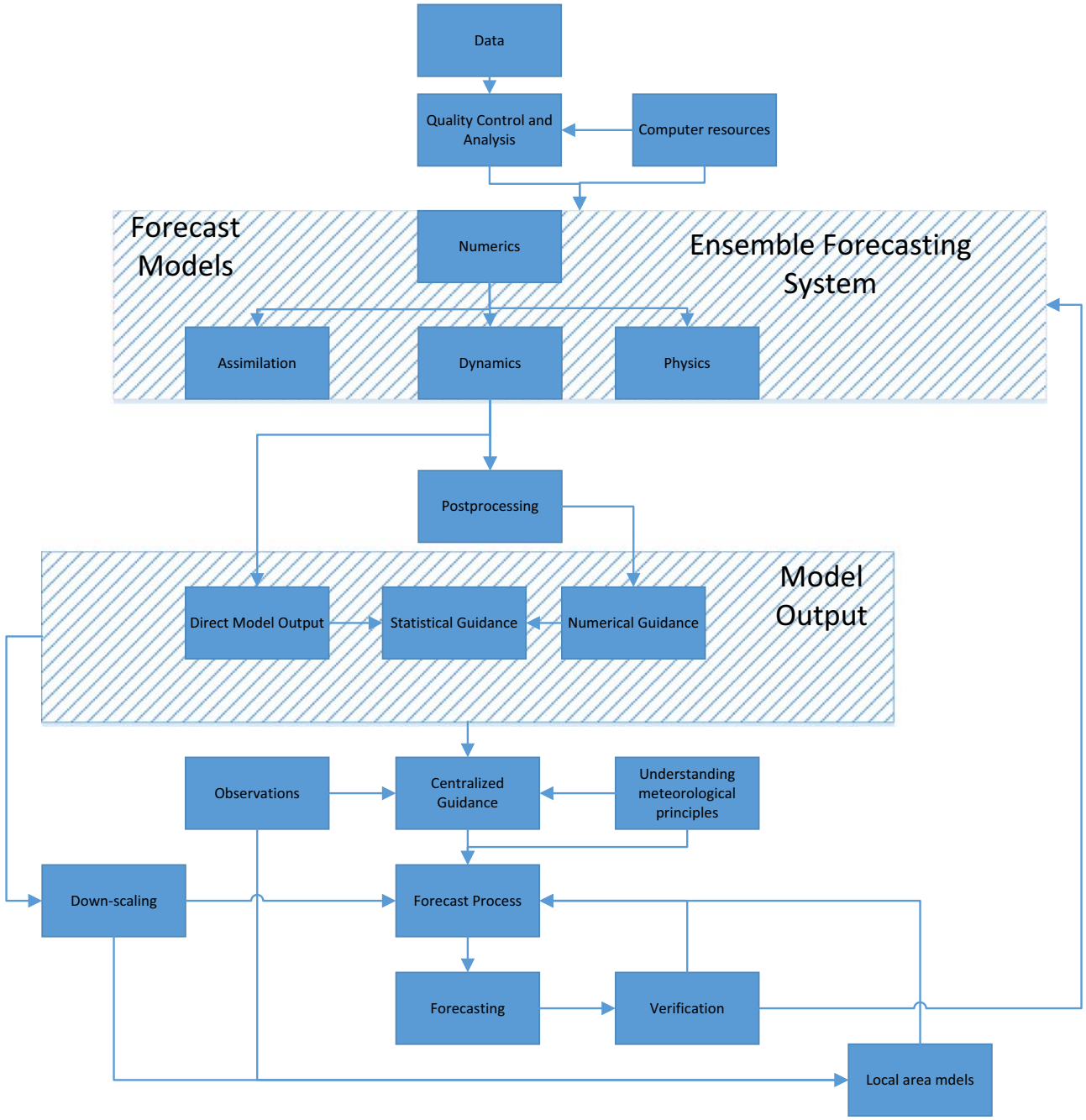

FIGURE 4.3 Components of the mesoscale numerical weather prediction systems [58].

as the percentage of the terrain that has a slope greater than the threshold value. By calculating the index, it is possible to develop correction procedures for the estimates obtained from the WAsP model for more complex terrains [65].

Various sources of uncertainties exist that might impede the accurate assessment of wind potential at a particular site. These uncertainties can be classified as:

- Uncertainties due to the measurement accuracy
- Uncertainties due to historical wind resources
- Uncertainties due to the change in the climate over the long term in the future
- Change of the wind shear
- Wind flow modeling

For a project with a lifespan of 10 years, the total compounded effect of uncertainties from different sources might vary between 4.1% and 7.5% [8].

The estimation of losses affects the wind potential assessment. As a rule of thumb, for the losses associated with a small wind turbine, the theoretical output must be reduced for accommodating real-world operating conditions. This derating factor might reach up to 15%−30%. Usually, the following factors are cited as the sources of losses [66]:

- Density of air: Density of air decreases with the increases in temperature and elevation, and reduced air density leads to a decrease in wind power output.
- Turbine availability: Breakdowns, scheduled, and unscheduled maintenance might decrease the availability of a wind turbine. Various researchers have studied optimal preventive and scheduled maintenance strategies for maximizing turbine availability to minimize losses [67,68].
- Site availability: Due to factors associated with the grid (e.g., brownouts or blackouts), some losses might be encountered. As such, the temperature outside the operating range of the wind turbine might also contribute to the losses. The losses are higher when the electric power is transmitted at lower voltages.
- Site losses: Losses due to transmission of electric energy might be encountered.
- Turbulence: Due to the specific terrain factors, resulting turbulence might reduce wind power by up to 4%.

The wake of the turbines is another factor. It is suggested in the literature that to reduce wake losses at wind farms, turbines should be spaced between 5 and 9 rotor diameters in the prevailing wind direction, and between 3 and 5 rotor diameters in the direction perpendicular to the prevailing wind [64].

4.7 Wind speed and power forecasting

Since wind is an intermittent energy source, predicting a reliable supply of wind power is a challenging task that should be addressed accordingly. Accurate forecasting reduces the uncertainty and streamlines the planning activities associated with the grid. To forecast wind power and speed, numerous methods have been proposed in the literature. Depending on the time horizon associated with the forecasting period, wind forecasting can be divided into four distinct categories [69]:

- **Very short-term forecasting:** The time scale varies between a few seconds to 30 min, and forecasting is usually conducted for the electricity market for clearing and regulatory action.
- **Short-term forecasting:** The time scale is between 30 min and 6 h, and the forecasts are used for making economic load dispatching, and load increment/decrement decisions.
- **Medium-term forecasting:** The forecasting horizon varies between 6 h and 1 day. These forecasts are generally employed for online and offline decisions associated with the generator and operational security in the day ahead markets.
- **Long-term forecasting:** Long-term forecasting entails time period between 1 day and 1 week or more. Usually, this type of forecast is used to assist the decision-making processes for reserve requirement decisions, and maintenance scheduling for minimizing operating cost.

Various methods can be employed in terms of forecasting wind speed. Fig. 4.4 provides an overview of the general classification in the literature. Persistence-based models assume the previous period value as the forecast for a future period. This type of method works well, especially for very short-term and short-term forecasting [71]. This type of model is usually used for benchmarking purposes to test the forecasting quality of other methods.

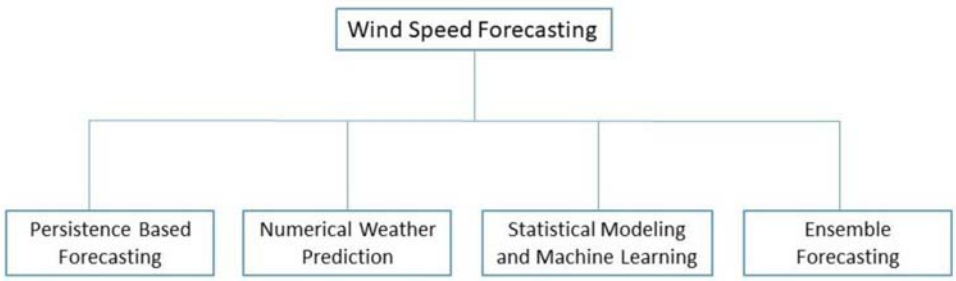

FIGURE 4.4 Classification of wind speed forecasting models [70].

Numerical weather prediction-based methods are usually used for forecasting the local weather and air-related attributes. Various software packages for numerical weather prediction methods have been developed and include the High-Resolution Local Area Model, the hydrostatic ETA model (i.e., a hydrostatic model that employs the eta vertical coordinate), Aire Limitée Adaptation dynamique Développement International model [72–74]. One striking difference between the numerical weather prediction model and the other models is that various wind attributes as well as the speed can be forecasted (e.g., pressure, density, direction, temperature, and humidity). Those models perform pretty well over the long term. However, the forecasts obtained by the numerical weather prediction models depend heavily on the initial conditions; therefore, providing an ensemble forecast increase the reliability. Unfortunately, the use of numerical weather prediction-based methods does require a large amount of computing power, and even with the right set of the inputs, due to the chaotic behavior, forecasting the wind attributes beyond a couple of weeks ahead is not possible. Generally, this model performs well for the long term, but short-term predictions are inferior compared to other methods. Moreover, those models, due to the high cost of collecting the input set and the high computing costs, are only used once or twice daily [65]. Since the numerical weather prediction method serves as a platform for forecasting the future weather state, the output might be further processed to obtain finer estimates with respect to the wind attributes. In that regard, Cassola and Burlando [75] apply the Kalman filtering method for improving the wind speed and wind power forecasts for the very short term. Some researchers also use neural networks for postprocessing model output forecasts obtained from the numerical weather prediction models [76]. In a similar sense, the output of the numerical weather prediction models might be further postprocessed for identifying certain deviating patterns. For instance, Bossavy et al. [77] use the derivative filtering approach for edge detection to characterize ramp events when the power production of the wind turbine significantly deviates from the usual electricity generation pattern.

Statistical and learning-based approaches incorporate various methods from statistics and artificial intelligence. Statistical-based approaches usually incorporate techniques applied on time series data such as Auto Regressive Integrated Moving Average (ARIMA) based methods. There are various implementations of ARIMA-based models in the literature, such as fractional ARIMA-based models and joint Auto Regressive Moving Average (i.e., ARMA) models for predicting wind attributes simultaneously [78,79]. ARMA-based models are based on the previous period's wind speeds/power and past error terms. In general, the ARMA-based model can be expressed as [80]:

$$y_t = \delta + \sum_{i=1}^{p} \phi_i y_{t-i} + \sum_{j=1}^{q} \varphi_j e_{t-j} + e_t, \tag{4.10}$$

where δ is the constant term associated with the stochastic process of the ARMA model, ϕ_i is the ith autoregressive coefficient, φ_j is the coefficient of jth moving average, e_t is the error term at time period t, and y_t represents the value of wind speed observed or forecasted at time period t.

In addition to traditional static ARMA models, researchers have developed dynamic versions for capturing inherent nonstationary wind speeds. In that regard, Huang and Chelebi [81] use the smoothed integrated random walk processes to model the coefficients of model parameters. Recently, there is a growing interest in combining the traditional ARMA-based models with other approaches. In that vein, Liu et al. [82] develop two approaches where the ARMA model is linked with artificial neural network (ANN) and Kalman filter-based methods, and Shi et al. [83] combine ARMA with ANN and support vector machines (SVM) for the same purpose. It is concluded that those models perform well for nonstationary wind speed prediction in wind power systems. The statistical-based methods are not only limited to the ARMA-based models. For instance, Liu et al. [84] adopt the Modified Taylor Kriging model and compare the forecast quality to ARMA-based approaches.

Researchers have also explored the possibility of implementing Auto-Regressive Conditional Heteroskedasticity and Generalized Auto-Regressive Conditional Heteroskedasticity (GARCH) based models for modeling the variability of wind speed. Those variance equations can be incorporated into the mean regression equation and (-M) counterparts can be created in this fashion. Liu et al. compare 10 different ARMA-GARCH(-M) based approaches for modeling the volatility and conclude that no model outperforms the other, and indicate that as the height increased, the power of the model decreased [85]. Those studies are important for providing the interval forecast and calculating the operation probability of the wind turbines and conditionally expected wind output [86,87].

On the other hand, artificial intelligence and machine learning based approaches for predicting the wind speed have found many application areas. In that regard, the ANN is a commonly used approach that has been used to map the random input vector(s) to outputs without prior assumptions of a fixed relationship. The neural network can learn, based on the existing data, discover the hidden patterns, and use the past data to predict future ones. Successful implementations of ANNs for wind speed forecasting exist in the literature [88,89]. Li and Shi [90] compare three different ANNs,

namely adaptive linear element (ADALINE), feed-forward back-propagation, and radial basis function for 1 h ahead of wind speed predictions and concluded that no model outperformed any other, and that wind sites should be evaluated in terms of the performance of the different ANN on a case-by-case approach. Khosravi et al. [91] compare six different customized algorithms namely multilayer feed-forward neural network, support vector regression, fuzzy inference system, adaptive neuro-fuzzy inference system, group method of data handling type neural network, adaptive neuro-fuzzy inference system optimized with genetic algorithms, and adaptive neuro-fuzzy inference system optimized with particle swarm optimization algorithm. The algorithms are tested on four different time intervals for the wind speed data (i.e., 5-min, 10-min, 15-min, and 30-min). It is indicated that group method of data handling type neural network can provide robust results over different datasets, and adaptive neuro-fuzzy inference system optimized with particle swarm optimization and with genetic algorithm optimization provides very accurate results with former outperforming the latter. Li and Jin [92] develop a multiobjective optimization based machine learning approach. Their research incorporates the feature selection methods for choosing most suitable modes for the time series and the optimal input form. On the output side, they implement machine learning and multiobjective optimization for the forecast module. The novelty is that interval estimates are conducted for the wind speed data in addition to point estimates, which address the uncertainty in the forecasts. Luo et al. [93] combine the extreme-learning machine method and deep learning model as the stacked extreme learning. For improving the forecast performance, the Euclidean norm of the mean square error is replaced by the nonlinear similarity measure-generalized correntropy for better handling of the outliers. Li [94] implements a two-stage approach, where the first stage incorporates the geographically weighted ensemble machine learning based on three learners (i.e., autoencoder-based deep residual network, XGBoost, and random forest), and heterogeneity and spatial correlation are also accounted for. The second stage consists of downscaling based on meteorological reanalysis data. Ensemble predictions fare better as compared to individual learner algorithms with an approximately 12%−16% improvement in R^2 and a decrease of 0.14−0.19 m/s in root mean square error based on the data obtained from mainland China.

Some authors also posit that the incorporation of some measure of turbulence or stability as an input parameter is important for improving the quality of the forecasts. In that regard, Optis and Perr-Sauer [95] adopt five machine learning algorithms (i.e., Generalized Additive Model, Neural Network, Gradient Boosting Method, Extremely Randomized Tree, and the SVM), and the authors indicate that the turbulence that can be represented as the ratio of the mean to the standard deviation of the wind speed is found to be the second most significant variable affecting the forecast quality after the wind speed. They report similar performance in the machine learning algorithms that are tested. The results show that the selection of the initial subset of the input parameter is a key component to determine the forecast quality. The conclusion is in parallel with the previous research where wind speed volatility is included in wind speed forecasting in the form of GARCH models. Yu et al. [96] indicate that the wind speed data can be decomposed into several subseries and the recurrent neural networks might be used to extract the features of the low-frequency subseries to be used in the subsequent forecasting stages. Salcedo-Sanz et al. [97] develop a unified search algorithm using the Coral Reefs Optimization Algorithm with the Substrate Layer for feature selection. The authors then employ extreme machine learning and indicate that up to 20% improvements for the prediction of hourly and daily data can be achieved as compared to the models which do not incorporate the feature selection component. Zhu et al. [98] implement a deep learning approach that integrates the convolutional neural network and a multilayer perceptron to capture the Spatio-temporal correlation to provide input for the subsequent phases, and the authors show that the proposed approach performs better as compared to conventional machine learning models, such as multilayer perceptron, support vector regressor, and decision tree. Valsaraj et al. [99] indicate that the neural networks trained in a specific region might be used to predict the wind speed for other geographical locations. The robustness also leads to less computational effort and enhanced speed and productivity. Researchers also compare the traditional statistical methods and machine learning based approaches. To cite an instance, Liu et al. [100] compare the seasonal autoregression moving average method with the deep learning based approaches consisting of the gated recurrent unit and long short-term memory. It is reported that despite the computational intensity of the machine learning approach, the seasonal autoregression moving average based method outperforms the machine learning based approach especially for the offshore region. This might be intuitive based on the fact that the wind flow is more persistent in the offshore location which increases the prediction power of the ARMA-based approaches. However, it should be noted that further research is needed to provide an overall picture for comparison of different approaches, and investigate the flexibility of the traditional statistical-based approach as compared to newer machine learning based approaches.

The wind speed prediction performance of the proposed models over the short-term and long-term forecasting horizon is usually not consistent. Generally, numerical weather prediction (i.e., NWP) based models are better at predicting the medium and long-term wind speed as compared to the statistical model. Research has also been conducted to

address this issue. To cite an instance, Cai et al. [101] combine the SVM, stack de-noising autoencoder, and unscented Kalman filter. The approach is flexible for short-term and long-term forecasting horizon, where SVM and unscented Kalman filter address mainly short-term prediction, whereas stack de-noising auto-encoder based on NWP model output improves the long-term forecasting accuracy. In line with the research on developing effective models that can provide quality forecasts both on short and long-term forecasting horizons, in a subsequent paper, Cai et al. [102] adopt the Multitask Gaussian Process Regression Model to complement the Support Vector Regressor, and report satisfactory results for both short and long-term forecasting horizons. Support Vector Regressor is used to extrapolate the coarse wind speed data obtained at the nodes based on the NWP model to the exact wind turbine location. The authors improve their forecast quality further (i.e., 46% in terms of root mean square error as the performance measure as compared to benchmark models) by adopting smoothing term based on the Bayesian filter in another study [103]. Li et al. [104] incorporate the wind speed turbulence for an integrated recursive neural network and test their approach for prediction of wind speed for an interval ranging from 10 min to 12 h. The results show that incorporating the wind turbulence data significantly improves the model prediction quality, especially for the medium and long term. A similar finding is also reported by Optis and Perr-Sauer [95].

Moreover, Bilgili et al., by using a logistic sigmoid transfer function as an activation function, and resilient propagation as a learning approach, develop a model for forecasting the wind speed based on the data obtained from neighboring locations [105]. Kani and Ardehali [106] combine ANNs and the Markov chain models to develop an integrated approach for very short-term forecasting of wind speed. Li et al. [107] use the novel Markov prediction model to predict wind speed. One of the distinguishing features of the research is that they also incorporate the wind acceleration data in terms of joint distribution that is used to calculate the transition probability matrix. The proposed approach might also be used for assessing the uncertainty. Fadare uses 200-year data obtained from 28 ground stations and develops a 3-layered, feed-forward, backpropagation network with different configurations to forecast the wind speed in Nigeria [108]. There are also other artificial intelligence methods developed for wind speed prediction purposes such as spatial correlation-based approaches, fuzzy logic based approaches, wavelet transforms based approaches, entropy-based training methods [109–111], and SVM approaches [112].

Ensemble forecasting usually involves a large set of runs to predict the wind speed. Those ensemble forecasts are used for examining the future forecasts and the similarities between those outcomes are examined to obtain an insight on the reliability of forecast. As previously indicated, these models are especially useful with NWP-based models [113]. Associated with ensemble forecasting, hybrid methods are also gaining popularity. Usually, hybrid methods fall into two categories. These categories can be expressed as follows [89]:

- Weighting-based approaches
- Other approaches that
  - **a)** Combined approaches including data preprocessing techniques
  - **b)** Combined approaches including parameter selection and optimization techniques
  - **c)** Combined approaches including error processing techniques

Weighting-based algorithms involve the determination of the relative effectiveness of each model and assigning them a value indicating the special importance in the combined models [114]. Han and Liu [115] adopt the maximum entropy principle to obtain weight coefficients for six individual models (persistent, ARIMA, and four ANN-based models) for different prediction horizon times (i.e., between 1 and 6 h). Recently reported research involves the combination of different regression algorithms by means of a so-called Multiple Architecture System (MAS). Bouzgou and Benoudjit [116] implement the MAS to combine different regression models to forecast wind speed. Li et al. [117] develop a two-stage approach where the outputs of the forecasts from different neural networks are combined using Bayesian adaptive combination and concluded that applying Bayesian combination on the top of the individual forecasts can significantly improve the accuracy as compared to forecasts obtained from stand-alone ANNs.

Combined approaches use preprocessing techniques, which involve decomposing the nonlinear wind speed data to stationary and regular subseries and applying filtering techniques for eliminating redundant parts [89]. Wavelet transformation based methods are gaining popularity with these combined techniques. Lei and Ran combine a wavelet transformation with the ARMA model and indicate that the particular combined approach performs better as compared to the stand-alone ARMA-based approaches [118]. Also, Zhang et al. combine a wavelet transformation with an ANN to obtain satisfactory results [119].

On the other hand, other approaches have taken a selection of explanatory variables and determined model parameters [89]. For example, Xingpei et al. [120] employ a back propagation neural network for this purpose, where the initial weights and biases are optimized by employing genetic algorithms. It is indicated that the proposed approach

performs better than the approach using only ANNs. Similarly, other researchers have experimented with a simulated annealing-based approach for finding the parameters of the SVMs [121].

Related research is also conducted based on the postprocessing of the error terms to identify the patterns of systematic underestimation and overestimation. For example, Louka et al. [122] apply the Kalman filtering method to reduce the error terms for two numerical weather prediction models, namely the SKIRON model which is named after the wind blowing from the Scironian rocks in Kineta, and the Greece and Regional Atmospheric Modeling System model. Wang et al. [123] adopt the ARMA models to provide a fit for the wind speed data where the error terms are modeled using the simulated GARCH(1,1) based approach.

4.8 Conclusions

In this chapter, we discuss various aspects of wind power assessment and forecasting. The main principles of developing successful wind assessment programs are outlined. Various models that might be used for the micro-siting decisions (i.e., mass-consistent based methods, Jackson-Hunt-based models, methods based on computational fluid dynamics, spatial correlation-based methods) are discussed. Also, the important aspects of wind resource assessment analysis such as the spacing between wind turbines, uncertainty analysis, and loss estimation are discussed. In the last section, we provide the classification on the types of methods used for wind speed and wind power forecasting. Here, the aim is to reduce the uncertainty in electricity generated from wind-based resources.

It is worth mentioning that a successful wind power assessment program entails the implementation of many tasks such as preliminary wind analysis, selection of wind sites, micro-siting, and the accurate capture of existing wind flow profiles. Not only is the assessment of the wind power but also the accurate forecast of wind speed and wind power are important considerations for tapping the full potential of wind-based resources. The full potential of the wind-based resources on the onshore locations has not been unleashed yet; moreover, recent developments such as floating wind farms that can be constructed in offshore locations further away from the coast can contribute to the proliferation of wind-based energy production. However, global political and economic agendas significantly affect the fate of wind-based energy production. The mandate on fossil fuels and the research on alternative energy sources such as the fusion energy are important considerations that will have a profound impact on the energy sector. There is a myriad of recently developed artificial intelligence-based approaches that promise better wind speed forecasting quality. The input parameter selection is very important on the quality of the wind forecasts, whereas the artificial intelligence−based methods have the upper hand for supporting a higher number of input variables compared to traditional methods. Although those approaches in general provide better results as compared to traditional methods, the findings are not conclusive. Additional research is called for developing a robust somewhat unified methodology that can provide quality forecasts over different regions, time periods, and forecasting horizons. However, due to the chaotic nature of the wind, this remains a challenging task.

References

[1] Wind Denmark. Current energy production, <https://en.winddenmark.dk/wind-in-denmark/current-energy-production>.

[2] Global Wind Energy Council. Global Wind Report, <https://gwec.net/global-wind-report-2021/>; 2021.

[3] US Energy Information Administration. Today in energy, The United States installed more wind turbine capacity in 2020 than in any other year, March 3, 2021, <https://www.eia.gov/todayinenergy/detail.php?id = 46976>.

[4] Bailey B.H., McDonald S.L., Bernadett D.W., Markus M.J., Elsholz K.V. Wind resource assessment handbook. Subcontract No. TAT-5−15283-01; 1997.

[5] Open Energy Information. <http://en.openei.org/doe-opendata/dataset/cecf687d-28e3-4e27-b3a4-269a02acd8a0/resource/190c9a87-e89a-48ef-bf27-68fae2e77bb9/download/global2windmaps.doc>; May 2016.

[6] ESMAP. Energy sector management assistance program, renewable energy resource mapping initiative, <http://esmap.org/RE_mapping>; 2016.

[7] Prasad RD, Bansal RC. Technologies and methods used in wind resource assessment. In: Zobaa Ahmed F, Bansal Ramesh, editors. Handbook of renewable energy technology. Singapore: World Scientific; 2011. p. 69−98. Available from: https://doi.org/10.1142/9789814289078_0004.

[8] New York State Energy Research and Development Authority, Wind resource assessment handbook, Final Report 10−30, <http://www.nyserda.ny.gov/-/media/Files/Publications/Research/Biomass-Solar-Wind/wind-resource-assessment-toolkit.pdf/>; October 2010.

[9] Windustry, Chapter 4: Wind Resource Assessment, May 2016. <http://www.windustry.org/community_wind_toolbox-4-wind-resource-assessment>.

[10] Bennui A, Rattanamanee P, Puetpaiboon U, Phukpattaranont P, Chetpattananondh K. Site selection for large wind turbine using GIS. Proceedings of the *PSU-UNS* international conference on engineering and environment, Phuket, Thailand; 2007.

[11] Lawan SM, Abidin WAWZ, Chai WY, Baharun A, Masri T. The status of wind resource assessment (WRA) techniques, wind energy potential and utilisation in Malaysia and other countries. ARPN J Eng Appl Sci 2013;8(12):1039–53.
[12] Corbett J, Whiting R, Bleeg J, Woodcock J, Horn U, Landberg L, et al. CFD can consistently improve wind speed predictions and reduce uncertainty in complex terrain. Proceedings of European wind energy conference, Copenhagen, Denmark; 2012.
[13] Wang Z, Qin H, Lewis JI. China's wind power industry: policy support, technological achievements, and emerging challenges. Energy Policy 2012;51:80–8.
[14] Brower M. Wind resource assessment: a practical guide to developing a wind project. John Wiley & Sons; 2012.
[15] Enercon. Calculated power curve, Enercon E141, EP4, May 2016. <http://www.enercon.de/en/products/ep-4/e-141-ep4/>.
[16] Gurit.com. Wind turbine blade aerodynamics, May 2016. <http://www.gurit.com/files/documents/2aerodynamicspdf.pdf>.
[17] Rodrigo JS, Guillén FB, Arranz PG, Courtney MS, Wagner R, Dupont E. Multi-site testing and evaluation of remote sensing instruments for wind energy applications. Renew Energy 2013;53:200–10.
[18] Nicholls-Lee R. A low motion floating platform for offshore wind resource assessment using lidars. In: Proceedings of ASME 2013 32nd international conference on ocean, offshore and arctic engineering (pp. V008T09A036-V008T09A036). American Society of Mechanical Engineers, Nantes, France; 2013.
[19] Gadad S, Deka PC. Offshore wind power resource assessment using Oceansat-2 scatterometer data at a regional scale. Appl Energy 2016;176:157–70.
[20] Soukissian T, Karathanasi F, Axaopoulos P. Satellite-based offshore wind resource assessment in the Mediterranean. IEEE J Ocean Eng 2017;42(1):73–86.
[21] AWS Truepower. Wind resource assessment practical guidance for developing a successful wind project, May 2016. <https://www.awstruepower.com/assets/Wind-Resource-Assessment-Practical-Guidance-for-Developing-a-Wind-Project-Brower-Dec20122.pdf>.
[22] Asian Development Bank. Guidelines for wind resource assessment: best practices for countries initiating wind development, May 2016. <http://www.adb.org/sites/default/files/publication/42032/guidelines-wind-resource-assessment.pdf>.
[23] Waewsak J, Chaichana T, Chancham C, Landry M, Gagnonc Y. Micro-siting wind resource assessment and near shore wind farm analysis in Pakpanang District, Nakhon Si Thammarat Province, Thailand. Energy Procedia 2014;52:204–15.
[24] Kim H, Kim B. Wind resource assessment and comparative economic analysis using AMOS data on a 30 MW wind farm at Yulchon district in Korea. Renew Energy 2016;85:96–103.
[25] Landberg L, Myllerup L, Rathmann O, Petersen EL, Jørgensen BH, Badger J, et al. Wind resource estimation—an overview. Wind Energy 2003;6(3):261–71.
[26] Carta JA, Velázquez S, Cabrera P. A review of measure-correlate-predict (MCP) methods used to estimate long-term wind characteristics at a target site. Renew Sustain Energy Rev 2013;27:362–400.
[27] Torres JL, Garcia A, De Blas M, De Francisco A. Forecast of hourly average wind speed with ARMA models in Navarre (Spain). Sol Energy 2005;79(1):65–77.
[28] Jangamshetti SH, Rau VG. Normalized power curves as a tool for identification of optimum wind turbine generator parameters. IEEE Trans Energy Convers 2001;16(3):283–8.
[29] Zhou J, Erdem E, Li G, Shi J. Comprehensive evaluation of wind speed distribution models: a case study for North Dakota sites. Energy Convers Manag 2010;51(7):1449–58.
[30] Erdem E, Shi J. Comparison of bivariate distribution construction approaches for analysing wind speed and direction data. Wind Energy 2011;14(1):27–41.
[31] Yu Z, Tuzuner A. Fractional weibull wind speed modeling for wind power production estimation. In: Proceedings of IEEE power & energy society general meeting, Calgary, Alberta, Canada; 2009.
[32] Li G, Shi J. Application of Bayesian model averaging in modeling long-term wind speed distributions. Renew Energy 2010;35(6):1192–202.
[33] Badger, J, Mortensen N, Hahmann A, Bingol A. Introduction to mesoscale and microscale wind resource mapping. In: Proceedings of mesoscale mapping of RE resources ESMAP knowledge exchange forum, Washington, DC; 2009.
[34] Díaz H, Soares CG. Review of the current status, technology and future trends of offshore wind farms. Ocean Eng 2020;209:107381.
[35] Tong D, Farnham DJ, Duan L, Zhang Q, Lewis NS, Caldeira K, et al. Geophysical constraints on the reliability of solar and wind power worldwide. Nat Commun 2021;12(1):1–12.
[36] Lu X, McElroy MB, Kiviluoma J. Global potential for wind-generated electricity. Proc Natl Acad Sci 2009;106(27):10933–8.
[37] Bosch J, Staffell I, Hawkes AD. Temporally explicit and spatially resolved global offshore wind energy potentials. Energy 2018;163:766–81.
[38] US Department of the Interior. Bureau of ocean energy management, renewable energy on the outer continental shelf, <https://www.boem.gov/renewable-energy/renewable-energy-program-overview>.
[39] Hoogwijk M, Graus W. Global potential of renewable energy sources: a literature assessment. Background Report Prepared by Order of REN21. Ecofys, PECSNL072975; 2008.
[40] Wilson JC, Elliott M, Cutts ND, Mander L, Mendão V, Perez-Dominguez R, et al. Coastal and offshore wind energy generation: is it environmentally benign? Energies 2010;3(7):1383–422.
[41] Battisti L, Benini E, Brighenti A, Castelli MR, Dell'Anna S, Dossena V, et al. Wind tunnel testing of the DeepWind demonstrator in design and tilted operating conditions. Energy 2016;111:484–97.
[42] Barranger N, Ternisien T, Kallos G. An intercomparison study between RAMS and CRES-Flow-NS models and evaluation with wind tunnel experimental data: Toward improving atmospheric modeling for wind resource assessment. J Wind Eng Ind Aerodyn 2015;142:272–88.
[43] Conan B, van Beeck J, Aubrun S. Sand erosion technique applied to wind resource assessment. J Wind Eng Ind Aerodyn 2012;104:322–9.

[44] Shahab S, Jozani MJ, Bibeau E, Molinski M. A statistical algorithm for predicting the energy storage capacity for baseload wind power generation in the future electric grids. Energy 2015;89:793–802.
[45] Foresti L, Tuia D, Kanevski M, Pozdnoukhov A. Learning wind fields with multiple kernels. Stoch Environ Res Risk Assess 2011;25(1):51–66.
[46] Ratto CF, Festa R, Romeo C, Frumento OA, Galluzzi M. Mass-consistent models for wind fields over complex terrain: the state of the art. Environ Softw 1994;9(4):247–68.
[47] Jackson PS, Hunt JCR. Turbulent wind flow over low hill. Q J R Meteorol. Soc 1975;101:929–55.
[48] Nouri A, Babram MA, Elwarraki E, Enzili M. Moroccan wind farm potential feasibility. Case study. Energy Convers Manag 2016;122:39–51.
[49] Finardi S, Brusasca G, Morselli MG, Trombetti F, Tampieri F. Boundary-layer flow over analytical two-dimensional hills: a systematic comparison of different models with wind tunnel data. Boundary-Layer Meteorol 1993;63(3):259–91.
[50] Ayotte KW. A nonlinear wind flow model for wind energy resource assessment in steep terrain. Proceedings of global windpower conference. Paris, France; 2002.
[51] Petersen EL, Mortensen NG, Landberg L, Højstrup J, Frank HP. Wind power meteorology. Risø Natl Laboratory, Roskilde, Denmark, Technical Doc No Risø-I-1206 (EN) 1997.
[52] Miljødata EO. Case studies calculating wind farm production-Main Report. Denmark: Energi- og Miljødata;; 2002.
[53] Berge E, Gravdahl AR, Schelling J, Tallhaug L, Undheim O. Wind in complex terrain. A comparison of WAsP and two CFD-models. Proc EWEC 2006;27 Athens, Greece.
[54] Toja-Silva F, Peralta C, Lopez-Garcia O, Navarro J, Cruz I. Roof region dependent wind potential assessment with different RANS turbulence models. J Wind Eng Ind Aerodyn 2015;142:258–71.
[55] Bitsuamlak GT, Stathopoulos T, Bédard C. Numerical evaluation of wind flow over complex terrain: review. J Aerosp Eng 2004;17:135–45.
[56] Murakami S, Mochida A, Kato S. Development of local area wind prediction system for selecting suitable site for windmill. J Wind Energy Ind Aerodyn 2003;91:1759–75.
[57] Sumner J, Watters CS, Masson C. CFD in wind energy: the virtual, multiscale wind tunnel. Energies 2010;3:989–1013.
[58] Comet Meted, NWP and ensemble model systems forecast, May 2016. <http://www.meted.ucar.edu/nwp/model_fundamentals/navmenu.php> [accessed 31.05.16].
[59] Brower M, Validation of the windmap program and development of MesoMap. In: Proceeding from AWEA's WindPower conference. Washington, DC, USA; 1999.
[60] Frank HP, Rathmann O, Mortensen N, Landberg L. The numerical wind atlas, the KAMM/WAsP method. Riso-R-1252 report from the Risoe National. Laboratory, Roskilde, Den 2001;59.
[61] Yu W, Benoit R, Girard C, Glazer A, Lemarquis D, Salmon JR, et al. Wind energy simulation toolkit (WEST): a wind mapping system for use by the wind-energy industry. Wind Eng 2006;30:15–33.
[62] García-Rojo R. Algorithm for the estimation of the long-term wind climate at a meteorological mast using a joint probabilistic approach. Wind Eng 2004;28(2):213–23.
[63] Đurišić Ž, Mikulović J. A model for vertical wind speed data extrapolation for improving wind resource assessment using WAsP. Renew Energy 2012;41:407–11.
[64] An Y, Pandey MD. A comparison of methods of extreme wind speed estimation. J Wind Eng Ind Aerodyn 2005;93(7):535–45.
[65] Mortensen NG, Bowen AJ, Antoniou I. Improving WAsP predictions in (too) complex terrain. In: Proceedings of the European wind energy conference and exhibition, Athens, Greece; 2006.
[66] Northern Power Systems, Engineering bulletin, Energy production estimating. Estimating annual energy production from a Northern Power® NPS 100™ wind turbine; May 2016. <http://www.northernpower.com/wp-content/uploads/2014/10/NPS-White-Paper-Energy-Production-Estimating.pdf>.
[67] Byon E, Ntaimo L, Ding Y. Optimal maintenance strategies for wind turbine systems under stochastic weather conditions. IEEE Trans Reliab 2010;59(2):393–404.
[68] Andrawus J, Watson J, Kishk M. Wind turbine maintenance optimisation: principles of quantitative maintenance optimisation. Wind Eng 2007;31(2):101–10.
[69] Soman SS, Zareipour H, Malik O, Mandal P. A review of wind power and wind speed forecasting methods with different time horizons. In: Proceedings of North American Power Symposium (NAPS), IEEE, Arlington, Texas, USA; 2010.
[70] Foley AM, Leahy PG, Marvuglia A, McKeogh EJ. Current methods and advances in forecasting of wind power generation. Renew Energy 2012;37(1):1–8.
[71] Lei M, Shiyan L, Chuanwen J, Hongling L, Yan Z. A review on the forecasting of wind speed and generated power. Renew Sustain Energy Rev 2009;13(4):915–20.
[72] Källén E. HIRLAM documentation manual, System 2.5, Technical Report. S-60176 Norrköping, Sweden; 1996.
[73] Lazić L, Pejanović G, Živković M. Wind forecasts for wind power generation using the Eta model. Renew Energy 2010;35(6):1236–43.
[74] Bubnova R, Hello G, Bénard P, Geleyn J-F. Integration of the fully-elastic equations cast in the hydrostatic pressure terrain-following coordinate in the framework of the ARPEGE/ALADIN NWP system. Monthly Weather Rev 1995;123:515–35.
[75] Cassola F, Burlando M. Wind speed and wind energy forecast through Kalman filtering of Numerical Weather Prediction model output. Appl Energy 2012;99:154–66.
[76] De Giorgi MG, Ficarella A, Tarantino M. Assessment of the benefits of numerical weather predictions in wind power forecasting based on statistical methods. Energy 2011;36(7):3968–78.

[77] Bossavy A, Girard R, Kariniotakis G. Forecasting ramps of wind power production with numerical weather prediction ensembles. Wind Energy 2013;16(1):51–63.
[78] Kavasseri RG, Seetharaman K. Day-ahead wind speed forecasting using f-ARIMA models. Renew Energy 2009;34(5):1388–93.
[79] Erdem E, Shi J. ARMA based approaches for forecasting the tuple of wind speed and direction. Appl Energy 2011;88(4):1405–14.
[80] Montgomery DC, Jennings CL, Kulahci M. Introduction to time series analysis and forecasting. John Wiley & Sons; 2015.
[81] Huang Z, Chalabi ZS. Use of time-series analysis to model and forecast wind speed. J Wind Eng Ind Aerodyn 1995;56(2):311–22.
[82] Liu H, Tian HQ, Li YF. Comparison of two new ARIMA-ANN and ARIMA-Kalman hybrid methods for wind speed prediction. Appl Energy 2012;98:415–24.
[83] Shi J, Zeng S. Evaluation of hybrid forecasting approaches for wind speed and power generation time series. Renew Sustain Energy Rev 2012;16(5):3471–80.
[84] Liu H, Shi J, Erdem E. Prediction of wind speed time series using modified Taylor Kriging method. Energy 2010;35(12):4870–9.
[85] Liu H, Erdem E, Shi J. Comprehensive evaluation of ARMA–GARCH (-M) approaches for modeling the mean and volatility of wind speed. Appl Energy 2011;88(3):724–32.
[86] Liu H, Shi J, Qu X. Empirical investigation on using wind speed volatility to estimate the operation probability and power output of wind turbines. Energy Convers Manag 2013;67:8–17.
[87] Liu H, Shi J, Erdem E. An integrated wind power forecasting methodology: interval estimation of wind speed, operation probability of wind turbine, and conditional expected wind power output of a wind farm. Int J Green Energy 2013;10(2):151–76.
[88] Salcedo-Sanz S, Perez-Bellido AM, Ortiz-García EG, Portilla-Figueras A, Prieto L, Paredes D. Hybridizing the fifth generation mesoscale model with artificial neural networks for short-term wind speed prediction. Renew Energy 2009;34(6):1451–7.
[89] Tascikaraoglu A, Uzunoglu M. A review of combined approaches for prediction of short-term wind speed and power. Renew Sustain Energy Rev 2014;34:243–54.
[90] Li G, Shi J. On comparing three artificial neural networks for wind speed forecasting. Appl Energy 2010;87(7):2313–20.
[91] Khosravi A, Machado L, Nunes RO. Time-series prediction of wind speed using machine learning algorithms: A case study Osorio wind farm, Brazil. Appl Energy 2018;224:550–66.
[92] Li R, Jin Y. A wind speed interval prediction system based on multi-objective optimization for machine learning method. Appl Energy 2018;228:2207–20.
[93] Luo X, Sun J, Wang L, Wang W, Zhao W, Wu J, et al. Short-term wind speed forecasting via stacked extreme learning machine with generalized correntropy. IEEE Trans Ind Inform 2018;14(11):4963–71.
[94] Li L. Geographically weighted machine learning and downscaling for high-resolution spatiotemporal estimations of wind speed. Remote Sens 2019;11(11):1378.
[95] Optis M, Perr-Sauer J. The importance of atmospheric turbulence and stability in machine-learning models of wind farm power production. Renew Sustain Energy Rev 2019;112:27–41.
[96] Yu C, Li Y, Bao Y, Tang H, Zhai G. A novel framework for wind speed prediction based on recurrent neural networks and support vector machine. Energy Convers Manag 2018;178:137–45.
[97] Salcedo-Sanz S, Cornejo-Bueno L, Prieto L, Paredes D, García-Herrera R. Feature selection in machine learning prediction systems for renewable energy applications. Renew Sustain Energy Rev 2018;90:728–41.
[98] Zhu Q, Chen J, Zhu L, Duan X, Liu Y. Wind speed prediction with spatio–temporal correlation: a deep learning approach. Energies 2018;11(4):705.
[99] Valsaraj P, Alex Thumba D, Satheesh Kumar K. Spatio-temporal independent applicability of one time trained machine learning wind forecast models: a promising case study from the wind energy perspective. Int J Sustain Energy 2022;1–19.
[100] Liu X, Lin Z, Feng Z. Short-term offshore wind speed forecast by seasonal ARIMA-A comparison against GRU and LSTM. Energy 2021;227:120492.
[101] Cai H, Jia X, Feng J, Yang Q, Hsu YM, Chen Y, et al. A combined filtering strategy for short term and long term wind speed prediction with improved accuracy. Renew Energy 2019;136:1082–90.
[102] Cai H, Jia X, Feng J, Li W, Hsu YM, Lee J. Gaussian Process Regression for numerical wind speed prediction enhancement. Renew Energy 2020;146:2112–23.
[103] Cai H, Jia X, Feng J, Yang Q, Li W, Li F, et al. A unified Bayesian filtering framework for multi-horizon wind speed prediction with improved accuracy. Renew Energy 2021;178:709–19.
[104] Li F, Ren G, Lee J. Multi-step wind speed prediction based on turbulence intensity and hybrid deep neural networks. Energy Convers Manag 2019;186:306–22.
[105] Bilgili M, Sahin B, Yasar A. Application of artificial neural networks for the wind speed prediction of target station using reference stations data. Renew Energy 2007;32(14):2350–60.
[106] Kani SP, Ardehali MM. Very short-term wind speed prediction: a new artificial neural network–Markov chain model. Energy Convers Manag 2011;52(1):738–45.
[107] Li W, Jia X, Li X, Wang Y, Lee J. A Markov model for short term wind speed prediction by integrating the wind acceleration information. Renew Energy 2021;164:242–53.
[108] Fadare DA. The application of artificial neural networks to mapping of wind speed profile for energy application in Nigeria. Appl Energy 2010;87(3):934–42.

[109] Alexiadis MC, Dokopoulos PS, Sahsamanoglou HS. Wind speed and power forecasting based on spatial correlation models. IEEE Trans Energy Convers 1999;14(3):836–42.
[110] Damousis IG, Dokopoulos P. A fuzzy expert system for the forecasting of wind speed and power generation in wind farms. Proceedings of power industry computer applications, 2001. In: PICA 2001. Innovative computing for power-electric energy meets the market. 22nd IEEE power engineering society international conference on (pp. 63–69). IEEE, Sydney, Australia; 2001.
[111] Liu D, Niu D, Wang H, Fan L. Short-term wind speed forecasting using wavelet transform and support vector machines optimized by genetic algorithm. Renew Energy 2014;62:592–7.
[112] Zhou J, Shi J, Li G. Fine tuning support vector machines for short-term wind speed forecasting. Energy Convers Manag 2011;52(4):1990–8.
[113] Giebel G, Badger J, Landberg L, Nielsen HA, Nielsen T, Madsen H, et al. Wind power prediction ensembles, Report 1527. Risø National Laboratory, Denmark; 2005.
[114] Sánchez I. Short-term prediction of wind energy production. Int J Forecast 2006;22:43–56.
[115] Han S, Liu Y. The study of wind power combination prediction. In: Proceedings of the Asia-Pacific power and energy engineering conference (APPEEC), Chengdu, China, 2010.
[116] Bouzgou H, Benoudjit N. Multiple architecture system for wind speed prediction. Appl Energy 2011;88:2463–71.
[117] Li G, Shi J, Zhou J. Bayesian adaptive combination of short-term wind speed forecasts from neural network models. Renew Energy 2011; 36(1):352–9.
[118] Lei C, Ran L. Short-term wind speed forecasting model for wind farm based on wavelet decomposition. In: Proceedings of the third international conference on electric utility deregulation and restructuring and power technologies (DRPT), NanJing, China; 2008.
[119] Zhang X, Chongchong C, Wang W, Dai Y. The intelligent methods used in prediction the wind speed and output power of wind farm. In: Proceedings of the Asia-Pacific power and energy engineering conference (APPEEC), Shanghai, China; 2012.
[120] Xingpei L, Yibing L, Weidong X. Wind speed prediction based on genetic neural network. In: Proceedings of the 4th IEEE conference on industrial electronics and applications (ICIEA), Hangzhou, China; 2009.
[121] Hui T, Dongxiao N. Combining simulate anneal algorithm with support vector regression to forecast wind speed. In: Proceedings of the second IITA international conference on geoscience and remote sensing (IITA-GRS), Qingdao, China; 2010.
[122] Louka P, Galanis G, Siebert N, Kariniotakis G, Katsafados P, Pytharoulis I, et al. Improvements in wind speed forecasts for wind power prediction purposes using Kalman filtering. J Wind Eng Ind Aerodyn 2008;96(12):2348–62.
[123] Wang MD, Qiu QR, Cui BW. Short-term wind speed forecasting combined time series method and arch model. In: Proceedings of the international conference on machine learning and cybernetics (ICMLC), Xian, China; 2012.

Chapter 5

Global potential for wind-generated electricity

Xi Lu[1] and Michael B. McElroy[2]

[1]School of Environment and State Key Joint Laboratory of Environment S imulation and Pollution Control, Tsinghua University, Beijing, P. R. China, [2]Harvard John A. Paulson School of Engineering and Applied Sciences, Department of Earth and Planetary Sciences, Harvard University, Cambridge, MA, United States

5.1 Introduction

Fossil fuels—coal, oil, and natural gas—currently account for close to 80% of total global primary consumption of energy and for the bulk of emissions of the key greenhouse gas CO2. The nations of the world at the 21st meeting of the Conference of the Parties to the UN Framework Convention on Climate Change in Paris in December 2015 committed to restricting future greenhouse gas emissions to ensure that the consequent increase in global average surface temperature should be limited to 2°C or less referenced with respect to conditions that applied in the preindustrial era. Meeting this objective will require no less than a sea change in the manner in which the world sources future energy [1]. Physical prospects for growth in hydro and biomass are limited. Nuclear is expensive. Geothermal could play a role though major investments in relevant research and development will be required to realistically evaluate its potential. The best options, given current understanding, involve combinations of wind and solar. This chapter offers an assessment of the overall wind potential.

The energy absorbed by the earth from the sun over the course of a year totals approximately 3.9×10^{24} J (3.7 million quads where 1 quad = 10^{15} BTU and 1 BTU = 1055.06 J). To place this number in context, the total energy consumed globally by humans amounted to 5.66×10^{20} J (536.9 quads) in 2014, a little more than 1 part in 10,000 of the total supplied by the sun. The solar energy absorbed by the earth is realized primarily initially as heat, manifest in the atmosphere as internal energy (IE) complemented by a source of potential energy supplied by evaporation of water. A fraction of IE (approximately 40%) is converted to potential energy (PE), energy the air includes by virtue of its elevation relative to the surface. The fraction of the energy of the atmosphere manifest in kinetic form (KE), wind, is extremely small relative to either IE or PE. It accounts for as little as 763.8×10^{18} J (724 quads), 0.06% of the total energy content of the atmosphere. It is replaced, however, on average every 6.9 days implying a global annual source of about 4.04×10^{22} J (38,300 quads), approximately 73 times the total global demand for commercial energy, 466 times global consumption of energy in the form of electricity.

There are two important sources for KE in the atmosphere: one results from work supplied by the force of gravity acting to change the elevation of specific air masses; the second relates to work performed by the force associated with spatial gradients of pressure driving air across isobars, causing it to move from regions of high to regions of low pressure. Dissipation by friction in the near-surface environment, at altitudes below about 1 km, is responsible for approximately 50% of the net global sink for KE with the balance contributed by viscous dissipation of small-scale turbulent elements at higher altitudes [2]. Huang and McElroy [3] using a temperature-pressure-wind record based on reanalysis of meteorological data covering the period January 1979 to December 2010, concluded that work supplied by gravitational and pressure forces was responsible for a globally averaged net source of KE equal to 2.46 W/m^2 over this time interval, slightly more in the southern hemisphere, less in the north (2.49 W/m^2 as compared to 2.44 W/m^2) [3]. As indicated earlier, this source would be sufficient to supply a quantity of kinetic energy significantly greater than the energy implicated in current demand for electricity or even in the demand for energy in all forms. Only a fraction of this global supply could be harnessed of course under realistic circumstances to produce electricity.

Wind Energy Engineering. DOI: https://doi.org/10.1016/B978-0-323-99353-1.00033-5

The electricity generated from an individual turbine is determined ultimately by the kinetic energy intercepted by the blades of the turbine. This depends in turn on the area swept out by the blades, on the density of the air intercepted by the blades, and on the cube of the wind speed (a factor proportional to the square of the wind speed defining the kinetic energy contained in a given volume of air, an additional factor to specify the rate at which this energy may be delivered to the turbine). In general, the greater the elevation of the rotor and the greater the diameter of the blades, the greater is the potential yield of electricity. Wind speeds increase typically as a function of elevation accounting for the advantage of the first of these considerations. The area intercepted by the blades of the turbine varies in proportion to the square of the diameter of the rotor accounting for the advantage of the second. In practice, there is a range of wind speeds over which a typical turbine may be expected to operate economically. At low speeds, frictional losses would be sufficient to offset any potential production of electricity. If wind speeds are too high, operation of the turbine could be hazardous and the blades are typically feathered to avoid damage. The quantity of electricity produced as a function of wind speed for a particular turbine design is defined in terms of what is referred to as the power curve. Power curves for the two representative turbine designs considered below, the GE 2.5 and 3.6 MW models, are displayed in Fig. 5.1.

The yield of electricity anticipated from a particular wind farm depends on several factors, including the quality of the wind resource, the design of the turbines included in the facility, and spacing between the turbines. The choice of spacing reflects a tradeoff involving considerations of costs for individual turbines, costs for development of the site, and costs for laying power cables, in addition to costs anticipated for routine operation and maintenance of the facility. Turbines must be spaced to minimize interference in airflow due to interactions among individual turbines. This requires a compromise between the objective of maximizing the power generated per turbine and the competing incentive to maximize the number of turbines sited per unit area.

Two sources of data have been employed in the literature to evaluate the global potential for generation of electricity from wind. One is based on surface and/or sounding measurements of winds. The second makes use of what is referred to as assimilated meteorological data, with wind speeds derived from retrospective analysis of global meteorological data using a state-of-the-art weather/climate model incorporating inputs from a wide variety of observational sources [5] including not only surface and sounding measurements but also results from a diverse suite of measurements and observations taken from a combination of aircraft, balloons, ships, buoys, dropsondes and satellites—in short, the gamut of all of the observational data employed to provide the world with the best possible meteorological forecasts, enhanced by the application of these data in a retrospective analysis. The former approach was adopted by Archer and Jacobsen

	GE 2.5 Turbine	GE 3.6 Turbine
Power Curve	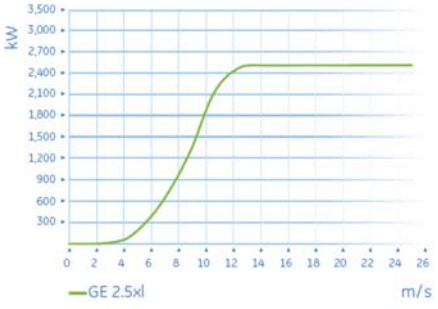	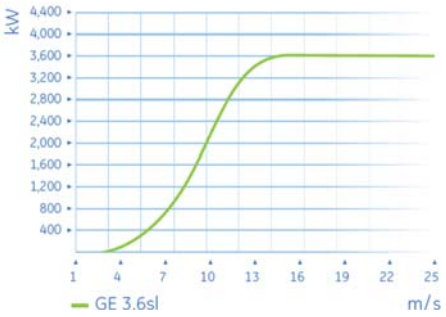
Technical Parameter	• Cut-in Wind Speed: 3.5 m s^{-1} • Cut-out Wind Speed: 25 m s^{-1} • Rated Wind Speed: 12.5 m s^{-1} • Rotor Diameter(D): 100 m	• Cut-in Wind Speed: 3.5 m s^{-1} • Cut-out Wind Speed: 27 m s^{-1} • Rated Wind Speed: 14 m s^{-1} • Rotor Diameter(D): 111 m

FIGURE 5.1 Power curves and representative technical parameters for the two GE turbines selected for purposes of the present investigation [4].

in their pioneering early study of potential global wind resources [6]. The latter was favored by Lu et al. and provides the basis for the bulk of the results discussed below [4].

The study by Archer and Jacobsen used data for the year 2000 incorporating inputs from 7753 individual surface meteorological stations complemented by results from 446 stations for which vertical soundings were available [6]. They restricted their attention to power that could be generated using a network of 1.5 MW turbines tapping wind resources from regions with annually averaged wind speeds in excess of 6.9 m/s (wind class 3 or better) at an elevation of 80 m. The meteorological stations employed in their analysis were concentrated to a significant extent in the United States, Europe, and Southeastern Asia. As a consequence, results inferred for other regions are subject to considerable uncertainty. To estimate the wind potential at a particular location, Archer and Jacobson used six empirical functions to develop the best least square fit to wind profiles observed at individual neighboring stations for which information was available from soundings [6]. They used an inverse square approach to average data from the five closest meteorological stations to select input for the wind profile adopted to calculate the power potential at a particular sample location. They argued that the estimates for wind power derived using this approach should be conservative on the low side for two reasons: first, the potential for bias introduced by the use of the least square methodology should trend in that direction; second, the fact that the meteorological stations employed in the analysis were not selected optimally to capture most favorable wind conditions. They concluded that 20% of the total available global wind power potential could be tapped to provide as much as 123 PW h of electricity annually, seven times total global consumption, comparable to the consumption of energy globally in all forms [6].

We outline in the next section the procedures adopted by Lu et al. [4] in their study of global wind potential. Results are presented and discussed in the sections that follow. The final section addresses limitations in our ability to respond definitively to the challenges posed in the title of this chapter: to define the ultimate global potential for the generation of electric power using wind.

5.2 Methodology

The Lu et al. study took advantage of a simulation of global wind fields provided by Version 5 of the Goddard Earth Observing System Data Assimilation System (GEOS-5 DAS) [4]. The GEOS-5 analysis employs a terrain-following coordinate system defined by 72 vertical layers extending from the surface to a pressure level of 0.01 hPa (an altitude of approximately 78.2 km) [5]. Pressure levels are selected to resolve features of the atmosphere including both troposphere and stratosphere. Individual volume elements are defined in terms of their horizontal boundaries (latitude and longitude) and by the pressures at their top and bottom. The horizontal resolution of the simulation is 2/3-degree longitude by 1/2-degree latitude (equivalent to approximately 67 km by 50 km at mid-latitudes). The model provides 3-dimensional pressure fields at both layer centers and at layer edges, in addition to wind speeds (meridional and zonal) and temperatures at the midpoint of individual layers with a time resolution of 6 h. The three lowest layers are centered at altitudes of approximately 71, 201, and 332 m. The 6-h data for the three lowest layers were employed in the Lu et al. [4] analysis using an interpolation scheme described as follows to estimate temperatures, pressures, and wind speeds at 100 m, the hub height for the 2.5 and 3.6 MW turbines considered as representative and illustrative for purposes of the present discussion.

Knowing the values of pressures at the lower and upper edges of individual layers, together with temperatures and pressures at the midpoints of the layers, Lu et al. [4] calculated altitudes corresponding to the mid-points of the layers using an iterative application of the barometric law assuming a linear variation of temperature between the midpoints of the individual layers. The barometric law was applied also to calculate the pressure at 100 m. Wind speeds and temperatures at 100 m were computed using a cubic spline fit to the corresponding data at the midpoints of the three lowest layers.

The power curves reported by the General Electric Company for the turbine models considered here assume an air density of 1.225 kg/m^3 under conditions corresponding to an air temperature of 15°C at a pressure of 1 atmosphere [7]. To account for the differences in air density at the rotor elevations as compared to this standard, wind speeds in the published power/wind speed curves (Fig. 5.1) were adjusted according to Eq. (5.1).

$$V_{corrected} = \left(\frac{P}{1.225 \bullet R \bullet T}\right)^{1/3} V_{original} \tag{5.1}$$

where P and T identify air pressures and temperatures at the hub height and R denotes the gas constant, 287.05 N m (kg/K) for dry air.

In estimating the global potential for wind-generated electricity, it will be important to exclude locations for which it would be either impractical or uneconomic to install turbines. To this end, Lu et al. [4] elected to eliminate areas classified as forested, areas occupied by permanent snow or ice, and areas identified as either developed or urban. They were guided in their selection of locations for turbine deployment by data from the Moderate-Resolution Imaging Spectroradiometer (MODIS) instruments included in the payloads of NASA's Terra and Aqua satellites.

MODIS provides a record of the spatial distribution of different types of land cover observed over the Earth in 2001. Following a classification introduced by the International Geosphere-Biosphere Programme, the record identifies 17 categories of land cover including 11 different classes of natural vegetation, 3 classes of developed areas, and 3 classes identifying areas occupied by permanent snow or ice (notably Greenland and Antarctica). It singles out also regions classified as barren, areas with at most a sparse coverage of vegetation, and regions covered by water. It pinpoints regions identified as either urban or heavily developed. The horizontal resolution of the record is approximately 1 km by 1 km. Lu et al. [4] used the MODIS record to exclude from their analysis areas classified as forested, areas occupied by permanent snow or ice, areas covered by water, and areas identified as either developed or urban. Environments identified by Lu et al. as inappropriate for wind resource development are indicated in Fig. 5.2.

Topographic relief data for both land and ocean areas were derived using the Global Digital Elevation Model (GTOPO30) of the Earth Resources Observation and Science Data Center of the U.S. Geological Survey. The spatial resolution of this data source for offshore environments (bottom topography) as applied here is approximately 1 km by 1 km [8]. Several factors conspire to limit the development of offshore wind farms. Esthetic considerations, for example, have restricted the development of wind resources in the near-shore environment in the United States (the Cape Wind controversy as a case in point) [9] although objections to near-shore installations in Europe appear to have been less influential. There is a need further to accommodate requirements for shipping, fishing, and for wildlife reserves and to minimize potential interference with radio and radar installations. To account for these limitations, Musial and colleagues, in studies of the offshore wind power potential for the contiguous United States, chose to exclude the placement of wind farms within 9.3 km (5 M where M refers to nautical mile) of shore and to limit development to 33% of the area between 9.3−37 km (5 and 20 M) offshore while expanding potential development to 67% of the area between 37−92.6 km (20 and 50 M) [9−12].

The expense of installing wind turbines offshore generally increases as a function of water depth and as a function of distance from shore. General Electric recommends that its turbines should be installed using state-of-the-art monopole structures fixed to the seabed for water depths less than 20 m. Water jacket tripod or quadruped structures can support towers in waters up to 50 m [13,14]. For greater depths, it is necessary to resort to floating structures using technology developed by the oil and gas extraction industry [15]. Experience with the use of floating structures in the

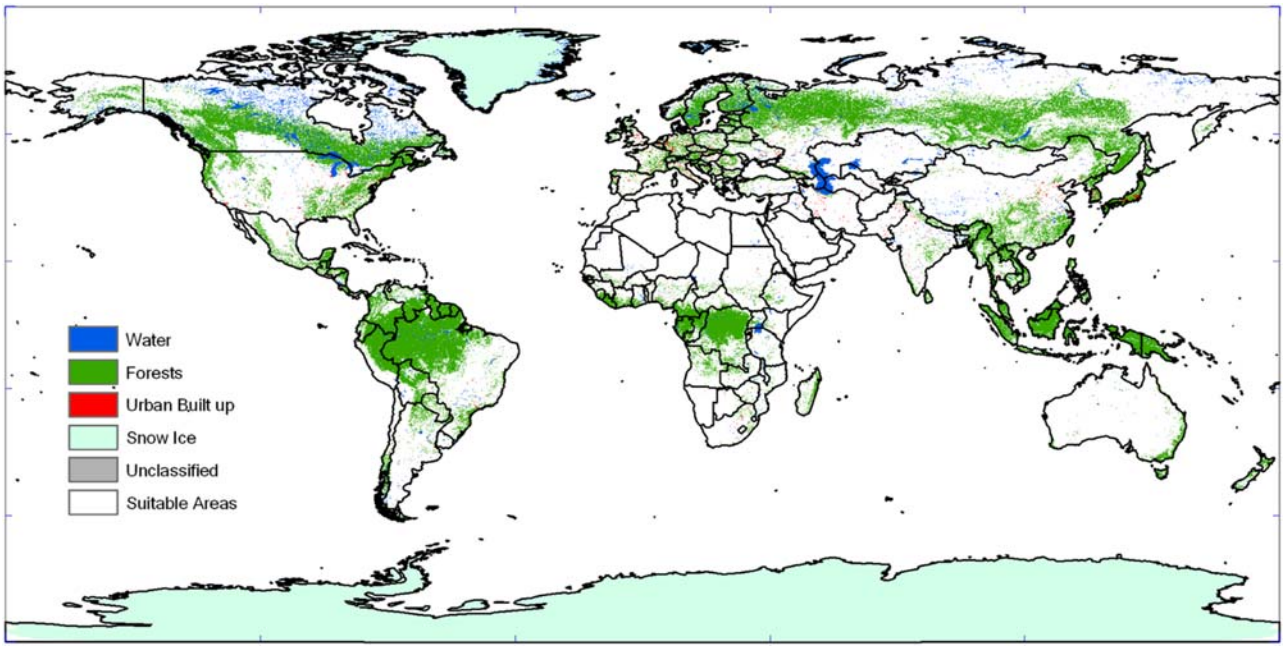

FIGURE 5.2 Global map of areas considered unsuitable for onshore wind turbine installation [4].

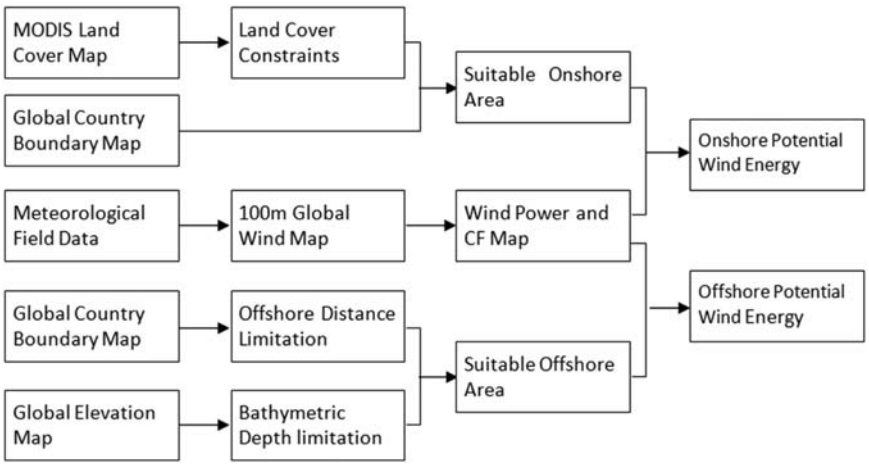

FIGURE 5.3 Schematic summary of the approach adopted to calculate potential wind energy both onshore and offshore [4].

wind power business is relatively limited to date but its development is not expected to pose insuperable problems in the future, although it will certainly be more expensive.

Lu et al. [4], followed by Dvorak et al. [14], considered three possible regimes for offshore development of wind power defined by water depths of 0−20 m, 20−50 m, and 50−200 m. Somewhat arbitrarily, they limited the potential deployment of wind farms to distances within 92.6 km (50 M) of the nearest shoreline, assuming that 100% of the area occupied by these waters could be available for development. A schematic summary of the approach they adopted in calculating wind power potential both onshore and offshore is presented in Fig. 5.3.

A further consideration in estimating the total global potential for wind-generated electricity concerns the criteria adopted to determine the spacing of turbines in particular wind farms. Restricting downstream interturbine wake power loss to less than 20% requires a downwind spacing of more than seven turbine rotor diameters with cross-wind spacing of at least four diameters [6,16]. Applying this constraint to the 2.5 MW GE turbines [17] (rotor diameter 100 m, radius 50 m) selected as representative for onshore wind deployment implies an interturbine spacing of one per 0.28 km^2. Given the much higher expense for the development of off-shore wind farms, Lu et al. [4] elected to impose a greater relative spacing in this case in order to limit interturbine interference to less than 10%. This translates to a requirement for an interturbine spacing of 5×10 rotor diameters. Assuming deployment of GE 3.6 MW turbine [18] (rotor diameter 111 m, radius 55.5 m), positioning of turbines, in this case, should be restricted to one every 0.62 km^2. The results presented in what follows reflect these assumptions.

5.3 Results

5.3.1 Global perspective

We restrict attention in what follows to locations in which wind conditions are projected to allow for the turbine choices considered here to function on an annual basis with capacity factors of no less than 20%.

Results on a country-by-country basis are summarized in Fig. 5.4A and B for onshore and offshore environments, respectively. Placement of the turbines onshore and offshore was restricted as discussed above. Table 5.1 presents a summary of results for the ten countries identified as the largest national emitters of CO_2. The data included here refer to national reporting of CO_2 emissions in 2012 and electricity consumption for these countries in 2011. Wind power potential for the world as a whole and for the contiguous United States is summarized in Table 5.2.

If the top ten CO_2 emitting countries were ordered in terms of wind power potential, Russia would rank number one, followed by Canada with the United States in the third position. There is an important difference to be emphasized, however, between wind power potential in the abstract and the fraction of the resource that is likely to be developed when subjected to realistic economic constraints. Much of the potential for wind power in Russia and Canada is located at large distances from population centers. Given the inevitably greater expense of establishing wind farms in remote locations and potential public opposition to such initiatives, it would appear unlikely that these resources will be developed in the near term. Despite these limitations, it is clear that wind power could make a significant contribution to the demand for electricity for the majority of the countries listed in Table 5.1, in particular for the four largest CO_2 emitters—China, the United States, India, and Russia. However, it should be noted that the resource for Japan is largely

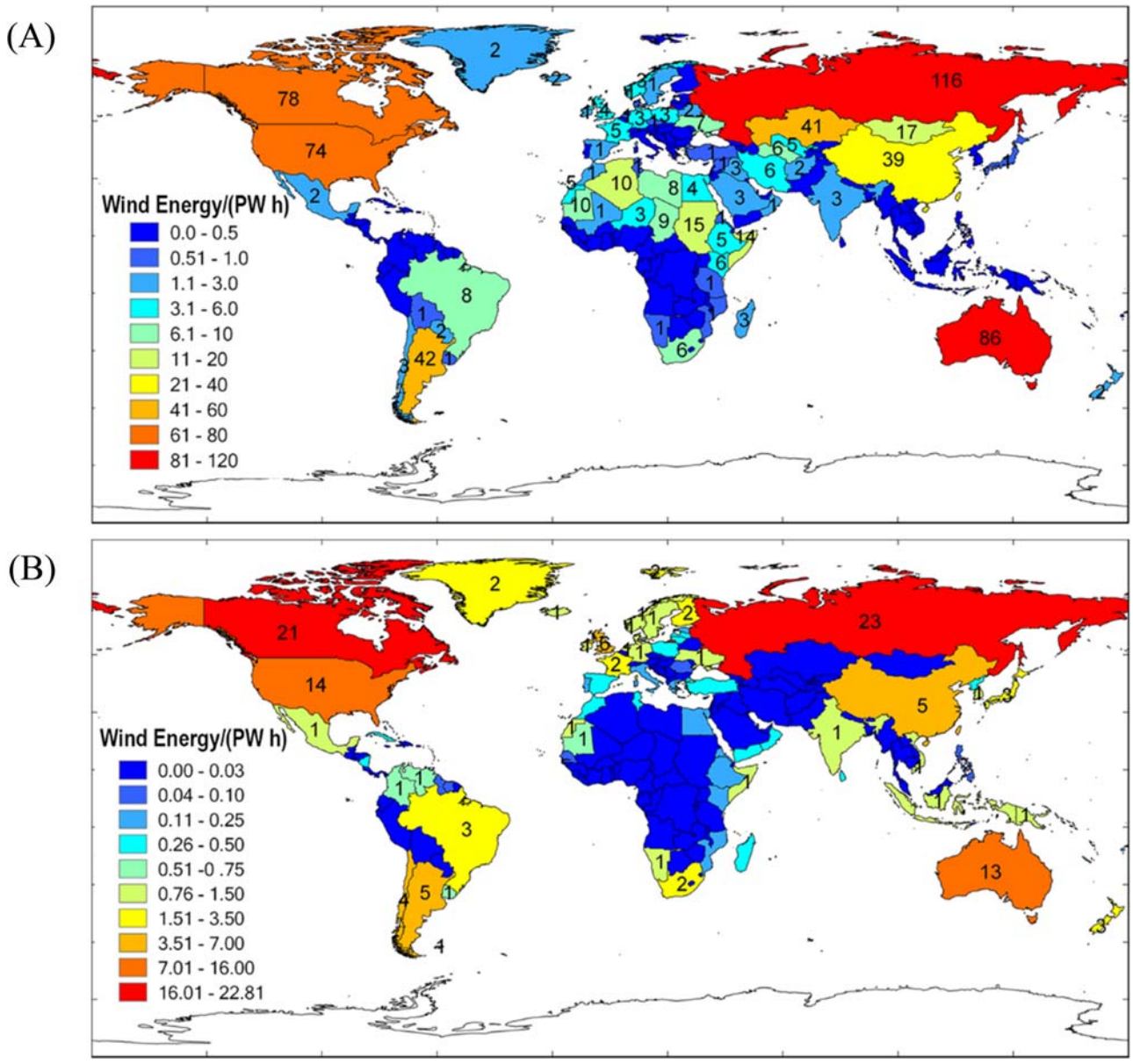

FIGURE 5.4 Annual wind energy potential country by country, restricted to installations with capacity factors greater than 20% with siting limited as discussed in the text: (A) onshore, (B) offshore [4].

confined to the offshore area, 82% of the national total. To fully exploit these global resources will require, inevitably, significant investment in transmission systems capable of delivering this power to regions of high load demand. Results for the contiguous United States and for China will be discussed in more detail in the following sections.

The electricity that could be generated potentially on a global basis using wind, displayed as a function of an assumed capacity factor cutoff on installed turbines, is presented in Fig. 5.5A and B for onshore and offshore environments respectively. The results in Fig. 5.5A suggest that the total current global consumption of electricity could be supplied by the wind while restricting the installation of land-based turbines to regions characterized by the most favorable wind conditions, regions where the turbines might be expected to function with capacity factors greater than 53%. If the cutoff capacity factor were lowered to 36%, the energy content of electricity generated using wind with land-based turbines globally would be equivalent to the total current global consumption of energy in all forms. Cutoff capacity factors needed to accommodate similar objectives using offshore resources would need to be reduced, as indicated in Fig. 5.5B. To place these considerations in context, we would note that capacity factors realized by turbines installed recently in the United States (in 2004 and 2005) have averaged close to 36% [21].

TABLE 5.1 Onshore and offshore wind potential for the 10 countries identified as the largest national emitters of CO_2 [4].

No	Country	CO_2 emission/ (10^6 metric tons)	Elec. consumption/ (TW h)	Potential wind energy/(TW h)		
				Onshore	Offshore	Total
1	China	8547.7	4207.7	39,000	4600	44,000
2	United States	5270.4	3882.6	74,000	14,000	89,000
3	India	1830.9	757.9	2900	1100	4000
4	Russia	1781.7	869.3	120,000	23,000	140,000
5	Japan	1259.1	983.1	570	2700	3200
6	Germany	788.3	537.9	3200	940	4100
7	S. Korea	657.1	472.2	130	990	1100
8	Iran	603.6	185.8	5600	–	5600
9	Saudi Arabia	582.7	211.6	3000	–	3000
10	Canada	499.1	551.6	78,000	21,000	99,000

Note: CO_2 emission for 2012 and electricity consumption for 2011, data source from CDIAC [19] and US EIA [20].

TABLE 5.2 Annual wind energy potential for installations onshore and offshore for the world as a whole and for the contiguous US analysis.

Areas		World wide		Contiguous United States	
		No CF limitation	20% CF limitation	No CF limitation	20% CF limitation
Energy (onshore areas)/(PW h)		1100	690	84	62
Energy (offshore areas)/(PW h)	0–20 m	47	42	1.9	1.2
	20–50 m	46	40	2.6	2.1
	50–200 m	87	75	2.4	2.2
Energy total/(PW h)		1300	840	91	68

The analysis assumes a loss of 20% and 10% of potential power for onshore and offshore respectively due to interturbine interference [4].
Note: All data assume offshore location distance within 92.6 km (50 nautical miles) of the nearest shoreline.

5.3.2 US perspective

An estimate of the electricity that could be generated for the contiguous United States every month (subject to the siting and capacity limitations noted above) is illustrated for both onshore and offshore environments in Fig. 5.6. Results presented here were computed using wind data for 2006. Not surprisingly, the wind power potential for both environments is greatest in winter, peaking in January, lowest in summer, with a minimum in August. Onshore potential for January, according to the results presented in Fig. 5.6, exceeds that for August by a factor of 2.5: the corresponding ratio computed for offshore locations is slightly larger, 2.9.

Fig. 5.6 also includes monthly data for consumption of electricity in the United States during 2006. Demand for electricity exhibits a bimodal variation over the course of a year with peaks in summer and winter, and minima in spring and fall. Demand is greatest in summer during the air conditioning season. Summer demand exceeds the minimum in spring/fall demand typically by between 25% and 35% on a US national basis depending on whether summers are unusually warm or relatively mild. The correlation between the monthly averages of wind power production and

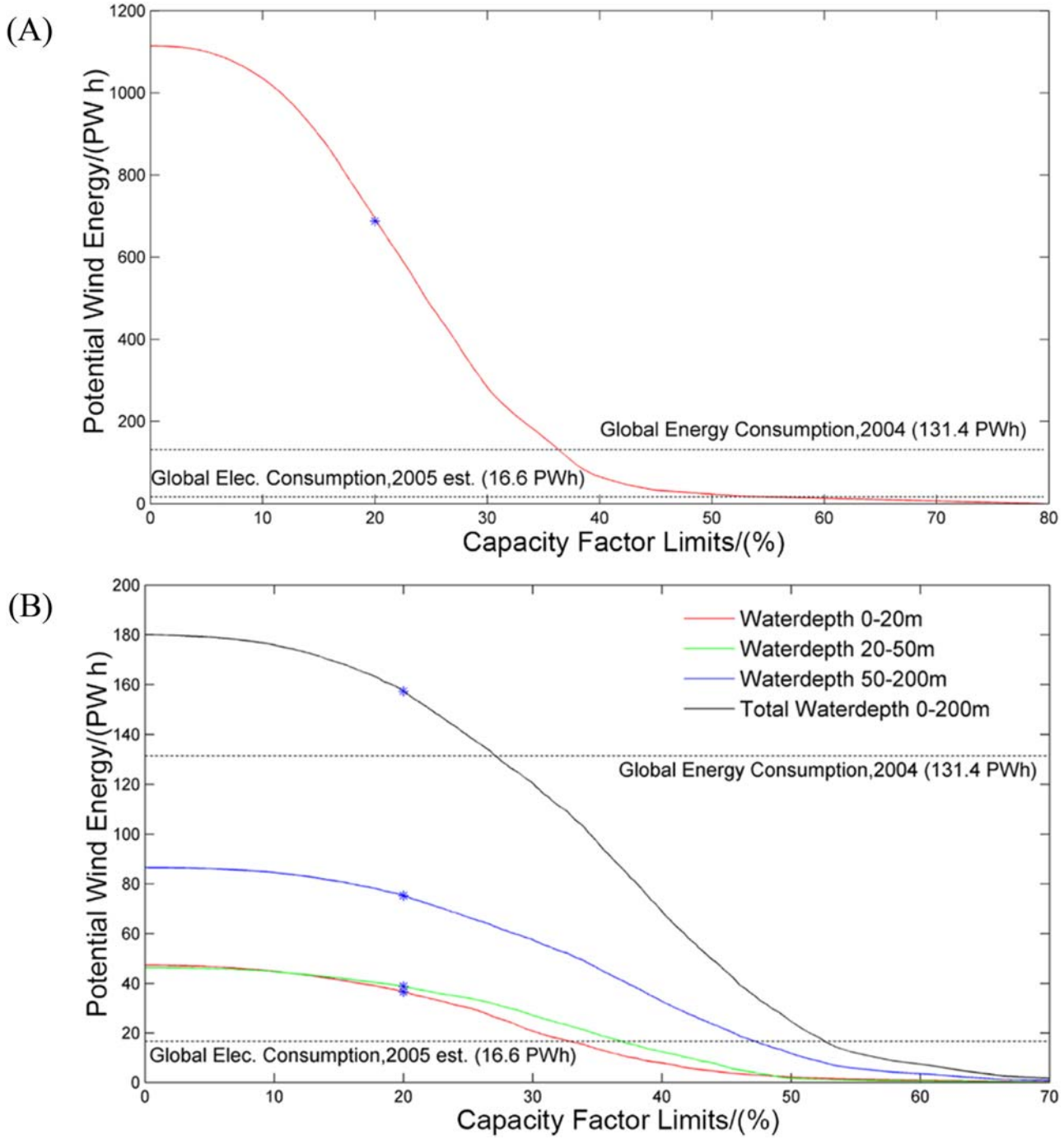

FIGURE 5.5 Annual wind energy potential as a function of assumed limits on capacity factors. Results corresponding to the capacity factor limit of 20% assumed in this study are indicated by *: (A) global onshore, (B) global offshore [4].

electricity consumption is negative. Very large wind power penetration can produce excess electricity during large parts of the year. This situation could allow options for the conversion of electricity to other energy forms. Plug-in electric vehicles, for example, could take advantage of short-term excesses in electricity systems, while energy-rich chemical species such as H_2 could provide a means for longer-term storage.

Potential wind-generated electricity available from onshore facilities on an annually averaged state-by-state basis is presented in Fig. 5.7A. Note the high concentration of the resource in the central plains region extending northward from Texas to the Dakotas, westward to Montana and Wyoming, and eastward to Minnesota and Iowa. The resource in

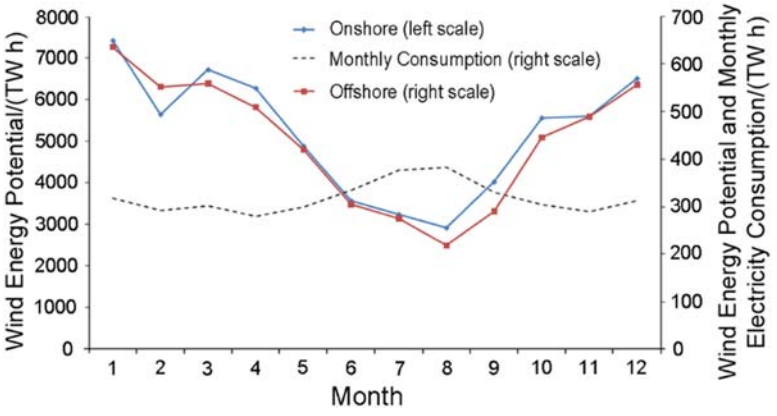

FIGURE 5.6 Monthly wind energy potential for the contiguous United States in 2006 with monthly electricity consumption for the entire United States [4].

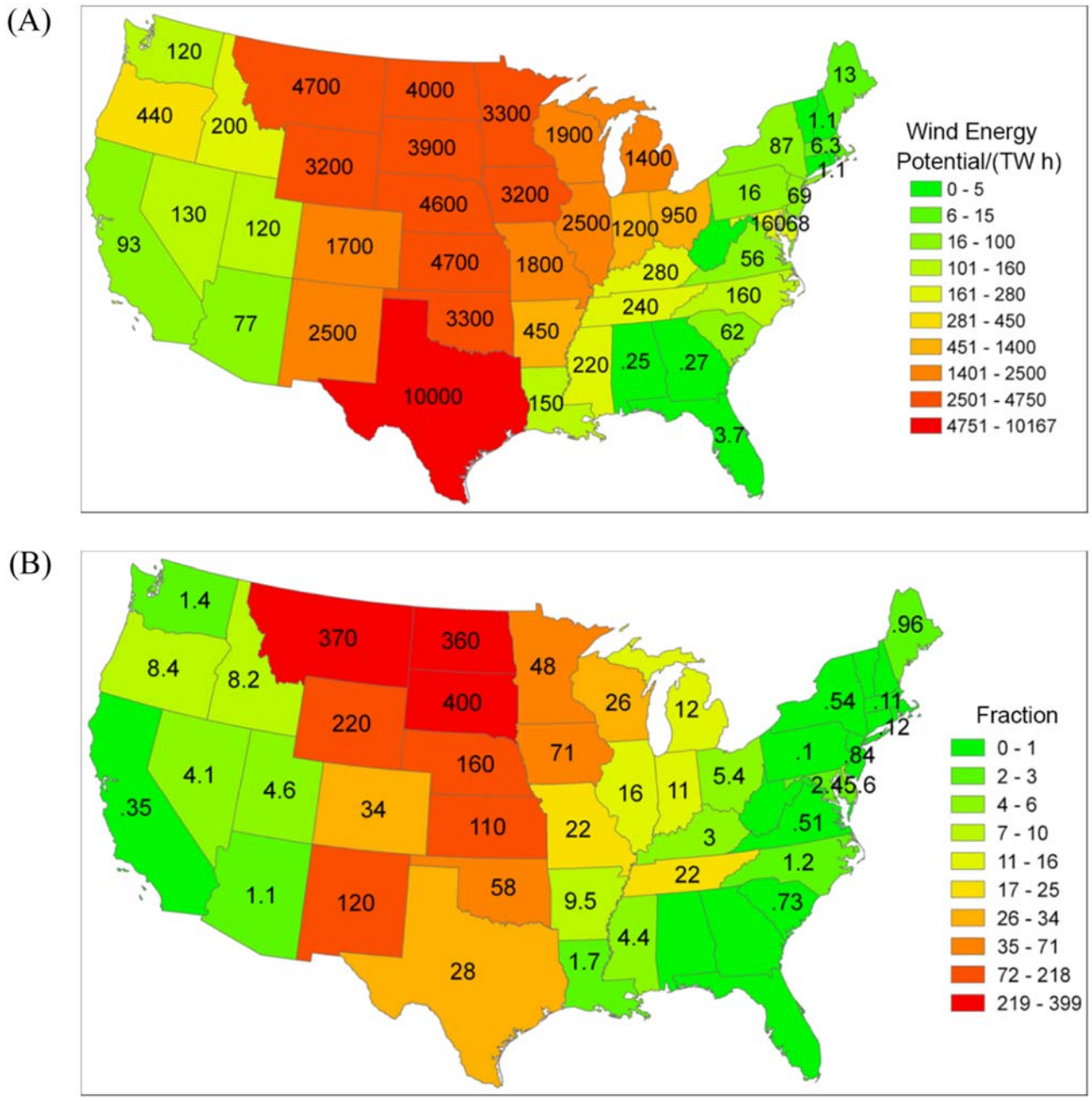

FIGURE 5.7 (A) Annual onshore wind energy potential on a state-by-state basis for the contiguous United States (B) Same with A, but expressed as a fraction of total electricity retail sales in the states (2006) [4]. For example, the potential source for North Dakota exceeds the current total electricity retail sales in that State by a factor of 360. *Data for total electricity retail sales from http://www.eia.doe.gov.*

this region, as illustrated in Fig. 5.7B, is significantly greater than the current local demand. Important exploitation of this resource will require, however, a significant extension of the existing power transmission grid. Expansion and upgrading of the grid will be required in any event to meet anticipated future growth in electricity demand. It will be important in planning for this expansion to recognize from the outset the need to accommodate contributions of power from regions rich in potential renewable resources, not only wind but also solar. The additional costs need not, however, be prohibitive [21]. ERCOT, the operator responsible for the bulk of electricity transmission in Texas, estimates the extra cost to transmit up to 4.6 GW of wind-generated electricity at about \$180 KW^{-1}, approximately 10% of the capital cost for installation of the wind power-generating equipment [22].

An important issue relating to the integration of electricity derived from wind into a grid incorporating contributions from a variety of sources relates to the challenge of matching supply with load demand incorporating a contribution from the supply that is intrinsically variable both in time and space and subject to prediction errors. This challenge can be mitigated to some extent if the variations of wind sources contributing to an integrated transmission grid from different regions are largely uncorrelated. An anomalously high contribution from one region can be compensated in this case by an anomalously low contribution from another. To investigate the significance of this potential compensation, Lu et al. [4] examined the covariance of wind resources from three specific regions, one in Montana, the second in Minnesota, and the third in Texas, as indicated in Fig. 5.8. Analysis of 6-h averaged potential wind-generated supplies of electricity from the three regions over the four seasons, winter, spring, summer and fall, yielded the results summarized in Table 5.3. Contributions from the three regions are essentially uncorrelated during the winter months (October through March) with r values of less than 0.07. Correlation coefficients (r values), however, are relatively high in summer (July through September) with values ranging from 0.28 (Montana versus Texas) to 0.37 (Montana versus Minnesota) with intermediate values in spring. The analysis suggests that wind power could make a relatively reliable contribution to anticipated base load demand in winter. It may be more difficult to incorporate wind power resources into projections of base load demand for other seasons, particularly for summer.

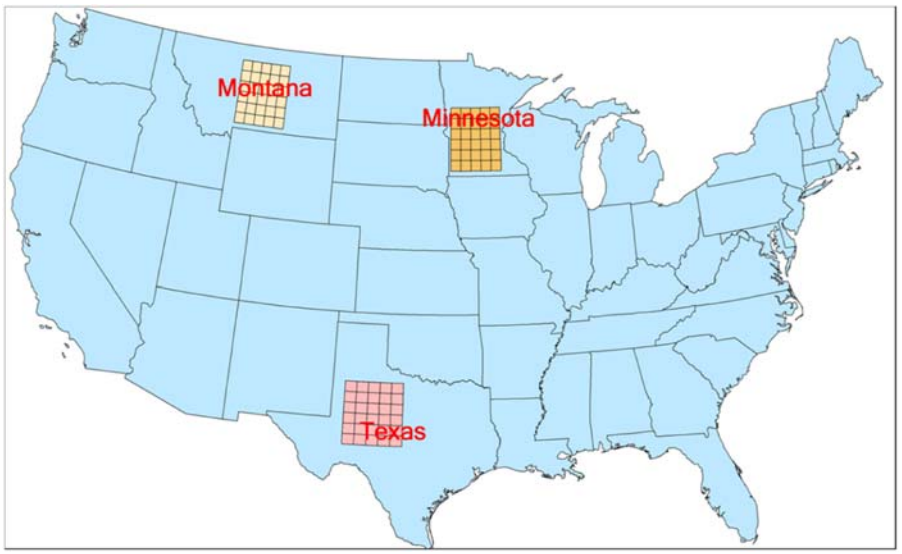

FIGURE 5.8 Locations of regions in Montana, Minnesota, and Texas were selected to explore the spatial correlation of wind resources [4].

TABLE 5.3 Correlations of wind power potential between selected regions of Montana (MT), Minnesota (MN), and Texas (TX) in different seasons for 2006 [4].

Correlation Coefficient (r)	Jan–Mar	Apr–Jun	Jul–Sep	Oct–Dec
MN-MT	0.027	0.11	0.37	−0.15
MN-TX	0.069	0.29	0.29	−0.060
MT-TX	0.065	0.26	0.28	−0.0024

5.3.3 China perspective

McElroy et al. [23] applied the assimilated meteorology data resource, as described earlier, to assess also the potential for wind-generated electricity in China. The approach they followed, in this case, was generally similar to that adopted for the global and US applications described by Lu et al. [4]. In particular, they elected to exclude as possible sites for turbine deployment forested areas, areas occupied by permanent snow or ice, areas covered by water, and areas identified as either developed or urban. They excluded in the Chinese application also land areas with slopes larger than 20% [21]. Recognizing that turbine sizes installed in China are generally smaller than those favored in the United States, they chose to focus their study on the deployment of a suite of 1.5 MW turbines, selecting for this purpose the GE 1.5 MW axle design [24]. The hub height for this model is 80 m and the rotor diameter measures 82.5 m. The spacing between turbines in representative wind farms was selected similar to that adopted for wind farms installed in Inner Mongolia, with 9 rotor diameters in the downwind direction, 5 rotor diameters in the direction perpendicular to the prevailing wind ($9D \times 5D$), slightly larger than the spacing of $7D \times 4D$, adopted by Lu et al. [4]. Overall power loss due to turbine−turbine interactions with the spacing assumed in the China application is estimated at about 10% [25].

The spatial distribution of capacity factors (CF's) evaluated for the deployment of the 1.5 MW turbines considered here is illustrated in Fig. 5.9. CF defines the fraction of the rated power potential of a turbine that is actually realized over the course of a year given expected variations in wind speed. CF values for wind farms deployed in Inner Mongolia, as illustrated for example in Fig. 5.9, are estimated to reach values as high as 40% indicating that 1.5 MW turbines installed in this region could potentially provide as much as 5.26 GW h of electricity over the course of a year. Wind conditions are notably favorable, and CF values are consequently large, over extensive regions of northern China (Inner Mongolia, Heilongjiang, Jilin, and Liaoning) and in parts of the west (Tibet, Xinjiang, Qinghai, and Gansu). Wind farms deployed recently in the United States have achieved operational CFs as high as 48%, with an average of close to 35% [26]. By way of comparison, CFs for wind farms installed in China has been significantly lower than for the United States, close to 23% on average [27]. The relatively low operational performance of wind farms in China is attributed to a combination of factors: lower quality of the largely and domestically produced turbines deployed in China as compared with turbines available on the international market; bottlenecks introduced by limitations imposed by the existing Chinese electricity grid; and suboptimal siting of wind farms due to inadequate prior screening of potentially available wind resources [28].

Electricity that could be generated from wind irrespective of price, restricted, however, to installations capable of operating with CF's greater than 20%, is illustrated for the existing seven electric grid areas of China in Fig. 5.10. The figure also includes results expressed as ratios with respect to the current production of electricity in these grid regions. The data displayed here suggest that a suite of 1.5 MW turbines deployed in onshore regions with favorable wind resources could provide potentially as much as 24.7 PW h of electricity annually, more than 7 times current national Chinese consumption.

Demand for electricity in China is spread more evenly throughout the year as compared to the United States where demand peaks in summer. The pattern for China reflects the fact that the largest fraction of electricity in the country is used by industry (70%) as compared to only 29% for industry in the United States where electricity demand is spread

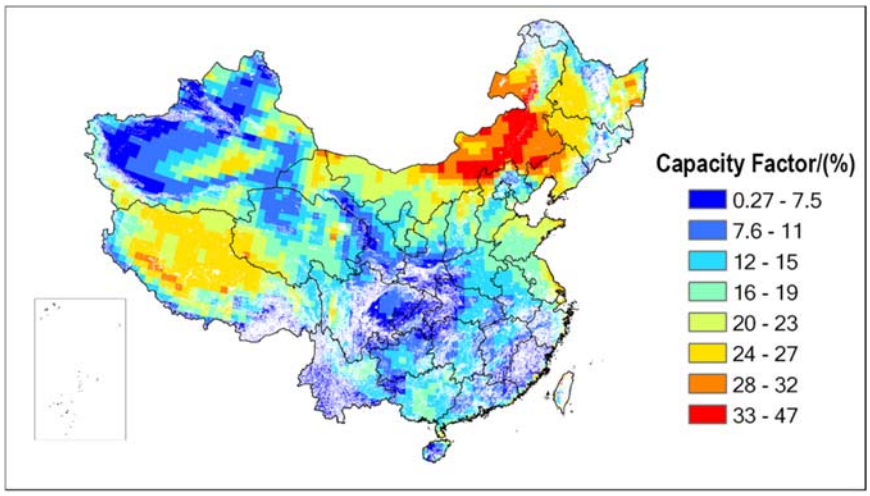

FIGURE 5.9 Spatial distribution of capacity factors (CFs) evaluated for deployment of the 1.5 MW turbines [23].

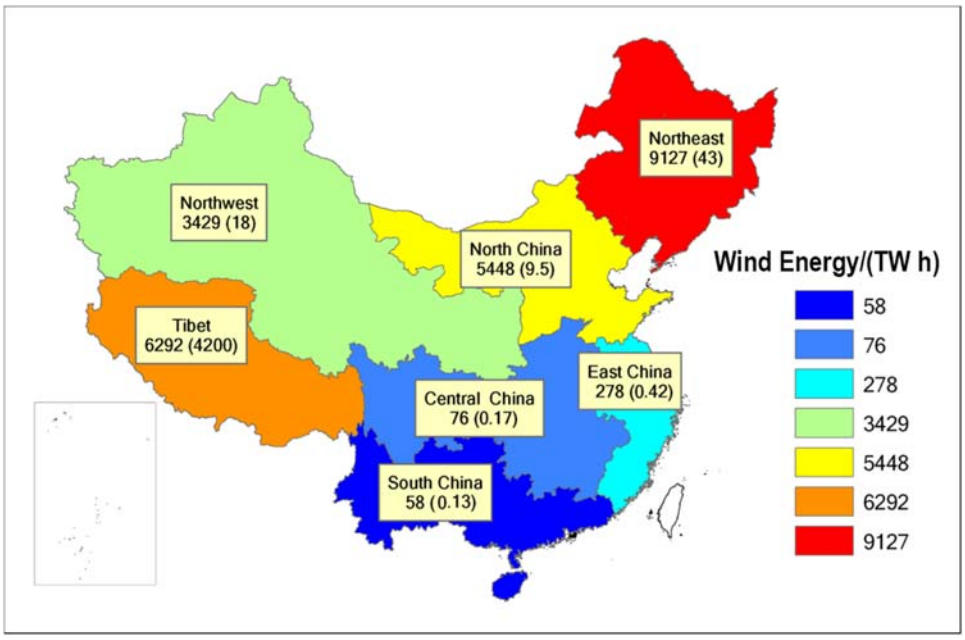

FIGURE 5.10 Potential electricity irrespective of price that could be generated over the 7 electric grid areas of the Chinese mainland [23].

more evenly among residential, commercial, and industrial usage. Incorporating baseload sources of electricity from coal-fired power plants poses relatively minor problems for grid managers charged with matching supplies of electricity with demand. Adjusting to an important, intrinsically variable, supply such as that from wind will require a more complex, and consequently more costly, grid management protocol.

Operators of an electric utility face a formidable and continuing challenge to ensure that the production of electricity is targeted in real time to meet projected demand. In a typical power system, nuclear and coal-fired systems provide sources of what is referred to as baseload power. That is to say, the assumption is that these systems will operate essentially continuously, with minimal opportunity to respond to either increases or decreases in demand. Typically, gas-fired systems, which can be turned on or off rapidly, provide the flexibility needed to react to changes in demand. Accommodating an input of power from an intrinsically variable source such as wind poses a particular problem for the orderly operation of a complex electric utility network.

Integration of wind energy into China's coal-heavy electricity system presents significant challenges owing to wind's variability and the grid's system-wide inflexibilities. As indicated in a recent study [28], China has a greater capacity for wind installation compared to the United States (145.1 GW versus 75.0 GW), but generates less electricity from wind (186.3 TW h versus 190.9 TW h). A study by Davidson et al. (2016) suggested a potential production of 2.6 PW h per year by 2030 [29]. Although this represents 26% of the total projected electricity demand, it is only 10% of the total estimated physical potential of wind resources in the country. Increasing the operational flexibility of China's coal fleet would allow wind to deliver nearly three-quarters of China's target of producing 20% of primary energy from nonfossil sources by 2030.

5.4 Concluding remarks

The discussion to this point has sought to estimate the quantity of electricity that could be generated by selective placement of state-of-the-art wind turbines in regions judged suitable for their deployment. As indicated, the wind data employed in this analysis were derived from retrospective analysis of past meteorological conditions. In this sense, the present analysis may be interpreted as identifying the electricity that could have been produced from turbines installed at some point in the past when wind conditions may have been similar, and remained similar, to those identified in the database adopted here. The past is of course at best an imperfect prologue for the future. But, in planning for the future it may be the best option at our disposal.

Reservations that should be noted in addressing the charge indicated in the title of this chapter—to define the global potential for wind-generated electricity—include the following. Placement of a concentration of wind turbines at a particular location could have the potential to alter local and potentially even regional wind conditions. Extensive deployment of

wind farms could have an impact on the budget of atmospheric kinetic energy leading to a potentially consequential change in the circulation of the global atmosphere. And, finally, in responding to increasing concentrations of greenhouse gases, climate and wind conditions in the future may differ significantly from conditions that prevailed in the past. Quantitative projections for future wind power potential will be subject therefore to a level of inevitable unavoidable uncertainty.

The impact of wind farms on local meteorological conditions has been explored in a number of recent studies. Zhou et al. [30]. used satellite data covering the period 2003−2011 to analyze the response of regional surface temperature to the development of a wind farm in Texas. They found evidence for a significant upward trend in surface temperature, by as much as 0.72°C per decade, particularly at night and especially in the immediate neighborhood of the wind farms. Roy and Traitner [31] found a similar pattern in their study of the response of temperatures to the development of a wind farm in San Gorgonio, California. They reported evidence for a statistically significant increase in temperature, by about 1°C, at an elevation of 5 m downwind of the wind farm at night. The increase persisted through the early morning, followed by modest cooling during the day. They suggested that the impacts of wind farms on local weather could be minimized by modifying the design of rotor systems, or by siting wind farms in regions defined by high levels of natural turbulence. They further identified the Midwest and Great Plains regions of the United States as ideal for the placement of low-impact wind farms.

If the entire demand for electricity in the United States were to be accommodated by wind, the accompanying sink for kinetic energy would amount to approximately 6% of the sink contributed naturally by surface friction over the entire contiguous US land area, 11% for the sink identified with the area indicated in the foregoing as most favorable for wind farm development. The impact on the circulation of the atmosphere of potentially major commitments to wind power was explored in a number of recent studies, notably by Kirk-Davidoff and Keith [32] and Keith et al. [33]. They concluded that exploitation of wind resources at high levels of penetration might be expected to lead to significant changes in the circulation of the atmosphere, even in regions remote from the location of the involved turbines. They argued that the budget for the global inventory of atmospheric kinetic energy is regulated primarily by processes on the input side of the ledger rather than by the sink. An increase in friction resulting from the operation of large numbers of power-generating turbines could be compensated in this case, they argued, by a decrease in the dissipation of momentum by friction elsewhere. The global average surface temperature, they concluded, would not be expected to change significantly in the face of a large investment in wind-generated electricity. Temperatures at high latitudes could decrease to a modest extent in response to an anticipated decrease in the efficiency of meridional heat transport. The impact could be viewed as positive in this case, an offset to some extent for the amplified warming projected to arise in this environment in response to the human-induced increase in the concentration of greenhouse gases.

The impact on the circulation of the atmosphere of a large-scale investment in wind farms was investigated also by Miller et al. [34] and by Marvel et al. [35]. Employing a simple parameterization approach to simulate the influence of turbine operations as a sink for atmospheric momentum, Miller et al. [34] concluded that turbines distributed uniformly over the Earth's surface could harvest kinetic energy sustainably at a rate ranging up to as much as 400 TW. If the turbines were deployed at an elevation of 100 m, the yield could be as great as 1800 TW. Using an alternate approach to parameterize the sink for momentum associated with the exploitation of wind resources, Jacobson and Archer [36] concluded that as the number of wind turbines increased over a large geographic region, extraction of power should first increase linearly, converging eventually to a limit, estimated as in excess of 250 TW for turbines sited at 100 m, rising to 380 TW for turbines deployed at an altitude of 10 km.

There is a notable discrepancy between these various estimates of wind potential. Adams and Keith [37] addressed the issue using a mesoscale model. They concluded that the generation of power from wind should be limited to an average of about 1 W/m^2 for facilities distributed over an area of approximately 100 km^2. They argued further that the results obtained using a mesoscale model should provide a useful guide to what might be expected on the basis of a more complete global model. The assertion, however, remains to be demonstrated.

Modern wind turbines are designed to operate effectively for life cycles ranging up to 25 years or even longer. Predictions of wind power for the next 25 years, including the need to anticipate the impact of intrinsic variability, will pose a challenge for prospective investors. Global and regional climate models have difficulty in accounting for historical trends in wind regimes. There is little reason to believe that they will be more successful in predicting the future. Pryor et al. [38], based on existing research, argued that the changes in mean wind speeds and energy density anticipated for the future are unlikely to exceed the year-to-year variability ($\pm$ 15%) observed most recently over much of Europe and North America. Surface winds have declined in intensity in China, the Netherlands, the Czech Republic, the United States, and Australia over the past few decades [39−42]. The precise cause of this decline is uncertain. Vautard et al. [43] analyzed the extent and potential cause for the changes in surface wind speeds observed over

northern mid-latitudes between 1979 and 2008, using data from 822 surface weather stations. They indicated that surface wind speeds declined by 5%−15% over almost all continental areas at northern mid-latitudes with the decrease greatest at higher wind speeds. In contrast, upper-air winds inferred from sea-level pressure gradients, and winds derived from weather re-analyses, exhibit no such trend. It has been suggested that an increase in surface roughness resulting from increases in biomass and related changes in land cover over Eurasia could account for as much as 25% to 65% of the decrease in surface winds observed over this region.

Huang and McElroy [3], using assimilated meteorological data for the period January 1979 to December 2010, investigated the origin of wind energy from both mechanical and thermodynamic perspectives. Their results indicate an upward trend in kinetic energy production over the past 32 years, suggesting that wind energy resources might increase in a warming climate. They further highlighted the fact that the total kinetic energy stock of the atmosphere displays significant interannual variability, responding notably to the changing phases of the ENSO cycle. The potential for wind as a source of electricity at any particular location may be expected thus to vary not only in the long-term but also interannually in response to natural fluctuations in the circulation of the atmosphere.

The overall conclusion from this chapter is that wind resources on a global scale could accommodate a large fraction of present and anticipated future demand for electricity. The concentration of facilities in specific regions might be expected to contribute to a change in prevailing local meteorological conditions. This change is unlikely however to be sufficiently disruptive as to offset the advantages that could be realized from the concentration in the first place. Generation of electricity by capturing kinetic energy from the wind may be considered as an additional contribution to the surface friction that serves as the natural offset to the atmosphere's global production of kinetic energy. At high levels of penetration, wind facilities could have an appreciable influence on the budget of this important quantity: climate might be expected to adjust accordingly. Given foreseeable near term expansion of wind systems, however, this is unlikely to pose a serious problem. The most important limitation for future growth is likely to involve rather the challenge of responding to the intrinsic variability of the input from wind, compounded by the fact that this source may not be matched ideally to patterns of power demand.

Acknowledgments

The work was supported by the State Environmental Protection Key Laboratory of Sources and Control of Air Pollution Complex, Collaborative Innovation Centre for Regional Environmental Quality, the National Key R&D Program "Formation mechanism and control technology of air pollution" (2016YFC0208900), and the Volvo Group in a research project of the Research Center for Green Economy and Sustainable Development, Tsinghua University. It was also supported by the Harvard Climate Change Solutions Fund and the Harvard Global Institute.

References

[1] McElroy MB. Energy and climate: vision for the future. Oxford: Oxford University Press; 2016. p. 280.
[2] Kung EC. Large-scale balance of kinetic energy in atmosphere. Mon Weather Rev 1966;4(11):627−40.
[3] Huang JL, McElroy MB. A 32-year perspective on the origin of wind energy in a warming climate. Renew Energy 2015;77:482−92.
[4] Lu X, McElroy MB, Kiviluoma J. Global potential for wind-generated electricity. Proc Natl Acad Sci USA 2009;106(27):10933−8.
[5] Rienecker M.M., et al. The GEOS-5 data assimilation system-documentation of versions 5.0.1, 5.1.0, and 5.2.0. In: Suarez MJ, editor Technical report series on global modeling and data assimilation. Washington, DC: NASA; 2007, p. 118.
[6] Archer CL, Jacobson MZ. Evaluation of global wind power. J Geophys Res 2005;110(D12):D12110.
[7] IEC, Wind turbines—part 12-1: power performance measurements of electricity producing wind turbines, editor Commission IE. Geneva, Switzerland: NYSE: IHS; 2005.
[8] USGS Global Digital Elevation Model. (GTOPO30). 30-arc seconds. Sioux Falls, South Dakota: U.S. Geological Survey, Center for Earth Resources Observation and Science (EROS); 2006.
[9] U.S. Department of Energy. Environmental impact statement for the proposed cape wind energy project U.S. Department of Energy, Washington, DC; 2012, p. 801.
[10] Musial W, Butterfield S. Future for offshore wind energy in the United States. EnergyOcean 2004. Palm Beach, Florida: National Renewable Energy Laboratory (NREL); 2004. p. 16.
[11] Musial W. Offshore wind energy potential for the United States. In: Wind Powering America—Annual State Summit, Evergreen, CO; 2005, p. 23.
[12] Musial W, Ram B. Large-scale offshore wind power in the united states: assessment of opportunites and barriers. Golden, CO: National Renewable Energy Laboratory; 2010. p. 108−28.
[13] Dvorak MJ, Archer CL, Jacobson MZ. California offshore wind energy potential. Renew Energy 2010;35(6):1244−54.
[14] Dvorak MJ, Stoutenburg ED, Archer CL, Kempton W, Jacobson MZ. Where is the ideal location for a US East Coast offshore grid? Geophys Res Lett 2012;39. Available from: https://doi.org/10.1029/2011GL050659.

[15] Sclavounos P, Tracy C, Lee S. Floating offshore wind turbines: responses in a seastate pareto optimal designs and economic assessment. New York: Amer Soc Mechanical Engineers; 2008.
[16] Masters GM. Renewable and efficient electric power systems. Hoboken, NJ: John Wiley & Sons, Inc; 2004.
[17] GE. 2.5 MW series wind turbine. Fairfield, CT: General Electric Energy; 2006.
[18] GE. 3.6 MW wind turbine technical specifications, ed. Energy G. Fairfield, CT: General Electric Energy; 2006.
[19] Boden TA, Andres RJ, Marland G. Preliminary 2011 and 2012 global & national estimates. *Fossil-fuel CO_2 emissions*. Oak Ridge, TN: Carbon Dioxide Information Analysis Center; 2013. p. 4.
[20] US EIA. International energy outlook. Washington, DC: U.S. Energy Information Administration; 2013. p. 312.
[21] US-DOE. 20% Wind energy by 2030, increasing wind energy's contribution to U.S. Electricity Supply. Washington, DC: U.S. Department of Energy; 2008.
[22] ERCOT. Analysis of transmission alternatives for competitive renewable energy zones in Texas. Austin, TX: Energy Reliability Council of Texas (ERCOT); 2006, p. 120.
[23] McElroy MB, Lu X, Nielsen CP, Wang Y. Potential for wind-generated electricity in China. Science 2009;325(5946):1378–80.
[24] GE. 1.5-MW series of wind turbines, ed. Energy GE. Fairfield, CT; 2009, p. 12.
[25] Kempton W, Archer CL, Dhanju A, Garvine RW, Jacobson MZ. Large CO_2 reductions via offshore wind power matched to inherent storage in energy end-uses. Geophys Res Lett 2007;34(2):5.
[26] Wiser R, Bolinger M. In: US-DOE, editor. Annual report on U.S. wind power installation, cost and performance trends: 2007. Washington, DC: U.S. Department of Energy; 2008. p. 32.
[27] Cyranoski D. Renewable energy: Beijing's windy bet. Nature 2009;457(7228):372–4.
[28] Xi L, McElroy MB, Peng W, Liu S, Nielsen CP, Wang H. Challenges faced by China compared with the US in developing wind power. Nat Energy 2016;1(6):6.
[29] Davidson MR, Zhang D, Xiong W, Zhang X, Karplus VJ. Modelling the potential for wind energy integration on China's coal-heavy electricity grid. Nat Energy 2016;1:7 July 2016.
[30] Zhou LM, Tian YH, Roy SB, Thorncroft C, Bosart LF, Hu YL. Impacts of wind farms on land surface temperature. Nat Clim Change 2012; 2(7):539–43.
[31] Roy SB, Traiteur JJ. Impacts of wind farms on surface air temperatures. Proc Natl Acad Sci U S Am 2010;107(42):17899–904.
[32] Kirk-Davidoff DB, Keith DW. On the climate impact of surface roughness anomalies. J Atmos Sci 2008;65(7):2215–34.
[33] Keith DW, DeCarolis JF, Denkenberger DC, Lenschow DH, Malysherv SL, Pacala S, et al. The influence of large-scale wind power on global climate. Proc Natl Acad Sci USA 2004;101(46):16115–20.
[34] Miller LM, Brunsell NA, Mechem DB, Gans F, Monaghan AJ, Vautard R, et al. Two methods for estimating limits to large-scale wind power generation. Proc Natl Acad Sci U S A 2015;112(36):11169–74.
[35] Marvel K, Kravitz B, Caldeira K. Geophysical limits to global wind power. Nat Clim Change 2013;3:118–21.
[36] Jacobson MZ, Archer CL. Saturation wind power potential and its implications for wind energy. Proc Natl Acad Sci U S A 2012;109(39):15679–84.
[37] Adams AS, Keith D. Are global wind power resource estimates overstated? Env Res Lett 2013;8.
[38] Pryor SC, Barthelmie RJ. Climate change impacts on wind energy: a review. Renew Sust Energ Rev 2010;14(1):430–7.
[39] Klink K. Trends in mean monthly maximum and minimum surface wind speeds in the coterminous United States, 1961 to 1990. Clim Res 1999;13(3):193–205.
[40] Smits A, Tank A, Konnen GP. Trends in storminess over the Netherlands, 1962–2002. Int J Climatol 2005;25(10):1331–44.
[41] Xu M, Chang C-P, Fu C, Qi Y, Robock A, Robinson D, et al. Steady decline of east Asian monsoon winds, 1969–2000: Evidence from direct ground measurements of wind speed. J Geophys Res-Atmos 2006;111(D24):8.
[42] McVicar TR, Van Niel TG, Li LT, Roderick ML, Rayner DP, Ricciardulli L, et al. Wind speed climatology and trends for Australia, 1975–2006: capturing the stilling phenomenon and comparison with near-surface reanalysis output. Geophys Res Lett 2008;35(20):6.
[43] Vautard R, Cattiaux J, Yiou P, Thepaut JN, Ciais P. Northern Hemisphere atmospheric stilling partly attributed to an increase in surface roughness. Nat Geosci 2010;3(11):756–61.

This page intentionally left blank

Chapter 6

Achieving carbon neutrality: the future of wind energy development in China

Jacqueline Lam[1,2], Victor O.K. Li[1,2], Shanshan Wang[1], Peiyang Guo[1] and Danyang Zhu[1]
[1]*Department of Electrical and Electronic Engineering, the University of Hong Kong, Hong Kong, P. R. China,* [2]*Energy Policy Research Group, the University of Cambridge, Cambridge, United Kingdom*

6.1 Introduction

Globally, energy is generated mainly from nonrenewable sources. This has resulted in serious environmental pollution and health degradation. By contrast, renewable energies (RE) are clean and sustainable, and emit fewer pollutants and greenhouse gases (GHG) [1]. REs include wind, solar, biomass, geothermal and hydro, all of which occur naturally on our planet. Like all renewable forms of energy, wind generates green electricity and provides a solution to reducing GHGs. It is expected that to achieve the target of controlling global temperature rise to below 2°C, wind energy must be an increase from a global share of power mix from approximately 6% in 2020 to 30% by 2050. The global new wind power installations have exceeded 90 GW in 2020 and achieved a 53% increase as compared to 2019, demonstrating strong demand for the adoption of wind energy technologies worldwide [2].

As the biggest GHG emitter in the world, China is facing increasing pressure to cut carbon emissions. The recent slowdown in economic development has prompted China to look for alternative economic solutions and develop new energy industries which include wind. In less than two decades of development, China's installed wind energy capacity has reached the stage of being greater than that of any other country in the world. In this chapter, we will first review the status of China's wind energy development, with a brief introduction to the electricity and wind energy market in China. Second, we identify the barriers and drivers to the country's wind energy development. Lastly, we outline the possible future pathways for achieving a sustainable wind energy industry in China.

6.2 Wind energy development in China

6.2.1 Overview

The Chinese economy has seen significant growth in recent decades, with the GDP per capita (PPP) increasing from US$982 in 1990 to US$17,211 in 2020 [3]. To maintain this high rate of economic growth, China needs to continue expanding its electricity supply. However, viable options for electricity generation are few. China is rich in coal reserves but limited in gas and oil supplies. Electricity generation based on coal is highly polluting and carbon-intensive, thus creating significant political and international pressure [4]. There is an urgent need for China to change from high-carbon to low-carbon electricity generation.

China has so far achieved remarkable progress in wind energy development. As of 2020, electricity from wind turbines represented 6% of the overall power generation in China [5]. This is largely due to the country's vast wind resources [6], relative technological maturity, and relatively low cost, compared to other renewable resources. From 2001 to 2020, China's accumulated wind power generation capacity increased from 383 MW to 282 GW. The newly installed wind energy capacity also increased to 72,411 MW in 2020 (see Fig. 6.1). China accounted for 56% of the new wind power installations in the world in 2020 [2]. Wind energy has constituted a key component of China's renewable energy strategy and is expected to play an increasingly significant role in China's energy mix. In terms of carbon neutrality, China targets to reach 1200 GW of total installed capacity of wind power and solar power by 2030, eventually reaching 80% of nonfossil energy consumption by 2060 [8]. In response to China's vision of carbon neutrality,

Wind Energy Engineering. DOI: https://doi.org/10.1016/B978-0-323-99353-1.00004-9

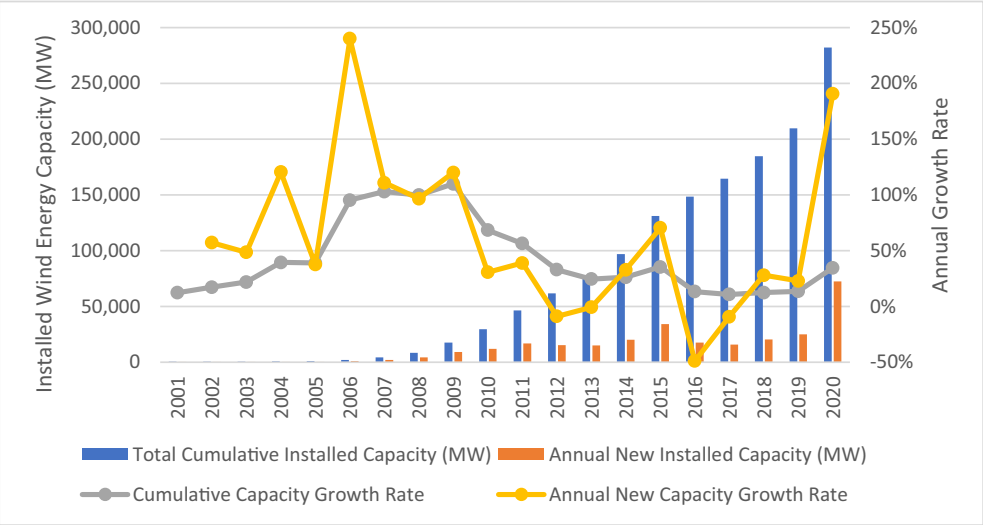

FIGURE 6.1 China's wind energy capacity development from 2001 to 2020 [7].

Beijing Declaration on Wind Energy sets an ambitious target of scaling up China's cumulative wind capacity to at least achieve a minimum of 800 GW by 2030 and 3000 GW by 2060 [9].

6.2.2 Electricity market and wind energy market in China

6.2.2.1 Electricity market and wind energy market

China's electricity market is heavily regulated. On the supply side, the government has established an on-grid tariff for each province. Each power plant must sell its outputs to the two national grid companies via the on-grid tariff. The grid companies then transmit and distribute the electricity to local utilities, which are subsidiaries of the two grid companies. On the demand side, consumers purchase electricity from local utilities at fixed prices set by the local governments. Since 2015, China has started revamping the electricity market and has attempted to liberalize the electricity supply [10]. In spite of the recent progress, the long-term market-oriented reforms have yet to fully replace the short-term administrative planning on renewable energy sources in China [11].

For a long time, two different pricing schemes have been in place in the Chinese electricity market in parallel to boost the integration of wind energy into the grid; auctioning and feed-in-tariffs (FIT). The auctioning scheme was introduced in 2003, when the National Development and Reform Commission (NDRC) organized national concession tendering for selected projects, and picked winners based on the lowest bidding price. However, it soon became evident that this process was dominated by state-owned enterprises (SOEs), which submitted bids at very low prices to secure projects. SOEs were keen to win these projects because (1) they were required by the government to purchase wind capacity to meet their renewable installation target; (2) they were able to compensate for wind project loss with revenues from conventional generation; (3) some parties hoped to win the bid first and postponed the development until the cost of wind power technology becomes sufficiently low. Such practices conducted by SOEs carried unintended consequences: the tariffs were too low to cover the project cost; auction winners resorted to corner-cutting to reduce costs; private investments were forced to exit the nascent wind power industry. After a few unsuccessful attempts to reform the auctioning process, the Chinese government eventually decided to abandon onshore wind auction.

In 2009, FITs were introduced to replace auctioning. China is divided into four regions based on wind resources and the existing grid infrastructure. Under each region, a benchmark price for wind power is issued by NDRC. Each tariff consists of two parts: a fixed on-grid tariff and a renewable subsidy. The fixed on-grid tariff is paid by the national grid companies. The renewable subsidy is covered by a national renewable fund, sustained by a surcharge levied on electricity consumers and fiscal transfer from the government. A high, fixed FIT has been considered by wind developers as one of the most important drivers of wind capacity installation [12]. As wind energy becomes increasingly cost-competitive, policymakers increasingly require it to compete with coal in the absence of any subsidies [11]. By the end of 2021, China officially ended the FIT program (USD134/MWh) for offshore wind farms. From 2022 onwards, NDRC requires that wind electricity tariffs are benchmarked to the coal baseline price [13].

6.2.2.2 Key players in the wind energy market in China

China's wind industry is shaped by five key types of stakeholders, including the wind developers, the wind turbine manufacturers, the central government, the local governments, and the national and local grid companies. Because of the strong role the state plays in the electricity market in China, the central and the local governments are dominant players shaping the wind energy market. The national and local grid companies are under the direct control of the state and the local governments.

6.2.2.2.1 Wind energy developers

Wind energy developers in China consist primarily of state-owned power generation companies. The unique feature of China's electricity system dates back to 2002 when its electricity market was restructured to allow competition in electricity supply. Five state-owned companies were spun off from the State Grid Corporation (SGC), then, the only vertically integrated utility. Since then, China's electricity generation has been dominated by five corporations plus a number of new entrants, most of which are SOEs such as Shenhua and CR power. After China increased the renewable penetration by taking up wind auctioning in 2003, these companies rapidly expanded their installed wind capacities via their deep pockets and their ability to subsidize the low strike price of wind renewables by the revenues obtained from nonrenewables. Only one new entrant has been able to obtain significant market share from any state-owned companies. This is Tianrun, a private power company specializing in wind power development and a subsidiary of Goldwind, the leading wind turbine manufacturer in China.

6.2.2.2.2 Wind turbine manufacturers

Chinese wind turbine manufacturers hold a significant share in the global wind energy market. In 2020 Goldwind and Envision, both Chinese with a combined installed capacity of 24 GW, are reported to rank the 3rd and the 4th among wind turbine equipment manufacturers (OEMs) in the world. A strong home market helps achieve such outstanding performance [14].

Chinese wind manufacturers started developing wind turbines at a much later stage than their European counterparts. Local wind turbine manufacturing began production in the mid-1990s. In 1996 the Chinese government unveiled a set of policy initiatives to speed up wind technology capacity. Chinese manufacturers gradually acquire advanced technologies via joint ventures or technology licensing and secure competitive positions in global turbine manufacturing [15,16]. A major policy reform was introduced in 2005, which required that 70% of wind turbine components be manufactured in China [17]. Though this policy was eventually abolished five years after the introduction due to international pressure, it significantly boosted the market share of domestic manufacturers and encouraged technology transfer from frontrunner companies in China. China has gradually reduced its reliance on imported turbine technologies and has accumulated its own innovative capacity [16]. Chinese manufacturers can produce large turbines of comparable size to their European counterparts.

6.2.2.2.3 The central government

The central government, including NDRC and the National Energy Agency, are the primary national policy-making bodies taking charge of wind power development and planning in China. Before 2010 when auctioning was applied to wind power pricing, NDRC was responsible for planning concession bidding, for any wind projects that exceed 50 MW. After China has adopted FIT, NDRC retains the authority to approve any wind projects that exceeded this threshold, while delegating the local government the authority to approve any projects that fall below the threshold. However, the overheated response of the local governments to approve wind projects that fall below the threshold, prompted NDRC, in 2011, to retake its authority to approve all types of wind projects. In 2013, NDRC decides to delegate the authority of wind projects approval back to the local governments, while retaining its overarching control over wind development planning. The central authority lays out plans for scheduled installation for individual provinces and coordinates transmission line construction [18].

6.2.2.2.4 The local governments

In parallel with the central government, the local governments have much control over local wind energy development. They are given the authority to propose annual plans for total local power generation, which will dictate the maximum wind capacity that each local province should take up. Before 2011, the local governments also gained considerable power on wind capacity installation as they enjoyed the authority to approve any wind projects falling below 50 MW.

For the local authorities, wind energy development is not taken as a zero-sum game; there are potential to boost local employment and economic growth and increase the local authority's tax revenue. However, some local governments also hold the belief that coal-fired electricity has a higher potential to boost local employment and economy [19]. Whenever there is an oversupply of electricity, local governments often attempt to save coal-fired power generation, at the expense of wind power development, via wind curtailment. Such a situation may improve with the outline of China's 14th Five Year Plan (2021−25) in 2021, requiring individual provinces to create their own development plans on RE and timetables for meeting the emission limits. Provinces like Jiangsu and Guangdong have set specific targets for wind electricity to incentivize the local authorities at different levels of administration to achieve the emission reduction goals [2].

6.2.2.2.5 Grid companies

Grid companies are tasked with ensuring grid access and priority dispatch of wind power. China's transmission and distribution are dominated by two national grid companies, namely, the National Grid and the Southern Power Grid. These two grid companies are not competitors as they are serving different regions. Local utility companies are subsidiaries of these two national companies and follow closely the policies laid down by their parent companies. Grid companies make a profit from procuring and selling electricity at state-sanctioned prices. They pay the on-grid tariff for wind electricity at the same rate as their coal counterpart, whereas the difference between the FIT price and the on-grid tariff is covered by the renewable fund. The renewable fund is supported by government subsidies and surcharge levied on the consumers.

6.3 Wind energy development in China: barriers and drivers

The wind energy output in China is less than satisfactory in view of the massive wind capacity installed. This can be witnessed by comparing wind development in China with that of the United States. In 2015, The installed wind energy capacity in China was double that of the States [20]. However, the wind energy output generated in China was slightly lower than that of the States, and only 186 TW h of wind energy output was generated in 2015, as compared to 190 TW h generated in the States. The mismatch in wind energy capacity and output is partly due to the fact that wind resources are intrinsically less abundant in China [21,22]. Other factors beyond the scarcity of wind resource have also contributed to the less well-performed wind energy output, including poor grid connectivity and wind curtailment [19,21,23]. In Sections 3.1 and Sections 3.2, we will highlight the barriers to (Sections 3.1) and drivers of (Sections 3.2) wind energy development in China and provide an account of the relatively less well-performed wind energy output in China.

6.3.1 Barriers to wind energy development in China

6.3.1.1 Overcapacity in nonrenewable power plants

Overcapacity in electricity generation from nonrenewables has become increasingly evident due to the slowdown in capacity investment and economy in China. The cooling effect on capacity investment is closely linked to its long history of capacity shortage. In the 1980s, after the introduction of the open-door policy, electricity demand increased dramatically and most provinces began experiencing severe electricity shortages. Industrial users in China were only allowed to access electricity only on government-planned schedules, depending on how much capacity was generated in total. Such a move went against the generally accepted international practice [24]. To spur capacity investment, the central government liberalized the electricity supply, allowing provincial governments and private companies to build their own power plants. Preferential pricing was introduced to fix procurement prices at a rate that guaranteed revenues. Such measures have produced huge financial incentives for grid companies to invest in generation capacity. Over the last few decades, the growth in electricity supply has gradually been catching up with the growth in electricity demand.

As a result of the economic slowdown in 2015, with the growth rate in China dropping from double digits to single digits, electricity demand followed the same pattern. However, capacity investment irrationally grew despite the economic trend. Growth in investment capacity outstripped electricity demand. Electricity demand increased marginally by 0.5% [25], while the total installed capacity increased by more than 10% in 2015 [26].

Over-capacity implies that wind energy will play an increasingly weaker role in electricity generation. Gansu, a remote inland province in Northwest China, has an installed capacity of 27 GW of wind and solar energy, in addition to the 104 TW h thermal or hydro capacity [27]. Given that its average annual electricity demand is 109 TW h, without

cutting thermal power or hydro generation or transmitting the excessive capacity to other provinces, installed wind energy capacity could hardly be put into any meaningful use in Gansu. This is also true for other provinces that display similar electricity supply and demand characteristics.

6.3.1.2 Wind curtailment

Wind curtailment is a particularly acute challenge to wind energy integration in China. Wind curtailment refers to the situation where the output of wind plants is reduced to a level below its maximum generation capacity. China has experienced curtailment since 2010 and curtailment peaked at 17% in 2012 and 2017 [28]. In some places, the curtailment rate reached as much as 39% for a particular year [20]. Despite its recent improvement that wind curtailment rate dropped to 4% in 2019 [28], it remains staggering when compared to other renewable energy development leaders such as Germany, which had a curtailment rate of below 1% in 2013 [29].

Wind curtailment should be considered within the context of China's priority dispatch policy. Internationally, procurement of output from generation sources other than wind is not guaranteed. The various generation sources are dispatched based on the structure of the competitive wholesale market, such as the US and Germany; or local policies or regulations, such as China. Under the priority dispatch policy, however, system operators are obliged to dispatch wind output first before they dispatch other sources. In China, the Renewable Energy Law provides that renewable energy such as wind be awarded a dispatch priority, which means that grid companies must procure all power from wind developers at the FIT price.

However, priority dispatch has not been strictly implemented. Local governments sometimes misinterpret or distort the policy in favor of thermal power generation, which has been taken as a more important means for enhancing economic growth and employment [19]. Local policies that attempt to restrict wind power development include setting the total generation hours for wind power, ordering the wind developers to purchase generation rights from thermal power plants, thereby forcing wind power to compete with thermal power in the newly established electricity market. This situation would not occur in other countries as hefty compensation has to be paid to wind farm owners for every kilowatt hour the operator fails to procure. In China, because no penalty or compensation is required legally in case of any wind procurement failure, the local governments are free to interpret the priority dispatch provision, resulting in a violation of priority dispatch.

6.3.1.3 Poor grid connectivity

Poor grid connectivity arises from the geographic distribution of wind farms and the centralized development of generation capacity. A key feature of China's wind power is centralized utility-scale generation. Large wind farms are mostly located in the vast inland regions, including North China, the Northeast, and the Northwest ("Three North" regions), where wind resources are abundant. Because of the sheer expansion and sparse distribution of population in these regions, wind energy needs to be transmitted across thousands of miles before consumption. Very often, wind generation within these inland provinces greatly outstrips demand, making it necessary to export excessive energy to coastal or southern provinces, and triggering the need for long-distance transmission.

Transmission planning often lags behind the speed of wind capacity installation. The time spent in obtaining official approval of new transmission lines greatly exceeds that of new wind power development. Construction of new transmission lines has to go through onerous planning, environmental impact, and feasibility assessments before it is assessed by various divisions of the central government [23]. Besides, a huge delay may occur due to the lengthy process involved in land acquisition. Long-distance transmission also requires considerable coordination among the local governments, whenever transmission lines have to pass through their own jurisdictions [4]. In comparison, planning for wind projects is relatively easy. The local governments have much say in the installation of new wind capacity and the approval procedures are often simple and easy. The speed of installing wind turbines thus often outpaces that of constructing transmission lines.

6.3.1.4 Lack of a well-functioned ancillary service market

Integrating renewables calls for flexible power sources to provide ancillary services. Wind energy outputs are inherently variable and uncertain. Therefore, the power system must be flexible enough to accommodate rapid change. However, power supply flexibility is low in China. Coal-fired power plants dominate the power generation, accounting for 64% of the total electricity supply as of 2020 [5]. Unlike gas power which could ramp up and down quickly, coal-fired power plants are usually designed to serve base load and run at a constant output. Large deviation from the designed

output is often seen as ill-advised as it reduces efficiency, increases costs, and lowers equipment lifetime [30]. As such, no coal-fired power plants will be motivated to provide ancillary services for renewables without proper compensation.

China lacks a well-functioned ancillary service market to provide power plants with incentives to balance the grid. In other countries with a large share of coal power, such as Germany, any plant capable of providing ancillary service is eligible to enter the market. At a time when renewable output changes drastically, the price of ancillary service provision would surge to an extremely high level to compensate for the sudden change. This price signal would encourage investment in flexible power sources such as natural gas and provide the necessary financial incentives for coal-fired power plants to retrofit and increase flexibility. However, in China, such market design is still largely elusive. Very often, coal-fired power plants are required by the government to provide ancillary services free of charge. In some regions where remuneration schemes do exist for ancillary services, the payment is often low and fixed by the government. The incentive for investment in flexibility remains weak.

6.3.1.5 Lack of demand response and energy storage

Demand response (DR) offers a promising solution to increase power system flexibility from the demand side. DR refers to all intentional modifications to consumers' electricity consumption patterns such as altering the duration of use, the level of instantaneous demand, and the total electricity consumption [31]. DR programs enable timely adjustment of consumer demand according to electricity supply conditions, which helps to accommodate intermittency of electricity output and levels out its variation. The DR programs that are most relevant to wind energy integration include direct load control, interruptible or curtailable load, demand side bidding or buyback programme, and emergency DR programs.

China's DR development is in its infancy. Because of the lack of electricity wholesale market, DR programs are rolled out under the strong supervision of the government, which would set the amount and price for curtailment. The state-owned grid companies are responsible for implementing the DR programs. However, because the grid companies earn profits from the fixed price difference of electricity procurement and sales, they are reluctant to promote DR as curtailment from DR would reduce their revenues. DR is therefore undervalued as a tool to integrate wind energy into the grid in China.

China also lacks energy storage technologies, particularly thermal storage, that can level wind output variation by absorbing and releasing wind energy from the grid. Such technologies are particularly important given the prevalence of combined-heat-and-power (CHP). CHP has been promoted by the government for decades due to its high efficiency in heat and electricity generation. However, most CHP plants are not designed for flexibility, and the proportion of electricity output to heat output is fixed. As a result, CHPs could not be ramped down during peak wind output seasons because residents are relying on them for heating. In principle, thermal energy storage could effectively decouple electricity generation from heat production, allowing CHP power plants to vary electricity output without affecting heat supply, thus enabling CHP plants to respond flexibly to variation in wind output. However, such a thermal energy storage system is not yet available in China.

6.3.1.6 Differential priorities between the central government and the local governments

The policy objectives of promoting wind energy differ between the central and the local governments. The central government values increasing wind energy share to reduce emissions and enlarge economic benefits. The local governments, however, prioritize large-scale investment in wind power and wind turbines, partly for local economic development and for extending their personal ambitions. Given that the performance of local officials is tied to local economic growth, large-scale wind energy projects that involve huge financial investments are preferred by the local governments. Wind power investment becomes a desirable option for local governments to strengthen their own political portfolio. Sometimes, the local governments would push for wind investment even when such development has proven to be redundant from environmental or economic perspectives.

The tussle between the central government (mainly NDRC) and the local governments is most evident in the transfer of authority for wind project approval. Before 2011, all wind projects above 50 MW had to obtain approval from the NDRC. To circumvent the approval procedure, the local governments came up with a strategy of dividing a large wind project into smaller ones for wind projects below 50 MW. A rush to wind power installation by the local governments soon resulted in severe wind curtailment. To control the rush for wind investment, NDRC began asserting its authority over all wind projects in 2011. In 2013, however, under the banner of "streamlining administration and delegating power" proposed by the new administration, project approval authority was re-delegated to local governments.

Nevertheless, the NDRC still tries to control the wind development pace by issuing an annual wind development plan [18].

The relationship among the local governments is characterized by increasing protectionism. Provinces experiencing electricity overcapacity are not able to export excessive power to other provinces experiencing power shortages. This is because local governments believe that importing electricity will reduce the local need for new capacity investment, thus hurting local employment and economy [19]. An example is the construction of a long-distance transmission line, which connects the wind power plants in Gansu province to the southern provinces of Hunan, Hubei, and Jiangxi. Government officials from the receiving provinces displayed their reluctance in purchasing wind energy from Gansu. Instead, they continued to approve new generation plants to reduce the import of electricity.

6.3.1.7 Vested interests between coal companies and the government

Local governments are influenced by their vested interest in coal companies. Local governments must balance the interests of coal-fired plants, which dominate generation and contribute immensely to the local economy and taxation. Wind energy will impact coal-fired power plants and the local governments in the following ways:

1. An increase in wind dispatch would crowd out a share of output that would otherwise belong to coal. This is particularly evident in places where large, centralized wind capacity is installed. For example, in Gansu province, if its total wind capacity of 12.5 GW operates at its legally guaranteed 1800 h/year [32], the average utilization hours of coal-fired power plants would be reduced by 1406 h per year. This would slash the revenue of coal-fired plants by 30% and the value-added tax by at least 30%.[1]
2. Accommodating wind intermittency increases ancillary service costs borne by coal-fired power plants. Integrating wind energy to the grid requires the provision of ancillary services by coal-fired power plants, such that the thermal power outputs can vary based on variations in wind outputs. In China, many provinces still demand compulsory ancillary services from coal-fired power plants. In the few provinces that do offer compensation for ancillary services, coal-fired generators are required to share the compensation [19]. An increase in wind integration would adversely impact the total revenue of coal-fired power plants.
3. From the perspective of local governments, coal-fired power plants contribute more in terms of employment and economic growth [19].

As a result, in face of an oversupply of electricity, the local governments are either inclined to compromise on the priority dispatch rule or invite the wind power generators to share profits with the coal-fired power plants. These measures have exacerbated the wind curtailment and thwarted the integration of wind energy into the grid. In Section 3.2, we will outline the existing drivers of wind energy development in China.

6.3.2 Drivers of wind energy development in China

6.3.2.1 Energy coordination

Tackling wind curtailment requires coordination among capacity installation, transmission planning, and consumer demand. Transmission must keep up with capacity installation. New wind energy projects should not be undertaken if the output could not be utilized or otherwise matched by demand.

Starting in 2015, China begins improving the coordination of energy sources. The central government tries to control the overheated capacity installation with an annual development plan [18]. It provides a guideline that decides on the total planned capacity for each province according to wind resource endowment and severity of curtailment. Provincial governments are held responsible for approving individual projects and arranging grid connections and transmission within the province. The NDRC plans large interregional transmission lines. Plans are underway to shift wind development from the remote regions, the "Three North," to the south, where wind output could be transmitted and utilized by load within a short distance. Ultra-high voltage (UHV) transmission lines are scheduled to deliver wind energy from inland regions to the South.

1. The calculation is based on the assumption that the average utilization hour of coal-fired power plants is 5000 h per year. The calculation for valued-added tax is based on the formula provided by reference [17] *Notice on wind power development and management*, 2005.

6.3.2.2 Coal-fired power plants retrofit and energy storage

China must still rely on coal power to reduce wind output variation, as coal power still dominates electricity generation and China has very limited flexible energy sources other than the natural gas. At present, coal power in China is highly inflexible. Most coal-fired power plants could only ramp down to a minimum level of 60%−70% rated output, while in western countries such as Denmark such level could reach as low as 20% [30]. For the CHP power plants that are dominant in the north, they are often not allowed to ramp down the output, as they are badly needed for heating. Wind energy is therefore frequently curtailed because few coal-fired power plants in China can provide high flexibility in energy output.

Since 2016, 15 pilot programs addressing coal-fired power plant generation flexibility enhancement were set up in regions with severe wind curtailment [33]. It is expected that through retrofits, the coal-fired power plants could further ramp down by an additional 20% of rated output. Recent regulations also seek to enhance the flexibility of CHP plants with thermal storage. Traditional CHP plants will be complemented with hot water tanks, which serve to decouple electricity output and heat output [34]. Pilot programs on electrical storage have also been launched in the "Three North" region which refers to the seven provinces in the northwest (Xinjiang and Gansu), northeast (Heilongjiang, Jilin, and Liaoning), and north (Hebei and Inner Mongolia). These pilots will allow electrical storage to be compensated for their ancillary service [35]. The "Three North" region plays an important role in the Chinese wind energy market development. In 2016, it represented 71.5% total capacity of the nation, while accounting for 99% of the total wind curtailment. Despite policy nudges from the national level, the outcome is not as effective as expected. More fundamental reformations of the electricity market are needed [36].

6.3.2.3 Smart demand response

Smart DR utilizes smart infrastructure and management system to increase demand flexibility. Currently, the Chinese government is aggressively pursuing smart infrastructure deployment. China is committed to rolling out new advanced meters with smart functionalities to 90% of all users by 2020 [37]. In 2015 alone, more than 90 million units were installed [38].

Equipped with smart infrastructure, the electricity system presents abundant opportunities for smart DR. Four pilot cities have been chosen for DR programs: Beijing, Suzhou, Tangshan, and Foshan [39]. Jiangsu has already rolled out its first interruptible load program that could respond to contingency events within seconds [40]. China has established an annual demand side management target which requires utilities to achieve an annual saving of at least 0.3% in sales volume, and 0.3% in demand [41]. Wind energy integration is set to benefit immensely from these measures.

6.3.2.4 Emerging ancillary service market

China has made some progress in setting up ancillary service markets, though it is less than satisfactory. In 2006 a new regulation by NDRC was implemented to require generators to be compensated for the ancillary service they provide above the legally required level [42]. Before 2006, all ancillary services were provided free of charge. Up till now, nearly all regional grids have established rules on ancillary service compensation. Usually, the rules will define an obligatory ancillary service level, above which payment would apply. Some provinces adopted a fixed formula. For example, the Southern grid provides that thermal plants could receive 3 RMB/(kW h) for plants operating at 40%−50% of rated capacity, and 6 RMB/(kW h) for 30%−40% of rated capacity [43]. Some other provinces went further to allow market pricing. For example, the Northeast Grid has established that provincial and regional ancillary service markets should adopt market pricing.

6.3.2.5 Carbon trading and carbon reduction target

Carbon trading is an important instrument for internalizing the external costs of air pollution. Zero-emission wind power produces energy that contributes to the efforts to combat climate change. However, plants producing nonrenewable energy freely emit at zero cost as the cost associated with emissions is not reflected in its pricing. As a result, wind energy is at a price disadvantage. A fundamental approach to rectify such free-riding behavior is to let the thermal power plants pay for carbon emissions through carbon trading. By setting a legally binding carbon reduction target and assigning permits for each thermal power plant, plants with emissions exceeding their caps must purchase permits from others who meet or exceed the emission target. In this way, wind energy and thermal energy are put on a level playing field where they could compete fairly. Given that traditional regulatory, nonmarket-based command, and control policies perform less in reducing carbon, carbon trading has been increasingly hailed as a possible option on the national

policy agenda [44]. On 16 July 2021, China's national emissions trading scheme (ETS) finally makes its debut. Though the total carbon emission allowance traded in China in 2021 was only 412.05 million tons comparing with 12 billion in the European ETS market for the same year [45], this was an important step for introducing carbon pricing as a market instrument to incentivize the adoption of wind electricity.

6.4 The future of wind energy development in China

Despite efforts introduced by the government to overcome barriers, several challenges have yet to be fully addressed. Present implemented measures are insufficient in addressing the poor compliance with the priority dispatch measures. In terms of grid connectivity, although the annual development plan delineates the responsibilities of local governments to promote transmission line construction and introduce UHV transmission, transmission approval and construction procedures are still cumbersome. In addition, reform that could address the political tussle between the central and local governments is particularly difficult to carry out. We recognize that such barriers will not be overcome in the short term. Rather, it requires stakeholder engagement and reform over a long period of time. However, we believe that the following technologies and mechanisms reform, if followed through, would greatly improve the integration of renewable to the electricity supply system in the future.

6.4.1 Distributed generation deployment and proactive transmission planning

Grid-connection delay and geographic mismatch between generators and loads could be alleviated by distributed generation deployment and proactive transmission planning [21]. Proactive transmission planning has been widely implemented in the US, and the option of exporting excess output in China could be supported by the UHV lines. Some scholars have shown that proactive construction of large-scale transmission line is more cost-efficient than smaller transmission investments on individual projects [46]. Distributed generation can be found in the Eastern regions of China, where low-speed wind resources abound and electricity demand is substantial. With the distributed energy system installed near a load center, it could achieve greater energy conservation, lower investment cost, and a flexible operation pattern [47]. The savings in the transmission cost and curtailment loss outweigh the higher energy generation cost under relatively low wind speed [21]. In the future, distributed wind generation is more likely to be integrated with solar generation, establishing the "wind and solar" complementary power generation system [48].

6.4.2 Offshore wind power planning

While the remarkable achievement of the Chinese wind power industry is attributed to onshore wind power, the geographic mismatch of generation and demand places a heavy burden on transmission and grid planning. Since there are abundant offshore wind resources along the Southeast coastline where electricity demand is strong, the trend of promoting offshore wind power development is inevitable [49]. Scholars have suggested several approaches to offshore wind power development in China, including: (1) improve independent research and development in wind technologies (e.g., wind turbine manufacture, installation, construction, etc.) through spiral interactive innovation; (2) modify and upgrade the policy framework, especially the tariff policy and the financial subsidy policy; (3) encourage the local governments to guide the development through a market-based mechanism; and (4) integrate wind energy to the grid [50]. In 2020 China invested US$303 billion and installed 3 GW of new offshore wind capacities, equivalent to more than half of all global new offshore installations [2].

6.4.3 Smart grid

The smart grid will contribute to advancing the integration of renewables through advanced information, communication, and management technologies [51,52]. A typical smart grid system consists of variable energy sources, energy storage, power electronic interface, power control, and power grid load [53]. Based on the metering records of consumers' energy consumption, the trend in wind power penetration in the local grid distribution system could be predicted [54]. On the other hand, electricity generation is presently monitored and controlled remotely via Advanced Metering Infrastructure and Supervisory Control and Data Acquisition. Smart homes, intelligent buildings, and electrical vehicles can also serve as smart grid components. For instance, electric vehicles can be considered distributed energy storage units [53]. The European Union is moving into the field of Smart Grid proactively, and China is making similar moves.

The SGC of China has committed to invest USD 350 billion between 2021 and 2025 to upgrade the current power grids while building new power systems with improved voltage regulation capability and better compatibility with RE [55].

6.4.4 Merit-order-based dispatch

The merit-order-based dispatch tends to give priority to power plants to deliver and dispatch according to marginal generation costs. Because of the close-to-zero marginal cost of wind, a merit-order-based dispatch would favor the purchase of power from wind farms. The conventional energy sources would then compete for the remaining demand not covered by the renewables (hard coal and fuel oil, etc.). In China, the dispatch order was characterized by inefficient dispatch, implying that the grid company would try to distribute equal shares of operating hours to all thermal power plants [56]. Since 2009, an energy-saving and environmentally friendly generation dispatching (ESGD) model, which preestablishes the dispatch order based on pollutant emission, has been carried out in five provinces [57]. However, as an administrative measure, ESGD provides relatively small improvement. It does not change economic incentives and potentially exacerbates center-provincial tensions [56]. A full market-based ESGD model would require bidding for dispatch, based on the marginal cost which may only be realized in the long-term future.

6.5 Conclusion

Over the last two decades, China has made remarkable progress in wind energy development. China leads the world in wind capacity installation and wind turbine manufacturing output. However, such a leading position has not resulted in a correspondingly superior wind energy output. China still suffers from transmission and grid connectivity challenges, alongside curtailment problems. The electricity system is not flexible enough to accommodate wind intermittency. The local and central governments have different wind development priorities, resulting in irrational investment decisions and ineffective management.

Currently, the integration of wind energy into the grid is a key priority in China. Reforms via transmission planning, increasing system flexibility through retrofitting coal-fired power plants, introducing DR programs, and improving energy storage are ongoing. To ensure a level playing field for wind and thermal power plants, a legally binding carbon reduction target and carbon-trading initiatives have been established. However, such initiatives have already begun with anticipations for full legal implementations. In the future, market reform in the electricity market should be continued, alongside merit-order-based dispatch and the development of a well-functioned ancillary market. By addressing these key challenges, a clean, smart, and sustainable electricity system is highly foreseeable in China.

Acknowledgment

We gratefully acknowledge the editorial assistance of Miss Melody Ma.

References

[1] Peidong Z, Yanli Y, Yonghong Z, Lisheng W, Xinrong L. Opportunities and challenges for renewable energy policy in China. Renew Sustain Energy Rev 2009;13(2):439–49.
[2] Global Wind Energy Council. Global wind report 2021; 25 March 2021.
[3] The World Bank. GDP per capita, PPP (current international $)—China (1990—2020), <https://data.worldbank.org/indicator/NY.GDP.PCAP.PP.CD?end = 2020&locations = CN&start = 1979&view = chart> [accessed 21.03.22].
[4] Kahrl F, Williams J, Jianhua D, Junfeng H. Challenges to China's transition to a low carbon electricity system. Energy Policy 2011;39(7):4032–41.
[5] International Energy Agency. Electricity generation by source, People's Republic of China 1990–2020, <https://www.iea.org/fuels-and-technologies/electricity>.
[6] McElroy MB, Lu X, Nielsen CP, Wang Y. Potential for wind-generated electricity in China. Science 2009;325(5946):1378–80.
[7] IRENA Renewable Energy Statistics database. Installed electricity capacity by country/area (MW) by Country/area, Technology, Grid connection and Year, <http://pxweb.irena.org/pxweb/en/IRENASTAT/IRENASTAT__Power%20Capacity%20and%20Generation/ELECCAP_2021_cycle2.px/>.
[8] Working guidance for carbon dioxide peaking and carbon neutrality in full and faithful implementation of the new development philosophy, <https://en.ndrc.gov.cn/policies/202110/t20211024_1300725.html>; 2021.
[9] Beijing declaration on wind energy, <https://gwec.net/wp-content/uploads/2020/11/Beijing-Declaration-EN.pdf>; 2020.
[10] Notice of CPC Central Committee and the State Council on further deepening reform on the electricity market structure, <http://drc.gd.gov.cn/gdsnyj/gkmlpt/content/3/3736/mpost_3736971.html#3862>; 2015.

[11] Hove A. Trends and contradictions in China's renewable energy policy, <https://www.energypolicy.columbia.edu/research/commentary/trends-and-contradictions-china-s-renewable-energy-policy> [accessed 22.03.22].
[12] Lam J, Woo C-K, Kahrl F, Yu W. What moves wind energy development in China? Show me the money!. Appl Energy 2013;105:423–9.
[13] Lin MT. China continues strong renewables policy support after record PV, offshore wind power expansion in 2021. IHS Markit. <https://cleanenergynews.ihsmarkit.com/research-analysis/china-continues-strong-renewables-policy-support-after-record-.html> [accessed 22.03.22].
[14] Pek A. GWEC releases global wind turbine supplier ranking for 2020. Global Wind Energy Council. <https://gwec.net/gwec-releases-global-wind-turbine-supplier-ranking-for-2020/> [accessed 22.03.22].
[15] Liao C, Jochem E, Zhang Y, Farid NR. Wind power development and policies in China. Renew Energy 2010;35(9):1879–86.
[16] Dai Y, Xue L. China's policy initiatives for the development of wind energy technology. Clim policy 2015;15(1):30–57.
[17] Notice on wind power development and management; 2005.
[18] NEA, Notice on improving the management of annual wind development. <http://zfxxgk.nea.gov.cn/auto87/201505/t20150520_1930.htm>; 2015.
[19] Zhao X, Zhang S, Zou Y, Yao J. To what extent does wind power deployment affect vested interests? A case study of the Northeast China Grid. Energy Policy 2013;63:814–22.
[20] GWEC, Global wind report: annual market update 2015, GWEC, Brussels; 2016.
[21] Lu X, McElroy MB, Peng W, Liu S, Nielsen CP, Wang H. Challenges faced by China compared with the US in developing wind power. Nat Energy 2016;1:16061.
[22] Zhou Y, Luckow P, Smith SJ, Clarke L. Evaluation of global onshore wind energy potential and generation costs. Environ Sci Technol 2012;46(14):7857–64.
[23] Yang M, Patiño-Echeverri D, Yang F. Wind power generation in China: understanding the mismatch between capacity and generation. Renew Energy 2012;41:145–51.
[24] KahrlF., Wang,X. Integrating renewable energy into power systems in China: a technical primer, Regulatory Assistance Project, Beijing; 2014.
[25] NEA. NEA publishes total electricity demand in 2015, <http://www.nea.gov.cn/2016-01/15/c_135013789.htm>; 2016.
[26] NBS. Communique on economy and social development in 2015. National Bureau of Statistics. <http://www.stats.gov.cn/tjsj/zxfb/201602/t20160229_1323991.html>; 2016.
[27] Plan on renewable consumption near production site; 2016.
[28] Feng S. As China's energy mix shifts to renewables, how can power markets evolve? China Dialogue. <https://chinadialogue.net/en/energy/power-markets-chinas-energy-mix-shifts-to-renewables/> [accessed 22.03.22].
[29] FNA. Monitoringbericht 2014. Federal Network Agency; 2014. <http://www.bundesnetzagentur.de/SharedDocs/Downloads/DE/Allgemeines/Bundesnetzagentur/Publikationen/Berichte/2014/Monitoringbericht_2014_BF.pdf?__blob = publicationFile&v = 4>.
[30] Martinot E. Grid integration of renewables in China: learning from the cases of California, Germany, and Denmark. <http://www.martinot.info/Martinot_CVIG_2015_DE-DK-CA.pdf>; 2015.
[31] Albadi M.H., El-Saadany E., Demand response in electricity markets: an overview. In: 2007 IEEE power engineering society general meeting; 2007.
[32] Notice on guaranteed procurement of wind and solar energy, <http://www.gov.cn/xinwen/2016-06/01/content_5078698.htm>; 2016.
[33] Notice on enhancing accommodation of renewable power in three-north regions, <https://www.66law.cn/tiaoli/34699.aspx>; 2016.
[34] Notice on initiating pilot programs on increasing thermal power flexibility, <http://fzggw.jiangsu.gov.cn/art/2016/7/7/art_284_6648515.html>; 2016.
[35] Notice on initiating pilot programs on admission of electrical storage for ancillary service in the "Three North" region, <https://www.waizi.org.cn/law/.11395.html>; 2016.
[36] Qi Y, Dong W, Dong C, Huang C. Understanding institutional barriers for wind curtailment in China. Renew Sustain Energy Rev 2019;105:476–86. Available from: https://doi.org/10.1016/j.rser.2019.01.061.
[37] Action plan on power distribution network construction and transformation for 2015–2020; 2015.
[38] Reportlinker. China smart electric meter industry report, 2016–2020, <https://www.reportlinker.com/p03837879/China-Smart-Electric-Meter-Industry-Report.html>; 2016.
[39] Interim management methods for a new central incentive fund in support of comprehensive demand side management (DSM) pilot cities. N. d. a. r. commission and M. o. Finance; 2012.
[40] Xinhua. China's first grid-load interaction system goes into operation. <http://news.xinhuanet.com/fortune/2016-06/15/c_1119049318.htm>.
[41] NDRC, Interim measures for assessment of grid companies on meeting the demand side management target. <http://www.nea.gov.cn/131300574_31n.pdf>; 2011.
[42] SERC. Interim measures for the management of ancillary service by grid-connected power plant; 2006.
[43] NEA. Notice on management of ancillary service in southern grid. <http://nfj.nea.gov.cn/action/front/contentAction_initViewContent?content.contentId = 402881e54e7bcc28014f2520b4a90036>; 2015.
[44] Lo AY. Carbon trading in a socialist market economy: can China make a difference? Ecol Econ 2013;87:72–4.
[45] Tan L. The first year of China's national carbon market, reviewed. China Dialogue. <https://chinadialogue.net/en/climate/the-first-year-of-chinas-national-carbon-market-reviewed/> [accessed 24.03.22].
[46] Mills A, Wiser R, Porter K. The cost of transmission for wind energy in the United States: a review of transmission planning studies. Renew Sustain Energy Rev 2012;16(1):1–19.

[47] Dong L, Liang H, Gao Z, Luo X, Ren J. Spatial distribution of China's renewable energy industry: regional features and implications for a harmonious development future. Renew Sustain Energy Rev 2016;58:1521–31.
[48] Ming Z, Shaojie O, Hui S, Yujian G, Qiqi Q. Overall review of distributed energy development in China: status quo, barriers and solutions. Renew Sustain Energy Rev 2015;50:1226–38.
[49] Feng Y, et al. Overview of wind power generation in China: status and development. Renew Sustain Energy Rev 2015;50:847–58.
[50] He D-X. Coping with climate change and China's wind energy sustainable development. Adv Clim Change Res 2016;7(1):3–9.
[51] Gao M, Jian L, Li W, Yao X. A stochastic programming based scheduling and dispatch for smart grid with intermittent wind power. Glob J Technol Optim 2016;2016.
[52] Hossain M, Madlool N, Rahim N, Selvaraj J, Pandey A, Khan AF. Role of smart grid in renewable energy: an overview. Renew Sustain Energy Rev 2016;60:1168–84.
[53] Colak I, Fulli G, Bayhan S, Chondrogiannis S, Demirbas S. Critical aspects of wind energy systems in smart grid applications. Renew Sustain Energy Rev 2015;52:155–71.
[54] Keyhani A. Design of smart power grid renewable energy systems. John Wiley & Sons; 2016.
[55] IRENA and China state grid pave way towards smart electrification. IRENA. <https://irena.org/newsroom/articles/2022/Feb/IRENA-and-China-State-Grid-Pave-Way-Towards-Smart-Electrification> [accessed 24.03.22].
[56] Kahrl F, Williams JH, Hu J. The political economy of electricity dispatch reform in China. Energy Policy 2013;53:361–9.
[57] Zhong H, Xia Q, Chen Y, Kang C. Energy-saving generation dispatch toward a sustainable electric power industry in China. Energy Policy 2015;83:14–25.

Chapter 7

Vertical wind speed profiles in atmospheric boundary layer flows

Sukanta Basu
Faculty of Civil Engineering and Geosciences, Delft University of Technology, Delft, the Netherlands

7.1 Introduction

The vertical profile of wind speed, extending up to a few hundreds of meters above ground or sea level, is a critical meteorological variable for several application arenas, including (but not limited to) wind resource assessments [1,2], wind engineering [3,4], air pollutant dispersion [5,6], aviation [7], and bird migration studies [8]. Such profiles are typically measured by tall meteorological masts, sodars, lidars, wind profilers, aircraft, balloons, and kites [9–13]. Given the high cost of the instruments/infrastructures and other logistical issues, in general, there is a dearth of tall wind profile measurements around the world. In the absence of observational wind data, high-resolution atmospheric models (e.g., mesoscale models) are often utilized to generate synthetic wind data. Even though this numerical approach has been showing significant promise, there is room for improvement in terms of increasing the accuracy and reliability of the simulated wind data. In the absence of either observed or reliable atmospheric model-generated wind profiles, a wide range of similarity theory-based and empirical equations of varying complexity have been proposed as viable alternatives for wind profile estimations. These equations utilize near ground/sea level wind data (either measured by automated weather stations, mesonets, ocean buoys, or estimated via satellite remote-sensing) and other ancillary data to estimate winds at higher altitudes.

In this chapter, we first provide some examples of vertical wind speed profiles based on field observations from around the world. These examples provide a glimpse into the diversity of wind speed profiles in our atmosphere. Next, we discuss various similarity theory-based and empirical wind profile equations. None of these profiles are generic in nature; rather they are only applicable for specific atmospheric conditions (e.g., neutral stability), suitable for specific locations (e.g., surface layer), or only valid for certain phenomena (e.g., hurricane). Throughout this chapter, we provide numerous illustrative examples from offshore wind energy literature.

7.2 Diversity of wind speed profiles

Wind speed profiles in the atmospheric boundary layer (ABL; the lowest part of our atmosphere) exhibit a myriad of shapes. Sometimes the profiles are approximately logarithmic in nature; other times they can portray somewhat linear trends. There are specific meteorological conditions when wind speeds are more-or-less uniform with height. Certain other conditions can promote "jet" shapes with low-level wind maxima. Some of these shapes can be seen in Fig. 7.1.

The well-known "Leipzig wind profile" is shown in the left panel of Fig. 7.1. The wind data were measured by Mildner [14] using pilot-balloons more than ninety years ago. This specific profile played a pivotal role in early ABL studies (e.g., [15]). Two wind profiles from the well-known Wangara field campaign [16] are documented in the middle and right panels of Fig. 7.1. This campaign was conducted in July and August of 1967 at Hay, Australia [16]. The landscape was flat and almost homogeneous. Given the ideal site condition, the observed wind profiles and other meteorological data have been used for model validation over the years (see [17] and the references therein). The middle panel of Fig. 7.1 represents a daytime unstable condition. Due to strong turbulent mixing, the wind profile is close to being uniform with height. In contrast, the right panel of Fig. 7.1 shows the presence of a low-level jet (LLJ); the nose of the

Wind Energy Engineering. DOI: https://doi.org/10.1016/B978-0-323-99353-1.00031-1

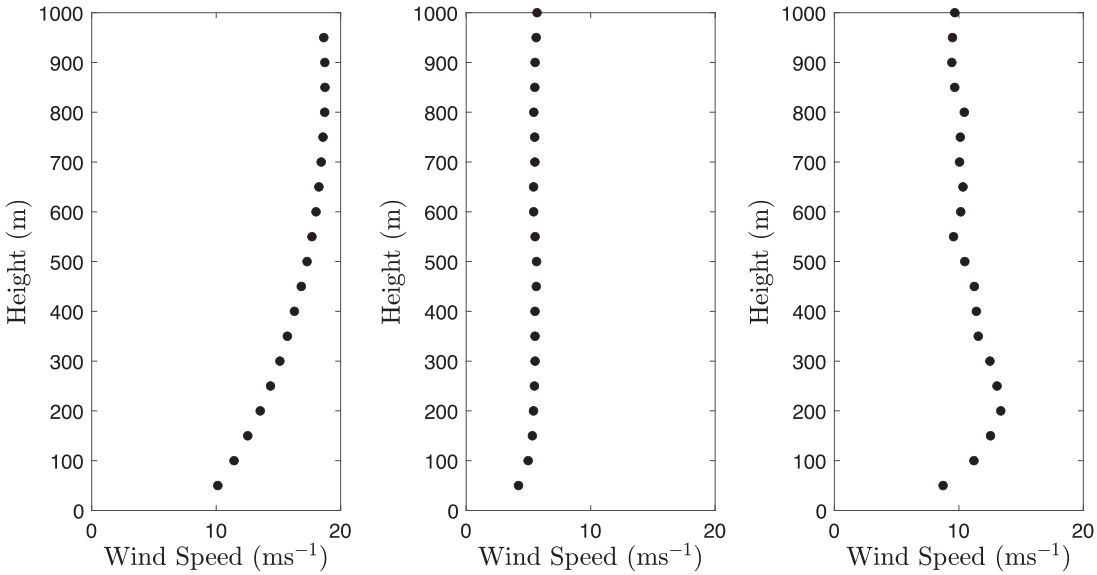

FIGURE 7.1 Observed wind profiles at Leipzig, Germany (*left panel*) and at Wangara, Australia (*middle and right panels*).

LLJ is around 200 m above ground level. This profile was measured during nighttime stably stratified condition. Under such a scenario, turbulent mixing is weak and various atmospheric layers can be partially decoupled from each other and from the underlying surface. As a result, a low-level wind maximum can form; the physical mechanism associated with this phenomenon is called inertial oscillation. More information on LLJs can be found in standard textbooks of ABL (e.g., [18,19]).

A few years ago, Peña et al. [20] attempted to identify canonical wind profiles measured at a coastal onshore location in Denmark. Based on visual inspection, they identified ten different shapes from an extensive observational database composed of sonic anemometers and lidar measurements. Instead of laborious manual identification, Durán et al. [21] proposed an automated wind profile classification approach by using self-organizing feature maps [22]. The readers are encouraged to peruse Peña et al. [20] and Durán et al. [21] to appreciate the diversity of wind profiles.

At present, only atmospheric models [23] with appropriate physical parameterizations [24] have the ability to capture the rich diversity of wind profiles. However, these models are computationally expensive and often suffer from different biases and errors. Instead, for certain applications, one can make use of similarity theory-based and/or empirical equations. In the following section, we delve into various types of similarity theories.

7.3 Similarity theory

Arya [5] defined similarity theory in a succinct manner:

> *A similarity theory, based on dimensional analysis, provides a means of grouping the variables into some dimensionless similarity parameters and organizing the experimental data in the most efficient manner to derive universal similarity relationships.*

In the ABL literature, a wide range of similarity theories have been proposed over the past century (see [9,18,19]). We only discuss the ones which are relevant for wind energy applications.

7.3.1 Logarithmic law of the wall

The logarithmic law of the wall (henceforth Π_{LOG}) is quite often used in wind energy applications:

$$U = \frac{u_*}{\kappa} \ln\left(\frac{z}{z_\circ}\right), \tag{7.1}$$

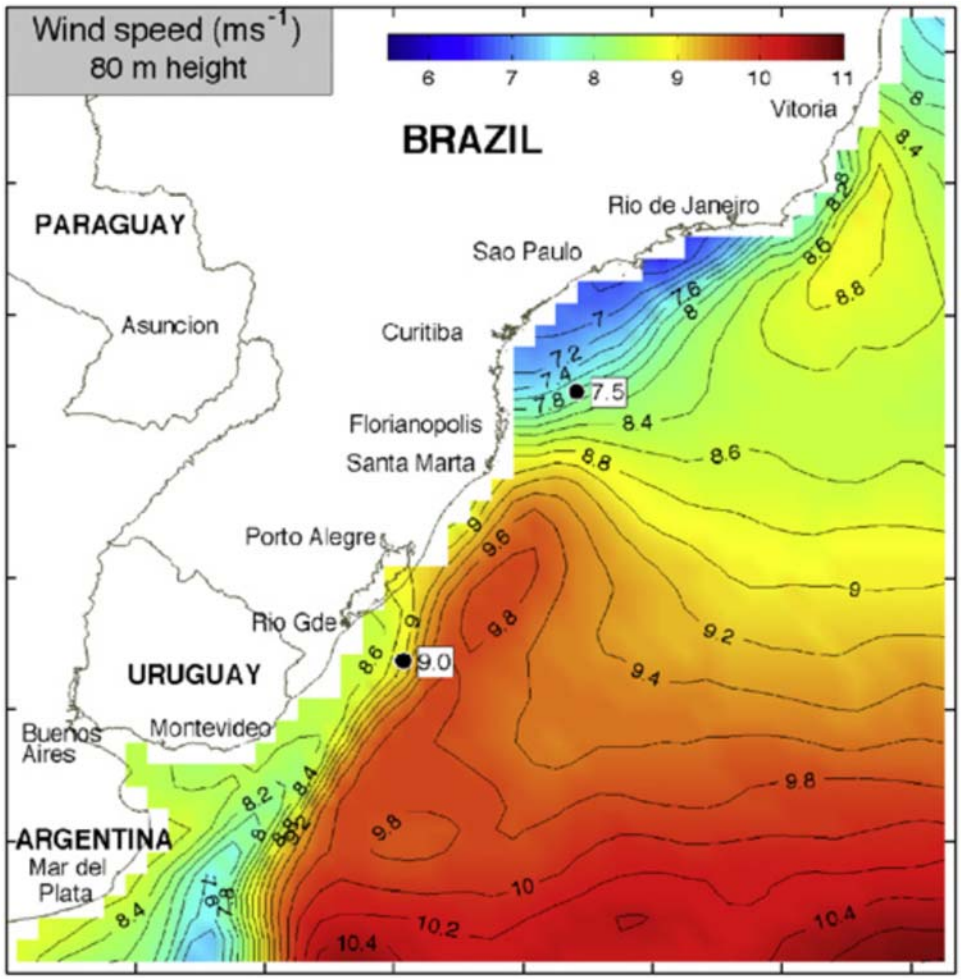

FIGURE 7.2 Offshore wind resource map of southeastern Brazil. This map was created by extrapolating QuikSCAT wind data using Π_{LOG} with $z_\circ = 0.2$ mm. Dates: August 1999–June 2007. *Reproduced with permission from Pimenta F, Kemptona W, Garvinea R. Combining meteorological stations and satellite data to evaluate the offshore wind power resource of Southeastern Brazil. Renew Energy 2008;33:2375–87.*

where $z_\circ$ is the so-called aerodynamic roughness length. Surface friction velocity is represented by u_*. von Kármán constant is denoted by κ. Eq. (7.1) could be re-written as follows:

$$\frac{U_H}{U_r} = \frac{\ln\left(\frac{H}{z_\circ}\right)}{\ln\left(\frac{z_r}{z_\circ}\right)}, \tag{7.2}$$

where U_r is the reference (or measured) wind speed at a given height (z_r), U_H is the estimated wind speed at hub-height (H).

Π_{LOG} has a firm physical basis. It can be derived by a dimensional analysis as well as by more formal approaches (e.g., Millikan's approach). In theory, Π_{LOG} is only applicable in the surface layer[1] for neutrally stratified atmospheric conditions (the regime where the buoyancy effects are virtually insignificant). However, in various wind resource assessment projects, Π_{LOG} has been (quite inappropriately) utilized for the extrapolation of nonneutral (aka diabatic) wind speed profiles.

For example, Pimenta et al. [25] created an offshore wind map ($H = 80$m) of southeastern Brazil by extrapolating satellite remote-sensing (QuikSCAT)-based wind data using Π_{LOG} (Fig. 7.2). Even though this wind map shows heterogeneous spatial distribution of wind speeds, the omission of atmospheric stability makes this wind map less than useful.

1. The lowest part of the ABL is called the surface layer. In this layer, the Coriolis effects can be neglected. Turbulent fluxes of momentum, heat, moisture, and other scalars are assumed to be invariant with height in the surface layer.

7.3.2 Monin–Obukhov similarity theory

Differentiating Eq. (7.1) with respect to z leads to the following equation:

$$\left(\frac{\kappa z}{u_*}\right)\left(\frac{\partial U}{\partial z}\right) = 1. \tag{7.3}$$

This equation is only valid for neutrally stratified conditions. For nonneutral cases, based on dimensional analysis, Monin and Obukhov [26] hypothesized that:

$$\left(\frac{\kappa z}{u_*}\right)\left(\frac{\partial U}{\partial z}\right) = \phi_m\left(\frac{z}{L}\right), \tag{7.4}$$

where L is the Obukhov length [18,19]. The ratio z/L is called the stability parameter (ζ). The function ϕ_m is commonly known as the gradient stability function. By definition, $\phi_m(0)$ equals to 1 (neutral condition).

The exact form of $\phi_m\left(\frac{z}{L}\right)$ cannot be derived solely based on a dimensional analysis; rather, observational (or simulated by high-fidelity models) datasets are needed to derive these functions. In the literature, numerous $\phi_m\left(\frac{z}{L}\right)$ functions have been proposed; please refer to Table 3 of Ref. [27] for some examples.

Eq. (7.4) can be integrated to yield:

$$U = \frac{u_*}{k}\left[\ln\left(\frac{z}{z_\circ}\right) - \psi_m\left(\frac{z}{L}, \frac{z_\circ}{L}\right)\right], \tag{7.5}$$

where $\psi_m\left(\frac{z}{L}, \frac{z_\circ}{L}\right) = \int_{z_\circ/L}^{z/L} \frac{1-\phi_m(\zeta)}{\zeta} d\zeta$ and $\zeta = \frac{z}{L}$. The function ψ_m is widely known as the stability correction term. In this chapter, Eq. (7.5) will be referred to as Π_{MO}. It can be re-written as follows:

$$\frac{U_H}{U_r} = \frac{\ln\left(\frac{H}{z_\circ}\right) - \psi_m\left(\frac{H}{L}, \frac{z_\circ}{L}\right)}{\ln\left(\frac{z_r}{z_\circ}\right) - \psi_m\left(\frac{z_r}{L}, \frac{z_\circ}{L}\right)}. \tag{7.6}$$

Since $z_\circ \ll z_r < H$, it is a common practice to neglect the effect of roughness in the stability correction terms. In other words, Eq. (7.6) can be simplified to:

$$\frac{U_H}{U_r} = \frac{\ln\left(\frac{H}{z_\circ}\right) - \psi_m\left(\frac{H}{L}\right)}{\ln\left(\frac{z_r}{z_\circ}\right) - \psi_m\left(\frac{z_r}{L}\right)}. \tag{7.7}$$

By convention, the stability correction terms (ψ_m) are "subtracted" from the log-law. Thus, with respect to the neutral condition, the wind speeds are supposed to increase (decrease) for stable (unstable) conditions. Several formulations for ψ_m exists in the literature akin to ϕ_m functions. For example, Barthelmie [28] and Holtslag et al. [29] utilized the so-called Businger-Dyer correction terms [30–32]:

$$\psi_m = -\frac{5z}{L}; \text{for} \frac{z}{L} \geq 0 \tag{7.8a}$$

$$\psi_m = 2\ln\left(\frac{1+x}{2}\right) + \ln\left(\frac{1+x^2}{2}\right) - 2\tan^{-1}x + \frac{\pi}{2}; \quad \text{for } \frac{z}{L} \leq 0 \tag{7.8b}$$

where

$$x = \left(1 - \frac{16z}{L}\right)^{1/4}.$$

It should be noted that Monin-Obukhov Similarity Theory (MOST, Π_{MO}) is strictly valid in the surface layer. For typical stably stratified conditions (i.e., $\frac{z}{L} \geq 0$), hub-heights of 100–150 m are much higher than the top of the surface layer. Under this scenario, the applicability of Π_{MO}, Eqs. (7.4–7.7), is highly questionable.

Holtslag et al. [29] analyzed offshore wind data from the Ijmuiden tower in the North Sea (close to the Dutch coastline). They plotted the ratio U_{92}/U_{58} as a function of the stability parameter (z/L); see Fig. 7.3. In addition to the

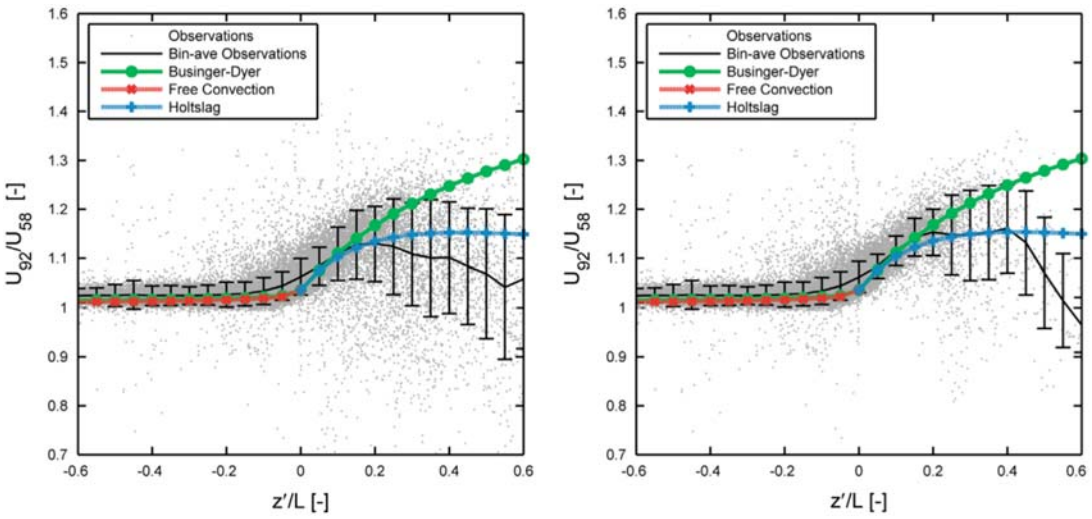

FIGURE 7.3 *Left panel*: the ratio of wind speeds at 92 and 58 m as a function of the stability parameter. Observational data from the IJmuiden tower were used for making this plot. Several empirical formulations (e.g., Businger-Dyer functions) for wind shear are overlaid for direct comparison. *Right panel*: same as left panel; except, filtered data are used in this plot. Basically, for stable conditions, cases with $u_* < 0.2$ m/s were removed. In these plots, $z' = 13.5$ m. *Reproduced with permission from Holtslag MC, Bierbooms WAAM, van Bussel GJW. Validation of surface layer similarity theory to describe far offshore marine conditions in the Dutch North Sea in scope of wind energy research. J Wind Eng Ind Aerodyn 2015;136:180–91.*

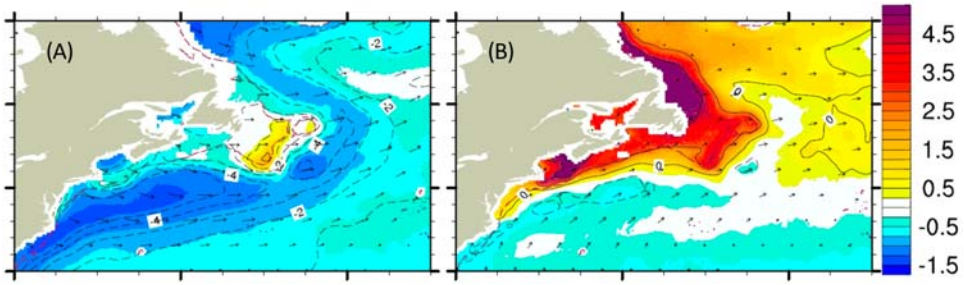

FIGURE 7.4 Π_{MO}-based 80 m wind speed minus Π_{LOG}-based 80 m wind speed (m/s). (A) The winter months (DJF) of 2000–06. (B) The summer months (JJA) of 2000–06. *Reproduced with permission from Capps SB, Zender CS. Global ocean wind power sensitivity to surface layer stability. Geophys Res Lett 2009;36:L09801.*

Businger-Dyer functions [i.e., Eqs. (7.8a) and (7.8b)], they overlaid other empirical stability correction formulations. For example, the ψ_m function proposed by Beljaars and Holtslag [33] was invoked. Based on Fig. 7.3, one can conclude that for unstable conditions, the scatter of the observed data is marginal. More importantly, all the empirical formulations are more-or-less in-line with the observations. However, for stable conditions, the scatter increases tremendously. The empirical formulations performed reasonably well for weakly stable conditions; however, they were not able to capture the observed decrease of wind shear for very stable conditions.

Capps and Zender [34] compared Π_{LOG} and Π_{MO} for the estimation of the global ocean wind energy at 80 m above sea level. They used QuikSCAT-based 10 m wind data and other data sources (e.g., NCEP-DOE AMIP-II Reanalysis). In Fig. 7.4, $U(80\text{m})_{\Pi_{MO}} - U(80\text{m})_{\Pi_{LOG}}$ values are shown for eastern North America. The extrapolated wind profiles are nearly logarithmic during the winter months (*left panel*). However, during the summer months, when stability effects are generally more important, Π_{LOG} underestimates the 80 m wind speed values substantially (3 m/s or more) in extended regions. This figure clearly underscores the need for stability correction functions in the extrapolation methodologies, which have been historically neglected in wind resource estimation projects.

7.3.3 Extension of Monin–Obukhov similarity theory

As mentioned earlier, MOST is strictly valid in the surface layer. Gryning et al. [35] extended the MOST-based wind profiles for the entire boundary layer. In conventional MOST, only a surface layer length scale (l_S) is involved. Gryning et al. [35] hypothesized that an integrated length scale (l) for the entire boundary layer can be written as:

$$\frac{1}{l} = \frac{1}{l_S} + \frac{1}{l_M} + \frac{1}{l_U}; \tag{7.9}$$

where l_M and l_U represent middle and upper boundary layer length scales, respectively. For neutral conditions, they assumed $l_S = z$ and $l_U = (h - z)$; where the variable h denotes boundary layer height. For nonneutral conditions, they followed the MOST prescription of $l_S = \frac{z}{\phi_m}$; where, ϕ_m is the gradient stability function described earlier.

Gryning et al. [35] made another crucial assumption regarding the dependency of friction velocity (u_*) with height; for simplicity, they assumed that u_* decreases linearly with height and goes to zero at the top of the boundary layer. With all these assumptions, they arrived at the following equations for wind speed profiles for different stability conditions (see also [36]):

$$U = \frac{u_*}{\kappa}\left[\ln\left(\frac{z}{z_0}\right) + \frac{z}{l_M} - \frac{z}{h}\left(\frac{z}{2l_M}\right)\right]; \text{for} \frac{z}{L} = 0 \tag{7.10a}$$

$$U = \frac{u_*}{\kappa}\left[\ln\left(\frac{z}{z_0}\right) - \psi_m\left(\frac{z}{L}\right)\left(1 - \frac{z}{2h}\right) + \frac{z}{l_M} - \frac{z}{h}\left(\frac{z}{2l_M}\right)\right]; \text{for} \frac{z}{L} < 0 \tag{7.10b}$$

$$U = \frac{u_*}{\kappa}\left[\ln\left(\frac{z}{z_0}\right) - \psi_m\left(\frac{z}{L}\right) + \frac{z}{l_M} - \frac{z}{h}\left(\frac{z}{2l_M}\right)\right]; \text{for} \frac{z}{L} > 0 \tag{7.10c}$$

Collectively, these wind speed profile equations are termed as Π_{MOX} in this chapter. The stability correction terms (ψ_m) were discussed in the context of Π_{MO}. Identical formulations are also used by [35]. However, in contrast to Π_{MO}, the Π_{MOX} equations require additional parameterizations for h and l_M. Please refer to [35] for further technical details.

Sathe et al. [36] analyzed observational data from a 116 m tall meteorological mast near the Egmond aan Zee offshore wind farm (OWEZ), the Netherlands. They compared Π_{MO} and Π_{MOX} for the OWEZ case under a range of stably stratified conditions (see Table 7.1). Given the complexity of the l_M parameterization in Π_{MOX}, they also explored a slightly simplified formulation in which the length scale l_M is neglected. From Table 7.1, it is evident that Π_{MO} performs quite poorly in the case of very stable condition at upper elevations (i.e., at 70 m and 116 m). The Π_{MOX} formulation with or without l_M performs much better for these scenarios. In the case of near-neutral stability, the performances of Π_{MO} and Π_{MOX} are nearly identical.

We would like to note that Sathe et al. [36] used Businger-Dyer's ψ_m functions [i.e., Eqs. (7.8a) and (7.8b)] in their study. It will be worthwhile revisiting their study with a diverse suite of ψ_m parameterizations (e.g., [33]) in conjunction with Π_{MO}.

TABLE 7.1 Root mean squared error (m/s) between observed and various extrapolated wind profiles.

	21 m	70 m	116 m
Near-neutral stable			
Π_{MO}	0	1.47	2.66
Π_{MOX}	0.02	1.46	2.62
Π_{MOX}, neglecting l_M	0.03	1.47	2.62
Stable			
Π_{MO}	0	2.36	5.71
Π_{MOX}	0.08	2.50	4.35
Π_{MOX}, neglecting l_M	0.03	2.62	4.39
Very stable			
Π_{MO}	0	8.48	21.97
Π_{MOX}	0.48	5.91	9.22
Π_{MOX}, neglecting l_M	0.62	6.06	9.24

Observational data from OWEZ in the wind sector of 225–315 degrees are utilized here.
Source: Sathe A, Gryning S-E, Peña A. Comparison of the atmospheric stability and wind profiles at two wind farm sites over a long marine fetch in the North Sea. Wind Energy 2011;14:767–80.

7.3.4 Geostrophic drag laws

Following the seminal work by Kazanski and Monin [37], various wind profile relationships were proposed in the atmospheric science literature [38–40]. These relationships make use of various boundary layer scaling hypotheses and are collectively known as geostrophic drag laws (Π_{GDL}). In principle, they are applicable in the outer part of the ABL (i.e., above the surface layer) and asymptotically match with Π_{MO} in the surface layer. Unfortunately, due to the lack of reliable high-altitude wind data, Π_{GDL} formulations have not been properly validated and their accuracy remains questionable. Furthermore, their usage requires the availability of different meteorological variables as input: geostrophic wind speed, boundary layer height, Brunt-Väisälä frequency, Obukhov length, friction velocity, roughness length, and Coriolis parameter. Since some of these variables are not routinely available, it is not surprising that Π_{GDL} formulations have not been popular in practical applications (including wind energy). In this respect, the papers by Cvitan et al. [41] and Emeis [42] are worth mentioning as they utilize simplified versions of Π_{GDL} formulations.

7.4 Empirical formulations

In parallel to the development of various similarity theories, a number of empirical formulations of wind speed profiles have been proposed in the literature. In this section, we summarize a few of them.

7.4.1 Power law

Even though Π_{LOG}, Π_{MO}, and Π_{MOX} formulations have been used by the wind energy industry, they are much less popular than the following power-law relationship (Π_{PL}):

$$\frac{U_H}{U_r} = \left(\frac{H}{z_r}\right)^{\alpha}; \tag{7.11}$$

Here α is the so-called shear exponent or the Hellmann exponent [43]. If a reference wind speed is available (e.g., from an ocean buoy), the only unknown in Eq. (7.11) is α. It is well-established in the literature that α strongly varies with atmospheric stability and surface roughness [44–47]. Thus, α is expected to exhibit diurnal, seasonal, and interannual variations. The value of α may also depend on advection and nonequilibrium conditions, which are common in the coastal zone. Nevertheless, constant values of α are often used in wind energy projects. Without any doubt, $\alpha = 1/7$ or 0.14 is the most commonly used value in wind resource estimations. Please note that $\alpha = 1/7$ does not have any physical basis for turbulent boundary layers. It is empirically estimated and has been found to approximately hold under near-neutral conditions over flat terrains with low roughness [43].

Intuitively, a parameterization for α which reliably takes into account the effects of atmospheric stability and surface roughness should yield an improvement over the traditional constant α-based extrapolation approach. Keeping this in mind, Hsu [48] created a simple lookup table for α (Table 7.2) based on a field study on the flat southern coast of St. Croix, U. S. Virgin Islands. To the best of our knowledge, the errors and uncertainties associated with this lookup table for other locations have never been evaluated.

Instead of using the aforementioned lookup table and/or other ad-hoc parameterizations, a far better option is to estimate α from near-surface wind data and utilize it in Π_{PL} for vertical extrapolation. For example, if wind speed measurements (U_1 and U_2) corresponding to two observational levels (z_1 and z_2) are available, α can be easily estimated by inverting Eq. (7.11):

$$\alpha = \frac{\ln(U_2/U_1)}{\ln(z_2/z_1)}. \tag{7.12}$$

TABLE 7.2 Approximate values of α as functions of various coastal environments and atmospheric stabilities.

Stability	Offshore waters	Flat, open coast	Towns or cities
Unstable	0.06	0.11	0.27
Neutral	0.10	0.16	0.34
Stable	0.27	0.40	0.60

Source: Hsu SA. Coastal meteorology. San Diego, CA: Academic Press, Inc.; 1988.

However, if more than two levels of wind data are measured, it is statistically more robust to utilize a standard (ordinary least squares-based) linear regression approach between $\ln(U_k)$ and $\ln(z_k)$; where the subscript k refers to different sensor levels. Please note that, in this regression approach, one implicitly assumes that α remains invariant with height which may not be physically very realistic.

Whether Π_{LOG} can be approximated by Π_{PL} was investigated by Sedefian [49] and Emeis [50]. By matching local slopes, it is straightforward to derive:

$$\alpha = \left[\ln\left(\frac{z}{z_\circ}\right)\right]^{-1}. \tag{7.13}$$

Hsu et al. [51] utilized this equation in an offshore setting. If one assumes $z = 10$ m and $z_\circ = 2 \times 10^{-4}$ m (commonly used in offshore wind energy literature, for example, [52]), α becomes approximately equal to 0.09 ($\ll 0.14$).

Corrigan and Matthiesen [53] analyzed offshore wind data taken over lake Erie in Canada. A ZephIR lidar system was deployed between May 2 and June 10 of 2013 to measure wind speeds and directions at heights of 40, 80, 120, 160, and 200 m, respectively. Even though the lidar's sampling frequency was 15 s, Corrigan and Matthiesen [53] averaged the wind data over 10 min intervals to reduce inherent fluctuations and noise. Then, using Eq. (7.12) in conjunction with wind data from the 80 and 200 m levels, they estimated α. The histogram of estimated values is shown in Fig. 7.5. The mean value of α was only 0.09, much smaller than the conventional value of 0.14. They also reported strong dependence of α on the prevalent wind direction.

7.4.2 Profiles for strong winds

In the wind engineering community, the Deaves and Harris equation [54,55] is quite popular. According to this formulation (Π_{DH}):

$$U(z) = \frac{u_*}{\kappa}\left[\ln\left(\frac{z}{z_\circ}\right) + 5.75\left(\frac{z}{h}\right) - 1.88\left(\frac{z}{h}\right)^2 - 1.33\left(\frac{z}{h}\right)^3 + 0.25\left(\frac{z}{h}\right)^4\right]. \tag{7.14}$$

Here h is the ABL height parameterized by $u_*/6f$. The Coriolis parameter is denoted by f. Even though the Π_{DH} formulation was originally proposed for strong wind and neutral condition, it has been used for other meteorological conditions (see [56]).

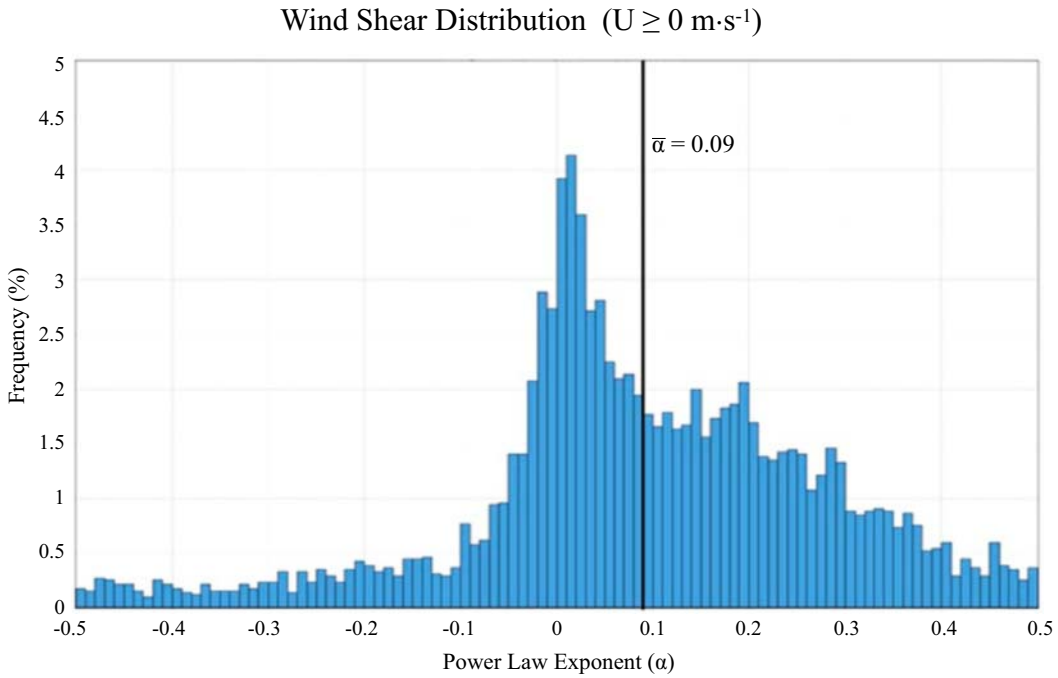

FIGURE 7.5 Histogram of estimated α from wind measurements taken over lake Erie, Canada. *Reproduced with permission from Corrigan D, Matthiesen DH. Analysis of the power law exponent applied to Lake Erie wind shear. Wind Eng 2017;41:103–13.*

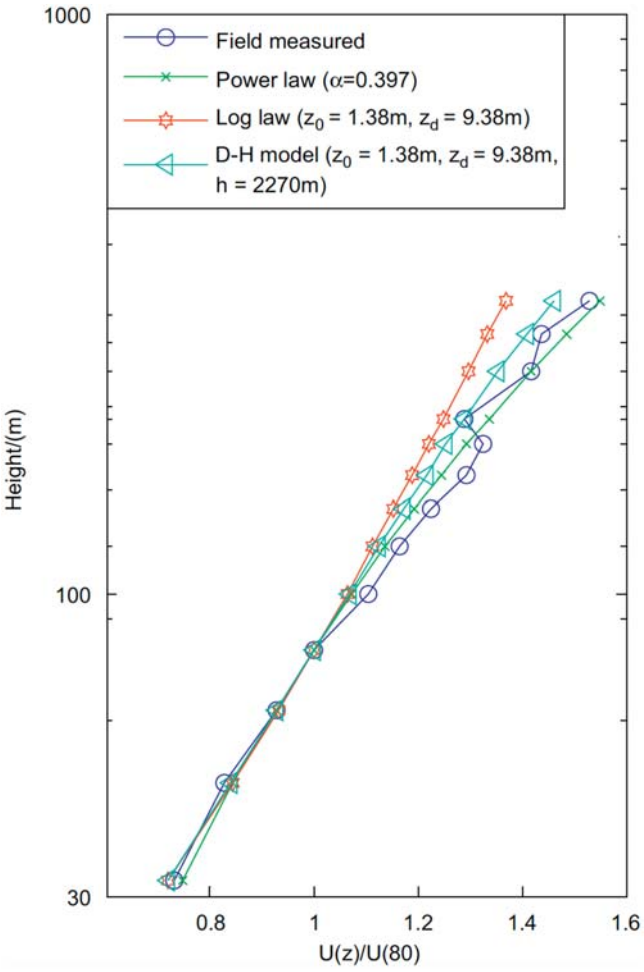

FIGURE 7.6 Comparison of measured and predicted wind speeds during windstorms [57]. *Reproduced with permission from Li Q, Zhi L, Hu F. Boundary layer wind structure from observations on a 325 m tower. J Wind Eng Ind Aerodyn 2010;98:818–32.*

Li et al. [57] analyzed wind data from a 325 m tall tower during twelve windstorms. The measured mean wind speed profile is shown in Fig. 7.6. They compared Π_{LOG}, Π_{PL}, and Π_{DH} against observations. The performance of Π_{PL} and Π_{DH} is comparable. However, Π_{LOG} significantly underestimates the observed wind speeds.

Vickery et al. [58] parameterized wind profiles in hurricanes as follows:

$$U(z) = \frac{u_*}{\kappa}\left[\ln\left(\frac{z}{z_\circ}\right) - a\left(\frac{z}{H^*}\right)^n\right], \tag{7.15}$$

where a and n are free parameters. H^* is the boundary layer height (or jet height) in a hurricane. Recently, an alternate formulation has been proposed by [59]:

$$U(z) = \frac{u_*}{\kappa}\left[\ln\left(\frac{z}{z_\circ}\right) + \eta_0 \sin\left(\frac{z}{H*}\right)\exp\left(-\frac{z}{H*}\right)\right], \tag{7.16}$$

where η_0 is equal to 9.026.

7.5 Concluding remarks

In this chapter, we have discussed various similarity theory-based and empirical wind profile formulations. In terms of model complexity (loosely based on the input data requirements), one can write:

$$\Pi_{PL} \subset \Pi_{LOG} \subset \Pi_{MO} \subset \Pi_{MOX} \subset \Pi_{\mathrm{GDL}}$$

Even though each of these formulations has its own strengths and weaknesses, some of them are clearly more suitable than others for practical applications.

We recommend that the usage of Π_{LOG} should be limited as it is only applicable for neutral conditions; such conditions are rarely present over land and offshore regions. On the same token, Π_{PL} should also not be used with constant α values. As a poor man's approach to account for stability, one can use Π_{PL} with variable α; in this strategy, wind data from the lowest two sensor levels can be utilized to estimate α as a function of time. If more sensor levels are available, one can utilize a more accurate linear regression approach.

Π_{MO} should be utilized for most situations for wind profile estimation within the surface layer. However, the selection of stability correction functions (ψ_m) will be extremely important. For unstable, neutral, and weakly stable conditions, the formulations by Businger and Dyer are adequate. However, for stronger stability conditions, one should experiment with alternative ψ_m formulations.

Π_{MOX} formulation performs better than Π_{MO} for heights above the surface layer. However, Π_{MOX} is much more complicated than Π_{MO} and includes ad-hoc parameterizations (with tuning parameters). Furthermore, by construction, Π_{MOX} cannot be used for heights above the ABL. Thus, for moderately stable and very stable conditions, this approach cannot be used beyond tens of m above the surface.

Arguably, Π_{GDL} are the most suitable formulations for the entire ABL and for a wide range of stability conditions. However, they require numerous inputs and are quite uncertain due to the lack of rigorous validation. With the advent of long-range lidars, reliable high-altitude wind data are becoming more and more readily available. We encourage the wind community to leverage these new datasets and perform comprehensive validation of Π_{MOX} and Π_{GDL} formulations.

Acknowledgments

The author is grateful to Simon Watson and Bert Holtslag for their constructive feedback.

References

[1] Brower MC. Wind resource assessment: a practical guide to developing a wind project. Hoboken, NJ: John Wiley & Sons, Inc; 2012. p. 280.
[2] Emeis S. Wind energy meteorology. Berlin: Springer; 2013. p. 196.
[3] Holmes JD. Wind loading of structures. Taylor & Francis; 2001. p. 379.
[4] Simiu E, Scanlan RH. Wind effects on structures: fundamentals and applications to design. 3rd ed. New York: John Wiley & Sons, Inc; 1996. p. 688.
[5] Arya SP. Air pollution meteorology and dispersion. New York: Oxford University Press, Inc.; 1999. p. 310.
[6] de Visscher A. Air dispersion modeling: foundations and applications. Hoboken, NJ: John Wiley & Sons, Inc; 2014. p. 634.
[7] Lester PF. Turbulence: a new perspective for pilots. Jeppesen Sanderson, Inc.; 1994. p. 290.
[8] Chilson PB, Frick WF, Kelly JF, Liechti F. Aeroecology. Springer; 2017. p. 497.
[9] Sorbjan Z. Structure of the atmospheric boundary layer. Englewood Cliffs, NJ: Prentice Hall; 1989. p. 317.
[10] DeFelice TP. An introduction to meteorological instrumentation and measurement. Upper Saddle River, NJ: Prentice Hall; 1998. p. 229.
[11] Bradley S. Atmospheric acoustic remote sensing. Boca Raton, FL: CRC Press; 2008. p. 271.
[12] Emeis S. Surface-based remote sensing of the atmospheric boundary layer. Springer; 2011. p. 190.
[13] Solari G. Wind science and engineering. Springer; 2019. p. 944.
[14] Mildner P. Über Reibung in einer speziellen Luftmasse. Beitr Phys fr Atmosph 1932;19:151.
[15] Lettau H. A re-examination of the "Leipzig Wind Profile" considering some relations between wind and turbulence in the friction layer. Tellus 1950;2:125–9.
[16] Clarke RH, Dyer AJ, Brook RR, Reid DG, Troup AJ. The Wangara experiment: boundary layer data. Div Meteorol Phys Tech 1971;362.
[17] Basu S, Vinuesa J-F, Swift A. Dynamic LES modeling of a diurnal cycle. J Appl Met Clim 2008;47:1156–74.
[18] Stull RB. An introduction to boundary layer meteorology. Dordrecht, The Netherlands: Kluwer Academic Publishers; 1988. p. 670.
[19] Arya SP. Introduction to micrometeorology. San Diego, California: Academic Press; 2001. p. 420.
[20] Peña A, Floors R, Gryning S-E. The Høvsøre tall wind-profile experiment: a description of wind profile observations in the atmospheric boundary layer. Boundary-Layer Meteorol 2014;150:69–89.
[21] Durán P, Basu S, Meißner C, Adaramola MS. Automated classification of simulated wind field patterns from multiphysics ensemble forecasts. Wind Energy 2020;23:898–914.
[22] Kohonen T. Self-organizing maps. 3rd ed. New York: Springer-Verlag; 2001.
[23] Warner TT. Numerical weather and climate prediction. New York: Cambridge University Press; 2011. p. 526.
[24] Stensrud DJ. Parameterization schemes. New York: Cambridge University Press; 2007. p. 459.

[25] Pimenta F, Kemptona W, Garvinea R. Combining meteorological stations and satellite data to evaluate the offshore wind power resource of Southeastern Brazil. Renew Energy 2008;33:2375–87.
[26] Monin A, Obukhov A. Basic laws of turbulent mixing in the atmosphere near the ground. Tr Akad Nauk SSSR Geo z Inst 1954;24:163–87.
[27] Optis M, Monahan A, Bosveld FC. Limitations and breakdown of Monin-Obukhov similarity theory for wind profile extrapolation under stable stratification. Wind Energy 2016;19:1053–72.
[28] Barthelmie RJ. The effects of atmospheric stability on coastal wind climates. Meteorol Appl 1999;6:39–47.
[29] Holtslag MC, Bierbooms WAAM, van Bussel GJW. Validation of surface layer similarity theory to describe far offshore marine conditions in the Dutch North Sea in scope of wind energy research. J Wind Eng Ind Aerodyn 2015;136:180–91.
[30] Dyer AJ, Hicks BB. Flux-gradient relationships in the constant flux layer. Q J R Meteorol Soc 1970;96:715–21.
[31] Businger JA, Wyngaard JC, Izumi Y, Bradley EF. Flux-profile relationships in the atmospheric boundary layer. J Atmos Sci 1971;28:181–9.
[32] Dyer AJ. A review of flux-profile relationships. Boundary-Layer Meteorol 1974;7:363–72.
[33] Beljaars ACM, Holtslag AAM. Flux parameterization over land surfaces for atmospheric models. J Appl Meteorol 1991;30:327–41.
[34] Capps SB, Zender CS. Global ocean wind power sensitivity to surface layer stability. Geophys Res Lett 2009;36:L09801.
[35] Gryning S-E, Batchvarova E, Brümmer B, Jørgensen H, Larsen S. On the extension of the wind profile over homogeneous terrain beyond the surface boundary layer. Boundary-Layer Meteorol 2007;124:251–68.
[36] Sathe A, Gryning S-E, Peña A. Comparison of the atmospheric stability and wind profiles at two wind farm sites over a long marine fetch in the North Sea. Wind Energy 2011;14:767–80.
[37] Kazanski AB, Monin AS. On the dynamic interaction between the atmosphere and earth's surface. Izv Akad Nauk SSSR, Ser Geofiz 1961;5:514–15.
[38] Blackadar AK, Tennekes H. Asymptotic similarity in neutral barotropic planetary boundary layers. J Atmos Sci 1968;25:1015–20.
[39] Zilitinkevich SS. Velocity profiles, the resistance laws and the dissipation rate of mean flow kinetic energy in a neutrally and stably stratified planetary boundary layer. Boundary-Layer Meteorol 1989;46:367–87.
[40] Zilitinkevich SS, Esau IN. Resistance and heat-transfer laws for stable and neutral planetary boundary layers: old theory advanced and re-evaluated. Quart J Roy Meteorol Soc 2005;131:1863–92.
[41] Cvitan L, Sinik N, Klaić ZB. Two simple wind speed models for practical application under stable conditions. Meteorol Appl 2002;9:423–32.
[42] Emeis S, Baumann-Stanzer K, Piringer M, Kallistratova M, Kouznetsov R, Yuhkov V. Wind and turbulence in the urban boundary layer—analysis from acoustic remote sensing data and fit to analytical relations. Meteorol Z 2007;16:393–406.
[43] Gualtieri G, Secci S. Comparing methods to calculate atmospheric stability dependent wind speed profiles: a case study on coastal location. Renew Energy 2011;36:2189–204.
[44] Frost R. The velocity profile in the lowest 400 feet. Meteorol Mag 1947;76:14–17.
[45] Sisterson DL, Frenzen P. Nocturnal boundary-layer wind maxima and the problem of wind power assessment. Environ Sci Technol 1978;12:218–21.
[46] Irwin J. A theoretical variation of the wind profile power-law exponent as a function of surface roughness and stability. Atmos Environ 1979;13:191–4.
[47] Bañuelos-Ruedas F, Angeles-Camacho C, Rios-Marcuello S. Analysis and validation of the methodology used in the extrapolation of wind speed data at different heights. Renew Sustain Energy Rev 2010;14:2383–91.
[48] Hsu SA. Coastal meteorology. San Diego, CA: Academic Press, Inc.; 1988.
[49] Sedefian L. On the vertical extrapolation of mean wind power density. J Appl Meteorol 1980;19:488–93.
[50] Emeis S. How well does a power law fit to a diabatic boundary-layer wind profile? DEWI Mag 2005;26:59–62.
[51] Hsu SA, Meindl EA, Gilhousen DB. Determining the power-law wind-profile exponent under near-neutral stability conditions at sea. J Appl Meteorol 1994;33:757–65.
[52] Motta M, Barthelmie RJ, Vølund P. The influence of non-logarithmic wind speed profiles on potential power output at Danish offshore sites. Wind Energy 2005;8:219–36.
[53] Corrigan D, Matthiesen DH. Analysis of the power law exponent applied to Lake Erie wind shear. Wind Eng 2017;41:103–13.
[54] Deaves DM, Harris RI. A mathematical model of the structure of strong winds. London: Construction Industry Research and Information Association; 1978. p. 76.
[55] Cook NJ. The Deaves and Harris ABL model applied to heterogeneous terrain. J Wind Eng Ind Aerodyn 1997;66:197–214.
[56] Gualtieri G. Wind resource extrapolating tools for modern multi-MW wind turbines: comparison of the Deaves and Harris model vs. the power law. J Wind Eng Ind Aerodyn 2017;170:107–17.
[57] Li Q, Zhi L, Hu F. Boundary layer wind structure from observations on a 325 m tower. J Wind Eng Ind Aerodyn 2010;98:818–32.
[58] Vickery PJ, Wadhera D, Powell MD, Chen Y. A hurricane boundary layer and wind field model for use in engineering applications. J Appl Meteorol Climatol 2009;48:381–405.
[59] Snaiki R, Wu T. A semi-empirical model for mean wind velocity profile of landfalling hurricane boundary layers. J Wind Eng Ind Aerodyn 2018;180:249–61.

This page intentionally left blank

Section C

Wind turbine technology

This page intentionally left blank

Chapter 8

Wind turbine technologies

Anca Daniela Hansen
DTU Wind and Energy Systems, Technical University of Denmark, Roskilde, Denmark

8.1 Introduction

Wind turbine technology is a very complex technology involving multidisciplinary and broad technical disciplines such as aerodynamics, mechanics, structure-dynamics, meteorology as well as electrical engineering addressing the generation, transmission, and integration of wind turbines into the power system.

Wind turbine technology has matured over the years and become the most promising and reliable renewable energy technology today. It has moved very fast, since the early 1980s, from wind turbines of a few kilowatts to today's multimegawatt-sized wind turbines [1−3]. Besides their size, the design of wind turbines has changed from being convention-driven to being optimized-driven within the operating regime and market environment. Wind turbine designs have progressed from fixed speed, passive controlled and with drive trains with gearboxes, to become variable speed, active-controlled and with or without gearboxes, using the latest in power electronics, aerodynamics, and mechanical drive train designs [4]. The main differences between all wind turbine concepts developed over the years concern their electrical design and control.

Today, the wind turbines on the market mix and match a variety of innovative concepts, with proven technology for both generators and power electronics [4]. The continuously increased and concentrated electrical penetration of large wind turbines into electrical power systems inspires the designers to develop both custom generators and power electronics [5,6] and to implement modern control system strategies.

8.2 Overview of wind turbine components

A wind turbine consists of a tower and a nacelle that is mounted on the top of a tower. The nacelle contains several components, which contribute with their specific function in the energy conversion process from wind energy to electrical energy. Fig. 8.1 shows the main components of a wind turbine including the turbine rotor, transmission system (gearbox), generator, possible power electronics, control system, transformer, and finally its connection to the grid.

8.2.1 Aerodynamic rotor

The aerodynamic rotor of a wind turbine captures the power from the wind and converts it to kinetic mechanical power. The aerodynamic rotor is mainly made up of a hub and blades, with the latter attached to the hub by mechanical joints. Modern wind turbines have typically two or three blades, made up by a matrix of fiberglass mats impregnated with polyester [8]. In the old wind turbines, the blades can be firmly attached to the hub, while in the more modern ones the blades can be turned around their longitudinal axes.

8.2.2 Transmission system

As depicted in Fig. 8.1, the kinetic mechanical power from the aerodynamic rotor is transmitted to the generator through a transmission system, which typically consists of the rotor shaft, mechanical brake (s), and a gearbox.

The mechanical brakes are usually used as a backup system for the aerodynamic braking system of the wind turbine and/or as a parking brake once the turbine is stopped. The aerodynamic brake system usually consists of turning the blade out of the wind, namely 90 degrees about the longitudinal axis of the blade.

Wind Energy Engineering. DOI: https://doi.org/10.1016/B978-0-323-99353-1.00020-7

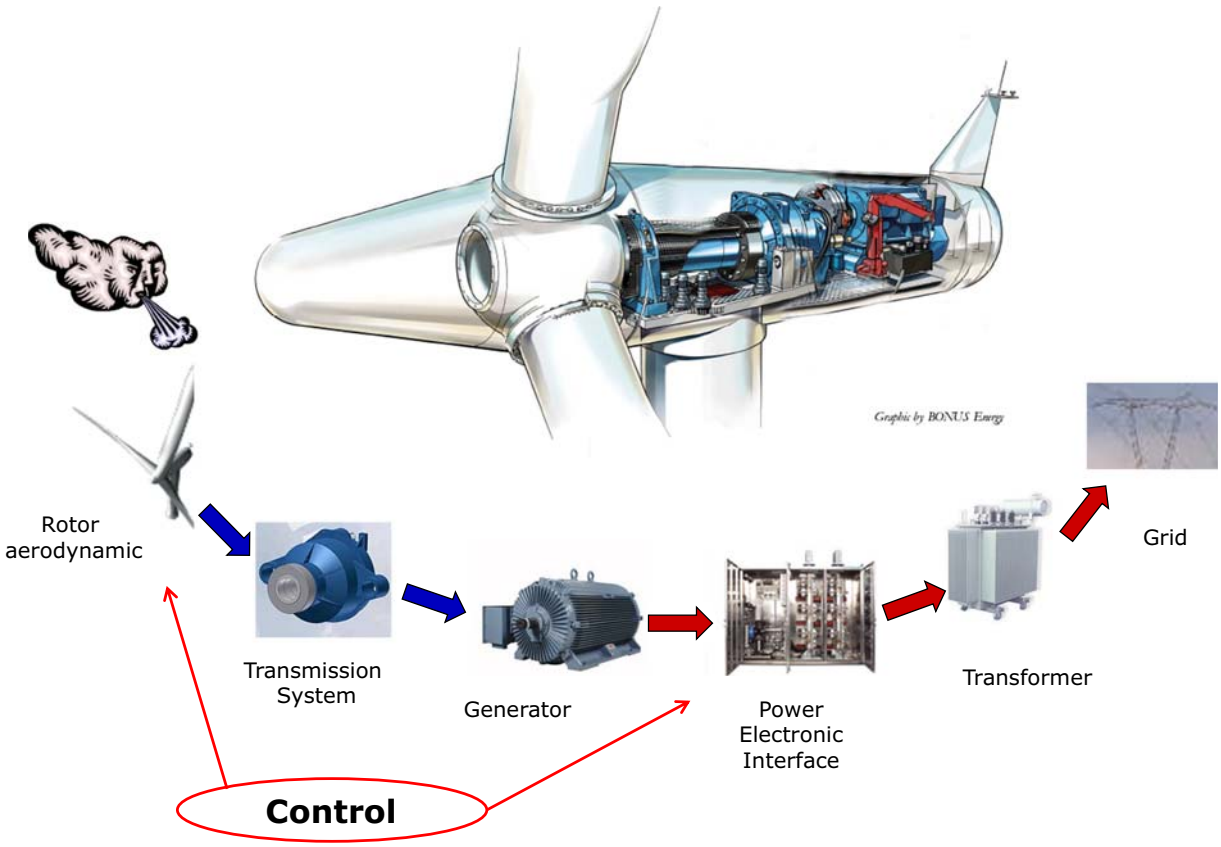

FIGURE 8.1 Wind turbine components—picture from Internet [7]. *Adapted with additional illustrations.*

The main purpose of the gearbox is to act as a rotational speed increaser; the gearbox of a wind turbine converts the slow high torque rotation of the aerodynamic rotor into the much faster rotation of the generator shaft. Depending on their geometrical designs, gearboxes are typically divided into two classes. The first one is the spur and helical gearboxes, which consists of a pair of gear wheels with parallel axes. The second one is the planetary gearbox which consists of epicyclic trains of gear wheels [9]. As the gearbox is continuously subjected to large and varying torques due to the increased size of wind turbines and wind speed variability, the gearbox is the weakest link in the wind turbines, many of them failing in less than two years of operation [9]. As result, in some newer wind turbine technologies, the gearbox has been removed, by designing generators, with a multipolar structure to adapt the rotor speed to the generator speed. The generator speed decreases by increasing number of polepairs, and therefore the gearbox may not be necessary for multipole wind turbine generator systems, i.e., where the number of polepairs may be higher than 100.

8.2.3 Generator

The generator is an electromechanical component, which converts mechanical power into electrical power. As indicated in Fig. 8.2, generators have typically a stator and a rotor. The stator is a stationary housing, which has coils of wire mounted in a certain pattern. The rotor is the rotating part of the generator and is responsible for the magnetic field of the generator.

A rotor can have a permanent magnet or an electromagnet, namely, a magnetic field is generated on the rotor and rotates with the rotor. By its rotation, the rotor and thus its magnetic field pass the stator windings and induce a voltage in the terminals of the stator. When the magnetic field of the stator is following the magnetic field of the rotor, the generator is called synchronous, otherwise, it is called asynchronous.

Two major types of generators used in the industry are synchronous generators and asynchronous (induction) generators. Descriptions of synchronous and asynchronous generators can be found in many standard textbooks. For example, [4,11,12] provide a good overview regarding the different generator technologies currently used by the wind industry as well as future options for the design of wind turbine generators.

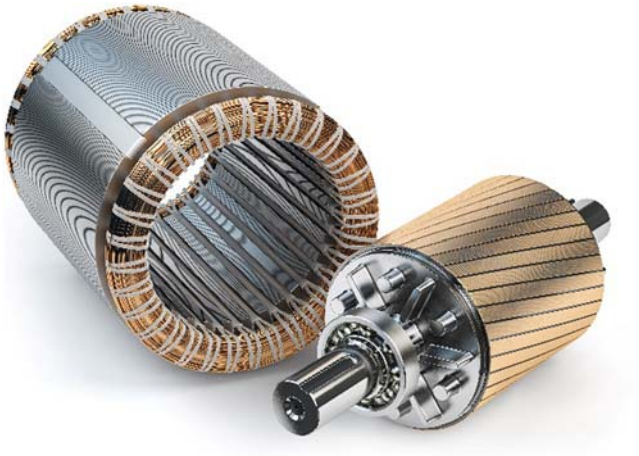

FIGURE 8.2 Generator's stator and rotor [10].

8.2.3.1 Synchronous generator

The synchronous generator is a generator, which operates at the synchronous speed, dictated by the frequency of the connected grid, regardless of the magnitude of the applied torque. The magnetic field in the synchronous generator can be created by using permanent magnets or with a conventional field winding.

The speed of the synchronous generator is determined by the frequency of the rotating field and by the number of polepairs of the rotor. If the synchronous generator has a suitable large number of poles (i.e., multipole structure) it can be used for direct-drive applications without the need for a gearbox.

The synchronous generator is more expensive and mechanically more complicated than an asynchronous generator of a similar size. However, it has one significant advantage compared with the asynchronous generator, namely, that it does not need reactive magnetizing current and thus no further power compensation equipment.

Two classical types of synchronous generators are often used in the wind turbine industry:

- Wound rotor synchronous generator (WRSG) is the workhorse of the electrical power industry and therefore very well documented in the literature [11–13]. Its stator windings are connected directly to the grid and hence the rotational speed is strictly fixed by the frequency of the supply grid. The rotor winding, through which direct current flows, generates the exciter field, which rotates with synchronous speed.
- A permanent magnet synchronous generator (PMSG) has a wound stator, while its rotor is provided with a permanent magnet pole system. It has a high efficiency as its excitation is provided without any energy supply. However, the materials used for producing permanent magnets are expensive and they are difficult to manufacture. Additionally, the use of permanent magnets excitation requires the use of a full-scale power converter to adjust the voltage and frequency of generation to the voltage and the frequency of transmission, respectively. Different topologies of PMSG are presented in the literature [14–16]. The most common types are the radial flux machine, the axial flux machine, and the transversal flux machine.

8.2.3.2 Asynchronous (induction) generator

The asynchronous generator has several advantages such as robustness and mechanical simplicity, and since it is produced in large series, it also has a low price. The major disadvantage is that the stator needs a reactive magnetizing current. As the asynchronous generator does not contain permanent magnets and is not separately excited, it consumes reactive power to get its excitation. The reactive power may be supplied by the grid or by power electronics.

In the asynchronous generator, an electric field is induced between the rotor and the rotating stator field by a relative motion called slip, which causes a current in the rotor windings. The interaction of the associated magnetic field of the rotor with the stator field results in a torque acting on the rotor.

The rotor of an asynchronous generator can be designed as a short-circuit rotor (squirrel-cage rotor) or as a wound rotor [11]:

- Squirrel-cage induction generator (SCIG)—It has been often used by the industry over the years, due to its mechanical simplicity, high efficiency, and low maintenance requirements. As depicted in Fig. 8.3, the rotor of this generator has conducting bars embedded in slots and shorted in both ends by end rings. The electrical characteristics of the rotor can therefore not be controlled from the outside.

FIGURE 8.3 Squirrel-cage induction generator [17].

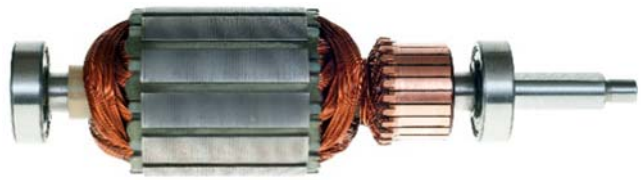

FIGURE 8.4 Wound rotor induction generator [19].

SCIG is a very robust and stable generator, its speed changes by only a few percent as its slip varies with the changes in the wind speed. Wind turbines based on SCIG are typically equipped with a soft-starter mechanism and an installation for reactive power compensation, as SCIGs consume reactive power. SCIGs have a steep torque speed characteristic and therefore fluctuations in wind power are transmitted directly to the grid. These transients are especially critical during the grid connection of the wind turbine, where the inrush current can be up to 7−8 times the rated current.

In a weak grid, this high inrush current can cause severe voltage disturbances [18]. Through the soft-starter, the generator is gradually connected to the grid to limit the inrush currents. The amount of reactive power for the generator varies depending on the wind conditions. This means that if the wind speed is high, the wind turbine can produce more active power, but only if the generator gets more reactive power. Without any electrical components to supply reactive power, the needed reactive power for the generator is taken directly from the grid and this might cause additional transmission losses and can, in some situations, make the grid unstable. To avoid this, capacitor banks or modern power electronic converters are typically used to provide the needed reactive power compensation.

- Wound rotor induction generator (WRIG)—the windings of the wound rotor can be externally connected through slip rings and brushes or by means of power electronic equipment, see Fig. 8.4. This means that this generator has the advantage that its electrical characteristics can be controlled from the outside, and thereby a rotor voltage can be impressed.

By using power electronics, the power can be extracted or impressed to the rotor circuit and the generator can be thus magnetized from either the stator circuit or the rotor circuit. The disadvantage of WRIG is that it is more expensive than, and not as simple and robust as, the SCIG. Two WRIG configurations are mainly used in the wind industry:

- **OptiSlip or FlexiSlip induction generators**: They were often used in the 1990s, as WRIGs with a variable external rotor resistance attached to the rotor windings, which can be changed by an optically controlled converter mounted on the rotor shaft, hence the name. This optical coupling eliminates the need for costly slip rings that need brushes and maintenance. The range of the dynamic speed control depends on the size of the variable rotor resistance. Typically, the slip for OptiSlip is 10%, while for FlexiSlip it is about 16% [4].
- **Doubly-fed induction generator (DFIG)**: It has the stator windings directly connected to the constant frequency grid, while the rotor is connected to the grid through a back-to-back power converter. The size of this converter is related to the selected speed range, namely, it is not a full-scale power converter, since typically only a fraction up to 70% of the speed range is utilized. The selection of the speed range is based on the economic optimization of investment costs and on increased efficiency. Thus, the cost of the converter increases when the speed range around the synchronous speed becomes wider. DFIG has the ability to control independently its active and reactive power. A drawback of the DFIG is the inevitable need for slip rings [13,20].

8.2.4 Power electronic interface

The generator converts the mechanical power into electrical power, which is fed into the power grid through a power electronic interface [5,21]. As it is placed between the wind turbine generator and power grid, the power electronic interface should satisfy both generator and grid side requirements with a cost-effective and easy maintenance solution. On the generator side, this interface ensures that the rotating speed of the turbine is continuously adjusted to extract maximum power out of the wind [15,16,22] following a maximum tracking point. On the grid side, the power electronic interface must comply with the grid codes [23] regardless of the wind speed, such as the ability to control active and reactive power, frequency, and voltage control.

The penetration of power electronics in wind turbine systems has been continuously growing since the 1980s, becoming gradually more and more advanced and bringing in significant performance improvements for the wind turbines—not only reducing the mechanical stress/loading and increasing the energy yield but also enabling wind turbines to behave as active controllable components in the power system and support the grid similar to the conventional power plants [20]. Nowadays, components can handle higher current and voltage ratings. Furthermore, the power losses decrease and as result the devices become more reliable.

The most commonly used power electronic interfaces in wind turbine applications over the years are:

- **Soft-starter** is a simple and cheap power electrical component used in the 1980s in wind turbines with SGIG to reduce the inrush current during wind turbine connections to the grid, thereby limiting the disturbances to the grid. Without a soft starter, the inrush current can be up to 7−8 times the rated current, which can cause severe voltage disturbances on the grid [21].
- **Capacitor bank** is an electrical component that supplies reactive power to the asynchronous generators of wind turbines [21]. Traditionally, mechanically switched capacitor banks are the easiest and most economical way to minimize the reactive power drawn by asynchronous generators from the grid. The generators of wind turbines can have a full load dynamic compensation, where a certain number of capacitors are connected or disconnected continuously, depending on the average reactive power demand of the generator over a predefined period of time. As the reactive power demand of an asynchronous generator is strongly dependent on wind speed, the capacitor banks can often be triggered by an extreme number of switching events.
- **Frequency converter**, typically used in wind turbines since 2000, is a device that facilitates the interconnection of two electrical systems with independent frequencies [21]. It makes the device possible to adjust and control the generator frequency and voltage, and thus enhance wind turbines capability to behave and act as active components in the power system. A traditional frequency converter, also called an adjustable speed drive, consists of:
  - AC/DC conversion unit (rectifier) converts alternating current into direct current, while the energy flows into the DC system;
  - Capacitors (energy storage);
  - DC/AC conversion unit (inverter) converts direct current into alternating current, while the energy flows to the AC side.

In recent years, different converter topologies (back-to-back /multilevel/tandem /matrix/resonant converters) have been investigated to test whether or not they can be used in wind turbines. The back-to-back converter is highly relevant to wind turbines today. It constitutes the state of the art and may therefore be used for benchmarking the other converter topologies. As discussed in reference [24], the matrix and multilevel converter are the most serious competitors to the back-to-back converter and thus are recommended for further studies.

8.2.5 Control system and wind turbine control capabilities

A wind turbine is typically equipped with a control system, necessary to assure a proper operation of the wind turbine under all operational conditions. The control system is meant to control and keep the wind turbine within its normal operating range by passive or active means. Passive controls use their own sensing and are exercised by use of natural forces, e.g., when the rotor “automatically” loses the aerodynamic efficiency (known as stall phenomena), when the wind speed exceeds a certain critical level. Active controls use electrical, mechanical, hydraulic, or pneumatic means and require transducers to sense the variables that will determine the control action needed. Typical variables which are monitored in a control system are wind speed, rotor speed, active and reactive power, voltage, and frequency of the wind turbine’s point of connection. In addition, the control system must be able to stop the wind turbine, if necessary.

The overall goal of wind turbine active control is to maximize the power production and to reduce the structural loads on the mechanical components and thus their costs and lifetime consumption. At low wind speeds, the control system has to ensure that the turbine produces optimal power, namely that the wind turbine is extracting power out of the wind with maximum efficiency. At high wind speeds, namely higher than the rated wind speed, the power production of the turbine should be limited to the rated power value and thereby reduce the driving forces on the blades as well as the load on the whole wind turbine structure.

All wind turbines are designed with some sort of power control [4]. Three options for the power output control are currently used: stall control, pitch control, and active stall control. The main differences between these options concern the way in which the aerodynamic efficiency of the rotor is limited during above the rated wind speed to prevent overloading.

- **Stall control (passive control)** is the simplest, most robust, and cheapest power control method. Here the blades are firmly attached to the hub and the wind attack angle of the wings is fixed. The design of rotor aerodynamics causes the rotor to stall "automatically" (so losing efficiency) when the wind speed exceeds a certain level, i.e., rated value.
- **Pitch control (active control)** means that the blades can be quickly turned away from or into the wind as the power output becomes too high or too low, respectively. In contrast to stall control, pitch control requires that the rotor geometry changes and it is, therefore, more expensive due to its pitching mechanism and controller. The pitching system can be based on a hydraulic system, controlled by a computer system, or an electronically controlled electric motor. The pitch control system must be able to adjust the pitch angle by a fraction of a degree at a time, corresponding to a change in the wind speed, to maintain a constant power output.
- **Active stall control**, as the name indicates, means that the stall of the blade is actively controlled by pitching the blades in the opposite direction as a pitch-controlled wind turbine does. This movement increases the angle of attack of the rotor blades to make the blades go into a deeper stall and into a larger angle of attack. In contrast to stall control, active stall control has the advantage of being able to compensate for variations in air density.

The wind turbines can also be classified according to their speed control ability into two significant classes such as fixed-speed wind turbines and variable speed wind turbines.

- **Fixed-speed wind turbines** were the most commonly installed wind turbines in the early 1990s. The characteristic of these wind turbines is that they are equipped with an sSCIG connected directly to the grid, a soft-starter, and a capacitor bank for the reduction of reactive power consumption. Regardless of the wind speed, the rotor speed of the wind turbine is almost fixed, stuck to the grid frequency, and cannot be changed. Fixed-speed wind turbines are designed to achieve maximum efficiency at one particular wind speed, namely at the most likely wind speed in the area where the wind turbine is placed. Fixed-speed wind turbines have the advantages of being simple, robust and reliable, well proven, and having a low cost of electrical parts. Its direct drawbacks are high mechanical stress, uncontrollable reactive power consumption, and limited power quality control [18].
- **Variable speed wind turbines** have become the dominant type among the installed wind turbines during the past decade. Variable speed operation can only be achieved by decoupling the electrical grid frequency and mechanical rotor frequency through a power electronic interface. The characteristic of these wind turbines is that they are designed to achieve maximum aerodynamic efficiency over a wide range of wind speeds. Within variable speed operation, it is possible to continuously adapt (accelerate or decelerate) the rotational speed of the wind turbine to the wind speed, in such a way that the turbine operates continuously at its highest level of aerodynamic efficiency. The advantages of variable speed wind turbines are an increased annual energy capture (this is about 5% more than the fixed-speed technology) and that the active and reactive power can be easily controlled [15,16]. They have also less mechanical stress, improved power quality and, not least, controllability and "grid friendliness," which is a prime concern for the grid integration of large wind farms. The disadvantages are the additional losses due to power electronics that increase the component count and make the control system more complex. Besides these, they have also an increased cost due to the power electronics, which is about 7% of the whole wind turbine [15,16,22,25].

Fixed-speed wind turbines have been used with all three types of power control options by the industry. Until the mid-1990s, when the size of wind turbines reached the megawatt range, the stall control fixed-speed wind turbines, were the predominant type.

Pitch control applied to fixed-speed wind turbines has not been very attractive due to the large inherent power fluctuations at high wind speeds; the pitch mechanism is not fast enough to avoid power fluctuations in case of gusts at high wind speeds.

Active stall fixed-speed wind turbines have been popular in the 1990s, due to their smooth limitation in power. However, as they have very slow control, their success is strongly conditioned by their ability to comply with the stringent requirements imposed these days by utility companies.

The pitch control method has proved to be a very attractive option for variable speed operation and for larger wind turbines than 1 MW. The variable speed wind turbines are today only used in practice together with a fast pitch mechanism, due to power limitation considerations [4]. The reason why variable speed stall or variable speed active stall control wind turbines are not considered is their lack of ability for rapid reduction of power. If such variable active stall controlled wind turbine is running at maximum speed and encounters a large wind gust, the aerodynamic torque can become critically large and may result in a run-away situation.

8.3 Contemporary wind turbine technologies

This section presents an overview of the contemporary wind turbine technologies with their configurations, characteristics, advantages, and drawbacks. Depending on the generator type, power electronics, power, and speed controllability, wind turbines can generally be categorized into four categories.

8.3.1 Fixed-speed wind turbines (Type 1)

The fixed-speed wind turbine configuration uses a multiple-stage gearbox and a SCIG to convert the mechanical energy from the wind into electrical energy. This is the conventional concept applied by many Danish wind turbine manufacturers during the 1980s and 1990s, and therefore it is also referred to as "Danish concept" [4].

As illustrated in Fig. 8.5, in this configuration the generator is directly connected to the grid via a transformer. Besides the generator, the electrical system of fixed-speed wind turbines also contains a soft-starter for smoother grid connection and a capacitor bank for reactive power compensation.

Since SCIG operates in a narrow range around the synchronous speed, this turbine operates with almost constant speed, regardless of the wind speed. This concept has been very popular because of its relatively low price for mass production, its simplicity, and its robustness. However, as the fixed-speed wind turbine concept implies that the wind speed fluctuations are converted into mechanical fluctuations and consequently into electrical power fluctuations, this type of wind turbine experiences high mechanical and fatigue stress. Furthermore, it has limited power quality control, no control of its reactive power consumption, and no speed control to optimize its aerodynamic efficiency.

A pole-changeable SCIG configuration corresponding to two rotation speeds has been used in some commercial wind turbines to increase the power production of these turbines, namely, a generator winding set with typically 8 poles for low wind speeds and another one with 4−6 poles for medium and high wind speeds (typically 4−6 poles) [13,15].

8.3.2 Limited variable speed wind turbines (Type 2)

This configuration corresponds to the limited variable speed controlled wind turbine, known as OptiSlip or FlexiSlip. This type of wind turbine was promoted by the Danish manufacturer VESTAS since the mid-1990s up to 2006, and it has subsequently been used by the Indian manufacturer SUZLON [4].

As illustrated in Fig. 8.6, in this configuration, the stator of a WRIG is directly connected to the grid, whereas the rotor winding is connected in series with a variable additional rotor resistance, which is controlled optically and is changed dynamically by power electronics. By changing the rotor resistance size, the speed of the turbine can be modified and thus a variable speed operation can be achieved by controlling the energy extracted from the WRIG rotor. Thus, the size of this resistance defines the range of the variable speed (typically from 0% to 10%). However, some energy

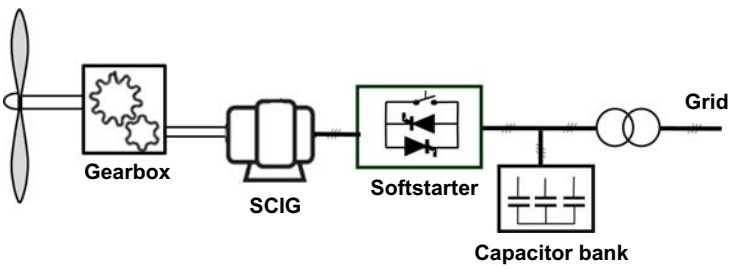

FIGURE 8.5 Fixed-speed wind turbine—Type 1.

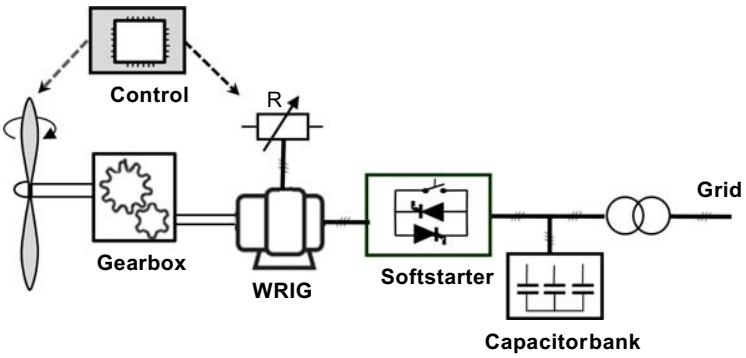

FIGURE 8.6 Limited variable speed wind turbine—Type 2.

extracted from the controllable resistance is dumped as heat loss. This concept still needs a soft-starter to reduce the inrush current and a reactive power compensator to provide the reactive power for the magnetization of the generator. The control system includes the control of the variable resistance and the pitch control of the blades.

The advantages are a simple circuit topology without slip rings and an improved operating speed range compared to that found in Type 1. To a certain extent, this concept can reduce the mechanical loads and power fluctuations caused by gusts. Some of the disadvantages are: limited speed range, as it is dependent on the size of the additional resistance; some power is dissipated in the variable resistance as losses; poor control of active and reactive power.

In summary, this concept partially solves the need for variable speed operation to increase aerodynamic efficiency. It is thus the first step toward the variable speed wind turbine concept, which is the main dominating concept found in the market today.

8.3.3 Variable speed wind turbines with partial scale power converter (Type 3)

Type 3 configuration denotes the variable speed wind turbine concept with a doubly-fed induction generator. It uses a partial scale back-to-back power converter connected to the rotor of the generator, typically through slip rings. This concept supports a wide speed range operation, depending on the size of the power converter [22,26].

As illustrated in Fig. 8.7, the stator is directly connected to the grid, while the rotor is connected through a partial scale power converter (rated at approximately 30% of nominal generator power). The power rating of this partial scale converter defines the speed range (typically $\pm 30\%$ around synchronous speed). This converter decouples mechanical and electrical frequencies making variable speed operation possible as it can vary the electrical rotor frequency. Moreover, this converter performs reactive power compensation and a smooth grid interconnection and therefore this configuration needs neither a soft-starter nor a reactive power compensator. A slip ring is used to transfer the rotor power by means of a partial scale converter. The power converter controls the rotor frequency, i.e., the rotor speed, enabling thus the variable speed operation of the wind turbine [18,21]. Besides this, it also controls the active and reactive power of the generator. The control system includes the electrical control of the converter and the pitch controller of the blades to limit the power when the turbine is above the rated power.

This concept is naturally more expensive when compared with Type 1 and Type 2 solutions, however, it is still attractive and popular option. The power converter enables the wind turbine to act as an actively controllable unit in the power system. Compared with Type 2, the rotor energy, instead of being dissipated, can be fed into the grid by the power electronic converter. It has a wider range of dynamic speed control compared to Type 2, depending on the size of the power converter. In addition to the fact that the converter is smaller, the losses are also lower. Its main drawbacks are the additional protection of the power converter in the case of grid faults and the use of slip rings, which requires a regular maintenance, and can result in machine failure and electrical loss [18,21].

8.3.4 Variable speed wind turbines with full-scale power converter (Type 4)

Type 4 corresponds to the variable speed concept with full-scale power converter. The generator is connected to the grid through a full-scale power converter as illustrated in Fig. 8.8. The full-scale converter allows for the control of the generator in a speed range of up to 100%. Besides this, it supports a smooth grid connection and reactive power compensation over the entire speed range. Similarly to Type 3, the control system of this concept includes the electrical control to control active and reactive power, as well as the pitch control to limit the rotor speed.

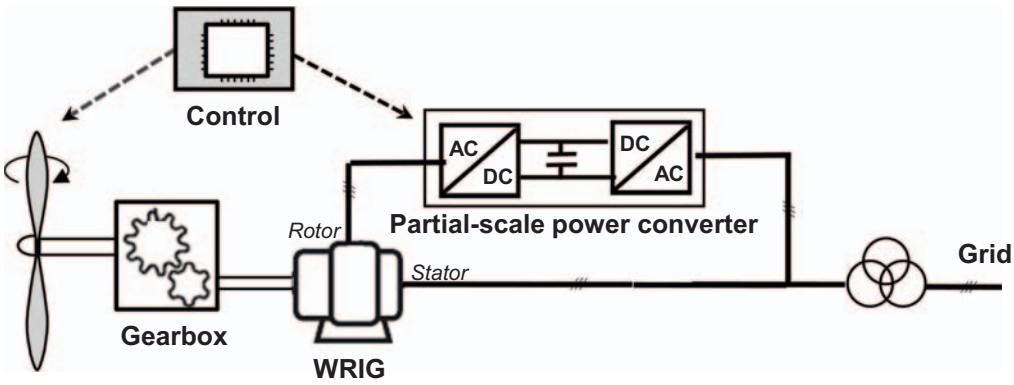

FIGURE 8.7 Variable speed wind turbine with partial-scale power converter—Type 3.

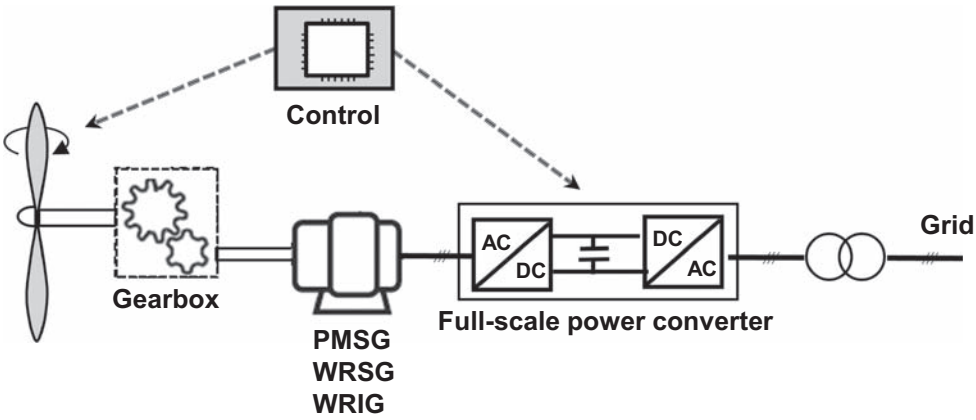

FIGURE 8.8 Variable speed wind turbine with full-scale power converter—Type 4.

As depicted in Fig. 8.8, this concept can be implemented for different types of generators; namely, the generator can be excited electrically (i.e., WRSG or WRIG) or by a permanent magnet (PMSG).

Some full variable speed wind turbine systems have no gearbox, as depicted by the dotted gearbox in Fig. 8.8. In these cases, a direct-driven multipole generator is used. The difference between wind turbines with and without gearboxes is the generator rotor speed. The direct-driven multipole generator rotates at a low speed because the generator rotor is directly connected to the hub of the aerodynamic rotor. The lower speed makes it necessary to produce a higher torque and therefore a large generator with large number of poles is needed. The wind turbine companies Enercon, Made, and Lagerwey supply this technology [25].

Compared with the Type 3 system, Type 4 has the advantages of a generator with better efficiency, no slip rings, simpler or even removed gearbox, full power and speed controllability, as well as better grid support ability, and a less complex grid-fault ride-through capability. Some important benefits of removing the gearbox are reduced losses, lower costs, and increased reliability due to the elimination of rotating mechanical components.

Its main disadvantages are the more expensive converter (100% of rated power instead of 30%) and the losses in the converter, which are higher because all the power is processed by the power electronic converter. However, the continuously decreasing cost of power electronics (roughly a factor of 10 over the past 10 years) and the absence of brushes might make this configuration the dominant one for development in the near future [27].

8.4 Conclusions

Over the years wind turbine technology has developed and reached a very reliable and advanced level. The wind turbine technology has changed and progressed from fixed speed, stall controlled and with drive trains with gearboxes, to become variable speed, pitch controlled and with or without gearboxes.

Today, the most dominating and promising wind turbine technologies are based on variable speed operation concepts. The increased interest in variable speed wind turbines is due to the presence of the power electronics, which facilitate many attractive features, including reduced mechanical stress, increased power capture, as well as their ability to support the grid by complying with the increasingly onerous grid requirements. The presence of power electronics makes it thus possible for wind turbines to behave in a similar way to conventional power plants and hence actively support the grid.

As with all technologies, the future is difficult to predict. However, it is clear that future improvement of wind turbine technology will be strongly dependent on the further development of power electronics technology for wind power applications.

References

[1] Herbert GMJ, Iniyan S, Sreevalsan E, Rajapandian S. A review of wind energy technologies. Renew Sustain Energy Rev 2007;11:1117–45.

[2] Chen Z, Blaabjerg F. Wind energy-the world's fastest growing energy source. IEEE Power Electron Soc Newsl 2006;18:15–19.

[3] Li H, Chen Z. Overview of different wind generator systems and their comparisons. Renew Power Generation, IET 2008;2:123–38.

[4] Hansen AD. In: Ackermann T, editor. Wind power in power systems. 2nd ed. Chichester: John Wiley and Sons; 2010.

[5] Chen Z, Guerrero JM, Blaabjerg F. A review of the state of the art of power electronics for wind turbines. IEEE Trans Power Electron 2009;24:1859–75.

[6] Blaabjerg F, Liserre M, Ma K. Power electronics converters for wind turbine systems. IEEE 2011;48:708–19.

[7] https://www.google.dk/search?q = bonus + wind + turbine + picture&espv = 2&biw = 1280&bih = 621&tbm = isch&tbo = u&source = univ&sa = X&ved = 0ahUKEwis9Pj3iafNAhVGXCwKHZuSAqIQ7AkIOA#imgrc = kYwk2sNT_vaJ8M%3A.

[8] Mandell JF, Samborsky DD, Wang L, Wahl N. New fatigue data for wind turbine blade materials. In: ASME wind energy symposium, Nevada: USA, January 6–9; 2003.

[9] Ragheb A, Ragheb M. Wind turbine gearbox technologies. In: Proceedings of the 1st international nuclear and renewable energy conference (INREC10), Amman, Jordan, March 21–24; 2010.

[10] Rotor and Stator of Electric Motor. Isolated on white background stock photo—download image now, iStock (istockphoto.com).

[11] Heier S. Grid integration of wind energy conversion systems. Germany: Chichester, and Kassel University, John Wiley & Sons Ltd.; 1998.

[12] Boldea I. The electric generators handbook- variable speed generators. Boca Raton, FL: Taylor & Francis; 2006.

[13] Orabi M, El-Sousy F, Godah H, Youssef MZ. High-performance induction generator wind turbine connected to utility grid. In: Proc 26th Annu. INTELEC, Sep. 19–23, 2004, p. 697–704.

[14] Alatalo M. Permanent magnet machines with air gap windings and integrated teeth windings. Technical Report 288. Sweden: Chalmers University of Technology; 1996.

[15] Hansen LH, Helle L, Blaabjerg F, Ritchie A, Munk-Nielsen S, Bindner H, et al. Conceptual survey of generators and power electronics for wind turbines. Risø National Laboratory Technical Report Riso-R-1205(EN) Roskilde, Denmark; December 2001.

[16] Parviainen A. Design of axial-flux permanent magnet low-speed machines and performance comparison between radial flux and axial flux machines [Ph.D. Lappeenranta University of Technology, Acta universitatis Lappeenrantaensis; 2005.

[17] Squirrel cage. Rotor shaft and bearings used for asynchronous electric motor 3d rendering on isolated white background stock photo—download image now—iStock (istockphoto.com).

[18] Larsson A. PhD dissertation The power quality of wind turbines. Goteborg, Sweden: Chalmers University of Technology; 2000.

[19] Electric motor. stock photo—download image now—engine, electronics industry, business finance and industry—iStock (istockphoto.com).

[20] Muller S, Deicke M, De Doncker RW. Doubly fed induction generator systems for wind turbines. IEEE Ind Appl Mag 2002;8:26–33.

[21] Erickson RW, Maksimovic D. Fundamentals of power electronics. Boulder, CO: Springer Science + Business Media; 2001.

[22] Michalke G, Hansen AD, Hartkopf T. Modelling and control of variable speed wind turbines for power system studies. Wind Energy 2010;13:307–22.

[23] Altin M, Goksu O, Teodorescu R, Rodriguez P, Bak-Jensen B, Helle L. Overview of recent grid codes for wind power integration. Proc OPTIM 2010;11521160.

[24] Blaabjerg F, Teodorescu R, Chen Z, Liserre M. Power converters and control of renewable energy systems. In: Proc. 6th international conference power electronics, Oct. 18–22; 2004;1:1–20.

[25] Carlson O, Hylander J, Thorborg K. Survey of variable speed operation of wind turbines, In: European Union wind energy conference, Sweden; 1996. p. 406–409.

[26] Hansen AD, Sørensen P, Iov F, Blaabjerg F. Centralised power control of wind farm with doubly-fed induction generators. Renew Energy 2006;31:935–51.

[27] Kazmierkowski MP, Krishnan R, Blaabjerg F. Control in power electronics—selected probles. London and New York: Academic Press; 2002.

Chapter 9

Small-scale wind turbines

Patrick A.B. James and AbuBakr S. Bahaj

Energy & Climate Change Divisions, & Sustainable Energy Research Group, Faculty of Engineering and the Environment, University of Southampton, Southampton, United Kingdom

This chapter deals with micro and small wind turbines. Micro-wind turbines are typically defined as having a rated power of up to 1.5 kWp (where p refers to peak power) and their most widely used application is in yachts for battery charging. Small wind turbines are rated between 1.5 and 100 kWp and are generally free-standing, pole, or tower-mounted turbines. Small wind turbines at the lower end of this range are sometimes used in off-grid systems, but turbines above 20 kWp are almost always grid-connected (Fig. 9.1). The majority of micro and small wind turbines are horizontal axis three-blade designs. Vertical axis small wind turbines represent a small fraction of the market (see UK installations 2005−14 in Fig. 9.5) despite their claimed performance benefits over horizontal axis turbines, particularly in relation to turbulent wind response.

This chapter focuses on small wind turbines in the United Kingdom over the past decade (2005−15) which represents a period of "boom and bust" for building mounted micro-wind turbines in particular. The sector was trying to break out from yacht battery charging to the emerging grid-connected micro-generation sector during this period (Figs. 9.2−9.5).

Grid-connected micro-generation carries high front capital costs which is often the key barrier to commercial uptake. To encourage "early adopter" to take new technology, grants are initially used to cover a fraction of the capital cost. Later, as the market penetration of technology grows, more radical policy approaches such as enabling businesses to apply enhanced capital allowances to micro-generation investment or feed-in tariffs may emerge [2,3].

Grant subsidies are, however, not taking place without their problems. Whilst they enable micro-generation technologies to become visible to the public and so encourage wider take-up, as a subsidy they financially reward installation of a system and not generation. This is a fundamental weakness of grant subsidy, it risks rapid deployment of a technology with potentially limited regard to the long-term performance. Poor energy yield performance is to the detriment of primarily the turbine owner but also to the grant funder in the longer term. The installer, however, has already been paid, and whilst reputational damage may occur, this may take several years to emerge and will affect the wider industry.

In the case of micro-wind turbines, the predictive performance problem is exacerbated by the fact that the wind resource at a site is very difficult to quantify with any level of confidence without undertaking prior measurements. Field measurements are expensive to undertake, even placing an anemometer in an appropriate location for 6−12 months would

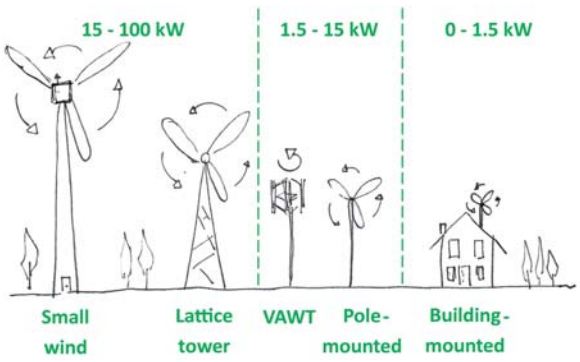

FIGURE 9.1 Small and micro-wind turbine scales, 1−100 kWp.

Wind Energy Engineering. DOI: https://doi.org/10.1016/B978-0-323-99353-1.00005-0

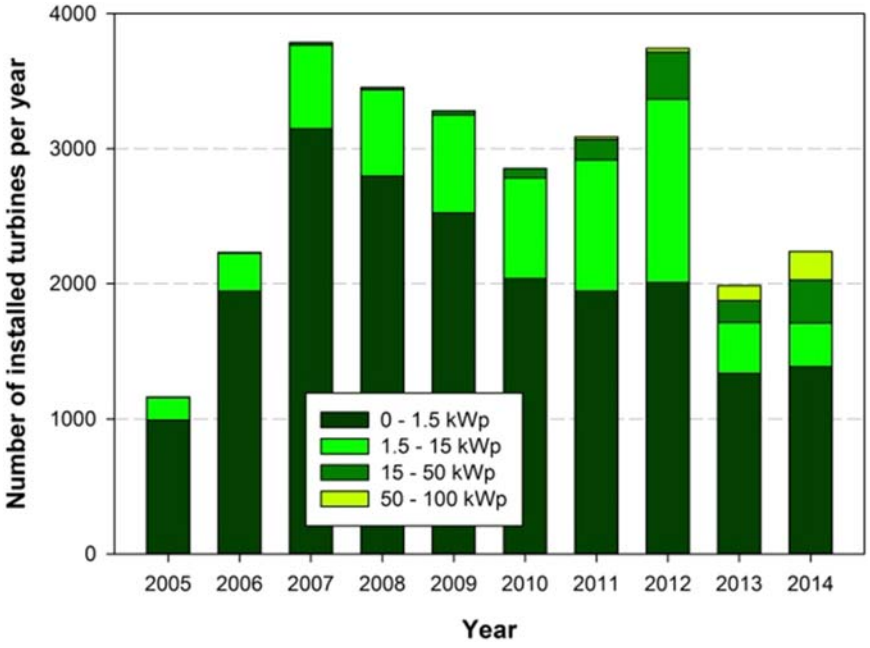

FIGURE 9.2 Number of installed small wind turbines per year by size category, 2005–14 in the United Kingdom [1]. *Courtesy Renewable UK. Small and medium wind UK market report. RUK-003-5, March 2015; 2015.*

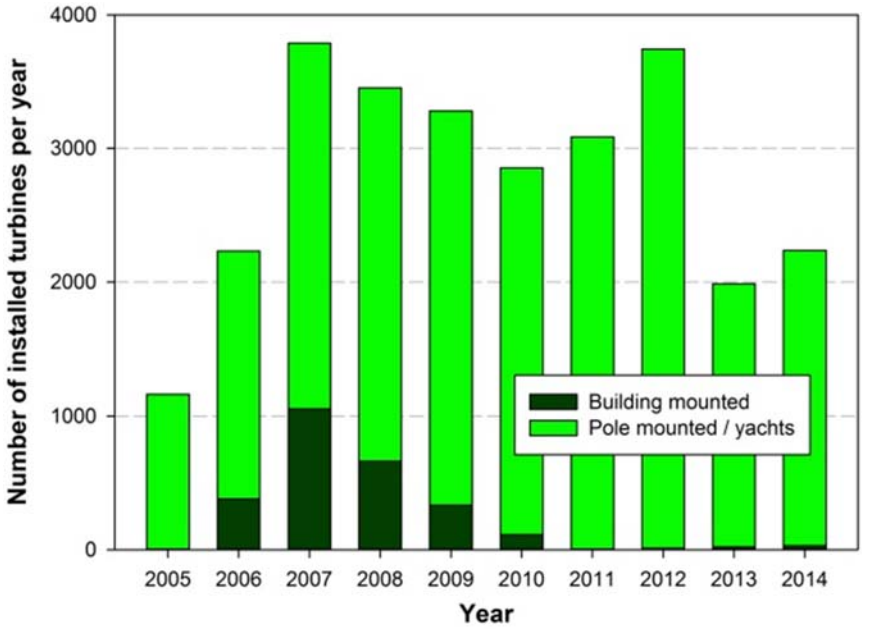

FIGURE 9.3 Number of installed small wind turbines per year by application sector, building mounted compared to pole mounted and marine, 2005–14 in the United Kingdom. *Courtesy Renewable UK. Small and medium wind UK market report. RUK-003-5, March 2015; 2015.*

cost at least £1000. This cost alone would make most micro-wind turbines financially unattractive. For installers, undertaking site wind measurements also delay the actual deployment of the turbine and the installer payment.

Guidance documents in the United Kingdom at this time [4,5] stated threshold wind speeds of 5 m/s for installation. The primary data source for this information was the Numerical Objective Analysis Boundary Layer (NOABL) wind speed modeling tool [6] and the underlying UK weather station dataset. NOABL tool was developed as a wind resource assessment for large-scale on-shore wind turbines located in clean air, rural locations. The modeling interpolates wind speeds from meteorological weather stations across the entire United Kingdom assuming rural landform with no obstructions throughout. If NOABL is used to assess wind speeds without the use of correction factors to account for built-form density, it will significantly overestimate the wind speed resource. The tool was never developed with

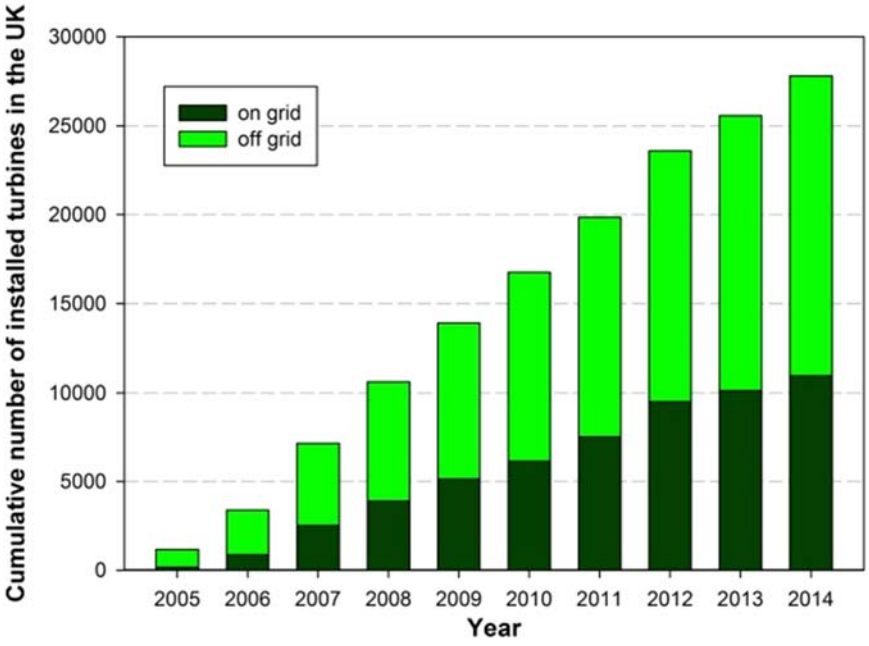

FIGURE 9.4 Cumulative number of installed small wind turbines both "on" and "off" grid, 2005−14 in the United Kingdom. *Courtesy Renewable UK. Small and medium wind UK market report. RUK-003-5, March 2015; 2015.*

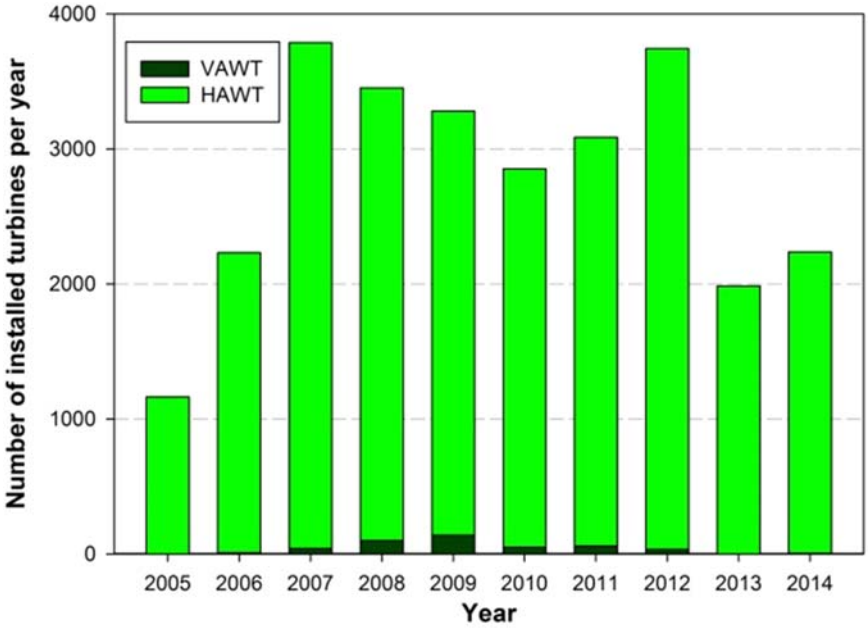

FIGURE 9.5 Number of installed horizontal axis (HAWT) and vertical axis (VAWT) small wind turbines (<100 kWp) per year, 2005−14 in the United Kingdom. *Courtesy Renewable UK. Small and medium wind UK market report. RUK-003-5, March 2015; 2015.*

micro-wind turbines as the application but it has become the starting point for site resource assessment and this was part of the problem in the United Kingdom.

In 2008, the British Wind Energy Association (BWEA), now RenewableUK, published its annual report on the state of the micro-wind industry [7]. It is instructive to look at some of the data published for this year in terms of the claimed typical load factors for small wind turbines and market projections. In the United Kingdom, large onshore wind farms have an average load factor of around 28% with offshore wind farms at around 38% [8]. The 2008 BWEA report provides average annual energy production (AEP) data, which corresponds to load factors of 10% and 17% for building mounted and small pole-mounted wind turbines, respectively. The building-mounted turbine market was predicted to grow by over 400% to ~11,700 turbines per annum in the United Kingdom from 2007 to 2009, as highlighted in Fig. 9.6.

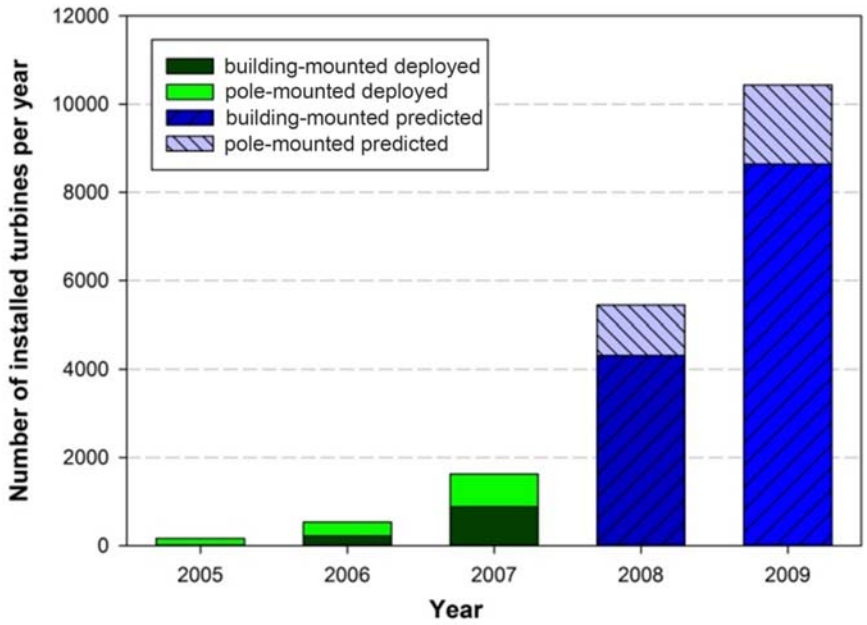

FIGURE 9.6 BWEA Small wind report 2008. Annual building and pole mounted turbine installations (2005–07) and year 2007 projections for 2008 and 2009 (all sizes below 15 kWp). *Courtesy British Wind Energy Association. BWEA small wind systems. UK Market Report 2008, (now renewable UK); 2008.*

B&Q, a major DIY (Do-It-Yourself) retailer started to sell a 1.0 kWp wind turbine, the WS1000, produced by Windsave Ltd in 2006. The micro-wind turbine was sold as a complete, fully installed system (turnkey solution of turbine, grid-connected inverter, and wiring). The total cost of the B&Q Windsave system was £1498 fully installed.

To stimulate the micro-generation sector the United Kingdom launched the Low Carbon Buildings Program [9] in April 2006, funding projects across four streams: households, communities, medium scale, and large scale. In total, the government-funded £91 m of micro-generation demonstration projects. In relation to small wind, 940 wind turbines (0.5–50 kWp) were installed through LCBP (total wind turbine grant value £4.7 m), representing 4.9% of all micro-generation installations and 5.1% of the total budget.

1. *Households:* A total of 762 wind turbine grants were awarded at an average value of £2304, total LCBP cost of £1.8 m. Maximum grant subsidies were £1000 per kW installed, up to a maximum of £5000 per installation subject to an overall 30% limit of the installed cost (exclusive of VAT). 44 grants with a value of £24,510 were returned (39 of which were building mounted turbines) due to the de-installation of systems owing to issues of poor performance.
2. *Communities:* (18 wind turbines, average grant £15,726)
3. *Medium scale:* (27 wind turbines, average grant £17,809) and,
4. *Large scale:* (1 wind turbine, average grant £32,924).

It is instructive to consider what the 2008 report BWEA claimed typical load factors [7] would mean for the economics of such a Windsave turbine.

Annual generation (kWh = load factor (%/100) × rated power (kW) × hours in the year)
= 0.10 × 1.0 × 8760 = 876 kWh/annum
Typical electricity tariff = 12 p/kWh, £105 per annum.

With an LCBP grant of £500 on proof of installation, this would give a simple payback time of fewer than 9 years at a discount rate of 0%. At the time, residential solar photovoltaic (PV) systems were, in comparison, far more expensive at around £8000 for a 3 kWp system. There was also no feed-in tariff in place at this point in the United Kingdom. In addition, an outlay of £1500 was seen by the micro-generation industry as a more affordable "discretionary" purchase for early adopters compared with the far higher cost in 2006 of a home PV system.

By 2006, the micro-wind turbine market was growing rapidly in the United Kingdom, primarily driven by B&Q's selling of the Windsave WS1000 turbine. However, concerns began to emerge about the claimed energy performance figures of turbines, especially in the built environment. The *WarwickWindTrial* study of 26 turbines in locations ranging from "theoretically poor" to "theoretically excellent" produced an average load factor of 4.1% [10]. The BWEA's 2008 published average load factor figures of 10% (building mounted) and 17% (pole mounted) started to look very optimistic. B&Q suspended the selling of micro-wind turbines in February 2009 following the WarwickWindTrial report, pending the findings of the larger national micro-wind trial undertaken by the Energy Saving Trust [11].

In July 2009, when the National Micro-wind Trial report, "Location, Location, Location: Domestic small-scale wind field trial report" was released [11], B&Q offered all micro-wind turbine customers a full refund and free decommissioning of their system. Windsave, the supplier to B&Q, filed for bankruptcy in September 2009 when B&Q effectively ended its relationship with them.

The 2008 BWEA small wind systems report uses the assumption that building mounted or off-grid (on a boat) turbines (up to 1.5 kW) have an average load factor of 10% [7]. There is no differentiation in load factor regardless of the application. The assumed load factor increases to 17% for free-standing, pole-mounted turbines, but again is regardless of the application (1.5−10 kW).

This EST micro-wind field trial was established to address a number of key questions:

1. Are UK manufacturers' performance claims in terms of predicted annual electricity generation realistic?
2. What is the relationship between NOABL wind-speed data for a location and measured turbine hub-height wind speeds? Are the proposed correction factors for NOABL wind speeds to real sites realistic?
3. How sensitive are micro-wind turbines to turbulence and to what extent does this compromise theoretical performance?
4. What is the future potential market for building mounted and pole-mounted micro-wind turbines in the United Kingdom?

9.1 The fundamental concern for micro-wind: the wind resource

The fundamental issue for micro-wind is the wind resource. It does not matter if a micro-wind turbine is able to rapidly respond to changing wind speeds or work well in the turbulent wind if the overall wind resource is poor. To illustrate this issue, the example of the wind resource on the roof of a University of Southampton (UoS) building is considered (Fig. 9.7,

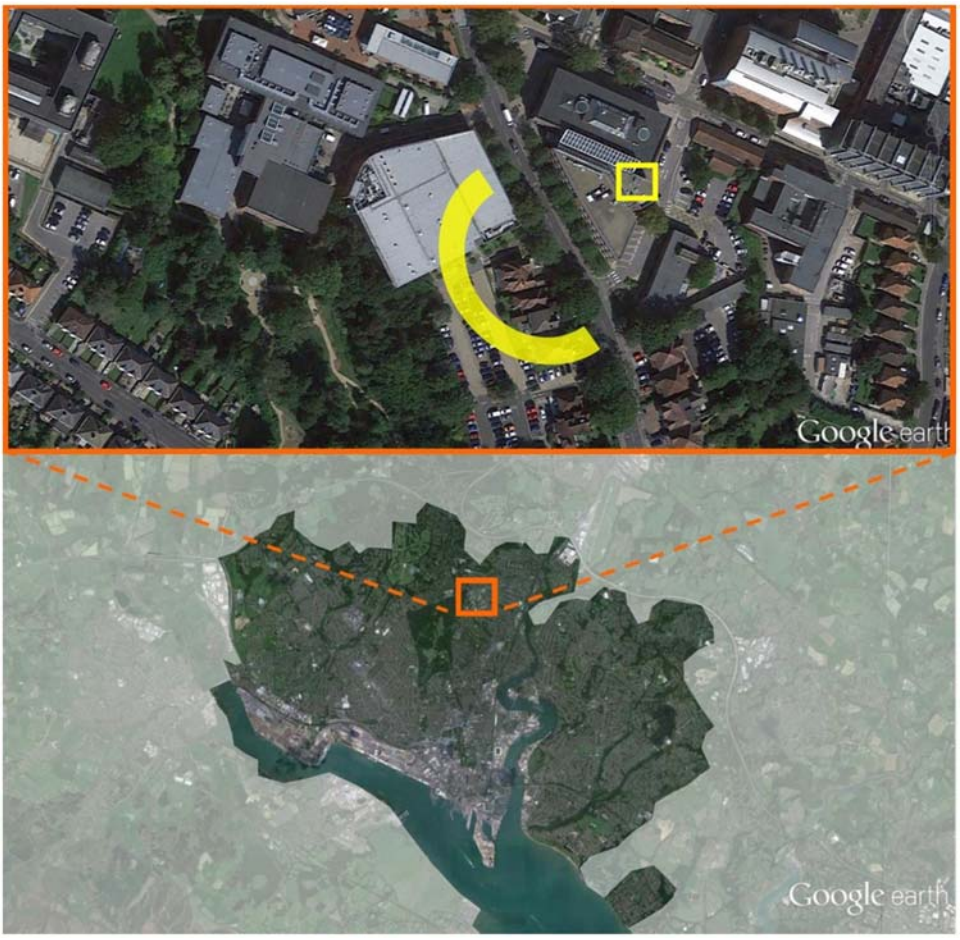

FIGURE 9.7 Location of University of Southampton weather station (*top yellow*) in the northern part of the port city of Southampton. The prevailing wind is from the South West (*yellow arc*) where the topography slopes away from the building. *Aerial images adapted from Google Earth.*

weather station highlighted as a yellow square). Southampton is located on the South Coast of the United Kingdom, it is a port city of around 250,000 people. The University is located to the north of the city in an urban area (orange square in Fig. 9.7). The weather station is on the top of a three-story building on the main campus. The prevailing wind is from the South West in the United Kingdom and in this direction, the land falls away at the site as the campus is on a slope. The roof of the building would be considered to be fairly unobstructed in the prevailing wind direction for an urban environment (yellow arc in Fig. 9.7).

NOABL provides the predicted wind-speed for any 1 km grid square in the United Kingdom at 45, 25, and 10 m above ground level (AGL). These wind speeds are for clean air and unobstructed terrain. The UoS NOABL 1 km grid square reference 445 111 (SU4511), NOABL output: 45 m AGL = 6.5 m/s, 25 m AGL = 6.0 m/s, 10 m AGL = 5.2 m/s.

The NOABL-MCS correction factor [4] for the UoS weather station anemometer would be 0.35 × NOABL = 1.8 m/s, to account for built-up location and an anemometer height of 2 m above the roof. This would correspond to a building-mounted turbine where the turbine blade tip comes within 2 m of the roof during a rotation (dense urban 35% correction factor, see Table 9.1).

The Microgeneration Installation Standard MIS3003 issue 2.0 [4] has three wind-speed categories as shown in Table 9.1. The 2015 revision [12] increased this to five essentially splitting rural category into three, to provide better prediction in the key rural sector and provide better hub height correction. The underlying scaling factor analysis remains unchanged and relates to the work of Harris and Deaves in 1980 [13]. The stated threshold wind-speed for installing a micro-wind turbine is 5.0 m/s which this site achieves as a NOABL estimate, although with urbanization correction applied this estimate is reduced to 1.8 m/s. Fig. 9.8 compares a NOABL wind-speed average as a Weibull distribution with a shape factor of 2 with the observed wind speed data over a 12-month period. The observed wind speed has an average of 2.35 m/s and fits well with a Weibull distribution with a shape factor of 2. This one graph serves to highlight the issue of micro-wind, uncorrected clean air wind speeds are not appropriate and should not be used.

Fig. 9.9 compares the predicted yield of a Windsave WS1000 turbine if mounted at the position of the UoS anemometer in terms of the NOABL wind-speed and the measured anemometer. The power curve for the WS1000 turbine has been applied to the wind-speed cubed but no cut-in or cut-out speed has been applied. The predicted energy output is shown as a binned distribution of the wind-speed cubed (0.5 m/s bin width). The NOABL wind-speed gives an estimated annual yield of 836 kWh/annum, compared to 94 kWh/annum which can be achieved for the actual wind resource. In reality, the WS1000 turbine has a cut-in speed of 4.5 m/s so the potential generation is around half of the 836 kWh/annum estimate.

This analysis does not consider the power requirements of the inverter which is a further complication for grid-connected systems in particular. In the United Kingdom, there are specific performance characteristics that inverters must comply with for grid connection. Systems less than 16 A per phase (3.68 kWp single phase) follow guidance under Engineering Recommendation G83/2, [*Recommendations for the Connection of Type Tested Small-scale Embedded Generators (Up to 16 A per Phase) in Parallel with Low-Voltage Distribution Systems*] [14]. Systems above 16 A need to be compliant with G59 [15]. In the case of G83/2, there is a requirement that a minimum reconnection period of 20 s occurs when an inverter senses the grid voltage and frequency within acceptable limits. Therefore, an inverter must always be synchronized with the utility grid to be able to immediately export generated power. In the case of PV, there is always enough dc power on even the dullest of days from a PV array to power the inverter and keep it synchronized. Micro-wind is more problematic, if the wind is infrequent and gusty, the inverter will be off and may not complete its synchronization cycle in time to export the potential generation from a gust. For this reason, a micro-wind inverter may take its synchronization power from the utility grid rather than the dc side as is the case with PV. In some of the field trial examples shown in this chapter, this can actually lead to a "negative load factor" where, in extreme cases, the parasitic load of the turbine is actually greater than the annual generation (see case study example of an *Urban Building Mounted Turbine*, Fig. 9.22, below). If we consider that an inverter might have a parasitic ac load of up to 10 W, this would correspond to approximately 88 kWh/annum, which in the case of the UoS's example given above and Fig. 9.9, would cancel out all theoretical generation.

It is with these performance concerns in mind that the UK's National Micro-wind Filed Trial became established building on the work of the WarwickWindTrials [10]. Under the UK's national micro-wind trial, nine different types of the turbine were assessed: 5 building mounted and 4 pole-mounted (Table 9.1). These turbines had predominantly either

TABLE 9.1 NOABL MCS3003, issue 2.0 (2010) wind-speed correction factors for level of urbanization of a site and proximity of a turbine to roof and nearest obstructions.

NOABL correction classification	Proximity of turbine to roof or nearest obstruction	Lowest point of turbine above roof (m)	NOABL wind speed scaling factor
Rural			
Open country with occasional houses and trees	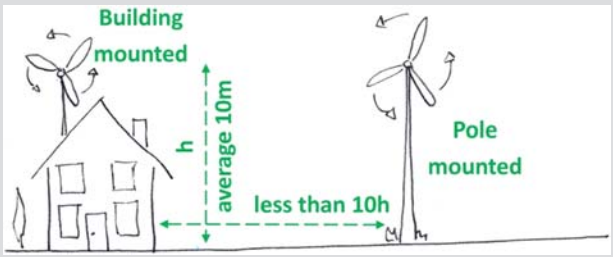	12 7 2 0	100% 94% 86% 82%
Low-rise urban/suburban			
Typically town/village situations with other buildings well-spaced		6 4 2 0	67% 61% 53% 39%
Dense urban			
City centers of most closely spaced 4-storey buildings or higher		10 5 3 1	56% 51% 44% 35%

Scaling factors derived from data given in Harris RI, Deaves DM, The structure of strong winds. In: Wind engineering in the eighties proceedings of the CIRIA conference held on 12/13 November. London, UK; 1980.

been installed through the Low Carbon Buildings Program [9] or were Windsave turbines purchased through B&Q. Table 9.1 shows the specifications of the turbines and it is interesting to note that there is no specific wind-speed at which manufacturers choose to rate their turbine. A total of 64 building-mounted and 22 pole-mounted turbines were monitored for a period of 12 months across urban, suburban, and rural locations (Table 9.2).

In addition to the fully monitored sites of *UK's National Micro-wind Field Trial*, provided monthly generation readings from an additional 68 micro-wind turbines were provided to the trial. Building-mounted and pole-mounted turbines are considered separately in the next two sections. The *UK's National Micro-wind Field Trial* study forms the basis of the data presented here and further information can be found in two *Energy Policy* publications by the authors [16,17].

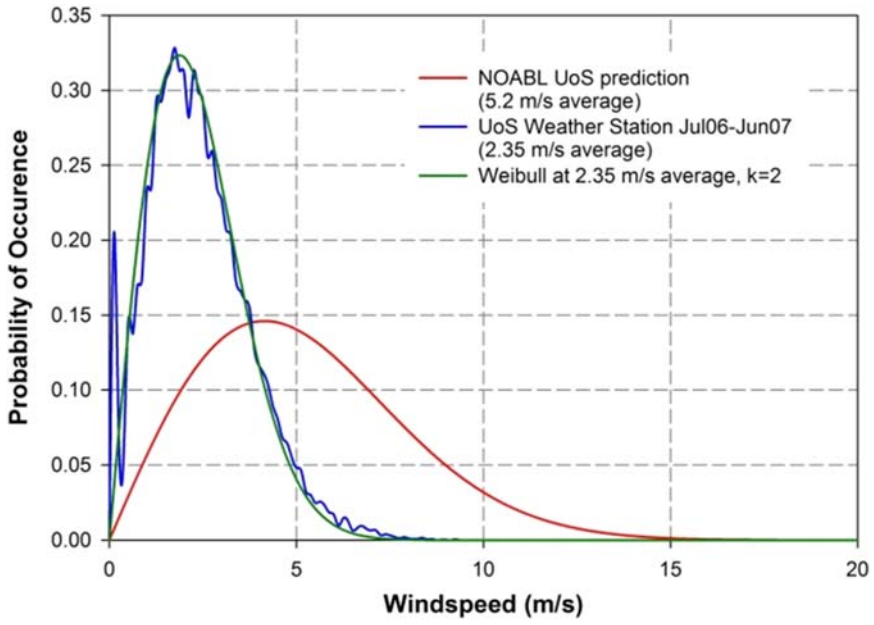

FIGURE 9.8 Comparison of NOABL wind-speed estimate and measured data for the roof of B37, University of Southampton (UoS) (July 2006–June 2007).

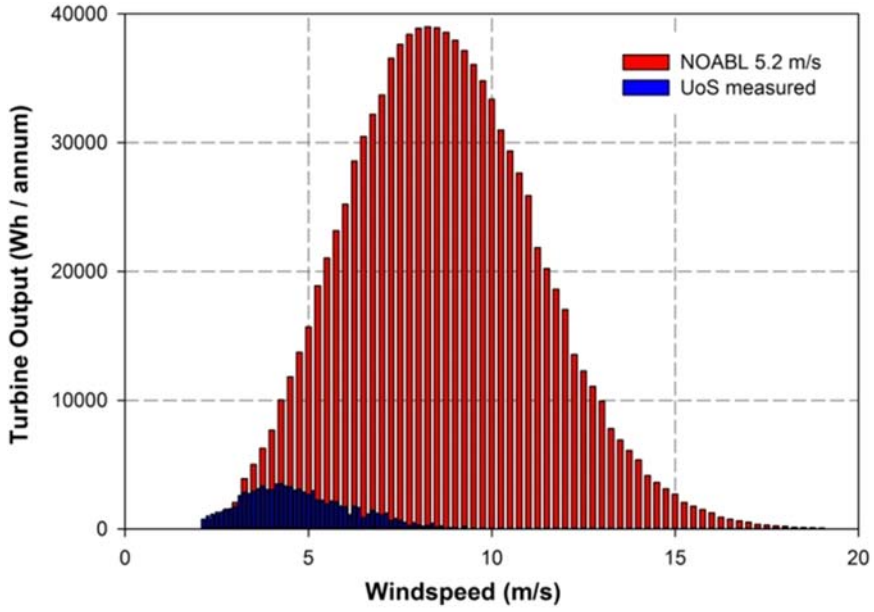

FIGURE 9.9 Comparison of predicted output (0.5 m/s width wind-speed binned distribution) from a WS1000 building mounted micro-wind turbine at the University of Southampton, comparing uncorrected NOABL prediction (836 kWh/annum) and actual wind-speed measurements (94 kWh/annum).

9.1.1 Building-mounted turbines

Fig. 9.10 shows the distribution of building-mounted wind turbines in the United Kingdom for the national micro-wind field trial. Five case study sites are highlighted: Southampton (Dense Urban), South East London (Dense Urban), Felixstowe (Low rise urban/suburban), King's Lynn (Rural), and Silsoe (Rural).

It is instructive to compare the manufacturer's published power curves of the various building-mounted turbines with a commonly used large-scale turbine of the period, a 1.8 MW Vestas V90. Peak efficiencies at realistic wind speeds for operation (above 4 m/s) are around 40% and as you would expect are lower than that of the large V90 turbine (45%) and occur at a lower wind-speed (Fig. 9.11). The corresponding AEP is shown in Fig. 9.12. The Windsave WS1000 is predicted to generate ~900 kWh/annum for an average annual wind-speed of 5 m/s. It is interesting to note

TABLE 9.2 Specifications of micro-wind turbines which participated in the UK's National Micro-wind Field Trial.

Turbine	Number in trial	Diameter (m)	Rated power (kW)	Rated wind speed (m/s)	Cut-in wind speed (m/s)	Cut-out wind speed (m/s)
Building-mounted turbines						
Air Dolphin	5	1.8	1.0	12.0	2.5	50
Ampair 600	14	1.7	0.6	12.5	3.5	None
Eclectic D400	4	1.1	0.4	15.5	2.5	None
Swift	5	2.1	1.5	12.5	2.3	None
Windsave, WS1000	36	1.75	1.0	12.5	4.5	15
Free standing, pole mounted turbines						
Eoltec	5	5.6	6.0	11.5	2.7	None
Iskra AT5−1	6	5.4	5.0	11.0	3.0	None
Proven 2.5	4	3.5	2.5	12.0	2.5	None
Proven 6	7	5.5	6.0	12.0	2.5	None

NOTE: Specifications relate to micro-wind turbines installed at the time of the UK's National Micro-wind Field Trial (2008).

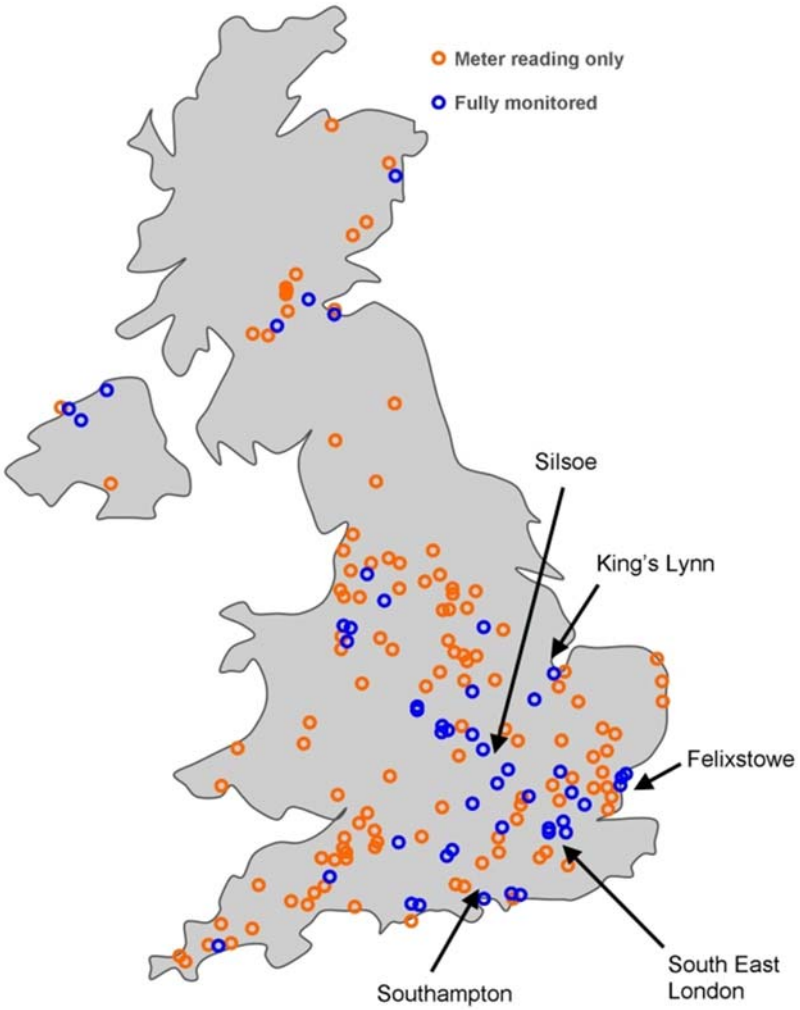

FIGURE 9.10 Location of building mounted turbines of the national micro-wind trial. Blue circles show fully monitored sites, and orange circles show meter readings only. Five case study sites are highlighted: Southampton (Dense Urban), South East London (Dense Urban), Felixstowe (Low rise urban/suburban), King's Lynn (Rural), and Silsoe (Rural).

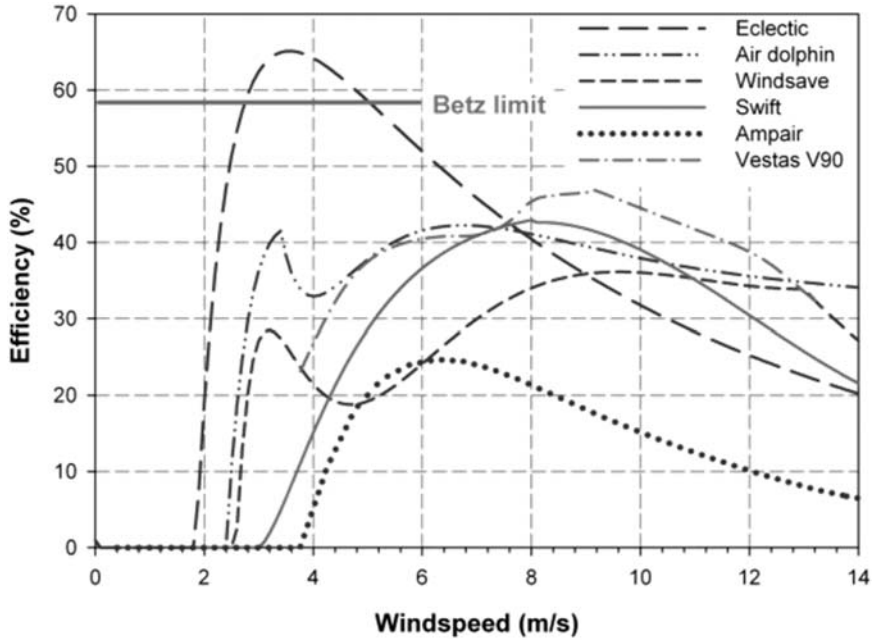

FIGURE 9.11 Calculated manufacturers' turbine efficiency as a function of wind-speed from manufacturers' stated power curve (at time of field trial).

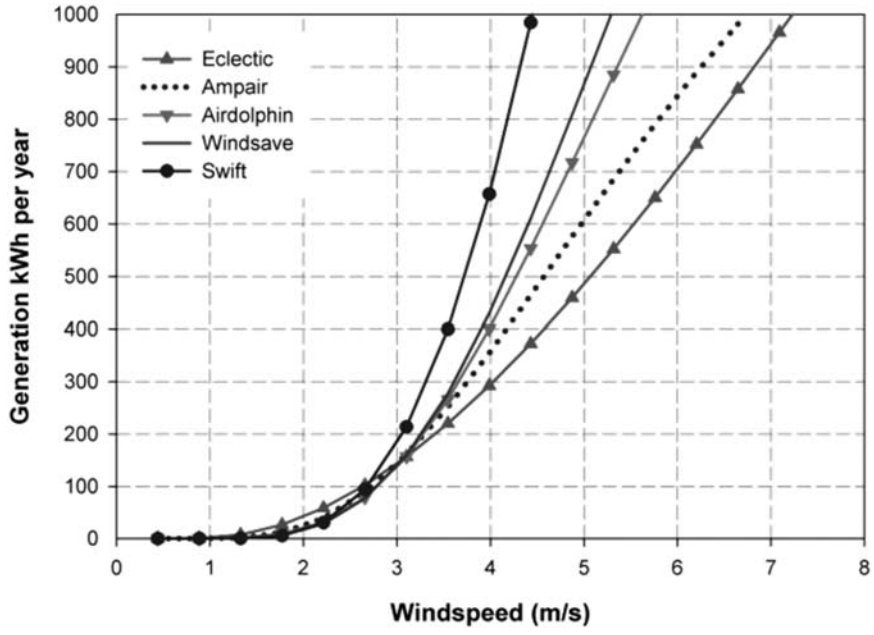

FIGURE 9.12 Annual Energy Production (AEP) estimates for building-mounted wind turbines as a function of annual average wind-speed, assumed Weibull distribution with a shape factor of 2.0.

that this AEP is similar to that of 1 kWp of roof-mounted PV in the South of the United Kingdom [18], but obviously at a higher capital cost (at the time of the trial) than the micro-wind turbine. Driven by economies of scale through mass manufacturing, predominantly in China, the Levelised Cost of Energy of PV has since fallen dramatically. The global average of utility-scale renewable power from PV was 0.381 US$/kWh in 2010, by 2020 this was 0.057 US $/kWh, showing an 85% reduction (refer IRENA, 2021). As of the end of 2020, there were 1,048,328 PV installations in the United Kingdom with a combined capacity of 13,435 MW compared to only 96 MW in 2010 [statista, 2021]. The average installation cost of a 0−4 kWp PV system in the United Kingdom in March 2021 was £1691 kW^{-1}.

[IRENA, 2021] IRENA (2021), Renewable Power Generation Costs in 2020, International Renewable Energy Agency, Abu Dhabi. ISBN 978-92-9260-348-9.

[statista, 2022] Statista, Cumulative capacity of solar PV installed by accreditation in the United Kingdom (UK) from 2010 to 2020, https://www.statista.com/statistics/494156/monthly-cumulative-capacity-installed-by-scheme-of-solar-power-in-the-uk/.

The initial data monitoring testing for the field trial was undertaken at Silsoe in Bedfordshire. An industrial shed surrounded by low-lying fields was used to assess the performance of a WS1000 turbine (Fig. 9.13).

Silsoe is not in a particularly windy location in the United Kingdom, with a stated NOABL wind speed of 4.6 m/s. The site is classified as rural and has a 2010 MIS3003 MCS 0.82 correction factor (3.8 m/s). Fig. 9.14 compares the 5-min average anemometer measurements with turbine power over a period of 4 winter months (periods of highest wind speeds). The power curve shown is interpolated from the measured dataset and shows close agreement with the manufacturer's published data. It is interesting to note the scatter in power points above 5-min average wind speeds of 11 m/s. This is where, over a 5-min period, the peak wind-speed may exceed the cut-out speed of 15 m/s leading to a loss of output.

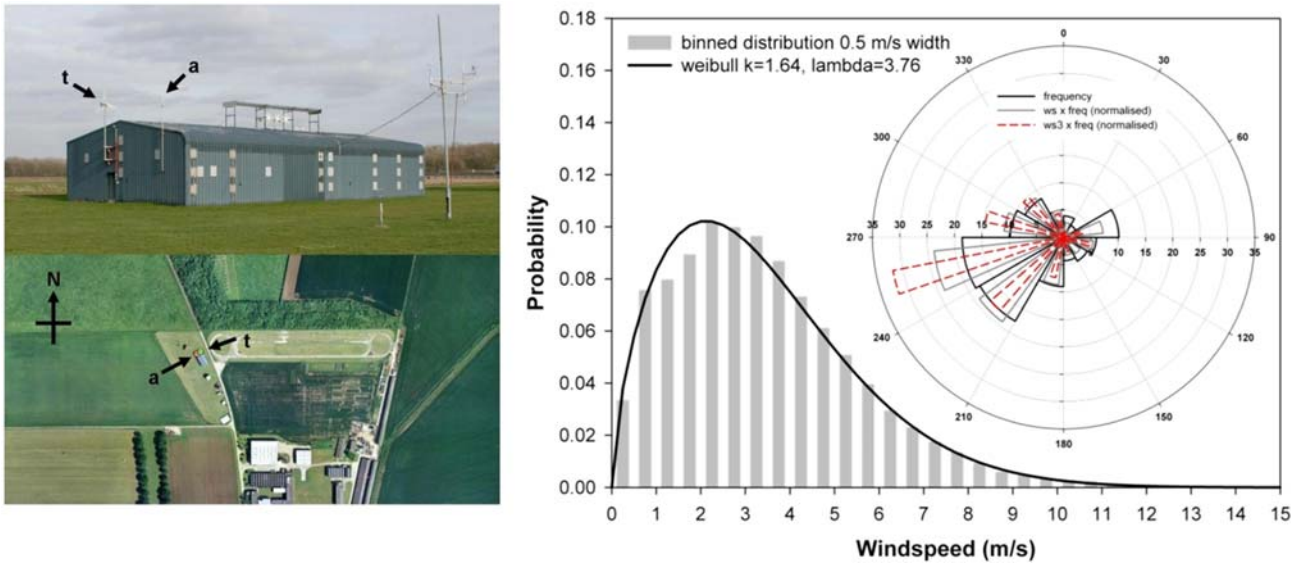

FIGURE 9.13 Windsave WS1000 turbine (*t*) and ultrasonic anemometer (Vaisala WMT50, *a*) on South West side of an industrial shed surrounded by low-lying fields. Silsoe site measured wind-speed data, March 2008−February 2009. NOABL wind-speed is 4.6 m/s, and for NOABL-MCS, 3.8 m/s.

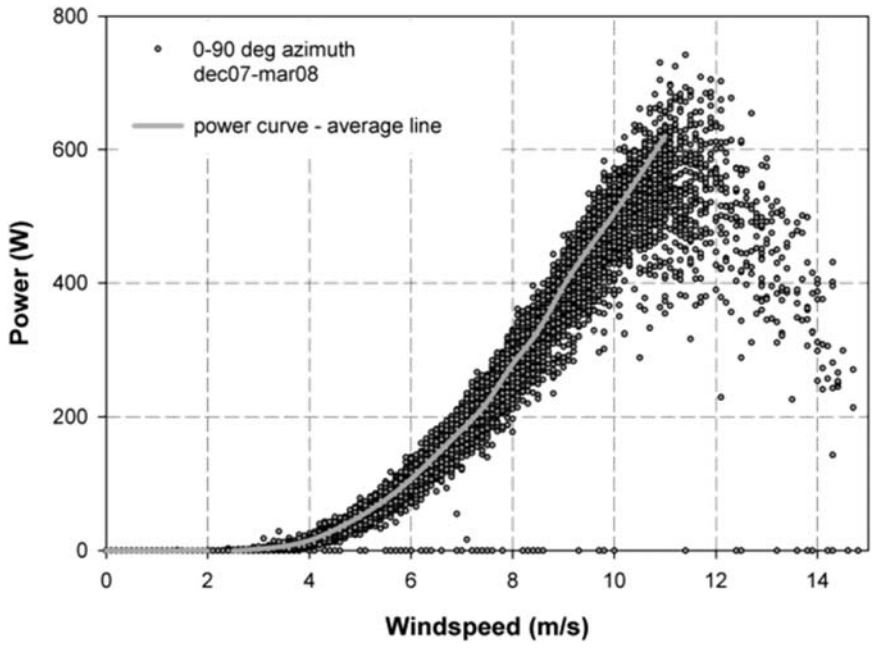

FIGURE 9.14 Comparison of WS1000 published power curve and Silsoe site measurements, 5-min averages.

The measured wind-speed distribution and turbine performance over a 12-month period (March 2008–February 2009) is shown in Figs. 9.13 and 9.15, respectively. The overall generation was 244 kWh (103 kWh/m^2 swept area), with an average wind-speed of 3.4 m/s. This corresponds to a load factor of 2.8%.

The data monitoring at the Silsoe site was reconfigured to record 1-second interval data of wind-speed and power to assess the speed of response of the WS1000 turbine. Fig. 9.16 shows the wind-speed and turbine power output over an example 300-second period. There is a clear correlation between wind-speed and power output suggesting the response of the turbine is indeed fast in the order of seconds. If one compares the Turbulent Intensity, TI, which is defined as the (*standard deviation of wind-speed over a 10-min period*)/(*average wind-speed over a 10-min period*), over a 10-min period with the output of the turbine, this rapid response is evident (Fig. 9.16).

Periods of high turbulent intensity correspond to rapid changes in wind-speed. The energy (proportional to wind-speed cubed) in 10 min of high TI will be larger than for a low TI period. This is illustrated in Fig. 9.17, where the power output of the turbine as a function of TI (low and high) is shown. High TI periods produce greater power output

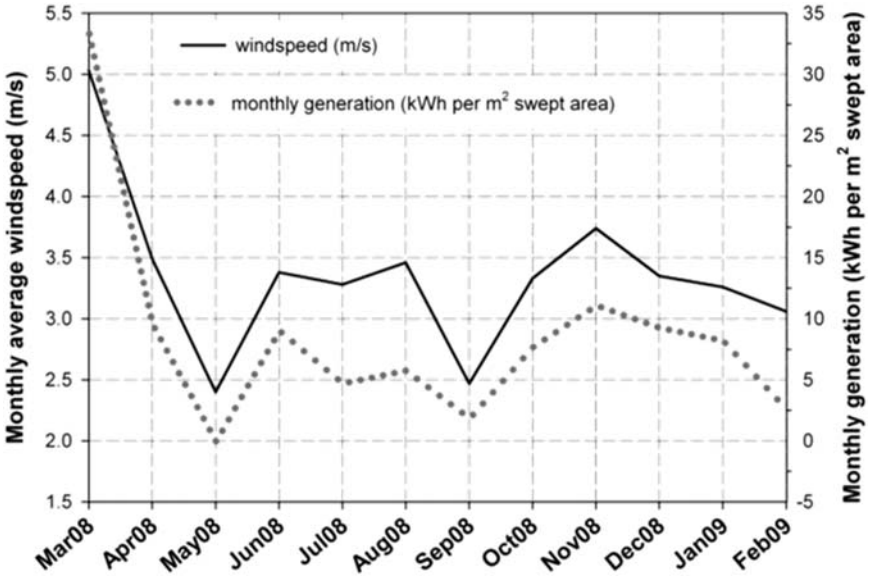

FIGURE 9.15 12 months of Silsoe site WS1000 micro-wind turbine performance data, March 2008–February 2009. The average wind-speed of 3.4 m/s, and the annual load factor is 2.8%.

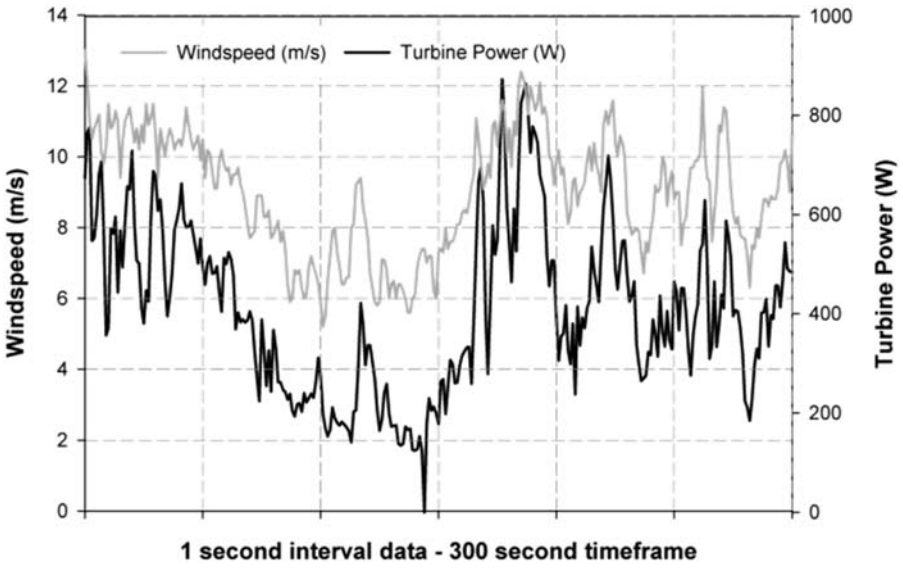

FIGURE 9.16 One-second interval wind-speed and turbine power response, Windsave WS1000 turbine at Silsoe.

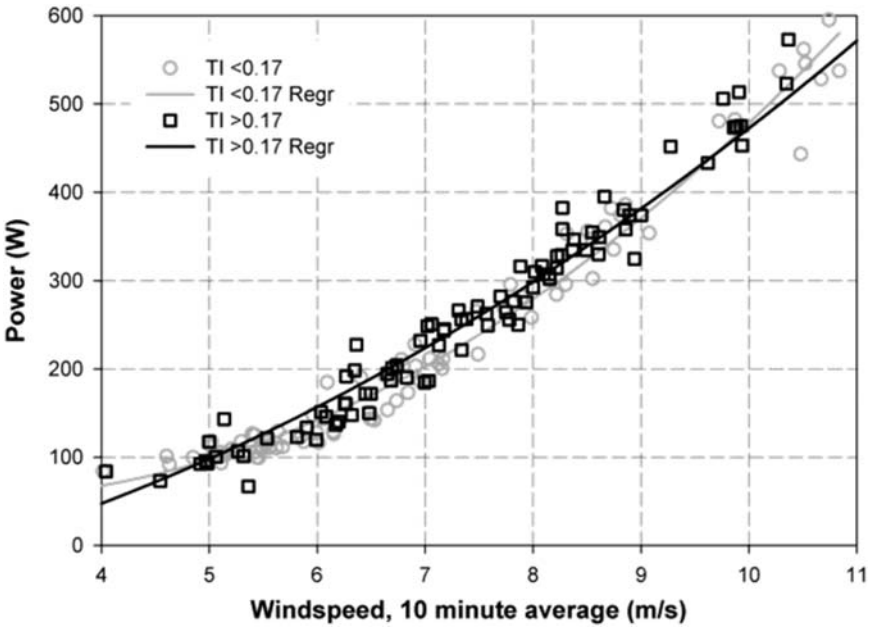

FIGURE 9.17 Power output as a function of wind speed turbulent intensity, TI, for a WS1000 turbine, averaged over a 10-min period. Higher turbulent intensity results in higher power output from the turbine, demonstrating the rapid response of the turbine.

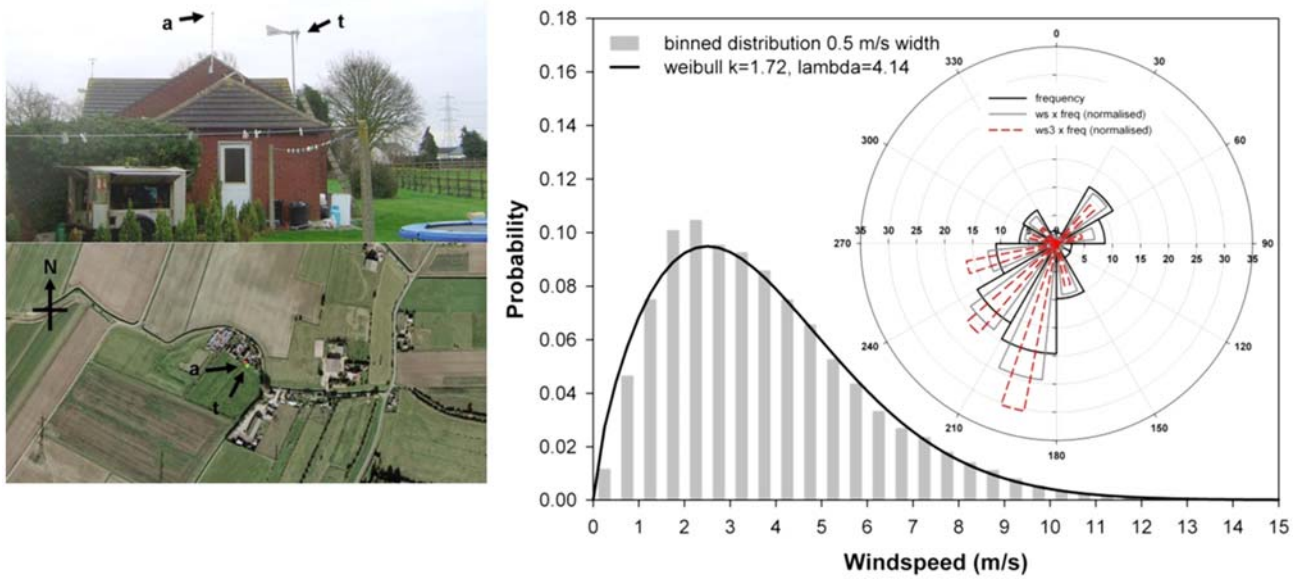

FIGURE 9.18 Windsave WS1000 turbine (*t*) and ultrasonic anemometer (Vaisala WMT50, *a*) on rural house near King's Lynn. Site measured wind-speed data, March 2008−February 2009. The average wind-speed is 3.65 m/s. NOABL wind-speed is 5.0 m/s, and for NOABL-MCS (2010), 4.3 m/s.

from the turbine than periods of lower TI with the same average wind-speed. The performance benefit of high TI reduces at higher wind speeds as it increases the probability of the cut-out wind-speed (15 m/s) being reached in that 10-min period.

9.2 Rural building mounted turbine

Fig. 9.18 shows a rural class site [4] building a mounted turbine near King's Lynn. The prevailing wind is from the South West with an average wind speed of 3.65 m/s. The NOABL and NOABL-MCS (2010) wind speed estimates for

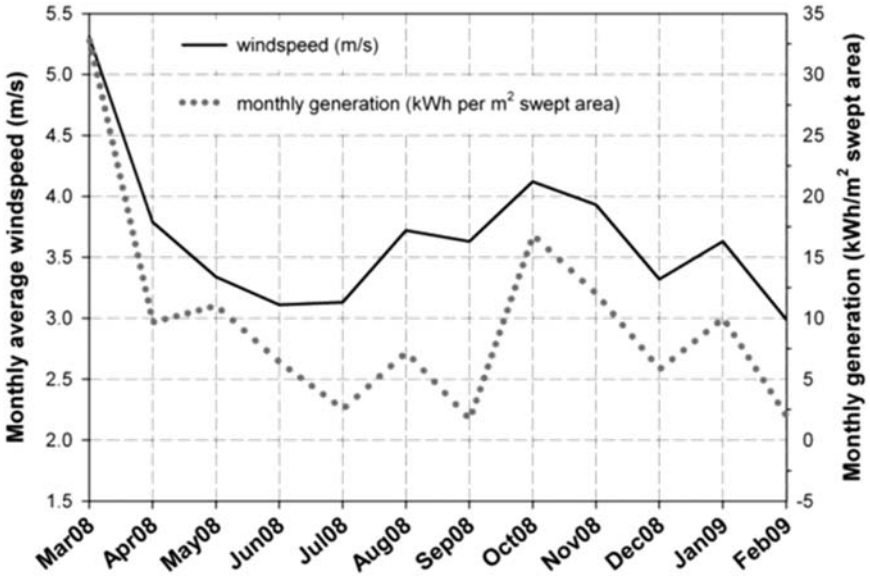

FIGURE 9.19 Measured wind-speed at King's Lynn site and WS1000 wind turbine monthly output, March 2008–February 2009. The average wind speed is 3.65 m/s, and the load factor is 3.1%.

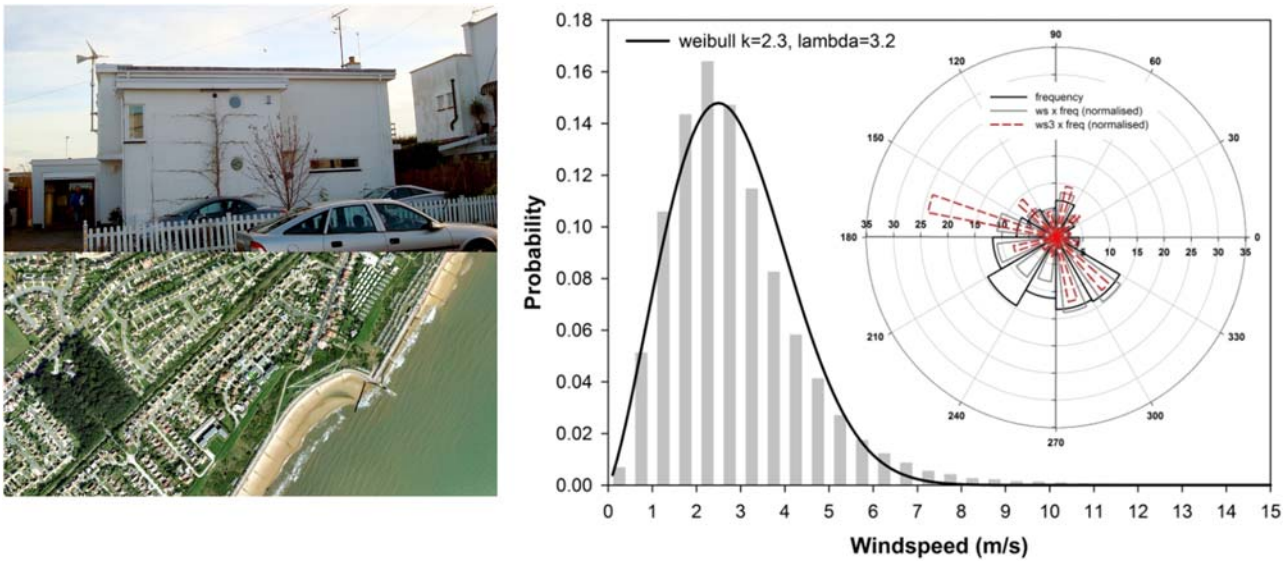

FIGURE 9.20 Windsave WS1000 turbine (*t*) and ultrasonic anemometer (Vaisala WMT50, *a*) on house in the coastal town of Felixstowe. Measured wind-speed data, March 2008–February 2009. Average wind-speed is 2.83 m/s. NOABL wind-speed is 5.7 m/s, and for NOABL-MCS (2010), 2.2 m/s.

the site are 5.0 and 4.3 m/s, respectively. The measured load factor, including inverter power draw, was 3.1% over the 12-month monitoring period (Fig. 9.19).

9.3 Suburban building mounted turbine

Fig. 9.20 shows a coastal, suburban turbine in Felixstowe on the East coast of the United Kingdom. The NOABL and NOABL-MCS (2010) wind speed estimates for the site are 5.7 and 2.2 m/s, respectively. The measured wind speed was 2.83 m/s which resulted in an annual load factor of 0.6% (Fig. 9.21).

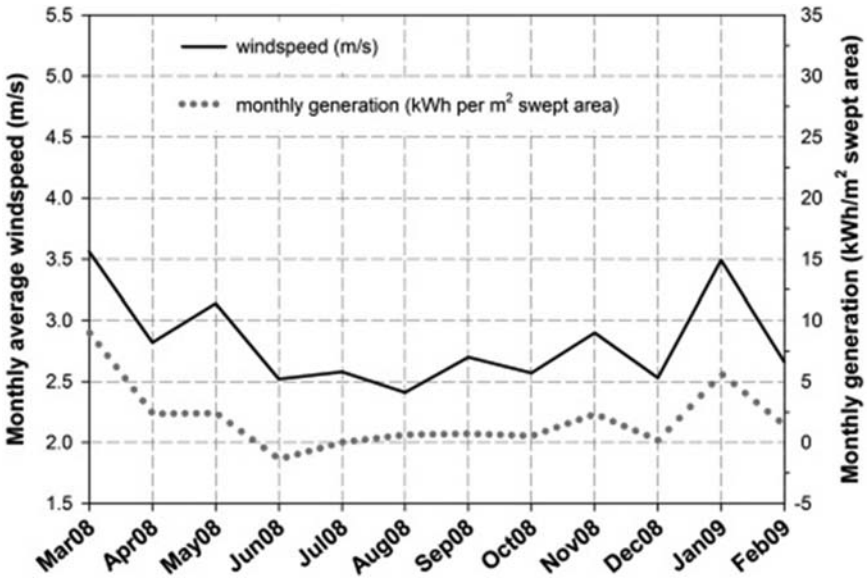

FIGURE 9.21 Measured wind-speed at Felixstowe site and WS1000 wind turbine monthly output. March 2008–February 2009. The average wind-speed is 2.83 m/s, and the load factor is 0.6%.

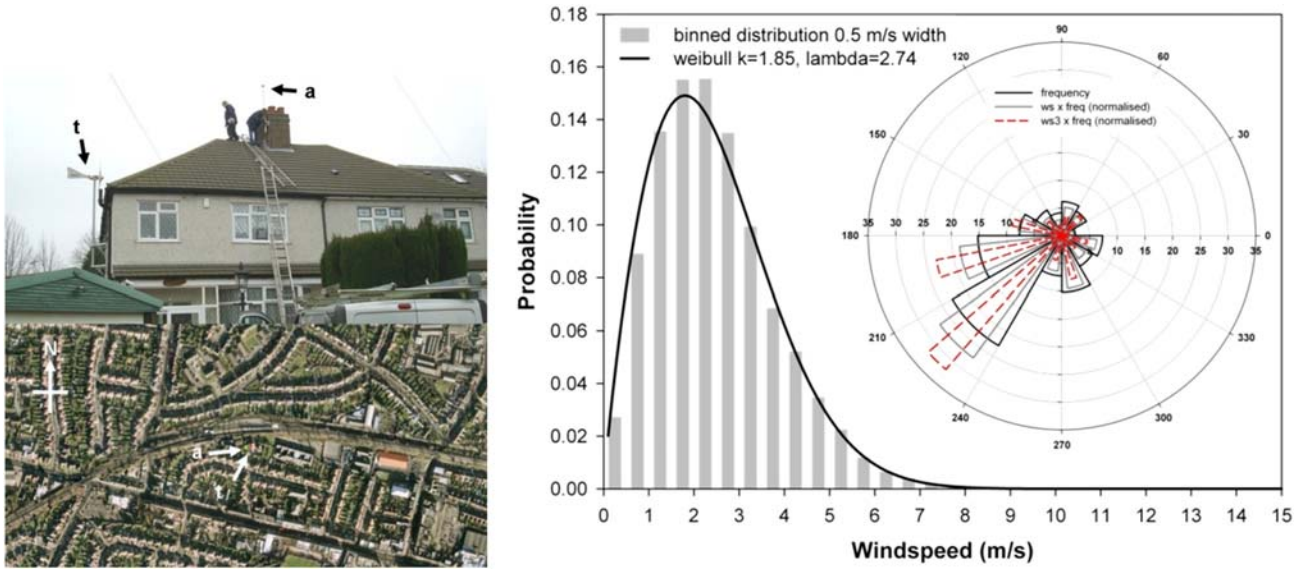

FIGURE 9.22 Windsave WS1000 turbine (*t*) and ultrasonic anemometer (Vaisala WMT50, *a*) on house in South London. The average wind-speed is 2.4 m/s. NOABL wind-speed is 5.0 m/s and for NOABL-MCS (2010), 1.8 m/s.

9.4 Urban building mounted turbine

Fig. 9.22 shows a highly urbanized site in South London. The turbine has been installed at the eaves height of the roof, whereas the wind speed anemometer is above roof height. The NOABL and NOABL-MCS (2010) wind speeds for the anemometer location are 5.0 and 1.8 m/s. The site is clearly not appropriate for micro-wind and this is reflected in the measured wind speeds and turbine output (Fig. 9.23). In this case, the parasitic ac demand of the inverter is actually greater than the generation of the turbine resulting in an overall negative load factor. If the turbine has been located at the anemometer position, the higher generation would have just exceeded the inverter power requirements over the year.

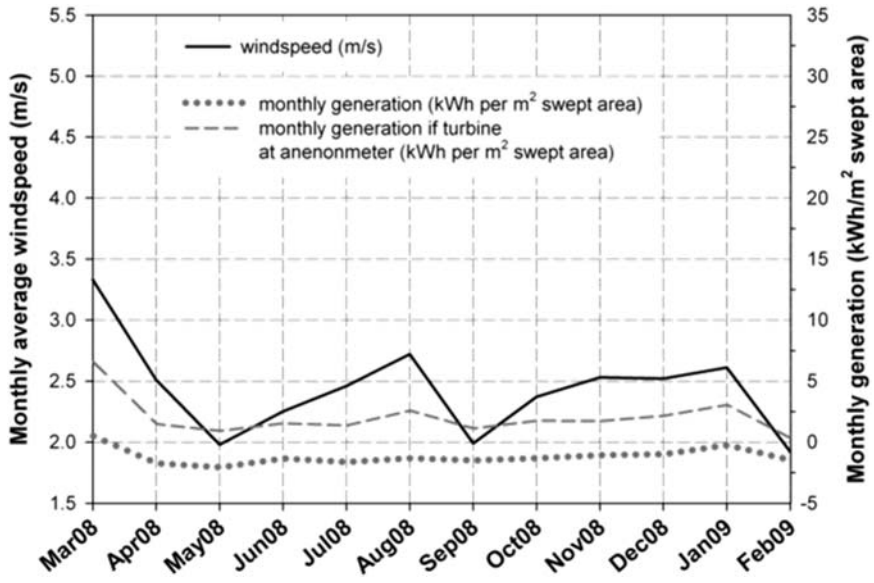

FIGURE 9.23 Measured wind-speed at the South London site and WS1000 wind turbine monthly output, March 2008–February 2009. Average wind-speed is 2.4 m/s, and the load factor is -0.42%. Potential turbine generation if located at anemometer height is shown (dashed grey line).

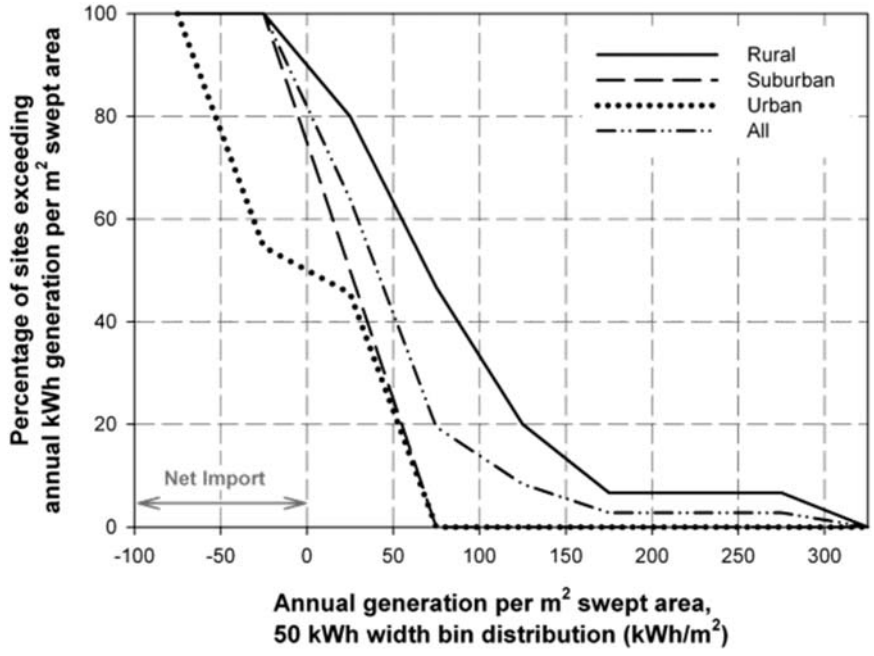

FIGURE 9.24 Binned distribution (50 kWh width) of building mounted micro-wind turbine sites, annual generation per m^2 swept area, as a function of site type: Rural, Suburban, Urban.

9.5 Summary findings: building mounted turbines

Fig. 9.24 shows the performance analysis of the building-mounted turbines. It is important to note that half of the urban turbines have a negative load factor (they consume more power than they generate over the year). The best performing rural wind turbines generated around 300 kWh/m^2 annum which corresponds to a load factor of ~8%. The field trial data has shown this very poor performance compared to the claimed typical load factor of 10%.

Fig. 9.25 compares the measured wind speeds at the building-mounted turbine sites with that predicted by NOABL-MCS [4]. The solid grey line shows a 1:1 (perfect) relationship between prediction and observation. For urban and rural sites, there is a fairly even scatter on either side of the perfect fit line. The NOABL-MCS 2010 correction appears appropriate for both Urban and Suburban sites. However, this correction merely serves to confirm that there is no wind resource in such locations. The threshold wind speed for installation of micro-wind turbine is 5.0 m/s. only two sites in

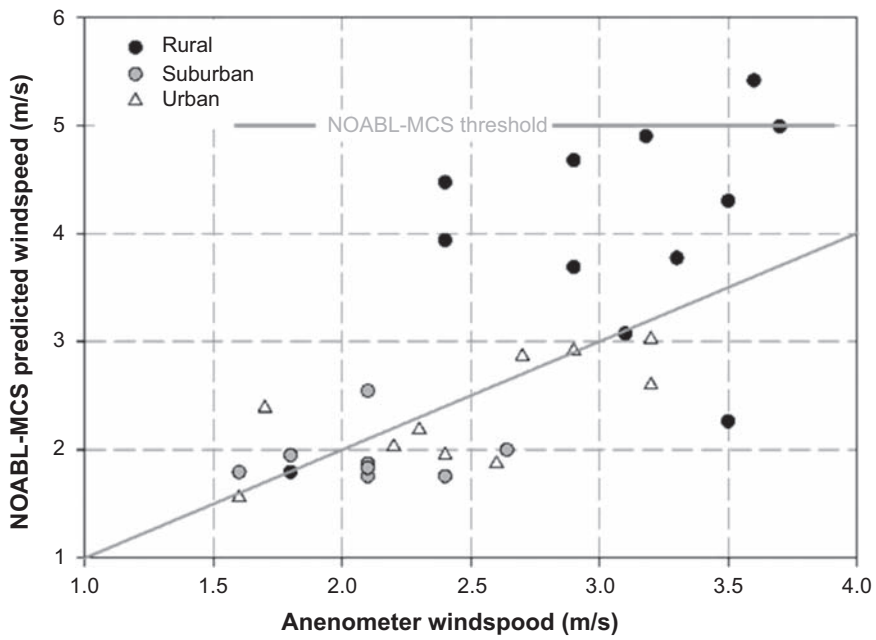

FIGURE 9.25 EST micro-wind trial building mounted turbine summary. Comparison between measured annual wind speeds at sites with NOABL-MCS 2010 estimates. Rural NOABL-MCS 2010 correction is seen to overestimate the wind resource.

the trial achieved this design threshold, although no sites had a measured wind-speed of above 4.0 m/s. It appears that the NOABL-MCS 2010 correction still represents an overestimate of wind resource for rural locations.

9.6 Field trial observations: pole mounted turbines

Fig. 9.26 shows the location of pole-mounted turbines in the UK's National Micro-wind Trial. These are generally located on farmland in what would be considered good wind resource locations.

The calculated manufacturer's efficiency curves and AEP as a function of wind speed are shown in Figs. 9.27 and 9.28. All the pole-mounted turbines show very similar AEP predictions for the expected wind speed ranges (4.8 m/s annual average).

Fig. 9.29 shows a typical farm-based pole-mounted turbine wind trial site. A proven 6 kW turbine is located in a field near the main farm buildings. Scaffold poles have been used to mount an anemometer at the same height as the turbine hub (12 m). The predominant wind speed direction is from the South West. The average wind speed of the site was 4.62 m/s compared to NOABL and NOABL-MCS 2010 estimates of 7.7 and 6.8 m/s. The load factor of the site was 20.6% (Fig. 9.30).

Fig. 9.31 compares the NOABL-MCS estimate of annual generation [4] with the measured performance of pole-mounted turbines in the trial. Whilst there is still a high level of variability in site-specific prediction, the overall relationship is consistent.

9.7 The future for micro-wind

Pole-mounted turbines were shown to perform well in the UK's National Micro-wind Trial. An average load factor of 19% was measured with the best turbine sites having load factors above 30% (Orkney Islands). Rural landowners, especially farmers, are a clear market for pole-mounted turbines. In some cases, the groundwork installation costs, such as foundations and underground cable laying, can be undertaken by the farmer at a marginal cost. An assessment in 2009 by the authors of the potential pole mount turbine market in the United Kingdom was based on the premise of 50 kWp being installed on each farm in the United Kingdom which achieved a threshold wind-speed [19]. For a threshold NOABL-MCS [4] wind-speed of 5.0 m/s this suggested a resource-based potential UK market of around 87,000 farm sites (achieving a load factor threshold of 17%), predominantly in Scotland.

Feed-in tariffs transformed the micro-generation sector in the United Kingdom between 2011 and 2015, where PV became almost ubiquitous either on household roofs or ground mounted in fields. As of May 2016, there was 10,265 MW of PV capacity in the United Kingdom across 882,440 installations.

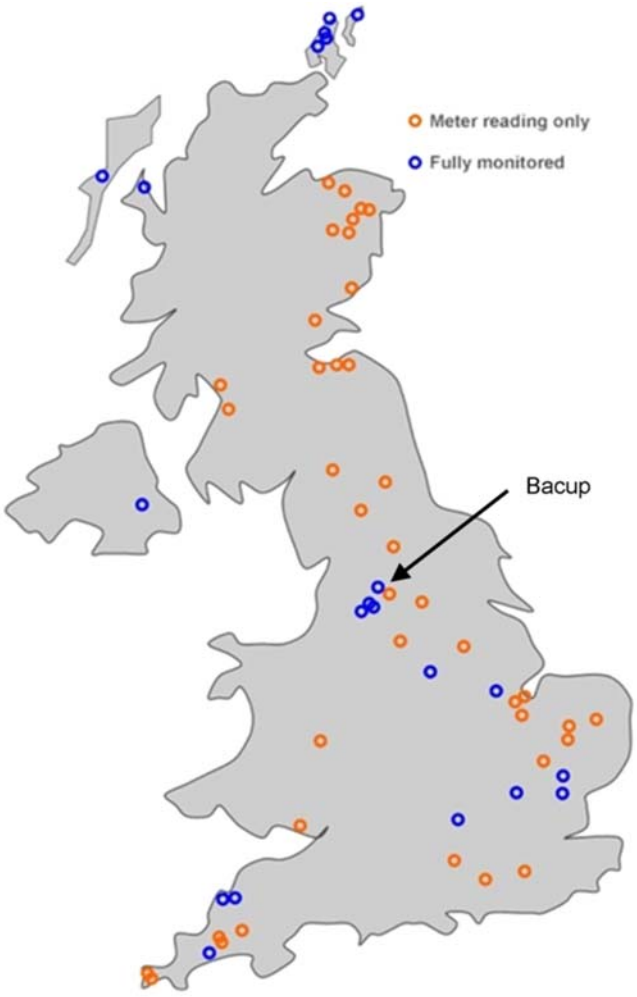

FIGURE 9.26 Location of Pole mounted turbines for UK national micro-wind trial. The case study site Bacup (Rural) is highlighted.

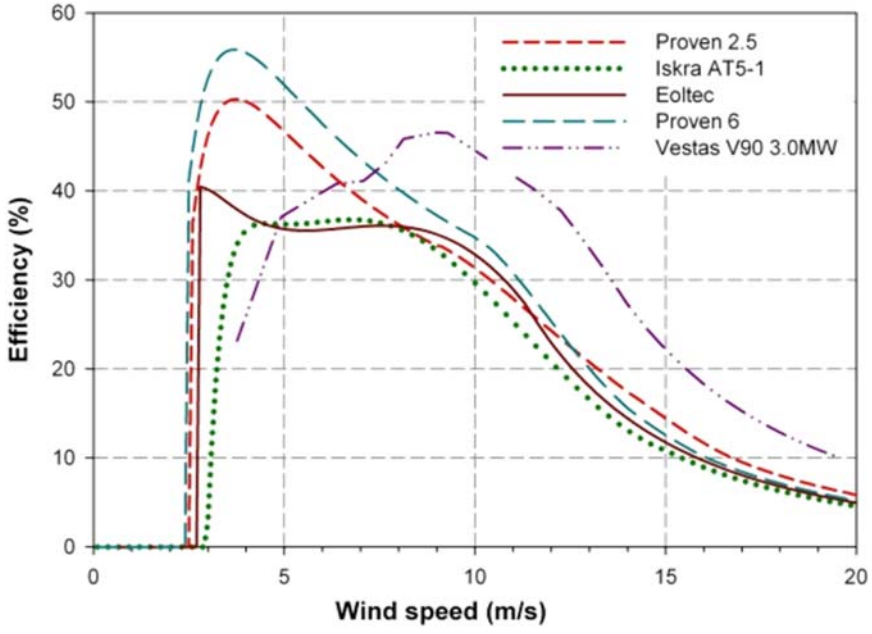

FIGURE 9.27 Calculated manufacturers' pole-mounted turbine efficiency as a function of wind-speed from manufacturers' stated power curve (at time of field trial).

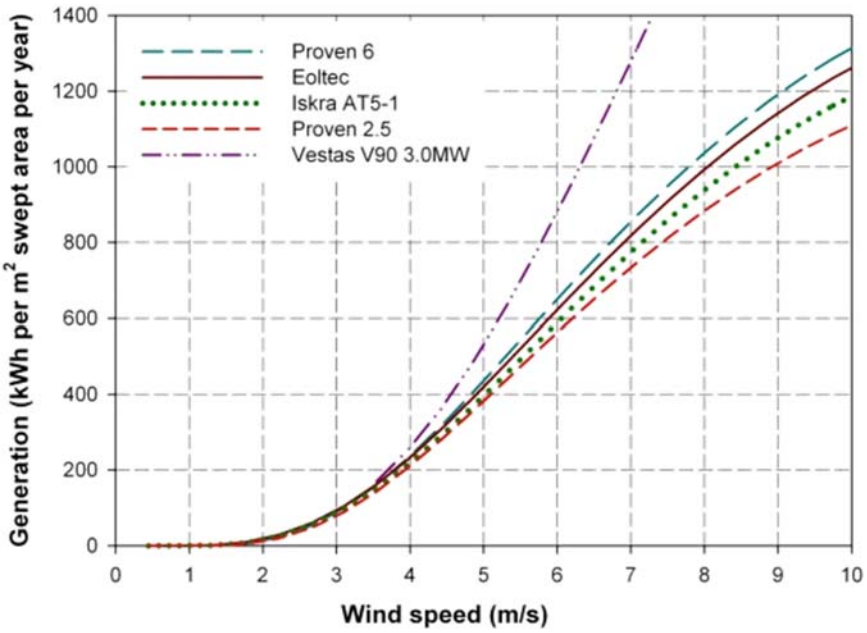

FIGURE 9.28 Annual Energy Production (AEP) estimates for pole-mounted wind turbines as a function of annual average wind-speed, assumed Weibull distribution with a shape factor of 2.0.

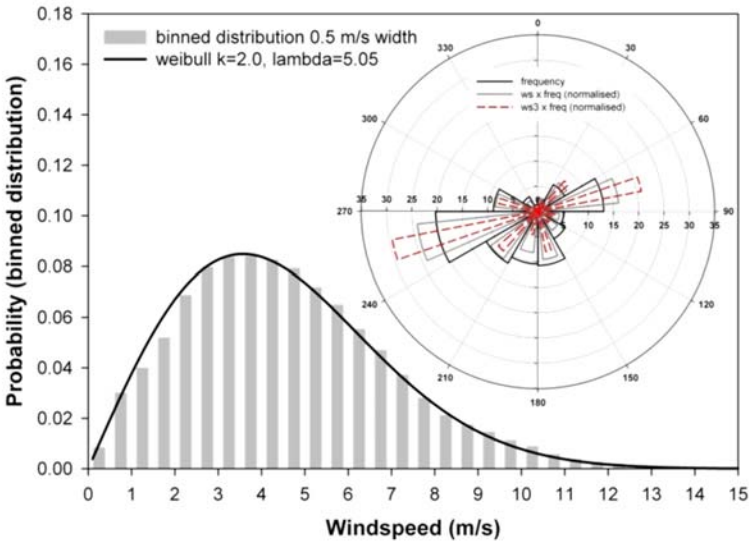

FIGURE 9.29 Proven 6 kW turbine and ultrasonic anemometer (Vaisala WMT50) on a farm near Bacup, South Pennines, Lancashire. Average wind-speed is 4.62 m/s. NOABL wind speed is 7.7 m/s, and NOABL-MCS 2010 wind speed is 6.8 m/s.

Around 40% of this capacity is in the 5−25 MWp capacity range [20]. By comparison, the cumulative number of small wind turbines (<50 kW) was very small. There were 4226 turbines in the range of 1.5−15 kW and 749 in the 15−50 kW range, with an overall capacity of 52 MW. For all but the windiest of sites in the United Kingdom, PV will offer a better financial return and is a lower-risk investment with an established supply chain and easy resource assessment. PV has a typical load factor of ~11% in the South of the United Kingdom, whereas an excellent pole-mounted small wind site might achieve ~30%, but more typically 19%. In 2016 the grid-connected PV cost was around £1265/kWp installed (10−50 kW range 2016), [21], whereas a high-quality pole-mounted turbine was £5000−7000 k/Wp that is fully installed.

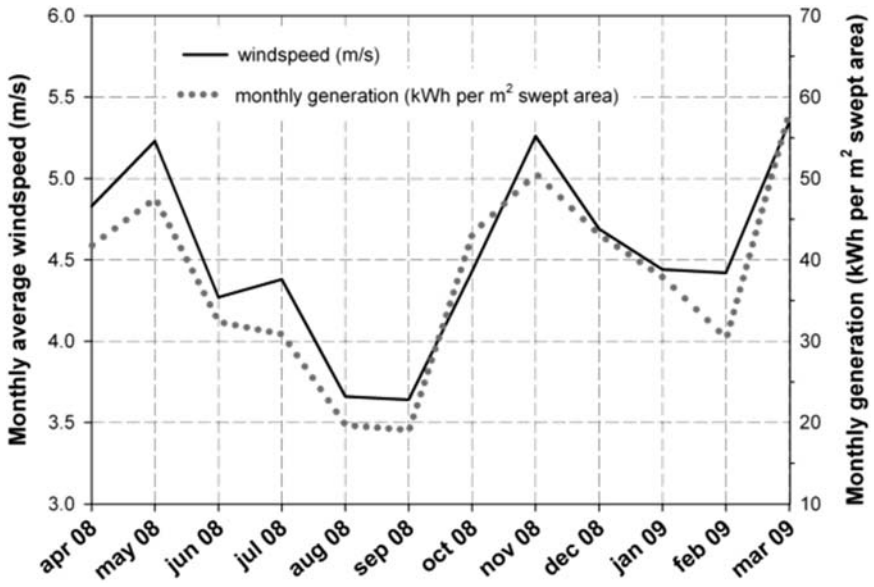

FIGURE 9.30 Measured wind-speed at Bacup, South Pennines site and proven 6 kWp wind turbine monthly output, March 2008–February 2009. Average wind-speed is 4.62 m/s, and the load factor is 20.6%.

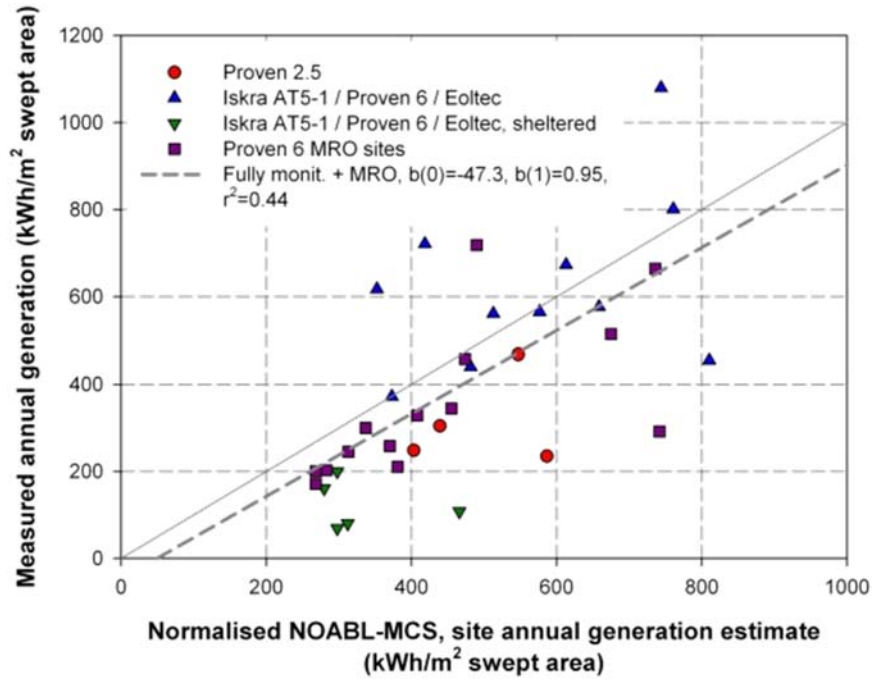

FIGURE 9.31 Comparison of NOABL-MCS [4] AEP estimate and measured annual generation across pole-mounted turbines of the national micro-wind trial.

To qualify for feed-in tariffs, a system must be installed by an MCS-certified contractor (that is, Micro-generation Certification Scheme) [12]. As of June 2016, the most generous feed-in tariff in the United Kingdom was 4.32 p/kWh for generation from PV and 8.46 p/kWh for generation from wind [22]. The overall economics are sensitive to the level of export to the grid, and therefore "avoided import" which has a value of ~12 p/kWh. If we were to assume a 50% level of export for the case of PV and wind [23,24], a £5000 kW/p turbine would need to have a load factor of ~28% to achieve the same financial payback time (14 years in each case at 0% discount rate). The twin issues of an unstable feed-in tariff policy in the United Kingdom and the rapidly falling price of PV make the market challenging for small wind. This is outlined clearly in RenewableUK's [25] report "Small and Medium Wind Strategy: The current and future potential of the sub-500 kW wind industry in the UK" which states that "experience shows mounting challenges, and our industry is at a crossroads that will determine its future" [25].

Today (in 2022), the microgeneration landscape has changed significantly from what is described above with PV becoming the renewable of choice for most applications. The government closed the feed-in tariff scheme to new customers in April 2019 further weakening the economic case for small wind. The small wind turbine sector is now restricted to off-grid or remote, and high-wind resource locations. Micro-wind turbines are no longer installed in the urban environment.

9.8 Conclusions

The main lesson from the UK's National Micro-wind Trial study is borne out in its formal report title "Location, Location, Location: Domestic small-scale wind field trial report." It is that there is simply insufficient wind resource in urban and suburban locations [11]. Deploying micro-wind turbines in these locations will lead to very poor load factors (typically 2%) and in some cases, they may even be negative due to the parasitic ac power draw of the inverter.

The study suggests that vertical axis micro-wind turbines are able to respond quickly to changes in wind-speed, in essence that turbulence is not the key issue in relation to poor performance. The best performing rural building mounted turbines had to load factors up to 8% which is still less than PV in the United Kingdom. The building-mounted turbine MCS correction factors for NOABL wind speeds [4] show good agreement for urban and suburban sites, but the NOABL-MCS rural value appeared high in this study.

Pole-mounted turbines performed well in this study achieving the expected load factors (average of 19%). The NOABL-MCS correction to wind-speed for rural pole-mounted turbines is far better, but still on an individual site basis, it can lead to a large overuse or underestimate of the resource.

For off-grid systems, wind and PV are complementary technologies having higher generation in different seasons of the year. In relation to grid-connected systems, the dramatic reduction in the cost of PV, driven by generous feed-in tariffs has transformed the micro-generation sector in the United Kingdom. This has made the economics of small grid-connected wind much more difficult in a highly competitive market. The deployment of medium wind (100−500 kW) on rural farms is a sector that has significant potential but this also faces the challenge of PV in particular. Large-scale onshore wind in the United Kingdom has faced challenges with planning acceptance in recent years which has pushed renewable expansion offshore. Recent events (COVID-19, Ukraine conflict) have created unprecedented rises in wholesale gas prices, with associated increases in electricity costs. The pressure of energy costs and the acceptance of the need to provide security of supply may lead to increased interest in the medium wind at the higher end of the power range going forward.

Acknowledgments

This work is part of the activities of the Energy and Climate Change Division and the Sustainable Energy Research Group (http://www.energy.soton.ac.uk). The work presented here was undertaken as part of the UK's National Microwind Trial. The field trial was developed and delivered with funding and support from a wide variety of stakeholders including the Energy Saving Trust (EST); The Scottish Government; DEFRA; B&Q; and the UK's main energy suppliers including EDFEnergy, RWEN power, NIE Energy, Centrica plc, ScottishPower Ltd, Scottish&Southern Energy, and E.ON UK. These funders were represented on the project's advisory group and were influential in the trial's site selection and communications.

Aspects of this work formed the basis of the 2011 PhD study of Dr. Matthew Sissons entitled "Micro-wind power in the UK: Experimental datasets and theoretical models for site-specific yield analysis" [19].

References

[1] Renewable UK. Small and medium wind UK market report. RUK-003-5, March 2015; 2015.

[2] Watson J, Sauter R, Bahaj AS, James PAB, Myers LE, Wing R. Unlocking the power house: policy and system change for domestic micro-generation in the UK. 2006, p. 1−32, ISBN 1-903721-02-04.

[3] Watson J, Sauter R, Bahaj AS, James PAB, Myers LE, Wing R. Domestic micro-generation: economic, regulatory and policy issues for the UK. Energy Policy 2008;36(8):3095−106.

[4] MIS3003. Requirements for contractors undertaking the supply, design, installation, set to work commissioning and handover of micro and small wind turbine systems issue 2.0, 26/08/2010. 2010.

[5] Energy Saving Trust (EST). CE72: Installing small wind-powered electricity generating systems − guidance for installers and specifiers. 2004.

[6] NOABL. Numerical objective analysis boundary layer tool database, <http://tools.decc.gov.uk/en/windspeed/default.aspx>; 2016.

[7] British Wind Energy Association. BWEA small wind systems. UK Market Report 2008, (now renewable UK); 2008.

[8] DUKES Digest UK Energy Statistics. Chapter 6: renewable sources of energy, <https://www.gov.uk/government/uploads/system/uploads/attachment_data/file/450298/DUKES_2015_Chapter_6.pdf>; 2015.
[9] LCBP. Low carbon building programme. Final Report, DECC, <https://www.gov.uk/government/uploads/system/uploads/attachment_data/file/48160/2578-lcb-programme-2006-11-final-report.pdf>; 2011.
[10] WarwickWindTrials. WarwickWindTrials final report, <http://www.warwickwindtrials.org.uk/resources/Warwick + Wind + Trials + Final + Report + .pdf>; 2009.
[11] Energy Saving Trust (EST). Location, location, location: domestic small scale wind field trial report; July 2009.
[12] MIS3003. Requirements for contractors undertaking the supply, design, installation, set to work commissioning and handover of micro and small wind turbine systems issue 3.4, 01/05/2015; 2015.
[13] Harris RI Deaves DM. The structure of strong winds. In: Wind engineering in the eighties proceedings of the CIRIA conference held on 12/13 November. London, UK; 1980.
[14] G83/2. G83: recommendations for the connection of small scale embedded generators (up to 16 A per phase) in parallel with public low voltage distribution networks. Available from The Energy Networks Association: <http://www.energynetworks.org>; 2012.
[15] G59/3. G59: recommendations for the connection of embedded generating plant to the public electricity suppliers' distribution systems. Available from The Energy Networks Association <http://www.energynetworks.org>; 2014.
[16] James PAB, Sissons MF, Bradford J, Myers LE, Bahaj AS, Anwar A. Implications of the UK field trial of building mounted horizontal axis micro-wind turbines. Energy Policy 2010;38(10):6130−44.
[17] Sissons MF, James PAB, Bradford J, Myers LE, Bahaj AS, Anwar A, et al. Pole-mounted horizontal axis micro-wind turbines: UK field trial findings and market size assessment. Energy Policy 2011;39(6):3822−31.
[18] James PAB, Jentsch MF, Bahaj AS. Quantifying the added value of BiPV as a shading solution in atria. Sol Energy 2009;83(2):220−31.
[19] Sissons MF. Micro-wind power in the UK: experimental datasets and theoretical models for site-specific yield analysis [Ph.D. thesis]. Southampton, England: University of Southampton; 2011.
[20] DECC (Department of Energy and Climate Change). Solar photovoltaics deployment, 30 June, <https://www.gov.uk/government/statistics/solar-photovoltaics-deployment>; 2016a.
[21] DECC. Department of energy and climate change, solar PV cost data, 23 July, <https://www.gov.uk/government/statistics/solar-pv-cost-data>; 2016b.
[22] Ofgem. Feed in tariff tables 01 July−30 September, <https://www.ofgem.gov.uk/environmental-programmes/feed-tariff-fit-scheme/tariff-tables>; 2016.
[23] Bahaj AS, James PAB. Urban energy generation: the added value of photovoltaics in social housing. Renew Sustain Energy Rev 2007;11(9):2121−36.
[24] Bahaj AS, Myers LE, James PAB. Urban energy generation: Influence of micro-wind turbine output on electricity consumption in buildings. Energy Build 2007;39(2):154−65.
[25] Renewable UK. Small and medium wind strategy: the current and future potential of the sub-500kW wind industry in the UK; November. 2014.

Chapter 10

Civil engineering aspects of a wind farm and wind turbine structures

Subhamoy Bhattacharya
Department of Sustainability, Civil and Environmental Engineering, University of Surrey, Guildford, London, United Kingdom

10.1 Energy challenge

Energy challenge: With the discovery of shale gas (fracking) and the lowering of oil prices, it is predicted that reliance on oil (often termed as oil age) may have gone. With the increasing use of electric cars and wind turbines, it may be argued that this change of moving toward low carbon energy (LCE) is irreversible and quite similar to the transition from *Stone Age* to *Bronze Age*. Offshore wind energy is considered promising technology to move toward LCE.

10.2 Wind farm and Fukushima nuclear disaster

10.2.1 Case study: performance of near-shore wind farm during 2012 Tohoku earthquake

A devastating earthquake of moment magnitude M_w9.0 struck the Tohoku and Kanto regions of Japan on 12th March at 2:46 PM which also triggered a tsunami, see Fig. 10.1 for the location of the earthquake and the operating wind farms. The earthquake and the associated effects such as liquefaction and tsunami caused great economic loss, loss of life, and tremendous damage to structures and national infrastructures but very little damage to the wind farms. Extensive damage was also caused by the massive tsunami in many cities and towns along the coast. Fig. 10.2A shows photographs of

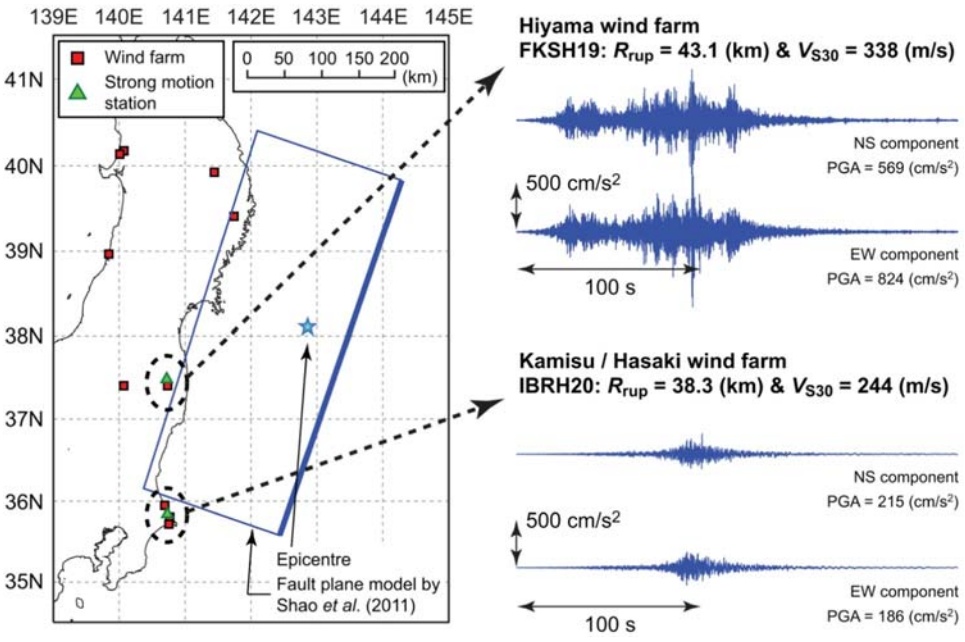

FIGURE 10.1 Details of the 2012 Tohoku earthquake and locations of the wind farms.

Wind Energy Engineering. DOI: https://doi.org/10.1016/B978-0-323-99353-1.00008-6

FIGURE 10.2 (A) Photograph of the Kamisu (Hasaki) wind farm following the 2012 Tohoku earthquake; (B) collapse of the pile-supported building following the same earthquake.

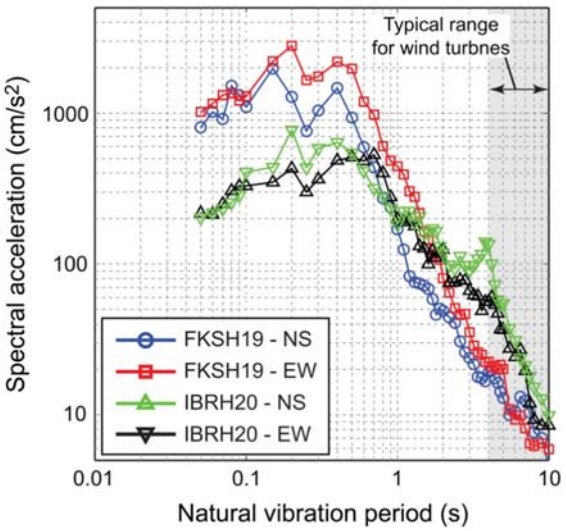

FIGURE 10.3 Power spectra of the earthquake and natural frequency of wind turbines.

a wind farm at Kamisu (Hasaki) after the earthquake and Fig. 10.2B shows the collapse of pile-supported building at Onagawa. At many locations (e.g., Natori, Oofunato, and Onagawa), tsunami heights exceeded 10 m, and sea walls and other coastal defense systems failed to prevent the disaster.

The earthquake and its associated effects (i.e., tsunami) also initiated the crisis of the Fukushima Dai-ichi nuclear power plants (NPP). The tsunami, which arrived around 50 min following the initial earthquake, was 14 m high and it overwhelmed the 10 m high plant sea walls flooding the emergency generator rooms and causing the power failure of the active cooling system. Limited emergency battery power ran out on 12th March and subsequently led to the reactor heating up and the subsequent meltdown leading to the release of harmful radioactive material into the atmosphere. Power failure also meant that many of the safety control systems were not operational. The release of radioactive materials caused a large-scale evacuation of over 300,000 people and the cleanup costs are expected to be of the order of tens of billions of dollars. On the other hand, following/during the earthquake the wind turbines were automatically shut down (like all escalators or lifts) and following an inspection—they were restarted.

10.2.1.1 Why did the wind farm stand up?

Recorded ground acceleration time-series data in two directions [North-South (NS) and East-West (EW)] at Kamisu and Hiyama wind farms [FKSH 19 and IBRH20] are presented in Fig. 10.3 in the frequency domain. The dominant period ranges, of the recorded ground motions at the wind farm sites, were around 0.07−1 s and on the other hand, the periods of the offshore wind turbine systems are in the range of 3 s. Due to the nonoverlapping of the vibration periods, these structures will not get tuned in and as a result, there are relatively insensitive to earthquake shaking. However, earthquake-induced effects such as liquefaction may cause some damage. Further details can be found in Bhattacharya and Goda [1]. Further details of the dynamics of wind turbine structures together with the effects of foundation

flexibility can be found in Adhikari and Bhattacharya [2,3], Bhattacharya and Adhikari [4], Bhattacharya et al. [5–7], and Lombardi et al. [8]

ASIDE: One may argue that had there been few offshore wind turbines operating, the disaster may have been averted or the scale of damages could have certainly been reduced. The wind turbines could have run the emergency cooling system and prevented the reactor meltdown. In this context, it is interesting to note that there are plans to replace the Fukushima NPP with a floating wind farm. The project is in an advanced stage whereby involving a 2 MW semisub floating turbine that has been operational for a few years. An innovative 7 MW oil pressure drive type wind turbine on a three-column semisub floater has recently been tested.

10.3 Wind farm site selection

Fig. 10.4 shows the operating or planned wind farms along the UK coast. Fig. 10.5, on the other hand, shows wind farms along the coasts of the United Kingdom and Europe together with the installed capacity. This section of the chapter will detail the considerations for choosing a particular site.

The main considerations are:

1. **Wind resources**: A thorough knowledge of wind resources in an area is fundamental as it allows an estimation to be made of the wind farms' productivity and therefore the financial viability of the project. As a thumb rule, a project is not financially viable if the average wind speed at the hub height is below 6 m/s and it is considered a safe investment if the average wind speed at the hub is more than 8.5 m/s.
2. **Marine aspects:** Marine aspects would include water depth, wave spectrum at the site (wave height, wave period), current and tide data, exposure to waves and sediment transport, identification of scour-related issues, and if scour protection is needed. Often installation of foundations creates obstacles in the local flow pattern of water which may create turbulence leading to a scouring effect.
3. **Environmental impact**: For all wind farm, an EIA (Environmental Impact Assessment) must be completed as a part of the planning process and it covers the physical, biological, and human environment. This would involve collecting all types of existing environmental data and assessing all the potential impacts that could arise due to the construction and operation of the wind farm. The impacts can range from favorable to less favorable and then to detrimental. Potential aspects of the biological environment include marine mammals, sea birds that use the area on a regular basis, birds from nearby areas that pass through the area during flight, fish, etc. Other aspects include the effect of flora and fauna during the construction (for example noise due to piling or operating noise), the electromagnetic field generated by subsea cable. The human environment includes a change of landscape. Marine archeology aspects such as shipwrecks are also taken in consideration. To carry out the assessment, samples of seabed may be collected and analyzed for worms, barnacles, or other species.
4. **Power export/grid connection:** One of the important deciding factors is the location of onshore grid connections. The deciding factor includes the length of submarine cable required which is dependent on the turbine layout, substation location, identify export cable routing (landfall), risk assessment of buried cables, and the transformer options—AC or DC.
5. **Economics:** Modeling of capital costs and Levelised cost of energy (LCOE) is a function involving many parameters: depth of water, distance from shore, wind speed at the site, port and harbor facilities near the site, Socio-economic condition and access to skilled labor, location of National Grid, and hinterland for the proposed development.
6. **Navigation:** This navigation risk assessment survey investigates whether or not there is a need for an exclusion zone due to fishing or navigation or military operations. Cables connecting the wind farms and the export cables are buried to depths of 2–3 m to avoid the risk of entanglement with nets.
7. **Consents and legislations:** Depending on the country, the consent requirements may change. For example, in the United Kingdom, any development of more than 100 MW is classified as a significant infrastructure project and requires a development consent order from IPC (Infrastructure Planning Commission). These rules are subject to amendment and currently, the final decision rests with the Secretary of State for Energy and Climate Change (Fig. 10.6).

10.3.1 Case studies: Burbo wind farm (see Fig. 10.6 for location)

The Burbo Wind Farm was fitted with 3 MW wind turbines of Vestas V80 make.

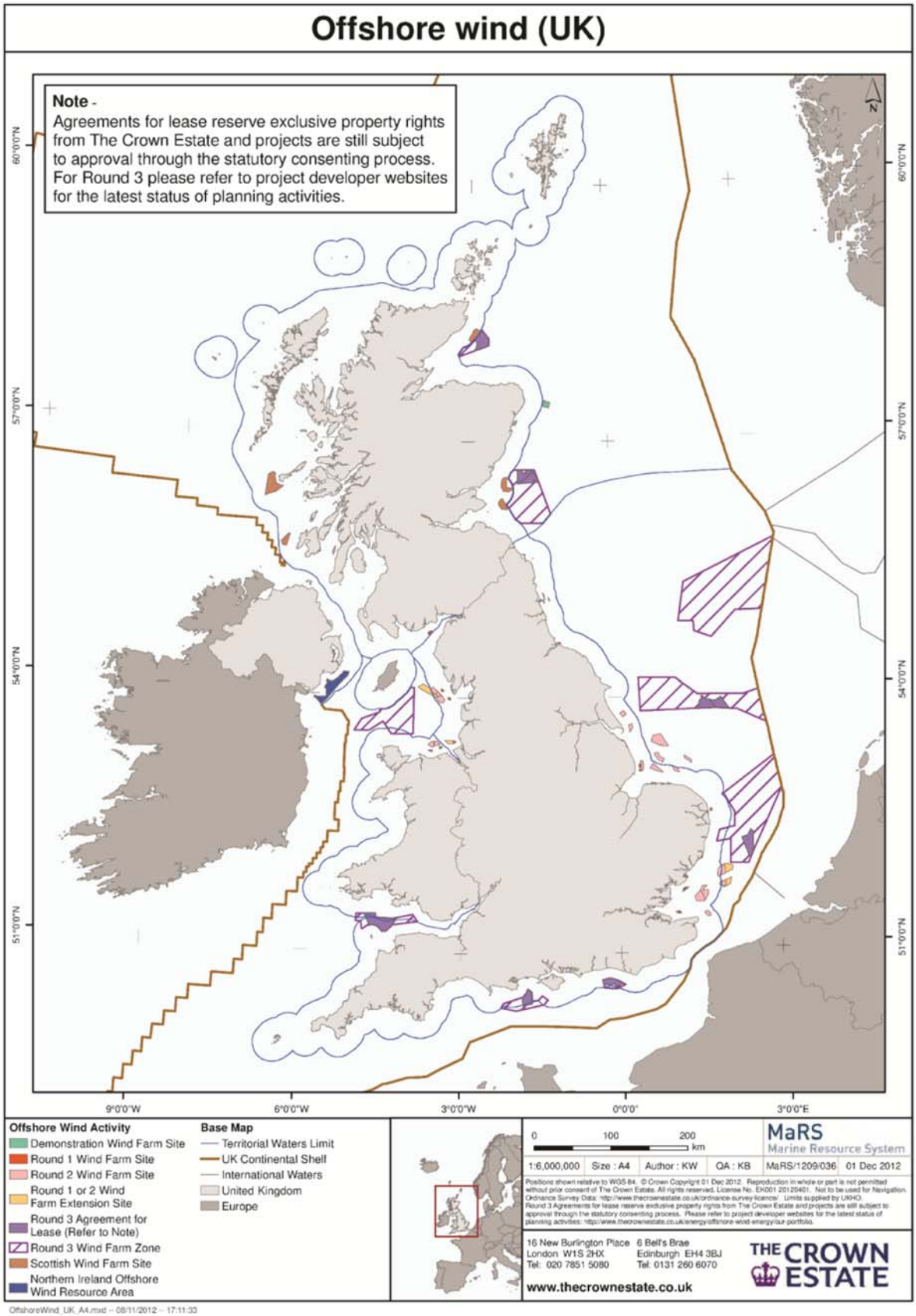

FIGURE 10.4 Offshore wind farms around the United Kingdom.

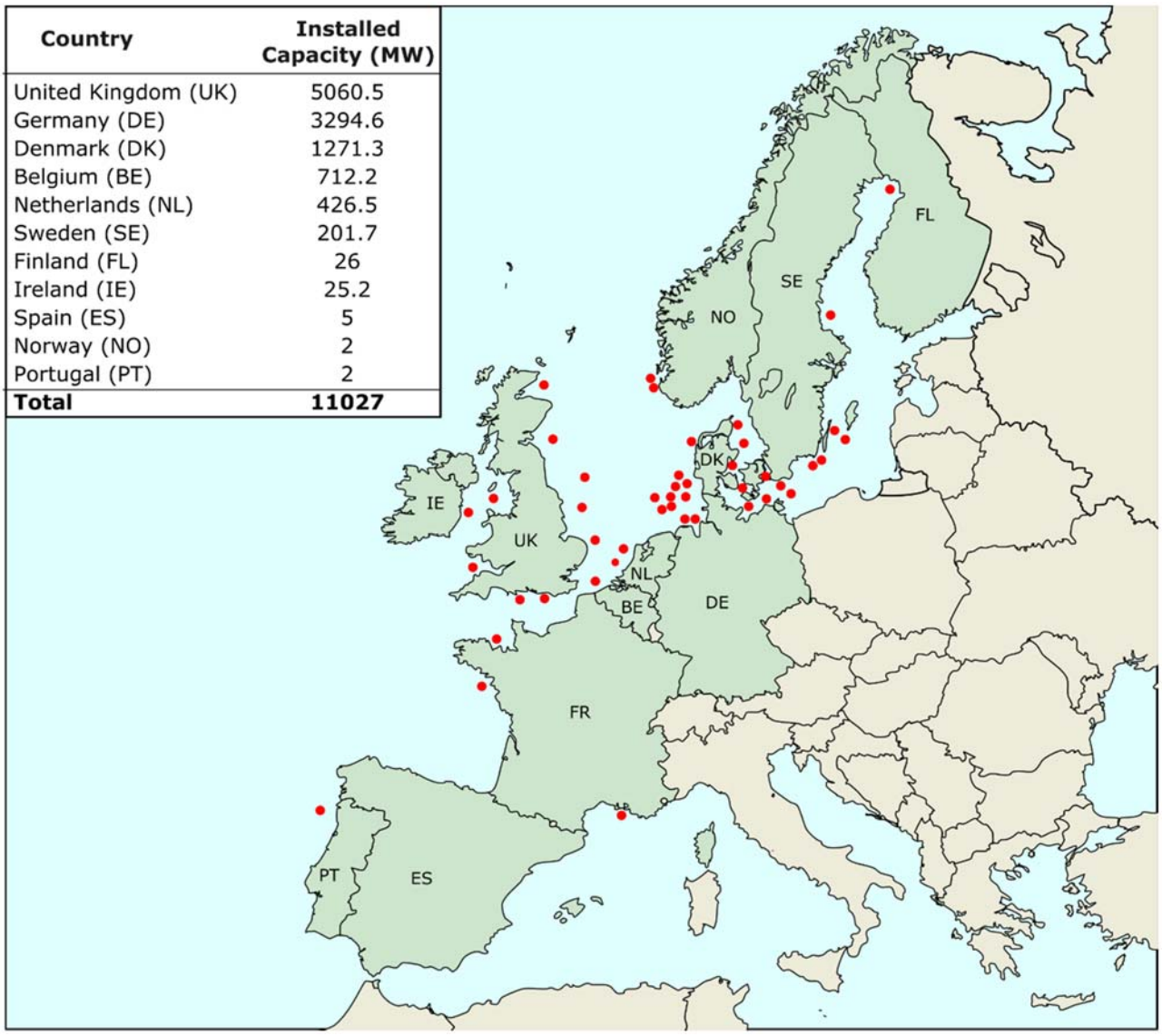

FIGURE 10.5 Wind farms in Europe.

The location of Burbo wind farm is influenced by the following:

1. Average wind speed more than 7 m/s
2. Shallow water depth is 0.5 m to 8 m at Low tide
3. Good seabed condition for the construction of the foundation
4. Close to entrance of Mersey river
5. Proximity to Liverpool port
6. 6.4 km from Sefton coastline
7. Safe distance from navigation channel
8. Onshore export cable traveled 3.5 km underground to a substation to be fed into the grid

The following consents were taken for Burbo:

1. Consents are Section 36 of Electricity Act 1989 for wind turbine and cabling
2. Consent under Section 34 of Coastal Protection Act 1949 for Construction in navigable waters
3. Permission from Port Authority

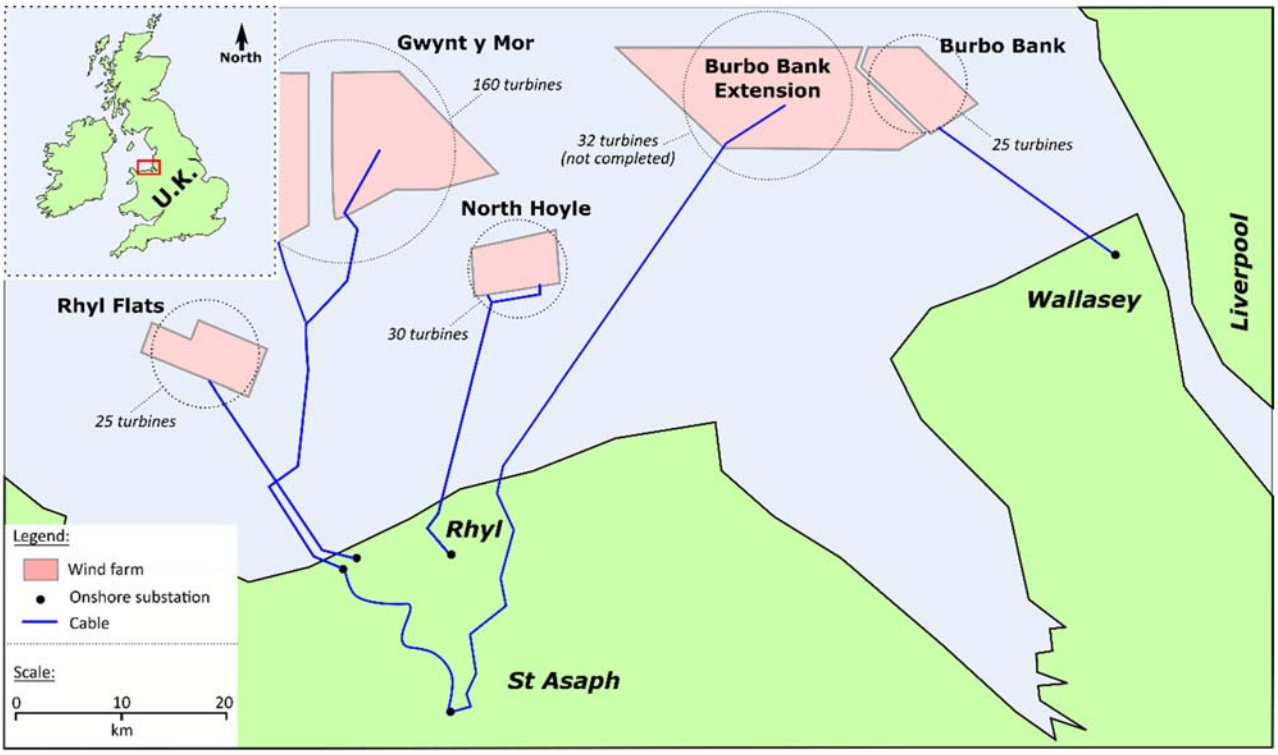

FIGURE 10.6 Location of the Burbo wind farm.

4. Permission under Section 57 of the Town and Country Planning Act 1990 for onshore cabling, interconnection facilities, and substation
5. License under Section 10.5 of Food and Environment Protection Act 1985 for the siting of Wind Turbines and deposit of scour protection material

10.3.2 ASIDE on the economics

Currently, many wind farms are operating from the subsidy provided by the government. For example, in the United Kingdom, there are schemes such as cfD (Contract for Difference) are in use. However, in order to be sustainable, large wind farms are to be constructed and built to achieve the economy of scales to produce electricity at the lowest possible cost. Therefore, the cost of electricity from different sources is compared using LCOE or SCOE (Society's Cost of Energy). As many of the installation, operation, and maintenance (O&M) will be carried out in rougher waters, time in construction is also a driving factor for site selection. Therefore, every cost that increases part of the construction has to be lowered in such a manner that an optimal method for the construction and installation will be established.

10.4 General arrangement of a wind farm

Fig. 10.7 shows the components of a typical Wind Farm. The turbines in a wind farm are connected by interturbine cables (electrical collection system) and are connected to the offshore substation. There are export cables from offshore to onshore. Figs. 10.8 and 10.9 shows photographs of some of the components. Fig. 10.8A shows the photograph of a wind farm with many wind turbines and a substation. Fig. 10.8B shows the details of the substructure of a monopile with J tubes for the electrical collection system. Fig. 10.9 shows the photograph of a jacket-supported substation.

10.5 Choice of foundations for a site

The choice of foundation will depend on the following: site conditions (wind, wave, current, seabed condition, ground profile, water depth, etc), available fabrication and installation expertise, operation and maintenance, decommissioning laws of the land, and finally economics. The definition of an ideal foundation is as follows:

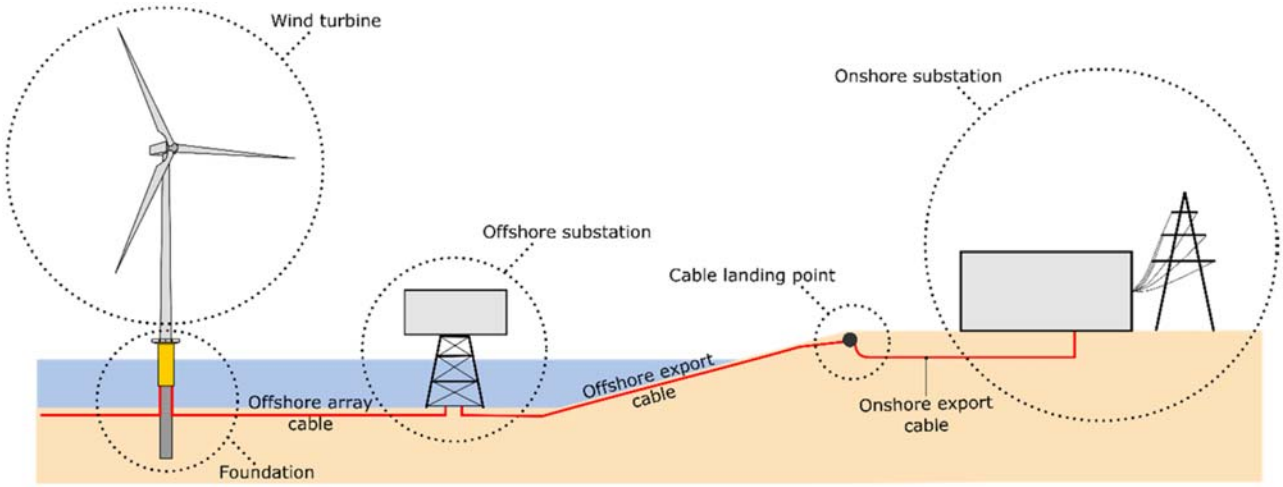

FIGURE 10.7 Overview of a wind farm.

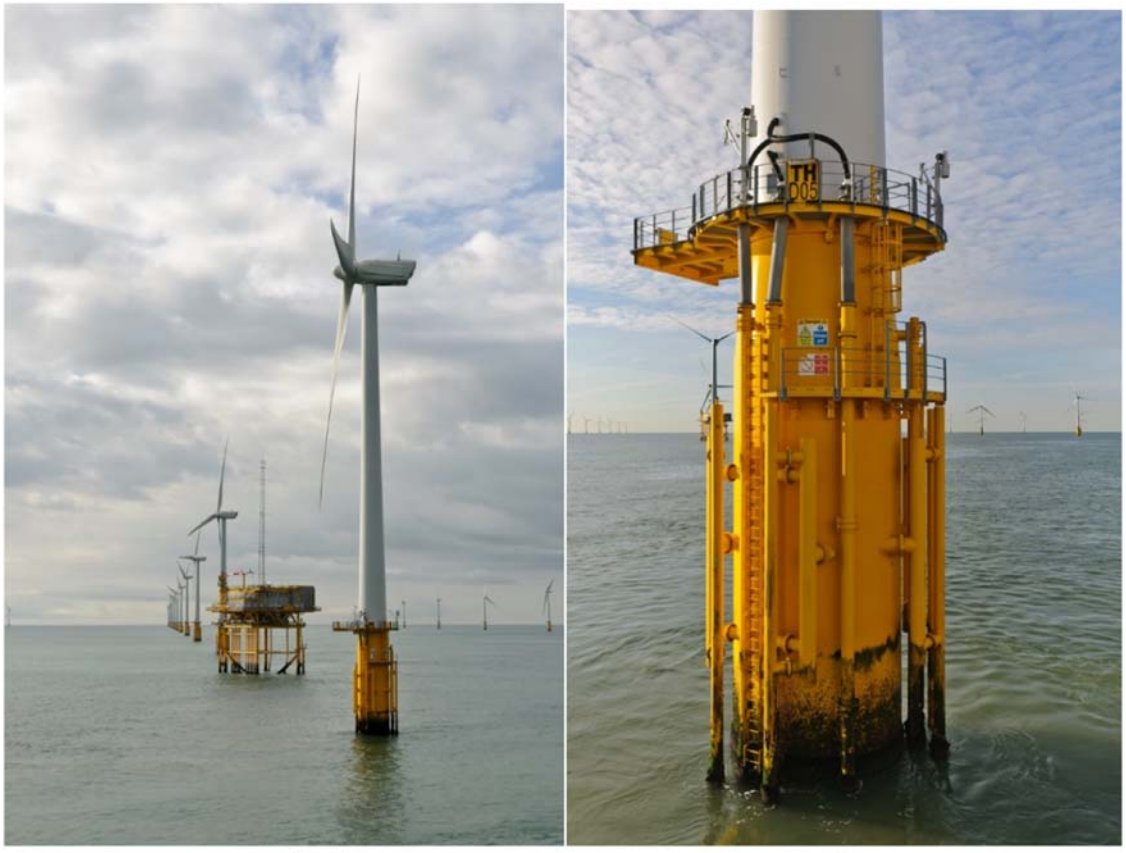

FIGURE 10.8 (A) Wind farm with offshore substation; (B) Turbine J tubes for interturbine cables and electrical collection system.

1. A foundation which is capacity or "*rated power*" specific (i.e., 5 MW or 8 MW rated power) specific but not turbine manufacturer specific. In other words, a foundation is designed to support 5 MW turbine but can support turbines of any make. There are other advantages in the sense that turbines can be easily replaced even if a particular manufacturer stops manufacturing them.

FIGURE 10.9 Offshore substation.

2. Installation of a foundation is not weather sensitive, that is, not dependent on having a calm sea or a particular wind condition. The installation of the first offshore wind farm in the United States took more time due to the unavailability of a suitable weather window.
3. Low maintenance and operational costs, that is, need the least amount of inspection. For example, a jacket-type foundation needs inspection at the weld joints.

It is economical to have a large number of turbines in a wind farm to have the economy of scale and therefore it also requires a large area. If the continental shelf is very steep, grounded (fixed) turbines are not economically viable and a floating system is desirable.

10.6 Foundation types

Foundations constitute the most important design consideration and often determine the financial viability of a project. Typically foundations cost 25% to 34% of the whole project and there are attempts to get the costs down. Many aspects must be considered while choosing and designing the foundation for a particular site. They include ease of installation under most weather conditions, varying seabed conditions, aspects of installation including vessels and equipment required, and local regulations concerning the environment (noise). Fig. 10.10 shows a schematic diagram of a wind turbine supported on a large diameter column inserted deep into the ground (known as monopile). This is the most used foundation so far in the offshore wind industry due to its simplicity.

Fig. 10.11 shows the various types of foundations commonly used today for different depths of water. Monopile (Fig. 10.11C), gravity-based foundations (Fig. 10.11B), and suction caissons (Fig. 10.11A) are currently being used or considered for water depths of about 30 m. For water depth between 30 and 60 m, jackets or seabed frame structures supported on piles or caissons are either used or planned. A floating system is being considered for deeper waters, typically more than 60 m. However, the selection of foundations depends on seabed, site conditions, turbine and loading characteristics, and economics but not always on the water depth.

The substructure can be classified into two types:

1. Grounded system or fixed structure where the structure is anchored to the seabed. Grounded system can be further subdivided into two types in the terminology of conventional foundation/geotechnical engineering: shallow foundation (gravity base solution and suction caisson) and deep foundation.
2. Floating system where the system is allowed to float is anchored to the seabed by a mooring system. Floating systems have a certain ecological advantage in the sense that the foundations leave a very low seabed footprint, easy to decommission and maintain as the system can be de-anchored and floated out to a harbor.

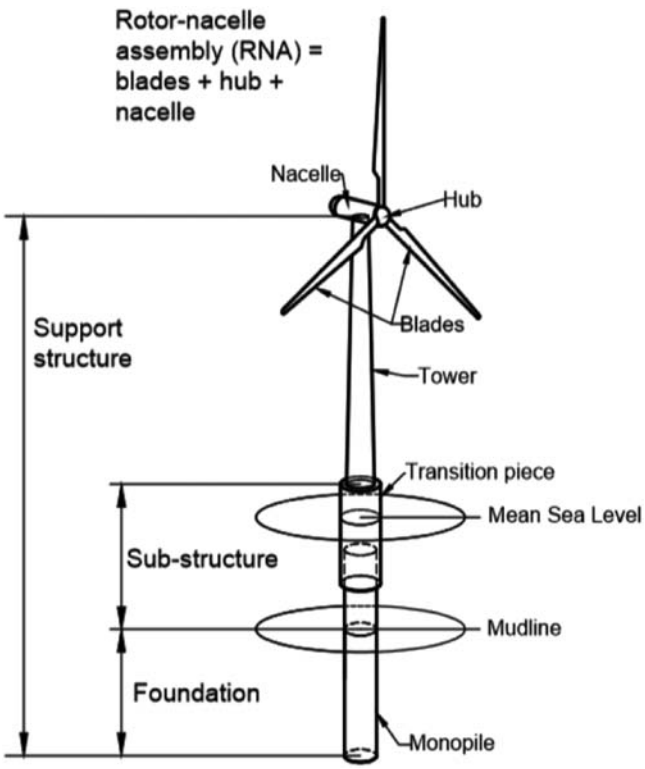

FIGURE 10.10 Monopile foundation.

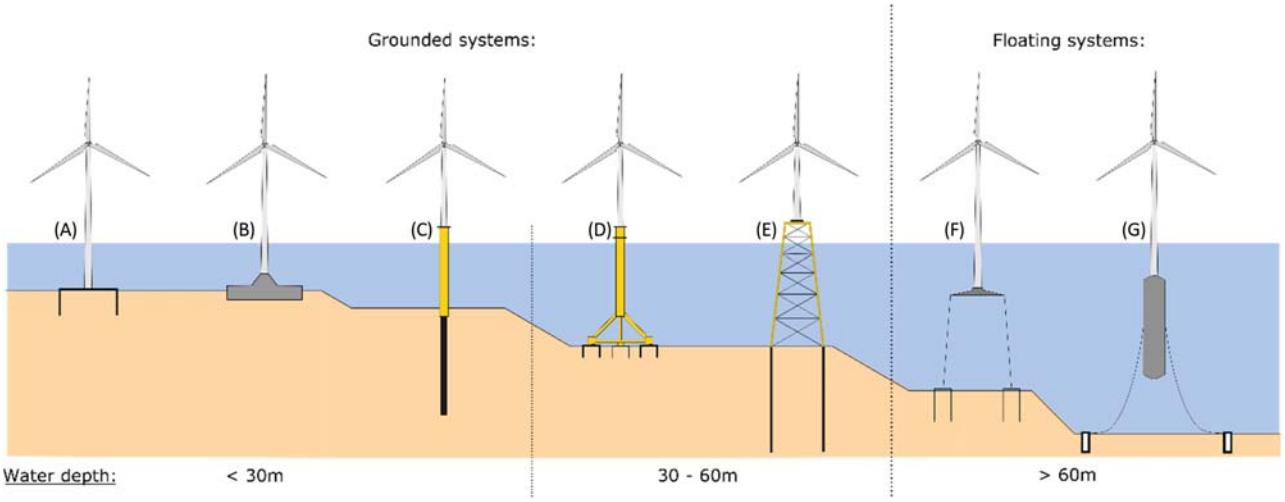

FIGURE 10.11 (A) Bucket/suction caisson; (B) gravity based, (C) monopile, (D) tripod on bucket/suction caisson; (E) jacket/lattice structure; (F) tension leg platform; (G) spar buoy floating concept.

10.7 Gravity-based foundation system

The gravity foundation is designed to avoid uplift or overturning, that is, no tensile load between the support structure and the seabed. This is achieved by providing adequate dead load to provide stability to the structure under the action of overturning moments. If the dead loads from the support structure and the superstructure (tower + RNA) are not sufficient, additional ballast will be necessary. The ballast consists of rock, iron ore, or concrete. Installation of these foundations often requires seabed preparation to avoid inclination. The gravity-based structures in most cases are constructed in-situ concrete or with precast concrete units. The gravity-based concept can be classified into two types depending on the method of transportation and installation:

1. Crane-free solution also known as "*float-out and sink*" solution: These types of foundations will be floated (either self-buoyant or with some mechanism) and towed to the offshore site. At the site, the foundation will be filled with ballast causing it to sink to the seabed. This can be attractive solution for sites having very hard or rocky soil conditions. This operation does not require a crane and is thus known as a "crane-free" solution.
2. Crane-assisted solution: In this type, the foundation does have the capacity to float and is therefore towed to the site onboard a vessel. They are then lowered to the seabed using cranes. An example is the Thornton Bank, shown in Fig. 10.12 where the shape of the gravity-based substructure is compared to a champagne bottle.

10.8 Suction buckets or caissons

Suction buckets (sometimes referred to as suction caissons) are similar in appearance to gravity-based foundations but with long skirts around the perimeter. Essentially, they are a hybrid foundation taking design aspects from both shallow and pile foundation arrangements. A caisson consists of a ridged circular lid with a thin tubular skirt of the finite length extending below, giving it the appearance of a bucket. Typically, such foundations will have a diameter-to-length ratio (D/Z) of around 1 making them significantly shorter than a pile but deeper than a shallow foundation. A sketch of a suction caisson with the terminology can be seen in Fig. 10.13. Suction caissons themselves are a fairly recent development in the offshore industry. Caissons first came into use around 30 years ago as a foundation structure for offshore oil and gas production platforms.

10.9 Pile foundations

Single large diameter steel tubular pile also known as monopile is the most common form of foundation for supporting offshore wind turbines. Fig. 10.14 shows the monopile type of foundation which is essentially a large steel pile (3−7 m in diameter) driven into the seabed with a typical penetration depth of 25−40 m. A steel tube, commonly called the transition piece (TP), is connected to the steel pile and the tower is attached to it. The TP supports the boat landings and ladders used for entering the turbine. Currently, this type of foundation is extensively used for water depths up to 25−30 m.

These foundations can be reliability driven into the seabed using a steam or hydraulically driven hammer and the practice is very standardized due to the offshore oil and gas industry. The handling and driving of these foundations require the use of either floating vessels or jackup vessels which must be equipped with large cranes, a suite of hammers, and drilling equipment. If the ground profile at the site contains stiff clay or rock, the drive-drill-drive procedure

FIGURE 10.12 GBS from Thornton Bank Project.

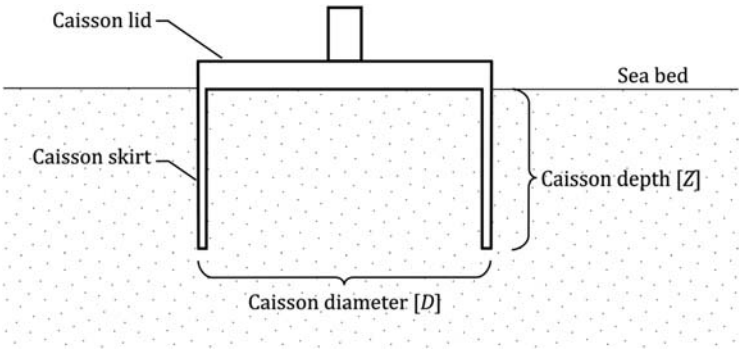

FIGURE 10.13 Typical layout of a suction caisson foundation.

FIGURE 10.14 Large diameter monopile.

may need to be adopted. Pile driving results in noise and vibrations. Therefore, the installation of the turbine (Nacelle and Rotor) is always carried out after the piling has been completed.

10.10 Seabed frame or jacket supporting supported on pile or caissons

Often a seabed frame or a jacket supported on piles or caissons can act as a support structure and they can be classified as Multipods, see Fig. 10.15. Multipods have more than one point of contact between the foundation and the soil. Soil-embedded elements may include flexible piles, gravity bases, and suction caissons which can also be used. Fig. 10.16 shows an example from a wind farm in China. Further details on the foundations used in China can be found in Chapter 13.

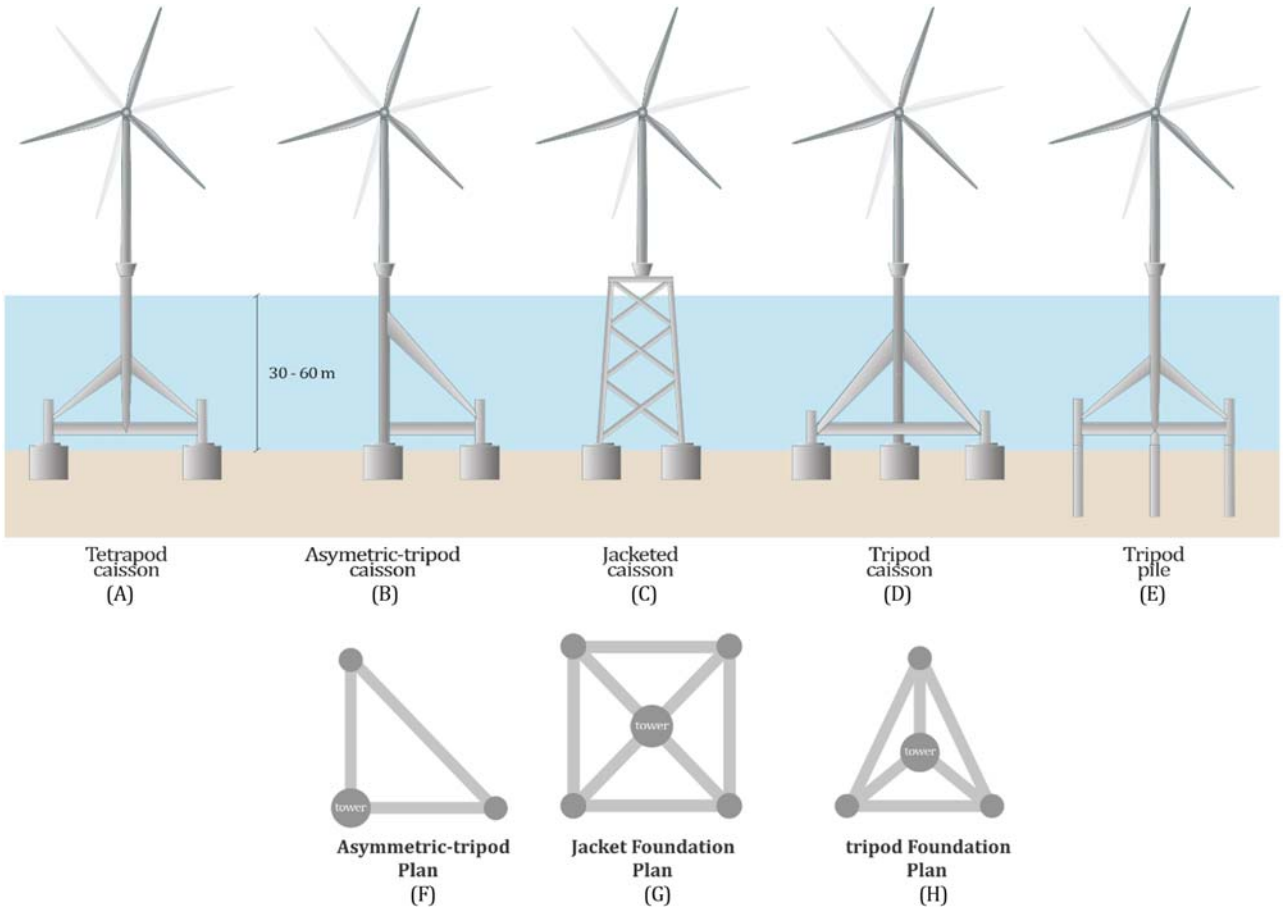

FIGURE 10.15 Multipod foundations.

FIGURE 10.16 Different types of support structures for a wind farm in China.

10.11 Floating turbine system

The floating system can be classified into three main types, see Fig. 10.17A:

1. Mooring stabilized TLP (Tension Leg Platform) concept: This type of system is stabilized with tensioned mooring and is anchored to the seabed for buoyancy and stability.
2. Ballast stabilized *Spar buoy* concept with or without motion control stabilizer: This type of system will have a relatively deep cylindrical base providing the ballast whereby the lower part of the structure is much heavier than the upper part. This would raise the center of buoyancy about the center of gravity of the system. While these are simple structures having a low capex cost, it needs a deeper draft, that is, deeper water, and is not feasible in shallow water. A motion stabilizer can be used to reduce the overall tilt of the system
3. Buoyancy stabilized semisubmersible: This concept is a combination of ballasting and tensioning principle and consumes a large amount of steel, see Fig. 10.17B.

There are varieties of anchors that can be used to moor the floating system and they can be classified into surface anchors and embedded anchors. An example of surface anchors is a large heavy box containing rocks or iron ore and the holding capacity depends on the weight of the anchor itself and the friction between the base of the anchor and the seabed. On the other hand, examples of embedded anchors include anchor piles, (see Fig. 10.17C; Fig. 10.17B and C) which are floating wind turbine concepts suitable for deeper waters. Fig. 10.17A shows the floating concept (semisub) implemented in a wind farm in Japan (offshore Fukushima) and Fig. 10.17C shows the Hywind concept (spar).

10.12 Site layout, spacing of turbines, and geology of the site

Wind turbines in a wind farm are spaced to maximize the amount of energy that can be generated without substantially increasing the CAPEX (Capital expenditure, that is, upfront cost). If the farm is significantly spread out, that is, large

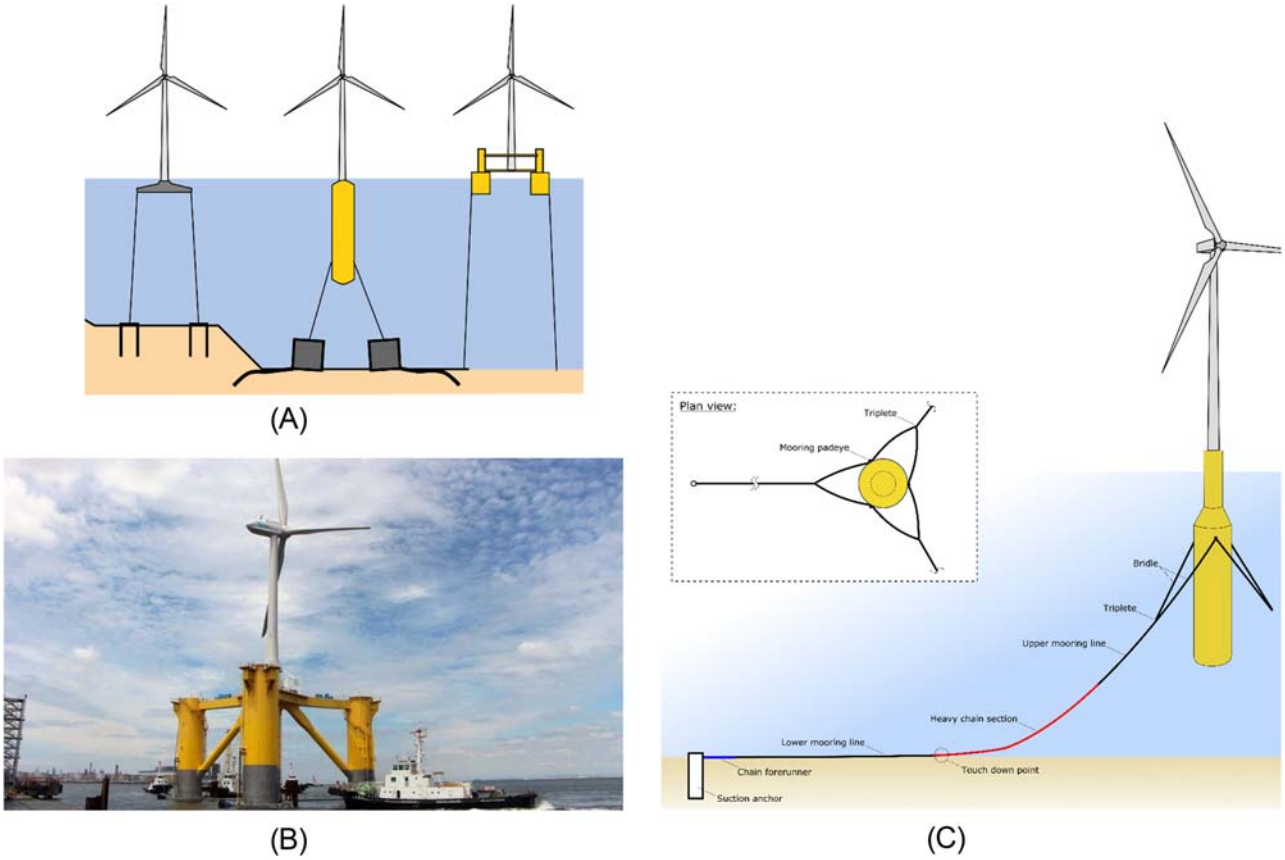

FIGURE 10.17 (A) Three main types of floating systems to support WTG (Wind Turbine Generator). (B) Semisubmersible foundation for Offshore Fukushima (Japan). (C) Details of Hywind Wind Turbine Installation which is Spar buoy—Floating system.

FIGURE 10.18 Wake turbulence. *Photo credit Vattenfall Wind Power, Denmark.*

spacing of the turbines, the interarray cable length will increase. The spacing is therefore an optimization problem between the compactness of the wind farm (which minimizes the CAPEX cost due to subsea cables) and the adequate separations between turbines so as to minimize the energy loss due to wind shadowing from upstream turbines. Fig. 10.18 shows the aerial photo of wake turbulence behind individual wind turbines that can be seen in the fog of the Horns Rev wind farm off the Western coast of Denmark (Photo credit Vattenfall Wind Power, Denmark).

The geometric layout of a wind farm can be a single line of array, or a square, or a rectangular configuration. Due to advanced methods for optimization having different constraints as well as site conditions, a different layout pattern is increasingly being used. Typically, the spacing between turbines is equivalent to 3−10 times the rotor diameter and it depends on the prevailing wind direction. The spacing should be larger than 3−4 rotor diameter perpendicular to the prevailing wind direction and 8−10 diameters for direction parallel to the wind direction. For example, for a prevailing South Westerly wind direction (which is typical of Northern Ireland), a possible site layout for a wind farm located in the area is shown in Fig. 10.19. The spacing along the wind direction is kept at 6 times the rotor diameter (6D) but across the wind, the spacing can be kept a bit lower (4D).

Due to the large spacing of the turbines (typically 800−1200 m apart), a small to medium size wind farm would extend over a substantial area. The typical size for a modern-day wind farm is 20 km × 6.5 km (for example, Sandbank wind farm of the German North Sea). Due to the large coverage of the area for a wind farm, there may be significant variation in the geological and subsurface conditions as well as practical restraints. Examples include a sudden drop in the sea floor causing a change in water depth, paleochannels, change in ground stratification, submarine slopes, presence of foreign objects such as shipwrecks, location of important utility lines (gas pipeline, fiber optic cables), etc. A detailed site investigation program consisting of geotechnical and geophysical tests is carried out to establish a 3D geological model which often dictates the layout.

10.12.1 Case study: Westermost Rough

Fig. 10.20 shows the ground profile from Westermost Rough Offshore Wind Farm (located in the United Kingdom) approximately 8 km off the Yorkshire coast, near the town of Withernsea following Kalleheve et al. [9]. It may be observed that the monopile passes through different geologies denoted in the figure. Therefore, the foundation consists of monopiles of varying length, wall thickness, and diameter. This also shows that not only geotechnical but also geological study needs to be carried out.

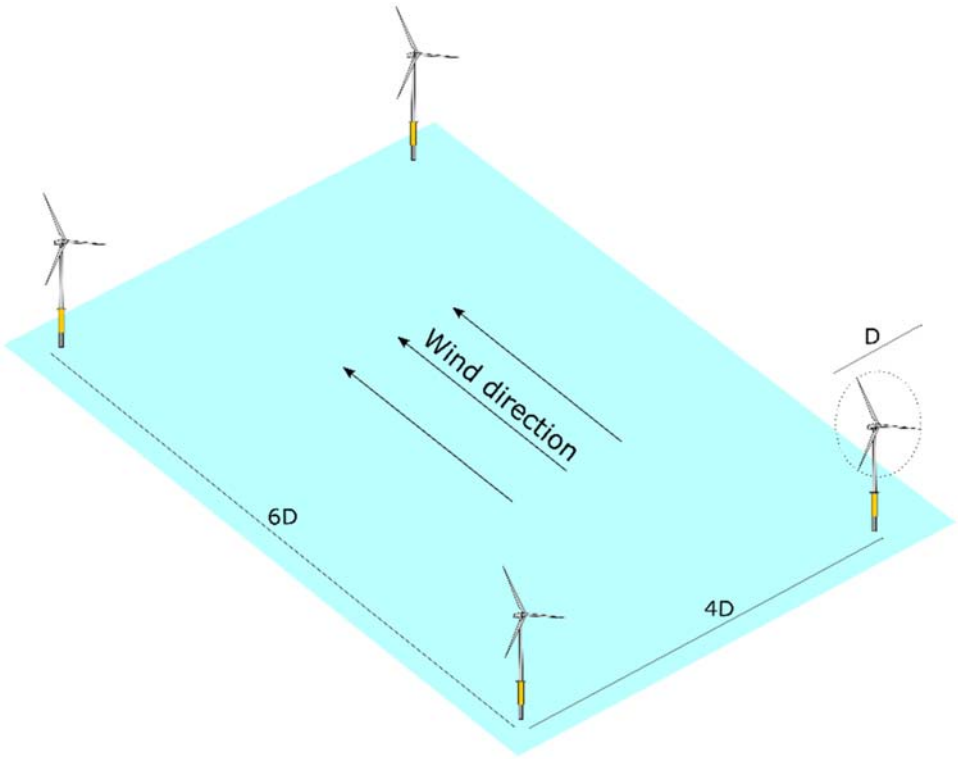

FIGURE 10.19 Spacing of turbines.

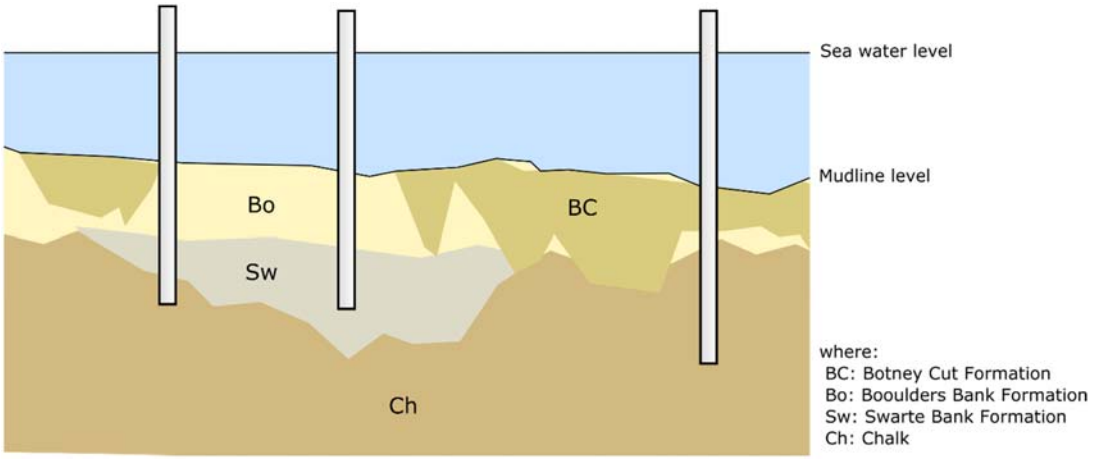

FIGURE 10.20 Monopile foundation in Westermost Rough. *Adapted from Kallehave D, Byrne BW, LeBlanc Thilsted C, Mikkelsen KK. Optimization of monopiles for offshore wind turbines. Phil Trans R Soc 2015; A373:2035. https://doi.org/10.1098/rsta.2014.0100.*

10.13 Economy of scales for foundation

Monopiles are currently preferred for water depths of upto 30 m. The simple geometry makes it possible to automate the manufacturing and fabrication process and the typical manufacturing cost related to monopile steel is two euros per kilogram. Welding can be carried out by robots and installation is relatively simple. However, if the diameter becomes large (knowns as XL or XXL piles which are over 8 m in diameter and weigh 1200 tons), the transportation and installation become challenging and limit the number of installation contractors that can carry out the work. Innovations are underway to install large diameter piles using a Vibro method where a foundation is installed through the vibration of the soil and thus effectively liquefying the soil around it.

An alternative to large-diameter monopiles is the 3 or 4-legged jacket on small diameter piles. Steel for jackets costs around five euros per kilogram to manufacture which is more than double that of monopiles due to many tubular joints which are often welded manually.

Gravity-based foundations are cheaper to manufacture as compared to steel but require a large fabrication yard and storing area. As concrete foundations will be much heavier than an equivalent steel foundation, large crane and vessels are required for installation. For an offshore site where the surface ground is rock, a gravity-based structure will be a preferred choice; this is the situation in French waters.

Due to the vast size of a wind farm, there will be varying seabed conditions including water depth and distance from the shore. As a result, the loads on the foundations will change and ideally, the best design will be to design each foundation individually which will give rise to a customized foundation design for each turbine location. However, from an economic point of view, it is desirable to have a few foundation types so that the overall economy is achieved and the process of fabrication and installation can be carried out efficiently using the same installation vessel. Most North European developers prefer one type of foundation (either monopiles or jackets) on a site. This consideration often dictates the layout of the farm to avoid deeper water or soft locally available mud.

References

[1] Bhattacharya S, Goda K. Use of offshore wind farms to increase seismic resilience of Nuclear Power Plants. Soil Dyn Earthq Eng 2016;80:65−8. Available from: https://doi.org/10.1016/j.soildyn.2015.10.001.

[2] Adhikari S, Bhattacharya S. Dynamic analysis of wind turbine towers on flexible foundations. Shock Vib 2012;19:37−56.

[3] Adhikari S, Bhattacharya S. Vibrations of wind-turbines considering soil-structure interaction. Wind Struct—An Int J 2012;14:85−122.

[4] Bhattacharya S, Adhikari S. Experimental validation of soil−structure interaction of offshore wind turbines. Soil Dyn Earthq Eng 2012;31 (5−6):805−16.

[5] Bhattacharya S, Lombardi D, Muir Wood DM. Similitude relationships for physical modelling of monopile- supported offshore wind turbines. Int J Phys Model Geotech 2012;12(2):58−68.

[6] Bhattacharya S, Cox J, Lombardi D, Muir Wood D. Dynamics of offshore wind turbines supported on two foundations. Proc ICE Geotech Eng. 2013;166(2):159−69.

[7] Bhattacharya S, Nikitas N, Garnsey J, Alexander NA, Cox J, Lombardi D, et al. Observed dynamic soil−structure interaction in scale testing of offshore wind turbine foundations. Soil Dyn Earthq Eng 2013;54:47−60 2013.

[8] Lombardi D, Bhattacharya S, Muir Wood D. Dynamic soil-structure interaction of monopile supported wind turbines in cohesive soil. Soil Dyn Earthq Eng 2013;49:165−80.

[9] Kallehave D, Byrne BW, LeBlanc Thilsted C, Mikkelsen KK. Optimization of monopiles for offshore wind turbines. Phil Trans R Soc 2015;A 373:2035. Available from: http://doi.org/10.1098/rsta.2014.0100.

Chapter 11

Aerodynamics and the design of horizontal axis wind turbine

Martin Otto Lavér Hansen
DTU Wind and Energy Systems, Technical University of Denmark, Lyngby, Denmark

11.1 Introduction

A wind turbine is a device that transforms the kinetic energy in the wind into electricity, and the overall object is to make a machine that will survive all the expected loads (ultimate and fatigue) in the design lifetime of typically 20 years and to produce electrical energy as cheap as possible, more formally to minimize the Levelized Cost of Energy (LCoE) [$/kWh]. To do this, one must know something about the environmental input to the wind turbine in the form of wind speed distribution, atmospheric turbulence, and for an offshore wind turbine also a description of the sea state. Standards/norms, such as IEC 61400-3, have been made that compile all the load cases that must be considered to have a safe design.

The various environmental inputs and load cases must be transformed into forces including aerodynamic loads to verify the structural integrity of the wind turbine. Being able to compute accurately, the aerodynamic loads is also needed when calculating the power production for a given wind speed and is thus an important element in the optimization process minimizing the LCoE. The objective of this chapter is to describe the aerodynamics of a wind turbine both qualitatively and quantitatively to have some tools for designing an aerodynamically efficient rotor. To fully follow all the derivations, requires basic knowledge in fluid mechanics, but only at a fundamental level since exclusively very basic conservation laws from classic physics are applied.

To understand the power contained in the wind, one can consider an area normal to the wind velocity, as shown in Fig. 11.1. After a time Δt, the volume of air particles that have passed this area is $A \cdot V_o \cdot \Delta t$, weighing $\Delta m = \rho \cdot A \cdot V_o \cdot \Delta t$ and having a kinetic energy of $E_{kin} = \frac{1}{2}\Delta m V_o^2 = \frac{1}{2}\rho V_o^3 A \Delta t$ and thus the available power (energy per time) in the wind is $P_{avail} = \frac{1}{2}\rho V_o^3 A$. The available power is thus proportional to the density of the air, the rotor area and very importantly the wind speed cubed, and it is the purpose of any wind turbine to transform, as cheaply as possible, some of this into useful power.

11.2 A short description on how a wind turbine works

To comprehend the equations used to compute the aerodynamic loads on a wind turbine rotor, it is very useful first to learn how a wind turbine basically works. It is clear that a device is needed that will slow down the wind speed to extract kinetic energy from the air and at the same time, a torque must be created that eventually can drive an electrical generator. Both can be accomplished by a few spinning blades having cross sections shaped as conventional airfoils, as shown in Fig. 11.2.

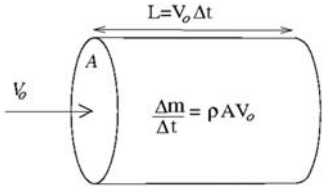

FIGURE 11.1 Air flow passing the area, *A*.

Wind Energy Engineering. DOI: https://doi.org/10.1016/B978-0-323-99353-1.00019-0

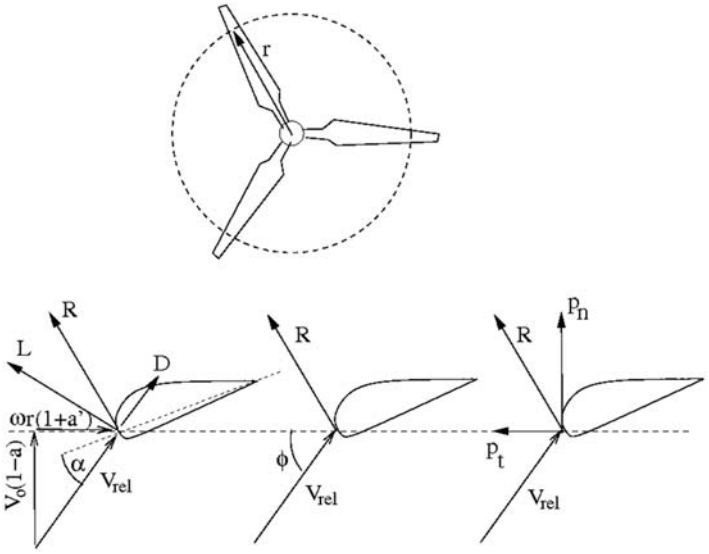

FIGURE 11.2 Local flow at the rotor blades at radial position r.

The upper part of Fig. 11.2 shows the rotor from the front and the lower part displays the unfolded cut in the rotor plane at the radial position, r, indicated by the dashed line and can be seen directly from above. The first thing to note in the lower part of Fig. 11.2 is that the wind speed approaching the rotor has been reduced by a factor $a \cdot V_o$, so that the apparent wind at the rotor plane is $(1 - a)V_o$. The in plane velocity is mainly the rotational speed of the blade at the radial distance r from the rotor axis, ωr, but also a small extra contribution, $a'\ \omega r$, is present, so that the effective tangential velocity experienced by the rotor is $(1 + a')\omega r$. The two nondimensionalized velocities, a, and, a', are called the axial- and the tangential induction factors, respectively, and if they were known, the relative wind, V_{rel}, approaching the rotor plane can be drawn in the so-called velocity triangle, see the lower left sketch in Fig. 11.2. By definition, the lift is perpendicular and the drag is parallel to the relative velocity as also sketched in Fig. 11.2. The net aerodynamic loading is the vector sum of the lift and drag and denoted, R, in the Figure and is the integral of the pressure and skin friction distribution on the airfoil at this radial position. It is seen that this resulting aerodynamic load vector has a component into the wind, p_n, and an in-plane component, p_t. The in-plane component, p_t, delivers the required torque to the shaft and the normal loading provides a contribution to the necessary thrust force that is reducing the wind speed to extract power from the wind. It is also, p_n, and, p_t, that are responsible for the induced wind speeds $a \cdot V_o$ and $a'\ \omega r$, since these are the reactions on the wind velocity from the blade loadings. Now after having described how a wind turbine works, the equations necessary to compute the aerodynamic loads are derived in the following sections.

11.3 1-D momentum equations

The 1-D momentum theory goes back more than 100 years and was developed by Froude and Rankine and is therefore often called the Rankine−Froude theory. The theory was originally developed for marine propulsion but will be shown here for a wind turbine rotor. The rotor is modeled as a permeable disk with a normal load equally distributed over the rotor plane giving rise to a constant velocity profile in the wake. The integral of the normal loading can be integrated into one thrust force, T, as shown in Fig. 11.3. Only the flow confined by the streamlines touching the rotor tip is affected by the thrust force and the free wind speed upstream is gradually reduced to a lower value in the wake, as sketched in Fig. 11.3.

It is seen in Fig. 11.3 that the velocity due to the thrust force, T, is decreasing with the downstream distance and since the massflow is the same at any downstream plane the streamlines have to expand. The undisturbed wind speed is denoted by V_o, the reduced velocity in the rotor plane is u and the velocity in the wake is u_1. According to the previous section, the velocity in the rotor plane u may also be written as $u = (1 - a)V_o$. Since there is no flow across the lateral streamlines touching the rotor tip the conservation of energy assuming no loss for the control volume confined by these is easily determined as:

$$P = \tfrac{1}{2}\dot{m}(V_o^2 - u_1^2) = \tfrac{1}{2}\rho u A(V_o^2 - u_1^2) \tag{11.1}$$

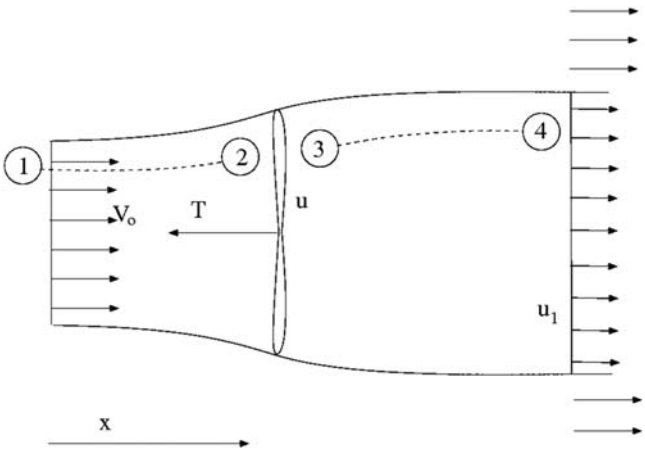

FIGURE 11.3 A simple wind turbine rotor model made as a permeable disk with constant loading giving basically a 1-D flow.

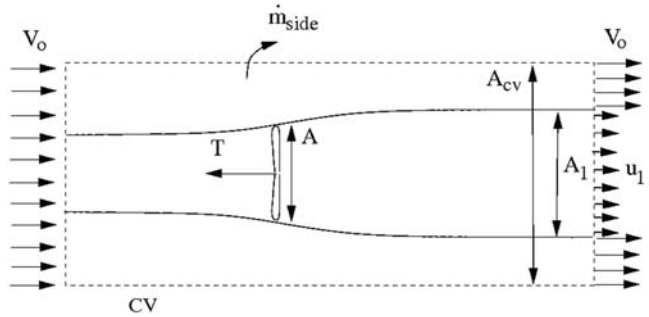

FIGURE 11.4 The dashed line indicates a cylindrical control volume enclosing the flow through the ideal wind turbine rotor and is used for evaluating the relationship between the flow and thrust force.

where ρ is the density of the air, A is the rotor area, and P is the power extracted from the wind. In deriving Eq. (11.1), it is assumed that the pressure at the outlet has recovered to the ambient pressure, since the streamlines are now parallel again and also that none of the mechanical energy is dissipated into heat. Further, one may apply the Bernoulli equation along the streamline from 1 to 2 and again from 3 to 4, as indicated in Fig. 11.3.

$$\begin{aligned} p_o + \frac{1}{2}\rho V_o^2 &= p^+ + \frac{1}{2}\rho u^2 \\ p^- + \frac{1}{2}\rho u^2 &= p_o + \frac{1}{2}\rho u_1^2 \end{aligned} \tag{11.2}$$

where p_o denotes the ambient pressure, p^+ denotes the pressure just upstream of the rotor, and p^- denotes the pressure just behind the rotor. These equations may be combined to form the following equation:

$$\Delta p = p^+ - p^- = \tfrac{1}{2}\rho(V_o^2 - u_1^2) = \tfrac{1}{2}\rho(V_o + u_1)(V_o - u_1) \tag{11.3}$$

where Δp is the pressure drop over the rotor disk. Next, a cylindrical control volume totally enclosing the flow through the rotor is considered as drawn by the dashed line in Fig. 11.4. Since the lateral boundary of this control volume is horizontal, the pressure around the control volume can only contribute to an axial force at the in- and outlet planes, and here the pressure is assumed as the ambient value. Therefore, the net pressure force is zero and the only remaining force in the flow direction is the unknown thrust force, T. The lateral boundaries are no longer streamlined so there is a mass flow crossing the lateral boundaries of the control volume and that is carrying axial momentum. The conservation of axial momentum thus becomes:

$$-T = \rho A_1 u_1^2 + \rho(A_{cv} - A_1)V_0^2 + \dot{m}_{side}V_0 - \rho A_{cv}V_0^2 \tag{11.4}$$

And combining this with the conservation of mass, we get:

$$\dot{m}_{side} = \rho A_{cv}V_0 - \rho A_1 u_1 - \rho(A_{cv} - A_1)V_0 = \rho A_1(V_0 - u_1) \tag{11.5}$$

Yields

$$T = \rho A u(V_o - u_1) \tag{11.6}$$

Now since the thrust can also be expressed as the pressure drop over the rotor disk times the area, the combination of (11.3) and (11.6) gives us the following:

$$u = \tfrac{1}{2}(V_o + u_1) \tag{11.7}$$

Since by definition $u = (1-a)V_o$ Eq. (11.7) gives that the velocity in the wake becomes $u_1 = (1-2a)V_o$ and if this is introduced into Eq. (11.1), the power can written as:

$$P = 2\rho a(1-a)^2 V_o^3 A \tag{11.8}$$

The power is often nondimensionalized with the available power in the wind into the so-called power coefficient, which is shown as:

$$C_p = \frac{P}{\frac{1}{2}\rho V_o^3 A} \tag{11.9}$$

And introducing Eq. (11.8) into (11.9) a simple expression is derived for an ideal power coefficient assuming 1-D flow and no losses, that is:

$$C_p = 4a(1-a)^2 \tag{11.10}$$

It is seen that the maximum value of Eq. (11.10) is $C_p = 16/27 \approx 60\%$ and occurs for a = 1/3. This is known as the Betz limit and is an upper theoretical value for the power coefficient of a wind turbine.

Also, a thrust coefficient is defined as:

$$C_T = \frac{T}{\frac{1}{2}\rho V_o^2 A} \tag{11.11}$$

And it can be shown that using the definition of the axial induction factor and Eqs. (11.6) and (11.7) that the thrust coefficient for an ideal rotor becomes

$$C_T = 4a(1-a) \tag{11.12}$$

The value of the thrust coefficient giving the theoretical maximum power coefficient is thus $C_T = 8/9$.

Even though a real rotor is not ideal and cannot be modeled simply as a permeable disk leading to Eqs. (11.10) and (11.12), they still tell us something about what can maximally be achieved and that this happens for a thrust force giving an axial induction factor of approximately $a = 1/3$. Measurements verify that Eq. (11.12) is valid up to approximately $a = 1/3$ and for higher values of the axial induction factor an empirical correlation called the Glauert correction is used, and one often used expression is shown as follows:

$$C_T(a) = \begin{cases} 4a(1-a) & \text{for } a < 0.3 \\ 4a(1-\frac{1}{4}(5-3a)a & \text{for } a \geq 0.3 \end{cases} \tag{11.13}$$

11.4 Blade element momentum

The blade element momentum method as described by Glauert [1] is a generalization of the momentum theory coupled to the blade element theory often attributed to Drzewiecki. The blade element theory is that the flow past a given section is considered 2D and that the effective inflow velocity can be constructed as the vector sum of the incoming velocity and the rotational speed. However, when doing this one must also, as was shown by Glauert, include the induced velocities that are the reaction to the incoming flow from the aerodynamic blade loads. When doing this one can draw the so-called velocity triangle as shown in Fig. 11.5, where the induced velocity is included as **W**, the axial component is given as aV_o (consistent with the 1-D momentum theory), and the tangential component as $a'\omega r$. Provided that the induced velocity is known, one can calculate the size and direction of the relative velocity. Assuming locally a 2D flow past an airfoil and that the lift and drag coefficients are available as function of angle of

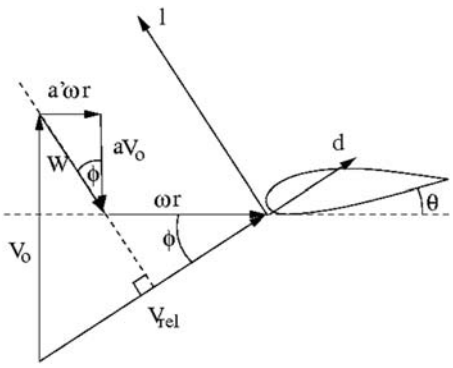

FIGURE 11.5 The velocity triangle used to compose the relative velocity approaching an element of the rotor at a radial distance, *r*, from the rotational axis.

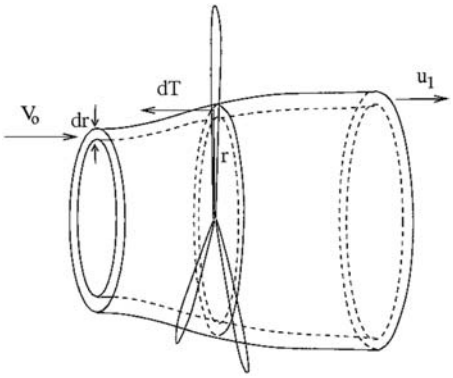

FIGURE 11.6 A streamtube of thickness, *Dr*, intersecting the radial position, *r*, on the rotorplane.

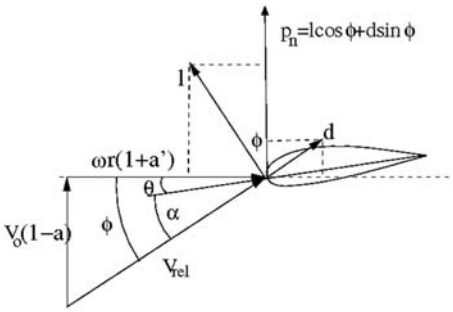

FIGURE 11.7 Velocities and aerodynamic loads at a blade element at a radial distance, *r*, from the rotational axis of rotation.

attack and Reynolds number, the lift and drag can be calculated, as shown later. The problem left is then to estimate the induced velocities that are in equilibrium with the aerodynamic loads, and this is exactly what the Blade Element Momentum theory (BEM), does.

In BEM, the loads and induced wind speeds are computed at a finite number of radial positions also denoted elements. Further, it is assumed that these elements are independent. A stream tube with thickness, dr, around each element is considered as shown in Fig. 11.6. The two lateral sides are assumed to be comprised of streamlines and the partly empirical Eq. (11.13) is presumed also to be valid for the streamtube in Fig. 11.6. Further, it is assumed that there are no azimuthal variations of the velocities at the outlet, u_1, and in the rotorplane, u, which is only true if the thrust is also azimuthally constant corresponding to an infinite number of blades. A correction to this, denoted Prandtl's tip loss correction, is introduced later. But for the moment the equations are derived as if the aerodynamic loads are distributed evenly at the area of the strip cutting the rotor plane $dA = 2\pi r dr$. The thrust from one blade can be estimated from the blade element at the same radial position, *r*, from Fig. 11.7.

Provided that the axial and tangential induction factors, a, and a', are known the angle of the incoming relative wind with the rotor plane, ϕ, called the flowangle, see Fig. 11.7, can be computed as:

$$\tan\varphi = \frac{(1-a)V_o}{(1+a')\omega r} \tag{11.14}$$

And the size of the relative wind speed is shown as:

$$V_{rel}^2 = (1-a)^2 V_o^2 + (1+a')^2(\omega r)^2 \tag{11.15}$$

Knowing the angle between the rotor plane and the airfoil chord, θ, the local angle of attack is given as follows:

$$\alpha = \phi - \theta \tag{11.16}$$

The lift and drag coefficients are then found by a table look-up, $C_l(\alpha, \mathrm{Re})$ and $C_d(\alpha, \mathrm{Re})$, for the airfoil applied at this radial position, and from these the lift and drag [N/m] can be computed as:

$$\begin{aligned} l &= \frac{1}{2}\rho V_{rel}^2 c C_l(\alpha, \mathrm{Re}) \\ d &= \frac{1}{2}\rho V_{rel}^2 c C_d(\alpha, \mathrm{Re}) \end{aligned} \tag{11.17}$$

Next, these aerodynamic loads are projected normal (see also Fig. 11.7) and tangential to the rotor plane as shown below:

$$\begin{aligned} p_n &= l\cos\phi + d\sin\phi \\ p_t &= l\sin\phi - d\cos\phi \end{aligned} \tag{11.18}$$

Finally, the thrust force at the streamtube in Fig. 11.6, can be calculated as:

$$dT = Bp_n dr, \tag{11.19}$$

since p_n multiplied by dr is the force from one blade and B is the number of blades. Eq. (11.19) is nondimensionalized as in the definition for the thrust coefficient Eq. (11.11), but using the strip area of the streamtube intersecting the rotor plane and using Eqs. (11.18) and (11.17) to determine the normal load and introduce the solidity, $\sigma = \mathrm{Bc}/2\pi r$

$$C_T = \frac{dT}{\frac{1}{2}\rho V_o^2 2\pi r dr} = \frac{\sigma(1-a)^2(C_l\cos\phi + C_d\sin\phi)}{\sin^2\phi} \tag{11.20}$$

One can also apply the conservation of angular momentum for the control volume in Fig. 11.6 to find a relationship between a' and the torque from the aerodynamic loads noting that the angular velocity upstream of the rotor is 0 and $2a'\omega r$ in the wake

$$dM = \dot{m} r 2a'\omega r = 2\pi r dr \rho(1-a)V_o r 2a'\omega r = 4\pi r^3 \rho V_o \omega a'(1-a)dr \tag{11.21}$$

The torque can also be found directly from the tangential loads as follows:

$$dM = Brp_t dr = Br\tfrac{1}{2}\rho V_{rel}^2 c C_t dr = \frac{1}{2}\rho B \frac{V_o(1-a)\,\omega r\,(1+a')}{\sin\phi\cos\phi} r c C_t dr \tag{11.22}$$

Please note that C_t in Eq. (11.22) is not the thrust coefficient but the tangential force coefficient given as follows:

$$C_t = C_l\sin\phi - C_d\cos\phi \tag{11.23}$$

From Eqs. (11.21) and (11.22) an expression for the tangential induction factor is derived as:

$$a' = \frac{1}{\frac{4\sin\phi\cos\phi}{\sigma C_t} - 1} \tag{11.24}$$

To describe the blade geometry one needs to have at some discrete radial positions (typically around 10−15 stations) the chord, $c(r)$, the twist, $\beta(r)$, and a table with the lift and drag coefficients as a function of angle of attack. The chord, $c(r)$, is the local width of the blade, the pitch, θ_p, is the angle between the rotorplane and the tip airfoil and the twist the angle between a local airfoil along the blade and the tip airfoil as shown in Fig. 11.8.

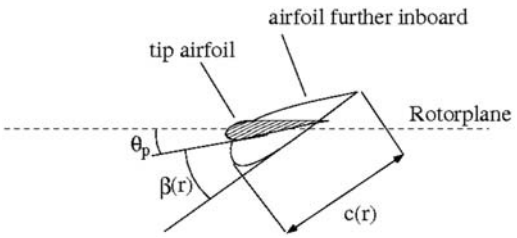

FIGURE 11.8 Sketch showing the chord, the twist, and the pitch angle on a blade.

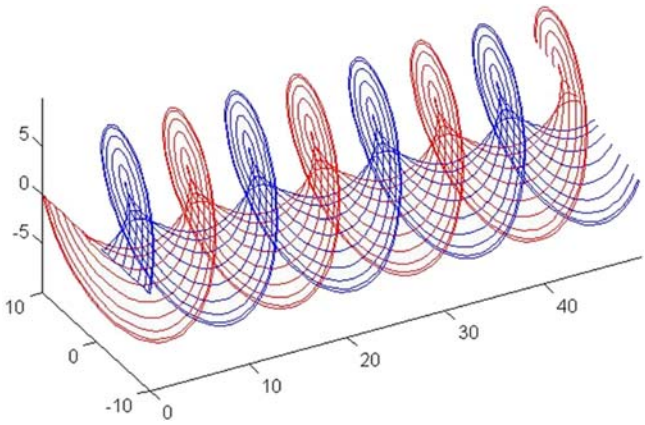

FIGURE 11.9 The vortex system behind a wind turbine rotor, $B = 2$.

The angle between one blade element and the rotor plane θ in Eq. (11.16) is thus given as follows:

$$\theta(r) = \theta_p + \beta(r) \tag{11.25}$$

To evaluate the momentum equations from the control volume in Fig. 11.6, it has been assumed that there is no azimuthal variation of the induced velocities at the outlet, which would only be true for a rotor with an infinite number of blades. Prandtl made a correction to the aerodynamic loads evaluated from the velocity triangle as in Fig. 11.7 so that when these are used for a rotor with infinitely number of blades one gets approximately the same induction as the real rotor with B blades. Prandtl evaluated the induced velocities from a lifting line model, where the blades are modeled as lines with a bound circulation distribution along the span. The local bound circulation can be estimated from the Kutta−Joukowski theorem and the definition of the lift coefficient as follows:

$$\Gamma(r) = \tfrac{1}{2}\rho V_{rel} c C_l \tag{11.26}$$

Next, there are vortices trailed from the blades and lying in a helical path as shown in Fig. 11.9 for a two-bladed rotor. The strength of the trailed vortices is given as the gradient of the bound circulation according to Helmholtz theorem. The only free parameter is then the helical pitch angle of the trailed vortex lines that must be specified since the resulting induced velocities on the blades from this vortex system is a function of this pitch. But for a lightly loaded rotor the pitch can be approximated from the free wind speed and the angular velocity only. Knowing the geometry and the strength of the vortex lines the induced velocity, $\boldsymbol{W}$, can be computed on the blades using the Biot-Savart law for every vortex line as follows:

$$\mathbf{W} = \frac{\Gamma}{4\pi}\int \frac{\mathbf{ds} \times \mathbf{r}}{|\mathbf{r}|^3} \tag{11.27}$$

Where Γ is the circulation of one vortex line, **ds**, a small piece of the line with direction tangent to the line, and **r** is the radius vector from that small piece to the point where the induced velocity is evaluated.

Prandtl solved this system using potential flow and a simple assumption of the wake geometry and came up with a correction to the loads so that the induction at the blades becomes the same as a rotor with an infinite number of blades. The loads from the velocity triangle shown in Fig. 11.7 is divided by a factor, F, denoted by Prandtl's tip loss correction, to model a system with an infinite number of blades that gives approximately the same solution as the vortex

system shown in Fig. 11.9 for a finite number of blades. Then one can apply these loads to the momentum equations derived for an infinite number of blades.

$$F = \frac{2}{\pi}\arccos\left(\exp\left(-\frac{B}{2}\frac{R-r}{r\sin\phi}\right)\right) \tag{11.28}$$

where R is the rotor radius, r is the local radius, and ϕ is the local flow angle. When this correction is applied to the momentum Eqs. (11.13) and (11.24) these become:

$$C_T(a) = \begin{cases} 4aF(1-a) \text{ for } a < 0.3 \\ 4aF(1-\frac{1}{4}(5-3a)a \text{ for } a \geq 0.3 \end{cases} \tag{11.29}$$

and

$$a' = \frac{1}{\frac{4F\ \sin\phi\ \cos\phi}{\sigma C_t} - 1} \tag{11.30}$$

Now one has, finally, all the equations needed to calculate the aerodynamic loads on a wind turbine rotor for a given blade geometry.

11.4.1 The blade element momentum method

Necessary input: First, one has to decide the number of elements, typically 10−15, and their radial positions. The airfoil data in the form of lift and drag coefficients at each station as a function of angle of attack and possibly Reynolds number must be obtained. Further, the chord and twist must be known in the elements. With the geometry given one must also define the operational parameters in the form of wind speed V_o, pitch angle θ_p, and rotational speed, ω.

For each element:

1. Guess a value of the induction factors, a, and a'
2. Calculate flow angle ϕ using Eq. (11.14)
3. Calculate angle of attack using Eqs. (11.16) and (11.25)
4. Determine lift and drag coefficients from tabulated airfoil data
5. Calculate Prandt's tip loss factor Eq. (11.28)
6. Calculate thrust coefficient using Eq. (11.20)
7. Calculate new value of axial induction factor a^{new} from Eq. (11.29)
8. Calculate tangential force coefficient using Eq. (11.23)
9. Solve Eq. (11.30) for a new value of the tangential induction factor a'^{new}
10. Compare the new values of a and a' with the values from the previous iteration and if $|a^{new}\text{-}a^{old}| < \varepsilon$ stop else go back to step (2) and calculate a new flowangle.

The BEM method described above is the classical one derived by Glauert [1] and is sufficient for blade design. But for unsteady load estimation, this must be complemented by more submodels to handle the dynamic response of the induced wind to time-varying loads from the angle of attack changing due to, for example, atmospheric turbulence, tower passage, and wind shear. To read more about this, we refer to textbooks such as Hansen [2], Manwell et al. [3], Burton et al. [4], and Schaffarczyk [5].

11.5 Use of steady blade element momentum method

The BEM method can be used to analyze a given rotor design by computing the loads for varying operational parameters: angular velocity ω, pitch angle θ_p, and wind speed V_o. On a stalled controlled wind turbine the blades are rigidly mounted to the hub and the pitch angle is thus constant. Further, an asynchronous generator is typically used where the rotational speed is almost constant, leaving only the wind speed a free parameter. Fig. 11.10 shows the measured and computed power as function of wind speed for the Tellus 100 kW. The geometry for this rotor is reported in Schepers et al. [6]. It is seen that for low wind speeds, where the angles of attack are also low and the local flow attached, there is a very good agreement between the measured and computed power using 2-D airfoil data. However,

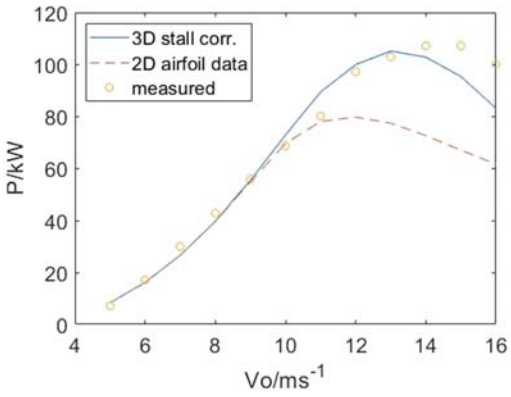

FIGURE 11.10 The measured and computed power curve for a 100 kW Tellus wind turbine as described in [6].

TABLE 11.1 Global blade data for the 100 kW Tellus wind turbine as described in [6].

Radial position [m]	Twist β [deg.]	Chord [m]	Airfoil thickness %
2.70	15.0	1.090	24.6
3.55	9.5	1.005	20.7
4.40	6.1	0.925	18.1
5.25	3.9	0.845	17.6
6.10	2.4	0.765	16.6
6.95	1.5	0.685	15.6
7.80	0.9	0.605	14.6
8.65	0.4	0.525	13.6
9.50	0	0.445	12.6

when using pure 2-D airfoil the flow seems to stall too early with a resulting underestimation of the power at high wind speeds, and to improve the numerical results one must correct the 2D airfoil data in stall using a stall delay model that takes into account the effects of rotation on the stalled boundary layer. The model used here is found in Chaviaropoulos and Hansen [7] and alters the lift coefficient as follows:

$$C_{l,3D}(\alpha) = C_{l,2D}(\alpha) + 2.2 \cdot \left(\frac{c}{r}\right) \cdot \Delta C_l(\alpha)$$
$$\Delta C_l = C_{l,inv} - C_{l,2D} \tag{11.31}$$

where r is the radial distance to the rotational axis, c is the chord and $C_{l,inv}$ is the inviscid lift coefficient. It should also be mentioned that the correction is only applied up to deep stall, where the 2D data are again applied. The Tellus turbine is a relatively small rotor with a radius of only 9.5 m and the rotational effects are thus stronger than on larger wind turbines, where the term (c/r) becomes small at the outer part of the blades. The overall blade data for the Tellus turbine is shown in Table 11.1 and the NACA 63n-2nn airfoil is used, where the two last digits denote the thickness. 2-D airfoil data can be found in airfoil catalogs such as [8], but are given in [6] for thicknesses 12, 15, 18, 21 and 25 and to find the actual airfoil data for a given thickness one has to interpolate among these 5 thicknesses. The rotational speed is 47.5 RPM and the pitch angle is $\theta_p = -1.5$ degrees.

Fig. 11.11 shows the computed thrust force as function of wind speed for the stalled regulated Tellus wind turbine and it is seen the thrust force increases with wind speed and stays high at high wind speeds, and Fig. 11.12 is plotted the computed power and thrust coefficients and it is seen that this wind turbine runs most efficiently between 6 and 9 m/s, where Cp is around 0.44.

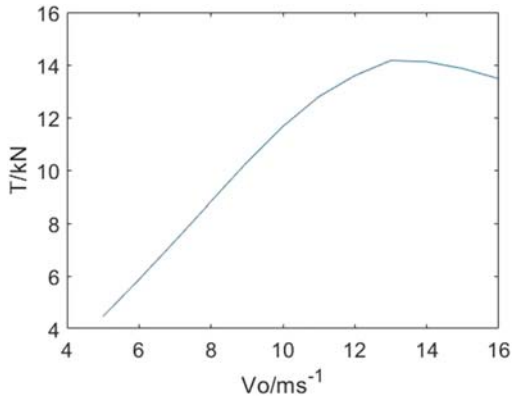

FIGURE 11.11 Computed thrust curve for the Tellus 100 kW wind turbine.

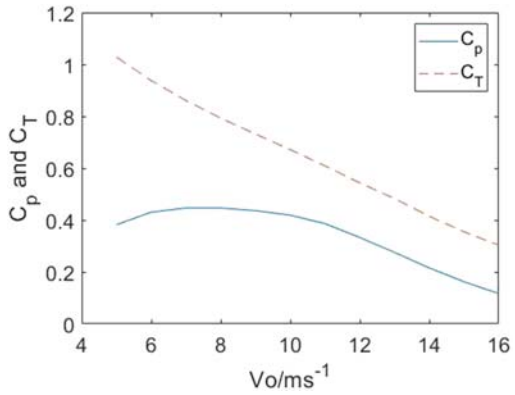

FIGURE 11.12 Computed thrust and power coefficients for the Tellus 100 kW wind turbine.

The large MW wind turbines of today run at variable speed and the entire blades are actively pitched to control the angles of attack along the blade (VSPR Variable Speed Pitch Regulated). An example of a VSPR wind turbine is the virtual DTU 10 MW reference wind turbine as described in [9]. For a given wind turbine the power depends on the air density, the viscosity, the wind speed, the rotor radius, the angular velocity, and the pitch angle are shown as follows:

$$P = f(\rho, \mu, V_o, R, \omega, \theta_p) \tag{11.32}$$

And using dimensional analysis one finds that:

$$C_p = f\left(\frac{\rho V_o R}{\mu}, \frac{\omega R}{V_o}, \theta_p\right) \tag{11.33}$$

The first parameter is the Reynolds number, this effect is small for large rotors, and the second parameter is called the tip speed ratio λ. For a large wind turbine, there is thus one combination of the tip speed ratio and pitch angle (λ_{opt}, $\theta_{p,opt}$) maximizing the aerodynamic efficiency. By running a BEM code this variation can be found and the values giving the highest possible $C_{p,max}$ determined. For the DTU 10 MW reference wind turbine, the values are $\lambda = 7.9$ and $\theta_p = 0°$, see Fig. 11.13.

This then requires that the rotational speed varies shown as follows:

$$\omega(V_o) = \frac{\lambda_{opt}}{R} V_o \tag{11.34}$$

and that the pitch angle is kept at $\theta_{p,opt}$. However, this is in practice only possible up to a certain wind speed, since the rotational speed from Eq. (11.34) will become too large so that the tip speed exceeds approximately 80−90 m/s where the aerodynamic noise becomes unacceptable. For such a turbine the power and thrust coefficients will be constant at their optimum value for the lower wind speeds and then start to decrease as, shown in Fig. 11.16, when the optimum tip speed ratio no longer can be kept as required by Eq. (11.34). Figs. 11.14 and 11.15 show the computed power and thrust as function of wind speed, where the rotational speed is governed by Eq. (11.34) but limited to 1.01 rad/s corresponding to a tip speed of 90 m/s. Further, after reaching rated power the pitch has been adjusted to obtain a rated

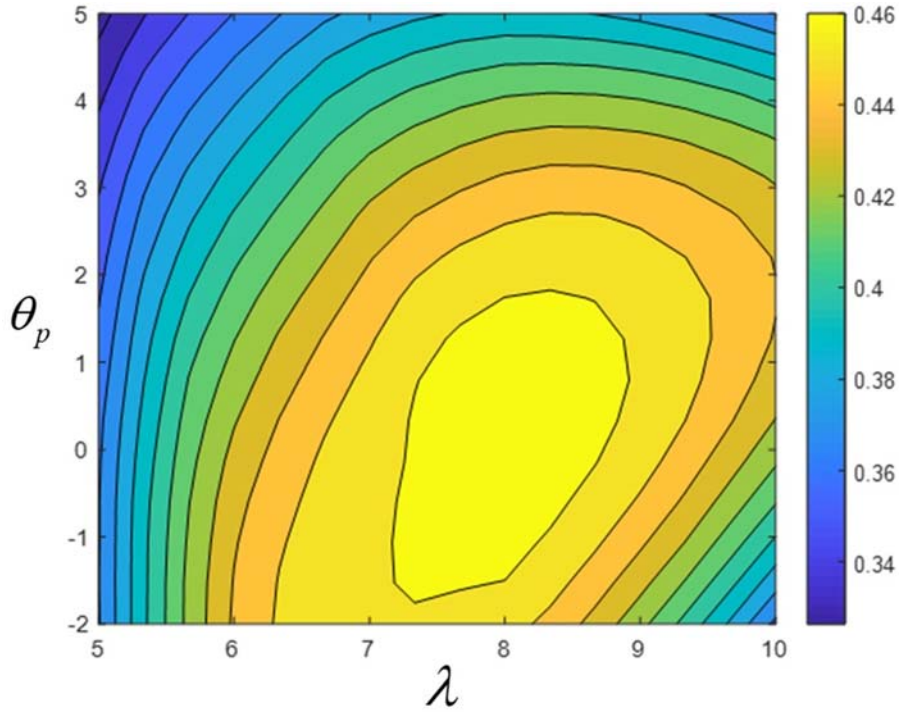

FIGURE 11.13 Computed $C_p(\lambda, \theta_p)$ variation for the DTU 10 MW reference wind turbine.

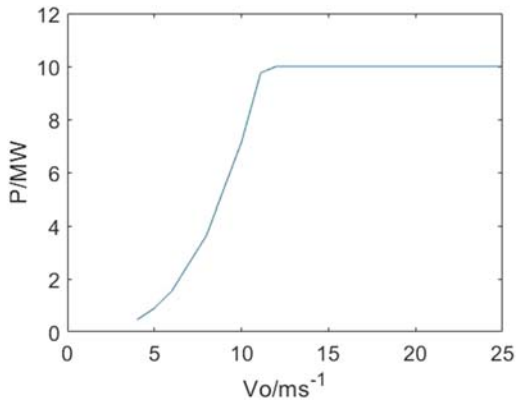

FIGURE 11.14 The BEM computed power curve for the DTU 10 MW reference wind turbine.

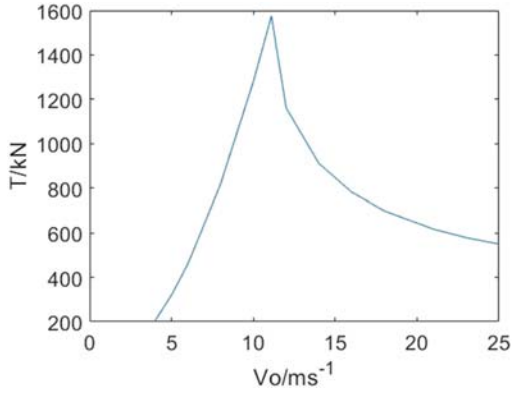

FIGURE 11.15 The BEM computed thrust curve for the DTU 10 MW reference wind turbine.

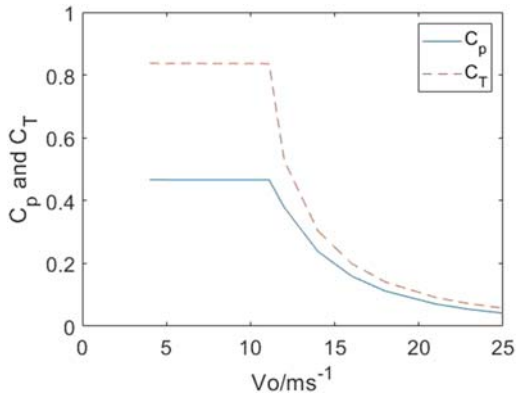

FIGURE 11.16 The computed thrust and power coefficients for the DTU 10 MW reference wind turbine.

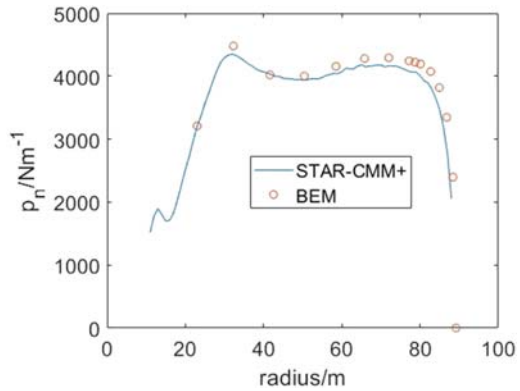

FIGURE 11.17 The computed normal load distribution for the DTU 10 MW reference turbine at $V_o = 16$ m/s.

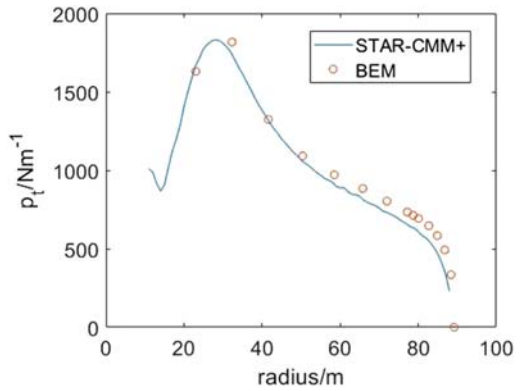

FIGURE 11.18 The computed tangential load distribution for the DTU 10 MW reference turbine at $V_o = 16$ m/s.

power of 10 MW. From Fig. 11.15, it is seen that the thrust strongly decreases with wind speed as the blades are deloaded by increasing the pitch angle to limit the power to the rated value. Increasing pitch angle means lowering the angle of attack Eqs. (11.16) and (11.25).

An alternative to the Blade Element Momentum method and vortex methods is using full Computational Fluid Dynamics, CFD, solving numerically the Navier−Stokes equations in the computational grid surrounding the wind turbine rotor. The earliest attempt to compute a rotating wind turbine blade was done in 1994 [10], but the breakthrough for CFD in wind energy came with the NREL blind test of a full-scale experiment conducted in the NASA-Ames wind tunnel in the year 2000 [11]. The CFD solver EllipSys came out as far the best of all the applied models and the comparison was later published in [12]. Today many commercial CFD programs are available, and Figs. 11.17 and 11.18 show some resulting load distributions from [13] computed using the STAR-CCM + software for the DTU 10 MW reference wind turbine for a wind speed of 16 m/s. Figures also show that a very good agreement is achieved with BEM. This is, however, not necessarily always the case and CFD is therefore always used to check the design based on BEM calculations to avoid surprises.

11.6 Aerodynamic blade design

Before describing a blade design process and how the BEM method can be used one needs first to define a good design. The object of any wind turbine-related project is to reduce the price of producing one kWh considering the overall costs over the entire lifetime. To do this one must have a reliable cost model including materials, manufacturing and operation and maintenance cost, which is outside the scope of this chapter. Instead focus will be purely on obtaining an aerodynamically efficient rotor producing as many kWh/m^2/year as possible, assuming this will also be the most economically profitable design. The actual design depends on whether the turbine is stall regulated, pitch regulated or VSPR. But in all cases, one must combine the power curve, $P(V_o)$, with a given site-specific wind distribution $H(V_o)$ where H is the actual annual number of hours in the wind speed interval of $Vo \pm 0.5$ m/s. The total annual energy production is the sum of $\sum H \cdot P$ [kWh] for all wind speed intervals between start and stop. Especially for a stall-regulated wind turbine, the actual design will depend strongly on the actual wind distribution at a given site. First one must decide on a rotor radius and the airfoils. Today there exist airfoils specifically designed for wind turbine blades as for example, the Risø-A1 (fixed rotor speed, stall or pitch), Risø-B1 (Variable speed and pitch control), and Risø-P (pitch regulated, variable or constant rotor speed) families, see Fuglsang and Bak [14]. The shape of these airfoils was described by only a few degrees of freedom, DOFs, and a 5th order B-spline and the optimum values for the DOFs were found using a Simplex method optimizing various object functions, depending on whether the airfoil is to be used at the root, the mid or tip of the blade. The aerodynamics for a given set of DOFs was determined using the XFOIL code [15]. The important properties of a wind turbine airfoil are summarized and prioritized in Table 11.2 (inspired by Fuglsang and Bak) [14] depending on its radial placement. It is clear that the main purpose of the root sections is to carry a high bending moment and therefore the structural properties are most important; hence, the high thickness to chord ratio. However, also geometrical compatibility is important since these airfoils must morph smoothly with the geometries at the mid and tip part of the blade. At the outer part of the blade contributing mostly to the thrust and power production the aerodynamic properties such as high lift, high lift-to-drag ratio, benign poststall behavior, low roughness sensitivity, and low noise are all very important. And the airfoils at the mid part of the blades should be able to both carry loads and produce power and be geometrically compatible with the root and tip airfoils. It is very important to verify the designs found using preferably both CFD and wind tunnel experiments, since XFOIL is based on the integral boundary layer equations not fully valid after stall, and therefore especially the real poststall behavior may be different than predicted using XFOIL. Further, it is possible to cure some of the bad aerodynamic properties of the thick root airfoils by applying vortex generators and Gourney flaps, see Timmer and Rooij [16].

Now having decided on the airfoils one can start to think about how to design a good blade with respect to chord and twist distribution. The most straightforward design is a so-called one-point design, where the blade layout is calculated to obtain the highest possible power coefficient for one specific tip speed ratio and pitch angle. Since the BEM assumes that the different elements along the blade are independent they can be individually optimized to maximize the local power coefficient at each element, dC_p, defined as follows:

$$dC_p = \frac{\omega dM}{\frac{1}{2}\rho V_o^3 2\pi r dr} \tag{11.35}$$

TABLE 11.2 Relative importance of airfoil properties.

	Root	Mid part	Tip
Thickness to chord ratio %	>27	21–27	15–21
Structure	+++	++	+
Geometrical compatibility	++	++	++
Maximum roughness insensitivity		+	+++
High max lift coefficient		+	+++
Benign poststall behavior		+	+++
Low aerodynamic noise			+++

And can be combined with Eq. (11.22) to give the following equation:

$$dC_p = \frac{B\lambda^2(1-a)(1+a')\frac{c}{R}\cdot\frac{r}{R}C_t}{2\pi\sin\phi\cos\phi} \tag{11.36}$$

The input to the design is a specified rotor radius, R, a given tip speed ratio, λ, and given airfoils along the blade. The design angle of attack, α_d, is for the radial element the one giving the highest lift-to-drag ratio and thus fixed. That means that also the lift and drag coefficients are fixed corresponding to their value at the design angle of attack. Now for every radial position following algorithm is made for various chord lengths.

1. Guess on a and a'
2. $\tan\phi = \frac{(1-a)R}{(1+a')\lambda r}$
3. $\theta = \phi - \alpha_d$
4. $C_n = C_l(\alpha_d)\cos\phi + C_d(\alpha_d)\sin\phi$ and $C_t = C_l(\alpha_d)\sin\phi - C_d(\alpha_d)\cos\phi$
5. $F = \frac{2}{\pi}\arccos\left(\exp\left(-\frac{B}{2}\frac{R-r}{r\sin\phi}\right)\right)$
6. Update a and a' using Eqs. (11.29) and (11.30)
7. Check convergence, if not go back to (2) with new values of a and a'
8. Calculate $dC_p(c/R)$ using Eq. (11.36)

Pick the value giving the highest local power coefficient and also note the local pitch, $\theta(r)$, and chord, $c(r)$ and continue with the next element. Figs. 11.19 and 11.20 show the result using this 1-point optimization for the following parameters $\lambda = 6$, $B = 3$, $\alpha_d = 4$, Cl = 0.8, and $Cd = 0.012$. The overall power coefficient for this design is 0.44, which is not impressive and can be improved by choosing more efficient airfoils with less drag, especially for the outer part of the blade.

One could further improve the 1-point design by slightly adjusting locally the twist angle at every element to maximize energy production in a wind speed interval, between 6 and 9 m/s where most energy is typically produced. To do

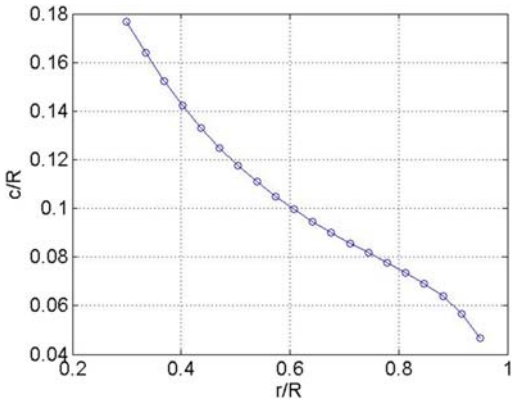

FIGURE 11.19 Dimensionless chord, c/R, for 1-point design. $\lambda = 6$, $B = 3$, $\alpha_d = 4$, $Cl = 0.8$, and $Cd = 0.012$.

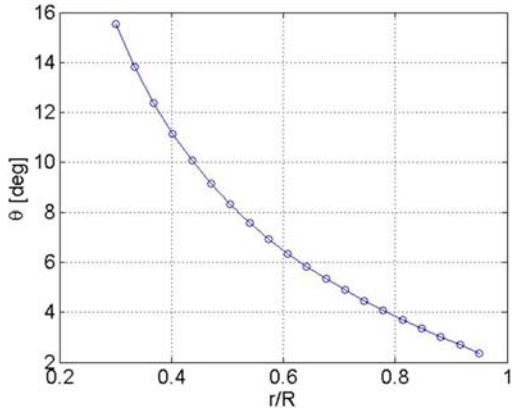

FIGURE 11.20 Twist distribution for 1-point design. $\lambda = 6$, $B = 3$, $\alpha_d = 4$, $Cl = 0.8$, and $Cd = 0.012$.

so, one can for each section calculate, using a BEM code, the local power production [kW/m] as function of twist angle and wind speed as:

$$\frac{dP}{dr}(\theta, V_o) = B\omega r p_t \tag{11.37}$$

Next, the produced energy in the chosen wind speed interval as a function of twist angle is computed, $\frac{dE}{dr}(\theta)$ [kWh/m/year] by combining the local power production with the annual number of hours in each wind speed interval as described earlier, and the twist angle producing most energy per meter blade is finally adopted.

An alternative 1-point optimization would be to replace the BEM code with a lifting line using Eqs. (11.26) and (11.27) and letting the trailed vortex lines follow a helical pitch as shown in Fig. 11.9 and requiring that the axially induced velocity along the rotor blades should be constant. This would, however, give something very close to the 1-point optimized blade using the BEM equations, since these have been calibrated through Prandtl's tip loss correction to give approximately the same as this vortex model. In doing this, one should change the pitch of the helical wake iteratively as a function of the computed induction.

For more complete optimization, one could still use the BEM code to calculate the power and thrust as function of the rotational speed, the wind speed, the pitch angle, and the chord and twist distribution. The chord and twist distribution is then typically described by a limited number of DOFs, for example, a spline, and the BEM model is coupled to a formal optimization algorithm as for example, the Simplex method, finding the geometry and operational parameters that maximize the annual energy yield under certain constraints for given wind distribution.

11.7 Unsteady loads and fatigue

A big challenge for a wind turbine is that the loads are inherently unsteady, mainly due to atmospheric turbulence and gravity. The wind speed in one fixed point in space is constantly due to atmospheric turbulence fluctuating around a mean value as shown in Fig. 11.21 for a mean wind speed of $V_o = 18$ m/s and a turbulence intensity of $I = \sigma/V_o = 12\%$. When a wind turbine blade spins around in a turbulent wind field, both the size and direction of the wind velocity in the velocity triangle drawn in Fig. 11.7 is changing in time and thus also the aerodynamic loads. Further gravity gives a large one per revolution (1-P) periodic load mainly in the edgewise direction of a blade, as indicated in Fig. 11.22. Other unsteady loads come from wind shear, tower passage, and if the rotor in a wind farm is partly in the wake of an upstream turbine. Wind shear is when the wind speed increases with height so that the apparent wind speed is higher at the top position than when a blade half a revolution later is pointing down, and this gives a sinusoidal variation with the frequency of the rotation (1-P). The time it takes for a blade to pass the tower is small, but during this time the wind speed is reduced giving a sudden drop in the loads that acts as an impulsive loading.

Further, the blades will respond elastically to the time-varying loads and the velocities from the vibrations also change the angles of attack, and to solve for the time-dependent loads and deflections one needs to calculate in the time

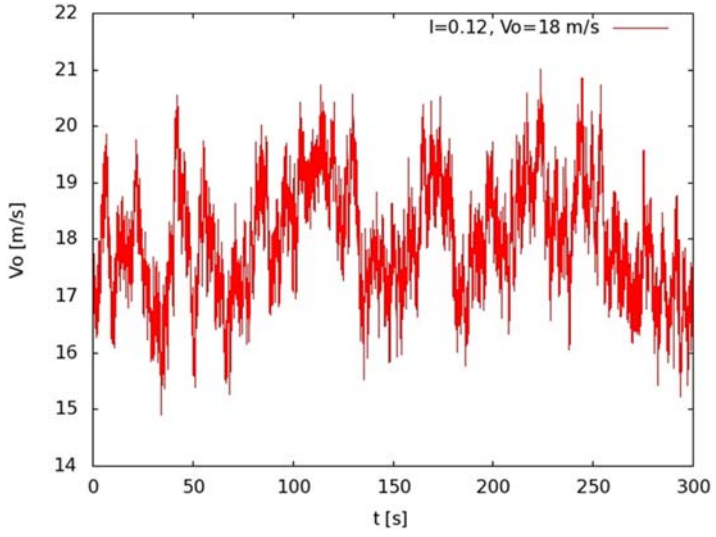

FIGURE 11.21 Example of a 5 min time history of a turbulent wind speed measured in one fixed point in space, having a mean speed of $V_o = 18$ m/s and standard deviation $\sigma = 0.12 \cdot V_o = 2.2$ m/s.

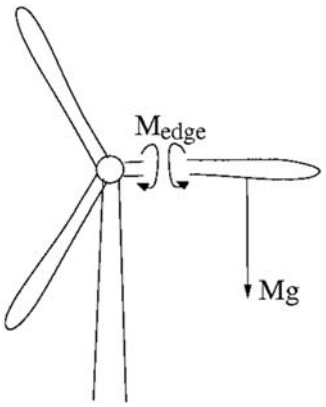

FIGURE 11.22 Simple drawing of the edgewise bending moment due to gravity.

domain the coupled structural and aerodynamic problem using a so-called aeroelastic code. To reduce the risk of a blade failure different norms/standards exist, for example, IEC 61400-3 that describe the load cases that a wind turbine is expected to experience during its design lifetime including: normal operation, extreme situations such as extreme wind and wave situations, fault conditions, starts, stops, etc. Each of these load cases must, for a given design, be simulated in time and the accumulated fatigue damage weighted with the expected occurrence of the various load cases must not lead to failure; also, it must be checked that the ultimate loads do not cause any structural damage.

11.8 Brief description of design process

A typical design process will then be something like this. First, the wind turbine is designed by combining a simple aerodynamic model as described in the previous sections with an optimization algorithm, where the object is to minimize the LCoE. Now for this design, all the load cases described in the standards are then simulated aeroelastically in the time domain including the structural response to the time-varying loads, and the extreme and fatigue loads are input to more advanced structural models, such as Finite Element Models, for the various components used in the turbine. If these FEM-based calculations reveal some structural problems, one has to go back and change the design and redo all the cases to make new load input to the structural models, and so on until one believes to have an optimized design that with a very high probability will survive all the expected dynamic loads experienced during the entire design lifetime. Now, typically also the final blade design is checked using advanced flow solvers such as Computational Fluid Dynamic CFD codes to verify the aerodynamic loads found using the simpler models relying on tabulated airfoil data. And now the design can be physically built and tested before it is allowed to be erected outside test stands and sold commercially.

References

[1] Glauert H. Airplane propellers. In: Durand WF, editor. Aerodynamic theory, Vol. 4. Berlin: Springer; 1976. ISBN 0844606065.
[2] Hansen MOL. Aerodynamics of wind turbines. 3rd ed. London and New York: Routledge; 2015. ISBN 9781138775077.
[3] Manwell FM, McGowan JG, Rogers AL. Wind energy explained:theory, design and application. 2nd ed. New York: Wiley; 2009. ISBN 9780470015001.
[4] Burton T, Jenkins N, Sharpe D, Bossanyi E. Wind energy handbook. 2nd ed. New York: Wiley; 2011. ISBN 9781119993926.
[5] Schaffarczyk AP. Introduction to wind turbine aerodynamics. Dordrecht: Springer; 2011. ISBN 13:9783642364082.
[6] Schepers JG, Brand AJ, Bruining A, Graham JMR, Hand MM, Infield DG et al., Rotor aerodynamics database. ECN-C−02−016 report; 2002.
[7] Chaviarropoulos PK, Hansen MOL. 'Investigating three-dimensional and rotational effects on wind turbine blades by means of a Quaso-3D Navier-Stokes solver. J Fluids Eng 2000;122:330−6.
[8] Abbott IH, Doenhoff AE. Theory of wing sections. New York: Dover; 1959.
[9] Bak C et al., Description of the DTU 10 MW reference wind turbine. DTU wind energy report-I-0092; July 2013.
[10] Hansen MOL, Michelsen JA, Sorensen NN. Navier Stokes solver for a rotating wing. In: Proc. European wind energy conference. Thessaloniki; October 1994, p. 557−561.
[11] Simms D, Schreck S, Hand M, Fingersh LJ. NREL unsteady aerodynamics experiment in the NASA-Ames wind tunnel: a comparison of predictions to measurements, doi: 10.2172/783409.
[12] Sørensen NN, Michelsen JA, Schreck S. Navier-Stokes predictions of the NREL phase VI rotor in the NASA Ames 80 ft X 120 ft wind tunnel. Wind Energy 2000;5(2−3):151−69.

[13] Shamik MM. Study of a full 3D rotating wind turbine using CFD [MSc thesis-M-0449]. DTU Wind Energy; 2001.
[14] Fuglsang P, Bak C. Status of the Risø wind turbine airfoils. In: European wind energy conference, Madrid; 16–19 June; 2003.
[15] Drela M. An analysis and design system for low reynolds number airfoils. Low Reynolds Number Aerodynamics, vol. 54. Berlin: Springer; 1989. p. 1989.
[16] Timmer WA, van Rooij RPJOM. Summary of the Delft University wind turbine dedicated airfoils AIAA-2003-0352 J Sol Energy Eng 2003;125(4):488–96.

This page intentionally left blank

Chapter 12

Civil engineering challenges associated with design of offshore wind turbines with special reference to China

Subhamoy Bhattacharya[1], Lizhong Wang[2], Junwei Liu[3] and Yi Hong[2]
[1]Department of Sustainability, Civil and Environmental Engineering, University of Surrey, Guildford, London, United Kingdom, [2]Zhejiang University, P.R. China, [3]Qingdao University of Technology, P.R. China

12.1 Offshore wind potential in China

Due to the rapid and consistent economic growth and prosperity, the demand for energy in China has grown enormously. Due to the extensive coastline and to comply with the global climate agreements, the offshore wind power sector has been expanding. The wind power industry has grown steadily since 2006. Up to about 2010, the turbines were mostly built onshore in areas with high wind speed (e.g., Xinjiang Province) and offshore potentials were not investigated. However, the 12th Five Year Plan (2011−15) of the PRC (People's Republic of China) Government gave a boost to expand the offshore capability and the target was to develop offshore wind turbines (OWTs) farms of 5 GW capacity by 2015 and 30 GW capacity by 2020. Furthermore, there was an announcement of a "National Offshore Wind Power Development and Construction Plan (2014−2016)" to develop offshore wind farms in Chinese waters/China sea. Fig. 12.1 shows the location of the development of the wind farms in Chinese waters.

China completed the first OWT installation (Suizhong 35-1 Oil Field Turbine) in 2007. Subsequently, the first offshore wind farm in Asia was developed in 2010 through the Donghai Bridge 100 MW Offshore Wind Power Demonstration Project. In 2010, a wind farm was also constructed in the intertidal area of Longyuan Rudong. After successful construction and operation of the first three wind farms, a large number of wind farm projects were consented/authorized and construction is underway. Table 12.1 shows the statistics of the work in progress.

As shown in Fig. 12.1A, there are five main sea areas in China: (1) Bohai Sea (enclosed sea); (2) Yellow Sea; (3) East China Sea; (4) South China Sea; and (5) Taiwan Strait. The locations and capacities of offshore wind farms (in operation or still under construction) in China are illustrated in Fig. 12.1B.

The long stretch of the China Sea is becoming attractive for many scientific surveys related to wind energy, as a result of the rapid development of the economy in the adjoining areas, leading to energy demand. As the wind speed offshore is much larger and more stable than onshore counterpart, offshore wind power developments in these zones are attracting serious investors. The three main economic zones (Beijing Zone, Yangtze River Delta, and Pearl River Delta) are also very close to the long coastline of China and are therefore convenient for electricity transport to the regional economic zones. Therefore, these sea regions are suitable for the construction and application of offshore wind farms.

The distributions of offshore wind farms in those five sea regions are different in both number and density. It can be seen from Fig. 12.1 that offshore wind farms are densely distributed along the Yellow Sea coast and Hangzhou Bay. However, compared with the Yangtze River Delta Economic Region (around Shanghai), there are few offshore wind farms in the Pearl River Delta Economic Region (Guangzhou—Hong Kong). Table 12.2 provides statistics on the distribution of the projects in the China Sea.

12.2 Dynamic sensitivity of offshore wind turbine structures

OWTs, due to their shape and form (i.e., a long slender column with a heavy mass as well as a rotating mass at the top) are dynamically sensitive because the natural frequencies of these slender structures are very close to the excitation

Wind Energy Engineering. DOI: https://doi.org/10.1016/B978-0-323-99353-1.00026-8

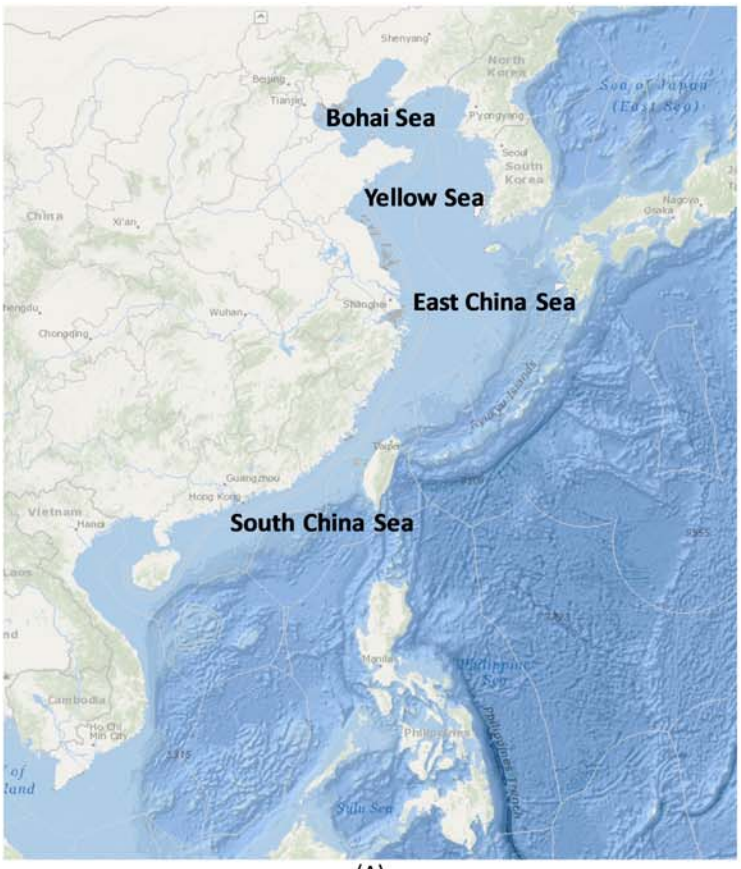

FIGURE 12.1 (A) A map showing the main developments of offshore wind projects in China; (B) locations and capacities of offshore wind farms in China.

TABLE 12.1 Offshore wind farms in China.

Development status	No. of farms
Fully commissioned	23
Partial generation	3
Under construction	2
Preconstruction	14
Consent authorized	>100

TABLE 12.2 Offshore wind farms in China sea.

Offshore wind development (Fig. 12.1)	Fully commissioned	Partial generation	Under construction	Preconstruction
Bohai Sea	4	0	0	3
Yellow Sea	14	0	0	0
East China Sea	3	2	2	7
Taiwan Strait	2	1	0	2
South China Sea	0	0	0	2

frequencies imposed by the environmental and mechanical loads [1]. Fig. 12.2 shows a simple mechanical model of the whole system including the different components and the design variables. In the model, the foundation is replaced by four springs: K_L (lateral spring), K_R (rocking spring), K_V (vertical spring), and K_{LR} (cross-coupling spring). The stability and deformation of the system is very much dependent on these four springs; a few things may be noted regarding these springs:

1. The properties and shape of the springs (load-deformation characteristics) should be such that the whole structure should not collapse under the action of extreme loads and the deformation is acceptable under the working loads;
2. The values of the spring (stiffness of the foundation) are necessary to compute the natural period of the whole structure as this is a linear Eigenvalue analysis. Further details on the analysis required can be found in work by Adhikari and Bhattacharya [2] and by Bhattacharya and Adhikari [3].
3. The values of the springs will also dictate the overall dynamic stability of the system due to its nonlinear nature. It must be mentioned that these springs are not only frequency dependent but also change with cycles of loading due to dynamic soil-structure interaction. Further details on the dynamic interaction can be found in the work of Bhattacharya et al. [4,5].

Fig. 12.3 shows typical wind and wave power spectral densities for offshore sites which essentially describe the frequency content of dynamic excitations from wind turbulence and waves. The graph also shows the turbine's rotational frequency range (1P) and the turbine's blade passing frequency range (3P) for a range of commercial wind turbines of different capacities (2−8 MW). A simplified way of translating the wind turbulence spectrum and the wave spectrum into mudline bending moment spectra through linear transfer functions has been presented by Arany et al. [6] The peak frequencies of loading have been shown to coincide with the peak frequencies of wind turbulence and waves. However, loads at the 1 and 3P frequencies can also be observed through effects such as aerodynamic and mass imbalance of the rotor and rotational sampling of turbulence by the blades, for 1 and 3P loads, respectively [6,7]. Further details on the estimations of the loads can be found in the work by Bhattacharya [6,8]. For the widely used soft-stiff design, the target Eigen frequency (for practical purposes, the first natural frequency) is a frequency in the narrow gap between 1 and 3P. Fig. 12.3 also shows measured natural frequencies of a wide array of OWTs from several different wind farms across Europe (see Table 12.3 for the nomenclature on the wind turbine structure for which the measured natural frequencies

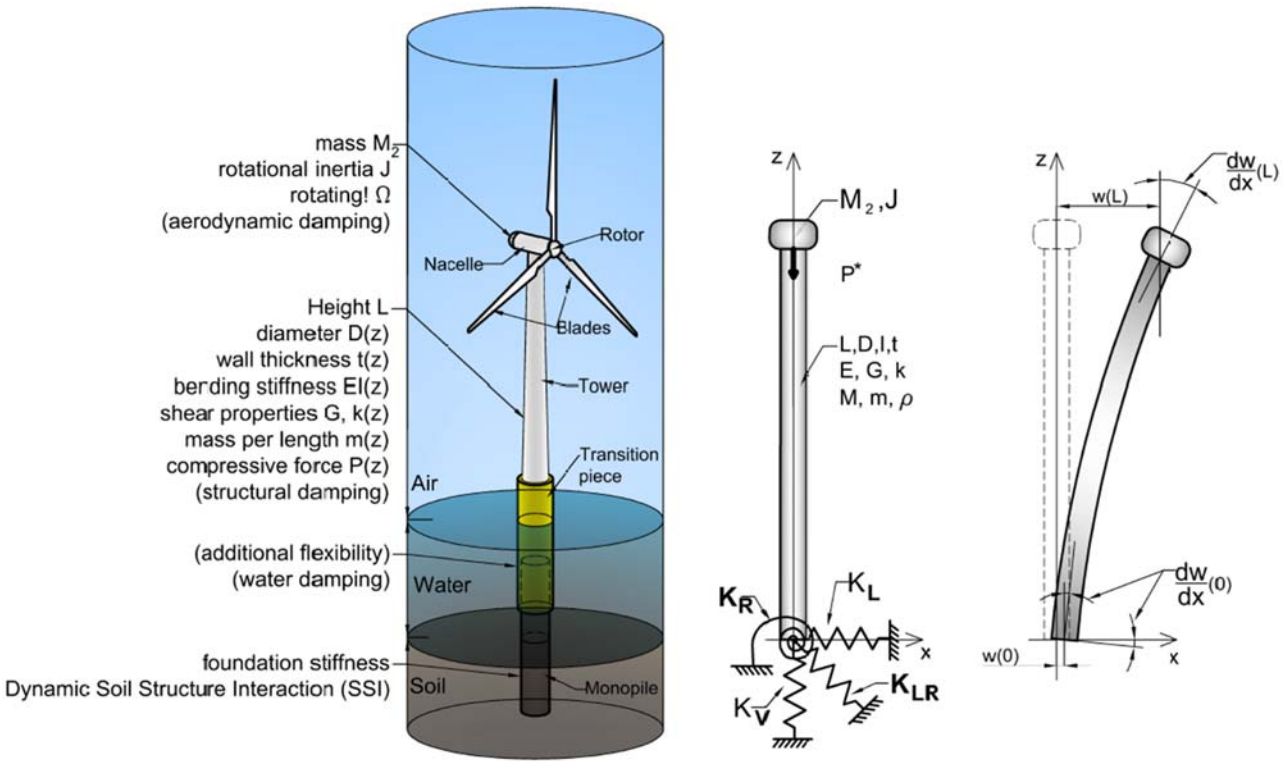

FIGURE 12.2 Simplified mechanical model of an offshore wind turbine.

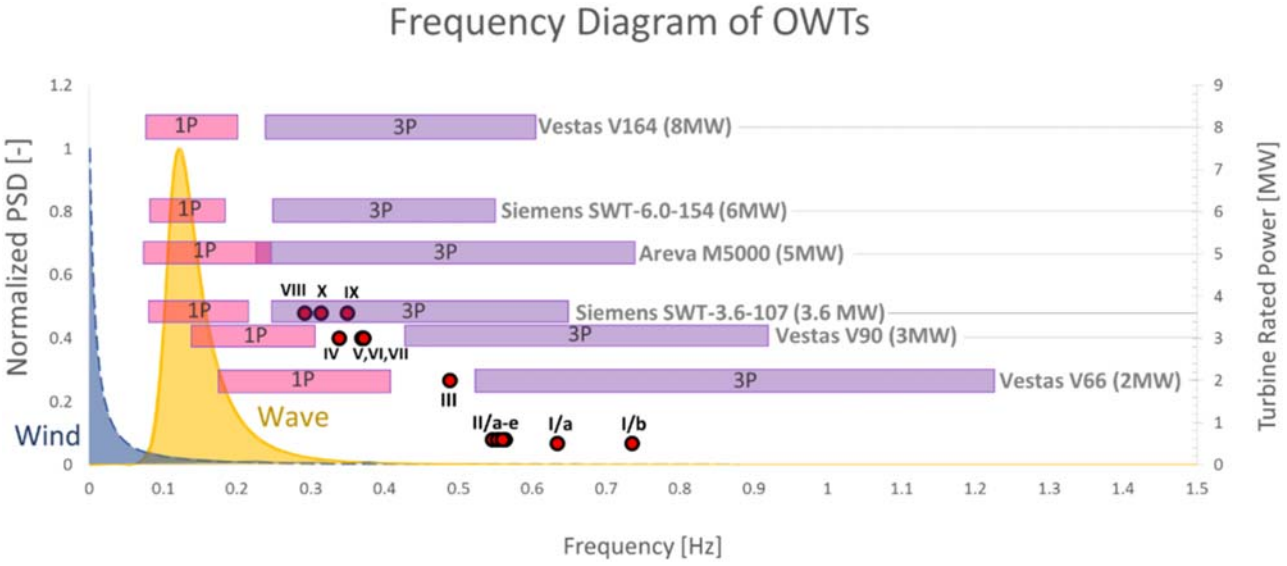

FIGURE 12.3 Typical wind and wave spectra, rotational speed (1P), and blade passing (3P) frequency bands for six commercial turbines and measured natural frequencies of the OWTs (given in Table 12.3).

are shown). The figure clearly shows the trend that the target natural frequencies of heavier turbines (8 MW) are indeed closer to the excitation frequencies of the wave and wind, making these structures even more sensitive to dynamics. It is of interest to review the codes of practice in this regard. DNV code [9] suggests that the first natural frequency should not be within 10% of the 1 and 3P ranges. It is apparent from Fig. 12.4 that for soft-stiff design, the first natural frequency of the wind turbine needs to be fitted in a very narrow band (in some cases the 1 and 3P ranges may even coincide leaving no gap) which is a significant challenge.

TABLE 12.3 Analyzed offshore wind farms with the used wind turbines and soil conditions at the sites.

No.	Wind farm name and location	Turbine type and rated power	Soil conditions at the site
I.	Lely Offshore Wind Farm (The Netherlands)	NedWind 40/500 2-bladed 500 kW study purpose wind turbine	Soft clay in the uppermost layer to dense and very dense sand layers below.
II.	Irene Vorrink Offshore Wind Farm (The Netherlands)	NordtankNTK600/43 600 kW study purpose wind turbine	Soft layers of silt and clay in the upper seabed to dense and very dense sand below.
III.	Blyth Offshore Wind Farm (United Kingdom)	Vestas V66 2 MW industrial offshore wind turbine	Rocky seabed (weathered bedrock)
IV.	Kentish Flats Offshore Wind Farm (United Kingdom)	Vestas V90 3 MW industrial offshore wind turbine	Layers of dense sand and firm clay
V.	Barrow Offshore Wind Farm (United Kingdom)	Vestas V90 3 MW industrial offshore wind turbine	Layers of dense sand and stiff clay
VI.	Thanet Offshore Wind Farm (United Kingdom)	Vestas V90 3 MW industrial offshore wind turbine	Fine sand and stiff clay
VII.	Belwind 1 Offshore Wind Farm (Belgium)	Vestas V90 3 MW industrial offshore wind turbine	Dense sand and stiff clay
VIII.	Burbo Bank Offshore Wind Farm (United Kingdom)	Vestas V90 3 MW industrial offshore wind turbine	Saturated dense sand
IX.	Walney 1 Offshore Wind Farm (United Kingdom)	Siemens SWT-3.6-107 3.6 MW industrial offshore wind turbine	Medium and dense sand layers.
X.	Gunfleet Sands Offshore Wind Farm (United Kingdom)	Siemens SWT-3.6-107 3.6 MW industrial offshore wind turbine	Sand and clay layers

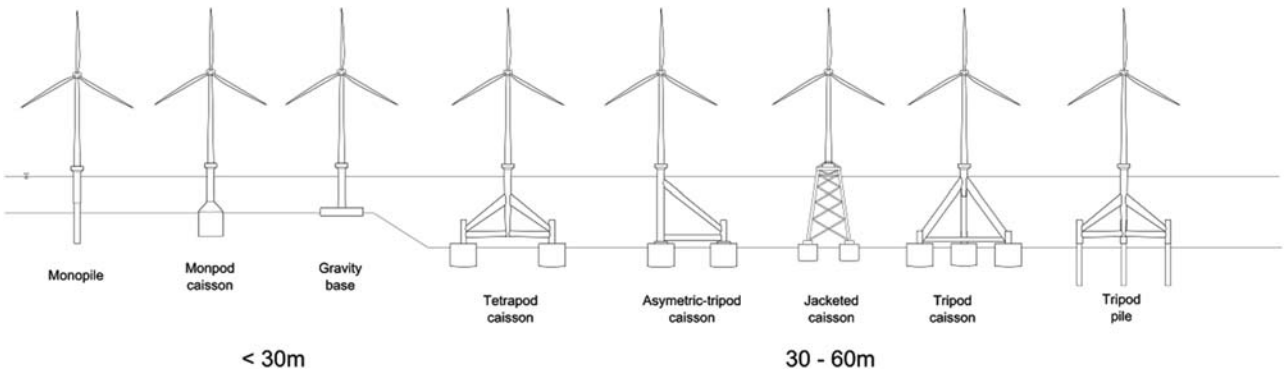

FIGURE 12.4 Figure showing different types of foundations for fixed (grounded) systems.

12.3 Dynamic issues in support structure design

The schematic diagram of a wind turbine system model shown in Fig. 12.2 is relevant to the study of the overall system dynamics which is important for many design calculations such as Eigen frequencies and fatigue. In practice, the support structure is the whole structure that supports the heavy turbine, that is, the components below the rotor nacelle assembly (RNA) which includes the tower, substructure, and foundation. The foundation is defined as the part of the support structure that is embedded in the ground below the mudline. The tower is typically a tubular tapered column. As the natural frequencies of these systems are very close to the forcing frequencies, the dynamics pose multiple design challenges and the scale of the challenges will vary depending on turbine types and site characteristics. These issues are briefly mentioned in the next section:

There are two main categories of modern wind turbines based on the operational range:

1. Variable rotational speed machines have an operational speed range (1P range).
2. Constant rotational speed wind turbines that operate at a single rotational speed (fixed 1P).

Variable speed machines have 1 and 2P/3P frequency bands which must be avoided, as opposed to a single frequency (applicable to constant rotational speed machines). They are more restrictive from the point of view of foundation design as the forcing frequency is a band rather than a unique value. The turbines currently used in practice (under operation) are variable speed machines. Fig. 12.3 shows the 1 and 3P bands for typical OWTs ranging from 2 MW (not in production anymore) turbines to commercially not yet available 8 MW turbines. It may be observed from Fig. 12.3 that for most wind turbines, 1 and 3P excitation cover wide frequency bands. To avoid these ranges, the designer of the support structure has three options from the point of view of the stiffness of the tower and the foundation:

1. Soft-soft structures: Whereby the natural frequency lies below the 1P frequency range. This design is typical for floating offshore platforms, but is practically impossible to achieve for fixed (grounded) structures. Also, soft-soft fixed structures would likely be subject to high dynamic amplification of wave load response.
2. Soft-stiff structures: Whereby the natural frequency lies above the 1P frequency range. This is the typical design choice for practical bottom fixed structures, such as monopile-founded OWTs. All wind turbines in Fig. 12.3 are designed soft-stiff.
3. Stiff-stiff structures: Whereby the natural frequency lies above the 3P range. Such designs are typically considered to have a massive support structure and therefore uneconomic.

It is quite clear from Fig. 12.3 that designing a soft-stiff system that avoids both the 1 and 3P frequency bands is challenging because of the tight tolerance of the target natural frequency. Indeed, some OWTs with a wide rotational speed range, such as the Areva M5000 5 MW in Fig. 12.3 with 0.075−0.25 Hz (4.5−14.8 rpm) do not even have a gap between 1 and 3P and they are overlapping. Modern wind turbines often feature a sophisticated pitch control system designed to leap-frog the rotational frequency range that would cause resonance of the structure due to the corresponding 3P frequency. For example, if the rotational speed range is 5−12 rpm, equivalent to 0.083−0.216 Hz, then the 3P frequency band is 0.25−0.65 Hz. If the structural natural frequency is 0.35 Hz, then the pitch control may regulate the rotational speed such that the corresponding 3P frequency avoids $\pm$ 10% of the structural natural frequency, that is, the frequency band 0.315−0.385 Hz to comply with the DNV code [9]. This would result in a jump in the rotational speed from 6.3 rpm to 7.7 rpm, avoiding operation between these values. Obviously, this is also not without cost, both in terms of initial cost, maintenance, and power production.

The second issue is the top head mass, that is, the mass of the RNA (i.e., M_2 in Fig. 12.2). With the increasing capacity of the turbine, the mass of the rotor-nacelle assembly increases, and the natural frequency will also decrease keeping other factors constant. Furthermore, the hub height is also higher due to longer blades (associated with heavier turbines) which increases the flexibility of the taller towers causing further reduction in the natural frequency. This trend can also be seen in Fig. 12.3, the target natural frequency of wind turbines (in soft-stiff design) with higher power output is typically lower. Fortunately, the large rotor diameter wind turbines also tend to have lower rotational speeds. This is because for optimum power production, the tip speed ratios (ratio of the speed of the tip of the blades and the incoming wind speed) are maintained at a favorable value, also to avoid blade damage. Furthermore, the top head mass is dependent on the choice of drive (with or without a gearbox). Direct drive wind turbines do not need gearboxes, and thus significant weight reduction can be achieved (theoretically). However, the weight reduction is not obvious because the power of an electric generator is proportional to its rotational speed

12.3.1 Importance of foundation design

Designing foundations for OWTs is challenging as these are dynamically sensitive structures in the sense that the natural frequencies of these structures are very close to the forcing frequencies of the wind, wave, 1P (rotor frequency) and 2P/3P (blade shadowing frequency) loading. Typically, for the widely used soft-stiff design (target frequency of the overall wind turbine is between 1P and 2P/3P) the ratio of forcing frequency, f_f, to natural frequency, f_n, is very close to 1 and as a result is prone to dynamic amplification of responses such as deflection/rotation which may enhance the fatigue damage, thereby reducing the intended design life. Therefore, a designer apart from accurately predicting the natural frequency of the structure, must also ensure that the overall natural frequency due to dynamic-soil-structure-interaction does not shift toward the forcing frequencies making the value of f_f/f_n even closer to 1. Therefore, foundations are one of the critical components of OWTs not only because of the overall stability of the structure but also due

to the financial viability of the project. Foundation selection plays an important role in the overall concept design for offshore wind farms as there are large financial implications attached to the choices made. The selection of foundation type and the design is a complex task, which strongly depends not only on the site characteristics (wind, wave, ground type), and turbine type but also on the maturity and track record of the design concepts. Fig. 12.4 shows different types of foundations either in use or proposed to be used. One of the main aims of a foundation is to transfer all the loads from the wind turbine structure to the ground safely and within the allowable deformations. Guided by the Limit State Design philosophy, the design considerations are to satisfy the following:

1. Ultimate Limit State (ULS): The first step in design is to estimate the maximum loads on the foundations (predominantly overturning moment, lateral load, and vertical load) due to all possible design load cases and compare them with the capacity of the chosen foundation. For monopile type of foundations, this would require computation of ultimate moment, lateral and axial load carrying capacity. Therefore, inevitably, ULS design consideration will provide the minimum dimension (length and diameter) of the monopile and also the wall thickness required. The input required for such calculations is site characteristics (for example, wind and wave data) and turbine data. At some sites, some other loads (for example, ice loads or earthquake loads) may need to be considered. Particularly, in Chinese waters, the loads from extreme events such as typhoons may govern.
2. Target Natural Frequency (Eigen Frequency) and Serviceability Limit State (SLS): This requires the prediction of the natural frequency of the whole system (Eigen Frequency) and the deformation of the foundation at the mudline level (which can be further extrapolated to the hub level) over the lifetime of the wind turbine. As the natural frequency is concerned with very small amplitude vibrations (linear Eigen Value Analysis will suffice) the deformation of the foundation will be small and prediction of initial foundation stiffness would suffice for this purpose. Therefore, the second major calculation is the determination of the stiffness of the foundation. Closed-form solutions to obtain the foundation stiffness for rigid monopiles as well as flexible monopiles are developed by Shadlou and Bhattacharya [10] and used in Arany et al. [11] for the simplified design of monopiles. These foundation stiffness values can be used to estimate the deformation (pile head rotation and displacement) in the linear range and natural frequency of the whole system.
3. Fatigue Limit State and long-term deformation: This would require predicting the fatigue life of the monopile as well as the effects of long-term cyclic loading on the foundation.
4. Robustness and ease of installation: This step will ascertain that the foundation can be installed and that there is adequate redundancy in the system [12].

Typically, foundations cost between 25% and 34% of the overall cost. For the North Hoyle project in the United Kingdom, the cost of the foundation was 34% [13], and it has been reported that the development of the Atlantic Array wind farm did not go ahead and one of the main reasons was the expense of the foundation. Foundations for wind turbines can be classified into two main types: fixed (or grounded to the seabed) and floating. While most of the currently installed or operating turbines are supported by fixed/grounded foundation systems, research and development of floating foundations are underway. Fig. 12.4 shows the different types of grounded (fixed to the seabed) and foundation systems either in use or proposed and will constitute the main part of this chapter.

Compared to the design of OWTs in the North Sea, additional challenges are posed in wind turbine design in China, due to the presence of the unfavorable yet widely distributed soft clayey seabed in the Chinese waters. It is well recognized that soft clays (frequently encountered in Chinese waters) are much more susceptible to stiffness degradation [14] than stiff clay and dense sand (typically found in the North Sea, see Table 12.3), at a given undrained cyclic loading. In other words, the natural frequencies of wind turbine structures in Chinese water are more likely to be altered by the environmental loadings than those of the turbines in the North Sea, causing the former to be more sensitive to dynamics. Figs. 12.5–12.7 show fixed foundations used in Chinese waters and Fig. 12.8 shows the method of installation.

12.4 Types and nature of the loads acting on the foundations

12.4.1 Loads acting on the foundations

The loads acting on the wind turbine tower are ultimately transferred to the foundation and can be classified into two types: static or dead load due to the self-weight of the components and the dynamic loads (or in some instances, this can be cyclic). However, the challenging part is the dynamic loads acting on the wind turbine which are discussed below:

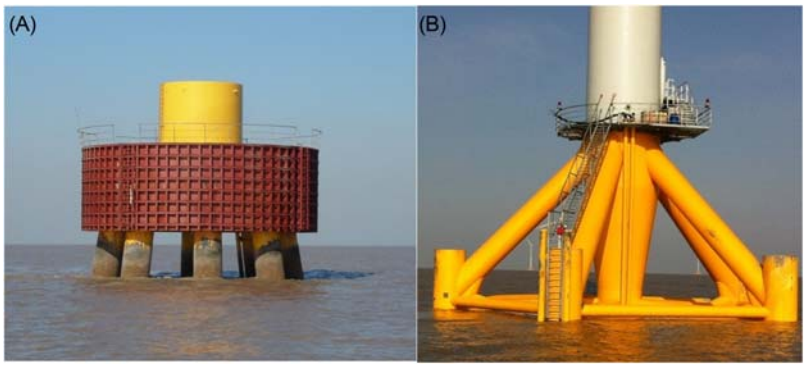

FIGURE 12.5 Foundations supporting wind turbines used in Chinese waters: (A) Group of 8 piles supporting a high rise pilecap used in soft soil sites; (B) multipod foundation.

FIGURE 12.6 Large scale prestressed concrete bucket foundation in water depth of 6 m (the caisson dimensions are 30 m in diameter and 7 m in depth).

FIGURE 12.7 Rudong Intertidal wind farm.

1. The lateral load acting at the hub level (top of the tower) from the rotating blades is produced by the turbulence in the wind. The magnitude of the dynamic component depends on the turbulent wind speed;
2. The load is caused by waves crashing against the substructure very close to the foundation. The magnitude of this load depends on the wave height and wave period;
3. The load is caused by the vibration at the hub level due to the mass and aerodynamic imbalances of the rotor. This load has a frequency equal to the rotational frequency of the rotor (referred to as 1P loading, as defined in Section 2). Since most industrial wind turbines are variable speed machines, 1P is not a single frequency but a frequency band between the frequencies associated with the lowest and the highest rpm (revolutions per minute);

FIGURE 12.8 Installation of the wind turbine in China.

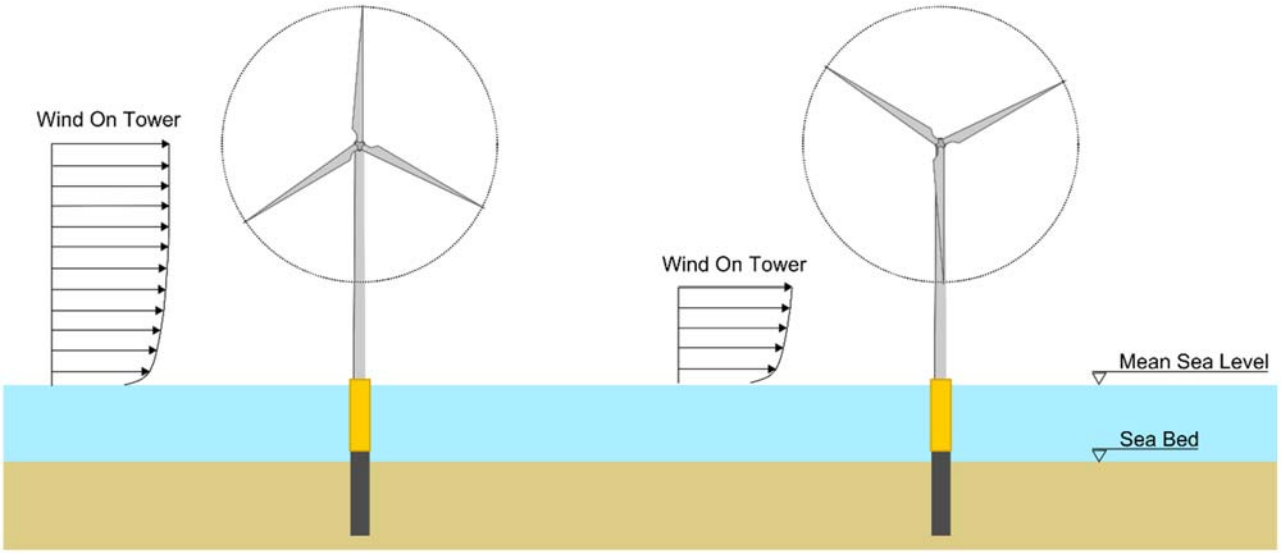

FIGURE 12.9 Blade shadowing load on the tower (3P load). The left-hand diagram shows the wind load on the tower when the blades do not shadow the tower.

4. Loads in the tower due to the vibrations caused by blade shadowing effects (referred to as 2P/3P, as defined in Section 2). The blades of the wind turbine passing in front of the tower cause a shadowing effect and produce a loss of wind load on the tower, as shown in Fig. 12.9. This is a dynamic load having a frequency equal to three times (3P) the rotational frequency of the turbine for three-bladed wind turbines and two times (2P) the rotational frequency of the turbine for a two-bladed turbine. The 2P/3P loading is also a frequency band like 1P and is simply obtained by multiplying the limits of the 1P band by the number of the turbine blades.

The turbulent wind velocity and the wave height on the sea are both variables and best treated statistically using Power Spectral Density functions. In other words, instead of time domain analysis, the produced loads are more effectively analyzed in the frequency domain whereby the contribution of each frequency to the total power in wind turbulence and in ocean waves is described. Representative wave and wind (turbulence) spectra can be constructed by a Discrete Fourier Transform from site-specific data. However, in absence of such data, theoretical spectra can be used. The DNV standard specifies the Kaimal spectrum for wind and the JONSWAP (Joint North Sea Wave Project) spectrum for waves in OWT applications.

It is clear from the above discussion that designing soft-stiff wind turbine systems demands the consideration of dynamic amplification and also any potential change in system frequency due to the effects of cyclic/dynamic loading on the system, that is, Dynamic-Structure-Foundation-Soil-Interaction. Typically, the first modal frequency of the wind turbine system lies in the range of 75% to 120% of the excitation frequencies (see Fig. 12.3) and as a result, dynamic amplifications of responses are expected.

Clearly, for soft-stiff design, any change in natural frequency over the design/operation period of the turbine will enhance the dynamic amplifications which will increase the vibration amplitudes and thus the stresses and fatigue damage on the structure. Therefore, fatigue is one of the main design drivers for these structures. Predicting fatigue damage is undoubtedly a formidable task due to the complexity associated with the uncertainty in the dynamic amplification (owing to changes in system characteristics over time and number of cycles), randomness of the environmental loading, and last but not the least, the impact of climate change.

12.4.2 Extreme wind and wave loading conditions in Chinese waters

Typhoons, which can lead to failure or even collapse of wind turbines, hit the region of the East and South China Sea almost every year, but rarely occur in the North Sea. Typhoons can have a negative effect on wind turbine systems ranging from fracture of blades, damage to braking system, yielding of tower, and even excessive rotation foundation. However, the direct effect of a typhoon is loss of power supply and emergently shut down which may damage the weakest part (e.g., blade and nacelle). It is, therefore, necessary to understand the wind condition in the Chinese waters and this section provides a brief summary.

Bohai Sea: The total area of the Bohai Sea in China is approximately 77 284 km^2 and is classified into four parts: west, middle, Jinzhou, and Suizhong. Bohai Sea is the only inner sea region of China and is a shallow sea with an average water depth of about 18 m. In winter, due to the flow of cold air from Siberia, the average wind speed is about 6−7 m/s. On the other hand, in summer, due to warm airflow from the Western Pacific Ocean, the average wind speed is 4−5 m/s. In August, the wind speed is quite low. In this sea, wind farms are located in Jinzhou and the predominant wind directions for high wind speeds are southeast and southwest with mean annual wind speed of 7.21 m/s (100 m height over sea level). Typhoons and cyclones are not normal in the Bohai Sea and the wind condition is stable throughout the year. The Bohai Sea has a cold climate and in the winter period, the onshore near the coastline is almost frozen for 3−4 months.

Yellow sea: The total area of the Yellow Sea 380,000 km^2 and comprises Shandong, Jiangsu, and the Korean Peninsula. There are many offshore wind farms built along the coastline of the Yellow Sea from north to south. In winter, the wind is stable but in summer it varies in both magnitude and direction. Typhoons are very frequent in summer throughout the Shanghai area, which is located in the south of the Yellow Sea. The annual average wind speed in the north of the Yellow Sea is 6.80−6.88 m/s but in the south, the value is larger and the average value is 7.45−7.55 m/s.

East China Sea: The total area of the East China Sea is 770,000 km^2 and is comprised of the continental coastline of Japan and Taiwan. There are many offshore wind farm projects located in Hangzhou Bay. The annual mean wind speed tested at 100 m in height over sea level is generally around 9.6−9.8 m/s at the exit of Hangzhou Bay. However, in terms of frequent typhoon phenomena in summer from May to September each year, wind speed remains unstable and the amplitudes are quite large, even greater than 14 m/s. The cyclone effect is very important and governs the design of an OWT.

Taiwan Strait: Taiwan Strait is one part of the East China Sea, connected with the South China Sea in the south of China. In summer, it is common to see strong winds (e.g., typhoons) that damage the cities and structures along the coastline. Usually, typhoons in summertime will come from the south-east and the wind speed is quite high. The annual wind speed in Taiwan Strait is about 11.5−12 m/s and is even higher when a typhoon appears (20 m/s or more). Each year, typhoons are responsible for serious damage to the economy and structures in Taiwan and in particular to Fujian and Zhejiang, located on the two sides of the Taiwan Strait.

South China Sea: The total area of the South China Sea is about 3,500,000 km^2. It is surrounded by the continent of South China mostly, northeast to Taiwan Strait, southwest to Singapore Strait. Most wind projects are newly built or under construction. It is also common to see strong wind (e.g., typhoons) and high rainwater during each summer. The annual mean wind speed in the South China Sea is 9−11 m/s. When a typhoon comes, the wind speed is usually over 17 m/s (at 100 m in height). Table 12.4 summarizes the wind condition in the Chinese waters.

12.4.2.1 Case study: Typhoon-related damage to wind turbines in China

Zhejiang Province, located on the west of the East China Sea, experienced 23 typhoons since 1997 (the starting year of wind farming projects), causing hundreds of millions of dollars of economic loss. It is of interest to discuss the effects of the 10th August 2006 Typhoon "*Saomai*" which had wind speeds of 68 m/s that devastated many wind farms. This is the most powerful typhoon to hit China over the past 50 years; it killed 104 people and left at least 190 missing. Furthermore, it blacked out cities and destroyed over 50,000 houses in the southeast part of the country.

TABLE 12.4 Wind condition summary in China Seas (unit: m/s).

Sea name	Wind speed range (m/s)	Mean wind speed (m/s)
Bohai Sea	6.4–8.2	7.45
Yellow Sea (north)	6.8–7.5	6.86
Yellow Sea (south)	7.0–8.2	7.48
East China Sea	7–11	9.68
Taiwan Strait	11.5–12	12.04
South China Sea	8.8–9.8	9.18

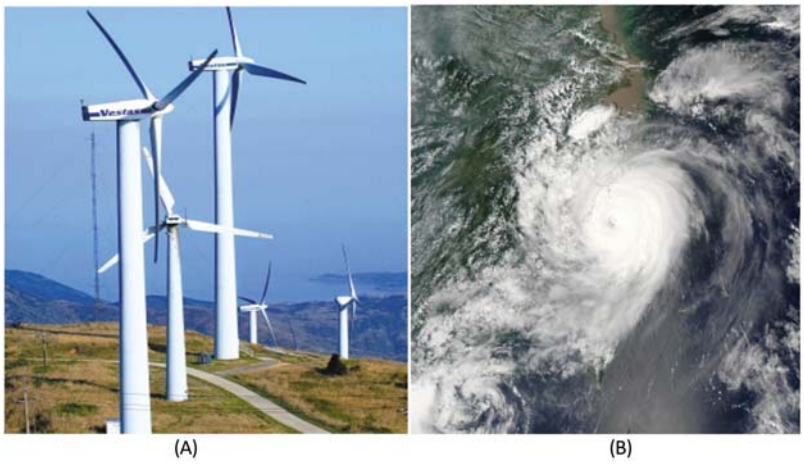

FIGURE 12.10 (A) Hedingshan wind farm (before typhoon Saomai); (B) aerial view of the typhoon.

FIGURE 12.11 Damages to blades and tower due to hurricane Saomai.

Fig. 12.10A and B shows the Hedingshan wind farm in Zhejiang province (before the cyclone) along with the aerial photograph of the typhoon. The typhoon destroyed 28 wind turbine structures and blades which included five collapsed towers (600 kW turbines) with a total a loss of about 70 million RMB (Figs. 12.11–12.13).

12.4.3 Wave condition

Bohai Sea, Yellow Sea, and East and the South China Sea are connected to each other, in a bow shape from north to south along the China coastline. Tropical and subtropical monsoon climate also influence the wave height in China Sea. Thus, in Chinese offshore wind farm projects, sea waves are a major influence in the design. The wave height distribution in the South China Sea is variable owing to the large sea area. High wave heights occur in the north-east of the South China Sea and in the south-east of the Indo-China Peninsula, with wave heights of 2.4–2.6 m. The maximum significant wave height is however larger than 2.8 m in the west of the Luzon Strait. Comparatively, the significant wave

FIGURE 12.12 Damages to the connections due to hurricane Saomai.

FIGURE 12.13 Damages to the foundations due to hurricane Saomai.

height in the north is less than 2 m. Wave period ranges from 6 to 10 s. Table 12.5 shows the distribution of wave height and period for the Chinese waters.

12.5 Ground conditions in Chinese waters

Ground condition is fundamental in designing wind turbine foundations. Many elements should be considered: The depth of seawater, salinity content in ocean, and ground stiffness variation with depth. Generally, the ground condition in China Seas is not as stiff as that in North Europe. A summary of the ground conditions is given below.

12.5.1 Bohai Sea

The Bohai Sea is a low-lying land settled by North China Plain, where the soil consists of sediments brought from mountains and the Yellow River and is soft silty clay or clayey silt. The drilling of a borehole is the usual method used for underground geology surveys. There are many records of boreholes in the Bohai Sea and a typical profile (from top to bottom) is as follows:

1. Soft clay silt (Layer 1): The depth of this layer varies and is typically 0−7.4 m in the Western Bohai.
2. Mucky clay to silty clay (Layer 2): In this layer, the clay is changing from soft to stiff, with materials of mucky clay, silt, and loose sand. The depth of the clay layer varies (thickness 2.5−9.0 m in Western Bohai), center Bohai (thickness 4.0−10.0 m), Jinzhou (thickness 2.7−14.8 m), and Suizhong (thickness 0.8−5.8 m).
3. Combination of silty clay, clay, and loose sand (Layer 3). Again the thickness of this layer varies: 2.5−7.0 m in Western Bohai.

TABLE 12.5 Wave height and period in the Chinese waters.

China Sea	Region	Wave height (m)	Wave period (s)
Bohai Sea	Bohai Strait	1.2	4.8
	Others	<1	<4.5
Yellow Sea	North	1.2	5
	Center	1.4	5
	South	1.6	6
East China Sea	Shanghai coastline	1.6	6
	Zhejiang coastline	1.8	7
	Taiwan Strait	2.4	9
South China Sea	Luzon Strait	2.8	10
	Indo-China Peninsula	2.6	8
	Others	<2	6

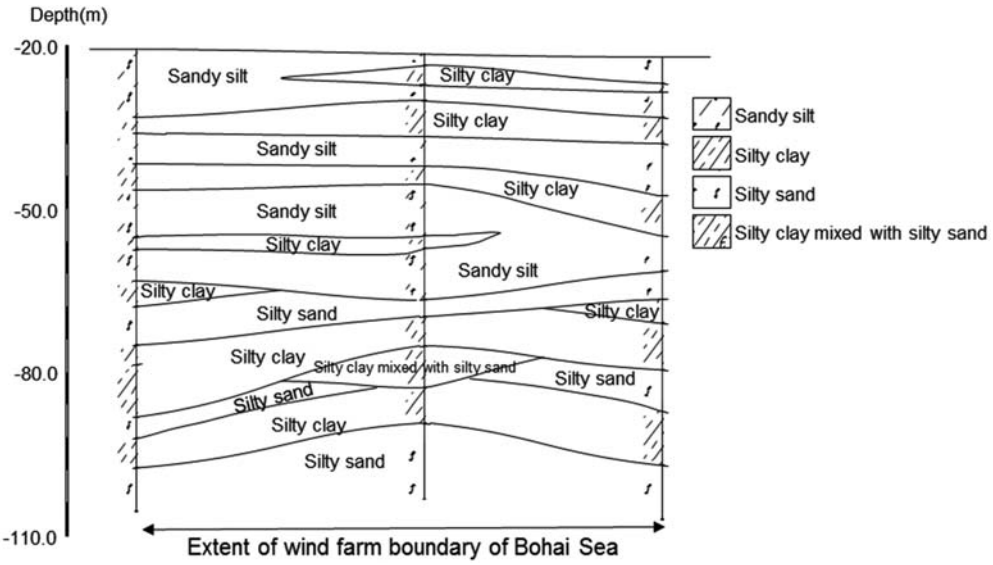

FIGURE 12.14 Ground profile in Bohai Sea wind farm.

4. Fine sand and silt: In this layer, the main material is fine sand, combined with silty sand and clay. The stiffness is that of medium-dense sand. The thickness in the western Bohai Sea is 4.0−15.0 m, in the center of Bohai it is 4.0−12.0 m, in Jinzhou it is 3.0−15.0 m and in Suizhong, it is 0−14.2 m.
5. Clay: In this layer, the clay is quite stiff and hard, combined with some silty clay. The thickness in western Bohai is 2.0−18.0 m, in the center of Bohai it is 3.0−15.0 m, in Jinzhou it is 3.0−17.0 m and in Suizhong it is 0−15.0 m.
6. Fine sand and silt.

In this layer, the main material is fine sand, combined with silty clay where the layer is thin. The stiffness is quite dense. The thickness in western Bohai is 5.0−11.0 m, in the center of Bohai it is 6.0−15.0 m, in Jinzhou it is 7.0−15.0 m and in Suizhong it is 12.0−18.0 m.

A typical ground profile for Bohai Sea is given in Fig. 12.14 and it is clear that the ground is variable. On the other hand, Figs. 12.15 and 12.16 show ground profiles for the Yellow Sea and Fujian Sea, respectively. It is evident that the ground profiles are variable which calls for detailed site investigation to minimize risks during construction.

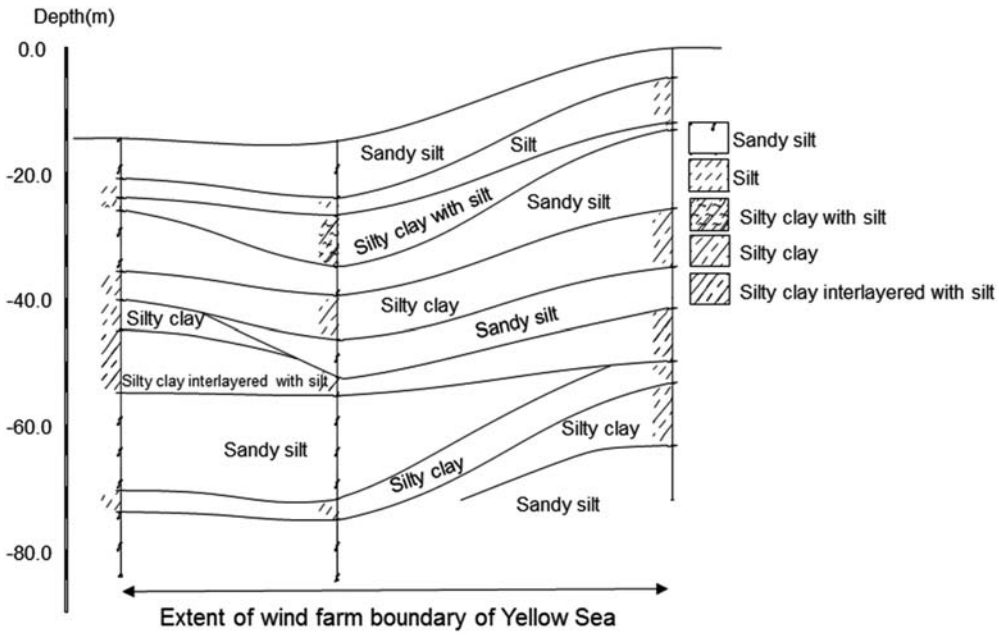

FIGURE 12.15 A section of a ground profile in the Yellow sea showing the extreme geology.

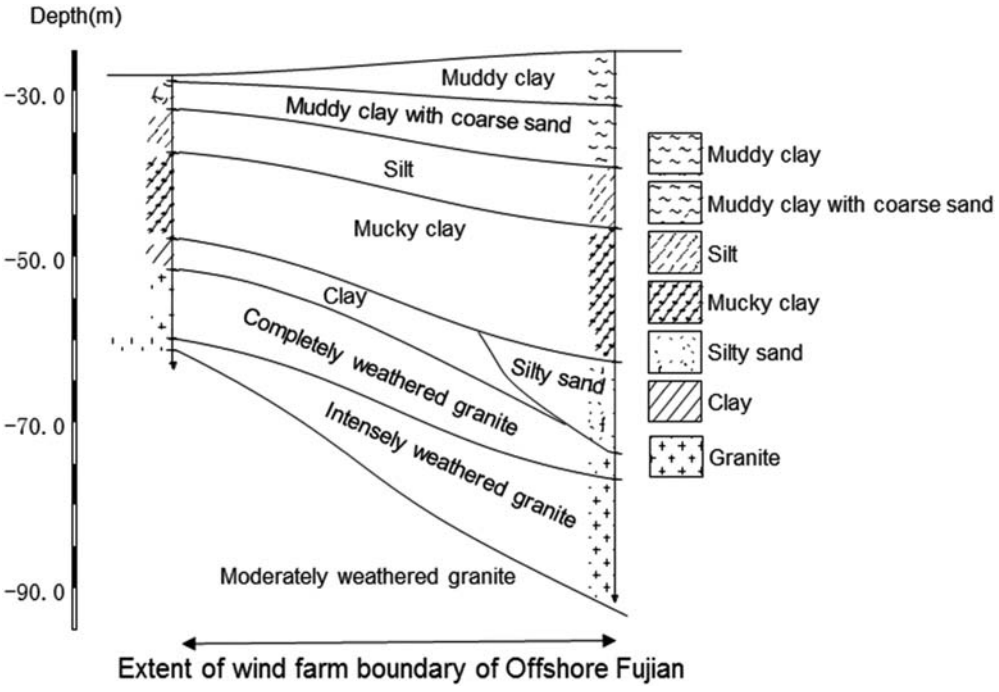

FIGURE 12.16 Ground profile in offshore Fujian sea (Taiwan Strait).

Multilayering soft marine sediments are also widely formed in the regions in and adjacent to the East China Sea [15,16]. A typical ground profile in the East China Sea is illustrated in Fig. 12.17.

Table 12.6 shows the multilayered ground profile in the South China Sea. A general observation can be made that the ground profile in Chinese Waters is variable and it shows the importance of a comprehensive site investigation.

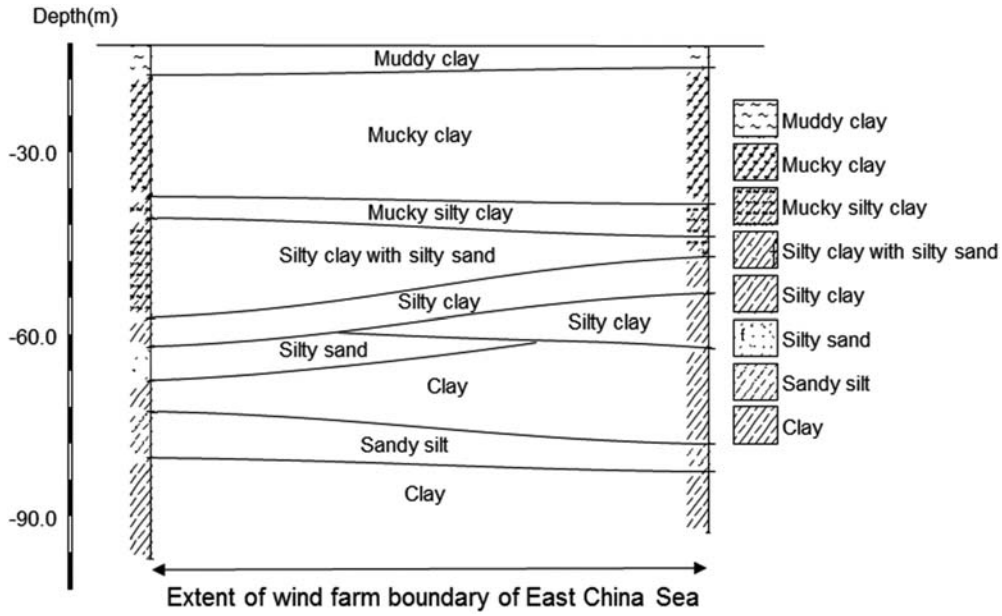

FIGURE 12.17 A section of the ground profile in the East China Sea.

TABLE 12.6 A typical ground profile in the South China Sea.

Position no.	Depth (m)	Soil
1	0–4.2	Silty clay
	4.2–19.4	Laminated soil
	19.4–40.0	Silty clay
2	0–3.0	Sandy soil
	3.0–7.4	Silty clay
	7.4–27.0	Laminated soil
	27.0–35.3	Silty clay
3	0–1.9	Silty clay
	1.9–2.6	Silty sand
	2.6–5.5	Silty clay
	5.5–9.0	Sandy soil
	9.0–15.0	Laminated soil
	15.0–39.8	Silty clay
4	0–1.5	Sandy soil
	1.5–4.9	Silty clay
	4.9–7.0	Silty sand
	7.0–12.7	Laminated soil
	12.7–25.4	Silty clay
	25.4–40.6	Sandy soil

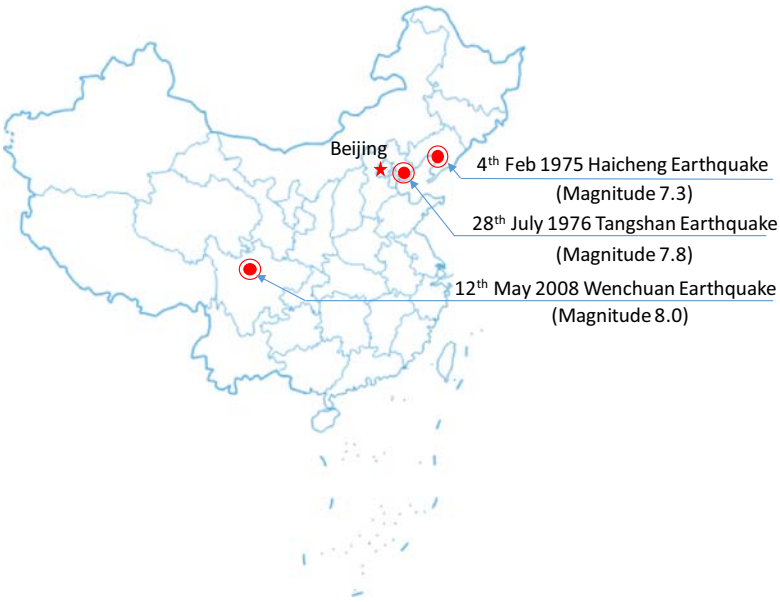

FIGURE 12.18 Location of three major earthquakes in China.

12.6 Seismic effects

Fig. 12.18 shows the map of China, which includes three major earthquake locations. It is of interest to note that the location of the earthquakes of 4th Feb 1965 Haicheng and 28th July 1976 Tangshan were close to the Bohai Sea. The effect of an earthquake on a wind turbine structure can be summarized as follows:

1. Loose to medium dense sandy soil around the foundation may liquefy which will affect the behavior of the foundation. In the case of monopile foundations not having sufficient embedment in nonliquefiable soil beneath the liquefiable soil, there may be a settlement which may cause tilting or in extreme situations a bearing failure. The time period of the wind turbine structure will increase owing to liquefaction and the structure will shift away from the predominant frequency of the earthquake causing higher displacement at the nacelle level.
2. Clay soils may soften depending on the layering/ground profile and the earthquake type. It may either attenuate or amplify the motion experienced by the structure.
3. Behavior of intermediate soils, that is, sandy silt or silty sand or silty clay under seismic loading is difficult to predict and advanced element tests and characterization are required. Cyclic triaxial tests can be carried out to assess the liquefaction potential of the soils.

12.7 A note on serviceability limit state design criteria

Serviceability criteria will be defined based on the tolerance requirements for the operation of the wind turbine and are often described as "turbine manufacturer requirements." Ideally, these should be turbine specific, that is, size and the hub height, gear boxed, or direct drive. Typically, these tolerances are specified in some codes of practice (e.g., DNV) or a design specification supplied by the client which may be dictated by the turbine manufacturer. Some of the specific requirements are:

1. Maximum allowable rotation at pile head after installation. DNV code specifies a 0.25-degree limit on "tilt" at the nacelle level.
2. Maximum accumulated permanent rotation resulting from cyclic and dynamic loading over the design life.

12.7.1 An example of a method to predict the required foundation stiffness

For a wind farm, it has been estimated that the maximum moment at the mudline level is 125 MN m and if the allowable tilt is 0.25 degrees at the foundation level, one can therefore estimate the rotational foundation stiffness required as given by Eq. (12.1):

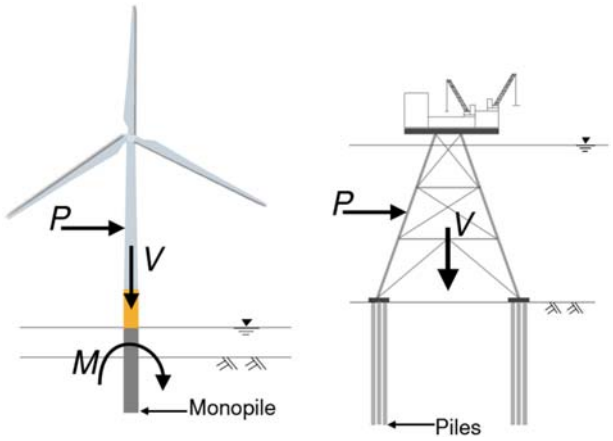

FIGURE 12.19 Monopile supported wind turbine and piles supported oil and gas platform.

$$K_R = \frac{125\ \text{MNm}}{4.36 \times 10^{-3}\text{rad}} = 28.6\ \text{GNm/rad} \tag{12.1}$$

This is a very large number and would require a large diameter monopile or equally alternative multiple pod foundations. In this context, it may be mentioned that SLS criteria impact the foundation design and thereby costs. It has been reported that floating wind turbines are allowed to tilt by up to ± 5 degrees in the worst sea states. Therefore, it is necessary to understand the stringent criteria of 0.25 degrees for a grounded wind turbine system. A value of 0.25 degrees represents a horizontal deflection of 450 mm for a typical 80 m tower. Clearly, a less stringent tilt criterion will save on foundation costs and installation time and make wind energy cheaper.

12.8 Challenges in analysis of dynamic soil-structure interaction

OWTs are new types of offshore structures and are unique in their features. The most important difference with respect to oil and gas installation structures is that they are dynamically sensitive (as explained in Section 12.2) and moment-resisting. Fig. 12.19 shows a typical monopile-supported wind turbine and a pile-supported fixed offshore jacket structure. There are, however, obvious differences between those two types of foundations. Piles for offshore structures (such as oil and gas platforms) are typically 60−110 m long and 1.8−2.7 m in diameter and monopiles for OWTs are commonly 30−40 m long and 3.5−6 m in diameter. Degradation in the upper soil layers resulting from cyclic loading is less severe for offshore oil and gas platform piles which are significantly restrained from pile head rotation, whereas monopiles are free-headed. The commonly used design method using a beam on nonlinear Winkler springs ("p-y" method in API code or DNV code) may be used to obtain pile head deflection under cyclic loading, but its use is limited for wind turbines because:

1. The widely used API model is calibrated against response to a small number of cycles (maximum 200 cycles) of flexible piles for offshore fixed platform applications. In contrast, for a real OWT, 10^7-10^8 cycles of loading are expected for the rigid piles over a lifetime of 20−25 years.
2. Under cyclic loading, the API or DNV model always predicts the degradation of foundation stiffness in sandy soil. However, recent work by Bhattacharya and Adhikari [17], Cuellar et al. [18], and Leblanc [19] suggested that the foundation stiffness for a monopile in sandy soil will actually increase as a result of densification of the soil next to the pile.
3. The ratio of horizontal load (P) to a vertical load (V) is very high in OWTs when compared with fixed jacket structures.

While OWT structures are designed for an intended life of 25−30 years, little is known about their long-term dynamic behavior under millions of cycles of loading. While it is possible to monitor existing OWT installations at a reasonable cost, full-scale testing is very expensive. An alternative method is to carry out carefully planned scaled dynamic testing to understand the scaling/similitude relationships which can be later used for interpretation of the experimental data and also for scaling up the results to real prototypes. There are mainly two approaches to scale up the model test results to prototype consequences: first is to use standard tables for scaling and multiply the model observations by the scale factor to predict the prototype response and the alternative is to study the underlying

mechanics/physics of the problem based on the model tests recognizing that not all interactions can be scaled accurately in a particular test. Once the mechanics/physics of the problem are understood, the prototype response can be predicted through analytical and/or numerical modeling in which the physics/mechanics discovered will be implemented in a suitable way. The second approach is particularly useful to study the dynamics of OWTs as it involves complex dynamic wind-wave-foundation-structure interaction and none of the physical modeling techniques can simultaneously satisfy all the interactions to the appropriate scale. Ideally, a wind tunnel combined with a wave tank on a geotechnical centrifuge would serve the purpose but this is unfortunately not feasible. It is recognized that not all physical mechanisms can be modeled adequately and therefore those need special consideration while interpreting the test results. As dynamic soil structure interactions of wind turbines are being studied, stiffness of the system is a top priority. Bhattacharya et al. [4,5,20] carried out experimental testing of a 1:100 scaled wind turbine to characterize the free dynamics of the system and to study the long-term behavior under the action of the dynamic loading.

The following conclusions could be reached from the study:

1. The change in natural frequencies of the wind turbine system may be affected by the choice of foundation system, that is, deep foundation or multiple pods (symmetric or asymmetric) on shallow foundations. Deep foundations such as monopiles will exhibit sway-bending mode, that is, the first two vibration modes are widely spaced—typical ratio is 4−5. However, multiple pod foundations supported on shallow foundations (such as tetrapod or tripod on suction caisson) will exhibit rocking modes in two principle planes (which are of course orthogonal). Fig. 12.20 shows the dynamic response of monopile-supported wind turbine and tetrapod foundation plotted in the loading spectrum diagram.
2. The natural frequencies of wind turbine systems change with repeated cyclic/dynamic loading. In the case of strain-hardening sites (such as loose to medium dense sandy sites) the natural frequency is expected to increase and for strain-softening sites (such as normally consolidated clay) [21−23] the natural frequency will decrease.
3. The results showed that the multipod foundations (symmetric or asymmetric) exhibit two closely spaced natural frequencies corresponding to the rocking modes of vibration in two principle axes. Furthermore, the corresponding two spectral peaks change with repeated cycles of loading and they converge for symmetric tetrapods but not for asymmetric tripods. From the fatigue design point of view, the two spectral peaks for multipod foundations broaden the range of frequencies that can be excited by the broadband nature of the environmental loading (wind and wave)

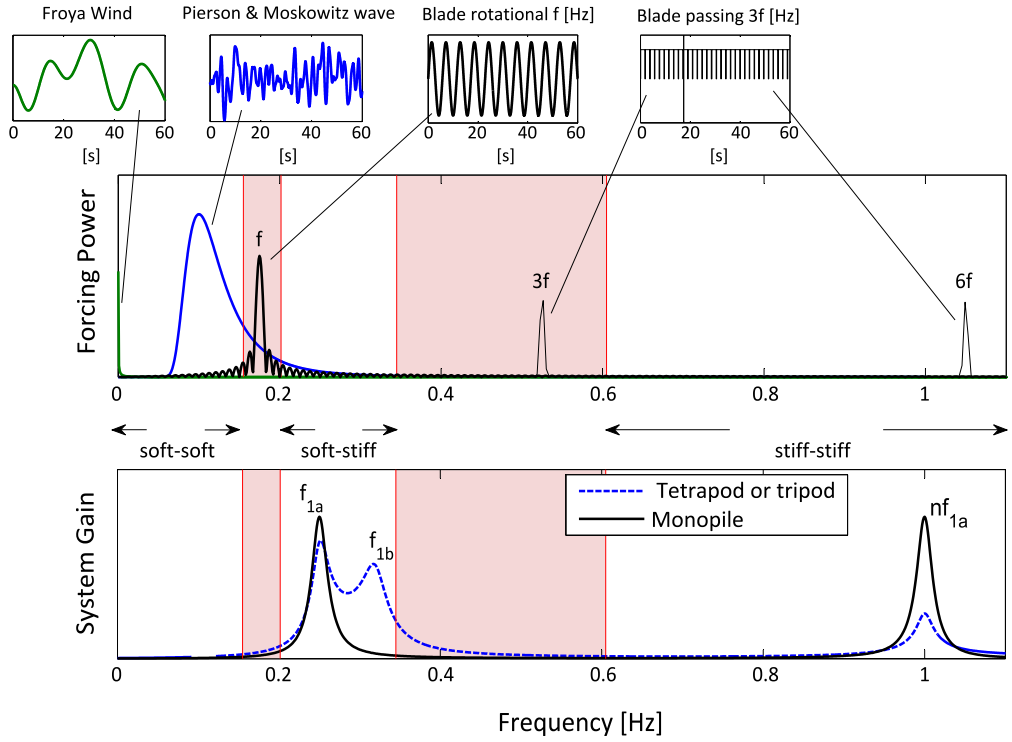

FIGURE 12.20 Relationship between effect of natural frequency of tripod and monopile on the forcing frequencies.

thereby impacting the extent of motions. Thus the system lifespan (number of cycles to failure) may effectively increase for symmetric foundations as the two peaks will tend to converge. However, for asymmetric foundations, the system life may continue to be affected adversely as the two peaks will not converge. In this sense, designers should prefer symmetric foundations to asymmetric foundations.

12.9 Foundation design

While design guidelines are available for offshore oil and gas installation foundations, its direct extrapolation/interpolation to OWT foundation design is not always possible, the reasons which are explored in the earlier section. There are two reasons: (1) The foundations of these structures are moment resisting, that is, large overturning moments at the foundation which are disproportionately higher than the vertical load; (2) The structure is dynamically sensitive, and therefore fatigue is a design driver. This section, therefore, explores a simplified foundation design methodology that may be used during option engineering or preliminary design for foundations supporting OWTs.

1. Compute the maximum mudline bending moment considering the different load combinations. The overturning moments due to 1P (misalignment) and 3P (blade shadowing) may be neglected in this step.
2. Based on the allowable tilt criteria for the particular project, determine the foundation stiffness required as discussed in Section 12.6. This is the minimum stiffness that is required to satisfy the SLS.
3. It is then required to check the ULS criteria, that is, the foundation capacity. If the foundation is not adequate, the size must be increased.
4. The soil surrounding the foundations will be subjected to tens of millions of cycles of cyclic and dynamic loading of varying strain as well as varying frequency. It must be ensured that the soil remains in the linear elastic range so as not to alter the dynamic stiffness of the foundation. For detailed design, resonant column testing is recommended to find the threshold strains of the ground. Further details on the use of the threshold strain concept in monopile design can be found in the work by Lombardi et al. [24].
5. Beam on Nonlinear Winkler Model or Finite Element Analysis can be carried out and it must be ensured that the p-y curves in soil are within the linear elastic section at all depths. However, 3D Finite Element Analyses are recommended to understand the strains around the foundation.
6. It is now required to obtain the stiffness of the foundation to calculate natural frequency of the whole system to check where the overall system is placed: soft-soft, soft-stiff, or stiff-stiff (see Fig. 12.3). If the natural frequency is not acceptable, the design parameters such as foundation stiffness, tower stiffness, and mass may be altered so that the desired frequency is obtained. This is an iterative process.
7. The foundation stiffness may change over the lifetime of the wind turbine due to soil-structure interaction which will have an impact on the natural frequency of the system and tilt. If the ground is sandy site, the natural frequency is expected to increase and if it is a clay site, the natural frequency may decrease. If the site is layered (as often encountered in Chinese waters, see Figs. 12.14–12.17), the change in natural frequency cannot be ascertained a priory and depends on various factors including the geometry of layering. Engineers need to carry out calculations to predict the change in frequency which is also necessary to compute the fatigue loading.

12.9.1 Challenges in monopile foundation design and installation

Monopiles have been predominantly used to support wind turbine generators in water depths up to 30 m. However, there are discussions with regard to the use of monopiles in deeper water depths termed as "XL" monopile. Preliminary calculations suggest that 10 m diameter monopiles weighing 1200 t (where t refers to metric tonnes) may be suitable for 45 m water depth and of course dependent on ground conditions. However, the use is uncertain due to the following: (1) no codified cyclic design to predict long-term tilt; (2) lack of redundancy in foundation system and therefore chance of single-point failure; (3) Installation costs and lack of adequate specialized vessels; (4) Connection among the foundation, transition piece, and the tower. Some of these aspects are described below in further detail.

1. *Lack of redundancy*: Monopiles are "overturning moment" resisting structures and there are two main components: (1) overturning moment arising from the thrust acting at the hub level; (2) overturning moment due to the wave loading. Also, these two moments can act in two different planes and will vary constantly depending on the time of the day and time of the year. Monopiles are rigid piles and the foundation collapse can occur if the soil around the pile fails, that is, there would be rigid body movement. If the foundation starts to tilt, it is very expensive to rectify.

2. *Cyclic (rather dynamic) design of monopile:* The response of monopile under cyclic/dynamic load is not well understood and there is lack of guidance in codes of practice. If the cyclic design is incorrect, monopile can tilt in the long term. If the tilt is more than the allowable limit, the turbine may need a shutdown. Monopile design is usually (also wrongly) carried out using API design procedure calibrated for flexible pile design where the pile is expected to fail by plastic hinge.
3. *Issues related to installation of monopiles*: Large monopile installation requires suitable vessel availability as well as specialized heavy lifting equipment. Other issues are noise refusals, buckling of the pile tip, drilling out, and grouted connections. If the site contains weak rock (siltstone/sandstone/mudstone) and where the local geology shows bedrock or hard glacial soils at shallow depths, drive-drill-drive techniques may be required, with subsequent increases in cost and schedule. It must be mentioned here that driving reduces the fatigue life.

12.9.2 Jacket on flexible piles

There has been considerable interest in jacket-type structures for deeper water applications but are perceived to be expensive due to the amount of steel required. However, jackets supported on piles can be considered a safe solution due to the excellent track record of good performance in offshore oil and gas industry. Offshore oil and gas industry has been using long flexible piles (diameters up to 2.4 m) which are easy to drive and the necessary vessels are available (relatively as opposed to vessels to install monopiles). This aspect will drive down the time in construction costs regarding piling and also large vessels are not required for pile installation. However, there are costs associated with jacket installation. One of the requirements is the optimization of the jacket so as to consume minimum steel. There are two types of jacket: normal jacket and twisted jacket. The advantage of twisted jacket over normal jacket is fewer numbers of joints and therefore fewer fatigue issues.

12.10 Concluding remarks

OWTs are new types of offshore structures characterized by low stiffness (as a result flexible and have low natural frequency) and therefore sensitive to the dynamic loadings. Additional challenges are imposed on OWTs in China over and above those in North Sea, as the turbines in China are subjected to much harsher environmental loadings (particularly typhoons and earthquakes) and are founded on a softer and more complex multi-layering seabed. This chapter discusses the complexity involved in designing the foundation of these structures. It has been shown that design guidelines available for offshore oil and gas installation foundations cannot be direct extrapolated/interpolated to OWT foundation design. It is also highlighted that any extrapolation from the design experiences for wind turbine foundations in the North Sea to those in China should be treated with great caution.

References

[1] Guo Z, Yu LQ, Wang LZ, Bhattacharya S, Nikita G, Xing YL. Model tests on the long-term dynamic performance of offshore wind turbines founded on monopiles in sand. J Offshore Mech Arct Eng 2015;127(4) 041902-1-11.
[2] Adhikari S, Bhattacharya S. Dynamic analysis of wind turbine towers on flexible foundations. Shock Vib 2012;19:37–56.
[3] Adhikari S, Bhattacharya S. Vibrations of wind-turbines considering soil-structure interaction. Wind Struct—An Int J 2011;14:85–112.
[4] Bhattacharya S, Cox J, Lombardi D, Muir Wood D. Dynamics of offshore wind turbines supported on two foundations. Geotech Eng: Proc ICE 2012 2012;166(2):159–69.
[5] Bhattacharya S, Nikitas N, Garnsey J, Alexander NA, Cox J, Lombardi D, et al. Observed dynamic soil–structure interaction in scale testing of offshore wind turbine foundations. Soil Dyn Earthq Eng 2012;54:47–60.
[6] Arany L, Bhattacharya S, Macdonald J, Hogan SJ. Simplified critical mudline bending moment spectra of offshore wind turbine support structures. Wind Energy 2015;18:2171–97. Available from: https://doi.org/10.1002/we.1812.
[7] Burton T, Jenkins N, Sharpe D, Bossanyi E. Wind energy handbook. Chichester, West Sussex: John Wiley & Sons, Ltd.; 2001.
[8] Bhattacharya S. Challenges in design of foundations for offshore wind turbines. Wiley; 2019.
[9] DNV (Det Norske Veritas). Guidelines for design of wind turbines. 2nd ed. London: DNV; 2002.
[10] Shadlou M, Bhattacharya S. Dynamic stiffness of monopiles supporting offshore wind turbine generators. Soil Dyn Earthq Eng 2016;15–32. Available from: https://doi.org/10.1016/j.soildyn.2016.04.002.
[11] Laszlo A, Bhattacharya S, Macdonald J, Hogan SJ. Design of monopiles for offshore wind turbines in 10 steps. Soil Dyn Earthq Eng 2017;92:126–52. Available from: https://doi.org/10.1016/j.soildyn.2016.09.024 ISSN 0267-7261.
[12] Wang LZ, Yu LQ, Guo Z, Wang ZY. Seepage induced soil failure and its mitigation during suction caisson installation in silt. J Offshore Mech Arct Eng 2014;126 011103-1-11.
[13] Carter JMF. North Hoyle offshore wind farm: design and build. Energy: Proc Inst Civ Eng EN1 2007;160(1):21–9.

[14] Li LL, Dan HB, Wang LZ. Undrained behaviour of natural marine clay under cyclic loading. Ocean Eng 2011;38(16):1792–805.
[15] Hong Y, Ng CWW, Chen YM, Wang LZ, Chan VSY. Field study of down drag and drag load of bored piles in consolidating ground. J Perform Constr Facil 2015; ASCE.10.1061/(ASCE)CF.1943-5509.0000790, 04015050.
[16] Ng CWW, Hong Y, Liu GB, Liu T. Ground deformations and soil-structure interaction of a multi-propped excavation in Shanghai soft clays. Géotechnique 2012;63(12):912–1007.
[17] Bhattacharya S, Adhikari S. Experimental validation of soil–structure interaction of offshore wind turbines. Soil Dyn Earthq Eng 2011;31 (5–6):805–16.
[18] Cuéllar P, Georgi S, Baeßler M, Rücker W. On the quasi-static granular convective flow and sand densification around pile foundations under cyclic lateral loading. Granul Matter 2012;14(1):11–25.
[19] Leblanc C. Design of offshore wind turbine support structures—selected topics in the field of geotechnical engineering. Denmark: Aalborg University; 2009.
[20] Bhattacharya S, Lombardi D, Muir Wood DM. Similitude relationships for physical modelling of monopile- supported offshore wind turbines. Int J Phys Model Geotech 2011;11(2):58–68.
[21] Wang LZ, He B, Hong Y, Guo Z, Li LL. Field tests of the lateral monotonic and cyclic performance of jet-grouting reinforced cast-in-place piles. J Geotech Geo-environ Eng, ASCE 2015;141(5):06015001.
[22] He B, Wang LZ, Hong Y. Capacity and failure mechanism of laterally loaded jet-grouting reinforced pile: field and numerical investigation. Sci China Technol Sci 2015;59(5):763–76.
[23] He B, Wang LZ, Hong Y. Field testing of one-way and two-way cyclic lateral responses of single and jet-grouting reinforced piles in soft clay. Acta Geotech 2016 [provisionally accepted].
[24] Lombardi D, Bhattacharya S, Muir Wood D. Dynamic soil-structure interaction of monopile supported wind turbines in cohesive soil. Soil Dyn Earthq Eng 2012;49:165–80.

This page intentionally left blank

Chapter 13

Numerical methods for soil-structure interaction analysis of offshore wind turbine foundations

Susana Lopez-Querol[1], **Liang Cui**[2] **and Subhamoy Bhattacharya**[2]

[1]*University College London, London, United Kingdom,* [2]*Department of Sustainability, Civil and Environmental Engineering, University of Surrey, Guildford, London, United Kingdom*

13.1 Introduction

Offshore wind turbine installation is a unique type of structure due to its geometry (i.e., mass and stiffness distribution along the height) and the cyclic/dynamic loads acting on it. There are four main loadings on the offshore wind turbine: wind, wave, 1 and 3P, see Fig. 13.1. Each of these loads has unique characteristics in terms of magnitude, frequency, and the number of cycles applied to the foundation. The loads imposed by the wind and the wave are random in both space (spatial) and time (temporal) and therefore, they are better described statistically. Apart from the random nature,

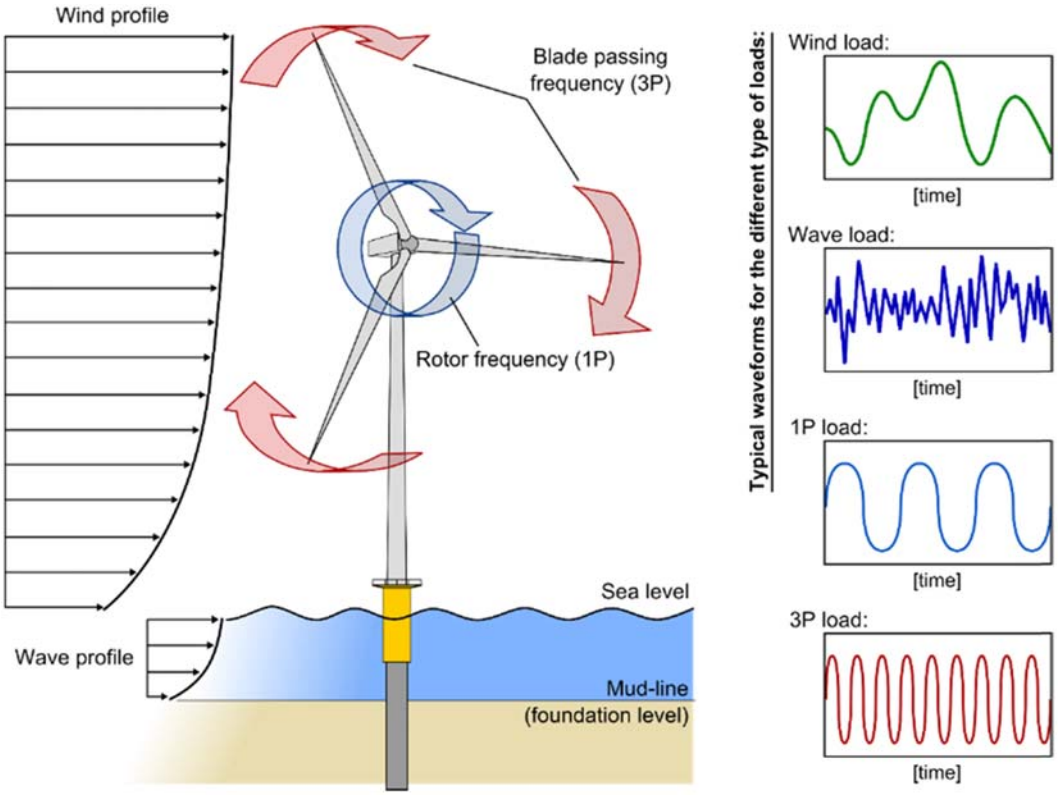

FIGURE 13.1 External loads acting on an offshore wind turbine, along with their typical waveforms.

Wind Energy Engineering. DOI: https://doi.org/10.1016/B978-0-323-99353-1.00003-7

these two loads may also act in two different directions. 1P loading is caused by mass and aerodynamic imbalances of the rotor and the forcing frequency equals the rotational frequency of the rotor. On the other hand, 2P/3P loading is caused by the blade shadowing effect and is simply two or three times the 1P frequency. Fig. 13.1 shows the typical waveforms of the four types of loads. On the other hand, Fig. 13.2 presents a schematic diagram of the main frequencies of the loads together with the natural frequency of two Vestas V90 3 MW wind turbines from two wind farms: Kentish Flats and Thanet (United Kingdom).

Fig. 13.3 describes schematically the mechanism to be considered at the design stage guided by Limit State Design philosophy. A commentary on the diagram is given below.

1. Ultimate Limit State (ULS): the first step in the design is to estimate the maximum loads on the foundations (predominantly overturning moment, lateral load, and the vertical load) due to all possible design load cases and compare them with the capacity of the chosen foundation. For monopile type of foundations, this would require computation of ultimate moment, lateral and axial load carrying capacity.
2. Target Natural Frequency (Eigen Frequency) and Serviceability Limit State (SLS): this requires the prediction of the natural frequency of the whole system (Eigen Frequency) and the deformation of the foundation at the mudline level (which can be further extrapolated to the hub level) over the lifetime of the wind turbine.
3. Fatigue Limit State and long-term deformation: this would require predicting the fatigue life of the monopile as well as the effects of long-term cyclic loading on the foundation.
4. Robustness and ease of installation: This step will ascertain that the foundation can be installed and there is adequate redundancy in the system.

One of the major uncertainties in the design of offshore wind turbines is the prediction of long-term performance of the foundation, i.e., the effect of millions of cycles of cyclic and dynamic loads on the foundation. The three main long-term design issues are:

1. Whether or not the foundation will tilt progressively under the combined action of millions of cycles of loads arising from the wind, wave and 1P (rotor frequency) and 2P/3P (blade passing frequency). It must be mentioned that if the foundation tilts more than the allowable, it may be considered failed, based on SLS (SLS) criteria and may also lose the warranty from the turbine manufacturer. The loads acting on the foundation are typically one-way cyclic and many loads are also dynamic in nature. Further details of the loading can be found in Arany et al. [1].

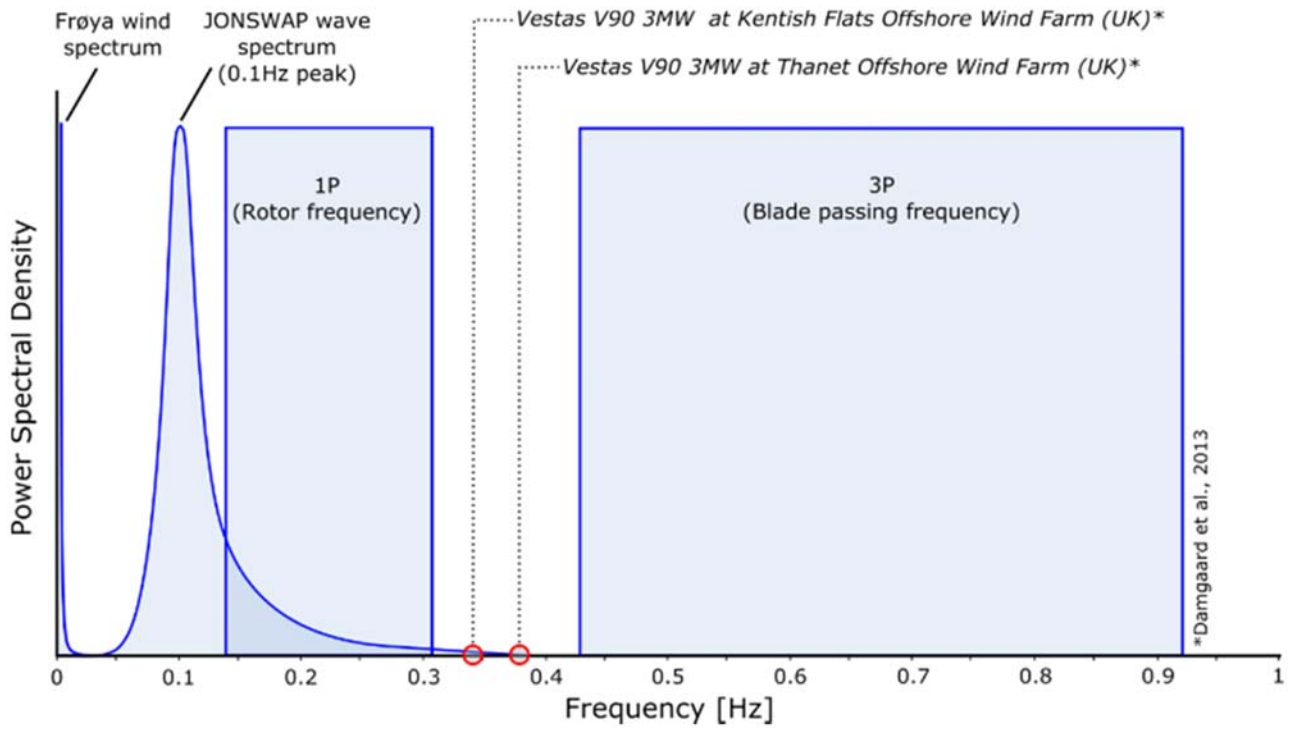

FIGURE 13.2 Forcing frequencies plotted against power spectra densities for Vestas V90 3 MW wind turbines.

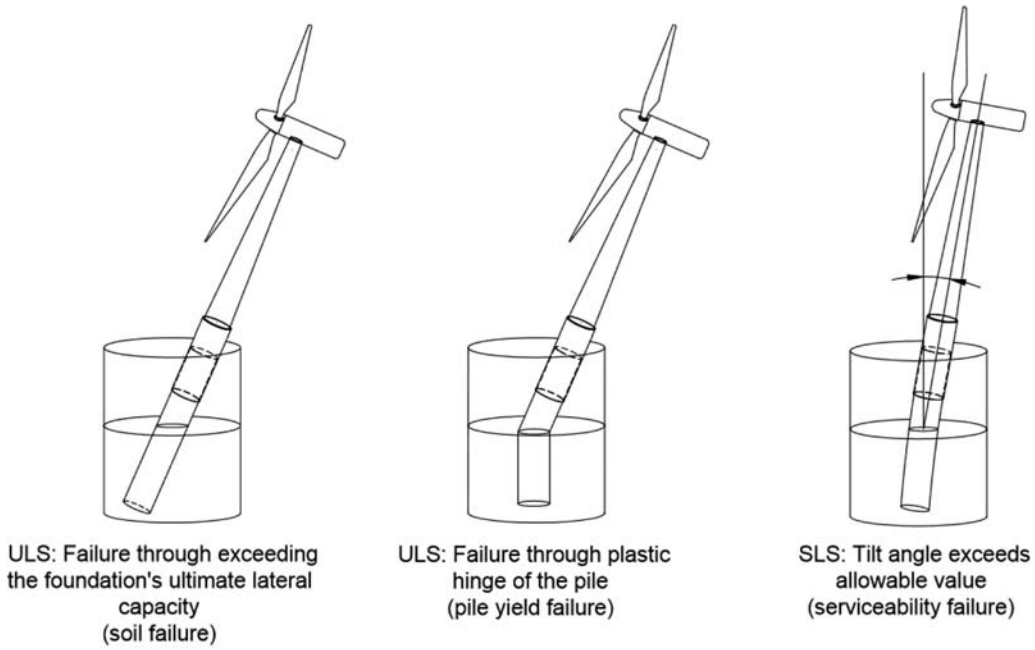

FIGURE 13.3 Examples of ULS and SLS failure [1].

2. It is well known from the literature that repeated cyclic or dynamic loads on a soil cause a change in the properties which in turn can alter the stiffness of the foundation, see Bhattacharya and Adhikari [2] and Bhattacharya [3]. A wind turbine structure derives its stiffness from the support stiffness (i.e., the foundation) and any change in natural frequency may lead to the shift from the design/target value and as a result, the system may get closer to the forcing frequencies. This issue is particularly problematic for soft-stiff design (i.e., the natural or resonant frequency of the whole system is placed between the upper bound of 1P and the lower bound of 3P) as any increase or decrease in natural frequency will impinge on the forcing frequencies and may lead to unplanned resonance. This may lead to loss of years of service, which is to be avoided.
3. Predicting the long-term behavior of the turbine takes into consideration wind and wave misalignment aspects [4,5].

The SLS and ULS modes of failure are schematically described in Fig. 13.3. ULS failure (which can also be described as collapse) can be of two types: (1) where the soil fails; (2) where the pile fails by forming a plastic hinge [6,7]. On the other hand, in SLS failure, the deformation will exceed the allowable limits. While the ULS calculations can be carried through standard methods, the SLS calculations and long-term issues require a detailed understanding of the Cyclic Soil-Structure Interaction as well as Dynamic Soil-Structure Interaction.

Fig. 13.4 shows a typical mudline bending moment acting on a wind turbine. Typically, in shallow to medium deep waters, the wind thrust loading at the hub will produce the highest cyclic overturning moment at the mudline. However, the frequency of this loading is extremely low and is in the order of magnitude of 100 s (see Fig. 13.4). Typical period of wind turbine structures is in the range of about 3 s; therefore, no resonance of structure due to wind turbulence is expected resulting in *cyclic* soil-structure interaction [8,9].

On the other hand, the wave loading will also apply overturning moment at the mudline and the magnitude depends on water depth, significant wave height, and the peak wave period. Typical wave periods will be in the order of 10 s (for the North Sea) and will therefore have *dynamic* soil-structure interaction. A calculation procedure was developed by Arany et al. [1] and the output of such a calculation will be relative wind and the wave loads; an example is shown in Fig. 13.4. It is assumed in the analysis that the wind and the wave are perfectly aligned which is a fair assumption for deeper water further offshore projects (i.e., fetch distance is high). Analysis carried out by Arany et al. [1] showed that the loads from 1 and 3P are orders of magnitude lower than wind and wave but they will have the highest dynamic amplifications. The effect of dynamic amplifications due to 1 and 3P will be small amplitude vibrations. Resonance has been reported in operational wind farms in the German North Sea, see Hu et al. [10]. Furthermore, there are added soil-structure interactions due to many cycles of loading and wind-wave misalignments. Typical estimates will suggest that offshore wind turbine foundations are subjected to 10−100 million load cycles of varying amplitudes over their lifetime

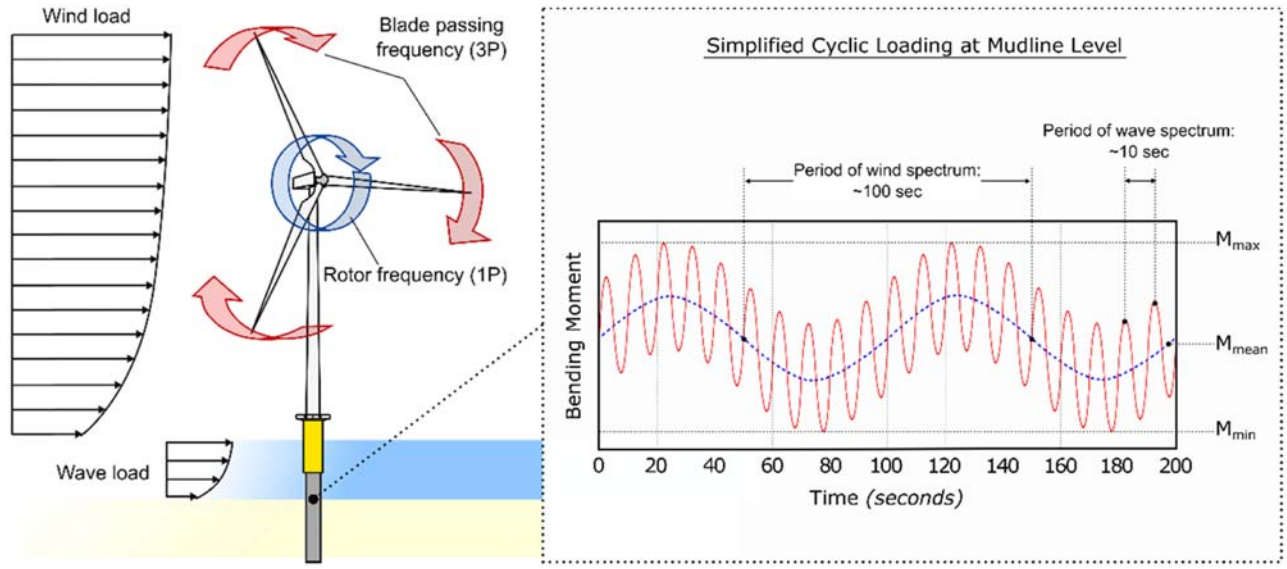

FIGURE 13.4 Loads acting on a typical offshore wind turbine foundation and typical mudline moment.

(25−30 years). The load cycle amplitudes will be random/irregular and have broadband frequencies ranging several orders of magnitudes from about 0.001−1 Hz.

Based on the discussion above, the soil-structure interaction can be simplified into two superimposed cases and is discussed below:

1. Cyclic overturning moments (typical frequency of 0.01 Hz) due to lateral loads of the wind acting at the hub. This will be similar to a "*fatigue type*" problem for the soil and may lead to strain accumulation in the soil giving rise to progressive tilting. Due to wind and wave load misalignment, the problem can be bi-axial. For example, under operating conditions, for deeper water and further offshore sites, wind−wave misalignment will be limited for most practical scenarios. Wave loading, on the other hand, will be moderately dynamic as the frequency of these loads are close to the natural frequency of the whole wind turbine system (typical wind turbine frequency is about 0.3 Hz).
2. Due to the proximity of the frequencies of 1, 3P, wind, and wave loading to the natural frequency of the structure, resonance in the wind turbine system is expected and has been reported in German Wind farm projects [10,11]. This resonant dynamic bending moment will cause strain in the pile wall in the fore-aft direction which will eventually be transferred to the soil next to it. This resonant type mechanism may lead to compaction of the soil in front and behind the pile (in the fore-aft direction).

Deformation of the pile under the action of the loading described in Fig. 13.4 will lead to three-dimensional soil-pile interactions, as shown schematically in Fig. 13.5. Simplistically, there would be two main interactions: (1) due to pile bending (which is cyclic in nature) and the bending strain in the pile will transfer (through contact friction) strain in the soil which will be cyclic in nature; (2) due to lateral deflection of the pile there will be strain developed in the soil around the pile. Fig. 13.5 shows a simple methodology to estimate the levels of strains in a soil for the two types of interactions and is given by Eq. (13.1) and Eq. (13.2). The average strain in the soil at any section in a pile due to deflection can be estimated using Bouzid et al. [12] as follows:

$$\gamma = 2.6\frac{\delta}{D_P} \tag{13.1}$$

where δ is the pile deflection at that section (e.g., A-A in Fig. 13.5) and D_P is the pile diameter.

On the other hand, the shear strain in the soil next to the pile due to pile bending can be estimated using Eq. (13.2).

$$\gamma_1 = \frac{M \times D_P}{2 \times I \times E_P} \tag{13.2}$$

where M is the bending moment in the pile, I is the second moment of area of the pile, and E_P is the Young's Modulus of the pile material. It must be mentioned that Eq. (13.2) assumes that 100% of the strain is transmitted to the soil

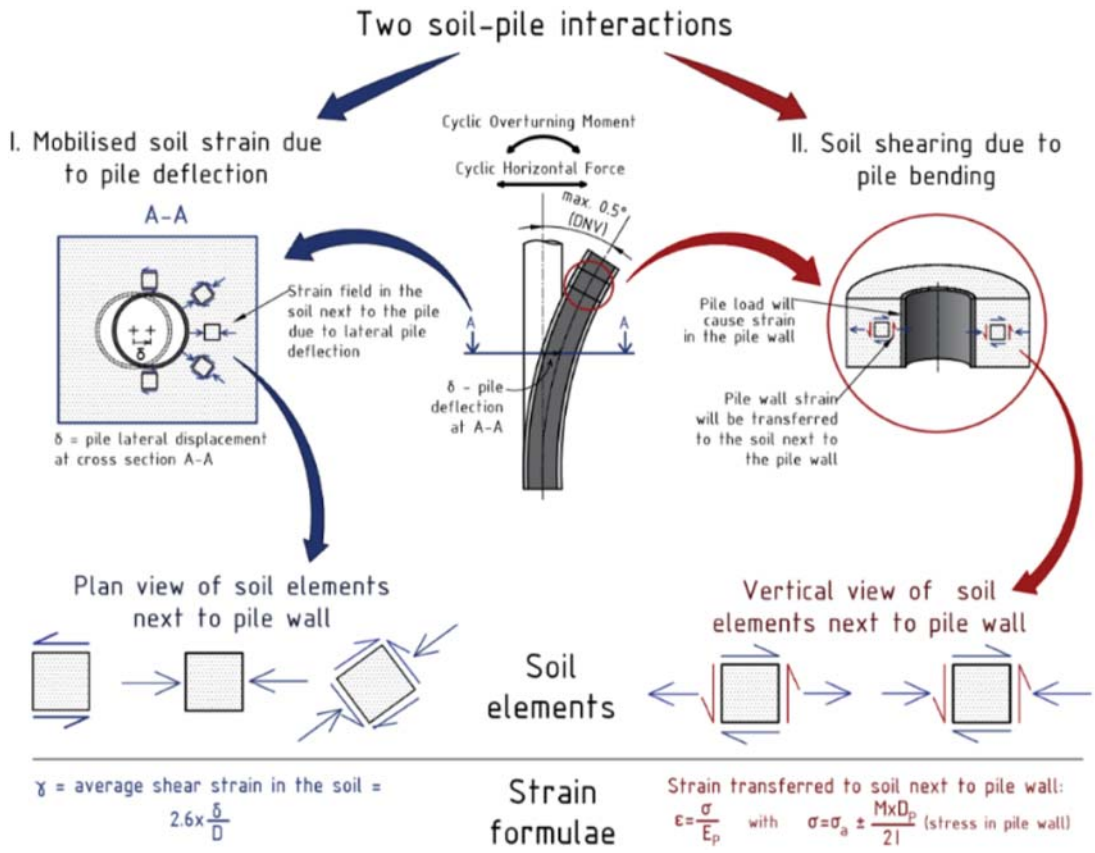

FIGURE 13.5 Two types of soil-pile interaction on a monopile-supported wind turbine.

which is a conservative assumption and calls for further study. In practice, this will be limited to the friction between the pile and the soil.

13.1.1 Need for numerical analysis for carrying out the design

The previous section showed a simplified procedure to estimate Soil-Structure Interaction (SSI). However, this approach is grossly oversimplified and has limitations in the sense that the changes in soil properties due to cyclic loading cannot be considered. Also, whether or not the foundation will progressive tilt cannot be studied. While the two simple interaction phenomena (i.e., due to pile bending and to lateral deflection of the pile) are taken into consideration, other aspects, such as interface opening (gap formation) or possible impacts between pile and soils during the dynamic loading cannot be accounted for. Moreover, the nature of dynamic loadings is complicated due to the wind wave misalignment. These considerations make it necessary to use numerical simulations which allow one to precisely define the geometry of the problem and can also encompass different types of soils. Furthermore, changes in the behavior of the soil surrounding the pile are expected to occur as a consequence of the repetition of cycles. Advanced constitutive models, suitable to reproduce different aspects of cyclic/dynamic behavior, are therefore required for analysis. Classical elastic-plastic models cannot estimate the accumulation of plastic volumetric strains due to the repetition of cycles (densification). Therefore, advanced constitutive laws capable of simulating the plastic strains in soils not due to the magnitude of the loading, but due to the repetition of cycles are needed [13–15].

13.2 Types of numerical analysis

Different types of numerical analysis ranging from very simple and practical to more theoretical and standardized can be carried out depending on the application. The methods can be classified into three groups: (1) Simplified where closed form solutions are used and useful during the conceptual and financial feasibility stage; (2) Standard method where code-based calculations are carried out. In the context of monopile, the standard analysis is the p-y analysis

(nonlinear Beam on Winkler Foundations), Winkler [16]; (3) Advanced analysis which requires specialist knowledge and expertise. In the detailed design stage, advanced analysis is necessary to predict the long-term prediction. This chapter aims to present advanced numerical models that are suitable to model the SSI [17].

13.2.1 Standard method based on beam on nonlinear Winkler spring

The American Petroleum Institute (API) code prescribes a methodology known as "*p-y" method* which is widely used for design of offshore piles. This is a subgrade modulus method with nonlinear depth-dependent load−deformation characteristics representing the pile-soil interaction. This procedure is calibrated to provide the worst-case scenario for the foundation behavior under static and cyclic loading. The *p-y* curve has been adopted in most offshore standards (like API, 2007; GL, 2005; DNV, 2004 or ISO) as it has been considered, for many years, as the best method available to determine the displacements of the head of the pile under various loading conditions. Fig. 13.6 represents a typical $p-y$ curve and in the Figure, from *a* to b, an increase in the loading carries an increasing rate of degradation. This nonlinear behavior can be determined empirically or using field tests, under either static or monotonic loading conditions. On the other hand, Fig. 13.6B shows the degradation suffered by the soil as the pile deflection increases [19−21].

Terzaghi [22] demonstrated that the linear relationship between p and y (from the origin to *a* in Fig. 13.6A) was only valid for values of p lower than a half of the ultimate bearing capacity of the soil [22]. This criterion is assumed in the construction of the $p-y$ curves by many methodologies. API (2007) [23] takes into account a number of factors for the construction of the curves, which can be summarized as follows:

- Type of soil: Basically either sandy or clayey material, considering their different properties.
- Type of loading: Monotonic or cyclic loading.

Some other aspects, such as the effects of pile installations on the soils and the scour, are taken into account, although it is fully recognized that these factors require further analysis and research.

The main limitations of this API (2007) are:

- The $p-y$ curve is a procedure verified for piles up to 2 m diameter [19] and this is one of the main limitations of this methodology, as the monopiles in OWT currently have diameters of around 6 m. Extrapolation of a calibrated method is not advisable in geotechnical engineering. Achmus and Abdel-Rahman [19] demonstrated that $p-y$ curve underestimates the deflections of piles, compare to some numerical simulations. Other researches also demonstrate that $p-y$ curve overestimates the pile-soil stiffness for large diameter piles [24].
- The nonlinear behavior expected for very high loads in large diameter piles is not covered by this methodology, because the calculated displacements are small if related to the pile diameter (although they can be very big in absolute terms) [19].
- When the piles are installed in layered soil, the material is taken as continuous and the interaction between the different layers is neglected. This limitation does not occur when the curves are derived on the basis of full-scale tests [18].
- The subgrade reaction coefficient, k, does not contain any effect related to the flexural stiffness of the pile or the type of loading.

Computational simulations are the alternative to overcome those limitations. Different trends in these methodologies and few worked-out examples are presented next, in order to address their suitability and reliability.

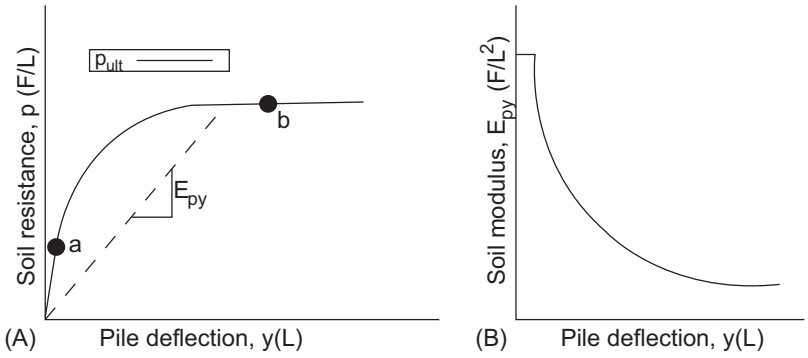

FIGURE 13.6 Examples of $p-y$ curves [18].

13.2.2 Advanced analysis (finite element analysis & discrete element modeling) to study foundation-soil interaction

13.2.2.1 Different soil models used in finite element analysis

To account for accumulated strains in the numerical simulations, it is necessary to employ a suitable constitutive model, capable of reproducing realistic soil behavior when subjected to cyclic/dynamic loading conditions. Simple elastoplastic models are usually based on one yield surface without hardening (e.g., the Mohr−Coulomb model), with isotropic hardening (e.g., the Cam−Clay model), or on two yield surfaces (isotropic loading and deviatoric loading) for example, Lade's. They are ideal and efficient in simulating the soil behavior under monotonic conditions but are not suitable to model cyclic loading. Essentially, in such models, plastic deformations start to appear for a certain magnitude of loading, usually higher than the amplitude of the cycles, and hence, the simulated soil behavior remains elastic under that limit, which is against experimental evidences, particularly for granular soils [25]. Fig. 13.7 shows the different phenomena which can take place in the soil during cyclic loading.

The plastic phenomenon for cyclic loading can either be based on "constant stress amplitude" (so-called stress controlled) or "constant strain amplitude" (strain controlled). The phenomenon called "adaptation" refers to less dissipation of energy in each cycle of loading as the number of cycles increases, until convergence to nondissipative elastic cycles. On the other hand, "accommodation" refers to the change of the dissipation of energy from the beginning with an irreversible cumulative deformation and evolves toward a stabilized cycle. This is experienced in laboratory experiments for drained samples. "Ratcheting" is an irreversible strain accumulation that keeps the same shape as that of the beginning [25].

Constant strain amplitude cyclic loading phenomenon results in the cyclic hardening or softening. Cyclic hardening occurs when there is an increase in the cyclic stress amplitude with an increase in the number of cycles, for example, densification during testing of drained soil. On the contrary, cyclic softening occurs when there is a reduction in the cyclic stress amplitude as the number of cycles increases, for example, an increase in pore pressure during the testing of undrained soil samples (decrease in the effective stress).

In one of the examples presented in this chapter, a kinematic hardening law has been employed by coupling the elastic moduli and a hardening parameter. Kinematic hardening is used to model plastic ratcheting, which is the buildup of plastic strain during cyclic loading, as previously explained. Other hardening behaviors include changes in the shape of the yield surface in which the hardening rule affects only a local region of the yield surface, and softening behavior in which the yield stress decreases with plastic loading. The kinematic hardening model only involves one plastic

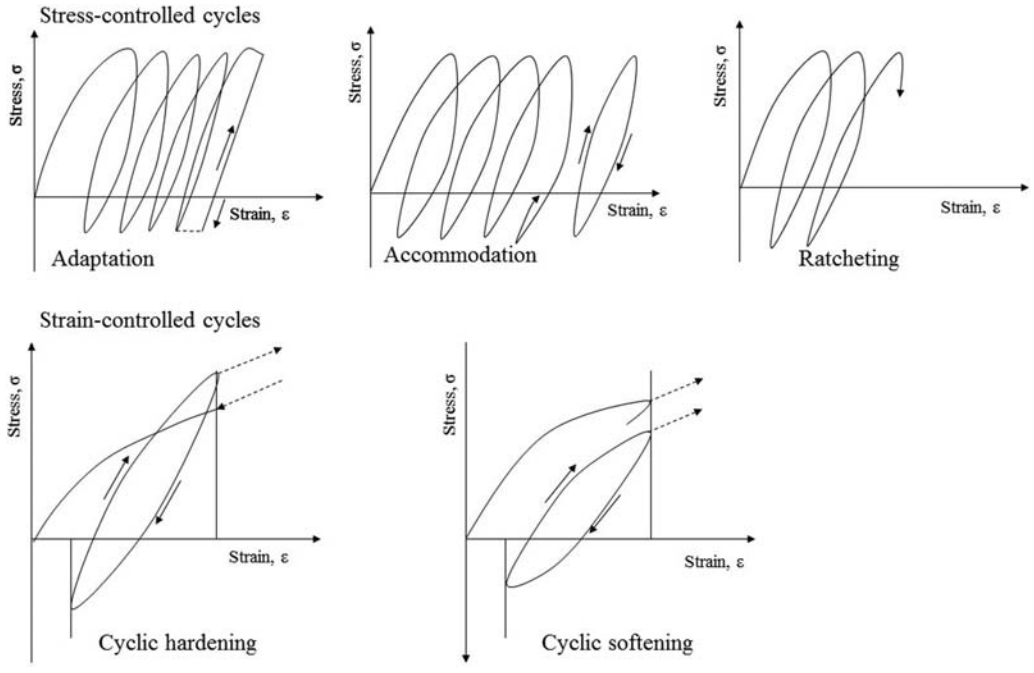

FIGURE 13.7 Different cyclic behaviors after [25].

mechanism with a smooth yield surface. For nonlinear modeling, the material behavior is characterized by an initial elastic response, followed by plastic deformation and unloading from the plastic state. The plasticity is a result of the microscopic nature of the material particles and includes shear loading that causes particles to move past one another, changes in void or fluid content that result in volumetric plasticity, and exceeding the cohesive forces between the particles or aggregates. The material is defined by model materials subject to loading beyond their elastic limit. See Refs. [25,26] for more details.

13.2.2.2 Discrete element model analysis basics

Originally proposed by Cundall and Strack [26], the Discrete Element Method (DEM) simulates granular materials as assemblies of individual particles which respond to given load conditions. The interactions between particles are simulated by contact laws, for example, linear contact model, Hertz–Mindlin contact model Mindlin and Deresiewicz [27], and parallel bond model, where the normal and tangential contact forces are dependent on the overlap and relative displacement between two contact particles. The contact forces, accelerations, velocities, and displacements of all particles are updated in each small time-step using the central difference time integration method (Fig. 13.8). Stresses and strains are then calculated from the contact forces within a representative volume element or along a boundary. The DEM is superior to other numerical methods (e.g., FEM) as it allows the direct monitoring of change in soil stiffness, and more importantly, it offers a method to analyze the micromechanics, which underlies the stiffness changes. Fig. 13.9 shows a flowchart of a typical DEM calculation.

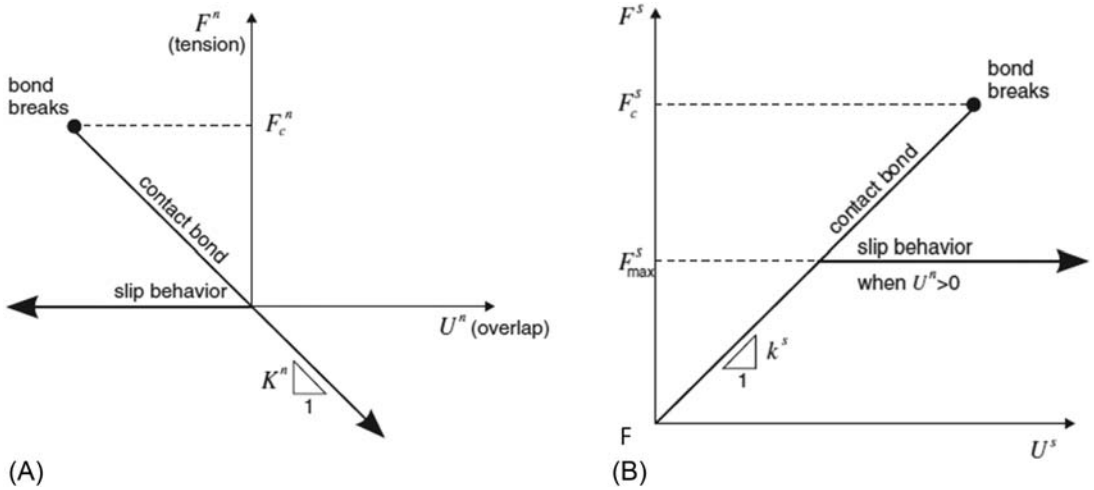

FIGURE 13.8 Force–displacement behavior for contact occurring at a point Itasca [28]: (A) Normal component of contact force and (B) shear component of contact force.

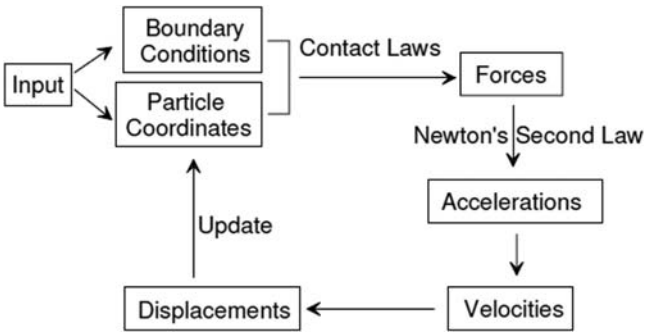

FIGURE 13.9 Flowchart to illustrate the calculation cycles performed in discrete element simulations.

13.3 Example application of numerical analysis to study soil-structure interaction of monopile

This section of the chapter shows different applications of numerical analysis to investigate phenomena related to long-term performance as explained in Section 13.1.

13.3.1 Monopile analysis using discrete element method

An analysis of monopile-soil interactions and stiffness variations was carried out using an open-sourced DEM code modified and validated in previous studies (Cui) [29], Cui et al. [30], O'Sullivan et al. [31]. More details can be found in Cui and Bhattacharya [32]. A DEM model of a soil tank (100 mm × 100 mm × 50 mm) was first created, which was filled with about 13,000 spherical particles of radii in the range of 1.1−2.2 mm. The particles were deposited under gravity. The pile was 20 mm in diameter and was embedded to a depth of 40 mm by removing particles located in the space which was to be occupied by the pile. Particles were allowed to settle down again following the installation of the pile. Once the soil particles were settled down in the soil tank, cyclically horizontal movements were assigned to the pile to simulate the cyclic movements of the OWT mono-pile due to the cyclic loadings. Translational movements rather than rotational movements were assigned to the pile at this stage. Three different strain amplitudes, 0.1%, 0.01%, and 0.001%, were chosen to examine the effects of strain levels. For each strain amplitude, two types of cyclic loading were applied: symmetric cyclic loading with stains in the ranges of (−0.1%, 0.1%), (−0.01%, 0.01%) and (−0.001%, 0.001%) and asymmetric cyclic loading with stains in the ranges of (0, 0.2%), (0, 0.02%), and (0, 0.002%). As constrained by the computational costs, 500 cycles were simulated for strain amplitude of 0.1%, and 1000 cycles were simulated for other strain amplitudes. The simulation parameters are listed in Table 13.1.

The resultant horizontal stress applied on the pile versus the horizontal strain of soil is illustrated in Fig. 13.10. It can be observed that the stress−strain curves form hysteresis loops, indicating the energy dissipations during the cyclic loading. It is also interesting to observe that, though the stresses in the first half cycle for the asymmetric cyclic loading is positive, it is reduced to negative when the strain goes to zero. Following a few cycles, the minimum negative stress approaches the same magnitude as the maximum positive stress. Moreover, the magnitude of stresses and the shape of the hysteresis loops for both symmetric cyclic loading and asymmetric cyclic loading are almost identical after many cycles. The system under asymmetric cyclic loading behaves the same as symmetric cyclic loading with the same strain amplitude after many cycles, indicating that the strain amplitude, rather than the maximum strain, dominate the long-term cyclic behavior.

The secant Young's Modulus of soil in each cycle was calculated by determining the slope of a line connecting the maximum and minimum points of each full loop and is shown in Fig. 13.11. It is evident that the secant Young's Modulus of soil increased during the cyclic loading. The initial stiffness of asymmetric cyclic loading is lower than that of symmetric cyclic loading with the same strain amplitude due to the higher maximum strain applied. However, following a few cycles, the stiffness for both types of cyclic loading approaches the same value. The Young's Modulus versus horizontal strain in the first half cycle and in the 500th cycle for strain amplitude of 0.1% is shown in Fig. 13.12. The stiffness-strain curve in the first cycle displays the similar "S" shape as expected for the shear modulus-shear strain curve. Following cyclic loadings, stiffness at different strain levels all increases significantly.

TABLE 13.1 Input parameters for DEM simulation.

Parameters	Value
Soil particle density ρ_s (kg/m^3)	2650
Particle sizes (mm)	1.1, 1.376, 1.651, 1.926, 2.2
Interparticle frictional coefficient μ	0.3
Particle-boundary frictional coefficient μ	0.1
G_s (Hertz-Mindlin contact model)	2.868×10^7
Poisson's ratio	0.22
Initial void ratio e	0.539

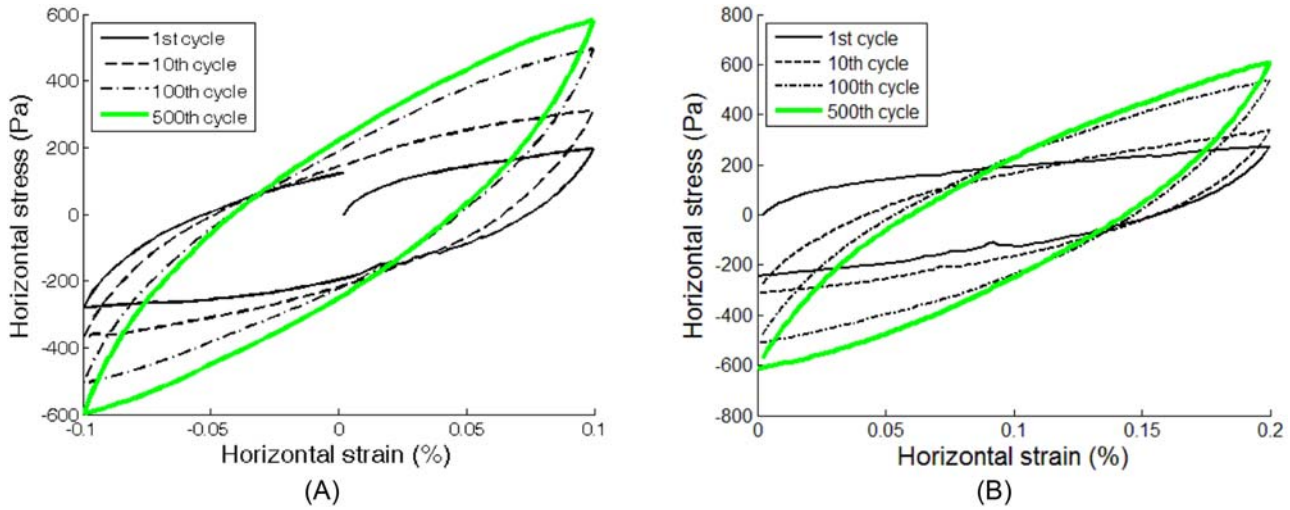

FIGURE 13.10 Hysteresis loops formed by stress−strain curves during cyclic loadings: (A) strain (−0.1%, 0.1%) and (B) strain (0, 0.2%).

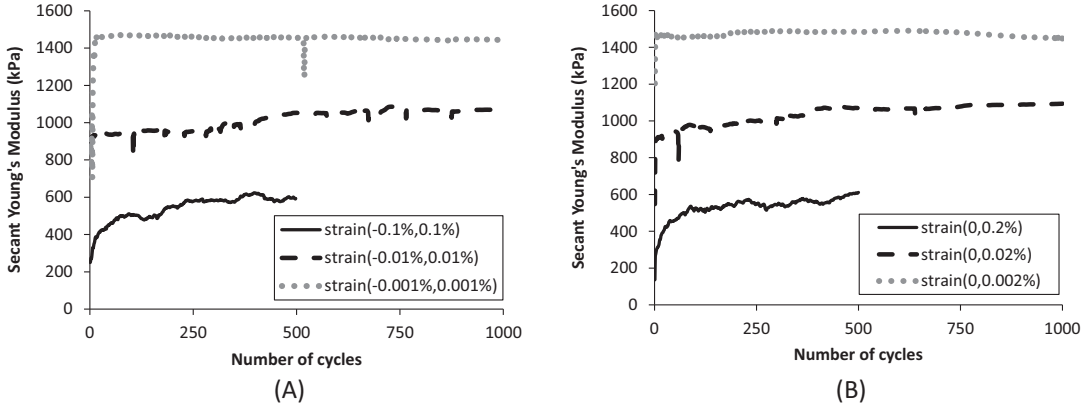

FIGURE 13.11 Secant Young's Modulus of soil at the end of each cycle: (A) symmetric loading and (B) asymmetric loading.

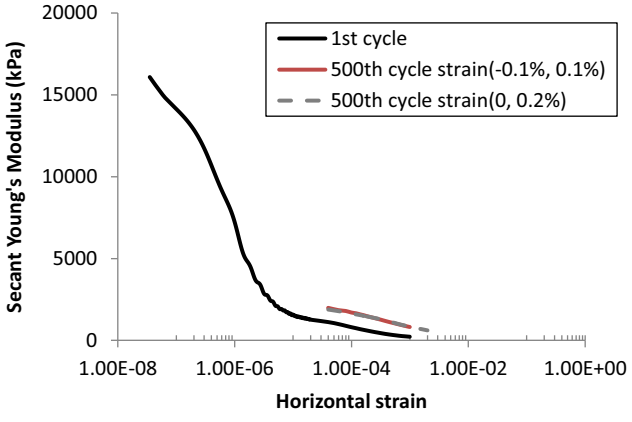

FIGURE 13.12 Secant Young's Modulus versus horizontal strain.

To illustrate the ground settlement, plots of incremental soil particle displacements in the symmetric cyclic loading with strain amplitude of 0.1% in the first 50 cycles and in the next 50 cycles are given in Fig. 13.13. Each arrow in the plot starts from the original center of a particle and ends at the new center at the end of a given cycle. It is evident that

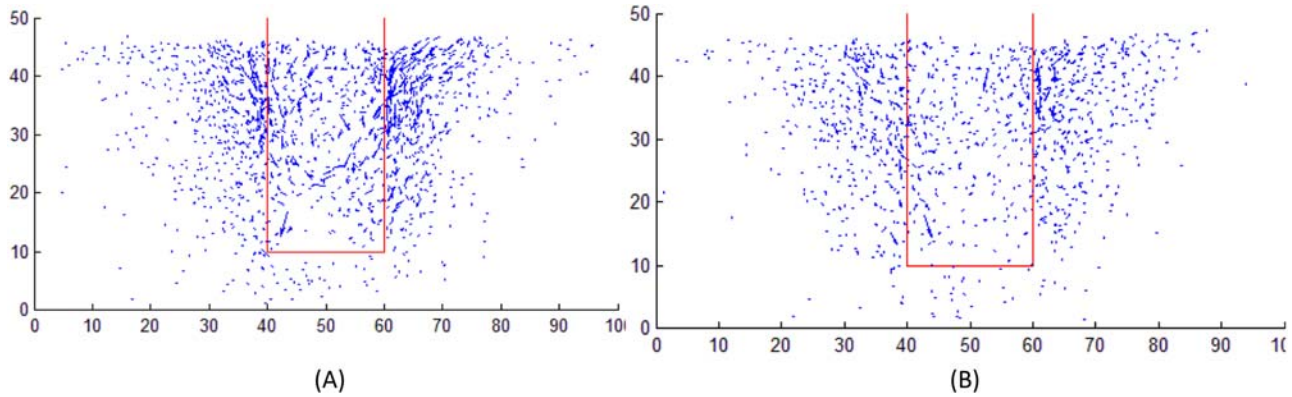

FIGURE 13.13 Incremental soil displacements at the end of the given cycle (Unit: mm): (A) symmetric loading and (B) asymmetric loading.

soil particles surrounding the pile moved downwards, causing ground settlement. Soil densification around the pile is the main reason causing the increase in soil stiffness. It is also clear that the soil particle displacements are only significant in the first 50 cycles, underlying the significant increase in the soil stiffness in the first 50 cycles. In the current DEM simulations, samples with same initial void ratio of 0.539 (medium dense sample) all showed densification behavior and stiffness increase under cyclic loading. It would be interesting to investigate soil behaviors and stiffness evolutions for a wide range of initial void ratios in future study.

The evolutions of average radial stress in representative cycles are illustrated in Fig. 13.14. Due to the soil densification, the radial stress increased significantly for strain amplitude of 0.1% under cyclic loading. The shapes of the radial stress−strain curves are quite different for different strain amplitudes. For symmetric cyclic loading with 0.01% strain amplitude (Fig. 13.14C), the radial stress increases at positive strain values but decreases slightly at negative strain values. However, for 0.1% strain amplitude (Fig. 13.14A), the radial stress increases at both positive and negative strains, forming a "butterfly" shaped curve. It is also interesting to observe that, for the asymmetric cyclic loading (Fig. 13.14B), the stress−strain response in the first few cycles is different from that in the correlated symmetric cyclic loading, However, it eventually evolves to the same "butterfly" shape after many cycles. It confirms again that the influence of different maximum strain of a cyclic loading can be eliminated after many cycles and the dominant factor for cyclic soil response is strain amplitude.

The evolution of unbalanced horizontal force at the end of each cycle is illustrated in Fig. 13.15. It is evident that the unbalanced horizontal force is more significant with increasing strain amplitude. It can also be seen that the unbalanced force for asymmetric cyclic loading is much larger in magnitude and is oriented in the opposite direction compared with that for symmetric cyclic loading. It is because, for asymmetric cyclic loading, the pile only moves to the right side and compresses the soils on the right side significantly; therefore, the horizontal force on the pile at the end of each cycle is oriented to the left. However, for the symmetric cyclic loading, the pile compressed the soils on both sides to the same strain level. At the end of a full cycle, the residual horizontal force is oriented to the right. In the presented study, monopile was driven to move by a predefined constant velocity. It is more realistic to simulate the free-motions of the monopile under the action of resultant external force/moment, including the interaction force/pressure between the monopile and the soil.

13.3.2 Monopile analysis using FEM using ANSYS software

This section of the chapter presents the analysis of a monopile embedded 30 m in a cylindrical soil layer (90 m wide, 45 m deep), see Fig. 13.16. The steel pile is open-ended with a wall thickness of 90 mm and a diameter of 7.5 m. It is worth noting that monopile diameters of up to 7 m are designed to maintain the serviceability of the wind energy converters over several years as a result of harsh environmental conditions offshore. The monopile extended 30 m above the sea bed to the point where it was loaded and driven 30 m into the sea bed where the water depth was 10 m. The software ANSYS 17.0 was used to create the three-dimensional model of wind turbine foundation. Static Structural Analysis was used to analyze static conditions, while the Transient Structural was used for the cyclic load.

The soil-pile model took advantage of the symmetry in geometry and load, hence, only one-half of the soil-pile model was modeled, as shown in Fig. 13.17 which means that the transversal displacements at the symmetry plane were set to zero. A fine mesh size was selected for the system as shown in Fig. 13.17 resulting in 50622 nodes and

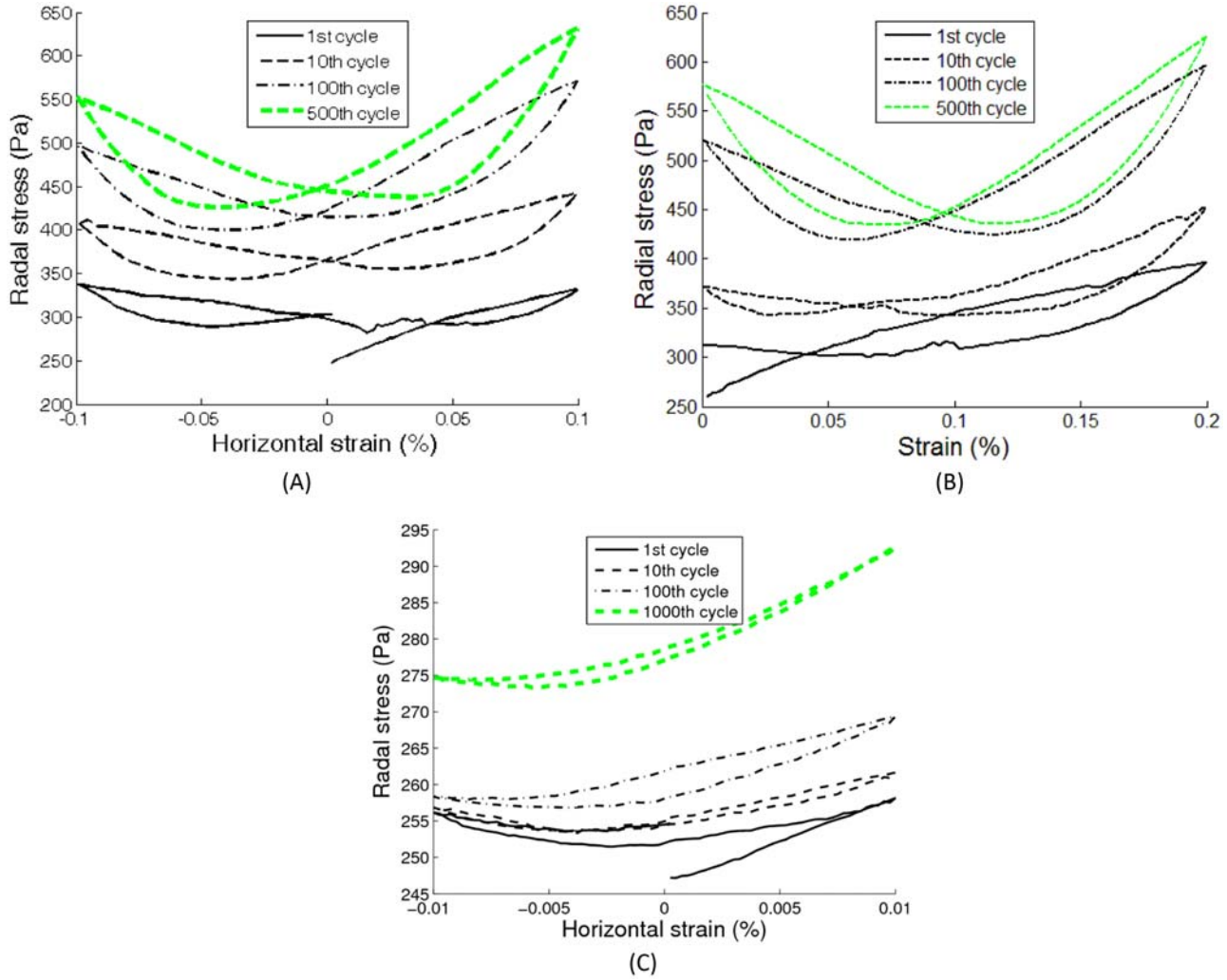

FIGURE 13.14 Evolution of average radial stresses in representative cycles: (A) strain (−0.1%, 0.1%), (B) strain (0, 0.2%), and (C) strain (−0.01%, 0.01%).

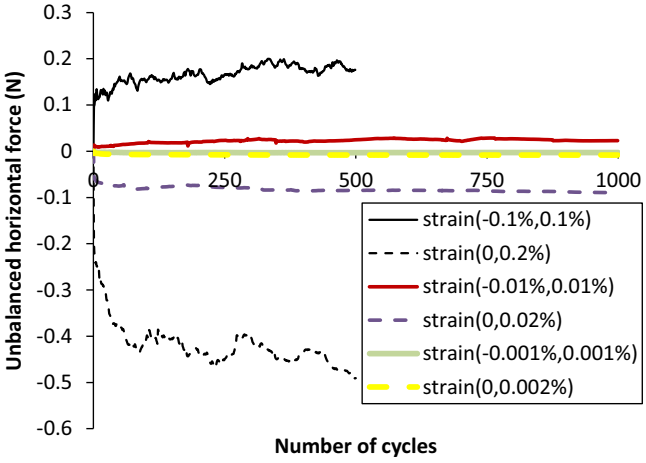

FIGURE 13.15 Evolution of unbalanced horizontal force on the pile at the end of each cycle.

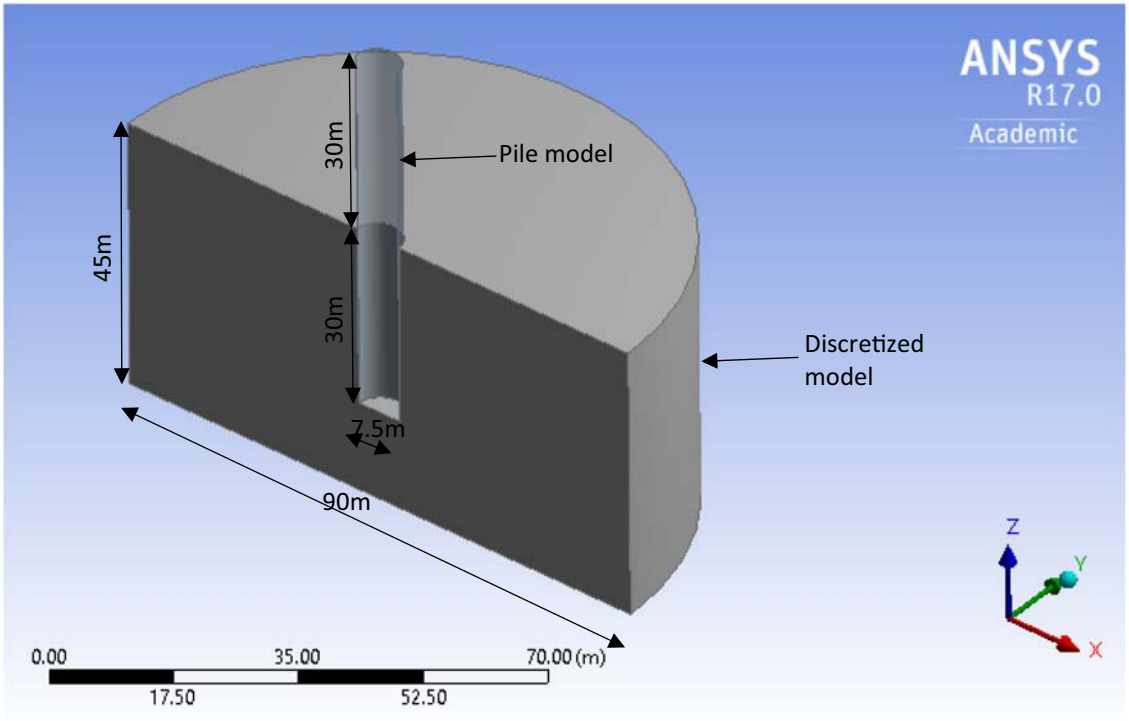

FIGURE 13.16 3D view of the monopile system.

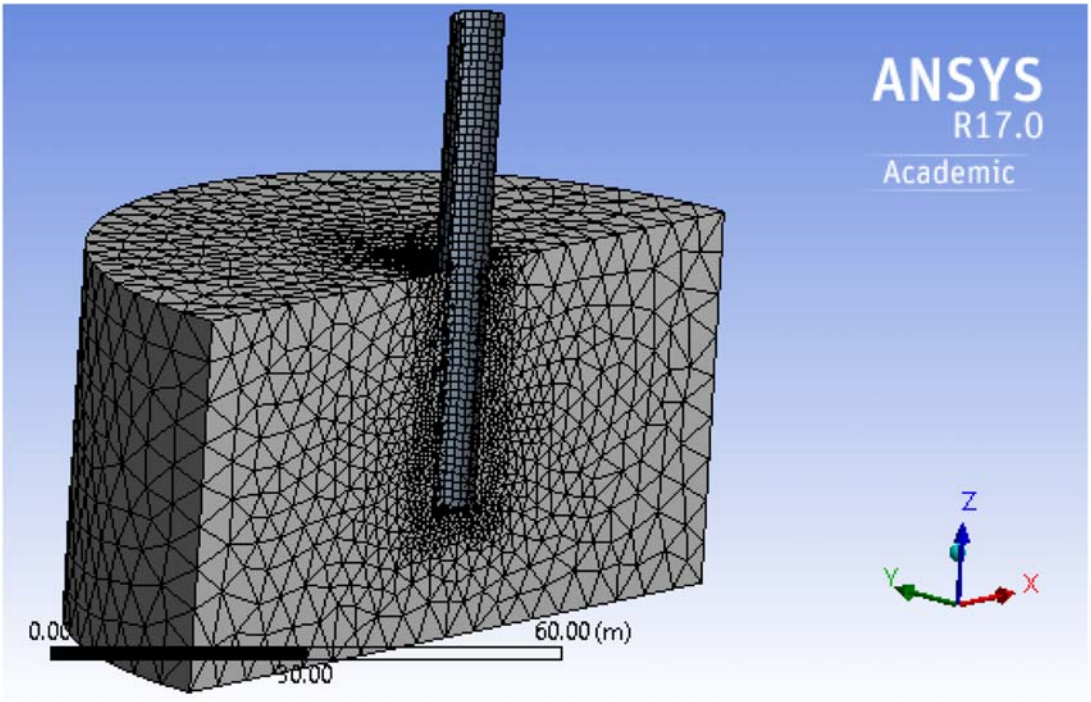

FIGURE 13.17 Mesh sizing of the system.

36816 elements. Previous studies demonstrated that the minimum number of elements required for an accurate enough model of monopile wind turbine foundations may be in the range of 30,000−40,000. The interaction between pile and structure was modeled as a frictional interface with a friction coefficient of 0.4.

The time step was taken as 0.5 s which was derived by the integration time step method [33]. The force was applied by an idealized system described by Bryne and Houlsby [34] with a generalized loading case for a 3.5 MW turbine in which a 4 MN horizontal load and a 6 MN vertical load applied 30 m above the soil surface were used. This can be represented as:

$$F(t) = F_{max}\sin(2\pi ft) \tag{13.3}$$

The one-way lateral load was applied with a sinusoidal character of 0.1 Hz (typical frequency ranges in these infrastructures are 0−1 Hz for environmental loads and 5−200 Hz for machine loads) [34]. A fixed end time, t of 1000 s was used, this gave one hundred cycles (frequency = 0.1 Hz) which was used in analyzing the results. The input parameters for the pile were calibrated for offshore installation in the United Kingdom using typical test results while those obtained after calibration for the soil are shown in Table 13.2. The steel monopile was represented as a linear-elastic, isotropic, homogeneous material. For the soil properties, the Kinematic Hardening law has been employed.

The elastic modulus of the soil was derived from Janbu (1963) as presented in Eq. (13.2):

$$E = 60\text{MPa} * \frac{5}{6} * \sqrt{2} * \left(\frac{\sigma_y}{\sigma_{at}}\right)^{\lambda} \tag{13.4}$$

where σ_y denotes the soil vertical effective stress, and σ_{at} is the atmospheric pressure.

The plot of the applied horizontal load versus the pile-head displacement for dynamic loading, $p-y$ (Fig. 13.18) shows a progressive inclination of the hysteretic loops, for every subsequent increase in the number of cycles, resulting in an increasing pile head displacement. A similar trend can be observed in the result reported by [13], although that analysis was carried out for a clayey soil under the influence of a two-way lateral loading, which resulted in equal but opposite pile displacements in both directions. This result trend can be referred to as accommodation cyclic behavior (previously presented in this paper) and is mostly found in laboratory experiments [25].

A closer observation of pile-head displacement (Fig. 13.19) shows an increase in displacement with time. This can be observed in drained cyclic tests with an increase in density (densification) [25]. However, instabilities caused by alternating degradation and compaction are observed in the earlier cycles, causing negative displacement accumulation at the initial stages of loading. The pile head displacement at the end of the 1st cycle equals 1.36 and 2.06 cm at the end of 100 cycles, which is the maximum displacement of the sea bed in front of the pile. This gives a total increased displacement of 0.7 cm. The accumulation rate from the 1st to the 100th cycle equals 1.51 cm. The displacement accumulation per cycle reduces drastically for the first 10 cycles, and then tends toward zero as the number of cycles increases because at deflections larger than that of static loading, the value of soil resistance, p, decreases sharply due to cyclic loading, while afterward it remains pretty much constant [18]. This is a result of the kinematic hardening

TABLE 13.2 Soil model material parameters for medium dense sand (after) [19].

Parameter	Symbol	Value
Oedometric stiffness parameter	κ	600
	λ	0.55
Poisson's ratio	Y	0.25
Unit buoyant weight (kN/m^3)	γ'	15.5
Internal friction angle (deg)	Ø′	35
Dilation angle (deg)	ψ	5
Cohesion (kN/m^2)	c	0.1
Yield surface parameter	α	0.127
Yield surface parameter (kPa)	k	1.8
Plastic potential	β	$4.05*10^{-2}$
Hardening law (MPa)	C D	22 1200

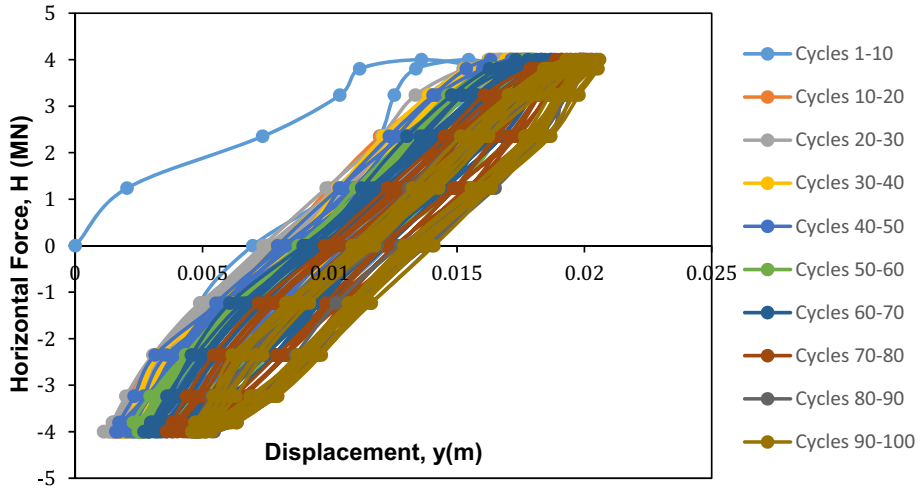

FIGURE 13.18 $p-y$ curve obtained from harmonic loading.

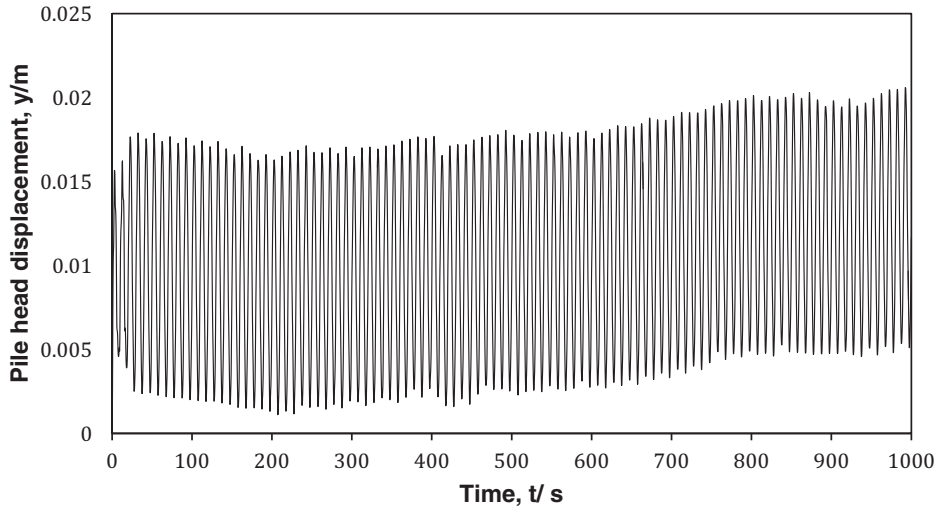

FIGURE 13.19 Plot of pile head displacement with time.

parameter, as also reported by [25] which stated that the cycles become reversible until a complete stabilization is reached for very high numbers of cycles. Similar results are observed along radial stress paths [35,36].

A comparison of the load-displacement response at the pile head between results from finite element modeling (static and dynamic) and API $p-y$ curve method is provided in Fig. 13.20. The dynamic loading is represented by the curve for the 1st, 50th, and 100th cycle. From the figure, it is observed that at very low lateral horizontal forces, the API method is in agreement with numerical simulations for static loading and 1st cycle dynamic loading. This supports the statement that the API method is a pseudo-static approach [18]. However, at low lateral horizontal forces and a high number of cycles, the API method underestimates the pile displacement. This can be observed by the difference in pile displacements between the API method and numerical simulations; calling Δ to the displacement obtained when the applied load is 4 MN, we can see that Δ equals 0.3 cm for the 1st cycle, 0.8 cm for the 50th cycle, and 1 cm for the 100th cycle. This underestimation of the pile displacement by the API method at low lateral displacement was also observed by Hearn [37]. This also represents the conclusion presented by [38] who stated that "the cyclic bearing capacity may be significantly lower than the static bearing capacity." This is true as the displacement increases with an increase in the number of cycles. Thus, the displacement as a result of several cycles goes further away from the displacement from static load/one cycle, since there is an accumulation of volumetric strains in the soil surrounding the pile. The plot also shows that the curve for the static loading and the 1st cycle dynamic loading are similar but the difference in pile displacement at the maximum applied lateral load of 4 MN is 0.3 cm. This gives a percentage difference

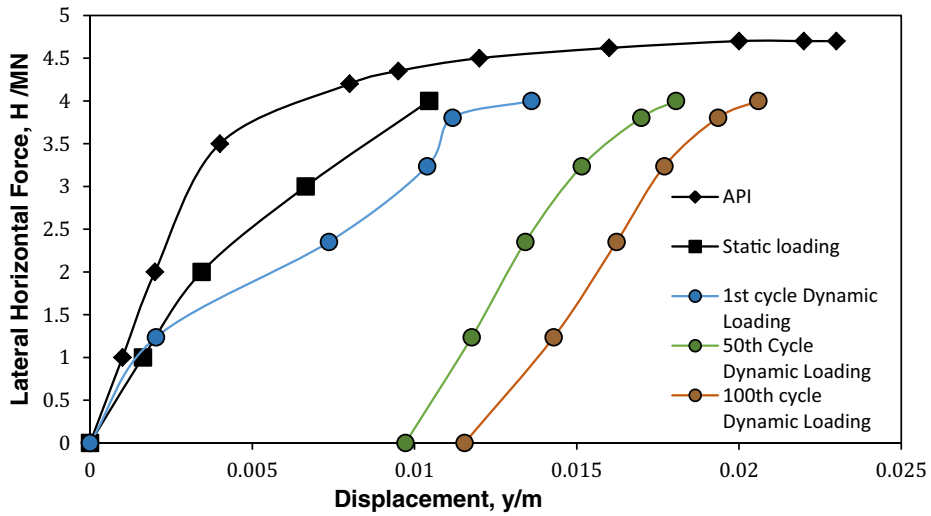

FIGURE 13.20 Comparison plot of the $p-y$ curve between the API method and numerical simulations.

of 30%. This may be because simulations for transient analysis are based on the division of time or steps: therefore, there is a progressive accumulation of residual errors with an increase in the number of time steps [39].

References

[1] Arany L, Bhattacharya S, Macdonald J, Hogan SJ. Design of monopiles for offshore wind turbines in 10 steps. Soil Dyn Earthq Eng 2017;92:126–52. Available from: https://doi.org/10.1016/j.soildyn.2016.09.024.

[2] Bhattacharya S, Adhikar S. Experimental validation of soil–structure interaction of offshore wind turbines. Soil Dyn Earthq Eng 2011;31 (5–6):805–16.

[3] Bhattacharya S. Challenges in design of foundations for offshore wind turbines. IET J, Eng Technol Ref 2014;9. Available from: https://doi.org/10.1049/etr.2014.0041 Online ISSN 2056–4007.

[4] Bhattacharya S, Lombardi D, Muir Wood D. Similitude relationships for physical modelling of monopile-supported offshore wind turbines. Int J Phys Model Geotech 2011;11(2):28–68.

[5] Guo Z, Yu L, Wang L, Bhattacharya S, Nikitas G, Xing Y. Model tests on the long-term dynamic performance of offshore wind turbines founded on monopiles in sand. J Offshore Mech Arct Eng 2015;. Available from: https://doi.org/10.1115/1.4030682 Paper No: OMAE-14-1142.

[6] Bhattacharya S, Cox JA, Lombardi D, Muir Wood D. Dynamics of offshore wind turbines on two types of foundations. Proc Inst Civ Eng: Geotech Eng 2012;166:159–69. Available from: https://doi.org/10.1680/geng.11.00015.

[7] Bhatthcharya S, Nikitas N, Garnsey J, Alexander NA, Cox J, Lombardi D, et al. Observed dynamic soil–structure interaction in scale testing of offshore wind turbine foundations. Soil Dyn Earthq Eng 2013;54:47–60.

[8] Arany L, Bhattacharya S, Macdonald J, Hogan SJ. Simplified critical bending moment spectra of offshore wind turbine support structures. Wind Energy 2014;. Available from: https://doi.org/10.1002/we.1812.

[9] Arany L, Bhattacharya S, Macdonald JHG, Hogan SJ. Closed form solution of Eigen frequency of monopile supported offshore wind turbines in deeper waters incorporating stiffness of substructure and SSI Soil Dyn Earthq Eng 2016;83:18–32ISSN 0267-7261. Available from: http://doi.org/10.1016/j.soildyn.2015.12.011.

[10] Hu W.-H., Thöns S., Said S., Rücker W. Resonance phenomenon in a wind turbine system under operational conditions. In: Cunha A, Caetano E, Ribeiro P, Müller G, editors. Proceedings of the 9th International Conference on Structural Dynamics, EURODYN 2014, Porto, Portugal, 30 June–2 July 2014. ISSN: 2311-9020; ISBN: 978-972-752-165-4.

[11] Nikitas G, Vimalan N, Bhattacharya S. An innovative cyclic loading device to study long term performance of offshore wind turbines. J Soil Dyn Earthq Eng 2016;82:154–60.

[12] Bouzid D. p-y curves from stress-strain of a soil: FE assessment. Geomech Eng, 5. Techno-Press; 2013. p. 379–99. Available from: http://doi.org/10.12989/gae.2013.5.5.379.

[13] Cuéllar P. Pile foundations for offshore wind turbines: numerical and experimental investigations on the behaviour under short-term and long-term cyclic loading [Ph.D. thesis]. Technical University of Berlin; 2011.

[14] Wichtmann T, Niemunis A, Triantafyllidis T. Strain accumulation in sand due to cyclic loading: drained triaxial tests. Soil Dyn Earthq Eng 2005;25(12):967–79. Available from: https://doi.org/10.1016/j.soildyn.2005.02.022.

[15] Blazquez R, Lopez-Querol S. Generalized densification law for dry sand subjected to dynamic loading. Soil Dyn Earthq Eng 2006;26 (9):888–98. Available from: https://doi.org/10.1016/j.soildyn.2005.09.001.

[16] Winkler E. Die Lehre von der Elasticitaet und Festigkeit mit besonderer Rucksicht auf ihre Anwen- dung in der Technik fur polytechnische Shulen, Bauakademien, Ingenieure, Maschinenbauer, Architek- ten, etc. Verlag von H. Domenicus, Prag; 1867.
[17] McClelland B, Focht JA. Soil modulus for laterally loaded piles. Trans Am Soc Civ Eng 1958;123(2954):1049–86.
[18] Reese CL, Van Impe FW. Single piles and pile groups under lateral loading. 2nd ed. CRC Press/Balkema; 2001.
[19] Achmus M, Abdel-Rahman K. Finite element modelling of horizontally loaded monopile foundations for offshore wind energy converters in Germany. In: Proc int symp front offshore geotech ISFOG; 2005. p. 391–6. https://doi.org/10.1201/NOE0415390637.ch38.
[20] Ashour M, Norris G. Modeling lateral soil-pile response based on soil pile interaction. J Geotech Geoenviron Eng 2000;126(5):420–8.
[21] Matlock H. Correlations of design of laterally loaded piles in soft clay. In: Proceedings of the II annual offshore technology conference, Houston, TX (OTC 1204); 1970. p. 577–94.
[22] Terzaghi K. Evaluation of coefficients of subgrade modulus. Geotechnique 1955;297–326.
[23] API. Recommended practice for planning, designing and constructing fixed offshore platforms—working stress design. In: API recommenced practice, 2A-WSD (RP 2A-WSD); 2007.
[24] Lesny K, Wiemann J. Design aspects of monopiles in German offshore wind farms. Frontiers in offshore geotechnics. ISFOG 2005;383–9.
[25] Cambou B, Hicher PY. Elastoplastic modeling of soils: cyclic loading. Const Model Soils Rocks 2010;143–86. Available from: https://doi.org/10.1002/9780470611081.ch4.
[26] Cundall P, Strack O. A discrete numerical model for granular assemblies. Geotechnique. 1979;29(1):47–65.
[27] Mindlin R, Deresiewicz H. Elastic spheres in contact under varying oblique forces. ASME J Appl Mech 1953;20:327–44.
[28] Itasca PFC2D manual 4.0; 2008.
[29] Cui L. Developing a virtual test environment for granular materials using discrete element modelling [Ph.D. thesis]. Ireland: University College Dublin; 2006.
[30] Cui L, O'Sullivan C, O'Neill S. An analysis of the triaxial apparatus using a mixed boundary three-dimensional discrete element model. Geotechnique 2007;57(10):831–44.
[31] O'Sullivan C, Cui L, O'Neil S. Discrete element analysis of the response of granular materials during cyclic loading. Soils Found 2008;48(4):511–30.
[32] Cui L, Bhattacharya S. Soil-monopile interactions for offshore wind turbine. Eng Comput Mech, Proc Inst Civ Eng 2016;169:171–82.
[33] Hamming R.W. Digital filters. Prentice-Hall signal processing series; 1977.
[34] Byrne BW, Houlsby GT. Foundations for offshore wind turbines. Philos Trans A Math Phys Eng Sci 2003;361:2909–30. Available from: https://doi.org/10.1098/rsta.2003.1286.
[35] Sa'don NM, Pender MJ, Abdul Karim AR, Orense R. Pile head cyclic lateral loading of single pile. Geotech Geol Eng 2014;32:1053–64. Available from: https://doi.org/10.1007/s10706-014-9780-5.
[36] Jardine RJ, Yang ZX, Foray P, Zhu B. Interpretation of stress measurements made around closed-ended displacement piles in sand. Géotechnique 2013;63:613–27. Available from: https://doi.org/10.1680/geot.9.P.138.
[37] Hearn E. Finite element analysis of an offshore wind turbine monopile [Master's thesis]. Medford, MA: Dep Civ Environ Eng Tufts Univ; 2009. https://doi.org/10.1061/41095(365)188.
[38] Yang M, Ge B, Li W, Zhu B. Dimension effect on P-y model used for design of laterally loaded piles. Proc Eng 2016;143:598–606. Available from: https://doi.org/10.1016/j.proeng.2016.06.079.
[39] Wichtmann T. Explicit accumulation model for non-cohesive soils under cyclic loading. Inst Für Grundbau Und Bodenmechanik: 274 [Ph.D. thesis]. Germany: University of Karlsruhe; 2005.

This page intentionally left blank

Chapter 14

Reliability of wind turbines

Shawn Sheng[1] **and Ryan O'Connor**[2]
[1]*National Renewable Energy Laboratory, Golden, CO, United States,* [2]*EDF Renewables North America, Denver, CO, United States*

14.1 Introduction

Modern utility-scale wind turbines are complex systems that include both hardware—structural, mechanical, electrical, thermal, and hydraulic—and software—data acquisition, control, or monitoring—components. They are designed to convert kinetic energy from the wind into electrical power. The development of modern large wind turbines dates back to the 1970s and 1980s and has expanded dramatically during the past few decades, with the global cumulative installed wind power generation capacity reaching 743 gigawatts by the end of 2020 [1,2]. The evolution, however, has been profoundly influenced by reliability and availability issues [2], ranging from structural collapses in the early prototypes to the recent premature component failures on commercial wind turbines. The encouraging fact is that nowadays most modern, land-based wind turbines can achieve an availability of about 98% and a mean time between failures (MTBFs) of more than 7000 hours, implying a failure rate of a little over 1 failure(s)/turbine/year [2]. The challenge is a few overhauls or replacements of major components are normally needed throughout the design life of a modern wind turbine, despite the fact that structural components, such as the foundation and tower, can normally last longer. These overhauls or replacements of major components, which are infrequent but typically associated with long downtime, compounded with frequent failures of other components that have short downtime, lead to increased operation and maintenance (O&M) costs of wind turbines and subsequently, the levelized cost of energy for wind power. The cost can increase as wind turbines age and become much higher for offshore wind power plants. Based on European experience, on average, the availability of offshore wind plants is about 7% lower than land-based plants [3], and the O&M costs for an offshore wind plant are twice as much as for a land-based plant [4]. As a result, there is a clear need for the wind energy industry to improve reliability and reduce O&M costs, especially when turbines are installed offshore.

There are a few different factors to consider when improving turbine reliability and reducing O&M costs, such as design [5], testing [6], and O&M [7]. The wind turbine application is uniquely featured by a stochastic duty cycle, which is similar to automotive applications, and an expected long asset lifetime, which is more similar to aerospace applications. It is also characterized by difficult access, remote and regional resources, strained supply chains, and new functional requirements. The majority of wind turbine components are designed to be dependable and have no redundancy. For example, a typical wind turbine has about 5000 parts, which can lead to around half a million possible turbine failures at a wind plant with 100 turbines. Current turbine design standards focus on component survival against damage from hazards throughout a turbine design lifetime. This is compounded by the use of custom parts, and designers are driven by certification, not regulation. Reliability demonstration is difficult as specific designs and parts become obsolete. Reputation of a turbine technology also has an influence, which is supported by anecdotes, analysis, witnesses to failures, and reporting. Oftentimes severe events are overstated. Considering these facts, the lack of reliability:

- Increases capital expenditures through overdesign, excessive prototyping and testing, and warranty and insurance requirements
- Increases financing costs due to uncertainties as well as operational expenditures from both scheduled and unscheduled events
- Reduces annual energy production.

Once turbines are installed in a wind plant, the main opportunity for cost of energy (COE) reduction lies in the improvement of O&M practices, which is the perspective taken in this chapter. The intention of this chapter is to

Wind Energy Engineering. DOI: https://doi.org/10.1016/B978-0-323-99353-1.00016-5

highlight the current reliability statistics of wind turbines, and describe how the wind industry's O&M practices can benefit from reliability engineerings, such as warranty planning, maintenance planning, supply-chain planning, and risk management. Reliability engineering is a mature discipline, ready to be widely adopted and practiced by the wind industry, and can help reduce O&M costs. The authors hope that the materials presented in this chapter can help stimulate the integration of reliability engineering methods by the global wind energy industry and benefit O&M practices overall. This chapter is not intended to provide a comprehensive discussion on wind turbine reliability or O&M practice improvements through condition-based maintenance or prognostics and health management, for which the audience can refer to such books as Ref. [2].

Given that wind turbines have various types of components, a wind turbine reliability evaluation needs to consider them accordingly. However, this chapter focuses on mechanical components and uses them to demonstrate the potential benefits of reliability engineering to wind. In addition, various sectors of the wind industry may have different interests in terms of wind turbine reliability. For example, manufacturers may be more interested in improving wind turbine reliability through design improvements; whereas owners and operators may be more interested in improving wind turbine reliability through O&M practice enhancements. This chapter takes the owners' and operators' perspectives, focusing on reliability analyses to determine efficient maintenance practices [8]. Specifically, failure analysis identifies certain component failure rates and life characteristics over time or operating conditions to help determine maintenance or component replacement intervals. If root causes for certain failures were identified, these failure modes could be mitigated through either O&M practices or replacements with improved products. Another type of practice, such as failure-mode-effect-criticality analysis performed for product design or improvements, can also be conducted to benefit O&M [9].

In the next few sections, a brief discussion on terminology and reliability metrics is provided. Then, the current status of wind turbine reliability is presented. Next, the reliability engineering methodology that can potentially benefit wind plant O&M, including data collection, model development, and forecasting, is discussed. Two case studies are then presented to illustrate how the reliability engineering methodology can be utilized to benefit wind plant O&M. The chapter concludes with some final remarks on potential opportunities to improve wind turbine reliability.

14.2 Fundamentals

14.2.1 Terminology

14.2.1.1 Reliability

Reliability is the *probability* that a product or a system will perform its *intended functions* satisfactorily (i.e., without failure and within specified performance limits) for *a specified length of time*, when operating under *specified environmental and usage conditions* [10]. Depending on the perspective, reliability can be inherent as designed and manufactured or operational as observed in the field [11]. To use wind turbines as the context, the product or system can be a wind turbine or a turbine component. The specified length of time is normally treated as the design life of 20−25 years for a wind turbine, which only specifies the duration and is not a complete reliability statement. Two other factors in the definition are to perform intended functions and under specified conditions. Reliability is a probability that changes if the application or design is changed. When wind turbine reliability is discussed, often it is based on anecdotes, not thorough and systematic analyses using data collected from the field. A failure occurs when the intended functions of a wind turbine component cannot be performed satisfactorily.

For complex machines like a wind turbine, the reliability of the entire turbine is affected by the reliability of its subsystems, including both hardware and software, and how those components are connected. When analyzing the reliability of a wind turbine or a wind turbine subsystem like a gearbox, it is recommended to use a comprehensive and normalized grouping of components according to their functions and positions. One method is to use reliability block diagrams [12], which show the functional components and their relationships within a wind turbine. They consider the relationship between all competing and independent failure modes impacting the components of a wind turbine. The reliability of a wind turbine is also affected by environmental conditions, such as wind and wave conditions in offshore wind plants. It is worth noting that improvements in major turbine subsystems or component reliability alone are not sufficient and the impacts of connecting components also need to be considered. The economies of wind turbines and other independent power generation plants generally prohibit the use of redundant components.[1] In addition, components in wind turbines are generally nonrepairable, implying when failed, the components cannot be repaired without

1. This does not include safety equipment.

maintenance intervention. All components must function for the wind turbine to generate electricity. This dependency on all turbine subsystems and components negatively impacts the reliability of a wind turbine as it leads to lower system reliability than individual component reliability. For more information on system and component reliability, refer to Chapter 6 in Ref. [13].

14.2.1.2 Metrics

To evaluate the reliability of a wind turbine, its major components normally need to be grouped into three categories: structural, electrical, and mechanical. The reason for this grouping is that they typically need different reliability evaluation metrics and methods. For structural components, such as the blades, tower, and foundation, the probability of failure can be used as the metric and evaluated using structural reliability theory [14,15]. For electrical and mechanical components, their life is assumed to follow the classical bathtub curve. Its failure rate, λ, is a very popular measure, which is normally treated as the inverse of *MTBF*. These metrics can be calculated using classic reliability theory [13]. Some work on wind turbine reliability evaluation by integrating structural subsystems with electrical and mechanical components was reported in Ref. [16]. This chapter focuses on the mechanical components.

Below is a brief list of metrics and expressions that are useful for reliability evaluation, as stated in Chapter 1 of Ref. [2].

- Mean time to failure: *MTTF* (nonrepairable components)
- Mean time to repair or replacement: *MTTR*
- Logistic delay time: *LDT*
- Downtime: $MTTR + LDT$
- Mean time between failure: $MTBF = MTTF + MTTR + LDT$ (repairable systems, such as a wind turbine or a wind turbine gearbox)
- Failure rate:

$$\lambda = \frac{1}{MTBF} \tag{14.1}$$

- Repair rate:

$$\mu = \frac{1}{MTTR} \tag{14.2}$$

The *MTTF* often is used on nonrepairable turbine components that need to be replaced after they fail. These are often the lowest-level actionable components within a wind turbine. For a wind turbine gearbox or the entire turbine, which both comprise many low-level actionable components, *MTBF* is more appropriate. Among these metrics, *MTBF*, or failure rate, and downtime are often used in the wind industry to evaluate relative improvements in turbine reliability. No matter which metric is used, the key is to trend the chosen metric over time. On the other hand, using *MTTF* or *MTBF* alone is not sufficient [17] for reliability engineering analysis. When discussing wind turbine reliability within the community of peers, reliability engineers are better served by expressing the reliability in terms of life distributions and parameters, which will be discussed in Section 14.4.

14.2.2 Taxonomy

Different parties may use various sets of taxonomies when talking about wind turbines. In terms of wind turbine reliability, it is essential to know the taxonomy and chain of dependability. The set of taxonomy introduced by the ReliaWind consortium is adopted in this chapter. It uses a five-level system to describe a wind plant and the definitions include [2]:

- The system, which could be the wind plant including wind turbines, the substation, and cables
- The subsystem, which could be an individual wind turbine or a substation at the wind plant
- The assembly, which could be the gearbox in a wind turbine or the high-voltage system in the substation
- The subassembly, which could be the high-speed shaft in the gearbox
- A component, which could be the high-speed shaft bearing.

The set of taxonomy is also helpful when conducting reliability data collection. For more details on this set of taxonomy, please refer to Chapter 11 in Ref. [2]. If cost analysis is also of interest, refer to the land-based and offshore wind plant cost breakdown structures developed by the National Renewable Energy Laboratory (NREL) in Appendixes E and F of Ref. [18].

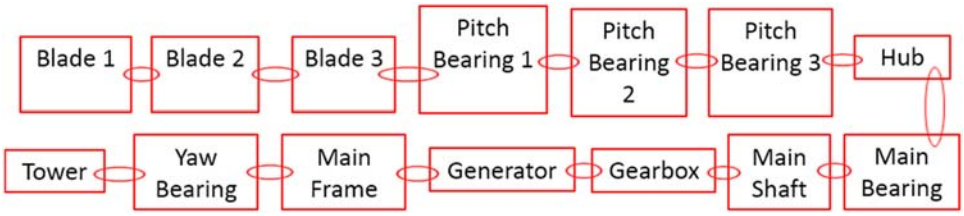

FIGURE 14.1 Figurative chain of dependability showing the relationship between the various major components in a wind turbine [19].

14.2.3 Failure types

Wind turbine systems are nonrepairable during operation and function similar to a chain under tension. All components must survive or the system fails. The length of the chain is not constant for all wind turbine designs [19]. The chain shown in Fig. 14.1 includes the fourteen major components common to many modern wind turbines: three blades, three-pitch bearings, a hub, main bearing, main shaft, gearbox, generator, main frame, yaw bearing, and tower. Some turbine designs may include more or fewer major components [19].

Component life cycle reliability includes all independent failure modes of the component. Wind turbine components commonly suffer from four types of failures: infant, premature, random, and wear-out.

Infant failures are those events mostly due to wear-in problems or quality defects from the material manufacturing process. These types of failures are more likely to occur early in life and have a decreasing incidence rate with age. Preventing all infant failures is prohibitively expensive and every manufacturer must allow some defect rate for each component. The allowable defect rate is a function of the manufacturer's quality management and risk assessment. For wind energy project owners, the majority of infant failures are mitigated by a supplier warranty. Performing life data analysis on an infant failure provides wind turbine owners with a way to measure the quality management of the supplier and to understand the value of a supplier warranty.

Premature failures include those events due to a latent defect in the design, manufacturing process, or application (including maintenance activities). Premature failures are often detected after some period of operation and may progress to show signs of degradation and wear before functional failures. Axial cracks are a common premature failure of wind turbine gearbox bearings. Corrosion is another premature failure seen on wind turbine components. Premature failures can impact a small or large portion of an aging turbine population and these failures often disrupt operations either mildly or catastrophically.

Random failures are expected to appear throughout the wind turbine life cycle. These failures are caused mostly by an unlikely string of preceding events, or can be an overload event like a 50-year extreme gust or a lightning strike. The rate of a random failure is constant regardless of the equipment age. As with infant failures, it is prohibitively expensive to overdesign wind turbine components to survive all likely random, extreme failures. Experienced owners and original equipment manufacturers with a large fleet of wind turbines expect some failures due to random strength exceedances. The risk of these random failures is typically mitigated by insurance. Life data analysis of random failures provides wind turbine owners with a method to quantify their wind turbine insurance needs.

As strange as it may sound, wear-out failures are the way in which owners hope wind turbine components fail. If a majority of the failures are wear-out, it is likely that the owner has selected a quality manufactured product, operated and maintained the asset effectively, avoided random failures from a host of causes, and finally failed the components by "old age." This is the ideal way a component will break down at the end of its life and the failure for which the component lifetimes are often specified (e.g., a 20-year design life refers to the classic fatigue "wear out" of materials). These failures are more likely to happen later in the life cycle and related life data analysis helps owners plan for maintenance and spare parts.

Table 14.1 provides a list of failure modes typically seen in major wind turbine assemblies (i.e., gearboxes, blades, pitch bearings,[2] and generators) by grouping them according to the four failure types discussed above. For each failure mode, a failure mechanism is present and needs to be modeled and analyzed [16]. It is clear that reliability analysis of wind turbines can be conducted at different levels, for various components, and on certain failure modes. As a result, when analyzing or discussing wind turbine reliability, it is beneficial to specify as many of the details as possible.

The stacked bar plot in Fig. 14.2 shows the relative behavior of these common failure types for a large number of wind turbine equipment, i.e., assemblies or components. Note that they can experience any of these types of failures at any time during their life cycle.

2. A wind turbine typically has three pitch bearings, which are treated together as an assembly.

TABLE 14.1 Typical failures seen in major wind turbine assemblies.

Failure types	Assemblies			
	Gearboxes	**Blades**	**Pitch bearings**	**Generators**
Infant	• Gear mesh o Timing errors o Macrogeometry o Skidding o Abrasion o Adhesion o Foreign object debris/damage • Bearings o Mounting failure o Macrogeometry o Skidding o Abrasion o Adhesion o Thermal runaway o Foreign object debris/damage	• Composite delamination • Adhesive bond line failure • Mounting error • Transportation and handling • Lightning protection system • Laminate wrinkles	• Mounting failure • Actuation system failure • Seal failure	• Insulation failure • High-resistance connection
Premature	• Gear mesh o Micropitting o Nonconforming inclusions o Grinding temper o Tooth interior fatigue failure o Corrosion o Lubricant degradation o Microgeometry errors • Bearings o Irregular white etching areas raceways o Grinding temper raceways and rollers o Nonconforming inclusions raceways and rollers o Skidding o Micropitting o Cage failure o Raceway creep o Shoulder and lip fatigue o Corrosion o Lubricant degradation o Preload errors o Microgeometry errors	• Bond line cracks • Leading-edge erosion (accelerated) • Composite delamination • Laminate wrinkles • Blade add-on failures (e.g., spoilers, vortex generators) • Moisture ingress and icing • Balancing mass rupture • Lightning protection system	• Raceway fatigue cracks • Cage bunching • Raceway contact ellipse spill • Inadequate lubricant/ maintenance • False brinelling • Actuation system failure	• Wedge failure • Bearing failure • Insulation failure • Dust/debris buildup • Slip-ring failure
Random	• Gear mesh o Characteristic load exceedance o Material strength exceedance o Foreign object debris/damage following routine service o Nonconformity from allowable defect rate o Nacelle fire • Bearings o Characteristic load exceedance o Material strength exceedance o Foreign object debris/damage following routine service o Nonconformity from allowable defect rate o Nacelle fire	• Characteristic load exceedance • Material strength exceedance • Nonconformity from allowable defect rate • Nacelle fire • Lightning strike overload • Pitch bearing failure • Tower strike	• Characteristic load exceedance • Material strength exceedance • Nonconformity from allowable defect rate • Nacelle fire • Actuation system failure	• Low-voltage, high-current event • Lightning surge; nacelle fire

(*Continued*)

TABLE 14.1 (Continued)

Failure types	Assemblies			
	Gearboxes	**Blades**	**Pitch bearings**	**Generators**
Wear	• Gear mesh o Bending fatigue o Surface fatigue • Bearings o Subsurface rolling contact fatigue	• Bond line fatigue failures: edge loading • Root fatigue cracks: flap and edge loading • Leading-edge erosion • Foreign object debris buildup • Composite fatigue failure • Hardware fatigue	• Raceway rolling contact fatigue • Gear mesh bending fatigue • Gear mesh surface fatigue	• Insulation fatigue • Bearing failure

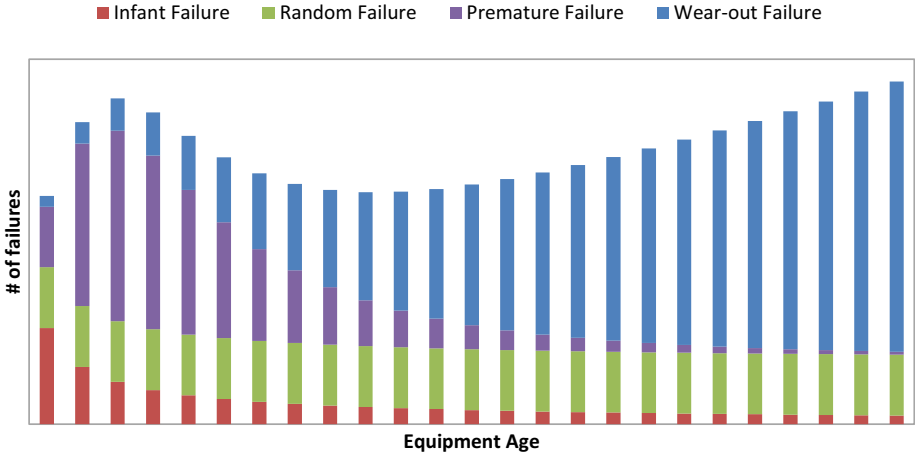

FIGURE 14.2 Common failure types for wind turbine equipment during the project life cycle [19].

14.3 Current status

To accurately evaluate the current status of wind turbine reliability, it is necessary to calculate consistent metrics based on data collected through standardized practices, including analysis and reporting. However, these types of metrics, such as *MTBF*, are typically not easy, if not impossible, to obtain due to the lack of needed information in various data collection initiatives in the wind energy industry, especially for relatively older projects. Nevertheless, wind turbine reliability is so critical that there are various benchmarking efforts around the globe. This section gives a brief overview of these efforts, which were indirectly referenced in one survey [20] and one recent publication [21], highlighting where the industry is in terms of wind turbine reliability.

The survey reported in Ref. [20] was conducted in 2013 and reviewed reliability data collection and analysis efforts mainly in Europe and the United States. The European efforts include Wissenschaftliches Mess-und Evaluierungsprogramm (WMEP) [22], Landwirtschaftskammer Schleswig-Holstein [23], VTT [24], Vindstat [25], WindStats [26], and ReliaWind [27]. WMEP was the earliest among these efforts and started in 1989. Similar efforts in the United States were not started until about 2010, represented by Continuous Reliability Enhancement for Wind (CREW) [28], and a project conducted by Det Norske Veritas-Keuring van Elektrotechnische Materialen te Arnhem (DNV KEMA) and Germanischer Lloyd (GL) Garrard Hassan under the sponsorship of NREL [29]. Another effort from the United States is the gearbox failure database [30], which was started as part of the Gearbox Reliability Collaborative [31] project and focuses on gearbox failure modes and possible root causes. After the completion of the survey, there were a few new reliability data collection and analysis efforts, including offshore wind applications, started in both Europe (e.g., Wind energy-Information-Data-Pool [32],

CIRCE [33], and SPARTA) [34] and Asia (e.g., Huadian) [35]. There are variations among different reliability data collection and analysis efforts and there is a need for the wind industry to develop and adopt a standardized approach. To correctly understand results reported by different data collection efforts, it is necessary to consider the population of turbines each database recorded, including turbine age, technology, site location, etc.

Based on various reliability data collection and reporting efforts, including most discussed earlier, a few reviews [21,36–38] were conducted by various researcher groups. Fig. 14.3, extracted from Ref. [21], shows median values of downtime per failure (hours) caused by different subassemblies. It was compiled based on 10 out of 15 data sources the authors reviewed, as the other five do not have downtime information. The top few are gearbox, generator, shaft and bearings, and structure. Cross-checking against the statistics extracted from Ref. [39], as previously reported in this chapter, there is no change with power module, including generator subassembly, and drivetrain module, including the gearbox and shaft and bearing subassemblies, being the top downtime drivers. The reason for structure subassembly to show up as one of the top downtime drivers might be because the data sources used in Ref. [21] include offshore wind power plants. If this information was removed from Fig. 14.3, the next in the line will be the blade and hub, as well as the air brake subassemblies, which are part of the rotor module and consistent with the previous statistics reported in this chapter.

Fig. 14.4, extracted from Ref. [21], shows median values of failures per turbine per year by different subassemblies. The top few subassemblies are electrical, control, pitch, and blades and hub, and the subassemblies with lower failure rates include brakes, shafts and bearings, nacelle, and structure. Comparing with the statistics, extracted from Ref. [40], as previously reported in this chapter, which had control, blades/pitch, and electric system as the top drivers, and hubs, drivetrains, including shaft and bearings, and structures as the bottom few. Both are in agreement except hub rises to the top in the new statistics, which could also be caused by the inclusion of offshore wind turbines.

A few observations from the aforementioned efforts in the United States include [20]:

- The 2012 CREW data show the top four identifiable drivers in terms of the average number of events per turbine were the rotor/blades, electric generator, balance of plant, and controls, and the top four identifiable drivers in terms of the mean downtime per event were the braking system, controls, yaw, and power distribution. The unidentified events caused the longest downtime per event, indicating the need to clarify what it specifically covers to better understand the downtime drivers.

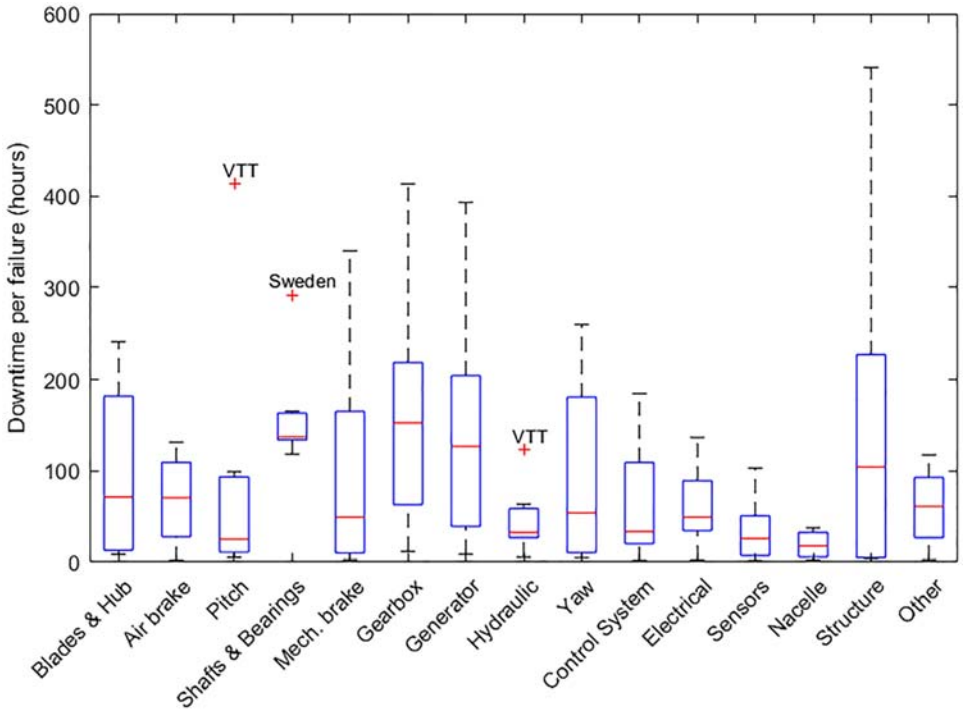

FIGURE 14.3 Box plot of downtime caused by different subassemblies [21].

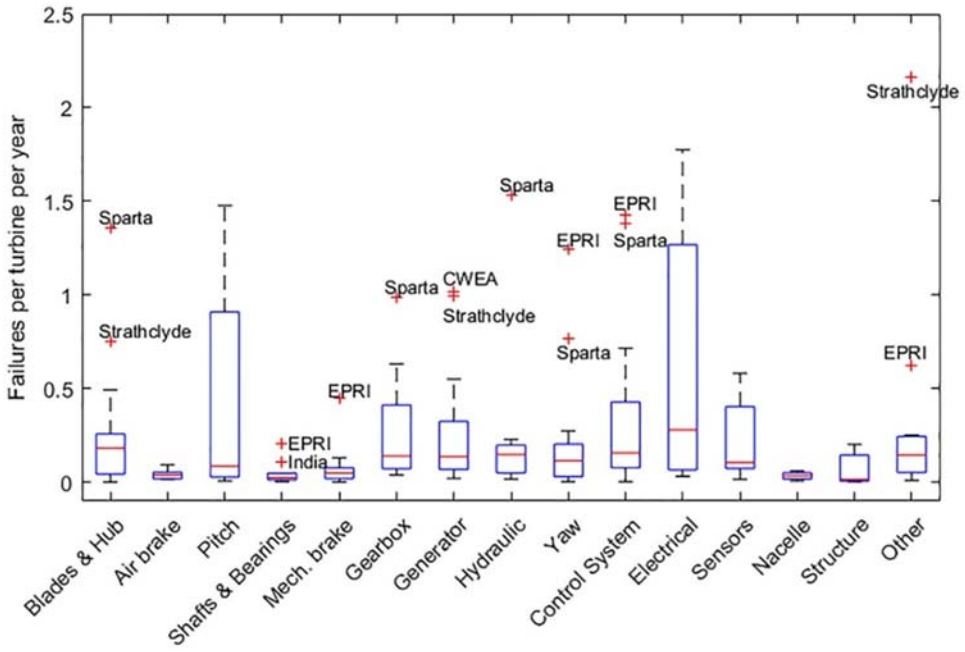

FIGURE 14.4 Box plot of failures caused by different subassemblies [21].

- The data collected by DNV KEMA and GL Garrard Hassan (newly formed DNV GL) show from 1999 to 2011 the average yearly replacement rates for gearboxes was about 5% and peaked in years 4, 5, and 8. Generators were about 3.5% and peaked in years 6 and 7, and blades were about 2% and peaked in years 1 and 5.
- The gearbox failure data collected from 2013 to 2016 show that wind turbine gearboxes could fail in different ways drastically. Bearing and gear failures were concentrated in the parallel stages, and the top gearbox failure mode was high-speed or intermediate bearing axial cracks.

For offshore wind turbines, generators and converters were observed to have higher failure rates than land-based turbines [41]. Assuming that the definition of failures is similar in Refs. [40,41], the average failure rate for an offshore wind turbine is approximately 10 failures/turbine/year by a wind plant's third operational year, which is more than five times the land-based failure rate. For offshore wind turbines, the subassemblies/components that fail the most are the pitch/hydraulic system, the "other" component group (i.e., door/hatch, cover, bolts, lightning protection system, and lift), and the generator [41]. Offshore wind turbines show a stronger correlation between rising average failure rates and rising average wind speeds than land-based wind turbines [41]. The observation from study [40] that medium-size direct-drive wind turbines have more frequent electrical and electronic failures but higher availability than geared turbines for land-based turbines appears to also apply to offshore turbines [38].

There are a few conservative observations in terms of current wind turbine reliability status that can be made [2,20,38]:

- Mature technologies have lower failure rates and new technologies have higher failure rates
- Failure rates vary with turbine configurations, resources (e.g., gusts), and environmental conditions (e.g., humidity)
- Reliability benefits from direct-drive wind turbines versus geared wind turbines throughout the entire life cycle are not yet conclusive
- The power module fails more frequently than other modules, but the drivetrain or rotor module failures typically have higher downtime and costs
- Offshore wind plants require improved reliability due to potential higher failure rates and longer downtime per failure event.

A typical wind plant has tens or hundreds of turbines, thereby generating a huge amount of data continuously. There are opportunities to make use of data analysis techniques to better harvest data, thereby gaining knowledge so the reliability and availability of wind plants can be improved. One such opportunity is life data analysis based on reliability engineering, which can provide immediate benefits to wind plant O&M if appropriately adopted and practiced. It will be addressed in the next section.

14.4 Reliability engineering

Reliability engineering focuses on equipment life cycle management. Life data analysis is one of the most powerful tools in reliability engineering [13], providing a forward look based on past and present observations. There are several approaches available for performing life data analysis and this section presents one approach that is well-suited for wind turbine technology. Similar to other properties of the equipment (e.g., rating, ampacity, and height), if appropriate life data are not captured and analyzed, reliability cannot be evaluated, controlled, and improved. To benefit from reliability engineering through life data analysis, the practices typically include three steps: data collection, model development, and failure forecasting. For the analysis, it is helpful to clearly define the reliability relationships among turbine components. As shown in Fig. 14.1, the dependability between a series of major turbine components is illustrated through a system reliability block diagram. It features a representative wind turbine configuration including a gearbox, a generator, three blades, and three pitch bearings and assumes the failures that occurred to these components are independent [12].

14.4.1 Data collection

Wind turbine equipment records and failure reports can be highly variable, from the level of detail and format to data integrity. Fortunately for wind turbine reliability engineers, there are often several data sources, such as supervisory control and data acquisition (SCADA), inspection reports, and maintenance work orders, which are available to investigate and characterize equipment records for life data analysis. One challenge with the life data analysis is that it may take more than 80% of the effort to collect and validate data. Another challenge is inconsistent definitions of failure events, as they may vary throughout the life cycle of a wind turbine or for different purposes, even within an organization. In addition, there are no mandatory and standardized practices for reliable data collection to support systematic life analysis.

Analysts should plan to drill down the turbine equipment hierarchy to the lowest actionable element. Developers of wind energy projects consider the wind turbines and balance-of-plant equipment as the lowest actionable items. Long-term owners and operators of wind projects are interested in the major assemblies and subassemblies in the wind turbines and balance-of-plant systems. A manufacturer may consider the raw materials and surface finishes at the lowest actionable level to track data.

The data collection begins by evaluating the major failures that are likely to happen during the life cycle of a wind turbine and the repairs that the wind turbine owner is likely to perform. Regardless of the equipment being analyzed, the data requirements for life data analysis can be satisfied by tracking just two fields: age and failure status. In practice, it is helpful to record a minimum of four fields for all equipment including:

- Installation date
- Last known operating date
- Status
- Equipment key.

The *installation date* is the first day the equipment enters service. For original equipment, this is the first day generation is reported through the SCADA system or otherwise assumed as the commercial operation date of the turbine. For replacement equipment, this is the date when the wind turbine returns to service following a repair. The *last known operating date* is either: (1) the date the equipment was taken offline, or (2) the latest date turbine operation can be verified. For most modern wind turbines, the operating status can be verified in real-time, and the *last known operating date* can therefore be updated constantly for equipment in service. Together, the *installation date* and *last known operating date* provide the bounds to measure the component's lifetime *usage*. For developing reliability models as functions of load cycles or other age measures, these two dates are useful to bound queries of a lifetime SCADA database. For convenience, equipment age is often measured with calendar time as it translates well with maintenance planning and risk analyses. The benefit of collecting the *installation date* and the *last known operating date* is the ability to measure lifetimes in several different ways.

The *status* identifies the state of the equipment on the *last known operating date*. Entries for the *status* field identify equipment as either a *failure* event, *F*, or a *suspended* event, *S*. Suspended events, or *suspensions*, are cases when the equipment has not failed by the specific failure mechanism being analyzed. *Suspensions* may be the default *status* when the equipment was commissioned as it is still in service, or maybe equipment removed preventively, or otherwise failed by another failure mode than the one being analyzed. Strict failure logic should be used to categorize the *status* of each

equipment record. The *equipment key* links the equipment record with an instance on a wind turbine at a plant. All asset and plant records and properties are related to the equipment in this field.

Failure and repair events are unwelcome by wind plant owners and operators, but reliability engineers normally view them as opportunities to improve knowledge. The reliability engineers need to stay aware of all equipment status changes in the fleet, and ensure that the necessary detail is recovered for all failure and repair events as accurately as possible. Some questions and details to consider when recording failure and repair events include:

- *When and how was the failure detected?* A failure is called an event, but it is often a process. Damage can be detected in several ways as it progresses to a failure. Catastrophic failures can be detected by turbine faults or local landowners reporting noticeable problems with surrounding turbines. Progressive failure events may be detected in the same ways earlier in the failure process, and also by routine maintenance, prognostics, and health management systems, or during an offline inspection campaign. Recording the failure detection method lets owners evaluate the most popular methods for each failure mode and compare how alternative methods of detection correlate with subsequent repair event costs and production losses. Reliability engineers can analyze *when* and *how* the failure modes are detected to inform owners of the best methods to manage the failure mode risks and mitigate losses.
- *When was the wind turbine taken offline to replace the failed equipment?* This date is equivalent to the *last known operating date* for the failed equipment. This date can be on, after, or even before the failure detection date. If the offline date is the same as the failure detection date, the equipment was likely run to failure. If the offline date is after the failure detection date, the failing equipment may have been operated and monitored while the replacement was being planned. If the offline date is before the failure detection date, the turbine was most likely taken offline due to some other cause and the component was determined to require replacement.
- *When was the failed equipment replaced?* This is the date when the turbine returns to service following the replacement of the failed equipment. Together, the *offline date* and *replacement date* allow the reliability engineers to measure the total event downtime and production losses.
- *What is the failure mode of the failed equipment?* A failure mode describes how the equipment fails. Wind turbine equipment can fail by many independent and competing failure modes, as illustrated in Table 14.1. Recovering the failure mode detail can require considerable time and resources, but categorizing and grouping events by failure modes allows the reliability engineers to develop the most informative and specific reliability models. In a system reliability analysis, the reliability engineers develop a specific reliability model for each distinguishable failure mode of the equipment.
- *What type of maintenance was done?* The maintenance type can be either corrective, preventive, or planned preventive. Corrective maintenance is performed on equipment that has functionally failed or is unfit for service. Preventive maintenance is performed to replace equipment on the condition of some other event, with no indication of catastrophic failure on the equipment replaced. For example, when gearbox replacement is determined as necessary for a wind turbine, the main shaft bearing may be replaced at the same time as a preventive maintenance practice. Planned preventive maintenance is recorded when replacements are scheduled or planned based on early detection of the failure process. The maintenance type field helps owners to group and analyze total event downtimes and detection methods.

To facilitate the data collection and subsequent model development and life forecasting, an equipment and event record database typically needs to be developed. When developing such a database, it is necessary to consider how the data will be accessed and maintained. It is recommended to use a central repository if planning to perform routine analysis for a large fleet of equipment, as this helps to organize and manage the data entries.

14.4.2 Model development

Good data collection facilitates efficient model development. But first, it is important to discuss what differentiates the models. Reliability models are functions of time that show the evolution of equipment risk of failures. The reliability models are lifetime distributions that can be expressed in several forms, all of which define the distribution of a continuous random variable lifetime, t. These forms include but are not limited to:

- Reliability function, $R(t)$
- Unreliability function, $Q(t) = 1 - R(t)$
- Probability density function, $f(t)$
- Hazard rate function, $h(t) = f(t)/R(t)$.

TABLE 14.2 Various forms of reliability models for lifetime distributions.

Lifetime distribution	Parameters	$R(t)$	$f(t)$	$h(t)$	$Q(t)$
Exponential	$\lambda > 0$	$e^{-\lambda t}$	$\lambda e^{-\lambda t}$	λ	$1-e^{-\lambda t}$
Weibull	$\eta > 0;\ \beta > 0$	$e^{-\left(\frac{t}{\eta}\right)^{\beta}}$	$\frac{\beta}{\eta}\left(\frac{t}{\eta}\right)^{\beta-1} e^{-\left(\frac{t}{\eta}\right)^{\beta}}$	$\frac{\beta}{\eta}\left(\frac{t}{\eta}\right)^{\beta-1}$	$1-e^{-\left(\frac{t}{\eta}\right)^{\beta}}$
Gamma	$\lambda > 0;\ \kappa > 0$	$1 - I(\kappa, \lambda t)$	$\frac{\lambda(\lambda t)^{\kappa-1} e^{-\lambda t}}{\Gamma(\kappa)}$	$\frac{\lambda(\lambda t)^{\kappa-1} e^{-\lambda t}}{\Gamma(\kappa)[1 - I(\kappa,\lambda t)]}$	$I(\kappa, \lambda t)$
Lognormal	$-\infty < \mu' < \infty;\ \sigma' > 0$	$\int_{\ln(t)}^{\infty} \frac{1}{\sigma'\sqrt{2\pi}} e^{-\frac{1}{2}\left(\frac{x-\mu'}{\sigma'}\right)^2} dx$	$\frac{1}{\sigma'\sqrt{2\pi}} e^{-\frac{1}{2}\left(\frac{t'-\mu'}{\sigma'}\right)^2}$	$\frac{f(t)}{R(t)}$	$1 - R(t)$
Log-logistic	$\lambda > 0;\ \kappa > 0$	$\frac{1}{1+(\lambda t)^{\kappa}}$	$\frac{\lambda\kappa(\lambda t)^{\kappa-1}}{[1+(\lambda t)^{\kappa}]^2}$	$\frac{\lambda\kappa(\lambda t)^{\kappa-1}}{1+(\lambda t)^{\kappa}}$	$1 - \frac{1}{1+(\lambda t)^{\kappa}}$

Γ is the gamma function.
I is the incomplete gamma function.

TABLE 14.3 Classification of lifetime distributions.

Lifetime distribution	Increasing failure rate	Decreasing failure rate	Bathtub-shaped failure rate	Upside-down bathtub-shaped failure rate
Exponential	Yes	Yes	No	No
Weibull	$\text{Yes}_{\beta \geq 1}$	$\text{Yes}_{\beta \leq 1}$	No	No
Gamma	$\text{Yes}_{\kappa \geq 1}$	$\text{Yes}_{\kappa \leq 1}$	No	No
Lognormal	No	No	No	Yes
Log-logistic	No	$\text{Yes}_{\kappa \leq 1}$	No	Yes

Detailed expressions of these forms for some common lifetime distributions are shown in Table 14.2 [42].

The hazard rate function, also known as failure rate in reliability, is perhaps the most popular expression of a lifetime distribution[3] due to its intuitive interpretation of the amount of reliability risk associated with a component at time, t. The shape of the failure rate function indicates how the equipment ages. An increasing failure rate shows equipment is more likely to fail as time passes. This is common with mechanical items that undergo wear or fatigue. A decreasing failure rate means equipment is less likely to fail as time passes. This can occur with computer software or with some metals that work-harden through use and increase strength with time. Failure rates can follow a bathtub shape, wherein equipment reliability improves initially and then degrades as time passes. Failure rates can even follow an upside-down bathtub shape. The shape of the failure rate function is useful in determining the appropriate distribution to use when modeling equipment lifetimes. The lifetime distributions can be classified by their modeling capabilities for different behaviors of failure rate functions. Table 14.3 shows the classification of some common lifetime distributions for modeling strictly increasing failure rates, strictly decreasing failure rates, bathtub-shaped failure rates, and upside-down bathtub-shaped failure rates. The classification can be used as a guideline to choose the appropriate life distributions for different types of failure rates when starting the modeling efforts. However, the final distribution that can give the best possible modeling results may only be determined through a systematic evaluation based on the methods to be introduced next.

The reliability engineers rely on their experiences with failure mechanisms and lifetime data to determine the appropriate lifetime distribution(s) for the analysis. Two common methods used to analyze time-to-failure data sets and

3. The hazard function goes by several aliases: in reliability it is also known as the hazard rate or failure rate. In actuarial science it is known as the force of mortality or force of decrement. In point process and extreme value theory it is known as the rate or intensity function. In vital statistics it is known as the age-specific death rate, and in economics its reciprocal is known as Mill's ratio.

TABLE 14.4 Common methods used to analyze lifetime data for wind turbine equipment.

Maximum likelihood estimation	Rank regression
Find the distribution most likely to produce the historical data	Find the distribution resulting in the shortest distance between the expected values and the observed values
Estimate parameters independent of any ranking of failure time	Requires rank estimates of each failure time
Considers all equipment in the estimation of parameters; not just failures	Based on the total sample size and failure order number
Best with censored data	Best with complete data

develop lifetime distributions are *Rank Regression* and *Maximum Likelihood Estimation* (*MLE*). In short, rank regression solutions find the distribution that minimizes the error between observed values and expected values of unreliability, whereas MLE solutions find the distribution that is most likely to reproduce the historical data set. Both methods develop parametric lifetime distributions that handle a random continuous variable lifetime. These two methods are compared in Table 14.4 and the selection of the method is based on the properties of the data set. MLE is the preferred method to develop lifetime distributions when analyzing the *censored* data[4] for wind turbine equipment [35].

Development of the reliability model using the MLE method begins with an assumed distribution that could fit the data set representing reliability for one turbine subsystem or component at either a plant or fleet level. This initial distribution may be determined based on prior knowledge of the failure mechanism and equipment lifetimes (e.g., by following recommendations given in Table 14.3). Often prior knowledge is missing, and this initial assumption is left up to the reliability engineers. Still, reliability software can make this initial guess programmatically without inputs from the analysts and this initial guess typically has little impact on the final results. The initial distribution is used to evaluate the likelihood that the historical events in the data set would occur if the distribution truly characterized the equipment's lifetimes. The measure commonly used to characterize the distribution with the data set is called the *log-likelihood* value. A *log-likelihood* value is calculated based on the equipment record *status* and *age* and the assumed distribution. For *failure* records, the log-likelihood value, L_F, is calculated:

$$L_F = \ln f(t) \tag{14.3}$$

and for *censored* data records (i.e., *suspensions*), the log-likelihood value, L_S, is:

$$L_S = \ln R(t) \tag{14.4}$$

Log-likelihood values are calculated for all *failure* and *suspension* records in the data set and these values are summed to show the total log-likelihood value, L, as:

$$L = \sum L_F + \sum L_S \tag{14.5}$$

The reliability engineers then iterate on the distribution and calculate a new log-likelihood value for each record. The sum of the log-likelihood values for the new distribution is compared with the sum from the initial distribution. The distribution with the *maximum log-likelihood* value is ranked best for the data set. More and more iterations are made by the analysts with the goal of finding the distribution that maximizes the log-likelihood value for the data set. Typically, this iterative process is aided by computer software evaluating thousands, or even millions, of potential distributions for the data set. The results from the MLE method are a lifetime distribution that can serve to estimate equipment lifetimes and fully describe the reliability of the equipment throughout its life cycle.

14.4.3 Forecasting

Data collection and equipment lifetime estimates alone can inform many decisions wind plant owners need to make. However, decision-makers rely on reliability engineers to understand how the equipment reliability impacts their assets.

4. Wind turbine equipment lifetime data are often incomplete with *censored* observations. A *censored* observation occurs when only a bound is known on the time to failure. *Censoring* appears frequently with lifetime data because it is impractical to observe all of the equipment failures.

Forecasting is the primary reason to perform life data analysis and this section discusses an approach to apply the data collection and model development efforts for performing these failure forecasts.

Recall that the probability of failure for mechanical equipment is typically a continuous value starting from 0 and increasing monotonically to 1 over time. If we know that some equipment has operated for some period of time, t_0, and has not failed [status = S], the *probability of failure* over some additional operating time, t, is still a continuous value starting from zero at age t_0 that increases to one as t approaches infinite. This value is known as the *conditional probability of failure* and is what wind turbine reliability engineers use to forecast failures. Often the *conditional probability of failure* is found easier by solving for the *conditional reliability* and then taking the mathematical complement[5]:

$$Q(t_0 + t|, t_0) = 1 - \left[\frac{R(t_0 + t)}{R(t_0)}\right] \tag{14.6}$$

where $Q(t_0 + t|t_0)$ is the *conditional probability of failure* for some additional service time, t, provided the equipment has operated without failure for time, t_0, and $R()$ is the *reliability function*. For a population of similar equipment at a wind energy project, the total number of equipment failures in a period of time is equal to the sum of the *conditional probabilities of failure* for all equipment during that time such that:

$$n(t) = \sum_{i=1}^{U} Q_i(t_0 + t|, t_0) \tag{14.7}$$

where $n(t)$ is the *total number of failures* expected during some additional time, t, for a population of U total equipment and Q_i is the *conditional probability of failure* for each ith instance of equipment in the at-risk population. Equipment is *at risk* if it did not fail at t_0 and is expected to be operating during the time, t.

At a very high level, the top business decisions involve values of just two types: time and currency. Regardless of the units used in the failure forecast, all forecast results should be presented with respect to calendar time or the asset life cycle cost.

When a reliability engineer performs a failure forecast based on *causal measures* other than calendar time, such as total production or load cycles, the reliability engineer must forecast the duty cycle of the *causal metric* with respect to calendar time before presenting the failure forecast. This approach adds complexity and uncertainty to the failure forecast but it also offers higher fidelity and sensitivity for modeling application stress profiles consistent with the diurnal and seasonal variability common to wind energy projects.

14.5 Case studies

To demonstrate the reliability engineering life data analysis method discussed in Section 14.4, two case studies are presented in this section: one on gearbox spares planning and the other on pitch-bearing maintenance scheduling.

14.5.1 Gearbox spares planning

An example wind energy project with 10 turbines has an inventory with one spare gearbox. Its asset manager wants to know if the project will likely need another spare gearbox in the next 2 years. She asks for a forecast showing the expected failures of the gearbox equipment at this project. The reliability engineer plans to provide the failure forecast by computing the *conditional probability of failure* for each gearbox at the project in the next 2 years. First, the data collection effort brings in gearbox equipment records with the *status*, the *age* in calendar days, and other classified details about the design and application. Review of the data set shows this project has 10 gearboxes of varying ages at risk in the next 2 years. The reliability engineer happens to have access to a larger data set of assets under management and she finds 313 similar instances of gearbox equipment and lifetime records.

The reliability engineer reviews the censored lifetime data from the total 323 gearbox records and identifies a common gearbox failure mode in the records. For each record, she delineates the age and assigns a failure status: F for failure or S for suspension, based on her failure mode criteria. She selects three initial distributions to model the time-to-failure data and decides to use the MLE method to analyze the data. To execute the MLE method, she develops a logic that first evaluates the status of each record and then calculates the log-likelihood value for that record. If the record status is S for *suspension*, she calculates the natural log of the reliability function at the age of the record. Or if the record

5. The term in brackets [ ] is known as the *conditional reliability*.

status is *F* for *failure*, she calculates the natural log of the probability density function at the age of the record. She then uses software to iterate the parameters for the distributions with a goal to maximize the log-likelihood values. An excerpt of the MLE solutions for the data set is shown in Table 14.5 along with the log-likelihood values calculated for some of the equipment records. Evaluating the maximum log-likelihood values between the three distributions, the reliability engineer chooses the Weibull distribution with a slope of 1.402 and scale parameter of 13,088 days as the best reliability model for the gearbox lifetime data.

Now that the reliability engineer has collected the data and developed the reliability model, they are ready to run the failure forecast. They list out the current age of the gearboxes at their project as t_0 along with the age of each gearbox in 2 years from now as $t_0 + t$. Note that, because the equipment age and reliability model units are in calendar days, the expected future age in 2 years is deterministic, but this is not always the case for other aging metrics (e.g., production forecasts are probabilistic). The failure forecast results for the 10 gearboxes over the next 2 years are shown in Table 14.6 along with informative measures of the current and future reliability of each gearbox.

TABLE 14.5 Example spreadsheet results of MLE analysis with three-lifetime distributions.

	Distribution	**Weibull**	**Lognormal**	**Gamma**
	Parameter 1	1.402	1.434	9320
	Parameter 2	13,088	9.583	1.459
Equipment age, days	**Failure status**	**Log − likelihood**	**Log − likelihood**	**Log − likelihood**
985	**S**	−0.027	−0.031	−0.02779
1492	**S**	−0.048	−0.058	−0.04987
1491	**S**	−0.048	−0.058	−0.04983
810	**F**	−10.280	−10.001	−10.2264
1812	**S**	−0.063	−0.076	−0.06541
1505	**F**	−10.059	−9.845	−10.0167
⋮	⋮	⋮	⋮	⋮
	Total log likelihood value	−530.5	−534.7	−531.0

TABLE 14.6 Failure forecast results for 10 gearboxes at a project.

Gearbox instance	Current age t_0/ days	Future age $(t_0 + t)$/ days	Current reliability R (t_0)/%	Future reliability R $(t_0 + t)$/%	Conditional probability of failure $Q(t_0 + t\|, t_0)$/%	Number of failures $n(t_0 + t)$
Turbine 01	1825	2555	93.9	90.4	3.7	0.037
Turbine 02	3285	4015	86.6	82.6	4.6	0.046
Turbine 03	3285	4015	86.6	82.6	4.6	0.046
Turbine 04	2920	3650	88.5	84.6	4.4	0.044
Turbine 05	3285	4015	86.6	82.6	4.6	0.046
Turbine 06	3650	4380	84.6	80.6	4.7	0.047
Turbine 07	2920	3650	88.5	84.6	4.4	0.044
Turbine 08	3650	4380	84.6	80.6	4.7	0.047
Turbine 09	3285	4015	86.6	82.6	4.6	0.046
Turbine 10	2190	2920	92.2	88.5	4.0	0.040
The total number of gearbox failures expected at the project in the next 2 years is						**0.443**

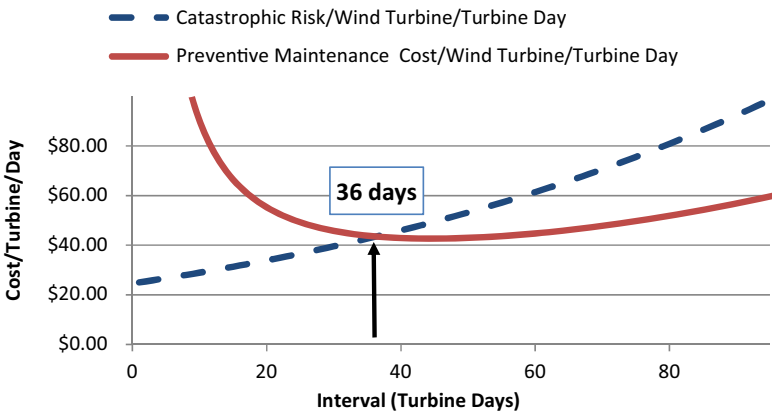

FIGURE 14.5 Pitch bearing maintenance strategies.

Finally, the reliability engineer adds the number of failures expected for all gearboxes and compares this sum to the number of gearboxes available in the inventory. In this case, the reliability engineer advises the asset manager that the project is expected to suffer less than one gearbox failure from the identified common failure mode in the next 2 years and a gearbox spare is likely not needed.

14.5.2 Pitch bearing maintenance scheduling

In another example project, the wind turbines are suffering a fatigue failure of pitch bearings that can result in catastrophic losses if undetected. This project cannot tolerate a catastrophic loss and the asset manager wants to know how often to inspect the pitch bearings to mitigate the risk. The nominal maintenance plan requires an offline inspection of each turbine every 6 months but the failure rate of the pitch bearings at this project suggests more frequent inspections are needed. The reliability engineer plans to use life data analysis and a risk-based inspection approach to find out an appropriate maintenance interval for this project.

The risk-based inspection approach requires a failure forecasting model and some additional data for calculating risks. These data include the cost of inspection, the failure mode detectability, and the planned replacement cost and catastrophic event cost, which the reliability engineer normally gathers or assumes. The "cost" terms here are inclusive of the material and labor costs plus the lost production revenue during the event downtime. The detectability shows the likelihood of detecting failures with the inspection.

The reliability engineer prepares outlooks of two maintenance strategies: the first showing the catastrophic risk of a "do-nothing" run-to-failure strategy and the other showing the risk of a preventive maintenance strategy through offline inspections. The catastrophic risk is the calculated product of the expected failures and the cost of a catastrophic event. The preventive maintenance costs include the sum of the total cost of the inspections, the expected replacement costs when failures are found during inspections, plus the risk of a catastrophic loss from misdetection during offline inspections. Because the project cannot tolerate catastrophic risk, the reliability engineer sets the preventive maintenance costs equal to the catastrophic risk to determine the most appropriate interval for offline inspections.

The reliability model for the pitch bearing failure at this project is found, using the MLE method, to be a lognormal distribution with a log mean of 8.12 log days and a log-standard deviation of 0.454 log days. The current age of the pitch bearings at the project is 560 days. The cost of an offline inspection is $750 and the detectability of the failure with this inspection is 95%. The cost of a planned replacement of the pitch bearing failure is $325,000 and the cost of a catastrophic event is $650,000. The reliability engineer evaluates the risk outlooks for the two maintenance strategies as shown in Fig. 14.5 and advises the asset manager that a 36-day inspection interval is equivalent in cost to the run-to-failure strategy and has the highest likelihood of detecting a failure and avoiding a catastrophic loss.

14.6 Conclusions

This chapter briefly discussed the fundamentals of wind turbine reliability and the current industry status. Then, the reliability engineering method for life analysis was presented in detail and illustrated through two case studies. An owner and operator's perspective is taken, and mechanical components are used to exemplify the potential benefits of reliability engineering analysis to wind power plant O&M. These analyses have been practiced by the wind industry

increasingly to reduce O&M risks and improve finance. This is only one type of data analysis from a relatively mature discipline that the wind industry can benefit from. Because wind energy is a data-rich industry, there are numerous opportunities to benefit from advanced computational and data analysis techniques for improving reliability and availability, especially as wind turbines get more and more instrumentation.

Wind turbine reliability is a complex issue. Many components can fail in vastly different ways. The turbines often operate in harsh environments yet are expected to have a longer life while the economic margins reduce over time. However, to make wind power competitive and successful, the industry must improve both turbine reliability and plant availability. This improvement is even more critical for offshore wind applications. The areas of focus can start with mission-critical and costly assemblies. An immediate opportunity for the wind industry is through the adoption of reliability engineering life data analysis as discussed in this chapter. To truly address the wind turbine reliability challenge systematically and thoroughly as a global industry, all parties within the entire wind turbine supply chain have to come together and share data and knowledge in a way that is useful to both the partners and the entire industry. The task is challenging but rewarding.

Acknowledgments

The contribution from the NREL to this work was supported by the U.S. Department of Energy (DOE) under Contract No. DE-AC36−08GO28308. Funding for the work was provided by the DOE Office of Energy Efficiency and Renewable Energy Wind Energy Technologies Office. The support from eDF Renewable Energy is greatly appreciated.

References

[1] Global Energy Research Council. Global Wind Report; 2021. <https://gwec.net/global-wind-report-2021/>.
[2] Tavner P. Offshore Wind Turbines Reliability Availability and Maintenance. The Institution of Engineering and Technology, UK.
[3] Tavner P. Offshore Wind Turbine Reliability, Supergen Wind Training, Manchester, UK; 2011.
[4] International Renewable Energy Agency, Renewable energy technologies: cost analysis series, volume 1: power sector, wind power; May, 2012.
[5] Guo Y, Bergua R, van Dam J, Jove J, Campbell J. Improved wind turbine drivetrain designs to minimize the impacts of non-torque loads. Wind Energy 2015;18(12):2199−222.
[6] Guo Y, Keller J, LaCava W. Planetary gear load sharing of wind turbine drivetrains subjected to non-torque loads. Wind Energy 2015; 18(4):757−68.
[7] Sheng S. Monitoring of wind turbine gearbox condition through oil and wear debris analysis: a full-scale testing perspective. Tribol Trans 2016;59(1):149−62.
[8] Gonzalez D, Wagner PD, Wisniewski R, Lein PJ, MacDiarmid A, Rose D et al. The impact of "Green" technology on system reliability, Utica, NY: Reliability Information Analysis Center; 2012.
[9] Andrawus J, Watson J, Kishk M, Adam A. The selection of a suitable maintenance strategy for wind turbines. Wind Eng 2006;30(6):471−86.
[10] Rademakers, et al. Reliability analysis methods for wind turbines. Task 1 of the project: probabilistic safety assessment for wind turbines. <ftp://ftp.ecn.nl/pub/www/library/report/1992/c92018.pdf>.
[11] Safie F. Understanding the elements of operational reliability a key for achieving high reliability, presented at Trilateral Safety and Mission Assurance Conference, Cleveland, OH; October 26−28, 2010.
[12] IEC 61078, Analysis techniques for dependability—reliability block diagram and Boolean methods; 2006.
[13] O'Connor PDT, Kleyner A. Practical Reliability Engineering, Fifth Edition. John Wiley & Sons, Ltd.; 2012.
[14] Gintautas T, Sørensen JD. Integrated system reliability analysis. <http://www.innwind.eu/-/media/Sites/innwind/Publications/Deliverables/D1_34_REPORT_revised_2015.ashx?la = da>.
[15] Winterstein SR, Veers P. A numerical analysis of the fatigue and reliability of wind turbine components. SAND94−2459, Sandia National Laboratories, Albuquerque, New Mexico; 2000.
[16] Kostandyan EE, Reliability modeling of wind turbines: exemplified by power converter systems as basis for O&M planning, Ph.D. Thesis, Alborg University; 2013.
[17] Schenkelberg F. Replace after MTTF time to avoid failures—right? <http://nomtbf.com/2016/09/replace-mttf-time-avoid-failures-right>.
[18] Mone C, Smith A, Maples B, Hand M. Cost of wind energy review. Golden, CO: National Renewable Energy Laboratory; 2015 <http://www.nrel.gov/docs/fy15osti/63267.pdf>.
[19] O'Connor R. Approach to quantify the inherent reliability of a wind turbine system. AWEA Windpower; 2014.
[20] Sheng S. Report on wind turbine subsystem reliability—a survey of various databases. Golden, CO: National Renewable Energy Laboratory; 2013. <http://www.nrel.gov/docs/fy13osti/59111.pdf>.

[21] Dao C, Kazemtabrizi B, Crabtree C. Wind turbine reliability data review and impacts on levelised cost of energy. Wind Energy 2019; 22(12):1848–71.
[22] Tavner P, Spinato F, van Bussel GJW, Koutoulakos E. Reliability of different wind turbine concepts with relevance to offshore application, In: Presented at the European Wind Energy Conference, March 31–April 3, Brussels, Belgium; 2008.
[23] Pettersson L, Andersson J- O, Orbert C, Skagerman S. RAMS-database for wind turbines—pre-study. Elforsk Rep 2010;10:67.
[24] Wind Energy Statistics in Finland. <http://www.vtt.fi/proj/windenergystatistics/?lang = en>.
[25] Carlsson F, Eriksson E, Dahlberg M. Damage preventing measures for wind turbines—phase 1 reliability data. Elforsk Rep 2010;10:68.
[26] Windstats Newsletter. vols. 16–25, Q1 2003–Q4; 2012.
[27] Wilkinson M, Hendriks B. Report on wind turbine reliability profiles, reliawind deliverable D.1.3; 2011.
[28] Peters V, Ogilvie A, Bond C. CREW database: wind plant reliability benchmark, SAND2012–7328; 2012.
[29] Lantz E. Operations expenditures: historical trends and continuing challenges. In: Presented at AWEA Wind Power Conference, May 5–8, Chicago, IL. NREL/PR-6A20–58606; 2013.
[30] Sheng S. Gearbox reliability database: yesterday, today, and tomorrow. Wind Turbine Tribology Seminar, Chicago, IL. <http://www.nrel.gov/docs/fy15osti/63106.pdf>; 2014.
[31] Link H, LaCava W, van Dam J, McNiff B, Sheng S, Wallen R, et al., Gearbox reliability collaborative project report: findings from phase 1 and phase 2 testing; 2011 <http://www.nrel.gov/docs/fy11osti/51885.pdf>.
[32] Fraunhofer Institut for Energy Economics and Energy System Technology. <http://www.wind-pool.de/>.
[33] Reder MD, Gonzalez E, Melero JJ. Wind turbine failures—tackling current problems in failure data analysis. J Phys: Conf Ser 2016; 753:072027. Available from: https://doi.org/10.1088/1742-6596/753/7/072027.
[34] SPARTA. System performance, availability and reliability trend analysis, portfolio review 2018/19.
[35] Ma Z, An G, Sun X, Chai J. a study of fault statistical analysis and maintenance policy of wind turbine system. In: International conference on renewable power generation, October 17–18; 2015, Beijing, China. Available from: https://doi.org/10.1049/cp.2015.0443.
[36] Artigao E, Martín-Martínez S, Honrubia-Escribano A, Gómez-Lázaro E. Wind turbine reliability: a comprehensive review towards effective condition monitoring development. Appl Energy 2018;228:1569–83. Available from: https://doi.org/10.1016/j.apenergy.2018.07.037.
[37] Pfaffel S, Faulstich S, Rohrig K. Performance and reliability of wind turbines: a review. Energies 2017;10(11):1904. Available from: https://www.mdpi.com/1996-1073/10/11/1904.
[38] Cevasco D, Koukoura S, Kolios AJ. Reliability, availability, maintainability data review for the identification of trends in offshore wind energy applications. Renew Sustain Energy Rev 2021;136:110414. Available from: https://doi.org/10.1016/j.rser.2020.110414.
[39] Lange M, Wilkinson M, van Delft T. Wind turbine reliability analysis. In: Presented at the 10th German Wind Energy Conference, November 17–18, Bremen, Germany; 2010.
[40] Pinar Pérez JM, García Márquez FP, Tobias A, Papaelias M. Wind turbine reliability analysis. Renew Sustain Energy Rev 2013;23:463–72.
[41] Carroll J, McDonald A, McMillan D. Failure rate, repair time and unscheduled O&M cost analysis of offshore wind turbines. Wind Energy 2016;19(6):1107–19.
[42] Leenmis LM. Reliability probabilistic models and statistical methods. 2nd ed. United States: Ascended Ideas; 2009.

This page intentionally left blank

Chapter 15

Practical method to estimate foundation stiffness for design of offshore wind turbines

Saleh Jalbi, Masoud Shadlou and Subhamoy Bhattacharya
Department of Sustainability, Civil and Environmental Engineering, University of Surrey, Guildford, London, United Kingdom

15.1 Introduction

Fig. 15.1 shows a typical itemized cost of different components of an offshore wind farm and it is clear that the foundation is one of the most expensive items covering almost 34% of the overall cost. One of the main reasons for this high cost is the uncertainty associated with long-term loading conditions, ground profile, and lack of track record of performance on these structures. Research is currently underway to reduce the cost of foundations thereby reducing Levelised Cost of Energy. The principle aim of a foundation is to transfer all the loads from the wind turbine structure to the ground safely and within the allowable deformations. Guided by the Limit State Design philosophy, the design considerations are to satisfy the following:

1. Ultimate Limit State (ULS): This is to ensure that the maximum loads on the foundations are much lower than the capacity of the chosen foundation. This calculation is dependent on the strength of the soil.
2. Target Natural Frequency (Eigen Frequency) and Serviceability Limit State (SLS): This requires the prediction of the natural frequency of the whole system (Eigen Frequency) and the deformation of the foundation at the mudline level. As the natural frequency is concerned with very small amplitude vibrations, linear Eigen Value Analysis will

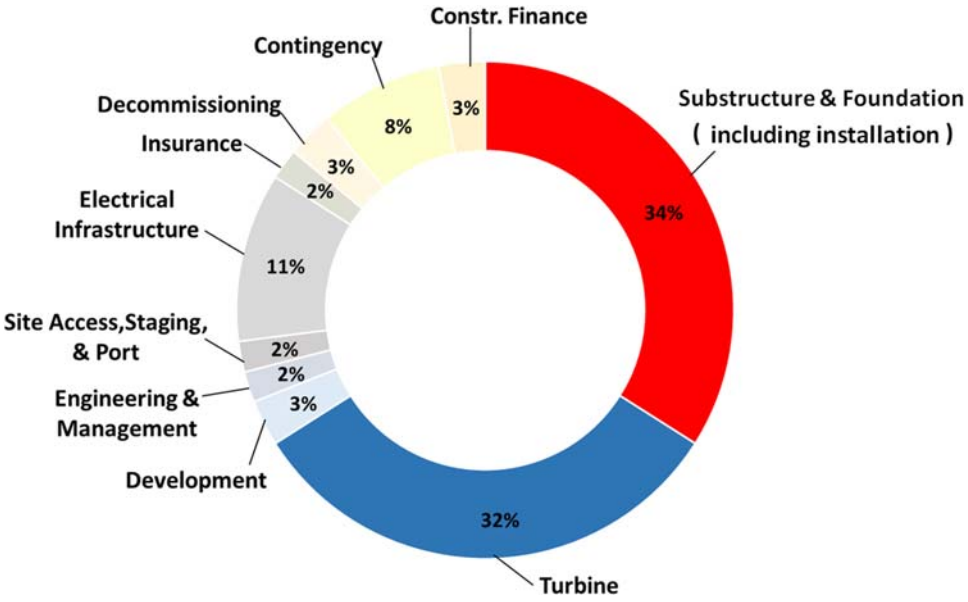

FIGURE 15.1 Cost of different components of a typical offshore wind farm.

Wind Energy Engineering. DOI: https://doi.org/10.1016/B978-0-323-99353-1.00012-8

suffice. The deformation of the foundation will be small and the prediction of initial foundation stiffness would suffice for this purpose. This requires the determination of stiffness of the foundation.

3. Fatigue Limit State and long-term deformation: This would require predicting the fatigue life of the monopile as well as the effects of long-term cyclic loading on the foundation. Again this step requires stiffness of the foundation.
4. Robustness and ease of installation: This step will ascertain that the foundation can be installed and that there is adequate redundancy in the system.

Design of foundation is an iterative process and Fig. 15.2 shows a flowchart for the design of monopiles suggested by Arany et al. [1]. It is clear from the flowchart that foundation stiffness plays a key role in the design. This chapter, therefore, focuses on the different methods of estimating the foundation stiffness and this is one of the critical parameters for design.

Fig. 15.3 shows a mathematical model where the foundation is replaced by a set of springs: K_V (vertical stiffness), K_L (Lateral stiffness) K_R (Rocking stiffness), and K_{LR} (Cross-Coupling). The input required to obtain K_L, K_R, and K_{LR} are: (a) pile dimensions; (b) ground profile, that is, soil stiffness along the length of the pile. In this context, it must be mentioned that the foundation stiffness is required for two calculations: Deformation (deflection ρ and rotation θ at mudline) and natural frequency estimation.

Few points may be noted regarding these springs:

(a) The properties and shape of the springs (load-deformation characteristics, that is, lateral load-deflection or moment-rotation) should be such that the deformation is acceptable under the working load scenarios expected in the lifetime of the turbine. Further details of shape of these springs associated with stress−strain of the supporting soil can be found in Bouzid et al. [2].

(b) The values of the springs (stiffness of the foundation) are necessary to compute the natural period of the structure using linear Eigenvalue analysis. Further details on the analysis required can be found in Adhikari and Bhattacharya [3], Adhikari and Bhattacharya [4], Arany et al. [5], and Arany et al. [6].

The values of the springs will also dictate the overall dynamic stability of the system due to its nonlinear nature. It must be mentioned that these springs are not only frequency dependent but also change with cycles of loading due to dynamic soil-structure interaction. Further details on the dynamic interaction can be found in Bhattacharya et al. [7], Bhattacharya et al. [8], Bhattacharya [9], Lombardi et al. [10], Zania [11], and Damgaard et al. [12].

15.2 Methods to estimate foundation stiffness

In this section, three methods are discussed:

1. ***Simplified method***: Closed-form solutions for foundation stiffness can be obtained *for simple ground profiles*, see Fig. 15.4. Any spreadsheet program or even a simple calculator can be used to compute them and typically time taken is only a few minutes. This method can be useful in the preliminary design and during the optimization stage or even financial feasibility study. In this context, it must be remembered that the foundation constitutes 34% of the overall cost.
2. ***Standard method***: This is one of the most common methods used in industry, see Fig. 15.5. Foundation-soil interaction is represented by a set of discrete Winkler springs where the spring stiffness is obtained through p−y curves which are provided in different design standards. Standard software are available at reasonable costs to carry out the analysis and will only take a few hours to carry out an analysis. *Complex ground soil profiles can be analyzed for standard soils* that is *sand and clay*. Few soil parameters are required and the effects of cyclic load are taken empirically.
3. ***Advanced methods***: These are continuum models (see Fig. 15.6) and advanced 3D finite element software packages or programs are necessary. Such packages are expensive, computationally demanding, and require an experienced engineer to carry out the simulations. These models are *versatile and can model complex ground profile and any type of soils*. Cyclic loading can also be applied.

15.2.1 Simplified method (closed form solutions)

Closed-form solutions have been proposed by Shadlou and Bhattacharya [13]. The values of K_L, K_R, and K_{LR} are summarized in Tables 15.1 and 15.2 for rigid and flexible piles for three types of ground profile: Homogenous, Linear and

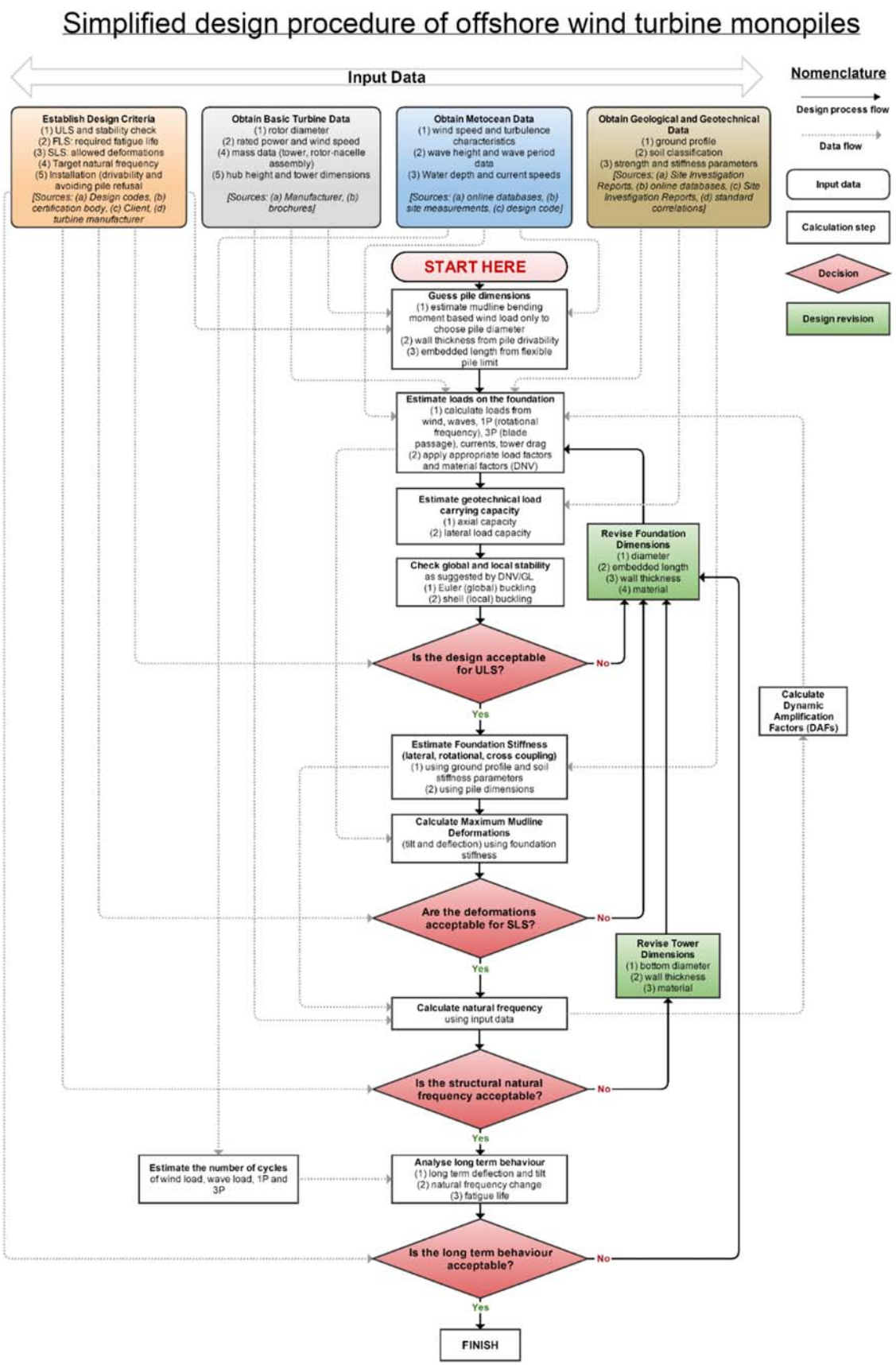

FIGURE 15.2 Flowchart of the design process for monopole.

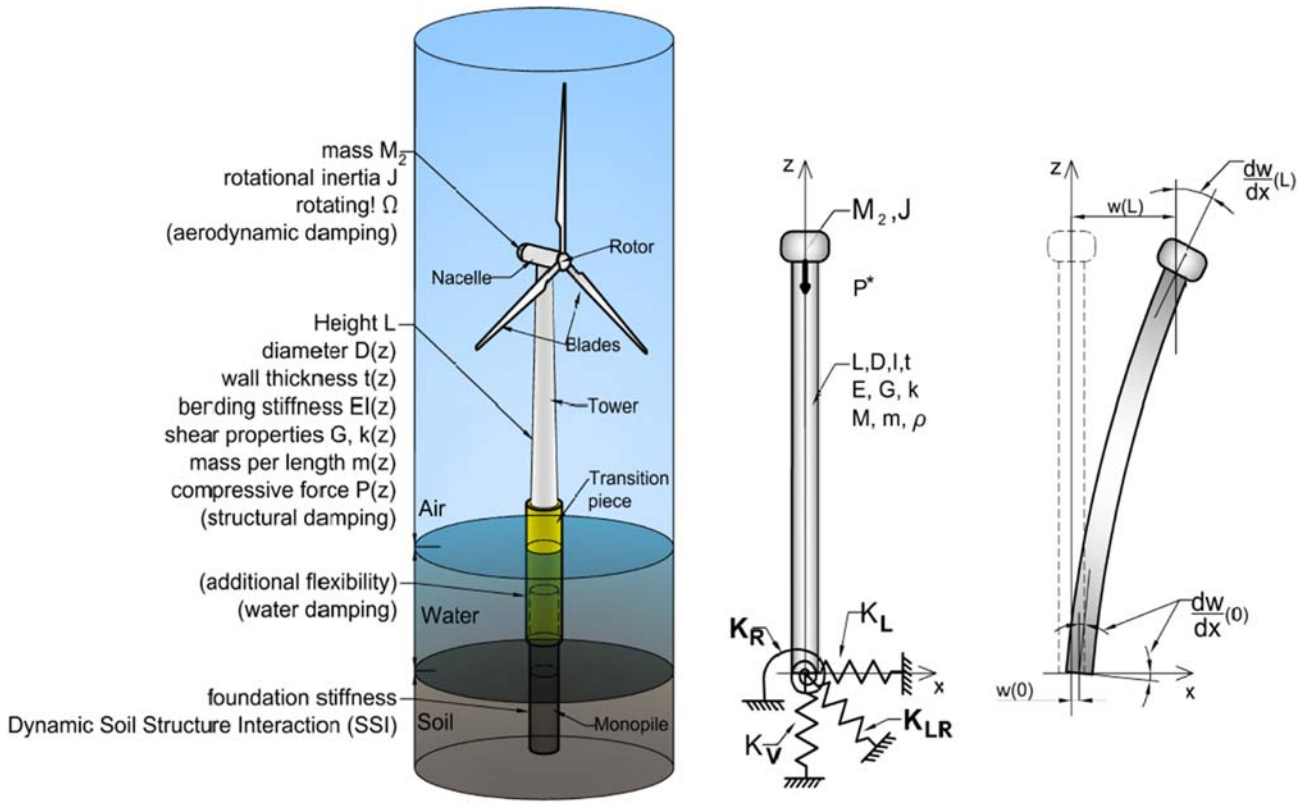

FIGURE 15.3 Mathematical model and importance of foundation stiffness.

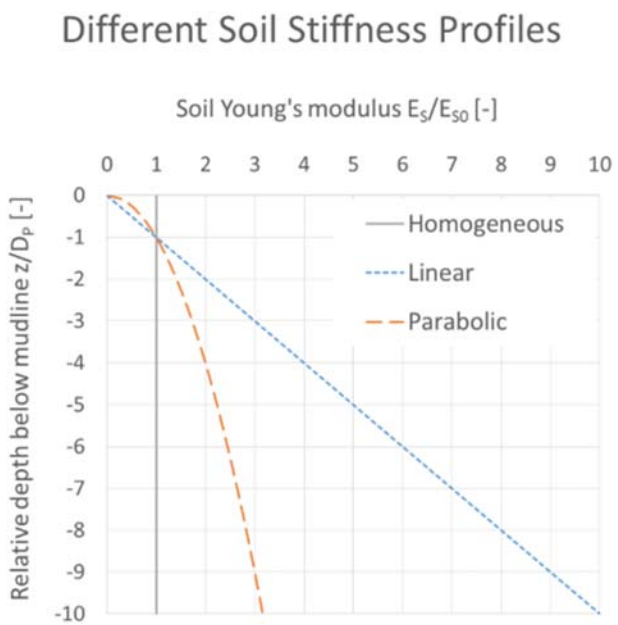

FIGURE 15.4 Homogeneous, linear, and parabolic soil stiffness profiles.

Parabolic, see Fig. 15.4. Homogeneous soils are soils that have a constant stiffness with depth such as overconsolidated clays. On the other hand, a linear profile is typical for normally consolidated clays and parabolic behavior can be used for sandy soils. It may be observed from Table 15.1 that the stiffness term is a function of the aspect ratio (L/D_P) of the pile and soil stiffness (E_{S0}) and this is a characteristic of rigid behavior. On the other hand, Table 15.2 is a function of

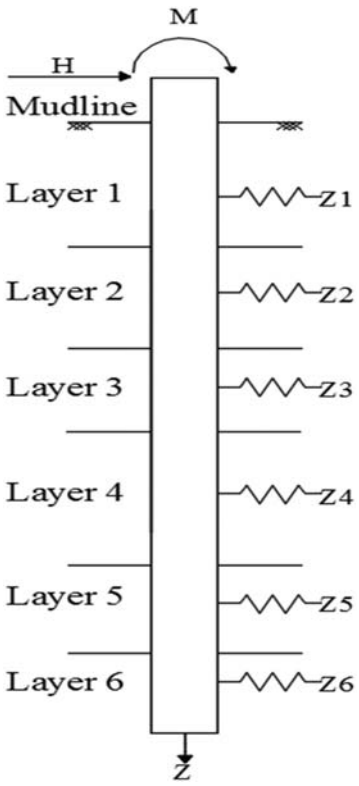

FIGURE 15.5 Monopile supported on discrete winkler springs.

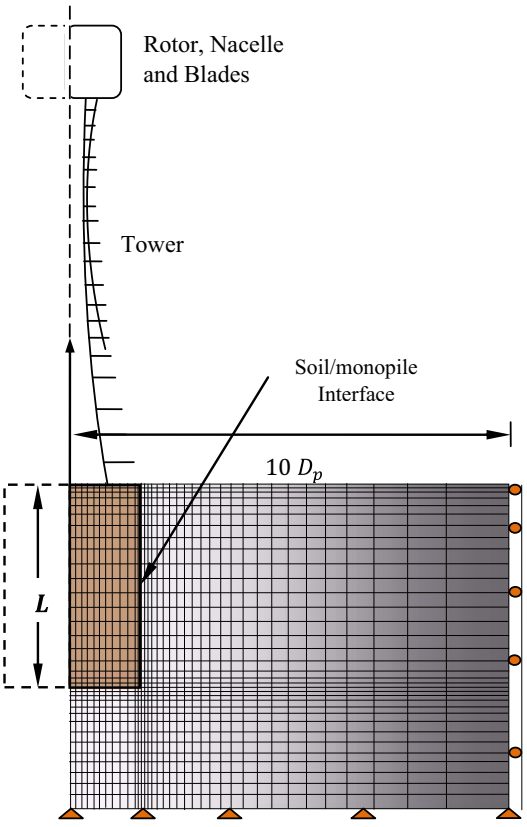

FIGURE 15.6 Finite element method.

TABLE 15.1 Formulas for stiffness of monopiles exhibiting rigid behavior.

Ground profile (see Fig. 15.4)	K_L	K_{LR}	K_R
Homogeneous	$3.2\left(\frac{L}{D_P}\right)^{0.62} f_{(vs)} E_{SO} D_P$	$-1.8\left(\frac{L}{D_P}\right)^{1.56} f_{(vs)} E_{SO} D_P{}^2$	$1.65\left(\frac{L}{D_P}\right)^{2.5} f_{(vs)} E_{SO} D_P{}^3$
Parabolic	$2.65\left(\frac{L}{D_P}\right)^{1.07} f_{(vs)} E_{SO} D_P$	$-1.8\left(\frac{L}{D_P}\right)^{2} f_{(vs)} E_{SO} D_P{}^2$	$1.63\left(\frac{L}{D_P}\right)^{3} f_{(vs)} E_{SO} D_P{}^3$
Linear	$2.35\left(\frac{L}{D_P}\right)^{1.53} f_{(vs)} E_{SO} D_P$	$-1.8\left(\frac{L}{D_P}\right)^{2.5} f_{(vs)} E_{SO} D_P{}^2$	$1.58\left(\frac{L}{D_P}\right)^{3.45} f_{(vs)} E_{SO} D_P{}^3$

TABLE 15.2 Tables for monopiles exhibiting flexible behavior.

Ground profile (see Fig. 15.4)	K_L	K_{LR}	K_R
Homogeneous	$1.45\left(\frac{E_P}{E_{SO}}\right)^{0.186} f_{(vs)} E_{SO} D_P$	$-0.3\left(\frac{E_P}{E_{SO}}\right)^{0.5} f_{(vs)} E_{SO} D_P{}^2$	$0.19\left(\frac{E_P}{E_{SO}}\right)^{0.73} f_{(vs)} E_{SO} D_P{}^3$
Parabolic	$1.015\left(\frac{E_P}{E_{SO}}\right)^{0.27} f_{(vs)} E_{SO} D_P$	$-0.29\left(\frac{E_P}{E_{SO}}\right)^{0.52} f_{(vs)} E_{SO} D_P{}^2$	$0.18\left(\frac{E_P}{E_{SO}}\right)^{0.76} f_{(vs)} E_{SO} D_P{}^3$
Linear	$0.79\left(\frac{E_P}{E_{SO}}\right)^{0.34} f_{(vs)} E_{SO} D_P$	$-0.27\left(\frac{E_P}{E_{SO}}\right)^{0.567} f_{(vs)} E_{SO} D_P{}^2$	$0.17\left(\frac{E_P}{E_{SO}}\right)^{0.78} f_{(vs)} E_{SO} D_P{}^3$

relative pile-soil stiffness (E_P/E_S). Further details on the classification of rigid and flexible piles in relation to monopile application can be found in Shadlou and Bhattacharya [13].

$$* f_{(vs)} = 1 + 0.6|\upsilon_s - 0.25|$$

$$f_{(\nu s)} = 1 + 0.6|\nu_s - 0.25|$$

15.2.2 Standard method

Traditionally in the offshore industry, a nonlinear p−y method is employed to find out pile head deformations (deflection and rotation) and foundation stiffness. The approach can be found in API (2005) and also suggested in DNV [14]. Originally it was developed by Matlock [15]; Reese, Cox, and Koop [16]; O'Neill and Murchinson [17], and the basis of this methodology is the Winkler approach [2] whereby the soil is modeled as independent springs along the length of the pile, see Fig. 15.5. The p−y approach uses nonlinear springs and produces reliable results for the cases for which it was developed, that is small diameter piles and for few cycles of loading. The method is not validated for large diameter piles, in fact, using this method, under prediction of foundation stiffness has been reported by Kallehave and Thilsted [18], who also proposed an updated p−y formulation. Many researchers have recently worked on developing design methodologies for the large diameter more stocky monopiles with length-to-diameter ratios typically in the range between 4 and 10.

15.2.3 Advanced method

In this method, soil structure interaction is carried out using 2D and 3D FEA (Finite Element Analysis) and different sophisticated soil models can be used. This requires advanced soil testing to feed the soil parameters. It is important to note that such models usually require not only knowledge but also expertise and experience. It is not advisable to use this method during the preliminary and optimization stages due to the high cost and the time required for calculation. This method best serves as a final check to a few optimized cases as the results obtained are usually of high accuracy. Fig. 15.6 shows a typical section through a finite element model with various degrees of freedom showing the soil mass, the pile, the pile-soil interface, and the boundary conditions.

15.3 Obtaining foundation stiffness from standard and advanced method

The analysis method presented in Sections 15.2.2 and 15.2.3 is numerical methods and the output from such analysis with being pile-head load−deflection and moment−rotation curves. However, following Fig. 15.3, one needs three stiffness terms (K_L, K_R, and K_{LR}) to carry out dynamic and SLS calculations. This section of the chapter explains a simple methodology to extract the stiffness terms from the analysis results obtained in Sections 15.2.2 and 15.2.3.

While K_L (Lateral stiffness, i.e., force required for unit lateral deflection and the unit is MN/m) and K_R (Rocking Stiffness is the moment required for unit rotation and the unit is MNm/Rad) are easy to appreciate and visualize, the cross-coupling term (K_{LR}) is more involved and arises from matrix compliance. Arany et al. [5] showed cross-coupling stiffness (K_{LR}) of the foundation is an important parameter and must be considered for dynamic analysis of monopiles. Gazetas [19] explains the coupling effect in foundations as a consequence of the inertia of the structure and where the foundation's center of gravity is above the center of soil reaction pressure. This means as the structure is being displaced laterally, an inertial force arises at the center of gravity and produces a net moment thereby rocking occurs. It is, therefore, necessary to explain the cross-coupling term (K_{LR}) through a simple cantilever beam example shown in Fig. 15.7.

Fig. 15.7A shows a cantilever beam subjected to a moment at the free end (M) causing deflection (ρ_1) and rotation (θ_1). On the other hand, Fig. 15.7B shows another cantilever beam where the lateral load (P) at the tip causes deflection (ρ_2) and rotation (θ_2). The expressions for deflection and rotation are given by Eqs. (15.1) and (15.2).

$$\rho_1 = \frac{ML^2}{3EI} \quad \theta_1 = \frac{ML}{EI} \tag{15.1}$$

For a point load

$$\rho_2 = \frac{PL^3}{3EI} \quad \theta_2 = \frac{PL^2}{2EI} \tag{15.2}$$

It is clear that both the moment and the point load produce a rotation as well as a deflection and in effect the rotation caused by the point load or the deflection caused by the moment is indicative of the cross-coupling stiffness term. By definition, the stiffness is the force/moment required to move the body by a unit displacement/rotation respectively, and thus for this example, K_{11} is the stiffness resisting the point load, K_{12} and K_{21} are cross-coupling stiffness, and K_{22} is the stiffness resisting rotation. For "unit" values for P and M, the stiffness terms are given by Eqs. (15.3) and (15.4).

$$K_{11} = \frac{1}{\rho_2} = \frac{1}{\frac{1\times L^3}{3EI}} = \frac{3EI}{L^3} \quad K_{12} = \frac{1}{\theta_2} = \frac{1}{\frac{1\times L^2}{2EI}} = \frac{2EI}{L^2} \tag{15.3}$$

$$K_{21} = \frac{1}{\rho_1} = \frac{1}{\frac{1\times L^2}{2EI}} = \frac{2EI}{L^2} \quad K_{22} = \frac{1}{\theta_1} = \frac{1}{\frac{1\times L}{EI}} = \frac{EI}{L} \tag{15.4}$$

It may be noted that the cross-coupling stiffness of K_{12} and K_{21} are equal for the same magnitude of loading. This method can be extended to the results obtained from standard and advanced methods to find the three stiffness terms (K_L, K_{LR}, and K_R). Typically, (pile head load)-deflection and (pile head moment)-rotation curves are nonlinear depending on the soil type. However, the linear range of the curves can be used to estimate pile-head rotation and deflection based on Eq. (15.5) and one can understand the importance of the cross-coupling term.

$$\begin{bmatrix} H \\ M \end{bmatrix} = \begin{bmatrix} K_L & K_{LR} \\ K_{LR} & K_R \end{bmatrix} \begin{bmatrix} \rho \\ \theta \end{bmatrix} \tag{15.5}$$

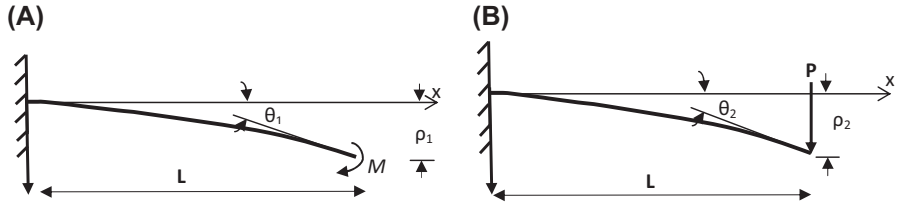

FIGURE 15.7 Explanation of cantilever cross-coupling term.

Eq. 15.5 can be rewritten as Eq. (15.6) through matrix operation where I (Impedance Matrix) is a 2x2 matrix given by Eq. (15.7).

$$\begin{bmatrix} \rho \\ \theta \end{bmatrix} = [I] \times \begin{bmatrix} H \\ M \end{bmatrix} \tag{15.6}$$

$$I = \begin{bmatrix} I_L & I_{LR} \\ I_{RL} & I_R \end{bmatrix} \tag{15.7}$$

To obtain the stiffness terms, one can run a numerical model (either standard or advanced) for a lateral load (say $H = H_1$) with zero moment ($M = 0$) and obtain values of deflection and rotation (ρ_1 and θ_1). The results can be expressed through Eqs. (15.8) and (15.9).

$$\begin{bmatrix} \rho_1 \\ \theta_1 \end{bmatrix} = \begin{bmatrix} I_L & I_{LR} \\ I_{RL} & I_R \end{bmatrix} \times \begin{bmatrix} H_1 \\ 0 \end{bmatrix} \tag{15.8}$$

$$\rho_1 = H_1 \times I_L \Rightarrow I_L = \frac{\rho_1}{H_1} \quad \theta_1 = H_1 \times I_{RL} \Rightarrow I_{RL} = \frac{\theta_1}{H_1} \tag{15.9}$$

Similarly, another numerical analysis can be done for a defined moment ($M = M_1$) and zero lateral load ($H = 0$), and the results are shown in Eqs. (15.10) and (15.11).

$$\begin{bmatrix} \rho_2 \\ \theta_2 \end{bmatrix} = \begin{bmatrix} I_L & I_{LR} \\ I_{RL} & I_R \end{bmatrix} \times \begin{bmatrix} 0 \\ M_1 \end{bmatrix} \tag{15.10}$$

$$\rho_2 = M_1 \times I_{LR} \Rightarrow I_{LR} = \frac{\rho_2}{M_1} \quad \theta_2 = M_1 \times I_R \Rightarrow I_R = \frac{\theta_2}{M_1} \tag{15.11}$$

From the above analysis (Eqs. 15.8−15.11), terms for the I matrix (Eq. 15.7) can be obtained. Eq. (15.6) can be rewritten as Eq. (15.12) through matrix operation.

$$[I]^{-1} \times \begin{bmatrix} \rho \\ \theta \end{bmatrix} = \begin{bmatrix} H \\ M \end{bmatrix} \tag{15.12}$$

Comparing Eqs. (15.5 and 15.12), one can easily see the relationship between the stiffness matrix and the inverse of the Impedance matrix (I) given by Eq. (15.13). Eqs. (15.14 and 15.15) are matrix operations that can be carried out easily to obtain K_L, K_R, and K_{LR}.

$$K = \begin{bmatrix} K_L & K_{LR} \\ K_{RL} & K_R \end{bmatrix} = I^{-1} = \begin{bmatrix} I_L & I_{LR} \\ I_{RL} & I_R \end{bmatrix}^{-1} \tag{15.13}$$

$$K = I^{-1} = \begin{bmatrix} \frac{\rho_1}{H_1} & \frac{\rho_2}{M_2} \\ \frac{\theta_1}{H_1} & \frac{\theta_2}{M_2} \end{bmatrix}^{-1} \tag{15.14}$$

$$K = \frac{1}{\left(\frac{\rho_1}{H_1} \times \frac{\theta_2}{M_2}\right) - \left(\frac{\rho_2}{M_2} \times \frac{\theta_1}{H_1}\right)} \times \begin{bmatrix} \frac{\theta_2}{M_2} & -\frac{\rho_2}{M_2} \\ -\frac{\theta_1}{H_1} & \frac{\rho_1}{H_1} \end{bmatrix} = \begin{bmatrix} K_L & K_{LR} \\ K_{RL} & K_R \end{bmatrix} \tag{15.15}$$

Therefore, mathematically, one needs to run only two cases, that is, p−y analyses or FEA analysis to obtain the three spring stiffness. It is important to note that the above methodology is only applicable in the linear range and therefore it is advisable to obtain a load-deflection and moment-rotation curve to check the range of linearity. If the analysis is used beyond the linear range, underestimations of deflections and rotations will occur. Also, the natural frequency of the whole system will be underestimated.

15.4 Example problem [monopile for Horns Rev 1]

The case study of Horns Rev 1 is used to show the application of the methodology. Various data on the case study can be found in Augustensen et al. [20]. The monopile foundation supports a 60 m long tower carrying a Vestas V80 2 MW

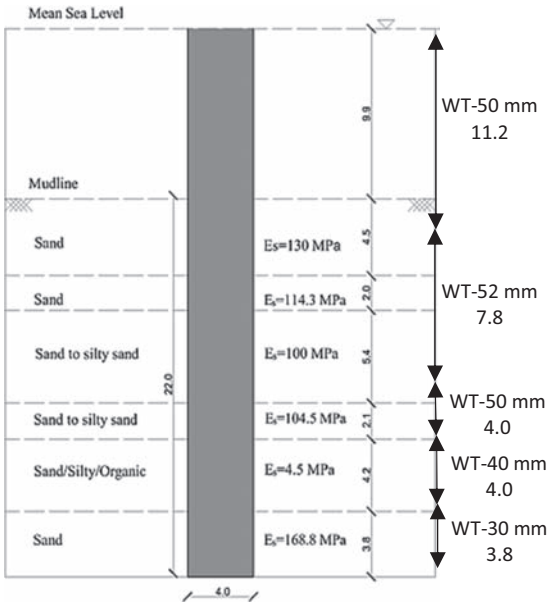

FIGURE 15.8 Pile details.

TABLE 15.3 Soil properties.

Soil layer	Soil type	Depth/m	*Es*/MPa	ϕ/deg	γ'/(kN/m^3)
1	Sand	0–4.5	130	45.4	10
2	Sand	4.5–6.5	114.3	40.7	10
3	Sand to silty sand	6.5–11.9	100	38	10
4	Sand to silty sand	11.9–14.0	104.5	36.6	10
5	Sand/silt/organic	14.0–18.2	4.5	27	7
6	Sand	18.2	158.8	38.7	10

wind turbine. The pile has a diameter of 4.0 m and varying wall thickness (WT in Fig. 15.8). The reported ultimate loads on the pile head were $H = 4.6$ MN and $M = 95$ MN.m. Table 15.3 provides a detailed description of the soil layers which w obtained through an extensive test program including geotechnical borings, CPTs and triaxial tests given in Augustensen et al. [20]. ALP (Oasys) has been used for the p-y analysis of the monopile which can compute deflections, rotations, and bending moments along the pile. Several other software packages such as (PYGM and LPILE) can also be used and are available for this type of analysis, or can be solved numerically through a MATLAB® program. In this study, p−y curves along different depths are modeled in two ways: (a) Elastic-Plastic springs by taking the soil properties given in Table 15.3; (b) API recommended p−y springs.

The API code provides the following formulations for sandy soils:

$$p = Ap_u \tanh\left(\frac{kx}{Ap_u}y\right) \tag{15.15}$$

where A is a factor that depends on the type of loading, and p_u depends on the depth and angle of internal friction ϕ'.

However, for the Elastic-Plastic model used in the study, the following equations were used to construct the p−y curves.

$$p = ky \;\; k = (E_s h) \tag{15.17}$$

where h is the midpoint of the elements immediately above and below the spring under consideration.

The plastic phase of the curve is given by:

$$F_p = \left(K_q \sigma'_v + cK_c\right) hD_P \tag{15.18}$$

where Kq and Kc are factors that depend on depth and ϕ'

Fig. 15.9A–D shows the results obtained from the analysis.

It is evident from Fig. 15.9A–D, that the ULS loads lie within the linear range which means the deflections and rotations arising from such forces can be estimated using K_L, K_R, and K_{LR}. Table 15.4 summarizes the results for the analysis where two load cases have been applied ($H = 0.2$ MN and $M = 0$), and ($H = 0$ and $M = 0.2$ MN m) where the

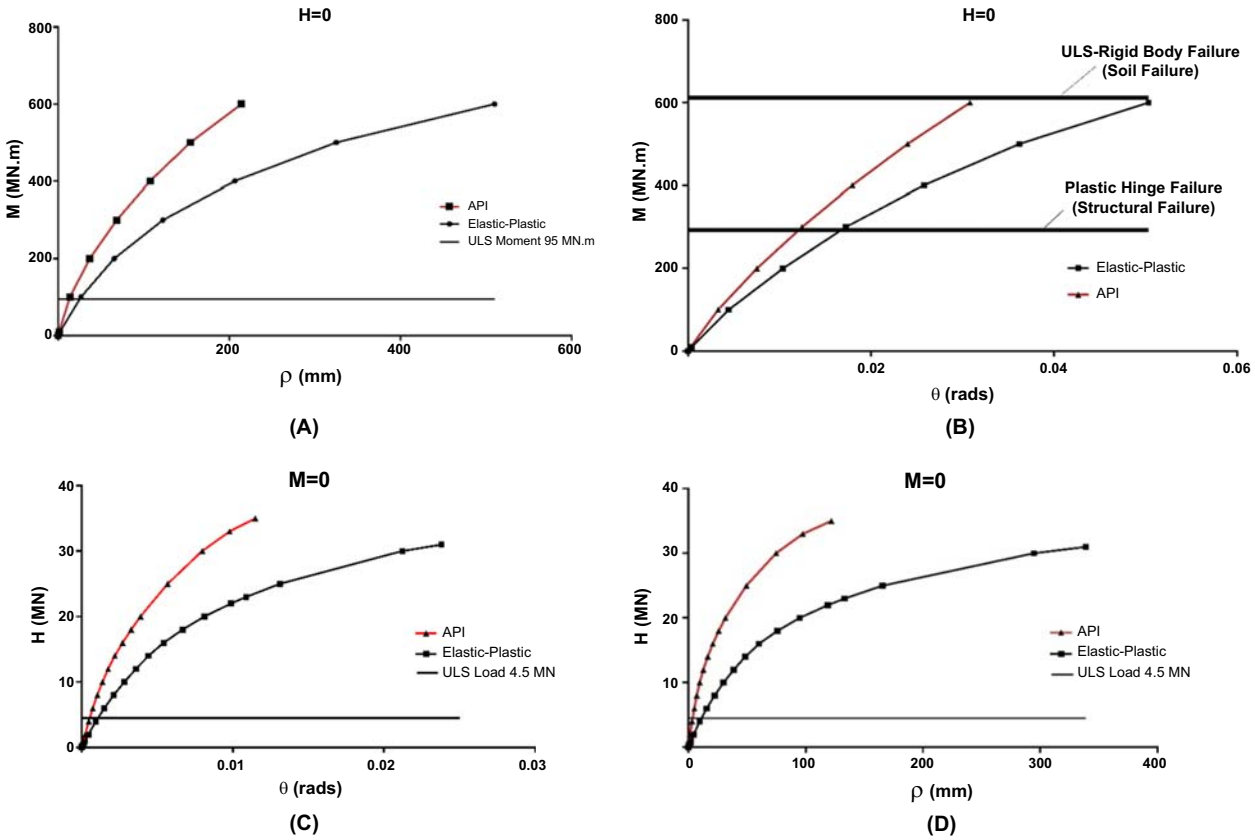

FIGURE 15.9 Analysis of Elastic-Plastic Model: (A) Moment–deflection curve. (B) Moment–rotation. (C) Lateral load–rotation curve. (D) Lateral load–deflection curve.

TABLE 15.4 Results from analysis using equation 15.13.

Model	Loads	ρ/(mm)	θ/(rad)	I_L	I_{LR}	I_{RL}	I_R
Elastic-plastic	H = 0.2 MN.m M = 0 MN.m	0.43	4.1E − 05	2.15E − 03	2.1E − 04	–	–
API code	H = 0.2 MN.m M = 0 MN.m	0.15	2.3E − 05	7.60E − 03	1.1E − 04	–	–
Elastic-plastic	M = 2 MN.m H = 0 MN	0.41	8.3E − 05	–	–	2.1E − 04	4.2E − 05
API code	M = 2 MN.m H = 0 MN.m	0.223	6.0E − 05	–	–	1.1E − 04	3.0E − 05

major steps are also shown. It may also be noted that Fig. 15.9B plots the ultimate capacity of the pile based on two considerations: (a) Soil fails and the pile fails as rigid body failure; (b) Pile fails by forming a plastic hinge.

Using Eq. (15.13) and applying to the results obtained and shown in Table 15.4, stiffness terms as predicted by Elastic-Plastic model are given by Eq. (15.19).

15.4.1 Elastic-plastic formulation

$$I = \begin{bmatrix} 0.00215 & 0.00021 \\ 0.00021 & 0.000042 \end{bmatrix} => I^{-1} = K = \begin{bmatrix} K_L & K_{LR} \\ K_{RL} & K_R \end{bmatrix} = \begin{bmatrix} 894.1 & -4451.3 \\ -4451.3 & 46,252.1 \end{bmatrix}$$

$$K_L = 894.1 \text{ MN}/m \quad K_{LR} = -4451.3\text{MN} \quad K_R = 46,252.1 \text{ MN.m/Rad} \tag{15.19}$$

The same approach has been use for the API model and the results are shown in Eq. (15.20).

15.4.2 API formulation

$$I = \begin{bmatrix} 0.0076 & 0.00011 \\ 0.00011 & 0.00003 \end{bmatrix} => I^{-1} = K = \begin{bmatrix} K_L & K_{LR} \\ K_{RL} & K_R \end{bmatrix} = \begin{bmatrix} 3102 & -11,823.7 \\ -11,823.7 & 78,275.5 \end{bmatrix}$$

$$K_L = 3102 \text{ MN}/m \quad K_{LR} = -11,823.7\text{MN} \quad K_R = 78,275.5 \text{ MN.m/Rad} \tag{15.20}$$

It may be noted that the stiffness terms are quite different in the two formulations given by Eqs. (15.19 and 15.20). This is because the API formulation is empirical and is calibrated against small diameter piles and the extrapolation to large diameter piles is not validated or verified.

Finite Element Software package PLAXIS 3D was also used to evaluate the deflection and rotation due to the pile head loads. To save computational efforts space, half the pile was modeled, see Figs. 15.10 and 15.11. A classical Mohr−Columb material model was set for the soil with the same stiffness and strength properties provided in Table 15.3. For the pile material, elastic perfectly plastic model was used. Ten node tetrahedral elements were assigned to the soil volume and six node triangular plate elements for were used for the pile. The interface between the soil and the pile was modeled with double-noded elements. The soil extents were set as $20D_p$, and a medium-dense mesh was used. The pile was extended by 21 m above the ground to simulate the effect of the applied moment. Similar plots shown in Fig. 15.9 were obtained. Fig. 15.12 plots the deflection along the length of the pile obtained for $H = 4.6$ MN and $M = 95$ MN m.

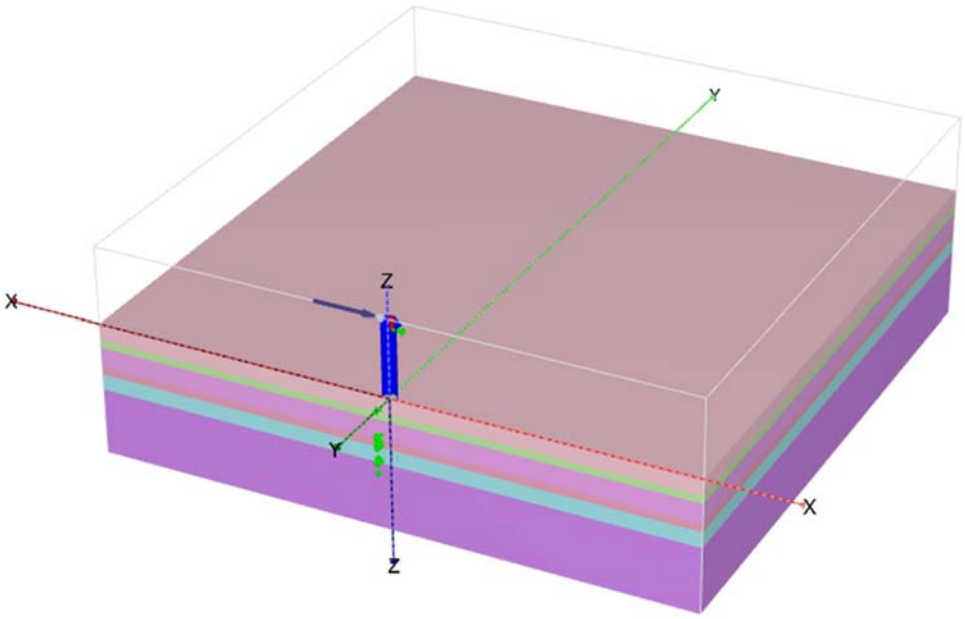

FIGURE 15.10 Geometry used in Plaxis model.

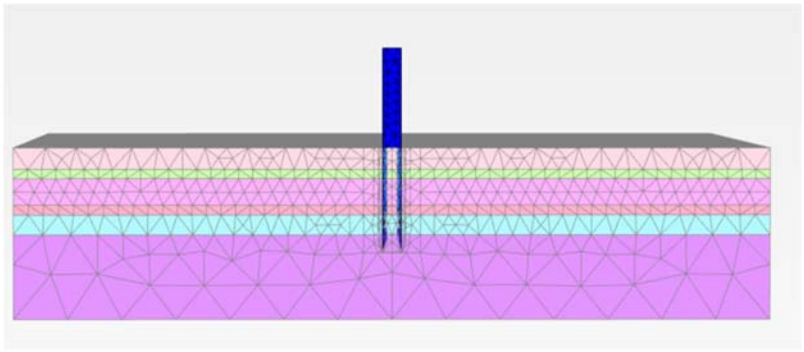

FIGURE 15.11 Mesh used in Plaxis model.

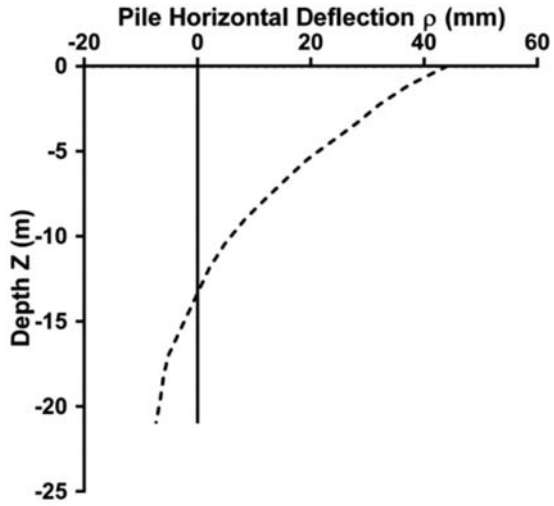

FIGURE 15.12 Plots the deflection of the pile obtained from the PLAXIS analysis for pile head loads of H = 4.6 MN and M = 95 MNm.

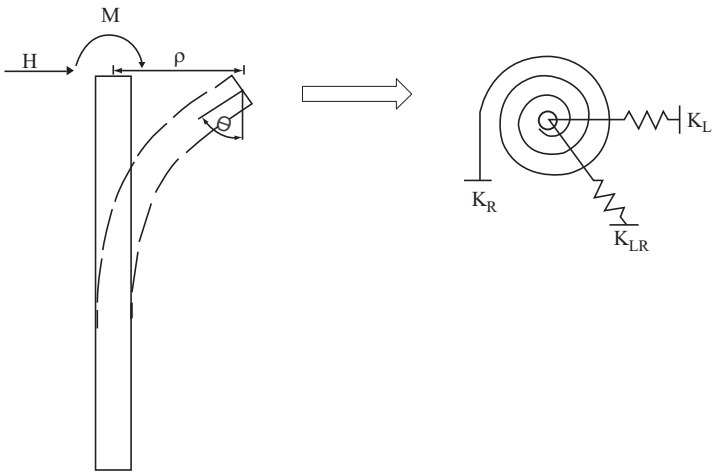

FIGURE 15.13 Simplified spring model.

15.5 Discussion and application of foundation stiffness

Fig. 15.13 schematically shows the essence of the matrix operations presented in the earlier section. Essentially, the foundation is replaced by a set of springs which are obtained from lateral load/moment analysis of piles. This is quite similar to the substructure method.

15.5.1 Pile head deflections and rotations

Eq. (15.5) can be used to predict pile head deflections and rotations as shown below (Eq. 15.21). It may be noted from Fig. 15.9A–D that the ultimate loads were within the linear range.

15.5.1.1 Elastic-plastic

$$\begin{bmatrix}\rho\\ \theta\end{bmatrix}=\begin{bmatrix}894.1 & -4451.3\\ -4451.3 & 46,252.1\end{bmatrix}^{-1}\begin{bmatrix}4.6\\ 9.5\end{bmatrix}=\begin{bmatrix}0.03\\ 4.8E-03\end{bmatrix}$$

15.5.1.2 API formulation

$$\begin{bmatrix}\rho\\ \theta\end{bmatrix}=\begin{bmatrix}3102 & -11,823.7\\ -11,823.7 & 78,275.5\end{bmatrix}^{-1}\begin{bmatrix}4.6\\ 9.5\end{bmatrix}=\begin{bmatrix}0.014\\ 3.5E-03\end{bmatrix} \tag{15.21}$$

The results predict a deflection of 30 mm and a rotation of 0.280 degree using the Elastic-Plastic model. On the other hand, the results predict 14 mm of deflection and 0.20 degree using the API model. The advanced model based on PLAXIS 3D shown in Fig. 15.12 predicts a deflection of 42.5 mm and rotation of 0.3 degree.

15.5.2 Prediction of the natural frequency

These foundation stiffness values can be used to predict natural frequency following the method proposed by Arany et al. [1]. The steps are also shown below.

Step 1: (Fixed Based Natural Frequency of the Tower)

Calculate the bending stiffness ratio of Tower to the pile

$$\chi=\frac{E_T I_T}{E_P I_P} \tag{15.22}$$

Calculate the platform/tower length ratio

$$\psi=\frac{L_s}{L_T} \tag{15.23}$$

Calculate the substructure flexibility coefficient to account for the enhanced stiffness of the Transition piece

$$C_{MP}=\sqrt{\frac{1}{1+\left(1+\psi^3\right)\chi-\chi}} \tag{15.24}$$

Obtain the fixed base natural frequency of the tower

$$f_{FB}=\frac{1}{2\pi}C_{MP}\sqrt{\frac{3E_T I_T}{\left(mRNA+\frac{33mT}{140}\right){L_T}^3}} \tag{15.25}$$

where the cross-sectional properties of the tower can be calculated as

$$D_T=\frac{D_b+D_t}{2}\quad I_T=\frac{1}{8}(D_T-t_T)^3 t_T\pi \tag{15.26}$$

Step 2: Calculate the nondimensional foundation stiffness parameters

The equivalent bending stiffness of the tower needed for this step:

$$q=\frac{D_b}{D_T}\quad f(q)=\frac{1}{3}\times\frac{2q^2(q-1)^3}{2q^2\ln q-3q^2+4q-1}\quad EI_\eta=EI_{top}\times f(q) \tag{15.27}$$

TABLE 15.5 Tower properties. Note that t refers to metric tonnes.

Top Diameter/m	2.3
Bottom Diameter/m	4.0
Wall Thickness/mm	35
Tower Height/m	70
Mass of RNA/t	100
Mass of Tower/t	130

where I_{top} is the second moment of area of the top section of the tower

$$\eta_L = \frac{K_L L^3}{EI_\eta} \tag{15.28}$$

$$\eta_{LR} = \frac{K_{LR} L^2}{EI_\eta} \tag{15.29}$$

$$\eta_R = \frac{KR_R L}{EI_\eta} \tag{15.30}$$

Step 3: Calculate the foundation flexibility factors

$$C_R(\eta_L, \eta_{LR}, \eta_R) = 1 - \frac{1}{1 + 0.6\left(\eta_R - \frac{\eta_{LR}^2}{\eta_L}\right)} \tag{15.31}$$

$$C_L(\eta_L, \eta_{LR}, \eta_R) = 1 - \frac{1}{1 + 0.5\left(\eta_L - \frac{\eta_{LR}^2}{\eta_R}\right)} \tag{15.32}$$

Step 4: Calculate the flexible natural frequency of the OWT system

$$f_0 = C_L C_R f_{FB} \tag{15.33}$$

Due to a lack of some aspects of tower data, a similar 2 MW wind turbine from North Hoyle has been used. Table 15.5 summarizes the tower properties used for the calculations.

For simplicity, the substructure flexibility coefficient (C_{MP}) is considered to be 1. Therefore, following Eqs. (15.22−15.33) we obtain:

$$D_T = \frac{D_b + D_t}{2} = > \frac{4 + 2.3}{2} = 3.15 \quad I_T = \frac{1}{8}(3.15 - 0.035)^3 \times 0.035 \times \pi = 0.415 \text{ m}^4$$

$$f_{FB} = \frac{1}{2\pi}\sqrt{\frac{3 \times 210E9 \times 0.415}{(100{,}000 + \frac{33 \times 130{,}000}{140})70^3}} = 0.385 \text{ Hz}$$

The fixed base frequency is therefore 0.385 Hz.

$$q = \frac{4}{2.3} = 1.74 \quad f(q) = \frac{1}{3} \times \frac{2 \times 1.74^2(1.74-1)^3}{2 \times 1.74^2 \ln 1.74 - 3 \times 1.74^2 + 4 \times 1.74 - 1} = 3.56$$

$$EI_\eta = 210 \times \frac{1}{8}(2.3 - 0.035)^3 \times 0.035 \times \pi \times 3.56 = 119.4 \text{ GPa}$$

The nondimensional groups are:

$$\eta_L = \frac{0.8941 \times 70^3}{119.4} = 2568 \quad \eta_{LR} = \frac{-4.45 \times 70^2}{119.4} = -182.6 \quad \eta_R = \frac{46.25 \times 70}{119.4} = 27.1$$

The foundation flexibility coefficients are given as follows:

$$C_R(\eta_L, \eta_{LR}, \eta_R) = 1 - \frac{1}{1 + 0.6\left(27.1 - \frac{-182.6^2}{2568}\right)} = 0.894 \quad C_L(\eta_L, \eta_{LR}, \eta_R) = 1 - \frac{1}{1 + 0.5\left(2568 - \frac{-182.6^2}{27.1}\right)} = 0.999$$

The natural frequency is therefore given by:

$$f_0 = 0.894 \times 0.999 \times 0.385 = 0.344Hz$$

15.5.3 Comparison with SAP 2000 analysis

The system was modeled using SAP 2000 and modal analysis is carried out to obtain the natural frequency. Nonprismatic beam elements of varying diameter were assigned to the tower while the soil structure interaction was represented by discrete linear Winkler springs. The spring stiffness values were taken from the soil properties (Table 15.3) and are a function of modulus of elasticity at the location of the spring and the spacing between two adjacent springs. A lumped mass was assigned at the tower head to model the dead mass of the RNA (Rotor Nacelle Assembly). The first natural frequency recorded was 0.351 Hz and Fig. 15.14 shows the first mode of vibration.

Nomenclature

C_L,C_R	Lateral and rotational flexibility coefficient
C_{MP}	Substructure flexibility coefficient
D_b	Tower bottom diameter
D_p	Pile diameter
D_t	Tower top diameter
D_T	Average tower diameter
E_p	Pile Young's modulus
E_S	Vertical distribution of soil's Young's modulus
E_{SO}	Initial soil Young's modulus at $1D_p$ depth
$E_{I\eta}$	Equivalent bending stiffness for tower top loading
f_0	First natural frequency (flexible)
f_{FB}	Fixed base (cantilever) natural frequency
H	Horizontal load at pile head
I_p	Pile second moment of area
I_T	Tower second moment of area
K_L	Lateral stiffness of the foundation
K_{LR}	Cross-coupling stiffness of the foundation
K_R	Rotational Stiffness of the foundation
L_P	Pile embedded length
L_S	Platform height
L_T	Tower height
M	Applied moment at the pile head
m_{RNA}	Mass of Rotor Nacelle assembly
m_T	Mass of tower
θ	Pile head rotation
t_T	Tower wall thickness
η_L	Nondimensional lateral stiffness
η_{LR}	Nondimensional cross-coupling stiffness
η_R	Nondimensional rotational stiffness
ρ	Pile head deflection
Ψ	Length ratio
χ	Bending stiffness ratio
υ_s	Soil Poisson's ratio
ϕ'	Soil angle of internal friction

FIGURE 15.14 First mode of vibration.

References

[1] Arany L, Bhattacharya S, Macdonald J, Hogan SJ. Design of monopiles for offshore wind turbines in 10 steps. Soil Dyn Earthq Eng 2017;92:126−52. Available from: https://doi.org/10.1015/j.soildyn.2015.09.024 ISSN 0267-7261.

[2] Bouzid DA, Bhattacharya S, Dash SR. Winkler Springs (p-y curves) for pile design from stress-strain of soils: FE assessment of scaling coefficients using the mobilized strength design concept. Geomech Eng 2013;5:379−99. Available from: https://doi.org/10.12989/gae.2013.5.5.379.

[3] Adhikari S, Bhattacharya S. Vibrations of wind-turbines considering soil-structure interaction. Wind Struct 2011;14:85−112.

[4] Adhikari S, Bhattacharya S. Dynamic analysis of wind turbine towers on flexible foundations. Shock Vib 2012;19:37−56.

[5] Arany L, Bhattacharya S, Adhikari S, et al. An analytical model to predict the natural frequency of offshore wind turbines on three-spring flexible foundations using two different beam models. Soil Dyn Earthq Eng 2015;74:40−5. Available from: https://doi.org/10.1015/j.soildyn.2015.03.007.

[6] Arany L, Bhattacharya S, Macdonald JHG, Hogan SJ. Closed form solution of Eigen frequency of monopile supported offshore wind turbines in deeper waters incorporating stiffness of substructure and SSI Soil Dyn Earthq Eng 2016;83:18−32. Available from: https://doi.org/10.1015/j.soildyn.2015.12.011ISSN 0267-7261. Available from: http://www.sciencedirect.com/science/article/pii/S0267726115003206.

[7] Bhattacharya S, Cox JA, Lombardi D, Wood DM, Wood M. Dynamics of offshore wind turbines supported on two foundations. Proc ICE—Geotech Eng 2013;156:159. Available from: https://doi.org/10.1580/geng.11.00015.

[8] Bhattacharya S, Nikitas N, Garnsey J, et al. Observed dynamic soil−structure interaction in scale testing of offshore wind turbine foundations. Soil Dyn Earthq Eng 2013;54:47−60. Available from: https://doi.org/10.1015/j.soildyn.2013.07.012.

[9] Bhattacharya S. Challenges in the design of foundations for offshore wind turbines;. Engineering and Technology Reference, 9. Institute of Engineering and Technology; 2014. Available from: http://doi.org/10.1049/etr.2014.0041. ISSN 2056-4007.

[10] Lombardi D, Bhattacharya S, Muir D, Wood M. Dynamic soil−structure interaction of monopile supported wind turbines in cohesive soil. Soil Dyn Earthq Eng 2013;49:155−80. Available from: https://doi.org/10.1015/j.soildyn.2013.01.015.

[11] Zania V. Natural vibration frequency and damping of slender structures found on monopiles. Soil Dyn Earthq Eng 2014;59:8−20. Available from: https://doi.org/10.1015/j.soildyn.2014.01.007.

[12] Damgaard M, Zania V, Andersen L, Ibsen LB. Effects of soil−structure interaction on real time dynamic response of offshore wind turbines on monopile. Eng Struct 2014;75:388−401. Available from: https://doi.org/10.1015/j.engstruct.2014.06.006.

[13] Shadlou M, Bhattacharya S. Dynamic stiffness of monopiles supporting offshore wind turbine generators. Soil Dyn Earthq Eng 2015;15−32. Available from: https://doi.org/10.1015/j.soildyn.2015.04.002.

[14] DNV; 2004.

[15] Matlock H. Correlations for design of laterally loaded piles in soft clay. In: Proceedings of the Second Annual Offshore Technology Conference; 1970.

[16] Reese LC, Cox WR, Koop FD. Analysis of Laterally Loaded Piles in Sand. Pap. No. 2080. In: Proceedings of the Sixth Annual Offshore Technology Conference; 1974.

[17] O'Neill MW, Murchinson JM. An evaluation of p-y relationships in sands. Houston, TX: University of Houston;; 1983.

[18] Kallehave D., Thilsted C.L. Modification of the API p-y formulation of initial stiffness of sand. Offshore Site Investigation Geotechnique Integrated Geotechnologies−Present Futur; 2012.

[19] Gazetas G. Analysis of machine foundation vibrations: state of the art. Int J Soil Dyn Earthq Eng 1983;2:2−42. Available from: https://doi.org/10.1015/0261-7277(83)90025-6 ISSN 0261-7277.

[20] Augustesen AH, Brødbæk KT, Møller M, Sørensen, SPH, Ibsen LB, Pedersen TS, et al. Numerical modelling of large-diameter steel piles at horns rev. In: Topping BHV, Neves LFC, Barros RC, editors, Proceedings of the twelfth international conference on civil, structural and environmental engineering computing. Civil-Comp Press (Civil-Comp Proceedings; No. 91); 2009.

This page intentionally left blank

Chapter 16

Physical modeling of offshore wind turbine model for prediction of prototype response

Domenico Lombardi[1], Subhamoy Bhattacharya[2] and George Nikitas[2]
[1]Department of Geotechnical Engineering, The University of Manchester, United Kingdom, [2]Department of Geomechanics, University of Surrey, United Kingdom

16.1 Introduction

Offshore wind turbines (OWTs) are providing an increasing proportion of wind energy generation capacity because offshore sites are characterized by stronger and more stable wind conditions than comparable onshore sites. Owing to the higher capacity factor (i.e., the ratio of the actual amount of power produced over a period of time to the rated turbine power) and decreasing Levelised Cost of Energy (LCOE) (i.e., the ratio of the total cost of an offshore wind farm to the total amount of electricity expected to be generated over the wind farm's lifetime), OWTs are currently installed in high numbers in Northern Europe. The industry is rapidly developing worldwide, particularly in countries such as China, South Korea, Taiwan, and Japan, whereas the US has recently installed its first pilot offshore wind farm on Block Island. The design and construction of offshore turbines, however, are more challenging when compared with onshore counterparts, owing to the harsh environmental conditions existing at the offshore sites.

16.1.1 Complexity of external loading conditions

OWTs are characterized by a unique set of dynamic loading conditions that is schematically depicted in Fig. 16.1. These include: (1) load produced by the turbulence in the wind, whose amplitude is the function of the wind speed; (2) load caused by waves crashing against the substructure, whose magnitude depends on the height and period of waves; (3) load caused by mass and aerodynamic imbalances of the rotor, whose forcing frequency equals the rotational frequency of the rotor (referred to as 1 P loading in the literature); (4) loads in the tower due to the vibrations caused by blade shadowing effect (referred to as 3 P loading in the literature), which occurs as each blade passes through the shadow of the tower.

The loads imposed by wind and wave are random in both space and time, as a result, these are better described statistically by using the Pierson–Moskowitz wave spectrum and Kaimal wind spectrum, shown in Fig. 16.2. It is clear from the frequency content of the applied loads that the designer in order to avoid the resonance of the OWT has to select a design frequency that lies outside the ranges of forcing frequencies. Specifically, the Det Norske Veritas (DNV) code [1] recommends that the natural frequency of the wind turbine should be at least $\pm 10\%$ away from the main forcing frequencies introduced earlier. Depending on the design value of natural frequency, three design approaches are possible, namely: Soft-Soft (natural frequency <1 P), Soft-Stiff (natural frequency between 1 P and 3 P), and Stiff-Stiff (natural frequency >3 P).

It is worth noting that the design procedure requires an accurate evaluation of the natural frequency, which is dependent on the support condition (i.e., the stiffness of the foundation) that in turn relies on the strength and stiffness of the surrounding soil. Furthermore, as the natural frequencies of OWTs are very close to the forcing frequencies, the dynamics pose multiple design challenges because of the tight tolerance of the target natural frequency, whereby the scale of

Wind Energy Engineering. DOI: https://doi.org/10.1016/B978-0-323-99353-1.00021-9

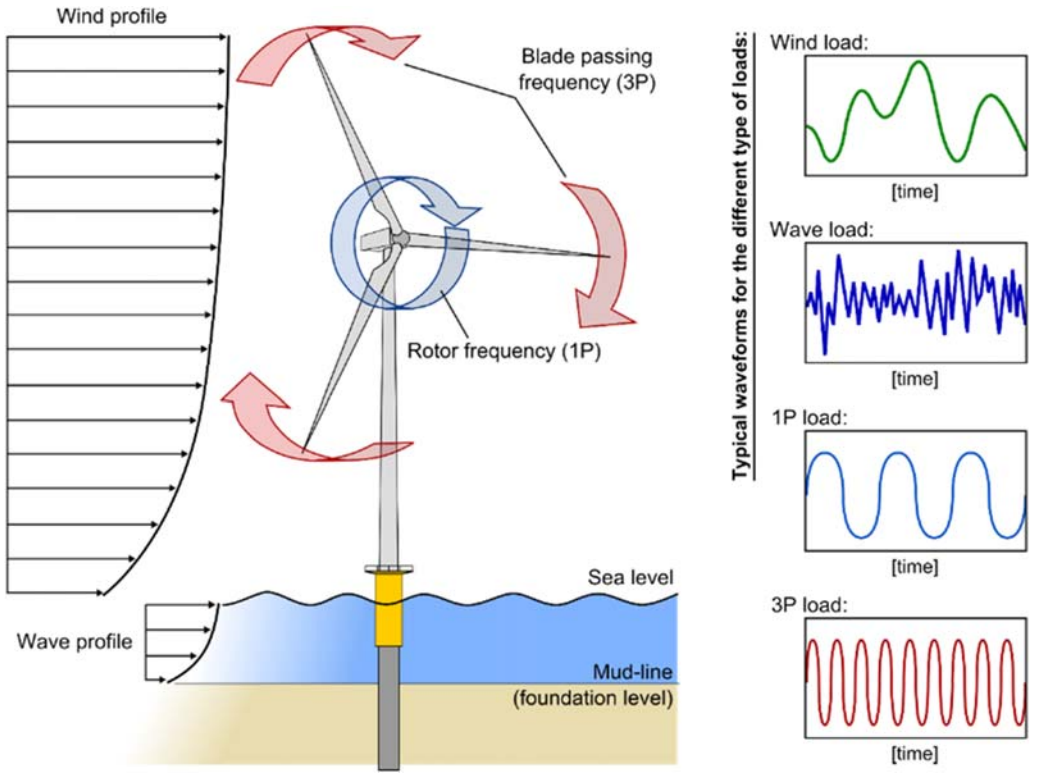

FIGURE 16.1 Typical loads acting on an offshore wind turbine.

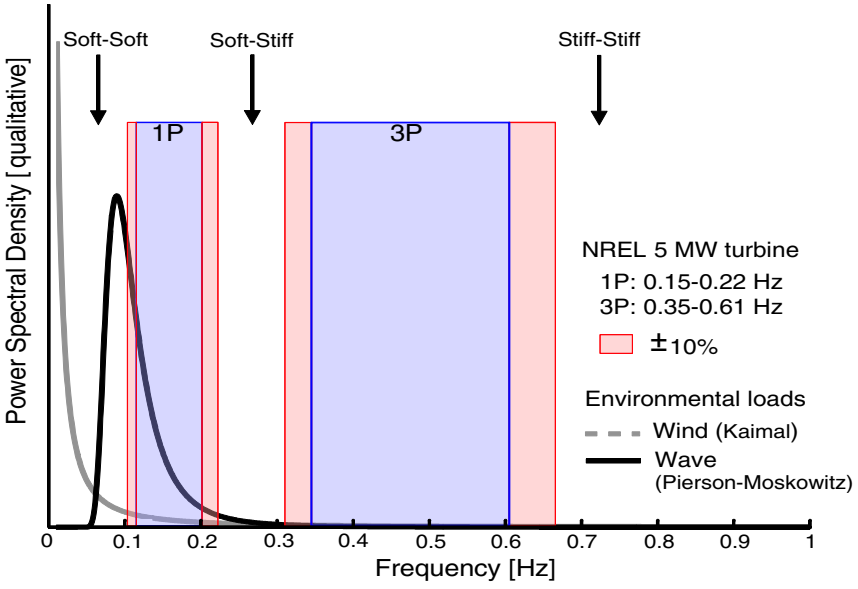

FIGURE 16.2 Qualitative power spectrum of main forcing frequencies and different design approaches considering an NREL 5 MW wind turbine.

the challenges will vary depending on turbine types and site characteristics. Typical values of vibration characteristics and site characteristics of operating wind turbines are listed in Table 16.1.

16.1.2 Design challenges

There are two main aspects related to cyclic loading conditions, see Nikitas et al. [3], that have to be taken into account during design: (1) soil behavior due to nondynamic repeated loading, that is, fatigue type problem and this is mainly

TABLE 16.1 Analysed offshore wind farms with the used wind turbines and soil conditions at the sites.

No.	Wind farm name and location	Turbine type and rated power	Soil conditions at the site	Natural frequencies[a]/ Hz
I.	Lely Offsore Wind Farm (Netherlands)	NedWind 40/500 2-bladed 500 kW study purpose wind turbine	Soft clay in the uppermost layer to dense and very dense sand layers below.	0.63–0.74
II.	Irene Vorrink Offshore Wind Farm (Netherlands)	Nordtank NTK600/43 600 kW study purpose wind turbine	Soft layers of silt and clay in the upper seabed to dense and very dense sand below.	0.55–0.56
III.	Blyth Offshore Wind Farm (UK)	Vestas V66 2 MW industrial offshore wind turbine	Rocky seabed (weathered bedrock)	0.49
IV.	Kentish Flats Offshore Wind Farm (UK)	Vestas V90 3 MW industrial offshore wind turbine	Layers of dense sand and firm clay	0.34
V.	Barrow Offshore Wind Farm (UK)	Vestas V90 3 MW industrial offshore wind turbine	Layers of dense sand and stiff clay	0.37
VI.	Thanet Offshore Wind Farm (UK)	Vestas V90 3 MW industrial offshore wind turbine	Fine sand and stiff clay	0.37
VII	Belwind 1 Offshore Wind Farm (Belgium)	Vestas V90 3 MW industrial offshore wind turbine	Dense sand and stiff clay	0.37
VIII	Burbo Bank Offshore Wind Farm (UK)	Vestas V90 3 MW industrial offshore wind turbine	Saturated dense sand (2090)	0.29
IX	Walney 1 Offshore Wind Farm (UK)	Siemens SWT-3.6–107 3.6 MW industrial offshore wind turbine	Medium and dense sand layers.	0.35
X	Gunfleet Sands Offshore Wind Farm (UK)	Siemens SWT-3.6–107 3.6 MW industrial offshore wind turbine	Sand and clay layers	0.31

[a]*Estimated based on reference [2].*

attributable to wind loading which has a very low frequency; (2) soil behavior due to dynamic loading which will cause dynamic amplification of the foundation response, that is, the resonance type problem. This is mainly due to 1 P and 3 P loading but wave loading can also be dynamic for deeper waters and heavier turbines. A breakdown of the overall problem of soil-structure interaction into two types of soil shearing is schematically represented in Fig. 16.3. The current codes of practice (e.g., DNV [1], American Petroleum Institute [3,4], Institute of Electrical Engineers) [5] for the design of monopile foundations of OWTs recommend the application of the p–y curves primarily for the evaluation of lateral pile capacity in the ultimate limit state. The codes provide limited guidance in predicting the change of the foundation stiffness and consequent change of natural frequency, which are both design drivers for serviceability limit state requirements.

Furthermore, it is important to note that the vibration of the foundation will induce cyclic strains in the soil in its vicinity. Under moderate-to-high amplitudes of cyclic loading most soils change their stiffness and strength. In order to study the changes in soil stiffness due to these cyclic strains, the developing strain in the soil around the shear zone must be taken into consideration. Soils in offshore sites can be fully saturated and therefore pore pressures are likely to develop as a result of these cyclic strains. The pore pressure developed may dissipate to the surrounding soil depending on factors including frequency of loading, the permeability of the soil, and diameter of the pile. Pore water pressure may also develop in unsaturated soils under cyclic shearing. It should be noted that due to the nature of the external excitation, wave and wind-induced loads may impose either one-way or two-way cyclic loading on the monopile, whereby one-way loading develops more soil deformation and consequently more change in foundation stiffness.

OWTs are relatively new structures without any track record of long-term performance. Therefore, the uncertainties of their long-term response pose additional challenges to developers and designers of offshore wind farms. In fact,

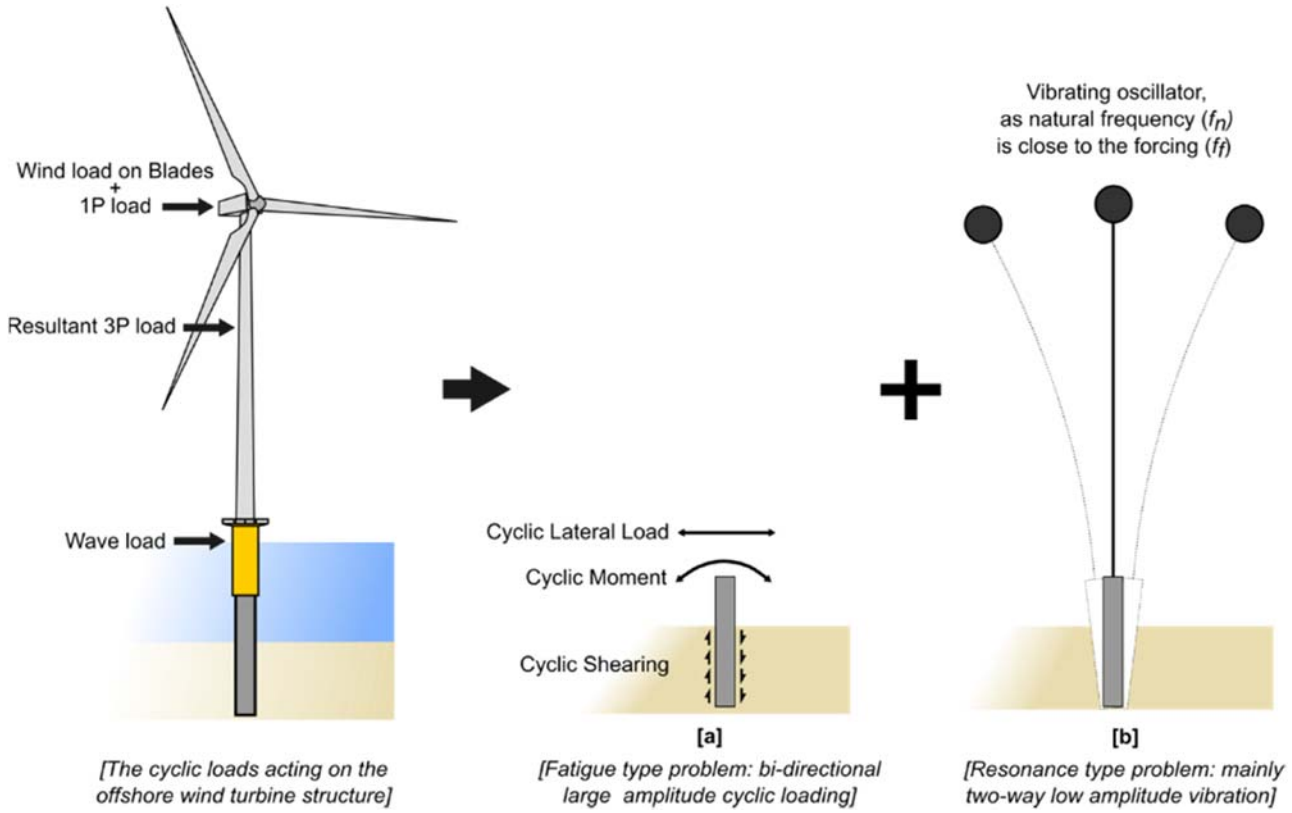

FIGURE 16.3 Breakdown of soil-structure interaction of offshore wind turbines into two types of problems.

monitoring of a limited number of installed wind turbines has indicated a gradual departure of the overall system dynamics from the design requirements (e.g., the data from Lely wind farm data) [6], which may lead to amplification of the dynamic response of the turbines, leading to larger tower deflections and/or rotations beyond the allowable limits tolerated by the manufacturer. The latter is often considered responsible for the damage observed in gearboxes and other electrical rotating equipment.

16.1.3 Technical review/appraisal of new types of foundations

Foundations typically cost 25%−35% of an overall offshore wind farm project and in order to reduce the LCOE, new innovative foundations are being proposed. However, before any new type of foundation can actually be used in a project, a thorough technology review is often carried out to de-risk it. European Commission defines this through TRL (Technology Readiness Level) numbering starting from 1 to 9, see Table 16.2 for different stages of the process. One of the early works that needs to be carried out is technology validation in the laboratory environment (TRL-4). In this context of foundations, it would mean carrying out tests to verify the long-term performance. It must be realized that it is very expensive and operationally challenging to validate in a relevant environment and therefore laboratory-based evaluation has to be robust so as to justify the next stages of investment. This is another motivation for scaled model testing.

16.1.4 Physical modeling for prediction of prototype response

Experimental investigations on physical wind turbine models can provide valuable information for understanding the dynamic behavior and long-term performance of OWTs. While physical modeling at normal gravity (often known as 1-g testing) can be used for modeling different loading conditions experienced by structures, its application in tackling soil-structure interaction needs additional consideration. In such cases, geotechnical centrifuge facilities are often used where 1: N scale model can be subjected to N-g (N times earth gravity) to replicate the prototype stresses. However, OWTs are very complex structures involving aerodynamics (wind turbulence at the blades), hydrodynamics (wave

TABLE 16.2 Definition of TRL.

TRL level as European Commission
TRL-1: Basic principles verified
TRL-2: Technology concept formulated
TRL-3: Experimental proof of concept
TRL-4: Technology validated in lab
TRL-5 Technology validated in relevant environment
TRL-6: Technology demonstrated in relevant environment
TRL-7: System prototype demonstration in the operational environment
TRL-8: System complete and qualified
TRL-9: Actual system proven in the operational environment

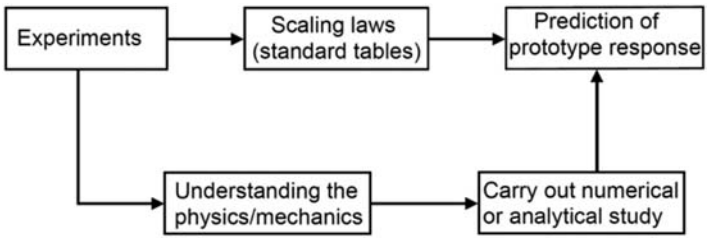

FIGURE 16.4 Reflective loop for physical modeling.

slamming the tower and the part of the tower under water), cyclic and dynamic soil-structure interaction. Ideally, a wind tunnel and a wave tank onboard a geotechnical centrifuge are suitable which seems to be unlikely with the current technology development. For such problems involving many interactions, where overall system dynamics and long-term performance needs to be studied, the centrifuge is not well-suited due to the unwanted parasitic vibration of the geotechnical centrifuge and the lack of a stable platform. Another important limitation of centrifuge facilities is the limited number of cycles that can reasonably be applied when compared with the expected number of cycles that a typical offshore wind turbine experiences over its lifespan of 25 years, which is in the range of 10^7-10^8. This calls for alternative modeling techniques where a problem will be studied through a set of nondimensional groups and is explained in the next section.

16.2 Physical modeling of offshore wind turbines

Derivation of correct scaling laws constitutes the first step in an experimental study. The similitude relationships are essential for the interpretation of the experimental data and for scaling up the results for the prediction of the prototypes' responses. As shown in Fig. 16.4, there are two approaches for deriving the scaling law relationships. The first is to use standard tables for scaling and multiply the model observations by the scale factor to predict the prototype response, for example, see Wood [7]. The alternative is to study the underlying mechanics/physics of the problem based on the model tests, recognizing that not all the interactions can be scaled accurately in a particular test. Once the mechanics/physics of the problem are understood, the prototype response can be predicted through analytical and/or numerical modeling in which the physics/mechanics discovered will be implemented in a suitable way. As shown by Bhattacharya et al. [8] and Lombardi et al. [9], the second method is well-suited for investigating the dynamics of OWTs, which involves complex dynamic wind−wave−foundation−structure interaction, and no physical modeling technique can simultaneously satisfy all the interactions at a single scale. Ideally, a wind tunnel combined with a wave tank on a geotechnical centrifuge would serve the purpose but this is unfortunately not feasible. Special consideration is required when interpreting the test results.

The design and interpretation of the test carried out on a small-scale model require the assessment of a set of laws of similitude that relate the model to the prototype structure. These can be derived from dimensional analysis from the

assumptions that every physical process can be expressed in terms of nondimensional groups and the fundamental aspects of physics must be preserved in the design of model tests. The necessary steps associated with designing such a model can be stated as follows:

- to deduce the relevant nondimensional groups by thinking of the mechanisms that govern the particular behavior of interest both at the model and prototype scale;
- to ensure that a set of crucial scaling laws are simultaneously conserved between model and prototype through pertinent similitude relationships;
- to identify scaling laws that are approximately satisfied, and those which are violated and therefore require special consideration.

16.2.1 Dimensional analysis

Dimensional analysis refers to a method of great generality and mathematical simplicity that can be conveniently used for studying phenomena that at first appear to be very complex but which can be qualitatively analyzed and described in more simplified terms [10]. Although the basis of dimensional analysis was set in the nineteenth century by Fourier in his work on the theory of the heat flow, only in the twentieth century the method has been extensively used in different fields of physics and engineering. The approach is based on the concept of similarity, which in physical terms implies that any phenomenon can be studied through a finite number of independent quantities expressed in a nondimensional form, that is, unit-free. In this context, dimensional analysis aims to determine these nondimensional quantities, which constitutes the first step in an experimental study

16.2.2 Definition of scaling laws for investigating offshore wind turbines

As discussed earlier, OWTs are dynamically sensitive structures because of the multiple frequencies that contribute to the complexity of the interaction of the foundation with the supporting soil. To study the dynamics and predict the long-term performance of OWTs, the following phenomena have to be considered and correctly replicated in the model tests, namely:

- vibration of the pile owing to the environmental loads will induce cyclic strains in the soil in the vicinity of the pile. In order to study the changes in soil stiffness owing to these cyclic strains, the developing soil strain around the field must be monitored. These soils are saturated and therefore pore pressures are likely to develop as a result of these cyclic strains. The pore pressure developed may dissipate to the surrounding soil, depending on the frequency of the loading;
- changes in the soil stiffness owing to the cyclic loading may lead to changes in foundation stiffness, which in turn will alter the natural frequency of the system. Therefore, the relationship between the foundation characteristics and the overall system dynamics, in other words, the soil−structure interaction, is important for overall system performance;
- repeated cyclic stresses will be generated in the pile owing to cyclic loading. Therefore, foundation fatigue is also a design issue.

Based on the above discussion, the following physical mechanisms are considered for the derivation of the nondimensional groups:

1. strain field in the soil around a laterally loaded pile which will control the degradation of soil stiffness;
2. cyclic stress ratio (CSR) in the soil in the shear zone;
3. rate of soil loading which will influence the dissipation of pore water pressure;
4. system dynamics, the relative spacing of the system frequency and the loading frequency;
5. bending strain in the monopile foundation for considering the nonlinearity in the material of the pile;
6. fatigue in the monopile foundation.

16.3 Scaling laws for offshore wind turbines supported monopiles

16.3.1 Monopile foundation

Most of the OWTs currently in operation are supported on monopiles. Monopiles consist of tubular steel tubes having a diameter in the range of 3.5−10 m. The choice of monopiles results from their simplicity of installation and the proven success of conventional piles—characterized by smaller diameters, that is, 1.5−3.0 m, in supporting offshore oil and gas infrastructures.

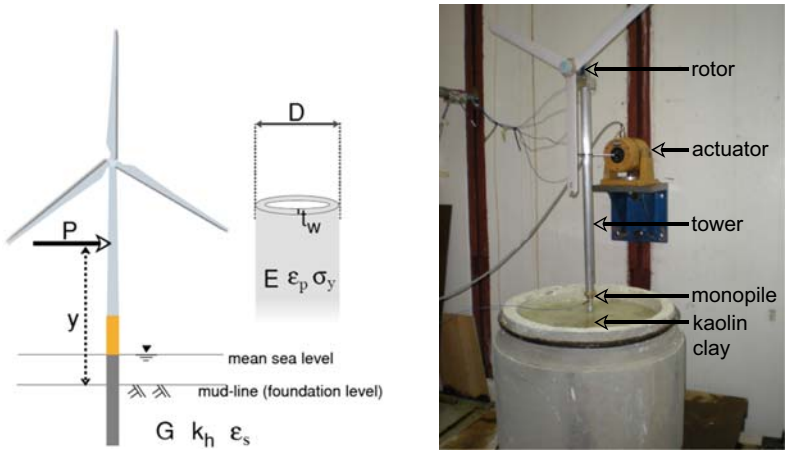

(A) (B)

FIGURE 16.5 (A) Definition of the main parameters used in the nondimensional analysis. (B) Small-scale physical model of offshore wind turbine used in the pilot studies.

16.3.2 Strain field in the soil around the laterally loaded pile

Repeated shear strain may reduce the stiffness of saturated soils. Assuming that the changes in soil stiffness drive long-term performance, the average strain next to a pile is a governing criterion and must be preserved in order to ensure similar stiffness degradation in both model and prototype. The relevant nondimensional group can be derived by considering that the average shear strain field around a laterally moving pile is a function of pile head deflection (δ) and pile outer diameter (D), mathematically expressed by:

$$\varepsilon_s \propto \frac{\delta}{D} \tag{16.1}$$

Klar [11] suggested a value of 2.6 for the coefficient of proportionality between the average strain in the soil and the ratio of head deflection and pile diameter. However, there is a lack of consensus in the literature on this proportionality coefficient. The pile head deflection is a function of the external load (P) the shear modulus of the soil (G) and the pile diameter. Therefore, the average strain field in the soil around a pile can be expressed as a function of only three parameters (see Fig. 16.5A):

$$\varepsilon_s = f(P, D, G) \tag{16.2}$$

The parameters in Eq. (16.2) can be used to obtain a dimensionless group as follows:

$$\varepsilon_s = f\left(\frac{P}{GD^2}\right)\frac{[F]}{[FL^{-2}][L]^2} \tag{16.3}$$

Eq. (16.3) describes the nondimensional group that takes into account the strain field in the soil generated by a laterally loaded pile. Eq. (16.3) shows that the strain in the soil is directly proportional to the horizontal load applied at the pile head, inversely proportional to the soil stiffness, and inversely proportional to the square of the pile diameter.

16.3.3 Cyclic stress ratio in the soil in the shear zone

In geotechnical earthquake engineering, it is well established that degradation of a soil due to liquefaction-type failure is a function of CSR which is defined as the ratio of the shear stress to the effective vertical stress at a particular depth, defined by Eq. (16.4) [12]. The CSR can be expressed by Eq. (16.4):

$$CSR = \frac{\tau_{cyc}}{\sigma'_v} \tag{16.4}$$

$$\tau_{\text{cyc}} \propto \frac{P}{D^2}\,\frac{[F]}{[L]^2} \tag{16.5}$$

where:

τ_{cyc} = cyclic shear stress imposed by the pile on the soil at a particular depth
σ'_v = effective vertical stress on the soil at the same depth

The vertical effective stress can be related to the shear modulus of the soil:

$$\sigma'_v \propto G\frac{[F]}{[L]^2} \tag{16.6}$$

It is usually found that G is proportional to $\sigma'_v n$, where the exponent n is a function of the type of soil, varying from 0.435 to 0.765 for sandy soil, although a value of 0.5 is commonly used in practice. For clayey soil, the value of n is generally larger and usually taken as 1 [13].

Combining Eqs. (16.4−16.6), one can see that the nondimensional group expressed by Eq. 16.3 can also guarantee the similarity of CSR. This leads us to a nondimensional group, expressed by Eqs. (16.7a) and (16.7b), that must be satisfied by the following equation:

$$\left(\frac{P}{GD^2}\right)_{\text{model}} = \left(\frac{P}{GD^2}\right)_{\text{prototype}} \tag{16.7a}$$

It is interesting to note that using two different approaches based on average strain in the soil, and on the CSR, the dimensional analysis leads to a unique nondimensional group given by Eq. (16.7a). It can be easily shown that considering the overturning moment (M) at the head of the foundation, that is, pile head; for example, the group in Eq. (16.7b) can equally be used, which is shown below:

$$\left(\frac{M}{GD^3}\right)_{\text{model}} = \left(\frac{M}{GD^3}\right)_{\text{prototype}} \tag{16.7b}$$

16.3.4 Rate of soil loading

Pore pressure generation and subsequent dissipation are a function of the frequency of loading exerted on the soil. The time (t) in which the pore pressure dissipates will be directly proportional to the soil permeability (k_h) and inversely proportional to characteristic length, for example, monopile diameter:

$$t \propto \frac{k_h}{D} \tag{16.8}$$

Considering the variables in Eq. (16.8), one can obtain the only possible dimensionless group:

$$\left(\frac{k_h t}{D}\right) \quad \frac{[LT^{-1}][T]}{[L]} \tag{16.9}$$

Replacing time by forcing frequency (f_f), the pore pressure dissipation is therefore correctly modeled when:

$$\left(\frac{k_h}{f_f D}\right)_{\text{model}} = \left(\frac{k_h}{f_f D}\right)_{\text{prototype}} \tag{16.10}$$

16.3.5 System dynamics

In order to correctly simulate the system dynamics resulting from the interaction between the external loads (i.e., forcing frequency) and the wind turbine (i.e., natural frequency), the ratio between the forcing frequency and the natural frequency of the turbine should be of the same order in the physical model and prototype. The main forcing frequencies are as follows (also see Fig. 16.2):

- Environmental loading: the predominant wave and wind forcing frequency is typically around 0.1 Hz;
- Rotor frequency: it represents the frequency of the blade rotation, and is generally indicated by 1 P. As shown in Fig. 16.2, typical values are in the range of 0.15−0.22 Hz;
- Wind shielding effects of the blade on the tower: when the blade passes the tower the shadowing effect of the wind load causes a cyclic load on the tower. This frequency is indicated by 3 P (or 2 P for a two-bladed rotor). Evidently, the blade passing frequency is the product of the rotor frequency and the number of blades.

From Fig. 16.2, it may be noted that for any of the three design approaches possible (i.e., soft-soft, soft-stiff, and stiff-stiff), the ratio between the forcing and the natural frequency is close to 1. This aspect must be preserved also in the physical model. Therefore the nondimensional groups for the correct modeling of the dynamics of the system can be expressed as a ratio between the forcing and natural frequency:

$$\left(\frac{f_f}{f_n}\right)_{\text{model}} = \left(\frac{f_f}{f_n}\right)_{\text{prototype}} \tag{16.11}$$

Lombardi et al. [9] pointed out that the two groups for "rate of soil loading," given by Eq. (16.10), and "system dynamics," given by Eq. (16.11), cannot be simultaneously satisfied with the same pore fluid in model and prototype. It is obvious that both coefficients of permeability and diameter of the monopile affect the drainage condition. Modeling both the nondimensional groups together can be conveniently accommodated through the use of a different pore fluid such as silicone oil or methylcellulose solution for the model tests.

16.3.6 Bending strain in the monopile

The strain in the monopile is a function of its mechanical properties and the characteristics of the external loads. As shown in Fig. 16.1, the external loads due to the wind and the waves can be conveniently modeled as a horizontal force acting at the distance y above the foundation level (see Figs. 16.3 and 16.5A). Assuming that the monopiles remains elastic, the strain in the pile wall will be a function given by Eq. (16.12).

$$\varepsilon_p = f(P, y, D, E, t_w) \tag{16.12}$$

where:

t_w is the pile wall thickness;
E is the Young's modulus of the pile

The parameters in Eq. (16.12) can be combined to obtain a dimensionless group:

$$\varepsilon_p = f\left(\frac{Py}{ED^2t_w}\right)\frac{[F][L]}{[FL^{-2}][L]^2[L]} \tag{16.13}$$

In order to correctly model the material nonlinearity of the pile, the nondimensional group expressed by Eq. (16.14) must be preserved in the model and the prototype:

$$\left(\frac{Py}{ED^2t_w}\right)_{\text{model}} = \left(\frac{Py}{ED^2t_w}\right)_{\text{prototype}} \tag{16.14}$$

16.3.7 Fatigue in the monopile

The stress in the monopile can be an important parameter influencing the fatigue phenomena. Fatigue relates to the degradation of the material after a large number of load cycles ($>10^7$ cycles). The design of an offshore wind turbine must ensure that the Fatigue Limit State is satisfied. The fatigue in the monopile can be expressed as a function of the external load, pile diameter, pile wall thickness, the vertical distance between the application point of the load P and the pile head, and the yield stress of the material (σ_y):

$$f\left(P, D, t_w, y, \sigma_y\right) \tag{16.15}$$

The parameters in Eq. (16.15) can be combined to obtain a dimensionless group:

$$f\left(\frac{Py}{\sigma_y D^2 t_w}\right)\frac{[F][L]}{[FL^{-2}][L]^2[L]} \tag{16.16}$$

Eq. (16.16) represents the nondimensional group required to take account of the fatigue phenomenon. This can be correctly modeled when Eq. (16.17) is satisfied, as shown below:

$$\left(\frac{Py}{\sigma_y D^2 t_w}\right)_{\text{model}} = \left(\frac{Py}{\sigma_y D^2 t_w}\right)_{\text{prototype}} \tag{16.17}$$

To explore the usefulness of these dimensionless groups derived so far, the next section of the paper describes typical results obtained from high-quality small-scale experiments.

16.3.8 Example of experimental investigation for studying the long-term response of 1−100 scale offshore wind turbine

This section describes an example of an experimental investigation carried out on a small-scale offshore wind turbine. The experimental apparatus is shown in Fig. 16.5B, however, more details regarding the experimental arrangement can be found in Lombardi et al. [9]. As it can be seen from the figure, modeling of the environmental dynamic loads can be achieved by using an electro-dynamic actuator fixed to the laboratory's strong wall and connected to the tower. The blades are rotated by a DC electric motor to model the 1 P loading, which also gives some aerodynamic damping to the system. An alternative cyclic loading system is proposed by Nikitas et al. [3]. This consists of two identical interlocking gears where masses can be attached, see Fig. 16.4. The working principle of this cyclic loading device is based on the unbalanced rotation of eccentric masses and is presented schematically in Fig. 16.6. This counter-rotating eccentric mass of equal magnitude is able to produce a unidirectional cyclic load on Y-axis only as the net force on X-axis is zero due to the cancellation of the equal and opposite forces. In the case when the two masses mounted on the interlocking gears are not equal, there will be a sinusoidal loading along two perpendicular directions (X and Y axis). The force resultants in the X and Y axes for two cases when the masses are equal and unequal are presented in Fig. 16.7.

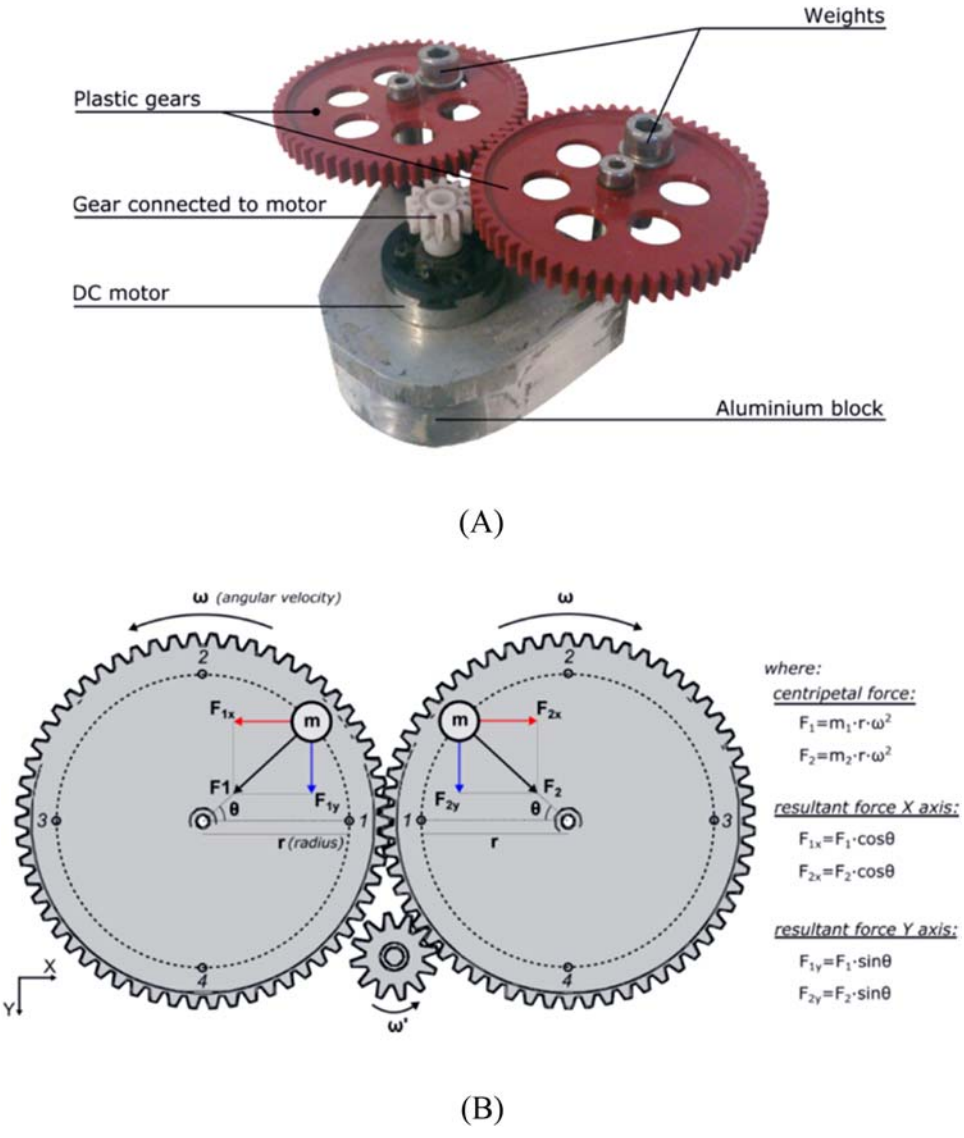

FIGURE 16.6 Cyclic loading system developed by Nikitas et al. [3]: (A) Photograph depicting different components; (B) Working principle.

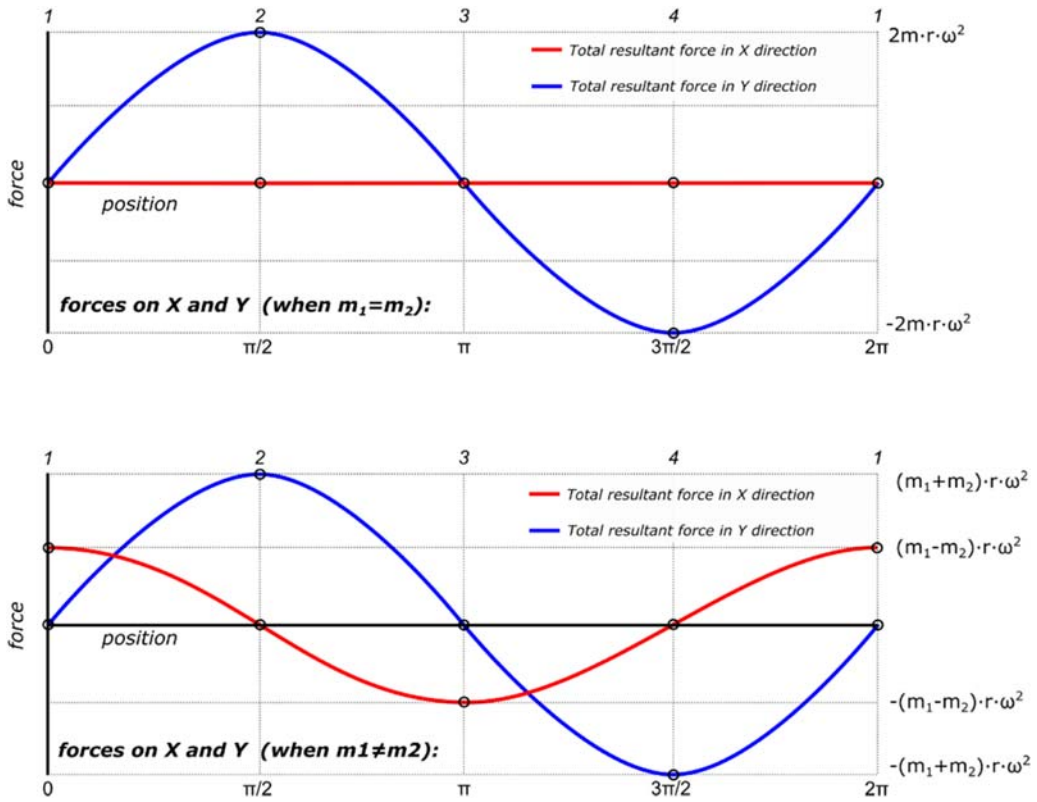

FIGURE 16.7 Force resultants in X and Y axes when the masses are equal (*top*) and not (*bottom*).

It may be noted that the excitation force produced by this device is dependent on three variables: mass of the weights attached to the gears (m), the radius of the gears (r), and the angular velocity of the gears (ω). The frequency (Hz) of the cyclic loading depends mainly on the angular velocity which can be easily controlled by the voltage (V) of the power supply. In order to control the force in the Y axis, the appropriate masses should be attached to the rotating gears, because the radius remains the same. Also, it is possible to change the frequency and amplitude by just replacing the type and the diameter of the gears. Once the amplitude and the frequency of the cyclic loads are defined, the device is mounted on the tower to simulate the desired overturning moment at the level of the foundation.

In a typical offshore project, the largest contribution towards the overturning moment is due to the wind and the wave loads having different magnitudes of the overturning moment, frequency, and also the number of cycles. A way to address this loading complexity in a scaled model test is by attaching two of these eccentric mass actuators, one to represent each load (frequency and amplitude), and placing them at the correct height in order to produce the desired scaled bending moment at the base of the model. The result of such an arrangement would provide realistic results for the foundation's long-term performance. Such a configuration is presented schematically in Fig. 16.8, where the wind and the wave are both acting along the same direction, that is, collinear. There can be loading scenarios, when the wind and the wave may not be aligned, and Fig. 16.9 shows a possible configuration that can be used for simulation.

Typical results presented by Lombardi et al. [9] highlighted that the long-term behavior of OWTs supported on monopiles is strongly affected by the level of strain generated in the soil adjacent to the foundation [given by Eq. (16.3)], whereby larger strains result in higher variation in foundation stiffness and natural frequency of the system. Evidently, the potential change in vibration characteristics has to be appropriately taken into account in the design and prediction of the long-term performance of OWTs.

16.4 Scaling laws for offshore wind turbines supported on multipod foundations

Offshore wind farm projects are increasingly turning to alternative foundations [14], which include jacket and multipod foundations. The scaling relations required to investigate such foundations need to take into account the geometric

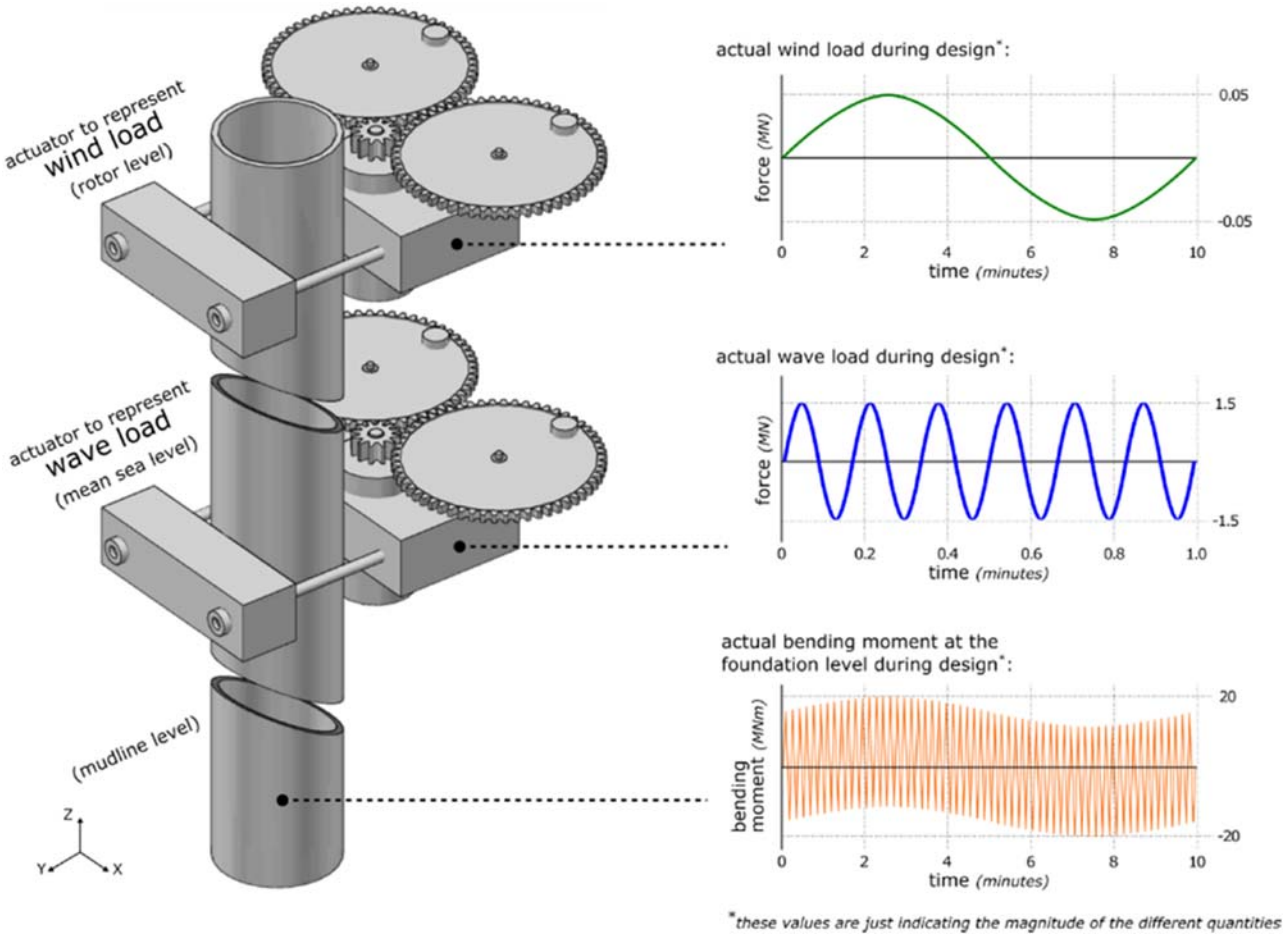

FIGURE 16.8 Configuration of two actuators to represent separately wind and wave loads, when these are acting along the same direction.

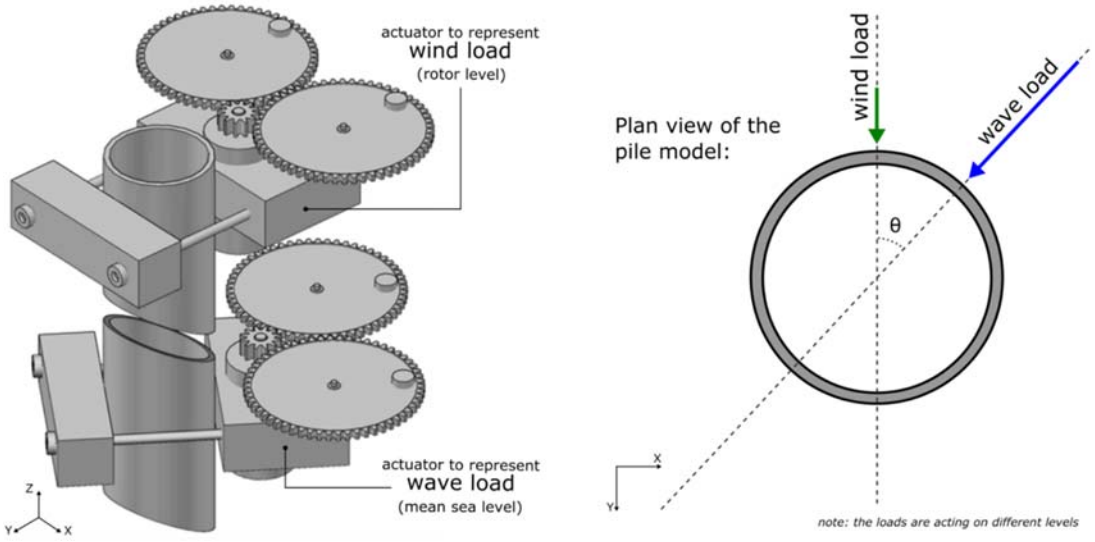

FIGURE 16.9 Configuration to study the wind-wave misalignment.

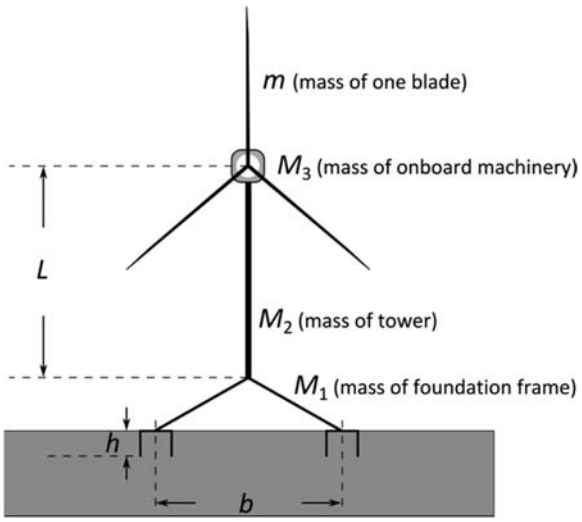

FIGURE 16.10 Schematic diagram for multipod foundation wind turbines.

arrangement (i.e., characterizing the asymmetry). Thus, this section of the chapter incorporates the additional scaling laws required to study generic multipod foundations, such as the one depicted in Fig. 16.10.

The rules of similarity between the model and prototype that need to be maintained are given in the following section.

The dimensions of the small-scale model need to be chosen in such a way that similar modes of vibration will be excited in the model and prototype. It is expected that rocking modes will govern the multipod (tripod or tetrapod suction piles or caissons) foundation and as a result relative spacing of individual pod foundations (b in Fig. 16.10) with respect to the tower height (L in Fig. 16.10) needs to be maintained, see Eq. (16.18). This geometrical scaling is also necessary to determine the point of application of the resultant force on the model. The aspect ratio of the caisson (diameter to depth ratio) should also be maintained to ensure the pore water flow is reproduced. This leads to the similitude relationship given by Eq. (16.19).

$$\left(\frac{L}{b}\right)_{\text{model}} = \left(\frac{L}{b}\right)_{\text{prototype}} \tag{16.18}$$

where L is the length of the tower and b is the spacing of the caissons

$$\left(\frac{D}{h}\right)_{\text{model}} = \left(\frac{D}{h}\right)_{\text{prototype}} \tag{16.19}$$

where D is the diameter of the caisson and h is the depth of the caisson.

To model the vibration of the tower, the mass distribution between the different components needs to be preserved. In other words, the ratios M_1:M_2:M_3:m in Fig. 16.10 need to be maintained in the model and prototype.

$$(M_1{:}M_2{:}M_3{:}m)_{\text{model}} = (M_1{:}M_2{:}M_3{:}m)_{\text{prototype}} \tag{16.20}$$

The relative stiffness between the suction caisson and the surrounding soil: The stiffness of the caissons relative to the soil needs to be preserved in the model so that the caisson interacts similarly with the soil as in the prototype. Caisson flexibility affects both the dynamics and the soil structure interaction and as a result, this mechanism is of particular interest. Based on the work of Doherty et al. [15], the nondimensional flexibility of a suction caisson is given by:

$$\frac{Et}{GD} \tag{16.21}$$

where

E = Elastic modulus of caisson skirt (GPa)
t = Thickness of caisson skirt (mm)

G = Shear modulus of surrounding soil (GPa)
D = Diameter of the caisson (m)

The above group can be derived from the expression of hoop stress (σ_θ) developed in a thin-walled cylindrical pressure vessel given by Eq. (16.5).

$$\sigma_\theta \propto \frac{pD}{t} \tag{16.22}$$

noting that σ_θ is the stress in the caisson which is proportional to the elastic modulus of the caisson skirt (E) and p is the pressure applied by the soil, dependent on the shear modulus. Therefore, the following relationship should be maintained:

$$\left(\frac{Et}{GD}\right)_{\text{model}} = \left(\frac{Et}{GD}\right)_{\text{prototype}} \tag{16.23}$$

The loading encountered in a single caisson in a multipod foundation is a combination of vertical and horizontal load. For a combination of lateral and vertical load, a failure envelope given by Eq. (16.24) is often used in practice.

$$\left(\frac{V}{V_{\max}}\right)^i + \left(\frac{H}{H_{\max}}\right)^j = 1 \tag{16.24}$$

where

$H_{\max}$ = Bearing capacity in horizontal direction
$V_{\max}$ = Bearing capacity in vertical direction
V = Vertical load on the individual caisson
H = Horizontal load on the caisson

with $i = j = 3$ (see) [8]

The nondimensional group to preserve is $V/V_{\max}$ which is proportional to $V/\gamma' D^3$ for sandy soil where γ' is the buoyant soil unit weight (kN/m^3) and D is the caisson diameter. The relationship for clay soil is given by Eq. (16.25c). Therefore, the following relationship should hold the following equations:

$$\left(\frac{V}{V_{\max}}\right)_{\text{model}} = \left(\frac{V}{V_{\max}}\right)_{\text{prototype}} \tag{16.25a}$$

$$\left(\frac{V}{\gamma' D^3}\right)_{\text{model}} = \left(\frac{V}{\gamma' D^3}\right)_{\text{prototype}} \quad \text{for sandy soil} \tag{16.25b}$$

$$\left(\frac{V}{s_u D^2}\right)_{\text{model}} = \left(\frac{V}{s_u D^2}\right)_{\text{prototype}} \quad \text{for clay soil} \tag{16.25c}$$

Details of the derivation are provided in [8]. The lateral load acting on the caisson can be derived from the CSR in the shear zone next to the footing which is quite similar to the case for pile as derived earlier for the monopile due to the fact that caissons and monopiles will act as a rigid body. This leads us to a nondimensional group (Eq. 16.26) that must be satisfied.

$$\left(\frac{H}{GD^2}\right)_{\text{model}} = \left(\frac{H}{GD^2}\right)_{\text{prototype}} \tag{16.26}$$

16.4.1 Typical experimental setups and results

A series of tests were carried out by Bhattacharya et al. [14] to investigate the dynamics and long-term performance of small-scale OWTs models supported on multipod foundations (see Fig. 16.11). Fig. 16.12 shows the asymmetric model arrangement in a typical setup. The results showed that the multipod foundations (symmetric or asymmetric) exhibit two closely spaced natural frequencies corresponding to the rocking modes of vibration in two principle axes. Furthermore, the corresponding two spectral peaks change with repeated cycles of loading and they converge for symmetric tetrapods but not for asymmetric tripods. From the fatigue design point of view,

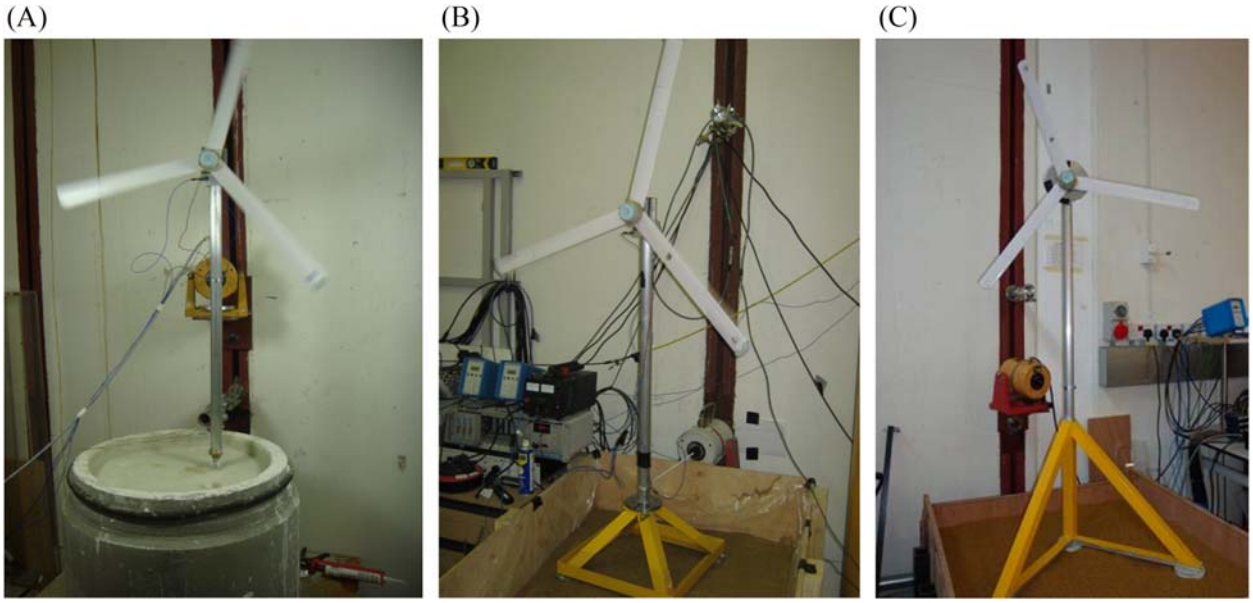

FIGURE 16.11 Small-scale wind turbine model supported on different types of foundation; (A) monopile; (B) symmetric tetrapod foundation; (C) asymmetric tripod.

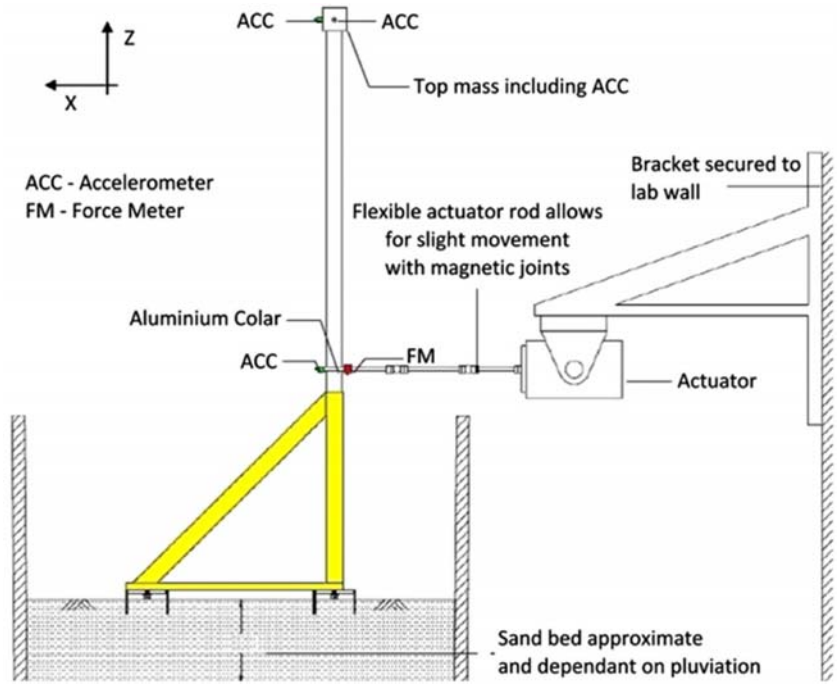

FIGURE 16.12 Schematic diagram of the test setup for asymmetric tripod.

the two spectral peaks for multipod foundations broaden the range of frequencies that can be excited by the broadband nature of the environmental loading (wind and wave) thereby impacting the extent of motions. Thus, the system lifespan (number of cycles to failure) may effectively increase for symmetric foundations as the two peaks will tend to converge. However, for asymmetric foundations, the system life may continue to be affected adversely as the two peaks will not converge. In this sense, designers should prefer symmetric foundations to asymmetric foundations.

16.5 Conclusions

This chapter shows that small-scale experimental studies can be carried out to study complex dynamic soil-structure interaction problems where there is no prior information. The long-term performance of OWTs has been studied because there is a real concern regarding the effect on the performance of changes in the foundation stiffness.

Mechanics-based nondimensional groups have been derived in order to study the various aspects of this problem and their validity has been verified using physical modeling. Under certain loading conditions, the natural frequency of the system decreases as a result of the effects of cyclic loading. These critical conditions relate to the strain level in the soil; and the relative position of the system frequency in comparison to the forcing frequency.

References

[1] DNV GL AS. Design of offshore wind turbine structures. DNV-OS-J101, Det Norske Veritas; 2014.
[2] Arany L, Bhattacharya S, Macdonald JH, Hogan SJ. Closed form solution of Eigen frequency of monopile supported offshore wind turbines in deeper waters incorporating stiffness of substructure and SSI. Soil Dyn Earthq Eng 2016;83:18−32.
[3] Nikitas G, Vimalan NJ, Bhattacharya S. An innovative cyclic loading device to study long term performance of offshore wind turbines. Soil Dyn Earthq Eng 2016;82:154−60.
[4] API. Recommended practice for planning, designing, and constructing fixed offshore platforms: working stress design. 20th ed. Washington, DC: American Petroleum Institute RP2A-WSD; 2007.
[5] IEC 61400-1. Wind turbine generator systems—part 1: design requirements, 3rd ed.; 2005.
[6] Kuhn M. Dynamics of offshore wind energy converters on mono-pile foundation experience from the Lely offshore wind turbine. In: OWEN Workshop; 2000.
[7] Wood DM. Geotechnical modelling. CRC Press; 2003. ISBN: 9780415343046.
[8] Bhattacharya S, Lombardi D, Wood DM. Similitude relationships for physical modelling of monopile-supported offshore wind turbines. Int J Phys Model Geotech 2011;11(2):58−68.
[9] Lombardi D, Bhattacharya S, Wood DM. Dynamic soil−structure interaction of monopile supported wind turbines in cohesive soil. Soil Dyn Earthq Eng 2013;49:165−80.
[10] Lombardi D, Bhattacharya S, Ghosh S, Alexander NA. Fundamentals of engineering mathematics. London: ICE Publishing; 2015.
[11] Klar A. Upper bound for cylinder movement using "Elastic" fields and its possible application to pile deformation analysis. Int J Geomech 2008;8(2):162−7.
[12] Seed HB, Idriss IM. Simplified procedure for evaluating soil liquefaction potential. J Soil Mech Found Div 1971;97(SM9):1249−73.
[13] Wroth CP, Randolph MF, Houlsby GT, Fahey M. A review of the engineering properties of soils with particular reference to the shear modulus. Report CUED/D-SOILS TR75. University of Cambridge; 1979.
[14] Bhattacharya S, Cox JA, Lombardi D. Dynamics of offshore wind turbines supported on two foundations. Inst Civ Eng Proc Geotech Eng 2013;166(2):159−69.
[15] Doherty JP, Houlsby GT, Deeks AJ. Stiffness of flexible caisson foundations embedded in non-homogeneous elastic soil. J Geotech Geoenviron Eng 2005;131(12):1498−508.

Chapter17

Seismic design and analysis of offshore wind turbines

Subhamoy Bhattacharya[1,2], **Sadra Amani**[1], **Athul Prabhakaran**[3] **and Surya Biswal**[1]

[1]Department of Sustainability, Civil and Environmental Engineering, University of Surrey, Guildford, London, United Kingdom, [2]Renew Risk (OWF-PRA Limited), London, United Kingdom, [3]Department of Structural Engineering, University of California, San Diego, CA, United States

17.1 Introduction

Around the world, offshore wind farms are increasingly constructed as a source of renewable energy, with more turbines deployed in regions of high seismicity. Fig. 17.1 shows the global development of offshore wind farms in terms of capacity by 2030.

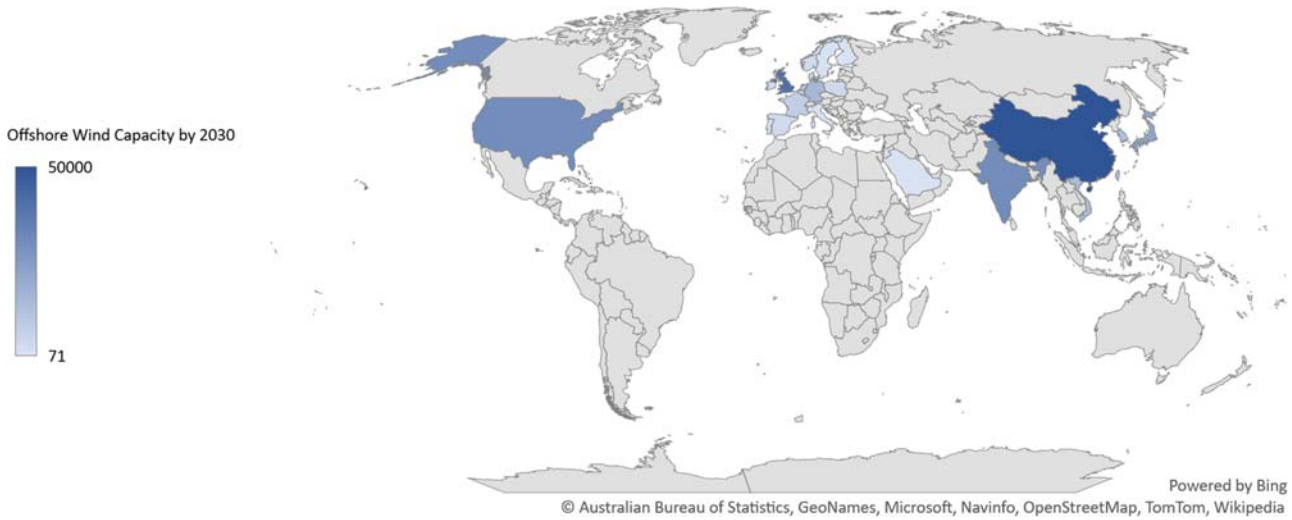

FIGURE 17.1 Projected offshore wind capacity in 2030 [1−7].

This chapter focuses on seismic design considerations of offshore wind turbines and introduces frameworks along with some examples. The foundations of offshore wind turbines are generally divided into two types: (i) bottom fixed and (ii) floating. Bottom fixed wind turbines could be subdivided into suction bucket caissons, gravity-based, monopiles, and jacket foundations as shown in Fig. 17.2 (1−5). Floating wind turbines also could be subdivided into semi-submersible, tension leg platform (TLP), barge, and spar type foundations as shown in Fig. 17.2 (6−9). Bottom-fixed foundations typically are installed in shallow waters, whereas floating wind turbines are deployed in deep waters [8]. The sections below illustrate simplified design considerations towards the seismic design of bottom fixed and floating wind turbines.

Wind Energy Engineering. DOI: https://doi.org/10.1016/B978-0-323-99353-1.00011-6

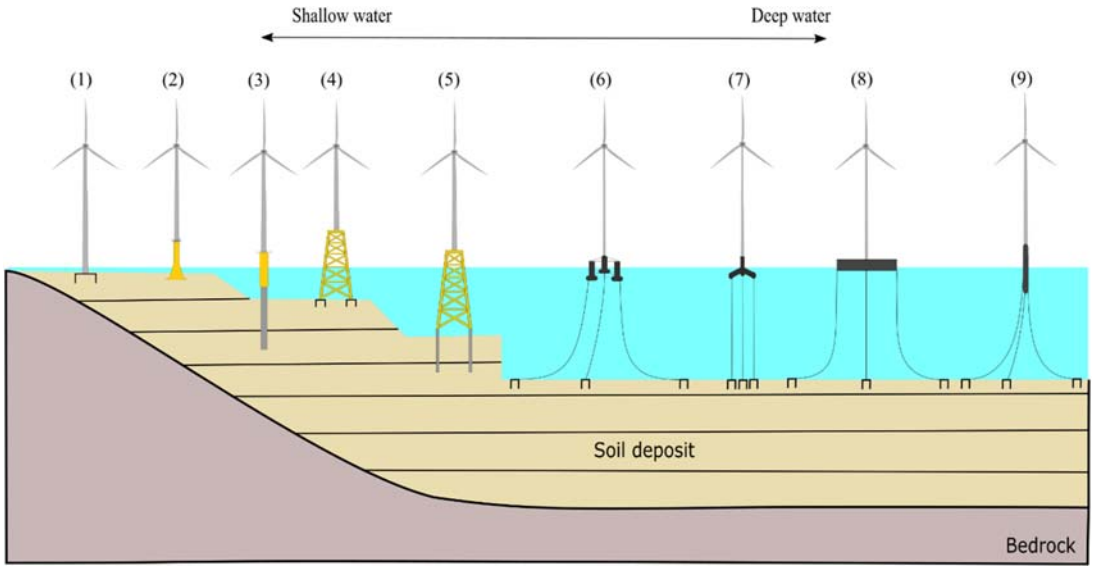

FIGURE 17.2 Typical bottom fixed and floating foundations. (1) Suction bucket caisson, (2) gravity-based foundation, (3) monopile, (4) jacket on suction caisson (5) jacket on monopile, (6) semisubmersible, (7) tension leg platform (TLP), (8) barge, (9) spar [9].

17.2 Methodology of design for bottom fixed offshore and nearshore wind farms

This section presents a methodology to design nearshore and offshore wind turbines in seismic regions. Typical limit states for OWT design include an ultimate limit state (ULS), serviceability limit state (SLS), and fatigue limit state (FLS) criteria. ULS criteria are necessary to ensure that the structure and foundation remain safe and exhibit minimal plastic deformations during extreme loading. SLS criteria are necessary to ensure that the pile head tilt, rotation, and RNA acceleration is within an acceptable range. Finally, FLS criteria are necessary to appraise the long-term life of the structure (*e.g.*, high cycle fatigue loading, seismic events, *etc.*). Limit states considered for seismic design are discussed below:

1. Seismic considerations-ULS: The presence of liquefaction/strain-softening susceptible layers in the soil can reduce the ultimate capacity of embedded foundations. Further, under static shear stresses, ground failure can lead to the mobilization of large soil masses and increased demands on the foundation system.
2. Seismic consideration-SLS: Strong shaking can increase demands on the rotor-nacelle assembly (RNA), and permanent tilt/deformation at the pile head.
3. Seismic consideration-FLS: The large number of cycles imposed by wind/wave load can induce high cycle fatigue. This condition must be accounted for in the seismic design of OWTs, where the capacity of the foundation system must be reduced to account for the fatigue load. It is noted that OWTs incur a much larger number of cycles during storm and typhoon loading compared to earthquake loads. However, seismic loads can incur large shear strains on the soil deposit. Therefore, considerations should be made toward changes to the fatigue life of the turbine, particularly during postseismic events.

A summary of typical limit states in OWT deep foundation design is detailed in Table 17.1 and Fig. 17.3. Readers are referred to Bhattacharya [10], Amani et al. [11] and Bhattacharya et al. [12] for further details.

TABLE 17.1 ULS, SLS, and FLS Criteria of bottom fixed wind turbines.

Limit state	Typical criteria
ULS	1. Ground failure (soil failure) causing foundation collapse 2. Foundation should remain elastic
SLS	1. Permanent tilt at pile head < 0.5 to 0.75 degree (these are typical for grounded systems) 2. RNA acceleration < 0.2 to 0.4 g 3. Acceptable pile head deformation
	*Please see Fig. 17.3
FLS	1. Wind + Wave loading imposes many cycles during the operational life of the turbines 2. Fatigue life needs to be quantified after a seismic event

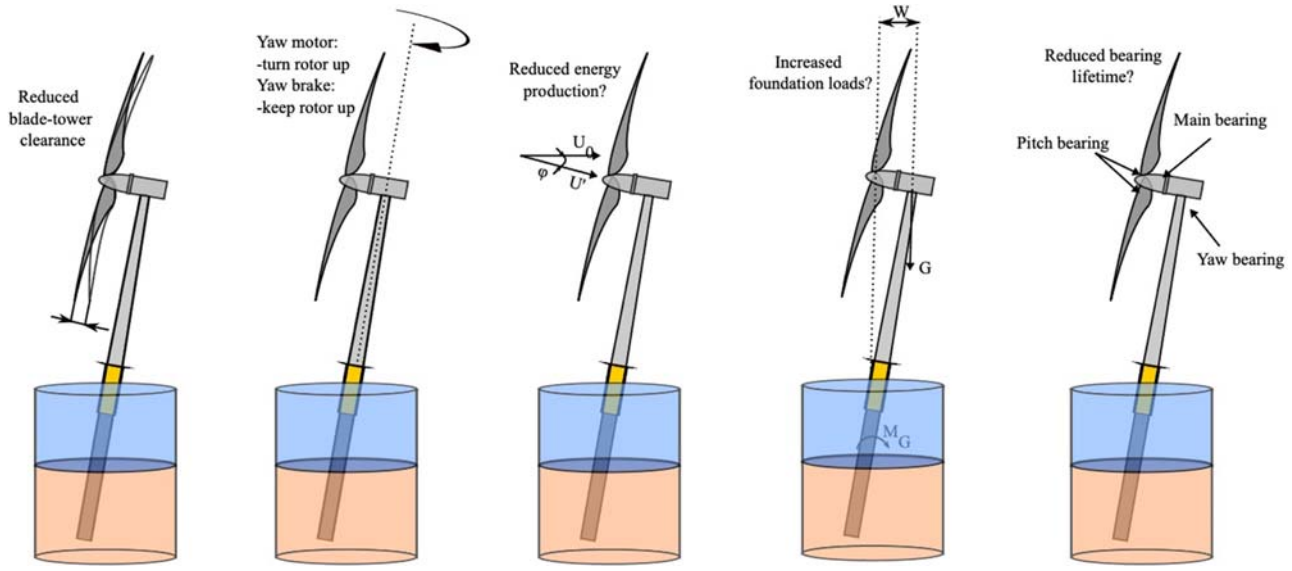

FIGURE 17.3 Aspects governing the SLS requirements for monopile foundation [10].

Furthermore, limit states considered for the seismic design of floating wind farms are discussed below:

4. Seismic considerations-ULS: The presence of liquefaction/strain-softening susceptible layers in the soil can reduce the ultimate capacity of embedded foundations. Further, under static shear stresses, ground failure can lead to the mobilization of large soil masses and increased demands on the foundation system.
5. Seismic consideration-SLS: Strong shaking can increase demand for RNA and permanent tilt/deformation at the pile head.
6. Seismic consideration-FLS: The large number of cycles imposed by wind/wave load can induce high cycle fatigue. This condition must be accounted for in the seismic design of OWTs, where the capacity of the foundation system must be reduced to account for the fatigue load.

Once the limit states at each hazard level are explicitly defined, the proposed methodology (outlined in Fig. 17.4) can be used to obtain a preliminary foundation design. These steps outlined in Fig. 17.4 are shown as below:

1. Input Data Assimilation:
   Prior to analyses, information regarding the turbine, site, and hazards needs to be obtained, including the following points:
   a. *Performance requirement (limit states)* includes ULS, SLS, and FLS checks. The readers are referred to Table 17.1 for further details on the performance requirements.
   b. *Turbine data* includes wind turbine specifications such as blade diameter, rotor, blade passing frequency (1P, 3P), tower specifications (height, thickness, diameter).
   c. *Metocean data* could be collected from metrological stations nearby the site. These data could be wind speed (operational, turbulent), wave height, and period.
   d. *Site characterization* study is required to investigate the soil properties, soil layers, types, and water depth.
   e. *Seismic and tsunami hazard analyses* should be conducted for seismic regions for different return periods.
2. Preliminary design: For the estimation of the pile dimensions, this step must be fulfilled. The preliminary design methodology could be carried out using the 10-step method presented in Arany et al. [13].
3. Identification of layers that can rapidly lose strength and stiffness during earthquake loading using liquefaction triggering analysis (only in seismic regions).
4. Site response analysis: Appropriate soil constitutive models should be used to obtain soil displacement histories along the length of the pile. The user can perform a total/effective stress analysis based on the soil profile and expected level of shaking.
5. Definition of appropriate $p-y$ curves for soil layers precluding and including strength loss (in the event of soil liquefaction/cyclic softening).

6. Structural modeling of the tower-monopile system using appropriate structural properties. Imposition of wind, wave, and tsunami load (if applicable) on the tower structure.
7. Imposition of soil displacement histories obtained from step (4) to the fixed end of the soil spring.
8. Dynamic foundation-structure interaction analysis.

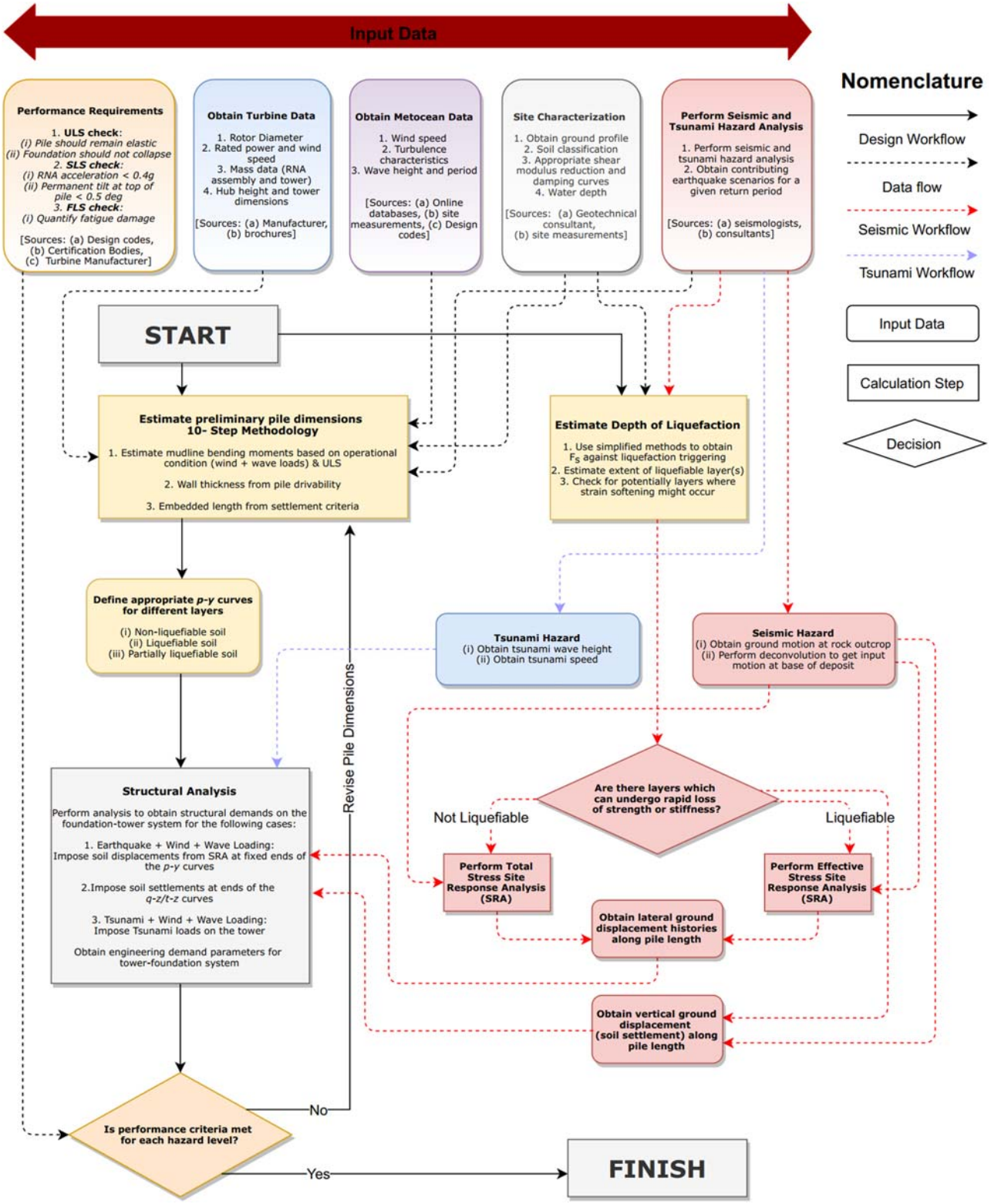

FIGURE 17.4 Workflow for monopile design for wind turbines in the seismic zone.

17.2.1 Ground motion selection

In design practice, the seismic hazard at a site is described in terms of a Uniform Hazard Spectra (UHS), obtained from a probabilistic seismic hazard analysis. However, selecting hazard-consistent ground motions using a UHS has proven to provide conservative estimates of structural response as the UHS is not defined through a single earthquake scenario. More appropriately, the conditional mean spectrum [14] and generalized conditional mean spectrum [15] can be used to obtain the suite of ground motions at the rock outcrop. A detailed review of possible ground motion selection methodologies could be found in Katsanos et al. [16].

The UHS is commonly prepared for rock outcrop sites. The methods discussed above could be utilized to obtain a suite of hazard-consistent ground motions (at the rock outcrop). Once the rock outcrop motion is obtained, deconvolution can be used to obtain the ground motion at bedrock [17]. The suite of ground motions developed for bedrock is the input to the site response analysis.

17.2.2 Site response analysis

The free-field response of the ground (away from the deep foundation) to the suite of ground motion developed at the bedrock level can be obtained through a site response analysis. If assumptions for 1D wave propagation hold [18], the shear stress−strain response of soil layers can be characterized through appropriate shear modulus reduction and damping curves. Based on project requirements, these curves can be site-specific or generic, based on the client's requirements. This approach would constitute a total stress-based site response analysis. Pore pressure, soil dilation, *etc*., can be incorporated using an effective stress-based approach with appropriate constitutive models. It is noted that equivalent linear analyses are usually performed in the frequency domain and cannot account for soil softening due to pore-pressure development [19]. Therefore, analysis of a deposit with liquefaction susceptible layers would require an appropriate soil constitutive model.

Displacement demands from the ground are then imposed on the pile through an appropriate set of load-deformation curves ($p-y$). It is noted that ground response analysis can account for the development of shear strain contrasts (based on the soil profile) and associated kinematic demands.

17.2.3 Soil-structure interaction

The free-field response of the soil deposit is connected to the response of deep foundations through appropriate $p-y$ curves. This method treats the pile as a beam on a nonlinear Winkler foundation, where pile−soil interaction is modeled using discrete nonlinear $p-y$ springs.

It is critical to note that $p-y$ curves employed in practice are often mechanism/hazard-specific. Therefore, considerations toward appropriate mechanisms should be accounted for in the selection of relevant $p-y$ curves. For example, in strain-softening/liquefaction susceptible deposits, appropriate modifications can be made to the $p-y$ curves to represent strength/stiffness loss. Several techniques currently exist in the literature to model the $p-y$ curve for liquefied soil, including p multiplier, reduced $p-y$ curves [20], hybrid curves [21], and zero strength $p-y$ curves [22]. Further after the onset of liquefaction, effects of soil dilation can be accounted for using strain hardening $p-y$ curves as mentioned in Lombardi et al. [23] or Dash et al. [24]. Therefore, the selection of inappropriate $p-y$ springs could lead to overestimation or underestimation in design based on the problem being analyzed. Typical $p-y$ springs for liquefied soil using the p multiplier (8%) reduced API and hyperelastic formulations, are shown below in Fig. 17.5.

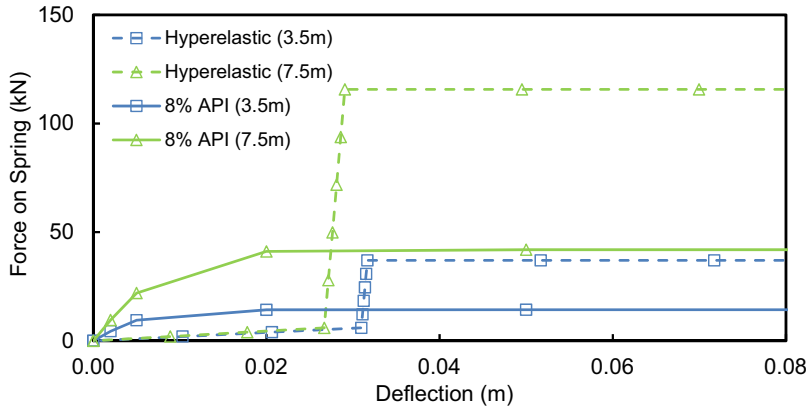

FIGURE 17.5 Typical hyperelastic and reduced API $p-y$ curves.

Fig. 17.6 describes the schematic concept of the soil-structure interaction (SSI) model using $p-y$ springs.

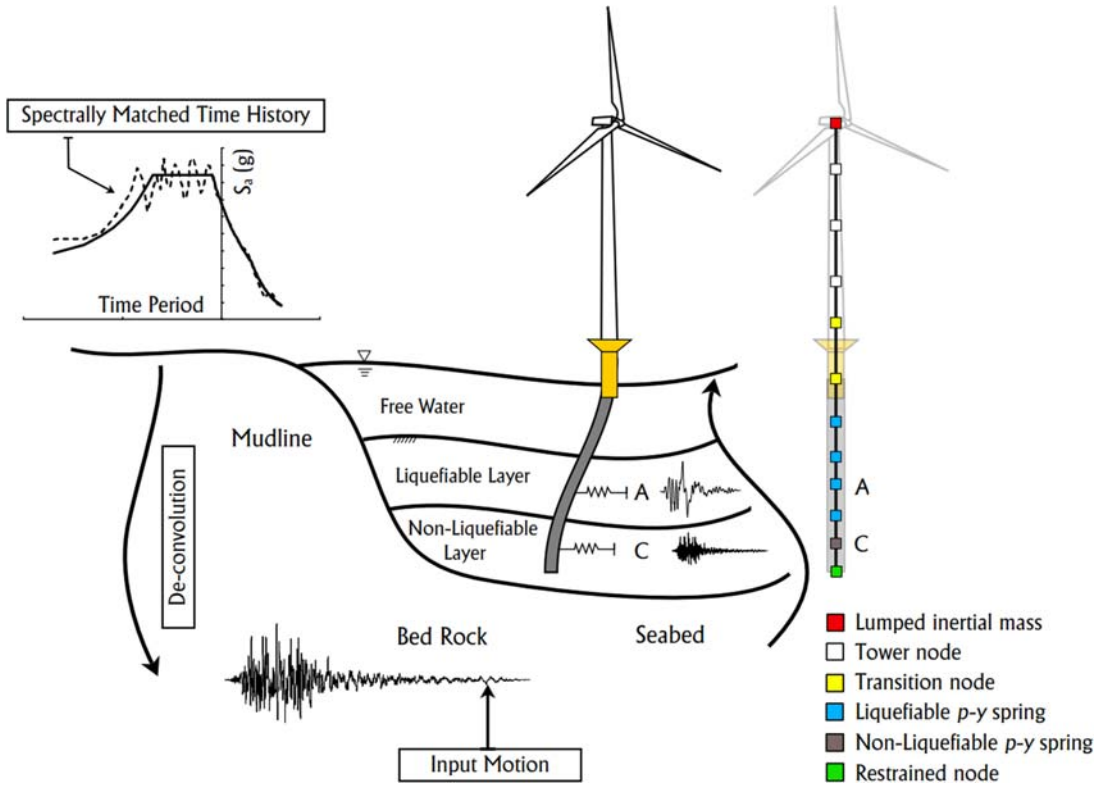

FIGURE 17.6 Schematic concept of soil−structure interaction model ($p-y$ spring).

17.2.4 Identification of liquefiable or strain softening layers

If layers are susceptible to soil liquefaction, simplified methods such as Idriss and Boulanger [25], Robertson and Wride [26], Kayen et al. [27], and Seed et al. [28] can be used to estimate the likelihood of triggering (check for initial liquefaction, *i.e.,* $r_u = 1$). However, sufficient strength loss can occur and lower r_u values, which must be considered from a design perspective. Further, simplified methods assume each layer acts independently, leading to challenges in stratified sites, as noted by Beyzaei et al. [29].

Determination of strain-softening layers can also be identified using the method presented by Idriss and Boulanger [25]. In addition, liquefaction triggering analysis is dependent on the hazard level considered (liquefaction might not trigger for low hazard levels, *e.g.*, design basis event, but might trigger for the maximum credible event).

17.2.5 Load utilization ratio analysis

The load utilization ratio of monopile can be used to obtain the demand/capacity ratio of a pile under combined lateral and flexural loading [30,31]. The utilization ratio can be easily depicted graphically (Fig. 17.7), where M_R and H_R represent the resistance capacity of a pile for the applied Moment (M) and Lateral load (H), which can be predicted using the $p-y$ spring method. The epistemic uncertainty of using specified $p-y$ curves can be treated using multiple constitutive models.

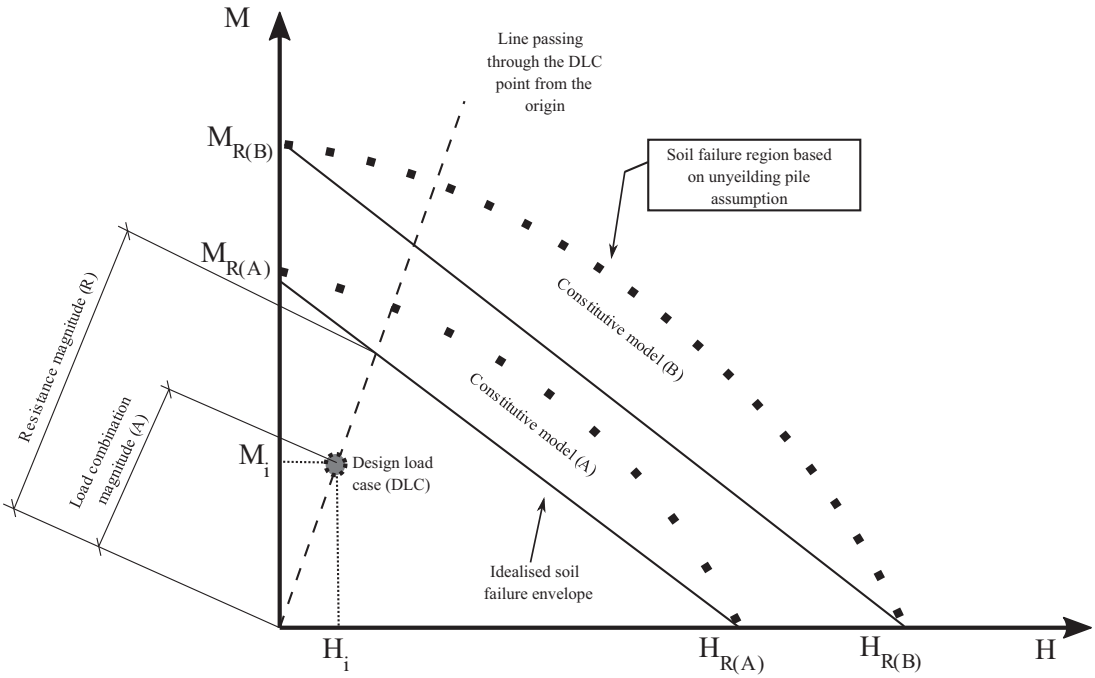

FIGURE 17.7 Construction of the load utilization ratio.

As shown in Fig. 17.7, the failure surface could vary based on the chosen soil constitutive model. Therefore, an idealized soil failure envelope line is defined. Then, knowing the distance of the design load case (DLC) point from the idealized line, the load utilization ratio *(R/A)* could be found.

Eq. 17.1 is derived based on the provided geometry to calculate the ratio between the resistance (R) and load (A) to obtain the load utilization ratio.

$$FOS(A,B) = \frac{R}{A} = \frac{\sqrt{\frac{(H_i M_R H_R)^2 + (M_i M_R H_R)^2}{(M_i H_R + M_R H_i)^2}}}{\sqrt{M_i^2 + H_i^2}} \tag{17.1}$$

17.2.6 Plotting the moment (MR) and lateral (HR) resisting capacity curve in liquefiable and nonliquefiable soil

Offshore wind farms constructed in potentially liquefiable soil are rising sharply. Moreover, young offshore deposits are particularly vulnerable to soil liquefaction during strong shaking. Soil liquefaction occurs in stages where the supporting ground behaves as a heavy fluid, resulting in lateral and vertical resistance loss. Further, upward artesian flow due to excess pore pressure generation can result in high buoyant forces resulting in cable floatation if not accounted for in the design. Aleem et al. [31] suggest a methodology to predict the load utilization ratio of monopiles supporting offshore wind turbines for nonliquefiable soils. This paper presents a method as an extension to adopt this method on liquefiable soils.

Fig. 17.8 presents a simplified sketch to plot the capacity of the foundation in two stages: No-Liquefaction (preliquefaction) and Maximum Liquefaction (post-liquefaction). The plot also includes the DLCs. The effect of soil liquefaction is the loss of the "foundation's lateral and moment-resisting capacity. Such a simplified approach estimates the capacity of pre and postliquefaction properties to help with the preliminary sizing of offshore wind turbine foundations. Once resistance capacity is estimated, a safety margin presents the action (demand) on the foundation.

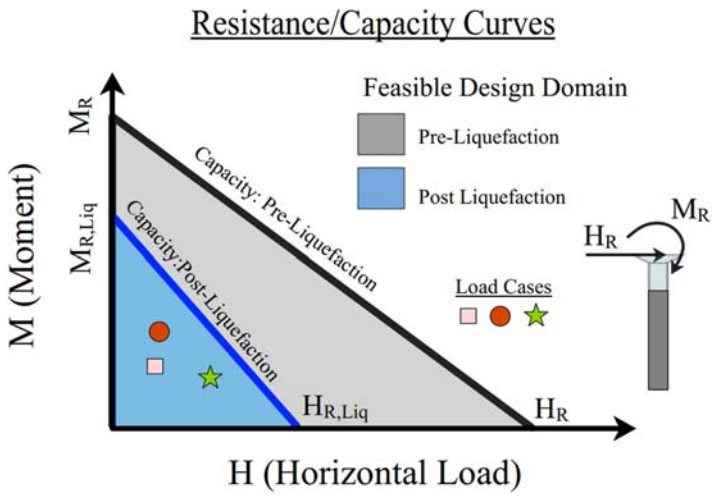

FIGURE 17.8 Schematic diagram showing the demand and capacity.

During earthquakes, soil deposits often liquefy top-down. The upper layers lose strength, and the liquefaction front progressively travels to deeper layers, as Scott [32] highlighted. Therefore, as presented in Fig. 17.9, it is expected that with progressive liquefaction, the foundation capacity will reduce in stages.

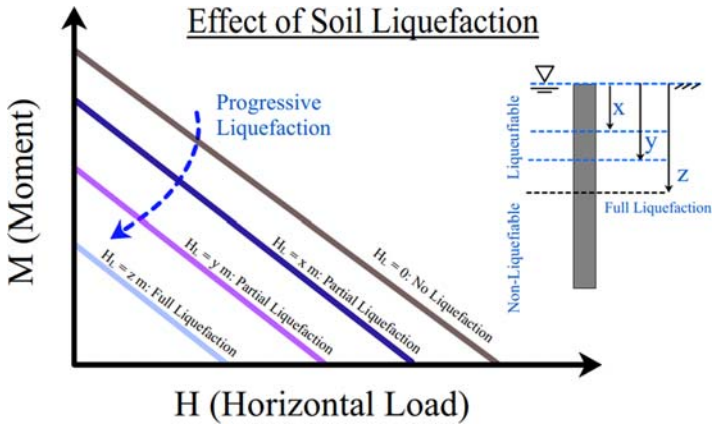

FIGURE 17.9 Schematic diagram of the load cases.

Therefore, considering the design life of the wind farm and tolerable risk, a probabilistic assessment can be performed for liquefaction triggering potential, thereby reducing the requirement for expensive ground remediation measures. An additional hazard due to loss of foundation capacity is the accumulated tilt of the system. As shown in Fig. 17.10, pre-liquefaction, the ground offers sufficient resistance (capacity) to prevent excessive tilt of the superstructure. However, strong shaking can result in high inertial demands at the hub level, resulting in significant moments on the mudline. These demands can lead to tilting of the foundation, which can be exacerbated by soil liquefaction and additional long-term loading if not corrected.

Two methods could conduct this assessment: (1) Complete removal of the $p-y$ springs in the liquefiable soil region; (2) Consideration of $p-y$ springs for the liquefiable region. Several techniques currently exist in the literature to model the $p-y$ curve for liquefied soil, including p multiplier, reduced $p-y$ curves [20], C_u-*factor* method [33], hybrid curves [21], and zero strength $p-y$ curves [22].

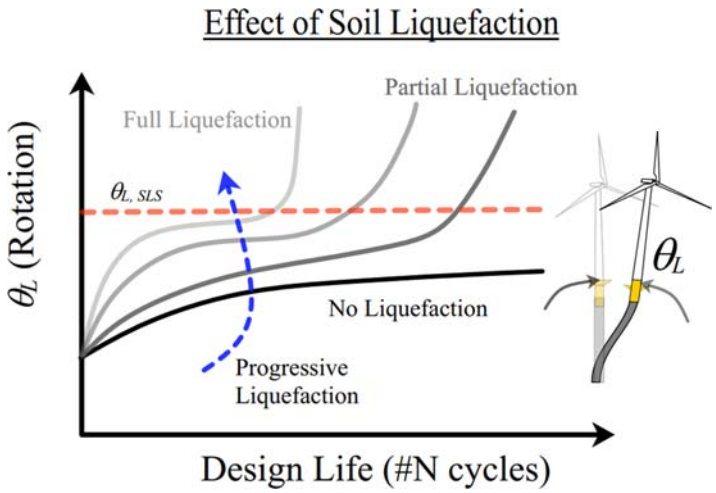

FIGURE 17.10 Long-term tilt of offshore wind turbines.

17.2.7 Examples of the moment and lateral resisting capacity curve in liquefiable soil

The moment and lateral resisting capacity curve plotted for a typical sandy soil—the depth of liquefied soil presented by the removal of $p-y$ springs. API [34] $p-y$ springs were assigned to represent the nonliquefiable depth. The results shown in Fig. 17.11 presented a nonlinear reduction for the Moment and Lateral resisting capacity.

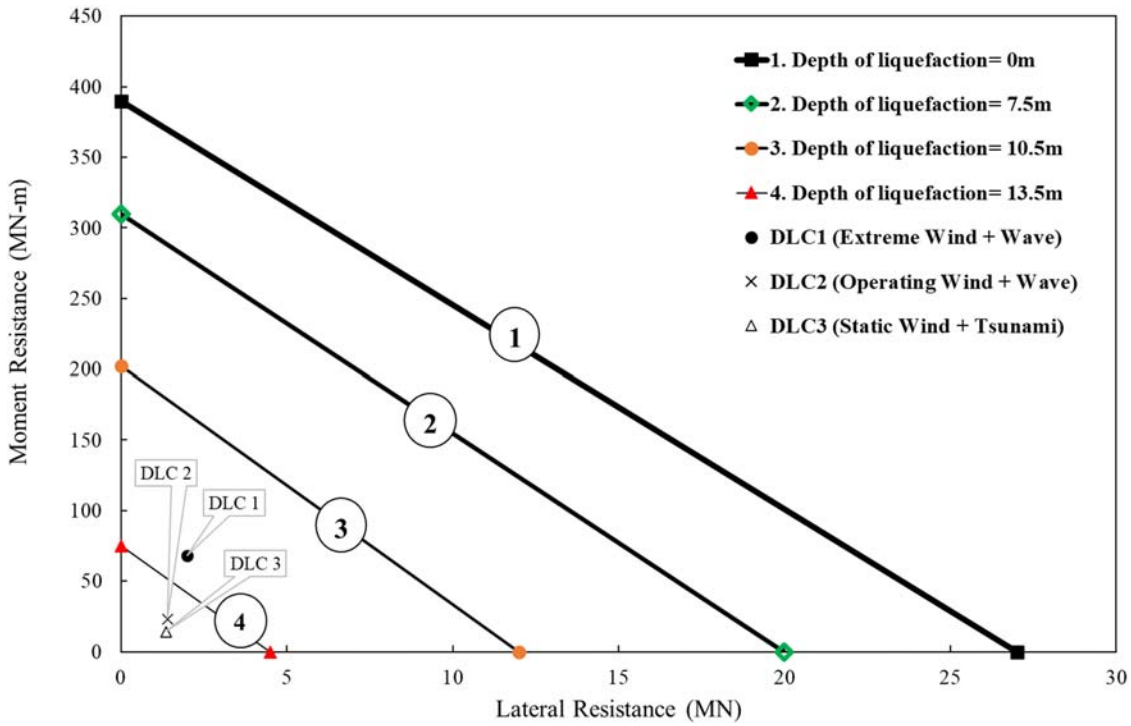

FIGURE 17.11 The moment resistance capacity reduction due to liquefaction.

17.2.8 Analysis of soil settlement postliquefaction

As a result of soil liquefaction, sand boil, land subsidence, or excessive settlement could be observed in the field [35]. Liquefaction-induced consolidation settlements in the free field can be reasonably predicted using Tokimatsu and Seed [9], Ishihara and Yoshimine [36], or Zhang et al. [37]. The parameters of this chart are based on CSR and the adjusted SPT N-value ($N_{1,60}$)

17.2.9 An example of 15 MW NREL wind turbine on jacket and monopile foundations

Amani et al. [38] studied the methodology and validation of offshore wind turbines for a 2 MW offshore wind turbine for the Kamisu wind farm, subjected to the Tohoku 2011 earthquake with the magnitude of 9.1 MW. Due to nonlinearity in the scaling of offshore wind turbines [39], the methodology outlined by Amani et al. [38] needs to be also studied for larger wind turbines to ensure its applicability to larger wind turbines. In this study, the 15 MW NREL [40] wind turbine model was tested on a jacket and monopile foundation using the methodology outlined by Amani et al. [38] to assess relative output differences. This study considers Chang-Bin offshore wind farm [41,42] with a proposed water depth of 40 m. The Chang-Bin wind farm is located at the coordinates of 24°08′59.9″N 119°57′00.0″E. Monopile and jacket foundations are typically installed within a 30−60 m water depth range [10]. A map of the considered site is shown below in Fig. 17.12.

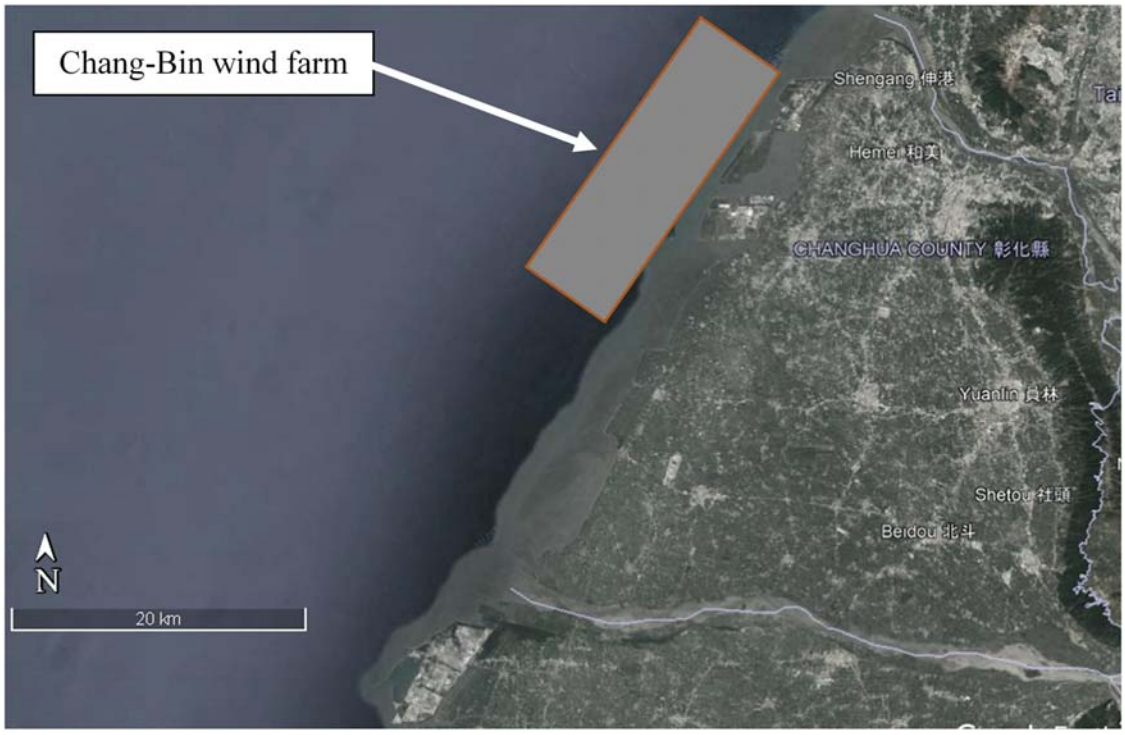

FIGURE 17.12 Chang-Bin wind farm location [43].

17.2.9.1 Soil profile and site response analysis

Strong motion data was selected from Engineering Strong Motion Database (ESM) [44] and the soil surface motions from stations TCU070 [44] station. The recorded motions and corresponding 5% damped response spectra are recorded as presented in Fig. 17.13. Deconvolution was performed employing *DeepSoil* [45] to obtain the "within" motions at a depth of 80 m for the soil profiles provided in the BH-01 (Please see Table 17.2). The output of the deconvoluted motion is shown in Fig. 17.14. The Modulus reduction and damping curves suggested by Anbazhagan et al. [46] were employed. Similarly, the displacement response of BH-01 to the given motion of Chi-Chi is presented in Figs. 17.15 and 17.16.

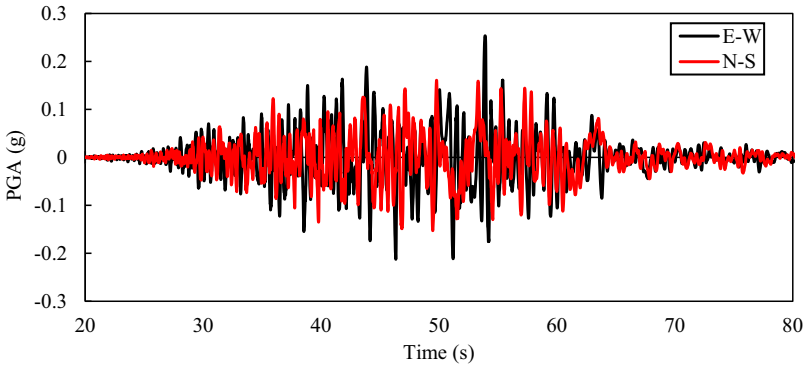

FIGURE 17.13 Recorded motion of Chi-Chi earthquake on the soil surface (station: TCU070).

TABLE 17.2 BH-01 (Taiwan Ocean Research Institute) simplified soil layers.

Layer	Depth Z (m) (elevation)	Soil type	γ' (kN/m^3)	φ'	Average SPT-N
1	0–10.8	Poorly graded sand with silt	8.5	29.5	7
2	10.8–26.1	Silty sand	9.5	32	28
3	26.1–47.2	Silty sand	9.6	32.3	32
4	47.2–71.5	Silty sand	9.5	33	42
5	71.5–73.8	Low plasticity clay	8.5	31	28
6	73.8–80.0	Silty sand	10.5	33	44

Source: Adopted from Wang Y-K, Chai J-F, Chang Y-W, Huang T-Y, Kuo Y-S. Development of seismic demand for chang-bin offshore wind farm in Taiwan Strait. Energies 2016;9:1036. https://doi.org/10.3390/en9121036.

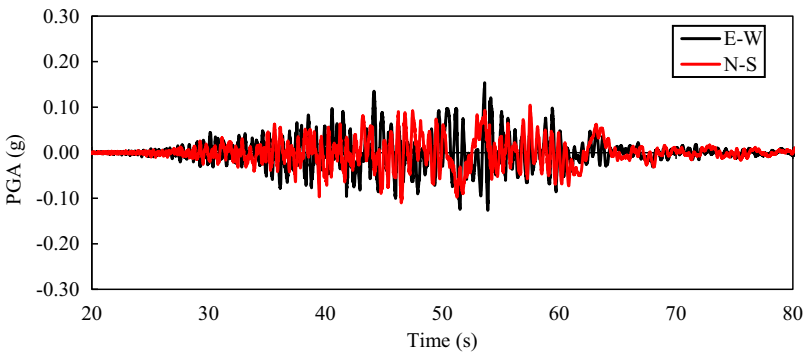

FIGURE 17.14 Deconvelouted motion at 80 m below the ground level for Chi-Chi earthquake (station: TCU070).

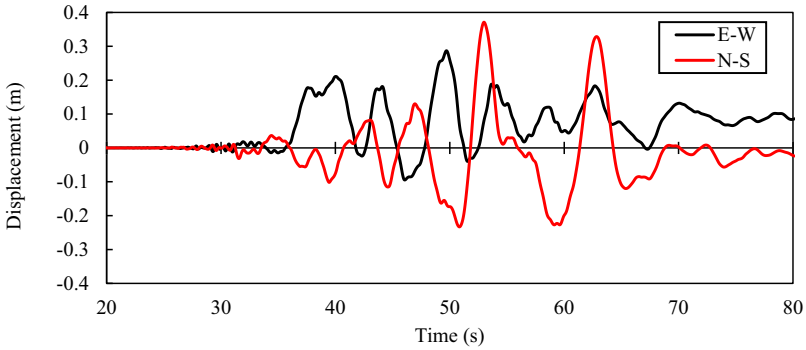

FIGURE 17.15 Displacement time history corresponding Chi-Chi earthquake (station: TCU070) for BH-01 soil profile at mudline level.

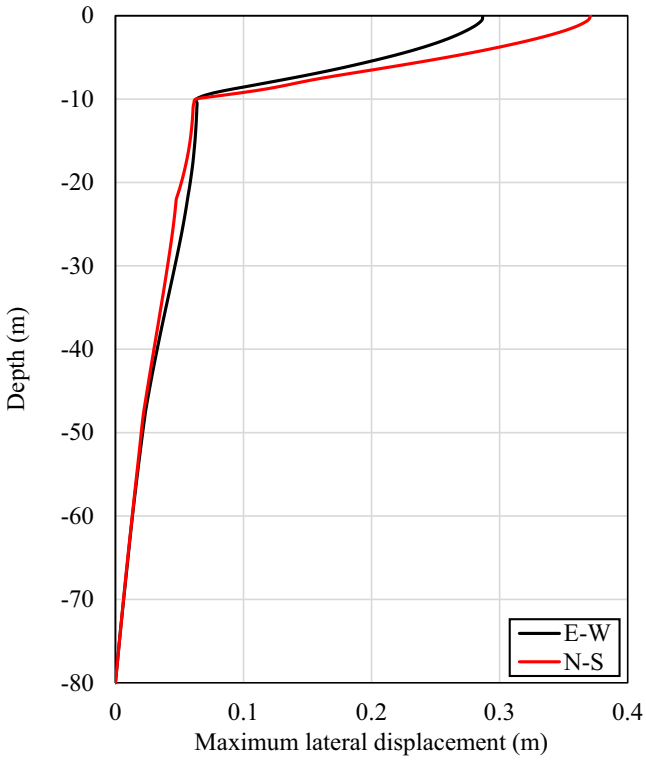

FIGURE 17.16 Maximum displacement estimated using *OpenSees* at BH-01 for Chi-Chi 1999 earthquake (Station: TCU070).

Soil profiles from boreholes closer to the turbines were obtained from Kao [42] and used to perform the site response analysis using the "within" motions obtained earlier. The soil profiles used are presented in Table 17.2. The groundwater table for the analysis is considered as 40 m for both jacket and monopile foundations.

The "within" motions obtained were propagated through a 1D effective stress site response analysis performed in *OpenSees* [47] to obtain the free-field response of both deposits. In each deposit, liquefiable layers were modeled using the Pressure-Dependent Multi-Yield surface (PDMY02) constitutive model developed by Elgamal et al. [48] and Yang et al. [49].

A modest stiffness proportional damping of 0.3% is considered in the site response analysis for numerical stability (the main source of damping arises from the hysteretic response of the soil). Parameters used in the model are presented in Table 17.3.

TABLE 17.3 Parameters considered in the site response analysis for the Changbin wind farm-BH01 [47].

Model parameters	Poorly graded sand with silt	Silty sand	Silty sand	Silty sand
Constitutive model	PDMY02			
Mass density, ρ (t/m^3)	1.7	1.95	1.95	2.1
Low strain shear modulus G_r (MPa)	55	110	130	130
Poisson's ratio for dynamic analysis	0.33	0.33	0.33	0.33
Friction angle describing strength as $p'\sin(f)$	29.5	3.5	32	33
Phase transformation angle (f_{PT})	26	26	26	26
Pressure dependence coefficient (n)	0.5			
Contraction parameter (c_1)	0.087	0.013	0.013	0.013
Dilation parameter (d_1)	0	0.3	0.3	0.3
Maximum shear strain (g_{max})	0.1			
Reference mean confinement p'_r (kPa)	101			
Permeability (m/s)	6.6×10^{-5}	1.0×10^{-7}		
Initial stiffness proportional damping (ξ)	0.003			
Convergence criteria based on norm of energy increment	1.0×10^{-7}			

Computed excessive pore water pressure obtained from the site response analysis is presented in Fig. 17.17. The responses indicate the mobilization of ground displacements, particularly at depths of stiffness contrast, after the onset of soil liquefaction. The free-field response of the ground is then imposed to the far ends of the compatible $p-y$ springs to obtain the demand on the monopile.

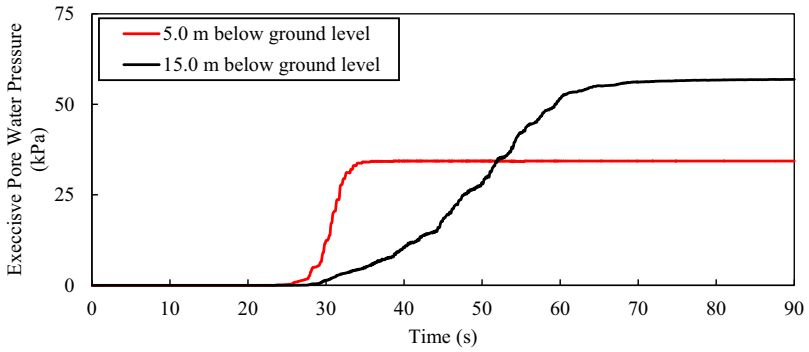

FIGURE 17.17 Computed excess pore pressure response. Changbin wind farm soil profile subjected to Chi-Chi earthquake.

Estimation of soil settlement at the considered site is assessed based on the stratigraphy shown in Fig. 17.18. The triggering analysis was carried out based on Idriss and Boulanger [25], and estimates of the consolidation-induced settlement were obtained from Ishihara and Yoshimine [36]. The analysis predicted initial liquefaction between depths of 10.5 m. Estimated postliquefaction consolidation settlements were generally about 0.4 m.

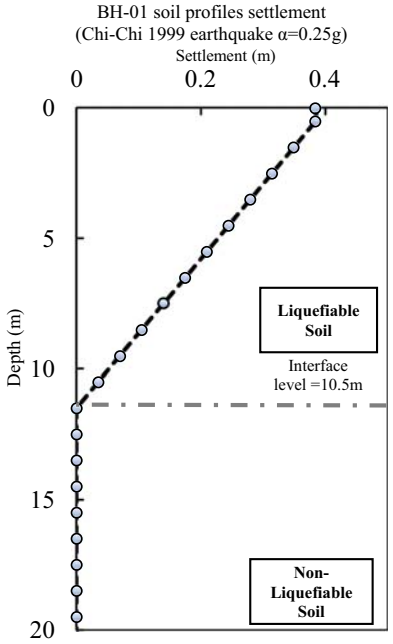

FIGURE 17.18 Chang-Bin wind farm settlement (Chi-Chi 1999 earthquake $\alpha = 0.25$ g).

17.2.9.2 Loads

17.2.9.2.1 Earthquake loads

The free-field response of the ground is obtained from the site response analysis and is imposed on the far ends of compatible $p-y$ curves for both offshore and nearshore turbines. The relative ground displacement was obtained from site response analysis, as shown in Fig. 17.16. The free-field response was obtained and assigned to the end of $p-y$ springs based on two directions (Bi-directional, X and Y). One direction represents the ground displacement in the north–south (NS) direction and the other east–west (EW).

17.2.9.2.2 Wind and wave loads

In this analysis, A generic U.S. East Coast site with a wind speed described by a Weibull distribution with a mean velocity of approximately 8.65 m/s and a shape parameter of 2.12 was considered [40]. In this analysis, the turbine-rated wind speed was considered as 10.59 m/s. And the 50-year significant wave height was considered as 11.3 m, with a 50-year significant wave period of 18.5 s [40].

Using the methodology outlined by Arany et al. [13], the wind and wave load for this wind farm were estimated. The summary of applied loads wind and wave loads is shown in Table 17.4.

TABLE 17.4 Estimated wind and wave loads.

Loads	Monopile	Jacket
Wind (ETM)	Uniformly Distributed Load (UDL) on blades (11 kN/m)	
Wave (50-year EWH)	UDL (considering the extreme wave height = 11.3 m) − 1560 kN/m	UDL on the surface of jacket (considering the extreme wave height = 11.3 m) − 258 kN/m

17.2.9.3 Soil-structure interaction analysis

Soil-pile interaction was modeled through nonlinear springs at regular intervals. Since only the lateral pile response is studied, soil springs are provided only in the two horizontal directions (i.e., earthquake motion direction). In both models, a combination of API $p-y$ springs [34] and hyperelastic $p-y$ springs proposed by Dash et al. [24] were employed to model the nonliquefiable layers and the liquefiable layers, respectively.

The wind turbine structure was modeled at the top of a monopile foundation, with aerodynamic mass dampers (bi-directional). The assigned aerodynamic damper parameters were found using the recommended range by Adhikari and Bhattacharya [50]. The translational and rotational inertia of the RNA mass was considered. Mass distribution of the tower is explicitly modeled through point masses specified along the tower length. The selection of appropriate damping is critical for the design and analysis of OWTs [51]. Results from the Cyclic Simple Shear test by [41] hinted that the Chang-Bin offshore wind farm could have a high damping ratio at higher shear strain. For high shear strain (0.01%) the damping ratio could be as high as 20% and as low as 5% for low shear strain (0.0001%). In this analysis due to cyclic seismic load consideration, 20% Rayleigh damping was considered in the analysis [50,52]. The turbine structure and foundation specifications are demonstrated in Table 17.5.

TABLE 17.5 Turbines and foundation specifications [40,53−55].

Jacket[a]		Monopile	
Turbine model	15 MW NREL	Turbine model	15 MW NREL
Hub height [m]	150	Hub height [m]	150
Pile length [m]	45	Pile length [m]	45
Tower height	114.85	Tower height	129.5
Number of legs	4	RNA mass [tons]	1070
RNA mass [tons]	1070	Blade length [m]	120
Blade length [m]	120	Blade weight [tons]	65
Blade weight [tons]	65	Tower top-bottom diameter & thickness [m]	6.5−10, 0.023−0.041
Tower top-bottom diameter & thickness [m]	6.5−10, 0.024−0.04	Transition piece length, diameter, and thickness [m]	15, 10, 0.041−0.045
Leg vertical height and spacing [m]	60.15−24 × 24	Upper monopile length, diameter, and thickness [m]	40, 10, 0.055

(Continued)

TABLE 17.5 (Continued)

Jacket[a]		Monopile	
Transition piece dimensions [m]	12 × 12	Pile diameter & thickness [m]	10–0.055
Transition piece mass [tons]	200	Water depth [m]	40
Jacket leg diameter & thickness [m]	2.5–0.05	Section material	S355
Jacket bracing diameter & thickness [m]	2.0–0.02		
Pile diameter & thickness [m]	4–0.05		
Water depth [m]	40		
Section material	S355		

[b]Blades are assuemd rigid in the 15 MW NREL wind turbine analysis and a concentrated mass at the center of gravity of the blade is assigned (26.8 m from the hub origin).
[a]*Proposed dimensions based on the findings for a typical jacket foundation by Alati, Failla, and Arena [56] to suit a 15 MW NREL wind turbine*

In this model, the lumped mass was assigned at the top of the tower based on the provided recommendation by NREL [40]. The summary of the lumped mass is shown in Table 17.6.

TABLE 17.6 Lumped masses and moments of inertia for the Nacelle assembly [40].

The coordinate system has its origin at the tower top, with *x* pointed downwind (parallel to ground/water and not the shaft) and *z* pointed up[b]

Name	X_{TT} [m]	Z_{TT} [m]	Mass [t]	I_{xx} [kg m^2]	I_{yy} [kg m^2]	I_{zz} [kg m^2]
Nacelle total[a]	5.486	3.978	820.888	12,607,277	21,433,958	18,682,468

[a]*The lumped mass doesn't include the blades- The blades were assigned at the 11.35 m overhang distance (x-direction) from the center.*
[b]*x, y, z are the local coordinates of the Nacelle assembly system*

The schematic concept of the monopile and jacket wind turbine models are demonstrated in Fig. 17.19.

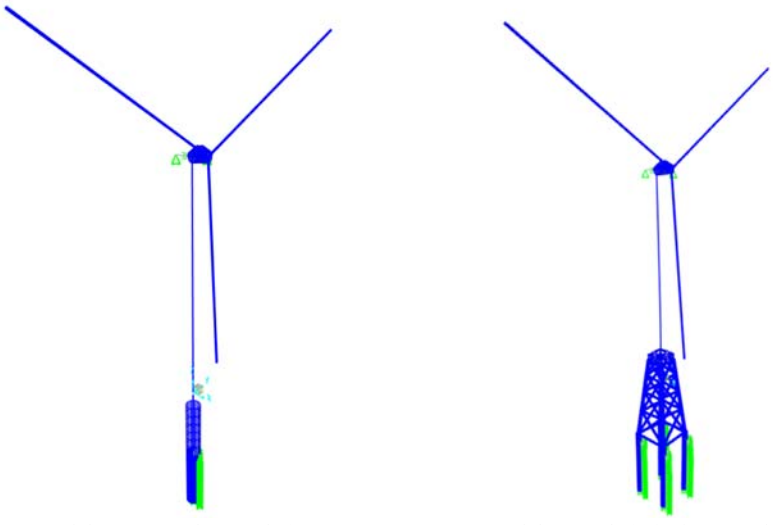

(A) Model of monopile foundations (B) Model of a pile in jacket foundations

FIGURE 17.19 Model of a turbine for 15 MW NREL wind turbine supported by (A) monopile and (B) jacket foundations.

After modeling the SSI model of the 15 MW NREL model, the natural frequency of the monopile and jacket model was estimated as 0.14 and 0.25 Hz respectively. The outlined natural frequency by NREL for the 15 MW model was found to be 0.17 Hz [40]. In these models, the liquefied ground and the increased water depth were considered. Therefore, a reduction in the natural frequency of the monopile was expected. The dynamic behavior of these foundations with respect to seismic demand, wind, and wave was assessed. The rotation (θ_{max}), displacement (Δ_{max}), and RNA acceleration (a_{RNA}) for monopile and jacket foundation were recorded. The summary of the maximum estimated parameters is shown in Table 17.7.

TABLE 17.7 Resultant (XY) pile head displacement (Δ), pile head rotation (θ), RNA acceleration (a_{RNA}) of Jacket and monopile foundation.

Analysis	Δ_{max} (mm) XY	θ_{max} (deg) XY	a_{RNA} (g) XY
Leg (Q1): Jacket (postliquefaction)	142	0.11	0.11
Leg (Q2): Jacket (postliquefaction)	169	0.45	
Leg (Q4): Jacket (postliquefaction)	166	0.46	
Leg (Q4): Jacket (postliquefaction)	141	0.37	
Monopile (postliquefaction)	227	0.68	0.17

For jacket the maximum response between all the piles is taken.

During seismic events, the foundations could experience unexpected deformations. For both the jacket and the monopile foundation the pile head response due to the considered earthquake is compared. This allowed visualizing the behavior of piles with respect to the applied loads. The recorded response to on monopile foundation was recorded and outlined in Fig. 17.20.

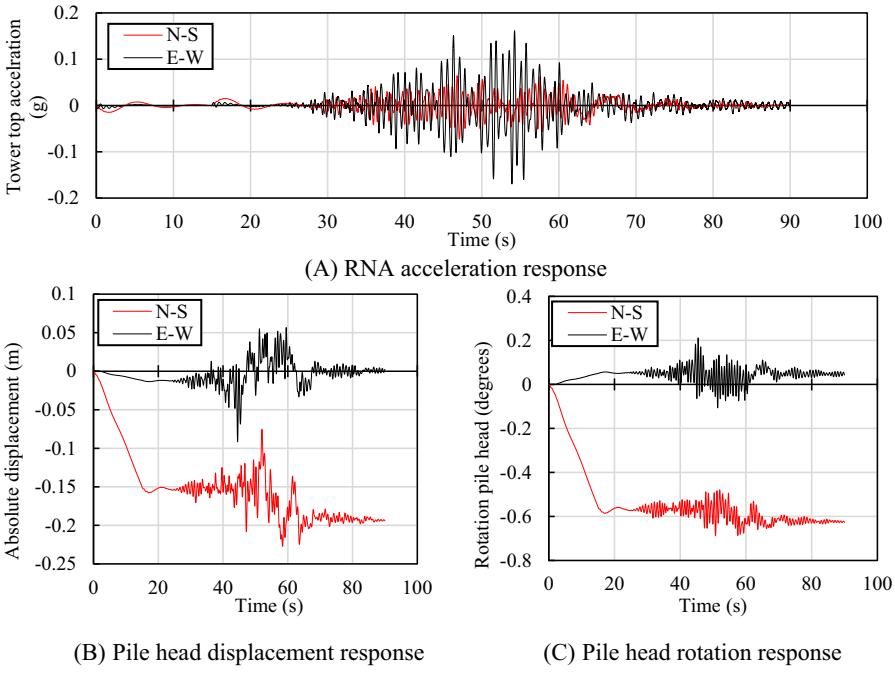

(A) RNA acceleration response

(B) Pile head displacement response

(C) Pile head rotation response

FIGURE 17.20 Pile head rotation, displacement, and RNA acceleration responses for a turbine for a 15 MW NREL wind turbine supported by a monopile . (A) RNA acceleration response, (B) Pile head displacement response, (C) Pile head rotation response.

Similarly, the outputs were recorded for 4 piles of the jacket (four quarters). The results are outlined in Fig. 17.21.

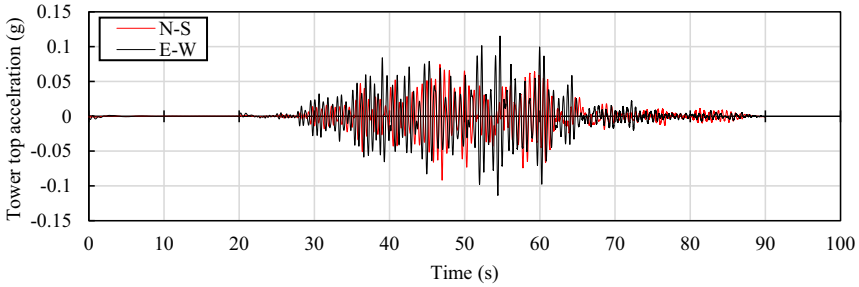

(A) RNA acceleration response

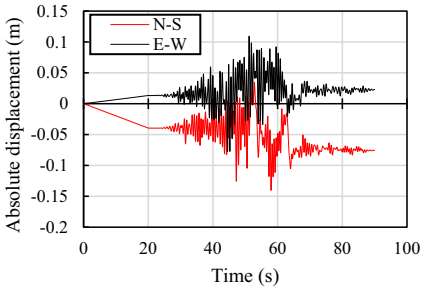

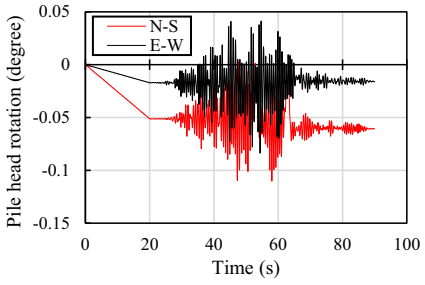

(B) Q1 pile head rotation and displacement

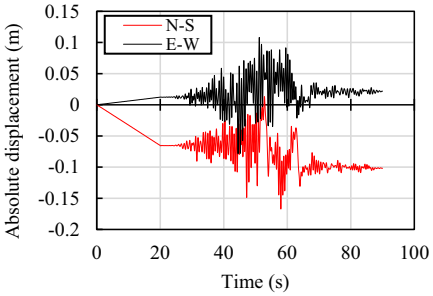

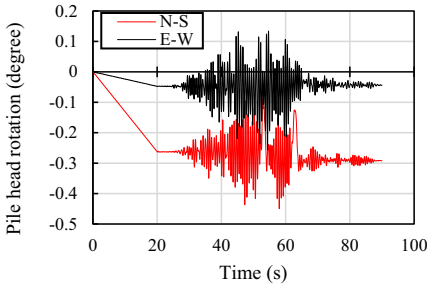

(C) Q2 pile head rotation and displacement

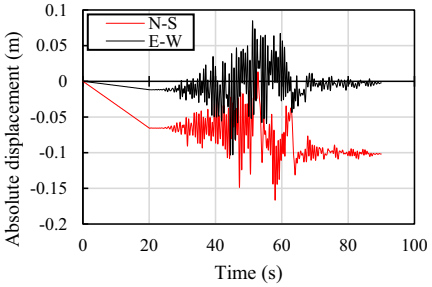

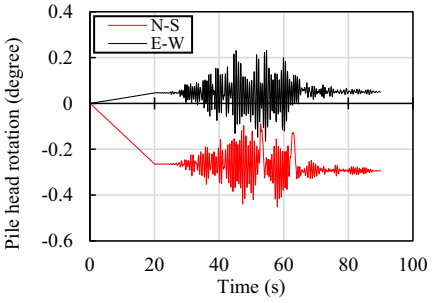

(D) Q3 pile head rotation and displacement

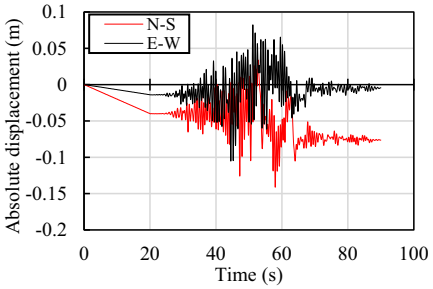

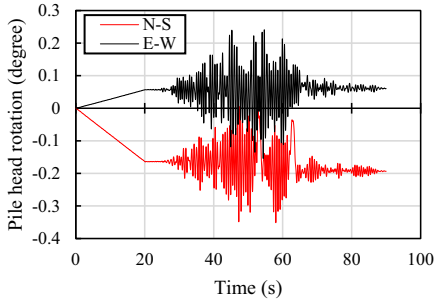

(E) Q4 pile head rotation and displacement

FIGURE 17.21 Pile head rotation, displacement, and RNA acceleration responses for a turbine for 15 MW NREL wind turbine supported by a jacket foundation . (A) RNA acceleration response, (B) Q1 pile head rotation and displacement, (C) Q2 pile head rotation and displacement, (D) Q3 pile head rotation and displacement, (E) Q4 pile head rotation and displacement.

The comparison between the 15 MW NREL offshore wind turbine supported by monopile and jacket foundation indicated that jacket foundations are less vulnerable to the applied external loads (wind, wave, and seismic loads). It might be a reasonable solution to consider jacket foundations for the seismic regions. In addition, it was observed that the RNA acceleration is much lower in the jacket foundation.

17.3 Methodology of analyzing floating wind turbines

This section explains the procedure to design floating offshore wind turbines with TLPs.

1. Data gathering: The data gathering needs to be carried out to have a clear vision for analyzing a problem. These data could be divided into four stages.
2. *Performance requirement (limit states) includes ULS, SLS, and FLS checks.*
   a. Under ULS criteria, it is expected to find the ultimate load that the foundation could carry.
   b. Under SLS criteria, it is expected to ensure that the tilt of the wind turbine platform under the operating stage is below the allowable limit (typically 7 degrees) [57].
   c. Under FLS criteria, it is expected to ensure that during the long term
3. *Turbine data* includes wind turbine specifications such as blade diameter, rotor, blade passing frequency (1P, 3P), and tower specifications (height, thickness, and diameter).
4. *Met-ocean data:* Obtaining the water depth is a critical player in the design of floating wind turbines. The readers are referred to the literature for more details.
5. *Seismic hazard analysis* is one of the main scopes of this paper to study the effect of fault rupture on the FWT system. Therefore, the fault rupture type, potential earthquake magnitude, and fault rupture displacement need to be estimated. In addition, the ground motion at the surface level needs to be obtained.
6. Estimation of dimensions for floating offshore wind turbine (platform and tower): An initial estimation could be achieved by considering overturning equilibrium in the floating foundation system.
7. Define appropriate tension leg dimensions: These dimensions could also be estimated by considering an equilibrium between the uplift force (buoyancy) and the cables. The tension of the legs (cables) should be within a safe zone to avoid unexpected plastic failure of the cables.
8. Structural modeling: Apart from structural modeling using appropriate properties. Imposition of the wind, wave, ground motion acceleration, and fault rupture need to be considered. The fault rupture should be applied first in the analysis and followed by earthquake motion.
9. Checking whether the design criteria meet the design demand. In case the foundation collapses or is under or over-designed, then the dimensions need to be revised.

Fig. 17.22 shows the workflow that needs to be carried out to assess the vulnerability of floating offshore wind turbines.

17.3.1 Employed Modeling Details

The equilibrium in floating structures is created by balancing the external loads and the reaction forces (generated due to buoyancy force). The external forces are moment (due to wind and wave load) and vertical load (due to self-weight). Furthermore, the reaction force is typically generated due to the buoyancy effect. The distance between the center of gravity (C_g) and the Metacenter (M) is called metacentric height (G.M.). This is a measurement of the initial static stability of a floating body [58]. The floating objects start to destabilize as the applied external moment nears the resisting moment due to the buoyancy force, as shown in Fig. 17.23.

Floating wind turbines could be modeled by benefiting from the main principles of floating objects' stability. The free body diagram of TLP wind turbines is shown in Fig. 17.24. The T_1 and T_2 represent the tension in the cables (tendons). Under the destabilization process, one of the cables (e.g., T_2) could loosen, and the other cable (T_1) started to generate excessive tension. Moreover, as a result, it increases the risk of tendon failure.

Modeling of floating structures often could be complex due to several uncertainties. These could be selecting an appropriate damping factor, stiffness, and definition of a proper tension parameter to the cables in a TLP system. Therefore, this paper proposes the following stages:

1. Tension legs were defined using cables with tendon properties (prestressed)
2. The full-scale RNA is considered in this study
3. Spring damper systems could be implemented at the interface between mast and rotor and between seabed and tension legs.

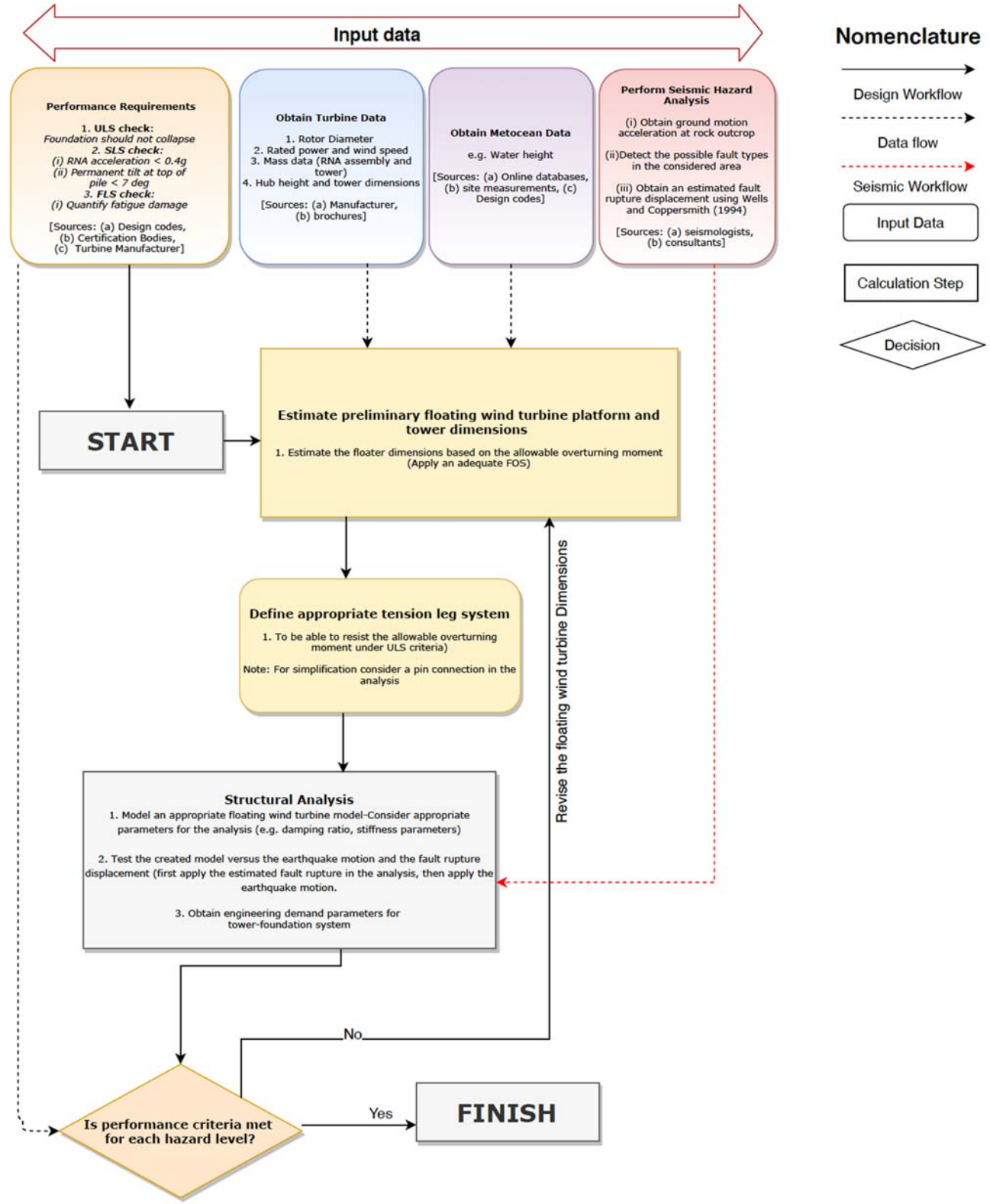

FIGURE 17.22 Workflow to analyze the vulnerability of FOWTs (TLP).

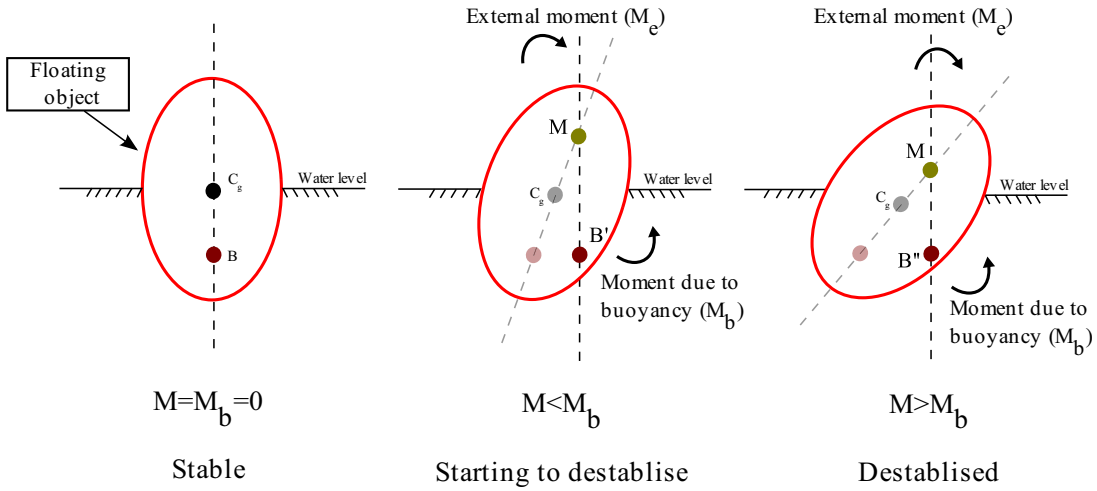

FIGURE 17.23 Destabilization due to overturning moment.

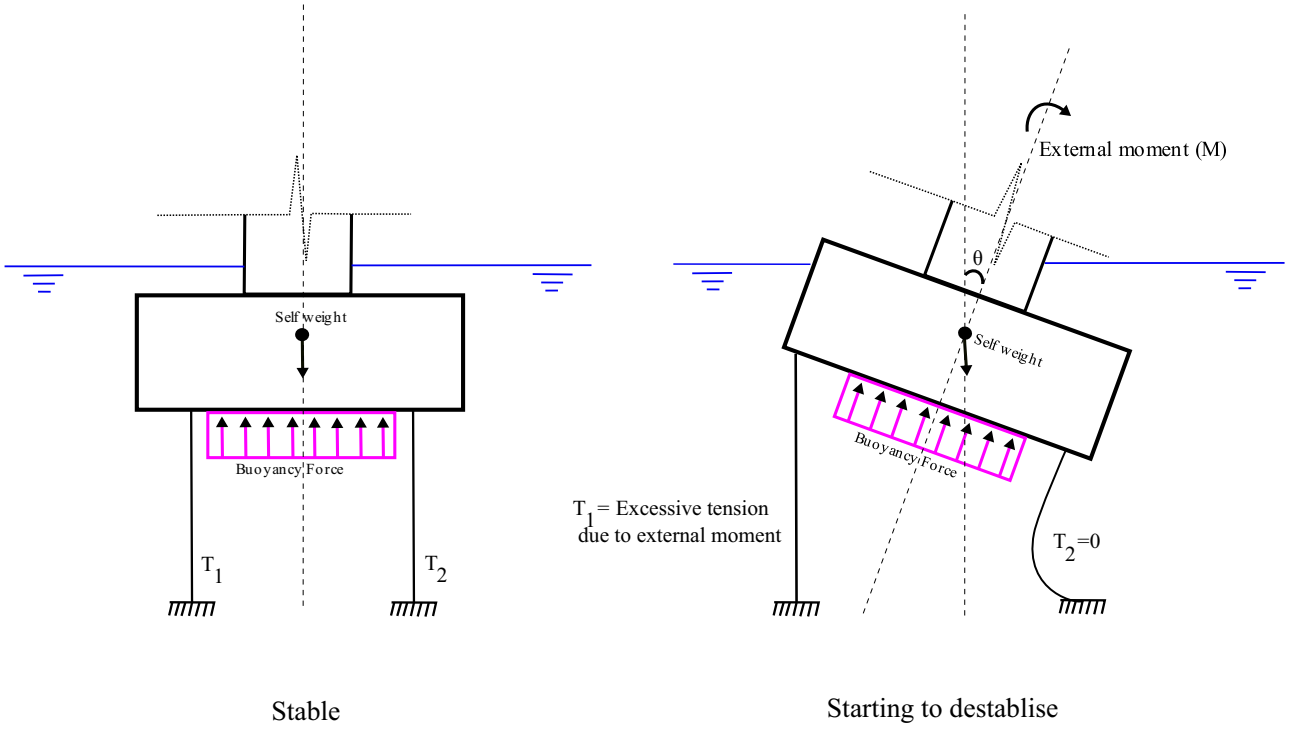

FIGURE 17.24 Application of destabilization principles on FWTs (TLP).

4. The buoyant force should be modeled as a uniformly distributed load acting upwards on the bottom surface of the floater.
5. The damping generated at the water and floater surface interface could be modeled through two viscous dampers on either side of the mast.
6. The pretension in the tension legs is achieved by introducing initial strain in the truss elements [59].

The structures schematic model is shown in Fig. 17.25.

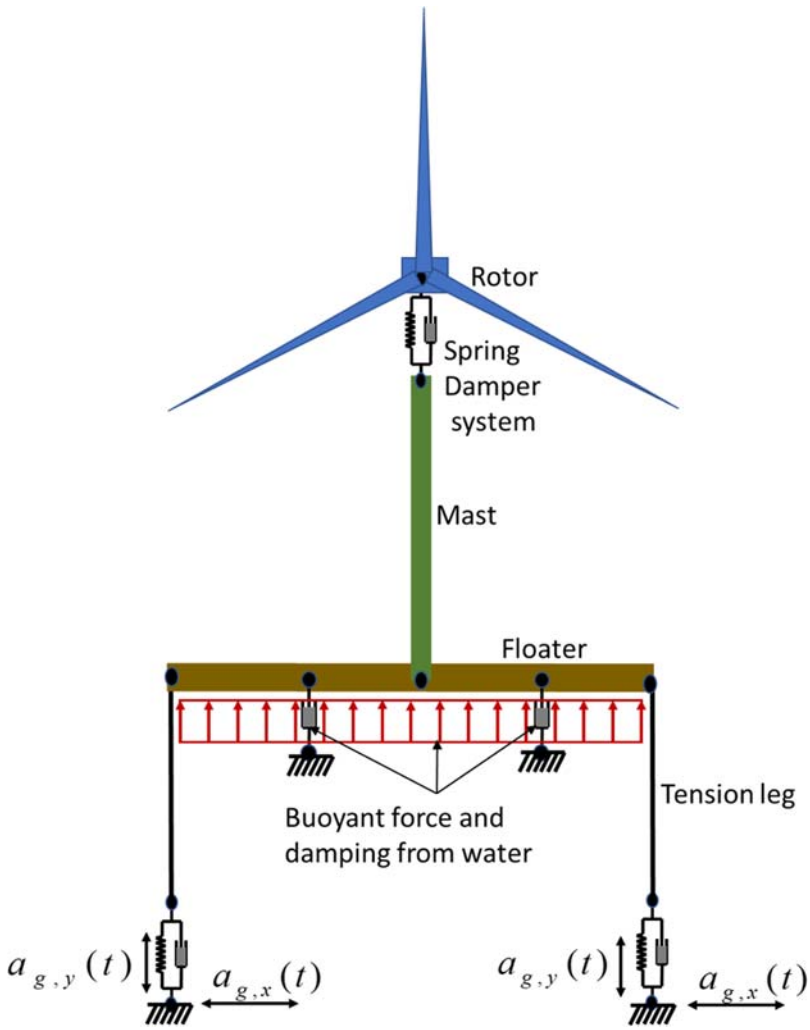

FIGURE 17.25 Schematic structural model to analyze TLP structures in seismic regions [59].

Summary

In this chapter, methodologies were presented for the design and analysis of offshore wind turbines in seismic regions. This includes bottom fixed (monopile and jacket structures) and floating wind turbines (TLP). The analysis conducted using the proposed method showed that jacket foundations are less vulnerable to the combination of earthquake, wind, and wave loads in comparison with monopile foundations. In addition, in large-sized wind turbines (e.g., 15 MW), the amplification of RNA spotted is higher than the smaller wind turbines (e.g., 2 MW). The concept to assess the floating wind turbines in seismic regions is proposed in Section 17.3, which could be used to estimate the effect of seismic demands on floating wind turbines.

References

[1] Nghiem A, Pineda I. Wind energy in Europe: scenarios for 2030. Brussels: Wind Europe; 2017.

[2] Wind Europe. Spain issues plan for up to 3 GW offshore wind by 2030—in perfect time for WindEurope 2022 in Bilbao. Wind Eur 2021, <https://windeurope.org/newsroom/news/spain-issues-plan-for-up-to-3-gw-offshore-wind-by-2030-in-perfect-time-for-windeurope-2022-in-bilbao/#:~:text = Spain> is already the second,on the back of this [accessed 13.02.22.].

[3] Christopher TR, Williams M, Goldstein M, Carter A. The road to 30 gigawatts: key actions to scale an offshore wind industry in the United States. Cent Am Prog 2022;. Available from: https://www.americanprogress.org/article/the-road-to-30-gigawatts-key-actions-to-scale-an-offshore-wind-industry-in-the-united-states/ [accessed 27.05.22.].

[4] Tachev V. Wind Energy in South Korea—Opportunities and Challenges 2021. https://energytracker.asia/wind-energy-in-south-korea-opportunities-and-challenges/#:~:text = As a part of its,MW the country has today [accessed 27.05.22.].

[5] GlobalData Energy. China to add significant offshore wind power capacity every year during 2023−2030. Power Technol 2021. https://www.power-technology.com/comment/china-offshore-wind-power/ [accessed 27.05.22.].
[6] Li CH. "Taiwan's new policy can turn it into a major regional offshore wind hub." NHST Media Gr 2021. https://www.rechargenews.com/wind/taiwans-new-policy-can-turn-it-into-a-major-regional-offshore-wind-hub/2-1-1010192 [accessed 27.05.22.].
[7] ABB/ZERO. Floating offshore wind Norway's next offshore boom? 2018.
[8] Bhattacharya S., Amani S., Prabhakaran A., Mistry H.K., Lombardi D., Seismic design of offshore wind turbines. In The 17th World Conference on Earthquake Engineering, 2021, Sendai, Japan.
[9] Tokimatsu K, Seed HB. Evaluation of settlements in sands due to earthquake shaking. J Geotech Eng 1987;113:861−78. Available from: https://doi.org/10.1061/(ASCE)0733-9410(1987)113:8(861).
[10] Bhattacharya S. Design of foundations for offshore wind turbines. 1st ed. Chichester: Wiley; 2019. Available from: https://doi.org/10.1002/9781119128137.
[11] Amani S, Prabhakaran A, Bhattacharya S. Design of monopiles for offshore and nearshore wind turbines in seismically liquefiable soils: Methodology and validation. Soil Dynamics and Earthquake Engineering 2022;157107252. Available from: https://doi.org/10.1016/j.soildyn.2022.107252.
[12] Bhattacharya S, Amani S, Prabhakaran A, Macabuag J. Hazard considerations in the vulnerability assessment of offshore wind farms in seismic zones. Reliability Engineering and Resilience 2022;1:88−109. Available from: https://doi.org/10.1002/eer2.11.
[13] Arany L, Bhattacharya S, Macdonald J, Hogan S. Design of monopiles for offshore wind turbines in 10 steps. Soil Dyn Earthq Eng 2017;92:126−52. Available from: https://doi.org/10.1016/j.soildyn.2016.09.024.
[14] Baker JW. Conditional mean spectrum: tool for ground-motion selection. J Struct Eng 2011;137:322−31. Available from: https://doi.org/10.1061/(ASCE)ST.1943-541X.0000215.
[15] Kwong NS, Chopra AK. A Generalized conditional mean spectrum and its application for intensity-based assessments of seismic demands. Earthq Spectra 2017;33:123−43. Available from: https://doi.org/10.1193/040416eqs050m.
[16] Katsanos EI, Sextos AG, Manolis GD. Selection of earthquake ground motion records: a state-of-the-art review from a structural engineering perspective. Soil Dyn Earthq Eng 2010;30:157−69. Available from: https://doi.org/10.1016/j.soildyn.2009.10.005.
[17] Idriss IM. Earthquake ground motions at soft soil sites. Int. Conf. Recent Adv. Geotech. Earthq. Eng. Soil Dyn., St. Louis, Missouri: University of Missouri-Rolla; 1991.
[18] Kramer SL. Geotechnical earthquake engineering. 1st ed. Prentice Hall; 1996.
[19] Idriss I, Sun JI. SHAKE91: a computer program for conducting equivalent linear seismic response analyses of horizontally layered soil deposits. Department of Civil and Environmental Engineering. Davis Calif.: Center for Geotechnical Modeling Dept. of Civil and Environmental Engineering University of California Davis; 1992.
[20] Boulanger RW, Kutter BL, Brandenberg SJ, Singh P, Chang D. Pile foundations in liquefied and laterally spreading ground during earthquakes: centrifuge experiments & analyses. Davis, CA; 2003.
[21] Franke KW, Rollins KM. Simplified hybrid p-y spring model for liquefied soils. J Geotech Geoenviron Eng 2013;139:564−76. Available from: https://doi.org/10.1061/(ASCE)GT.1943-5606.0000750.
[22] Railway Technical Research Institute (RTRI). Design standard for railway facilities-seismic design-Japan. Japan; 1999.
[23] Lombardi D, Dash SR, Bhattacharya S, Ibraim E, Muir Wood D, Taylor CA. Construction of simplified design p−y curves for liquefied soils. Géotechnique 2017;67:216−27. Available from: https://doi.org/10.1680/jgeot.15.P.116.
[24] Dash S, Rouholamin M, Lombardi D, Bhattacharya S. A practical method for construction of p-y curves for liquefiable soils. Soil Dyn Earthq Eng 2017;97:478−81. Available from: https://doi.org/10.1016/j.soildyn.2017.03.002.
[25] Idriss IM, Boulanger RW, Institute. EER. Soil liquefaction during earthquakes. 2nd ed. Oakland, CA: Earthquake Engineering Research Institute; 2008.
[26] Robertson PK, Wride C. Evaluating cyclic liquefaction potential using the cone penetration test FearCan Geotech J 1998;35:442−59. Available from: https://doi.org/10.1139/t98-017.
[27] Kayen R, Moss RES, Thompson EM, Seed RB, Cetin KO, Der Kiureghian A, et al. Shear-wave velocity−based probabilistic and deterministic assessment of seismic soil liquefaction potential. J Geotech Geoenviron Eng 2013;139:407−19. Available from: https://doi.org/10.1061/(ASCE)GT.1943-5606.0000743.
[28] Seed RB, Cetin KO, Kammerer AM, Wu J, Pestana JM, Riemer MF, et al. Recent advances in soil liquefaction engineering: a unified and consistent framework. In: 26th Annual ASCE Los Angeles Geotech. Spring Semin., CA; 2003.
[29] Beyzaei CZ, Bray JD, Cubrinovski M, Bastin S, Stringer M, Jacka M, et al. Characterization of silty soil thin layering and groundwater conditions for liquefaction assessment. Can Geotech J 2020;57:263−76. Available from: https://doi.org/10.1139/cgj-2018-0287.
[30] Aleem M, Emre Demerici H, Bhattacharya S, Demirci HE, Bhattacharya S, Kingdom U. Lateral and moment resisting capacity of monopiles in layered soils. ICEESEN 2020, Kayseri, Turkey; 2020, p. 19−21.
[31] Aleem M, Bhattacharya S, Cui L, Amani S, Salem AR, Jalbi S. Load utilisation (LU) ratio of monopiles supporting offshore wind turbines: formulation and examples from European wind farms. Ocean Eng 2022;248:110798. Available from: https://doi.org/10.1016/j.oceaneng.2022.110798.
[32] Scott RF. Soil properties from centrifuge liquefaction tests. Mech Mater 1986;5:199−206. Available from: https://doi.org/10.1016/0167-6636(86)90034-7.
[33] Lui L, Dobry R. Effect of liquefaction on lateral response of piles by centrifuge model tests. NCEER Bull 1995;9:7−11.

[34] API. Recommended practice for planning, designing and constructing fixed offshore platforms—working stress design. API Recomm Pract 2007; 24-WSD:242.
[35] Lee D.-H., Ku C.-S., Juang C.H. Soil liquefaction and ground settlement in Chi-Chi Taiwan, Earthquake. Int. Conf. Recent Adv. Geotech. Earthq. Eng. Soil Dyn.; 2001, p. 27.
[36] Ishihara K, Yoshimine M. Evaluation of settlements in sand deposits following liquefaction during earthquakes. Soils Found 1992;32:173−88. Available from: https://doi.org/10.3208/sandf1972.32.173.
[37] Zhang G, Robertson PK, Brachman RW. Estimating liquefaction-induced ground settlements from CPT for level ground. Can Geotech J 2002;39:1168−80. Available from: https://doi.org/10.1139/t02-047.
[38] Amani S, Prabhakaran A, Bhattacharya S. Design of monopiles for offshore and nearshore wind turbines in seismically liquefiable soils: methodology and validation. Soil Dyn Earthq Eng 2022;157:107252. Available from: https://doi.org/10.1016/j.soildyn.2022.107252.
[39] Bhattacharya S, Lombardi D, Amani S, Aleem M, Prakhya G, Adhikari S, et al. Physical modelling of offshore wind turbine foundations for TRL (technology readiness level) studies. J Mar Sci Eng 2021;9:589. Available from: https://doi.org/10.3390/jmse9060589.
[40] Gaertner E, Jennifer R, Latha S, Frederik Z, Benjamin A, Garrett B, Nikhar A, Fanzhong M, Pietro B, Witold S, George S, Roland F, Henrik B, Katherine D, Matt S, Christopher A, and Anthony V. Definition of the IEA 15-megawatt offshore reference wind. Golden, CO: National Renewable Energy Laboratory. 2020. NREL/TP-5000-75698. https://www.nrel.gov/docs/fy20osti/75698.pdf
[41] Yu-Shu K, Chi-Sheng L, Juin-Fu C, Yu-Wen C, Yu-Hsiu TS. Case study of the ground motion analyses and seabed soil liquefaction potential of changbin offshore wind farm. J Mar Sci Technol 2019;27:448−62. Available from: https://doi.org/10.6119/JMST.201910_27(5)0.0007.
[42] Wang Y-K, Chai J-F, Chang Y-W, Huang T-Y, Kuo Y-S. Development of seismic demand for chang-bin offshore wind farm in Taiwan Strait. Energies 2016;9:1036. Available from: https://doi.org/10.3390/en9121036.
[43] Google Earth Pro. Location of Chang-bin wind farm (24° 8' 59.9," 119° 57' 0"), n.d.
[44] Luzi L, Lanzano G, Felicetta C, DAmico MC, Russo E, Sgobba S, et al. Engineering strong motion database (ESM) (Version 2.0). Ist Naz Di Geofis e Vulcanol 2020. https://doi.org/10.13127/ESM.2 [accessed 29.4.22].
[45] Hashash YMA, Musgrove MI, Harmon JA, Ilhan O, Xing G, Numanoglu O, et al. DEEPSOIL V7.0, User Manual. Urbana, IL: Board of Trustees of University of Illinois at Urbana-Champaign; 2020.
[46] Anbazhagan P, Prabhakaran A, Madhura H, Moustafa SSR, Al-Arifi NSN. Selection of representative shear modulus reduction and damping curves for rock, gravel and sand sites from the KiK-Net downhole array. Nat Hazards 2017;88:1741−68. Available from: https://doi.org/10.1007/s11069-017-2944-x.
[47] Elgamal A, Yang Z, Lu J. Cyclic1D: a computer program for seismic ground response. Report No. SSRP-06/05. San Diego; 2006.
[48] Elgamal A, Yang Z, Parra E, Ragheb A. Modeling of cyclic mobility in saturated cohesionless soils. Int J Plast 2003;19:883−905. Available from: https://doi.org/10.1016/S0749-6419(02)00010-4.
[49] Yang Z, Elgamal A, Parra E. Computational model for cyclic mobility and associated shear deformation. J Geotech Geoenviron Eng 2003;129:1119−27. Available from: https://doi.org/10.1061/(ASCE)1090-0241(2003)129:12(1119).
[50] Adhikari S, Bhattacharya S. A general frequency adaptive framework for damped response analysis of wind turbines. Soil Dyn Earthq Eng 2021;143:106605. Available from: https://doi.org/10.1016/j.soildyn.2021.106605.
[51] Ko YY. A simplified structural model for monopile-supported offshore wind turbines with tapered towers. Renew Energy 2020;156:777−90. Available from: https://doi.org/10.1016/j.renene.2020.03.149.
[52] Lombardi D, Bhattacharya S. Modal analysis of pile-supported structures during seismic liquefaction. Earthq Eng Struct Dyn 2014;43:119−38. Available from: https://doi.org/10.1002/eqe.2336.
[53] Takashi M, Inoue S, Tsuji Y, Yoshida K, Komatsuzaki M. Seismic design of offshore wind turbine withstands Great East Japan Earthquake and Tsunami. J Energy Power Eng 2014;8:2039−44. Available from: https://doi.org/10.17265/1934-8975/2014.12.007.
[54] 4coffshore. Wind turbine information database 2021. <https://www.4coffshore.com/windfarms/turbines.aspx> [accessed 5.5.21].
[55] Tottori Prefectural Government. List of domestic offshore wind power generation 2013. <https://www.pref.tottori.lg.jp/secure/836760/siryou6-2-1.pdf> [accessed 10.06.21].
[56] Alati N, Failla G, Arena F. Seismic analysis of offshore wind turbines on bottom-fixed support structures. Philos Trans R Soc A Math Phys Eng Sci 2015;373:20140086. Available from: https://doi.org/10.1098/rsta.2014.0086.
[57] DNV GL Standards. DNVGL-ST-0119: floating wind turbine structures; 2018.
[58] Barrass CB, Derrett DR. Ship stability for masters and mates. Elsevier; 2012. Available from: https://doi.org/10.1016/C2010-0-68323-4.
[59] Bhattacharya S, Biswal S, Aleem M, Amani S, Prabhakaran A, Prakhya G, et al. Seismic design of offshore wind turbines: good, bad and unknowns. Energies 2021;14. Available from: https://doi.org/10.3390/en14123496.

This page intentionally left blank

Chapter 18

Seismic hazards associated with offshore wind farms

Sadra Amani[1], Athul Prabhakaran[2], Subhamoy Bhattacharya[1,5], Haroon Rashid[3] and Rajib Sarkar[4]

[1]Department of Sustainability, Civil and Environmental Engineering, University of Surrey, Guildford, London, United Kingdom, [2]Department of Structural Engineering, University of California, San Diego, CA, United States, [3]Department of Civil Engineering, Indian Institute of Technology Bombay, Mumbai, Maharashtra, India, [4]Department of Civil Engineering, IIT(ISM) Dhanbad, Dhanbad, Jharkhand, India, [5]Renew Risk (OWF-PRA Limited), London, United Kingdom

18.1 Introduction

Offshore wind farms are being constructed in seismic zones. In the design of offshore wind turbines (OWT) in seismic regions, identifying the potential hazards are necessary. Fig. 18.1 shows a global seismic hazard map based on the Global Environmental Multiscale Model (GEM) together with potential or existing locations of offshore wind farms.

Wind farms developed in offshore environment provide more stable wind condition in comparison with the onshore wind farms. And thisdemand for cost-efficient wind energy production has facilitated the industry to develop larger turbines with higher capacities. Countries are planning to diversify their investment in offshore wind farms. Table 18.1 show offshore wind farms' global development in terms of power by 2030.

A review of various sizes of OWTs was conducted. The findings indicate that the increase in the turbine capacity results in the exponential rise of RNA mass as shown in Fig. 18.2.

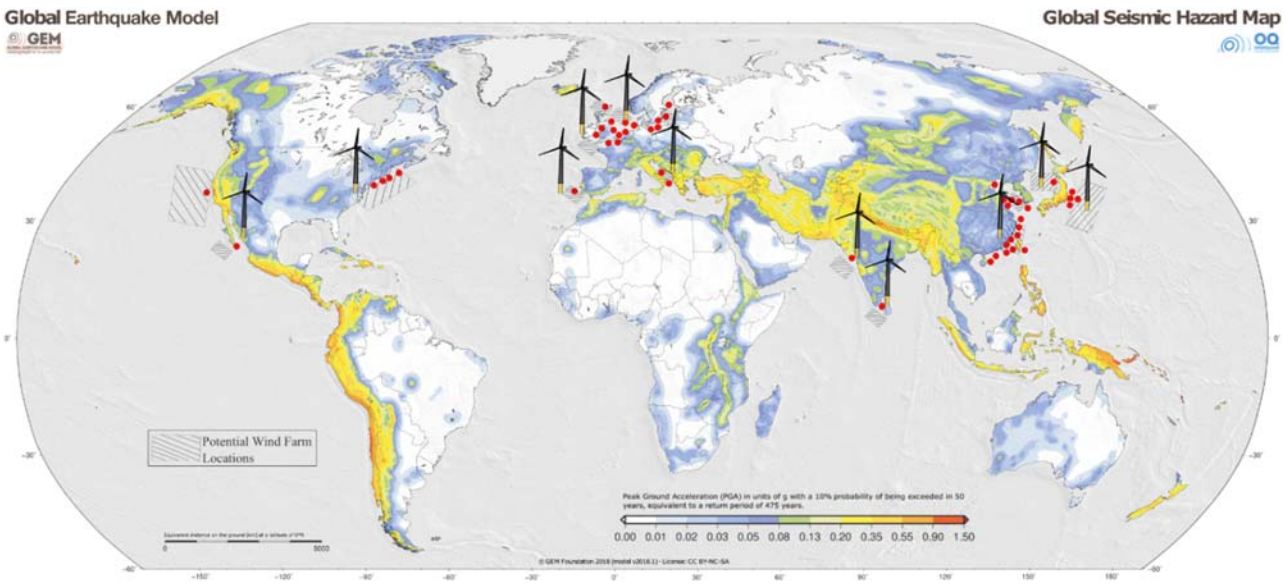

FIGURE 18.1 Investments in offshore wind farms together with seismicity [1,2]. *The base map of the GEM model is from Bhattacharya S, Biswal S, Aleem M, Amani S, Prabhakaran A, Prakhya G, et al. Seismic design of offshore wind turbines: good, bad and unknowns. Energies 2021;14. https://doi.org/10.3390/en14123496. Bhattacharya S, Lombardi D, Amani S, Aleem M, Prakhya G, Adhikari S, et al. Physical modelling of offshore wind turbine foundations for trl (technology readiness level) studies. J Mar Sci Eng 2021;9:589. https://doi.org/10.3390/jmse9060589.*

Wind Energy Engineering. DOI: https://doi.org/10.1016/B978-0-323-99353-1.00018-9

TABLE 18.1 Projected offshore wind capacity between 2022 to 2030 [3–9].

Number	Country	Year–capacity (MW)								
		2022	2023	2024	2025	2026	2027	2028	2029	2030
1	China	23108	26470	29831	33193	36554	39915	43277	46638	50000
2	United Kingdom	15361	18441	21521	24601	27680	30760	33840	36920	40000
3	Germany	8512	9323	10134	10945	11756	12567	13378	14189	15000
4	Netherlands	3953	4897	5840	6783	7727	8670	9613	10557	11500
5	Denmark	2558	2776	2993	3211	3429	3647	3864	4082	4300
6	Belgium	2456	2649	2842	3035	3228	3421	3614	3807	4000
7	Taiwan	1683	3130	4576	6022	7469	8915	10361	11807	13254
8	Sweden	203	215	227	239	252	264	276	288	300
9	South Korea	1425	2746	4067	5388	6709	8030	9351	10672	11993
10	Vietnam	1595	3091	4587	6082	7578	9074	10570	12066	13562
11	Japan	2449	4813	7177	9541	11905	14269	16633	18997	21360
12	Finland	71	No future plan outlined							
13	United States	3371	6699	10028	13357	16685	20014	23343	26671	30000
14	Ireland	222	419	617	814	1011	1208	1406	1603	1800
15	Portugal	39	53	67	81	94	108	122	136	150
16	Norway	339	671	1004	1337	1669	2002	2335	2668	3000
17	Spain	338	670	1003	1336	1669	2001	2334	2667	2999
18	France	780	1557	2335	3112	3890	4667	5445	6222	7000
18	Poland	356	711	1067	1422	1778	2133	2489	2844	3200
20	Estonia	67	133	200	267	333	400	467	533	600
21	India	5000	8125	11250	14375	17500	20625	23750	26875	30000
22	Saudi Arabia	Long-term plan outlined								500
23	Columbia	Long-term plan outlined								3000
24	Italy	72	144	217	289	361	433	506	578	650

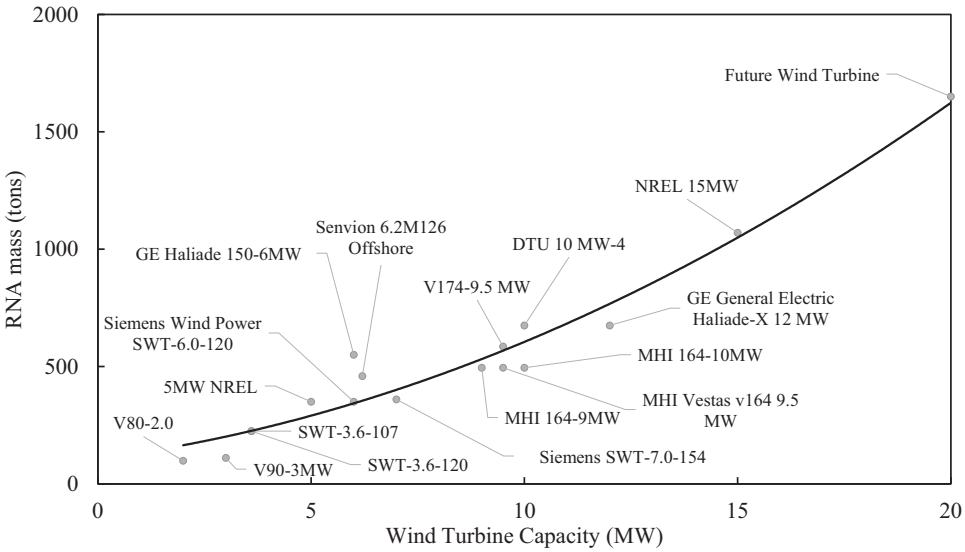

FIGURE 18.2 RNA mass variation with respect to wind turbine capacity [10–35].

Likewise, the natural frequency of the wind turbine system declines for a larger wind turbine capacity, as shown in Fig. 18.3.

Water depth and ground conditions typically govern the choice of the OWT foundation system. Bottom fixed foundations are typically deployed in water depths up to 60 m. For depths up to 30 m, monopiles are preferred. Typical foundation systems between 30 and 60 m include monopiles, suction caissons, and jacket structures [37]. As translational and rotational inertia is largely concentrated at the top of OWTs, dynamic wind/wave loads can generate substantial moment demands on the foundations. Further, due to the sensitivity in the dynamic response of OWTs to changes in their natural frequency, soil and foundation flexibility need to be accounted for in the design stage. The seismic design of OWT foundations typically considers self-weight, wind, wave, 1P (rotor frequency), 3P (blade passing frequency), and seismic loads [37]. Fig. 18.4 shows the different load types applied to a turbine structure. The time scales for wind, wave, and seismic loads add further complexity to the dynamics of OWTs. For example, cyclic wind loads

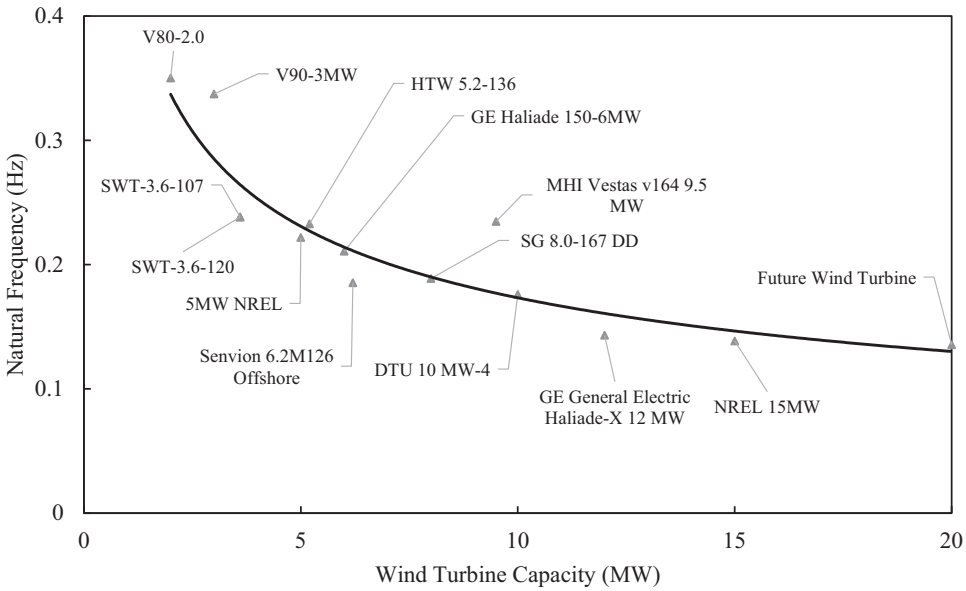

FIGURE 18.3 Natural frequency of the wind turbine system declines for a larger wind turbine capacity (Estimated using Arany et al. [36] for various wind farms based on the data collected from [10–35]).

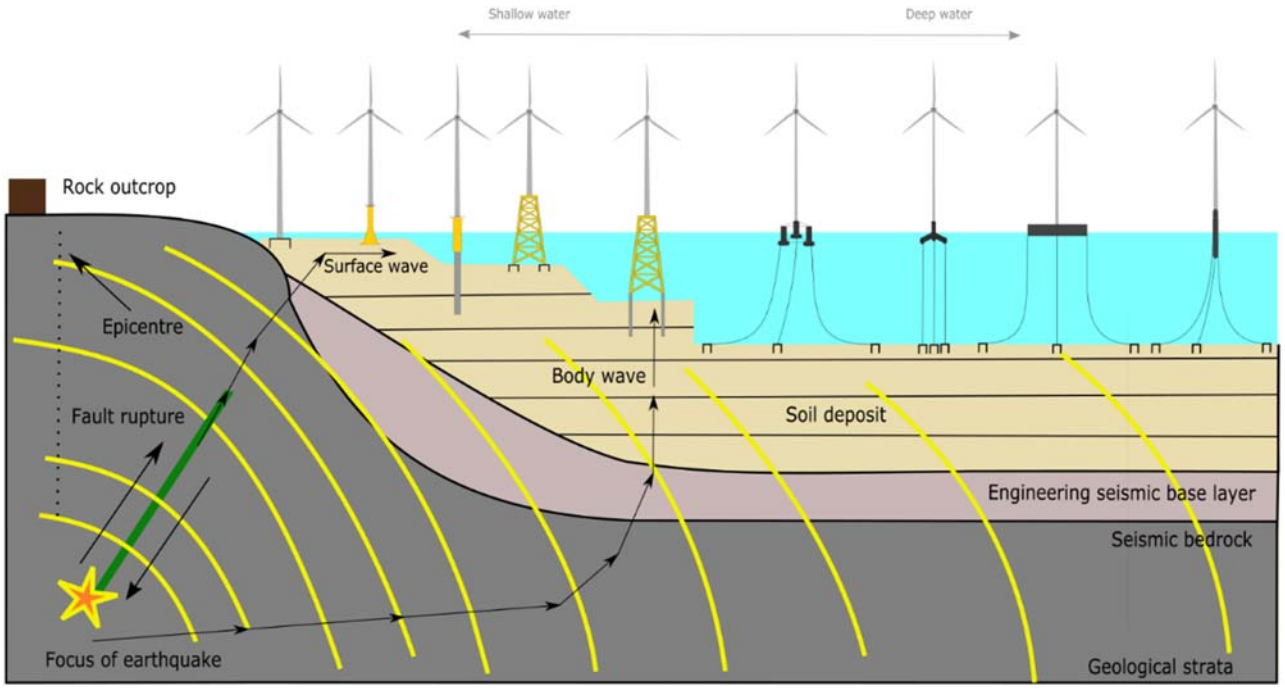

FIGURE 18.4 Wave propagation in layered media and common foundation types of offshore wind turbines [41,42].

have a period of around 100 s, whereas wave loads have a period of 10 s. Readers are referred to Arany et al. [36], Amani et al. [38], Bhattacharya [37] and Bhattacharya et al. [39,40] for further details.

The hypergraph of water range versus the capacity of OWTs is plotted. Fig. 18.5 illustrates the results. This is helpful to review the market expansion in different water ranges.

By carrying a regional review the seismic hazards st different regions are different, Table 18.2 summarizes some of the potential hazards in different regions.

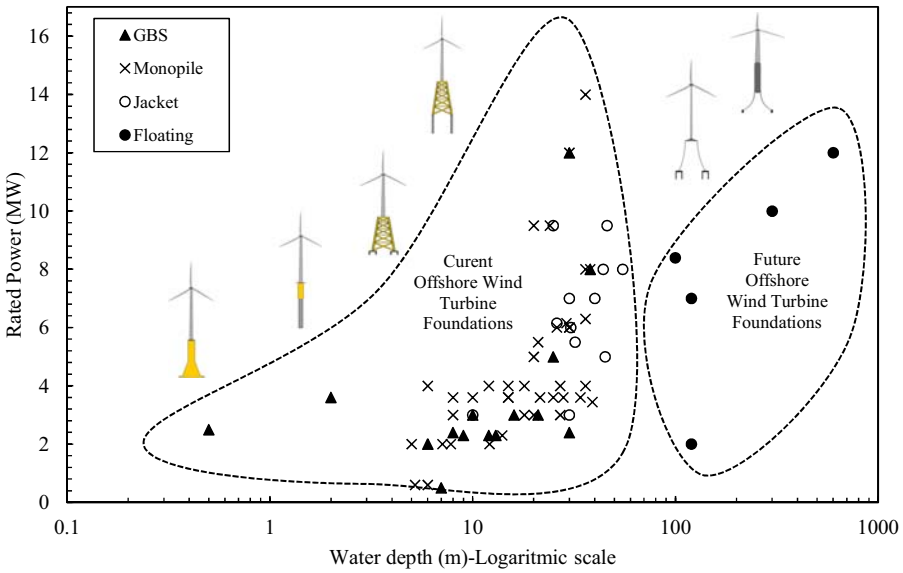

FIGURE 18.5 Compares the water range versus the rated power for different wind farm foundations in seismic regions [2,28,43].

TABLE 18.2 Seismic hazards for potential seismic zones [1].

Offshore Western United States (California)	High water depths and the required solution is floating technology. Seismically induced hazards include ground shaking, surface rupture, seabed liquefaction, submarine landslides, and tsunami loading. Additionally, the fault condition in relation to the electrical cables, the soil condition at the sites and its liquefaction or mud failure, mooring conditions, and loads imposed on the mooring and cables are some of the hazards on the floating foundations [44].
Offshore Eastern United States (Lake Eerie)	The eastern United States is an intraplate region, and the region has a relatively low seismic hazard compared to the west coast. Temperature-induced stresses can be a potential hazard at this site.
Offshore Canada (Pacific)	Offshore western Canada has the Cascadia subduction zone. Hazards include ground shaking, tsunami loading, seabed liquefaction, submarine landslides, basin effects, and surface rupture.
Offshore India	For the west coast, the significant seismic hazard (Gujarat) is ground shaking, For the southeast coast, (Tamil Nadu) major hazard is the tsunami.
Offshore Taiwan	Hazards include ground shaking, surface rupture, seabed liquefaction, tsunami loading and submarine landslides, slope failure, fluid seepage, volcanism, subsidence, bedforms, positive/negative reliefs, and diapers [45].
Offshore South America	Offshore South America has the Chilean subduction zone and can experience large earthquakes. Hazards include ground shaking, tsunami loading, submarine landslides, and seabed liquefaction.
Offshore Japan	Offshore Japan has a subduction zone and can experience large earthquakes. Hazards include ground shaking, tsunami loading, seabed liquefaction, and submarine landslides.
Offshore Italy	Adriatic Sea is located within the Adriatic plate. This is a continental crust by active compression and overridden by thrust belts on all sides. The region is prone to strong ground shaking, tsunami loading, and liquefaction.
Offshore Greece	Most of the seismicity is concentrated in the southern part of the Adriatic plate and between the Aegean and African plates into the southeast of Crete and is interpreted to be associated with the intracrustal graben system (Ptolemy and Pliny trenches). The region is prone to strong ground shaking, tsunami loading, and liquefaction.

18.2 Seismic hazard of bottom fixed offshore wind turbines

There are two types of OWT systems: (1) Grounded system where the turbine foundation is attached to the seabed; (2) Floating system where the anchor is attached to the seabed. Earthquake-induced hazards on OWTs require detailed investigation. In general, there are three types of categories in this field. (1) Effect of significant fault movement, (2) Ground shaking, (3) Liquefaction. Fig. 18.6 collates the possible hazards for an offshore wind farm.

Due to the highlighted hazards, the damage scale on OWTs could be different. To illustrate, foundation type, structural stiffness, and degree of the hazards are some examples that could impact the scale of damage [46].

18.2.1 Liquefaction and possible hazards

Due to the cyclic loading applied to the soil particle, the excess pore pressure will cause a reduction in the effective stress. This excess pore pressure loosens the contact between the soil particles, and as a result, a fluid-like behavior occurs in saturated soil, also known as liquefaction [47]. An increase in the pore pressure results in effective stress reduction, and therefore the stiffness of the soil also decreases. Therefore, this results in different types of failure mechanisms such as overall settlement, excessive rotation, and an increased period of the system. Fig. 18.7 schematically shows the liquefaction process. Further details can be found in Lombardi and Bhattacharya [48] and Bhattacharya et al. [37,49].

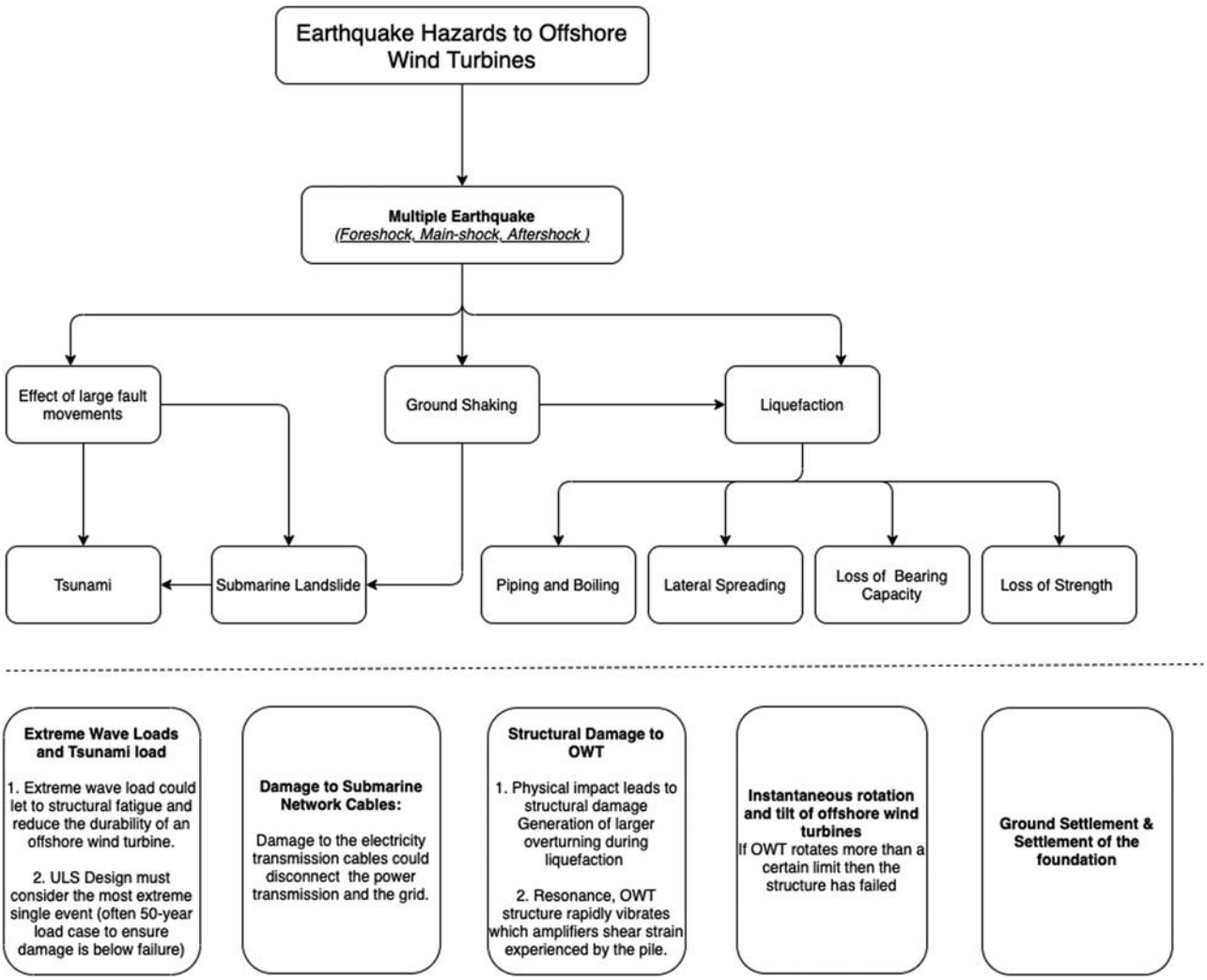

FIGURE 18.6 Shows the earthquake hazards to offshore wind turbine structures [1].

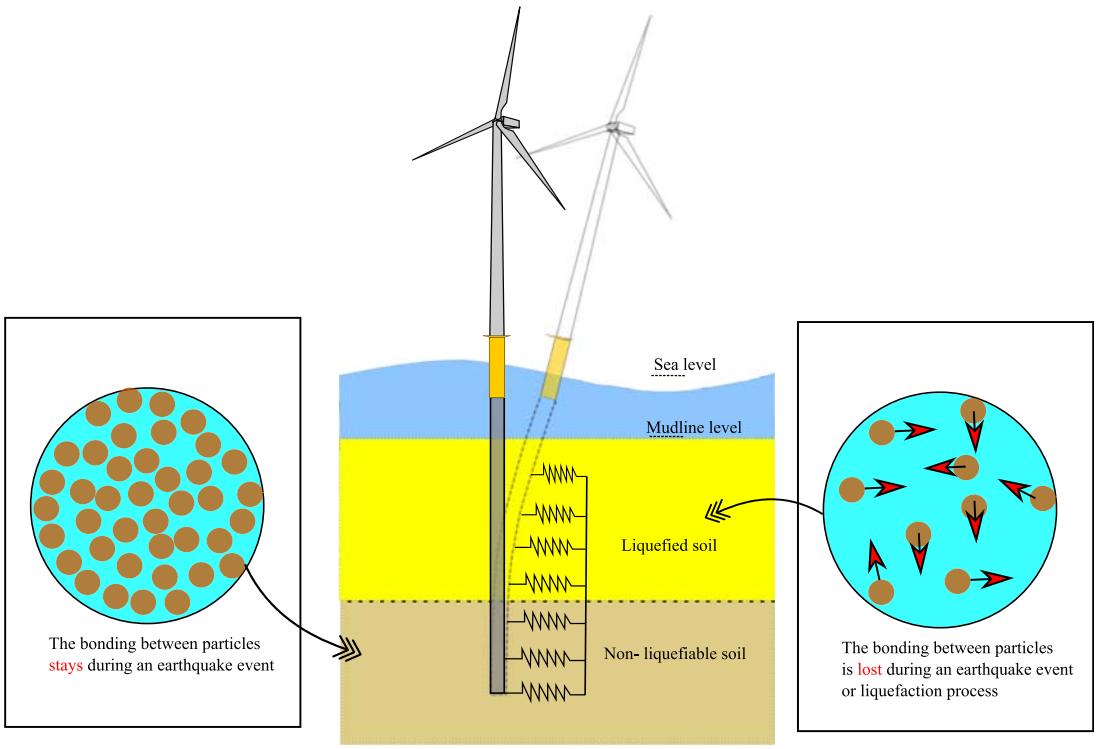

FIGURE 18.7 Schematic process of liquefaction phenomena and its possible effects on offshore wind turbines.

18.2.2 Tsunami

Tsunami loads are loads induced by the elevation of seawater surface level and current. The seawater elevation due to tsunami depends on water depth. In deep waters, tsunami elevation is minor and may be nondetectable. When the tsunami arrives in shallow water, the tsunami elevation is amplified [50]. Fig. 18.8 shows the tsunami wave propagation offshore and nearshore. In general, there are three main parameters to define the magnitude and application of tsunami forces. These include (1) inundation depth, (2) the tsunami flow velocity, and (3) the impact direction. And these are dependent on (1) tsunami wave height, (2) topography of the wave travel distance, and (3) roughness of the coastal inland [51]. Several codes of practice are available to estimate the tsunami load on the structures. For example, the Japanese code of practice MLIT 2570 [11] provides a static loading recommendation to design the tsunami load. This guideline applies the water depth coefficient based on the distance from the source to the static load configuration. The Japanese code of practice assumes a triangular force distribution on the structure. In contrast, the US guidance recommends considering hydrodynamic forces for tsunami event design. This code of practice recommends the consideration of the coefficient of drag, the momentum of flux, and the accumulated debris in the flow [52–54].

18.2.3 Example of deterministic seismic hazard analysis of Gujarat Coast, India [56]

Gujarat is one of the most seismically active regions of India. As per the data of the Global Seismic Hazard Assessment Program, the Gujarat region lies in a moderate to high seismic risk region. All four seismic zones of India are known to lie in this region (BIS IS 1893 [Part-1]) [57]. Thus, an evaluation of the seismic hazard of Gujarat Coastline for the safe design of offshore wind farms is necessary. For carrying out DSHA analysis, details of potential seismic sources are obtained from the seismotectonic atlas [58], published by the Geological Survey of India. Linear seismic sources within a radius of 500 km are considered. The maps have been digitized and georeferenced in Arcgis [59].

A 5 MW OWT system was analyzed for the expected ground motions at all the forty-four sites along the Gujarat coast. Deterministic seismic hazard analysis is being carried out for obtaining the site-specific ground motions considering the ground motion prediction equation proposed by NDMA [61] applicable for the specific region. PGA at each site is estimated from all the seismic sources and the maximum PGA obtained is assigned to the particular site. The site-

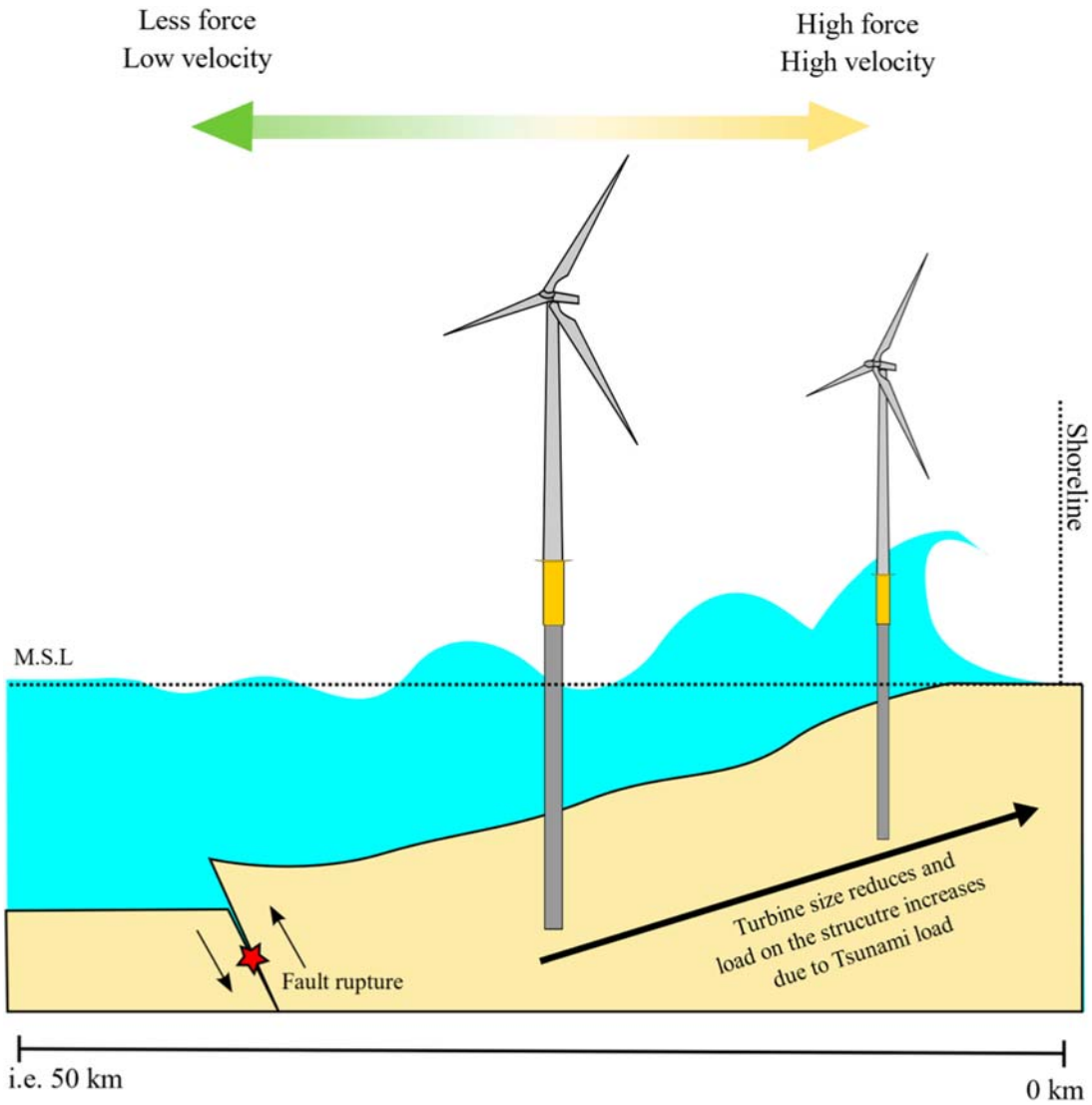

FIGURE 18.8 Tsunami wave propagation on offshore wind turbines [55].

specific response spectrum is evaluated for all the sites corresponding to the source giving maximum PGA. Site-specific response spectrum of a few selected sites. Table 18.3 mentions the derived peak ground acceleration (PGA) values for the sites. From Table 18.3, it may be observed that PGA values are in the range of 0.04−0.31 g. The PGA for sites that lie between the Kachchh and Saurashtra region (i.e., Sites 1−7) are found in the range of 0.18−0.31 g, and for the remaining sites, between 0.04 and 0.16 g. Choudhury, Chopra, and Kumar [62] have reviewed the seismic hazard of the region. They reported that PGA values in the Kachchh region had an average value of 0.35 g, while in Saurashtra average value of 0.175 g was reported at the bedrock level. It may be noted that they have obtained PGA values for the onshore regions of Gujarat. Since sites 1−7 lie in between Kachchh and Saurashtra, the PGA values are expected to be in the range of average values of Kachchh and Saurashtra region reported by Choudhury, Chopra, and Kumar [62]. In line with this, PGA values for sites 1−7 were observed to be in the range of average values (0.175−0.35 g) reported by the literature. The PGA values of the sites of the Saurashtra region also follow the range provided by the same literature. According to IS 1893(Part-1): 2016 [57], the Kachchh region lies in Zone V (PGA 0.36 g), northern parts of Saurashtra lie in Zone IV (PGA 0.24 g), and the remaining parts of Saurashtra in Zone III (PGA 0.16 g). It is observed that the PGA values of sites 1−7 lie in between PGA values of 0.24 and 0.36 g as recommended by IS 1893 (Part-1): 2016 [57] for Zone IV and Zone V respectively. The remaining sites are found to be in

proximity to Zone III with the PGA values in the range of 0.04−0.16 g. The diverse range of PGA values for the sites warrants the need for site-specific seismic hazard assessment. As per Chopra et al. [63], damage to structure usually begins around the PGA value of 0.10 g. Seismic hazard is severe in areas where the PGA values lie between 0.50 and 0.65 g. When the PGA values are in the range of 0.25−0.50 g, the seismic hazard is high, and when the PGA values are in the range of 0.15−0.25 g, the seismic hazard is moderate. In line with this observation, damage for any structure is expected to be high for sites lying between Kachchh and Saurashtra (Sites 1−7), and for the remaining sites, moderate damage is expected.

18.3 Seismic hazards of floating offshore wind farms

Floating offshore wind (FOWTs) installed capacity is estimated to reach 1000 GW by 2050 globally [64]. Floating foundations are expected to be used widely in the USA and East Asian countries such as Taiwan, Japan, China, and South Korea [2]. Fig. 18.9 and Table 18.3 illustrate the location and the details of some important floating wind turbine projects around the globe projected on the major tectonic plates map. OWT foundation is a solution that enables cheaper installation costs and lower damage to marine life. Therefore, it is becoming a preferable concept for developers. Floating wind turbines offer a lower installation cost than the bottom fixed foundations. And are suitable for water depths greater than 60 m [65]. The application of floating foundations on OWTs is relatively novel, and currently, there is a limited study on the design of these foundations in seismic regions.

Fault rupture in floating foundations could cause rupture and destabilization of the structure. Fig. 18.10 shows two main floating systems classified based on mooring lines. In one case, the mooring line is taut, which restricts movement, and the system is known as Tension Leg Platform (TLP). The mooring system allows excursion, known as the catenary mooring system. Fig. 18.10A shows the OWT systems supported on a barge system and suspended with catenary cables. The fault rupture between the supports could cause cables to loosen and a minor tilt in the

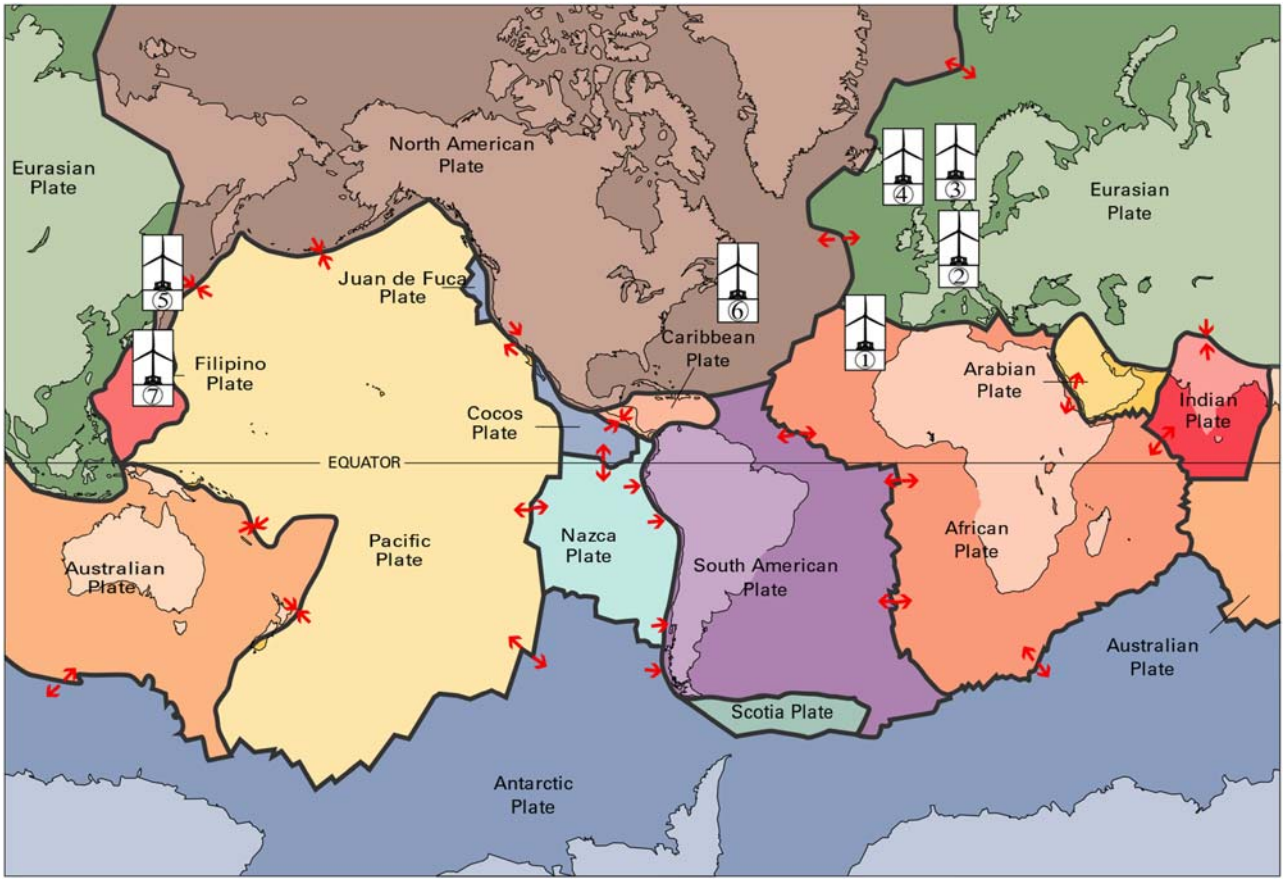

FIGURE 18.9 Location of floating wind farms projected on the map of the tectonic plates [66]. *The base map is from Nash S. USGS-tectonic plates; 2011.*

TABLE 18.3 Table of some key floating wind turbine projects.

#	Name	Location	Type of foundation	Total capacity (MW)	Type of turbine	Water depth (m)	Installed	References
Commissioned, under construction								
1	Wind Float Atlantic	Portugal	Semisubmersible	25	MHI V164–8.4 MW	100	2020	[67,68]
2	Kincardine	UK	Semisubmersible	50	5 × (V164–9.5 MW) 1 × (V80–2 MW)	60–80	2021	[69]
3	Hywind Tampen	Norway	Spar-buoy	88	SG 8.0–167 DD	260–300	2022	[70]
4	Hywind Scotland	UK	Spar-buoy	30	SWT-6.0–154	95–120	2017	[71]
Planned, future								
5	KF wind	Korea	Semisubmersible	1200	IEA 15-theoritical 16 MW	>200	–	[72]
6	Redwood coast offshore wind project	USA	Semisubmersible	120–150	–	610–1100	2024	[73,74]
7	Hibiki wind farm	Japan	(Barge)	–	V174–9.5 MW	55	2030	[75,76]

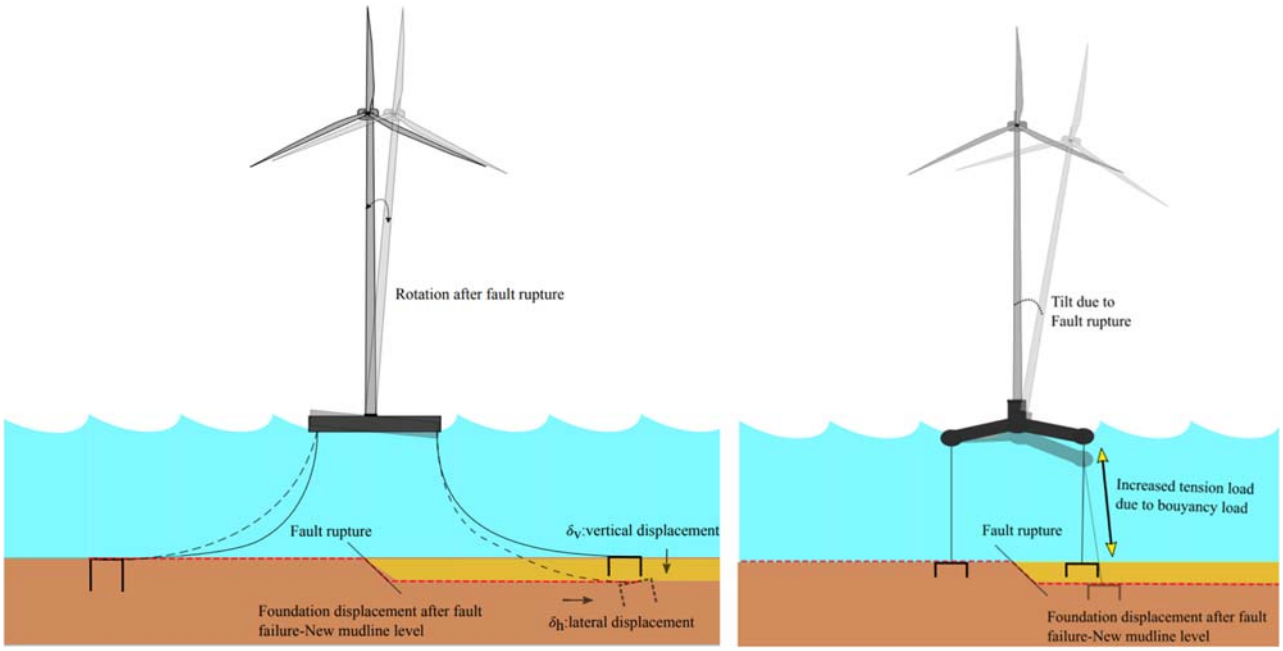

(A) Catenary mooringsystem (barge, semi-submersible, Spar buoy)

(B) Taut mooring system (tension leg platform)

FIGURE 18.10 Fault rupture induced hazard on floating offshore wind turbine. (A) Caternary mooring system, (B) Taut mooring system [1,2].

tower system. However, in a prestressed mooring system, for example, TLP, any amount of fault rupture between the supports could lead to a considerable amount of tilt, as shown in Fig. 18.10B. The tilt significance is proportional to the displacement at fault rupture location or even due to the response of earthquake motion at the surface level [1,77].

Additionally, different hazards for TLP floating structures are shown below in Fig. 18.11.

18.3.1 Fault rupture

Fault rupture occurrence could create cyclic stress with a large magnitude in the tension leg system of floating OWTs and create excessive strain on the cables and result in breakage. The mechanism of earthquake slip could be divided into three main stages [79]. (1) Initiation of the sliding (generation of the crack), (2) Expansion of the crack within the rupture zone, and (3) Rupture termination. Two methods could provide an estimate for the fault rupture displacement. One could be by carrying probabilistic surface fault displacement hazard analysis (PFDHA) or it could be estimated by conducting deterministic fault displacement hazard analysis [80]. Several papers studied the fault rupture displacement along the piles using the PFDHA approach, these are summarized in Petersen and Wesnousky [81]. Wells and Coppersmith [82] outlined formulas based on studying several earthquake events to obtain the displacement created by different types of fault rupture. Wells and Coppersmith [82] characterized the displacement based on the magnitude and the type of fault rupture [83]. Wells and Coppersmith [82] equations can be used to assess the vulnerability of floating OWTs to fault rupture. The readers are referred to Bhattacharya [37,84] and Bhattacharya et al. [1] for more details. The formulation depends on the magnitude of an earthquake event and the type of fault rupture (i.e., Strike-Slip, Reverse, Normal, and Thrust) as shown in Fig. 18.12. These input parameters are surface rupture length, subsurface rupture length, downdip rupture width, rupture area, maximum displacement, and average displacement.

18.3.2 Submarine landslide

Installation of offshore wind farms typically involves a detailed site investigation and ground improvement works if necessary. However, due to earthquakes, landslides are also possible.

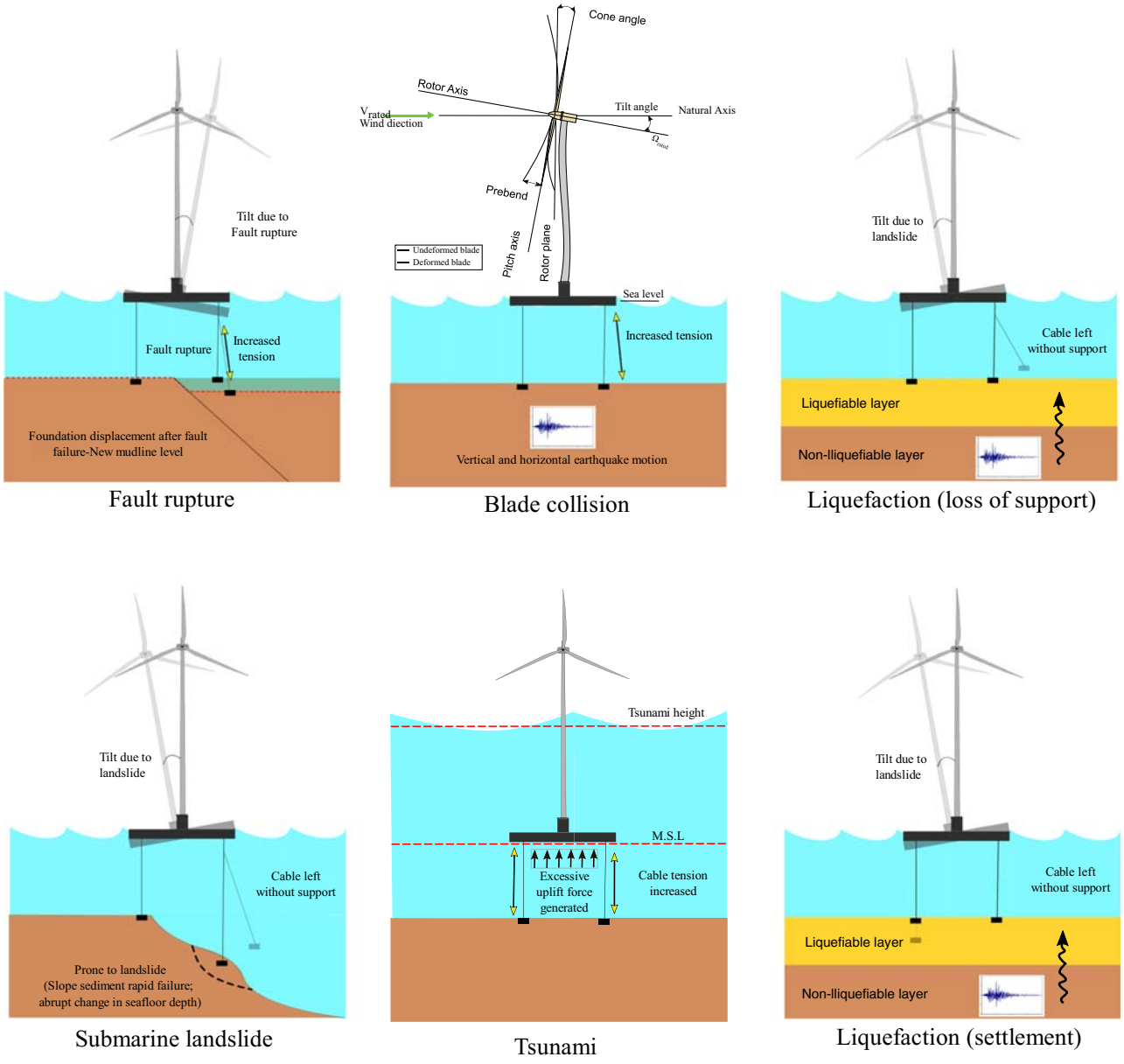

FIGURE 18.11 Typical hazards for TLPs [78].

18.3.3 Tsunami

Tsunami could danger the foundation system in two ways. It could increase the buoyancy force and increase the tension on the platform cables. It could even cause the foundation to tilt, which would increase the risk of instability in the whole wind turbine system.

18.3.4 Liquefaction

Due to cyclic loading, pore pressure increases in liquefiable soil, and therefore, the effective stress of soil reduces. FWT foundations are mostly supported by cables (either tensioned cable or catenary). The reduction in the effective stress results in a weaker anchor condition and therefore the anchors will become redundant. Therefore, it is recommended to use cables supported by piles in liquefiable soil.

Under seismic excitation, deep foundations experience demands due to (1) their inability to match free-field deformation (kinematic response) and (2) inertia arising from superstructure (inertial response). Appraisal of these

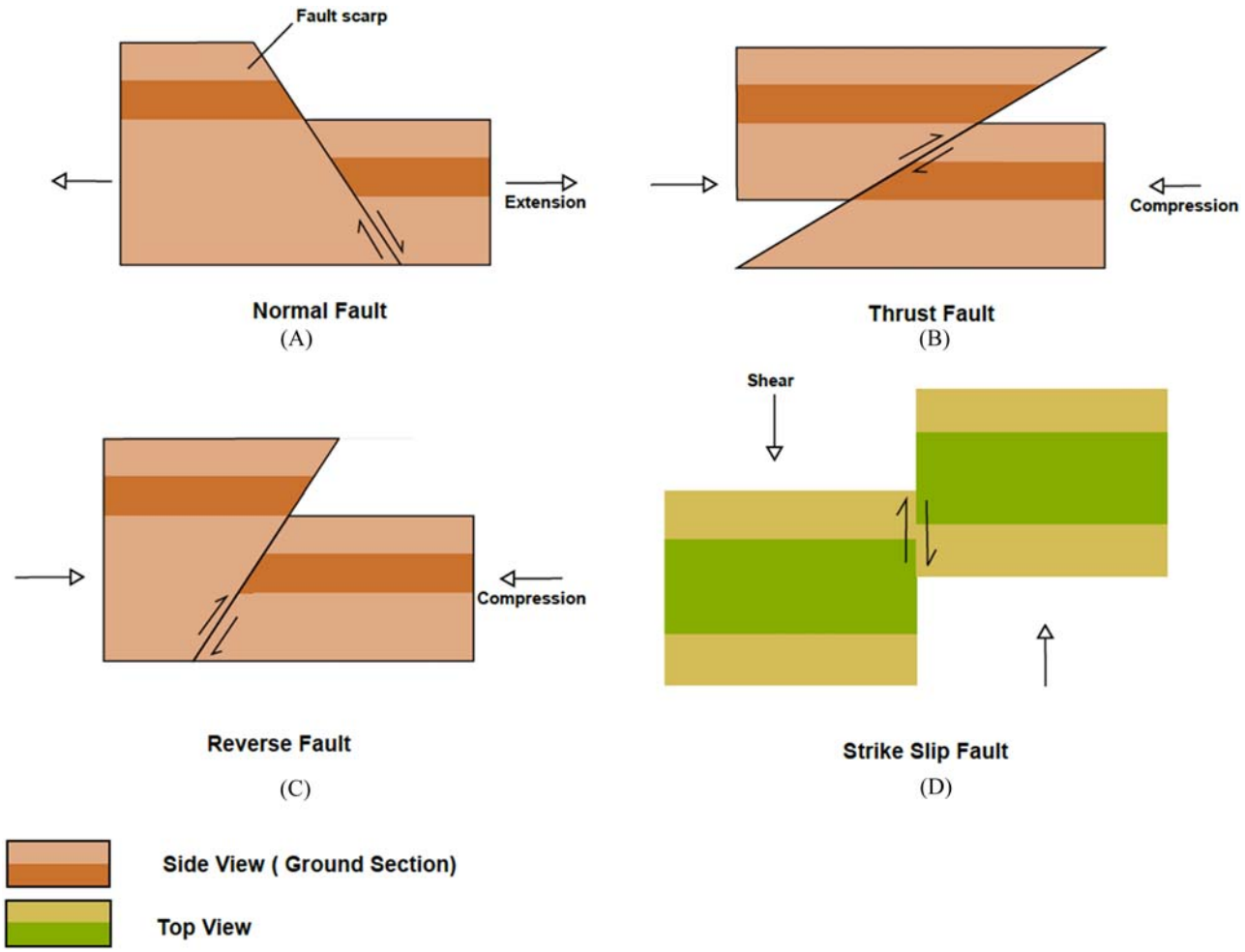

FIGURE 18.12 It shows different types of fault failures: (A) normal, (B) thrust, (C) reverse, and (D) strike-slip faults.

interactions is a necessary step toward the design of deep foundations for OWTs [85,86]. Regarding the floating wind turbines. There are two main types of mooring systems for floating wind turbines: (1) Vertical mooring (Taut mooring); (2) Catenary mooring, as shown in Fig. 18.13.

An example of taut mooring system is a TLP system where the cables are prestressed to increase the stability of the floater due to waves, wind, and other external loads, whereas the catenary system has a loose cable system and is allowed to move sideways up to a limited distance. Some examples of catenary mooring systems are barge, spar-buoy, and semisubmersible. There are different anchoring options available for floating wind turbines. These includes driven, drilled, or grouted piles, suction anchor, gravity-based anchor, and drag-embedded anchors. Seismic waves originated due to fault rupture are mainly in a form of body waves and surface waves. The wave propagation initiates by the travel of body waves [Primary (P) and Secondary (S) waves] and the surface waves (Rayleigh and Love waves). Fig. 18.14 shows the seismic waves' travel path in a floating wind farm.

This section introduces a methodology for the seismic design of monopile-supported OWTs accounting for kinematic and inertial effects. In the following section, the methodology is presented, with considerations to ground motion selection, site response analysis, and dynamic soil-structure interaction. Further, a case study is presented to validate the methodology based on observed response to a set of turbines from Japan during the 2011 Great East Japan (Tohoku) earthquake.

1. OWTs are sensitive to tsunami loads. The local tsunami depth is proportional to the increase in tsunami loads applied over the structure. Therefore, OWTs could collapse as a result of large tsunami loads.
2. RNA acceleration is typically smaller than the given PGA. Therefore, RNA experiences much lesser acceleration due to earthquakes in liquefiable soil.

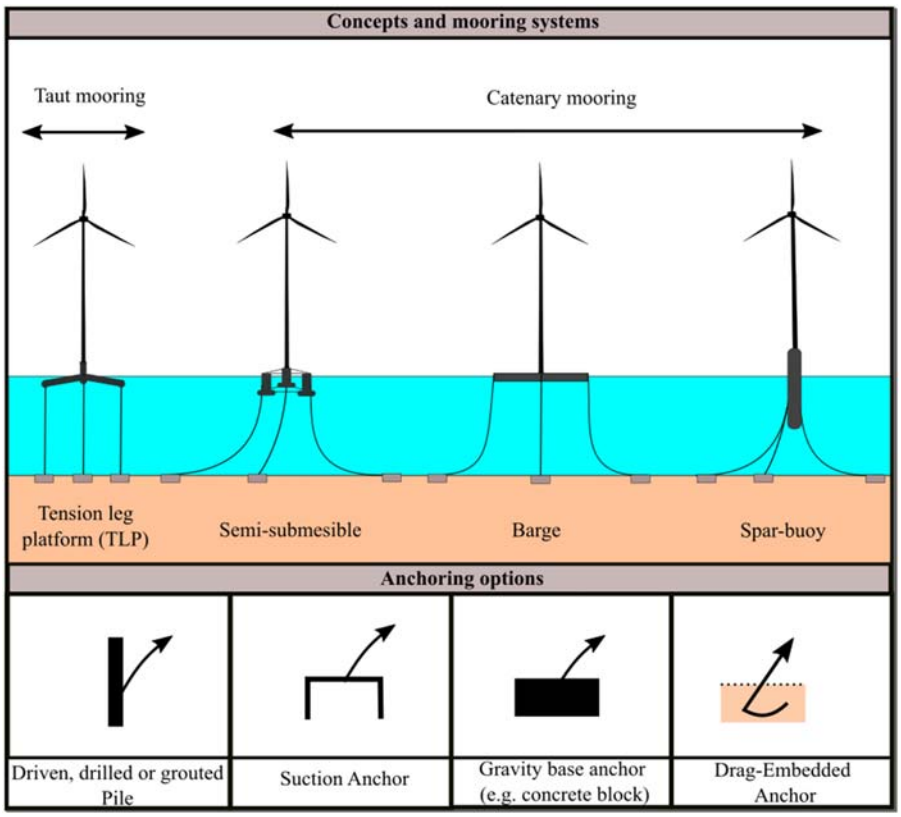

FIGURE 18.13 Different types of FOWTs.

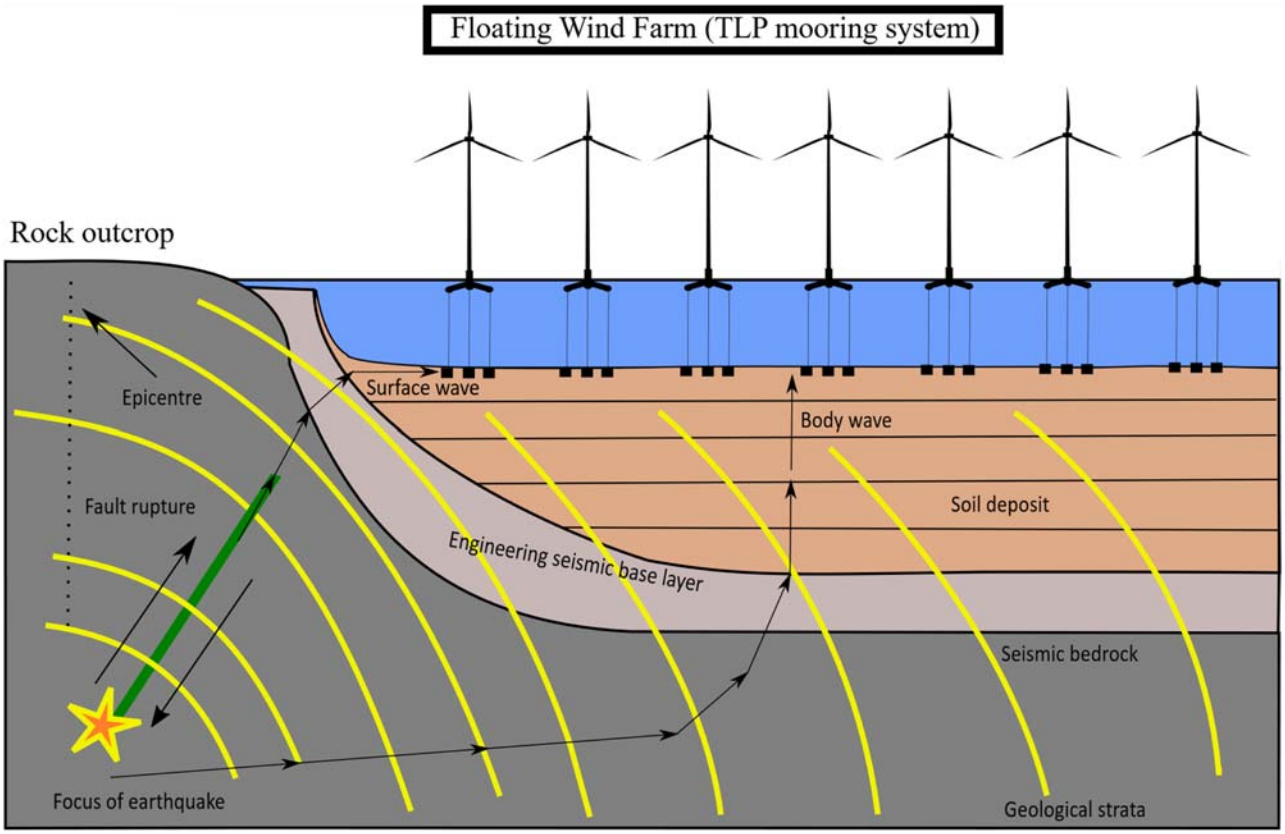

FIGURE 18.14 Seismic waves travel through the subsurface layers from the earthquake's origin.

3. The bending strain of the pile is vulnerable to the change in pile diameter and is almost constant for the pile length change.
4. The moment and lateral resisting capacity of the pile could be an excellent check to determine the performance of the wind turbine foundations in liquefiable soil.
5. Blade collision in seismic events with high PGAs is likely. Therefore, OWTs should consider blade effects for the seismic zones.
6. Floating wind turbines with TLP systems are more vulnerable to fault ruptures than the OWTFs with catenary systems. The authors recommend considering catenary mooring systems (e.g., semi-submersibles) for seismic regions.
7. There is limited information on the tsunami load calculation offshore; therefore, this needs further verification.

18.4 Miscellaneous hazards

Some of the hazards are shared between the floating and bottom fixed wind turbines. This section discusses the shared hazards.

18.4.1 Blade collision during a seismic event

One of the other possible hazards during the cyclic loading event (particularly in the seismic event) is the crash of the blade with the tower. Improving the wind turbine's rated power requires a higher wind capture area and longer blades. Longer blades during seismic events are more likely to cause higher deformation and, therefore, collision. Besides, the importance of other parameters such as the tower specification, RNA mass, tsunami loads, and unexpected ground accelerations is not negligible. This hazard is demonstrated schematically in Fig. 18.15.

For floating wind turbines, ground vibration induced from an earthquake could transmit through the tension leg system to the platform and therefore to the wind turbine system. This vibration could cause instability in the structure and therefore blade collision is expected. Most offshore wind farms are equipped with seismometers. Once the ground shake is detected by the system, the whole wind farm will be automatically shut down by the embedded sensors in the offshore wind turbine systems. However, blade collision could occur if the seismic hazard detection sensors carry faulty or malfunctioned . Furthermore, during the shutdown process if seismic motions reach the surface level during the slowdown period of the wind turbines, there could be still risks exist for the catastrophic failure of wind turbines.

18.4.2 Electrical cables failure

Energy infrastructure assets are of two types: generation and transmission assets. While the turbines fall under generation asset in the sense that these produce power, the electric cables that transfer electricity from the turbines to the onshore grid is transmission asset. Potential hazards related to large fault ruptures include anchor/mooring line failure in floating OWTs and electrical cable failure. There are two types of cables: (1) interarray cables, which connect different turbines and links with the offshore substation; (2) export cable, which connects the offshore substation to the onshore grid, i.e., exports power. The cable (interarray and export) design of OWTs in seismic regions will need some extra considerations. A study conducted by KIS-ORCA [87] concludes that seismic activities, landslides, and current abrasion in water depths exceeding 1000 m could be associated with cable failures. For water depths less than 200 m, cable failures mainly occur due to anchoring and fishing activities. Statistics revealed that 70% of cable failures are due to human-related activities (i.e., fishing and anchoring), and the remaining are due to natural calamities, i.e., earthquakes. Therefore, it is highly likely that for the current installation depths (which are less than 200 m), the risk of cables failure due to only seismic effects (such as shaking, i.e., inertia) is low. However, since OWTs are relatively expensive assets, 'cable failure (array cables) could cut power. Therefore, no risk should be left unconsidered.

18.5 Summary of demands of offshore wind turbines

This chapter outlined some of the important risks and hazards for the design and analysis of offshore wind turbines. The summary of some of the engineering risks for different foundation types have been outlined in Table 18.4.

In addition, for the floating wind turbine, it could be concluded that TLP type foundations are not a suitable solution for the areas where the fault rupture hazard exist. The mooring system of TLP foundations is pretensioned, whereby,

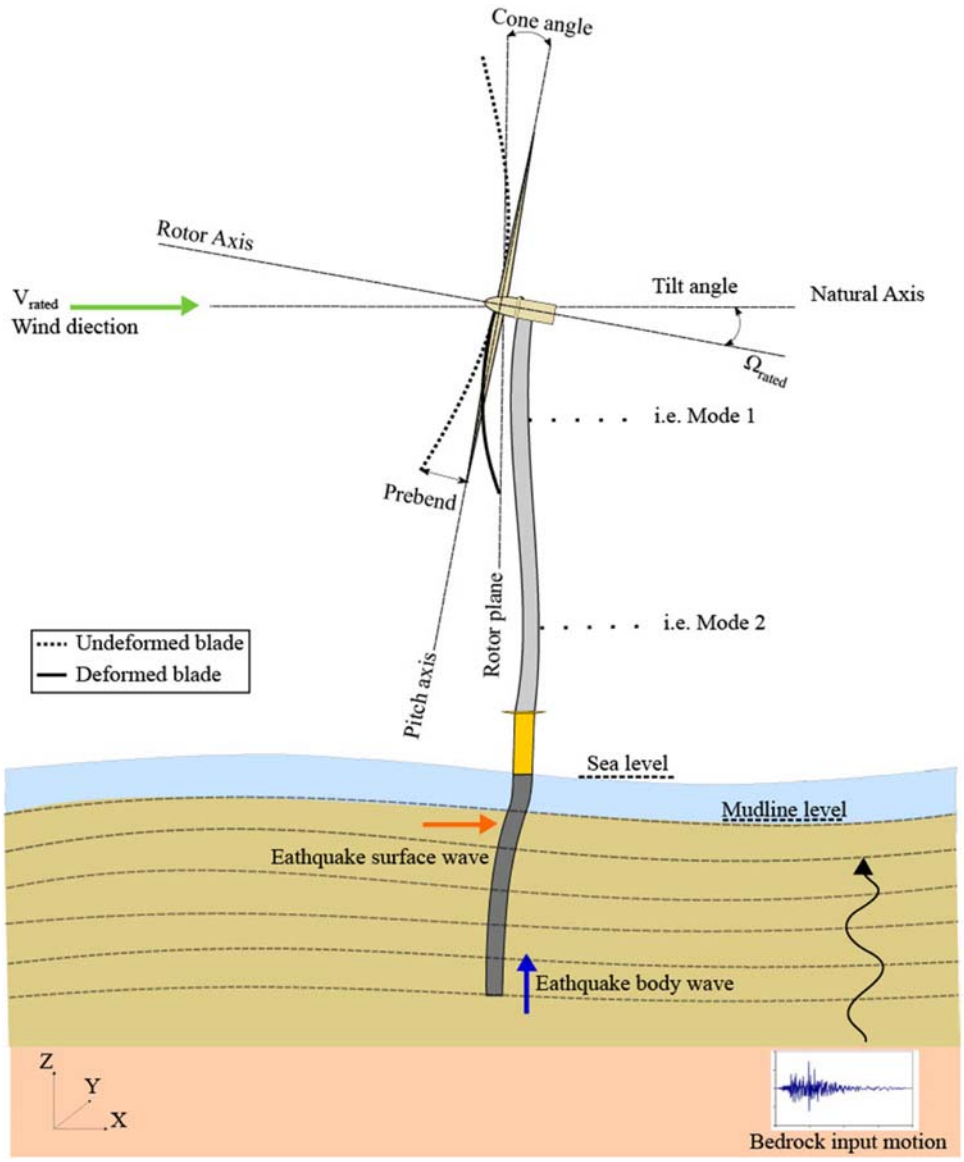

FIGURE 18.15 Seismic response and the possibility of blade collision with the turbine tower.

TABLE 18.4 Engineering risk to different foundation types for OWTs [1].

Foundation type	Engineering risk in seismic areas
Monopile	1. High moment demand on foundations due to inertia loading + Emergency Braking (if any) 2. Kinematic moments in layered soils 3. Loss of lateral load/moment carrying capacity due to seabed liquefaction
Jacket foundation	1. Buckling of braces 2. Small diameter piles (as opposed to monopile foundations) are prone to buckling instability and P-delta effects
Caissons	1. Overturning due to tsunami loading
Floating system	1. Less vulnerable to ground shaking and therefore applicable to high seismic regions with deeper waters. However, surface fault rupture can cause high tensile forces on cables.

such systems become vulnerable to vertical vibration . Vertical ground motion could destabilize the floating system or increase the risk of cable failure due to excessive design tension. However, horizontal displacement of ground due to the earthquake is relatively small compared to the cable length; therefore, minimal to no vulnerability was observed due to applied horizontal ground motions. Fault rupture is a critical risk for the TLP foundations and could cause tendon failure in large ruptures. However, in this study, failure is not observed. The readers of this paper are referred to Wells and Coppersmith [82] for further details on fault displacement estimation.

References

[1] Bhattacharya S, Biswal S, Aleem M, Amani S, Prabhakaran A, Prakhya G, et al. Seismic design of offshore wind turbines: good, bad and unknowns. Energies 2021;14. Available from: https://doi.org/10.3390/en14123496.

[2] Bhattacharya S, Lombardi D, Amani S, Aleem M, Prakhya G, Adhikari S, et al. Physical modelling of offshore wind turbine foundations for TRL (technology readiness level) Studies. J Mar Sci Eng 2021;9:589. Available from: https://doi.org/10.3390/jmse9060589.

[3] Nghiem A, Pineda I. Wind energy in Europe: scenarios for 2030. Brussels: Wind Europe; 2017.

[4] Wind Europe. Spain issues plan for up to 3 GW offshore wind by 2030—in perfect time for Wind Europe 2022 in Bilbao. Wind Eur 2021. <https://windeurope.org/newsroom/news/spain-issues-plan-for-up-to-3-gw-offshore-wind-by-2030-in-perfect-time-for-windeurope-2022-in-bilbao/#:~:text=> Spain is already the second, on the back of this [accessed 27.02.22].

[5] Christopher TR, Williams M, Goldstein M, Carter A. The road to 30 gigawatts: key actions to scale an offshore wind industry in the United States. Cent Am Prog 2022; <https://www.americanprogress.org/article/the-road-to-30-gigawatts-key-actions-to-scale-an-offshore-wind-industry-in-the-united-states/> [accessed 27.05.22].

[6] Tachev V. Wind energy in South Korea—opportunities and challenges 2021. <https://energytracker.asia/wind-energy-in-south-korea-opportunities-and-challenges/#:~:text=> As a part of its, MW the country has today. [accessed 27.05.22].

[7] GlobalData Energy. China to add significant offshore wind power capacity every year during 2023−2030. Power Technol 2021. <https://www.power-technology.com/comment/china-offshore-wind-power/> [accessed 27.05.22].

[8] Li CH. Taiwan's new policy can turn it into a major regional offshore wind hub. NHST Media Gr 2021. <https://www.rechargenews.com/wind/taiwans-new-policy-can-turn-it-into-a-major-regional-offshore-wind-hub/2-1-1010192> [accessed 27.05.22].

[9] ABB/ZERO. Floating offshore wind Norway's next offshore boom?; 2018.

[10] TritonKnoll. Triton Knoll Offshore Wind Farm Project: Decommissioning Programme for Triton Knoll Offshore Wind Farm; 2018.

[11] Bauer L, Matysik S. Siemens Gamesa SG 7.0−154. Big Portal Wind Energy; 2020. <https://en.wind-turbine-models.com/turbines/1810-siemens-gamesa-sg-7.0-154> [accessed 24.11.20].

[12] Jonkman J, Butterfield S, Musial W, Scott G. Definition of a 5-MW reference wind turbine for offshore system development; 2009. <https://doi.org/NREL/TP-500-38060>.

[13] Vestas. V90-3.0 MW-an efficient way to more power; 2009. <https://www.maine.gov/dacf/lupc/projects/windpower/transcanada/Volume3/Volume3_Section2/Appendix2-I.pdf>.

[14] Tande JO. EERA DeepWind'2018 conference 17−19 January 2018. In: Tande JO, editor. SINTEF Energy Res. AS, Trondheim: SINTEF; 2018.

[15] Bauer L, Matysik S. GE General Electric GE 4.1−113 2013. <https://en.wind-turbine-models.com/turbines/479-ge-general-electric-ge-4.1-113> [accessed 25.11.20].

[16] GE Renewable Energy. GE's Haliade-150-6MW-high yield offshore wind turbine; 2015.

[17] Alstom. Alstoms 6 MW Haliade offshore wind turbine loaded at Ostend 2013. <https://www.alstom.com/press-releases-news/2013/9/alstoms-6mw-haliade-offshore-wind-turbine-loaded-at-ostend#:~:text=> The nacelle weighs around 400, of more than 2.9 GW. [accessed 25.11.20].

[18] Alstom. Haliade 150-6MW. Barcelona; 2014.

[19] Senvion. 6.3M152 n.d. <https://www.senvion.com/global/en/products-services/wind-turbines/6xm/63m152/> [accessed 25.11.20].

[20] Sun&Wind Energy. Senvion delivers turbines for offshore wind farm Nordsee One 2015. <https://www.sunwindenergy.com/wind-energy/senvion-delivers-turbines-offshore-wind-farm-nordsee-one> [accessed 25.11.20].

[21] Siemens Gamesa Renewable Energy. Wind Turbines & Services Highly profitable n.d. <https://www.siemensgamesa.com/en-int/products-and-services> [accessed 25.11.20].

[22] Matt Whitby. MHI Vestas offshore wind signs conditional contract for 330 MW Walney extension phase 1. MHI Vestas Offshore Wind n.d. <https://mhivestasoffshore.com/mhi-vestas-offshore-wind-signs-conditional-contract-for-330-mw-walney-extension-phase-1/> [accessed 24.11.20].

[23] Hitachi Ltd. HITACHI 5200kW Wind Turbine. Tokyo: n.d.

[24] Bauer L, Matysik S. Hitachi, Ltd. HTW5.2−136 2016. <https://en.wind-turbine-models.com/turbines/1553-hitachi-ltd.-htw5.2-136> [accessed 25.11.20].

[25] Ichter B, Steele A, Loth E, Moriarty P, Selig M. A morphing downwind-aligned rotor concept based on a 13-MW wind turbine. Wind Energy 2016;19:625−37. Available from: https://doi.org/10.1002/we.1855.

[26] Bauer L, Matysik S. The big portal for wind energy 2020. <https://en.wind-turbine-models.com> [accessed 25.11.20].

[27] Kiyoki S, Sakamoto K, Kakuya DEH, Saeki M. 5-MW downwind wind turbine demonstration and work toward smart operation control. Next-Generation Energy Solut Aimed Symbiosis F E A T U R E D A R T I C L E S with Glob Environ 2017:38−44.

[28] 4coffshore. Wind turbine information database 2021. <https://www.4coffshore.com/windfarms/turbines.aspx> [accessed 5.5.21].
[29] Orsted. Offshore wind; n.d. <https://orsted.co.uk/energy-solutions/offshore-wind/our-wind-farms> [accessed 24.11.20].
[30] IECRE. IECRE. WE. CC. 20. 0038-R0 (Provisional component certificate wind turbine). Hamburg; 2020.
[31] Reve. NREL unveils 15 MW wind turbine developed with DTU 2020. <https://www.evwind.es/2020/02/13/nrel-unveils-15-mw-wind-turbine-developed-with-dtu/73570> [accessed 25.11.20].
[32] Gaertner E., Rinker J., Sethuraman L., Zahle F., Anderson B., Barter G., et al. IEA Wind TCP Task 37-Definition of the IEA Wind 15-Megawatt Offshore Reference Wind Turbine-Technical Report. Denver: 2020. https://doi.org/NREL/TP-5000-75698.
[33] IECRE. IECRE. WE. CC. 19.0020-R0. Hamburg; 2019.
[34] SIEMENS. New dimensions (Siemens Wind Turbine SWT-3.6−107). Erlangen; 2011.
[35] Siemens A.G. Turbina Sapiens in its natural habitat-Siemens 6.0 MW offshore wind turbine. Erlangen; 2011.
[36] Arany L, Bhattacharya S, Macdonald J, Hogan S. Design of monopiles for offshore wind turbines in 10 steps. Soil Dyn Earthq Eng 2017;92:126−52. Available from: https://doi.org/10.1016/j.soildyn.2016.09.024.
[37] Bhattacharya S. Design of foundations for offshore wind turbines. 1st ed. Chichester: Wiley; 2019. Available from: https://doi.org/10.1002/9781119128137.
[38] Amani S, Prabhakaran A, Bhattacharya S. Design of monopiles for offshore and nearshore wind turbines in seismically liquefiable soils: Methodology and validation. Soil Dynamics and Earthquake Engineering 2022;157:107252. Available from: https://doi.org/10.1016/j.soildyn.2022.107252.
[39] Bhattacharya S, Lombardi D, Praphakaran A, Mistry HK, Amani S, Prakhya G, et al. Risks and Vulnerabilities in the Design, Construction, and Operation of Offshore Wind Turbine Farms in Seismic Areas. Tracts in Civil Engineering. Singapore: Springer; 2023. Available from: https://doi.org/10.1007/978-981-19-3330-1_1.
[40] Bhattacharya S, Amani S, Prabhakaran A, Macabuag J. Hazard considerations in the vulnerability assessment of offshore wind farms in seismic zones. Earthquake Engineering and Resilience 2022;1:88−109. Available from: https://doi.org/10.1002/eer2.11.
[41] Yoshida N. Engineering seismic base layer for defining design earthquake motion. AIP Conf Proc 2008;1020:346−53. Available from: https://doi.org/10.1063/1.2963855.
[42] Santini A, Moraci N. 2008 Seismic engineering conference commemorating the 1908 Messina and Reggio Calabria Eartquake: [MERCEA '08]; Reggio Calabria, Italy, 8−11 July 2008/ed. Adolfo Santini. . .; Pt. 1. AIP Conf. Proc., vol. 1020,1, Melville, NY: American Inst. of Physics; 2008.
[43] Jalbi S, Arany L, Salem A, Cui L, Bhattacharya S. A method to predict the cyclic loading profiles (one-way or two-way) for monopile supported offshore wind turbines. Mar Struct 2019;63:65−83. Available from: https://doi.org/10.1016/j.marstruc.2018.09.002.
[44] USGS. Main faults of northern and central California. Pacific Coast Mar Sci Cent; n.d.<https://www.usgs.gov/media/images/main-faults-northern-and-central-california> [accessed 23.02.20].
[45] Song G. Types of marine geohazards investigated in offshore wind farm construction. Open Access Gov 2020; <https://www.openaccessgovernment.org/marine-geohazards-offshore-wind-farm-construction-2/97663/> [accessed 23.02.20].
[46] Macabuag J, Rossetto T, Ioannou I, Suppasri A, Sugawara D, Adriano B, et al. A proposed methodology for deriving tsunami fragility functions for buildings using optimum intensity measures. Nat Hazards 2016;84:1257−85. Available from: https://doi.org/10.1007/s11069-016-2485-8.
[47] PLAXIS. PLAXIS 3D Material Models Manual, 2019.
[48] Lombardi D, Bhattacharya S. Evaluation of seismic performance of pile-supported models in liquefiable soils. Earthq Eng Struct Dyn 2016;45:1019−38. Available from: https://doi.org/10.1002/eqe.2716.
[49] Bhattacharya S, Demirci HE, Nikitas G, Prakhya GKV, Lombardi D, Alexander NA, et al. Physical modeling of interaction problems in geotechnical engineering. In: Samui P, Kumari S, Makarov V, Kurup P, editors. Model. Geotech. Eng. Elsevier; 2021. p. 205−56. Available from: https://doi.org/10.1016/B978-0-12-821205-9.00017-4.
[50] Bureau Veritas. Classification and certification of floating offshore wind turbines-rule note NI 572 DT R02 E. France: Bureau Veritas; 2019.
[51] Palermo D, Nistor I, Nouri Y, Cornett A. Tsunami loading of near-shoreline structures: a primer. Can J Civ Eng 2009;36:1804−15. Available from: https://doi.org/10.1139/L09-104.
[52] Macabuag J, Raby A, Pomonis A, Nistor I, Wilkinson S, Rossetto T. Tsunami design procedures for engineered buildings: a critical review. Proc Inst Civ Eng—Civ Eng 2018;171:166−78. Available from: https://doi.org/10.1680/jcien.17.00043.
[53] MLIT. Further information concerning the design method of safe buildings that are structurally resistant to Tsunamis—Technical Advice No. 2570. Tokyo, Japan; 2011.
[54] Chock GYK. Dist. M. ASCE. Design for Tsunami loads and effects in the ASCE 7−16 standard. J Struct Eng 2016;142. Available from: https://doi.org/10.1061/(ASCE)ST.1943-541X.0001565.
[55] Bhattacharya S, Amani S, Prabhakaran A, Macabuag J. Hazard considerations in the vulnerability assessment of offshore wind farms in seismic zones. Earthq Eng Resil 2022;1:88−109. Available from: https://doi.org/10.1002/eer2.11.
[56] Rashid H, Sarkar R. Site-specific response of a 5 MW offshore wind turbine for Gujarat Coast of India. Mar Georesour Geotechnol 2021;1−20. Available from: https://doi.org/10.1080/1064119X.2021.1972062.
[57] IS 1893 (Part 1). Criteria for Earthquake Resistant Design of Strucutre. New Delhi; 2016.
[58] Kumar P, Tewari HC, Sreenivas B. Seismic structure of the Central Indian Crust and its implications on the crustal evolution. J Geol Soc India 2019;93:163−70. Available from: https://doi.org/10.1007/s12594-019-1146-4.
[59] ESRI (Environmental Systems Resource Institute). ArcGIS desktop: Release 10.4; n.d.

[60] Dasgupta S, Pande P, Ganguly D, Iqbal Z, Sanyal K, Venkatraman NV, et al. Seismotectonic Atlas of India and Its Environs,. Geological Survey of India 2000;86.
[61] NDMA. Development of probabilistic seismic hazard Map of India Technical Report. National Disaster Management Authority. India: NDMA; 2010.
[62] Choudhury P, Chopra S, Kumar MR. A review of seismic hazard assessment of Gujarat: a highly active intra-plate region. Earth-Sci. Rev 2018;187:205−18. Available from: https://doi.org/10.1016/j.earscirev.2018.09.014.
[63] Chopra VS, Kong N, Levine M. Transcriptional repression via antilooping in the Drosophila embryo. Proc Natl Acad Sci 2012;109:9460−4. Available from: https://doi.org/10.1073/pnas.1102625108.
[64] IRENA. Future of wind: deployment, investment, technology, grid integration and socio-economic aspects (A Global Energy Transformation Paper). Abu Dhabi; 2019.
[65] Goupee AJ, Koo BJ, Kimball RW, Lambrakos KF, Dagher HJ. Experimental comparison of three floating wind turbine concepts. J Offshore Mech Arct Eng 2014;136. Available from: https://doi.org/10.1115/1.4025804.
[66] Nash S. USGS-tectonic plates; 2011.
[67] Durakovic A. WindFloat atlantic fully up and running. OffshoreWINDBiz 2020. <https://www.offshorewind.biz/2020/07/27/windfloat-atlantic-fully-up-and-running/> [accessed 6.02.22].
[68] OW Ocean Winds. Windfloat Atlantic Project 2021. <https://www.oceanwinds.com/projects/windfloat-atlantic-project/> [accessed 6.02.22].
[69] Durakovic A. World's largest floating offshore wind farm fully operational. OffshorewindBiz 2021. <https://www.offshorewind.biz/2021/10/19/worlds-largest-floating-offshore-wind-farm-fully-operational/#:~:text=The> 50 MW Kincardine floating, largest operating floating wind farm [accessed 6.02.22].
[70] Equinor ASA. Hywind Tampen 2022. <https://www.equinor.com/en/what-we-do/hywind-tampen.html> [accessed 6.02.22].
[71] Equinor ASA. Industrialising floating offshore wind 2022. <https://www.equinor.com/en/what-we-do/floating-wind.html> [accessed 6.02.22].
[72] OW Ocean Winds. Korea floating wind farm project 2021. <https://www.oceanwinds.com/projects/korea-floating-wind-farm/> [accessed 6.02.22].
[73] OW Ocean Winds. Redwood coast offshore wind project 2021. <https://www.oceanwinds.com/projects/redwood/> [accessed 6.02.22].
[74] Redwood Coast Energy Authority. Redwood coast offshore wind 2022. <https://redwoodenergy.org/redwood-coast-offshore-wind/> [accessed 6.02.22].
[75] Skopljak N. MHI Vestas 9.5MW turbines in the game for Japanese offshore wind farm 2019. <https://www.offshorewind.biz/2019/11/06/mhi-vestas-9-5mw-turbines-in-the-game-for-japanese-offshore-wind-farm/> [accessed 6.02.22].
[76] Ikhennicheu M., Lynch M., Doole S., Borisade F., Matha D., Dominguez J.L., et al. D2.1 Review of the state of the art of mooring and anchoring designs, technical challenges and identification of relevant DLCs; 2020.
[77] Bhattacharya S, Amani S, Prabhakaran A, Mistry H, Lombardi D. Seismic design of offshore wind turbines. In: 17th World Conf. Earthq. Eng., Sendai, Japan: The 17th World Conference on Earthquake Engineering; 2021.
[78] Tajalli Bakhsh T, Monim M, Kent S, Lapierre T, Dahl J, Rowe J, et al. Potential earthquake, landslide, Tsunami and geo-hazards for the U.S. Offshore Pacific Wind Farms (19-P-202745); 2020.
[79] Ammon CJ, Velasco AA, Lay T, Wallace TC. Earthquake rupture and source time functions. Found. Mod. Glob. Seismol. Elsevier; 2021. p. 485−513. Available from: https://doi.org/10.1016/B978-0-12-815679-7.00026-4.
[80] Youngs RR, Arabasz WJ, Anderson RE, Ramelli AR, Ake JP, Slemmons DB, et al. A Methodology for probabilistic fault displacement hazard analysis (PFDHA). Earthq Spectra 2003;19:191−219. Available from: https://doi.org/10.1193/1.1542891.
[81] Petersen M, Wesnousky S. Fault slip rates and earthquake histories for active faults in southern California. Bull Seismol Soc Am 1994;84:1608−49.
[82] Wells D, Coppersmith K. New empirical relationships among magnitude, rupture length, rupture width, rupture area, and surface displacement. Bull Seismol Soc Am 1994;84:974−1002.
[83] Petersen MD, Dawson TE, Chen R, Cao T, Wills CJ, Schwartz DP, et al. Fault displacement hazard for strike-slip faults. Bull Seismol Soc Am 2011;101:805−25. Available from: https://doi.org/10.1785/0120100035.
[84] Bhattacharya S, Orense RP, Lombardi D. Seismic design of foundations. London: ICE Publishing; 2019. Available from: https://doi.org/10.1680/sdof.61668.
[85] Nikolaou S, Mylonakis G, Gazetas G, Tazoh T. Kinematic pile bending during earthquakes: analysis and field measurements. Géotechnique 2001;51:425−40. Available from: https://doi.org/10.1680/geot.2001.51.5.425.
[86] Tokimatsu K, Asaka Y. Effects of liquefaction-induced ground displacements on pile performance in the 1995 hyogoken-nambu earthquake. Soils Found 1998;38:163−77. Available from: https://doi.org/10.3208/sandf.38.special_163.
[87] KIS-ORCA. Maintenance/repair operations. Seafish 2019. <https://kis-orca.org/subsea-cables/maintenance-repair-operations/> [accessed 11.01.21].

Chapter 19

Some challenges and opportunities around lifetime performance and durability of wind turbines

V. Pakrashi[1], Kieran Ruane[2], Vesna Jaksic[2], Abdollah Malekjafarian[3], Michael O'Byrne[4], Franck Schoefs[5], Bidisha Ghosh[4], Luke J. Prendergast[6], Madjid Karimirad[7], Jimmy Murphy[8], Christopher Simon Wright[8,9], Deirdre O'Donnell[1], Gohar Shoukat[1], Ramon Varghese[1], Cian Desmond[9] and S. Bhattacharya[10]

[1]*Centre for Mechanics, Dynamical Systems and Risk Laboratory, School of Mechanical and Materials Engineering, University College Dublin, Dublin, Ireland,* [2]*Civil Structural and Environmental Engineering Department, Munster Technological University, Cork, Ireland,* [3]*School of Civil Engineering, University College Dublin, Dublin, Ireland,* [4]*School of Civil, Structural and Environmental Engineering, Trinity College Dublin, Dublin, Ireland,* [5]*Institut Universitaire Mer et Littoral, Nantes University, Nantes, France,* [6]*Department of Civil Engineering, Faculty of Engineering, University of Nottingham, Nottingham, United Kingdom,* [7]*School of Natural and Built Environment, Queen's University Belfast, Belfast, United Kingdom,* [8]*School of Civil Engineering, University College Cork, Cork, Ireland,* [9]*Gavin and Doherty Geosolutions Ltd., Dublin, Ireland,* [10]*Department of Civil Engineering, University of Surrey, Surrey, United Kingdom*

19.1 Introduction

While the design of turbine technology is rapidly developing and new materials continue to be developed, there are several sectors where information, knowledge, and insights remain lacking for this sector to make further progress, especially when lifetime performance aspects are considered. We often know how to make a certain structure or operation safe against known conditions, but lifetime needs require a deeper understanding of the challenges, both qualitatively and quantitatively. As a result, there are issues related to safety and operations that can be addressed to improve the competitiveness of this sector.

On the other hand, the availability and variety of technologies for monitoring, data communication, and analyses have increased sharply over time and several computational limitations do not exist. Availability of data is increased and so have the locations and frequency of them. However, the fundamental nature of the data, design of experiments, sensor placement strategies, and development of robust features of interest are often required to make sense of significant data. Choice of models, sensors, analysis, and interpretation along with possibilities of intercomparison, apportionment, and explanation of errors require more effort and consensus. An integrated approach utilizing a digital twin is required for improving and planning decisions from data but is not yet mature.

New materials, methods of analysis, availability of data, and communication protocols have thus opened new doors of opportunities. However, uncertainties or lack of information around lifetime needs and the interpretation of measured data and the lack of benchmarks around them continue to make the process challenging, which must be overcome and is being overcome often in an interdisciplinary environment. Relevant solutions around these topics will lead to better safety and savings in both operations and capital expenditures.

19.2 Fatigue, repowering, and repurposing

As new generations of wind turbines and new technologies make them bigger and more efficient, the question of fatigue, repowering, and repurposing of wind turbines is coming up as a core question in this sector. The turbines undergo site-specific lifetime impacts of stress on them and this influences their fatigue performance. At a foundation level, such performance is closely linked to the reuse of the site after the lifetime of a turbine or a farm, and inadequacy of foundations will require obtaining new sites, which poses a significant challenge to the owners. On the other hand, there is also a question of the future of a wind turbine after its useful service life is over. Rather than using it for landfills or recycling, there is a recent push toward repurposing it for different engineering sectors and giving it a second useful life with lower performance requirements.

Wind Energy Engineering. DOI: https://doi.org/10.1016/B978-0-323-99353-1.00032-3

19.2.1 Fatigue

Despite the first generation of offshore wind turbine monopiles (OWTMs) coming to the end of their lifespan, wind turbines remain an interdisciplinary and fast-changing sector with complex processes governing their structural risks over their lifetime. A core topic that requires further attention in this regard is fatigue [1]. Fatigue is instrumental in determining the remaining service life of OWTMs and guides their maintenance, monitoring, and site repowering feasibility. Fatigue models with probabilistic representations [2], damage/degradation models for OWTMs [3], geotechnical [4], and wind and wave models considering nonlinearity and stochasticity [5] exist independently—but a combined model is often absent or inadequate despite the need for their assimilation. Moreover, a real-time dependent fatigue reliability analysis is still at a basic stage of development [6]. Despite the opportunities of offshore wind becoming viable and sustainable as a clean energy source, there are critical challenges that must be overcome in this regard. Fixed-bottom monopiles still dominate this industry, despite advances in floating offshore wind, and will continue to influence offshore wind sector for the foreseeable future. De-carbonising the energy sector through offshore wind is thus fundamentally related to de-risking of these monopiles over their lifetime, minimizing their operational/capital expenditure and repowering sites after a typical design life (e.g., 20 years, but expected to increase over generations). These, in turn, are closely related to understanding fatigue at a site-specific level.

OWTMs are complex, dynamic structures with lifetime fatigue effects and their foundations often govern the lifetime safety levels and the feasibility of reuse or repowering of their sites. Estimating lifetime fatigue effects is challenging due to simultaneous presence of complex processes. These include random environmental excitation (e.g., wind, wave), system uncertainties (e.g., soil parameters), damage/degradation (e.g., corrosion, biofouling), environmental effects (e.g., temperature), and nonlinearities (e.g., blade-tower coupling; foundation scour). Design for longer-lasting turbines, service life extension of site repowering thus needs reliable lifetime estimates of fatigue by assimilating the abovementioned effects.

19.2.2 Repowering

Monopiles have been used extensively over the last two decades in offshore wind development as shown in Fig. 19.1. However, depth is not the only deciding factor, other factors like experience in designing, deploying, and maintaining certain technologies also come into play. Europe, for instance, has an extremely high percentage of monopile foundations (about 77%) than other types [7]. Acquired expertise through years of experience makes it a popular foundation type as well. Offshore wind turbines (OWTs) are usually designed to last between 20 and 25 years and once they reach their end of life, they are either dismantled or undergo end-of-life (EoL) extensions to ensure fitness for safe continued operation. This, however, would depend on economic and technical assessments carried out. There are three possibilities exist for site EoL decisions [8]:

- Partial repowering: Repair and/or replacement of turbine components (blades, nacelle, drive train, etc.)
- Full repowering: Replacing old turbines with new turbines.
- Decommissioning: Attempt to return the site to its former form as much as possible. It involves reversing the commissioning and installation

By 2030, approximately 3.5 GW of global offshore wind capacity will complete its 25-year life. In the early phase of offshore wind development, EoL decisions were chalked down as a long-term process and so the guidelines for them have not fully materialized. However, it is often felt that complete decommissioning is not economically the most feasible option to pursue as it can lead to negative cash flow on a site that would produce no further revenue. This is an issue that repowering can address, at least partially. Foundations have to remain intact with potential strengthening to cater for corrosion and scouring though and it is only the turbine that undergoes partial or full replacement. Here, an accurate assessment for the accumulated fatigue to the foundation has to be made.

19.2.3 Repurposing

Wind turbines are typically designed for 20−25 years of service life [9]. For example, Ireland issues a planning permission for 20 years [10]. In 2016, 12% of the installed wind turbine capacity in Europe was older than 15 years, while by 2020 this number increased to 28% [11]. Fig. 19.2 shows the number of onshore wind turbines reaching 20 years of operation from 2005−2035 in different countries in Europe [11]. A significant number of wind turbines will reach the end of their design life now and this number will only increase in future. To deal with this contemporary and upcoming

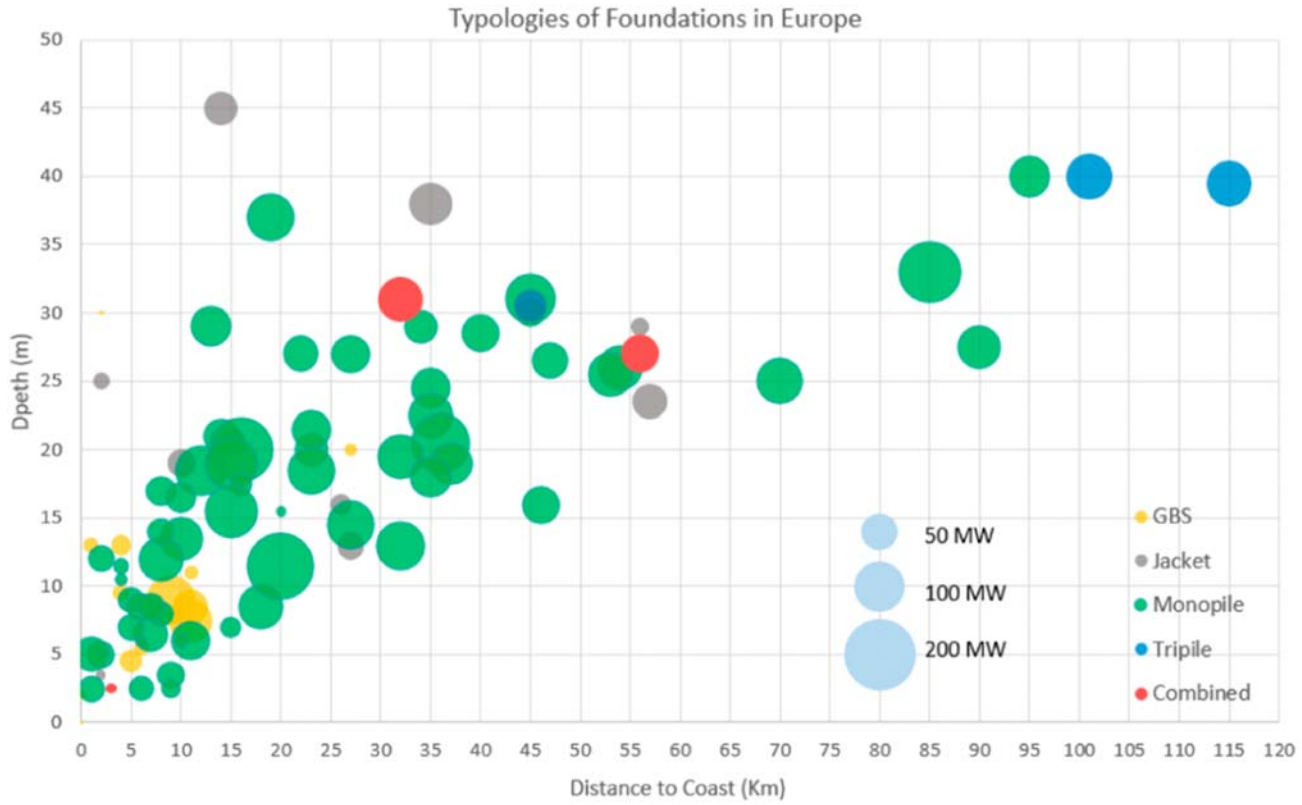

FIGURE 19.1 Typical foundations in Europe and their distribution in terms of distance to coast versus depth. *From Sánchez S, et al., Foundations in offshore wind farms: Evolution, characteristics and range of use. Analysis of main dimensional parameters in monopile foundations. J Mar Sci Eng 2019;7(12):441.*

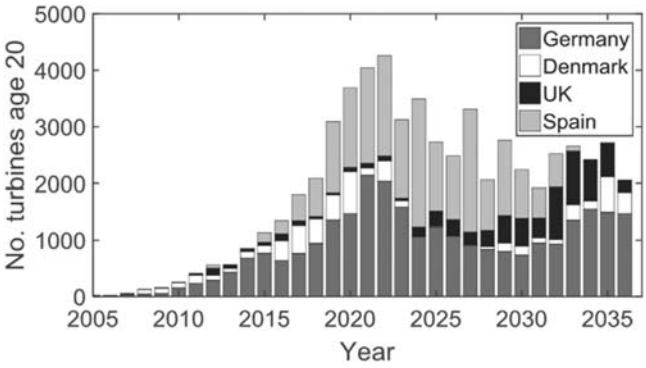

FIGURE 19.2 Wind turbines reaching the end of service life by year [2].

challenge, the wind industry requires to look into lifetime extension of the turbines and decisions on them after decommissioning while keeping technical, economic, legal, and social parameters of these aging assets in mind [11]. A number of recent projects globally have been addressing these challenges. They include SusWIND project on recyclable composites [12], Re-Wind Network on EoL alternatives [13], FiberEUse on composite recycling and reuse [14], EA Wind Task 45 [15], and ZEBRA Project on fully recyclable wind turbine blades [16].

Wind turbine rotor diameter has kept increasing in size over the last three decades, with typical diameters currently reaching 145 m [17]. On the other hand, it is estimated that 80%−85% of the wind turbine structure is made from metals, which can be recycled (e.g., steel tower, nacelle made of steel, aluminum, copper, etc.). However, the blades are made of fiber reinforced polymers, which is a recycling challenge [18] and solutions are rare and yet to be implemented on a large scale [17].

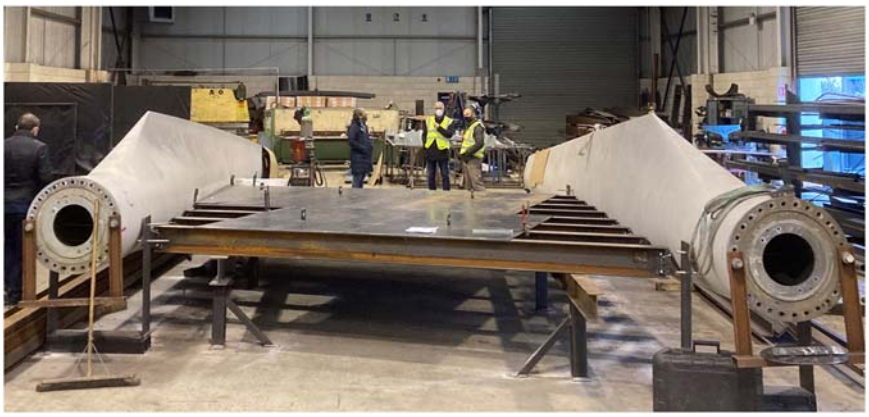

FIGURE 19.3 Connection test on wind turbine blades in Munster Technological University Ireland (Heavy Structure Lab).

Glass fiber reinforced polymer is currently the main material of choice for wind turbine blades, and the majority of the decommissioned blades in next 20 years will fall under this category [19]. A typical wind turbine blade is composed of around 60% reinforced, mainly glass, fibers, 23% of mainly thermosetting resins and adhesives, 9% of core materials (e.g., balsa wood, thermoplastic polymer-based foams, etc.), and the remaining 8% is metals, including steel and copper [20]. Some of the challenges preventing the implementation of sustainable recycling solutions include the technical difficulty of recycling glass fiber reinforced thermoset composite, the low cost of landfill, and precise assessment of waste volume [21]. Fig. 19.3 shows a recent experiment on an integrated approach for repurposing wind turbine blades, where the waste management options for composite blade materials in relation to their position on the waste hierarchy are discussed [22,23]. Reuse and repurposing are often more favorable options than recycling, recovery, and disposal. The reuse of the blade is possible if its condition allows refurbishment to serve again in a second-hand wind market while establishing its performance.

There are two main issues in relation to reuse: (1) blade design is specific to the turbine size and environmental conditions and it can be re-employed only in similar conditions, and (2) structural capacity of the refurbished blade must satisfy standards at its new deployment [10]. Repurposing is understood as the reuse of the entire blade or parts of the wind turbine blade in new structural or semistructural applications. A number of constructions have been made around the world with decommissioned turbine blades [24]. However, this solution is yet to be implemented on an industrial scale, capable of treating a large volume of blades and significant work is required to achieve this.

19.3 Scour aspects

Another important challenge around the lifetime performance of wind turbines, especially offshore, is that of scour. Scour is soil removal by currents/waves from around OWTs which reduces foundation strength, stiffness and capacity, ultimately reducing their lifespan. Scour is thus a key hazard and must be understood, estimated, monitored, controlled, and repaired if possible. Better understanding and management of scour will reduce risk, facilitate service life extension, repowering decisions, and lower lifetime O&M costs, making power more competitive. As an asset in harsh or changing environment, with uncertain operating conditions (e.g., wind speed/energy requirements) OWTs inevitably have an unpredictable design life and understanding scour to bring in more predictability to this sector, which is rapidly developing.

Vestas announced the launch of the V236−15MW wind turbine, overtaking GE's 14 MW Halide-X to become the world's largest wind turbine. This offshore scaleup continues and structures are being pushed to their performance limits over their lifetime. Increased and more stable energy production and better capacity factor come at the price of more onerous structural demands. This race continues as China's MingYang Smart Energy announced the MySE16.0−242 16 MW turbine (242 m tall) in August 2021. The rapid and interdisciplinary upscaling presents a range of complex scientific/technical challenges to overcome and understanding, designing, monitoring, and managing OWTs for scour will be a key aspect for resilient and longer service life. Unresolved scour issues will lead to failure or early shutdown of wind farms which are expensive, risky and lowers the credibility of this technology. Consider the relatively recent lawsuit for Robin Rigg farm, where the cost of remedial work around scour issues was £23 million, resulting in it being the largest case of its kind. This, if left unsolved, lack of knowledge around scour risks can lead to expensive and dangerous decisions. Fig. 19.4 presents examples of scour impacts for OW farms in the UK and Ireland, including Robin Rigg.

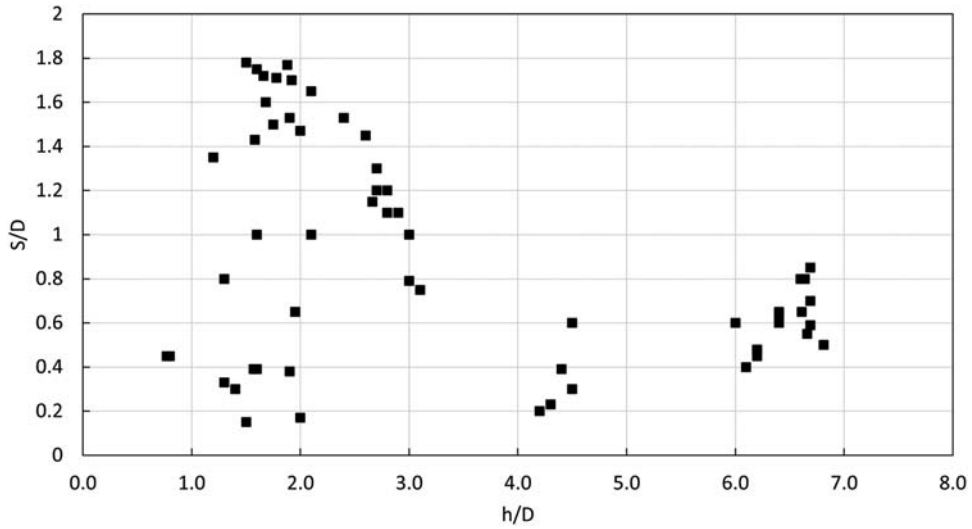

FIGURE 19.4 Nondimensional foundation scour depth (S) for OWTs in without scour protection (*D*, monopile diameter; *h*, water depth to mean sea level) [25]. *Carroll B, et al. A further review of sediment monitoring data. Cowrie ScourSed-09, Southampton, UK, 2010. p. 106.*

Following the award of seabed rights from The Crown Estate, the recent Moray West OW farm development considered scour protection extensively. Scientifically, there needs more work on understanding the complex interaction between nonlinearities (e.g., geometric: tower slenderness; material: soil models/use of composites; boundary: soil-structure interaction) and stochasticity (wind, wave), compounded with phenomena of interest at different timescales (e.g., damage/degradation, biofouling, rehabilitation/repair). This becomes further complicated by poor understanding of environmental uncertainties, evolving design constraints, and a lack of suitable analysis tools. Technological readiness levels (TRLs) of OWTs, including contemporary scour protection (e.g., armor, rip-rap) are often based on ocean wave basin tests and cannot consider all issues around structural, fluid and geotechnical scaling, and the interactions between them.

Scaled geotechnical testing in soil-structure interaction for OWT foundations, for example, suffers from issues related to particle size to diameter ratios, variations in elemental scaling laws (fluid, soil, structure), data reproducibility, and mapping from scaled to full-scale behavior. These problems must be integrated through multiscale modeling. However, it is not trivial and has not yet been comprehensively carried out.

19.4 Degradation aspects

Degradation aspects influence the turbines in many ways, including the timescale over which they happen. There seems to be a range of areas over which more information and benchmarking are required. The sources are diverse and the life challenges are only being understood now in a multidisciplinary environment, a trend that is expected to continue in the future as well.

Leading edge erosion [26] and its protection forms one of the important aspects which are being investigated globally. One such example is the current International Energy Agency Wind TCP Task 46, where climatic conditions, operations of wind turbines with erosion, laboratory testing for erosion, and related mechanics and materials properties have been identified as important. Protection technologies for blades can lead to lifetime extension.

A less investigated but well-observed damage is from lightning strikes [27]. Contemporary investigations are looking into protection systems for strikes, along with the consequence of lightning strike in a damage sense. This type of investigation includes their models, testing, examples, and case studies [28,29]. While an evidence base in this sector is evolving, there needs to be a further investigation around this topic.

Another important impact, which was less investigated before but has come up now as an important topic is that of biofouling and marine growth [30]. These growths increase the stresses on a structure, along with the cycles of stresses, thereby having a potential impact on fatigue, but also link itself to other types of degradation processes like scour and worsening them. The growth can also impact corrosion aspects but overall, there are significant challenges around their inspection, classification, and impact of them in terms of structural analysis and consequence on lifetime performance [31,32]. With more flexible structures being developed in this sector, the importance of biofouling and marine growth will continue to grow, as will the need to engage closely with biologists and ecologists.

Degradation aspects impact modern materials as well, increasing uncertainties around their performance. Composite materials have been considered to be useful and important for the evolution of OWT sector [33]. However, the durability aspects continue to hinder its progress, despite significant advancements in strength and analysis aspects. In particular, durability in the presence of seawater [34] and pressure continues to be a major problem in predicting structural and material performance [35]. Degradation levels and rates over time are thus often unknown, uncertain, or not replicable. This uncertainty is also observed in terms of thermal changes and exposure to other chemicals or conditions over its lifetime. Under such circumstances, the reliability of use of composites for lifetime performance demands gets lowered and unless there is more certainty around failure modes, fatigue, and degradation aspects over time, confidence around extensive use in several areas will remain limited. Overall laboratory testing or controlled testing of several such influential factors can be improved and new benchmarks will improve our understanding of lifetime performance of these turbines and make it more predictable.

19.5 Monitoring aspects

Laboratory testing is common for wind turbine components, especially blades. Froude scaled tests are often carried out in wave basins and they provide critical information for transitioning over TRLs, despite their limitations in terms of not being able to scale everything. For such tests, and even for deployed wind turbines, sensing can play a key role and is becoming increasingly popular. The recent VDI 4551 on structure monitoring and assessment of wind turbines and offshore stations document is a particular example of where this idea has been transitioning to practice guidelines. Fig. 19.5 shows small-scale testing of the wind turbine blade for dynamic loading in a laboratory and in a multisensor environment [36,37], which can inform the behavior of composites that dominate the manufacturing of wind turbine blades but where further information is required [33].

Recently, extensive research is being carried out for full-scale and in-operation turbines. Additionally, there is more work around the topic of damage and decommissioning coming up as well. With time, it is expected that the structural data and supervisory control and data acquisition systems will start interacting more and provide improved information.

FIGURE 19.5 Wind turbine blade exposed to dynamic loading testing [36].

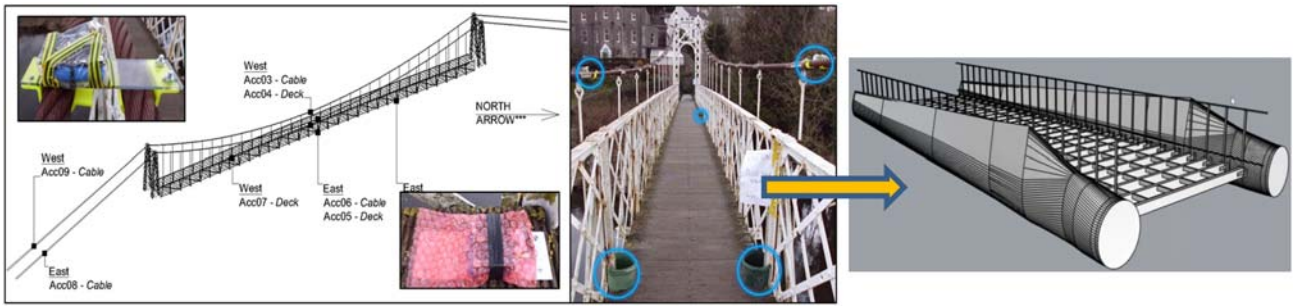

FIGURE 19.6 The role of monitoring in the repurposing of wind turbine blades.

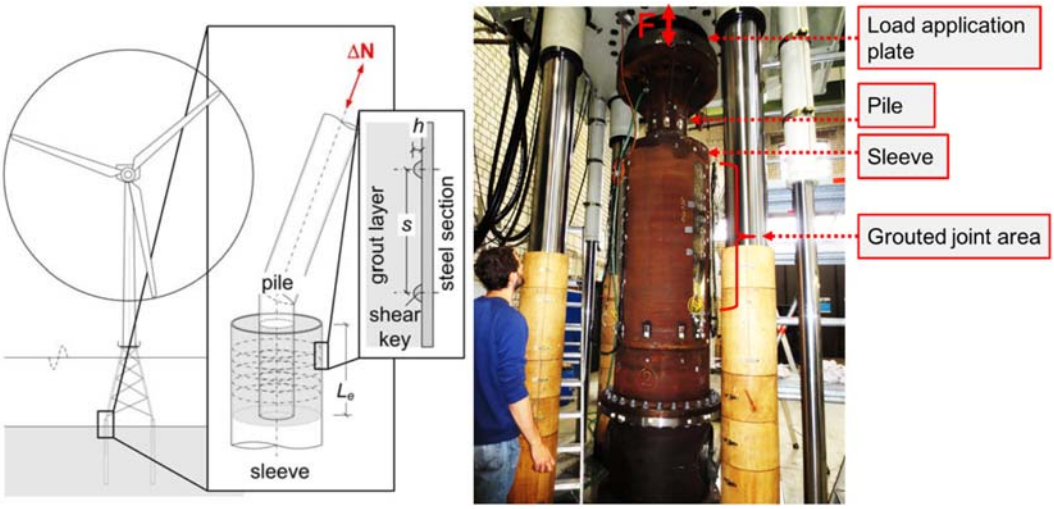

FIGURE 19.7 The details of an atypical grouted joint between a jacket substructure and a monopole and a laboratory scale instrument specimen in a servo-hydraulic testing machine. *Reused with Permissions from the copyright holder, International Society of Offshore and Polar Engineers and the authors, Müller N, et al., FBG sensors and signal-based detection method for failure detection of an offshore wind turbine grouted connection. Int J Offshore Polar Eng, 2019;29(01):1–7.*

Monitoring can also be relevant for repurposing of wind turbine components. Fig. 19.6 shows an example of a monitoring carried on Daly's Bridge, Cork [38], and how such monitoring can be adapted to repurposed blades as pedestrian bridges. Model updating, in a Bayesian sense [39], will ensure that the remaining capacity or service life of such bridges can be estimated through monitoring (including rapid, noncontact options) [40].

Monitoring in scaled tests not only allows for a better understanding of responses but can also lead to further investigations into how they are estimated and how scaling should be interpreted. This is a key issue because the increase in the power of the wind turbines and the size of each component generate new mechanisms: that was the case for the understanding of degradation mechanism of grouted connections of monopiles [41,42]. The grouted connection between the sleeve and the monopile of an OWT is a critical structural part that is subjected to axial forces. Fig. 19.7 presents the details of the grouted joint and a photograph of the laboratory testing of a scaled model with a fiber optic sensor-type structural health monitoring system, carried out at the Leibniz University of Hannover. In many ways, scaling remains one of the most challenging problems in this sector, despite extensive work that has been carried out. Fig. 19.8 presents one such example where scaled testing has resulted in a better understanding of response amplitude operators of floating platforms for offshore renewable energy systems.

19.6 Understanding uncertainties

There remains a wide variability in the choice and use of technology to harness natural resources like wind and wave. To make such choices viable and competitive, significant work is needed to de-risk the technologies against challenges over their lifetime for different stages of technological readiness, design, and performance after being installed. To this

effect, there is a need to better understand uncertainties and risks in relation to the environment and these offshore renewable energy systems are exposed to:

- the structural system itself
- its mechanical interaction with the environment
- the operational processes, and
- energy production aspects.

Through this approach, it is possible to address the input, the system, and the output of these technologies. The uncertainties can come from modeling, scaling, experimentation, inspection, data analysis, interpretation, and the impacts they have. These uncertainties also have an impact on social aspects. A better understanding of uncertainties and hazards will not only quantify but also the quality and identify these aspects and their interrelationships are improved. Successfully understanding and addressing uncertainties can facilitate early and robust decisions on interventions, repairs, or even "do-nothing" options. On the other hand, efficient quantification of performance assessment, hazard, and repowering possibilities of a site at the end of turbine service life can significantly improve competitiveness through a lower levelised cost of energy. A better framework to advise on OWT life extension using structural performance information would be very helpful in this regard. Fig. 19.9 demonstrates how the safety of a structure degrades

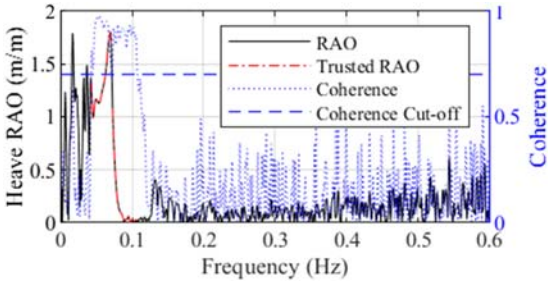

FIGURE 19.8 Comparison of response amplitude operators through scaled testing [43]. *From O'Donnell D, Murphy J, Pakrashi V, Comparison of response amplitude operator curve generation methods for scaled floating renewable energy platforms in ocean wave basin. ASME Lett Dyn Syst Control 2021;1(2).*

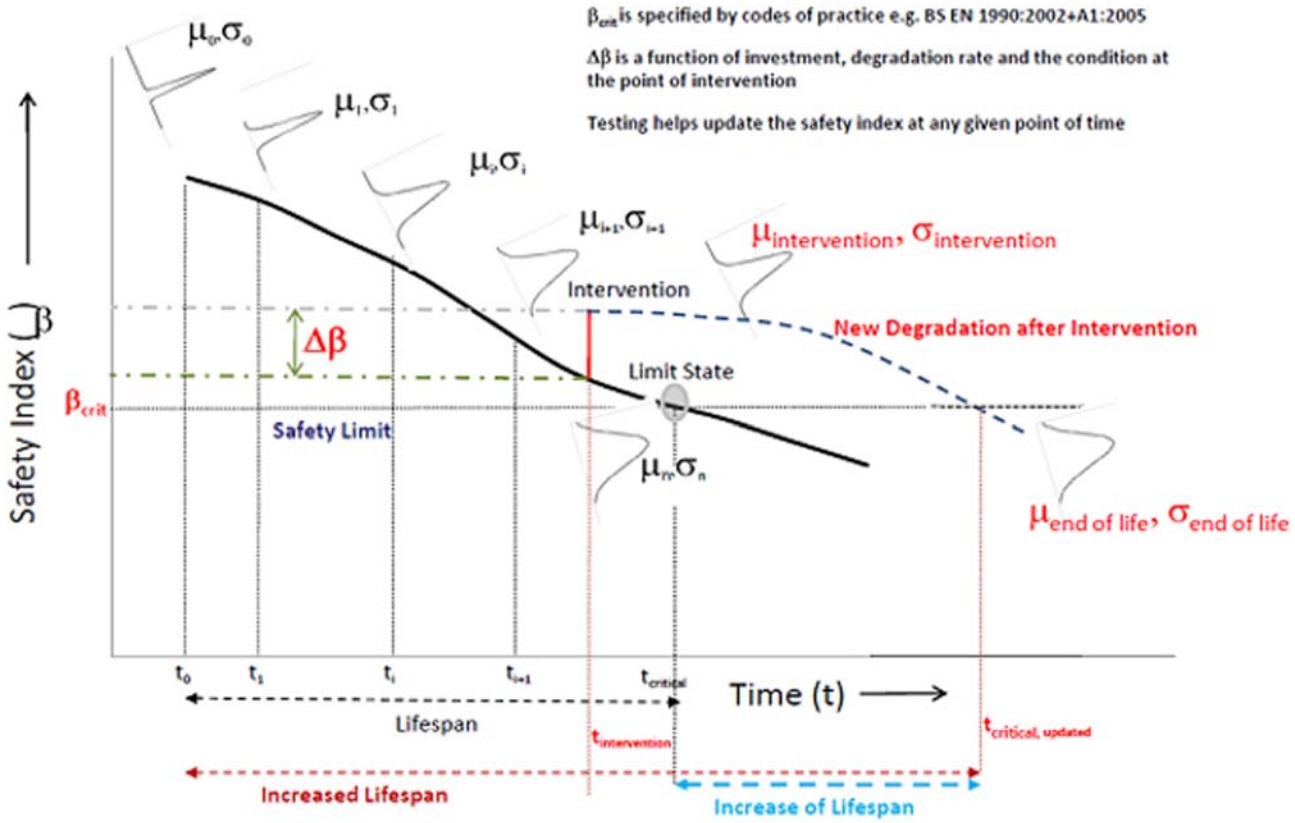

FIGURE 19.9 A risk-based approach for infrastructure asset management.

over time, while uncertainties about them also increase. Appropriate decisions on rehabilitation can provide important lifetime extensions for these assets, as well as ensure that unnecessary and expensive interventions are not carried out, where it is better to install a new one. A deep understanding of the type and extent of uncertainties in the system is fundamental to taking such decisions.

19.7 Conclusions

The needs and challenges of wind turbines, especially for the offshore wind sector are diverse and often novel. Consequently, technological advancement and fundamental insights are particularly important for their evolution. In this regard, there is a need to identify, understand, and address such challenges over their lifetime performance requirements. Here, there is a need to better deal with the exposure conditions, the various designs and solutions in the technology of the turbine, and additionally the degradation aspects. Repowering, repurposing, and performance criteria of this sector will continue to be important, as the technology matures and diversifies. This area can be better understood with the support of monitoring technology and related data analytics, with a clear idea about the possible physical processes and physics behind them. This combination of understanding of fundamental processes, monitoring, analysis, and related identification and quantification of uncertainties in the sector will de-risk it and make it more competitive, while making it safer over a lifetime.

References

[1] Luna J, et al. Wind turbine fatigue reduction based on economic-tracking NMPC with direct ANN fatigue estimation. Renew Energy 2020;147:1632–41.
[2] Righiniotis T, Chryssanthopoulos M. Probabilistic fatigue analysis under constant amplitude loading. J Constr Steel Res 2003;59(7):867–86.
[3] Ciang CC, Lee J-R, Bang H-J. Structural health monitoring for a wind turbine system: a review of damage detection methods. Meas Sci Technol 2008;19(12).
[4] Lombardi D, Bhattacharya S, Wood DM. Dynamic soil–structure interaction of monopile supported wind turbines in cohesive soil. Soil Dyn Earthq Eng 2013;49:165–80.
[5] Larsen JW, Iwankiewicz R, Nielsen SRK. Nonlinear stochastic stability analysis of wind turbine wings by Monte Carlo simulations. Probabilistic Eng Mech 2007;22(2):181–93.
[6] Rocher B, et al. Bayesian updating of probabilistic time-dependent fatigue model: application to jacket foundations of wind turbines. EWSHM-7th Eur Workshop Struct Health Monit 2014;.
[7] Sánchez S, et al. Foundations in offshore wind farms: evolution, characteristics and range of use. Analysis of main dimensional parameters in monopile foundations. J Mar Sci Eng 2019;7(12):441.
[8] Topham E, McMillan D. Sustainable decommissioning of an offshore wind farm. Renew Energy 2017;102:470–80.
[9] Sandström M, Haraldsdóttir H. Lifetime analysis of a wind turbine component. Gothenburg, Sweden: Breeze; 2020. p. 31.
[10] Sakellariou N. Current and potential decommissioning scenarios for end-of-life composite wind blades. Energy Syst 2018;9(4):981–1023.
[11] Ziegler L, et al. Lifetime extension of onshore wind turbines: A review covering Germany, Spain, Denmark, and the UK. Renew Sustain Energy Rev 2018;82:1261–71.
[12] SusWIND. <https://www.nccuk.com/sustainable-composites/activities/suswind/?acceptcookies = true>; 2021.
[13] RE-WIND Network. <https://www.re-wind.info/>; 2020.
[14] FiberEUse. <http://fibereuse.eu/>; 2017.
[15] IEA. EA Wind Task 45: Recycling Wind Turbine BladesAvailable from: EA Wind Task 45: Recycling Wind Turbine Blades; 2019.
[16] Durakovic A. Recyclable wind turbine blade. OffshoreWIND.biz. 2020;.
[17] Larsen K. Recycling wind turbine blades. Renew Energy Focus 2009;9(7):70–3.
[18] Psomopoulos CS, et al. A review of the potential for the recovery of wind turbine blade waste materials. Recycling 2019;4(1):7.
[19] Gurit, Gurit materials for wind turbine blades. In: Wind energy composite materials handbook. Gurit; 2014.
[20] Fingersh L, et al., Wind turbine design cost and scaling model. Golden, CO; 2006.
[21] Yazdanbakhsh A, Bank LC. A critical review of research on reuse of mechanically recycled FRP production and end-of-life waste for construction. Polymers 2014;6(6):1810–26.
[22] Delaney EL, et al. An integrated geospatial approach for repurposing wind turbine blades. Resour, Conserv Recycl 2021;170:105601.
[23] Ierides M, et al. Polymer composites circularity, vol. 2018. SusChem Mater Working Group 2018;.
[24] Alshannaq AA, et al. Structural analysis of a wind turbine blade repurposed as an electrical transmission pole. J Compos Constr 2021;25(4):04021023.
[25] Carroll, B, et al., A further review of sediment monitoring data. Cowrie ScourSed-09, Southampton, UK, 2010. 106.
[26] Mishnaevsky Jr L, et al. Leading edge erosion of wind turbine blades: Understanding, prevention and protection. Renew Energy 2021;169:953–69.

[27] Rachidi F, et al. A review of current issues in lightning protection of new-generation wind-turbine blades. IEEE Trans Ind Electron 2008;55 (6):2489–96.
[28] Wang Y, Zhupanska O. Lightning strike thermal damage model for glass fiber reinforced polymer matrix composites and its application to wind turbine blades. Compos. Struct 2015;132:1182–91.
[29] Radičević BM, et al. Impact of wind turbine blade rotation on the lightning strike incidence–a theoretical and experimental study using a reduced-size model. Energy 2012;45(1):644–54.
[30] Vinagre PA, et al. Marine biofouling: a European database for the marine renewable energy sector. J Mar Sci Eng 2020;8(7).
[31] Qiu W, Pakrashi V, Ghosh B. Fishing net health state estimation using underwater imaging. J Mar Sci Eng 2020;8(9).
[32] Schoefs F, et al. Fractal dimension as an effective feature for characterizing hard marine growth roughness from underwater image processing in controlled and uncontrolled image environments. J Mar Sci Eng 2021;9(12):1344.
[33] O'Leary K, Pakrashi V, Kelliher D. Optimization of composite material tower for offshore wind turbine structures. Renew Energy 2019;140:928–42.
[34] Jaksic V, et al. Influence of composite fatigue properties on marine tidal turbine blade design. Durability of composites in a marine environment, 2. Springer; 2018. p. 195–223.
[35] Davies P, Rajapakse YD. Durability of composites in a marine environment, Vol. 10. Springer; 2014.
[36] Jaksic V, et al. A comprehensive study of the delay vector variance method for quantification of nonlinearity in dynamical systems. R Soc Open Sci 2016;3(1).
[37] Buckley T, et al. Mitigating the structural vibrations of wind turbines using tuned liquid column damper considering soil-structure interaction. Renew Energy 2018;120:322–41.
[38] O'Donnell D, et al. Modelling and testing of a historic steel suspension footbridge in Ireland. Proc Inst Civ Eng—Bridge Eng 2017;170 (2):116–32.
[39] Argyris C, et al. Bayesian model-updating using features of modal data: application to the metsovo bridge. J Sens Actuator Netw 2020;9(2):27.
[40] Pakrashi V, Basu B, RyanKey K. Rapid assessment of natural periods of large short-period civil engineering structures. Eng Mater 2013;569–70.
[41] Müller N, et al. FBG sensors and signal-based detection method for failure detection of an offshore wind turbine grouted connection. Int J Offshore Polar Eng 2019;29(01):1–7.
[42] Schaumann P, Lochte-Holtgreven S, Bechtel A. Fatigue design for axially loaded grouted connections of offshore wind turbine support structures in deeper waters. Earth and Space 2010: Engineering, Science, Construction, and Operations in Challenging Environments 2010;2047–54.
[43] O'Donnell D, Murphy J, Pakrashi V. Comparison of response amplitude operator curve generation methods for scaled floating renewable energy platforms in ocean wave basin. ASME Lett Dyn Syst Control 2021;1(2).

Chapter 20

A review of wind power in grid codes: current state and future challenges

Antonio Alonso-Cepeda[1], Wes Baker[2], Raquel Villena-Ruiz[1], Eduard Muljadi[3], Andrés Honrubia-Escribano[1] and Emilio Gómez-Lázaro[1]

[1]Renewable Energy Research Institute and DIEEAC-ETSII-AB, Universidad de Castilla-La Mancha, Albacete, Castilla-La Mancha, Spain, [2]Electric Power Research Institute (EPRI), Palo Alto, CA, United States, [3]Department of Electrical and Computer Engineering, Samuel Ginn College of Engineering, Auburn University, Auburn, AL, United States

20.1 Introduction

In the early development of power systems, electricity was generated and consumed within a low voltage distribution network in the same small town. As the alternating current generation gained popularity, the size of the power generation increased, the power was generated in three-phase, and the transmission voltage was increased to reduce losses as the transmission network expanded to neighboring towns. The early utility companies discovered that paralleling multiple loads and generation is possible as a synchronized network. For example, the first hydroelectric power plant in the US (1889), the Willamette Falls station, transmits single-phase power 13 miles away from Oregon City, Oregon, to Portland at 4000 volts and steps the voltage down to 50 volts for distribution. In the case of Europe, the Rheinfelden (Germany) power plant was the first to use a three-phase alternative current at 50 Hz in 1898.

The power system as we know it today consists of three major components: generation, transmission, and distribution. For a long time, the three components belonged to the same utility. Utilities are often considered monopolies in regulated areas; they control the entire energy process from generation to customer support and service. Today, many customers across the globe do not have a choice over their utility. Only one to two utilities provide service to a particular area for most consumers.

As the same company owns a fully integrated system (generation, transmission, and distribution), the power system operation can maintain a safe, secure, reliable, and efficient electric power system. The overall revenues of the utility company collected from the consumers do not affect the operation of individual generation, transmission, and distribution.

When a market transforms into a deregulated one, it breaks up a utility's monopoly over all elements of the energy process. This change benefits customers because it allows organizations called retail electric providers to form and sell energy. With multiple organizations competing for the same business, customers have different options to choose from. And with competition, utilities have the incentives to keep rates low, and provide the best customer service. Because of deregulation, separate unique providers may compete to provide the best prices for generation, transmission, and distribution.

In the late eighties, the wind power technology was mature enough enabling practical deployment into the power grid. When the contribution of wind power to the grid was negligible during the disturbance, the reliability of the power system was not affected when the wind plant is disconnected from the grid. However, as the level of wind penetration into the grid reaches higher levels, we can no longer ignore the contribution of wind power generation as the primary power source of energy to the power grid. Thus, during the disturbance, the wind power plant must stay connected to the grid to keep the supply-demand balance. The grid code governs the conditions when the wind plant must stay connected to the grid.

20.1.1 Near horizon overview of power systems

In the past decade, the level of rotating inertia within power systems has continued to decrease due to the retirement of fossil fuel power plants. This trend of reducing inertia is magnified as the Levelized Cost of Energy (LCOE) of

Wind Energy Engineering. DOI: https://doi.org/10.1016/B978-0-323-99353-1.00035-9

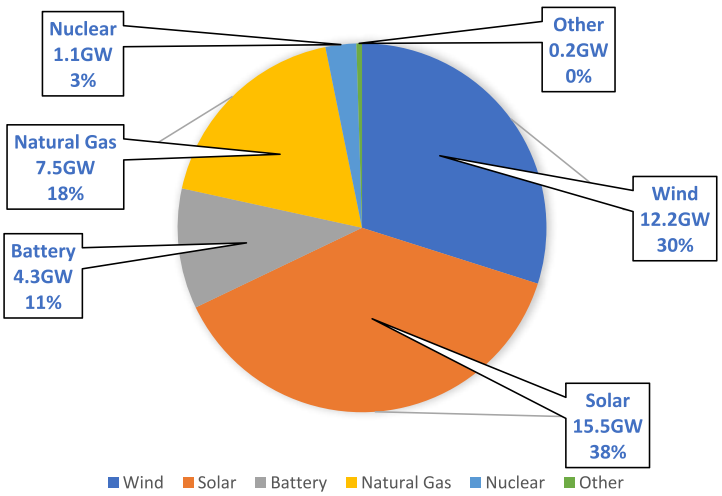

FIGURE 20.1 Planned generation capacity additions by resource type in the US for 2021. *Developed from data in Renewables account for most new U.S. electricity generating capacity in 2021, U.S. Energy Information Administration; 2021. https://www.eia.gov/todayinenergy/detail.php?id = 46416.*

renewable energy, for example, wind and solar, has decreased significantly. The reduced LCOE of renewable energy plants and other factors such as climate change results in the increased proposed connections and penetration level of renewable energy. These resources are typically connected to the grid via a power converter at the grid interface without inertial response capability like the synchronous generator. The dynamics of the renewable energy generators coupled to the grid via power electronic converters are largely dictated by the grid side inverter. Therefore, they have been commonly referred to as Inverter-Based Resources (IBR), Inverter-Based Generators (IBG), or Converter-Based Generators. Due to the converter interface with the grid, the IBR has significant advantages in flexibility and response time, allowing them to be controlled to provide a range of responses to support grid stability.

Recent reports summarizing the connection of new resources to the grid in the United States (US) show that recent and future resources are primarily IBR. For example, from 2015 to 2019, 59% of all new generation capacity added in the US was either wind or solar [1]. In Fig. 20.1, we see approximately 79% of the planned generation capacity additions in the US in 2021 are IBR [2]. Further, a snapshot of all the generation interconnection queues in the US at the end of 2020 shows 755 GW of proposed generation additions, of which 90% is IBR [3]. Historically, less than 25% of proposed plants in the generation queue are built. However, for perspective, the total generation capacity in the US is approximately 1200 GW [4].

20.1.2 Grid code

Network Codes (NC) or Grid Codes (GC) are the national normative documents that regulate the operation of the electrical systems of a region or a country. A GC defines technical characteristics that these systems must comply with in their connection and operation to the public grid to guarantee a correct and safe operation. There are notable differences between NCs of the European countries until the second decade of the 2000s. Thus, it is impossible to form a single and standardized European electricity system that would favor the optimized and flexible management of energy flows necessary to increase the penetration of renewable energy.

Contents of a GC vary depending on the transmission company's requirements. Typically, a GC specifies the required behavior of a connected generator during system disturbances. These include voltage regulation, power factor limits and reactive power supply, response to a system fault (e.g., short-circuit), response to frequency changes on the grid, and requirement to "ride through" short interruptions of the connection. There is no standard GC in all countries, and each electric grid has its GC. Even in North America, no GC applies to all territories.

Why do we need a GC? Significant changes have been occurring in the power system network and operation in the past decades. The deregulation of the power system in many different parts of the world has initiated and continues to affect the restructuring of power system management. Among the many others, the following factors are the key drivers or agents of change:

- The transition from Bulk Power Systems (BPS), that is, transmission, to Distributed Energy Resource systems, that is, distribution systems.
- Synchronous generator to IBR.

- Analog to digital system protection.
- Introduction of adaptive control and system protection.
- Faster communication and computation technologies.
- Introduction of machine learning Artificial Intelligence (AI) to power system.

20.1.3 Challenges in modern power systems

Power system dynamics. Reduction of kinetic energy in the power system due to the retirement of coal power plants and other rotating synchronous generators from the grid. This reduction of kinetic energy has an impact on power system dynamics. The net load determines the level of synchronous generation connected to the grid. The nature of generating fleets connected to the grid and the level of kinetic energy in the power system varies time-of-day, daily, day-of-the-week, and seasonally. As the number, location, and size of the synchronous generators and the renewable power plant connected to the grid vary with time, each bus's Thevenin or short circuit impedance varies throughout the day. Similarly, the rotating inertia available on the grid varies with time. These changes affect the voltage and frequency regulations and the dynamic behavior during normal or disturbance. The inertial response, the ramping rates, and the system damping differ from night and daytime and from winter to summer. In summary, the reduction of kinetic energy makes the power system become more dynamic. In low rotating inertia conditions, minor disturbances may excite power system oscillations and instabilities. Further, the range of bandwidths of the different controllers of IBR may result in dynamics that span a wide frequency range.

Power electronics. Power electronics switches have limited voltage and current ratings. Unlike electric machines, the p-n junction of the power electronics has a limited thermal capacity, thus preventing them from operating in overload conditions. Recent development in wide-band-gap devices promises significant improvements in the technical performance of power electronic switches; perhaps, short-term overloads may enhance the device's capability [5].

Unique characteristics of resource. Each renewable energy source has its unique characteristics. For example, wind generation tends to be high during the winter season, and wind power plant tends to generate during the nights. Solar power has the opposite characteristic; it has maximum generation during summer and the daytime. The daily and seasonal changes of the resources affect the net-load behavior of the power systems (i.e., the duck-curve first recognized in California ISO).

Impacts on the system protection. Traditional protection philosophies rely on the fault current contributions inherent to synchronous generators. The fault current contribution depends on the collective behavior of generators connected to the grid for a given fault location. As the size, location, , and proportion of the generating fleets (IBRs and synchronous generators) operating on the grid changes with time, the fault current may chnage significantly. For areas with high penetration levels of IBR, the fault current will be highly dependent on how the IBR is controlled and limited.

Ancillary services. Ancillary services aid the reliable transfer of power from generation resources to loads. Ancillary services function as reliability insurance to cover unexpected and unpredictable events on the grid. These services can be broadly categorized into frequency support and voltage support. The level of headroom of individual generators and energy storage on the grid available to provide spinning reserves, nonspinning reserves, the ramping capabilities, and kinetic energy in the power system depend on the type and size of the renewables. Renewable generators are typically operated to extract the maximum power from the resource (e.g., wind) at any given time resulting in zero headroom. Fortunately, the computing power, communication, and forecasting technologies for renewable sources and loads has progressed. Generation resources also contribute to the regulation of the system voltage through ancillary services.

20.1.4 Promising technologies for modern power systems

As modern technologies progress in many different sectors, the available modern and intelligent sensors, measurements, monitoring hardware/software must also be considered when developing future GCs. Utilities and system operators have adopted new technologies in their service territory. Advanced Metering Infrastructure, synchrophasors, situational awareness, substation automation, fault location identification and Restoration of Services, and digital system protection are well known and widely accepted within the power system communities. Similarly, the application of machine learning and AI in resource and load forecasts is gaining trust among power system engineers and planners.

Forecasting. The forecast of the level of inertia, short circuit current contribution, Thevenin impedance, the available headroom from the operating generators, and the ramp rates representations of the generating fleets should be developed and implemented to make it possible to adapt the system protections (adaptive system protection) and to empower the smaller utilities to compromise the system reliability within their footprints.

Flexible Consumer Rates. Adjustable rates should be made available to allow the consumers to sign a contract with the load aggregators and provide load services as part of the ancillary services provided to the grid. By providing incentives to the consumers to participate in ancillary services, the reliability of the power system can be warranted.

Aggregated Energy Storage. Aggregated energy storage can grow significantly with the wide adoption of electric vehicles. Home storage power banks are commercially available and can also be aggregated by storage aggregators to participate in the ancillary services.

20.2 Wind power in European grid codes

The electric network in Europe consists of five wide area interconnected and synchronous grids (Continental, United Kingdom, Ireland, Baltic, and Nordic) and two isolated ones (Iceland and Cyprus). These areas can be observed in Fig. 20.2. Frequency for all these grids is set to 50 Hz.

Those grids covering more than a country, allow facing punctual electricity demands that a member may need, providing a seamless power flux interconnection among countries. Each synchronous grid maintains a precise frequency control and, small perturbations of this variable in a point, could affect other locations belonging to the same grid [6].

New energy transition plans, drawn up by the European Union (EU), plan to implement a high penetration of wind and solar photovoltaic renewable energies in the electricity grid. Based on its estimations, renewable energy resources will cover up to 50% of electricity demand by 2030. Thus, the progress is continued as effective decarbonization of electricity production, implementing an increasingly ecological and renewable model and less dependent on primary energy sources related to the combustion of hydrocarbons.

The common characteristic of all renewable energies is their variability in power generation. As an opportunistic generator, the output power is not controlled, and often difficult to predict when the energy resource is available (when the wind will blow and under what conditions or direct solar radiation will be available). While it is necessary to reach the EU's energy transition objectives to avoid global warming of the planet, incorporating a more significant proportion of renewable energies into the electricity system has begun to generate a series of stability problems in national electricity systems. Different regulations and standards throughout the EU can solve the adverse impacts of the output variability of renewables.

This greater incorporation of renewable energies into the electricity mix is also known as the penetration level of renewable energies. High penetration of renewables causes different challenges that must be faced in a coordinated and

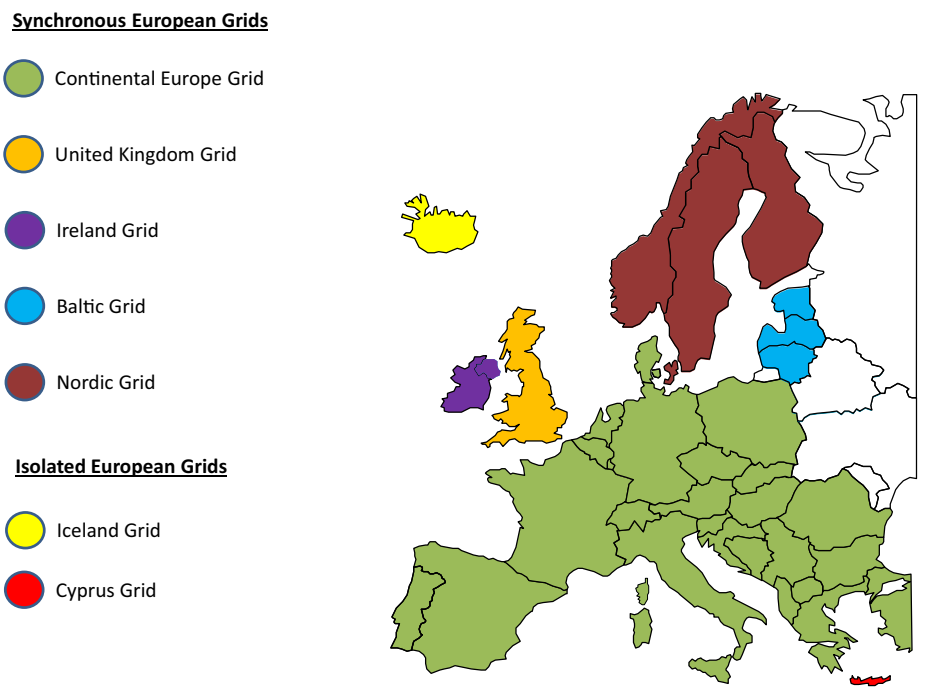

FIGURE 20.2 European transmission system map.

global way, not only at the national level but also at the EU level. Some of the most important causes are listed as follows:

- Distributed generation significantly complicates power generation management, making it more challenging to control tens of thousands of individual renewable producers than hundreds of stable conventional energy producers.
- A highly meshed transmission network, makes it difficult to manage and balance power flows during transport to the consumer.
- Congestion due to overcapacity when renewable production has a surplus due to weather conditions, and hence it must be stored or shed as renewable energy waste.
- Response to disturbances should be improved, so that the electrical system is more stable during some system incidents, such as voltage dips.
- Different adjustment services in cases where renewable resources are abundant; it implies flexibility in conventional production, moving it to other time bands.
- Minimizing forecast errors. Knowing as precisely as possible when energy resources will be produced is key to managing an electrical system.

*These new challenges require a change in the way of dealing with the adjustment between electricity generation and demand, the main actions of which at the operational level should be based on:

- An improvement in the forecasts estimating renewable resources reduces the uncertainty of this type of production as much as possible.
- Greater integration of power electronics in energy production, perfectly controlling all wave quality parameters.
- Better management strategies for the decentralization of electricity generation, assuming that distribution and self-consumption should have a greater weight.
- An increase and improvement in the electrical interconnection capacity between neighboring countries allow flexibility in the use of energy flow. The energy exchange depends on the instantaneous balance of energy production and consumption conditions of each country. Thus, providing an additional tool in the complex management between the electricity supply and demand with a high percentage of renewable penetration.

All these factors have generated a supranational context in which the development of European regulations and the creation of new NC have been necessary to manage the new challenges that lie ahead.

20.2.1 European network codes development

In 2010, the European Commission (EC) began to draft a new network code at the European level that allows the integration of the entire European electricity system in a harmonized manner. The Agency for the Cooperation of Energy Regulators (ACER) prepared the guidelines and foundations on which to develop the new network code. The writing of the code was carried out by the European Network of Transmission System Operators (TSO) for Electricity, involving different electricity sector stakeholders. After being drafted and reviewed by ACER, they were approved by the EC.

The NC formulates two types of network requirements. Some stricter ones, which are mandatory and of automatic application by each member state (applied without modifications), and others, more open, must be completed by each member country under its current legislation and the peculiar characteristics of its network and its management.

According to ENTSO-E [7], the structure of the European network code is shown in Table 20.1:

Three families (connection, operations, and market) and eight codes in total form it. In this chapter, we are going to focus on the requirements for generators called "COMMISSION REGULATION (EU) 2016/631." It was established on

TABLE 20.1 The code families in Europe.

The code families		
Connection	**Operations**	**Market**
Demand connection code	Emergency and restoration	Forward capacity allocation
Requirements for generators	Operations	Capacity allocation and congestion management
High voltage direct current connections	–	Electricity balancing

April 14, 2016, as a NC on requirements for grid connection of generators. The NC was entitled "Network Code Requirements for Generators" (NC RfG), or simply RfG. The enforcement of RfG began on April 27, 2019. It establishes the requirements for a generator, which can be wind power, photovoltaic, or otherwise, to be connected to the grid in a technically safe and equitable way, complying with market regulations. This code was developed to guarantee the optimal and coordinated management of the European electricity grid, giving importance to the security of the network, free competition, and the integration of renewable energies.

RfG provides a pan-European harmonization of connection requirements that is legally binding, establishing a standard set of requirements and a global structure for compliance assessment. On the other hand, and as we have indicated previously, it allows each member country to implement the RfG very customized. This document focuses on guaranteeing the safety of the electricity grid by foreseeing scenarios of significant renewable penetration whose generation is intermittent [8].

20.2.2 Structure and characteristics of network code requirements

The RfG structures the following requirements applicable to wind power generation:

1. Determination of significance and generator types. Generators will be classified based on their maximum capacity (active power) and voltage level (at the point where the generator is connected to the grid). As shown in Table 20.2, there are four types of generators, A, B, C, and D, with different power and connection voltage characteristics depending on the country of reference. A type of generator must meet the requirements of its category and all those of the lower categories (e.g., a type D generator must meet its requirements and those of generators C, B, and A). The TSO can modify the values in the table according to each country. Table 20.3 shows how other European countries establish different requirements for A to D generators.

TABLE 20.2 Classification of generators in Europe—I.

Generator types						
Type	Capacity					Voltage level
	Europe continental	Great Britain	Nordic	Ireland and North Ireland	Baltic	
A	> 0.8 kW	> 0.8 kW	> 0.8 kW	> 0.8 kW	> 0.8 kW	< 110 kV
B	> 1 MW	> 1 MW	> 1.5 MW	> 0.1 MW	> 0.5 MW	< 110 kV
C	> 50 MW	> 50 MW	> 10 MW	> 5 MW	> 10 MW	< 110 kV
D	> 75 MW	> 75 MW	> 30 MW	> 10 MW	> 15 MW	≥ 110 kV

TABLE 20.3 Classification of generators in Europe—II.

Generator types				
Type	Capacity			Voltage level
	Spain	Germany	The Netherlands	
A	> 0.8 kW	> 0.8 kW	> 0.8 kW	< 110 kV
B	> 100 kW	≥ 135 kW	≥ 1 MW	< 110 kV
C	> 5 MW	≥ 36 MW	≥ 50 MW	< 110 kV
D	> 50 MW	≥ 45 MW	≥ 60 MW	≥ 110 kV

2. RfG considers its application to different electricity generation modules, which can include pumping and heat production simultaneously in industrial facilities. Specifically, it refers to offshore generation facilities in which it is indicated that this type of system must meet the same requirements as terrestrial modules (onshore), unless the network manager modifies these requirements, or the connection is made using direct current voltage in which its frequency is not synchronously coupled to the main system (e.g., back-to-back converters).
3. RfG provides a large number of frequency stability requirements to keep frequency within safe productivity margins. Articles 13, 14, 15, and 16 establish these requirements for generator types A, B, C, and D respectively. Depending on the type of generator you have, different sections of each article should be applied. Thus, frequency ranges generators must withstand for a specific time without disconnecting are evaluated, as well as the amount of active power that the generator must inject to adapt to frequency variations and how to manage the control of this power. Finally, requirements are given for the maximum frequency variation rate that the generator can withstand.
4. In addition, voltage stability requirements are established so that they are within specific operating ranges. Time slots are specified when the generator should run out of range without shutting down. On the other hand, values of Reactive Power (Q) are established (controlling their ranges, slopes, and precision) at Maximum Active Power (P_{max}) and for values lower than it. Additionally, the fast fault current injection values that the power park itself must supply are established to normalize the voltage drop when a fault occurs.
5. Control values specified in the previous section will be used to act in the event of various disturbances that may occur. Thus, generators must be capable of damping and withstanding automatic reconnections that produce variations in Active Power (P). On the other hand, when a voltage dip occurs, limit voltage and frequency requirements are defined, which a generator must withstand for a while without disconnecting. Finally, as mentioned in the previous section, it is required that, after a fault, the generator must be capable of providing P recovery. TSOs are responsible for defining the time and magnitude of P recovery.

RfG defines other management aspects in the conventional operation of the power plant, such as simulation models, which will be static and dynamic and will be used to calculate the behavior of the power plant and participate in the validation procedures when faults occur. The RfG also defines the type of protection and control that a power plant must have and the synchronization conditions and equipment necessary to connect to the electrical grid. This code incorporates the conditions to recover a set of generators when an incident has occurred that isolates it or turns it off. Thus, we will have requirements for these generators to operate in island mode (disconnected from the main network). We will also have requirements to produce a reconnection when the system has been disconnected, and even procedures for autonomous starts without external power. It is essential to consider all these aspects in the operation of wind power plants.

The above requirements can be found in articles 17, 18, and 19 of the RfG for synchronous modules generators of type B, C, and D, respectively. In the case of power parks (such as wind power), the above requirements are found in articles 20, 21, and 22 for type B, C, and D power park modules, respectively.

Articles 23 to 28 define these requirements for offshore wind power parks.

To give a brief general idea of their content, apart from what has already been commented, it can be indicated that these three sets of articles provide a series of graphs in which the voltage in per unit (pu) is represented against the dimensionless Q obtained dividing Q by P_{max} (Q/P_{max}). It defines a series of ranges (minimum and maximum values of each magnitude) that graphically form a rectangle. The RfG allows each country to be at the point of operating conditions that it prefers as long as it is within the limits of this rectangle.

20.2.3 Grid code compliance—general aspects

As we have seen previously, NC establishes a series of technical operating requirements for electrical systems, which must be met to ensure the correct operation and safety provided by the execution of systems, following these documents.

Based on this idea, we can suggest an intuitive approximation of what Grid Code Compliance (GCC) is, indicating that it comprises all those activities related to the evaluation, verification, and certification of these requirements in the NC. Furthermore, GCC comprises different types of documents of a legal nature or test procedures that introduce technical conditions: connection to the network, purchase or transmission, and power distribution, which must be met and therefore be taken as part of the GCC.

Thus, if an entity wants to perform the installation connection (e.g., renewable offshore wind power type) to the electricity grid, a series of steps and tests must be followed to comply with the corresponding GC. Once it is estimated

that the NC has been met to make the connection in the example, it will be necessary to verify that this compliance is true, that is, obtain objective evidence that confirms that the requirements indicated in the code have been met, and for this step, we will have two types of compliance assessment: (1) compliance by testing and simulation; and (2) compliance by certification.

The NC RfG in its article 2 indicates that it will be necessary to have a power-generating module document (PGMD) that the power-generating facility owner will provide to the operators of type B or C generation modules. This document will confirm that the power generation module complies with the technical criteria established in this regulation and meets all compliance requirements. Member States may provide that an authorized certifier shall issue the PGMD.

ENTSO-E guides on:

- Compliance Testing (CT).
- Compliance Simulation (CS).
- Compliance Monitoring (CM).

To comply with testing, the RfG in its Title IV, Chapters 2, 3, and 4 indicates the conditions to carry out tests. It is important to note that the power-generating facility owner will ensure compliance throughout the life of their equipment, being possible for him/her to rely upon equipment certificates. At the same time, the relevant system operator will assess the compliance of a power-generating module under this regulation (throughout the facility's lifetime).

20.2.4 RfG by countries

ENTSO-E publishes updated information at [9] for the types of RfG implementation in different countries, many of which are still under development.

Considering the two types of compliance assessment that were explained above (certification and testing & simulation), each country has opted for one of them. In the first case, compliance by certification is carried out by generating a project certificate. This form of compliance is used only in Germany and Spain. Other countries like The Netherlands and Poland discuss this type of procedure. Many countries have opted for this type of procedure in the second case (testing and simulation).

In France, UK, Italy, Greece, The Netherlands, Austria, Poland, and Denmark is common that ISO/IEC 17065 accredited certification bodies issue equipment certificates as proof of compliance for specific capabilities (typically used in verification by certification). Despite that, some additional CT tasks, and CSs (performed by service providers without accreditation or certification bodies) are frequent.

Table 20.4 shows the GCC requirements for five countries and the summary of implementation in their national regulations.

TABLE 20.4 Technical requirements summary by country.

Requirements summary by countries				
Country	**National laws**	**Requirements**	**Compliance**	**Verification**
Spain	NTS v1.0 "Norma Técnica de Supervisión de la conformidad de los módulos de generación de electricidad según el Reglamento UE 2016/631"	Limited Frequency Sensitive Mode (LFSM-O)	Equipment certificate	Certification of the project based on NTS v1.0
	P.O. 9.0 "Información intercambiada por el operador del sistema"	Active power (P) and Reactive power (Q) control, V control and cos ϕ control	Simulation model using either PowerFactory or PSS/E simulation software	
	P.O. 12.2 "Instalaciones conectadas a la red de transporte: requisitos mínimos de diseño, equipamiento, funcionamiento y seguridad y puesta en servicio"			

(Continued)

TABLE 20.4 (Continued)

Requirements summary by countries				
Country	**National laws**	**Requirements**	**Compliance**	**Verification**
Germany	VDE-AR-N 4110 "Technische Regeln für den Anschluss von Kundenanlagen an das Mittelspannungsnetz und deren Betrieb (TAR Mittelspannung)," VDE|FNN, 11/2018	Limited Frequency Sensitive Mode (LFSM-O) with inverter capability	Component or Unit certificate	Certification of the project based on FGW TG8
		Active power (P) control using ramp rate limiting	Component testing (it is not mandatory—supplementary)	
	VDE-AR-N 4120, "Technische Regeln für den Anschluss von Kundenanlagen an das Hochspannungsnetz und deren Betrieb (TAR Hochspannung)" VDE|FNN, 11/2018	Reactive power (Q) as Q (U), Q(P), and Q set	Compliance simulations (a certification body carries them out)	
	FGW Technical guidelines for testing (TG3), simulations (TG4) & certification (TG8)	cos ϕ set		
UK	Energy Networks Association (ENA) Engineering Recommendation (EREC) G99 "Requirements for the connection of generation equipment in parallel with public distribution networks on or after 27 April 2019, 09/03/2020"	Limited Frequency Sensitive Mode (LFSM-O)	Equipment certificate	Compliance by mandatory testing (G99, Annex B.6, C.9)
		Active power (P) and Reactive power (Q) control, V control and cos ϕ control	Compliance testing	Compliance by mandatory simulation (G99, Annex B.4, C.7)
			Compliance simulations	
The Netherlands	Netbeheer Nederland "Power-Generating Modules compliance verification—Power-Generating Modules type B, C and D according to NC RfG and Netcode elektriciteit," Version 1.1, 01/12/2019	Limited Frequency Sensitive Mode (LFSM-O)	Equipment certificate	Certification of the project based on Compliance verification procedure
		Active power (P) and Reactive power (Q) control, V control (V1 & V2 mode), and cos ϕ control	Compliance testing	
	Netbeheer Nederland "Netcode elektriciteit," text as from 1 January 2020, last updated on 2020-02-11 (including ACM proposals), 01/01/2020		Simulation model using either PowerFactor or PSS/E simulation software	
Poland	PSE S.A. "Wymogi ogólnego stosowania wynikajace z Rozporzadzenia Komisji (UE) 2016/631 z dnia 14 kwietnia 2016 r. ustanawiajacego kodeks sieci dotyczacy wymogów w zakresie przylaczenia jednostek wytwórczych do sieci (NC RfG)", 18/12/2018	Limited Frequency Sensitive Mode (LFSM-O)	Equipment certificate	Compliance testing and simulations
	PTPiREE "Warunki i procedury wykorzystania certyfikatów w procesie przylaczenia modulów wytwarzania energii do sieci elektroenergetycznych," 20/03/2020	Active power (P) and Reactive power (Q) control, V control and cos ϕ control	Compliance testing	
			Simulations for compliance	

In the case of CT and CS, the following work plan is proposed:

- To set up a test procedure (plan).
- Tests carried out for verification.
- To set up a simulation procedure (plan).
- Simulations (set up model, calculation, and reporting) carried out.

In the case of certification, a compliance assessment will be carried out based on a certificate or through the Statement of Compliance (SoC). For this, the following points will be considered:

- Component certificate
- Equipment certificate
- Type certificate
- Project certificate

Finally, CM will consider the revision of the previous certificate or the SoC, according to the particular case [10].

20.3 Wind power performance requirements in North America

The electric grid in North America consists of four interconnections, shown in Fig. 20.3: the Eastern interconnection, the Western interconnection, the Texas interconnection, and the Quebec interconnection. The Eastern and Western interconnections are the largest, and both span parts of the United States (US) and Canada. The Western interconnection also includes the northern portion of Baja California, Mexico.

In the US, there is no universal GC. The performance requirements for generation facilities, including wind plants, are determined by the Federal Energy Regulatory Commission (FERC), the North American Electric Reliability Corporation (NERC), Independent System Operators (ISO), Regional Transmission Organizations (RTO), and transmission owners.

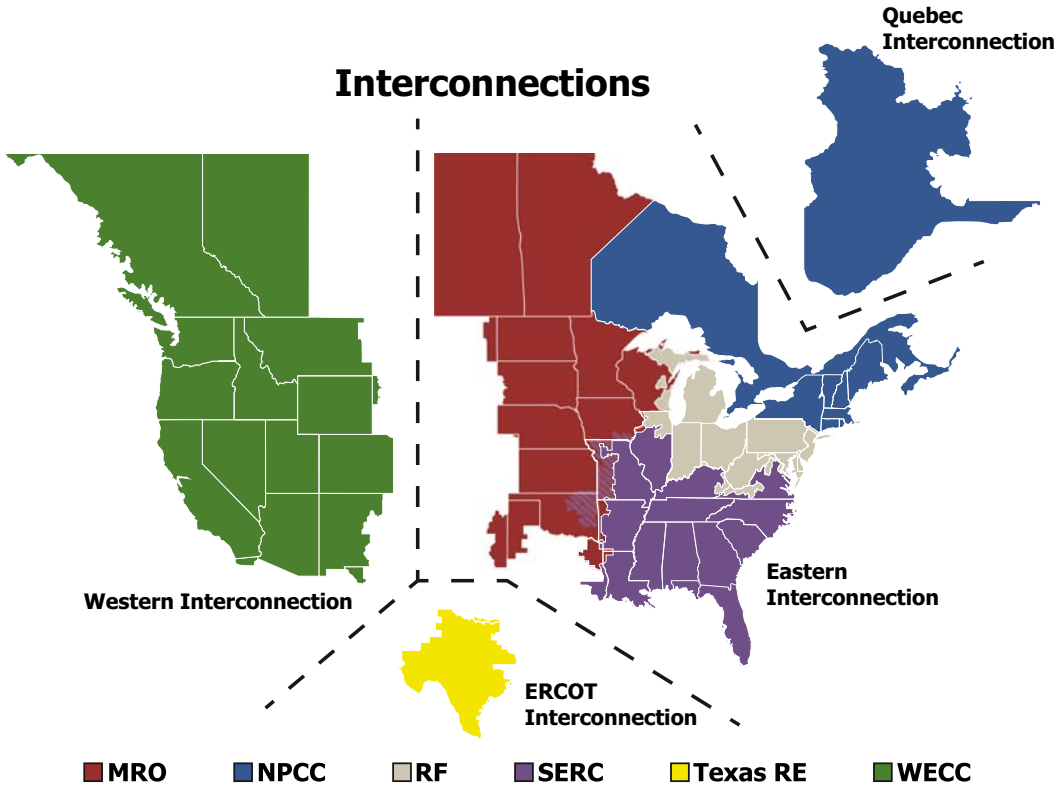

FIGURE 20.3 North America Interconnections [11].

20.3.1 Federal energy regulatory commission

FERC regulates the interstate transmission of natural gas, oil, and electricity in the US. The interconnection of generation to the transmission system falls under the jurisdiction of FERC; however, not all transmission owners in the US are under FERC's jurisdiction. For example, municipalities and federal power marketing agencies are not under FERC's jurisdiction [12].

20.3.1.1 Wind generation interconnection requirements

FERC establishes the standard interconnection procedures and agreements for the interconnection of generators. The Large Generator Interconnection Procedures (LGIP) and Interconnection Agreement (LGIA) apply to generating facilities with a capacity greater than 20 MW. The Small Generator Interconnection Procedures and Interconnection Agreements (SGIA) apply to generating facilities with a capacity of less than or equal to 20 MW. FERC Order 661 and Order 661-A, both issued in 2005, append the LGIP and LGIA to include technical requirements for large wind generation interconnections. The requirements are added as Appendix G to the LGIA. Appendix G of the LGIA also states that all other requirements of the LGIA continue to apply to wind-generating plant interconnections. Table 20.5 summarizes the performance requirements specified in the LGIA and the SGIA.

20.3.1.2 Incentives to support the grid reliability

FERC Order 755, "Frequency Regulation Compensation in the Organized Wholesale Power Market," requires RTOs and ISOs to adopt a two-part market-based compensation method for frequency regulation services—a capacity payment reflecting opportunity costs and a market-based performance payment—rewarding faster-ramping resources, such as batteries and flywheels. Frequency regulation, an ancillary service, facilitates grid stabilization by enabling supply-demand balance. It has been provided by slow-responding, fossil-fuel-centered gas turbines and coal-powered generators until the emergence of energy storage technologies.

On July 18, 2013, the FERC issued FERC Order 784, which revises its Avista policy regulating ancillary-service sales at market-based rates to public utility transmission providers. The rule aims to increase competition and transparency in ancillary service markets. FERC Order 784 revises regulations governing sales of frequency regulation services, thereby increasing the opportunities for energy storage projects in the ancillary services market.

20.3.2 Electric reliability organization

The US Energy Policy Act of 2005 establishes a single Electric Reliability Organization (ERO) in the US responsible for developing and certifying mandatory reliability standards for the bulk power system[1] subject to FERC approval. In 2006, FERC certified NERC as the ERO. This resulted in the NERC reliability standards, which were previously voluntary, becoming mandatory upon FERC approval. The ERO can also delegate its enforcement responsibilities to regional entities. Fig. 20.4 shows the six regional entities in the US.

Table 20.6 provides an overview of the relevant standards related to wind generation performance requirements. NERC standards are applicable to generating facilities, including wind plants, that aggregate to a total capacity greater than 75 MVA and have a common connection point at a voltage greater than or equal to 100 kV.

NERC also develops reliability guidelines based on the "collective experience, expertise, and judgment of the industry." NERC reliability guidelines are voluntary and are not subject to enforcement. In 2018, the NERC IBR Performance Working Group published a reliability guideline for BPS Connected IBR Performance [16]. This reliability guideline provides performance guidance for: (1) active power—frequency response; (2) reactive power—voltage response; (3) protection; (4) measurement data; and (5) performance monitoring.

20.3.3 Transmission owner

Transmission owners may also have specific performance requirements for newly interconnecting wind generation facilities. The transmission owner is required to document interconnection requirements under NERC standard FAC-001-3. NERC standard FAC-002-2 requires studies to evaluate the reliability impact of new generating facilities. Further, there

1. Bulk power system is defined in FERC Order 672 "facilities and control systems necessary for operating an interconnected electric energy transmission network (or any portion thereof), and electric energy from generating facilities needed to maintain transmission system reliability. The term does not include facilities used in the local distribution of electric energy."

TABLE 20.5 LGIA and SGIA interconnection performance requirements applicable to wind generation.

	LGIA [13]	SGIA [14]
Applicability	Generating facilities with a capacity greater than 20 MW.	Generating facilities with a capacity less than or equal to 20 MW.
Power factor design criteria	The generating facility shall be designed to maintain a composite power delivery at continuous rated output power at the high-side of the generator substation at a power factor within the range of 0.95 lagging to 0.95. The power factor range shall be dynamic and can be a combination of power electronics, fixed capacitors, and switched capacitors.	Same as LGIA
Voltage control	The large generating facility shall be operated to maintain the specified output voltage or power factor at the point of interconnection[a] within the facility's design limits. Further, the Large Generating Facility shall operate its voltage regulators in automatic operation.	Not explicitly specified.
Primary frequency response	The generating facility shall install, operate, and maintain frequency-responsive real power control with the ability to sense frequency changes and respond autonomously by changing the real power output in accordance with the droop and deadband parameters in the direction needed to correct the frequency deviation. The specification includes: 5% maximum droop based on the nameplate capacity of the generating facility and linear in the range of 59 Hz to 61 Hz ± 0.036 Hz deadband without a step to the droop curve	The generating facility shall install, operarate, and maintain a functioning governor or equivalent controls. The specified capabilities of the governor or equivalent control are the same as the LGIA.
Low voltage ride-through capability	Wind generating plants are to remain in-service during three-phase faults with normal clearing and single line to ground faults with delayed clearing, and subsequent postfault voltage recovery to prefault voltage unless fault clearing disconnects the plant from the system. The LGIA further specifies the wind generating plant shall remain interconnected for a voltage as low as zero volts at the high side of the wind GSU for a maximum of 9 cycles.	The generating facility shall not disconnect automatically or instantaneously from the transmission system for a defined under or over voltage condition. The defined conditions shall be in accordance with good utility practice and consistent with any standards and guidelines that are applied to other generating facilities in the Balancing Authority Area on a comparable basis.
Abnormal frequency events	The generating facility shall not disconnect automatically or instantaneously from the transmission system for an under or overfrequency condition. The generating facility can disconnect if the abnormal frequency condition persists beyond the limits set forth in ANSI/IEEE Standard C37.106 or other standards applied to other generators in the control area on a comparable basis.	The generating facility shall not disconnect automatically or instantaneously from the transmission system for a defined under or overfrequency condition. The defined conditions shall be in accordance with good utility practice and consistent with any standards and guidelines that are applied to other generating facilities in the balancing authority area on a comparable basis.

[a]*Defined in the LGIA as the point where the interconnection customer's interconnection facilities connect to the transmission provider's interconnection facilities.*

may be region-specific requirements from the ISO, RTO, or regional ERO entity. Similarly, the FERC LGIP describes a series of studies required as part of the interconnection process. Therefore, additional interconnection requirements may be identified through the study process of proposed interconnections.

20.3.4 Future standards

As noted previously, there is no universal GC in the US. The FERC and NERC standards allow the flexibility for transmission owners to develop performance requirements applicable to their grids. However, with the significant increase in proposed connections of IBR, an argument can be made for the need to establish technical minimum performance requirements for IBR in the US. Recently, standards development in the IEEE has taken on this topic. IEEE Std 2800™-2022, Standard for Interconnection and Interoperability of IBR Interconnecting with Associated Transmission Systems,

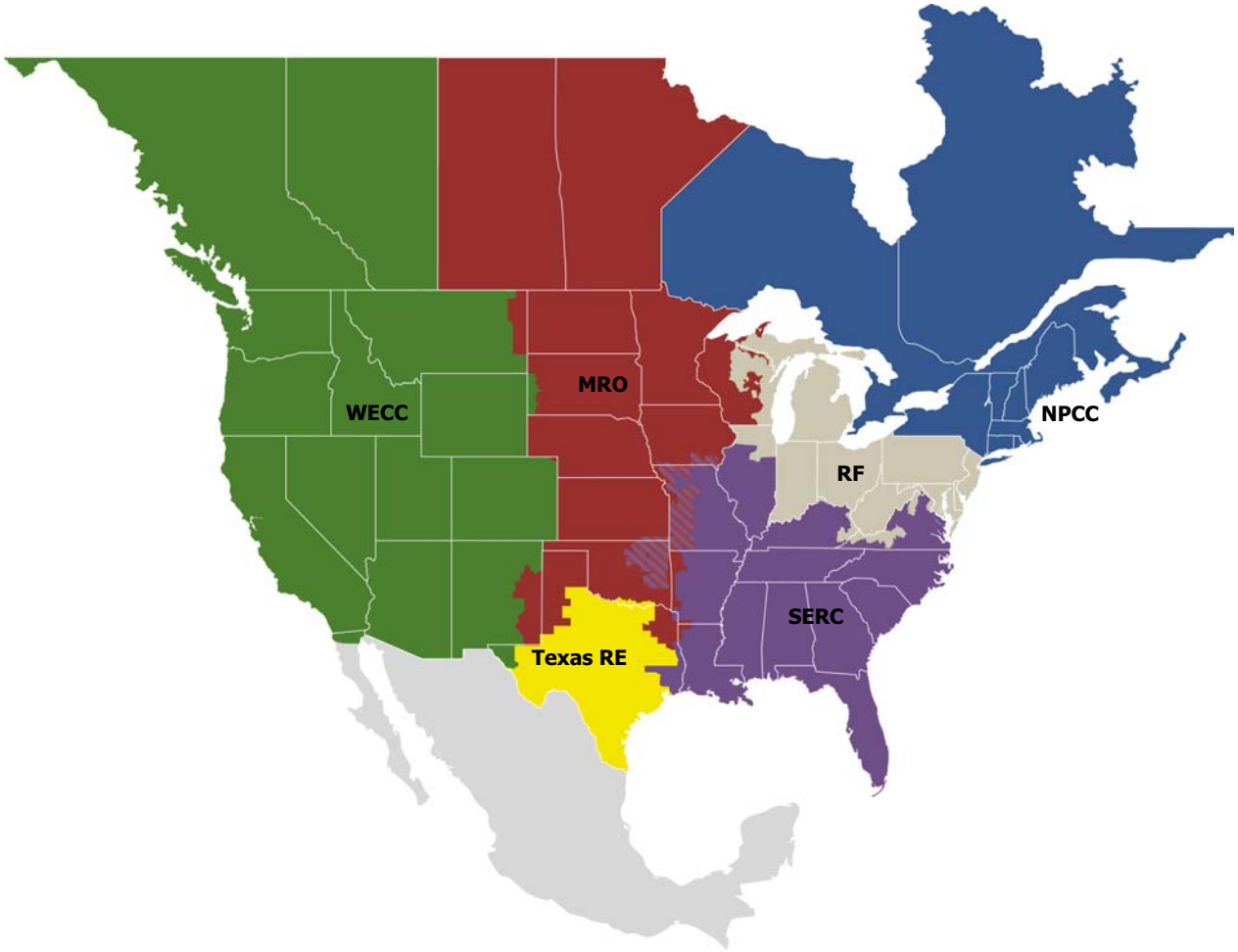

FIGURE 20.4 Map of the regional reliability entities in the US [15].

TABLE 20.6 NERC standard requirements relevant to wind generation performance requirements.

NERC standard	Requirement
FAC-001-3 facility interconnection requirements	Requires transmission owners to document and make interconnection requirements for generation facilities available.
FAC-002-2 facility interconnection studies	Requires studies evaluating the reliability impact of interconnecting new generator and materially modifying existing interconnections of generation.
VAR-002-4.1 generator operation for maintaining network voltage schedules	Requires generator owners to operate in automatic voltage control mode to maintain the voltage schedule provided by the transmission operator.
PRC-024-3 frequency and voltage protection settings	Generator owners are to ensure frequency and voltage protection does not cause the generating resource to trip of cease injecting current within the no trip zone. Note that this is a protection standard and not a ride-through standard.

prescribes minimum technical performance capability requirements for IBR connecting to the transmission system [17]. The standard includes performance capability requirements for active power—frequency response, reactive power—voltage control, voltage ride-through, frequency ride-through, protection, power quality, modeling data, measurement data for performance monitoring and validation, and test and verification requirements. The IEEE Std 2800™-2022 has

been approved by the IEEE Standards Association Standards Board in February 2022. To be enforced, this standard will need to be adopted by the transmission owner or another regulating authority such as FERC or NERC.

20.4 Future grid code challenges

The GCs are implemented in power systems through system protection at the device, distribution, and transmission levels. The system protection is programmed to ensure the system's reliability and availability can be maintained at a very high level according to the requirement stated within the area of the GC enforcement. The enforcer of the GC is the municipalities, utility, and system operators covering the system interconnection. Several challenges in developing future GCs can be listed as follows:

- The continuous changes in technologies improve the performance of devices, sensors, computation, and communication. Thus, new technologies tend to improve the reliability of the power system.
- The new sciences in forecasting, market design, and energy storage improve power system operation and make it more robust and resilient to withstand disturbances.
- The GC must be adaptable but also realistic. However, the question is how often the GC must be reviewed, what triggers the necessary changes, who decides the change, etc.
- As the GC is modified, we need to consider: (1) the burden on manufacturers to upgrade the devices (generator, control, protection, sensors, etc. to adapt to the GC of the targeted markets); (2) the education of existing engineers and technicians on implementing the modified GCs; and (3) the cost of modification on labor hours spent to change the setting of the control and system protection, the learning curves, the validation, and testing and commissioning of the new GC implementation on devices levels and plant levels.

Thus, we can conclude that the GC development or modification is a balance between the continuous deterioration of the power system dynamic performance and the continuous improvement in technologies and sciences in many aspects of power systems.

Acknowledgements

This research was partially funded by the Council of Communities of Castilla-La Mancha (Junta de Comunidades de Castilla-La Mancha, JCCM) through project SBPLY/19/180501/000287 and by the European Regional Development Fund (Fondo Europeo de Desarrollo Regional, FEDER). Raquel Villena-Ruiz is also a postdoctoral researcher Margarita Salas, with a contract within the framework of the call for grants for the requalification of the Spanish university system, funded by the European Union Recovery Instrument NextGenerationEU and obtained through the Universidad de Castilla-La Mancha (UCLM).

References

[1] Mark Bolinger JS, Robson Dana, Warner Cody. Utility-scale solar data update: 2020 edition. Lawrence Berkeley National Laboratory 2020;. Available from: https://emp.lbl.gov/sites/default/files/2020_utility-scale_solar_data_update.pdf.

[2] Renewables account for most new U.S. electricity generating capacity in 2021, U.S. Energy Information Administration, 2021. https://www.eia.gov/todayinenergy/detail.php?id = 46416.

[3] Joseph R, Mark B, Ryan HW, Seongeun J, Bentham P. Queued up: characteristics of power plants seeking transmission interconnection as of the end of 2020, 2021. <https://eta-publications.lbl.gov/sites/default/files/queued_up_may_2021.pdf> [accessed 08.02.22].

[4] Zummo P. America's electricity generation capacity: 2021 update, American Public Power Association. <https://www.publicpower.org/system/files/documents/Americas-Electricity-Generation-Capacity_2021-update.pdf>; 2021.

[5] Hoke Anderson, Bennion Kevin, Gevorgian Vahan, Chakraborty Sudipta, Muljadi E. Sizing SiC Storage Invert Fast Grid Frequency Support 2015;328–33. Available from: https://ieeexplore.ieee.org/document/7369262.

[6] ENTSO-E Grid Map. <https://www.entsoe.eu/data/map/>.

[7] What are network codes? <https://www.entsoe.eu/network_codes/>; 2021.

[8] Commission Regulation (EU) 2016/631 of 14 April 2016 establishing a network code on requirements for grid connection of generators. <https://eur-lex.europa.eu/legal-content/EN/TXT/HTML/?uri = CELEX:32016R0631&from = PL#d1e7449-1-1>; 2016.

[9] Progress of connection network code implementation. <https://www.entsoe.eu/active-library/codes/cnc/>; 2022.

[10] Holzapfel B, Holzapfel M., Grid code compliance in Europe. Ways to a fast and safe grid connection. <https://16iwyl195vvfgoqu3136p2ly-wpengine.netdna-ssl.com/wp-content/uploads/2020/06/2020-07-16_pv_magazine_Webinar_Grid_Code_Compliance_in_Europe_en.pdf>; 2020 [accessed 08.02.22].

[11] North American Electric Reliability Corporation (NERC) interconnections. <https://www.nerc.com/AboutNERC/keyplayers/PublishingImages/NERC%20Interconnections.pdf>; 2022.

[12] What FERC does. <https://www.ferc.gov/about/what-ferc/what-ferc-does>; 2020.
[13] Standard large generator interconnection agreement, FERC. <https://www.ferc.gov/sites/default/files/2020-04/LGIA-agreement.pdf>; 2019.
[14] Small generator interconnection agreement, FERC. <https://www.ferc.gov/sites/default/files/2020-04/sm-gen-agreement.pdf>.
[15] ERO Enterprise | Regional Entities. <https://www.nerc.com/AboutNERC/keyplayers/Pages/default.aspx>.
[16] Reliability Guideline-BPS-connected inverter-based resource performance, NERC. <https://www.nerc.com/comm/%E2%80%8COC_Reliability_Guidelines_DL/Inverter-Based_Resource_Performance_Guideline.pdf>; 2018.
[17] IEEE draft standard for interconnection and interoperability of inverter-based resources (IBR) interconnecting with associated transmission electric power systems, in P2800/D6.3, December 2021, p. 1−181.

This page intentionally left blank

Chapter 21

Intelligent design and optimization of wind turbines

Weifei Hu[1,2,3], Jianhao Fang[3], Zhenyu Liu[1,2,3] and Jianrong Tan[1,2,3]

[1]State Key Laboratory of Fluid Power and Mechatronic Systems, Zhejiang University, Hangzhou, P. R. China, [2]Engineering Research Center for Design Engineering and Digital Twin of Zhejiang Province, Hangzhou, P. R. China, [3]School of Mechanical Engineering, Zhejiang University, Hangzhou, P. R. China

21.1 Introduction

The booming energy demands combined with the dramatic depletion of conventional energies (e.g., fossil fuels) require the development of renewable energies [1]. As one of the most promising renewable energy resources [2], wind energy has attracted increasing interest from researchers due to its appropriate cost-effectiveness, environmental friendliness, and sustainability. Specifically, wind turbines (WTs) can generate electric energy by converting captured wind energy and can be located onshore (on land) or offshore (at sea). Today, large WTs are being deployed, especially on offshore wind farms to convert stronger and more stable wind energy. However, larger WTs, especially those offshore, are expected to place high demands on the design associated with the operations & maintenance cost, manufacturing process, performance, etc. [3]. To harness the wind at a maximum level, optimization is always crucial in the WTs design process.

Recent approaches in the literature have covered many aspects of the optimization of WTs [4], such as the optimization of the blade shape [5], the optimization of the wind farm [6], maintenance planning [7], and cost optimization [8]. In addition, due to the complexity of WT systems and their nonlinear and fully coupled aero-hydro-servo-elastic behavior, physics-based analysis modeling and iterative simulation are introduced to find an optimal solution in the design optimization process. Moreover, the optimized components could range from blades, rotors, towers, etc. The range of components varies, while the considered factors of WTs increase (e.g., load types, failure types, and structural analysis types). The increasing number of design variables and objectives, as well as the complexity of the physics-based analysis model, cause a struggling computing efficiency in the design optimization process. Compared with traditional methods, recent developments in intelligent design and optimization of WTs [e.g., artificial intelligence (AI) and machine learning (ML)] are being utilized to facilitate informed, reliable, cost-effective, and robust design optimization processes [9], including big data intelligence [10], optimized decision-making [11], and improvements in computational capabilities.

Based on a literature survey, this chapter provides a comprehensive review of recent approaches to the intelligent design and optimization of WTs. The chapter is organized as follows: Section 21.2 summarizes the different intelligent design and optimization methods for WTs. Section 21.3 elaborates on the applications of different components of WTs. The key challenges of the intelligent design and optimization of WTs, as well as future work, are concluded in Section 21.4.

21.2 Intelligent design and optimization methods for wind turbines

As one type of commonly used intelligent design and optimization methods, ML is a kind of algorithm for building an inductive model that learns from a limited amount of data without any specialist intervention [12,13]. In the past 20 years, different ML algorithms have been discovered and developed to cover a wide variety of input data in different problems, including regression, classification, and clustering [14]. Different ML methods can be used for different tasks, including condition monitoring (CM), design optimization, and real-time control of WTs. This section focuses on the

Wind Energy Engineering. DOI: https://doi.org/10.1016/B978-0-323-99353-1.00024-4

design and optimization methods for WTs, which are further grouped into three main categories, supervised learning, nonsupervised learning, and reinforcement learning (RL).

21.2.1 Supervised learning-based methods

In the process of design optimization, performance evaluation of WTs is always carried out by physics-based simulation and analysis. Hence, a highly accurate surrogate model to replace the computationally expensive simulation and analysis is of great importance for the WT design and optimization processes. However, the traditional surrogate methods based on parametric or semiparametric approaches may not show their efficiency in some cases, and the features are strongly nonlinear and multimodal with the input. To overcome these shortcomings, there is emerging research on ML for improving the runtime of the analysis. Supervised learning methods are found to be an efficient surrogate model for reducing the calculation time while maintaining the fidelity of the physics-based simulation.

Supervised learning is the method to train a model by labeled data for the particular output, which is good at addressing classification and regression problems by generally forming the predictor through a learned mapping $f(x)$ to predict the output (usually the performance) for each input x (or a probability distribution over y given x) [13]. The advantage of supervised learning-based methods is that there is no need for prior domain knowledge, but there is only the need to use the existing sensors or the simulation result to train models [15]. First, the parameterization of the specific part is obtained. Then, the performances (e.g., stress and/or deflection) of the part are obtained by finite element analysis (FEA) methods or experiments. Next, the surrogate model is established and predicts the performance instead of the expensive FEA solver [16]. Finally, the optimization algorithm is adopted to search for a better design [17]. Hence, the cost of the simulation time [e.g., expensive computational fluid dynamics (CFD) solver] or external experimental tools (e.g., wind tunnels) can be saved. Many different kinds of supervised learning methods are utilized for building surrogate models for design optimization, which can be grouped as shallow ML [e.g., artificial neural networks (ANNs) [18,19], support vector machines [20], random forest [21]] and deep learning [e.g., convolutional neural networks (CNNs) [15], and recurrent neural networks (RNNs) [22]].

While different methods could be utilized in various types of mapping, shallow machine-learning-based methods are suitable for predicting the performance of WTs (i.e., the power production curve and the fatigue life curve) with simulation or experimental data [23,24]. For instance, Sessarego et al. [25] applied an ANN for the design optimization of a curved wind turbine blade, which was trained with the simulation data generated by an aeroelastic simulator considering synthetic inflow turbulence. Sun et al. [26] used the experimental results of WTs to train an ANN to investigate the optimization strategies during wake steering. A CNN can reduce the dimension of the collected original data while extracting features of the original data, which shows the superiority in processing high-dimensional data (e.g., the stress distribution of CFD [15]) to the ANN-based methods. Wang et al. [27] verified the effectiveness of field reconstruction and performance prediction of a CNN by sampling 1500 cases for eight design variables in its dataset. Du et al. [15] established a CNN model to accomplish the accuracy and fast prediction of the flow field of the blade, where the training data was generated by CFD simulation. An RNN is a kind of deep learning algorithm that is quite effective in forecasting time series data. Mardani et al. [28] decomposed time series data to predict wind power using long short-term memory (LSTM). Similarly, Hu et al. [22] proposed an ensemble empirical mode decomposition method combined with LSTM for wind speed prediction. In conclusion, the different supervised learning-based methods are selected according to different forms of the dataset.

Supervised learning-based surrogate models are frequently combined with other optimization algorithms to improve and evaluate the performance of the system. The WT system is often converted to an optimization problem, mostly considering the optimization problem as a power production-based function [25,29] or a cost-based function [30]. In addition, other variables, such as fatigue life [31], environmental conditions [32], and system maintenance [33] are also often considered. In addition, deep learning methods enable the surrogate model to predict, under a higher dimension, a greater capacity, than shallow machine-learning-based methods. Table 21.1 summarizes the cited references in this section, separating them by the key method, the specific applications, and the data sources. It can be inferred that the ANN is the most frequently used method.

21.2.2 Unsupervised learning-based methods

Unsupervised learning is a type of method that can automatically classify or group input data without labeling. When searching the global optimization in the design process, the number of analyses (e.g., CFD) increases as the number of design variables (i.e., design space dimensionality) increases [34]. Meanwhile, too many sample types often lead to

TABLE 21.1 Supervised learning-based methods for WTs.

References	Supervised learning-based methods	Specific applications	Data source for training methods
[15]	Series CNN	Surrogate model; End wall profile performance prediction	CFD simulation
[17]	ANN, LSTM	Surrogate model; drag, lift, moment, pressure distribution prediction airfoil design performance	CFD simulation
[23]	ANN	Wind turbine power curve estimation	Met tower
[24]	ANN	Wind turbine wake prediction	CFD simulation
[25]	ANN	Surrogate model; Power coefficient. thrust coefficient prediction	Aeroelastic simulator (MIRAS)
[26]	ANN	Surrogate model; power generation prediction considering wake effect	Acquisition in wind field
[27]	Dual-CNN	Surrogate model; aerodynamic performance, temperature filds prediction	CFD simulation
[22]	LSTM	Wind field procasting	Acquisition in wind field

inaccurate model construction in the design process, further extending the number of model constructions and time. The calculation time of analysis and optimization increases exponentially with the design space dimensionality [35].

To combat the problem of dimensionality, dimensionality reduction methods are proposed. Dimensionality reduction refers to an unsupervised technology that can reduce the number of input datasets or features. By utilizing the unsupervised learning-based method including principal components analysis (PCA) [36], factor analysis [37], manifold learning [20], etc., those dimensions that affect the performance in WTs' design can be captured [38]. For instance, Wang et al. [39] introduced PCA for the dimensionality reduction of supervisory control and data acquisition (SCADA) data, which were more suitable for constructing a performance model. Some deep learning algorithms were also applied in dimensionality reduction, such as variational autoencoders (VAEs) [40] and generative adversarial networks (GANs) [41]. Deep learning algorithms are superior in terms of learning arbitrary dataset distributions compared to traditional dimensionality reduction methods. For example, Chen et al. [34] applied a Bézier-GAN for airfoil design and optimization by learning the shape variation in the database, which can accelerate convergence by improving the compactness of the design space while maintaining the features. Yang et al. [42] used VAE in the aerodynamic shape optimization of a WT airfoil by reducing the design variable as a realistic target distribution, and then predicting the quantities of interest. The unsupervised method could also be used to train the healthy model based on the healthy data of WT. When the data (e.g., frequency, acceleration) of actual WTs do not fit with the data predicted by the trained model, this can indicate that the WT may be failing [43].

When modeling for the WT (e.g., forecasting the WT power in a wind farm), it is inaccurate to predict the performance by a dataset of single WT or to choose a representative WT. Conversely, modeling separately for WT is a huge computational task [44]. To balance the accuracy associated with utilizing a single WT and ensure computational efficiency, clustering methods, which are also a part of unsupervised learning, are introduced to cluster WTs or divide WTs into several groups taking into account the similarity among the WTs [45]. Traditional clustering methods involve clustering data by minimizing the within-cluster sum of the Euclidean metric or introducing specific methods (e.g., spectral graph theory) for extracting similar features, such as k-means [46] and spectral clustering [47]. In addition, the ANN could also be utilized for clustering [e.g., self-organizing map (SOM)], which may show higher cluster effectiveness [48]. Then, the modeling process could be carried out for each group, which accomplishes a higher accuracy than that obtained without applying clustering methods. Liu et al. [49] verified the effectiveness of k-means, SOM, and spectral clustering methods in a wind farm, improving the prediction accuracy of the established model by 1.35%, 1.67%, and 1.43%, respectively.

In conclusion, the most common applications of unsupervised learning in the WTs' design and optimization are dimensionality reduction and clustering, while its most relevant applications include reducing the number of design variables and clustering similar WTs in a wind farm. Both dimensionality reduction and clustering are needed, and the

TABLE 21.2 Unsupervised learning-based methods for WTs.

References	Unsupervised learning-based methods	Specific applications	Data source for training methods
[34]	GAN	Dimensionality reduction; reduce the dimension of design variable	UIUC airfoil database
[39]	PCA	Dimensionality reduction; reduce the time series for model e	SCADA data
[42]	DAE	Dimensionality reduction; reduce the dimension of design variable	Frey face dataset
[43]	Autoencoder	Healthy condition modeling for foundation	Experiment
[44]	Support vector clustering	Cluster for similar WTs in wind farms	Experiment
[45]	SOM	Cluster for similar WTs in wind farms	SCADA data
[48]	SOM	Cluster for loads model parameters data in wind farms	Experiment
[49]	k-means, SOM, and spectral clustering methods	Clustered WTs in wind farms into several groups by identifying similar characteristics of wind speed and output power	SCADA data

prediction model of WT can be established quickly and accurately, which results in an efficient search in the optimization process. Table 21.2 summarizes the main application of the unsupervised learning mentioned in this section.

21.2.3 Reinforcement learning-based methods

Optimization methods always operate iteratively and modify the design variables, which makes the values of objective functions satisfy the goals. However, such methods often do not utilize the previous data when exploring the same design space, which induces computational inefficiency [50]. In addition, a large design space, as well as multiobjective functions, cause a heavy computational burden [51]. RL, which is also a type of ML, is introduced in the field of WT design and optimization to resolve these issues. RL can be used to find the optimal solution to exact problems by following the rule of "trial and error" in the searching process of the design space, where the searching mode is quite different from the method of gradient-based or nongradient-based methods.

The key idea of RL applied in WT design optimization is to train the agent (algorithm) to make the decision (optimization) referring to the reward evaluation at each step. Through a sequence of actions (design variables) in the feasible region in the design space, the agent could approximately achieve an optimal solution. Hence, the agent can learn not only the optimum but also how to find it (through the agent) [52]. For instance, Q-learning (a kind of reinforcement algorithm) is applied for the yaw angle design of WTs [53] or sequential decision-making problems [52]. The application of Q-learning algorithm has been applied in dynamic load distribution optimization, which shows good performance in a two-area power system [54]. In addition, as an extension of the value-based method, methods such as policy gradient can be utilized for continuous design space searching [55].

As an extension of RL, deep reinforcement learning (DRL) is proposed by combining RL methods with the supervised learning method, which can address design optimization problems of WTs. As mentioned above, the performance features of each state can be extracted by utilizing supervised learning. For example, Chen et al. [56] utilized a deep Q-network (DQN, a DRL method combining supervised learning with Q-learning) for online WT speed optimization. However, DQN is limited to solving discrete design optimization issues [52]. For continuous problems, DRL methods, such as the deterministic policy gradient (DPG) and the deep deterministic policy gradient (DDPG) can be applied in similar ways. In particular, the DDPG [57] could further address more comprehensive stochastic problems. For instance, Qin et al. [58] used the DDPG for a cascade blade profile design optimization with multiobjective functions.

To summarize, the RL method could be used as an optimization algorithm in the design optimization process, which is found to be efficient in particular issues, such as combination optimization and decision-making problems. By combining with other ML methods, RL can address more complicated problems, such as high-dimensional continuous optimization. Table 21.3 summarizes the references cited in this section, classifying them by algorithms used, applications, and design variables.

TABLE 21.3 Reinforcement learning-based methods for WTs.

References	Reinforcement learning-based methods	Objective function	Design variables
[52]	Actor-critic method	Power productions	Twist angle distribution in different wind speeds
[53]	Q-learning	Minimized cost	Yaw angle in different wind field
[54]	Q-learning	Error between prediction and actual	Portional and integral coefficients of controller
[59]	Q-learning	Lift-drag ratio	Airfoil
[56]	DQN	Error between two values of the electrical output power	Rotor speed
[58]	DDPG	Total pressure loss, laminar flow area	Profile parameter

21.3 Intelligent design and optimization applications for wind turbines

21.3.1 Blades

The design and optimization process for blades is essential for the wind energy industry due to their server loading conditions, long-term lifespan, and high cost [60]. In addition, the WT system design lifespan needs to be designed for 15−20 years under external and internal loads, for example, aerodynamic load, gyroscopic load, gravity load, as well as the dynamic interactions between the turbine system and other subassemblies. Hence, most of the design optimization processes aim to make WTs produce more energy (maximize annual energy production (AEP) [61], be power coefficient (C_p) [52], and to improve the lift-drag ratio (L/D) [19,59]) while avoiding extra cost and load (minimizing inertia moment (IM) [61], mass [61], and general load [15]).

As an important aspect of aerodynamics, wind load is modeled by the Weibull distribution (e.g., [62,63]). The hourly or 10-min distribution could be used for estimating the wind speed of WTs experienced in the lifespan. The wind load corresponding to damage under different wind speeds can be further estimated. However, extreme loads, which are low-probability events, can cause severe damage to WTs. Hence, research is carried out for accurate wind speed prediction. Supervised learning, especially deep learning, is considered the best way to anticipate extremely nonlinear environmental data [64]. Ramasamy et al. [65] proposed that ANNs have higher accuracy in wind speed prediction than other supervised learning methods. In addition, LSTM is more suitable for expressing wind speeds. To construct an optimal ANN architecture and to improve predictability, Hu et al. [22] proposed a method combining ensemble empirical mode decomposition, LSTM, and Bayesian optimization.

Considering different design variables, the optimization process of blades can be categorized into three groups: (1) airfoil optimization [19,52,59], (2) geometry optimization [61,66,67], and (3) structure optimization [67]. For simplification, such objectives (e.g., AEP, C_p, and coefficient of energy) could be expressed by explicit formulas. However, detailed fatigue damage may not be evaluated at specific locations on WT blades (e.g., erosion at the blade tips) [68]. However, CFD and BEM are considered one of the most popular methods for evaluating aerodynamic performance before the optimization process [61]; thus, obtaining the external stress. For example, Mishal et al. aimed to maximize the AEP within the minimum mass, which was evaluated by the BEM, by changing the blades' geometry coefficient (chord distribution, twist angle distribution, tip-speed ratio). The surrogate model was utilized to accelerate the evaluation speed and was always linked to supervised learning, such as an ANN [64] or a CNN [15,27]. Then, optimization was carried out for a higher design performance in the design space, which was always done by using a genetic algorithm (GA) or particle swarm optimization (PSO). Recently, RL has attracted more attention due to its superior capacity in solving multiobject functions and online learning. Jia et al. [52] constructed an "offline-online learning" RL framework for twist angle distribution optimization. In the stage of offline, the agent was trained and evaluated by CFD, which guided twist angle searching at different wind speeds. Table 21.4 shows the optimization application in WT blades categorized by methods, optimization goals, optimization variables, and data sources.

TABLE 21.4 Design and optimization methods for WT blades.

References	Optimization Methods	Objective function	Optimization Type	Data Source for optimization
[52]	RL	C_p	Airfoil	CFD, ML
[19]	GA	L/D	Airfoil	official data for S809 airfoil
[61]	SQP	AEP, IM	Geometry	BEM
[59]	RL	L/D	Airfoil	CFD
[15]	GD	Load	Geometry	CFD
[66]	NSGA-II	L/D, lift coefficient	Geometry	CFD
[67]	Differential Evolution	Load, Mass	Structural	CFD

21.3.2 Towers

WT towers support the rotor, blade, and nacelle all of which cause a complex load. As the size of the WT increases, the WT towers are required to have a greater thickness and diameter to achieve sufficient strength and bending stiffness [69]. Moreover, the material and manufacturing cost contains 15%−20% of the total cost. The WT towers can be divided into onshore structures and offshore structures. Both of them have been investigated for decades.

Design optimization for the tower should ensure an optimal construction cost for structural safety and functionality. Hence, the objective function can be the stiffness-to-mass ratio, minimum weight, minimum vibration, etc. [70]. When defining the constraints, the strength requirements under extreme loads (e.g., maximum principal stress, horizontal displacement on the top, etc.) need to be considered. Most of the design parameters are geometric parameters, such as diameter, thickness, and height due to the simple structure of the tower [71]. When considering offshore structures, parameters, such as submerged depth should also be included. To analyze the variation in towers, Taddei et al. [72] indicated that FEA could also be applied in shallow soil considering soil-structure interactions. The most frequent ML-based method is ANN, which is utilized to improve the computational speed with minimum accuracy loss. For example, Qiu et al. [73] utilized the ANN as a surrogate model improved by GA for damage degree to alternate the mathematical finite element method (FEM) calculations in frequency prediction. Lee et al. [74] used the backpropagation ANN as a neuro-response surface to surrogate the stress analysis result of FEM, which was utilized to optimize the geometric structures. Dai et al. [75] optimized the structural parameters of a WT tower by establishing a multiobjective optimization model, where the relationship between the design variable and stress, top displacement, and natural frequency was based on a backpropagation ANN. Research on ML-based tower design and optimization is summarized in Table 21.5, including optimization methods, the analysis target, and the simulation methods/tools.

21.3.3 Generators

During the wind energy capture process, the blades and rotors of WTs transfer wind energy to rotational mechanical energy, while the generators convert the rotational mechanical energy of the blade into electrical energy. The generator may be based on a doubly fed induction generator (DFIG) [18] or a permanent magnet synchronous generator (PMSG) [76]. In a real wind field, the actual wind speed varies, which considerably influences energy capturing [77]. To maximize the efficiency of the system with the minimum installation return, maximum power point tracking (MPPT) becomes one of the key research points in the wind energy conversion system [78].

The ML-based method is widely used in design for optimal power extraction, which is shown in Table 21.6, including its algorithm used, the data and variables applied, and its applications. For example, Alizadeh et al. [79] introduced a wavelet neural network to dynamically optimize coefficients of the proportional-integral (PI) controller for a PMSG. Meanwhile, Hong et al. [80] developed a BPNN with a modified PSO to optimize the PI parameter of a PMSG, which could minimize the loss of a MPPT. However, in terms of achieving nonlinear control, an ANN-based RL has been applied for a PMSG to achieve MPPT, which the agent learnt from existing simulation results by the SimPower Systems [56]. Wei et al. [81] introduced a model-free q-learning algorithm to train the agent with simulation data by PSCAD/EMTDC, and then optimized the rotor speed to achieve fast MPPT tracking. The ML-based method was also introduced in wind speed prediction, which could be efficient in finding the goal power points. For example, Ali et al.

TABLE 21.5 Design and optimization methods for WT towers.

References	Surrogate model/optimization methods	Analysis targets	Simulation methods/ tools
[73]	ANN, GA	Frequency	CFD
[74]	ANN, NSGA-II	Stress	Ansys
[75]	BP-ANN, NSGA-II	Stress, top displacement, and natural frequency	BEM, ANSYS

TABLE 21.6 Design and optimized methods for WT generators.

References	Methods	Data/variables	Applications
[79]	WNN	Power output, current	Coefficient of PI controller optimization
[80]	BPNN, modified-PSO	Rotational speed, power, power coefficient	Coefficient of PI controller optimization
[56]	ANN, RL	Rotor speed	MPPT
[81]	Q-learning	Rotor speed	MPPT
[18]	ANN, PSO	Rotor speed	Wind speed prediction

[18] applied an ANN to estimate the wind speed, while a PSO was used to optimize the PI controller against the classical controller, thus tracking the available MPPT at varying wind speeds for the DFIG.

21.3.4 Other mechanical and electrical components

Many other mechanical and electrical components are installed in WTs, such as gearboxes, shafts, hub castings, pitch mechanisms, nacelles, wind vanes, anemometers, etc. Even though many WTs are located onshore, their components still need to be frequently inspected and repaired throughout the lifespan of 15−20 years [60]. The ML-based method is also widely applied in these components. However, most of the ML-based methods are applied in detecting the failures that occur in WTs instead of design and optimization, (i.e., CM techniques [4]), including the CMS data-driven ML-based CM [82], ML-based maintenance management [83], and ML-based fatigue pattern recognition [84]. ML-based methods are utilized in the CM due to their capability to associate nonlinear and high-dimensional sensor data and features, which are widely used when indicating the signal of faults.

21.4 Conclusions

Various intelligent design and optimization methods have been applied for WT systems. This chapter summarizes the research work of ML applied in designing and optimizing WTs, which are categorized into three groups, supervised learning-based methods, unsupervised learning-based methods, and RL-based methods. Some concluding remarks on these three groups and their applications are provided below:

1. Supervised learning: The supervised learning methods of ML mostly act as surrogate models in the design and optimization of WTs, which can reduce the comprehensive calculation time in a physics-based analysis. The most commonly used method is the ANN and its derivation approaches.
2. Unsupervised learning: The applications of unsupervised learning in WT design and optimization can be grouped into dimensionality reduction and clustering. In detail, the performance prediction is established quickly and accurately by reducing the number of design variables or clustering similar features in the data.
3. RL: The RL method could be utilized to replace the traditional design and optimization process of WTs, which demonstrates its superiority in optimization and decision-making problems. The RL method can also address complicated problems, such as high-dimensional continuous optimization.

4. Applications: The most studied components of WT design and optimization are blades, generators, and foundations, which are carried out by combining ML-based methods and traditional optimization methods.

Considering the related research, intelligent design and optimization methods have proven to be efficient tools in the design and optimization of WTs. However, these methods can still be improved. For example, the prediction accuracy of some design and optimization methods using a physics-based model can be further improved by associating it with virtually generated training data, which may be realized through digital twin technology. Additionally, the uncertainty is not considered in the many existing intelligent design and optimization methods for WTs. To facilitate the reliable design of WTs, future work needs to investigate reliability-based design optimization by considering various uncertainties and using intelligent methods and algorithms.

Acknowledgments

This work is supported by the National Natural Science Foundation of China (Grant No. 52275275, 51905475, 52111540267), the Zhejiang Provincial Natural Science Foundation of China (Grant No. LZ22E050006), and the State Key Laboratory of Fluid Power and Mechatronic Systems (Grant No. SKLoFP_ZZ_2102).

Nomenclacture

AEP	Annual energy production
ANN	Artificial neural network
CFD	Computational fluid dynamics
CM	Condition monitoring
CNN	Convolutional neural network
C_p	Power coefficient
DRL	Deep reinforcement learning
DDPG	Deep deterministic policy gradient
DFIG	Doubly fed induction generator
DPG	Deterministic policy gradient
DQN	Deep Q-network
FEA	Finite element analysis
FEM	Finite element method
GAN	Generative adversarial networks
GA	Genetic algorithm
IM	Inertia moment
LSTM	Long short-term memory
L/D	Lift-drag ratio
ML	Machine learning
MPPT	Maximum power point tracking
PMSG	Permanent magnet synchronous generator
PSO	Partical swarm optimization
RL	Reinforcement learning
RNN	Recurrent neural network
SCADA	Supervisory Control And Data Acquisition
SOM	Self-organizing map
WT	Wind turbine
VAE	Variational autoencoder

References

[1] Bhattacharya M, et al. The effect of renewable energy consumption on economic growth: evidence from top 38 countries. Appl Energy 2016;162:733−41.
[2] Hernandez-Estrada E, et al. Considerations for the structural analysis and design of wind turbine towers: a review. Renew Sustain Energy Rev 2021;137:110447.
[3] Leimeister M, Kolios A, Collu M. Development of a framework for wind turbine design and optimization. Modelling 2021;2(1):105−28.
[4] Marugán AP, et al. A survey of artificial neural network in wind energy systems. Appl Energy 2018;228:1822−36.

[5] Chan CM, Bai H, He D. Blade shape optimization of the Savonius wind turbine using a genetic algorithm. Appl Energy 2018;213:148–57.
[6] Pagnini LC, Burlando M, Repetto MP. Experimental power curve of small-size wind turbines in turbulent urban environment. Appl Energy 2015;154:112–21.
[7] Sinha Y, Steel JA. Failure prognostic schemes and database design of a software tool for efficient management of wind turbine maintenance. Wind Eng 2015;39(4):453–77.
[8] Obdam T, Rademakers L, Braam H. Flight leader concept for wind farm load counting and performance assessment. In: European Wind Energy Conference. Citeseer; 2009.
[9] Stetco A, et al. Machine learning methods for wind turbine condition monitoring: a review. Renew Energy 2019;133:620–35.
[10] Gómez CQ, et al. Big data and web intelligence for condition monitoring: a case study on wind turbines. Handbook of Research on Trends and Future Directions in Big Data and Web Intelligence. IGI Global; 2015. p. 149–63.
[11] García Márquez FP, Segovia Ramírez I, Pliego Marugán A. Decision making using logical decision tree and binary decision diagrams: a real case study of wind turbine manufacturing. Energies 2019;12(9):1753.
[12] Clifton A, et al. Using machine learning to predict wind turbine power output. Environ Res Lett 2013;8(2):024009.
[13] Jordan MI, Mitchell TM. Machine learning: trends, perspectives, and prospects. Science 2015;349(6245):255–60.
[14] Hastie T, et al. The elements of statistical learning: data mining, inference, and prediction, 2. Springer; 2009.
[15] Du Q, et al. Aerodynamic design and optimization of blade end wall profile of turbomachinery based on series convolutional neural network. Energy 2022;244:122617.
[16] Raul V, Leifsson L. Surrogate-based aerodynamic shape optimization for delaying airfoil dynamic stall using Kriging regression and infill criteria. Aerosp Sci Technol 2021;111:106555.
[17] Du X, He P, Martins JR. Rapid airfoil design optimization via neural networks-based parameterization and surrogate modeling. Aerosp Sci Technol 2021;113:106701.
[18] Ali YA, Ouassaid M. Advanced control strategy of dfig based wind turbine using combined artificial neural network and PSO algorithm. In: 2020 International conference on electrical and information technologies (ICEIT). IEEE; 2020.
[19] Wen H, et al. A new optimization method of wind turbine airfoil performance based on Bessel equation and GABP artificial neural network. Energy 2019;187:116106.
[20] Tang B, et al. Fault diagnosis for a wind turbine transmission system based on manifold learning and Shannon wavelet support vector machine. Renew Energy 2014;62:1–9.
[21] Zhang L, et al. Ice detection model of wind turbine blades based on random forest classifier. Energies 2018;11(10):2548.
[22] Hu W, et al. Toward a digital twin: time series prediction based on a hybrid ensemble empirical mode decomposition and BO-LSTM neural networks. J Mech Design 2021;143(5).
[23] Li S, et al. Comparative analysis of regression and artificial neural network models for wind turbine power curve estimation. J Sol Energy Eng 2001;123(4):327–32.
[24] Ti Z, Deng XW, Yang H. Wake modeling of wind turbines using machine learning. Appl Energy 2020;257:114025.
[25] Sessarego M, et al. Design optimization of a curved wind turbine blade using neural networks and an aero-elastic vortex method under turbulent inflow. Renew Energy 2020;146:1524–35.
[26] Sun H, et al. Wind turbine power modelling and optimization using artificial neural network with wind field experimental data. Appl Energy 2020;280:115880.
[27] Wang Y, et al. Dual-convolutional neural network based aerodynamic prediction and multi-objective optimization of a compact turbine rotor. Aerosp Sci Technol 2021;116:106869.
[28] Mardani A, et al. Sustainable and renewable energy: an overview of the application of multiple criteria decision making techniques and approaches. Sustainability 2015;7(10):13947–84.
[29] Ribeiro A, Awruch A, Gomes H. An airfoil optimization technique for wind turbines. Appl Math Model 2012;36(10):4898–907.
[30] Elfarra MA, Sezer-Uzol N, Akmandor IS. NREL VI rotor blade: numerical investigation and winglet design and optimization using CFD. Wind Energy 2014;17(4):605–26.
[31] Su Y, et al. A coordinative optimization method of active power and fatigue distribution in onshore wind farms. Int Trans Elect Energy Syst 2017;27(10):e2392.
[32] Miao J., et al. The bio-objective long term maintenance scheduling for wind turbines considering weather conditions. In: 2018 Prognostics and System Health Management Conference (PHM-Chongqing). IEEE; 2018.
[33] Jin-He W, Xiao-Hong Z, Jian-Chao Z. Optimal maintenance decision for wind turbines based on imperfect maintenance model. Comput Integr Manuf Syst 2019;25(5):1151–60.
[34] Chen W, Chiu K, Fuge MD. Airfoil design parameterization and optimization using bézier generative adversarial networks. AIAA J 2020;58(11):4723–35.
[35] Regier JC, Stark PB. Mini-minimax uncertainty quantification for emulators. SIAM/ASA J Uncertain 2015;3(1):686–708.
[36] Wang Y, Ma X, Qian P. Wind turbine fault detection and identification through PCA-based optimal variable selection. IEEE Trans Sustain Energy 2018;9(4):1627–35.
[37] Muskulus M, Schafhirt S. Design optimization of wind turbine support structures-a review. J Ocean Wind Energy 2014;1(1):12–22.
[38] Grey ZJ, Constantine PG. Active subspaces of airfoil shape parameterizations. AIAA J 2018;56(5):2003–17.
[39] Wang Y, et al. Prediction of wind turbine-grid interaction based on a principal component analysis-long short term memory model. Energies 2018;11(11):3221.
[40] Kingma D.P., Welling M., Auto-encoding variational bayes. arXiv preprint arXiv:1312.6114; 2013.

[41] Goodfellow I, et al. Generative adversarial nets. Adv Neural Inf Process Syst 2014;27.
[42] Yang S, Lee S, Yee K. Inverse design optimization framework via a two-step deep learning approach: application to a wind turbine airfoil. Eng Comput 2022;1–17.
[43] Feijóo MDC, et al. Unsupervised damage detection for offshore jacket wind turbine foundations based on an autoencoder neural network. Sensors 2021;21(10):3333.
[44] Ali M, et al. Probabilistic clustering of wind generators. In: IEEE PES General Meeting. IEEE; 2010.
[45] Yan J, et al. Wind power grouping forecasts and its uncertainty analysis using optimized relevance vector machine. Renew Sustain Energy Rev 2013;27:613–21.
[46] Fahim A, et al. An efficient enhanced k-means clustering algorithm. J Zhejiang Univ-Sci A 2006;7(10):1626–33.
[47] Nie F, et al. Spectral embedded clustering: a framework for in-sample and out-of-sample spectral clustering. IEEE Trans Neural Networks 2011;22(11):1796–808.
[48] Wang W-S, Wang J, Wang K-W. Application of SOM neural network and C means method in load classification. In: Proceedings of the Chinese Society of Universities for Electric Power System and its Automation, 2011.
[49] Liu Y, et al. Clustering methods of wind turbines and its application in short-term wind power forecasts. J Renew Sustain Energy 2014; 6(5):053119.
[50] Lee XY, et al. A case study of deep reinforcement learning for engineering design: application to microfluidic devices for flow sculpting. J Mech Design 2019;141(11).
[51] Long W, et al. Refraction-learning-based whale optimization algorithm for high-dimensional problems and parameter estimation of PV model. Eng Appl Artif Intell 2020;89:103457.
[52] Jia L, et al. A reinforcement learning based blade twist angle distribution searching method for optimizing wind turbine energy power. Energy 2021;215:119148.
[53] Meng F, Bai Y, Jin J. An advanced real-time dispatching strategy for a distributed energy system based on the reinforcement learning algorithm. Renew Energy 2021;178:13–24.
[54] Wang Y, Liu Q, Yu T. A reinforcement learning approach to dynamic optimization of load allocation in AGC system. In: 2009 IEEE Power & Energy Society General Meeting. IEEE; 2009.
[55] Sutton RS, et al. Policy gradient methods for reinforcement learning with function approximation. Adv Neural Inf Process Syst 1999;12.
[56] Wei C, et al. An adaptive network-based reinforcement learning method for MPPT control of PMSG wind energy conversion systems. IEEE Trans Power Electron 2016;31(11):7837–48.
[57] Casas N., Deep deterministic policy gradient for urban traffic light control. arXiv preprint arXiv:1703.09035; 2017.
[58] Qin S, et al. Multi-objective optimization of cascade blade profile based on reinforcement learning. Appl Sci 2020;11(1):106.
[59] Yonekura K, Hattori H. Framework for design optimization using deep reinforcement learning. Struct Multidiscip Optim 2019;60(4):1709–13.
[60] Jiang Z, et al. Structural reliability analysis of wind turbines: a review. Energies 2017;10(12):2099.
[61] Thapa M, Missoum S. Surrogate-based stochastic optimization of horizontal-axis wind turbine composite blades. Struct Multidiscip Optim 2022;65(2):1–18.
[62] Hu W, Choi K, Cho H. Reliability-based design optimization of wind turbine blades for fatigue life under dynamic wind load uncertainty. Struct Multidiscip Optim 2016;54(4):953–70.
[63] Wais P. A review of Weibull functions in wind sector. Renew Sustain Energy Rev 2017;70:1099–107.
[64] Malik P, et al. A review on ANN based model for solar radiation and wind speed prediction with real-time data. Arch Computat Methods Eng 2022;1–19.
[65] Ramasamy P, Chandel S, Yadav AK. Wind speed prediction in the mountainous region of India using an artificial neural network model. Renew Energy 2015;80:338–47.
[66] Ju Y, Zhang C. Multi-point robust design optimization of wind turbine airfoil under geometric uncertainty. Proc Inst Mech Eng A J Power Energy 2012;226(2):245–61.
[67] Leloudas SN, et al. A robust methodology for the design optimization of diffuser augmented wind turbine shrouds. Renew Energy 2020;150:722–42.
[68] Hu W, et al. A computational framework for coating fatigue analysis of wind turbine blades due to rain erosion. Renew Energy 2021;170:236–50.
[69] Chen J, Li J, He X. Design optimization of steel–concrete hybrid wind turbine tower based on improved genetic algorithm. Struct Des Tall Spec Build 2020;29(10):e1741.
[70] Oest J, et al. On gradient-based optimization of jacket structures for offshore wind turbines. Wind Energy 2018;21(11):953–67.
[71] Bukala J, et al. Evolutionary computing methodology for small wind turbine supporting structures. Int J Adv Manuf Technol 2019; 100(9):2741–52.
[72] Taddei F, Butenweg C, Klinkel S. Parametric investigation of the soil–structure interaction effects on the dynamic behaviour of a shallow foundation supported wind turbine considering a layered soil. Wind Energy 2015;18(3):399–417.
[73] Qiu B, et al. Research on the damage prediction method of offshore wind turbine tower structure based on improved neural network. Measurement 2020;151:107141.
[74] Lee J-C, Shin S-C, Kim S-Y. An optimal design of wind turbine and ship structure based on neuro-response surface method. Int J Nav Arch Ocean Eng 2015;7(4):750–69.
[75] Dai J, et al. Structural parameters multi-objective optimisation and dynamic characteristics analysis of large-scale wind turbine towers. Aust J Mech Eng 2018;16(1):43–9.

[76] Yang B, et al. Passivity-based sliding-mode control design for optimal power extraction of a PMSG based variable speed wind turbine. Renew Energy 2018;119:577–89.
[77] Yang B, et al. Nonlinear maximum power point tracking control and modal analysis of DFIG based wind turbine. Int J Electr Power Energy Syst 2016;74:429–36.
[78] Jaramillo-Lopez F, Kenne G, Lamnabhi-Lagarrigue F. A novel online training neural network-based algorithm for wind speed estimation and adaptive control of PMSG wind turbine system for maximum power extraction. Renew Energy 2016;86:38–48.
[79] Alizadeh M, Kojori SS. Augmenting effectiveness of control loops of a PMSG (permanent magnet synchronous generator) based wind energy conversion system by a virtually adaptive PI (proportional integral) controller. Energy 2015;91:610–29.
[80] Hong C-M, Chen C-H, Tu C-S. Maximum power point tracking-based control algorithm for PMSG wind generation system without mechanical sensors. Energy Convers Manag 2013;69:58–67.
[81] Wei C, et al. Reinforcement-learning-based intelligent maximum power point tracking control for wind energy conversion systems. IEEE Trans Ind Electron 2015;62(10):6360–70.
[82] Lu B, et al. A review of recent advances in wind turbine condition monitoring and fault diagnosis. In: 2009 IEEE Power Electronics and Machines in Wind Applications. IEEE; 2009.
[83] Kusiak A, Li W. The prediction and diagnosis of wind turbine faults. Renew Energy 2011;36(1):16–23.
[84] Márquez FPG, Muñoz JMC. A pattern recognition and data analysis method for maintenance management. Int J Syst Sci 2012;43(6):1014–28.

This page intentionally left blank

Chapter 22

Wind and hybrid power systems: reliability-based assessment

Serkan Eryilmaz[1] **and Yilser Devrim**[2]

[1]Department of Industrial Engineering, Atilim University, Ankara, Turkey, [2]Department of Energy Systems Engineering, Atilim University, Ankara, Turkey

22.1 Introduction

Energy resources have been one of the most important research topics of humanity for centuries. People's interest in energy sources and their needs has gradually increased after the industrial revolution and has continued until today [1]. Today, most of the energy needs are provided by fossil fuels. In the past years, the economic viability of fossil fuels, the development of production systems, and due to their widespread use, its use has been at the highest level. The use of fossil fuels, which started with coal, has become more and more common with the addition of oil and natural gas. However, the oil crisis that broke out towards the end of the 20th century reduced the confidence in these resources. The gradual decrease of fossil fuel resources emerges as a serious problem. In addition to all these, the negative effects of fossil fuels on the environment, global warming, and environmental pollution have increased the use of renewable energy. Renewable energy sources have had great importance in recent years because they do not have a depletion problem and can be used in many regions around the world [2].

Clean energy sources such as solar, wind, geothermal energy, biomass, and hydro energy are important renewable energy sources. However, one of the important drawbacks of renewable energy resources is their interrupted nature [3]. Some renewable energy sources can complement each other, and multisource alternative energy systems have great potential to deliver higher quality and greater energy production. The geographical conditions and climatic conditions depending on the seasons influence electricity generation from wind and solar power [4]. For example, the inability to produce electricity at night or on cloudy days significantly affects the generation of electricity from solar energy. Accordingly, when the power of the wind is too low to support a wind turbine (WT), the required power cannot be produced. For this reason, a second energy system is used as a complement to solar and wind energy to ensure the reliability and continuity of the system.

Reliability of a power system, in a general sense, is a measure of the ability of the system to generate and supply electrical energy [5]. For a power system, the reliability has two main parts which are system adequacy and system security parts. The system adequacy is related to the existence of sufficient facilities within the system to satisfy the load demand. The system security aspect is concerned with the ability of the system to respond to the disturbances arising within the system.

In this chapter, wind and hybrid power systems are analyzed from the reliability point of view. In particular, the stochastic models that are necessary for reliability assessment of wind and hybrid power systems are presented, and a linkage between these stochastic models and well-known reliability indices is established.

The chapter is organized as follows. In Section 22.2, the stochastic models and reliability evaluation for the wind power systems are presented. Section 22.3 involves hybrid power systems. Finally, in Section 22.4, summary and some pointers for future are presented.

Wind Energy Engineering. DOI: https://doi.org/10.1016/B978-0-323-99353-1.00006-2

22.2 Wind power systems

A reliability model for a WT generator is based on three main factors which affect the output of the WT [6]:

1. The random behavior of the wind speed at the location which is modeled by a proper probability distribution.
2. The functional relationship between wind speed and power output of the WT.
3. The Forced-Outage-Rate (FOR) or equivalently the unreliability of the WT generator.

Assume that the random nature of the wind speed is represented by a random variable V. For given $V = v$, the functional relationship between the wind speed and the power output of the WT is characterized by $g(v)$, and the long-term reliability of the WT is denoted by p. Note that $1 - p$ gives the FOR of the WT.

Thus, the stochastic model that describes the long-term performance, that is the output of the WT can be represented as

$$P_{WT} = X. \quad g(V),$$

where X denotes the binary state of the WT such that $p = P\{X = 1\}$. The distribution of the WT output P_{WT} has been studied in the literature under various assumptions, see, for example, Giorsetto and Utsurogi [6], Louie and Sloughter [7], Eryilmaz and Devrim [8], Kan et al. [9]. For a given function $g(v)$ that describes the relationship between the wind speed and the WT output, the computation of the probability distribution and other statistical characteristics of the random variable P_{WT} needs the distribution of the wind speed, that is, $F(v) = P\{V \le v\}$ and the value of p. Note that the WT characteristics (cut-in wind speed, rated wind speed, cut-out wind speed, and rated power) are involved by the function $g(v)$. For example, if there is a cubic relationship between the wind speed and WT output, then one of the widely used equations is

$$g(v) = \begin{cases} 0, & v < v_{ci} \text{or} v \ge v_{co}, \\ P_r \dfrac{\left(v^3 - v_{ci}^3\right)}{\left(v_r^3 - v_{ci}^3\right)}, & v_{ci} \le v < v_r, \\ P_r, & v_r \le v < v_{co}, \end{cases} \tag{22.1}$$

where v_{ci}, v_{co}, v_r, and P_r respectively denote cut-in wind speed, cut-out wind speed, rated wind speed values, and rated power of the WT. See, for example, Villanueva and Feijoo [10] for other power curve models.

For a wind farm (WF) that consists of n WTs, the output of the WF is modeled by:

$$P_{WF} = S_n. \quad g(V),$$

where S_n denotes the total number of available WTs within the farm. If the WTs are identical and work independently, then we get:

$$P\{S_n = i\} = \binom{n}{i} p^i (1-p)^{n-i}, \quad i = 0, 1, \ldots, n.$$

In the literature, various methods have been proposed to compute the reliability p of a WT. See, for example, Tavner et al. [11] and Pérez et al. [12].

22.2.1 Stochastic modeling of wind power

The derivation of the probability distribution of the WF output heavily depends on the model of the wind speed distribution. The random variable V may be modeled by either a discrete or continuous probability distribution. First, assume that the distribution $F(v) = P\{V \le v\}$ is continuous. If the relationship between the wind speed and the power output of the WT is described by Eq. (22.1), then as shown by Eryilmaz and Devrim [8],

$$P\{P_{WF} \le x\} = \sum_{i=0}^{n} \binom{n}{i} p^i (1-p)^{n-i} Q_i(x), \tag{22.2}$$

where

$$Q_i(x) = \begin{cases} 0, & if\ x < 0 \\ H_i(x), & if\ 0 \le x \le iP_r \\ 1, & if\ x \ge iP_r, \end{cases}$$

and

$$H_i(x) = 1 - F(v_{co}) + F\left(\left[\frac{x}{iP_r}\left(v_r^3 - v_{ci}^3\right) + v_{ci}^3\right]^{\frac{1}{3}}\right),$$

and $Q_0(x) = 0$ if $x < 0$, and $Q_0(x) = 1$ if $x \geq 0$. In the case when the distribution of the random variable V is described by a discrete probability distribution, Giorsetto and Utsurogi [6] obtained the following expression:

$$P\{P_{WF} \leq x\} = \sum_{l=0}^{n}\sum_{j=1}^{s} u\left(x - l.g\left(\overline{v}_j\right)\right)P\left\{V = \overline{v}_j\right\}\binom{n}{l}p^l(1-p)^{n-l}, \tag{22.3}$$

where s represents the total number of possible states for the wind speed, and $u(x) = 1$ if $x \geq 0$ and $u(x) = 0$ if $x < 0$. The discretization process and determination of the value of s depend on various factors such as wind speed variation and WT characteristics (see, e.g., Ettoumi et al. [13], Shamshad et al. [14], Tang et al. [15]).

It should be noted that in Eqs. (22.2) and (22.3), the WT reliabilities are assumed to be independent of the wind speed. That is, the WT reliabilities are not influenced by the wind speed. The distribution of P_{WF} has been obtained by Kan et al. [9] when there is a correlation between wind speed and WT availability. Under dependence, the random variables X (the state of the WT) and V (wind speed) are no longer independent. Arwade et al. [16] used the following conditional probabilities to define a dependence model between WT reliabilities and wind speed:

$$p_q = P\{X = 1|, V = v\}, \quad v \in \left[v_{q-1}, v_q\right),$$

for $q = 1, 2, \ldots, m$. Under this dependence model, a WT has a different frequency of operation for each wind speed interval.

Manifestly, the probability distribution of the wind speed plays an important role in computing the probability distribution of P_{WF}. The wind speed distribution can be estimated based on the data collected at the corresponding location. Indeed, in the literature, many works have been published on wind speed probability distribution estimation. Among the others, Weibull, Gamma, and Birnbaum-Saunders distributions have been used to model wind speed at various locations (see, e.g., Chang [17], Wais [18], Mohammadia et al. [19]).

22.2.2 Reliability-based assessment

There are various reliability indices to evaluate the performance of power systems. In the following, we present definitions of well-known reliability measures:

Loss-of-Load Probability (LOLP)

For a given load L and a WF that has power output P_{WF}, the *LOLP* is defined as follows:

$$LOLP = P\{P_{WF} < L\}.$$

Depending on the wind speed modeling, the *LOLP* can be computed either from Eqs. (22.2) or (22.3).

Loss-of-Load Expectation (LOLE)

LOLE is defined to be the expected period during which the load demand is greater than the available power generation. Let t be the equally sized time step (e.g., hour, day), T be the total number of time steps, and L_t be the load demand at time period t.

$$LOLE = \sum_{t=1}^{T} P\left\{P_{WF}^t < L_t\right\}.$$

If $L_t = L$ for all t, then $LOLE = T.LOLP$.

Expected Energy not Supplied (EENS)

EENS is the expected energy that will not be supplied when the load exceeds the available generation. It is defined by the following expected value:

$$EENS = E(\max(L - P_{WF}, 0)).$$

The higher the value of *EENS* the less reliable the power system. For a given load, based on *EENS*, the Energy Index of Reliability (EIR) is calculated from

$$EIR = 1 - \frac{EENS}{L}.$$

The abovementioned reliability indices have been widely used in reliability and performance evaluation, and optimization of power systems. Reliability-based selection of WTs for a specific WF has been discussed by computing reliability indices such as LOLP, LOLE and EENS for selected WF compositions (see, e.g., Fotuhi-Firuzabad and Dobakhshari [20], Nemes and Munteanu [5], Mohiley and Moharil [21]). Volkanovski et al. [22] proposed a method for the optimization of maintenance scheduling of generating units in power system by minimizing the LOLE. Wen et al. [23] presented a review on reliability assessment of wind power. Dobakhshari and Fotuhi-Firuzabad [24] presented an analytical approach for the reliability modeling of large WFs using LOLE. Karki et al. [25] presented reliability analysis considering wind and hydropower coordination using LOLE. Mabel et al. [26] investigated the effect of increasing the hub height of wind energy conversion systems using LOLE. Volkanovski [27] used LOLP to investigate the impact of the introduction of the wind generating units in the power system. Beyza et al. [28] studied the performance of interconnection lines by measuring their impacts on the main reliability indicators LOLP, LOLE and EENS of interconnected power systems.

Very recently, Eryilmaz and Navarro [29] presented general theoretical results to compare performance of WFs. In particular, they have obtained conditions on WT characteristics and availability values of WTs to compare WTs and WFs in terms of *EENS*. Consider two WF compositions which are denoted by WF1 and WF2. The WF1 consists of n_1 identical WTs having common availability p_1, and turbine characteristics $v_{ci,1}$, $v_{co,1}$, $v_{r,1}$ and $P_{r,1}$, and the WF2 consists of n_2 identical WTs having common availability p_2, and turbine characteristics $v_{ci,2}$, $v_{co,2}$, $v_{r,2}$ and $P_{r,2}$. Assume that the relationship between the wind speed and the power output of the WT is described by (1) and $v_{co,1} = v_{co,2}$, $P_{r,1} = P_{r,2}$, $p_1 = p_2$. As shown by Eryilmaz and Navarro [29], if $v_{ci,1} \leq v_{ci,2}$ and $v_{r,1}^3 - v_{ci,1}^3 \leq v_{r,2}^3 - v_{ci,2}^3$, then WF1 is preferred to WF2 with respect to *EENS*. That is, the WF1 has a smaller *EENS* value.

Eryilmaz and Navarro [29] proved the following Theorem to compare the power outputs of two different WF compositions.

Theorem 1.: Let $v_{co,1} = v_{co,2}$, $P_{r,1} = P_{r,2}$. For $n_1 \geq n_2$, if the following three conditions hold true, then $P_{WF1} \geq_{st} P_{WF2}$.

a.
$(1-p_1)^{n_1} \leq (1-p_2)^{n_2}$,

b.
$v_{ci,1} \leq v_{ci,2}$,

c.
$v_{r,1}^3 - v_{ci,1}^3 \leq v_{r,2}^3 - v_{ci,2}^3$. In Theorem 1, $\geq_{st}$ represents usual stochastic ordering and the relationship between the wind speed and the power output of the WT is described by (1). A random variable X is stochastically greater than the random variable Y if $P\{X > x\} \geq P\{Y > x\}$ for all x, and this relation is denoted by $X \geq_{st} Y$.

As a direct consequence of Theorem 1, for two WFs that are installed at the same location, if $v_{co,1} = v_{co,2}$, $P_{r,1} = P_{r,2}$ and $n_1 \geq n_2$, and (a)−(c) hold true, then

$$P\{P_{WF1} > L\} \geq P\{P_{WF2} > L\}$$

which implies that LOLP for WF1 is smaller than the LOLP of WF2. That is WF1 is more reliable in terms of LOLP.

As it is seen, the reliability-based comparisons among possible WF compositions heavily depend on WT characteristics and reliability values of WTs. The reliability-based comparison results are potentially useful to make decision about the optimal choice of WF composition before installation of the WF at a specific site.

22.3 Hybrid power systems

Consider a hybrid power system that consists of n WTs and a photovoltaic system (PVS) that has a certain surface area. The power output of such a hybrid system can be defined as

$$P_h = S_n. \quad g(V) + Y.P_{PV},$$

where $P_{PV} = S\eta_{PV}A_{PV}$ is the power produced by the PVS, A_{PV} denotes PV array surface area (m^2), η_{PV} is the efficiency of the PVS, and S is random variable that represents solar irradiation (kw/m^2). Y is a binary random variable taking values "0" and "1," and the availability of the PVS is $r = P\{Y = 1\}$.

The cumulative distribution of the random variable P_h has been obtained by Eryilmaz et al. [30] as a function of wind speed and solar irradiation distributions, and reliability values p and r:

$$\begin{aligned} P\{P_h \le x\} &= \sum_{i=1}^{n} \binom{n}{i} p^i (1-p)^{n-i} r K_i(x) \\ &+ \sum_{i=1}^{n} \binom{n}{i} p^i (1-p)^{n-i} (1-r) Q_i(x) \\ &+ (1-p)^n r R(x) + (1-p)^n (1-r), \end{aligned} \tag{22.4}$$

where

$$R(x) = P\{P_{PV} \le x\} = P\left\{S \le \frac{x}{\eta_{PV}.\ A_{PV}}\right\} = G\left(\frac{x}{\eta_{PV}.\ A_{PV}}\right),$$

and

$$K_i(x) = \begin{cases} 0, if \quad x < 0 \\ \int_0^{min\left(\frac{x}{\eta_{PV}A_{PV}}, 1\right)} Z_F(x,s,i) \quad dG(s), if \quad 0 \le x < iP_r \\ \int_{\frac{x-iP_r}{\eta_{PV}A_{PV}}}^{min\left(\frac{x}{\eta_{PV}A_{PV}}, 1\right)} Z_F(x,s,i) \quad dG(s) + G\left(\frac{x-iP_r}{\eta_{PV}A_{PV}}\right), \quad if \quad iP_r \le x < \eta_{PV}A_{PV} + iP_r \\ 1, \quad if x \ge \eta_{PV}A_{PV} + iP_r, \end{cases}$$

where

$$Z_F(x,s,i) = 1 - F(v_{co}) + F\left(\left[\frac{x-\eta_{PV}A_{PV}}{iP_r}\left(v_r^3 - v_{ci}^3\right) + v_{ci}^3\right]^{\frac{1}{3}}\right).$$

As expected, the probability distribution of the hybrid power system depend on both the probability distribution of the wind speed $F(v) = P\{V \le v\}$ and the probability distribution of the solar irradiation $G(s) = P\{S \le s\}$. It should be noted that the random variables V and S are assumed to be independent and have continuous probability distributions in deriving Eq. (22.4). To compute the probability distribution of P_h and related reliability indices for the hybrid power system, both wind speed and solar irradiation distributions, and reliabilities of WTs and PVS, that is p and r must be known.

Eryilmaz et al. [30] have also obtained the following expression for the *EENS* of the hybrid power system.

$$EENS = L - \int 0\min(L, P_{hmax})P(P_h \ge u)du, \tag{22.5}$$

where P_{hmax} is the maximum power generated by the hybrid system. Eq. (22.5) is alternative to the *EENS* equation that has been obtained by Tina et al. [31].

22.4 Concluding remarks

As it has been pointed out throughout the chapter, the performance and reliability of wind and hybrid power systems depend on many internal and external factors. Thus, a robust reliability evaluation should consider these factors. The calculation of reliability indices needs the theoretical probability distribution of the power produced by the system. Therefore, the reliability-based assessment of power systems requires the derivation of this distribution which is in fact a probabilistic problem.

The assumptions of the stochastic model for the power output of the system heavily affect the values of reliability indices *LOLP, LOLE* and *EENS*. Although the assumption of independence between wind speed and WT availability is

mathematically more tractable, the ignorance of the dependence between wind speed and WT availability may result in a significant error in reliability evaluation. Indeed, as pointed out by Nguyen et al. [32], although the higher speed of wind within cut-in and cut-out speed produces higher power output, it also decreases the reliability of WTs. Therefore, the future works should focus more on the case of dependence. Another important assumption is on the independence between wind speed and solar irradiation. Manifestly, at a certain location, there might be statistical dependence between wind speed and solar irradiation. Such a dependence may also have an effect on the reliability evaluation of hybrid power systems.

References

[1] Kolar JL. Alternative energy technologies. Env Qual Manag 2000;10:45–54.
[2] Nehrir MH, et al. A review of hybrid renewable/alternative energy systems for electric power generation: configurations, control, and applications. IEEE Trans Sustain Energy 2011;2:392–403.
[3] Devrim Y, Bilir L. Performance investigation of a wind turbine–solar photovoltaic panels–fuel cell hybrid system installed at İncek region—Ankara. Turk Energy Convers Manag 2016;126:759–66.
[4] Degeilh Y, Singh C. A quantitative approach to wind farm diversification and reliability. Int J Electr Power Energy Syst 2011;33:303–14.
[5] Nemes C, Munteanu F. Optimal selection of wind turbine for a specific area. 12th Int Conf Optim Electr Electr Equip 2010;1224–9.
[6] Giorsetto P, Utsurogi KF. Development of a new procedure fo reliability modeling of wind turbine generators. IEEE Trans Power Appar Syst 1983;PAS-102:134–43.
[7] Louie H, Sloughter JM. Probabilistic modeling and statistical characteristics of aggregate wind power. Large Scale Renewable Power Generation Green Energy Technol 2014;19–51.
[8] Eryilmaz S, Devrim Y. Theoretical derivation of wind plant power distribution with the consideration of wind turbine reliability. Reliab Eng Syst Saf 2019;185:192–7.
[9] Kan C, Devrim Y, Eryilmaz S. On the theoretical distribution of the wind farm power when there is a correlation between wind speed and wind turbine availability. Reliab Eng Syst Saf 2020;203:107115.
[10] Villanueva D, Feijoo A. A review on wind turbine deterministic power curve models. Appl Sci 2020;10:4186.
[11] Tavner PJ, Xiang J, Spinato F. Reliability analysis for wind turbines. Wind Energy 2007;10:1–18.
[12] Pérez JMP, Márquez FPG, Tobias A, Papaelias M. Wind turbine reliability analysis. Renew Sustain Energy Rev 2013;23:463–72.
[13] Ettoumi FY, Sauvageot H, Adane A-E-H. Statistical bivariate modelling of wind using first-order Markov chain and Weibull distribution. Renew Energy 2003;28:1787–802.
[14] Shamshad A, Bawadi MA, Hussin W, Majid TA, Sanusi SAM. First and second order Markov chain models for synthetic generation of wind speed time series. Energy 2005;30:693–708.
[15] Tang J, Brouste A, Tsui KL. Some improvements of wind speed Markov chain modeling. Renew Energy 2015;81:52–6.
[16] Arwade SR, Lackner MA, Grigoriu MD. Probabilistic models for wind turbine and wind farm performance. J Sol Energy Eng 2011;133.
[17] Chang TP. Performance comparison of six numerical methods in estimating weibull parameters for wind energy application. Appl Energy 2011;32:88–272.
[18] Wais P. Two and three-parameter weibull distribution in available wind power analysis. Renew Energy 2017;32:103–15.
[19] Mohammadia K, Alavi O, McGowana JG. Use of Birnbaum–Saunders distribution for estimating wind speed and wind power probability distributions. Rev Energy Convers Manage 2017;32 143–109.
[20] Fotuhi-Firuzabad M, Dobakhshari AS. Reliability-based selection of wind turbines for large-scale wind farms. Int J Electr Comput Eng 2009;3:52–8.
[21] Mohiley AU, Moharil RM. Selection of wind generators for optimal utilization of wind energy using reliability constraint. Third Int Conf Adv Comput Commun 2013;367–71.
[22] Volkanovski A, Mavko B, Bosevski T, Causevski A, Čepin M. Genetic algorithm optimisation of the maintenance scheduling of generating units in a power system. Reliab Eng Syst Saf 2008;93:757–67.
[23] Wen J, Zheng Y, Donghan F. A review on reliability assessment for wind power. Renew Sustain Energy Rev 2009;13:2485–94.
[24] Dobakhshari AS, Fotuhi-Firuzabad M. A reliability model for large wind farms for power system adequacy studies. IEEE Trans Energy Convers 2009;24:792–801.
[25] Karki R, Hu P, Billinton R. Reliability evaluation considering wind and hydro power coordination. IEEE Trans Power Syst 2011;25:685–93.
[26] Mabel MC, Raj RE, Fernandez E. Analysis on reliability aspects of wind power. Renew Sustain Energy Rev 2011;15:1210–16.
[27] Volkanovski A. Wind generation impact on electricity generation adequacy and nuclear safety. Reliab Eng Syst Saf 2017;158:85–92.
[28] Beyza J, Gil P, Masera M, Yusta JM. Security assessment of cross-border electricity interconnections. Reliab Eng Syst Saf 2020;201:106950.
[29] Eryilmaz S, Navarro J. A decision theoretic framework for reliability-based optimal wind turbine selection. Reliab Eng Syst Saf 2022;221:108291.
[30] Eryilmaz S, Bulanik I, Devrim Y. Reliability based modeling of hybrid solar/wind power system for long term performance assessment. Reliab Eng Syst Saf 2021;209:107478.
[31] Tina G, Gagliano S, Rait S. Hybrid solar/wind power system probabilistic modelling for long-term performance assessment. Sol Energy 2006;80:578–88.
[32] Nguyen N, Almasabi S, Mitra J. Impact of correlation between wind speed and turbine availability on wind farm reliability. IEEE Trans Ind Appl 2019;55:2392–400.

Chapter 23

Multifidelity simulation tools for modern wind turbines

Luca Greco[1], Claudio Testa[1] and Alessandro Bianchini[2]
[1]CNR-INM INstitute of Marine Engineering, Rome, Italy, [2]Department of Industrial Engineering, Università degli Studi di Firenze, Firenze, Italy

23.1 Introduction

Simulation techniques have represented one of the key enablers of recent advancements in wind energy and are pivotal for any future progress. This is mostly due to the fact that wind energy, like very few other sciences, deals with problems involving contemporarily both different disciplines [1] and different scales [2]. For example, the new generation of wind turbines, having blades much longer than 100 m, implies solving flow scales ranging from the order of 10^2 m for the description of atmospheric flows to the order of 10^{-3} m for the blade-flow interaction. This of course makes experiments prohibitive or, at least, extremely costly and not easily replicable; on the other hand, although simulation can help tackle these problems, several issues need to be addressed to overcome this scale mismatch [3].

Focusing here the attention on the blade/turbine level, it is undisputed that up to now engineering methods, like the ubiquitous Blade Element Momentum (BEM) theory, have supported all the repetitive tasks necessary for design, control optimization, load analysis, certification, etc. [4]. BEM methods do represent the *comfort zone* for wind engineers, with almost all turbines available on the market today that have been designed and verified using some form of BEM modeling of their aerodynamics [5]. While modern BEM implementations use a number of correction submodels to account for various phenomena (e.g., dynamic inflow), the theory is still based on assumptions that are challenged by modern and future turbines. Large turbines now even exceed the atmospheric boundary layer for large parts of blade revolution, exposing them to inflow conditions never experienced so far, including non-Gaussian, nonuniform turbulence, atmospheric phenomena like tornadoes, marine jets, etc. Similarly, turbines can operate in yawed conditions to implement wake-steering wind plant control [4]. Furthermore, if aeroelasticity has represented the key enabler to support turbine upscaling, with blades highly curved and flexed in 3D, large rotors are now subject to deformation never experienced before. Indeed, to achieve these sizes, slender and stretched blades are needed. In turn, designing this type of blades without increasing the specific loads was allowed by two main factors, that is, aeroelastic-tailoring [6] and smart blade technology [7]. This latter, in particular, involves the introduction of a variety of aerodynamic appendices (like vortex generators, flaps, etc.), whose simulation is not at hand with simple engineering methods [8]. Finally, Floating Offshore Wind Turbines (FOWTs), representing one of the most effective technologies to reduce human environmental footprint, stretch these challenges further ahead due to the sea motion, continuously modifying the placement of the rotor disk with respect to the wind direction.

Overall, the described scenario shows that, while engineering methods will still provide the backbone of the majority of preliminary design analyses, the fidelity of numerical tools needs to be quickly expanded. Going beyond BEM, while retaining its desirable features and moderate computational cost includes, for example, learning how to generate more accurate 2D airfoil sectional characteristics (e.g., with more effective corrections for unsteady phenomena like dynamic stall), with more focus on dynamic corrections and in general moving toward a full 3D aerodynamic design [9]. In doing that, the use of higher-fidelity techniques, mostly connected to the numerical solution of the Navier−Stokes (NS) equations by using computational fluid dynamics (CFD), is needed.

Advancements in aerodynamic modeling are also required at the rotor level, with more detailed resolution of the flow past the rotors and a more accurate resolution of the blade deformation and the resulting fluid-structure interaction (FSI). A wide range of approaches has been developed to this end, focusing on different targeted accuracy. These are

Wind Energy Engineering. DOI: https://doi.org/10.1016/B978-0-323-99353-1.00013-X

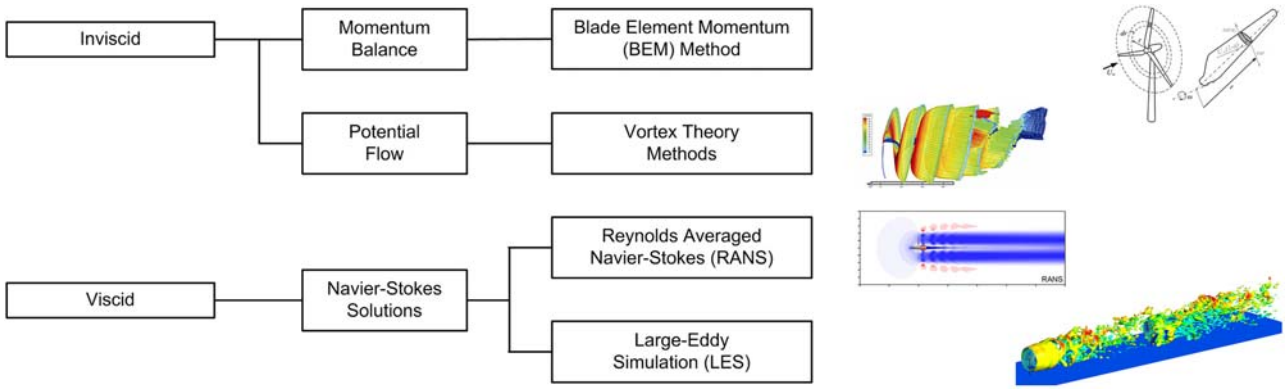

FIGURE 23.1 An overview of the hierarchy of different aerodynamic simulation models for wind turbines.

schematically represented in Fig. 23.1, where the level of fidelity and the computational cost increase from the left upper corner to the right lower one.

Viscid methods differ not only in how the NS equations are approximated and solved but also in the way the rotor is modeled. At the highest end of the fidelity spectrum (corresponding to the lower right corner of Fig. 23.1) are the so-called *blade-resolved* methods, in which the blade is actually modeled, and the flow is solved up to the blade surface. The flourishing of modern high-performance computing architectures and solution methods is bringing such methods finally within reach even. However, high-fidelity methods are extremely computationally expensive because they need to resolve small spatial and temporal scales, at the same time as they represent a very large structure and even larger fluid domain over a long time, spanning many orders of magnitude in both time and space, which hinders their use for repetitive simulations [4]. Indeed, many wind energy problems involve massively iterative tasks, such as the ones necessary for design, the exploration of the solution space, optimization, and uncertainty quantification [10,11]. To this end, there is the need to develop methods that are not only fast, but also accurate enough and with the necessary range of validity. The use of excessively simplified methods can lead to suboptimal solutions and may miss relevant couplings, in turn affecting performance and even safety. Many of the so-called *hybrid methods* are therefore being developed (e.g., [12–14]), in which accurate CFD solution is obtained for the larger scales of the problem (i.e., to solve the flow field past the turbine and in the wake), while the blade-flow interaction is not solved but replaced with equivalent forces inserted in the CFD domain via sources of momentum. These methods are offering unprecedented possibilities, especially in studying the interactions between multiple rotors in a farm.

Similar needs are relevant for the structural dynamics aspects of the problem, in which high-fidelity methods are needed to model generic geometries, exactly accounting for large deflections and couplings induced by the use of anisotropic composite materials (e.g., [15–17]).

In general, for both aerodynamics and structures, it is apparent that wind energy research is going towards the use of a multifidelity approach, that is, a progressively inner integration of higher-fidelity models in automated design frameworks, where they can be combined with those low- or medium-fidelity engineering methods to achieve a suitable balance between efficiency and accuracy. The first one is in fact needed to explore the design space in computational times compatible with industrial processes, while accuracy is necessary to ensure that all relevant couplings among the various fields and design choices are properly captured. As correctly discussed by [4], multifidelity platforms additionally allow the design procedures to zoom in on specific details and zoom out to speed up the calculations where possible. A variable level of fidelity also helps expand the range of design variables. For example, most optimization approaches use existing airfoils (somehow corrected for spanwise effects), while it would be definitely better to perform a full 3D design of the blade.

In this chapter, some perspectives of multifidelity approaches to wind turbine problems are presented, ranging from those connected to airfoil and blade aerodynamics up to structural dynamics. While specific research examples are provided, the aim is to give the reader the flavor of what could be at hand in the near future thanks to this new simulation paradigm.

23.2 Blade aerodynamics

For many years, classical 2D aerodynamics has been based on the assumption of mimicking the airfoil-flow interaction with a set of coefficients able to define an equivalent force exchanged between the two. The use of airfoil polars (i.e., lift,

drag, and moment coefficients) is the basis not only of BEM-based methods, but also of all those higher-fidelity models that do not solve the NS equations in proximity of the blade, like the Lifting Line Free-Vortex Wake (LLFVW) methods or the Actuator Line Model (ALM) [18]. Their importance, however, goes beyond the simple *functioning* of these methods, since they actually represent the most important *tuning knob* determining their accuracy to a large extent. To ensure that aerodynamic coefficients are predictive of the actual behavior of the airfoils when applied on wind turbine blades, two main aspects must be addressed:

1. The original *quality* of the data should be high—While apparently obvious, providing data of high quality for each specific airfoil is not always easy [19]. On the one hand, simulations may not be as accurate as needed; on the other hand, experiments in the wind tunnel are costly, often fail in matching Reynolds similitude due to the chords necessarily much shorter than those of real blades, and can be influenced by a variety of factors that are barely predictable like airfoil surface roughness, turbulence level, etc. [20].
2. A number of submodels are needed to adapt the basic coefficients to the functioning conditions seen onboard wind turbines—These methods, usually based on semiempirical corrections, address several phenomena among which the most relevant are the 3D effects (i.e., the presence of spanwise phenomena altering the individual sectional properties of the blade like tip-effects or rotational effects) [21] and dynamic effects (e.g., the periodic variation of the angle of attack resulting in the dynamic stall or stall delay [22]).

These effects are becoming relevant in many modern wind energy applications, prompting a larger use of genuine 3D approaches for the determination of the polars since the very beginning of the design phase. As discussed, going in this direction using experiments is of course always advisable, but often impractical. On the other hand, the application of blade-resolved CFD simulations, while powerful, is hindered by the high calculation costs, especially when multivariate analyses are needed for a complete characterization of the polars.

Within this context, an interesting example is the use of CFD as a *virtual test rig*. An approach recently proposed by some authors (e.g., [23,24]) is to use high-fidelity simulations for 2D analyses of the airfoils undergoing complex motions to derive more accurate polars than those usually obtained with ubiquitous panel methods for use in engineering simulation tools. For example, in the study of Holst et al. [23], a NACA0021 airfoil has been tested in a laboratory-scale wind tunnel at low Reynolds numbers (around 150,000) using a servo-motor able to make it rotate around 360 degrees with different revolution frequencies. As shown in Fig. 23.2A, this allowed not only to show the impact of a forced transition in static-type polars (dashed vs solid black lines) but also to highlight the onset of the dynamic stall hysteresis cycle (clearly visible in the figure), which was nicely matched by a transitional Unsteady Reynolds Averaged Navier−Stokes CFD simulation (*red line*). Having such experiments at hand is key for example to calibrate appropriately the dynamic stall models available in engineering methods, so as to accurately reproduce the real hysteresis cycle.

Overall, the possibility of tuning high-fidelity models on few experiments and then using them for multivariate analyses has several advantages, including: (1) CFD simulations offer an unprecedented level of flexibility in handling both complex geometries and varying inflow conditions; (2) if properly set, the accuracy is theoretically much higher than that of the conventional panel methods [26]; (3) the time-marching solution of NS equations allows tackling complex

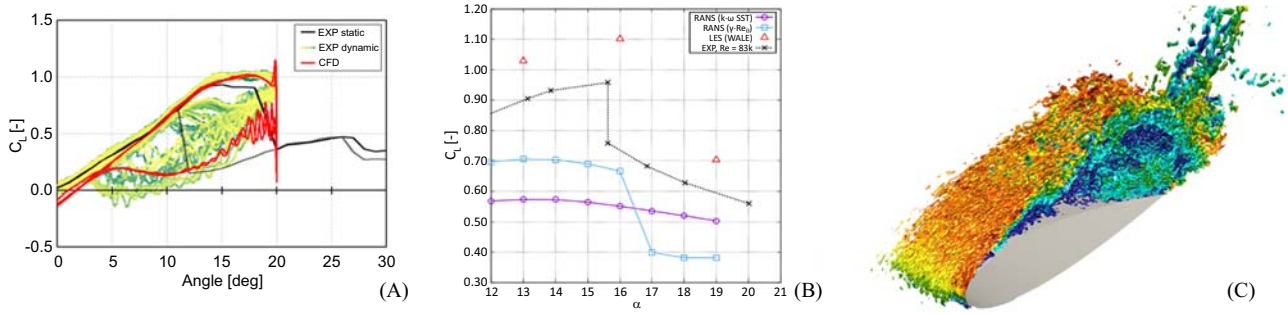

FIGURE 23.2 Examples of multifidelity analyses on the NACA0021 airfoil. (A) Comparison between static and dynamic experiments and CFD simulations; (B) Comparison between experiments and different CFD solution methods [25]; (C) Q-criterion for the LES approach showing flow separation at high angles of attack. *Data from (A) Holst D, Balduzzi F, Bianchini A, Church B, Wegner F, Pechlivanoglou G, et al. 2019 Static and dynamic analysis of a NACA0021 airfoil section at low reynolds numbers based on experiments and computational fluid dynamics. J Eng Gas Turbines Power 141; (B), (C) Giaccherini S, Mariotti F, Pinelli L, Marconcini M, Bianchini A. On the prospects of improving the numerical analysis of symmetric airfoils at low Reynolds numbers and high angles of attack by a LES approach: the case of NACA0021 profile. Ed ATI Associazione Termotecnica Italiana E3S Web Conf. 2020;197:08015.*

function conditions like dynamic change of the angle of attack, as shown in the experiments before; (4) having the entire flow field solved allows for more detailed validation (e.g., against experiments including Particle Image Velocimetry, pressure sensitive paints, photography, etc. [27]). In turn, in some cases, CFD can even allow for a critical revision or an improvement of the experimental setup [23].

While the approach described so far is usually thought for RANS (Reynolds Averaged Navier−Stokes)-based simulations (due to the more favorable ratio between accuracy and cost), there are several cases in which an even higher fidelity is needed. For example, the determination of airfoil performance in deep-stall conditions is key for a variety of applications, from turbines working in yaw, to parked conditions, up to vertical-axis turbines. In these cases, the range of fidelities needed starts from unsteady RANS and extends up to Large Eddy Simulations (LES). For example, Fig. 23.2B reports an analysis [25] on the same NACA0021 airfoil examined in the poststall region of angles of attack. In this case, it is apparent how a RANS approach (even if using a transitional model) is not able to capture the complex flow evolution around the blade (Fig. 23.2C) and thus reproduce the correct behavior of the poststall lift curve, which is instead provided by a LES approach.

To summarize, the wind industry needs higher-quality data for airfoil performance in a variety of working conditions that have been only roughly modeled to date, with a recognized *better-than-nothing* approach. To this end, the ubiquitous use of very high-fidelity CFD is still prohibitive due to the calculation cost. However, a multifidelity approach can fit the scope, in which a few high-fidelity simulations and experimental results can be used to validate/verify intermediate fidelity methods. This latter can be then used as a virtual test rig to produce those multivariate databases that are needed for the blade and turbine simulations that will be described in the following sections.

23.3 Rotor aerodynamics

Wind turbine rotors operate in complex environmental conditions, characterized by the coexistence of different phenomena such as atmospheric turbulence, ground boundary layer effects, directional and spatial variations in wind shear, thermal stratifications, and the possible effects of an upstream unsteady wake from a support structure or from other turbines. These phenomena, in turn, give rise to strong unsteady aerodynamic phenomena such as skewed wake flow [28,29], dynamic stall [30], and rotor-wake interaction [31−33]. Although onshore wind turbines represent today a mature technology, the global need for revamping old wind farms with the aim of reducing land occupation by adopting larger and more efficient rotors still put aeroelastic optimization within the list of primary research actions [4]. Moreover, recent outcomes of the Offshore Code Comparison, Collaboration, Continued, with Correlation project (OC5/OC6) [34] show that many additional technological challenges must be faced when dealing with offshore wind turbines, especially if they are mounted on floating platforms for deepsea installations, where bottom-fixed solutions are unfeasible. In these environments, characterized by average wind speeds up to 90% greater than onshore ones, besides considerations related to a shortened turbine lifetime and additional Operation & Maintenance (O&M) costs, operating conditions of FOWTs are also more severe than those onshore due to waves and currents, which continuously modify the relative orientation of the rotor disk with respect to the wind direction. On these bases, the challenge of cost reduction and O&M optimization must be tackled in a multidisciplinary context, in which a consistent prediction of turbine performance is the result of a comprehensive analysis where tower-blade aeroelasticity is strictly coupled with the floater-waves hydrodynamic interaction. For these reasons, the development of more reliable and accurate numerical tools is seen as a key way to address FOWTs analysis.

From a general standpoint, performance predictions with good levels of accuracy and low computational burden are of great interest to those involved in the preliminary design of on/off-shore wind turbines. In order to support the conceptual design of the new generation turbines, a comprehensive and fast understanding of the system dynamics is crucial to saving costs in later design phases. This requires low- and medium-fidelity models that are currently still used and enhanced. Nevertheless, recent results from the IEA Task 29 Phase IV on Detailed Aerodynamics of Wind Turbines [35] highlight the limitations of Blade Element Momentum Theory (BEMT), widely used by the industry, in predicting blade aeroloads under unsteady flow conditions. A thorough analysis of these topics is addressed in [36] by comparison of *blade-resolved* potential flow methods with BEMT models for the analysis of a wind turbine installed on a spar-buoy floating platform. This study demonstrates that differences in terms of predicted power, as well as mean and amplitude variations of the controlled blade pitch, can be observed between BEMT and vortex theory methods, especially at high tip speed ratio, for which unsteady aerodynamic phenomena and complex wake dynamics occur. These discrepancies are observed both under regular waves and constant wind as well as under irregular waves and turbulent wind conditions.

Within the model classification described in Fig. 23.1, some examples of beyond state-of-the-art wind turbine rotor aerodynamic modeling are presented in this section. These methodologies are currently starting to be at hand for industrial applications and represent fundamental complementary tools with respect to ubiquitous BEMT-based engineering models. These tools can be broadly categorized into inviscid (potential) and viscid flow methods and they represent two different levels in a hierarchy of aerodynamic formulations.

Potential flow formulations show a good trade-off among accuracy of simulation, CPU time demand, and out-of-the-box functionality. The outcomes of EU project AVATAR, of IEA Task 29 Phase IV and several literature works [37,38] demonstrate that three-dimensional (3D) unsteady panel methods for subsonic inviscid and irrotational flows [39–44] provide predictions in good agreement with experimental results for a variety of operational and inflow conditions. Within these formulations (see [44]), the blade shape is explicitly modeled by means of singularities (source/doublet panels) placed on its surface, whereas the wake is represented by a zero-thickness layer departing from the blade trailing edge where the vorticity generated on the blade surface is released downstream (see Fig. 23.3). The pressure distribution upon the blade(s) is computed by the Bernoulli equation, then aerodynamic forces and moments are obtained through the surface integration of the contribution of the elemental force due to the pressure field and stresses (tangential and normal) associated with viscosity.

Differently from lifting lines/surface formulations, these methodologies do not rely on airfoils polar data, thus needing a very limited number of tuning parameters (if any). Their major limitation is represented by viscous effects modeling, which is roughly achieved by invoking the behavior of an equivalent flat plate whose local Reynolds number matches the blade operating conditions. However, better predictions able to account for flow separation effects, such as those occurring in off-design, may be achieved through Integral Boundary Layer (IBL) techniques [45] or Reduced Order Models [30]. Within this family of methodologies, in order to accurately predict rotor loads, it is fundamental to achieve a physically consistent representation of the unsteady wake behavior as long as vorticity-driven phenomena are concerned. To this aim, Free Vortex Methods based on potential flow assumption consider wake points aligned to the local flow, that is moving with the wind and convected by the local fluid velocity due to the rotor blades and their wakes (self-induced effect).

Two examples of complex operating conditions where these methodologies are successfully stretched to their applicability limits are represented by the analysis of a rotor under extreme yaw, or that of a floating wind turbine working in Vortex Ring State (VRS). The first case refers, for example, to the Mexico rotor (a fully instrumented 4.5 m diameter three-blade turbine) tested at 30 degrees yaw in the large open jet facility of the German Dutch Windtunnels DNW [46]. Considering a blade radial section at $r/R = 0.82$, the analysis of pressure distributions at different azimuthal positions, shown in Fig. 23.4, demonstrates that, under the fully-attached flow conditions experienced by that section, the agreement between panel methods (*Funaero*, [44]) and experiments is excellent. Moving inboard, due to local flow conditions yielding to separation near the sectional trailing edge, panel codes tend to overpredict blade pressure. A view of the predicted three-dimensional shape of the wake, depicted in Fig. 23.5, reveals the well-known curled-wake mechanism starting at a distance from the rotor disk of about 2 diameters. This is the formation of a counter-rotating vortex pair in the wake of a turbine under highly yawed conditions [28,29].

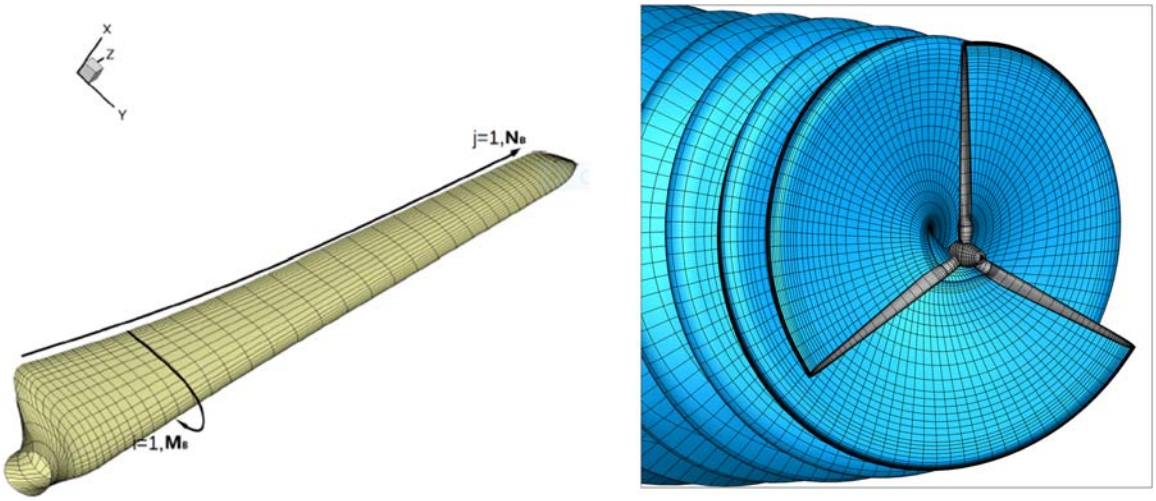

FIGURE 23.3 Example of blade (*grey*) and wake (*blue*) mesh for a panel method solver.

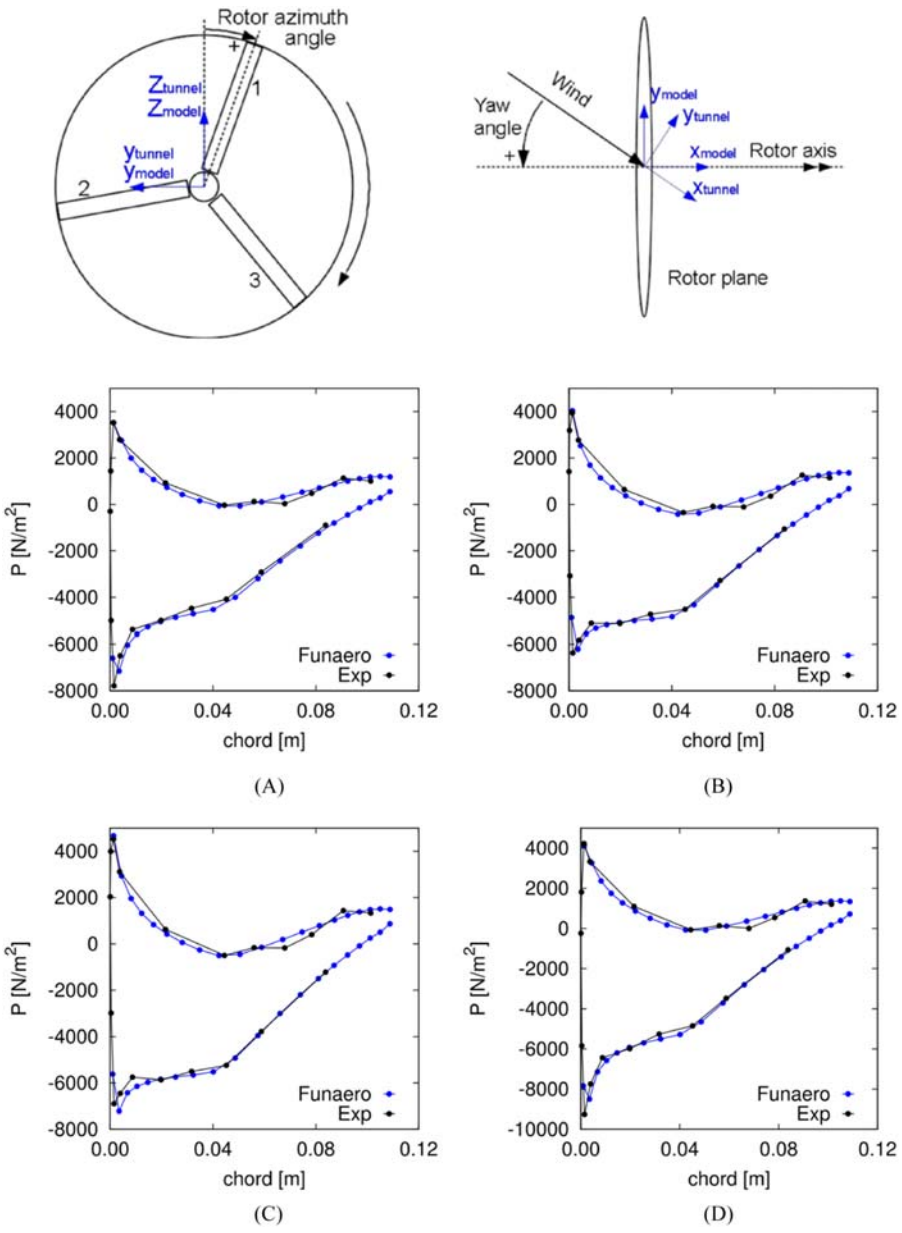

FIGURE 23.4 Blade pressure distribution at section $r/R = 0.82$ at four azimuth positions: $\psi = 0$ degrees (A), $\psi = 90$ degrees (B), $\psi = 180$ degrees (C) and $\psi = 270$ degrees (D). *From Greco L, Testa C. Wind turbine unsteady aerodynamics and performance by a free-wake panel method. Renew. Energy 2021;164:444–459.*

The characterization of the aerodynamic behavior of floating wind turbines represents another very relevant and challenging field of application for potential flow-based methodologies. Figs. 23.6 and 23.7 show the analysis of the NREL 5 MW rotor (a conventional three-bladed upwind turbine, with a rotor diameter of 126 m) undergoing an imposed pitch motion, that is, a rotation about the lateral axis (see Fig. 23.6). The sinusoidal pitch angle time history corresponding to an amplitude equal to 4 degrees and frequency equal to 1 Hz is shown in Fig. 23.6 (*right*). Under this rotation (which is representative of actual FOWT operating conditions) the rotor operates in VRS conditions with a close interaction between the blades and their wakes, especially during the backward motion phases. Fig. 23.7 (*left*) shows with gray levels the RANS-computed vorticity field [33] corresponding to the time instant T3 of Fig. 23.6 (*right*) compared to the location of wake points on the longitudinal plane predicted by a 3D unsteady panel code. Sound agreement between the numerical outcomes is shown up to 1D from the rotor disk, while further downstream the upper portion of the potential wake diverges from CFD-predicted vorticity clusters. Nevertheless, in terms of predicted power, panel codes provide an excellent accuracy compared to CFD data (see Fig. 23.7, *right*) and demonstrate how, for these operating conditions, relevant overshoot and undershoot with respect to the rated value are observed.

FIGURE 23.5 Mexico rotor in yawed flow: predicted three-dimensional shape of rotor wake by a panel code. *From Greco L, Testa C. Wind turbine unsteady aerodynamics and performance by a free-wake panel method. Renew. Energy 2021;164:444–459.*

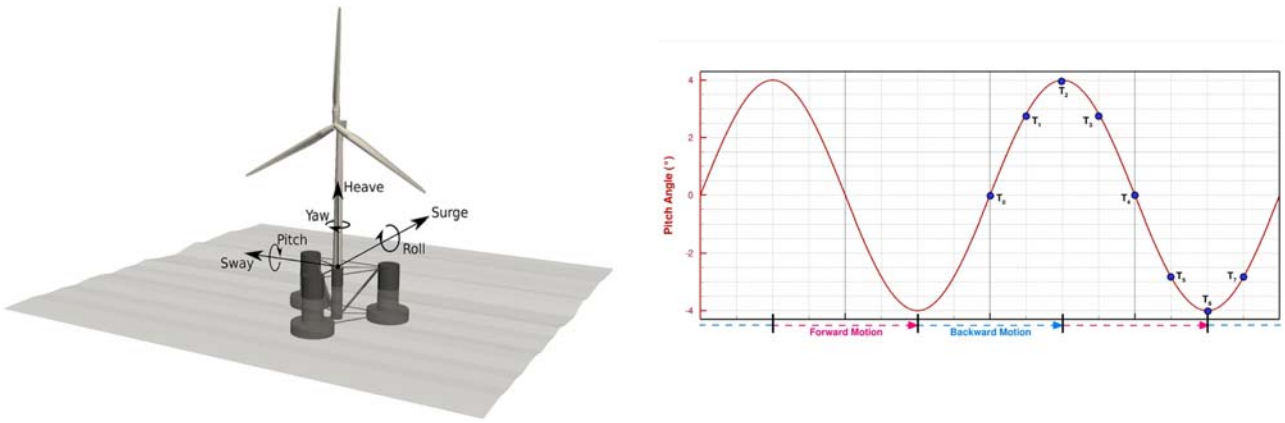

FIGURE 23.6 Degrees of freedom for an offshore floating wind turbine (*left*) [47]. *Right*: pitch motion analysis (amplitude 4 degrees and frequency 0.1 Hz). *From Papi F, Bianchini A. Technical challenges in floating offshore wind turbine upscaling: a critical analysis based on the NREL 5 MW and IEA 15 MW reference turbines. Renew. Sustain. Energy Rev. 2022;162:112489.*

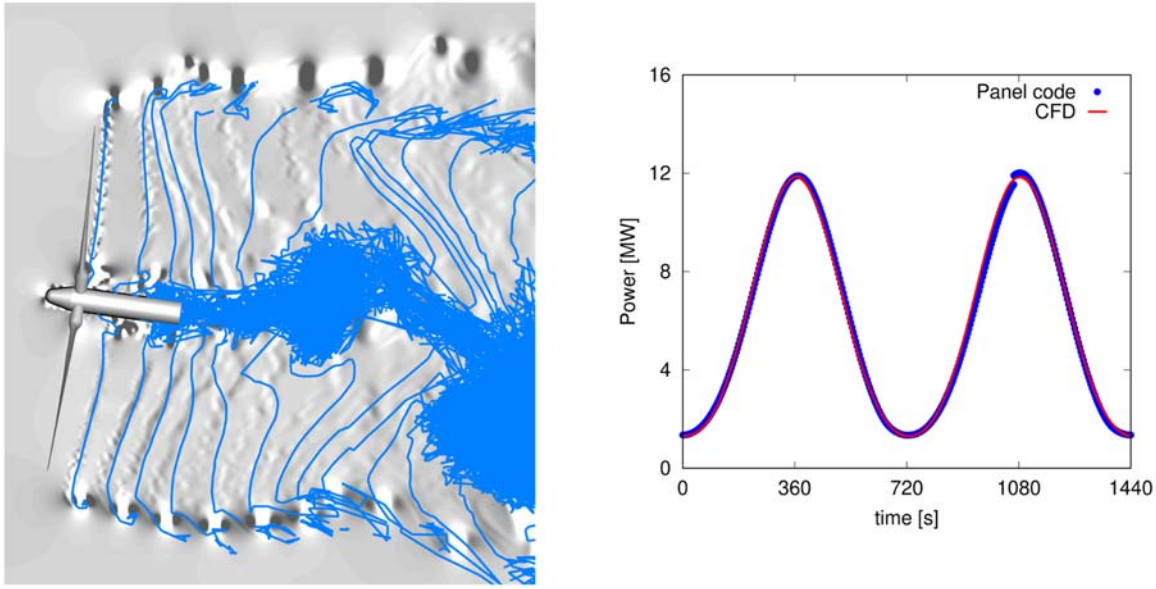

FIGURE 23.7 NREL 5 MW rotor in pitching conditions: comparison of wake shape (*left*) and predicted power (*right*) between RANSE and panel codes. *From Lienard C, Boisard R, Daudin C. Aerodynamic behavior of a floating offshore wind turbine. AIAA J 2020;58(9):3835–3847.*

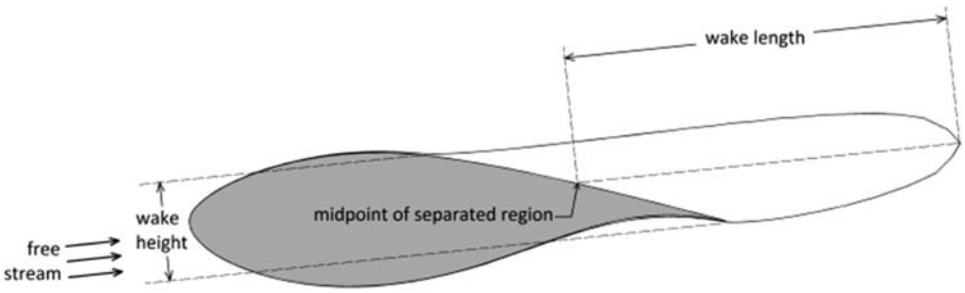

FIGURE 23.8 Sketch of the separated wake model. *From Nelson B, Kouh JS. The aerodynamic analysis of a rotating wind turbine by viscous-coupled 3D panel method. Appl. Sci. 2017;7(6) 1–15.*

Several other literature works demonstrate how potential flow aerodynamic methods are widely used in the prediction of turbine performance. In detail, many research studies address the issue of wake modeling and the ways to reduce the corresponding computational effort. Among these, Ref. [48] proposes a wake stabilization method freezing the free-wake after one-third of rotor revolution within the coupled hydro/aerodynamic analysis of the NREL 5 MW turbine on a semisubmersible floating platform. A comparison with the extensive BEMT codes used in the Offshore Code Comparison Collaboration Continuation (OC4) project [49] carried out in terms of platform motions shows that potential (aerodynamic and hydrodynamic) predictions for a steady wind/regular waves condition are in very good agreement with reference literature results. Furthermore, methodologies to improve viscous effects modeling are widely proposed. For example, Ref. [50] introduces a novel approach to model severe separation phenomena within potential flow methods where the onset of flow separation is predicted by the IBL analysis, with the separated wake resolved via a *thick wake* method treating the separated wake as a region of constant total pressure (see Fig. 23.8).

Even though BEMT-based aerodynamics is nowadays used in the majority of state-of-the-art aero-servo-elastic codes (see Section 23.3), the good trade-off between accuracy and reduced computational costs is the main driver for the application of this family of aerodynamic modeling techniques for wind turbine rotor aeroelastic analyses. Among literature examples, an investigation of the FSI of a floating wind turbine by means of potential flow aerodynamics is presented in [51]. In this work, a partitioned approach is used to couple a first-order panel method for simulating FOWTs in time domain with a detailed finite element CFD model built to analyze the global deformations, and corresponding stresses, on blades, tower, and floater.

On the other side of a hierarchy of aerodynamic formulations, CFD tools based on RANS [52], Detached Eddy Simulation (DES) [52–54], or LES [55,56] have shown the capability to yield physically consistent predictions of turbine performance and aerodynamics, thus interest in coupled CFD–CSD (Computational Structural Dynamics) techniques is increasing as well. Nevertheless, the high computational costs of such simulations make their application impractical during the earlier stages of the design, especially in view of massive aeroelastic and aeroservoelastic analyses required to comply with IEC-61400 standard regulations. Focusing on the challenging applications related to FOWTs, CFD studies of the coupled aerodynamic-hydrodynamic response of such systems are typically addressed under the assumptions of rigid bodies for the rotor, tower, and platform, while the lumped mass approach is used for the mooring lines.

An example of such high-fidelity and detailed simulations is reported in [57], where the commercial code STAR-CCM + is used to perform a multiphysical simulation including simultaneously the 6-DOF platform motions, the rotating blades, and the constraint effects of catenary lines. The volume of fraction method is applied to investigate the complex wave interference effect on the moving platform structure. In addition, a moving overset grid technique to effectively solve the large dynamic behavior of a FOWT due to the combined wind-wave coupling is considered. The computational mesh used for the calculations is shown in Fig. 23.9. The analysis of the DeepCwind semisubmersible floating platform with the NREL 5 MW wind turbine rotor is compared with outcomes from FAST, a widely used code implementing low-fidelity engineering models for unsteady aerodynamics based on the Generalized Dynamic Wake (GDW), the dynamic stall model by Beddoes–Leishman and tower shadow modeling. Under uniform wind conditions, the calculated blade aerodynamic loads show good agreement. Under the combined effect of uniform wind and regular waves, it is observed that the average values of heave and pitch response of the platform are in good agreement, whilst the amplitudes show some discrepancies. Moreover, the percentage differences between the average values of the surge and the mooring line tensions are relatively large (see Fig. 23.10).

A detailed CFD investigation about the onset of propeller and VRS conditions for a FOWT is addressed in [31], where the effect of surge motion on the thrust is investigated with OpenFOAM, a general purpose widely used software based on the finite volume method and solving the incompressible RANS equations. In this work, an overset mesh method is used to create separate individual submeshes (for the rotor, tower, and background domain) and then merge

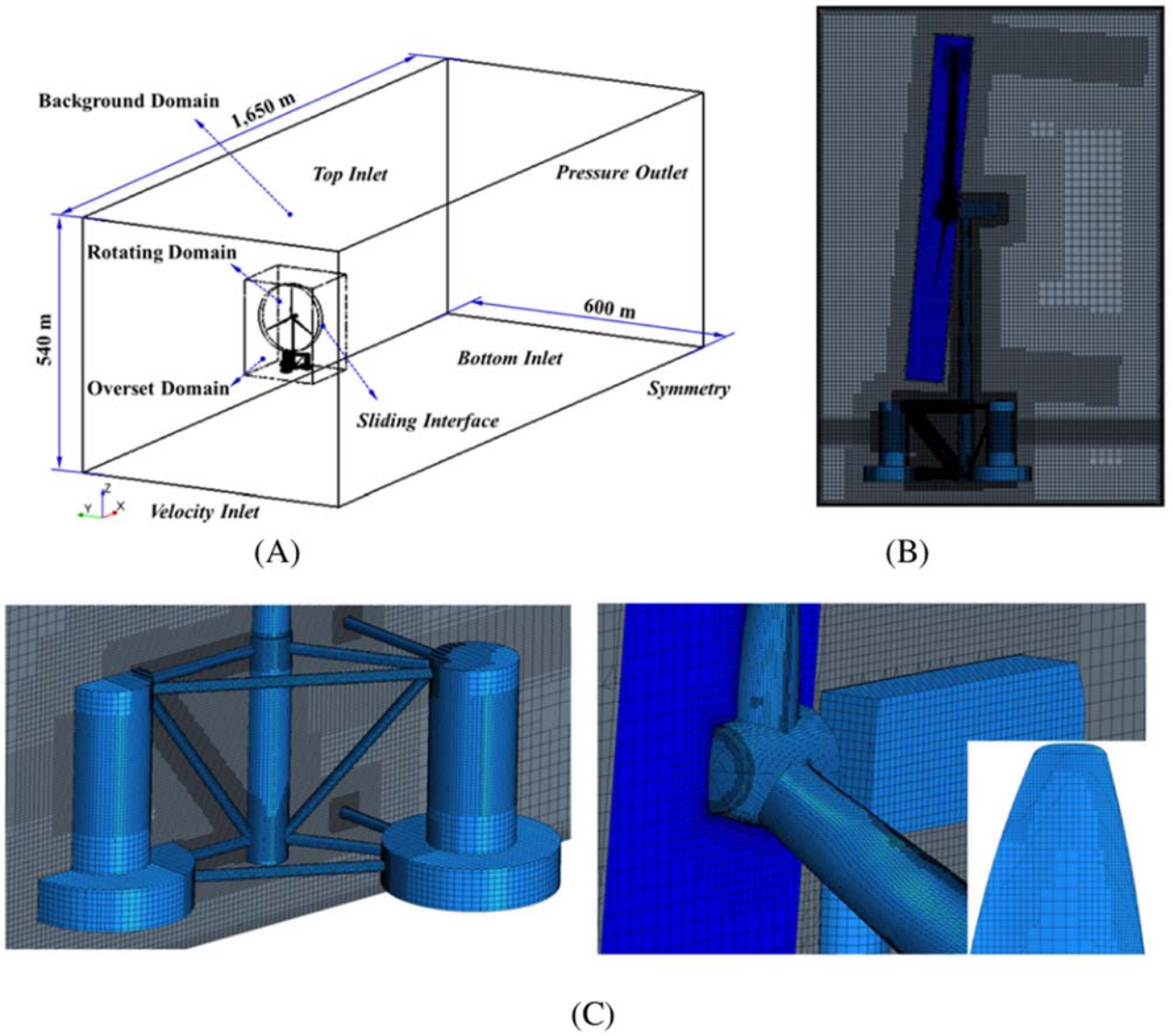

FIGURE 23.9 Computational mesh for floating offshore wind turbine model. (A) Computational domain, (B) entire turbine model with overset region, and (C) close view of turbine parts and platform surface mesh. *From Tran T, Kim D. A CFD study of coupled aerodynamic-hydrodynamic loads on a semisubmersible floating offshore wind turbine. Wind Energy 2018;21:70–85.*

them into one, with the boundaries between each individual submesh overlapping to act as a bridge between the various subdomains. The analysis addresses the NREL 5 MW wind turbine undergoing an imposed sinusoidal surge motion of amplitude 9.4 m and period 8.1 s at different wind speeds. The analysis shows that the combination of strong waves with low/moderate wind speeds (below rated) leads to propeller-like conditions: a negative thrust for the entire rotor is observed during part of the surging cycle (see Fig. 23.11). Moreover, VRS is observed with blade tip-vortex interaction and root vortex recirculation (see Fig. 23.12).

Although very accurate, CFD methodologies mentioned above require very high computational costs and cannot, therefore, represent the backbone of a design tool able to simulate several load cases for the single rotor and many wind turbines in an array for the different wave and wind conditions experienced in an installation site. Indeed, this family of tools is necessary to develop a better understanding of the conditions giving rise to unsteady aerodynamics phenomena like propeller and VRSs and their effect on turbine performance and blade loadings.

In order to reduce the computational costs of wind turbine simulations, hybrid formulations where low/mid-fidelity rotor aerodynamics models are coupled with high-fidelity tools for the analysis of the floater hydrodynamics have been recently proposed. This kind of approach aims at including also rotor aeroelastic effects within the simulations. An

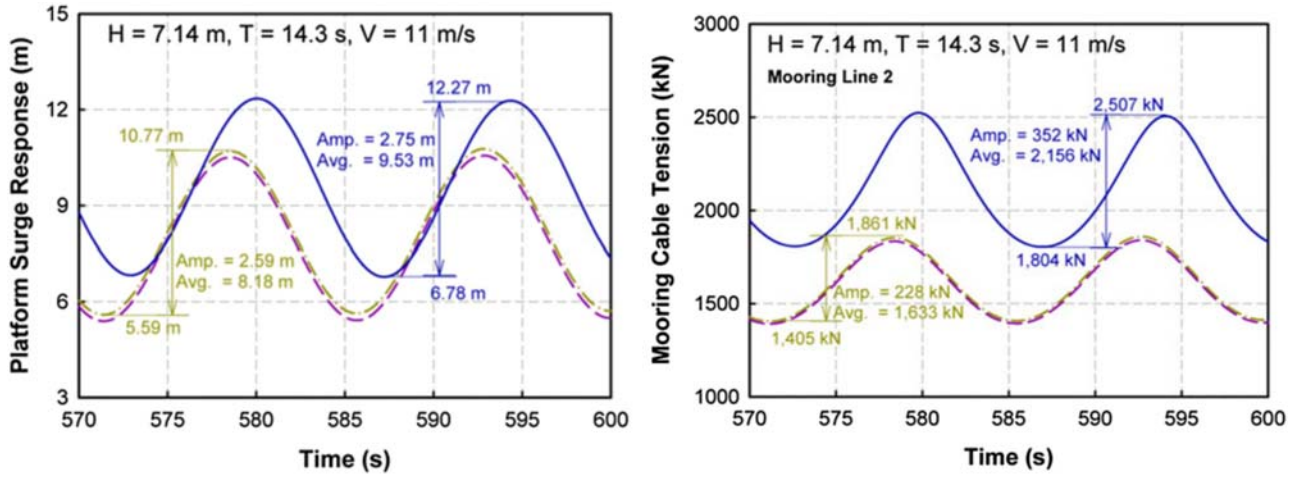

FIGURE 23.10 Prediction of platform surge (*left*) and mooring line tension (*right*). Comparison between FAST-BEM (*purple line*), FAST-GDW (*green line*), and CFD (*blue line*). *From Tran T, Kim D. A CFD study of coupled aerodynamic-hydrodynamic loads on a semisubmersible floating offshore wind turbine. Wind Energy 2018;21:70–85.*

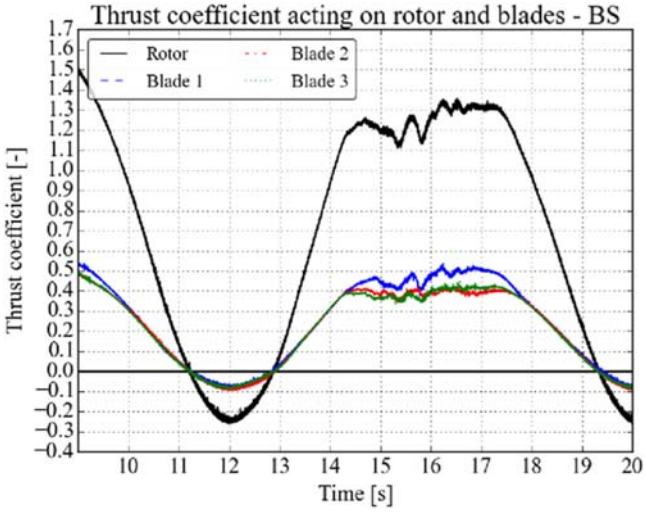

FIGURE 23.11 Thrust coefficient acting on the rotor as a whole and each blade individually under below-rated conditions in surge motion. *From Ryan Kyle R, Lee YC, Früh W-G. Propeller and vortex ring state for floating offshore wind turbines during surge. Renew. Energy 2020;155:645–657.*

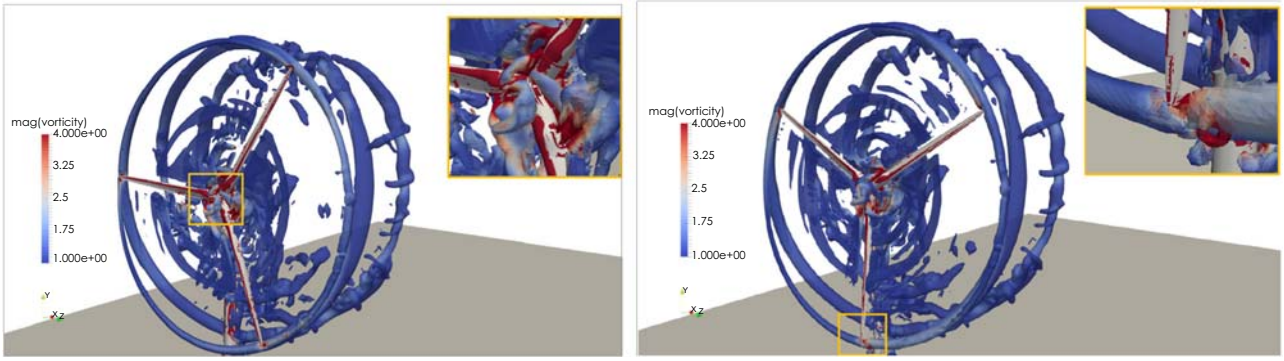

FIGURE 23.12 Vorticity iso-volumes for the below-rated surge case during propeller state. Blade vortex interaction at the tip as well as flow recirculation at the root is seen to occur in the left and right snapshots, respectively, reflecting VRS conditions. *From Ryan Kyle R, Lee YC, Früh W-G. Propeller and vortex ring state for floating offshore wind turbines during surge. Renew. Energy 2020;155:645–657.*

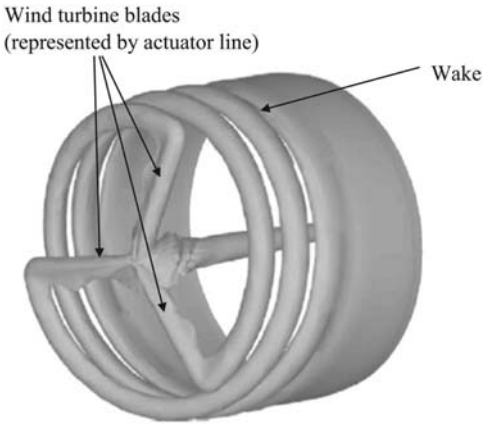

FIGURE 23.13 Blade modeling of a three-bladed wind turbine rotor based on the Actuator Line Model [59]. *From Wang L, Liu X and Kolios A. State of the art in the aeroelasticity of wind turbine blades: aeroelastic modelling. Renew Sustain Energy Rev 2016;64:195–210.*

example of such methods, although still applied under the rigid body assumption for all FOWT components (except the moorings) is presented in [58], where an unsteady ALM for rotor aerodynamics is coupled with the three-dimensional RANS solver OpenFoam. In these methodologies, the loads exerted by the blades on the fluid are computed by BEMT and then applied to the CFD solver at blade locations by means of a source term in the momentum equation (see Fig. 23.13). The NS equations are then solved numerically in order to obtain flow quantities such as velocity and pressure. The application of this solver to the analysis of the NREL 5 MW wind turbine mounted on a semisubmersible platform shows that the incoming wave frequency is the main driver of rotor unsteady aerodynamic loads, whose amplitude increases with the wave height. Differently, little influence of the wave is found on rotor average loads. The analysis of the platform dynamics shows that the effect of turbine aerodynamics as an external load on the supporting platform has a relevant impact on the average values of platform surge, heave, and pitch, whereas the influence of turbine loads on the fluctuation of the platform is negligible.

As a matter of fact, limits exist in the capabilities of all aerodynamic formulations, and ambiguities can also arise in how these models should be properly applied. Hence, the complementary use of numerical modeling of different accuracy seems to represent the best choice if one wants to better understand the aerodynamic phenomena affecting wind turbines, while ensuring that an effective compromise between accuracy and computational cost is ensured for each application.

23.4 Rotor blades' structural dynamics for aeroelasticity

During the last decades, the size of wind turbines has increased dramatically from a rated power of 50 kW with rotors of 10–15 m diameter up to nowadays commercial 14 MW turbines with rotors of more than 200 m diameters. As a consequence, rotor blades with unprecedented levels of flexibility have been proposed, increasing in turn the relevance of FSI phenomena. As a matter of fact, FSI is a crucial issue to be faced by designers for the deployment of the next generation of even longer and slender wind turbine blades. In particular, during predesign, the availability of fast and reliable numerical prediction tools is mandatory in that several engineering choices must be verified by multidisciplinary optimization tools.

For wind turbine aeroelastic predictions, suitable structural models are needed in order to yield blade(s) elastic displacements that, within the aeroelastic loop, affect the time-varying aerodynamic loads during the revolution period. Typically, wind turbines structural formulations fall into three-dimensional (3D) Finite Element Method (FEM) approaches or one-dimensional (1D) beam modeling. In principle, the high level of complexibility of rotor blades (made of many layers of fiber-reinforced composite material with the required shear webs, and tapering cross sections), requires devoted 3D FEM modeling to describe composite layer characteristics throughout the shell thickness of the blade (see Fig. 23.14).

This family of structural solvers provides accurate and detailed stress and deformation distributions on rotor blades when coupled with suitable aerodynamic models within an aeroelastic loop. Generally, they are coupled with CFD solvers as, for example, in [60–62]. In particular, in Ref. [60], it is demonstrated that coupling of a 3D shell structural model with the NS equations for incompressible flow in the Arbitrary Lagrangian–Eulerian (ALE) method yields relevant torque (hence power) overshoot with respect to lower-fidelity models.

Aeroelastic modeling based on coupled 3D FEM and CFD is able to provide accurate results, but it is extremely computationally expensive. A way to save computational cost is to couple the 3D FEM with efficient aerodynamic models such as BEMT engineering codes, thus again going in the direction of a multifidelity approach.

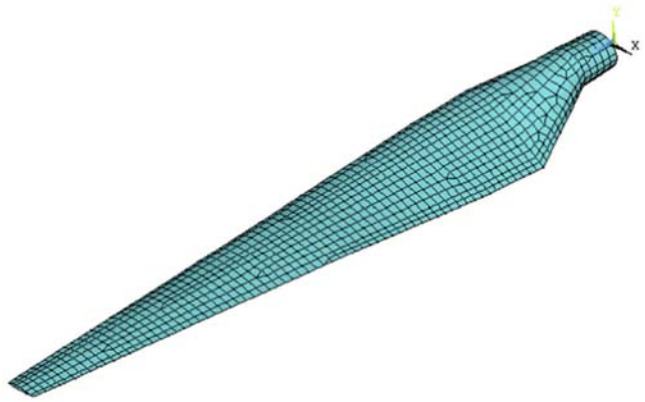

FIGURE 23.14 Example of a 3D FEM model of a wind turbine blade. *From Wang L, Liu X and Kolios A. State of the art in the aeroelasticity of wind turbine blades: aeroelastic modelling. Renew Sustain Energy Rev 2016;64:195–210.*

Despite the high level of accuracy obtained (for instance, in terms of free vibration characteristics, internal stresses distribution, and rotor dynamics), the use of 3D composite shell elements discussed so far is computationally expensive and so rarely used in practical applications. To reduce the computational costs of the analysis, 1D beam models are efficiently applied for wind turbine applications, since one blade dimension is significantly larger than the other two. The beam axis is defined along the largest dimension, with cross sections assumed perpendicular to it and characterized by structural properties equivalent to those of the real blade. In this context, several beam formulations have been developed over the years: among them, the Euler–Bernoulli and Timoshenko beam linear modelings are widely used for their simplicity. However, their drawback resides in the intrinsic assumption of small deflections that is not appropriate for the current and next generation wind turbine rotor blades undergoing large deflections. Handling these conditions requires a nonlinear beam model, taking account the geometric nonlinearities caused by large deflections. A well-known example is the Geometrically Exact Beam Theory (GEBT) [63], in which the deformed beam geometry (i.e., the displacements and rotations of the beam reference line) is represented exactly.

The use of 1D FEM is widely found in wind turbines' structural dynamics because it allows a more comprehensive and accurate deformation description by analyzing an assembly of finite elements connected by nodes. To this aim, FEM blade modeling schemes for moderate/large displacements have been proposed and successfully applied, starting from the knowledge gained in the past on helicopter rotor aeroelasticity, whose rotor blades share similar aeroelastic problems (in terms of overall performance, vibration, loads, and stability [64]) with wind turbine blades. For instance, Durocher and Kane [65] investigated the blade deflections including the effects of shear stress, axial-torsion coupling and torsional stiffness; Ormiston and Hodges [66] included the effects of precone, variable elastic coupling, and pitch-lag coupling; Belo and Marques [67] proposed a FEM analysis to study a helicopter blade undergoing the coupled motions of flapping, lead-lagging, axial stretching, and torsion, accounting for the pretwist angle and offsets between the mass and the elastic axes. In this context, a widely used set of nonlinear governing equations for rotating blade dynamics was developed by Hodges and Dowell [68] to capture the coupled motions in flapwise bending, lead-lag bending, axial deformation, and torsion. It is based on a fifteen Degree Of Freedom (DOF) FEM model where four DOF are used in flapwise, lead-lag bending and axial displacements, respectively, and three DOF for torsion. The theoretical modeling presented in [68] is applicable to nonuniform rotor blades, described as long, straight, slender, homogeneous isotropic beams undergoing axial, lag, flap, and torsion displacements. The theory is intended for moderate displacements, accurate to second order, and based on the hypothesis that squares of bending slopes, twist, thickness-radius, and chord-radius ratios are small with respect to unity. Rotor blades with pretwist, precone, and chordwise offsets of the center of mass, aerodynamic center, and tension center from the elastic axis may be modeled; structural dissimilarity among rotor blades are neglected whereas advanced tip shapes, such as swept-tip or tapered-tip, are not considered. The formulation is general, and when applied to wind turbine rotors it might be extended to configurations including the presence of the tower and floating structures for offshore applications. It represents a valuable starting point for wind energy investigations aimed at meeting the growing demand to better predict the delivered power of horizontal-axis wind turbines. This FEM model has been successfully applied to the study of rotorcraft aeroelasticity and the level of accuracy in the physical description of the FSI makes this approach among those having a leading position in wind turbine aeroelastic simulations.

Along with the definition of the most suitable structural and aerodynamic solvers, a fundamental step in rotor aeroelastic modeling is the FSI coupling strategy which aims at mapping together aerodynamic forces and structural deformation.

Currently, the fidelity requirements for FSI analysis are constantly increasing in order to include modeling details such as turbulence [69], nonlinear composite layered blades and large deformation [70]. In parallel, very good accuracy *vs* computational cost compromises are acceptable for the design of the high-efficiency next-generation rotors. A generally accepted categorization distinguishes FSI coupling strategies in monolithic and partitioned approaches (see Fig. 23.15). In monolithic formulations, fluid and structural state equations are combined to create a single monolithic system of equations, which is solved simultaneously by a single algorithm. This approach can potentially achieve better accuracy for a multidisciplinary problem, and, since the interaction of the fluid and the structure at the mutual interface is tackled synchronously, conservation properties at the interface are assured, which guarantees unconditional stability. Despite this attractiveness, the challenges associated with this approach often outweigh the benefits. In fact, fluid and structural solvers are usually very different, each using its own optimized tool specific to the fields of applications. Furthermore, a monolithic solver might be very inefficient, since structural and fluid problems are often characterized by different temporal and spatial scales. Moreover, monolithic methods are characterized by less modularity and require more coding than partitioned ones.

Differently, in partitioned FSI methods, the structural and fluid fields are solved using two different codes, and the interaction between them is limited to the exchange of surface loads and deformations by updating the related boundary conditions of the state equation of each domain.

Within partitioned formulations, two different approaches can be used to transfer the information between the fluid and the structural solvers. In the one-way FSI coupling, the fluid field is solved preliminarily and the obtained data (pressure and shear stress field) are transferred to the structural model as boundary conditions. The obtained structural displacement is not fed back into the fluid solver, allowing for independent CFD and CSD simulations. In the two-way FSI coupling, the fluid pressure is transferred to the structure and the induced structural deformation is used to update the fluid domain; therefore, fluid and structural domains are solved simultaneously, with bidirectional data transfer. In general, the two-way coupling solution is more accurate, especially for large deflections, where the fluid field is strongly influenced by structural deformation, whereas the applicability of one-way FSI is generally limited to problems characterized by small structural deformations. To provide a flavor of the role of FSI coupling strategies, the aeroelastic analysis of the NREL 5 MW wind turbine rotor is shown considering one-way and two-way coupling procedures [71]. In Fig. 23.16, the total blade tip deflection computed by a CFD/CSD solver for half a rotor revolution is depicted showing about 10% underestimation by the one-way coupling. This is a generally observed trend in the literature. Although

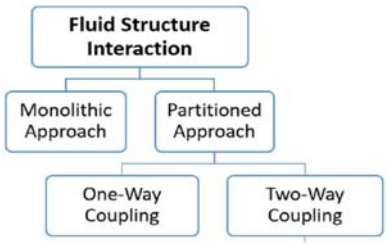

FIGURE 23.15 Categorization of coupling strategies for FSI simulations.

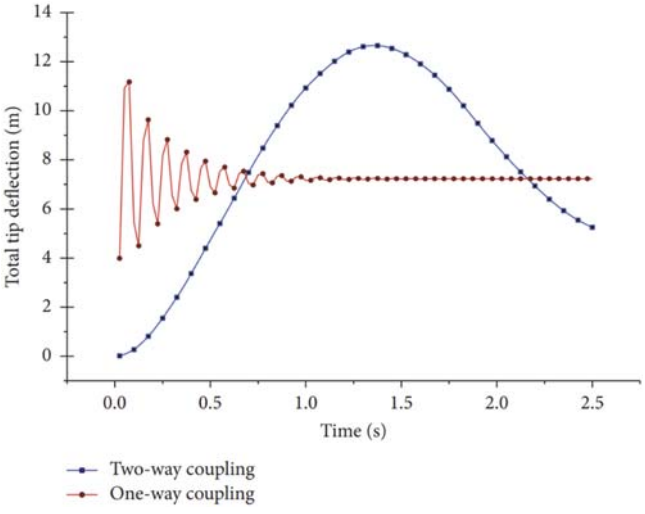

FIGURE 23.16 Blade tip deflection for half cycle of operation. *From Belayneh Ageze M, Hu Y, Wu H. Wind turbine aeroelastic modeling: basics and cutting edge trends. Int. J. Aerosp. Eng. 2017;Article ID 5263897:1–15.*

there is an enormous amount of computation effort required for strong coupling between fluid and structure, the application of two-way FSI coupling strategies is mandatory to simulate the full aeroelasticity characteristics of a wind turbine with a proper degree of fidelity.

23.5 Concluding remarks

While of course, the present chapter cannot provide a comprehensive analysis of all the multifidelity methods available today for wind turbine rotors, the technical analysis provided in previous sections aims at highlighting how the holistic approach unanimously invoked in support of the design of the next generation of wind turbines cannot be based entirely on the best available technique for any application. Modern simulation methods and increasing computational resources indeed allow for a high-fidelity modeling in almost every aspect of wind turbine design/simulation tasks, from airfoil aerodynamics to rotor aeroelasticity. However, if indeed a holistic approach needs to be pursued, making use only of these techniques would make the computational cost prohibitive and the problems too complex to be handled at the industrial level. To this end, multifidelity simulations are increasingly welcome in wind energy problems, so as to tailor the approach to each specific application, in terms of both accuracy/cost compromise and targeted outcomes.

References

[1] van Kuik GAM, Peinke J, Nijssen R, Lekou D, Mann J, Sørensen JN, et al. Long-term research challenges in wind energy—a research agenda by the European Academy of Wind Energy. Wind Energ Sci 2016;1:1–39.

[2] Veers P, Dykes K, Lantz E, Barth S, Bottasso CL, Carlson O, et al. Grand challenges in the science of wind energy. Science 2019.

[3] Hewitt S, Margetts L, Revell A. Building a digital wind farm. Arch Computat Methods Eng 2018;25:879–99.

[4] Veers P, Bottasso C, Manuel L, Naughton J, Pao L, Paquette J, et al. Grand challenges in the design, manufacture, and operation of future wind turbine systems (aerodynamics and hydrodynamics), 2022.

[5] Bianchini A. Trends, prospects, and R&D directions in wind turbine technology. In: Reference module in earth systems and environmental sciences. Elsevier; 2019.

[6] Scott S, Capuzzi M, Langston D, Bossanyi E, McCann G, Weaver PM, et al. Effects of aeroelastic tailoring on performance characteristics of wind turbine systems. Renew Energy 2017;114:887–903.

[7] Pechlivanoglou G. Passive and active flow control solutions for wind turbine blades; 2013.

[8] Alber J, Manolesos M, Weinzierl-Dlugosch G, Fischer J, Schönmeier A, Nayeri CN, et al. Experimental investigation of mini Gurney flaps in combination with vortex generators for improved wind turbine blade performance. Wind Energ Sci 2022;7:943–65.

[9] Bak C, Fuglsang P, Sørensen N, Madsen H, Shen WZ, Sørensen J. Airfoil characteristics for wind turbines. Electronic networking: research, applications and policy—EN 1999.

[10] Dimitrov N, Kelly MC, Vignaroli A, Berg J. From wind to loads: wind turbine site-specific load estimation with surrogate models trained on high-fidelity load databases. Wind Energ Sci 2018;3:767–90.

[11] Bortolotti P, Canet H, Bottasso CL, Loganathan J. Performance of non-intrusive uncertainty quantification in the aeroservoelastic simulation of wind turbines. Wind Energ Sci 2019;4:397–406.

[12] Thé J, Yu H. A critical review on the simulations of wind turbine aerodynamics focusing on hybrid RANS-LES methods. Energy 2017;138:257–89.

[13] Sørensen JN, Mikkelsen RF, Henningson DS, Ivanell S, Sarmast S, Andersen SJ. Simulation of wind turbine wakes using the actuator line technique. Phil Trans R Soc A 2015;373:20140071.

[14] Bianchini A, Balduzzi F, Gentiluomo D, Ferrara G, Ferrari L. Comparative analysis of different numerical techniques to analyze the wake of a wind turbine. In: Proceedings of the ASME Turbo Expo vol. 9, 2017.

[15] Ageze MB, Hu Y, Wu H. Wind turbine aeroelastic modeling: basics and cutting edge trends. Int J Aerosp Eng 2017;2017:e5263897.

[16] Hernandez-Estrada E, Lastres-Danguillecourt O, Robles-Ocampo JB, Lopez-Lopez A, Sevilla-Camacho PY, Perez-Sariñana BY, et al. Considerations for the structural analysis and design of wind turbine towers: a review. Renew Sustain Energy Rev 2021;137:110447.

[17] Otter A, Murphy J, Pakrashi V, Robertson A, Desmond C. A review of modelling techniques for floating offshore wind turbines. Wind Energy 2022;25:831–57.

[18] Papi F, Melani PF, Xie S, Perrone C, Scienza P, Balduzzi F, et al. Development and validation of an advanced actuator line model for wind turbines. E3S Web Conf 2021;312:08004.

[19] Schreck SJ, Robinson MC. Horizontal axis wind turbine blade aerodynamics in experiments and modeling. IEEE Trans Energy Convers 2007;22:61–70.

[20] Abbott IH, Von Doenhoff AE. Theory of wing sections: including a summary of airfoil data. New York: Dover Publ; 2010.

[21] Bak C, Andersen PB. Three-dimensional corrections of airfoil characteristics based on pressure distributions.

[22] Bangga G, Lutz T, Arnold M. An improved second-order dynamic stall model for wind turbine airfoils. Wind Energ Sci 2020;5:1037–58.

[23] Holst D, Balduzzi F, Bianchini A, Church B, Wegner F, Pechlivanoglou G, et al. Static and dynamic analysis of a NACA 0021 airfoil section at low reynolds numbers based on experiments and computational fluid dynamics. J Eng Gas Turbines Power 2019;141.

[24] Wiśniewski P, Balduzzi F, Buliński Z, Bianchini A. Numerical analysis on the effectiveness of gurney flaps as power augmentation devices for airfoils subject to a continuous variation of the angle of attack by use of full and surrogate models. Energies 2020;13:1877.
[25] Giaccherini S, Mariotti F, Pinelli L, Marconcini M, Bianchini A. On the prospects of improving the numerical analysis of symmetric airfoils at low Reynolds numbers and high angles of attack by a LES approach: the case of NACA0021 profile. Ed ATI Associazione Termotecnica Italiana E3S Web Conf. 2020;197:08015.
[26] XFoil. Available from: https://web.mit.edu/drela/Public/web/xfoil/.
[27] Ferreira CS, Van Bussel G, Van Kuik G. 2D CFD simulation of dynamic stall on a vertical axis wind turbine: verification and validation with PIV measurements. Collection of Technical Papers—45th AIAA Aerospace Sciences Meeting 2007;23:16191−16201.
[28] Bastankhah M, Porté-Agel F. Experimental and theoretical study of wind turbine wakes in yawed conditions. J Fluid Mech 2016;806:506−41.
[29] Berdowski T. Three-dimensional free-wake vortex simulations of an actuator disc in yaw and tilt 2018. In: Wind Energy Symposium; 2018:0513.
[30] Calabretta A, Molica Colella M, Greco L, Gennaretti M. Assessment of a comprehensive aeroelastic tool for horizontal-axis wind turbine rotor analysis. Wind Energy 2016;19(12):2301−19.
[31] Ryan Kyle R, Lee YC, Früh W-G. Propeller and vortex ring state for floating offshore wind turbines during surge. Renew Energy 2020;155:645−57.
[32] Tran T-T, Kim D-H. The platform pitching motion of floating offshore wind turbine: a preliminary unsteady aerodynamic analysis. J Wind Eng Ind Aerodyn 2015;142:65−81.
[33] Lienard C, Boisard R, Daudin C. Aerodynamic behavior of a floating offshore wind turbine. AIAA J 2020;58(9):3835−47.
[34] Robertson A, et al. OC5 project phase II: validation of global loads of the DeepCwind floating semisubmersible wind turbine. Energy Proc 2017;137:38−57.
[35] Schepers JG, Boorsma K et al. IEA wind TCP task 29, Phase IV: detailed aerodynamics of wind turbines, 2021. https://doi.org/10.5281/zenodo.4817875.
[36] Leroy V, Gilloteaux J-C, Lynch M, Babarit A, Ferrant P. Impact of aerodynamic modeling on seakeeping performance of a floating horizontal axis wind turbine. Wind Energy 2019;22:1019−33.
[37] Boorsma K, Hartvelt M, Orsi ML. Application of the lifting line vortex wake method to dynamic load case simulations. J Phys Conf Ser 2016;753:022030.
[38] Boorsma K, Greco L, Bedon G. Rotor wake engineering models for aeroelastic applications. J Phys Conf Ser 2018;1037:062013.
[39] Greco L., Muscari R., Testa C., Di Mascio A.. Prediction by a free-wake panel method marine propellers performance, flow-field features. J Hydrodyn B 2014;26:780−795.
[40] Greco L, Testa C, Salvatore F. Design oriented aerodynamic modelling of wind turbine performance. J Phys Conf Ser 2007;75:012011.
[41] Testa C, Greco L. Prediction of submarine scattered noise by the acoustic analogy. J Sound Vib 2018;426(21):186−218.
[42] Durante D, Dubbioso G, Testa C. Simplified hydrodynamic models for the analysis of marine propellers in a wake-field. J Hydrodyn 2013; 25(6):954−65.
[43] Leone S, Testa C, Greco L, Salvatore F. Computational analysis of self-pitching propellers performance in open water. Ocean Eng 2013;64:122−34.
[44] Greco L, Testa C. Wind turbine unsteady aerodynamics and performance by a free-wake panel method. Renew Energy 2021;164:444−59.
[45] van Garrel A. Integral boundary layer methods for wind turbine aerodynamics, ECN-C-04e004 Energy Research Centre of the Netherlands; 2004.
[46] Boorsma K, Schepers JG. Rotor experiments in controlled conditions continued: New Mexico. J Phys: Conf Ser 2016;753:022004.
[47] Papi F, Bianchini A. Technical challenges in floating offshore wind turbine upscaling: a critical analysis based on the NREL 5 MW and IEA 15 MW reference turbines. Renew Sustain Energy Rev 2022;162:112489.
[48] Netzband S, Schulz CW, Göttsche U, Ferreira González D, Abdel-Maksoud M. A panel method for floating offshore wind turbine simulations with fully integrated aero- and hydrodynamic modelling in time domain. Ship Technol Res 2018;65(3):123−36.
[49] Robertson A, Jonkman J, Masciola M. Definition of the semisubmersible floating system for phase II of OC4. Golden, CO: NREL. Report No.: NREL/TP-5000−60601; 2014.
[50] Nelson B, Kouh JS. The aerodynamic analysis of a rotating wind turbine by viscous-coupled 3D panel method. Appl Sci 2017;7(6):1−15.
[51] Wiegard B, König M, Lund J, Radtke L, Netzband S, Abdel-Maksoud M, et al. Fluid-structure interaction and stress analysis of a floating wind turbine. Marine Struct 2021;78:102970.
[52] Porcacchia F, Testa C, Zaghi S, Muscari R, Gennaretti M. Assessment of permeable boundary integral formulations for rotating blades noise prediction (ICSV 2017). 2017.
[53] Boorsma K, Schepers JG et al., Final Report of IEA Task 29: Mexnext (Phase 3), ECN-E-18e1003, Energy Research Center of the Netherlands; 2018.
[54] Bangga G, Weihing P, Lutz T, Kramer E. Effect of computational grid on accurate prediction of a wind turbine rotor using delayed detached-eddy simulations. J Mech Sci Technol 2017;31(5):2359e2364.
[55] Sedaghatizadeh N, Arjomandi M, Kelso R, Cazzolato B, Ghayesh M. Modelling of wind turbine wake using large eddy simulation. Renew Energy 2018;115:1166−76.
[56] Benard P, Vire A, Moureau V, Lartigue G, Beaudet L, Deglaire P, et al. Large-eddy simulation of wind turbines wakes including geometrical effects. Comput Fluid 2018;173:133−9.
[57] Tran T, Kim D. A CFD study of coupled aerodynamic-hydrodynamic loads on a semisubmersible floating offshore wind turbine. Wind Energy 2018;21:70−85.

[58] Cheng P, Huang Y, Wan C. A numerical model for fully coupled aero-hydrodynamic analysis of floating offshore wind turbine. Ocean Eng 2019;173:183−96.
[59] Wang L, Liu X, Kolios A. State of the art in the aeroelasticity of wind turbine blades: aeroelastic modelling. Renew Sustain Energy Rev 2016;64:195−210.
[60] Bazilevs Y, Hsu MC, Kiendl J, Wüchner R, Bletzinger KU. 3D simulation of wind turbine rotors at full scale. Part II: fluid−structure interaction modeling with composite blades. Int J Numer Methods Fluids 2011;65:236−53.
[61] Do Y, Kwon OJ. Predicting wind turbine blade loads and aeroelastic response using a coupled CFD−CSD method. Renew Energy 2014;70:184−96.
[62] Bazilevs Y, Hsu M-C, Scott M. Isogeometric fluid−structure interaction analysis with emphasis on non-matching discretizations, and with application to wind turbines. Comput Methods Appl Mech Eng 2012;249:28−41.
[63] Hodges DH. Geometrically exact, intrinsic theory for dynamics of curved and twisted anisotropic beams. AIAA J 2003;41:1131−7.
[64] Xiong JJ, Yu X. Helicopter rotor-fuselage aeroelasticity modeling and solution using the partition-iteration method. J Sound Vib 2007; 302(4−5):821−40.
[65] Durocher LL, Kane J. Preliminary design tools for pretwisted tapered beams or turbine blades. J Mech Des Trans ASME 1980;102(4):742−8.
[66] Ormiston RA, Hodges DH. Linear flap-lag dynamics of hingeless helicopter rotor blades in hover. J Am Helicopter Soc 1972;17:2−14.
[67] Belo EM, Marques FD. Analysis and vibration control of a helicopter rotor blade. Conference Publication No. 389, IEE 1290−1295; 1994.
[68] Hodges D.H., Dowell E.H. Nonlinear equations of motion for the elastic bending and torsion of twisted nonuniform rotor blades NASA TN D-7818, Washington, DC; 1974.
[69] Li Y, Castro AM, Sinokrot T, Prescott W, Carrica PM. Coupled multi-body dynamics and CFD for wind turbine simulation including explicit wind turbulence. Renew Energy 2015;76:338−61.
[70] Kumar J, Wurm F-H. Bi-directional fluid-structure interaction for large deformation of layered composite propeller blades. J Fluids Struct 2015;57:32−48.
[71] Belayneh Ageze M, Hu Y, Wu H. Wind turbine aeroelastic modeling: basics and cutting edge trends. Int J Aerosp Eng 2017;1−15 Article ID 5263897.

Chapter 24

Wind turbine supporting tower structural health monitoring and vibration control

Kaoshan Dai[1,2,3,4], **Ying Wang**[5] **and Zhenhua Huang**[6]

[1]Department of Civil Engineering, Sichuan University, Chengdu, Sichuan, P. R. China, [2]MOE Key Lab of Deep Underground Science and Engineering, Sichuan University, Chengdu, Sichuan, P. R. China, [3]State Key Lab of Hydraulics and Mountain River Engineering, Sichuan University, Chengdu, Sichuan, P. R. China, [4]Institution of Disaster Management and Reconstruct, Sichuan University, Chengdu, Sichuan, P. R. China, [5]Department of Intelligent Construction and Management, Nanjing Tech University, Nanjing, Jiangsu Province, P. R. China, [6]Department of Mechanical and Energy Engineering, University of North Texas, Denton, TX, United States

24.1 Introduction

The development of renewable energy sources has attracted great interest as the greenhouse effect introduces the global warming problem. Wind power is one of the most mature renewable energy technologies and related industry has been experiencing accelerated growth during recent decades. The installation rate of wind turbines around the world is increasing significantly. Wind turbine farms are constructed in plentiful wind resource areas that put a considerable number of wind turbine towers under severe wind conditions. However, various engineering problems have been gradually exposed along with its growth and maintenance and repairs constitute significant costs for existing wind farms. Wind energy industry continuously develops larger wind turbines for new projects located in more challenging environments to increase productivity and reduce operating costs. These new wind power facilities are more prone to fatigue and malfunction and are more expensive to repair. In this chapter of the book, the authors review the studies of structural safety issues of wind turbine towers under severe environmental conditions and present some efficient vibration control systems of wind turbine towers under wind and seismic loads. The authors also discussed some structural health monitoring-related issues of wind turbine towers.

24.2 Dynamic response of wind turbine tower under severe environmental conditions

Wind turbines are typically designed to resist the synoptic wind loads specified in current International Electrotechnical Commission (IEC) guidelines, but these standards do not account for high-intensity wind events such as tornadoes or downbursts. Because of the localized nature of high-intensity wind events, identifying critical locations that result in peak forces acting on the tower and blades is a challenging task. Wind turbine towers are often constructed in open areas, which means an absence of any obstacles, such as the buildings in urban areas, that can dissipate the effects of such events.

The growth in global wind energy suggests that wind farms will increasingly be constructed in seismically active regions, and entire arrays of similarly designed structures may become at risk of failing simultaneously under an extreme seismic event. It is therefore important to understand the behavior of these structures under realistic assessments of seismic loading. There is a dearth of information in this regard, with studies in the field focusing mainly on assessing fatigue in the turbine machinery and on blade design. The static or dynamic response of the support tower itself has been considered mostly in the context of wind loading with seismic loading usually deemed to be only of secondary importance and treated according to simple codified provisions.

Wind Energy Engineering. DOI: https://doi.org/10.1016/B978-0-323-99353-1.00036-0

24.2.1 Analysis of wind turbine under tornado

Field observations have revealed several wind turbine failures during tornadoes, including May 14, 2012, for example, during the Harper County, Kansas, tornado in the United States. Similar failures have been seen in southern Ontario, Canada, as well. A series of investigations have been devoted to studying the tornado-induced loads on residential houses and low-rise buildings. However, there is a gap in knowledge on the effect of tornadoes on vital energy structures such as wind turbine towers [1]. Case et al. [2] studied tornado-induced loads on low-rise buildings considering different geometry and orientation while Razavi and Sarkar [3] studied the effect of using different values for swirl ratio and translation speed of a tornado on a gable roof of a low-rise building model. The swirl ratio is defined as the ratio between the maximum tangential and radial velocities in the flow of the tornado wind field [4]. Wang et al. [5] obtained the surface pressure on a cubic building model with openings experimentally under tornado loads. Hu et al. [6] measured the characteristics of the flow field around a gable-roof building model by a digital particle image velocimetry (PIV) system at different radial distances and orientation angles from the tornado center. Meanwhile, Yang et al. [7] used a PIV system and load transducer to characterize the wake vortex and the resultant loads on a rigid high-rise building model. An extensive research program was therefore launched to investigate wind turbine behavior under high-intensity wind events. The study presented here focuses on a numerical model developed in-house for predicting the straining action acting on wind turbine towers due to tornadoes. Hamada et al. [8] developed a numerical model to study the response of transmission line systems under tornadoes. The numerical model incorporated the data obtained from Hangan and Kim's [4] computational fluid dynamics (CFD) study to simulate the tornadic wind fields of F2 and F4 category tornadoes. This model was subsequently employed in several investigations assessing the behavior of transmission lines under tornadoes [9–11].

Because of the uniqueness of wind turbine structures, structural analyses under tornadoes involve several challenges, which can be summarized as follows:

1. Tornado wind fields, unlike synoptic boundary layer wind fields, have three components: radial, tangential, and vertical (axial). These components vary significantly in space, which means that the structural elements of the wind turbines will experience different velocities (in magnitude and direction).
2. There is a variation in wind turbine heights and this makes the task of analyzing such structures due to tornado wind fields (that change significantly with heights) more challenging.
3. Different tornado wind fields, even from the same category such as F2, have different properties for the velocity components (that vary differently in space), which result in different straining actions on the wind turbine's structural elements.
4. The technology of enhancing the blades' airfoils is developing rapidly. And since the loads acting on the blades are dependent on the airfoil properties, it needed to be considered in the current study.

To predict the response of wind turbines under tornado loading, a numerical model is developed [12]. The numerical model incorporates a wind field that was generated based on CFD data generated by Hangan and Kim [4] and corresponding scaling for tornadoes established by Hamada et al. [8]. The analyses are based on moving the tornado in space around the wind turbine in order to determine the critical tornado locations for both the tower and the blades for a variety of blade pitch angles. The findings show that changes in the tornado location and the pitch angle lead to significant variations in the base moment of the tower and root moments of the blades, and the considered tornado wind field presents a hazard for the investigated wind turbine.

24.2.2 Structural response of wind turbine to downburst

A downburst is defined as a territory of strong moving air that falls suddenly on the ground during a thunderstorm, then transfers outwards in all directions producing vortices [13]. A downburst is another form of extreme wind events. However, it is not considered in the design codes [14,15]. Climate change results in an apparent increase in the rate and magnitude of this type of extreme wind event. In addition to having different profiles and characteristics compared to large-scale wind events, the transient nature and unpredictability of downbursts impose challenges. The wind direction of large-scale wind events is often known and the configuration of the wind turbine in terms of the rotor plane and the blade pitch angle can be adjusted accordingly to minimize the straining actions on the tower and blades. However, a thunderstorm could occur at any random location within a short time interval, which makes it difficult to predict in advance its exact location relative to the tower. It is therefore difficult to identify the wind direction that the wind turbine will be exposed to during a downburst and to adjust the wind turbine configuration accordingly.

Nguyen et al. [16−18] and Lu et al. [19] used a deterministic-stochastic hybrid model to study a 5-MW wind turbine under a downburst wind effect. Their analysis was conducted using FAST as open-source software, which is used for the analysis and design of wind turbines. The downburst wind field adopted in their studies was generated using two approaches. Nguyen et al. [16,17] and Nguyen and Manuel [18] presented the downburst wind field as mean and turbulent components generated separately. The mean component was generated based on an analytical model developed by Chay et al. [20]. This analytical model was an extension of the model developed by Oseguera and Bowles [21] and Vicroy [22] by considering the variation of both the radial and the vertical velocities over time as well as the translation velocity of the storm. This analytical model requires defining specific downburst parameters, which were taken from the NIMROD and JAWS projects [23,24]. Meanwhile, the turbulent part was artificially generated as a random process with coherence and standard turbulence power spectral density functions using TurbSim [25], which is an open-source turbulence simulator. The turbulence was modeled using the same scheme adopted in nonthunderstorm boundary layer winds. The coherence function was modeled using the approach developed by Davenport [26], while Kaimal power spectra [27] were used as the basis for simulating the turbulence components. The generated turbulence was then superimposed on the mean component to produce a downburst time history. Meanwhile, Lu et al. [19] used the output of large eddy simulations (LES) conducted by Hawbecker et al. [28], based on a cooling source model. From the LES-generated fields, full-domain slices of 2D wind fields were extracted for each downburst, then fed into an NREL 5-MW turbine model. In their studies, the researchers presumed certain scenarios that could influence the findings, particularly under high wind speeds and the sudden change in wind direction, which are key characteristics of downbursts. They assumed that the wind turbine would remain in operation conditions even if the wind speed exceeds the cut-out speed. They allowed for yaw errors up to 45 degrees during the change in the wind direction. These assumptions might lead to excessive loads on both the wind turbine tower and blades. For simulating the downburst configurations, the storm was assumed to move with a translation speed in a constant route and a constant direction relative to the ambient wind. They selected storms with track lines inclined between $+45$ and -45 degrees with respect to the ambient wind direction. Only upwind storms, which can occur in front of the wind turbine, were considered. As such, the study did not fully consider the random nature of downbursts that could occur at any location relative to the wind turbine tower.

On the other hand, Kwon et al. [29] developed a formulation for assessing the gust effect on wind turbines under downburst loading. They stated that the downburst gust-front wind induces higher loads on wind turbines with a lower dynamic effect compared to boundary layer wind. All the above studies were conducted numerically. Meanwhile, only one experimental study was carried out by Zhang et al. [30] to evaluate the characteristics of the fluid-structure interaction for a scaled-down wind turbine model subjected to a microburst-like wind, generated using an impinging jet microburst simulator. The wind loads acting on the wind turbine model was measured for different downburst radial locations as well as for different wind turbine orientation angles with respect to the incoming wind direction. They concluded that the dynamic effect of the microburst-like wind is higher on wind turbines with free-rotating blades than that with stationary blades. This is due to the presence of large-scale primary vortices in the microburst-like wind interacting with the unsteady wake vortex resulting from the rotation of the blades.

A numerical model is developed and validated to investigate the effect of downburst wind loading on wind turbines [31]. The numerical model can predict the effect of downbursts on wind turbines taking into consideration different downburst parameters as well as the change in the pitch angle of the blades. The research gives critical downburst configurations that lead to peak responses. According to the result, a downburst with a maximum radial velocity of 70 m/s develops straining actions on the tower and the three blades, exceeding significantly those calculated using IEC61400-1 guideline for class I wind turbines. The main reason behind that is the random location of the downburst and, consequently the wind direction, which will not allow adjusting the rotor plane orientation as typically done under extreme synoptic winds. Downbursts with maximum radial velocities of 50 and 55 m/s are found to be critical for the tower and the blades, respectively. At those velocity values, the straining actions due to the downbursts become equivalent to those calculated based on IEC61400-1 guidelines using a synoptic hub wind velocity of 70 m/s.

24.2.3 Seismic response of wind turbine tower

Failures of wind turbine towers subject to ground motion are rare, but the risk should be carefully considered given the fact that it affects entire wind farms, where a considerable number of similarly designed and nonredundant wind turbine towers are subject to the same seismic actions.

Wind turbine towers under wind and seismic actions have been studied through experimental testing, field investigations, and numerical analysis. The experimental testing of the collapse of wind turbine towers under large dynamic excitations tends to be limited by the space and safety of the test site. Large-scale elastic testing has been performed,

such as the large-scale experimental program on a decommissioned wind turbine tower by Prowell et al. [32,33], but few wind turbine towers have been experimentally tested to failure. In addition, some scale issues are involved in the experimental testing of wind turbine towers in wind tunnels that may affect the accuracy of the results [34]. Field investigation of failed towers following disasters can provide forensic information that is valuable from a practical point of view, but these are the final stage results of extreme events for which the failure process cannot be described. Numerical simulation techniques based on nonlinear finite element (FE) analysis, if properly used, can demonstrate the progressive collapse of a structure under extreme loading.

Regarding previous numerical studies on the seismic response of wind turbine towers, Nuta et al. [35] performed incremental dynamic analysis (IDA) based on the FE method to obtain fragility curves. Afterward, Patil et al. [36] carried out a detailed fragility analysis under near-fault and far-fault ground motions. More recently, Sadowski et al. [37] compared the IDA results on a wind turbine tower with welding imperfections under near- and far-fault earthquakes. Regarding the FE analysis of wind turbine towers under extreme wind loads, Zhang et al. [38] performed a dynamic time-history analysis under simulated typhoon wind velocity histories to illustrate the wind turbine tower failure modes. Dai et al. [39] conducted an FE analysis of a typical 1.5 MW wind turbine tower and observed different failure stages in wind-induced collapse for different wind directions. Furthermore, wind turbine towers have been investigated under multiple hazard loads. Asareh et al. [40] combined seismic fragility analysis with operational wind loads based on FE analysis. Smith and Mahmoud [41] evaluated the performance of wind turbines of various heights under wind, operation, and seismic loads. Mo et al. [42] performed seismic fragility analysis considering different operating conditions. Although many studies have been conducted using nonlinear dynamic FE simulations, few of them specifically compared the failure process under strong ground motions or wind actions.

Sadowski et al. [37] present an extensive set of nonlinear history response analyses investigating the seismic behaviors of a slender metal wind turbine support tower, modeled as a thin-walled near-cylindrical shell, under a representative selection of 10 near-fault and 10 far-field earthquake records. The tower exhibits high membrane stiffness against seismic excitations, but once in the inelastic range a plastic hinge develops at a change of thickness potentially leading to catastrophic collapse, with very little prior energy dissipation and no alternate load paths. The imperfections of the wall significantly reduce (up to 17%) the spectral acceleration at which plastic damage initiates. An imperfect tower also exhibits more numerous potential hinge locations, increasing the variability in the seismic response. The inclusion of vertical accelerations is not necessarily more detrimental to the elastic response or the intensity at which damage initiates. However, it has the potential to shift the critical hinge location to a weaker part of the tower, particularly when imperfections are present. When scaled to the same spectral acceleration at fundamental periods, near-fault records with pulse-like effects and large vertical accelerations are more demanding in wind turbine towers with imperfections than far-fault records with rupture distances below 50 km. A preliminary investigation into the effects of scaling to attain target average spectral accelerations from spectra with different damping levels suggests that employing higher damping may be more damaging to the structure. This is attributed to differences in spectral ordinates at individual periods leading to larger scaled spectral displacements at the fundamental period and the proneness of the structure to ratcheting collapse. Wind turbines are dominated by the fundamental modes, and the intensity measure based on the geometric average of the spectral acceleration at the first periods in the three directions is a reasonable choice for multiple stripe analyses. However, further studies are necessary to investigate the efficiency of Intensity Measures that incorporate selected higher-order modes.

24.3 Wind turbine tower testing technique and structural health monitoring

Due to vibration during their operational life, the tower, blades, and other components of wind turbines are prone to fatigue damage, which needs to be carefully considered at the design stage or for the determination of the remaining life [43,44].

24.3.1 Noncontact vibration measurement methods for wind turbine tower

The long-term monitoring of wind turbine towers has been performed with sensors that require physical components attached to the structure [45–47]. However, the deployment of contact vibration sensors is labor-intensive and challenging from a logistical point of view. The height of most wind turbine towers combined with the lack of elevators hinders the deployment of sensors, data loggers, and computers needed in contact measurement methods. These also need long cables that increase the workload and the installation time unless wireless sensors are employed [46]. In addition,

researchers that are not staff members of the wind farm often need permission and specific safety training to access a wind turbine tower and install the sensors.

Noncontact measurement methods can significantly simplify the field-testing process because there is no need to access the wind turbine [45,47], although some measurement techniques may benefit from a reflection device attached to the structure to improve the quality of the signal [47]. Noncontact measurement methods, such as photogrammetry systems, laser Doppler vibrometer (LDV), and interferometric radar (IR), have also been used in the testing of wind turbine structures [47–51].

Probably the most cost-effective method is the assembly of a photogrammetry system constructed with a consumer-grade camera and image processing, but it may be influenced by natural background lighting conditions [47,48]. Based on Doppler shifts of a laser beam, laser vibrometers have been used in operational modal analysis (OMA) of wind turbine towers [47]. However, current LDV sensors can only measure from a single point. IR sensors, which are not influenced by weather conditions, have been used in field testing of historic buildings, television towers, and stay cables [49–51].

Vibration measurements of two wind turbine towers by using contact and noncontact sensors are studied [52]. The contact sensors included integrated circuits piezoelectric accelerometers and passive servo ultra-low frequency velocimeters; the noncontact sensors included a LDV sensor and an IR sensor. Although contact sensors generally failed to record low-frequency vibrations, they gave the most precise vibration measurements for the wind turbine towers, and they are particularly recommended for long-term monitoring in which an installation is permanent. As they are installed in towers in most cases, contact sensors are suitable for wind turbine tower measurements in both working and nonworking conditions. Leaving aside the cost, noncontact sensors, that is, LDV and IR sensors, significantly simplify testing onsite, because they can be set up at a distance from a tower. In addition, they capture the low-frequency vibration of towers more accurately than contact sensors. However, the quality of the signal recorded by noncontact sensors may be compromised by environmental conditions. The LDV sensor is suitable for one-off monitoring of several towers of wind farms in operation without accessing the towers. It can capture high-order vibration frequencies, well above the first one, with precision comparable to contact sensors. LDV sensors can be used in working conditions by selecting measurement points that are not blocked by obstacles. On the other hand, the use of an IR sensor is recommended to extract mode shapes, because it allows one to obtain a dense array of multipoint measurements from the lower portion of a tower, but not from its top portion due to interference introduced by the blades, and that effect can be stronger in working conditions. Measurements by an IR sensor can only be used to identify the first vibration mode because its output is in the form of displacement that has small amplitudes at high-order modes; the quality of the IR sensor output is poor in the high-frequency range.

24.3.2 Modal parameter identification of wind turbine tower

Wind turbine tower vibration parameters are critical for the design and maintenance of wind farms. Furthermore, the identification of the aerodynamic damping is challenging because of the complex fluid-structure interaction and the nature of turbulent wind [53]. Classical experimental modal analysis requires a controlled excitation to trigger a dynamic response [54]. OMA, which does not require controlled force excitation of large wind turbine structures, is usually preferred to measure aerodynamic damping in operation. However, methods with artificial excitations (such as boat impact [55] and hydraulic shaker [56]) have also been used. In the literature, a limited number of studies focused specifically on identifying this damping contribution [47,55–63]. Measuring damping in parked wind turbines has been proved easier than in operating conditions [58]. Studies by researchers such as Devriendt et al. [59] and Bajrić et al. [60] have successfully identified damping for parked turbines using different identification methods either in the time or frequency domain. The identification methods used for operating turbines are similar to those for parked turbines. Hansen et al. [57] used stochastic subspace identification to extract the damping ratios for an operating wind turbine but the resulting damping ratios were scattered and the contribution due to aerodynamic damping alone remains unclear. Ozbek and Rixen [60] used the least square complex exponential method to identify aerodynamic damping with data from strain gauges and photogrammetry measurements. The measured damping ratio values did not vary significantly and were close to simulation results obtained using HAWCStab [61]. Devriendt et al. [62] used the poly least-squares complex frequency-domain (p-LSCF) estimator to identify the total damping for an operational wind turbine. They emphasized that harmonics in the excitation would hinder the use of classical OMA methods which assumes that measured resonances are only caused by amplification of the broadband noise excitation at the natural frequencies of the system. Hu et al. [63] implemented the p-LSCF method to identify the total damping in an operating turbine with different rotation speeds. The resonance due to 3P loading was observed to have a significant effect on the identified total

damping. Koukoura et al. [55] studied the total damping in an operating offshore wind turbine under ambient excitation using the enhanced frequency domain decomposition method. They found that a beating phenomenon observed in the autocorrelation function of the response made the identification less reliable, especially for side-side vibration.

Although many research works have been conducted to identify the aerodynamic damping in operating wind turbines using traditional OMA methods, limitations in these methods still exist. For operating wind turbines, the validity of some basic assumptions underpinning the implementation of most OMA methods remain doubtful and this causes difficulties in applying OMA techniques to wind turbines. These difficulties have been described by Tcherniak et al. [64] and Ozbek et al. [58]. First, the excitations to the structure need to be uncorrelated, but the forces exciting a wind turbine are not uncorrelated as they are coupled due to the influence of the rotor rotation. Second, traditional OMA methods assume that the resultant responses due to ambient excitation only include harmonics caused by the natural modes of the structure but not harmonics due to ambient excitations themselves. This assumption is violated by the rotor rotation causing 1P, 3P, etc. loadings to the tower. Third, traditional OMA techniques require that the structure system itself is a time-invariant system, which is not the case for wind turbines. The rotor rotation causes the system to be time-periodic [65]. Moreover, aerodynamic damping is influenced by the inflow wind speed, the rotation speed, and the pitch angles. None of these parameters are constant for wind turbines in normal operation due to the stochastic nature of wind turbulence and the variability of controlled conditions [66]. Fourth, and maybe less important, the excitations caused by turbulent wind fields are not white noise. The effort to extract dynamic parameters for wind turbines resulted in the development of modified OMA methods suitable for large wind turbine structures under ambient excitations. The natural excitation technique OMA method developed by James et al. [67] was initially used for modal parameter extraction of operating vertical-axis wind turbines. Some researchers improved the traditional OMA methods so that these methods can identify the wind turbine system when the excitations contain harmonics.

Dai et al. [68] presented a new modified stochastic subspace identification method for system identification of a structure under excitation with harmonic components with frequencies close to the natural frequencies of the structure. Its basic idea is to modify the Hankel matrix by adding harmonic vectors. This method effectively works with no need of modifying existing stochastic subspace identification algorithms. The effectiveness, accuracy, and robustness of the proposed method were numerically verified through a simple lumped-mass system. Since the ERA method and the stochastic subspace identification method both use the singular value decomposition to extract information, comparisons were made between the ERA method and the proposed modified stochastic subspace identification method. The modified stochastic subspace identification method showed good noise resistance and stability. The method was then applied to a utility-scale wind turbine tower that operates at a fixed rotation speed for rated power output. Actual structural modes and virtual harmonic modes that are caused by harmonic components in excitation can be successfully distinguished by the method developed. The field-testing campaign and modal frequency and damping ratio identification, as well as structural assessment results, were presented. Dong et al. [69] applied a similar modified stochastic subspace identification method to identify the frequency and damping of an operating turbine and obtained a wide range of values in different operating conditions.

24.3.3 Damping identification and aerodynamic damping of wind turbine in operation for seismic analysis

Damping is a key parameter in wind turbine systems as it limits the vibration amplitude. Therefore, identifying damping reliably in these systems is an important issue. In practice, only the total damping can be measured directly. For wind turbines in operation, the fore-aft (FA) aerodynamic damping has the highest contribution, so the measured total damping could also be seen as a close substitute for the aerodynamic damping. In many published studies, the distinction between total damping and aerodynamic damping for operating wind turbines is not always clear [57]. Besides the difficulties mentioned above, all previously discussed studies assumed that the wind turbine system is decoupled in terms of the FA and aide-aide (SS) motions.

In recent years, a number of authors have studied the seismic behavior of wind turbines [36,37,70–72]. The aerodynamic loads were not considered in these works because it was assumed that an emergency shutdown would be triggered if the acceleration of the nacelle reaches the safety threshold [40]. However, it is likely that strong ground motions would strike operating wind turbines before the blades are fully feathered and stop rotating, adding potentially unfavorable loads that may govern the tower design [73]. In light of this, the seismic analysis of wind turbines under operational conditions has attracted increasing interest, the emphasis of which is on the interaction between the aerodynamic and the earthquake actions [74–77]. Earthquake-induced oscillations of the turbine affect the aerodynamic loads and vice versa [78]. Hence, full aeroelastic analysis including the inherent interaction is recommended. Software

packages that are specific for wind turbines such as FAST and GH bladed can be used to predict the seismic performance combined with the aerodynamic loading. These numerical tools can be accurate but they require a significant computational effort because of the need for repetitive simulations to be performed for all the selected earthquake records and the different wind environment scenarios [78,79]. On account of this, some international standards and design guidelines propose simplified uncoupled analyses in which the aerodynamic and the seismic responses are calculated separately and then combined [14,15,73].

The interaction between the vibrating blades and the wind field can be considered in a quasi-steady approach by means of the adequate definition of the aerodynamic damping in the seismic analysis [80]. The modification of the relative wind velocity at the blades induced by the blade vibration during the earthquake changes the local angle of attack and thus it affects the aerodynamic force. Before the blades enter a stall condition, the increment of the aerodynamic force is always opposite to the direction of the tower motion, which provides an effect equivalent to a viscous damper that mitigates the vibration of the tower [81]. The determination of this additional damping effect is necessary to obtain accurate design loads as well as to help propose vibration control schemes [82]. Dai et al. [68] conducted a field measurement of a 1.5-MW horizontal-axis wind turbine (HAWT). When the blades started rotating for rated-power generation, an increase in the damping ratio of the fundamental vibration mode of the tower (from 1.8% to 3.2%) was observed, which is due to the aerodynamic damping effect. Dong et al. [83] launched a long-term prototype observation of a 2.5-MW offshore HAWT. The overall damping ratio measured in this work ranges from 1.07% to 9.98% under different operational conditions. The overall damping includes the inherent dissipation from the structure and the soil, as well as the aerodynamic and the hydrodynamic (when applicable) damping effects [84]. The aerodynamic damping can be much higher than the other sources of dissipation, especially for large-scale wind turbines. Liu et al. [81] carried out a load analysis on a 5-MW offshore HAWT and reported a great reduction in the average vibration amplitudes of the tower (from 1.94 to 0.22 m) when the aerodynamic damping effect is included. Therefore, the inappropriate consideration of aerodynamic damping may change the response prediction significantly, leading to either unreliable or overconservative designs.

Increasing efforts have been made to quantify the aerodynamic damping effect in numerical analyses of the seismic response. Witcher [85] examined combined wind and earthquake loading in a 2-MW HAWT using the GH Bladed software. He noticed that the peak tower response obtained in the fully-coupled time-domain analysis could be approximated by the response-spectrum approach with a 5% damping ratio. This is convenient because the damping ratio reference in the seismic design spectra for buildings in ASCE/SEI 7−10 [86] is set to 5%. ASCE/AWEA [73] recommends that the overall damping ratio should be set to 1% for parked conditions and 5% for operational conditions (i.e., 1% structural damping ratio plus 4% aerodynamic damping ratio). Valamanesh and Myers [87] complemented the damping values provided by ASCE/AWEA [73] from numerical simulations conducted using FAST for the dynamic analysis of a 1.5-MW HAWT. They recommended a 5% damping ratio for the operational conditions in the FA direction, while 1% is used for parked conditions in both directions and operational conditions in the side-side direction. Avossa et al. [80] investigated a decoupled model for the vulnerability assessment of a 5-MW HAWT subjected to wind and seismic actions, within which the aerodynamic damping was predicted from the proposal of Valamanesh and Myers [87], namely 0.1% for the parked condition, 3.7% in the FA direction and 1% in the side-side direction for the operational condition. However, experimental studies on this topic are rather scarce. The exception is the shake table test on an actual 65-kW HAWT conducted at the University of California, San Diego [33]. This work concluded that the aerodynamic damping has an appreciable effect on the FA response, while it may be negligible in the SS direction.

Recent research [88] showed that the rotating blades introduce significant damping coupling between the FA and SS directions for an operating wind turbine and this coupling is nonclassical, that is, the coupling is through a damping matrix which, unusually, is not symmetric. From this different view of aerodynamic damping, a new operational identification method that extracts the aerodynamic damping matrix directly is developed [53]. The proposed new identification method can extract the 2×2 damping matrix with good accuracy, provided a force input with sufficient amplitude is applied. Additionally, In practice, the size of devices to generate external, harmonic forces needs careful consideration for large wind turbine structures. Analyzing a FE model representing the tower and simplified wind-rotor interaction based on blade element momentum, they also found that identifying the full 2×2 damping matrix including the coupling between the FA and SS motions is essential to correctly capture the vibration behavior in the SS direction.

To investigate a practical approach to estimate the responses of wind turbine towers by analyzing both actions separately, a 1/100-scaled model of a wind turbine tower with optimized blades is developed and it has been tested under simultaneous operational wind and earthquake actions [89]. The goal was, according to this research, the interaction between the wind and the seismic-induced loads could lead to a reduction in the overall response compared to the

earthquake-only scenario. The coupling effect between the wind and the earthquake responses tends to increase with the wind speed and decrease with the peak ground acceleration.

24.4 Vibration control of wind turbine tower

To improve the efficiency in the generation of electricity from the wind, large-diameter rotors and thin wall slender towers are usually adopted in current designs, which are vulnerable to external excitations such as wind and seismic actions during their lifetime. These excitations can lead to excessive vibrations in the wind turbine blades and the tower, resulting in a reduction in electricity generation or even in the failure of the blades or the tower [39,90]. Moreover, as wind turbine towers become taller, their safety and serviceability may be considerably reduced. Therefore, it is of great significance to develop vibration suppression techniques that protect wind turbines from these hazards and improve the overall dynamic performance of the structure.

In response to these challenges and design trends, extensive research has been carried out on various vibration control devices to mitigate wind turbines' vibrations. In general, these devices can be grouped into two categories: passive control systems and active or semiactive control systems [91,92]. Active control systems are usually more expensive and less robust as they require external power sources that may not be available in the event of a power shortage. Contrary to active control systems, passive control systems need no external power, and they are widely adopted in different engineering applications. Among all the devices used to control wind turbine towers, tuned-type dampers are well-established and commonly used in industry, and they received most of the attention in the literature. Murtagh et al., [93], Lackner and Rotea [94], and Stewart and Lackner [95] suggested using tuned mass dampers (TMDs) for the vibration control of wind turbines; Ghaemmaghami et al. [96] suggested annular tuned liquid dampers (TLDs), and Chen et al. [97] suggested spherical TLDs; Colwell and Basu [71], Mensah and Dueñas-Osorio [98], and Chen et al. [99] proposed tuned liquid column dampers; Chen and Georgakis [100] developed a rolling ball damper; Zhang et al. [101] introduced a ball vibration absorber; Zuo et al. [102] proposed using multiple tuned mass dampers; Zhao et al. [103] developed a novel scissor-jack braced viscous damper; Zhang et al. proposed using ungrounded tuned mass inerter system [104] or tuned parallel inerter mass system (TPIMS) [82]. In all the cases, the results showed the effectiveness of the proposed dampers in the mitigation of the wind turbine tower vibrations from these hazards and the improvement of the overall dynamic performance of the structure.

24.4.1 Effect of soil-structure interaction on the design of tuned mass dampers

The accurate prediction of the seismic response of wind turbines is of great significance for maintaining and achieving the right balance between safety and economic efficiency. Underpredicting the seismic hazard may result in significant damage or even failure of the wind turbine, causing great economical loss and social consequences. In the other extreme case, overestimating the seismic hazard may lead to high economic and environmental costs of wind turbine farms, hindering the growth and expansion of wind power. In this regard, considering the soil-structure interaction (SSI) is an important factor in the accurate evaluation of the seismic response of tall and slender structural systems like wind turbines [105]. Bazeos et al. [106] first studied the influence of SSI in wind turbines by introducing a set of linear springs and dashpots. The results from eigenvalue analysis showed that the fundamental frequency was significantly lower for the SSI system, which further influences the dynamic behavior of wind turbines. Similar results from other numerical [107–109] and experimental [110,111] studies confirmed the significant influence of SSI on the dynamic performance of wind turbine towers. Besides, the soil characteristics and its flexibility were also found to be of high relevance by other researchers [112,113]. Consequently, ignoring the SSI in the design of tuned-type dampers for wind turbines may result in detuning problems.

To highlight the SSI effect on the parameter design of TMD, Dai et al. [114–117] conducted a series of small-scale shaking table tests of wind turbine towers with soil and TMDs were conducted. The experimental results confirmed that TMDs designed considering SSI were more efficient in vibration reduction compared to those designed with a fixed-base assumption. Moreover, a simplified numerical model was developed to further discuss the effect of SSI on TMD efficiency. The effect of site and earthquake intensity on the response reduction efficiency of TMDs was discussed with numerical simulations under synthetic ground motions generated for three different types of foundation soil. In general, the softer the site soil and the larger the earthquake intensity results in lower TMD efficiency, but there are exceptions. This is because the vibration control of TMDs depends not only on the soil stiffness but also on the frequency content of the ground motions, both of which are affected by the site classes and the earthquake intensity levels.

24.4.2 Novel vibration control system for wind turbine tower

The largest challenge of employing energy-absorbing dampers in wind turbine towers is that the small tower deformations limit the damper stroke which bottlenecks the maximum damping effect. A possible solution to this problem is to use geometric amplification mechanisms such as toggle brace systems [118]. Toggle brace systems have been studied for two decades and modern incarnations include the open-space damper system by Polat and Constantinou [119–121]. Toggle brace systems have been studied comprehensively in frame structures [122,123] but only Brodersen et al. [124] have studied these systems in wind turbines.

Utilizing the vertical deformation of the tower wall, viscous damper or scissor-jack braced viscous damper can effectively reduce the wind turbine's vibration equally under both earthquake and wind conditions. Under earthquake conditions with an operational rotor, due to the aerodynamic damping effect in the FA direction, the mitigation effect of the dampers in the side-to-side direction is comparatively greater. Scissor-jack braced viscous dampers are not only able to magnify the stroke of the damper to practical levels but also can decrease the required damping force to obtain the same damping effect compared to the brace-less viscous damper. Thus, the implementation of scissor-jack braced viscous dampers appears to be a practical engineering solution for the problem of excessive wind turbine vibrations. Additionally, the proposed scissor-jack braced viscous damper system can be further explored. The performance-based response mitigation study is a promising direction. The code-based practical optimization design is an imperative development direction as well. Experimental studies are also necessary to test the applicability and practicality of the scissor-jack braced viscous damper system applied in wind turbines.

The TPIMS is effective for seismic response mitigation of the wind turbine tower. A much smaller tuned mass of the TPIMS can realize the same target displacement reduction compared with the traditional tuned-mass dampers. Therefore, the TPIMS is a suitable technique for the retrofit of in-service wind turbine towers with excessive vibrations. Zhang et al. [82] proposed a design optimization method for the TPIMS, and it was proved as an efficient method for the design of the TPIMS to achieve a target wind turbine tower vibration performance with a small relative displacement of the tuned mass in the TPIMS. The number of design parameters in the TPIMS can be reduced with this optimization approach, which enhances the computational efficiency of the TPIMS design. The TPIMS demonstrated great robustness. Under four different ground shakings, seismic responses of the tower are not sensitive to the variation of the damping ratio and stiffness of the TPIMS. Therefore, a proper design of the tuned mass of the TPIMS can suppress seismic vibrations of the wind turbine tower. The proposed design method can be potentially extended to other forms of excitations besides white-noise, as well as to the design of structures with other type inerter systems, which is to be studied soon.

Another challenge is, which may cause a significant $P-\Delta$ effect, caused by the extra loading of the traditional TMD. For this reason, a novel damping system, namely the cable-based energy dissipating system (CEDS), was proposed by Dai et al [125]. Being different from the former techniques, the cable is attached to the tower along with the height, which allows the bending deformation of the tower to be transformed into the rigid motions of the cable extremities. By this approach, the energy of the tower is collected and is then dissipated by the damping device connected with the cable. Compared with conventional TMDs, the damper can be placed directly on the ground, avoiding additional weight on the structure. Due to the flexible nature of cable, the energy of the tower can be sufficiently transformed into the cable system, enabling efficient energy dissipation. By simulating the behavior of the CEDS with a customized element is developed based on FE formulation, they found that for both seismic and wind-induced vibrations, the proposed CEDS is capable to reduce the peak response within a wide frequency range, achieving efficient energy dissipation with high robustness.

24.5 Summary

The wind energy industry has developed rapidly in recent years. To increase energy generation efficiency and reduce operating costs, an increasing number of wind farms are deployed in challenging environments. As the supporting structures of wind turbines, the safety of wind turbine towers is an important topic for researchers and engineers, which includes structure stabilities and fatigue resistance of wind turbine towers under operational vibrations, extreme wind loads, and earthquake effects. Tests and numerical simulations are the two basic research and design/analysis methods for wind turbine towers. For the numerical simulation, response spectrum and time history analysis are the two main procedures for calculating the resistances of wind turbine towers. For current research on wind turbine towers, the pulsating wind action for wind resistance studies and the tower coupling action for earthquake studies are the two popular topics. Health monitoring and vibration control of wind turbine towers is another significant research topic. Health

monitoring identifies structural damages and vibration control mitigates structural vibrations. Effective health monitoring and vibration control technologies can help construct taller wind turbine towers under lower budgets.

References

[1] Hou F, Sarkar PP. Aeroelastic model tests to study tall building vibration in boundary-layer and tornado winds. Eng Struct 2020;207:110259. Available from: https://doi.org/10.1016/j.engstruct.2020.110259.

[2] Case J, Sarkar P, Sritharan S. Effect of low-rise building geometry on tornado-induced loads. J Wind Eng Ind Aerodyn 2014;133:124−34. Available from: https://doi.org/10.1016/j.jweia.2014.02.001.

[3] Razavi A, Sarkar PP. Tornado-induced wind loads on a low-rise building: influence of swirl ratio, translation speed and building parameters. Eng Struct 2018;167:1−12. Available from: https://doi.org/10.1016/j.engstruct.2018.03.020.

[4] Hangan H, Kim JD. Swirl ratio effects on tornado vortices in relation to the Fujita scale. Wind Struct 2008;11:291−302. Available from: https://doi.org/10.12989/was.2008.11.4.291.

[5] Wang J, Cao S, Pang W, Cao J. Experimental study on Tornado-induced wind pressures on a cubic building with openings. J Struct Eng 2018;144:04017206. Available from: https://doi.org/10.1061/(ASCE)ST.1943-541X.0001952.

[6] Hu H, Yang Z, Sarkar P, Haan F. Characterization of the wind loads and flow fields around a gable-roof building model in tornado-like winds. Exp Fluids 2011;51:835−51. Available from: https://doi.org/10.1007/s00348-011-1102-6.

[7] Yang Z, Sarkar P, Hu H. An experimental study of a high-rise building model in tornado-like winds. J Fluids Struct 2011;27:471−86. Available from: https://doi.org/10.1016/j.jfluidstructs.2011.02.011.

[8] Hamada A, el Damatty AA, Hangan H, Shehata AY. Finite element modelling of transmission line structures under tornado wind loading. Wind Struct An Int J 2010;13:451−69. Available from: https://doi.org/10.12989/was.2010.13.5.451.

[9] Hamada A, el Damatty AA. Behaviour of guyed transmission line structures under tornado wind loading. Comput. Struct 2011;89:986−1003. Available from: https://doi.org/10.1016/j.compstruc.2011.01.015.

[10] Hamada A, el Damatty AA. Failure analysis of guyed transmission lines during F2 tornado event. Eng Struct 2015;85:11−25. Available from: https://doi.org/10.1016/j.engstruct.2014.11.045.

[11] Ibrahim AM, el Damatty AA, el Ansary AM. Finite element modelling of prestressed concrete poles under downbursts and tornadoes. Eng Struct 2017;153:370−82. Available from: https://doi.org/10.1016/j.engstruct.2017.10.047.

[12] AbuGazia M, el Damatty AA, Dai K, Lu W, Ibrahim A. Numerical model for analysis of wind turbines under tornadoes. Eng Struct 2020;223:111157. Available from: https://doi.org/10.1016/j.engstruct.2020.111157.

[13] Theodore Fujita T. Downbursts: meteorological features and wind field characteristics. J Wind Eng Ind Aerodyn 1990;36:75−86. Available from: https://doi.org/10.1016/0167-6105(90)90294-M.

[14] GL. Guideline for the certification of wind turbines. Germanischer Lloyd Ind Serv GmbH 2010;(2010).

[15] -1, International standard "Wind turbines—Part 1: design requirement," International Electro-Technical Commission; 2010.

[16] Nguyen H, Manuel L, Veers P, Simulation of Inflow Velocity Fields and Wind Turbine Loads during Thunderstorm Downbursts. In: 51st AIAA/ASME/ASCE/AHS/ASC Structures, Structural Dynamics, and Materials Conference 18th AIAA/ASME/AHS Adaptive Structures Conference, American Institute of Aeronautics and Astronautics, Reston, Virginia, 2010. https://doi.org/10.2514/6.2010-2651.

[17] Nguyen H, Manuel L, Veers P. Wind turbine loads during simulated thunderstorm microbursts. J Renew Sustain Energy 2011;3:053104. Available from: https://doi.org/10.1063/1.3646764.

[18] Nguyen H, Manuel L. Transient thunderstorm downbursts and their effects on wind turbines. Energies 2014;7:6527−48. Available from: https://doi.org/10.3390/en7106527.

[19] Lu N-Y, Hawbecker P, Basu S, Manuel L. On wind turbine loads during thunderstorm downbursts in contrasting atmospheric stability regimes. Energies 2019;12:2773. Available from: https://doi.org/10.3390/en12142773.

[20] Chay MT, Albermani F, Wilson R. Numerical and analytical simulation of downburst wind loads. Eng Struct 2006;28:240−54. Available from: https://doi.org/10.1016/j.engstruct.2005.07.007.

[21] Oseguera RM, Bowles RL. A simple, analytic 3-dimensional downburst model based on boundary layer stagnation flow. Virginia: Hampton; 1988.

[22] Vicroy DD. A simple, analytical, axisymmetric microburst model for downdraft estimation. Virginia: Hampton; 1991.

[23] Fujita TT. Downburst, Microburst Macroburst 1985;.

[24] Hjelmfelt MR. Structure and life cycle of microburst outflows observed in Colorado. J Appl Meteorol 1988;27:900−27 . Available from: https://doi.org/10.1175/1520-0450(1988)027 < 0900:SALCOM > 2.0.CO;2.

[25] Jonkman B.J. Turbsim user's guide: version 1.50, 2009.

[26] Simiu E, Yeo D. Wind Eff Struct. Chichester, UK: John Wiley & Sons, Ltd; 2019. Available from: https://doi.org/10.1002/9781119375890.

[27] Kaimal JC, Wyngaard JC, Izumi Y, Coté OR. Spectral characteristics of surface-layer turbulence. Q J R Meteorol. Soc 1972;98:563−89. Available from: https://doi.org/10.1002/qj.49709841707.

[28] Hawbecker P, Basu S, Manuel L. Investigating the impact of atmospheric stability on thunderstorm outflow winds and turbulence. Wind Energy Sci 2018;3:203−19. Available from: https://doi.org/10.5194/wes-3-203-2018.

[29] Kwon DK, Kareem A, Butler K. Gust-front loading effects on wind turbine tower systems. J Wind Eng Ind Aerodyn 2012;104−106:109−15. Available from: https://doi.org/10.1016/j.jweia.2012.03.030.

[30] Zhang Y, Sarkar PP, Hu H. An experimental investigation on the characteristics of fluid-structure interactions of a wind turbine model sited in microburst-like winds. J Fluids Struct 2015;57:206–18. Available from: https://doi.org/10.1016/j.jfluidstructs.2015.06.016.
[31] Ahmed MR, el Damatty AA, Dai K, Ibrahim A, Lu W. Parametric study of the quasi-static response of wind turbines in downburst conditions using a numerical model. Eng Struct 2022;250:113440. Available from: https://doi.org/10.1016/j.engstruct.2021.113440.
[32] Guo L, Uang C-M, Elgamal A, Prowell I, Zhang S. Pushover analysis of a 53 m high wind turbine tower. Adv Sci Lett 2011;4:656–62. Available from: https://doi.org/10.1166/asl.2011.1336.
[33] Prowell I, Elgamal A, Uang C-M, Enrique Luco J, Romanowitz H, Duggan E. Shake table testing and numerical simulation of a utility-scale wind turbine including operational effects. Wind Energy 2014;17:997–1016. Available from: https://doi.org/10.1002/we.1615.
[34] van Treuren KW. Small-scale wind turbine testing in wind tunnels under low Reynolds number conditions. J Energy Resour Technol 2015;137. Available from: https://doi.org/10.1115/1.4030617.
[35] Nuta E, Christopoulos C, Packer JA. Methodology for seismic risk assessment for tubular steel wind turbine towers: application to Canadian seismic environment. Can J Civ Eng 2011;38:293–304. Available from: https://doi.org/10.1139/L11-002.
[36] Patil A, Jung S, Kwon O-S. Structural performance of a parked wind turbine tower subjected to strong ground motions. Eng Struct 2016;120:92–102. Available from: https://doi.org/10.1016/j.engstruct.2016.04.020.
[37] Sadowski AJ, Camara A, Málaga-Chuquitaype C, Dai K. Seismic analysis of a tall metal wind turbine support tower with realistic geometric imperfections. Earthq Eng & Struct Dyn 2017;46:201–19. Available from: https://doi.org/10.1002/eqe.2785.
[38] Zhang Z, Li J, Zhuge P. Failure analysis of large-scale wind power structure under simulated typhoon. Math Probl Eng 2014;2014:1–10. Available from: https://doi.org/10.1155/2014/486524.
[39] Dai K, Sheng C, Zhao Z, Yi Z, Camara A, Bitsuamlak G. Nonlinear response history analysis and collapse mode study of a wind turbine tower subjected to tropical cyclonic winds. Wind Struct. An Int J 2017;25:79–100. Available from: https://doi.org/10.12989/was.2017.25.1.079.
[40] Asareh M-A, Schonberg W, Volz J. Fragility analysis of a 5-MW NREL wind turbine considering aero-elastic and seismic interaction using finite element method. Finite Elem Anal Des 2016;120:57–67. Available from: https://doi.org/10.1016/j.finel.2016.06.006.
[41] Smith V, Mahmoud H. Multihazard assessment of wind turbine towers under simultaneous application of wind, operation, and seismic loads. J Perform Constr Facil 2016;30:04016043. Available from: https://doi.org/10.1061/(ASCE)CF.1943-5509.0000898.
[42] Mo R, Kang H, Li M, Zhao X. Seismic fragility analysis of monopile offshore wind turbines under different operational conditions. Energies 2017;10:1037. Available from: https://doi.org/10.3390/en10071037.
[43] Rezaei R, Fromme P, Duffour P. Fatigue life sensitivity of monopile-supported offshore wind turbines to damping. Renew Energy 2018;123:450–9. Available from: https://doi.org/10.1016/j.renene.2018.02.086.
[44] Martinez-Luengo M, Kolios A, Wang L. Structural health monitoring of offshore wind turbines: a review through the statistical pattern recognition paradigm. Renew Sustain Energy Rev 2016;64:91–105. Available from: https://doi.org/10.1016/j.rser.2016.05.085.
[45] Pieraccini M, Parrini F, Fratini M, Atzeni C, Spinelli P. In-service testing of wind turbine towers using a microwave sensor. Renew Energy 2008;33:13–21. Available from: https://doi.org/10.1016/j.renene.2007.02.001.
[46] Swartz RA, Lynch JP, Zerbst S, Sweetman B, Rolfes R. Structural monitoring of wind turbines using wireless sensor networks. Smart Struct Syst 2010;6:183–96. Available from: https://doi.org/10.12989/sss.2010.6.3.183.
[47] Ozbek M, Rixen DJ. Operational modal analysis of a 2.5 MW wind turbine using optical measurement techniques and strain gauges. Wind Energy 2013;16:367–81. Available from: https://doi.org/10.1002/we.1493.
[48] Brownjohn JMW, Xu Y, Hester D. Vision-based bridge deformation monitoring. Front Built Environ 2017;3. Available from: https://doi.org/10.3389/fbuil.2017.00023.
[49] Pieraccini M. Monitoring of civil infrastructures by interferometric radar: a review. Sci World J 2013;2013:1–8. Available from: https://doi.org/10.1155/2013/786961.
[50] Luzi G, Crosetto M., Monserrat O. Monitoring a tall tower through radar interferometry: the case of the Collserola tower in Barcelona, 2014;171–179. https://doi.org/10.1063/1.4879579.
[51] Gentile C, Cabboi A. Vibration-based structural health monitoring of stay cables by microwave remote sensing. Smart Struct Syst 2015;16:263–80. Available from: https://doi.org/10.12989/sss.2015.16.2.263.
[52] Wang Y, Dai K, Xu Y, Zhu W, Lu W, Shi Y, et al. Field testing of wind turbine towers with contact and noncontact vibration measurement methods. J Perform Constr Facil 2020;34:04019094. Available from: https://doi.org/10.1061/(ASCE)CF.1943-5509.0001366.
[53] Chen C, Duffour P, Dai K, Wang Y, Fromme P. Identification of aerodynamic damping matrix for operating wind turbines. Mech Syst Signal Process 2021;154:107568. Available from: https://doi.org/10.1016/j.ymssp.2020.107568.
[54] Ewins DJ. Modal testing: theory, practice and application. 2nd ed John Wiley & Sons; 2000.
[55] Koukoura C, Natarajan A, Vesth A. Identification of support structure damping of a full-scale offshore wind turbine in normal operation. Renew Energy 2015;81:882–95. Available from: https://doi.org/10.1016/j.renene.2015.03.079.
[56] Osgood R, Bir G, Mutha H, Peeters B, Luczak M, Sablon G. Full-scale modal wind turbine tests: comparing shak excitation wind excitation. Structural Dynamics and Renewable Energy 2011;113–24. Available from: https://doi.org/10.1007/978-1-4419-9716-6_11.
[57] Hansen MH, Thomsen K, Fuglsang P, Knudsen T. Two methods for estimating aeroelastic damping of operational wind turbine modes from experiments. Wind Energy 2006;9:179–91. Available from: https://doi.org/10.1002/we.187.
[58] Ozbek M, Meng F, Rixen DJ. Challenges in testing and monitoring the in-operation vibration characteristics of wind turbines. Mech Syst Signal Process 2013;41:649–66. Available from: https://doi.org/10.1016/j.ymssp.2013.07.023.

[59] Devriendt C, Magalhães F, Weijtjens W, de Sitter G, Cunha Á, Guillaume P. Structural health monitoring of offshore wind turbines using automated operational modal analysis. Struct Health Monit 2014;13:644−59. Available from: https://doi.org/10.1177/1475921714556568.
[60] Bajrić A, Høgsberg J, Rüdinger F. Evaluation of damping estimates by automated Operational Modal Analysis for offshore wind turbine tower vibrations. Renew Energy 2018;116:153−63. Available from: https://doi.org/10.1016/j.renene.2017.03.043.
[61] Hansen MH. Aeroelastic stability analysis of wind turbines using an eigenvalue approach. Wind Energy 2004;7:133−43. Available from: https://doi.org/10.1002/we.116.
[62] Wout W, Rasoul S, Gert DS, Christof D. Classifying resonant frequencies and damping values of an offshore wind turbine on a monopile foundation for different operational conditions. In: EWEA Annual Event; 2014.
[63] Hu W-H, Thöns S, Rohrmann RG, Said S, Rücker W. Vibration-based structural health monitoring of a wind turbine system. Part I: resonance phenomenon. Eng Struct 2015;89:260−72. Available from: https://doi.org/10.1016/j.engstruct.2014.12.034.
[64] Tcherniak D, Chauhan S, Hansen MH. Applicability limits operational modal anal operational wind turbines. in 2011;317−27. Available from: https://doi.org/10.1007/978-1-4419-9716-6_29.
[65] Allen MS, Sracic MW, Chauhan S, Hansen MH. Output-only modal analysis of linear time-periodic systems with application to wind turbine simulation data. Mech Syst Signal Process 2011;25:1174−91. Available from: https://doi.org/10.1016/j.ymssp.2010.12.018.
[66] Chen C, Duffour P. Modelling damping sources in monopile-supported offshore wind turbines. Wind Energy 2018;21:1121−40. Available from: https://doi.org/10.1002/we.2218.
[67] James III, GH, Carne TG, Lauffer JP. Lauffer, Nat excitation Tech (NExT) modal parameter extraction operating wind turbines, 1993.
[68] Dai K, Wang Y, Huang Y, Zhu W, Xu Y. Development of a modified stochastic subspace identification method for rapid structural assessment of in-service utility-scale wind turbine towers. Wind Energy 2017;20:1687−710. Available from: https://doi.org/10.1002/we.2117.
[69] Dong X, Lian J, Yang M, Wang H. Operational modal identification of offshore wind turbine structure based on modified stochastic subspace identification method considering harmonic interference. J Renew Sustain Energy 2014;6:033128. Available from: https://doi.org/10.1063/1.4881876.
[70] de Risi R, Bhattacharya S, Goda K. Seismic performance assessment of monopile-supported offshore wind turbines using unscaled natural earthquake records. Soil Dyn Earthq Eng 2018;109:154−72. Available from: https://doi.org/10.1016/j.soildyn.2018.03.015.
[71] Dai K, Huang Y, Gong C, Huang Z, Ren X. Rapid seismic analysis methodology for in-service wind turbine towers. Earthq Eng Eng Vib 2015;14:539−48. Available from: https://doi.org/10.1007/s11803-015-0043-0.
[72] Zhao Z, Dai K, Camara A, Bitsuamlak G, Sheng C. Wind turbine tower failure modes under seismic and wind loads. J Perform Constr. Facilities 2019;33:04019015. Available from: https://doi.org/10.1061/(ASCE)CF.1943-5509.0001279.
[73] ASCE/AWEA. Committee and others, Recommended practice for compliance of large onshore wind turbine support structures, ASCE/AWEA RP2011; 2012.
[74] Prowell I. An exp numer study wind turbine seismic behav, 2011.
[75] Asareh M-A. Dynamic behavior operational wind turbines considering aerodynamic seismic load interact, 2015.
[76] Asareh M-A, Schonberg W, Volz J. Effects of seismic and aerodynamic load interaction on structural dynamic response of multi-megawatt utility-scale horizontal axis wind turbines. Renew Energy 2016;86:49−58. Available from: https://doi.org/10.1016/j.renene.2015.07.098.
[77] Yuan C, Chen J, Li J, Xu Q. Fragility analysis of large-scale wind turbines under the combination of seismic and aerodynamic loads. Renew Energy 2017;113:1122−34. Available from: https://doi.org/10.1016/j.renene.2017.06.068.
[78] Santangelo F, Failla G, Santini A, Arena F. Time-domain uncoupled analyses for seismic assessment of land-based wind turbines. Eng Struct 2016;123:275−99. Available from: https://doi.org/10.1016/j.engstruct.2016.05.043.
[79] Santangelo F, Failla G, Arena F, Ruzzo C. On time-domain uncoupled analyses for offshore wind turbines under seismic loads. Bull Earthq Eng 2018;16:1007−40. Available from: https://doi.org/10.1007/s10518-017-0191-x.
[80] Avossa A, Demartino C, Contestabile P, Ricciardelli F, Vicinanza D. Some results on the vulnerability assessment of HAWTS subjected to wind and seismic actions. Sustainability 2017;9:1525. Available from: https://doi.org/10.3390/su9091525.
[81] Liu X, Lu C, Li G, Godbole A, Chen Y. Effects of aerodynamic damping on the tower load of offshore horizontal axis wind turbines. Appl Energy 2017;204:1101−14. Available from: https://doi.org/10.1016/j.apenergy.2017.05.024.
[82] Zhang R, Zhao Z, Dai K. Seismic response mitigation of a wind turbine tower using a tuned parallel inerter mass system. Eng Struct 2019;180:29−39. Available from: https://doi.org/10.1016/j.engstruct.2018.11.020.
[83] Dong X, Lian J, Wang H, Yu T, Zhao Y. Structural vibration monitoring and operational modal analysis of offshore wind turbine structure. Ocean Eng 2018;150:280−97. Available from: https://doi.org/10.1016/j.oceaneng.2017.12.052.
[84] Carswell W, Johansson J, Løvholt F, Arwade SR, Madshus C, DeGroot DJ, et al. Foundation damping and the dynamics of offshore wind turbine monopiles. Renew Energy 2015;80:724−36. Available from: https://doi.org/10.1016/j.renene.2015.02.058.
[85] Witcher D. Seismic analysis of wind turbines in the time domain. Wind Energy 2005;8:81−91. Available from: https://doi.org/10.1002/we.135.
[86] ASCE. Minimum design loads for buildings and other structures, 2013.
[87] Valamanesh V, Myers AT. Aerodynamic damping and seismic response of horizontal axis wind turbine towers. J Struct Eng 2014;140:04014090. Available from: https://doi.org/10.1061/(ASCE)ST.1943-541X.0001018.
[88] Chen C, Duffour P, Fromme P. Modelling wind turbine tower-rotor interaction through an aerodynamic damping matrix. J Sound Vib 2020;489:115667. Available from: https://doi.org/10.1016/j.jsv.2020.115667.
[89] Meng J, Dai K, Zhao Z, Mao Z, Camara A, Zhang S, et al. Study on the aerodynamic damping for the seismic analysis of wind turbines in operation. Renew Energy 2020;159:1224−42. Available from: https://doi.org/10.1016/j.renene.2020.05.181.

[90] Chou J-S, Tu W-T. Failure analysis and risk management of a collapsed large wind turbine tower. Eng Fail Anal 2011;18:295–313. Available from: https://doi.org/10.1016/j.engfailanal.2010.09.008.
[91] Stewart GM, Lackner MA. The effect of actuator dynamics on active structural control of offshore wind turbines. Eng Struct 2011;33:1807–16. Available from: https://doi.org/10.1016/j.engstruct.2011.02.020.
[92] Caterino N. Semi-active control of a wind turbine via magnetorheological dampers. J Sound Vib 2015;345:1–17. Available from: https://doi.org/10.1016/j.jsv.2015.01.022.
[93] Murtagh PJ, Ghosh A, Basu B, Broderick BM. Passive control of wind turbine vibrations including blade/tower interaction and rotationally sampled turbulence. Wind Energy 2008;11:305–17. Available from: https://doi.org/10.1002/we.249.
[94] Lackner MA, Rotea MA. Passive structural control of offshore wind turbines. Wind Energy 2011;14:373–88. Available from: https://doi.org/10.1002/we.426.
[95] Stewart G, Lackner M. Offshore wind turbine load reduction employing optimal passive tuned mass damping systems. IEEE Trans Control Syst Technol 2013;21:1090–104. Available from: https://doi.org/10.1109/TCST.2013.2260825.
[96] Ghaemmaghami A, Kianoush R, Yuan X-X. Numerical modeling of dynamic behavior of annular tuned liquid dampers for applications in wind towers. Comput Civ Infrastruct Eng 2013;28:38–51. Available from: https://doi.org/10.1111/j.1467-8667.2012.00772.x.
[97] Chen J, Zhan G, Zhao Y. Application of spherical tuned liquid damper in vibration control of wind turbine due to earthquake excitations. Struct Des Tall Spec Build 2016;25:431–43. Available from: https://doi.org/10.1002/tal.1266.
[98] Mensah AF, Dueñas-Osorio L. Improved reliability of wind turbine towers with tuned liquid column dampers (TLCDs). Struct Saf 2014;47:78–86. Available from: https://doi.org/10.1016/j.strusafe.2013.08.004.
[99] Chen J, Liu Y, Bai X. Shaking table test and numerical analysis of offshore wind turbine tower systems controlled by TLCD. Earthq Eng Eng Vib 2015;14:55–75. Available from: https://doi.org/10.1007/s11803-015-0006-5.
[100] Chen J, Georgakis CT. Tuned rolling-ball dampers for vibration control in wind turbines. J Sound Vib 2013;332:5271–82. Available from: https://doi.org/10.1016/j.jsv.2013.05.019.
[101] Zhang Z-L, Chen J-B, Li J. Theoretical study and experimental verification of vibration control of offshore wind turbines by a ball vibration absorber. Struct Infrastruct Eng 2014;10:1087–100. Available from: https://doi.org/10.1080/15732479.2013.792098.
[102] Zuo H, Bi K, Hao H. Using multiple tuned mass dampers to control offshore wind turbine vibrations under multiple hazards. Eng Struct 2017;141:303–15. Available from: https://doi.org/10.1016/j.engstruct.2017.03.006.
[103] Zhao Z, Dai K, Lalonde ER, Meng J, Li B, Ding Z, et al. Studies on application of scissor-jack braced viscous damper system in wind turbines under seismic and wind loads. Eng Struct 2019;196:109294. Available from: https://doi.org/10.1016/j.engstruct.2019.109294.
[104] Zhang R, Cao Y, Dai K. Response control of wind turbines with ungrounded tuned mass inerter system (TMIS) under wind loads. Wind Struct 2021;32:573–86.
[105] Katsanos EI, Thöns S, Georgakis CT. Wind turbines and seismic hazard: a state-of-the-art review. Wind Energy 2016;19:2113–33. Available from: https://doi.org/10.1002/we.1968.
[106] Bazeos N, Hatzigeorgiou GD, Hondros ID, Karamaneas H, Karabalis DL, Beskos DE. Static, seismic and stability analyses of a prototype wind turbine steel tower. Eng Struct 2002;24:1015–25. Available from: https://doi.org/10.1016/S0141-0296(02)00021-4.
[107] Zhao X, Maißer P. Seismic response analysis of wind turbine towers including soil-structure interaction. Proc Inst Mech Eng Part K: J Multi-Body Dyn 2006;220:53–61. Available from: https://doi.org/10.1243/146441905X73691.
[108] Andersen LV, Vahdatirad MJ, Sichani MT, Sørensen JD. Natural frequencies of wind turbines on monopile foundations in clayey soils—a probabilistic approach. Computers Geotech 2012;43:1–11. Available from: https://doi.org/10.1016/j.compgeo.2012.01.010.
[109] Arany L, Bhattacharya S, Macdonald JHG, Hogan SJ. Closed form solution of Eigen frequency of monopile supported offshore wind turbines in deeper waters incorporating stiffness of substructure and SSI. Soil Dyn Earthq Eng 2016;83:18–32. Available from: https://doi.org/10.1016/j.soildyn.2015.12.011.
[110] Lombardi D, Bhattacharya S, Muir Wood D. Dynamic soil-structure interaction of monopile supported wind turbines in cohesive soil. Soil Dyn Earthq Eng 2013;49:165–80. Available from: https://doi.org/10.1016/j.soildyn.2013.01.015.
[111] Bhattacharya S, Adhikari S. Experimental validation of soil-structure interaction of offshore wind turbines. Soil Dyn Earthq Eng 2011;31:805–16. Available from: https://doi.org/10.1016/j.soildyn.2011.01.004.
[112] Harte M, Basu B, Nielsen SRK. Dynamic analysis of wind turbines including soil-structure interaction. Eng Struct 2012;45:509–18. Available from: https://doi.org/10.1016/j.engstruct.2012.06.041.
[113] Kim DH, Lee SG, Lee IK. Seismic fragility analysis of 5 MW offshore wind turbine. Renew Energy 2014;65:250–6. Available from: https://doi.org/10.1016/j.renene.2013.09.023.
[114] Lalonde ER, Vischschraper B, Bitsuamlak G, Dai K. Comparison of neural network types and architectures for generating a surrogate aerodynamic wind turbine blade model. J Wind Eng Ind Aerodyn 2021;216:104696. Available from: https://doi.org/10.1016/j.jweia.2021.104696.
[115] Lalonde ER, Dai K, Lu W, Bitsuamlak G. Wind turbine testing methods and application of hybrid testing: a review. Wind Struct 2019;29:195–207.
[116] Dai K, Huang H, Lu Y, Meng J, Mao Z, Camara A. Effects of soil-structure interaction on the design of tuned mass damper to control the seismic response of wind turbine towers with gravity base. Wind Energy 2021;24:323–44. Available from: https://doi.org/10.1002/we.2576.
[117] Lalonde ER, Dai K, Bitsuamlak G, Lu W, Zhao Z. Comparison of semi-active and passive tuned mass damper systems for vibration control of a wind turbine. Wind Struct 2020;30:663–78.

[118] Constantinou MC, Tsopelas P, Hammel W, Sigaher AN. Toggle-brace-damper seismic energy dissipation systems. J Struct Eng 2001;127:105−12. Available from: https://doi.org/10.1061/(ASCE)0733-9445(2001)127:2(105).

[119] Polat E, Constantinou MC. Open-space damping system description, theory, and verification. J Struct Eng 2017;143:04016201. Available from: https://doi.org/10.1061/(ASCE)ST.1943-541X.0001698.

[120] Polat E, Constantinou MC. Testing an open-space damping system. J Struct Eng 2017;143:04017082. Available from: https://doi.org/10.1061/(ASCE)ST.1943-541X.0001802.

[121] Polat E, Open-space damping system theory experimental validation, 2016.

[122] Rama Raju K, Jame A, Gopalakrishnan N, Muthumani K, Iyer NR. Experimental studies on seismic performance of three-storey steel moment-resisting frame model with scissor-jack-magnetorheological damper energy dissipation systems. Struct Control Health Monit 2013;n/a-n/a. https://doi.org/10.1002/stc.1598.

[123] Rama Raju K, Ansu M, Iyer NR. A methodology of design for seismic performance enhancement of buildings using viscous fluid dampers. Struct Control Health Monit 2014;21:342−55. Available from: https://doi.org/10.1002/stc.1568.

[124] Brodersen ML, Høgsberg J. Damping of offshore wind turbine tower vibrations by a stroke amplifying brace. Energy Procedia 2014;53:258−67. Available from: https://doi.org/10.1016/j.egypro.2014.07.235.

[125] Dai K, Fang C, Zhang S, Shi Y. Conceptual design and numerical study on a cable-based energy dissipating system for the vibration reduction of tower-like structures. Eng Struct 2021;237:112034.

Chapter 25

Innovative foundation design for offshore wind turbines

Muhammad Aleem[2], Hasan Emre Demirci[1], Subhamoy Bhattacharya[2] and Sachin Jindal[2]
[1]Izmir Katip Celebi University, Izmir, Turkey, [2]Department of Civil and Environmental Engineering, University of Surrey, Guildford, London, United Kingdom

25.1 Introduction

Offshore wind farms (OWF) are planned to be installed in challenging sea conditions, and new cost-effective foundations need to be found and investigated. Offshore wind turbines are currently considered a sustainable and reliable energy source in water depths of about 40 m. Wind turbines are usually supported by large diameter piles, known as XL piles, and are subjected to various loads. Monopiles account for 81.65% of total wind turbines installed and is the most preferred type of foundation; however, there are numerous problems associated with the XL piles. With technological developments, offshore wind turbines (OWTs) are getting taller, and their capacity increases (wider rotor diameter). Therefore, they are installed in deeper waters, particularly away from the coastline. It may be observed that the rated capacity and the height of towers increase with the increase in top mass, as depicted in Fig. 25.1. As the turbine sizes become larger, their foundations become uneconomical and pose different difficulties while manufacturing, transportation, installation, and further exploration are required to optimize a design. Wind turbine structures are relatively new, with a minimal track record of long-term performance. Hence, there is a need to explore innovative foundation types. In this chapter, a brief literature review is provided for various innovative foundations. A new type of foundation, termed as hybrid foundation with steel plate addition at the seabed level, is analyzed in detail.

25.2 Need for new types of foundations

OWTs are relatively new structures and differ considerably from the offshore infrastructure used in the offshore oil and gas industry. From a design perspective, one of the most important distinctions is that OWTs are extremely sensitive to dynamic loads arising from wind, waves, and earthquakes. Furthermore, they have stringent serviceability limit state (SLS) criteria compared to other structures due to vibration-sensitive electrical components, notably gearboxes. Therefore, research and development are crucial to significantly reducing the levelized cost of energy (LCOE) and cutting the subsidies on which offshore wind projects rely. One of the most promising research areas for reducing costs is to design cost-effective foundations. Fig. 25.2 shows a range of innovations being conceptualized to cater to challenging ground and environmental conditions and, in some cases, to support larger turbines in deeper water. Hybrid foundations can be of various shapes and different configurations.

25.3 Inspiration for hybrid foundations

This hybrid foundation shown in Fig. 25.2D has been inspired by a combination of shallow and deep roots, as shown in Fig. 25.3. There are no codes of practice or guidelines for such a bio-inspired hybrid foundation, and, in such cases, scaled model testing becomes necessary to validate numerical and analytical solutions.

At times, challenging soil profiles lead to innovation. As an example, at the Fujian province offshore wind farm site (Putan Pinhhai Phase II) in China, engineers faced the daunting challenge of installing monopiles due to rock formations at a shallow depth. The presence of rock caused unexpected issues during monopile construction, including borehole collapse, jamming of a drilling tool, and pile tip buckling. The engineers found a solution consisting of a hybrid

Wind Energy Engineering. DOI: https://doi.org/10.1016/B978-0-323-99353-1.00022-0

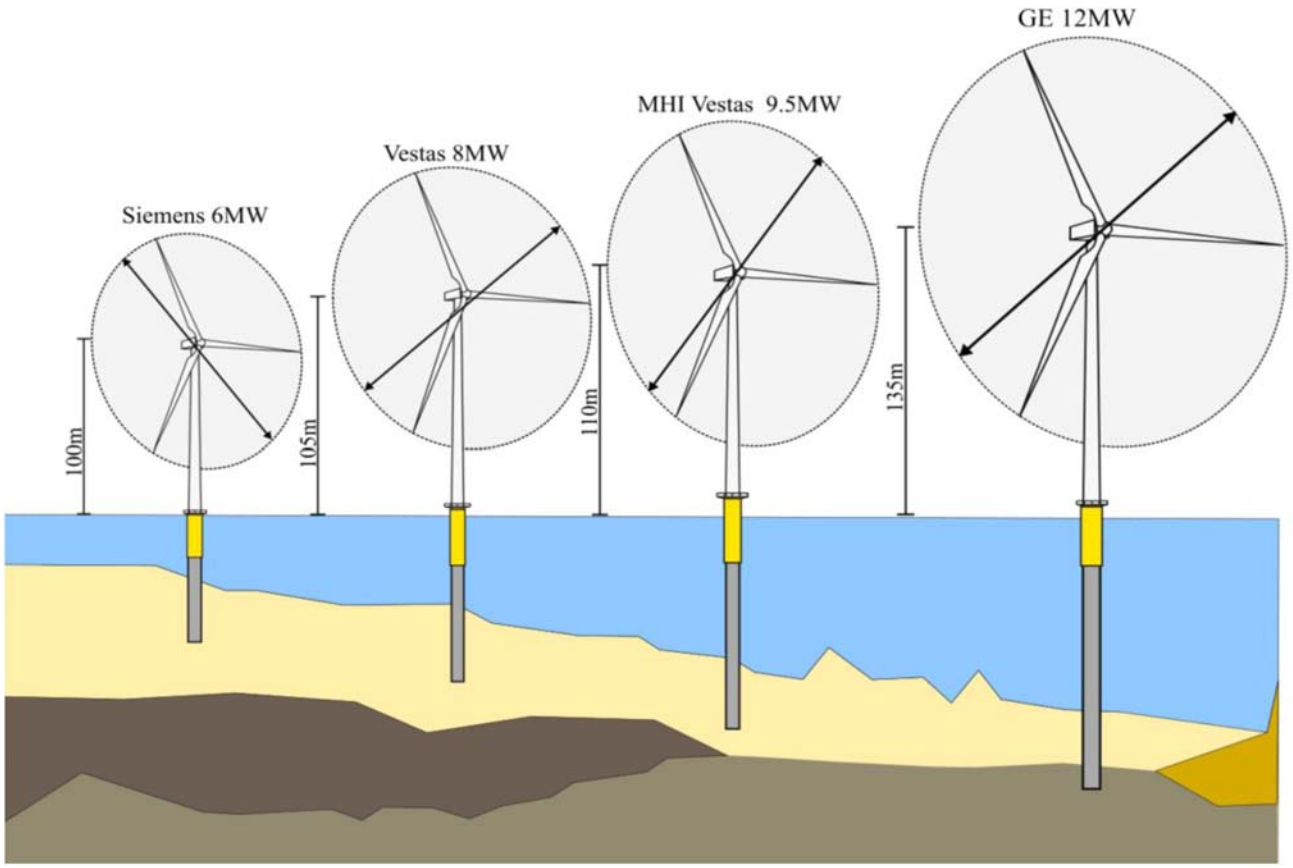

FIGURE 25.1 Evolution of offshore wind turbines.

shallow−deep foundation, which they named monopile−caisson hybrid foundation (Fig. 25.4). The main concept is that the top plate of the caisson (i.e., shallow foundation) will rest on the seabed, and the monopile will be fully embedded in the ground but not touch the rock.

25.4 Hybrid monopile foundation concept

A novel hybrid foundation concept has been analyzed to replace the typical monopile because of the reduced embedded length of the pile and enhance the offshore monopile's lateral bearing capacity. The improved design combines a monopile foundation and a plate at the mudline level (Fig. 25.5). Adding a circular steel plate at the mudline will stiffen the pile responses laterally. The main objective of this foundation is to reduce the LCOE. As the turbine sizes get larger, monopile foundations become uneconomical, and there is a need for an alternative foundation. The introduction of steel plates can provide additional shear stress to resist the lateral load and lower the pile rotations. The plate is a circular rigid lid. The benefits of using this hybrid type of foundation include the less embedded length of the pile, and the plate (large in diameter than a pile) is provided at the mud level to overcome the loose and weak soil. After the turbine's service life, it is easy to remove and decommission.

The concept is proposed to increase the lateral bearing capacity of original/existing offshore monopiles. The concept combines a monopile foundation and a gravity-based foundation. The gravity-based foundation is formed by introducing a circular friction wheel at the mudline level. The implementation of the friction wheel supplies additional shear stress at the soil and friction plate interface to resist larger moments and lateral loads. The lateral load and moment capacity increase lowers the lateral displacements and rotations at the pile head. This innovative concept can also be a reinforcement method for existing monopile foundations. Due to the wave and wind loads, foundations of OWTs are subjected to millions of cycles within their service lives. These cyclic loads may lead to fatigue of foundation materials and change in seabed conditions. An introduction of the concept of the hybrid foundation can provide additional bearing capacities as a retrofitting technique.

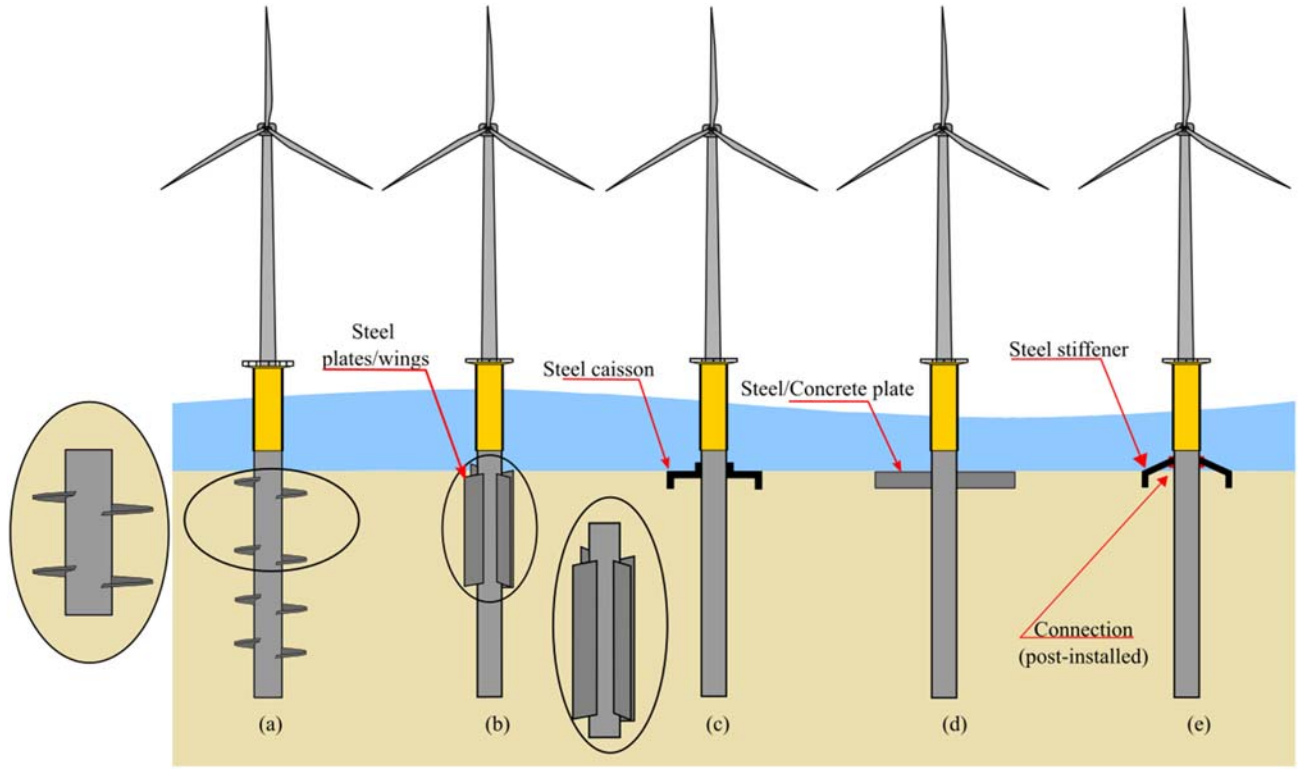

FIGURE 25.2 New foundation (A) helical monopiles (B) winged piles (C) collared monopile, caisson + monopile (D) hybrid monopile, (monopile with plate) (E) stiffened monopole.

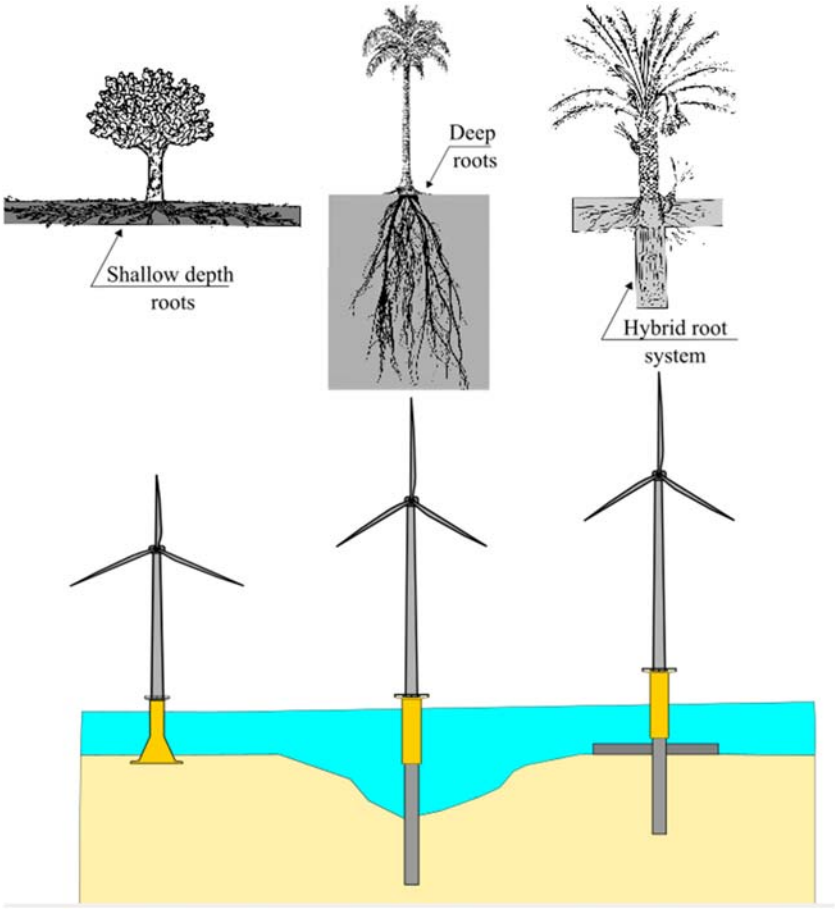

FIGURE 25.3 Biomimicry/bio-inspired.

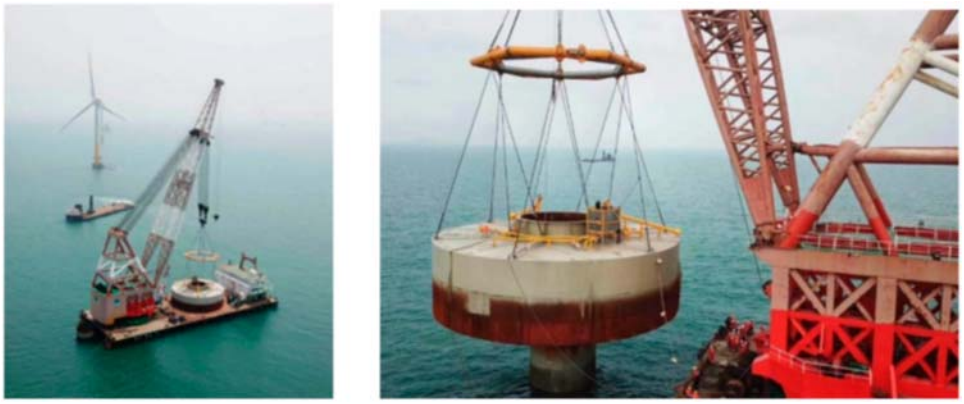

FIGURE 25.4 Concrete caisson or monopile suction caisson.

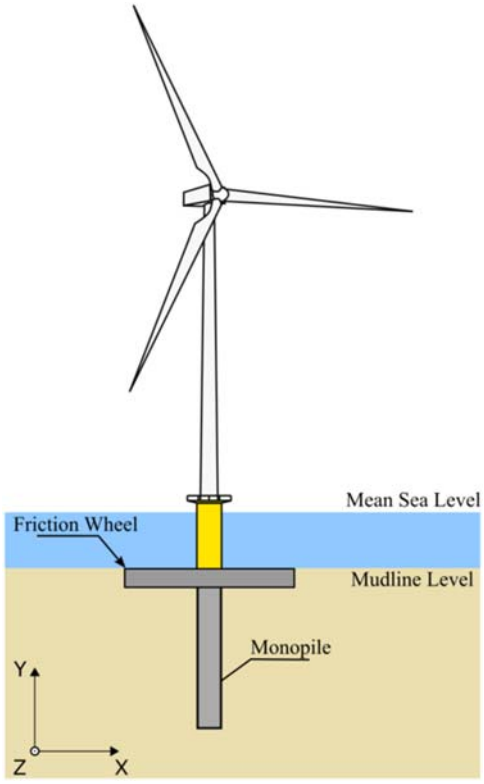

FIGURE 25.5 Hybrid monopile foundation.

25.5 Verification and validation

For innovative or new foundations, the generic codes and standards are not enough to justify the validation; hence, further studies are required, including experiment testing in the lab and detailed Finite Element (FE) models. For the above-stated hybrid foundation, a numerical study using the three-dimensional (3D) FE analysis is conducted to determine the impact of footing leads on the moment capacity. The added footing not only contributes to its moment capacity but also enhances the moment capacity of the pile, which acts as a rotational restraint. And a comparison has been made with the similar work conducted by Wang et al. [1] to study the performance of a hybrid foundation system consisting of a precast concrete plate and a central steel monopile using the FE analysis.

25.5.1 Validation step 1: numerical models validation via centrifuge test

Considering different loading conditions, the proposed setup was evaluated and concluded that the hybrid system may reduce construction costs using a shorter pile. The method can also be used to increase the existing capacity of the monopile foundation by adding the concrete plate (precast). The concept was to strengthen the typical monopile foundation by adding different materials at the mudline level. Wang et al. [1] tested five different types of foundations: (1) monopile, (2) monopile with steel plate, (3) monopile with gravel wheel, (4) gravel wheel only, and (5) steel plate. The results were compared with other techniques using the series of centrifuge tests. Adding a steel plate at the mudline level provides extra rotational resistance, ultimately improving the foundation's lateral bearing capacity. Besides the ultimate lateral capacity, the hybrid foundation showed an increase in lateral stiffness, concluding that adding a steel plate (frictional wheel) improves the lateral bearing capacity and provides extra moment resistance to the typical monopile foundation. Adding a steel plate results in larger bearing capacities than the other frictional wheels because the steel plate has a larger weight, and passive pressure on the embedded plate cannot be neglected.

3D FE models of the centrifuge tests were developed using Plaxis 3D software. The numerical models were validated via centrifuge test results of Wang et al. [1], where the lateral bearing capacity of monopile and hybrid foundations was investigated. The model pile was 7 m long, 1.1 m diameter solid steel rod, and 8 tonnes in weight. The steel friction wheel with 7 m diameter, 1.5 m thickness disc weighing 260 tonnes was used. The hybrid foundation was constructed by combining a pile and a friction wheel. A steel rod with a diameter of 0.5 and 13 m was used to construct the wind tower. The total weight of the tower and the tower head was 38.25 tonnes. All these values described here are in the prototype scale. These parameters of model geometry are shown in Table 25.1. A schematic sketch of an elevation view of the test setup demonstrating key dimensions is shown for two scenarios in Fig. 25.6. These scenarios are (1) wind turbine standing on a monopile foundation and (2) wind turbine standing on a hybrid (monopile +steel wheel) foundation, as shown in Fig. 25.6. The hybrid foundation and monopile were installed by pushing them into the soil under 1-g gravitational conditions. After installation, the steel friction wheel sat on the soil surface, and the pile foundation touched the container bottom. The embedment depth of the pile was 5.5 m, and the connection between the pile and container bottom was considered roller support. An actuator applied a monotonic lateral load 3 m above the pile head.

25.5.1.1 Comparison against the centrifuge tests of Wang et al. [1]

The lateral loads measured at 3 m above the pile head are plotted as a function of the lateral displacements measured at the same location in Fig. 25.7, along with those calculated from Plaxis 2D and Plaxis 3D numerical analysis. Two scenarios were used to validate the developed numerical models: (1) Case I: monopile in loose saturated Toyoura sand and

TABLE 25.1 Parameters used in model geometry (centrifuge tests).

Monopile		
Parameter	**Value**	**Units**
Diameter (D)	1.1	m
Length (L)	7	m
Embedment depth (H)	5.5	m
Weight (W)	8	tonnes
Steel friction wheel		
Diameter (D)	7	m
Thickness (t)	1.5	m
Weight (W)	260	tonnes
Tower and tower head		
Tower diameter (D)	0.5	m
Tower length (L)	13	m
Weight of tower and tower head	38.25	tonnes

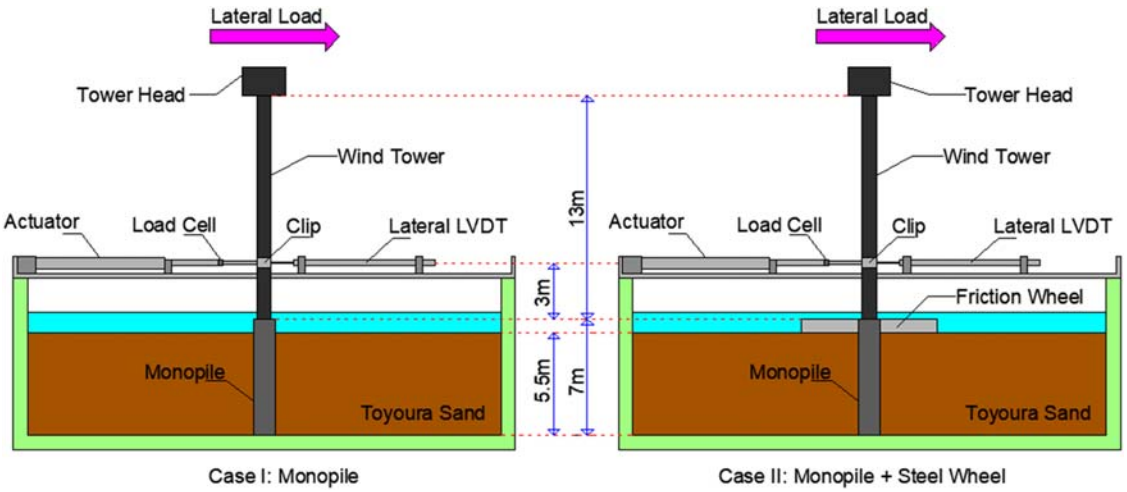

FIGURE 25.6 A schematic sketch of an elevation view of a test setup for Case I and Case II.

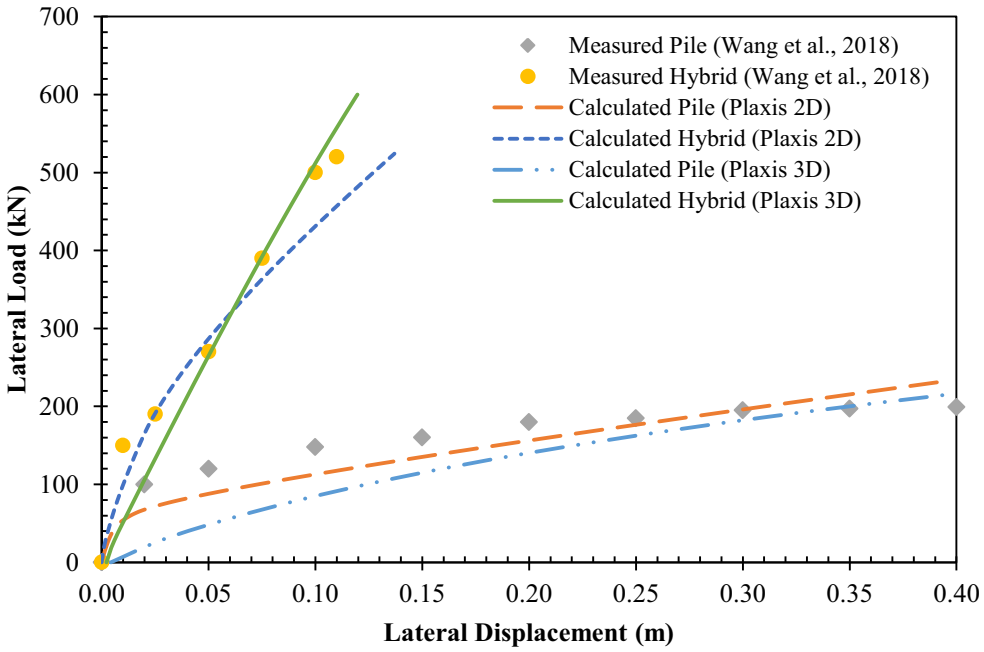

FIGURE 25.7 Comparison of the relationships of lateral loads and lateral displacements obtained from the centrifuge tests of Wang et al. [1] and numerical simulations.

(2) Case II: hybrid foundation in loose saturated Toyoura sand. Grey diamond data points show the measured lateral load−displacement data for Case I, while yellow circle data points show those measured for Case II.

For Case II, at a lateral displacement of 0.11 m, the lateral load is measured experimentally as 520 kN. The corresponding values are calculated as 543 and 464 kN for Plaxis 3D and Plaxis 2D, respectively. For Case I, at a lateral displacement of 0.30 m, the lateral load is measured experimentally as 195 kN, and the corresponding values are calculated numerically as 186 and 198 kN for Plaxis 3D and Plaxis 2D, respectively. In 2D plane-strain analysis, it is not possible to model the 3D nature of the pile. It is an efficient tool for estimating the loads taken by the structure. A 2D FE analysis analyses the structure in less time than a 3D. The comparison between these models showed that the 2D model described good behavior but underestimated it.

25.5.2 Validation step 2 experiment evaluation

25.5.2.1 1-g testing

The case study explained has been validated with 1-g testing. The experimental data for 1-g testing has been interpreted with the LU framework, which is explained further in this chapter.

25.5.2.2 Load utilization framework

This method was developed by Aleem et al. [2] to find out the various combinations of horizontal loads (H) and overturning moment loads (M), which lead to the failure of a foundation system, and the locus of such points will provide a 2D curve. This concept is similar to an Interaction diagram used in structural engineering and can generate a resistance curve (Eurocode concept of resistance). Any point inside the interaction diagram is SAFE, and these points can be considered load actions (Eurocode concept of Action) (Eurocode 2) [3]. See Figs. 25.8 and 25.9.

Finding the Moment Carrying Capacity (M_r) of a foundation system without any lateral load (i.e., a special case of $H = 0$) is relatively straightforward. Similarly, one can find the lateral load-carrying capacity (H_R) of the same foundation system in the absence of any moment (i.e., special case of $M = 0$).

Fig. 25.10 depicts the load utilization (LU) ratio for ULS loads (i.e., Resistance divided by Actions or R/A), which is also suggested in the Eurocode concept (Eurocode 2, 2011). As mentioned before, depending on the chosen soil model and the failure criteria, a yield surface can be mapped; therefore, this is nonunique. For standard engineering design calculations, a linear line joining M_r and H_R can be used as a simplified Yield Surface and is shown as Line 2 (idealized) in Fig. 25.10. Each design load case, that is, the combination of Hi and Mi, can be mapped in the H − M space. Fig. 25.10 shows a particular load case depicted by Hi and Mi, and a line may be drawn connecting this point and the origin (shown as Line 1 in Fig. 25.10). The LU ratio is given by the ratio of the load-carrying capacity of the foundation (R, i.e., resistance magnitude) to the Applied Load combination from wind and wave (A-Action), which can be visualized in Fig. 25.10. This geometrical representation of the safety factor against ULS considering lateral load and moment. The LU ratio for a particular load case is also the notional Factor of safety under a combined load. It can be defined as (R/A), and the definition of R and A is shown in Fig. 25.10; using elementary geometry, one can arrive at the following expression. Following the work of [2], a similar procedure was carried out to find the safety factor.

25.5.2.3 Test preparation

Most of the tests were conducted using a horizontal loading apparatus under 1g conditions. This was designed to apply the horizontal load to fail the turbine system. The testing arrangement consisted of a load cell connected/attached with the 12 V motor on the bespoke bracket/frame. The load in each experiment was applied at different levels/heights. The loading height was specified, and the horizontal and moment loads were applied to the structure. In all the tests,

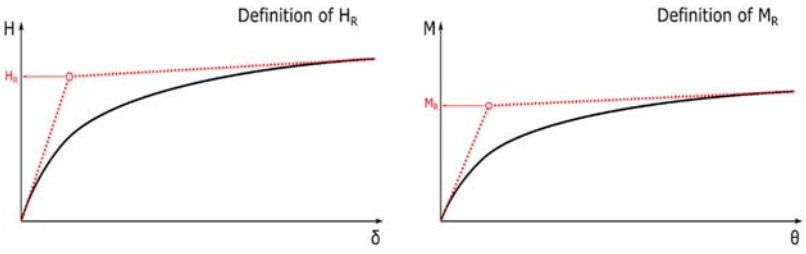

FIGURE 25.8 (A) Obtaining the HR from analysis (B) Obtaining MR from the analysis.

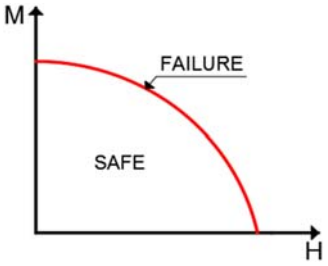

FIGURE 25.9 Typical moment-horizontal force interaction curve [4].

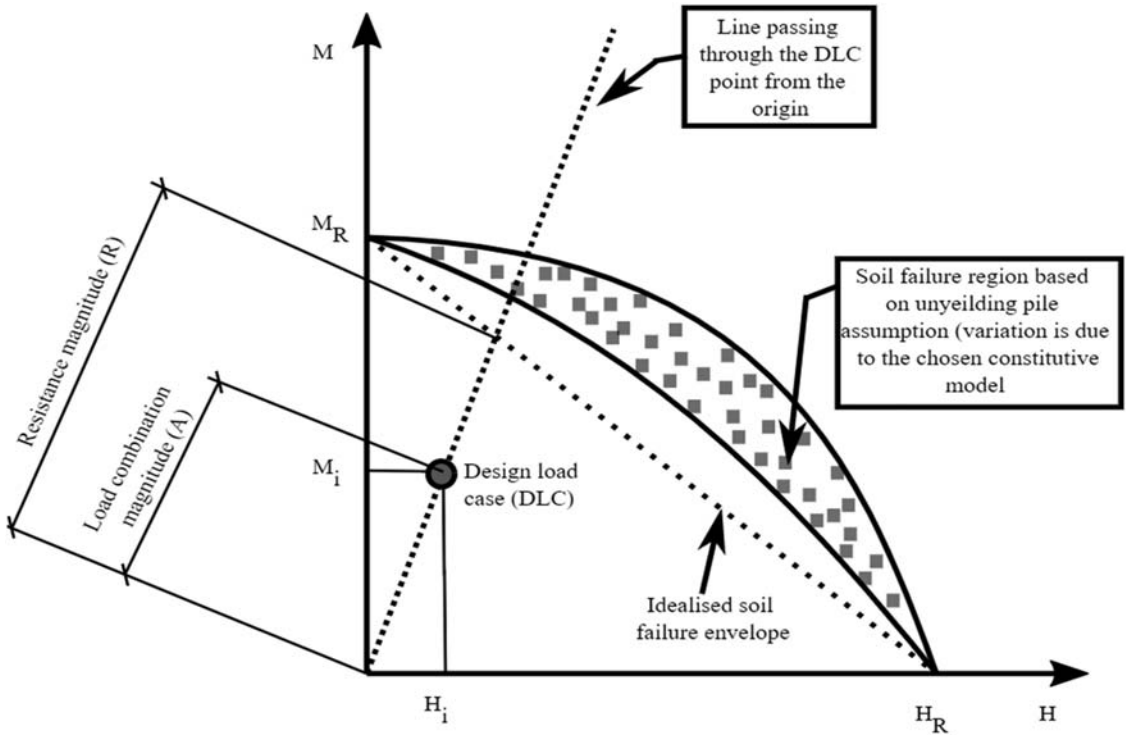

FIGURE 25.10 Moment and lateral load resistance capacity.

TABLE 25.2 Properties of Red Hill silica sand.

Items	Values
Specific gravity G_s	2.65
Median particle diameter D_{50}/mm	0.144
Internal friction angle (°)	36.0
Dry unit weight (kN·m^3)	16.8
Maximum void ratio e_{max}	1.035
Minimum void ratio e_{min}	0.608
Relative density	0.63
Shear modulus G/MPa	10.0

sand was enclosed in the tank consisting of 1150 mm long, 950 mm wide, and 600 mm high. The soil used in this experiment is Red Hill 110 silica sand with a mean particle size D_{50} of 0.14 mm. Other properties of the sand are provided in Table 25.2; throughout the test, the sand remained dry, replicating the fully drained offshore conditions. Red hill sand is quite typical in the North Sea and represents the soil along the southeast coastline of China. The sand bed is prepared by pouring sand from a hopper, maintaining the same flow rate and height. The final thickness of the sand bed was approximately 500 mm. The relative density is 63% as medium dense sand. The shear modulus of the sand bed G is obtained as approximately 10 MPa by the in-situ shear wave velocity method. Based on the scaling laws, the experimental setup is shown in Fig. 25.11. The model turbine mainly consists of 3 parts, and the cyclic loading device is connected to a volt generator and mounted on top of the tower (wind loading) and closer to the mudline (wave loading). Table 25.3 explain the 1-g testing program, with model description and its properties. Table 25.4 provide the comparison details for the LU framework.

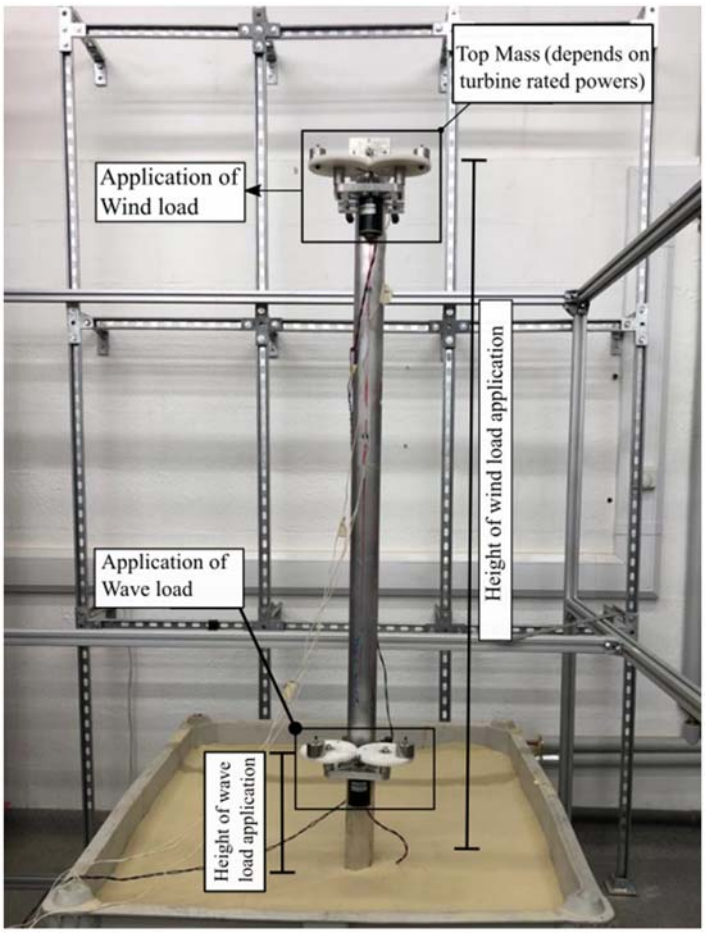

FIGURE 25.11 Test setup.

TABLE 25.3 1-g testing program.

Testing program model ID	Monopile diameter (mm)	Plate diameter (mm)	Wall thickness (mm)
Monopile	41	–	1.6
Monopile + Plate-I		100	9.5
Monopile + Plate-II		150	9.5
Monopile + Plate-III		200	9.5

TABLE 25.4 Comparison of LU.

	Monopile diameter and wall thickness (mm)	Plate diameter and wall thickness (mm)	Design load case	H_R (N)	Mr (Nm)	LU
Monopile	41 &1.6	–	9.5 N 7 Nm	64	19	1.93
Monopile + Plate-I		100 & 9.5		70	21	2.13
Monopile + Plate-II		150 & 9.5		72	27.5	2.58
Monopile + Plate-III		200 & 9.5		82	31	2.93

25.6 Steps to set up numerical model for hybrid monopile

Hybrid foundations are new foundations for which codes of practice do not exist. The behavior is a mix of elements from the shallow foundation and deep foundation, and a numerical model has been used to study the behavior. The critical outputs necessary for design are foundation stiffness and ultimate capacity. The former is required for SLS calculations as well as natural frequency estimates. This section describes the methodology for numerical analysis and the procedure to extract the stiffness. The method is calibrated based on a reported model test and is discussed later.

Fig. 25.12 shows a schematic diagram of a hybrid foundation with the parameters to define it. They are plate dimensions (Diameter D_p and plate thickness t_p), and monopile dimensions (D_m, L_p, and t_p). Numerical analysis can be conducted using the FE method and, in this study, Plaxis 3D has been used. The axisymmetric nature of the problem was not considered, and a complete model was used with the pile positioned at the center. The pile material was defined as steel that is not allowed to bend, and only the surrounding soil is mobilized (rigid body). Lateral loads and moments were monotonically applied at the head of the monopile. Soil layers were modeled by using the standard Mohr–Coulomb constitutive model. The interactions between the soil and pile, soil and the friction steel plate were simulated using interface elements. Plaxis 3D software was used to simulate this soil-structure interaction problem. The 3D model of the problem is demonstrated in Fig. 25.13. Fig. 25.13A shows different soil layers that are modeled by considering Fig. 25.15. Fig. 25.13B demonstrates the steel friction plate (*red*) and monopile (*blue*) used in the numerical models.

Material models and their corresponding input parameters critically affect the analysis results. Models suggest a mathematical description of the mechanical behavior of materials, which affects essential aspects of material behavior (see [2]).

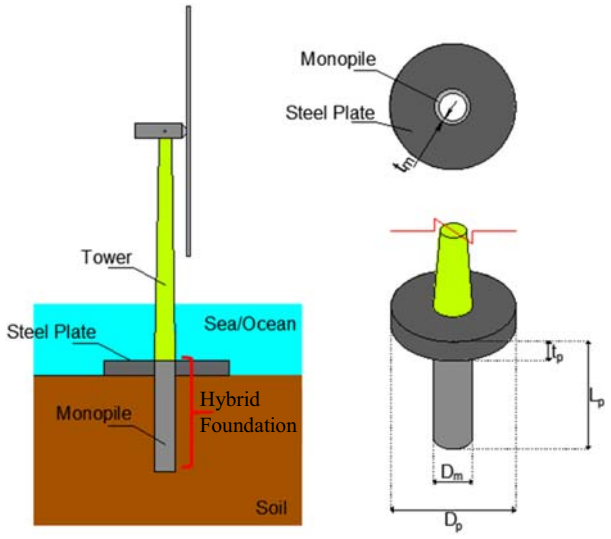

FIGURE 25.12 Schematic illustrations showing (A) an elevation view of offshore wind turbine with the proposed hybrid foundation, (B) a plan view of the hybrid foundation, and (C) an isometric view of the hybrid foundation.

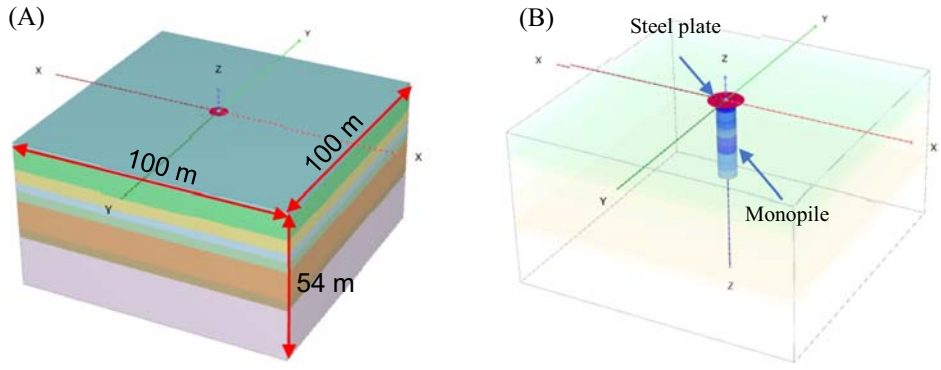

FIGURE 25.13 Numerical models showing (A) soil layers and steel plate (*red*), (B) monopile (*blue*), and steel plate (*red*).

TABLE 25.5 Geometric parameters used in numerical models, including monopile diameter (D_m), monopile wall thickness (t_m), the length of monopile (L_m), the steel plate diameter (D_p), and the thickness of steel plate (t_p).

Foundation	D_p(m)	t_p(m)	D_m(m)	t_m(m)	L_m(m)
Monopile	6.5	0.25	6.5	0.1	27
Hybrid I (HF I)	8				
Hybrid II (HF II)	12				
Hybrid III (HF III)	15				
Hybrid IV (HF IV)	20				
Hybrid V (HF V)	25				

25.6.1 Parametric study

The developed numerical model is used to carry out a parametric study to investigate the performance of hybrid foundations and the effect of the steel plate diameter (D_p) on the performance of hybrid foundations. The performance of hybrid foundations was evaluated by considering the relationships of lateral load-lateral displacement and resisting moment-rotation under applied monotonic loads. Six different numerical models were developed using Plaxis 3D software to evaluate the performance of hybrid foundations with various steel plate diameters. The geometric parameters used for these six numerical models are shown in Table 25.5. Fig. 25.12 shows a schematic illustration of the proposed hybrid foundation, consisting of the monopile diameter (D_m), the monopile wall thickness (t_m), the length of monopile (L_m), the diameter of the steel plate (D_p), and the thickness of steel plate (t_p). The 3D model with a monopile foundation was used as a benchmark to assess the performance of proposed hybrid foundations.

A monopile with 6.5 m diameter, 0.1 m thickness, and 27 m in length were used in each case. The steel plates with a thickness of 1.5 m and various diameters ranging from 8 to 25 m were used in numerical models, as shown in Fig. 25.12.

25.6.2 Soil profile

A typical North Sea ground profile was used in the numerical models. The soil profile used in the numerical models is adopted by considering Horn's Rev offshore wind farm in the North Sea, 25−40 km off the Danish Jutland coast. The Horn's Rev offshore wind farm location is shown on the map in Fig. 25.14. The soil profile used in the models is shown in Fig. 25.15. Sand layers and a silt layer are seen in the ground profile. The effective unit weights (γ') of the soil layers, strength parameters such as internal friction angle (φ) and undrained shear strength (c_u) are shown in Fig. 25.15.

25.6.3 Numerical results

Numerical results are presented by plotting the variation of lateral loads with lateral displacements and the resisting moment with rotations. Lateral displacements at the head of the monopile and hybrid foundations were calculated under monotonic lateral loads. Rotations at the head of the monopile and hybrid foundations were also calculated under monotonic loads. Fig. 25.16 shows the relationships between lateral loads and lateral displacements at the head of foundations for the monopile and hybrid foundations. The purple dashed line shows the serviceability limit for lateral displacement at the head of monopile and hybrid foundations. The serviceability limit for lateral displacement at the foundation's head was considered 0.2 m, as referenced in Fig. 25.16. The relationships between lateral load and displacement for each foundation show nonlinear behavior. Table 25.6 shows lateral loads at a lateral displacement of 0.2 m for different types of foundations. The change in lateral loads at a lateral displacement of 0.2 m is also shown in Table 25.6. It can be seen by comparing the monopile and HF V foundations' results that the lateral load capacity under serviceability limits can be increased by 37.7%. The use of HF V in Fig. 25.17 shows the effects of steel plate diameter on the lateral load capacity of hybrid foundations under serviceability limits. As shown in Fig. 25.17, the increase in the lateral load capacity of hybrid foundations is a function of the power of steel plate diameter.

FIGURE 25.14 A map showing the location of the Horn's Rev offshore wind farm.

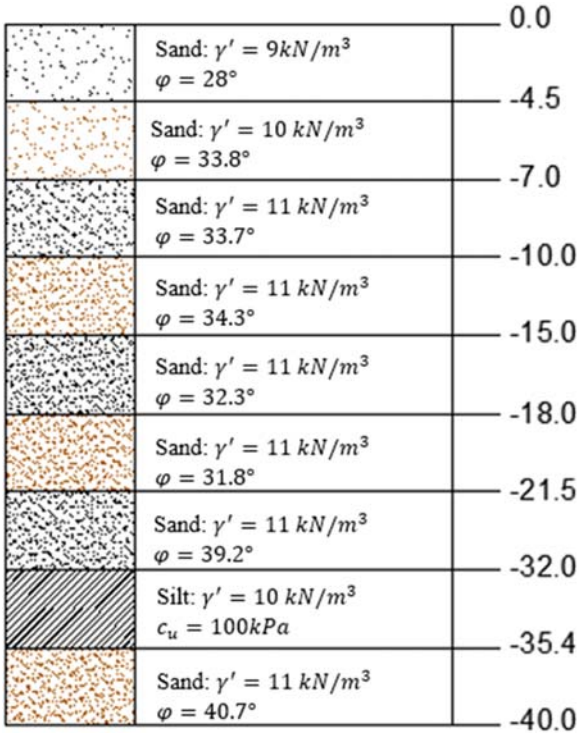

FIGURE 25.15 Soil profile adopted in numerical models.

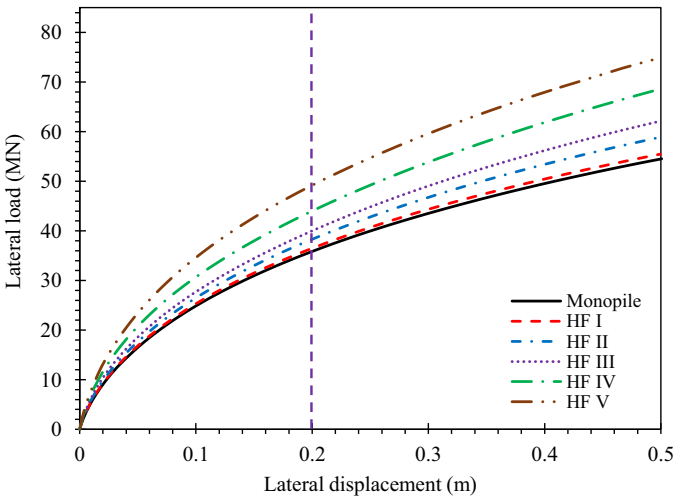

FIGURE 25.16 Lateral loads versus lateral displacements at the head of foundations for monopile and hybrid foundations.

TABLE 25.6 Lateral loads at a lateral displacement of 0.2 m for different types of foundations.

Lateral displacement (m)	Types of foundations	Lateral loads (MN)	Change in percentage (%)
0.2 (Serviceability limit)	Monopile	35.80	–
	HF I	37.20	3.9
	HF II	38.40	7.3
	HF III	40.20	12.3
	HF IV	44.10	23.2
	HF V	49.30	37.7

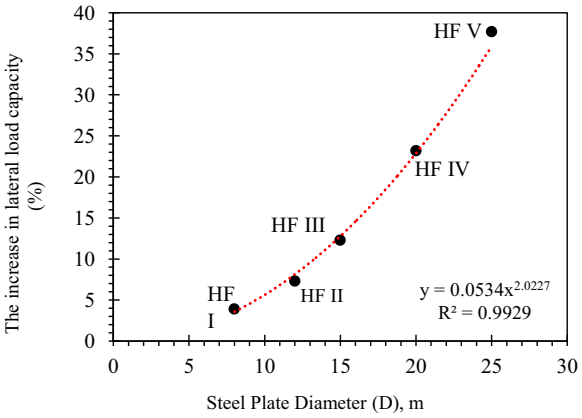

FIGURE 25.17 The increase in lateral load capacity of hybrid foundations with varying steel plate diameters under serviceability limits.

Fig. 25.18 shows the relationships between moments and rotations at the head of the monopile foundation and hybrid foundations. A purple dashed line shows the serviceability limit for rotations at the head of monopile and hybrid foundations. The serviceability limit for rotations at the foundation head was considered 0.5 degrees, as referenced in Fig. 25.18, and the relationships between moments and rotations for each foundation show nonlinear behavior.

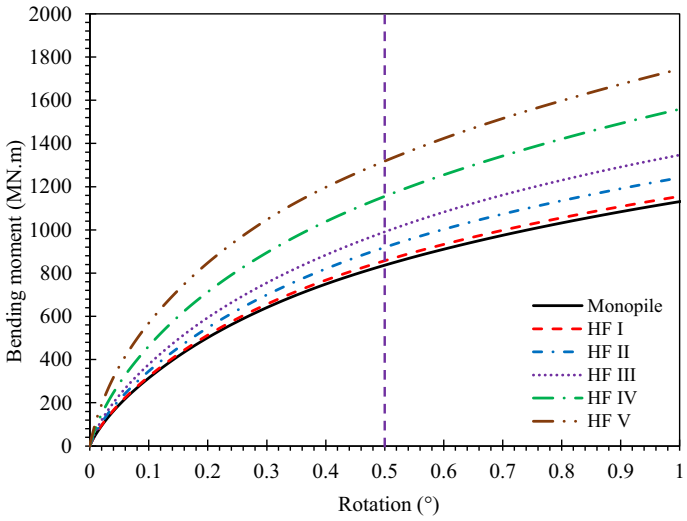

FIGURE 25.18 Moment versus rotations at the head of the foundation for monopile and hybrid foundations.

TABLE 25.7 Bending moments at a rotation of 0.5 degrees for different types of foundations.

Rotation (°)	Types of foundations	Bending moments (MN)	Change in percentage (%)
0.5 (serviceability limit)	Monopile	840.4	–
	HF I	866	3.0
	HF II	921	9.6
	HF III	992	18
	HF IV	1160	38
	HF V	1320	57

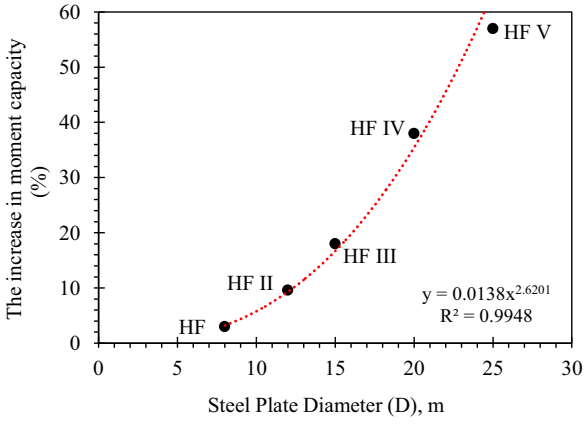

FIGURE 25.19 The increase in moment capacity of hybrid foundations with varying steel plate diameters under serviceability limits.

Table 25.7 shows bending moments at a rotation of 0.5 degrees for different types of foundations and the change in bending moments at a rotation of 0.5 degrees. It can be seen by comparing the results for the monopile and HF V foundations that the bending moment capacity under serviceability limits can be increased by 57% with the use of HF V. Figs. 25.19 and 25.20 show the effects of steel plate diameter on the bending moment capacity of hybrid foundations

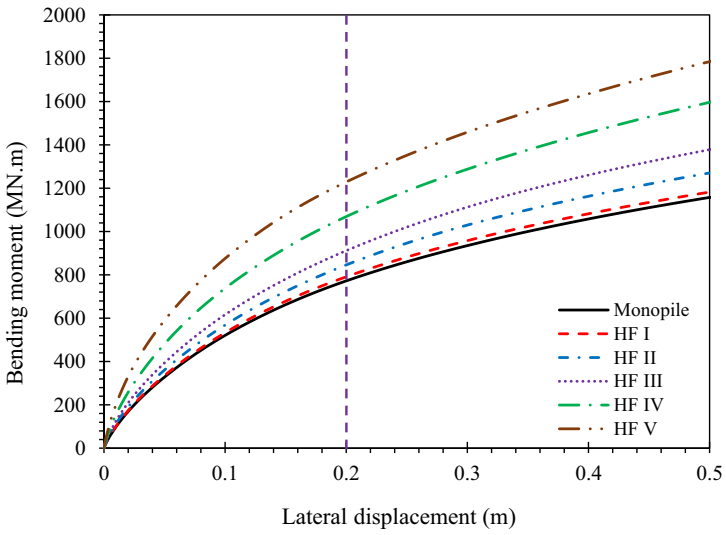

FIGURE 25.20 Moment versus displacement at the head of the foundation for monopile and hybrid foundation.

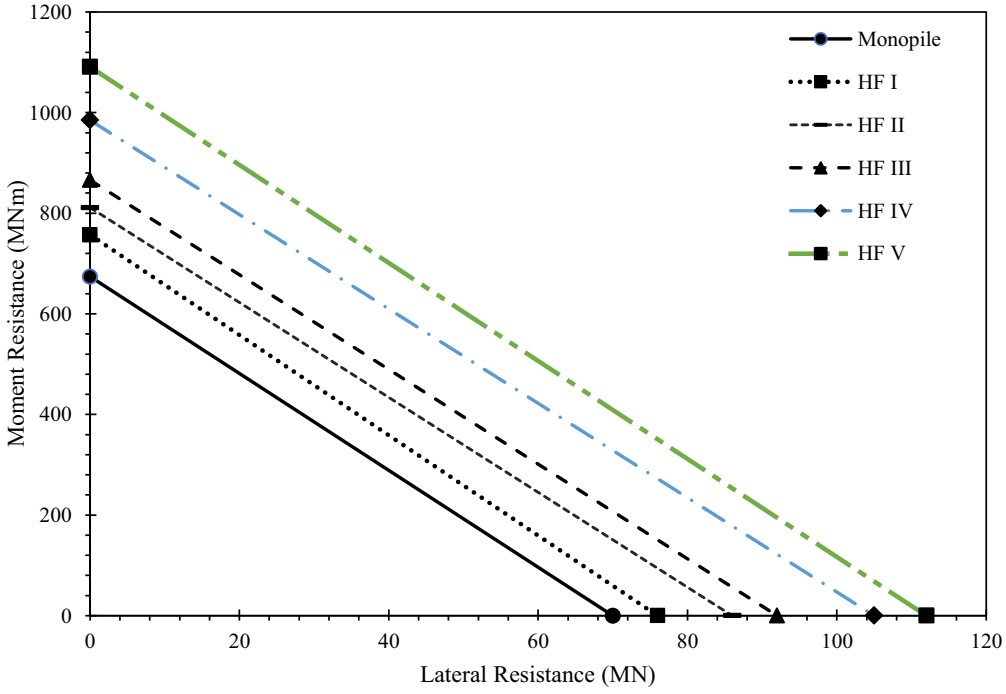

FIGURE 25.21 Comparison of capacity calculations.

under serviceability limits. As shown in Fig. 25.19, the increase in bending moment capacity of hybrid foundations is a function of the steel plate diameter's power. Fig. 25.21 shows the comparison of capacity calculation, that is, a relation between moment resistance and lateral resistance.

25.7 Further application of hybrid foundation study

25.7.1 Retrofitting of existing monopiles

This proposed concept of hybrid foundation can also be a reinforcement method for existing monopile foundations: the fatigue of materials, as well as the changing of seabed soil conditions, may influence behaviors of the pile foundation

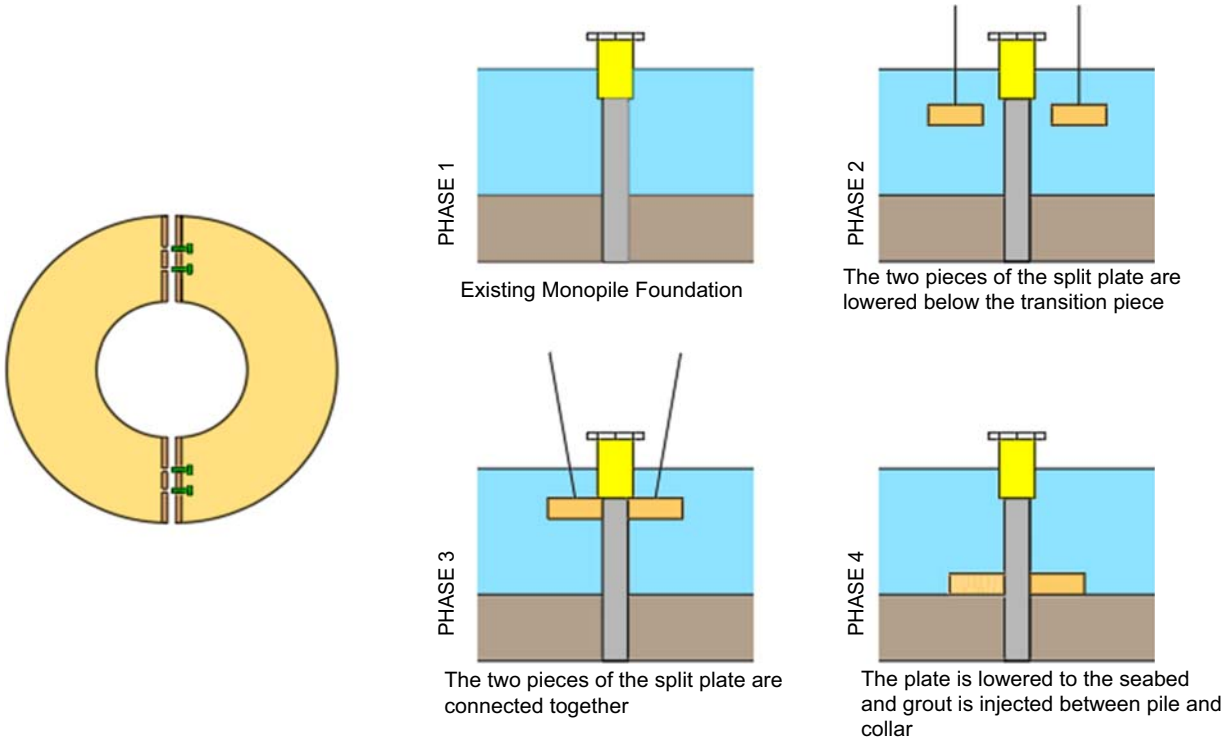

FIGURE 25.22 Retrofit technique.

in service, but it is unrealistic to rebuild the foundation, especially at offshore areas; therefore, a steel plate can be applied to provide additional bearing capacities as a practical modification to increase the service life of existing foundations (Fig. 25.22).

Retrofitting older wind turbines with advanced technological solutions increases the energy production of wind turbines. The lifetime of wind turbines can also be extended with better profitability. The introduced method is cost-effective for retrofitting the older, smaller wind turbines and making them more efficient. This solution will increase the performance of the foundation and provide a safe and effective way of upgrading the turbine with lower operational and maintenance costs. Horns Rev 2 wind farm is in the North Sea, approximately 30 km from the west of Esbjerg (Denmark). 2 MW turbines are supported on 4 m diameter, and 20 m long piles were driven into stiff sand. If the developer wishes to install turbines with higher specs in the same location, placing a steel plate around the piles can be a solution. Moreover, a similar wind turbine's service life could be increased by introducing a steel plate. The sensitivity analysis was conducted using the FE package to determine the model's suitable dimensions and compared it with the typical monopile.

Figs. 25.23 and 25.24 show the lateral and moment capacity comparison of monopile lengths with a hybrid foundation. Table 25.8 shows that the slight increase in material prices can be covered with speedy construction depending on the soil's nature on-site, with hybrid monopile foundations. Moreover, the hybrid monopile will bring high-cost benefits to rocky sites due to shorter pile lengths by reducing the cost and time spent drilling through rocks. In deeper waters, installing hybrid monopiles is expected to require fewer steps in terms of installation when compared to jackets. The hybrid type foundation is the solution where the water table is low (closer to the coastline), and shorter piles with the extra stiffness at the mudline level can be utilized. The installation and fabrication cost can be drastically reduced by providing a hybrid solution compared to XL-monopiles (Table 25.9).

Moreover, underground cables' cost to the substation can be reduced, considering the site close to the coastline. With a Vibro hammer, noise emissions can be reduced and faster penetration than hydraulic impact hammers (up to 10 times faster in sand). Further savings can be made by speeding up the installation process. This method of piling provides substantial savings in time and money. CAPE Holland started using the Vibro hammer technique in the North Sea (2011).

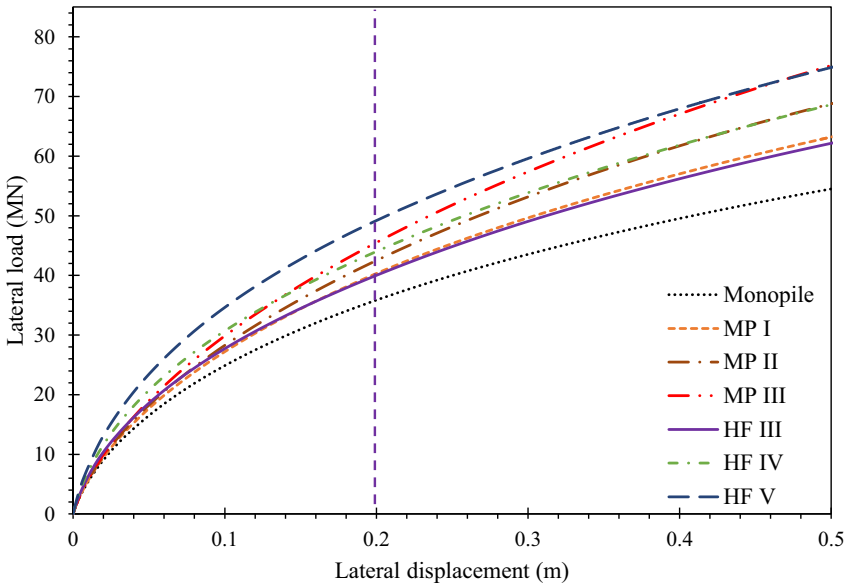

FIGURE 25.23 Lateral capacity comparison of monopile lengths with hybrid foundation.

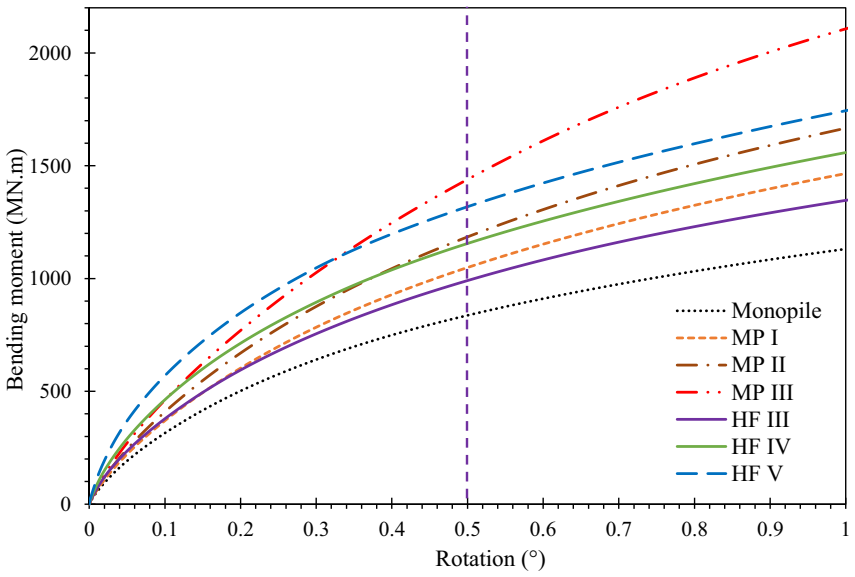

FIGURE 25.24 Moment capacity comparison of monopile lengths with hybrid foundation.

TABLE 25.8 Comparison of the proposed hybrid foundation with other monopile lengths.

	Hybrid foundation	Monopile			
Length of the pile (m)	27	27	30	33	36
Diameter of pile (m)	6.5	6.5	6.5	6.5	6.5
Thickness of pile (m)	0.1	0.1	0.1	0.1	0.1
Mass (tons)	426	426	473.5	521	568.2
Diameter of plate (m)	15	–	–	–	–
Plate thickness (m)	0.1	–	–	–	–
Mass of plate (tons)	113	–	–	–	–
Estimated price (Euros)	426000 × 2 + 113000 × 2 = 1078,000	426000 × 2 = 852000	473500 × 2 = 947,000	521000 × 2 = 1042,000	568200 × 2 = 1136,400

TABLE 25.9 Geometric parameters used in numerical models, including monopile diameter (D_m), monopile wall thickness (t_m), the length of monopile (L_m), the steel plate diameter (D_p) and the thickness of steel plate (t_p).

Foundation	D_p (m)	t_p (m)	D_m (m)	t_m (m)	L_m (m)
Monopile	6.5	–	6.5	0.10	27
MP I	6.5				30
MP II	6.5				33
MP III	6.5				36
Hybrid I (HF I)	8	0.10	6.5	0.10	27
Hybrid II (HF II)	12				
Hybrid III (HF III)	15				
Hybrid IV (HF IV)	20				
Hybrid V (HF V)	25				

25.8 Discussion and conclusions

The chapter aims to understand the need for innovative foundations to help reduce costs and increase efficiency. A study has been discussed to analyze how adding a plate or a skirt around the monopile improves foundation performance. The foundation of an offshore wind turbine accounts for up to 28% of the capital cost. The introduction of a hybrid foundation provides the additional shear stress to resist the lateral load and impart a larger restoring moment to lower pile rotations.

- This method increases the lateral resistance of the pile during the operational loading conditions, and the passive pressure in front of the steel reduced its lateral deflections.
- The effect of adding the steel plate has shown a further increase in the lateral performance of the hybrid system, and centrifuge tests are planned to investigate the hybrid system using the gravity base foundation in more detail.
- The hybrid foundation system can potentially reduce construction costs by employing a smaller/shorter pile. Adding a steel plate can also increase the capacity of an existing typical monopile foundation.
- Introducing a steel plate at the mudline level also significantly increased the moment and lateral load-carrying capacity (M_r, H_R), that is, there is a 37.7% increase in lateral load, and there is a 57% increase in M_r if a plate with a plate has a diameter of 25 m is added as discussed in the study.
- Increasing steel plate diameter exponentially increases the hybrid foundations' lateral load and moment carrying capacity (*HR*, *MR*).
- Required monopile lengths can be decreased by introducing a steel plate at the mudline level.

References

[1] Wang X, et al. Lateral bearing capacity of hybrid monopile-friction wheel foundation for offshore wind turbines by centrifuge modelling. Ocean Eng 2018;148(November 2017):182–92. Available from: https://doi.org/10.1016/j.oceaneng.2017.11.036.

[2] Aleem M, et al. Load utilisation (LU) ratio of monopiles supporting offshore wind turbines: formulation and examples from European Wind Farms. Ocean Eng 2022;248. Available from: https://doi.org/10.1016/j.oceaneng.2022.110798.

[3] BS EN 1992-1-1, Eurocode 2: Design of concrete structures—part 1-1: general rules and rules for buildings, British Standards Institution. Eurocode 2 (2011) Actions on structures, 2004.

[4] Aleem M, Demirci HE, Bhattacharya S. Lateral and moment-resisting capacity of monopiles in layered soils. Proceedings of ICEESEN. Kayseri-Turkey; 2020. p. 19–21.

Further reading

Abdelkader A, El Naggar MH. Hybrid foundation system for offshore wind turbine. Geotech Geol Eng 2018;36(5):2921−37. Available from: https://doi.org/10.1007/s10706-018-0513-z.

Anastasopoulos I, Theofilou M. Hybrid foundation for offshore wind turbines: environmental and seismic loading. Soil Dyn Earthq Eng 2016;80:192−209. Available from: https://doi.org/10.1016/j.soildyn.2015.10.015.

Bhattacharya S. Design of Foundations for Offshore Wind Turbines. 1st ed. Chichester: John Wiley & Sons Ltd; 2019.

Bhattacharya S, Lombardi D, Amani S, Aleem M, Prakhya G, Adhikari S, et al. Physical modelling of offshore wind turbine foundations for TRL (Technology Readiness Level) studies. J Mar Sci Eng 2021;9:589. Available from: https://doi.org/10.3390/jmse9060589.

Krishnaveni B. Generation of P-Y curves for large diameter monopiles through numerical modelling. Int J Res Eng Technol 2016;05(07):379−88. Available from: https://doi.org/10.15623/ijret.2016.0507060.

Nikitas G, Bhattacharya S. Chapter 16: Wind energy. Future energy (3rd ed): improved, sustainable and clean options for our planet, 2019 November. doi:10.1016/B978-0-08-102886-5.00016-5.

This page intentionally left blank

Chapter 26

Gravity-based foundation for offshore wind turbines

Muhammad Aleem[1], Subhamoy Bhattacharya[1], Surya Biswal[1] and Ganga Prakhya[2]
[1]*Department of Civil and Environmental Engineering, University of Surrey, Guildford, London, United Kingdom,* [2]*Sir Robert McAlpine, London, United Kingdom*

26.1 Introduction to gravity-based foundations

Offshore wind turbines (OWTs) are increasingly being installed worldwide as a reliable source of renewable energy with an expected operational design life of 25−30 years. Foundations play an important role in studying an offshore wind farm's viability as they are expensive in the overall cost breakdown. The foundation typically covers 16%−34% of the total cost and details can be found in Bhattacharya [1] and Stehly, Heimiller, and Scott [2]. Foundation selection is one of the important tasks and it depends on the metocean data, ground conditions, availability of construction expertise, and advances in foundation design. Monopiles are the preferred type of foundation; however, with turbines planned in shallower water depths, gravity-based supported foundations are currently being employed. Simplified and quick design methods are crucial in the preliminary design stage to assist in selecting the foundation type using the limited site and turbine data. Gravity-based foundations (GBFs) are often preferred for structures in shallow waters with stable ground conditions. Fig. 26.1 shows various types of GBS based on shape and water depths.

GBF, also known as gravity-based structure (GBS), needs to be designed to avoid uplift or overturning (i.e. no tensile load between the support structure and the seabed). This is achieved by providing adequate dead load to provide

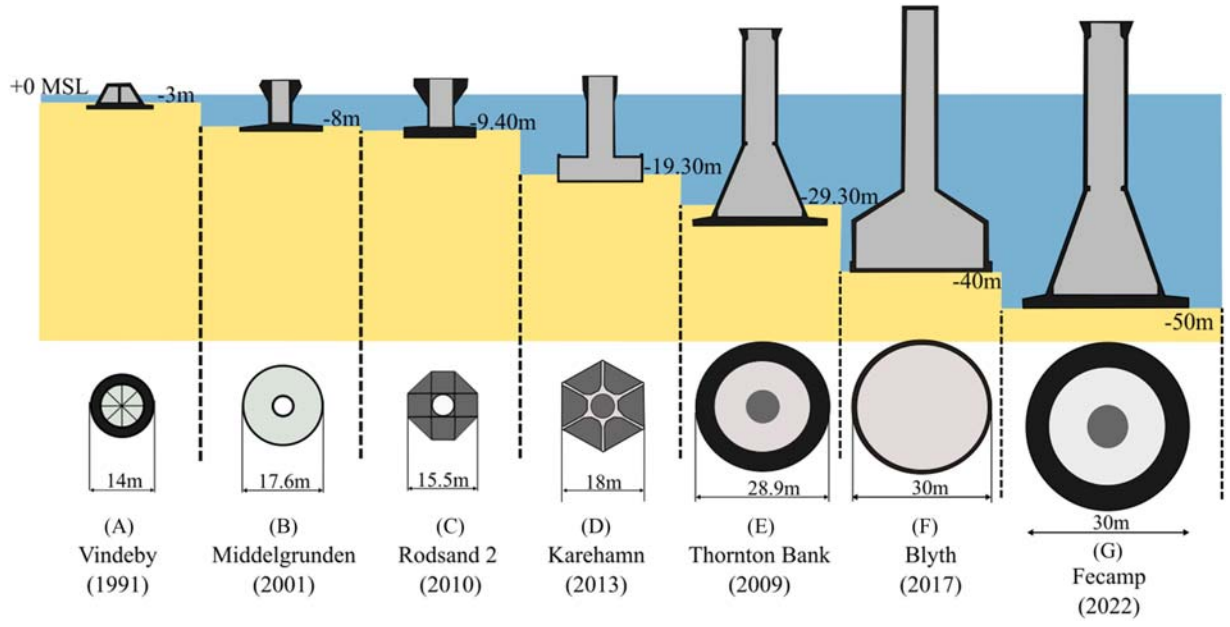

FIGURE 26.1 Development of gravity-based foundation.

Wind Energy Engineering. DOI: https://doi.org/10.1016/B978-0-323-99353-1.00014-1

stability to the structure against the action of overturning moments. If the dead loads from the support structure and the superstructure (Tower + RNA) are not enough, additional ballast will be necessary. The ballast consists of rock, iron ore, or concrete. Installation of these foundations often requires seabed preparation to avoid inclination. The GBS, in most cases, is constructed in-situ concrete or with precast concrete units. GBFs are cheaper to manufacture than steel but require a large fabrication yard and storing area. As concrete foundations will be much heavier than an equivalent steel foundation, larger cranes and vessels are required for installation. For an offshore site where the surface ground is rock, the GBS can be a preferred choice.

Case Study 1 (Empire Wind): Fig. 26.2 shows the location of the proposed 816 MW project in upstate New York port. Concrete GBFs are the preferred choice of foundation for this project, which will be manufactured in the capital region and would be floated out to the installation site, 20−30 miles from the south of Long Island. The water depth for the site is 20−30 m.

Case Study 2 (Fecamp, France): Fecamp offshore is a 498 MW wind farm located in the English Channel, off the Alabaster coast in shallow waters of approximately 30 m depth, see Fig. 26.3 for location. The offshore wind farm will extend over a 67 km^2 area and will be placed 500−1000 m apart.

26.1.1 Advantages and challenges of the gravity-based structure system

GBS can be described as a self-buoyant structure, also known as a "float-out and sink" solution. These foundations can be designed to float (either self-buoyant or with some mechanism) and towed to the offshore site. Subsequently, the foundation can be filled with ballast, causing it to sink and be placed in the seabed. This can be an attractive solution for sites having very hard or rocky soil condition and is an environment-friendly installation. Often, these operations do not require a crane and are thus known as a "crane-free" solution. Furthermore, concrete is readily available and economical compared to steel and needs low maintenance as it is inherently durable in marine environments. The following are some other benefits: minimizing the environmental impact and CO_2-intensity of concrete used is important.

Seabed preparation may be necessary before the deployment of the structure. Also, large space is required at the quayside for fabrication and storage before installation. In challenging geology, piled GBFs are often used. GBS is used in many Danish projects where the geology is shallow rock and clay. Lillgrund and Karehamn are in shallow rock and clay while Thornton Bank (Phase 1) is in medium grain dense sand.

26.1.2 Shapes and sizes

The geometry of the GBF system is an essential consideration in the design optimization process and is a function of site-specific needs. Fig. 26.1 shows a basic evolution of this geometry over the years (1991−2022) from a range of projects. Installed offshore wind GBF sizes range from 17 to 25 m in diameter for the conical designs and an average of 17 m × 17 m for the rectangular designs. Several different footing shapes have been used, which are as follows (Fig. 26.4):

- Circular base plate with a conical section and a cylindrical section
- Rectangular base plate with prestressed box
- Rectangular base plate with penetrative concrete legs
- Hexagonal base with concrete caisson structure
- Elliptical with partitioned cells for ballast
- Square based bottom

26.2 Load and design consideration

Loads on the foundation can be categorized as either static or cyclic loads. In the case of OWTs, static loads would be the vertical loads due to their superstructure and foundation mass, while the predominant cyclic loads are the lateral loads and overturning moment due to the wind and waves. It is worth mentioning that the vertical load is relatively small when compared to the lateral loads and overturning moments due to wind and waves. Cyclic loads are repeated loads and have a significant impact on the structure's lifetime, especially when the expected lifespan is between 20 and 25 years. The readers are referred to Chapter 2 of Bhattacharya [3].

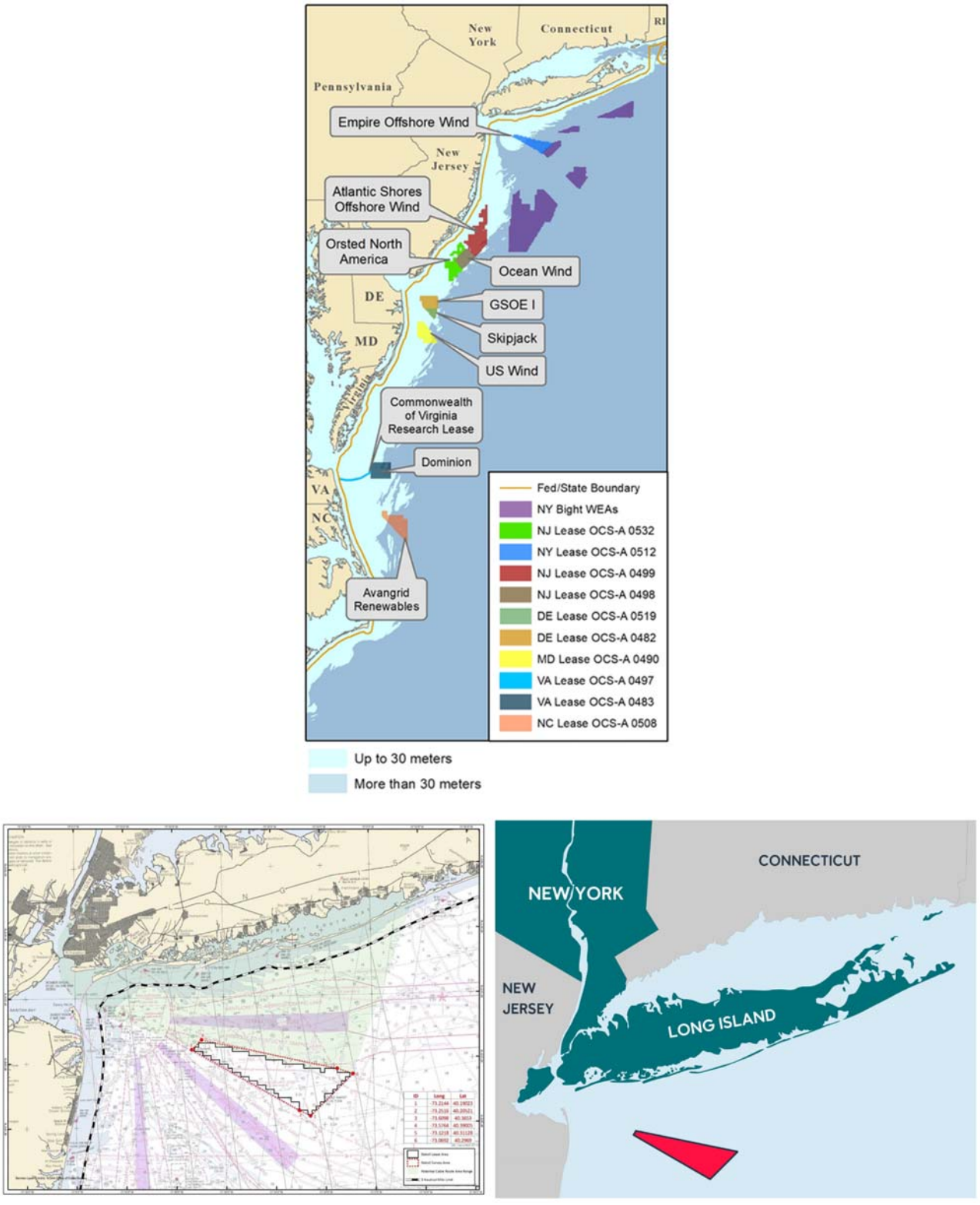

FIGURE 26.2 Proposed upstate New York port for concrete gravity base foundations (https://theconversation.com/offshore-wind-farms-could-help-capture-carbon-from-air-and-store-it-long-term-using-energy-that-would-otherwise-go-to-waste-173208).

FIGURE 26.3 Offshore Fecamp site.

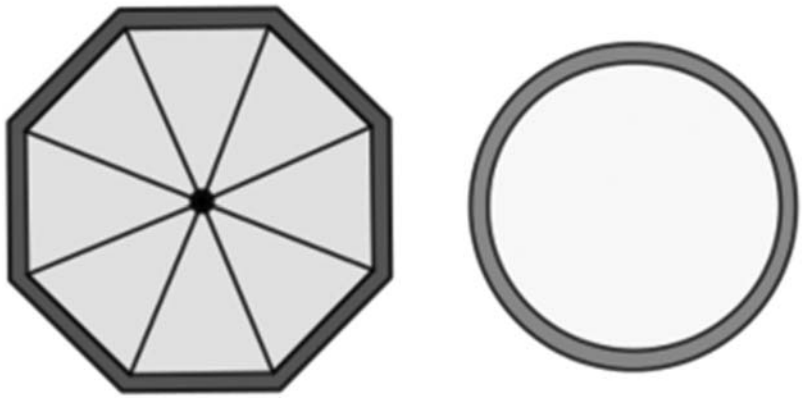

FIGURE 26.4 Plans of different shapes of gravity-based foundation (octagonal and circular).

TABLE 26.1 Summary of load scenarios.

Name	Wind model	Wave model
Normal operational conditions	Normal turbulence model (NTM) at the rated wind speed (U_R)	1-year extreme sea state (ESS)
Extreme wave load scenario	Extreme turbulence model (ETM) at the rated wind speed (U_R)	50-year extreme wave height (EWH)
Extreme wind load scenario	Extreme operating gust (EOG) at the rated wind speed (U_R)	1-year extreme wave height (EWH)

26.2.1 Load combination

Hundreds of load cases are provided in the DNVGL and the IEC codes for the design of OWTs to serve a service life of 25−30 years. However, not all are relevant for foundation design, and it has been identified for this study that the loading shown in Table 26.1 is the most applicable to analyze the foundations conservatively.

The wave conditions are considered independent of the wind conditions. However, this is not necessarily a true reflection of the problem as storms typically bring higher waves and winds simultaneously. It may be noted that this assumption is conservative as the maximum thrust force on the rotor does not correspond to the highest wind speed but those close to the rated wind speed.

26.2.2 Limit state design considerations

A limit state is a condition beyond which a structure or structural component will no longer satisfy the design requirements. For different situations, different requirements hold for the design of the offshore wind turbine foundation. According to DNV-OS-J101, the following design considerations are to satisfy:

- *Ultimate Limit State (ULS)*: This is to ensure that the maximum loads on the foundations are within the chosen members' capacity. The ULS considerations will provide the main dimensions of the foundations.
- *Target Natural Frequency*: This requires predicting the natural frequency of the whole system and the deformation of the structure at foundation and hub height levels. As the natural frequency is concerned with small amplitude vibrations, linear Eigen analysis would suffice.
- *The Fatigue Limit State (FLS)*: The FLS is related to cumulative. This would require predicting the fatigue life of the structure because of cumulative damage due to repeated loads.
- *Robustness and ease of installation*: This is to ensure the system's constructability and adequate redundancy.
- *Accidental limit states (ALS)*: Accidental conditions such as structural damage caused by accidental loads and damaged structures' resistance.
- *Serviceability limit states (SLS)*: This defines the deformations due to cyclic loading, which may alter the distribution of loads between supported rigid objects and the structure. These limits define the total deflection, instantaneous deflection, and differential settlement/accumulation of rotation allowable throughout the turbine system's lifetime. Excessive vibrations affecting nonstructural components (generator and gearbox) and differential settlements under the foundations may cause an intolerable tilt of the turbine, this must be checked within the SLS scope.

26.3 Sizing of gravity-based structure based on ultimate limit state and the effective area method

The ULS is of critical importance to the foundation design and is usually the first step. The methods are available in many textbooks and therefore are not repeated here. Some notable textbooks and monographs are Dean [4], Randolph and Gourvenec [5], Encyclopedia of Maritime and Offshore Engineering, and Salgado. Gravity foundations can transfer the loads through direct bearing if the soil underneath is stiff enough and these are stable due to their mass.

The loads acting on such foundations are vertical load (V), moment load (M), and horizontal load (H). The analysis of such foundations is carried out through the adaptation, modifications, and extension of Terzaghi's bearing capacity equations. The original bearing capacity equation given in Eq. (26.1) is developed for strip footing (i.e., footing under a long wall) resting on the surface of a homogenous deposit and for vertical loads (V) only. Offshore foundations are invariably subjected to lateral loads (H) and overturning moments (M) and can have different shapes, and in most cases, will be embedded in the seabed. The equation was first proposed by Terzaghi [6], and subsequently, Meyerhof [7] advocated a slightly modified bearing capacity equation to account for any embedment of the foundation. Hansen [8] described several alterations to the bearing capacity factors based upon theoretical foundation behavior. These methods have led to the generalized bearing capacity equation, detailed in almost all codes of practices such as BSI – British Standards Institution, DNV, etc. Eq. (26.2) shows a generalized form.

$$\frac{V}{A} = q_{ult} = c'N_c + \gamma z N_q + \frac{1}{2}\gamma B N_\gamma \tag{26.1}$$

$$q_{ult} = c'N_c b_c s_c i_c + \gamma z N_q b_q s_q i_q + \frac{1}{2}\gamma B N_\gamma b_\gamma s_\gamma i_\gamma \tag{26.2}$$

In the concept design stage, simplified methods are preferred. In this simplified approach, the generalized loading problem (V, M, H) is first transformed into a (V, H) problem by reducing the foundation area through a practical area approach, explained in the next section. The (V, H) problem is considered through the inclination factors i_c, i_q, and i_γ.

26.3.1 Converting (V, M, H) loading into (V, H) loading through an effective area approach

Moment (M) capacity can be considered as a function of the vertical capacity and the eccentric distance from the centreline that the resultant design loads will be applied. This can be expressed simply as:

$$e = \frac{M}{V} \tag{26.3}$$

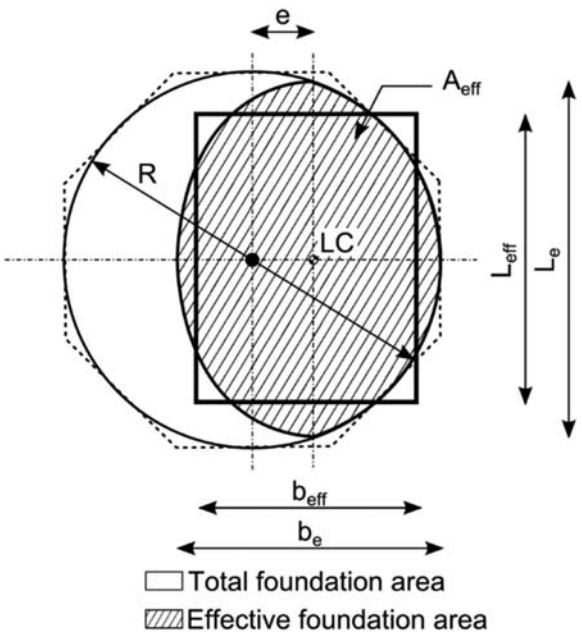

FIGURE 26.5 Effective foundation area after Det Norske Veritas.

where:

M	Moment	[Nm]
V	Vertical load	[N]
e	Eccentric loading point	[m]

When eccentric loading is considered, a reduction in the foundation area is required, this reduced area is called the effective foundation area. The effective area is defined such that its geometric center coincides with that of the resultant load. In the case of a circular foundation, the effective area can be calculated from the following formulation, see Fig. 26.5. The effective area can be further simplified into an equivalent rectangle having the same area and aspect ratio.

$$A_{eff} = 2\left[\frac{D^2}{4}\arccos\left(\frac{2e}{D}\right) - e\sqrt{\frac{D^2}{4} - e^2}\right] \tag{26.4}$$

where:

A_{eff}	Effective foundation area	[m^2]
D	Caisson diameter	[m]
e	Eccentric loading point	[m]

An example of how this reduction would be applied is shown later in the chapter. This is also recommended in API and DNV regulations.

26.4 Tower–gravity-based structure connection

Towers are made of steel and they must be connected to the GBF; large bending moments must be transferred and the connection is often bolted. Bolted connections are sensitive to corrosion and must be robustly protected from the marine environment to ensure their longevity. The factors to be accounted during the design of bolted joints include thorough consideration of shapes, functions, dimensions, materials, service environment, and working loads. These factors vary across industries and, usually, every industry has its own characteristic or typical joint configuration. The number of bolts depends on the flange radius and thickness, the size of the bolts, and predicted loads on the structure. These bolts serve the purpose of exerting a clamping force to keep the joint together (Figs. 26.6 and 26.7).

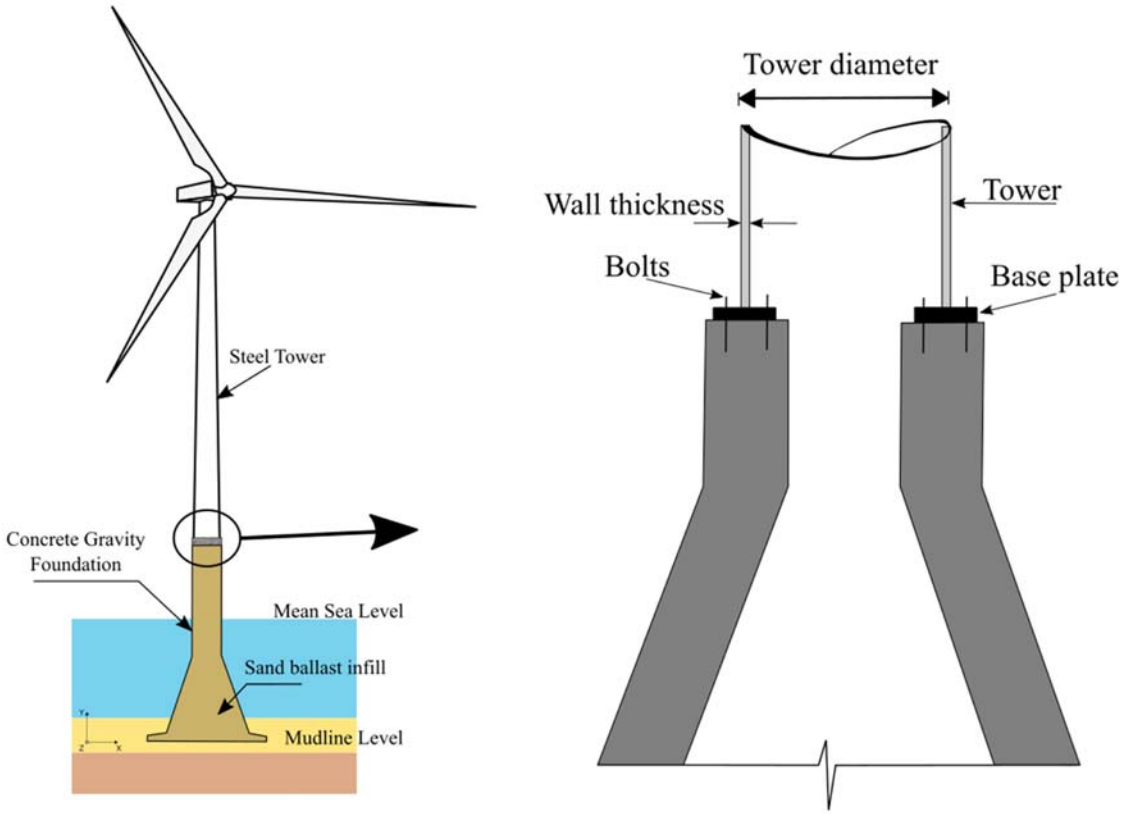

FIGURE 26.6 Tower connected to GBF.

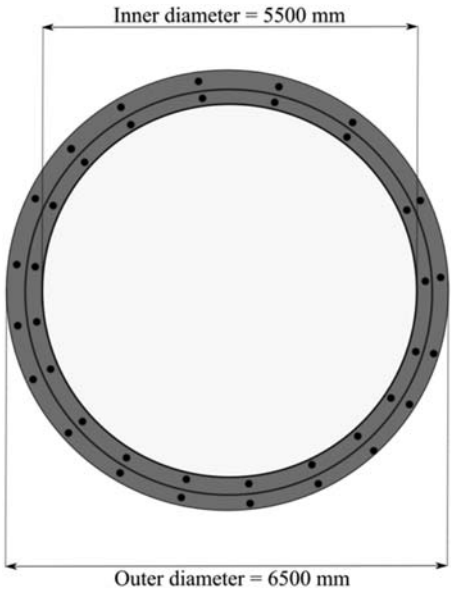

FIGURE 26.7 Plan view of the foundation.

Apart from the overall stability of the structure, the foundation must be checked against sliding. Sliding is usually prevented by ensuring the GBF has enough weight or ballast to develop sufficient friction at the base of the foundation. These two criteria often work against each other, that is, increasing the weight (or ballast) will increase the margin of safety for the sliding but reduce the margin of safety for the bearing capacity. Optimizing the costs of GBF is therefore often a trade-off between reducing ballast weight and increasing the base diameter.

26.4.1 Check for sliding resistance

Foundation subjected to horizontal loading must also be investigated for sliding resistance. The horizontal force can cause sliding of the foundation over the seabed. According to offshore standards, DNV (OS-J101) can determine the sliding resistance of the foundation. *Eurocode 7: Geotechnical design (BS EN 1997−1:2004 EN 1997−1:2004)*. Eq. (26.4) applies for drained conditions and Eq. (26.5) can be used for undrained conditions in clay ($\phi = 0$).

$$H_d < r\left(A_{eff}.c_d + V_d.tan\phi_d\right) \tag{26.5}$$

$$H_d < A_{eff}.r.s_{ud} \tag{26.6}$$

where; r: roughness parameter 1.0 for soil against soil (0.7 for soil to structure), A_{eff}: Effective Area, V_d: Effective vertical force.

Since the soil underneath the foundation consists of cohesionless sand, Eq. (26.5) can be used as:

$$H_d < r(V_d.tan\phi_d)$$

26.4.2 Work example for a gravity-based structure supporting 5 MW turbine

In this example, the GBF design for a typical 5 MW wind turbine is considered for moderate wind turbulence and a water depth of 28 m. The relevant information for the turbine is presented in Table 26.2. This design requires many checks and relevant clauses from Eurocode 2 (EC2) [9], Eurocode 7 (EC7) [10], and API, DnV has been used. The analysis part consists of the stability of GBFs (i.e., ULS checks), which will provide the minimum size of the foundation required to ensure safety against overturning and sliding. SLS, long-term performance requirements, and natural frequency of the whole system for dynamic response (vibration control) require foundation stiffness (Fig. 26.8).

This example takes a conical-shaped GBF (see Fig. 26.8B) with a circular foundation. A tapered steel tower (top diameter 3.87 m and bottom diameter 6 m) supporting the turbine rests on the GBF. The turbine data, together with the operating characteristics, along with metocean data is shown in Table 26.2. The geotechnical information is provided in Table 26.3 and the angle of internal friction φ of the soil is taken as 30 degrees for the entire stratum.

TABLE 26.2 Summary of a typical 5 MW wind turbine.

RNA mass (t)	353
Rotor diameter (m)	126
Rated wind speed, U_R (m/s)	13
Rotor speed range (RPM)	6.0−12.1
Cut-in (U_{in}) wind speed (m/s)	3.5
Cut-out (U_{out}) wind speed (m/s)	30
Tower data	
Tower height, h_t (m)	77
Bottom diameter, D_{bottom} (m)	6
Top diameter, D_{top} (m)	3.87
Weight of tower (t)	347
Summary of metocean and water depth conditions	
Mean water depth (m)	28
50-year significant wave height, $H_{s,50}$ (m)	7.8
50-year significant wave period, $T_{s,50}$ (s)	10.6

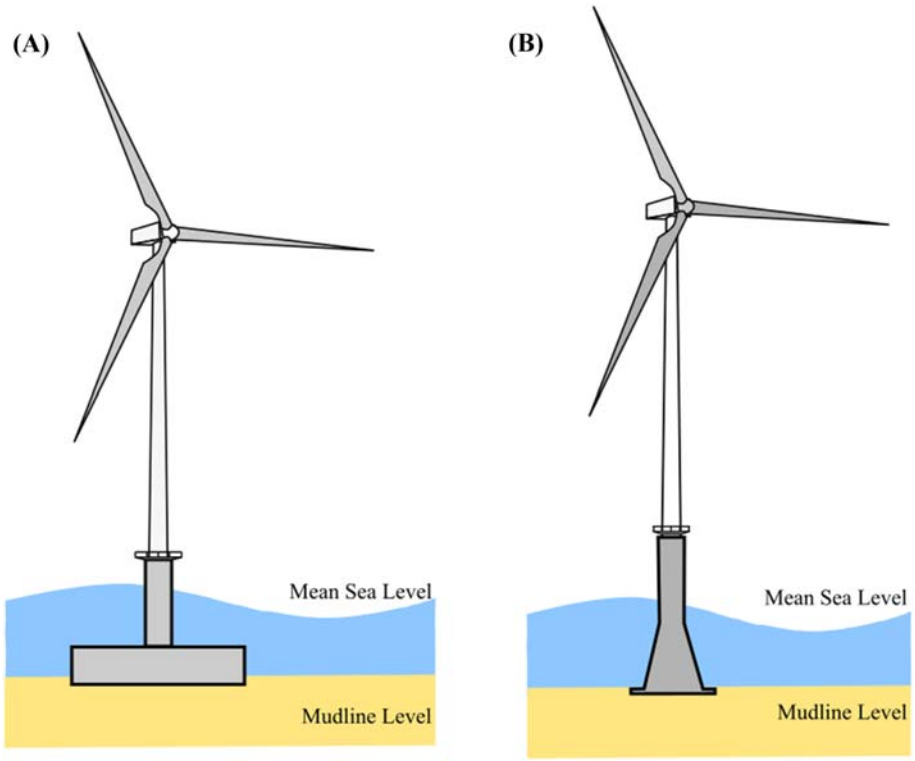

FIGURE 26.8 Schematic diagram of a rectangular gravity-based foundation system (A) and a circular gravity-based foundation system (B).

TABLE 26.3 Ground profile.

Type of soil	Depth (m)	φ (°)
Coarse to medium dense sand	0–20	30
Dense sand	20–23	30
Slightly silty to clayey fine sand	23–31	30

26.4.3 Loads on the foundation

The loads on the foundation can be calculated using the 10-step method discussed in Bhattacharya [3] and Arany et al. [11]. The design overturning moment (M) acting on the foundation is 275 MNm and the corresponding horizontal load (H) in the foundation is 6 MN. The design of footings based on UK-based projects and UK National Annex to EC7 Design Approach 1 is used.

26.4.4 Vertical load

A preliminary estimate of the GBF is circa 3,000 tonnes. Self-weight with a steel tower and RNA mass that acts on the foundation is 700 tonnes. The total vertical load is given in Table 26.4 (Fig. 26.9).

26.4.5 Initial dimensions and ballast load

26.4.5.1 Base of the tower

The top circular diameter of the GBF depends on the bottom diameter of the tower as the concrete pedestal needs to bear the load and transfer to the foundation. Because the bottom diameter of the tower in this example is 6 m, which will be bolted to the GBF, the top of the concrete is taken as 6.5 m (taken as an initial guess). The concrete thickness

TABLE 26.4 Vertical load.	
RNA + tower weight (t)	700
Self-weight of the structure (t)	3000
Total vertical load (V) = 3700 tonnes = 37 MN	

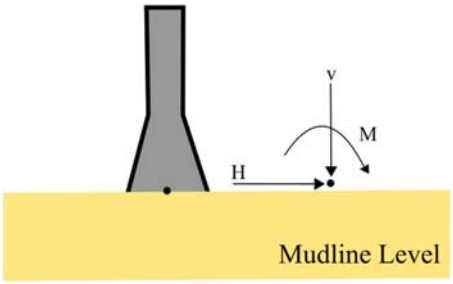

FIGURE 26.9 Gravity-based foundation details showing the loads.

will therefore be 0.5 m to take into account the concrete cover and the steel−concrete connections. As a rule of thumb, for load dispersion requirements, the foundation base will be approximately four times the top foundation diameter.

26.4.6 Calculation of ballast needed

The eccentricity of the loading is given as M/V and the vertical load provides the stability. The foundation is a GBF, and the overturning moment is resisted by the mass of the foundation. As mentioned previously, the total deadweight of the foundation without ballast is 3700 tonnes. It is necessary to check the capacity of the foundation by effective area method. Readers are referred to API [12] for further details on this method. Moment (M) capacity can be considered as a function of the vertical capacity and the eccentric distance from the centerline that the resultant design loads will be applied. This can be expressed simply as follows:

$$e = \frac{M}{V} = \frac{275}{37}$$

$$e = 7.45m$$

This "e" is due to the self-weight of RNA and the tower, and ballasting is carried out to reduce the eccentricity, "e". To prevent contact with the ground being lost at the edge of the footing, it is often advisable to keep the total action within the middle third of the foundation. In other words, the eccentricity of action from the center of the footing is kept within the following limits. Clause 6.5.4 of [10] (EC7) requires special precautions if the eccentricity of the loading exceeds one-third of the width of a rectangular footing or 0.6 of the radius of a circular footing. It should be noted that this is not the middle third rule, which requires the eccentricity not to exceed B/6 or L/6 to avoid a gap forming between the foundation and the soil if the soil behaves as a purely elastic material.

$$e < \frac{D}{6}$$

$$e < \frac{26}{6}$$

Assuming weight of ballast infill = 3000 tonnes = 30 MN

Revised $e = \frac{275}{67}$

$$e = 4.10m$$

When eccentric loading is considered, a reduction in the foundation area is required. This reduced area is called the effective foundation area. The effective area is defined such that its geometric center coincides with that of the resultant load. In the case of a circular foundation, the effective area can be calculated from the following formula given in Eq. (26.4).

$$A_{eff} = 321m^2$$

Equivalent rectangular:

$$A_{eff} = b_{eff} \times L_{eff}$$

$$321m^2 = b_{eff} \times L_{eff}$$

$$\frac{b_{eff}}{L_{eff}} = \frac{\sqrt{13-4.10}}{\sqrt{13+4.10}} = 0.72$$

$$b_{eff} = 0.72L_{eff}$$

$$b_{eff} = 15.20m$$

$$L_{eff} = 21.1m$$

26.4.7 Ultimate geotechnical capacity

The equations for bearing capacity factors and shape factors are given in Annex D, [10] (EC7). The bearing capacity of the subsoil is calculated for the stability of the foundation under extreme loads. Due to the combined loading of the vertical force and the bending moment, an eccentricity is created for the resulting bearing capacity and the center of the foundation. This eccentricity reduces the effective bearing area of the foundation and thus reduces the total bearing capacity. However, to be consistent, the bearing capacity factor is taken from API [12]. The depth of the foundation is taken as 3 m. N_c, N_q, and N_γ = Bearing Capacity Factors, which depend on the soil effective friction angle.

$$N_q = 18.40$$

$$N = 15.1$$

$$\begin{pmatrix} H = 6MN \\ V = 67MN \end{pmatrix}$$

Load inclination factors from API [12]:

$$i_q = \left(1 - 0.5 \times \frac{H}{V}\right)^5$$

$$i_q = 0.80$$

$$i_\gamma = \left(1 - 0.7 \times \frac{H}{V}\right)^5$$

$$i = 0.72$$

Shape factors from API [12]:

$$S_q = 1 + i_q\left(\frac{b_{eff}}{L_{eff}}\right) sin\varnothing$$

$$S_q = 1 + 0.80\left(\frac{15.20}{21.1}\right) sin30$$

$$S_q = 1.29$$

$$S_\gamma = 1 - 0.4i_\gamma\left(\frac{b_{eff}}{L_{eff}}\right)$$

$$S_\gamma = 1 - (0.4 \times 0.72)\left(\frac{15.20}{21.1}\right)$$

$$S_\gamma = 0.8$$

$$Q_{ult} = \left\{ p_0'(N_q - 1)i_q \times S_q + \frac{1}{2}\gamma' B' N_\gamma i_\gamma S_\gamma \right\}$$

The formula used to calculate the bearing capacity was obtained from the DNVGL codes

$$q_{ult} = (3 \times 9)(18.40 - 1)(0.80 \times 1.29) + 0.5 \times 9 \times 15.2 \times 15.1 \times 0.72 \times 0.8$$

$$\approx 1080kPa$$

$$\text{Bearingpressure} = \frac{67MN}{(21.1 \times 15.20)m^2} = 209\text{kPa}$$

$$FOS = \frac{1080}{209} \approx 5(\text{Acceptable})$$

26.4.8 Check for sliding resistance

Foundation subjected to horizontal loading must also be investigated for sliding resistance. The horizontal force can cause sliding of the foundation over the seabed. Section 6, "Spread Foundations" of [10] (EC7), can be used to determine the sliding resistance of the foundation. Eq. (26.5) applies for drained conditions and Eq. (26.6) can be used for undrained conditions in clay ($\phi = 0$).

$$H_d < r\left(A_{eff}.c_d + V_d.tan\phi_d\right)$$

$$H_d < A_{eff}.r.s_{ud}$$

Because it is assumed that the soil underneath the foundation consists of cohesionless sand, Eq. (26.5) can be used as follows:

$$H_d < r(V_d.\tan\phi_d)$$

$$H_d < 0.7(65.\tan 30)$$

$$6 < 26.3$$

$$\frac{F_{Ed}}{F_R} = \frac{6}{26.3} = 0.22$$

The unity check is below 0; thus, the foundation can resist the horizontal force for the sliding capacity.

26.4.9 Foundation stiffness

Different formulations for foundation stiffness are available in the literature. The foundation stiffness can be used to compute the natural frequency of the whole system (Table 26.5).

The foundation stiffness values can be used to check the natural frequency of the whole system for vibration response control, and the macro spring approach developed by Adhikari and Bhattacharya and Vargese et al. can be used. The stiffness can also be used to predict deformations as well.

TABLE 26.5 Formula for foundation stiffness.

Mode of motion	Foundation stiffness
Vertical	$K_v = \frac{4G_1R}{1-v_1}\cdot\frac{1+1.28\frac{R}{H}}{1+1.28\frac{RG_1}{HG_2}}; 1 \le \frac{H}{R} \le 5$
Horizontal	$K_H = \frac{8G_1R}{2-v_1}\cdot\frac{1+\frac{R}{H}}{1+\frac{RG_1}{HG_2}}; 1 \le \frac{H}{R} \le 4$
Rocking	$K_R = \frac{8G_1R^3}{3(1-v_1)}\cdot\frac{1+\frac{R}{6H}}{1+\frac{R}{6H}\frac{G_1}{G_2}}; 0.75 \le \frac{H}{R} \le 2$

G_1 and G_2: Shear modulus of upper two layers, v_1 and v_2: Poisson's ratio of upper two layers, R: Radius of the foundation, H: Height of the first soil layer.

$$K_v = \frac{4 \times 17.30 \times 13}{1-0.3}\cdot\frac{1+1.28\frac{13}{10}}{1+1.28\frac{13}{10}\times\frac{17.30}{5.76}}$$

$$K_v = 570.6\frac{MN}{m}$$

$$K_H = \frac{8G_1R}{2-v_1}\cdot\frac{1+\frac{R}{H}}{1+\frac{R}{H}\frac{G_1}{G_2}}$$

$$K_H = 554\frac{MN}{m}$$

$$K_R = \frac{8G_1R^3}{3(1-v_1)}\cdot\frac{1+\frac{R}{6H}}{1+\frac{R}{6H}\frac{G_1}{G_2}}$$

$$K_R = 106708\frac{MNm}{rad}$$

26.5 Summary

GBS is considered a plausible foundation type in many projects due to its better environmental credentials. Examples are less noise during installation, low-carbon concrete, and enhanced local content and supply chain. This chapter provides the fundamental aspects of GBS design. An example is taken to illustrate the GBS design for a 5 MW wind turbine generator.

References

[1] Bhattacharya S. Challenges in design of foundations for offshore wind turbines. Eng Technol Ref 2014;. Available from: https://doi.org/10.1049/etr.2014.0041.

[2] Stehly T, Heimiller D, Scott G. Cost of Wind Energy Review. (No. NREL/TP-6A20-70363).Golden, CO (United States). National Renewable Energy Lab.(NREL);2017. 2016;.

[3] Bhattacharya S. Design of foundations for offshore wind turbines. 1st ed. Chichester: John Wiley & Sons Ltd; 2019.

[4] Dean ET. Offshore Geotechnical Engineering Principles and Practice. In: Publishing.DNV-OS-J101. Design of offshore wind turbine structures, 1st ed. Det Norske Veritas; 2014.

[5] Gourvenec S, Randolph M. Offshore Geotechnical Engineering 2011;. Available from: https://doi.org/10.1201/9781315272474.

[6] Terzaghi K. Theoretical Soil Mechanics. New York; London: J. Wiley and Sons, Inc.; Chapman and Hall, Limited; 1943.

[7] Meyerhof GG. Penetration tests and bearing capacity of cohesionless soils. J Soil Mech Found Div 1956;82:1–19.

[8] Hansen J. Revised and extended formula for bearing capacity. Danish Geotech Institute, Copenhagen. Bull 1970;28.
[9] BS EN 1992-1-1:2004 + A1:2014. Eurocode 2: design of concrete structures—Part 1-1: general rules and rules for buildings.
[10] BS EN 1997−1:2004 + A1:2013. Eurocode 7: geotechnical design—Part 1: general rules.
[11] Arany L, et al. Design of monopiles for offshore wind turbines in 10 steps. Soil Dyn Earthq Eng 2017;92:126−52. Available from: https://doi.org/10.1016/j.soildyn.2016.09.024.
[12] API. Recommended practice 2GEO, geotechnical and foundation design considerations, American Petroleum Institute, 2011.

Section D

Storing energy

This page intentionally left blank

Chapter 27

Greenhouse gas emissions from storing energy from wind turbines

Charles J. Barnhart
Institute for Energy Studies, Western Washington University, Bellinghamm, WA, United States

27.1 The need for storage

The world needs affordable, accessible, sustainable, and low-carbon energy resources [1–3]. Of the renewable resources, solar PV and wind turbines have the highest technical potential to satisfy this need, but these technologies generate electricity from variable, weather-dependent resources [4–6]. Fig. 27.1 depicts a compelling visualization of 30 day superimposed power demand time series data (red), wind energy generation data (blue), and solar *insolation* data (yellow). Supply correlates poorly with demand.

The amount of storage needed for the operation of electrical grids incorporating increasing amounts of variable wind resources is a critical yet complicated question. It is complicated for two reasons: (1) the electrical grid, composed of myriad power sources and sinks, is conducted in real-time, and (2) the number of technologies and practices, their varied and evolving characteristics, and their possible implementations under differing and shifting policy landscapes present a grossly under-determined problem with several solutions. This chapter focuses on pairing storage with wind turbines to reduce GHG emissions.

Technologies and practices positioned to ensure grid reliability include flexible conventional energy generation (natural gas combustion turbines and diesel generation sets), flexible renewable energy generation (curtailment, hydropower, and concentrated solar power with thermal storage), flexible load (demand-side management), energy storage including thermal storage, and resource sharing (diversity and transmission). In the future, when greenhouse gas emissions are constrained, flexible energy generation will need to be achieved using low-carbon energy supplies.

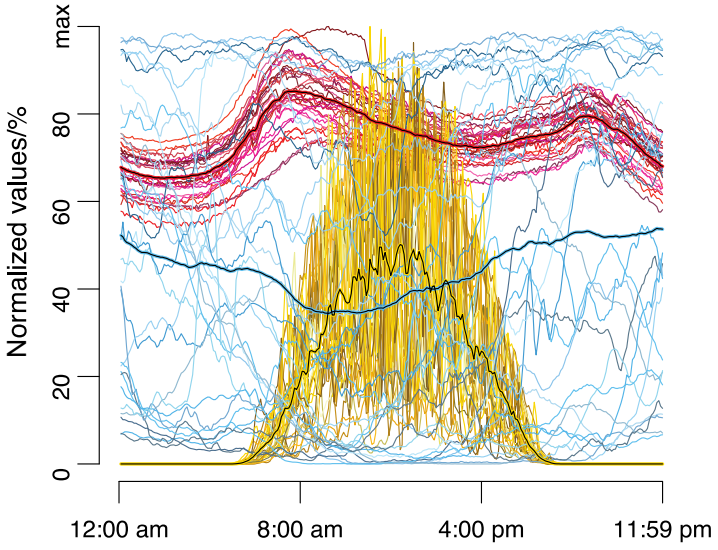

FIGURE 27.1 Wind-power generation (*blue*), insolation (*gold*), and power demand (*red*) time series data provide a compelling visualization of renewable energy's intermittent correlation with demand. Thirty days of data collected in April 2010 are superimposed and normalized to their maximum values. Average values are in color-highlighted black lines. *Data obtained from Bonneville Power Administration (Pacific Northwest, The United States).*

Wind Energy Engineering. DOI: https://doi.org/10.1016/B978-0-323-99353-1.00001-3

Studies have made efforts to determine the amount of renewable energy generation an electrical grid can support by bundling these technologies and practices into an abstract resource: grid flexibility is defined as the capacity to readily dispatch and halt the load and generation on [7]. Less flexible grids harbor high percentages of so-called baseload-generating plants such as nuclear, coal, and natural gas combined cycle plants. The amount of energy storage capacity required will depend firstly on grid flexibility. Secondly, it will depend on attributes of the renewable energy generation. The amount, type, mix, and degree of supply correlation affects how well supply satisfies demand. Today, storage on power grids is dominated by pumped storage hydro (PSH). Table 27.1 lists global storage energy capacity in MWh [8]. This chapter describes the effect storage has on the energy and carbon intensity of wind-generated electricity. First, key storage characteristics are listed. Second, energy return ratio results are presented. Third, carbon intensity calculations and results are presented.

27.1.1 Key characteristics for storage

Energy storage production incurs upfront energy costs and emits carbon into the atmosphere. While storage (apart from CAES) has no direct emissions of GHG, scope 2 emissions (from electricity generation) are associated with the round-trip efficiency and operation of the storage device. Scope 3 or life-cycle emissions are indirect, resulting from the process of mining the materials and manufacturing the storage and flexible generation technologies. The energetic and carbon intensity values for energy storage technologies were obtained from life cycle assessment (LCA) and net energy analysis (NEA) studies [9–12]. Key characteristics of grid-scale storage are safety, affordability, reliability, longevity, and efficiency. Technologies that satisfy these criteria include four electrochemical storage technologies—lithium-ion (Li-Ion), sodium sulfur (NaS), traditional lead-acid (Pb-Acid), vanadium redox flow batteries (VRB)—and two geological storage technologies—PSH and compressed air energy storage (CAES)—in this analysis.

Storage characteristics are listed in Table 27.2. This chapter focuses on how much energy it takes to store wind energy and how many GHGs are emitted. The energy intensity per unit energy storage capacity, ε_s (kWh/kWh), depends on the technology's depth of discharge (D), its total number of charge-discharge cycles (λ), and its cradle-to-gate (c2g) embodied electrical energy requirement per unit capacity of energy delivered to storage (CTG_e). Embodied energy accounts for energy expended in mining raw resources, manufacturing the device, and delivering the device to point of use. The per cycle carbon intensity (g CO_2eq/kWh) for storage technologies was calculated by adding capital ($GHG_{s,\ cap}$) and operational greenhouse gas ($GHG_{s,\ op}$) emissions per unit of electrical energy delivered per cycle.

A critical attribute of an energy storage technology is its round-trip efficiency, η. The carbon intensity of the discharged electricity is $\geq 1/\eta$ times the carbon intensity of the input electricity. Using storage increases the carbon intensity of delivered electricity by a factor, χ, as listed in Table 27.2. χ is a carbon intensity multiplier. If storage is 90% efficient, the carbon intensity of the delivered electricity increases by 11%, $\chi = 1.11\$$. Manufacturing storage technologies also incurs energy and carbon costs.

TABLE 27.1 Global storage energy capacity.

Technology	2010 (MWh)	2020 (MWh)	Percent growth	Percent total capacity
Flow	44	3221	7220	0.264
Latent heat	146	965	561	0.079
Lead-acid	36	166	361	0.014
Lithium-ion	16	868	5325	0.071
Nickel-based	18	19	6	0.002
Pumped hydro	862,484	1,178,193	37	96.477
Sensible heat	6091	34,770	471	2.847
Sodium-based	996	2161	117	0.177
Zinc-based	0	857		0.070
Total	869,831	1,221,220	40	100.000

Source: See Nguyen T. DOE global energy storage data. https://sandia.gov/ess-ssl/gesdb/public/index.html.

TABLE 27.2 Data used in net energy analysis of storage technologies.

Technology	CAES	Li-Ion	Sulfur	Lead	PSH	Flow
$GHG_{s,\ cap}$ (kg/MWh)	19,400	89,000	687,500	153,850	35,700	161,400
$GHG_{s,\ op}$ (kg/MWh)	288	0	0	0	1.8	3.3
D, discharge depth	1	0.8	0.8	0.8	1	1
λ, cycles	25,000	6000	4700	700	25,000	10,000
η, efficiency	0.7 (1.36)	0.9	0.75	0.9	0.85	0.75
CTG_e	22	136	145	96	30	208
χ, carbon multiplier	0.735[a]	1.111	1.333	1.111	1.764	1.333
ε_s, energy intensity	0.00088	0.028	0.039	0.17	0.0012	0.072

Definitions are in the text.
[a]*CAES operation delivers more electricity than enters storage by combusting natural gas.*
Source: Denholm P, Kulcinski. Life cycle energy requirements and greenhouse gas emissions from large scale energy storage systems. Energy Convers Manag 2004;45:2153–72. https://doi.org/10.1016/j.enconman.2003.10.014; Rydh C, Sandén B. Energy analysis of batteries in photovoltaic systems. Part I: Performance and energy requirements. Energy Convers Manag 2005;46:1957–9. https://doi.org/10.1016/j.enconman.2004.10.003; Sullivan JL, Gaines L. A review of battery life-cycle analysis: state of knowledge and critical needs ANL/ESD/10-7, transportation research. Oak Ridge, TN: Argonne National Laboratory; 2010.

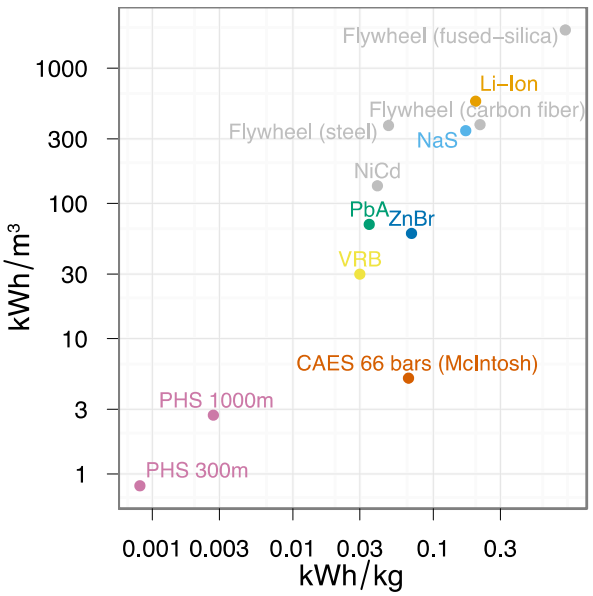

FIGURE 27.2 A plot comparing volumetric and specific energy densities for energy storage technologies. Technologies considered for large-scale energy storage have labels in color [13]. *Data obtained for PSH and CAES are calculated, and battery data are obtained from Beard KW. Linden's handbook of batteries, 5th ed. New York, Chicago, San Francisco, Athens, London, Madrid, Mexico City, Milan, New Delhi, Singapore, Sydney, Toronto: McGraw-Hill Education; 2019 and flywheel data from Semadeni M. Storage of energy, overview. Encycl Energy 2004;5:719–738.*

Despite higher energy and carbon intensities when compared to PSH, electrochemical storage technologies present one clear advantage: energy density. Batteries can store several hundred times the amount of energy per unit mass and volume than PSH (Fig. 27.2). Additionally, batteries do not require geological features, that is, steep topography, that PSH requires, and therefore can be deployed anywhere, including city centers, residences, and commercial buildings.

Lithium-ion technologies are experiencing the greatest amount of growth due to deployment in electric vehicles and personal devices. For this reason, rapid learning and advancement in lithium-ion development are driving reductions in cost, energy requirements, and associated scope 3 carbon emissions. Electrical energy storage (EES) technologies have developed rapidly over the last 50 years since the invention of the lithium-ion battery. This development has accelerated in the last two decades with the advent of ubiquitous personal electric devices and the exponential adoption of hybrid and electric vehicles. These growing economies of scale and associated learning-by-doing have led to reductions in cost, as well as embodied energy requirements and GHG emissions, during manufacturing. As such, this review of lithium-ion LCAs in the peer-reviewed literature reports historical analyses but emphasizes recent analyses. The body

of LCA literature for EES technologies is small, especially when compared to solar photovoltaic LCAs. Harmonization studies do not exist. However, this summary makes some efforts at harmonizing by breaking life cycle GHG emissions into the resource, manufacturing, use, and recycling stages. Furthermore, the focus is placed on recent LCAs due to "learning-by-doing" reductions in cost, energy use, and corresponding carbon emissions. It should be noted that as the power grid mixes supplying electricity for the manufacturing of batteries becomes less GHG intensive, the embodied GHGs of electrical energy storage (EES) will decrease.

27.1.2 Which lithium-ion chemistry should be used in grid storage?

Lithium batteries are generally categorized into five chemistries: lithium-cobalt oxide, lithium-titanate, lithium-iron phosphate, lithium-nickel manganese cobalt oxide, and lithium-manganese oxide. For stationary power backup and grid-tied services, lithium-nickel manganese cobalt oxide (Li-NMC) is often preferred due to its long life and inherent safety by being less prone to heating [14]. Drawbacks to this chemistry are lower energy densities (95−130 Wh/kg as compared to 150−190 Wh/kg for lithium-cobalt oxide used in cellphones). The Tesla-backed utility-scale Hornsdale Power Reserve in Australia (100 MW) and the proposed 409 MW, 900 MWh Florida Power and Light Manatee project operational in 2021 use Li-NMC chemistry. Thus, this review focuses on Li-NMC.

27.1.3 Published literature data survey and review for lithium-ion electrical energy storage

c2g GHG emissions occur during (1) the material acquisition phase, which includes mining, transport, and smelting or processing, (2) the cell production phase, which involves making the electrochemical pastes that constitute the battery anode and cathode and (3) the battery pack manufacturing phase, which involves building the case and battery management system (BMS), a computer that optimizes cell charging and discharge performance and safeguards against overheating (Table 27.3).

LCA studies of electrical energy storage (EES) technologies date back to the 1980s [15] with increased interest in the late 1990s and 2000s [9,10,16,17], but this paper will only review studies dated post-2010. Table 27.1 shows c2g GHG intensity (kg/kWh capacity) from several studies broken down by life-cycle stage (when available). Many of these studies are meta-analyses stemming from original 'tear-down' data produced by Linda Gaines's Transportation System Analysis group at Argonne National Laboratory. Sullivan and Gaines [11] produced a comprehensive review of material flows tracking energy intensity and GHG intensity for several battery chemistries. Their functional unit, kg of battery, requires assumptions about the energy density of the battery to report values on a per kWh capacity basis. Majeau-Bettez et al. [18] produced their own independent LCA inventory, later used by Hiremath et al. [2]. Majeau-Bettez et al. [18] broke GHG intensity down for major Li chemistries by component and found that Li-NMC production emissions are 200 kg CO_2e/kWh capacity with 27% from cell structure and components, 33% from the positive electrode, 8% from the negative electrode, 14% from BMS, and 18% from substrates and casing. Their study also found that China's coal-dominated electricity mix increases production emissions by 10%−16%.

TABLE 27.3 Reported GHG emissions (kg CO_2e/kWh capacity).

Study	Year	Upstream	Production	c2g
Sullivan and Gaines	2010	0	0	308
Sullivan and Gaines	2010	0	0	154
Sullivan and Gaines	2010	0	0	53
Majeau-Bettez et al.	2011	0	0	200
Hiremath et al.	2015	0	0	157
Dunn et al.	2015	0	0	50
Ambrose et al.	2016	33	157	190
Ambrose et al.	2016	36	475	511
Dai et al.	2019	59	30	89

Barnhart and Benson [12] brought focus to considering use phase, emphasizing the importance of efficiency and cycle life as key characteristics for maximizing life cycle energy return ratios. Hiremath et al. [2] compared several EES technologies' c2g and use-phase GHG intensities under various use-phase applications such as energy management and transmission and distribution investment deferral. Their study showed how the emissions from the generation source or power grid charging the battery can dominate life cycle emissions, up to 95% for particularly GHG-intensive grids. Ambrose and Kendall [1], focusing on traction batteries, used sophisticated statistical modeling to explore how variability in battery operations effect depth-of-discharge, cycle life, and capacity fade. They found that 80% depth-of-discharge maximizes total energy throughput and therefore minimizes per cycle embodied GHG intensity. They also found that the electricity grid dominates c2g and use-phase emissions, not the materials acquisition stage. Dunn et al. [19,20], both stemming from the Argonne group, further refined c2g energy and GHG intensity values for 5 Li chemistries producing the most comprehensive tear-down analyses to date. *For Li-NMC and a production factory powered by a grid with average California, USA emissions, c2g emissions are 89 kg/kWh capacity*. Recent studies from the Swedish Research Institute [21,22] are metanalyses of lithium-ion batteries [20] and report similar values.

Pellow et al. [23] explored battery recycling and highlighted critical gaps in LCA analysis and harmonization (e.g., electricity grid mix effect on manufacturing emissions) but did not address these gaps. Recycling displaces fossil fuel from mining and reduces bauxite residues, steel slags, and sulfide tailings from virgin aluminum, iron, and copper mining, respectively. Reference [23] reviews other recycling studies and finds end-of-life GHG intensities of 8−83.1 kg CO_2e/kWh capacity, settling on 27 kg/kWh as the most likely value. It is unknown how c2g emissions will be reduced for batteries manufactured with recycled materials. Results show the two trends: (1) reported c2g emissions are falling with time and (2) reported the GHG intensity of power grids is falling with increased renewable generation.

27.1.4 The case for considering use phase

27.1.4.1 GHG emissions associated with storing wind

Energy storage emits carbon into the atmosphere. Electricity sourced or Scope 2 emissions of carbon are those associated with the round-trip efficiency and operation of the storage device. Indirect emissions or Scope 3 emissions are those resulting from the process of mining the materials and manufacturing the storage and flexible generation technologies. The carbon intensity values for energy storage technologies were obtained from LCA and NEA studies. Carbon intensity values for the average United States power grid emissions and sub-grid emissions were obtained from the United States Environmental Protection Agency's Emissions and Generation Resource Integrated Database. Table 27.4 lists the life carbon intensity values for wind, PV, and gas.

The use phase for EES technologies can account for up to 95% of total life cycle emissions. Omitting the use phase would lead to an egregious underestimate and EES systems GHG footprint. The use phase emissions depend critically

TABLE 27.4 Generation technology life cycle, kWh($kg_{CO_2}eq$).

Wind	Onshore (harmonized) 107 estimates from 44 studies	22	50	91	119	333
PV	[24] Crystalline Silicon PV	5	20	22	25	38
	irradiation of 1700 (kWh)/m^2/a					
	41 estimates from 13 studies					
NGCC	[25] 51 estimates, 42 studies	1.4	2	2.2	2.4	3
	Capital emissions: 1 g/(kWh)					
NGCT		1.2	1.3	1.5	1.8	1.9
NGCC	[25]	–	15	21	36	–

Resource. Reference and notes Min 25th% median 75th% Max.
Source: References from [24–26].

on the EES roundtrip efficiency and the GHG intensity or emission factors of the charging source. The use phase emissions kg CO_2e per unit capacity (MWh) are calculated as follows:

$$\mathrm{GHG}_{\text{use phase}} = \frac{\mathrm{GHG}_{\text{charging source}}}{\mathrm{h}},$$

where η is the roundtrip efficiency. To avoid double counting generation emissions, the additional or add-on emissions from EES operations is,

$$\mathrm{GHG}_{\text{add-on}} = \frac{\mathrm{GHG}_{\text{charging source}}}{\mathrm{h}} - \mathrm{GHG}_{\text{charging source}}.$$

Fig. 27.3 shows these add-on emissions as a function of EES roundtrip efficiency (x-axis) and charging source generation emissions (y-axis). Representative source emissions for coal steam plants, natural gas combined cycle plants, solar PV, wind turbines, and hydroelectric turbines are listed along with average emissions for select US and the US average. The roundtrip efficiencies for various EES technologies are listed too. For Hawaii, as an example, a Li-NMC battery paired with average grid emissions would add an additional 37−78 g/kWh. If paired with solar PV it would add only 3−6 g/kWh, with wind, even less, 1−3 g/kWh. The energy lost due to inefficiencies is the same regardless of generation source, 0.05−0.11 kWh/kWh. However, that energy's GHG intensity is far lower for solar PV generation.

The life cycle emissions per cycle through the use phase consider all systems-level characteristics, including depth-of-discharge, cycle-life, round-trip efficiency, and source GHG intensity (Figs. 27.4 and 27.5):

$$\mathrm{GHG}_{\text{per cycle MWh}} = \frac{\mathrm{GHG}_{\mathrm{C2G}}}{\mathrm{lD}} + \frac{\mathrm{GHG}_{\text{charging source}}}{h}.$$

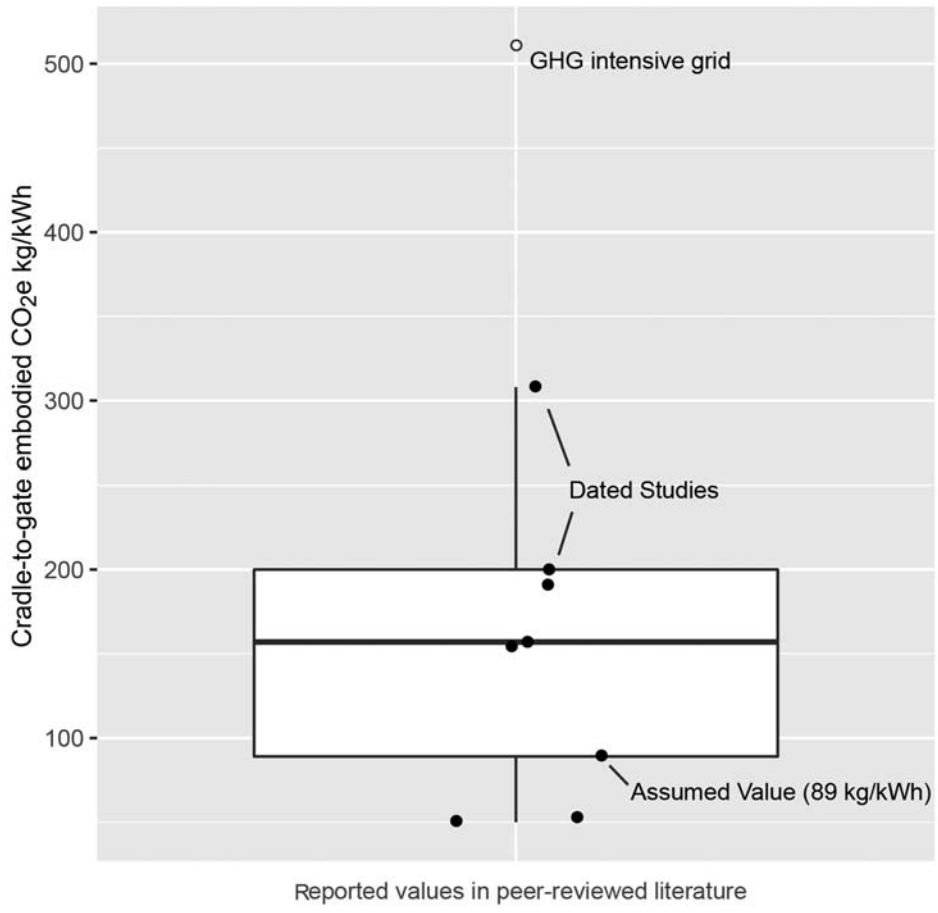

FIGURE 27.3 Reported c2g GHG values (kg CO_2e/kWh capacity) for Li-NMC batteries.

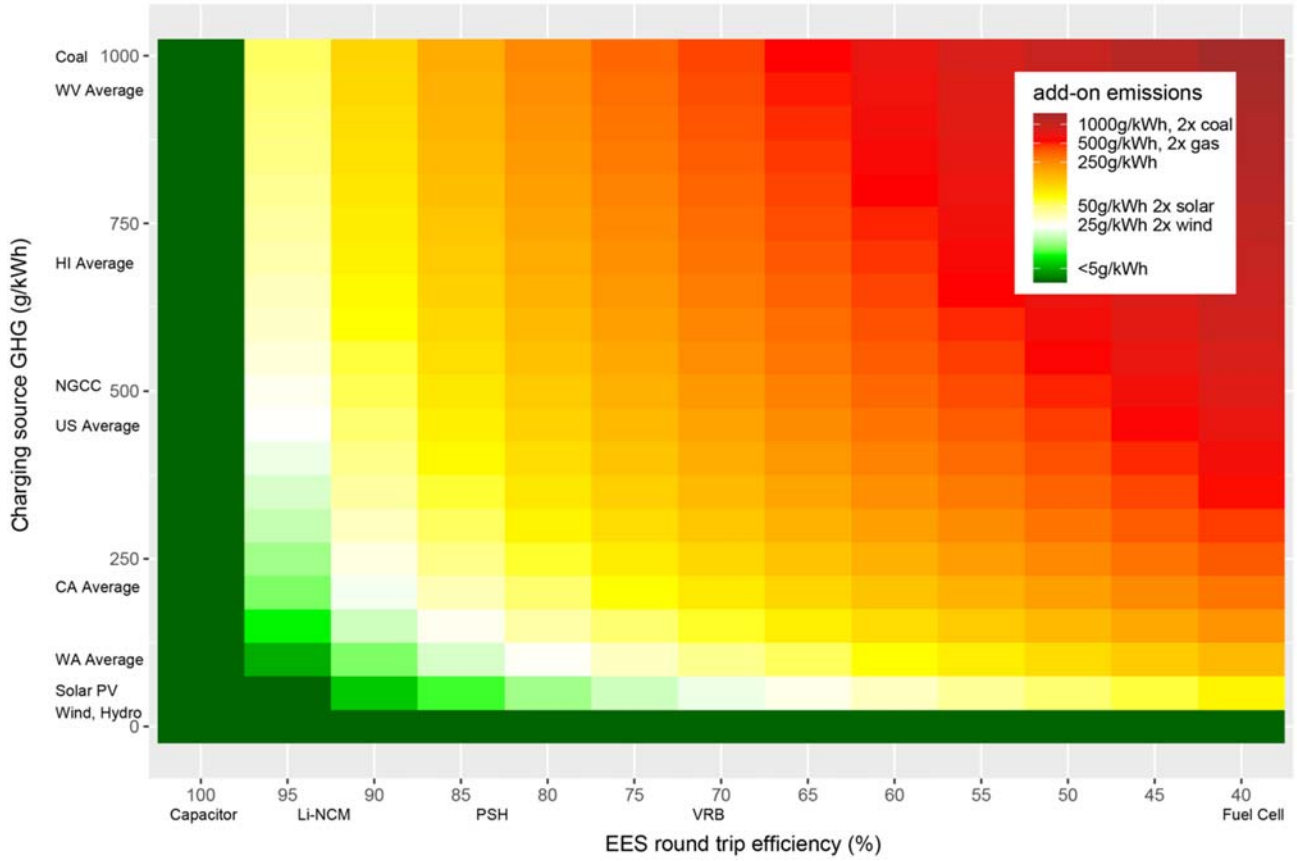

FIGURE 27.4 Additional emissions (kg/kWh) due to charging source and EES efficiency. The efficiency of the EES is shown by the x-axis in reverse order (highest/best on the left-hand side) with technologies labeled at corresponding percentages. The y-axis shows the GHG emission factor (g/kWh) of the electricity charging the EES. These sources are labeled with corresponding generation technologies or power grid averages.

27.1.5 Net energy analysis of storing and curtailing wind resources

Curtailing renewable resources results in an immediate and obvious forfeiture of energy. However, flexible grid technologies can also consume significant amounts of energy in their manufacturing and operation. These embodied energy costs are not as immediately apparent, but they are an energy sink from a societal perspective.

In this section, the energetic costs of EES are compared to the energetic costs of curtailment. In lieu of storage or other means of grid flexibility, variable resources are curtailed during periods of oversupply or of strong market disincentives [27,28]. Consequently, electricity is squandered, capacity factors are reduced, and revenue for turbine owners in certain markets is lost. In Texas, for example, 1.2%−17.1% of potential wind generation was curtailed on an annual basis between 2007 and 2012, equaling a total of 13 TWh of electrical energy. Worldwide, curtailment rates are projected to increase as wind and solar comprise a larger fraction of the generation mix [7,28]. We ask whether storage provides societal net-energy gains over curtailment. EES has significant value not quantified or analyzed in this study, including electricity market economics [29], ensuring reliable power supplies to critical infrastructure, ancillary benefits to power grid operation, and application in disaster relief and war zone scenarios.

The results shown here were originally presented in ref. [12], which presents a theoretical framework for quantifying how storage affects net energy ratios. This framework accommodates any type of generation or storage technology. Using LCA data for generation and storage technologies, we calculate which storage and generation technologies result in a net energy gain over curtailment. We present our data and results in terms of EROI: the amount of electrical energy returned per *unit* of electrical energy invested.

Fig. 27.6 shows calculated grid EROI values, $EROI_{grid}$ for PV (*top*), and wind resources (*bottom*) used with storage technologies (*colored lines*) as a function of φ. The solid black line bisecting the plots indicates the EROI value due to curtailment, spanning a range from original resource EROI to zero. The green region to the right of this line indicates

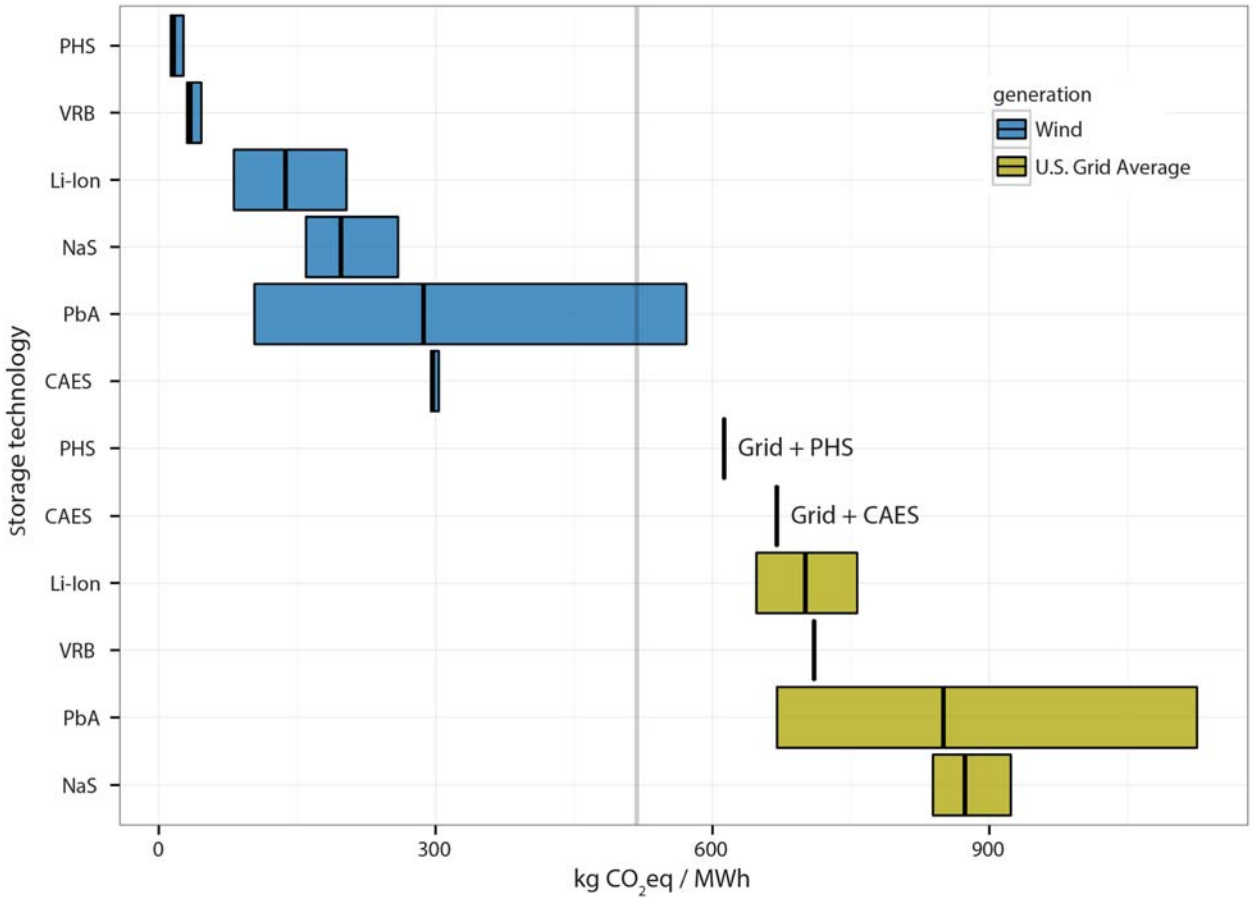

FIGURE 27.5 The carbon intensity of electricity provided by wind turbine-charged storage technologies. For comparison, the carbon intensity of electricity provided from storage technologies charged by a hypothetical U.S. average power grid is displayed on the right half of the bar chart. Vertical lines represent the average U.S. power grid carbon intensity and the intensity of a particularly low-carbon regional grid, the Northwest Western Electricity Coordinating Council (NW WECC).

combinations of EROI, $ESOI_e$, and φ, in which storage yields better energy returns than curtailment, $EROI_{grid} > EROI_{curt}$. To the left, in blue, $EROI_{grid} < EROI_{curt}$, storage implementation is more energetically costly than simply curtailing the resource.

Several interesting results emerge from Fig. 27.6. First, storage technologies with low $ESOI_e$ values, like Pb-Acid and ZnBr, reduce the grid EROI down much more severely than technologies with high $ESOI_e$ values, like PSH, CAES, and Li-Ion. Second, battery technologies paired with wind yield grid EROI values far below EROI values from curtailment alone for reasonable values of φ. However, these grid EROI values are greater than the average U.S. power grid values of ~ 20.

Ideally, storage technologies that support generation resources should not diminish energy−return ratios below curtailment energy-return ratios for reasonable values of ϕ. This means that geologic storage technologies, not contemporary battery technologies, are much more favorable for storing electricity generated from wind power.

Curtailment of wind resources during times of excess generation is a viable form of grid flexibility. Curtailment rates of up to 30% yield carbon and energy intensities that are lower than respective pairings with electrochemical storage technologies. While curtailment appears to be an immediate waste of a resource, the life-cycle energy costs of storage are greater than curtailment at reasonable rates below about 30%. Avoiding curtailment may not lead to the most environmentally sound decisions. Curtailment is not the only option, nor is it ideal. Useful applications for excess electricity occur beyond the power grid. Excess electricity could be used for thermal storage, producing heat or ice for later use. Additionally, electricity could be used to pump or desalinate water, smelt metal ores, or manufacture goods. The energy is 'stored', that is, embodied elsewhere in the economy.

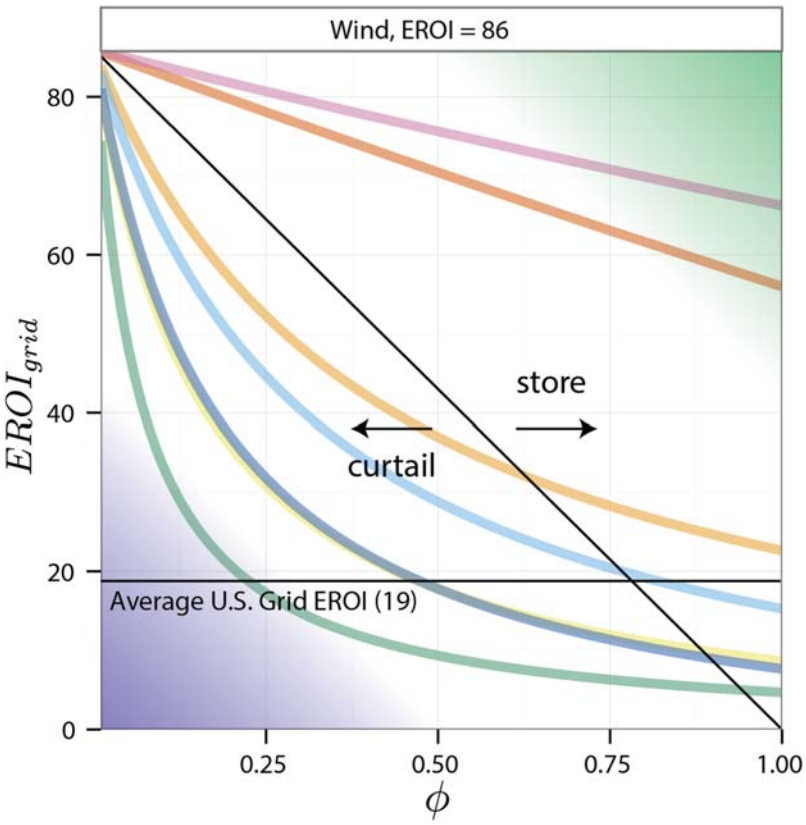

FIGURE 27.6 Grid $EROI_{grid}$ values as a function of storage or curtailment fraction, φ, and EES technology paired with wind. All technologies, except for PSH and CAES, perform worse than curtailment on a societal energy cost basis. Trading energy losses for lower GHG emissions is recommended, however, and pairing wind with lithium-ion and vanadium flow batteries still provides high energy returns, higher than the average U.S. power grid, with much lower GHG emissions.

27.2 Conclusion

The use of EES in power grids increases system-level GHG emissions in two ways: (1) embodied GHG emissions due to the mining and production of the EES and (2) emissions stemming from increased electricity production due to operational losses from the efficiency of the EES. For power grids, the Li-NMC chemistry has grown to be the EES of choice. Li-NMC batteries have c2g embodied emissions of 89 kg CO_2e/kWh of capacity. Li-NMC cells reliably achieve 3000 charge-discharge cycles and, as such, per cycle embodied emissions add 0.03 kg/kWh to delivered electricity. Additional use phase emissions due to battery efficiency (90%−95% roundtrip) depend on source generation and will add 1−3 g/kWh for wind turbines. Life cycle emissions will likely continue to decrease through the recycling of battery components, GHG intensity reductions in the electricity supply, and optimizations in EES operations.

Energy storage promises many benefits for electrical power grids and societal energy use in general. Our analysis shows how to calculate and compare their energy and carbon footprints. In conclusion, the analyses presented in this chapter reveal the following insights.

- Flexible power generation and energy storage come with a cost. Energy delivered from storage has greater carbon and energetic intensities than energy delivered directly from power generation technologies, and depending on the technology, the energy and carbon penalties for storage can be large.
- The energy and carbon intensities of wind plus storage are far lower than for the U.S. grid.
- Not all storage technologies are created equal. PSH performs best and traditional lead acid batteries perform worst. CAES trades low energy intensity for high carbon emissions associated with the combustion of natural gas. Li-Ion and VRB perform best among electrochemical storage solutions with Li-Ion providing the lowest energy intensity and VRB the lowest carbon intensity. Traditional lead acid batteries perform poorly by these metrics. Although they have low energy requirements for manufacture, their low number of charge-discharge cycles leads to frequent replacement and a high energy intensity of 0.17.

- The curtailment of wind resources provides flexibility with lower carbon and energy costs in comparison to the implementation of energy storage technologies until curtailment rates exceed about 30%. Simply put, more wind might be the answer.

Energy storage and curtailment can provide the flexibility the power grid will require as the fraction of intermittent wind resource supply increases. This chapter discusses the benefits of using systems-level energy intensity and carbon intensity analysis to compare the performance of flexible options for wind [30]. Policymakers and consumers that consider the effects of deploying storage with wind can better identify environmentally sound solutions.

References

[1] Ambrose H, Kendall A. Effects of battery chemistry and performance on the life cycle greenhouse gas intensity of electric mobility. Transportation Res D Transp Environ 2016. Available from: https://doi.org/10.1016/j.trd.2016.05.009.

[2] Hiremath M, Derendorf K, Vogt T. Comparative life cycle assessment of battery storage systems for stationary applications. Env Sci Technol 2015;49:4825–33. Available from: https://doi.org/10.1021/es504572q.

[3] Barnes FS, Levine JG. Large energy storage systems handbook. 1st ed. Boca Raton, FL: CRC Press; 2011.

[4] Denholm P. Improving the technical, environmental and social performance of wind energy systems using biomass-based energy storage. Renew Energy 2006;31:1355–70. Available from: https://doi.org/10.1016/j.renene.2005.07.001.

[5] Augustine C, Bain R, Chapman J, Denholm P, Drury E, Hall DG, et al. Renewable electricity futures study: volume 2 renewable electricity generation and storage technologies. NREL/TP-6A20-52409-2 2; 2012.

[6] Lew D, Piwko D, Miller N, Jordan G, Clark K, Freeman L. How do high levels of wind and solar impact the grid? The western wind and solar integration study (No. December), energy. National Renewable Energy Laboratory; 2010.

[7] Denholm P, Margolis RM. Evaluating the limits of solar photovoltaics (PV) in traditional electric power systems. Energy Policy 2007;35:2852–61. Available from: https://doi.org/10.1016/j.enpol.2006.10.014.

[8] Nguyen T. DOE Global Energy Storage database; 2022. https://sandia.gov/ess-ssl/gesdb/public/index.html.

[9] Denholm P, Kulcinski. Life cycle energy requirements and greenhouse gas emissions from large scale energy storage systems. Energy Convers Manag 2004;45:2153–72. Available from: https://doi.org/10.1016/j.enconman.2003.10.014.

[10] Rydh C, Sandén B. Energy analysis of batteries in photovoltaic systems. Part I: performance and energy requirements. Energy Convers Manag 2005;46:1957–79. Available from: https://doi.org/10.1016/j.enconman.2004.10.003.

[11] Sullivan JL, Gaines L. A review of battery life-cycle analysis: state of knowledge and critical needs ANL/ESD/10-7, transportation research. Oak Ridge, TN: Argonne National Laboratory; 2010.

[12] Barnhart CJ, Benson SM. On the importance of reducing the energetic and material demands of electrical energy storage. Energy Env Sci 2013;6:1083–92. Available from: https://doi.org/10.1039/C3EE24040A.

[13] Semadeni M. Storage of energy, overview. Encycl Energy 2004;5:719–38.

[14] Beard KW. Linden's handbook of batteries. 5th ed. New York, Chicago, San Francisco, Athens, London, Madrid, Mexico City, Milan, New Delhi, Singapore, Sydney, Toronto: McGraw-Hill Education; 2019.

[15] Hittman Associates. Life cycle analysis of electric vehicle storage batteries. U.S. Dept. of Energy H-1008/001-80-96; 1980.

[16] Rydh CJ. 99/03718 Environmental assessment of vanadium redox and lead-acid batteries for stationary energy storage Rydh, C. J. J. Power Sources, 1999;80:(1/2):21–29. Fuel Energy Abstr 1999;40:392. Available from: https://doi.org/10.1016/S0140-6701(99)98924-5.

[17] Chen H, Cong TN, Yang W, Tan C, Li Y, Ding Y. Progress in electrical energy storage system: a critical review. Prog Nat Sci 2009;19:291–312. Available from: https://doi.org/10.1016/j.pnsc.2008.07.014.

[18] Majeau-Bettez G, Hawkins TR, Strømman AH. Life cycle environmental assessment of lithium-ion and nickel metal hydride batteries for plug-in hybrid and battery electric vehicles. Env Sci Technol 2011;45:4548–54. Available from: https://doi.org/10.1021/es103607c.

[19] Dunn JB, Gaines L, Kelly JC, James C, Gallagher KG. The significance of Li-ion batteries in electric vehicle life-cycle energy and emissions and recycling's role in its reduction. Energy Environ Sci 2015;8:158–68. Available from: https://doi.org/10.1039/C4EE03029J.

[20] Dai Q, Kelly JC, Gaines L, Wang M. Life cycle analysis of lithium-ion batteries for automotive applications. Batteries 2019;5:48. Available from: https://doi.org/10.3390/batteries5020048.

[21] Emilsson E, Dahllöf L. Lithium-ion vehicle battery production 2019;47.

[22] Romare M, Dahllöf L. The life cycle energy consumption and greenhouse gas emissions from lithium-ion batteries 2017;58.

[23] Pellow MA, Ambrose H, Mulvaney D, Betita R, Shaw S. Research gaps in environmental life cycle assessments of lithium ion batteries for grid-scale stationary energy storage systems: end-of-life options and other issues. Sustain Mater Technol 2020;23:e00120. Available from: https://doi.org/10.1016/j.susmat.2019.e00120.

[24] Dolan SL, Heath GA. Life cycle greenhouse gas emissions of utility-scale wind power systematic review and harmonization. J Ind Ecol 2012;16:S136–54. Available from: https://doi.org/10.1111/j.1530-9290.2012.00464.x.

[25] Hsu DD, Donoughue PO, Fthenakis V, Heath GA, Kim HC, Sawyer P, et al. Of crystalline silicon photovoltaic systematic review and harmonization 2012;16. https://doi.org/10.1111/j.1530-9290.2011.00439.x.

[26] Donoughue PRO, Heath GA, Dolan SL, Vorum M. Life cycle greenhouse gas emissions of electricity generated from conventionally systematic review and harmonization. J Ind Ecol 2014;00. Available from: https://doi.org/10.1111/jiec.12084.
[27] Lannoye E, Flynn, DamianMalley MO. Evaluation of power system flexibility. IEEE Trans Power Syst 2012;27:922–31.
[28] Wiser R. Bolinger M. 2012 Wind Technologies Market Report—DOE/GO-102013-3948 (No. August). LBNL; 2013.
[29] Budischak C, Sewell D, Thomson H, Mach L, Veron DE, Kempton W. Cost-minimized combinations of wind power, solar power and electrochemical storage, powering the grid up to 99.9% of the time. J Power Sour 2013;225:60–74. Available from: https://doi.org/10.1016/j.jpowsour.2012.09.054.
[30] Carbajales-Dale M, Barnhart CJ, Brandt AR, Benson SM. A better currency for investing in a suitable future. Nature Climate Change 2014;4:524–7.

This page intentionally left blank

Section E

Environmental impacts of wind energy

This page intentionally left blank

Chapter 28

Climate change effects on offshore wind turbines

Maria James[1], Sumanta Haldar[1], Ramon Varghese[2], Subhamoy Bhattacharya[3] and Vikram Pakrashi[2]
[1]School of Infrastructure, Indian Institute of Technology Bhubaneswar, Odisha, India, [2]School of Mechanical and Materials Engineering, University College Dublin, Dublin, Ireland, [3]Department of Civil and Environmental Engineering, University of Surrey, Guildford, London, United Kingdom

28.1 Introduction and background

Climate change is the long-term shift in the climate that may occur over decades, centuries, or more. It is caused due to the increased emission of greenhouse gases into the atmosphere. Greenhouse gases absorb the outgoing longwave radiation and trap the heat, resulting in temperature rise, leading to changes in the ocean currents, sea-level rise, increase in extreme events, drought, heavy rainfall, etc. The offshore wind energy sector plays a prominent role in reducing these effects by shifting to a renewable energy source. According to the International Energy Association, offshore wind energy production is slated to represent 16% of the total energy generation in the European Union by 2040 [1]. But does climate change impact the design of offshore wind turbines (OWT)? Or will it affect the wind potential?

The Intergovernmental Panel on Climate Change (IPCC) issues a stark warning to policymakers on limiting global warming to 1.5 degrees in its largest ever assessment report produced on climate change [2]. The immediate, rapid, and large-scale reduction in greenhouse gas emissions would require a dramatic change in the wind and solar capacities [3]. Ironically, an increase in global temperature could lead to rising sea levels, more extreme weather, melting permafrost, and marine heat waves, all of which can affect the planning and maintenance of offshore wind power farms. Recent studies have also revealed a strong interhemispheric asymmetry in the future wind power potentials with decreases across the Northern mid-latitudes and increases across the Southern tropics and subtropics [4].

Climate change can affect the offshore wind power sector in two major ways. The primary and direct influence would be an alteration in the very resource that we try to tap into 3 wind. The offshore wind energy sector is heavily dependent on our ability to predict and foresee wind patterns, geographical distribution, and annual variability. Changing the interannual variability of the wind resource due to climate change poses a tough challenge to designers. Characterizing wind speeds is crucial in determining the mean power delivered by the wind turbine. The second major interference caused by climate change is the structural performance and maintenance of offshore wind farms. The change in environmental loads on an OWT caused by wind gusts, storms, icing, and sea ice poses an additional challenge to the structural designer, already dealing with a dynamically sensitive foundation-tower-turbine-rotor system. Wilkie and Galasso [5] investigated the sensitivity of various parameters such as fatigue life, structural loading, and financial loss (due to direct equipment damage) towards climate change. Fatigue life and structural loading are sensitive to climate change, while financial loss depends on nonstructural components that are independent of climate change. This chapter presents an overview of these effects and concludes with a few engaging case studies from around the world.

28.1.1 Rising temperatures, changing times

Reports show that a two to four degrees rise in temperature will result in a meter rise in sea-level, and intensification of extreme events such as cyclones and tsunamis. But this effect will vary from place to place. Hence, several researchers analyzed site-specific trends in the projected wind and wave patterns. An average 1 to 2 cm/s per year increase in wind intensity has been observed over the Southern Ocean surrounding Antarctica in the last three decades, and as a consequence, the average wave height has also risen. A 15% increase in the extreme wave is predicted over the southern

Wind Energy Engineering. DOI: https://doi.org/10.1016/B978-0-323-99353-1.00030-X

hemisphere and Northern Pacific due to 3-degree warming [6]. By 2100, a doubling of extreme events is projected over South Australia, the Arabian Sea, and the Gulf of Guinea by Grady et al. [7]. An increase in extreme events is also expected over the eastern tropical pacific and high latitudes of the southern hemisphere. A 10% rise in projected significant wave heights and a 5%−15% rise in 1 in 100-year significant wave height in the North Atlantic and North Pacific is predicted by Meucci et al. [8]. Hemer et al. [9] forecasted that 7.1% of the global ocean would experience a significant increase in the annual mean significant wave. Under the RCP8.5 scenario [representative concentration pathways (RCP); high emission scenario], an average 3 cm/year increase in significant wave height is predicted over many areas of the Arctic Ocean [10]. Under RCP8.5, doubling or tripping in the occurrence frequency of extreme events is forecasted by Lobeto et al. [11].

Meanwhile, Hemer et al. [9] projected that 25.8% of the global ocean would experience a reduction in significant wave height (e.g., the North Sea and the Mediterranean). The average significant wave height is expected to fall by 0.2 m in Europe near the coast [12]. A decreasing trend in the significant wave height is observed over the Mediterranean basin under the RCP8.5 scenario [13]. The studies by Casa-Prat et al. [14] projected a considerable decrease in wave height in North Atlantic Ocean due to the warmer climate and low surface wind speed. A 1.5 m extreme wave height decline is projected over the tropical North Pacific. Overall reduction in significant wave height is expected over Ireland also [15]. Similarly, on most North American Coastlines, the mean and extreme wave heights are projected to decrease [16].

Sea-level rise over time is another consequence of climate change. Higher sea levels will invite more destructive storm surges and frequent high tide flooding. The reports show that the 20 to 23 cm rise in sea level from 1880 and two-thirds of it happened in the last 25 years. And from 2006 to 2015, a 0.35- cm rise per year was observed, and if it continues, the model projects that the US sea level could rise to 2.2 m by 2100 and 3.9 m by 2150 (https://www.climate.gov/maps-data/dataset/sea-level-rise-map-viewer). These studies reveal that wind-wave patterns vary from place to place and time to time, depending on the prevailing climatic conditions. As wind turbines are susceptible to wind and wave climate, their effect on the design must be carefully examined.

28.2 Climate models

Energy balance, intermediate complexity, and general circulation models (GCM) are the three types of models commonly used for climate projections. The energy balance considers surface temperature from solar energy, reflectivity, and natural cooling from the earth emitting heat back into space. Intermediate complexity models are similar to energy balance models but combine many earth features such as land, oceans, and ice. Global climate models or GCMs are complex and precise models that consider information about the atmospheric chemistry and the land type, carbon cycle, ocean circulation, and glacial makeup of an isolated area. Projections of the effect of climate change on offshore wind power often utilize wind speeds simulated by GCMs and downscaled using regional climate models (RCM).

Global climate models are generally used worldwide for climate projections. Under GCM, there are 21 major climate models. Each model has its advantages and limitations. Studies by Pierce et al. [17] observed that none of the climate models shows a strong relationship between the score of the models of the matrices and the detection and attribution analysis results. Another advanced approach to improve accuracy is using a multimodel ensemble (MM) instead of individual models. MM models are superior to other individual models [18−22] because of the cancellation of offsetting errors in the individual climate models. A detailed description of different climate models can be obtained from Randall et al. [23] and Flato et al. [24].

The selection of particular GCMs varies from project to project and requires a significant understanding of climatology. Researchers have conducted sensitivity analyses to find out a suitable model for different study regions [25−32]. Chowdhury et al. [33] observed that GFDL, IPSL, CSIRO, and CNRM for obtaining ensemble CMIP5 GCM wind output had excellent accuracy for projecting the wave climate across the Indian Ocean (IO). Choudhary and Behera [34] suggested that RCMs could not provide reasonable wind inputs to predict the wave conditions over the IO. This is due to seasonal monsoons and swells from the southern IO on the wave climate. Another reason would be the arrival of the tropical storm from the southwest IO on the Indian coast [35].

Global climate models are constantly updated by incorporating higher resolution, additional Earth System processes and new components, and biochemical cycles. These updates are reflected in Coupled Model Intercomparison Projects (CMIP). CMIP aims to make a set of common input data in the form of future concentration of greenhouse gas emissions, aerosols, and other forcings so that comparison among models is possible. The fifth IPCC assessment report was based on CMIP5 models, while the latest sixth assessment report is based on CMIP6 models.

28.2.1 Comparison of CMIP5 and CMIP6 models

CMIP6 shows improvement over CMIP5 in terms of resolution, future scenarios considered, the number of groups that participated in modeling, and the number of conducted experiments. CMIP5 uses four RCPs, including RCP2.6, RCP4.5, RCP6.0, and RCP8.5. CMIP6 considers a set of updated pathways called shared socioeconomic pathways (SSP), including SSP1-1.9, SSP1-2.6, SSP4-3.4, SSP5-3.4OS, SSP2-4.5, SSP4-6.0, SSP5-3.4, SSP3-7.0 and SSP5-8.5 in terms of radioactive forcing levels by 2100. At the end of the century, the final forcing is the same for both, but the difference lies in the emission pathways.

CMIP6 shows higher equilibrium climate sensitivity than CMIP5 models. This could be due to the better representation of clouds and aerosols. However, studies by Nijsse et al. [36] and Tokarska et al. [37] pointed out that high-sensitivity climate models cannot replicate historical temperature. Compared to CMIP5, some models in CMIP6 show more mid and late-century warming. Many studies are being conducted to assess the performance of CMIP6 models in different regions. An analysis by Zhao et al. [38] over some areas of China observes that CMIP6 models have certain limitations in projecting wind speed in certain areas while showing realistic representation in some other regions. From the historical comparison of wind speed over the Bay of Bengal, Krishnan and Bhaskaran [39] observed that GISS-E2RCC, GISS-E2R, ACCESS 1.0, HadGEM2-AO CNRM-CM5, HadGEM2-ESCMIP 5 and CanESM2 from CMIP5 and GISS-E21G, MRI-ESM2, CaNESM5, and CC-ESM2-M from CMIP6 are the best performing models. Also, from the validation study, CMIP6 models perform better than CMIP5 models over the Bay of Bengal.

The above studies show that a detailed evaluation of CMIP6 models is required to assess the suitability to a particular region of interest. The selection of a specific GCM model for use in regional studies of climate change is based on the quality of the climate simulation in the area of interest [[26,40]]. Therefore, a proper selection of GCM models for climate projection is necessary. Some commonly used RCMs for wave projection are WAVEWATCH III, MIKE 21 SW, and the Multi-Grid WAVEWATCH III model. For a detailed description of different climate models, it is advised to refer to Randall et al. [23] and Flato et al. [24].

28.3 Impact of climate change on offshore wind turbines

28.3.1 Wind speed

From the 1970s onwards, the wind speed was lower than they are today. However, after 2010, the global average wind speed rose from 7 to 7.4 mph [41] which is attributed to climate change. Even though this surge in wind speed has a positive impact on wind energy production, this effect on the design of OWTs has to be analyzed in detail. Many studies are being conducted on the effects of climate change on OWTs. However, it is important to underline the uncertainty associated with the climate models.

There have been predictions of decreasing wind resources over much of the European domain. A decrease in wind power potential has been predicted over the Mediterranean region [42,43]. Tobin et al. [44] projected that climate change may affect current and near-term planned wind power production in Europe by under 10%−15% in magnitude at a country scale. Simulations reported by Davy et al. [42] show a general decrease in the wind power density across Europe with the exception of the region such as the Baltic Sea, and the Barents Sea. The potential loss of production could, however, be large enough to disturb the equilibrium of energy mix at the national scale. A study on the Irish region concluded that there is a seasonality associated with the effects of climate change on wind energy, with a more pronounced decrease predicted (<6%) for summer. The higher intra-annual variability in wind speeds could result in a higher variability in wind energy production. Hubler and Rolfes [45] studied the impact of increasing wind speed and air temperature on the fatigue life of OWTs in the Northern Sea. The study suggested that the inclusion of climate change has a marginal increase (< 5%) on the estimated fatigue load. This increase is mainly attributed to the rise in wind speed and not the rising air temperature.

Bisoi and Haldar [46−49], studied the effect of climate change on the dynamic behavior of monopile-supported OWT on the west coast of India. The study observed that the fatigue life of the OWTs is reduced substantially. At the same time, the serviceability responses are increased (20%−30%) after incorporating the future wind and wave inputs on the west coast of India. While the responses got reversed over the east coast of India. The typical graph delineating the impact of climate change is shown in Figs. 28.1 and 28.2. Zhang et al. [50] suggested that the load factor must increase from 1.35 to 1.7 if a 20% increase in 50 years of extreme wind speed occurs [50]. The initial capital cost is estimated to rise by 12% by the end of the twenty-first century on account of stronger wind in the future [50].

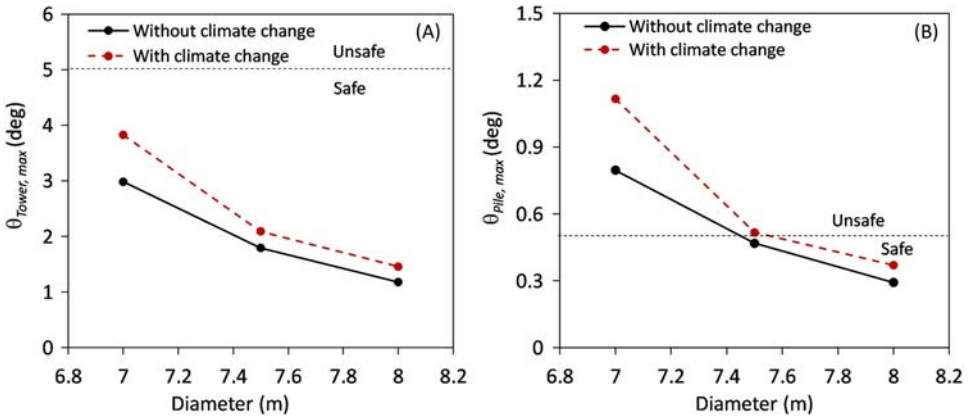

FIGURE 28.1 Rotational responses at the tower top and pile head with and without considering the climate change for soft clay [46].

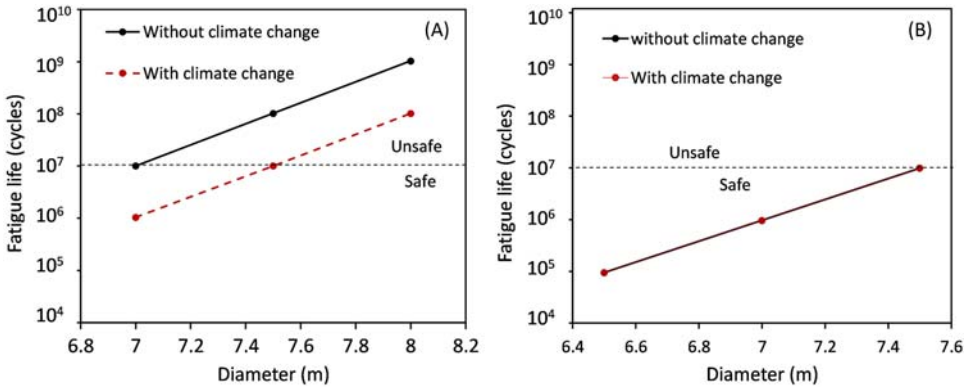

FIGURE 28.2 The fatigue life of OWT for (A) soft clay and (B) stiff clay [46].

Pinto et al. [51] predicted that the 98th percentile of wind gusts would rise by 5% by 2060 across western Germany. Even though the wind speed in that location (24 m/s at 10 m) coupled with the expected increase in gusts, it is still within the design criteria of wind turbines.

Another issue of climate change is storm surges. Storm surges are rising water levels caused due to the low pressure associated with cyclones. It produces additional vibration in foundations and towers due to collision. Moreover, frequent occurrences of these events would cause scour and sand wave migration, which affects the foundation and the exposure of embedded cable [52].

28.3.2 Sea ice

Apart from wind and wave loading, ice loading due to sea ice is another load case to be investigated, especially in high-altitude areas due to extreme minimum temperature. Piling up brash ice over the tower and foundation of a wind turbine in the northern part of the Baltic Sea is projected by Pryor and Barthelmie [52]. This can reach up to a height of 10 m with drift speeds of up to 1 m/sec [53] This generates additional static (ice load) and dynamic load (drifting ice) [54]. However, a significant reduction in mean total ice thickness, ice days, and sea ice extend is projected over the Baltic Sea [53,55–57]which leads to the reduction in ice loads in the near future. Therefore, reliable predictions on icing during the design life are required to assess the necessity and advantages of ice mitigation.

Drifting ice can collide with an OWT tower or foundation and is often considered in the design stage as additional ice loads. Dynamical ice loads can destabilize foundations or cause fatigue of the support structures. Measures such as ice-breaking cones can be attached to the tower structure at the water level as a mitigation measure for floating ice. In this context, the evaluation of region-specific sea ice parameters is important. Wang et al. [58] utilized satellite imagery to study sea ice parameters for the Bohai sea near China and concluded that the influence of sea ice on OWTs is diminishing due to climate change. The study categorized sea ice periods into three stages, namely freezing stage, heavy ice stage, and melting ice stage [58]. The periods of the three ice stages for the past 21 years are presented in Fig. 28.3. One could note

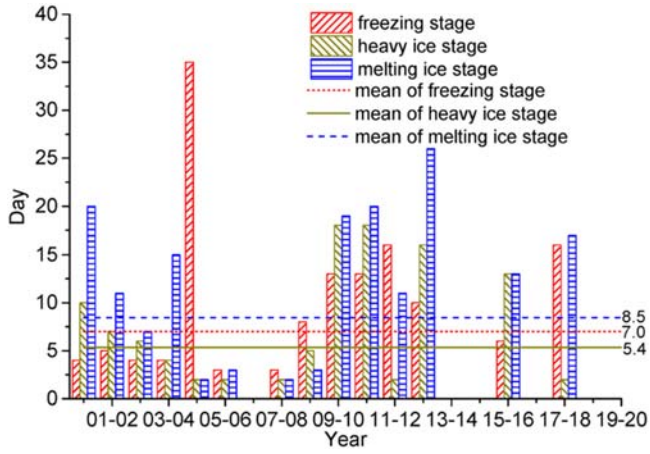

FIGURE 28.3 The number of days of the three ice stages and their averages in the Bohai sea over the past 21 years. *Reprinted with permission from Wang A, Tang M, Zhao Q, Liu Y, Li B, Shi Y, et al. Analysis of sea ice parameters for the design of an offshore wind farm in the Bohai Sea. Ocean Eng 2021;239:109902.*

the large interannual variability and six years without any sea ice. Climate change adds to the uncertainties in evaluating sea ice parameters [59].

Wind turbines are intended to withstand different loading conditions, including 10 min of turbulence intensity with a 50-year return period, wind gusts, and 10-min sustained wind speed, generating ultimate and fatigue loads. Based on the prevailing environmental conditions, in some places, OWT design experience a positive impact while there is a negative impact in other locations. Therefore, future wind and wave projections are extremely important for designing foundations for offshore structures.

28.3.3 Ice accretion

Ice accretion on wind turbine blades presents a challenge to the installation and operation of OWTs in arctic latitudes. Large ice accretion can degrade turbine durability and cause wind turbine vibrations [60,61]. The change in blade aerodynamics can lead to a decrease in electrical power production even for light ice accretion. The mechanism of ice accretion and the causative atmospheric processes are far too complex to predict with reasonable accuracy [62,63]. With a high have interannual variability, estimating the effects of climate change on icing would be a complex task. Studies on the effect of climate change on icing have been reported for OWTs. A study on Northern China region suggests that the effects of icing reduced over the period 1961−2015 owing to the increasing near-surface night-time temperatures [64]. A declining probability of icing by the end of the century has also been reported for Scandinavia and Continental Unites States [55,65]. Very less actionable information is available for the offshore wind power industry because meteorological-oceanographic factors that influence icing are hard to simulate. A study on icing conditions in the Baltic region suggests that the average number of icing events could decrease in the future owing to climate change warming [66].

28.4 Case studies

28.4.1 European region

The European Union's green deal plan for 2050 sets a carbon neutrality target that has emphasized the importance of offshore wind. Wind power is experiencing a considerable growth in Europe where 15.4 GW of capacity was installed in 2019 of which 3.3 GW was offshore-based [67]. A key factor in developing offshore wind power projects is selecting the best locations for installation. The locations are determined after careful consideration of wind energy estimates, European and national regulations, licensing process, and marine environmental protection. Estimating the regional change in wind power due to factors such as climate change plays an important role in offshore wind power projects of the future. Various ensembles of GCMs and RCMs, such as PRUDENCE, ENSEMBLES, and EURO-CORDEX have been utilized in projections for European offshore wind power for the 21st century [59,68,69].

Many climate projections have reported a general decrease in wind speed throughout Europe [[4,70,71]]. Davy et al. [42] assessed the impact of European wind resources using five GCMs from CMIP5 and a RCM developed at the Rossby centre, namely RCA4 [72]. Fig. 28.4 shows the projected changes in Wind Power Density between the historical and two future period representing the years 2021−50 and 2061−90. The two RCP scenarios represent weak (RCP 4.5) and strong global warming (RCP 8.5). The study found a strong similarity between the change from the historical period to Future 1

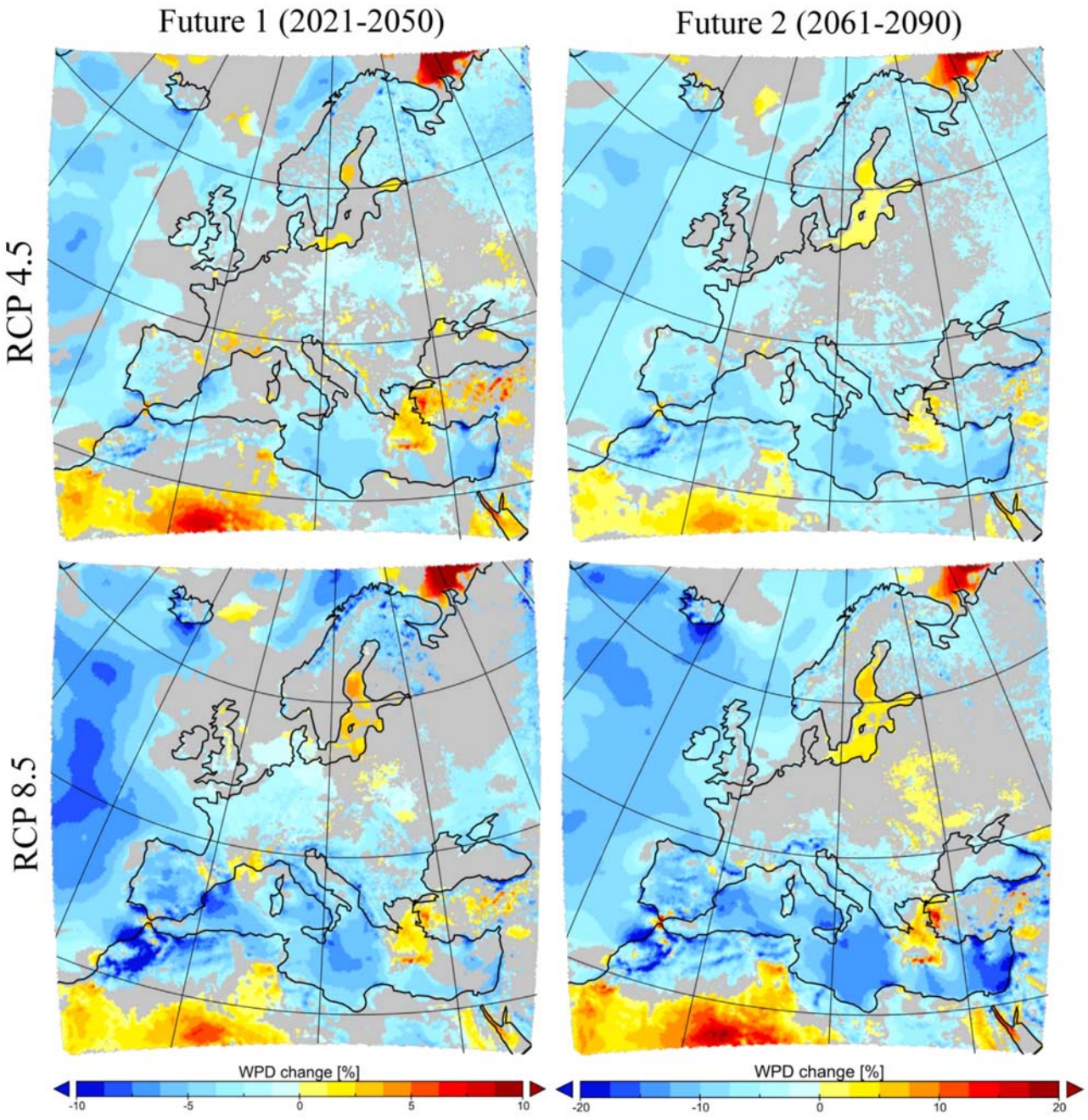

FIGURE 28.4 The ensemble-mean change (%) in wind power density from the historical period to the Future 1 period (left column) and to the Future 2 period (right column), under two different RCP scenarios. *With permission from Davy R, Gnatiuk N, Pettersson L, Bobylev L. Climate change impacts on wind energy potential in the European domain with a focus on the Black Sea. Renew Sustain Energy Rev 2018;81:1652–1659.*

period, and Future 1 to Future 2 periods. Only few locations such as the Baltic Sea, Barents Sea, and North Africa show signs of an increase in wind power density. It was found that the Black Sea region did not show any significant negative influence of climate change under either of the RCPs. The seasonality of wind resources in the region also matched the seasonality of power demand, making it a viable location for surrounding countries like Ukraine and Russia.

Around the countries of Ireland and the United Kingdom, wind power potential is slated to decrease in the range 0%–10% by the end of the century. Doddy Clarke et al. [73] utilized two RCMs, namely COSMO-CLM and RCA4 to scale down five different GCM datasets for offshore wind around Ireland. Apart from an overall decrease in wind energy (in the order of 0.2%–2%), certain seasonal changes such as the reversal of wind energy generation pattern during summer and winter were also observed. An interesting observation is the change in the duration of low power

events (less than 10% capacity factor for a minimum of 24 consecutive hours). Wind energy on the West-coast offshore was projected to have shorter low-power events than on the East-coast, suggesting the need to disperse wind farms geographically to ease the pressure on national power supply during low wind scenarios.

28.4.2 Indian Ocean region

India is the third-largest producer of greenhouse gas after US and China and is planning to invest in wind energy to tackle climate change. Studies [74] forecasted that the IO is significantly affected by the global wind-wave climate. Strengthening of extreme wind speed by 3 m/sec is projected by Krishnan et al. [75] in the Eastern south IO. Deepthi and Deo [76](predicted an increase in the wind speed of up to 74% for a 100-year period from 2030 to 2099 along the offshore basin of India. DHI [77] report predicts that the wave height can increase up to 26% for a 10% increase in wind speed. Moreover, recent studies indicate that climate change would increase the sea surface temperature and the tropical cyclone heat potential, leading to an increase in cyclone activity along the west coast of India [78,79], which is one of the strategic locations where OWTs are proposed. Pardikar [80] reported a significant increase of 82%, 52%, and 20% in the cyclone's duration, frequency, and intensity respectively, between 1982 and 2019.

Studies by Casas-Prat et al. [14] projected that the IO would experience an increased wave height and a higher peak wave period. The expected rise in maximum and significant wave height over the west coast (particularly Gujarat) is 15%, and the Tamil Nadu coast is 16% and 8%, respectively. Ten percent increase in the mean wave period is projected along the west coast of India by 2100 [33]. The West coast of India and Maldives have identified locations under the north IO region, which will undergo highly fluctuating wave scenarios over the next decades [81]. The El-Nino Southern Oscillation exacerbates intense significant wave height in the Bay of Bengal, Southwestern tropical IO, and Southern IO [82]. Another reason for the increase in wave height along the Indian coast is swell from the Southern Ocean [83] and wind speed [84].

The above studies stress that India will experience a noticeable climate change. However, only a few researchers have conducted studies to investigate the effect of climate change on the design life of OWTs in Indian offshores. Studies by Bisoi and Haldar [49] delineate that future climate projections are crucial for designing OWTs along the west coast of India. They examined the impact of climate change on design of a monopile-supported OWT for the two offshore locations in India. Fig. 28.5 shows an area corresponding to 5 × 5 NCEP grid lines of equal interval around

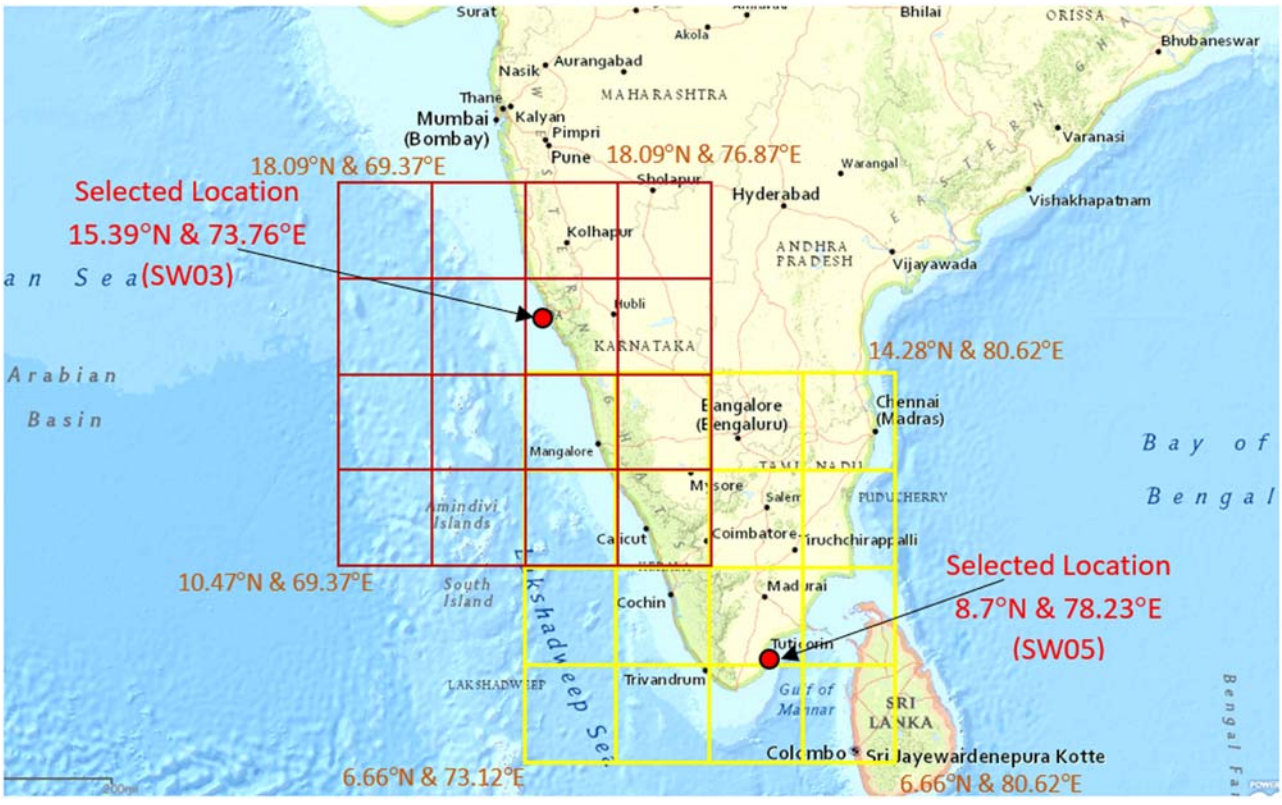

FIGURE 28.5 Offshore locations at the Indian coastline in which the NCEP grid is superimposed [49].

the selected locations in India. Maximum wind speed and corresponding wave height and wave period were forecasted using the statistical downscaling model for the GCM—A1B, A2, and B1 scenarios and CMIP5 output. Dynamic analysis was carried out in the time domain using nonlinear soil-structure interaction considering the forecasted met ocean data. It was observed that future wind and wave loads increase at the west coast of India, whereas environmental loads are found to be decreased at the east coast location of India due to the impact of climate change. The A2 scenario was found to be most aggressive and anticipates higher wind and wave load for the west and east coast locations of India.

References

[1] Birol F. Offshore wind outlook. *International Energy Agency*; 2019.

[2] IPCC. Climate change 2022: impacts, adaptation, and vulnerability. In: Pörtner H-O, Roberts DC, Tignor M, Poloczanska ES, Mintenbeck K, Alegría A, et al., editors. Contribution of working group ii to the sixth assessment report of the intergovernmental panel on climate change. Cambridge University Press; 2022.

[3] Victoria M, Zeyen E, Brown T. Speed of technological transformations required in Europe to achieve different climate goals. Joule 2022;6 (5):1066−86.

[4] Karnauskas KB, Lundquist JK, Zhang L. Southward shift of the global wind energy resource under high carbon dioxide emissions. Nat Geosci 2018;11(1):38−43.

[5] Wilkie D, Galasso C. Impact of climate-change scenarios on offshore wind turbine structural performance. Renew Sustain Energy Rev 2020;134:110323.

[6] Patra A, Min SK, Kumar P, Wang XL. Changes in extreme ocean wave heights under 1.5°C, 2°C, and 3°C global warming. Weather Clim Extremes 2021;33:100358.

[7] O'Grady JG, Hemer MA, McInnes KL, Trenham CE, Stephenson AG. Projected incremental changes to extreme wind-driven wave heights for the twenty-first century. Sci Rep 2021;11(1):1−8.

[8] Meucci A, Young IR, Hemer M, Kirezci E, Ranasinghe R. Projected 21st century changes in extreme wind-wave events. Sci Adv 2020;6(24): eaaz7295.

[9] Hemer MA, Fan Y, Mori N, Semedo A, Wang XL. Projected changes in wave climate from a multi-model ensemble. Nat Clim Chang 2013;3 (5):471−6.

[10] Casas-Prat M, Wang XL. Sea ice retreat contributes to projected increases in extreme Arctic ocean surface waves. Geophys Res Lett 2020;47 (15)e2020GL088100.

[11] Lobeto H, Menendez M, Losada IJ. Future behavior of wind wave extremes due to climate change. Sci Rep 2021;11(1):1−12.

[12] Bricheno LM, Wolf J. Future wave conditions of Europe, inresponse to high-end climate change scenarios. J Geophys Res Oceans 2018;123 (12):8762−91.

[13] De Leo F, Besio G, Mentaschi L. Trends and variability of ocean waves under RCP8. 5 emission scenario in the Mediterranean Sea. Ocean Dyn 2021;71(1):97−117.

[14] Casas-Prat M, Wang XL, Swart N. CMIP5-based global waveclimate projections, including the entire Arctic Ocean. Ocean Model 2018;123:66−85.

[15] Gallagher S, Gleeson E, Tiron R, McGrath R, Dias F. Twenty-first century wave climate projections for Ireland and surface winds in the North Atlantic Ocean. Adv Sci Res 2016;13:75−80.

[16] Erikson LH, Hegermiller CA, Barnard PL, Ruggiero P, van Ormondt M. Projected wave conditions in the Eastern North Pacific under the influence of two CMIP5 climate scenarios. Ocean Model 2015;96:171−85.

[17] Pierce DW, Barnett TP, Santer BD, Gleckler PJ. Selecting global climate models for regional climate change studies. Proc Nal Acad Sci U S A 2009;106(21):8441−6.

[18] Gleckler PJ, Taylor KE, Doutriaux C. Performance metrics for climate models. J Geophys Res 2008;. Available from: https://doi.org/10.1029/2007JD008972.

[19] Lambert SJ, Boer GJ. CMIP1 evaluation and intercomparison of coupled climate models. Clim Dyn 2001;17:83−106.

[20] Pincus R, Batstone CP, Hofmann RJP, Taylor KE, Gleckler PJ. Evaluating the present-day simulation of clouds, precipitation, and radiation in climate models. J Geophys Res 2008; Available from: https://doi.org/10.1029/2007JD009334.

[21] Reichler T, Kim J. How well do coupled models simulate today's climate? Bull Amer Meteor Soc 2008;89:303−11.

[22] Ziehmann C. Comparison of a single-model EPS with a multi-model ensemble consisting of a few operational models. Tellus A−Dyn Meteor Oceanog 2000;52:280−99.

[23] Randall DA, Wood RA, Bony S, et al. Cilmate models and their evaluation. In: Solomon S, Qin D, Manning M, Chen Z, Marquis M, Averyt KB, Tignor M, Miller HL, editors. Climate change 2007: the physical science basis. contribution of working group i to the fourth assessment report of the intergovernmental panel on climate change. Cambridge and New York: Cambridge University Press; 2007.

[24] Flato G, Marotzke J, Abiodun B, Braconnot P, Chou SC, Collins W, et al. Evaluation of climate models. In Climate change 2013: the physical science basis. In: Contribution of working group I to the fifth assessment report of the intergovernmental panel on climate change. Cambridge University Press; 2014. p. 741−866.

[25] Aflatooni M, Aghajanzadeh J. Comparison of different global climate models and statistical downscaling methods to forecast temperature changes in fars province of Iran. Environ Pollut 2013;2(4):135.

[26] Pierce DW, Barnett TP, Santer BD, Gleckler PJ. Selecting global climate models for regional climate change studies. Proc Natl Acad Sci 2009;106(21):8441–6.
[27] Leung LR, Mearns LO, Giorgi F, Wilby RL. Regional climate research: needs and opportunities. Bull Am Meteorol. Soc 2003;84(1):89–95.
[28] Feser F, Rockel B, von Storch H, Winterfeldt J, Zahn M. Regional climate models add value to global model data: a review and selected examples. Bull Am Meteorol. Soc 2011;92(9):1181–92.
[29] Luo M, Liu T, Meng F, Duan Y, Frankl A, Bao A, et al. Comparing bias correction methods used in downscaling precipitation and temperature from regional climate models: a case study from the Kaidu River Basin in Western China. Water 2018;10(8):1046.
[30] Giorgi F. Thirty years of regional climate modeling: where are we and where are we going next? J Geophys Res Atmos 2019;124 (11):5696–723.
[31] Prein AF, Bukovsky MS, Mearns LO, Bruyère CL, Done JM. Simulating North American weather types with regional climate models. Front Environ Sci 2019;7:36.
[32] Tapiador FJ, Navarro A, Moreno R, Sánchez JL, Garcia-Ortega E. Regional climate models: 30 years of dynamical downscaling. Atmos Res 2020;235:104785.
[33] Chowdhury P, Behera MR, Reeve DE. Wave climate projections along the Indian coast. Int J Climatol 2019;39(11):4531–42.
[34] Chowdhury P, Behera MR, Reeve DE. Wave climate projections along the Indian coast. Int J Climatol 2019;39(11):4531–42.
[35] Mawren D, Reason CJC. Variability of upper-ocean characteristics and tropical cyclones in the south west Indian Ocean. J Geophys Res Oceans 2017;122(3):2012–28.
[36] Nijsse FJMM, Cox PM, Williamson MS. Emergent constraints on transient climate response (TCR) and equilibrium climate sensitivity (ECS) from historical warming in CMIP5 and CMIP6 models. Earth Syst Dyn 2020;11.
[37] Tokarska K.B., Hegerl G.C., Schurer A.P., Forster P.M., Marvel K. Observational constraints on the effective climate sensit; 2022.
[38] Zhao L, Jin S, Liu X, Wang B, Song Z, Hu J, et al. Assessment of CMIP6 model performance for wind speed in China. Front Clim 2021;159.
[39] Krishnan A, Bhaskaran PK. Skill assessment of global climate model wind speed from CMIP5 and CMIP6 and evaluation of projections for the Bay of Bengal. Clim Dyn 2020;55(9):2667–87 ivity from the historical period. Environmental Research Letters, 15, 034043 (2020).
[40] McSweeney CF, Jones RG, Lee RW, Rowell DP. Selecting CMIP5 GCMs for downscaling over multiple regions. Clim Dyn 2015;44 (11):3237–60.
[41] Harvey C., Scientific American; November 19 2019.
[42] Davy R, Gnatiuk N, Pettersson L, Bobylev L. Climate change impacts on wind energy potential in the European domain with a focus on the Black Sea. Renew Sustain Energy Rev 2018;81:1652–9.
[43] Hueging H, Haas R, Born K, Jacob D, Pinto JG. Regional changes in wind energy potential over Europe using regional climate model ensemble projections. J Appl Meteorol Climatol 2013;52(4):903–17.
[44] Tobin I, Vautard R, Balog I, Bréon FM, Jerez S, Ruti PM, et al. Assessing climate change impacts on European wind energy from ENSEMBLES high-resolution climate projections. Climatic Change 2015;128(1):99–112.
[45] Hübler C, Rolfes R. Analysis of the influence of climate change on the fatigue lifetime of offshore wind turbines using imprecise probabilities. Wind Energy 2021;24(3):275–89.
[46] Bisoi S, Haldar S. Effect of climate change on dynamic behavior of monopile supported offshore wind turbine structure. Jpn Geotech Soc Spec Publ 2016;2(33):1189–93.
[47] Bisoi S, Haldar S. Sustainable design of monopile-supported offshore wind turbine considering climate change. Geoenvironmental practices and sustainability. Singapore: Springer; 2017. p. 129–39.
[48] Bisoi S, Haldar S. Impact of climate change on dynamic behavior of offshore wind turbine. Mar Georesourc Geotechnol 2017;35(7):905–20.
[49] Bisoi S, Haldar S. Impact of climate change on design of offshore wind turbine considering dynamic soil–structure interaction. J Offshore Mech Arct Eng 2017;139:6.
[50] Zhang D, Xu Z, Li C, Yang R, Shahidehpour M, Wu Q, et al. Economic and sustainability promises of wind energy considering the impacts of climate change and vulnerabilities to extreme conditions. Electr J 2019;32(6):7–12.
[51] Pinto JG, Neuhaus CP, Leckebusch GC, Reyers M, Kerschgens M. Estimation of wind storm impacts over Western Germany under future climate conditions using a statistical—dynamical downscaling approach. Tellus A Dyn Meteorol Oceanogr 2010;62(2):188–201.
[52] Pryor SC, Barthelmie RJ. Assessing the vulnerability of wind energy to climate change and extreme events. Clim Change 2013;121(1):79–91.
[53] Meier HM, Döscher R, Halkka A. Simulated distributions of Baltic Sea-ice in warming climate and consequences for the winter habitat of the Baltic ringed seal. AMBIO J Hum Environ 2004;33(4):249–56.
[54] Barker A, Timco G, Gravesen H, Vølund P. Ice loading on Danish wind turbines: part 1: dynamic model tests. Cold Regions Sci Technol 2005;41(1):1–23.
[55] Clausen, et al. Impacts of climate change on renewable energy sources. In: Fenger J, editor. Their role in the Nordic energy system. Nordic Council of Ministers; 2007. p. 105–28.
[56] Vihma T, Haapala J. Geophysics of sea ice in the Baltic Sea: a review. Prog Oceanogr 2009;80(3–4):129–48.
[57] Pryor SC, Barthelmie RJ, Bukovsky MS, Leung LR, Sakaguchi K. Climate change impacts on wind power generation. Nat Rev Earth Environ 2020;1(12):627–43.
[58] Wang A, Tang M, Zhao Q, Liu Y, Li B, Shi Y, et al. Analysis of sea ice parameters for the design of an offshore wind farm in the Bohai Sea. Ocean Eng 2021;239:109902.

[59] Pryor SC, Barthelmie R. Use of RCM simulations to assess the impact change on wind energy availability. Riso-R1477 (EN). Rep. No. 111; 2004.
[60] Alsabagh ASY, Tiu W, Xu Y, Virk MS. A review of the effects of ice accretion on the structural behavior of wind turbines. Wind Energy 2013;37(1):59−70.
[61] Hochart C, Fortin G, Perron J, Ilinca A. Wind turbine performance under icing conditions. Wind Energy 2008;11(4):319−33.
[62] Davis N, Hahmann AN, Clausen NE, Žagar M. Forecast of icing events at a wind farm in Sweden. J Appl Meteorol Climatol 2014;53 (2):262−81.
[63] Di Y, Lu J, Xu X, Feng T, Li L. A response characteristics study of widespread power grid icing to el nino. Math Probl Eng 2019;2019.
[64] Yu Y, Ren Z, Gao F, Meng X. Changes in surface icing duration over north China during 1961−2015. Atmos Sci Lett 2018;19(7):e827.
[65] Pryor SC, editor. Climate change in the Midwest: impacts, risks, vulnerability, and adaptation. Indiana University Press; 2013.
[66] Clausen NE, Gryning SE, Larsén XG, Tarp-Johansen NJ, Holttinen H, Barthelmie R, et al. Impact from climate change on extreme winds and icing conditions in the Baltic Region. CPH Offshore Wind 2005;.
[67] Martinez A, Iglesias G. Mapping of the levelised cost of energy for floating offshore wind in the European Atlantic. Renew Sustain Energy Rev 2022;154:111889.
[68] Giorgi F, Jones C, Asrar GR. Addressing climate information needs at the regional level: the CORDEX framework. World Meteorol Organ (WMO) Bull 2009;58(3):175.
[69] Van der Linden P., Mitchell J.F.B. ENSEMBLES: climate change and its impacts: summary of research and results from the ENSEMBLES project. Met Office Hadley Centre, Exeter, UK; 2009.
[70] Nolan P. Ensemble of regional climate model projections for Ireland. Environmental Protection Agency (EPA); 2015.
[71] Moemken J, Reyers M, Feldmann H, Pinto JG. Future changes of wind speed and wind energy potentials in EURO-CORDEX ensemble simulations. J Geophys Res: Atmos 2018;123(12):6373−89.
[72] Strandberg G, Bärring L, Hansson U, Jansson C, Jones C, Kjellström E, et al. CORDEX scenarios for Europe from the Rossby Centre regional climate model RCA4. SMHI; 2015.
[73] Doddy Clarke E, Sweeney C, McDermott F, Griffin S, Correia JM, Nolan P, et al. Climate change impacts on wind energy generation in Ireland. Wind Energy 2022;25(2):300−12.
[74] Schott FA, Xie SP, McCreary JP. Indian Ocean circulation and climate variability. Rev Geophys 2009;47(1). Available from: https://doi.org/10.1029/2007RG000245 RG1002.
[75] Krishnan A, Bhaskaran PK, Kumar P. Extreme wind-wave climate projections for the Indian Ocean under changing climate scenarios. Clim Dyn 2022;1−21.
[76] Deepthi R, Deo MC. Effect of climate change on design wind at the Indian offshore locations. Ocean Eng 2010;37(11−12):1061−9.
[77] Marine climate change guidelines. Denmark: Danish Hydraulic Institute; 2012.
[78] Kaur S, Kumar P, Weller E, Young IR. Positive relationship between seasonal Indo-Pacific Ocean wave power and SST. Sci Rep 2021;11 (1):1−9.
[79] Mohan S, Bhaskaran PK. Evaluation of CMIP5 climate model projections for surface wind speed over the Indian Ocean region. Clim Dyn 2019;53:5415−35.
[80] Pardikar, R. Climate change is making India's west coast more vulnerable to cyclones, Eos 2021, 102, https://doi.org/10.1029/2021EO163064. Published on 13 September 2021
[81] Kamranzad B, Mori N. Future wind and wave climate projections in the Indian Ocean based on a super-high-resolution MRI-AGCM3. 2S model projection. Clim Dyn 2019;53(3):2391−410.
[82] Kumar R, Stallard T, Stansby PK. Large-scale offshore wind energy installation in northwest India: assessment of wind resource using Weather Research and Forecasting and levelized cost of energy. Wind Energy 2021;24(2):174−92.
[83] Semedo A, Weisse R, Behrens A, Sterl A, Bengtsson L, Günther H. Projection of global wave climate change toward the end of the twenty-first century. J Clim 2012;26(21):8269−88. Available from: https://doi.org/10.1175/JCLI-D-12-00658.1.
[84] Kulkarni S, Deo MC, Ghosh S. Evaluation of wind extremes and wind potential under changing climate for Indian offshore using ensemble of 10 GCMs. Ocean Coast Manag 2016;121:141−52. Available from: https://doi.org/10.1016/j.ocecoaman.2015.12.008.

Further reading

1. Barstad I, Sorteberg A, Mesquita MDS. Present and future offshore wind power potential in northern Europe based on downscaled global climate runs with adjusted SST and sea ice cover. Renew Energy 2012;44:398−405.
2. Hansen MOL. Aerodynamics of wind turbines. Routledge; 2015.
3. Ruosteenoja K, Vihma T, Venäläinen A. Projected changes in European and North Atlantic seasonal wind climate derived from CMIP5 simulations. J Clim 2019;32(19):6467−90.

Chapter 29

Life cycle assessment: a meta-analysis of cumulative energy demand and greenhouse gas emissions for wind energy technologies

Michael Carbajales-Dale
Environmental Engineering and Earth Sciences, Clemson University, Clemson, SC, United States

29.1 Introduction

Technology assessment of energy production technologies is often computed in terms of the financial cost. The US Department of Energy and the National Renew Energy Laboratory (NREL) have been aggregating data on cost estimates for electricity generation in an online application: the Transparent Cost Database [1]. Two main metrics exist to assess the cost of, especially electricity generating, infrastructure investment: (1) *overnight capital cost*—combines all the capital cost data per unit of (peak) nameplate capacity without interest, as if built *overnight* [2], computed in $\$/(W_p)$,[1]; (2) *Levelized cost of electricity* (LCOE) —total costs (including annualized capital cost and yearly operating costs) divided by total lifetime electricity production [1], computed as $\$/(kW\ h_e)$.[2]

This chapter will advance the benefits of computation of analogous metrics for energetic and carbon "costs" associated with electricity production by wind energy technologies, such as cumulative energy demand (CED) or carbon footprint. The chapter then presents the results of a meta-analysis of energy inputs and greenhouse gas (GHG) emissions during the various life-cycle stages of wind electricity production, in terms of capital energy cost (CEC) and capital carbon cost (CCC)—equivalent to overnight capital cost (in Sections 29.5.1 and 29.5.2), life cycle energy cost (LCEC) and life cycle carbon cost (LCCC) —equivalent to LCOE (in Sections 29.5.3 and 29.5.4). The CED and carbon footprint are also assessed by a major component of the wind energy system (in Section 29.5.5 and trends in the parameters are assessed in Section 29.5.6 to determine if there are systematic reductions (e.g., due to learning) occurring within the wind industry. This information is then brought together in Sections 29.5.7 and 29.5.8, where the net energy and net carbon trajectories of the global wind industry are presented.

29.2 Wind energy technologies

Growth in the installed capacity of wind has been rapid in the last decade, with sustained growth rates of 16% during the period 2010−20. The global installed capacity of wind turbines, as depicted in Fig. 29.1, increased over 45 fold from 16 GW in 2000, to over 740 GW in 2020. Around 95% of wind deployment is currently on land, though deployment is increasingly occurring off-shore, in increasingly deeper waters, to make use of stronger and more steady winds.

The ratio of average power output to nameplate capacity $\left[\frac{W_{avg}}{W_p}\right]$ is termed the *capacity factor*. Fig. 29.2 uses data from [4,5] to display the distribution in capacity factor for the global installed capacity of wind. The peak in capacity

1. Units of nameplate capacity are presented with a subscript p to denote *peak* power.
2. Electrical energy is denoted with subscript e, primary energy is denoted with a subscript p.

Wind Energy Engineering. DOI: https://doi.org/10.1016/B978-0-323-99353-1.00028-1

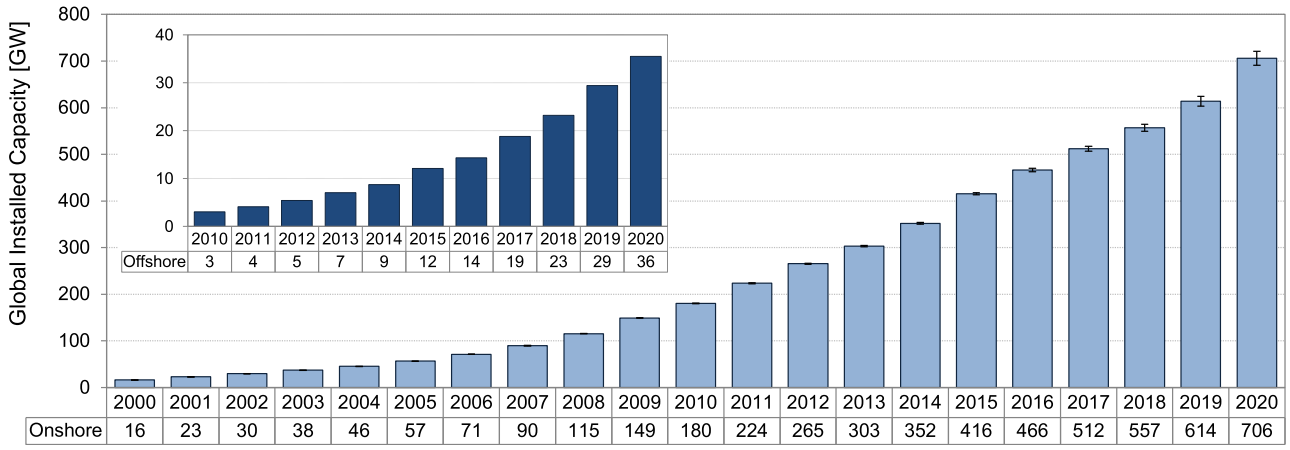

FIGURE 29.1 Global cumulative installed capacity [GW] of wind disaggregated by onshore and offshore compiled using data from [3–7].

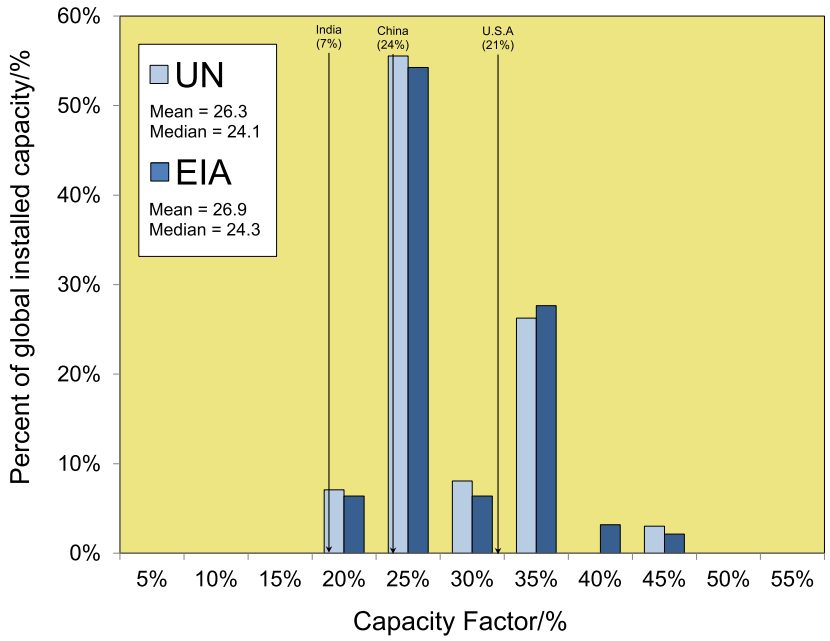

FIGURE 29.2 Distribution in global wind capacity factors using data from [4,5]. Average capacity factor for the three top wind capacity countries (China, United States, and India) is shown, with their proportion of global installed capacity in parentheses.

factor occurs around 25%, meaning that a 1 MW_p wind turbine will have an annual electricity production of 2.2 GW h_e/(year).[3]

The main technology for generating electricity from wind is the horizontal axis wind turbine, wherein airfoil-shaped blades spin around a central hub that sits at the top of a central tower.[4] The size of wind turbines has increased from a hub height of fewer than 30 m in the early 1990s to a hub height of over 100 m today [8,9]. Blade length has similarly increased. Power capacity is proportional to the area swept by the blades. The power that can be extracted from the wind is also proportional to the cube of the wind speed. As such, there is benefit to increasing the size of wind turbines, both to increase the capture area, but also to take advantage of the more frequent, higher wind speed at greater height. The power capacity of wind turbines has increased by two orders of magnitude from around 100 kW during the 1990s to 10 MW today. The main components of the wind system are rotor, nacelle housing the gearing and generator, tower, foundation, and the balance of system. These are described briefly below.

3. Generally speaking, offshore installments will have a higher capacity factor often greater than 35%.

4. Vertical axis wind turbines (VAWT) also exist, though generally not for the large, utilityscale turbines, ones as large as 6 MW have been built. Small-scale VAWTs (100–10,000 W) are favored in locations where wind direction changes rapidly and often, e.g., urban settings.

29.2.1 Rotor

The rotor is made up of the hub and blades.

29.2.1.1 Hub

The hub connects to the generator shaft by a bearing and also connects to the blades by bearing to allow control of the pitch of the blades. The hub is typically made primarily out of cast iron with a glass fiber reinforced polyester (or similar material) casing called the spinner [10].

29.2.1.2 Blades

The blades of modern turbines are airfoils, which can reach over 50 m in length, comprising a main spar glued between two shell sections. Primary materials used in blades are carbon fibers and woven glass fibers infused with epoxy resins and polyurethane glue used to assemble the blade shell.

29.2.2 Nacelle

The nacelle houses the electricity generating equipment including gearbox (if geared), generator, foundation, cover, yaw system (a bearing system that allows the wind turbine to change direction to face the wind), and controls.

29.2.2.1 Gearing and generator

The gearbox converts the low-speed rotation delivered by the blades to a high-speed (1500 rpm) rotation for electricity generation. Typical materials for the gearbox are iron and steel. The generator also consists mainly of iron and steel. Some manufacturers use lighter permanent magnets made from rare earth metals (e.g., neodymium or dysprosium) while others use heavier induction generators [10]. Although most wind turbines have gears, nongeared turbines are being built but must rely on heavier, low-speed generators.

29.2.2.2 Foundation and cover

The nacelle foundation provides the floor of the nacelle and is often made from cast iron. The cover to the nacelle is typically made from fiberglass, consisting of woven glass fibers, polyethylene, and styrene.

29.2.3 Tower

The hub height of turbines has increased significantly in recent decades, with the tallest turbines reaching over 150 m. As such, the turbine tower makes up a large proportion of the mass of the turbine. Typical materials are structural steel which is rolled and welded into tower sections or concrete.

29.2.4 Foundation

The foundation of wind turbines can change significantly, depending on the installation location. Onshore foundation designs include: tensionless pier, a cast-in-place concrete ring around 3−5 m in diameter and up to 10 m deep; anchor deep, a 2 m thick concrete ring supported by up to 20 steel anchors up to 15 m deep; and gravity spread, a broad steel-reinforced concrete disk up to 20 m in diameter [11]. Offshore designs include: gravity-based, using mass to prevent the turbine from tipping over; monopile, consisting of a single, hollow steel pile driven into the sea bed; tripod, consisting of a braced Y-frame and three, smaller piles into the sea bed; and floating, consisting of a floating ballast submerged and moored to the sea bed [12].

29.2.5 Balance of system

The balance of the system comprises all of the other components and installations to allow the wind system to operate. This includes inverters (if the turbine puts out DC electricity); electrical control systems; operational buildings and roads; spare equipment (e.g., replacement blades); grid interconnection; and energy storage (if required).

Nonequipment activities are also included in the balance of systems, such as transportation, which may be significant if it includes the construction or modification of roads to transport the large pieces of the turbine, for example, blades; and site preparation to enable installation of the turbine, such as leveling the ground.

29.2.6 Operation and maintenance

During their lifetime, the wind turbines will require regular servicing to maintain equipment and replacement of any worn-out parts. This typically will involve travel and transportation of additional equipment.

29.2.7 Disposal

At the end of its service life, typically defined as a period of 20−25 years, there is a choice that must be made. The turbines can be (1) *re-licensed*, which would require servicing and maybe replacement of parts; (2) *re-powered*, wherein the turbines are replaced with higher power new turbines, making use of as much of the balance of system as can be kept; or (3) *decommissioned*, where turbines are disassembled some parts, for example, the dynamo or steel tower, and are sold for reuse or scrap and the site is remediated.

29.3 Life-cycle assessment

Life-cycle assessment (LCA) is a system of methodologies and tools to evaluate the physical flows and environmental impacts associated with the production of goods and provision of services over the full life cycle from extraction and processing of raw materials through manufacture, operation, and finally to disposal [13]. The LCA is divided into four main phases: (1) *goal and scope*—including the definition of the *functional unit*, which quantifies the service delivered by the product system, definition of system boundaries, clarification of assumptions and limitations, allocation methods (e.g., between coproducts), and impact categories; (2) *life-cycle inventory* (LCI) —tracking material and energy flows from and to the environment, often involving either the creation of a "bottom-up" model of the production process, the use of input-output tables, or some hybrid of the two; (3) *life-cycle impact assessment* (LCIA) —evaluating the environmental impacts of flows associated with the LCI including selecting appropriate impact categories, indicators and environmental impact models, classification and measurement of impacts using a common metric to place different categories on an equivalent basis; (4) *interpretation*—including identification of significant issues arising from the LCI and LCIA stages, evaluation of completeness, sensitivity and consistency, and conclusions, limitations and recommendations.

29.3.1 Cumulative energy demand

CED is an impact metric that "represents the direct and indirect energy use, including the energy consumed during the extraction, manufacturing and disposal of the raw and auxiliary materials." [14] Certain environmental energy flows are not accounted for, such as the wind flowing through the turbine is not included in the CED for wind-generated electricity.

We may define CED on the basis of either nameplate capacity (to give CEC) or lifetime electricity generation (to give lifecycle energy cost, LCEC). Mathematically, we may say through the following equations:

$$\mathrm{CEC}\left[\frac{MJ_p}{W}\right] = \frac{\mathrm{CED}}{\kappa} \tag{29.1}$$

where κ is the nameplate capacity of the device; and

$$\mathrm{LCEC}\ \left[\frac{\mathrm{kW}|h_p}{\mathrm{kW}|h_e}\right] = \frac{\mathrm{CED}}{E} \tag{29.2}$$

where E is the electricity delivered by the device over its lifetime.

29.3.2 Carbon footprint

Carbon footprint sums up the GHG emissions of a product or service and may be thought of as the carbon "cost" (CC) for that product or service. For wind power, we may define CC on the basic of either nameplate capacity (to give CCC)

or lifetime electricity generation (to give lifecycle carbon cost, LCCC).Mathematically, we may say again, where κ is the nameplate capacity of the device:

$$\mathrm{CCC}\left[\frac{kg|CO_2\text{-eq}}{W}\right] = \frac{\mathrm{CC}}{\kappa} \tag{29.3}$$

$$\mathrm{LCCC}\left[\frac{\mathrm{kg}|CO_2\text{-eq}}{kW|h_e}\right] = \frac{CC}{E} \tag{29.4}$$

where E is the electricity delivered by the device over its lifetime.

29.3.3 Energy return on investment

Energy return on investment (EROI) compares the energy output from a technology with the energy that society must invest in delivering that energy [15]. Since the output energy from the wind turbine is in the form of electricity, we will convert this into primary energy equivalents (*p-eq*) to reflect the greater value that society places on electricity.[5] This electricity conversion factor is given by the average efficiency of the electricity grid, η, around 30%.

Mathematically, we can compute:

$$\mathrm{EROI}_{p-eq}\left[\frac{kW|h_{p\text{-eq out}}}{kW|h_{\mathrm{p\ in}}}\right] = \frac{1}{\eta \mathrm{LCEC}} \tag{29.5}$$

29.3.4 Carbon return on investment

Analogously to EROI, the carbon return on investment (CROI) compares the mitigation potential of a technology with the amount of carbon emitted in the production of that technology [16]. The mitigation potential of the electricity generated will depend on the carbon intensity of grid emissions for the location in which the electricity is generated. Since we don't know where the wind turbine is being installed, we can use the average global carbon intensity of 475 g CO_2 [17].

Mathematically, we can compute:

$$\mathrm{CROI}\left[\frac{kg|CO_2\text{-eq offset}}{kg|CO_2\text{-eq emitted}}\right] = \frac{\varepsilon_e}{\mathrm{LCCC}} \tag{29.6}$$

where ε_e is the carbon intensity of electricity being replaced by wind-generated electricity.

29.3.5 Energy payback time

Energy payback time (EPBT) is the amount of time that an energy technology takes to deliver the amount of energy required over its life cycle [18].

Mathematically, we may define this as follows:

$$\mathrm{EPBT}_{\mathrm{p\text{-}eq}}[yrs] = \frac{\mathrm{CED}}{\dot{E}_{\mathrm{p\text{-}eq}}} = \frac{L}{EROI_{p\text{-}eq}} \tag{29.7}$$

where E is the energy delivered by the device annually and L is the lifetime of the system. Again, we use the primary energy equivalent of the electricity produced by the wind turbine.

29.3.6 Carbon payback time

Carbon payback time (CPBT) is the amount of time that an energy technology takes to offset the amount of carbon released over its life cycle [19]. Mathematically, we may define this as follows:

$$\mathrm{CPBT}[years] = \mathrm{CC}\dot{C} \tag{29.8}$$

where C is the carbon offset by the device annually.

5. Society routinely accepts a three-to-one exchange of chemical fuel for electricity, since electricity is much easier to transport and convert into a variety of end uses.

29.3.7 Fractional electricity reinvestment

The fractional energy reinvestment, f_e, defines the amount of electricity that an industry composed of devises with a certain EPBT must invest in deploying new devices to maintain a certain growth rate [20,21]. Mathematically, we can define this as follows:

$$f_e[\%] = r\text{EPBT}_{\text{p-eq}} \tag{29.9}$$

where r is the industry growth rate in percent per year.

If $f_e > 100\%$, the industry is running in deficit, if $f_e < 100\%$, the industry can provide surplus electricity to society.

29.3.8 Fractional carbon emissions

The fractional carbon emissions, f_c, defines the amount of carbon that an industry composed of devises with a certain CPBT will emit in deploying new devices to maintain a certain growth rate, based on the fractional energy reinvestment concept [20,21].

$$f_c[\%] = r\text{CPBT} \tag{29.10}$$

29.4 Meta-analysis

The areas of interest for this analysis are: energy requirements and GHG emissions for the production of capital infrastructure, CEC and CCC analogs to overnight capital cost, measured on a per unit of nameplate capacity bases; and total life-cycle energy requirements and GHG emissions for the system, LCEC and LCCC, analogs to LCOE, measured on a per unit of electricity production basis.

A meta-analysis and harmonization project was carried out by researchers at the NREL and a number of other institutions to determine the distribution of GHG emissions from a variety of electricity production technologies over their entire life-cycle. Methodological details are provided in Heath and Mann [22]. The results have been published in a special issue of the Journal of Industrial Ecology. This analysis uses the NREL methodology to build upon previous meta-analyses which have been done for the energy inputs and GHG emissions to wind electricity production [8,9,20,23].

29.4.1 Literature search

In this literature search, we are building upon previous meta-analyses for energy requirements [24] and GHG emissions [25]. As such, the literature search was conducted on ScienceDirect with a publication date limited to 2015−22 using the search terms “wind” and “life cycle assessment” in the title, abstract, or keywords. This was supplemented with a search for technical reports, for example, from Vestas.

The initial search produced 402 items published since 2015. These were then passed to the screening process.

29.4.2 Literature screening

A number of criteria were used to screen the initial results in two rounds. In an initial screening, the following criteria were used: (1) the study should be in English; (2) the study should be original research or should reference data used; (3) the study should give numeric data on net energy metrics or GHG emissions; for example, CED, or net energy ratio. This screening eliminated 265 studies.

In a subsequent deeper screening, the following criteria were used. (1) the study should give data on wind turbine technologies; (2) the study should give sufficient information on assumptions and system boundaries to allow for harmonization; (3) cross-referenced estimates were also eliminated. This screening eliminated a further 61 studies. The studies used were Refs. [8,9,20,23,24,26−95].

A link to find more details of the studies remaining after screening is given in Appendix A.

29.5 Results and discussion

The raw data from the studies were used to calculate six metrics: (1) CEC; (2) CCC; (3) LCEC; (4) LCCC; (5) EPBT; and (6) CPBT. These are presented below. Further data was collected from the studies on the major components (e.g., tower, foundation, etc. as discussed in Section 29.2 above) and their contribution to either CED or GHG emissions.

29.5.1 Capital energy costs

CEC includes all the energy requirements to extract and process raw materials, manufacture and install the capital equipment including any site preparation and grid interconnection. This presentation does not account for changes in these values over time but instead shows the distribution across all studies over the more than forty-year period. Units of measurement for CEC are primary energy inputs per unit of nameplate capacity [$MJ_p/(W_p)$].

Fig. 29.3 shows the distribution in estimates of CEC for the various wind technologies and analysis methods. The boxes represent quartiles (Q1, Q2, and Q3) and whiskers plot minimum, and Q3 + 1.5 × interquartile range (IQR, Q3 minus Q2) values. Generally, there is a large min-max range in the data, with a much smaller IQR, that is, there are a lot of outlier values with a positive skew to the data. The median value for all estimates is 10.34 $MJ_p/(W_p)$. Onshore wind tends to have a lower CEC than offshore wind, due to the added costs of offshore deployment. Input–output analysis tends to produce higher estimates with a larger range, likely due to the inclusion of factors that are omitted from process-based analyses, that is cut-off. Summary statistics are presented below in Table 29.1.

29.5.2 Capital carbon costs

The distribution in estimates for CCC is presented in Fig. 29.4. The median value for all estimates is 0.65 kg CO_2-eq/(W_p). The general trends are somewhat similar to CEC. Offshore wind has a higher median value than onshore, but with comparable IQR in estimates. Input–output analysis produces higher estimates than the process-based. Summary statistics are presented below in Table 29.2.

29.5.3 Life-cycle energy costs

LCEC includes all of the energy inputs over the full lifecycle of the system, including end-of-life, normalized by the total lifetime electricity output from the system. The unit of measurement is primary energy per unit of electricity production [kW h_p/(kW h_e)]. Unlike the financial metric LCOE, no discounting of inputs and outputs has been made.

Fig. 29.5 shows the life-cycle energy requirements for onshore and offshore technologies and all of the different analysis methods. Similarly to CEC, we find a wide range in the data. Again, onshore has a lower median value than offshore and process analysis methods produce a lower variation in value. The median value for all estimates is 0.05 kW h_p/(kW h_e). Assuming a value of 30% to convert electricity output into primary energy equivalents gives an $EROI_{PE-eq}$ of 67. Assuming an average lifetime of 20 years gives an EPBT of 0.3 years or 3.6 months.

Equivalent values for onshore and offshore technologies are given in Table 29.3 (Table 29.4).

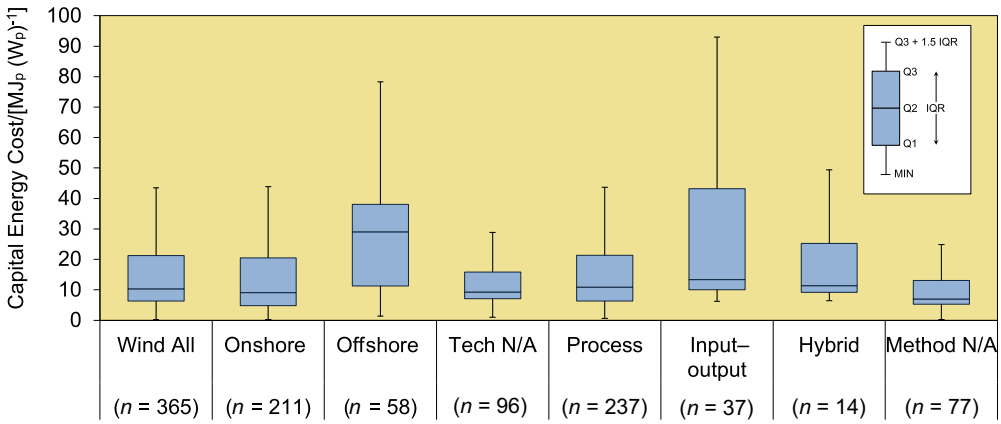

FIGURE 29.3 Capital energy cost [$MJ_p/(W_p)$] different wind technologies (onshore, offshore, unspecified) and when using different analysis methodologies (process-based, input–output, hybrid).

TABLE 29.1 Summary statistics of capital energy cost [$MJ_p/(W_p)$] estimates.

Statistic	Tech				Analysis method			
	All	On	Off	N/A	Process	IO	Hybrid	N/A
Count	365	211	58	96	237	37	14	77
Mean	30.23	26.27	63.40	18.88	31.47	33.24	16.90	27.39
SD	101.88	87.43	187.47	30.86	116.94	45.70	11.29	78.68
Min	0.25	0.25	1.39	1.01	0.67	6.20	6.40	0.25
Q1	6.36	4.81	11.30	7.09	6.36	10.00	9.19	5.26
Median	10.34	9.08	29.04	9.30	10.87	13.40	11.32	7.04
Q3	21.21	20.45	38.09	15.80	21.30	43.20	25.27	13.10
Max	1093	737	1093	221	1093	221	37	580
IQR	14.85	15.64	26.79	8.71	14.94	33.20	16.08	7.84
Range	1093	737	1091	220	1092	215	30	580

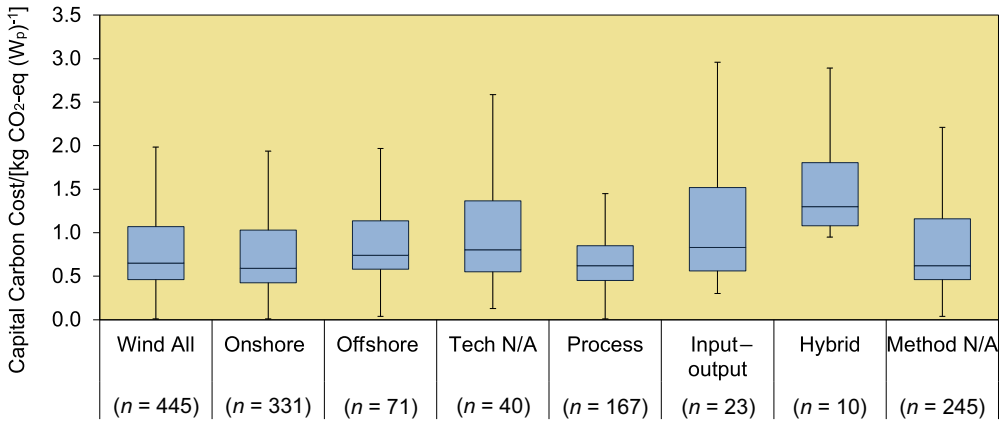

FIGURE 29.4 Capital carbon cost [kg CO_2-eq/(W_p)] of different wind technologies (onshore, offshore, unspecified) and when using different analysis methodologies (process-based, input−output, hybrid, unspecified).

TABLE 29.2 Summary statistics of capital carbon cost [kg CO_2-eq/(W_p)] estimates.

Statistic	Tech				Analysis method			
	All	On	Off	N/A	Process	IO	Hybrid	N/A
Count	445	331	71	40	167	23	10	245
Mean	109	143	1.47	25	283	1.57	1.48	4.94
SD	2234	2590	4.44	153	3646	1.70	0.53	61.67
Min	0.01	0.01	0.04	0.13	0.01	0.30	0.95	0.04
Q1	0.46	0.43	0.58	0.55	0.45	0.56	1.08	0.46
Median	0.65	0.59	0.74	0.81	0.62	0.83	1.30	0.62
Q3	1.07	1.03	1.14	1.37	0.85	1.52	1.81	1.16
Max	47121[a]	47121	37.95	966	47121	6.50	2.45	966
IQR	0.61	0.61	0.56	0.82	0.40	0.96	0.73	0.70
Range	47121	47121	37.91	966	47121	6.20	1.50	966

[a]*This estimate is for a 6 kW stand-alone system that includes battery storage.*

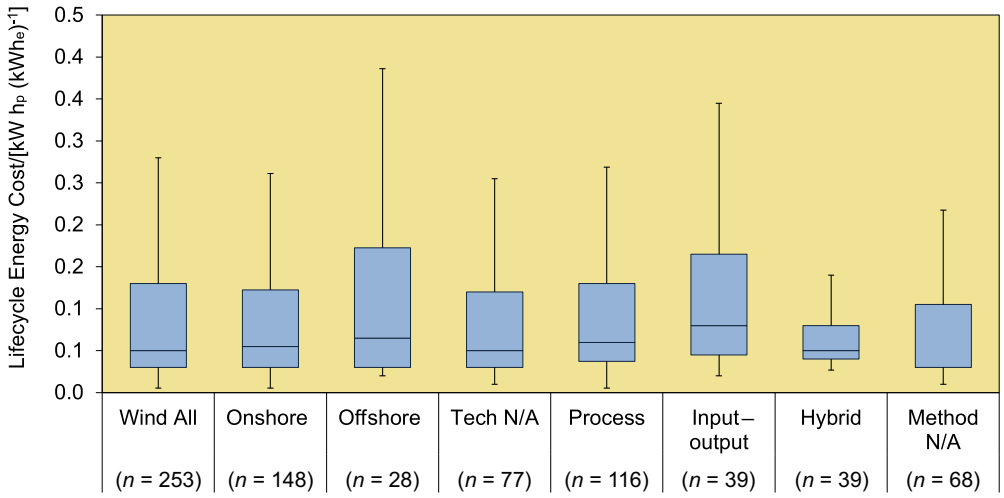

FIGURE 29.5 Life cycle energy cost [kW h_p/(kW h_e)] of different wind technologies (onshore, offshore, unspecified) and when using different analysis methodologies (process-based, input−output, hybrid).

TABLE 29.3 Net energy metrics for onshore and offshore wind technologies.

Tech	LCEC	EROI*PE − eq*	EPBT
	[kW h_p/(kW h_e)]	[kW h*PE − eq*/(kW h*p*)]	[years]
Onshore	0.06	61	0.33
Offshore	0.07	51	0.39

TABLE 29.4 Summary statistics of life cycle energy cost (LCEC) [kW h_p/(kW h_e)].

Statistic	Tech				Analysis method			
	All	On	Off	N/A	Process	IO	Hybrid	N/A
Count	253	148	28	77	116	39	39	68
Mean	0.12	0.12	0.14	0.11	0.10	0.16	0.07	0.16
SD	0.22	0.25	0.22	0.16	0.10	0.21	0.05	0.37
Min	0.01	0.01	0.02	0.01	0.01	0.02	0.03	0.01
Q1	0.03	0.03	0.03	0.03	0.04	0.05	0.04	0.03
Median	0.05	0.06	0.07	0.05	0.06	0.08	0.05	0.03
Q3	0.13	0.12	0.17	0.12	0.13	0.17	0.08	0.11
Max	2.56	2.56	1.17	1.00	0.66	1.00	0.21	2.56
IQR	0.10	0.09	0.14	0.09	0.09	0.12	0.04	0.08
Range	2.55	2.55	1.15	0.99	0.65	0.98	0.18	2.55

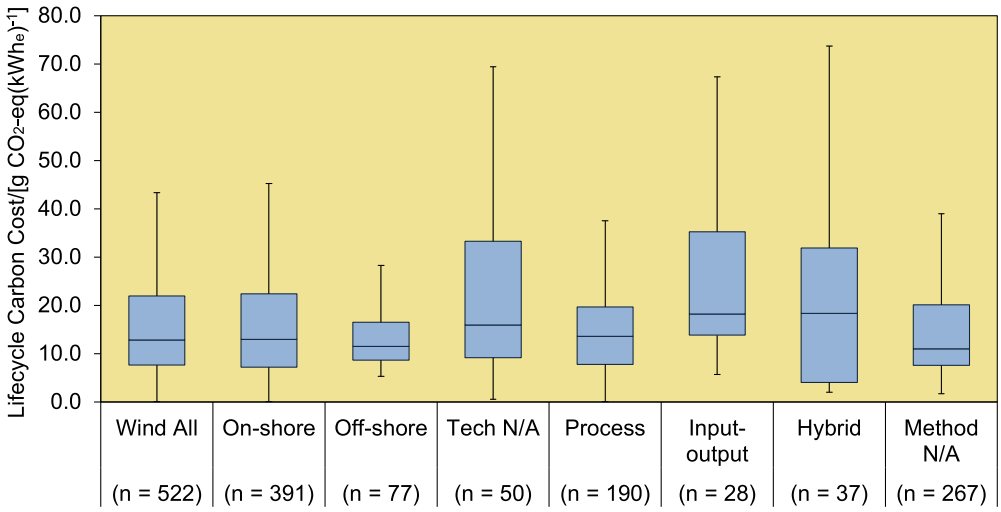

FIGURE 29.6 Life cycle carbon cost [g CO_2-eq/(kW h_e)] of different wind technologies (onshore, offshore, unspecified) and when using different analysis methodologies (process-based, input−output, hybrid).

TABLE 29.5 Net carbon metrics for onshore and offshore wind technologies.

Tech	LCCC	$CROI_{PE-eq}$	CPBT
	[g CO_2 − eq (kW h_e)$^{-1}$]	[g CO_2 − eq_{offset} (g CO_2 − eq)$^{-1}$]	[yrs]
Onshore	13.0	37	0.55
Offshore	11.5	41	0.49

29.5.4 Life-cycle carbon costs

Life cycle carbon-carbon cost (LCCC) includes all GHG emissions from the system over its full life cycle divided by the lifetime electricity production of the system. The unit of measurement is g CO_2-eq/(kW h_e).

Fig. 29.6 shows the distribution of estimates for LCCC. The median value for all technologies is 12.8 g CO_2-eq/(kW h_e). Using the global average carbon intensity, this gives a CROI of 37. Assuming a 20-year lifetime, offshore wind has a slightly lower median value than onshore with a much smaller IQR. Studies using input−output produce a high median value and a greater range of estimates (see Tables 29.5 and 29.6).

29.5.5 Components

Many of the studies provide a breakdown of CED and GHG emissions by different components. This data is presented in Tables A1 and A2, with distributions presented in Figs. 29.7 and 29.8. There is a large distribution of the values. The tower contributes the highest median value to the overall CED (23%). Transport has the highest range in values, which is greatly influenced by both location of the wind farm and the size of the system. The median value is 11%. Operation and maintenance (O&M) contribute a median value of 6% to total CED. Disposal presents an interesting case. Many studies give energy credits for recycling turbine materials (primarily steel), leading to a negative value, as much as 50% of the overall value. The median value for disposal is −21%.

Looking at GHG emissions, the picture is somewhat similar except that now the foundation has the highest median value to the overall emissions at 47%. This is due to the large use of concrete with associated emissions from cement manufacture. Surprisingly, transport contributes much less to GHG than to CED, with a median value of ¡1%. O&M contribute a median value of 4% to total GHG emissions. Again, disposal has a negative median value (−15%) with many studies attributing credits due to the recycling of components.

TABLE 29.6 Summary statistics of life cycle carbon cost (LCCC) [kg CO2-eq/(kW he)].

Statistic	Tech				Analysis method			
	All	On	Off	N/A	Process	IO	Hybrid	N/A
Count	522	391	77	50	190	28	37	267
Mean	577	763	19.31	25.48	1544	31.72	22.78	23.60
SD	12,362	14,283	52.42	27.55	20,488	32.80	20.38	48.96
Min	0.01	0.01	5.28	0.57	0.01	5.69	2.00	1.67
Q1	7.63	7.20	8.67	9.13	7.77	13.81	4.00	7.54
Median	12.83	12.96	11.52	15.95	13.57	18.23	18.33	11.00
Q3	21.92	22.41	16.50	33.25	19.67	35.21	31.88	20.10
Max	282,441	282,441	469	124	282,441	124	81	560
IQR	14.29	15.21	7.83	24.12	11.90	21.41	27.88	12.56
Range	282,441	282,441	464	123	282,441	118	79.00	558

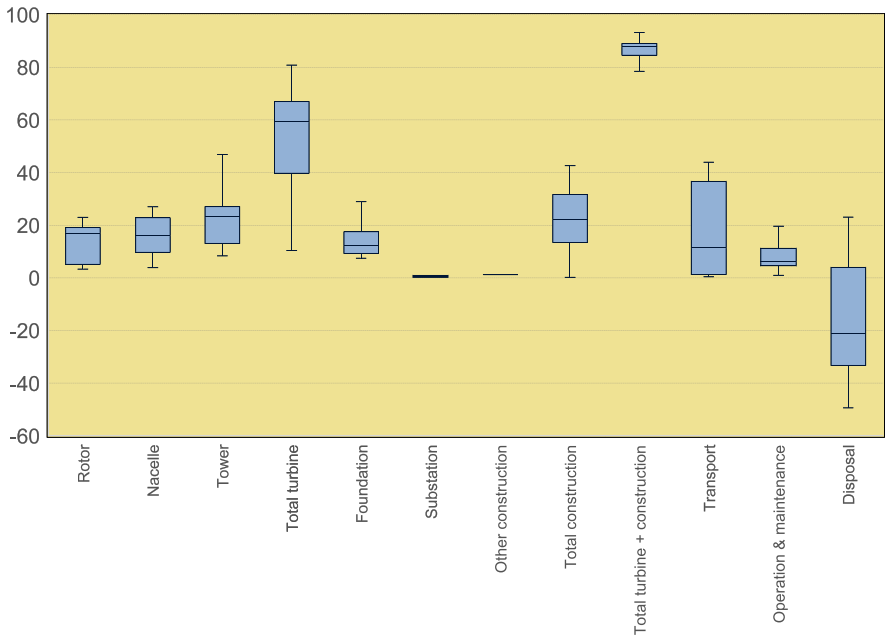

FIGURE 29.7 Percentage of cumulative energy demand (CED) made up of different components, based on data presented in Table A1. Disposal is often calculated to have negative embodied energy due to recycling credits.

29.5.6 Trends in parameters

The distributions presented above do not account for all physical attributes of the turbines or studies. For instance, we might expect that larger turbines might have a lower CEC or that a turbine built today would have a lower CED than the equivalent turbine built ten years ago.

There is a weak relationship between CEC and turbine power rating. CEC decreases slightly as turbine rating increases.

We also expect that as total global installed capacity increases, the industry decreases the cost of producing wind power systems. The energy learning curve for wind is depicted in Fig. 29.9 with a power curve fitted to the data. The learning rate is defined as the percent reduction in cost per doubling of installed capacity. The learning rate of CEC for the wind industry is approximately 11%.

Similarly, the carbon learning curve for wind is depicted in Fig. 29.10. The learning rate of CCC for the wind industry is 4%

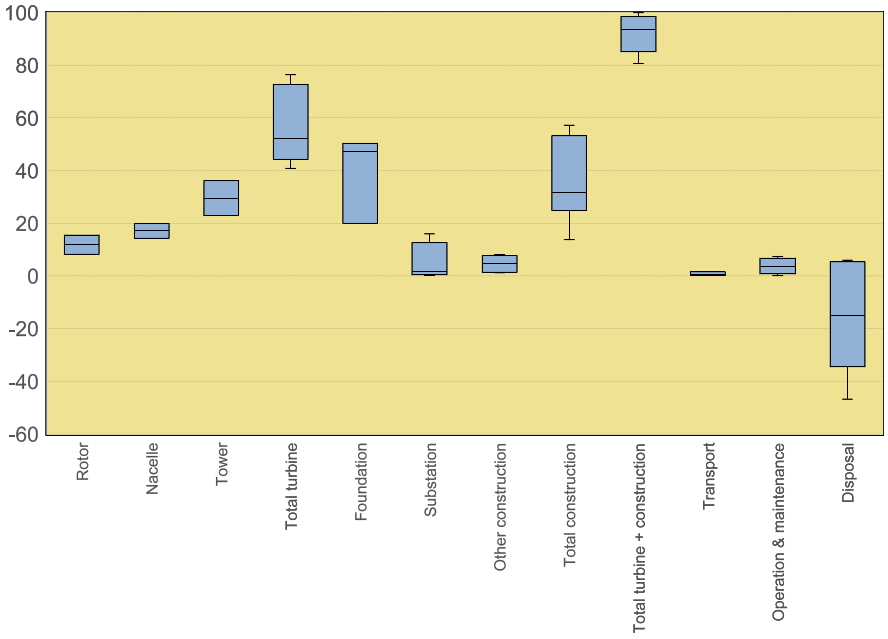

FIGURE 29.8 Proportion of greenhouse gas (GHG) emissions made up by different components, based on data presented in Table A2. Disposal is often calculated to have negative embodied energy due to recycling credits.

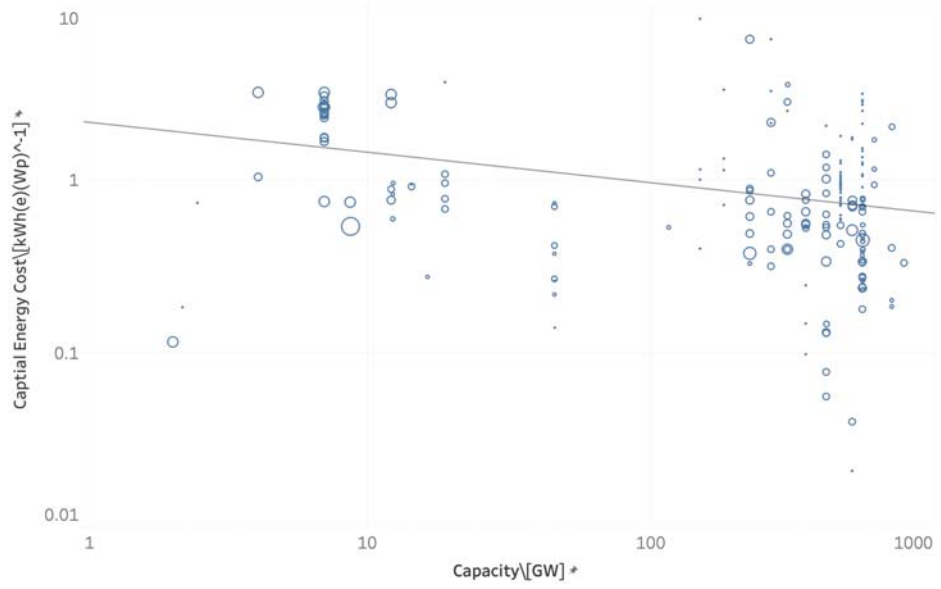

FIGURE 29.9 Estimates of capital energy cost (CEC) [$MJ_p/(W_p)$] as a function of the global installed capacity of wind [MW_p] on a log-log scale with a power curve fitted to the data. The sizes of the points represent the rated power. CEC decreases as the installed capacity increases.

29.5.7 Net energy trajectory of the global wind industry

Combining data on CEC and EPBT (including learning effects, see Section 29.5.6), as well as global wind industry capacity factors 21.2 and growth rate of installed capacity (see Fig. 29.1), we can determine the fractional reinvestment in each year. Combining these annual values, we can develop the net energy trajectory for the global wind industry, as shown in Fig. 29.11.[6]

As can be seen, both the onshore and offshore wind industries are operating with low fractional reinvestment. The onshore industry currently has a growth rate of around 11% $year^{-1}$ and wind turbines have an $EPBT_e$ of around 0.1 years, giving $f_{ON} = 1\%$. The offshore wind industry is currently growing more rapidly at a rate of around 60% in the previous year. and has a higher EPBT (since less offshore capacity has been installed) giving a higher fractional reinvestment, $f_{OFF} = 9\%$.

6. It is worth noting that these values are based on a capacity factor of 25%. In reality, offshore wind farms tend to have higher capacity factors (more like 35%−40%), so are likely to have shorter EPBT and correspondingly lower fractional reinvestment.

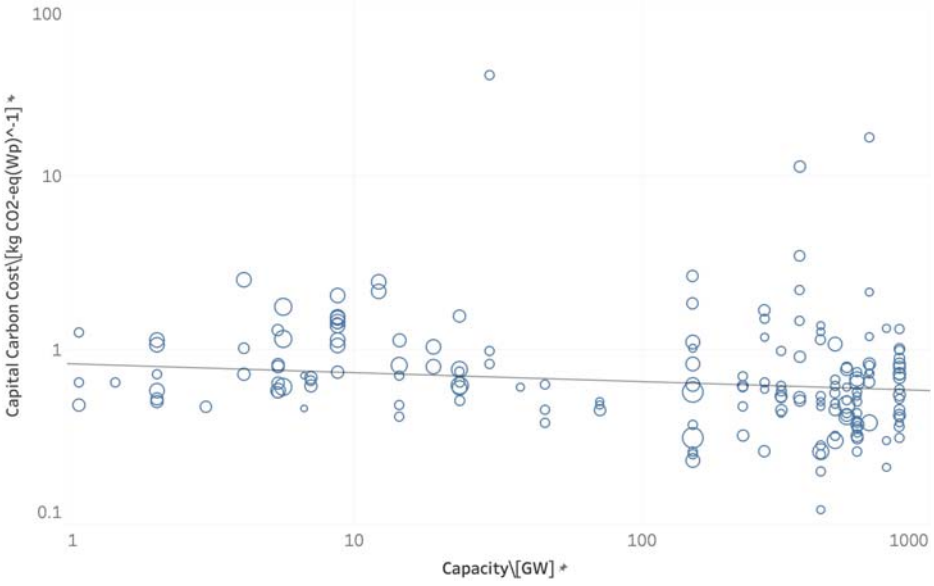

FIGURE 29.10 Estimates of capital carbon cost (CCC) [CO_2-eq/(W_p)] as a function of the global installed capacity of wind [MW_p] on a log-log scale with a power curve fitted to the data. Here, the turbine power rating is restricted to utility-scale, that is, above 1000 kW. Sizes of the points represent the rated power. CCC decreases as the installed capacity increases.

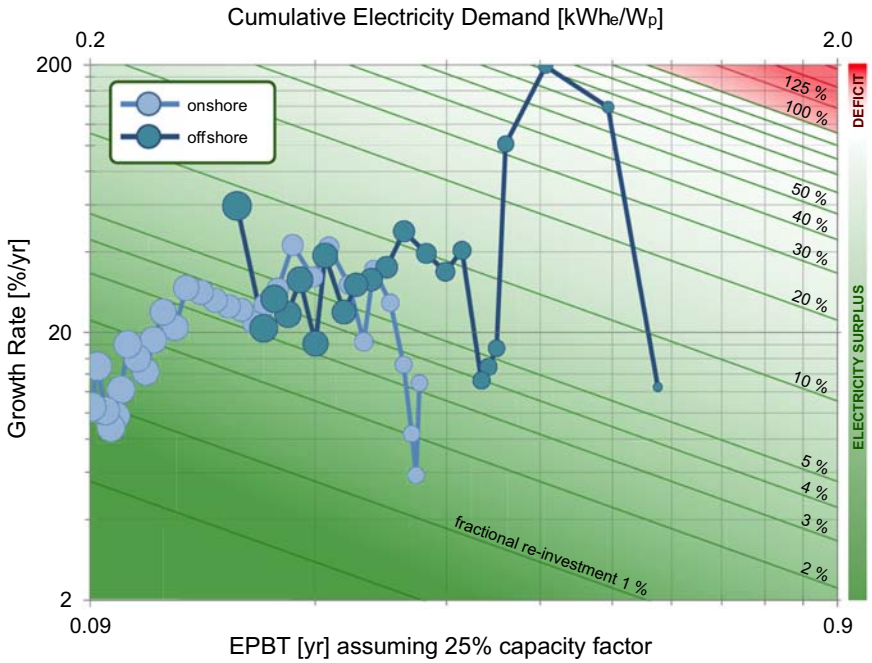

FIGURE 29.11 Net energy trajectory for the onshore and offshore wind industries between 2000 and 2021.

29.5.8 Net carbon trajectory of the global wind industry

Similarly to the net energy analysis in the previous section, we can calculate the fractional carbon emissions of the onshore and offshore wind industries based on CCC, CPBT (including learning rates discussed in Section 29.5.6) growth in installed capacity, the average capacity factor, and an offset of wind-generated electricity at the global average carbon intensity of 475 g CO_2/(kW h).

Bringing all of these annual values together, we can develop the net carbon trajectory for the global wind industry, as shown in Fig. 29.12. The onshore industry currently has a growth rate of around 11% year^{-1} and onshore wind turbines have a $CPBT_e$ of around 0.4 years, giving $f_{ON} = 4\%$. The offshore wind industry is currently growing more rapidly at a rate of around 60% in the previous year. and has a higher CPBT of 0.5 years, giving a higher fractional reinvestment, $f_{OFF} = 27\%$.

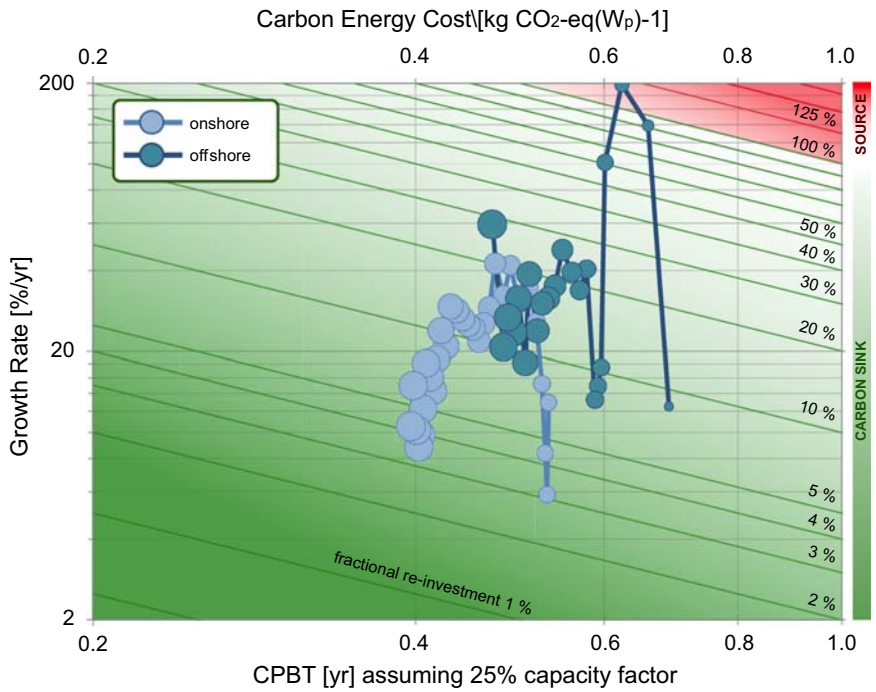

FIGURE 29.12 Net carbon trajectory for the onshore and offshore wind industries between 2000 and 2021.

29.6 Conclusions

The results of a meta-analysis of energy requirements (CED) and carbon emissions (carbon "cost," CC) for wind electricity production technologies has been presented. To facilitate the utility of this information, the metrics presented, CEC and CCC, as well as LCEC and LCCC are direct analogies of financial metrics commonly used to characterize electricity production technologies, overnight capital cost, and LCOE, respectively. The meta-analysis also determined another commonly used metric for assessing wind turbines, EPBT, and calculated an analogous metric CPBT based on an assumed offset for wind-generated electricity at the global average carbon intensity of electricity of 475 g CO_2/(kW h).

The results showed a large variation in both CEC and CCC, as well as LCEC and LCCC. We also presented a breakdown of CED and CC by major component/life cycle phase, which also showed a large range between studies. Disposal had the highest variation comprising between 22% and negative 50% of energetic and 10% to negative 50% of carbon costs if recycling credits were included.

Analyzing trends in the data showed that both CEC and CCC decrease as a function of global installed capacity with a learning rate of around 11% for energy costs and 4% for carbon costs. This compares with a learning rate in the PV industry of over 20% [15,21].

All of this information was combined to calculate the net energy trajectory of the global wind industry. The industry is clearly a net electricity provider and provides a net carbon benefit, both in terms of onshore as well as offshore installations, with both having fractional reinvestment rates of below 50%. In fact, the industry could be growing at over ten times its current rate and still be providing net electricity to society, over and above providing sufficient energy to meet its own needs.

Acknowledgments

The author would like to acknowledge financial support from the Environmental Engineering and Earth Sciences department at Clemson University.

Appendix A: Meta-analysis results

Data from the metaanalysis can be found at the following link: https://e3sa.sites.clemson.edu/Projects/WindTech.html

Appendix B: Contribution per component

(Tables A1 and A2)

TABLE A.1 Percentage of cumulative energy demand (CED) made up by different components.

Reference	Rotor	Nacelle	Tower	Total turbine	Foundation	Substation	Energy storage	Other buildings	Construction	Total turbine + construction	Transport	O&M	Disposal
	[%]	[%]	[%]	[%]	[%]	[%]	[%]	[%]	[%]	[%]	[%]	[%]	[%]
[96]	18.2	15.9	22.7	56.7	34.9	0.4		1.2	36.6	93.3	0.7	6.0	− 27.2
[97]	44.9	12.8	23.2	80.9	12.3				12.3	93.1		6.9	
[45]			10.4	10.4			74.3		74.3	84.7	13.4		
[98]	15.0	27.0	25.0	67.0	29.0	1.0			30.0	97.0	1.0	1.0	
[99]	7.2	11.0	46.8	65.0	19.8				19.8	84.8	7.0	5.5	3.1
[99]	5.1	23.6	46.0	74.7	9.7				9.7	84.4	7.0	5.5	3.1
[12]	3.6	4.3	9.0	16.9							38.2	15.1	23.1
[12]	5.2	6.2	13.1	24.5							11.5	26.2	8.7
[12]	3.3	4.0	10.7	18.0							11.3	19.6	8.7
[12]	3.3	3.9	8.3	15.5							13.7	27.5	10.3
[100]											32.5	6.5	
[100]											38.0	5.5	
[100]											39.0	3.0	
[100]											44.0	3.0	
[101]	7.8	23.5	31.2	62.6		0.2			0.2	62.8	0.4		− 46.7
[10]	16.0	16.0	25.0	57.0	15.0				29.0	86.0		7.0	− 20.0
[102]	18.0	15.0	24.0	57.0	15.0				28.0	85.0		7.0	− 20.0
[103]	22.0	20.0	23.0	65.0	10.0				23.0	88.0		5.0	− 22.2
[104]	21.0	19.0	27.0	67.0	9.0				21.0	88.0		4.0	− 33.3
[105]	18.5	16.5	33.5	68.5	10.5				20.5	89.0		4.0	− 33.3
[106]	18.0	16.0	24.0	58.0	9.0				30.0	88.0		6.0	− 33.3
[106]	23.0	22.5	22.0	67.5	7.5				21.5	89.0		5.0	− 25.0
[107]				53.7					42.7	96.3		3.7	− 49.4
[107]				60.4					13.6	74.0		26.0	− 44.5
[107]				45.0					39.9	84.9		15.1	− 35.8
[27]										87.8	0.5	7.4	4.4

TABLE A.8 Percentage of carbon cost (CC) made up by different components.

Reference	Rotor	Nacelle	Tower	Total turbine	Foundation	Substation	Energy storage	Other buildings	Construction	Total turbine + construction	Transport	O&M	Disposal
	[%]	[%]	[%]	[%]	[%]	[%]	[%]	[%]	[%]	[%]	[%]	[%]	[%]
[96]	8.2	14.3	22.9	45.4	50.3	0.3		1.2	51.8	97.3	0.2	2.6	−22.3
[27]				76.4					13.7	90.2	0.7	4.5	4.6
[41]				50.5		15.9		1.8	30.2	80.7	1.5	0.1	−46.8
[34]				40.8	47.2	2.5		7.6	57.2	98.0			−15.1
[56]	15.5	19.9	36.1	71.5	20.0	0.8		7.8	28.5	100.0			
[59]				53.4					33.2	86.6		7.4	6.0

References

[1] DOE, Transparent Cost Database, 2012. http://en.openei.org/apps/TCDB/ [accessed 16.12.12].
[2] Koomey J, Hultman N. A reactor-level analysis of busbar costs for us nuclear plants, 1970–2005. Energy Policy 2007;35:5630–42.
[3] GWEC, Global Wind Report 2021, Technical Report, Global Wind En-ergy Council, Brussels, Belgium, 2021 <https://gwec.net/global-wind-report-2021/>.
[4] EIA, International Energy Statistics, <http://www.eia.gov/countries/data.cfm>, 2021.
[5] UN, UN Energy Statistics Database, <http://data.un.org/Explorer.aspx?d = EDATA>, 2021.
[6] Jaganmohan M. Global cumulative installed wind power capacity from 2001 to 2021, <https://www.statista.com/statistics/268363/installed-wind-power-capacity-worldwide/>, 2022.
[7] WWEA, Worldwide wind capacity reaches 744 gigawatts—an unprecedented 93 gigawatts added in 2020. < https://wwindea.org/worldwide-wind-capacity-reaches-744-gigawatts/>, 2021.
[8] Lenzen M, Munksgaard J. Energy and CO_2 life-cycle analyses of wind turbines—review and applications. Renew Energy 2002;26:339–62.
[9] Kubiszewski I, Cleveland C, Endres P. Meta-analysis of net energy return for wind power systems. Renew Energy 2010;35:218–25.
[10] Vestas, Life cycle assessment of electricity production from an onshore V90-3.0 MW wind plant, 2013.
[11] Tong W. Wind Power Generation and Wind Turbine Design. Wit Press; 2010.
[12] Tsai L, An integrated assessment of offshore wind farm siting: a case study in the Great Lakes of Michigan, Ph.D. thesis, The University of Michigan, 2013.
[13] ISO, ISO 14040—environmental management—life cycle assessment—principles and framework, 1998.
[14] Huijbregts MA, Hellweg S, Frischknecht R, Hendriks HW, Hungerbühler K, Hendriks AJ. Cumulative energy demand as predictor for the environmental burden of commodity production. Environ Sci Technol 2010;44:2189–96.
[15] Dale M, Benson SM. Energy balance of the global photovoltaic (pv) industry-is the pv industry a net electricity producer? Environ Sci Technol 2013;47:3482–9.
[16] Singh U, Colosi LM. The case for estimating carbon return on investment (croi) for ccus platforms. Appl Energy 2021;285:116394.
[17] IEA, Global energy & CO2 status report 2019 <https://www.iea.org/reports/global-energy-co2-status-report-2019/emissions>.
[18] Teem JM, Erda, the option generator. In: Electron Devices Meeting, 1975 International, IEEE, 1975, pp. 275–278.
[19] Marimuthu C, Kirubakaran V. Carbon pay back period for solar and wind energy project installed in india: a critical review. Renew Sustain Energy Rev 2013;23:80–90.
[20] Dale M. A comparative analysis of energy costs of photovoltaic, solar thermal, and wind electricity generation technologies. Appl Sci 2013;3:325–37.
[21] Carbajales-Dale M, Barnhart CJ, Benson SM. Can we afford storage? A dynamic net energy analysis of renewable electricity generation supported by energy storage. Energy Environ Sci 2014;7:1538–44.
[22] Heath G, Mann M. Background and reflections on the life cycle assessment harmonization project. J Ind Ecol 2012;16:S8–11.
[23] Dolan SL, Heath GA. Life cycle greenhouse gas emissions of utilityscale wind power: systematic review and harmonization. J Ind Ecol 2012;16:S136–54.
[24] Carbajales-Dale M. Life cycle assessment: meta-analysis of cumulative energy demand for wind energy technologies. Wind Energy Engineering. Elsevier; 2017. p. 439–73.
[25] Concentrating Solar Power Projects <http://www.nrel.gov/csp/solarpaces/?> [accessed 16.12.12].
[26] Mendecka B, Lombardi L. Life cycle environmental impacts of wind energy technologies: a review of simplified models and harmonization of the results. Renew Sustain Energy Rev 2019;111:462–80.
[27] Li H, Jiang H-D, Dong K-Y, Wei Y-M, Liao H. A comparative analysis of the life cycle environmental emissions from wind and coal power: evidence from China. J Clean Prod 2020;248:119192.
[28] Wang L, Wang Y, Du H, Zuo J, Yi Man Li R, Zhou Z, et al. A comparative life-cycle assessment of hydro-, nuclear and wind power: a China study. Appl Energy 2019;249:37–45.
[29] Wang S, Wang S, Liu J. Life-cycle green-house gas emissions of onshore and offshore wind turbines. J Clean Prod 2019;210:804–10.
[30] Raugei M, Leccisi E. A comprehensive assessment of the energy performance of the full range of electricity generation technologies deployed in the United Kingdom. Energy Policy 2016;90:46–59.
[31] Cao Y, Wang X, Li Y, Tan Y, Xing J, Fan R. A comprehensive study on low-carbon impact of distributed generations on regional power grids: a case of Jiangxi provincial power grid in China. Renew Sustain Energy Rev 2016;53:766–78.
[32] Ozoemena M, Cheung WM, Hasan R, Fargani H. A hybrid stochastic approach for improving uncertainty analysis in the design and development of a wind turbine. Procedia CIRP 2016;56:19–24.
[33] Xue B, Ma Z, Geng Y, Heck P, Ren W, Tobias M, et al. A life cycle co-benefits assessment of wind power in China. Renew Sustain Energy Rev 2015;41:338–46.
[34] Kouloumpis V, Azapagic A. A model for estimating life cycle environmental impacts of offshore wind electricity considering specific characteristics of wind farms. Sustain Prod Consump 2022;29:495–506.
[35] Savino MM, Manzini R, Della Selva V, Accorsi R. A new model for environmental and economic evaluation of Renew Energy systems: the case of wind turbines. Appl Energy 2017;189:739–52.
[36] Atilgan B, Azapagic A. Renewable electricity in Turkey: life cycle environmental impacts. Renew Energy 2016;89:649–57.

[37] Ding N, Pan J, Liu J, Yang J. An optimization method for energy structures based on life cycle assessment and its application to the power grid in China. J Environ Manage 2019;238:18–24.
[38] Mendecka B, Lombardi L, Stanek W. Analysis of life cycle thermoecological cost of electricity from wind and its application for future incentive mechanism. Energy Convers Manag 2018;170:73–81.
[39] Bo Xie J, Xun Fu J, Yu Liu S, Sing Hwang W. Assessments of carbon footprint and energy analysis of three wind farms. J Clean Prod 2020;254:120159.
[40] Ji S, Chen B. Carbon footprint accounting of a typical wind farm in China. Appl Energy 2016;180:416–23.
[41] Liu P, Liu L, Xu X, Zhao Y, Niu J, Zhang Q. Carbon footprint and carbon emission intensity of grassland wind farms in Inner Mongolia. J Clean Prod 2021;313:127878.
[42] Wang L, Wang Y, Zhou Z, Garvlehn MP, Bi F. Comparative assessment of the environmental impacts of hydroelectric, nuclear and wind power plants in China: life cycle considerations. Energy Proc 2018;152:1009–14.
[43] Siddiqui O, Dincer I. Comparative assessment of the environmental impacts of nuclear, wind and hydro-electric power plants in Ontario: a life cycle assessment. J Clean Prod 2017;164:848–60.
[44] Martínez E, Blanco J, Jiménez E, Saenz-Díez J, Sanz F. Comparative evaluation of life cycle impact assessment software tools through a wind turbine case study. Renew Energy 2015;74:237–46.
[45] Fleck B, Huot M. Comparative life-cycle assessment of a small wind turbine for residential off-grid use. Renew Energy 2009;34:2688–96.
[46] Smith C, Burrows J, Scheier E, Young A, Smith J, Young T, et al. Comparative life cycle assessment of a Thai Island's diesel/PV/wind hybrid microgrid. Renew Energy 2015;80:85–100.
[47] Schreiber A, Marx J, Zapp P. Comparative life cycle assessment of electricity generation by different wind turbine types. J Clean Prod 2019;233:561–72.
[48] Ding N, Liu J, Yang J, Yang D. Comparative life cycle assessment of regional electricity supplies in China. Resour Conserv Recycl 2017;119:47–59.
[49] Gao C, Zhu S, An N, Na H, You H, Gao C. Comprehensive comparison of multiple renewable power generation methods: a combination analysis of life cycle assessment and ecological footprint. Renew Sustain Energy Rev 2021;147:111255.
[50] Aberilla JM, Gallego-Schmid A, Stamford L, Azapagic A. Design and environmental sustainability assessment of small-scale off-grid energy systems for remote rural communities. Appl Energy 2020;258:114004.
[51] Simons PJ, Cheung WM. Development of a quantitative analysis system for greener and economically sustainable wind farms. J Clean Prod 2016;133:886–98.
[52] Uddin MS, Kumar S. Energy, emissions and environmental impact analysis of wind turbine using life cycle assessment technique. J Clean Prod 2014;69:153–64.
[53] Zhao X, Liu S, Yan F, Yuan Z, Liu Z. Energy conservation, environmental and economic value of the wind power priority dispatch in China. Renew Energy 2017;111:666–75.
[54] Zhang J, Zhang J, Cai L, Ma L. Energy performance of wind power in China: a comparison among inland, coastal and offshore wind farms. J Clean Prod 2017;143:836–42.
[55] Walmsley TG, Walmsley MR, Atkins MJ. Energy return on energy and carbon investment of wind energy farms: a case study of New Zealand. J Clean Prod 2017;167:885–95.
[56] Nagashima S, Uchiyama Y, Okajima K. Environment, energy and economic analysis of wind power generation system installation with input-output table. Energy Proc 2015;75:683–90.
[57] Stanek W, Mendecka B, Lombardi L, Simla T. Environmental assessment of wind turbine systems based on thermo-ecological cost. Energy 2018;160:341–8.
[58] Danthurebandara M, Rajapaksha L. Environmental consequences of different electricity generation mixes in Sri Lanka by 2050. J Clean Prod 2019;210:432–44.
[59] Kang Gao C, Ming Na H, Hui Song K, Dyer N, Tian F, Jiang Xu Q, et al. Environmental impact analysis of power generation from biomass and wind farms in different locations. Renew Sustain Energy Rev 2019;102:307–17.
[60] Lombardi L, Mendecka B, Carnevale E, Stanek W. Environmental impacts of electricity production of micro wind turbines with vertical axis. Renew Energy 2018;128:553–64.
[61] Greening B, Azapagic A. Environmental impacts of micro-wind turbines and their potential to contribute to uk climate change targets. Energy 2013;59:454–66.
[62] Cherif H, Champenois G, Belhadj J. Environmental life cycle analysis of a water pumping and desalination process powered by intermittent Renew Energy sources. Renew Sustain Energy Rev 2016;59:1504–13.
[63] Sacchi R, Besseau R, Pérez-López P, Blanc I. Exploring technologically, temporally and geographically-sensitive life cycle inventories for wind turbines: a parameterized model for Denmark. Renew Energy 2019;132:1238–50.
[64] Lundie S, Wiedmann T, Welzel M, Busch T. Global supply chains hotspots of a wind energy company. J Clean Prod 2019;210:1042–50.
[65] Nock D, Baker E. Holistic multi-criteria decision analysis evaluation of sustainable electric generation portfolios: New England case study. Appl Energy 2019;242:655–73.
[66] Velez-Henao JA, Vivanco DF. Hybrid life cycle assessment of an onshore wind farm including direct and indirect services: a case study in Guajira, Colombia. J Environ Manage 2021;284.

[67] Kumar I, Tyner WE, Sinha KC. Input-output life cycle environmental assessment of greenhouse gas emissions from utility scale wind energy in the United States. Energy Policy 2016;89:294–301.
[68] Talens Peir'o L, Martin N, Villalba Mendez G, Madrid-L'opez C. Integration of raw materials indicators of energy technologies into energy system models. Appl Energy 2022;307.
[69] Maier M, Mueller M, Yan X. Introduction of a spatiotemporal life cycle inventory method using a wind energy example. Energy Proc 2017;142:3035–40.
[70] Angelakoglou K, Botsaris PN, Gaidajis G. Issues regarding wind turbines positioning: a benchmark study with the application of the life cycle assessment approach. Sustain Energy Technol Assess 2014;5:7–18.
[71] Vargas A, Zenón E, Oswald U, Islas J, Güereca L, Manzini F. Life cycle assessment: a case study of two wind turbines used in mexico. Appl Thermal Eng 2015;75:1210–16.
[72] Wang R, Lam CM, Hsu SC, Chen JH. Life cycle assessment and energy payback time of a standalone hybrid Renew Energy commercial microgrid: a case study of Town Island in Hong Kong. Appl Energy 2019;250:760–75.
[73] Li Q, Duan H, Xie M, Kang P, Ma Y, Zhong R, et al. Life cycle assessment and life cycle cost analysis of a 40 MW wind farm with consideration of the infrastructure. Renew Sustain Energy Rev 2021;138.
[74] Huang YF, Gan XJ, Chiueh PT. Life cycle assessment and net energy analysis of offshore wind power systems. Renew Energy 2017;102:98–106.
[75] Gibon T, Arvesen A, Hertwich EG. Life cycle assessment demonstrates environmental co-benefits and trade-offs of low-carbon electricity supply options. Renew Sustain Energy Rev 2017;76:1283–90.
[76] Elginoz N, Bas B. Life Cycle Assessment of a multi-use offshore platform: combining wind and wave energy production. Ocean Eng 2017;145:430–43.
[77] Martínez E, Latorre-Biel JI, Jiménez E, Sanz F, Blanco J. Life cycle assessment of a wind farm repowering process. Renew Sustain Energy Rev 2018;93:260–71.
[78] Oebels KB, Pacca S. Life cycle assessment of an onshore wind farm located at the northeastern coast of Brazil. Renew Energy 2013;53:60–70.
[79] Wang Y, Sun T. Life cycle assessment of CO 2 emissions from wind power plants: methodology and case studies. Renew Energy 2012;43:30–6.
[80] Al-Behadili S, El-Osta W. Life cycle assessment of dernah (libya) wind farm. Renew Energy 2015;83:1227–33.
[81] Garcia-Teruel A, Rinaldi G, Thies PR, Johanning L, Jeffrey H. Life cycle assessment of floating offshore wind farms: an evaluation of operation and maintenance. Appl Energy 2022;307:118067.
[82] Xu L, Pang M, Zhang L, Poganietz WR, Marathe SD. Life cycle assessment of onshore wind power systems in China. Resour Conserv Recycl 2018;132:361–8.
[83] Kabayo J, Marques P, Garcia R, Freire F. Life-cycle sustainability assessment of key electricity generation systems in Portugal. Energy 2019;176:131–42.
[84] Jung C, Schindler D. Modeling wind turbine-related greenhouse gas payback times in Europe at high spatial resolution. Energy Convers Manag 2021;243:114334.
[85] Raugei M, Leccisi E, Fthenakis V, Escobar Moragas R, Simsek Y. Net energy analysis and life cycle energy assessment of electricity supply in Chile: present status and future scenarios. Energy 2018;162:659–68.
[86] Tallaksen J, Bauer F, Hulteberg C, Reese M, Ahlgren S. Nitrogen fertilizers manufactured using wind power: greenhouse gas and energy balance of community-scale ammonia production. J Clean Prod 2015;107:626–35.
[87] Besseau R, Sacchi R, Blanc I, Perez-López P. Past, present and future environmental footprint of the Danish wind turbine fleet with LCA WIND DK, an online interactive platform. Renew Sustain Energy Rev 2019;108:274–88.
[88] Kouloumpis V, Sobolewski RA, Yan X. Performance and life cycle assessment of a small scale vertical axis wind turbine. J Clean Prod 2020;247:119520.
[89] Ortegon K, Nies LF, Sutherland JW. Preparing for end of service life of wind turbines. J Clean Prod 2013;39:191–9.
[90] Alvarez S, Sosab M, Rubioa A. Product and corporate carbon footprint using the compound method based on financial accounts. The case of Osorio wind farms. Appl Energy 2015;139:196–204.
[91] Stenzel P, Schreiber A, Marx J, Wulf C, Schreieder M, Stephan L. Renewable energies for Graciosa Island, Azores-Life Cycle Assessment of electricity generation. Energy Proc 2017;135:62–74.
[92] Eickelkamp T. Significance of fixed assets in life cycle assessments. J Clean Prod 2015;101:97–108.
[93] Wang M, Yao M, Wang S, Qian H, Zhang P, Wang Y, et al. Study of the emissions and spatial distributions of various powergeneration technologies in China. J Environ Manage 2021;278:111401.
[94] Treyer K, Bauer C. The environmental footprint of UAE's electricity sector: combining life cycle assessment and scenario modeling. Renew Sustain Energy Rev 2016;55:1234–47.
[95] Aso R, Cheung WM. Towards greener horizontal-axis wind turbines: analysis of carbon emissions, energy and costs at the early design stage. J Clean Prod 2015;87:263–74.
[96] Chen G, Yang Q, Zhao Y. Renewability of wind power in china: a case study of nonRenew Energy cost and greenhouse gas emission by a plant in guangxi. Renew Sustain Energy Rev 2011;15:2322–9.
[97] Martínez E, Sanz F, Pellegrini S, Jiménez E, Blanco J. Life-cycle assessment of a 2-MW rated power wind turbine: CML method. Int J Life Cycle Assess 2009;14:52–63.

[98] Demir N, Tąskın A. Life cycle assessment of wind turbines in pınarbąsıkayseri. J Clean Prod 2013;54:253–63.
[99] Guezuraga B, Zauner R, Pölz W. Life cycle assessment of two different 2 mw class wind turbines. Renew Energy 2012;37:37–44.
[100] Noori M, Kucukvar M, Tatari O. A macro-level decision analysis of wind power as a solution for sustainable energy in the usa. Int J Sustain Energy 2015;34:629–44.
[101] Yang J, Chen B. Integrated evaluation of embodied energy, greenhouse gas emission and economic performance of a typical wind farm in china. Renew Sustain Energy Rev 2013;27:559–68.
[102] Vestas, Life cycle assessment of electricity production from an onshore V100-2.6 MW wind plant, 2013.
[103] Vestas, Life cycle assessment of electricity production from an onshore V105-3.3 MW wind plant, 2014.
[104] Vestas, Life cycle assessment of electricity production from an onshore V117-3.3 MW wind plant, 2014.
[105] Vestas, Life cycle assessment of electricity production from an onshore V100-2.0 MW wind plant, 2015.
[106] Vestas, Life cycle assessment of electricity production from an onshore V112-3.3 MW wind plant, 2015.
[107] Kabir M, Rooke B, Dassanayake G, Fleck B. Comparative life cycle energy, emission, and economic analysis of 100 kw nameplate wind power generation. Renew Energy 2012;37:133–41.

Chapter 30

Wind turbines and landscape

Marc van Grieken and Beatrice Dower
MVGLA, Comrie, Perthshire, United Kingdom

30.1 A passion for landscape

Most people are passionate about landscape, whether as a source of inspiration for paintings or poetry; as the backdrop of a favorite walk; in providing the growing environment for food and livestock; as the setting of carefully crafted views; as the context of cultural associations and a timeline back into history; or simply as daily surroundings. Irrespective of whether the landscape has formal recognition as being of outstanding value or quality, changes in the landscape tend to invoke strong feelings and opinions in people. For example a landscape may have statutory protection as a World Heritage Site or National Park (see Fig. 30.1), or be protected by local designations such as special landscape areas in Scotland or areas of outstanding natural beauty in England; or it may be degraded land such as frequently found on the edges of our cities yet valued by people living nearby as local open space.

Onshore wind energy development is one of the measures being taken to combat climate change, and is resulting in rapid changes in our landscapes. In this chapter, we will discuss how wind energy developments affect people's perception of landscape and how the number, composition, and size of turbines that make up a wind farm influence this perception. We will discuss the meaning of landscape and consider how the development of wind farms in the landscape may affect the qualities and values that people attach to the landscape.

30.2 What is landscape?

Governments across the European Union ratified the European Landscape Convention (ELC) in 2000, which is designed to achieve improved approaches to the planning, management and protection of landscapes throughout Europe. It has also put people at the heart of this process. The ELC defines landscape as: "*an area, as perceived by people, whose character is the result of the action and interaction of natural and/or human factors*" [1]. As interpreted in the current UK Guidelines for Landscape and Visual Impact Assessment, "*landscape is about the relationship between people and place. It provides the setting for our day-to-day lives. The term does not mean just special or designated landscapes and it does not only apply to the countryside*" [2,3]. These descriptions confirm that landscape is important to people and therefore changes in the landscape may affect people in different ways.

Particularly in recent years, theories about the importance of landscape have evolved and the significance of the ELC definition is that it has moved thinking about landscape beyond the idea that landscape is only a matter of esthetics and visual amenity. The ELC encourages a focus on landscape as a resource in its own right and therefore not just as the setting for human activity (See Fig. 30.2). Understanding and evaluating landscape allows us to conceptualize our surroundings and consider the effects of introducing developments into our landscapes, and it can contribute to providing a spatial framework for managing landscape change. This enables informed discussion and debate about a wide range of environmental, land use and development issues—including wind farms.

30.3 Changing landscape

The description of landscape in the ELC [1] fully encompasses the changes that a landscape undergoes when humans live in it, aptly captured by Susan and Geoffrey Jellicoe in their book The Landscape of Man: "*Throughout history men have moulded their environment to express or to symbolize ideas − power, order, comfort, harmony, pleasure, mystery*" [4].

Wind Energy Engineering. DOI: https://doi.org/10.1016/B978-0-323-99353-1.00010-4

FIGURE 30.1 Glaciers across the world are retreating due to global temperature increases. Abel Tasman Glacier, Abel Tasman National Park, New Zealand. *Photo: M van Grieken. All rights reserved.*

Landscapes are constantly changing as a result of human intervention, such as intensification of agriculture, the felling of rainforests for cultivation, or the spread of urban development (see Fig. 30.3). Importantly, it is widely accepted that landscapes will change further through climate change. Some of our lands will be lost to the sea, some parts of the world will become arid and other areas may become wetter as a result of natural processes and these changes to our landscapes are among the consequences of climate change that people have limited control over. Notably, however, other significant changes in landscapes will be the result of the measures we take to address climate change.

Drastically cutting CO_2 emissions by reducing reliance on fossil fuels, especially for electricity generation is one of the primary measures to address climate change. This has led to governments across the world setting renewable energy targets to reduce CO_2 emission levels in accordance with the Kyoto protocol [5] and the Paris Agreement [6]. In many countries, the development, construction, and operation of wind farms (both onshore and offshore) are part of the mix of measures taken to address climate change. Introducing a wind farm in any landscape or in the sea (located 'inshore,' i.e., within sight of the land) has effects on the views of the landscape and may affect the perception of the landscape and seascape character and thus in doing so, the wind farm itself contributes to landscape change.

30.3.1 People's opinions

One of the most common comments made by local people who are consulted on a wind energy proposal in their local area is: "*I am all in favour of renewable energy and wind farms but this is not the right place*." Given that the primary

FIGURE 30.2 The Ring of Brodgar: Standing Stones illustrate ancient human activity in the landscape, Orkney, Scotland. *Photo: B Dower. All rights reserved.*

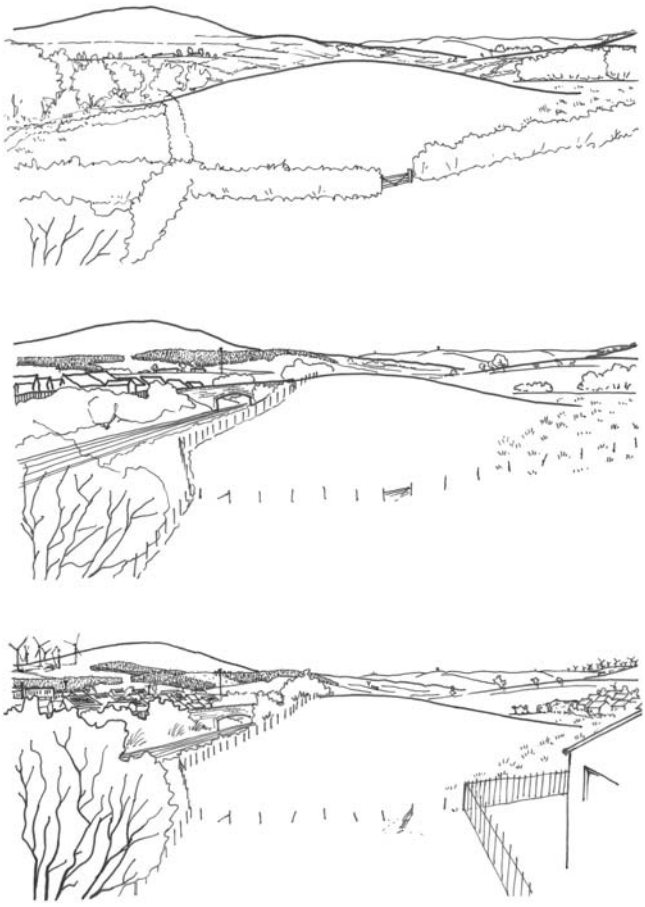

FIGURE 30.3 A changing landscape. *Reproduced with permission from MVGLA.*

FIGURE 30.4 Dounreay nuclear power plant, Scotland (now decommissioned). *Photo: B Dower. All rights reserved.*

concern of most people with respect to wind farms is the effect on landscape, views, and visual amenity, government support or otherwise for this type of development has therefore increasingly become a political issue. This is in itself not unique, as other forms of energy generation invoke equally strong opinions, as may be illustrated by the prolonged debate about new nuclear power plants in the UK or about fracking (Fig. 30.4).

While wind turbines are seen by some people as sculptural objects in the landscape, others see them as industrial monstrosities. Irrespective of this, wind farms are not being constructed for artistic reasons, but are designed and built to generate electricity, and the form of the turbines is driven by aerodynamic rather than sculptural considerations. They may therefore be comparable in scale, but not in function, to large sculptures such as the Angel of the North, near Gateshead, UK (see Fig. 30.5).

Landscape architects recognize that any type of development leads to changes in the landscape and therefore changes to views and visual amenities. Some of these changes resulting from development are very subtle or barely perceptible but other types of development lead to more substantive change in the physical landscape and in the perception of the landscape. The tall nature of modern wind turbines, currently up to around 150−180 m tall for the largest turbines in the UK, and the associated movement of the rotating blades, means that they are potentially visible from great distances: in some landscapes and visibility conditions up to 50−60 km.

Landscape architects describe the likely change in landscape by using readily recognizable terminology that will resonate with most people. Varying degrees of wind energy developments in the landscape can be described as ‘landscape without wind farms’; ‘landscape with occasional wind farms’; ‘landscape with wind farms’; and for the most developed landscapes ‘wind farm landscapes’ (see Fig. 30.6). Such terminology is not unique to wind energy development and may equally apply to, for example, coniferous plantations: ‘landscape without forest,’ ‘landscape with occasional forest,’ and ‘forest landscape.’

It is clear that landscapes are constantly changing, as a consequence of urban development; changes in farming practices; land use planning policies; and indeed as a consequence of wind farm development. Rather than ‘standing on the side lines’ and reactively responding to the effects of wind farms, we need to proactively debate and decide which landscapes are more suitable and capable of accommodating wind energy development and which landscapes are more vulnerable to losing their unique qualities. In our view, it is increasingly necessary to take control with respect to which landscapes can accommodate wind farm developments, and we must intentionally design how these landscapes will change in the future with wind energy development that is an essential part of our response to climate change.

FIGURE 30.5 The Angel of the North, near Gateshead, UK. *Photo: B Dower. All rights reserved.*

FIGURE 30.6 Wind farms can be seen to be a defining feature of this landscape. *Photo: M van Grieken. All rights reserved.*

30.4 Technological advancement

Wind energy is increasingly making a substantial contribution to our energy supply, even since the first edition of this chapter in 2017, and it will continue to increase markedly in the (relatively) short term of the next 25−50 years. In that timescale, it is possible that new technologies will come on stream that will potentially replace wind power, and may ultimately lead to the removal of wind turbines from our landscapes. The landscape implications of those new technologies may be similar or completely different from the changes that we see as a result of wind energy development.

There is plenty of evidence from history to demonstrate how the process of technological advancement led to the introduction and subsequent abandonment of power generation industries that have had a major effect on the landscape. In the 20th century, we saw the effect of the transition from coal-fired power stations to gas-fired power stations. The introduction of a very large coal-fired power station near Didcot raised considerable landscape and visual concerns in 1965. Sue and Geoffrey Jellicoe wrote: "*The cooling towers of Didcot Power Station, Berkshire, are symbolic of energy waste, destructive to the human scale and an intrusion into a famous rural vale that was almost universally resented*" [4]. Didcot was demolished between 2014 and 2020, but Drax Power Station in North Yorkshire, built in 1974, now runs largely on biomass fuel.

Wind energy has been harnessed for centuries with wind-driven mills draining the land in the Netherlands or milling grain into flour across the world. Many of these older windmills are now protected as valued historic structures (see Fig. 30.7).

Electricity-generating turbines are more recent and have become increasingly commonplace since the 1990s. Early turbines were relatively small, noisy, and inefficient with low energy yields. In recent years, however, driven by the pressing need for more efficient sources of renewable energy, technological advancement has accelerated rapidly. Modern machines are considerably more efficient, with greater energy yield per unit of swept area, but this has also led to the ever-increasing height and size of both onshore and offshore wind turbines.

The first commercially developed wind farm in Scotland, Hagshaw Hill in South Lanarkshire, used turbines with a hub height of 35 m and a rotor diameter of 41 m (therefore, 55.5 m to blade tip) generating 600 kW per turbine (see also Fig. 30.8). In 2022, planning consent was granted for the replacement of the Hagshaw Hill turbines with new

FIGURE 30.7 A wind-driven corn mill renovated and operated by volunteers. Colorful sails were an art installation, the lower floor was converted into a café. Boechout, Belgium. *Photo: B Dower. All rights reserved.*

FIGURE 30.8 Small, first-generation turbines in Flevoland, the Netherlands. *Photo: M van Grieken. All rights reserved.*

turbines of 200 m to blade tip. Fourteen of the new 6 MW turbines will generate six times as much energy as the original 26-turbine Hagshaw scheme.

The recently installed Westerwind turbines near Urk in the Netherlands have 135 m hub height and blades of 163 m length resulting in a tip height of 198 m, and can generate potentially 7.54 MW each. Notably, part of the Westerwind development is not on land, with the turbines set in the Zuiderzee, the large inland sea within the Netherlands. The offshore turbines of the Westerwind development are 'only' 165 m to tip high.

In the last few years, the most common commercial onshore wind turbine being used in the UK has been in the order of 125–150 m to blade tip, with a generating potential of 2–3.5 MW. 150 m to blade tip has been a 'glass ceiling' threshold as it is the height above which aviation safety lighting is required on tall structures in the UK (Fig. 30.9). However, current applications are usually for greater turbine sizes, with developers no longer limiting turbines to avoid aviation lighting, in the knowledge that turbine models of under 150 m are becoming increasingly difficult to source. This is understood to be because the international market for turbines is for larger machines, such that 'small' machines (and their component parts for maintenance) are being manufactured less. Indeed, several recent projects in Scotland given consent for turbines of about 125–150 m to blade tip have been returned to the consenting authorities with variations seeking to increase tip heights.

Over the last 15–20 years several local planning authorities in the UK have undertaken or commissioned so-called "wind farm capacity studies" trying to ascertain what size of turbine and size of wind farm can be accommodated without substantial landscape character change. These studies are informative with respect to relative landscape sensitivity, but focus on limiting wind farm development and avoiding landscape change. They do not proactively plan or design for the intended landscape change that is needed to accommodate the scale of wind energy required to meet renewable energy targets. Planning for and accommodating more wholescale landscape change through developing substantially larger wind farms with much greater power output and efficiency, as are now required in response to the climate change emergency and increasing electricity demand, requires development of design strategies and policies which are expressly supportive of this type of development and which actively embrace technology and size and scale advancement. However, most landscapes in the UK are subject to conservative strategies aimed at maintaining existing landscape character and 'fitting' turbines into the landscape rather than embracing necessary landscape change. Some would therefore consider that this 'lag' in technology in the UK is due to public objection to large structures in UK landscapes, and the reluctance of consenting authorities to support them for political reasons. While public opinions are changing, with turbines increasingly seen as doing their part towards the climate emergency, there are as yet few consents for very large-scale onshore wind farms in the UK.

Some professionals are of the view that the landscapes of the UK are smaller in scale than landscapes elsewhere in Europe or the world, and that as a result, the UK landscape is less capable of absorbing large turbines. This does not necessarily mean that the scale of the landscape features is smaller, but that the extent of each landscape type is small, and variation across the country is diverse. This is the case in some places but certainly not across the UK as a whole, and similar diversities of landscapes occur elsewhere in Europe and beyond. Different scale landscapes exist across the

FIGURE 30.9 Visible red aviation lights on turbine hubs, Middleton Wind Farm, Scotland. *Photo: B. Dower. All rights reserved.*

UK from the more densely populated parts of England to the less densely populated landscapes in the north and more rural parts of Wales and Scotland. If a country does not have landscapes of the similar extent to the vast plains of the USA or China that can accommodate hundreds of turbines extending for miles, one might ask whether it can only accommodate smaller technologies. The answer to this question depends to some extent on the level of suitability required. While purely considering landscape scale and size an argument can be had in favor of relatively small turbines. In practice, the economics of wind energy developments in the UK and the availability of commercially viable turbines pushes developments toward larger size machines. This is further driven by the observation that the best and most windy locations have been developed and new developments may require taller turbines with larger rotor diameters in order to be economically viable on lower wind yield sites.

Both of these trends, development on lower wind speed sites and the availability of turbines, drive developers towards increasing turbine size.

30.5 The perception of wind farms

There are three primary components of a wind farm that influence the perception of the development by people in the wider area around the wind farm.

First, the height and size of the turbines as objects are important factors. Introducing objects of the height and size currently commonly proposed for commercial scale wind energy development into any landscape represents a unique form of development that people are not necessarily familiar with, although wind farms are becoming increasingly common.

Second, the placement or composition of the individual turbines in different geometric formations greatly influences the perception of the wind farm, with turbines in lines, grids or groups creating strikingly different images.

The third unique aspect of wind energy development is the rotation of the blades, which introduces movements into the view while most landscapes are generally ‘still’ above ground level. The speed of rotation is a function of the size of the rotor (blade length) and the wind speed; with rotation commencing in winds of about 3.5 ms^{-1}, increasing gradually up to a

FIGURE 30.10 Two-bladed turbines create varied visual effects. *Photo: M van Grieken. All rights reserved.*

maximum speed at approximately 11 ms^{-1} wind speed, thereafter maintaining that maximum rotation speed till the turbines are shut down for safety at wind speeds of over 25 ms^{-1}. If the wind speed varies across a site, the speed of rotation can vary between turbines of the same dimensions and can be perceptible in some circumstances. Different rotor sizes have different minimum to maximum rotation speed ranges, and differences in rotation speed can emphasize size differences.

The relevance of movement is particularly evident when viewing two-bladed turbines. When the lower blade passes the tower, either in front or behind, this appears to interrupt the flow of rotation which some people may experience as an on/off effect (see Fig. 30.10).

30.5.1 Height and size

People are accustomed to proposals for new developments in their local landscape and in general most proposed developments are designed to limit landscape change and to provide as good a fit as possible to the host environment. For example, housing developments in rural areas tend to follow the vernacular design and be of a size and scale similar to existing buildings. Likewise, development of a city block in the center of New York may lead to the design of a skyscraper being in keeping with its surroundings.

Early onshore wind energy developments comprised turbines of 35–55 m tall and at this height, there is still a clear visual relationship between the turbine and other objects in the landscape such as trees that may be in the order of 20–30 m tall. Arguably at this height, turbines 'fit' into the landscape. With the increase in absolute height this 'connection' between the turbine and existing landscape features is broken: a 125 m turbine does not relate to the vertical dimension of common landscape features we humans are familiar with. Arguably this disparity increases with turbines of 150–198 m, but in fact, many people are incapable of readily estimating the actual height of turbines in excess of 100 m, because we are not used to those sorts of dimensions. This introduces a further factor that may influence people's response, namely the 'sense of scale' and a desire to relate the height of an object to something we know. Objections to wind farms often include references to the height of the proposed turbines relative to other known features in order to illustrate at these turbines are out of scale and therefore out of place. Some people also feel overawed when they know that turbines of a wind farm are similar or taller than, for example, the London Eye (135 m) or Salisbury Cathedral spire (123 m).

FIGURE 30.11 The height and size of these turbines is difficult to estimate despite the presence of clear scale indicators such as trees and pylons. *Photo: B Dower. All rights reserved.*

However, the actual ability to estimate the height of an object in the landscape depends on the availability of scale objects, the local context, and importantly on perspective. This is illustrated in Fig. 30.11. Furthermore in our experience, rather than absolute height, the predisposition of the observer to seeing wind turbines in the landscape is also an important factor in how he or she will perceive height. Since 2017, public awareness of the need to act over climate change has increased and there is a more widespread acknowledgment that renewable energy is needed. This has driven an increased level of understanding, if not acceptance, that wind farms are a necessary part of our landscapes.

30.5.2 Composition

Wind farms comprise more than one turbine. In the US and China, there are some wind farms with several hundred turbines, but in Western Europe, most wind farms comprise of 10−50 turbines. The placement of a number of towers in a group formation or in a grid or in a straight, curving or random line leads to a composition of objects which can be observed by people from different angles (see Fig. 30.12). Geometric layouts create very formal compositions and the effects of stacking and perspectives are predictable. Groupings or irregular layouts have less predictable compositional effects, and yet can be designed to relate to varied landform of a site, and arranged as a balanced array from key viewpoints or viewing directions.

Turbines must be separated from each other for safety and to avoid turbulence that reduces yield and causes additional wear and tear. This means that the turbines making up a wind farm must be spaced out, with distance increasing with increasing rotor diameter. Typically turbines have spaced a minimum of 6 times rotor diameter (some developers require 7 rotor diameters) from each other in the prevailing wind direction and 4 or 5 times across the wind. This represents a unique design challenge: four turbines with 100 m rotor diameters would be at least 600 m by 500 m apart. While the actual footprint of a turbine is quite small, the land taken per typical commercial-sized turbine (90−110 m rotor diameter) is therefore in the order of 30 hectares! This is illustrated in Fig. 30.13.

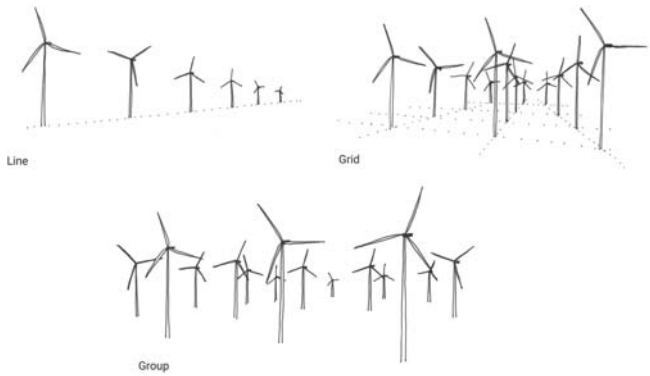

FIGURE 30.12 Lines, grids, and groups of turbines create different compositional effects. *Reproduced with permission from MVGLA.*

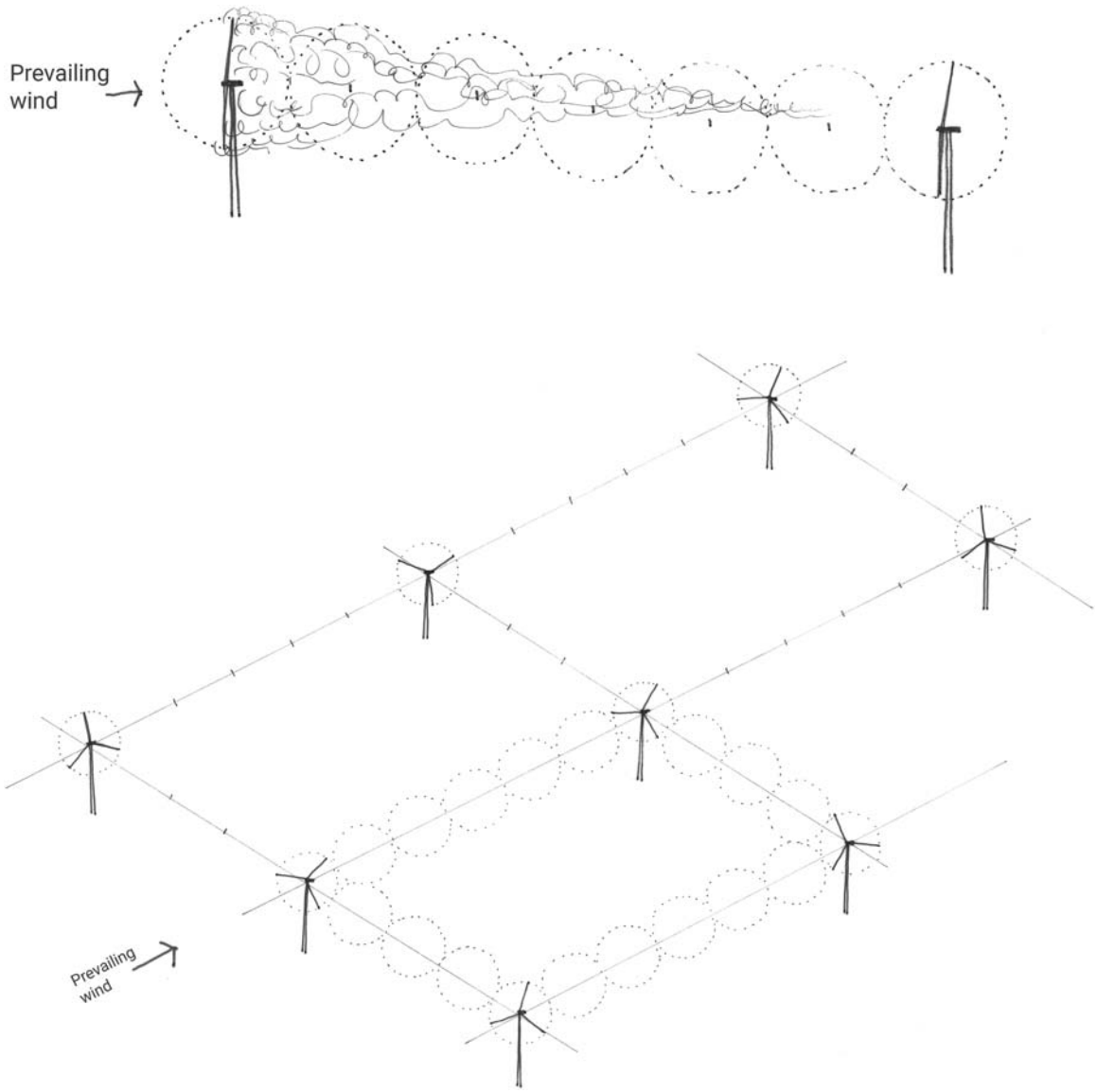

FIGURE 30.13 Turbine separation requirements take account of wake turbulence. *Reproduced with permission from MVGLA.*

30.5.3 Movement

The movement of the blades, especially when seen from greater distances, may be the primary factor for a wind turbine being noticed in the landscape. It is an instinctive defensive reaction to look at moving objects in our peripheral vision. There are different aspects to this movement: the movement of the blades themselves; the rotation of the turbine to follow the direction of the wind; and the extent of the turbine that is visible to the observer. The diagrams in Fig. 30.14 illustrate:

- a turbine which is visible in full;
- a turbine where the tower is largely hidden but the hub or nacelle is visible and therefore one or two of the blades are fully visible at any one time;
- a turbine that is largely hidden, with only part of a blade visible.

In the second scenario, people will perceive a full turbine even if they cannot see the full object, because the brain completes the picture. In the third scenario, we do not necessarily perceive the whole wind turbine and the movement of the blade can be disconcerting if it is seen as having a "windscreen wiper" effect (see Fig. 30.15).

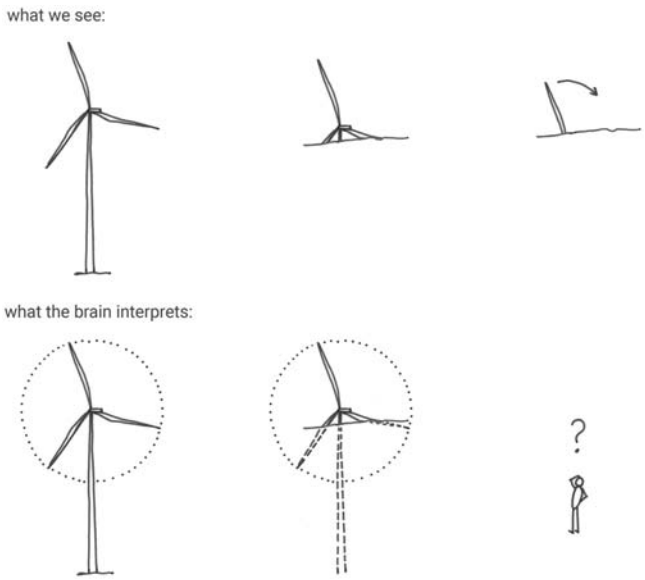

FIGURE 30.14 The proportion of a turbine visible affects our interpretation of it. *Reproduced with permission from MVGLA.*

FIGURE 30.15 An isolated blade tip creates a windscreen wiper effect. South Ronaldsay, UK. *Photo: B Dower. All rights reserved.*

30.6 Landscapes with power generation objects

As discussed in the introduction to this chapter, some landscape changes cause strong feelings, particularly when change is man-made, and none so more than for the industry of power generation. Coal mining, quarrying, oil refineries, power stations, hydroelectric dams, wind farms, fracking, and solar panels on agricultural land are among the types of development that trigger strong responses [7]. Some of those responses are influenced by the predisposition of the observer to the type of development proposed: people who are predisposed to supporting nuclear power and are of the view that wind farms are a waste of time may have strong negative responses to seeing wind turbines in the landscape, yet be more accepting of views of a nuclear power station. Opponents of nuclear power will not just 'see' the building housing the nuclear reactor but will also view this object as a facility they disagree with or are frightened of.

Current Scottish guidance on siting and designing wind farms points out that "*People's responses to wind farms vary—to some a wind farm may seem to dominate its surroundings, while others may view it as an exciting, modern addition with symbolic associations with clean energy and sustainability*" [8]. Opinions on wind energy have evoked strong reactions: "*Any windmill will wreck the scenery, it's what the Scots deserve if they want their countryside wrecked*" (Sir Bernard Ingham, former press officer for Margaret Thatcher [9]), though the younger generation are more imaginative: "*I can see a wind farm from my house, I think they look like angels*" (Jessica Dalgleish, age 9 [10]). Jessica has since had one of those "angels" named after her. Elsewhere, turbine have been given names: "*Gigha Wind Farm was the first community-owned project to be connected to the National Grid, and the turbines are locally known as the Three Dancing Ladies - Faith, Hope and Charity*" [11] (see Figs. 30.16 and 30.17).

It is important to be aware of these personal views and opinions with respect to seeing wind farms in the landscape. This is one of the most visible forms of renewable energy generation, as wind turbines are large, moving structures that have been put in prominent places seen by many people, while other renewable energy technologies such as biomass plants, hydro schemes and wave or tidal schemes are less visible and less frequent. Wind farms can be seen from long distances, and are becoming sufficiently numerous that they are unavoidably noticeable in some parts of the world.

With the increase in the number of wind energy developments in our landscapes, people's views, especially of those opposed to this type of development, have been increasingly vocal and planning decisions relating to wind power developments have been increasingly adversarial. In recognizing that personal opinions vary, it is therefore important that landscape and visual impact assessments that are undertaken as part of wind farm planning applications remain professionally objective, neutral, and remain free from the personal opinion of the assessor. The assessments need to present an impartial, well-reasoned, and logical evaluation of the effects of the proposed wind farm, so that they can inform the decision maker of the likely material effects of the proposed development, which can then be balanced (by the decision maker) with the policy context and the need for action against climate change.

Since the declaration of "climate emergency" by many countries since 2019, there has been growing awareness of the need for renewable energy, which will, slowly, lead to an acceptance that wind farms will have to be present in our landscapes as part of the efforts to curb climate change. However, planning decisions are still made in the context of out-of-date written planning policies, which often predate climate emergency declarations, and need to be updated to reflect the current situation and the current appetite for renewable energy generation.

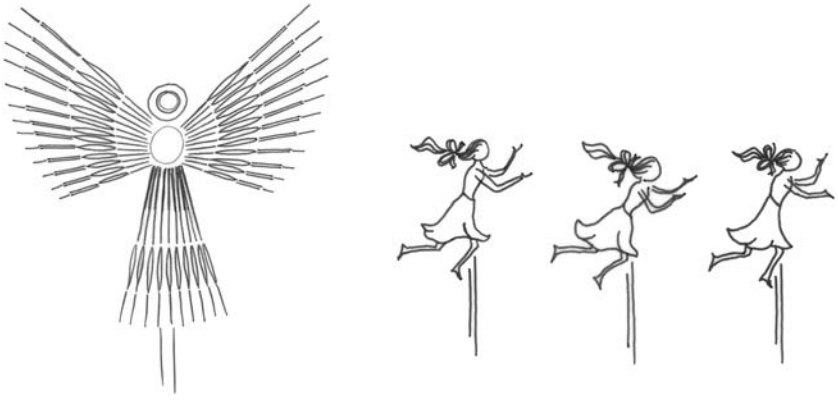

FIGURE 30.16 Turbines have been described as angels or dancing ladies. *Reproduced with permission from MVGLA.*

FIGURE 30.17 Wind Flower and Blade Song are two named turbines on North Uist, Scotland. *Photo: B Dower. All rights reserved.*

30.7 What are the effects of wind farms on our landscape?

Wind farms have a range of potential effects on our landscape, including direct effects on the site on which the turbines are built, effects upon character and effects on views and visual amenity of the local area. It is common practice to evaluate the likely effect of wind energy proposals on our landscape by considering effects on views and visual amenity as distinct from effects on the landscape fabric and its character. These latter effects are called landscape effects.

30.7.1 Landscape effects

Wind turbines alter the landscape by introducing large moving structures above ground level, as well as tracks and other infrastructure elements at ground level. Direct effects include the loss of existing land uses, such as arable or grazing land, forestry, etc. as a direct consequence of the construction of tracks, substation, works compounds, turbine foundations and other physical components of the wind farm (see Figs. 30.18 and 30.19). The power from each turbine needs to be cabled to an on-site substation from where it is exported to the National Grid: ground disturbance also occurs along buried grid connection routes. Track and cable route construction may involve the removal of features such as hedge or wall sections, and substations may need new screening planting. Wind farms on forested land commonly require complete or partial felling of plantations.

These changes directly affect features in the landscape at a local level, but can also affect landscape patterns. Landscapes with a simple pattern of rectilinear fields or open unenclosed moorland can be greatly affected by meandering tracks that do not respond to field boundaries or other existing features. Other more complex landscapes may be able to accommodate the development better, but may also become overwhelmed by it.

While the ground level land-take is small, and land uses can largely continue below the turbines (with the exception of forestry), the perception of the character of the landscape changes. An open, undisturbed moorland area would be altered to a wind energy generating site with areas of moorland between the tracks and turbines. The introduction of an industrial layer to the landscape is a greater change in some environments than in others. Lowland, settled landscapes where man-made features are more common, can potentially accommodate wind turbines without as much perceived change to the character of the landscape as remote undisturbed landscapes. However, settled landscapes have more

FIGURE 30.18 Newly constructed tracks cause ground disturbance. *Photos: M van Grieken. All rights reserved.*

FIGURE 30.19 Tracks, transformers, and meteorological mast are visible infrastructure elements, Braes of Doune Wind Farm, UK. *Photos: M van Grieken. All rights reserved.*

FIGURE 30.20 Trees cause turbulence that reduces yield. *Reproduced with permission from MVGLA.*

potential objectors living locally, and while remote landscapes often have better wind resources, they are also often more environmentally sensitive.

Commercial forest plantations are man-made land use areas, and are not as sensitive to development as open areas. However, forest trees cause turbulence above the canopy, which adversely affect the performance of the turbines. Because of this, manufacturers recommend that there should be a significant clearance between the lowest point of the swept circle and the tops of the trees (see Fig. 30.20). This means that full-grown forest trees are too tall to be allowed to grow below the turbines in most circumstances, and trees must be felled and the land left bare, or replanted with trees that must be felled early, before they grow too high. An alternative is to increase tower heights to lift the rotors out of the affected zone, or to allow turbines to be constructed in small clearings called 'key holes' in retained forest plantations.

An important consideration when considering effects on landscape is a perception of its character, and how the character of the landscape is affected or changed by introducing wind farms or turbines.

That turbines should 'fit' in the landscape has long been a recommendation with a view to minimizing landscape change. If turbines are in a similar height range to trees and buildings, it is possible to say that these can 'fit' in the landscape as features of similar scale to those existing. Turbines over 50−80 m to tip, however, can no longer be seen as fitting with other more human-scale elements. This is becoming more of an issue with turbines taller than 125 m and

certainly with turbines up to 200 m. In many places, turbines of this size will be perceived to be 'out of character' partly because we are unfamiliar with the size and height of these structures.

This poses unique challenges for the design of wind farms. It requires a different approach, recognizing that people find it hard to gauge the size of very large objects and may be overawed when they know the physical dimensions. Designing structures of a height and size very much larger than trees or buildings requires an approach that recognizes that they should be designed to be viewed from afar as well as from nearby. Indeed most views of a wind farm may be from far away.

30.7.2 Visual effects

Of interest to most people are the effects of wind farms on views and visual amenity. Visual effects of wind turbines relate to the appearance of the turbines, either as a single object or as a group of objects arranged as a wind farm when seen from different places within the surrounding area. Key factors in the assessment of visual effects are the number, size, scale, and composition of the turbines in a view. The wind farm may be described with reference to the prominence of turbines in the view, and what role the wind farm would have within the view, perhaps as a new focal feature or as a peripheral element on the horizon. Description of the composition of a wind farm may include references to the group of turbines having a 'balanced' appearance, and whether certain turbines appear separated from the main group as 'outliers' when seen from certain angles. Visual effects are normally assessed from representative locations such as popular scenic viewpoints or places where people stop to admire the view, as well as from settlements and places where people congregate. The potentially eye-catching effect of a moving object such as the rotation of turbine blades means that turbines are more noticeable than still structures, and they may affect the sense of tranquillity and stillness in remote landscapes. Conversely, the movement of turbines close to urban areas or within industrial areas can fit well with the perception of busy urban landscapes.

30.7.3 Landscape and visual effects

Although landscape and visual effects tend to be assessed separately and considered as different aspects of introducing turbines in our landscape, there is a clear relationship between the two: visual influence of turbines in a certain landscape will have an effect on how people perceive its character, and the loss of landscape features, for example, the felling of woodland, clearly also has visual effects. Landscape and visual effects may diverge, however, when more unique and rare qualities and perceptual aspects are being considered. In Scotland, this is the case when considering potential effects on so-called 'wild land.' 'Wild land' has been mapped in Scotland based on a systematic evaluation of aspects and qualities such as remoteness, naturalness, absence of human influences (such as telecommunication masts, powerlines, commercial forestry, etc.), and a sense of isolation. These areas of 'wild land' are neither generally accessible nor accessed: they are 'wild' because of the scarcity or absence of human influence. The potential effects on 'wild land' are therefore not experienced by being there, but rather by imagining the turbines in places where there are no other human artifacts or humans.

30.8 Mitigation

It is not possible to avoid all adverse effects on landscape and visual amenity of wind energy proposals, and all onshore and offshore wind energy developments visible from the land will have a number of adverse effects. In general, wind farms are designed to appear balanced and logical in terms of grouping, and to minimize the extent and number of significant effects while optimizing the generation capacity.

The design of a wind farm is critical to the appearance of the wind farm and its relationship with the landscape it is in. Wind farms should be designed with heed to the overall appearance of the development and how it relates to the existing pattern of the landscape. Structures can be placed in a landscape in ways that either detract or enhance the landscape: referring again to the cooling towers of Didcot Power Station, Berkshire: "*The cooling towers were re-composed from the purely functional into the picturesque so agreeably that horror at their presence is mitigated by an appreciation of their grandeur – gigantic follies composed like gods in converse*" [4].

In large flat open and geometric landscapes, such as the Fens in England or the polders in the Netherlands, formal geometric compositions of turbines in lines or grid formation, reflecting the underlying landscape pattern, may be most appropriate in terms of 'built-in' mitigation (see Fig. 30.21). In gently rolling uplands, a loose grouping may be more suitable (see Fig. 30.22), while in a landscape comprising of ridges, it may be appropriate to follow the ridge lines.

FIGURE 30.21 A geometric composition in a formal Dutch landscape. *Photo: M van Grieken. All rights reserved.*

FIGURE 30.22 An informal layout in rolling upland, Clyde Wind Farm, UK. *Photo: B Dower. All rights reserved.*

30.8.1 Strategic approach

When designing a wind farm it is important to ask the question to what extent the proposed wind farm will induce landscape change, and whether this change will mean that the landscape crosses a threshold, perhaps from a 'landscape with wind farms' to a 'wind farm landscape.' If this is the case, the designer needs to decide whether or not the development should be contained to avoid crossing that threshold, or whether it could be enlarged in order to maximize energy yield, given that the landscape change is inevitable.

To date, the approach to wind farm developments in the UK landscapes has been to minimize and limit landscape change, but this has led to subtle erosion of landscape character in many landscapes, and a gradual, reluctant response to increases in turbine size. An alternative, more proactive approach might have been (and might yet be) to allow more change in some areas, using larger turbines in larger scale landscapes and maximizing energy yield while minimizing the number of areas affected. With the existing, apparently haphazard, scattering of small groups of turbines with relatively small turbines across wide areas of the UK landscape, it is difficult to see a way forward toward a more coherent strategic approach without considerable effort in collaboration and removal of existing schemes to replace them with larger turbines as part of a wider development strategy. There are opportunities in the medium term, however, when wind farms come to the end of their operational lives, to redesign new wind farms for the same sites, a process known as repowering. If repowering can be done with a proactive approach taking in the larger turbine sizes available at the time, and exchanging a number of smaller developments with fewer, larger, well-designed developments, the landscape, and visual effects may be no more than before, in fact there may be improvement through reducing the 'clutter' of lots of smaller turbines, and the energy yields will certainly be considerably higher.

It is interesting to note that in the municipality of Zuid Flevoland in the Netherlands, the Westerwind Wind Park, owned by a collaboration of around 200 farmers and local residents, will comprise 83 new turbines with tip heights of up to 220 m, that will replace the current 220 turbines and generate almost three times the amount of electricity [12].

In the longer term, it is possible that wind turbines are a temporary measure, and as technology develops, they will probably be phased out in favor of some other, more efficient form of renewable power generation. In 25−50 years, it is possible that landscape architects will be designing new landscapes with new technologies while taking out some of the wind farms. Perhaps the composition of these new structures could be the emphasis for design, rather than the avoidance of landscape and visual effects.

30.9 Conclusion

The landscape around us is a valued resource and changes to it evoke passionate responses. The only constant in a landscape is that it will change. Change is happening through natural processes, human processes, and as a result of our measures to combat climate change. Wind farms are renewable energy technologies that are changing our landscapes, affecting both views and the perceived character of the areas into which they are introduced. The number, size, and composition of turbines in wind farms are the key factors that influence the appearance of a wind farm in the landscape, and how it relates to the landscape of the site. The design of wind farms must take into account the nature of the receiving landscape and the potential effects that a proposal may have on the local area, as well as the technological requirements of the development as a power generating facility.

References

[1] Council of Europe. European Landscape Convention. Council of Europe, 2000.
[2] Landscape Institute and the Institute of Environmental Management & Assessment. Guidelines for Landscape and Visual Impact Assessment. 3rd ed London and New York: Routledge; 2013.
[3] Swanwick C. Land Use Consultants. Landscape Character Assessment for England and Scotland. Countryside Agency and Scottish Natural Heritage. Cheltenham and Edinburgh, 2002.
[4] Jellicoe G, Jellicoe S. The Landscape of Man, Shaping the Environment from Prehistory to the Present Day. London: Thames and Hudson Ltd; 1975. p. 1975.
[5] United Nations Kyoto Protocol to the United Nations Framework Convention on Climate Change, 1998.
[6] Paris Agreement under the United Nations Framework Convention on Climate Change, 2016.
[7] Solar Panels in the Landscape. In: Letcher T, Fthenakis V, editors. A Comprehensive Guide to Solar Energy Systems. London: Academic Press; 2018.
[8] Scottish Natural Heritage, Siting and Designing Wind Farms in the Landscape. Version 3a, 2017.

[9] Sir Bernard Ingham, quoted in The Sunday Herald, 7th April 2002.
[10] Jessica Dalgleish, quoted in The Sunday Herald, 7th April 2002.
[11] Sunday Herald. Gigha: God's island of growth. Published 28 July 2008.
[12] Zuid Flevoland Westerwind Wind Park website <http://www.windparkzeewolde.nl> [accessed 25.04.22].

Chapter 31

Turbulent-boundary-layer trailing-edge noise reduction technologies including porous materials

Francesco Avallone and Daniele Ragni

Faculty of Aerospace Engineering, FPT Department, Wind Energy Section, Aeroacoustics Research Group, Delft University of Technology, Delft, The Netherlands

31.1 Noise sources in a wind turbine

Wind turbine noise is limiting the spreading of wind energy because of both its intensity and pitch, i.e. the characteristic swishing sound. The combination of the two makes wind turbine noise perceived as more annoying than other sources of noise with similar sound intensity [1] and it has a detrimental effect on health [2,3]. Since the pitch of the sound cannot be modified, stringent noise regulations, in terms of maximum acceptable noise amplitude, have been set in place. They limit both the locations where wind turbines can be installed and the day/night operations, therefore, affecting the generated power and the cost of energy [4,5]. For example, the noise limits, expressed in A-weighted continuous equivalent sound level (LAeq), set by several countries are reported in Fig. 31.1 [6,7]. Since noise regulations vary per country and per area, this further challenges the industrial development of wind turbines that are optimal for a large market share.

Wind turbine noise can be split into mechanical and aerodynamic noise. The former is generated by mechanical components such as the gearbox and the generator, while aerodynamic noise is generated by a flow interacting with an aerodynamic solid body. Although mechanical noise is several orders of magnitude louder than the aerodynamic one for a poorly maintained machine, periodical inspections and refurbishment of the inner turbine insulation are typically planned to keep the drive-train silent during the full life-span of the machine. Examples of aerodynamic noise are inflow-turbulent noise and airfoil-self noise. The former refers to the noise generated by a turbulent inflow interacting with an airfoil, while the latter is generated when an airfoil encounters a smooth nonturbulent inflow [8]. For wind turbines, airfoil-self noise is the most relevant.

Brooks et al. [9] identified five airfoil self-noise mechanisms: laminar boundary layer vortex shedding noise, turbulent boundary layer trailing edge (TBL-TE) noise, blunt trailing edge noise, boundary layer separation noise, and boundary layer stall noise. Because of the continuously increasing size of the wind turbine blade radius (i.e., longer than 100 m), the flow over the wind turbine airfoil close to the tip is at a Reynolds number in the order of 10^6, therefore, being turbulent. Then, TBL-TE noise is the dominant noise mechanism in an operating wind turbine. TBL-TE is also the most challenging one to reduce because strongly dependent on the boundary layer characteristics near the trailing edge, that is affected by many parameters such as operational conditions, free-stream turbulence, and blade surface roughness. For a comprehensive review on TBL-TE noise prediction, the reader can refer to Lee et al. [10].

TBL-TE noise is generated by the turbulent boundary layer approaching the trailing-edge of an airfoil, where energy is scattered as sound. It has dipolar features, that is, its directivity pattern has a form of 8 with the region of no-sound in the direction of the airfoil chord; it scales with the Mach number to the power of 5 (or 6), thus being dominant at low Mach numbers with respect to other noise sources such as the ones in the turbulent wake of the wind turbine that scale with the Mach number to the power of 8 [11]. Because of the Mach number dependence, TBL-TE noise is dominant toward the tip of the blades as experimentally showed by Oerlemans et al. [12]. They performed in-field measurements of a G58 wind turbine with a microphone array coupled with conventional beamforming [13]. An example of the measured beamforming map is reported in Fig. 31.2; it shows that aerodynamic noise is the dominant one, with mechanical noise being slightly larger only at about 630 Hz.

Wind Energy Engineering. DOI: https://doi.org/10.1016/B978-0-323-99353-1.00002-5

Standard	Quantity	Area	Time	Background $L_{A90(10min)}$	Limit
ETSU-R-97 England	$L_{A90(10min)}$	No financial Involvement	Day	≤30 to 35 dB	35 to 40 dB
ETSU-R-97 England	$L_{A90(10min)}$	No financial Involvement	Day	> 30 to 35 dB	BKGND + 5 dB
ETSU-R-97 England	$L_{A90(10min)}$	No financial Involvement	Night	≤38 dB	43 dB
ETSU-R-97 England	$L_{A90(10min)}$	No financial Involvement	Night	> 38 dB	BKGND + 5 dB
ETSU-R-97 England	$L_{A90(10min)}$	Financial Involvement	Any	≤40 dB	45 dB
ETSU-R-97 England	$L_{A90(10min)}$	Financial Involvement	Any	> 40 dB	BKGND + 5 dB
VIC NZS 6808:1998	$L_{A95(10min)}$	Any	Any	≤35 dB(L_{A95})	40 dB
VIC NZS 6808:1998	$L_{A95(10min)}$	Any	Any	> 35 dB(L_{A95})	BKGND + 5 dB
SA EPA 2003	$L_{Aeq(10min)}$ Prediction $L_{A90(10min)}$ Measurement	Any	Any	≤30 dB	35 dB
SA EPA 2003	$L_{Aeq(10min)}$ Prediction $L_{A90(10min)}$ Measurement	Any	Any	> 30 dB	BKGND + 5 dB
WA 2004	$L_{Aeq(10min)}$	Any	Any	≤30 dB	35 dB
WA 2004	$L_{Aeq(10min)}$	Any	Any	> 30 dB	BKGND + 5 dB
SA EPA 2009	$L_{Aeq(10min)}$ Prediction $L_{A90(10min)}$ Measurement	Standard	Any	≤35 dB	40 dB
SA EPA 2009	$L_{Aeq(10min)}$ Prediction $L_{A90(10min)}$ Measurement	Standard	Any	> 35 dB	BKGND + 5 dB
SA EPA 2009	$L_{Aeq(10min)}$ Prediction $L_{A90(10min)}$ Measurement	Rural Living	Any	≤30 dB	35 dB
SA EPA 2009	$L_{Aeq(10min)}$ Prediction $L_{A90(10min)}$ Measurement	Rural Living	Any	> 30 dB	BKGND + 5 dB
VIC NZS 6808:2010	$L_{A90(10min)}$	Standard	Any	≤35 dB	40 dB
VIC NZS 6808:2010	$L_{A90(10min)}$	Standard	Any	> 35 dB	BKGND + 5 dB
VIC NZS 6808:2010	$L_{A90(10min)}$	High Amenity	Day	≤35 dB	40 dB
VIC NZS 6808:2010	$L_{A90(10min)}$	High Amenity	Day	> 35 dB	BKGND + 5 dB
VIC NZS 6808:2010	$L_{A90(10min)}$	High Amenity	Evening or Night less than 6 m/s	≤30 dB	35 dB
VIC NZS 6808:2010	$L_{A90(10min)}$	High Amenity	Evening or Night less than 6 m/s	> 30 dB	BKGND + 5 dB
NSW Draft 2011	$L_{Aeq(10min)}$ $L_{A90(10min)}$ + 1.5 dB	Any	Day	≤30 dB	35 dB
NSW Draft 2011	$L_{Aeq(10min)}$ $L_{A90(10min)}$ + 1.5 dB	Any	Day	> 30 dB	BKGND + 5 dB
NSW Draft 2011	$L_{Aeq(10min)}$ $L_{A90(10min)}$ + 1.5 dB	Any	Night	≤30 dB	35 dB
NSW Draft 2011	$L_{Aeq(10min)}$ $L_{A90(10min)}$ + 1.5 dB	Any	Night	> 30 dB	BKGND + 5 dB
QLD 2016	L_{Aeq} Prediction	Non-host lot	Day and Evening	≤32 dB	37 dB
QLD 2016	L_{Aeq} Prediction	Non-host lot	Day and Evening	> 32 dB	BKGND + 5 dB
QLD 2016	L_{Aeq} Prediction	Non-host lot	Night	≤30 dB	35 dB
QLD 2016	L_{Aeq} Prediction	Non-host lot	Night	> 30 dB	BKGND + 5 dB
QLD 2016	L_{Aeq} Prediction	Host lot	Any	≤40 dB	45 dB
QLD 2016	L_{Aeq} Prediction	Host lot	Any	> 40 dB	BKGND + 5 dB
Demark	L_{Aeq}, 8 m/s@10 m	Standard	Any	Any	44 dB
Demark	L_{Aeq}, 6 m/s@10 m	Standard	Any	Any	42 dB
Demark	L_{Aeq}, 8 m/s@10 m	Noise Sensitive	Any	Any	39 dB
Demark	L_{Aeq}, 6 m/s@10 m	Noise Sensitive	Any	Any	37 dB
Canada, Ontario	L_{Aeq} (1hr)	Urban	Any	≤38 dB RefBG	45 dB
Canada, Ontario	L_{Aeq} (1hr)	Urban	Any	> 38 dB RefBG	RefBG + 7 dB
Canada, Ontario	L_{Aeq} (1hr)	Rural	Any	≤33 dB RefBG	40 dB
Canada, Ontario	L_{Aeq} (1hr)	Rural	Any	> 33 dB RefBG	RefBG + 7 dB
Sweden	L_{Aeq}, 8 m/s@10 m	Standard	Any	Any	40 dB
Sweden	L_{Aeq}, 8 m/s@10 m	Quiet	Any	Any	35 dB
Netherlands	L_{Aden}	Any	Any	Any	47 dB
Netherlands	L_{Aeq}	Any	Night	Any	41 dB

FIGURE 31.1 Comparison of wind turbine noise limits [7].

FIGURE 31.2 In-field beamforming measurements [12].

31.2 Noise reduction technologies

There are several noise reduction technologies have been developed to reduce TBL-TE noise.

The first method is based on the design of optimized blades for aeroacoustics purposes, that is, by changing the airfoil shape to control the development of the boundary layer on the blade, and therefore by reducing the amplitude of the turbulent pressure fluctuations near the trailing edge [14]. A second approach, which is the currently state-of-the-art in industry, relies on the application of trailing-edge serration add-ons. With this simple geometrical device, noise reduction is achieved by minimizing the scattering efficiency of the wall pressure fluctuations along the slanted edge [15,16]. A third and very recent approach is based upon the adoption of permeable trailing edges or permeable flaps. With these devices, noise reduction is achieved by the gradual mitigation of the unsteady pressure field mismatch near the trailing edge [17,18]. The advantage of the add-ons with respect to other solutions is that they can be added to existing operating wind turbines.

The first approach has shown promising noise reductions in wind tunnel tests [14,19,20]; for example, up to 4 dB noise reduction was achieved by a NACA 64418 airfoil. However, in-field measurements showed less noise reduction (up to 0.5 dB) than the one achieved with trailing edge serrations on the same 2.3 MW wind turbine [21].

1. *Trailing-edge serrations*

Trailing-edge serrations are widely adopted and a well-assessed noise reduction technology for TBL-TE noise. They are employed as attachable add-ons that modify the trailing-edge geometry [22−25] with a triangular shape; there can or cannot be combed in the empty space in between the solid triangles [4]. Oerlemans [4], van der Velden and Oerlemans [26], and Avallone et al. [15] have shown that the addition of combs is beneficial for noise reduction with respect to conventional serrations (Fig. 31.3).

Trailing-edge serrations reduce noise in the low-to-mid frequency range (Strouhal number based on the chord length up to 16) with maximum noise reduction at a Strouhal number based on the chord length equal to 8 [27]. At higher frequencies, trailing-edge serrations do not show noise reduction, but they even show noise increase [28].

It is well established that the serration length shall be at least equal to the boundary layer thickness at the trailing edge and that for length longer than 4 times the boundary layer thickness the increase in noise reduction is negligible. Furthermore, for a given serration length, sharper serrations (i.e., smaller wavelength) provide better noise reduction [23,29,30].

Howe [31] was the first to propose trailing-edge serrations as a noise reduction technology and showed that sharp serrations reduce noise more than ones with smooth tips (i.e., sinusoidal serrations). He developed an analytical method to predict noise reduction by trailing-edge serrations based on the assumption of frozen turbulence and a semiinfinite flat plate. The model predicts an asymptotic noise reduction at high frequency equal to $10\log10[1 + (4h/\lambda)^2]$ dB (where $2h$ and λ are the serration length and wavelength). The analytical prediction disagrees with measurements [16,21,25,28,29,32−36] because it overpredicts the maximum noise reduction and does not predict the noise increase at

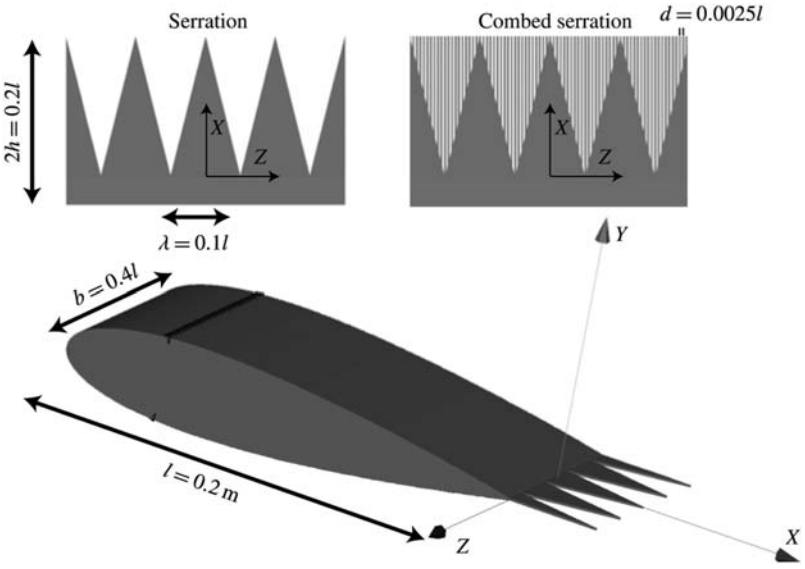

FIGURE 31.3 Conventional serration (*left*) and comb-serration (*right*) [15].

high frequency. More recently, Lyu et al. [37] proposed an analytical model that agrees better with measurements. The model shows that the serration shall be long enough to ensure a considerable phase difference between the acoustic wave scattered along the serration edge; furthermore, if the spatial range of the phase difference, that is, λ, is sufficiently small compared to the correlation length in the spanwise direction, radiated sound waves destructively interfere.

The challenge for analytical methods is to include complex flow physics over trailing edge serrations [38,39]. For this reason, advanced experimental methods and high-fidelity numerical simulations have been widely adopted to discover the physical mechanisms behind the noise reduction [25,27,35,36,40,41]. It has been shown that the dominant noise reduction mechanism is the destructive interference between acoustic wave scattered along the trailing edge of the serrations [15,39]. The wake flow, in the empty space between the serrations, affects the natural development of the turbulent boundary layer by creating streamwise oriented vortices and distorting the flow, which have a negative effect on the noise reduction capabilities of the serrations [15,16] (Fig. 31.4A).

It has been shown that low-frequency noise reduction is mainly driven by the pressure fluctuations near the root of the serrations, while the high-frequency noise behavior is driven by the flow features near the tip [16,29]. Therefore, the mitigation of the flow distortion near the root of the serrations can be obtained by mean of new shapes, such as the iron-shaped serrations [42], or the introduction of combs [4,15] (Fig. 31.4B).

More complex trailing-edge serration geometries have also been conceived in order to increase the frequency range of noise reduction [22]; they are based on multiscale concepts aiming at creating scattering interference between several scales of turbulence. However, these solutions are very complex to manufacture, and they have not spread yet in the industry.

In addition to the aeroacoustics benefits, trailing-edge serrations can offer also aerodynamic benefits, such as increasing lift because they act as a flap [34]. Llorente and Ragni [43,44] have shown that the change in lift due to serrations is similar to the one of a split plate with similar wetted area. Through experiments, carried out at high Reynolds numbers, they showed the positive impact of trailing-edge serrations; they quantified the effect of serrations as an increase of 5% in mean loading and 1% in power production. It is important to mention that the significant power increment results in higher loading and therefore it shortens the lifetime of the wind turbine.

2. *Porous material for noise reduction*

Flow permeable materials can be manufactured as porous foams or obtained as a series of deterministic geometries such as an ensemble of perforations or a repetition of elementary unit cells (Figs. 31.5 and 31.7). This distinction is very relevant because it affects the material characterization and therefore the aeroacoustics performances, which will be discussed in the following.

31.2.1 Characterization of the porous materials

A flow permeable material is characterized by geometrical properties such as shape and size of the pores, porosity (σ) or tortuosity (τ), and by parameters relating their effect on hydrodynamic quantities, such as permeability (K) or form coefficient (C), that quantify fluid energy losses when a fluid flows through them.

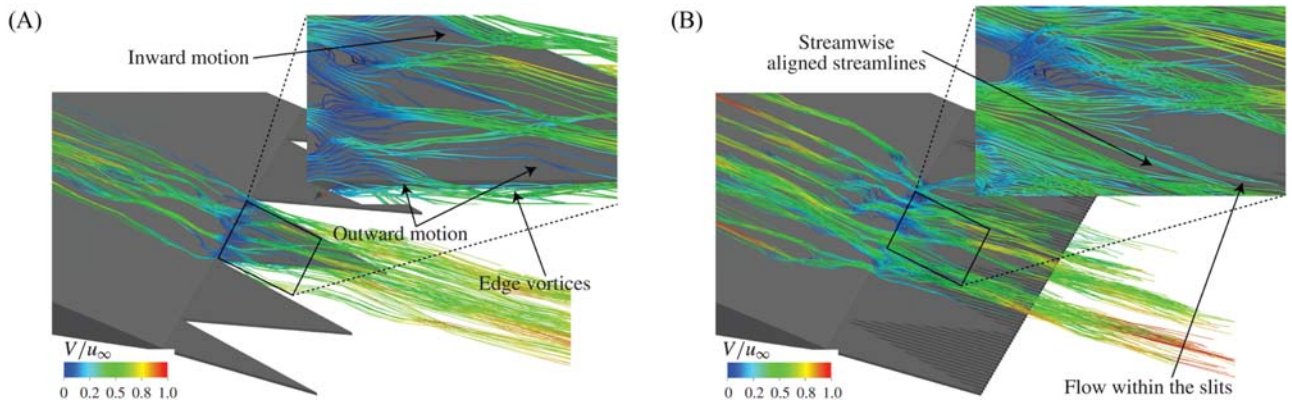

FIGURE 31.4 Streamlines over a conventional serration (A) and one with combs (B) [15].

FIGURE 31.5 Example of permeable trailing edges manufactured as (A) porous foam, and (B) an ensemble of straight channels [45].

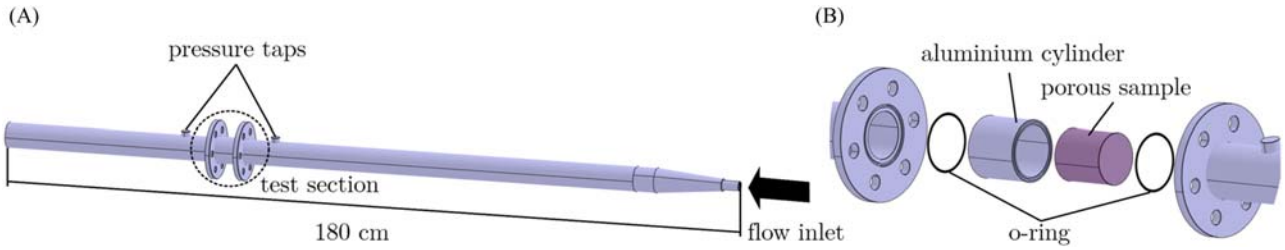

FIGURE 31.6 An example of the static pressure drop rig used to measure permeability and form coefficient (A). (B) The test section is represented [45].

The geometrical parameters are usually provided by the material manufacturer and can be controlled if deterministic geometries are used. They can be also measured by means of a microscope. It is worth mentioning that, when a conventional porous foam is considered, the inner structure might have several pores of different sizes.

The porosity of a material is defined as follows:

$$\sigma = 1 - \frac{\rho_p}{\rho_b} \tag{31.1}$$

where ρ_p and ρ_b are the density of the porous and base material. For a conventional porous foam, the density is obtained as the ratio between the weight and the volume of the sample. Conversely, if the flow permeable material is manufactured as a series of straight perforations, then the porosity can be defined starting from the geometrical features as:

$$\sigma = \pi \frac{d_h^2}{(2l_h^2)} \tag{31.2}$$

where d_h is the diameter of the orifice and l_h is the distance between the orifices' center.

Tortuosity is defined as the ratio between the average pore length and the thickness of the porous medium [46]. Therefore, a straight channel has tortuosity value equal to 1 in the direction of the perforation, and zero in all the others. If the geometry is complex, then statistical methods are used. An example is the random walk model that mimics the diffusion of walkers, randomly distributed within the porous material [47].

The macroscopic hydrodynamic quantities are instead obtained with pressure-drop measurements across a sample of permeable material (Fig. 31.6). The static pressure-drop Δp across a sample of homogeneous permeable material with thickness t is described by the Hazen–Dupuit–Darcy equation:

$$\frac{\Delta p}{t} = \frac{\mu}{K} v + \rho C v^2 \tag{31.3}$$

where ρ is the fluid density, μ is the dynamic viscosity, and v is the Darcian velocity, defined as the ratio between the volumetric flow rate and the cross-section area of the sample. The linear and quadratic terms in the equation account for pressure losses due to viscous dissipation and inertial effects respectively and depend on the permeability (K) and form coefficient (C), respectively.

It is worth mentioning that the equation is valid for the thickness of the material larger than the average pore size; in this case, the static-pressure drop is a linear function of the material thickness. For an airfoil, as application of interest, the thickness of the sample diminishes in the streamwise direction, and it is comparable to or smaller than the average pore size very close to the trailing edge. This makes very challenging the exact characterization of the material for wind turbine applications.

Employment of porous materials for noise reduction

The first example of flow permeable material for TBL-TE noise reduction is the application of brushes at the trailing edge of an airfoil [48]. However, this solution showed very small noise reduction (about 0.5 dB) when tested in-field during the SCIROCCO project [49].

More recently, the aerodynamic behavior and the aeroacoustics performance of porous foams at trailing edge have been investigated. Geyer et al. [50,51] were the first who proposed to use of porous materials as a solution to reduce TBL-TE noise. Initially, they performed aeroacoustics measurements of a fully permeable SD7003 airfoil. Results showed up to 20 dB noise reduction with respect to the fully solid baseline airfoil. As a countereffect, they measured a reduction up to 80% in lift and up to 10 times increase in drag. Because of such negative deterioration of the aerodynamic characteristics of the airfoil, in a second phase, they limited the application of the porous material to the last 5% of the chord length [52] showing noise reduction up to 8 dB, with almost no penalty for the lift and 6% drag increase with respect to the baseline solid airfoil.

Similar results were also obtained by the team at DLR. Herr et al. [48,53] tested several flow permeable trailing edges on a DLRF16 with extension equal to 10% of the chord. They reported noise reduction at low frequency and noise increase at high frequency. They found out that the material permeability is the driving parameter for noise reduction. A higher permeability results in larger noise reduction. The authors proposed that the noise reduction is caused by the gradual mitigation of the pressure mismatch at the trailing edge. On the other hand, the noise increase was attributed to the higher surface roughness with respect to the baseline solid trailing edge.

Data collected by Geyer et al. and Herr et al. [51,54] showed that another effect of a flow-permeable trailing edge is to modify the scaling law of the far-field noise with the free-stream Mach number. As a matter of fact, it was found that the power coefficient in presence of a porous trailing edge ranges between 5 and 7, while it is closer to 5 for a solid trailing edge. This has suggested that a different noise generation mechanism plays a role with respect to a solid trailing edge.

Such promising results have pushed the aeroacoustics community to understand the physical mechanisms behind noise reduction. Herr et al. [53] performed an extensive parametric study to discover the dependency of the far-field noise on the material properties. The materials were characterized in terms of permeability and form coefficient by using the same experimental approach as described above [45], and in terms of geometrical features by measuring the average pore size and the material tortuosity. They covered one side of the porous material with a nonpermeable tape in order to remove the aerodynamic communication between the pressure and suction side of the airfoil. They discovered that no far-field noise reduction is obtained when one side of the permeable material is covered. However, noise increase, due to the roughness effect, was still measured. Based on the two findings, the authors confirmed that the noise reduction is related to the mitigation of the pressure discontinuity across the streamwise extent of the porous medium; they named this phenomenon as the pressure-release process.

The previous findings were later confirmed by Rubio Carpio et al. [45,55,56]. In addition to far-field noise measurements, the authors measured the flow over the porous materials by means of particle image velocimetry. They found out that the effect of the porous surface is to increase the amplitude of the surface pressure fluctuations close to the surface and to reduce their coherence length near the wall. The porous materials used had minor influence, limited only near the wall, on the time-averaged turbulent boundary layer profile. Rubio Carpio et al. applied Amiet's theory [57,58] with the boundary layer integral parameters obtained from the experiments and they found that the variation of the boundary layer properties and of the statistical properties of the turbulent fluctuations were not sufficient to justify such a large noise reduction. This was further confirmed by the fact that the boundary layer integral parameters were very similar when comparing a porous trailing edge with and without a nonpermeable layer placed in the mid-section.

The same authors performed a parametric study on the effect of the streamwise extent of the porous medium on far-field noise by changing the extension of the nonpermeable layer in the mid-section of the trailing edge. For a NACA 0018 airfoil at 0-degree angle of attack, they found that noise reduction increases up to a nearly asymptotic value by increasing the streamwise extension of the permeable material. More in detail, most of the noise reduction was already obtained by using a length of the porous medium up to 5% of the chord length. For a larger extension of the porous medium length, a smaller increase in the noise reduction was achieved. This has suggested that two noise mechanisms play a role.

In order to investigate the noise reduction mechanisms, a detailed characterization of the flow within the porous medium is needed. This is extremely challenging from an experimental point of view because of complex installation of miniaturized microphones [59]. Therefore, numerical methods based on high-fidelity numerical simulations have been also used. Amongst the different approaches to simulate the porous medium, the ones based on impedance boundary conditions to represent the material cannot be used [60] because they discard the unsteady interaction between the suction and the pressure side. Alternative approaches rely upon fully resolving the material geometry [18], or representing the porous material with an equivalent fluid region [61–63]. The latter is often preferred for fully resolving the internal topology of the porous medium because computationally less expensive, particularly if the average pore size is way smaller than the characteristic length of the airfoil. When using the equivalent fluid approach, the flow equations within the equivalent fluid region are modified to include the Brinkman–Forchheimer–Darcy terms [64].

When adopting the equivalent fluid medium approach on an airfoil, it must be considered that the thickness of the porous material varies when approaching the trailing edge. Therefore, the values of characteristic parameters such as the form coefficient and the permeability vary along the streamwise extent of the porous medium. For this reason, "ad-hoc" measurements of the material form coefficient and permeability are needed. Teruna et al. [65] proposed the application of a multilayer approach to overcome this issue. They adopted two layers of permeable material, one exposed to the flow with material properties obtained from pressure drop measurements with sample thickness equal to the average pore size, and a second layer with properties obtained from measurements with a sample thickness such that the Darcy's equation provides asymptotic values of permeability and form coefficient. Furthermore, the first layer accounts for the effect of porosity with the mass-flux at the interface being a function of the porosity.

High-fidelity numerical simulations with both the equivalent fluid approach and fully resolved porous medium have been used to shed light on the physical mechanisms behind noise reduction. It has been found that two physical mechanisms play a role: the pressure release and the destructive interference between acoustic waves scattered along the porous extension [17,18].

The first flow mechanism is dominant near the trailing edge of the flow-permeable material where the thickness of the airfoil is comparable to the average pore size. In this region, there is an unsteady hydrodynamic interaction between the turbulent fluctuations on both the pressure and suction sides and, therefore, a strong mitigation of the pressure discontinuity at the trailing edge is obtained. When the thickness of the trailing edge is larger, then the direct interaction between the hydrodynamic pressure fluctuations is not possible and the relevance of the pressure release process diminishes (Fig. 31.7). However, the presence of the porous medium allows communication between the pressure and the suction side of the airfoil. For this reason, there is a gradual change in the pressure mismatch along the surface of the material thus allowing localized scattering of acoustic energy. Acoustic waves scattered along the streamwise extent

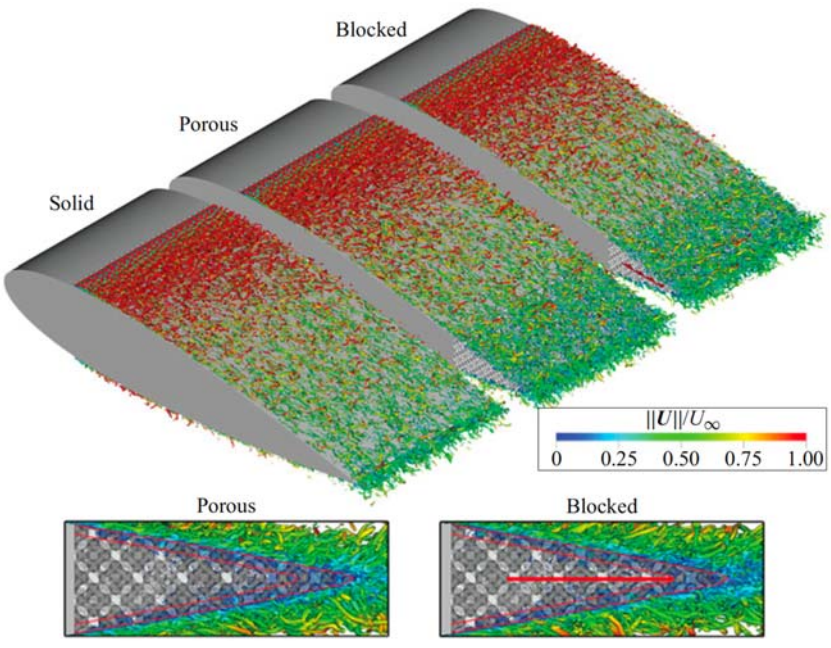

FIGURE 31.7 Snapshot of instantaneous isosurfaces of λ_2 criteria for vortex identification for three test cases. *Image is taken from Teruna et al. Teruna C, Avallone F, Ragni D, Rubio-Carpio A, Casalino D. J Fluid Mech 2021;926:17.*

create destructive interference and contribute to noise reduction. These findings are in line with the experimental evidence discussed above and highlight the relevant role of the pressure release process on noise reduction.

31.2.2 From porous foams to innovative metamaterials

Porous foams have been widely investigated as flow-permeable materials. However, the development of additive manufacturing has opened to the possibility to enlarge the design space [66] in order to obtain improved and tailored noise reduction performance. At the same time, thanks to additive manufacturing, it is possible to create modular geometries that can be easily reproduced and manufactured with robust precision. Furthermore, the exact same geometrical features can be also reproduced in high-fidelity numerical simulations. Therefore, additive manufacturing paves the way toward tailored optimization of the porous material geometry and properties, such as materials with varying properties (e.g., permeability and form coefficient) both along the thickness and the streamwise extent. For example, a flow-permeable trailing edge can be realized as an ensemble of deterministic unit cells geometries. An example is the diamond unit cells investigated by Teruna et al. [18] (Fig. 31.7). It has been shown that using this approach, it is possible to obtain noise reductions similar, both in amplitude and frequency distribution, to the ones that were achieved using conventional porous foams [67].

As mentioned earlier, the challenge for innovative flow-permeable material is to not increase drag and loose lift and to maintain good noise reduction levels also when changing the angle of attack with respect to the design condition. For this scope, several attempts have been proposed in the literature.

The team at DLR was the first to investigate flow-permeable trailing edge realized as a series of perforations [48,53,54,63,68,69]. Later Rubio Carpio et al. [70] investigated similar configurations (Fig. 31.5). In these studies, the authors realized different permeability values by changing the distance between the perforations while keeping the diameter of the perforations the same. Similarly, as for the conventional porous foams, trailing-edge geometries with larger permeability provide larger noise reduction. However, when comparing porous foams and perforated geometries, it has been found that, for a given permeability, the latter provides less noise reduction than the former. Therefore, the three components of the permeability tensor as well as the internal topology of the material play a relevant role in terms of noise reduction. This finding highlights the importance of tortuosity on noise reduction. Therefore, there is the need of further research on the link between the macroscopic material properties and the noise reduction to design optimized shapes. By using a similar concept, the effect of spatial change of permeability in the streamwise direction has been also investigated. Permeability was increased toward the trailing edge to increase the impact of the pressure-release effect. Several permeability distributions were tested with the same range of permeability variation along the streamwise extent. It was found that the noise reduction is larger in the entire range of angles of attack tested by decreasing the permeability at the root [59].

In order to maintain the noise reduction performance in a wide range of angles of attack, Luesutthiviboon et al. [66] covered a permeable trailing edge, manufactured as a series of wall-normal perforations, with a layer of Kevlar material. This resulted in investigating a new design space with respect to the one that can be inspected by using conventional porous foam; as a matter of fact, it allowed us to study the performance of materials with low flow resistivity but very large drag form coefficient. This solution showed average lower noise reduction levels with respect to conventional metal foams, but with minor variations when changing the angle of attack. Furthermore, because of the smoother surface to which the flow was exposed, the drag of the airfoil was lower than the one with conventional materials. This has opened the way toward optimal low-drag low-noise concepts with material topology changing both in the wall-normal and streamwise directions.

31.3 Conclusions

Reducing TBL-TE noise is a challenging but a needed task. Improvements in the state-of-the-art industrial solutions can be obtained by means of permeable materials at the trailing edge. However, the lack of fundamental knowledge on their effect on the flow and interaction between the pressure and suction sides of an airfoil, coupled with industrial challenges such as maintenance and worsening of the aerodynamic properties of the airfoil, make their application very challenging.

Based on the actual state of knowledge, additive manufacturing coupled with physic-based tailored designs of the permeable materials is the best way to research and invent new devices that can be applied, in the short term, by industry to increase the wind energy production and acceptance.

References

[1] Pedersen E, Persson WK. Perception and annoyance due to wind turbine noise—a dose−response relationship. J Acoust Soc Am 2004;116:3460. Available from: https://doi.org/10.1121/1.1815091.

[2] Michaud DS, Feder K, Keith SE, Voicescu SA, Marro L, Than J, et al. Exposure to wind turbine noise: perceptual responses and reported health effects. J Acoust Soc Am 2016;139:1443. Available from: https://doi.org/10.1121/1.4942391.

[3] Shepherd D, McBride D, Welch D, Dirks KN, Hill EM. Evaluating the impact of wind turbine noise on health-related quality of life. Noise Heal 2011;13:333−9. Available from: https://doi.org/10.4103/1463-1741.85502.

[4] Oerlemans S. Reduction of wind turbine noise using blade trailing edge devices. 22nd AIAA/CEAS Aeroacoustics Conference, American Institute of Aeronautics and Astronautics, Lyon, France; 2016. AIAA 2016-3018, p. 1−18.

[5] Wagner S, Bareiß R, Guidati G. Wind Turbine Noise. Berlin Heidelberg: Springer; 1996.

[6] Koppen E, Fowler K. International legislation for wind turbine noise. Euronoise 2015, Maastricht, The Netherlands; 2015. p. 321−326.

[7] Davy JL, Burgemeister K, Hillman D. Wind turbine sound limits: current status and recommendations based on mitigating noise annoyance. Appl Acoust 2018;140:288−95. Available from: https://doi.org/10.1016/J.APACOUST.2018.06.009.

[8] Blake WK. Mechanics of Flow-Induced Sound and Vibration V2: Complex Flow-Structure Interactions, Volume 2. Orlando, FL: Academic Press, Inc; 1986.

[9] Brooks TF, Pope DS. Airfoil self-noise and prediction. National Aeronautics and Space Administration, Scientific and Technical Information Division 1989.

[10] Lee S, Ayton L, Bertagnolio F, Moreau S, Chong TP, Joseph P. Turbulent boundary layer trailing-edge noise: theory, computation, experiment, and application. Prog Aerosp Sci 2021;100737. Available from: https://doi.org/10.1016/j.paerosci.2021.100737.

[11] Ffwocs Williams JE, Hawkings DL. Sound generation by turbulence and surfaces in arbitrary motion. Philos Trans R Soc Lond A Math Phys Eng Sci 1969;264:1151. Available from: https://doi.org/10.1098/rsta.1969.0031.

[12] Oerlemans S, Sijtsma P, Méndez López B. Location and quantification of noise sources on a wind turbine. J Sound Vib 2007;299(4–5):869−83. Available from: https://doi.org/10.1016/J.JSV.2006.07.032.

[13] Sijtsma P. Phased array beamforming appl wind tunn fly-over tests, NLR-TP-2010−549, 2010.

[14] Lutz T, Herrig A, Würz W, Kamruzzaman M, Krämer E. Design and wind-tunnel verification of low-noise airfoils for wind turbines. AIAA J 2007;45(4):779−85. Available from: https://doi.org/10.2514/1.27658.

[15] Avallone F, Van Der Velden WCP, Ragni D, Casalino D. Noise reduction mechanisms of Sawtooth and Combed-Sawtooth trailing-edge serrations. J Fluid Mech 2018;848:560−91. Available from: https://doi.org/10.1017/jfm.2018.377.

[16] Avallone F, Pröbsting S, Ragni D. Three-dimensional flow field over a trailing-edge serration and implications on broadband noise. Phys Fluids 2016;28(11):117101. Available from: https://doi.org/10.1063/1.4966633.

[17] Teruna C, Manegar F, Avallone F, Ragni D, Casalino D, Carolus T. Noise reduction mechanisms of an open-cell metal-foam trailing edge. J Fluid Mech 2020;898:A18. Available from: https://doi.org/10.1017/jfm.2020.363.

[18] Teruna C, Avallone F, Ragni D, Rubio-Carpio A, Casalino D. Numerical analysis of a 3-D printed porous trailing edge for broadband noise reduction. J Fluid Mech 2021;926:A17. Available from: https://doi.org/10.1017/JFM.2021.704.

[19] Bertagnolio F, Madsen HA, Bak C. Trailing edge noise model validation and application to airfoil optimization. J Sol Energy Eng Trans ASME 2010;132:0310101−9. Available from: https://doi.org/10.1115/1.4001462/475911.

[20] Guidati G, Wagner S. Design of reduced noise airfoils for wind turbines. Eur Congr Comput Methods Appl Sci Eng ECCOMAS 2000;11.

[21] Oerlemans S, Fisher M, Maeder T, Kögler K. Reduction of wind turbine noise using optimized airfoils and trailing-edge serrations. AIAA J 2009;47(6):1470−81. Available from: doi/10.2514/1.38888.

[22] Azarpeyvand M, Gruber M, Joseph PF. An analytical investigation of trailing edge noise reduction using novel serrations. 19th AIAA/CEAS Aeroacoustics Conference, American Institute of Aeronautics and Astronautics, Berlin, Germany; 2013, AIAA 2013−2009 p. 1−17.

[23] Gruber M, Joseph PF, Chong TP. On the mechanisms of serrated airfoil trailing edge noise reduction. 17th AIAA/CEAS Aeroacoustics Conference, American Institute of Aeronautics and Astronautics, Portland, OR; 2011, AIAA 2011-2781, p. 1−23.

[24] Avallone F, van der Velden WCP, Ragni D. Benefits of curved serrations on broadband trailing-edge noise reduction. J Sound Vib 2017;400:167−77. Available from: https://doi.org/10.1016/j.jsv.2017.04.007.

[25] Arce León C, Merino-Martínez R, Ragni D, Avallone F, Snellen M. Boundary layer characterization and acoustic measurements of flow-aligned trailing edge serrations. Exp Fluids 2016;57(12):182. Available from: https://doi.org/10.1007/s00348-016-2272-z.

[26] van der Velden WCP, Oerlemans S. Numerical analysis of noise reduction mechanisms on improved trailing edge serrations using the Lattice Boltzmann Method. 35th Wind Energy Symposium, American Institute of Aeronautics and Astronautics, Reston, VA; 2017, AIAA 2017-1379, p. 1−24.

[27] Jones LE, Sandberg RD. Acoustic and hydrodynamic analysis of the flow around an aerofoil with trailing-edge serrations. J Fluid Mech 2012;706:295−322. Available from: https://doi.org/10.1017/jfm.2012.254.

[28] Gruber M. Airfoil Noise Reduction by Edge Treatments. University of Southampton; 2012.

[29] Chong TP, Vathylakis A. On the aeroacoustic and flow structures developed on a flat plate with a serrated sawtooth trailing edge. J Sound Vib 2015;354:65−90. Available from: https://doi.org/10.1016/j.jsv.2015.05.019.

[30] Chong TP, Vathylakis A, Joseph PF, Gruber M. Self-noise produced by an airfoil with nonflat plate trailing-edge serrations. AIAA J 2013;51:2665−77. Available from: https://doi.org/10.2514/1.J052344.

[31] Howe MS. Aerodynamic noise of a serrated trailing edge. J Fluids Struct 1991;5(1):33−45. Available from: https://doi.org/10.1016/0889-9746(91)80010-B.
[32] Dassen T, Parchen R, Bruggeman J, Hagg F. Results of a wind tunnel study on the reduction of airfoil self-noise by the application of serrated blade trailing edges. Proceedings of the 1996 European Union Wind Energy Conference and Exhibition 1996;800−3.
[33] Gruber M, Joseph PF, Azarpeyvand M. An experimental investigation of novel trailing edge geometries on airfoil trailing edge noise reduction. 19th AIAA/CEAS Aeroacoustic Conference, American Institute of Aeronautics and Astronautics, Berlin, Germany; 2013, AIAA 2013−2011, p. 1−23.
[34] Arce León C, Ragni D, Pröbsting S, Scarano F, Madsen J. Flow topology and acoustic emissions of trailing edge serrations at incidence. Exp Fluids 2016;57(5):91. Available from: https://doi.org/10.1007/s00348-016-2181-1.
[35] Arce León C, Merino-Martínez R, Ragni D, Avallone F, Scarano F, Pröbsting S, et al. Effect of trailing edge serration-flow misalignment on airfoil noise emissions. J Sound Vib 2017;405:19−33. Available from: https://doi.org/10.1016/j.jsv.2017.05.035.
[36] Arce León C, Merino-Martínez R, Pröbsting S, Ragni D, Avallone F. Acoustic emissions of semi-permeable trailing edge serrations. Acoust Aust 2018;46(1):111−17. Available from: https://doi.org/10.1007/s40857-017-0093-8.
[37] Lyu B, Azarpeyvand M, Sinayoko S. Prediction of noise from serrated trailing edges. J Fluid Mech 2016;793:556−88. Available from: https://doi.org/10.1017/jfm.2016.132.
[38] Lima Pereira LT, Avallone F, Ragni D, Scarano F. A physics-based description and modelling of the wall-pressure fluctuations on a serrated trailing edge. J Fluid Mech 2022;938:A28. Available from: https://doi.org/10.1017/jfm.2022.173.
[39] Lima Pereira LT, Ragni D, Avallone F, Scarano F. Pressure fluctuations from large-scale PIV over a serrated trailing edge. Exp Fluids 2020;61(3):1−17. Available from: https://doi.org/10.1007/S00348-020-2888-X/FIGURES/16.
[40] Lima Pereira LT, Ragni D, Avallone F, Scarano F. Aeroacoustics of sawtooth trailing-edge serrations under aerodynamic loading. J Sound Vib 2022;537:117202. Available from: https://doi.org/10.1016/j.jsv.2022.117202.
[41] Sandberg RD, Jones LE. Direct numerical simulations of low Reynolds number flow over airfoils with trailing-edge serrations. J Sound Vib 2011;330(16):3818−31. Available from: https://doi.org/10.1016/j.jsv.2011.02.005.
[42] van der Velden WCP, Avallone F, Ragni D. Numerical analysis of noise reduction mechanisms of serrated trailing edges under zero lift condition. 23rd AIAA/CEAS Aeroacoustics Conference 2017; 2017, AIAA 2017−4173, pp. 1−14.
[43] Llorente E, Ragni D. Trailing edge serrations effects on the aerodynamic performance of a NACA 643418. Wind Energy 2019;22(3):392−406. Available from: https://doi.org/10.1002/WE.2293.
[44] Llorente E, Ragni D. Trailing-edge serrations effect on the performance of a wind turbine. Renew Energy 2020;147(3):437−46. Available from: https://doi.org/10.1002/WE.2293.
[45] Rubio Carpio A, Merino-Martínez R, Avallone F, Ragni D, Snellen M, van der Zwaag S, et al. Experimental characterization of the turbulent boundary layer over a porous trailing edge for noise abatement. J Sound Vib 2019;443:537−58. Available from: https://doi.org/10.1016/J.JSV.2018.12.010.
[46] Epstein N. On tortuosity and the tortuosity factor in flow and diffusion through porous media. Chem Eng Sci 1989;44(3):777−9. Available from: https://doi.org/10.1016/0009-2509(89)85053-5.
[47] Tranter TG, Kok MDR, Lam M, Gostick JT. Pytrax: a simple and efficient random walk implementation for calculating the directional tortuosity of images. SoftwareX 2019;10:100277. Available from: https://doi.org/10.1016/J.SOFTX.2019.100277.
[48] Herr M, Dobrzynski W. Experimental investigations in low-noise trailing edge design. AIAA J 2005;43(6):1167−75. Available from: https://doi.org/10.2514/1.11101.
[49] Nederland EC, Garcillán L, Fisher M, Koegler K, Maeder T. SIROCCO: Silent Rotors by Acoustic Optimisation. Second Int. Meet. Wind Turbine Noise, Lyon, France, 2007, ECN.
[50] Sarradj E, Geyer T. Noise generation by porous airfoils. 13th AIAA/CEAS Aeroacoustics Conference; 2007, AIAA 2007-3719, pp. 1−13.
[51] Geyer T, Sarradj E, Fritzsche C. Measurement of the noise generation at the trailing edge of porous airfoils. Exp Fluids 2009;48(2):291−308. Available from: https://doi.org/10.1007/s00348-009-0739-x.
[52] Geyer T, Sarradj E. 20th AIAA/CEAS Aeroacoustics Conference, American Institute of Aeronautics and Astronautics Inc.; 2014, AIAA 2014−3039, pp. 1−18.
[53] Herr M, Rossignol KS, Delfs J, Möβner M, Lippitz N. Specification of Porous Materials for Low-Noise Trailing-Edge Applications. 20th AIAA/CEAS Aeroacoustics Conference 2014;1−19.
[54] Herr M, Reichenberger J. 17th AIAA/CEAS Aeroacoustics Conference, American Institute of Aeronautics and Astronautics Inc.; 2011, AIAA 2011 - 2780, p. 1−25.
[55] Rubio Carpio A, Merino-Martínez R, Avallone F, Ragni D, Snellen M, van der Zwaag S. Broadband trailing edge noise reduction using permeable metal foams. INTER-NOISE 2017 46th International Congress and Exposition on Noise Control Engineering: Taming Noise and Moving Quiet 2017.
[56] Rubio Carpio A, Avallone F, Ragni D, Snellen M, Van Der Zwaag S. Mechanisms of broadband noise generation on metal foam edges. Phys Fluids 2019;31(10):105110. Available from: https://doi.org/10.1063/1.5121248.
[57] Amiet RK. Noise due to turbulent flow past a trailing edge. J Sound Vib 1976;47(3):387−93. Available from: https://doi.org/10.1016/0022-460X(76)90948-2.
[58] Moreau S, Roger M. Back-scattering correction and further extensions of Amiet's trailing-edge noise model. Part II: application. J Sound Vib 2009;323(1–2):397−425. Available from: https://doi.org/10.1016/j.jsv.2008.11.051.

[59] Rubio Carpio A. Innovative Permeable Materials for Broadband Trailing-Edge Noise Mitigation. Delft University of Technology; 2021.
[60] Scalo C, Bodart J, Lele SK. Compressible turbulent channel flow with impedance boundary conditions. Phys Fluids 2015;27(3):035107. Available from: https://doi.org/10.1063/1.4914099.
[61] Koh SR, Meinke M, Schröder W. Numerical analysis of the impact of permeability on trailing-edge noise. J Sound Vib 2018;421:348−76. Available from: https://doi.org/10.1016/J.JSV.2018.02.017.
[62] Zhou B, Ryong Koh S, Gauger NR, Meinke M, Schöder W. A discrete adjoint framework for trailing-edge noise minimization via porous material. Comput Fluids 2018;172:97−108. Available from: https://doi.org/10.1016/J.COMPFLUID.2018.06.017.
[63] Rossian L, Ewert R, Delfs JW. Prediction of airfoil trailing edge noise reduction by application of complex porous material. Notes Numer Fluid Mech Multidiscip Des 2018;136:647−57. Available from: https://doi.org/10.1007/978-3-319-64519-3_58.
[64] Ingham DB, Pop I. Transport Phenomena in Porous Media. Elsevier; 1998.
[65] Teruna C, Rego L, Avallone F, Ragni D, Casalino D. Applications of the multilayer porous medium modeling approach for noise mitigation. J Aerosp Eng 2021;34(6):04021074. Available from: https://doi.org/10.1061/(ASCE)AS.1943-5525.0001326.
[66] Luesutthiviboon S, Ragni D, Avallone F, Snellen M. An alternative permeable topology design space for trailing-edge noise attenuation. Int J Aeroacoust 2021;20(3–4):221−53. Available from: https://doi.org/10.1177/1475472X21100329.
[67] Rubio Carpio A, Avallone F, Ragni D. On the role of the flow permeability of metal foams on trailing edge noise reduction. 2018 AIAA/CEAS Aeroacoustics Conference, American Institute of Aeronautics and Astronautics Inc, AIAA; 2018, AIAA 2018−2964.
[68] Herr M. Design criteria for low-noise trailing-edges. 13th AIAA/CEAS Aeroacoustics Conference 28th AIAA Aeroacoustics Conference, American Institute of Aeronautics and Astronautics Inc.; 2007, AIAA 2007−3470.
[69] Rossian L, Fassmann BW, Ewert R, Delfs J. Prediction of porous trailing edge noise reduction using acoustic jump-conditions at porous interfaces. 22nd AIAA/CEAS Aeroacoustics Conference, American Institute of Aeronautics and Astronautics, Reston, VA; 2016, AIAA 2016−2920.
[70] Rubio Carpio A, Avallone F, Ragni D, Snellen M, van der Zwaag S. Quantitative criteria to design optimal permeable trailing edges for noise abatement. J Sound Vib 2020;485:115596. Available from: https://doi.org/10.1016/j.jsv.2020.115596.

This page intentionally left blank

Chapter 32

Global rare earth supply, life cycle assessment, and wind energy

Zhehan Weng and Gavin M. Mudd
Environmental Engineering, Monash University, Clayton, VIC, Australia

32.1 Background of rare earth elements

The rare earth elements (REE) are now considered key elements for various emerging technologies. In the early stages of their discovery (by Arrhenius in 1787 at Ytterby in Sweden), the term "rare" originated from the belief that the only known source of these new elements was at Ytterby [1,2]. The term "earth" was an archaic reference to oxidic materials in the 19th century [3], despite the fact they were metallic elements [4]. With scientific advancement in REE exploration and utilization, during the past two centuries, both the perceptions of REE's geological scarcity and its chemical properties, have proven to be obsolete. The International Union of Applied and Pure Chemistry defines REEs as the group of 15 lanthanide elements plus scandium and yttrium (as shown in Fig. 32.1). In general Sc is not extracted, and so in this paper, we use the abbreviation of TREO + Y to highlight that our data is rare earth oxides plus yttrium only.

It is important to understand that, each REE has distinctive physical and chemical characteristics, and hence, different downstream uses. The term light rare earth elements (LREE; La to Gd) and heavy rare earth elements (HREE; Tb to Lu), defined by similar electron shell configurations, are commonly used to classify the lanthanide elements more accurately. Despite having a relatively small molecular weight, yttrium is typically classified as an HREE, and scandium is not formally classified as either an LREE or an HREE due to the lack of similarities to either group; yet, it is included with the REE as a whole.

Since the latter part of the 20th century, the increasing demands for high-performance REE materials (see Fig. 32.2) in emerging technological applications have altered the global REE demands. This is exemplified by the utilizations of REE "mischmetals" in the permanent magnet industry. The superior magnetic strength of the neodymium iron boron ($Nd_2Fe_{14}B$) magnet and the ability of the samarium cobalt (SmCo) magnet to retain the magnetic characteristics even at elevated temperatures make them both essential components in precise weaponry systems, electric vehicles (EVs), and wind turbines [6,7].

However, the unique characteristics and the associated complexity of REE in the downstream applications often make them extremely difficult to recycle. Binnemans et al. [9] stated that, in 2011, less than 1% of REE was recycled. Finding substitutions for REE in most applications is also difficult, if not impossible [3,10–12]. For example, for NdFeB-based permanent magnets (generally regarded as the strongest permanent magnets yet discovered), the possible alternative for Nd is Pr, with a loss in magnetic strength. For Dy, there is no feasible alternative element to date [13,14]. As a result, the continuous growth of REE-dependent technologies in conjunction with new discoveries of REE applications aimed at a low-carbon society will significantly increase the future global demands for REE [8,15,16].

32.2 Global rare earth elements supply

In global terms, the REE are not "rare" from a geological abundance perspective, as some REE have a similar abundance to copper. Typical REE abundance in the Earth's crust varies significantly. For example, Ce has an average crustal concentration of 63 μmol/mol (63 ppm), which is higher than several base metal elements such as copper (Cu, 28 ppm) and lead (Pb, 17 ppm), on the Earth's upper crust [17]. In comparison, Tm and Lu have average upper crustal

Wind Energy Engineering. DOI: https://doi.org/10.1016/B978-0-323-99353-1.00015-3

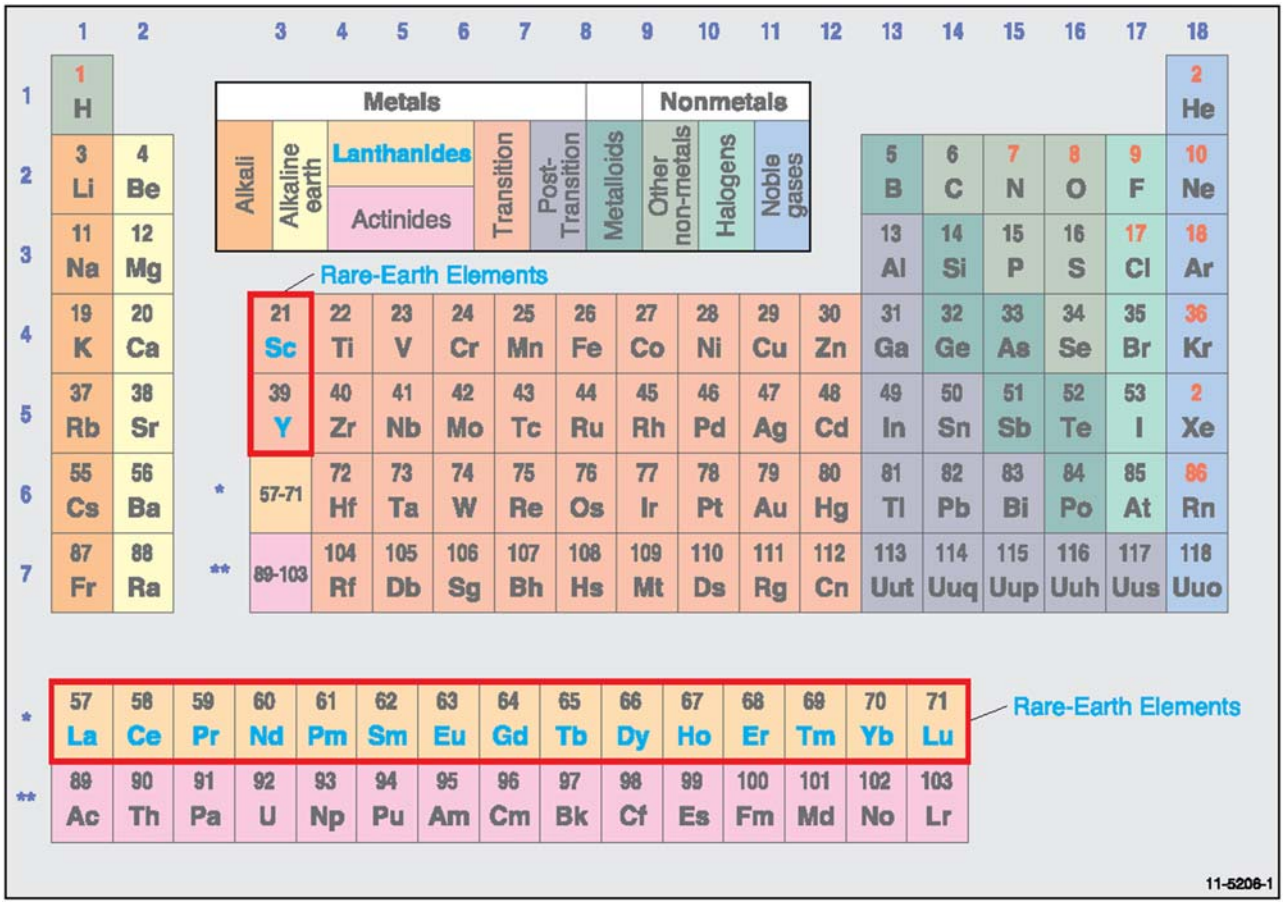

FIGURE 32.1 REE within the periodic table [5].

concentrations of 0.3 ppm and 0.31 ppm, respectively, which are much lower than the majority of other significant economic metals, but higher than gold (Au), silver (Ag) and the platinum group elements [17,18]. Similar results of REE abundances have also been reported by Hoatson et al. [5] (Fig. 32.3).

From a production perspective, the REE are primarily produced as rare earth oxides, or be more specifically, rare earth oxides plus yttrium (TREO + Y). Fig. 32.3 shows the historical TREO + Y production since 1950; the global production was dominated by monazite extraction until major weathered carbonatite projects came into production. The Mountain Pass Project ore body in California, United States was discovered in 1949 [19], and was the world's largest REE supplier until the early 1990s. During the same period, REE-enriched bastnäsite extracted from Mountain Pass become the primary global source for TREO + Y [20–22]. Since the 1990s, largely due to the rapid rise of Bayan Obo in northern China, the global TREO + Y market has been dominated by Chinese production. In 2006, China's annual production peaked at 133,000 t TREO + Y (where t refers to metric tonne), accounting for 97.1% of the global production that year. Since then, Chinese production has maintained its dominance. It also exemplifies the long-term supply risk inherent in having the global supply of the TREO + Y dependent on a single dominant supplier or country. As a result, concern about the long-term TREO + Y supply has become a strategic issue for major consumers like the USA and the European Union (EU) [13,14,23–25].

Weng et al. [26] reported a minimum global TREO + Y mineral resource of 619.5×10^6 t (619.5 million tonnes) with an average ore grade of 0.63%. In another word, there are abundant proven mineral resources hosted within a variety of different types of REE deposits, each of which has a diverse range of mineralogy. The study also suggests future global TREO + Y supply would shift from a few bastnäsite-based carbonatite mines toward a more diversified range of production from a range of different geological types. Demands for certain essential REE (especially HREE)-dependent products or applications (e.g., wind turbine) should be fulfilled by targeting suitable deposits (e.g., HREE enriched ionic clay deposits) with viable ore grades and implementing novel and site-specific mining, beneficiation, and refining

FIGURE 32.2 REE dependant techologies [8].

technologies and plant configurations to optimize the production efficiency of the desired end-products while minimizing environmental impacts.

32.3 Rare earth elements permanent magnets

The NdFeB permanent magnet is the key functional component in modern wind turbine industry. It is used for making permanent magnet synchronous generators (PMSG) and high-temperature superconductors [16,27,28]. The superior magnetic strength of NdFeB magnets, together with their special high induction and coercive force properties [29], has enabled the development and utilization of lighter and larger wind turbines with, greater aerodynamic efficiency, better reliability, and reduced maintenance requirements. As summarized by Wiser et al. [30], "the availability and cost of rare-earth permanent magnets are expected to affect significantly the size and cost of future direct-drive generator designs" (p. 580).

REE-dependent permanent magnets provide significantly better "maximum static energy product" capacity $BH(_{max})$ compared to traditional aluminum-nickel-cobalt (Alnico) and ceramic (Ferrite) magnets (see Fig. 32.4). Given their superior magnetic strength (e.g., NdFeB magnet) and excellent resistance to demagnetization at elevated temperatures (SmCo magnet) REE permanent magnets have become essential components for various modern wind turbine designs and manufacture [6,7].

Humphries [16] estimated that REE permanent magnet production is the single largest sector (approximately 20%) of global REE demands in 2010, and it was expected to grow by 10%−16% per year till 2015 (see Fig. 32.5). Lucas et al. [33] stated that wind turbine production uses about 10% of the global annual permanent magnet supply.

Given the importance of REE in facilitating clean energy technologies to help with addressing climate change, it is clear that there is a need to examine in finer detail the underlying basis of the criticality of REE—especially potential supply rates to meet growing demands for a variety of specific technologies. As systematically summarized by numerous articles, and governmental and industrial reports: the design, generation capacity, and efficiency of future wind

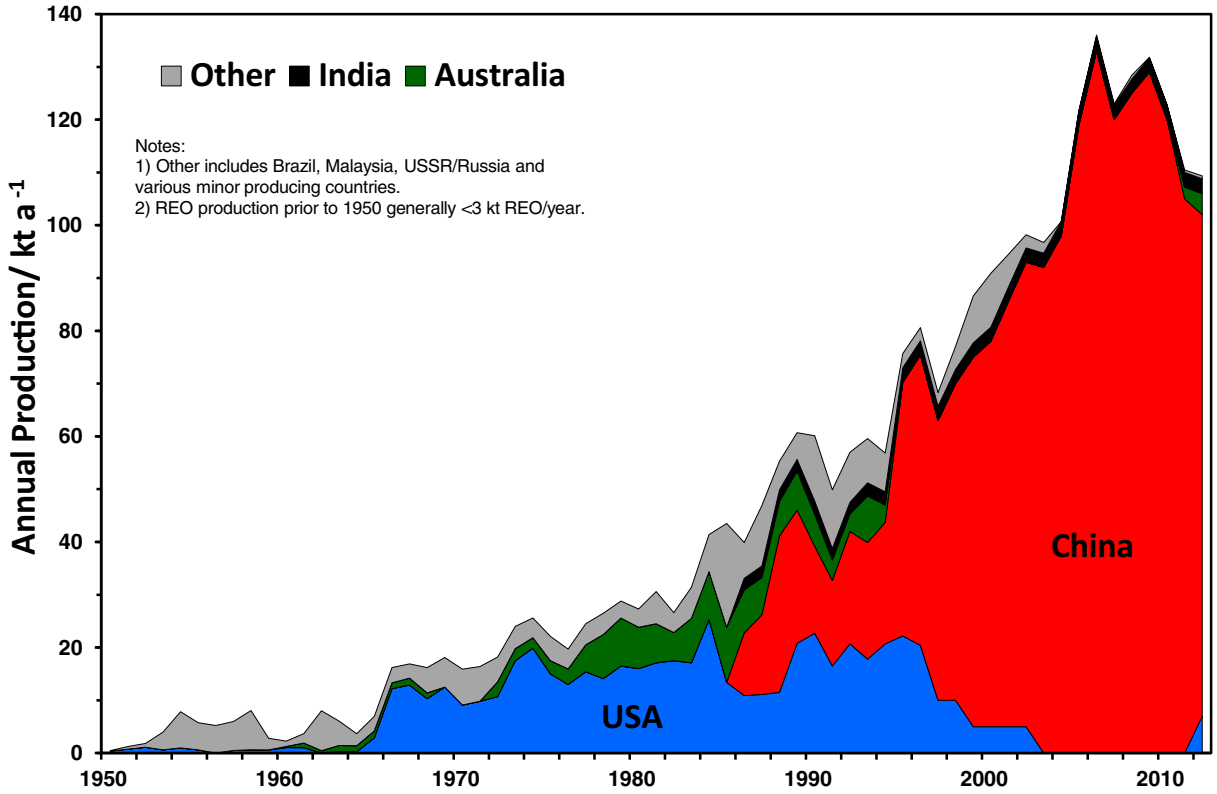

FIGURE 32.3 Global annual TREO + Y mine production. *Data sources: USBoM, Mineral resources of the United States, U.S. Bureau of Mines (USBoM), Washington, DC, 1927–34. USGS, various, Minerals commodity summaries. Reston, VA: U.S. Geological Survey (USGS), 1997–2015; Australian TREO + Y based on monazite production data from BoMRGG, The Australian mineral industry review, Australia. ACT, Australia: Bureau of Mineral Resources, Geology and Geophysics (BoMRGG), 1960–85 and under the assumption of minimum of 60% contained TREO + Y. Here a refers to annum.*

energy plants will be dependent on the availability of REE permanent magnets, especially the neodymium-iron-boron (NdFeB) permanent magnet. [27,30,33,34].

32.4 Life cycle assessment of the use of rare earth elements magnets in wind turbines

In this section, we compare two life cycle assessments (LCA) between two onshore low-medium speed wind turbines; namely: Vestas V112 3–3.45 MW with a PMSG [35] and Vestas V126 3.3 MW with single fed induction generator (SFIG) made of steel and copper [36], to demonstrate the importance of REE in wind turbine environmental footprints.

Table 32.1 summarized the raw material breakdowns for each system. Compared to V126, the V112 turbine contains an additional 485 kg of NdFeB permanent magnet, 3 t of copper, and 6 t of polymer materials to achieve remarkable savings of 86 t of steel and iron materials (22%), 1 t aluminum (23%) and electronics (30%), 480 kg lubricants (27%), and 364 kg other unspecified material. However, the irreplaceability and complex recycling process of REE unavoidably impacts the overall recyclability of PMSG wind turbines compared to other models which utilize more conventional (e.g., Alnico, Ferrite) magnets.

The overall life cycle impacts of a 100 MW wind plant (farm) (20 years life cycle) composed of 33 units of V112 or V126 are summarized (Table 32.2). Again, comparing the V126, to the V112, the V112 has much lower overall environmental profiles than the SFIG model in almost all impact categories, especially as related to human toxicity (54%), eutrophication (39%), and acidification (36%) potential. Moreover, a wind power plant is often considered one of the crucial "clean energy" systems that reduce greenhouse gas (GHG) emissions. The global warming potential (GWP), measured in carbon dioxide emissions equivalent (CO_{2e}), is an essential indicator to demonstrate overall environmental polluting capacity. Under the same operating conditions (e.g., operating hours, wind speed, plant life cycle, etc.), a wind power plant involving Vestas V112 turbines has a 15% lower GHG footprint than a plant involving V126 turbines

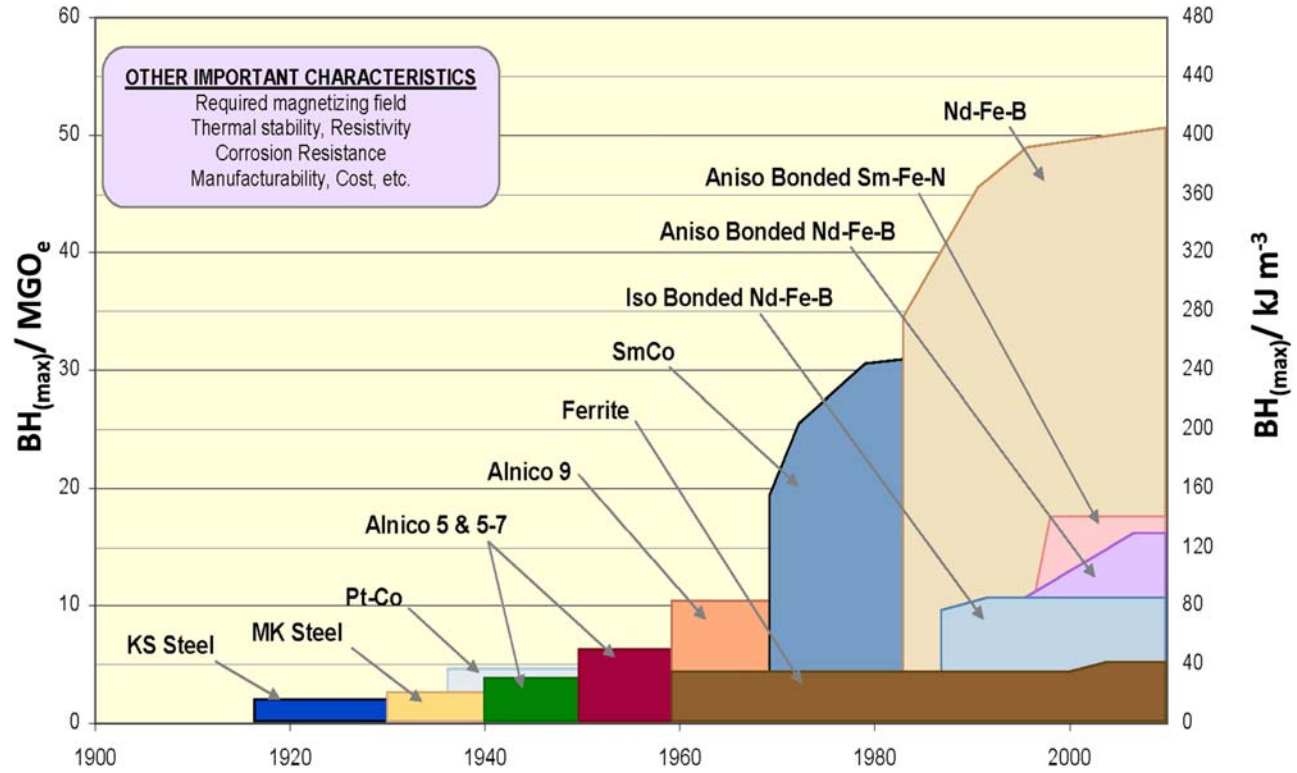

FIGURE 32.4 The development of permanent magnets [31,32].

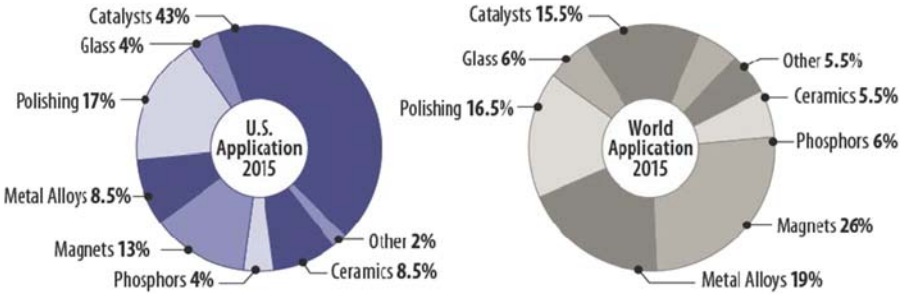

FIGURE 32.5 2015 REE demand estimate by application—U.S. and World [16].

per kilowatt-hour of electricity generated. This comparison highlights the critical role that REE permanent magnets play in the wind turbine industry by significantly reducing the raw material requirements and improving the overall environmental performance.

The detailed Nd, Dy, and Tb mineral resources data and corresponding environmental impacts in the production stage have been adopted from [26,37]; the NdFeB magnet production LCIA data adapted from [6] and LCIA of onshore and offshore wind turbines are based on data from [38]. The REE composition inventory of medium-high and low-speed PMSG wind turbines is shown in Table 32.3.

Principal assumptions include:

1. Typical life cycle period of a wind turbine is 25 years [40] with GWP as the primary environmental impact indicator of this assessment.
2. Medium-High speed PMSG is only utilized in onshore wind turbines.
3. Low-speed PMSG is only utilized in offshore wind turbines.
4. The average capacity factors (ratio of wind turbine's actual power output and peak power output under 100% nameplate capacity for the same period of time) for both onshore and offshore PMSG wind turbines are estimated as 28% [41] while the maximum and the minimum capacity factor is calculated based on full-load hours for corresponding systems [40].

TABLE 32.1 Material breakdowns for the Vestas V112 and V126 wind turbines [35,36].

Material inputs inventory	Units	V112	V126
Designed capacity	MW	3–3.45	3.3
Steel and iron materials	tonne	311	397
Aluminum and its alloys	tonne	3.4	4.5
Copper	tonne	4.8	1.8
Copper alloys	kg	9.1	30
Polymer materials	tonne	21	15
Process polymers	kg	765	1 939
Other materials and material compounds	tonne	27	25
Electronics/electrics	tonne	2.4	3.4
Lubricants and liquids	tonne	1.3	1.8
Not specified	kg	N/A	364
REE permanent magnets	kg	485	N/A
Recyclability	%	81	89

Notes: Average material inputs for each wind turbine are adapted from total 33 units of each system installed in 100 MW wind plant.

TABLE 32.2 Life cycle environmental impacts for 100 MW onshore wind power plant [35,36].

Life cycle environmental impacts	Units	V112	V126
Global warming potential (GWP)	g CO_{2e} $(kW\ h)^{-1}$	7.0	8.2
Eutrophication potential (EP)	mg PO_4 $(kW\ h)^{-1}$	2.7	4.4
Human toxicity potential (HTP)	mg DCBe/(kW h)	833	1 810
Acidification potential (AP)	mg SO_2e/(kW h)	28	44

TABLE 32.3 REE composition of medium-high and low-speed PMSG wind turbines.

System	REE	Value/kg/MW	Data sources
Medium-high speed PMSG (onshore wind turbine)	Nd	24	[14]
	Dy	2	[14]
	Tb	0.8	[39]
Low-speed PMSG (offshore wind turbine)	Nd	207	[14]
	Dy	18	[14]
	Tb	7	[39]

5. Other metal demands of permanent magnet production (e.g., Fe, Cu, Ni, B, etc.) are assumed to be covered by existing LCA studies with environmental impacts and have been included as part of the wind turbine's overall environmental footprint.

6. Environmental impacts of REE production and NdFeB magnet manufacturing characterizations and allocations are based on mass fractions of metal.

Table 32.4 shows the results of this LCA analysis. Regarding the GWP assessment, regardless of onshore or offshore wind turbine, the REE production and magnet production only accounts for a negligible proportion of the total GWP footprint for a wind turbine. This is expected given that the impact characterizations are based on the mass fractions of each material, and the relatively small amount of REE material in each turbine (Table 32.3). Our assessment also suggests that the overall GWP footprint for electricity generated from both onshore and offshore wind farms is the lowest when compared to power plants based on other energy sources (Fig. 32.6).

Compared to medium-high speed PMSGs, which dominate the current wind turbine market, low-speed generators have a significantly higher REE (i.e., Dy, Nd, Tb) amount per megawatt capacity, in exchange for lighter weight, better energy efficiency (or capacity factors) and lower GHG footprint. This is also seen in the lower average total GWP impact of low-speed PMSG as compared to the medium-high-speed PMSG units. Broadly speaking, it is reasonable to believe that extrapolating GWP impacts from REE production and permanent magnet manufacturing processing, to future wind turbine production (especially for low-speed PMSG), the utilization of REE permanent magnets will not compromise but will enhance the system's overall GWP footprint. Hence, REE permanent magnets will become even more important for future wind turbine designs and applications, especially given that the market is shifting toward high capacity low-speed PMSG wind plants.

It is also worth mentioning that, due to lack of good quality data, the current indicative LCA focus only on GWP impacts. The available data is insufficient to determine the overall environmental burden of global REE production. There is a broad range of other critical issues such as REE recovery efficiency, supply capacity, health concerns, acidification potential, and radiation exposure from hazardous by/coproducts (e.g., thorium and uranium, etc.) which should be addressed before concluding the overall impact of REEs. with relevance to future sustainable energy systems.

Table 32.5 presents the environmental benefits related to Vestas V112 and V126 wind turbines. The obvious result suggests the applications of REE magnets in modern wind turbine systems provide greater environmental benefits for wind turbines compared to the associated environmental costs from REE mineral extraction and magnet production stages.

32.5 Global wind energy projections

The International Energy Agency (IEA) predicts the evolution of the global energy sector toward 2040 [42]. The projections are divided into three primary scenarios that assess key aspects: energy sources by regions and sectors; energy

TABLE 32.4 LCA of medium-high and low-speed PMSG wind turbines.

System and process		Maximum	Average	Minimum
		gCO_{2e} $(kWh)^{-1}$	gCO_{2e} $(kWh)^{-1}$	gCO_{2e} $(kWh)^{-1}$
Onshore PMSG medium-high-speed	Nd production	2×10^{-3}	1×10^{-3}	1×10^{-3}
	Dy production	1×10^{-4}	9×10^{-5}	6×10^{-5}
	Tb production	$1 \times \times 10^{-5}$	8×10^{-6}	6×10^{-6}
	Magnet production	0.040	0.037	0.040
	Entire system	45	15	3
Offshore PMSG Low-speed	Nd production	1×10^{-2}	1×10^{-2}	9×10^{-3}
	Dy production	7×10^{-4}	7×10^{-4}	5×10^{-4}
	Tb production	7×10^{-5}	7×10^{-5}	4×10^{-5}
	Magnet production	0.23	0.29	0.29
	Entire system	23	12	7

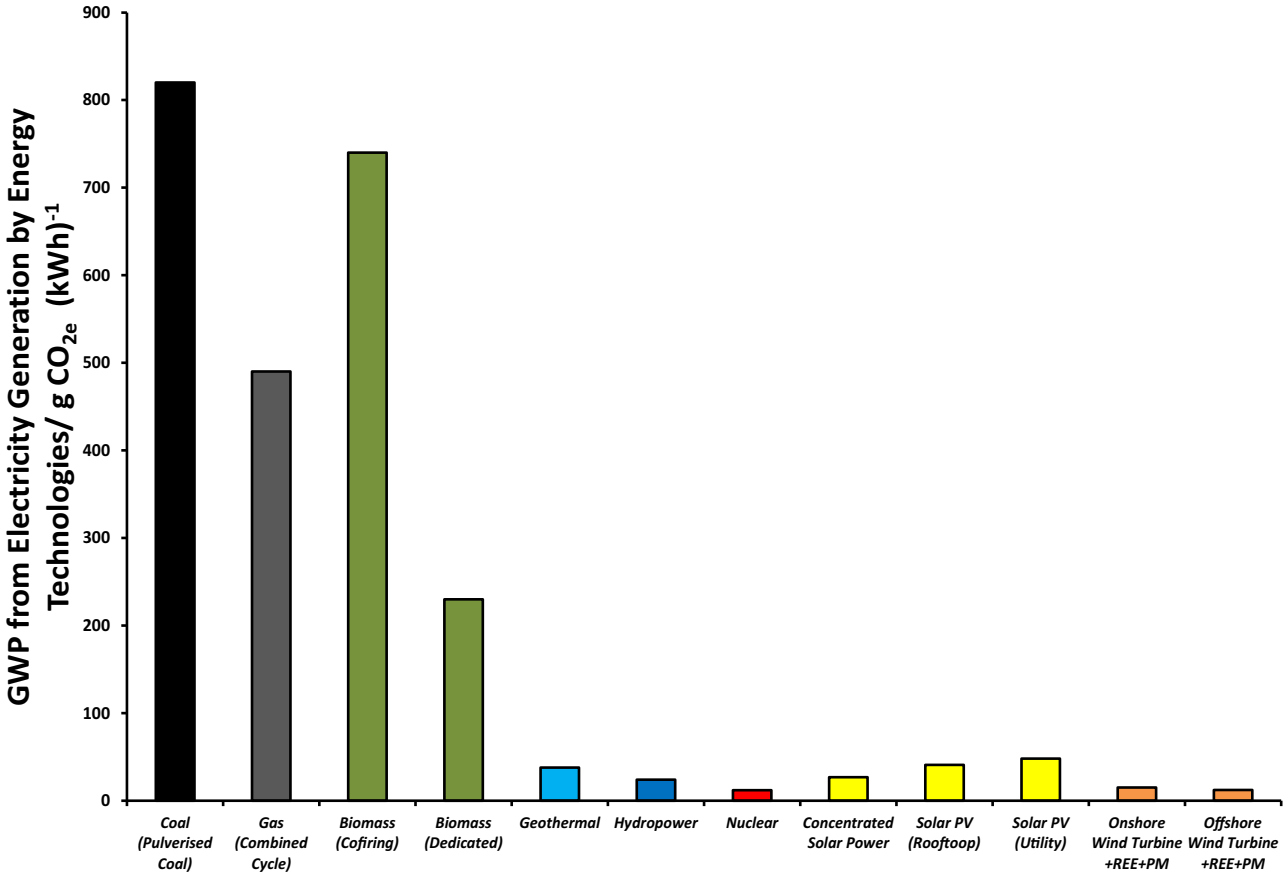

FIGURE 32.6 Emissions of selected electricity supply technologies. *From Average GWP impacts of other energy technologies are adapted from Schlömer S, Bruckner T, Fulton L, Hertwich E, McKinnon A, Perczyk D, et al., Annex III: technology-specific cost and performance parameters. In: Edenhofer O, Pichs-Madruga R, Sokona Y, Farahani E, Kadner S, Seyboth K, Adler A, Baum I, Brunner S, Eickemeier P, Kriemann B, Savolainen J, Schlömer S, von Stechow C, Zwickel T, Min JC, editors., Climate Change 2014: Mitigation of Climate Change. Contribution of Working Group III to the Fifth Assessment Report of the Intergovernmental Panel on Climate Change. Intergovernmental Panel on Climate Change (IPCC), Cambridge, 2014. p. 1331–54.*

TABLE 32.5 Benefit accounting based on Vestas V112 and V126 Systems with REE production stage footprints [35–37,40].

System & process	GWP reduction/mg CO_{2e} (kW h)$^{-1}$
Nd production	−3.3
Dy production	−0.2
Tb production	−0.02
REE magnet production	−290
GWP benefit	+1200
Overall benefit	+906

security and environmental protection; and economic development. The three core scenarios and their underlying assumptions about the evolution of energy-related government policies are summarized below:

1. *The Current Policies Scenario (CPS):* This scenario only considers existing energy policies for which implementing measures have been formally adopted as of mid-2015 and assume that these policies persist unchanged until 2040.

2. *The New Policies Scenario (NPS):* In addition to incorporating the policies and measures that affect energy markets that have been adopted as of mid-2015, it also takes into account other relevant intentions that have been announced, even when the precise implementing measures have yet to be fully defined. This includes the energy-related components of the Intended Nationally Determined Contributions, submitted by national governments by 1st October 2015 as pledges in the runup to the United Nations Framework Convention on Climate Change Conference of the Parties (COP21). These policies include programs to support renewable energy and improve energy efficiency, to promote alternative fuels and vehicles, carbon pricing, reform of energy subsidies, and the introduction, expansion, or phase-out of nuclear power. NPS is the moderate estimate of all three scenarios with considerations based on both existing and most likely developments for renewable energy growth.
3. *The 450 Scenario (450 S):* The "450" scenario assumes a set of policies based on the trajectory of GHG emissions from the energy sector that is consistent with the international goal to limit the rise in the long-term average global temperature to 2°C, compared with preindustrial levels. The policies collectively ensure an emissions trajectory consistent with stabilization of the GHG concentration after 2100 at around 450 ppm. Compared to the previous two scenarios, 450 s provides the most optimistic projection for renewable energy growth.

All scenarios have predicted a rapid growth of the renewable energy sector toward 2040. For example, in the NPS scenario, with increasing policy support from governments, reducing production and implementation costs, and greater scale use of new technologies, the fraction of renewable energy in the total global energy market is expected to rise from 14% in 2014 to 19% in 2040, with a total renewable power generation of $78\ 000 \times 10^{15}$ J (78 000 petajoules) in 2014 and 140,090 Mtoe (140,090 million tonnes of oil equivalent) in 2040 [42]. The electricity generation from renewable energy sources are projected to reach 13,429 TW h in 2040, with wind turbines expected to increase from 635 TW h in 2014 to 3568 TW h in 2040, an average 6.7% annual growth rate. The projected wind energy capacity requirements derived from all three scenarios are summarized in Fig. 32.7.

The substantial increase in global wind energy sector will require a corresponding growth in upstream REE-dependent component or material industries (e.g., NdFeB magnets) thus steering the economic drivers to increasing TREO + Y production over the coming decades along with other REE-dependant technologies.

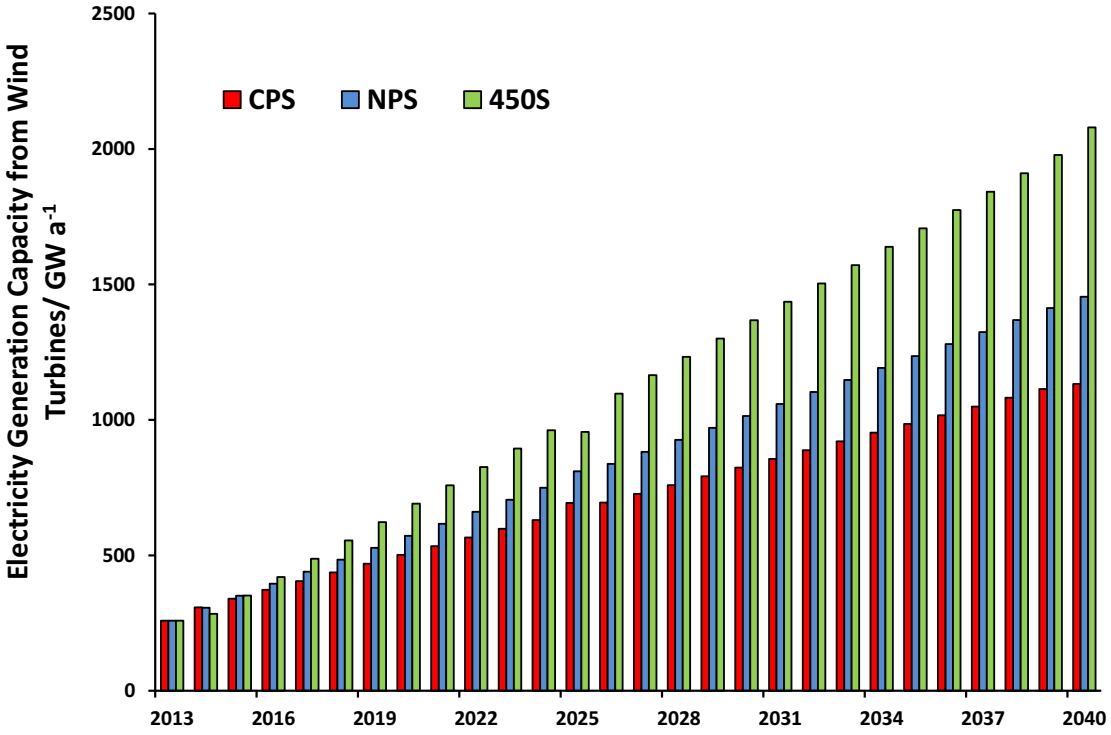

FIGURE 32.7 Projected Wind Energy Capacity Requirement to 2040; Notes: An average capacity factor used in this assessment is 28% [41]. *The annual electricity generation projection is adapted from IEA, World energy outlook 2015, International Energy Agency (IEA), Organisation for Economic Co-operation and Development (OCED), Paris, France, 2015; p. 718.*

32.6 Implications for future rare earth elements supply

The limited TREO + Y production capacity, China's monopoly position in REE processing, and commercial, geopolitical and environmental supply risks, all contribute to the implication that insufficient long-term REE supply will be the most severe constraint for wind energy to meet projected demands. In order to provide a more reliable and robust assessment of wind energy growth and expected demand, this sector presents a quantitative analysis of intercorrelations between available mineral resources [26], TREO + Y production capacity [26,37] and projected REE demands from IEA's three wind energy scenarios (i.e. CPS, NPS, and 450 S).

Fig. 32.8 shows the expected growth of global wind-based electricity generation capacity and evolution toward PMSG wind turbines. As estimated by Moss et al. [14], electricity production from PMSG wind farms will account for 15% of the European wind energy market and 20% global market in 2030. The European Wind Energy Association, EWEA, established an ambitious goal for global offshore wind energy of 4.3% of overall wind demand in 2020 [43]. This assessment uses the European wind energy targets based on the growth of various PMSG technologies (i.e., medium-high vs low-speed PMSG) as a benchmark for global wind energy evolution. The cumulative REE demands (2013−40) to meet these global energy targets are summarized in Table 32.6.

Again, as stated by Weng et al. [26], the geological scarcity of available mineral resources is not an immediate problem for wind energy development. This can be gauged by considering the most "rare" REE in the group—Tb. The estimated quantity of Tb in the world is 973 kt, which is more than enough to satisfy the most optimistic Tb (23.5 kt) demands, even considering the 450 S scenario. Nd is also widely considered one of the most critically scarce REE, however, as given in Table 32.6, the total Nd demands (considering the 450 S scenario) of 693 kt accounts for less than 0.1% of geologically available Nd. However, converting these geological resources into saleable commodities or functional materials will require complex mining, beneficiation, and refining processes. Hence, the real limitation is the annual REE production capacity instead of the REE geological scarcity.

Fig. 32.9 shows the projected annual TREO + Y production based on Tb demand in wind turbines. The projected Tb demand based on all three scenarios (CPS, NPS, and 450 S) increases from 63 t in 2013 to 1208, 1552, and 2218 t

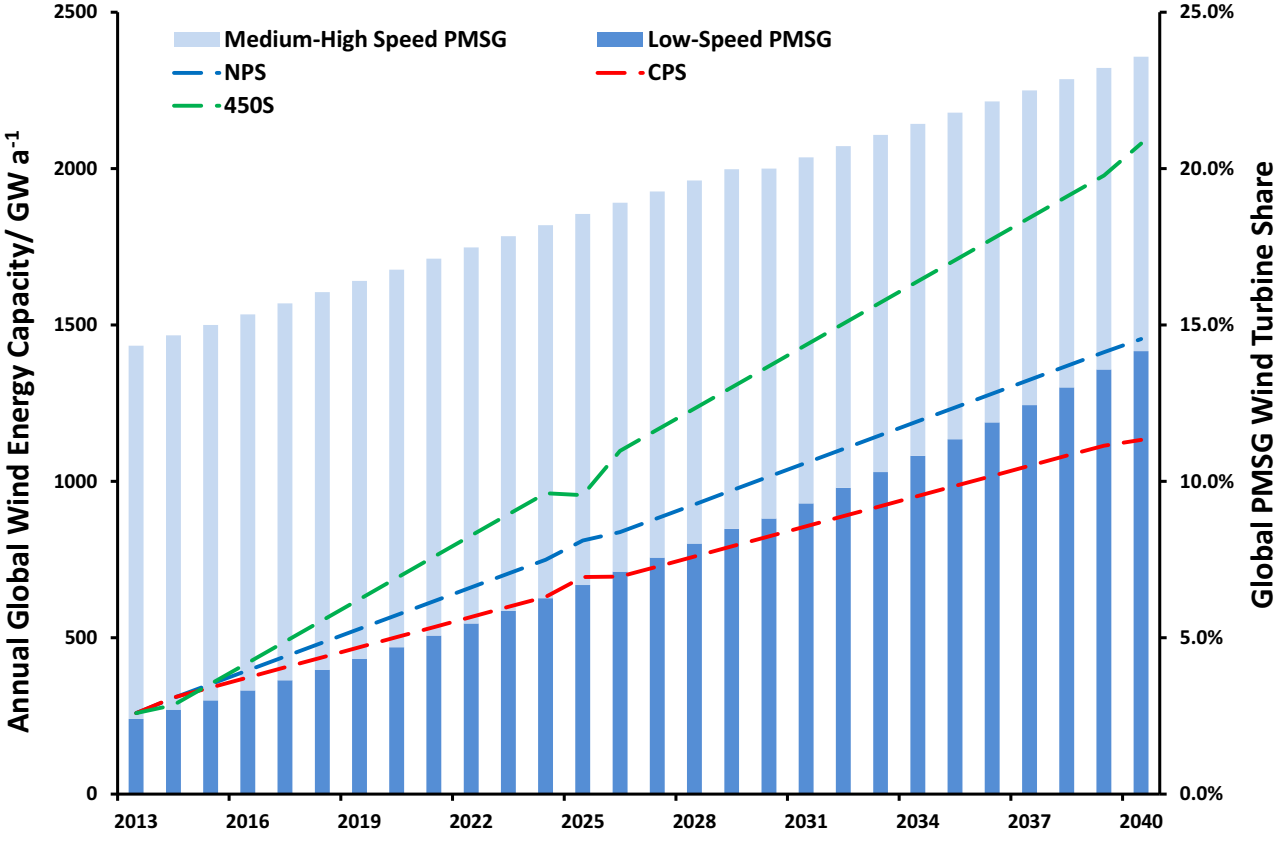

FIGURE 32.8 Projected global wind energy demands and PMSG share [13,42,44,45].

TABLE 32.6 Cumulative REE demand (2013–40) driven by medium-high and low-speed PMSG wind turbines.

REE	Wind energy scenario	Cumulative demands/ kt	Mineral resources/ kt
Dy	CPS	35	4601
	NPS	44	
	450 S	58.7	
Nd	CPS	419	72,821
	NPS	515	
	450 S	692.6	
Tb	CPS	14	973
	NPS	17	
	450 S	23.5	

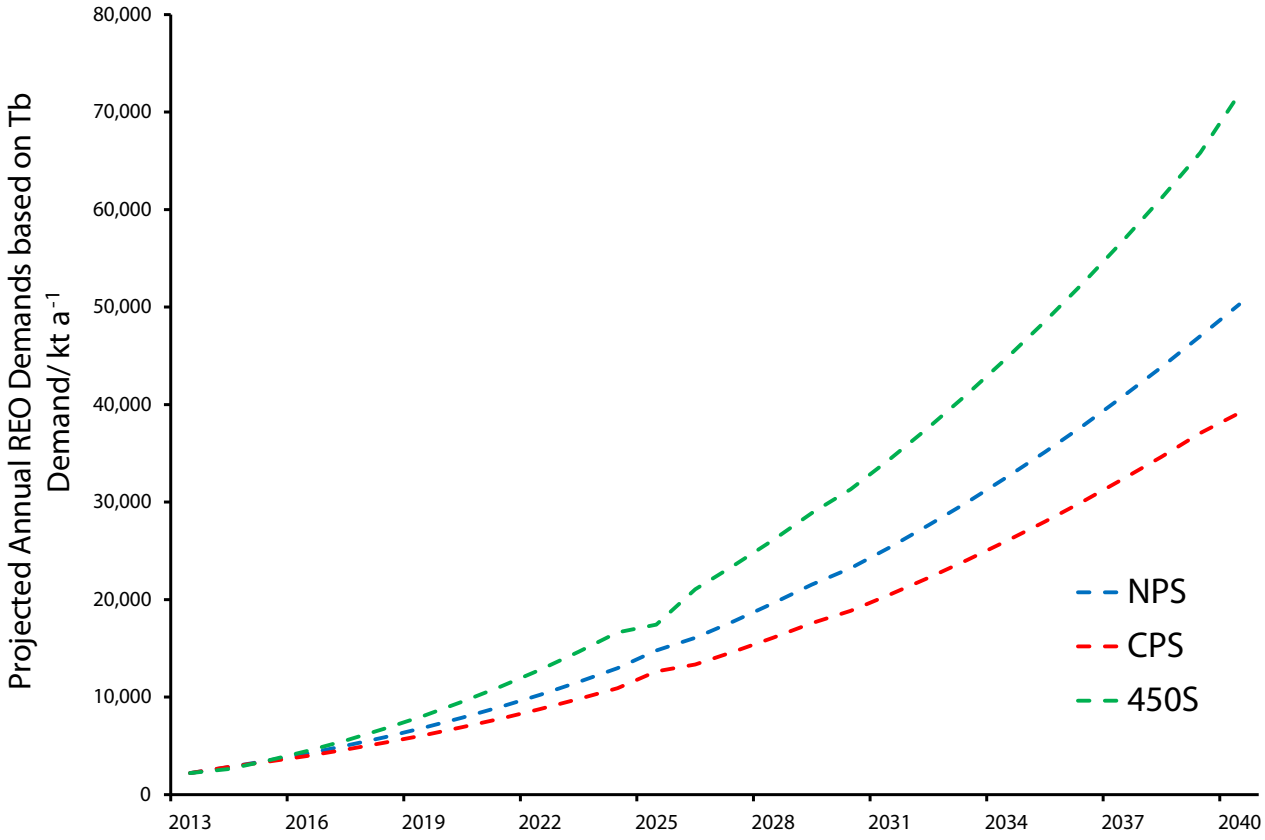

FIGURE 32.9 Projected annual REO production driven by estimated Tb demand.

in 2040, respectively. Corresponding annual production required to meet these demands has increased from 2.12×10^6 t (2.12 million tonnes) to 39×10^6 t, 50×10^6 t and 72×10^6 t TREO + Y, respectively, based on several key assumptions. These assumptions include: the average Tb proportion (0.11%) calculated from carbonatite REE deposits [26]; the average wind energy share (10%; [33]) of global REE permanent magnet market; and the permanent magnet share in global REE demand of 20% [16]. These assumptions were consistent throughout the modeling period (2013–14). According to [46,47], the reported annual global TREO + Y production is presently 110,000 t while the peak production

occurred in 2006 with 137,000 t produced; this being only 6% of the expected supply to meet Tb demands in 2013. The main explanation for such a significant difference between expected and reported TREO + Y production is that current global HREE are derived mainly from Southern China ionic clay projects instead of traditional carbonatite projects with a much higher average HREE concentrations.

32.7 Conclusion

The use of REE permanent magnets will not compromise but enhance the environmental footprint of wind turbines. Furthermore, they lead to greater environmental benefits for the life cycle of wind turbines which includes the associated environmental impacts from REE mineral production stages. Therefore, REE permanent magnets as key functional components will become even more critical for future wind turbine design and applications, especially given the market shifting toward high capacity low-speed PMSG wind turbines.

However, as a global industry, the overall environmental impact of increasing REE production is still significant especially considering the exponentially increasing global REE demands driven by other emerging technological applications like EV, photovoltaic thin films, and new sustainable system in future. Hence, novel REE extraction, recovery, and diverse supply chain based on various REE mineralogy are needed to cope with expected demands. Also, instead of the long-term availability of REE mineral resources, the short to medium-term TREO + Y production capacity and recovery efficiency are the main challenges for future REE supply.

Furthermore, current global REE mineral resources are dominated by LREE instead of HREE (e.g., Dy, Tb, Er, etc.) with an average ratio of LREE oxides to heavy rare earth element oxides of 13:1. The recent global REE supply has been dominated by the production of LREE-enriched bastnäsite-based carbonatite projects (e.g., Bayan Obo in China and the Mountain Pass in United States; the latter was shut down again in 2015). However, the predicted global REO consumption growth is mostly driven by increasing HREE (and particularly LREE such as Eu, Nd) demands from the emerging and advanced technology sector. Therefore, by simply increasing the production at the current carbonatite REE mines may result in an excess of LREE production while not being able to meet the demands for a particular HREE. As highlighted in Fig. 32.9, the expected Tb demands are simply too high based on traditional TREO + Y supply from bastnäsite-based carbonatite projects.

References

[1] Gschneider KA. 1787—1987 Two hundred years of rare earths. Rare Earth Informantion Center. Iowa, USA: Iowa State University; 1987. p. 32.
[2] Klinger JM. A historical geography of rare earth elements: From discovery to the atomic age. Extractive Industries Soc 2015;2:572–80.
[3] Zepf V. Chapter 1—An Overview of the Usefulness and Strategic Value of Rare Earth Metals A2—Filho, Ismar Borges De LimaWalter leal, rare earths industry. Boston, MA: Elsevier; 2016. p. 3–17.
[4] IUPAC, Nomenclature of inorganic chemistry IUPAC recommendations. International Union of Pure and Applied Chemistry (IUPAC). Switzerland: Zürich; 2005. p. 2005.
[5] Hoatson DM, Jaireth S, Miezitis Y. The major rare earth element deposits of Australia: geological setting, exploration, and resources. Geoscience 2011;204 Australia, ACT, Australia.
[6] Sprecher B, Xiao Y, Walton A, Speight J, Harris R, Kleijn R, et al. Life cycle inventory of the production of rare earths and the subsequent production of NdFeB rare earth permanent magnets. Environ Sci Technol 2014;48:3951–8.
[7] Zimmermann T, Gößling-Reisemann S. Critical materials and dissipative losses: a screening study. Sci Total Environ 2013;461–462:774–80.
[8] USDoE, Critical mineral strategies, U.S. Department of Energy, Washington, DC, 2011; p. 189.
[9] Binnemans K, Jones PT. Perspectives for the recovery of rare earths from end-of-life fluorescent lamps. J Rare Earths 2014;32:195–200.
[10] Graedel TE, Harper EM, Nassar NT, Nuss P, Reck BK. Criticality of metals and metalloids. Proc Natl Acad Sci USA 2015;112:4257–62.
[11] Graedel TE, Harper EM, Nassar NT, Reck BK. On the materials basis of modern society. Proc Natl Acad Sci USA 2015;112:6295–300.
[12] Habib K, Wenzel H. Exploring rare earths supply constraints for the emerging clean energy technologies and the role of recycling. J Clean Prod 2014;84:348–59.
[13] Moss RL, Tzimas E, Kara H, Willis P, Kooroshy J. The potential risks from metals bottlenecks to the deployment of strategic energy technologies. Energy Policy 2013;55:556–64.
[14] Moss RL, Tzimas E, Kara WP, Kooroshy J. Critical metals in strategic energy technologies. Eur Comm Jt Res Centre, Luxemb 2011;161.
[15] Hoenderdaal S, Espinoza LT, Marscheider-Weidemann F, Graus W. Can a dysprosium shortage threaten green energy technologies? Energy 2013;49:344–55.
[16] Humphries M. Rare Earth Elements: The Global Supply Chain. Washington, DC: U.S. Congressional Research Service; 2013. p. 27.
[17] Rudnick RL, Gao S. Composition of the continental crust. In: Holland HD, Turekian KK, editors. Treatise on Geochemistry, 3. Oxford: Elsevier Pergamon; 2014. p. 1–64.
[18] USBoM, Mineral resources of the United States. Washington, DC: U.S. Bureau of Mines (USBoM); 1927–1934.

[19] Olson JC, Shawe DR, Pray LC, Sharp WN. Rare-earth mineral deposits of the mountain pass district, San Bernardino County, California. Science 1954;119:325–6.
[20] Castor SB. The Mountain Pass rare earth carbonatite and associated ultrapotassic rocks, California. Can Mineral 2008;46:779–806.
[21] Mariano AN, Mariano Jr A. Rare earth mining and exploration in North America. Elements 2012;8:369–76.
[22] USEPA. Rare earth elements: a review of production, processing, recycling, and associated envrionmental issues. U.S. Environmental Protection Agency (USEPA), Washington, DC; 2012. p. 135.
[23] Hayes-Labruto L, Schillebeeckx SJD, Workman M, Shah N. Contrasting perspectives on China's rare earths policies: Reframing the debate through a stakeholder lens. Energy Policy 2013;63:55–68.
[24] Morrison WM, Tang R. China's Rare Earth Industry and Export Regime: Economic and Trade Implications for the United States. Washington, DC: U.S. Congressional Research Service; 2012. p. 17.
[25] Wübbeke J. Rare earth elements in China: policies and narratives of reinventing an industry. Resour Policy 2013;38:384–94.
[26] Weng Z, Jowitt SM, Mudd GM, Nawshad H. A detailed assessment of global rare earth element resources: opportunities and challenges. Econ Geol 2015;110:1925–52.
[27] Buchert M. Rare earths—A Bottleneck for Future Wind Turbine Technologies? Berlin: Oeko-Institut e.V.; 2011. p. 29.
[28] Wang RJ, Gerber S. Magnetically geared wind generator technologies: Opportunities and challenges. Appl Energy 2014;136:817–26.
[29] Dent PC. Rare earth elements and permanent magnets (invited). J Appl Phys 2012;111:7.
[30] Wiser R, Yang Z, Hand M, Hohmeyer O, Infi eld D, Jensen PH, et al. Wind energy. In: Edenhofer O, Pichs-Madruga R, Sokona Y, Seyboth K, Matschoss P, Kadner S, Zwickel T, Eickemeier P, Hansen G, Schlömer S, von Stechow C, editors. IPCC Special Report on Renewable Energy Sources and Climate Change Mitigation. New York: Intergovernmental Panel on Climate Change (IPCC); 2011. p. 539–96.
[31] Arnold. Market outlook for Ferrite, Rare Earth and other permanent magnets. Arnold Magnetic Technol (ARNOLD) 2016;43. Available from: http://www.magneticsmagazine.com/conferences/2016/Presentations/Arnold_Constantinides.pdf.
[32] Strnat KJ. Modern permanet magnets for applications in electro-technology. Proc Inst Electr Electron Eng 1990;78:923.
[33] Lucas J, Lucas P, Le Mercier T, Rollat A, Davenport W. Chapter 14—Rare earth-based permanent magnets preparation and uses. , Rare Earths. Amsterdam, Netherland: Elsevier; 2015. p. 231–49.
[34] Tripathi SM, Tiwari AN, Singh D. Grid-integrated permanent magnet synchronous generator based wind energy conversion systems: a technology review. Renew Sustain Energy Rev 2015;51:1288–305.
[35] D'Souza N, Gbegbaje-Das E, Shonfield P. Life cycle assessment of electricity production from a V112 turbine wind park. Vestas Wind Systems A/S (Vestas), Randers, Denmark; 2011. p. 87.
[36] Garrett P, Rønde K. Life cycle assessment of electricity production from an onshore V126-3.3 MW wind plant. Vestas Wind System A/S, Aaehus, Denmark; 2014. p. 116.
[37] Weng Z, Nawshad H, Mudd GM, Jowitt SM. Assessing energy and global warming potentials of rare earth production. J Clean Prod 2016;139:1282–97.
[38] Dolan S, Heath G. Life cycle greenhouse gasemissions of utility-scale wind power: systematic review and harmonization. J Ind Ecol 2012;16 (S1):136–54.
[39] Öhrlund, I., Future Metal Demand From Photovoltaic Cells and Wind Turbines, European Parliament Science and Technology Options Assess (EPSTOA), Brussels, Belgium, 2011; p. 72.
[40] Schlömer S, Bruckner T, Fulton L, Hertwich E, McKinnon A, Perczyk D, et al. Annex III: technology-specific cost and performance parameters. In: Edenhofer O, Pichs-Madruga R, Sokona Y, Farahani E, Kadner S, Seyboth K, Adler A, Baum I, Brunner S, Eickemeier P, Kriemann B, Savolainen J, Schlömer S, von Stechow C, Zwickel T, Min JC, editors. Climate Change 2014: Mitigation of Climate Change. Contribution of Working Group III to the Fifth Assessment Report of the Intergovernmental Panel on Climate Change. Cambridge, United Kingdom: Intergovernmental Panel on Climate Change (IPCC); 2014. p. 1331–54.
[41] GWEC. Global wind energy outlook 2014. Global Wind Energy Council (GWEC), Brussel, Belgium; 2015a. p. 60.
[42] IEA. World energy outlook 2015. International Energy Agency (IEA), Organisation for Economic Co-operation and Development (OCED), Paris, France; 2015. p. 718.
[43] EWEA. Pure power wind energy targets for 2020 and 2030—a report by the European Wind Energy Association—2009 update. European Wind Energy Association (EWEA), Stockholm, Swden; 2009. p. 78.
[44] EWEA. The European offshore wind industry—key trends and statistics 2014. European Wind Energy Association (EWEA); 2015. p. 25.
[45] GWEC. Global wind report annual market update 2014. Global Wind Energy Council (GWEC). Brussel, Belgium; 2015b. p. 80.
[46] USGS, various, Minerals commodity summaries. Reston, VA: U.S. Geological Survey (USGS); 1997–2015.
[47] BoMRGG. The Australian mineral industry review. ACT, Australia: Bureau of Mineral Resources, Geology and Geophysics (BoMRGG), 1960–85.

This page intentionally left blank

Chapter 33

Short-term power prediction and downtime classification

JM González-Sopeña[1], B Ghosh[1], P Mucchielli[2], B Bhowmik[2] and V. Pakrashi[2]

[1]QUANT Group, Department of Civil, Structural and Environmental Engineering, Trinity College Dublin, Dublin, Ireland, [2]UCD Centre for Mechanics, Dynamical Systems and Risk Laboratory, School of Mechanical and Materials Engineering, University College Dublin, Dublin, Ireland

33.1 Introduction

Wind power forecasting (WPF) and downtime detection are fast coming up as important aspects of operations, maintenance, and de-risking of the wind energy sector and data takes a center stage there. Our understanding of WPF, especially in the short term has become more important than ever and the availability of data from turbines, in conjunction with a wider range of methods that are available for analyses of such data has opened up newer avenues. Early downtime detection remains important and interesting, while its classification needs are becoming impactful. Modern data analysis and artificial intelligence can be of significant help, but they also come with the challenges of lack of benchmarking and inadequacy of guidelines and recommendations around their consistent use and comparison.

Investigation of such forecasts and proposing related guidelines by qualifying and quantifying the main sources of errors, and optimizing the currently available data is thus an important need. Novel statistical models are often used on high-resolution data from wind farms. The results not only improve operations & maintenance (O&M) costs but also increases the competitiveness of wind energy. Lack of standardization in terms of model evaluation and uncertainty quantification continues to be a problem and well-designed benchmark examples can address this for diverse datatypes. The robustness of developed methods is thus a key aspect to address, along with their original purpose of being accurate. There is a limited understanding in this field in terms of errors. Even if we do know the main existing sources of errors, we often do not have the tools to evaluate and quantify them during model development.

To this effect, analysis results on wind turbine data from Irish wind farms are considered in this chapter, especially in the context of the knowledge gap around short-term forecasting and downtime detection and classification.

33.2 Wind turbine data

WPFs are estimates of the power generation production of a wind turbine/wind farm in the foreseeable near future. For shorter-term prediction horizons, high-resolution measurements from SCADA (acronym for *Supervisory Control And Data Acquisition*) systems, including wind power generation data (Fig. 33.1) are used to build WPF models.

Accurate short-term WPFs contribute to keeping the stability of the grid and to the decision-making process in electricity markets. In the first case, the electricity generated from wind energy is not easily dispatchable due to the fluctuating nature of wind speeds, so WPFs allow to manage the required system flexibility to balance electricity consumption and generation. In the near future, such forecasts will only become more important as the electricity system flexibility must increase by at least two-thirds even for the most modest energy transition scenarios projected [1]. Apart from the technical aspects in relation to the grid, WPFs are an indispensable tool for participants in electricity markets. These markets emerge to meet the electricity consumption (namely load) profiles which are scheduled in advance in order to maintain the balance between electricity production and consumption. Having anticipated information on energy production in the form of forecasts lead to a more informed decision-making process in the different electricity markets.

Wind Energy Engineering. DOI: https://doi.org/10.1016/B978-0-323-99353-1.00009-8

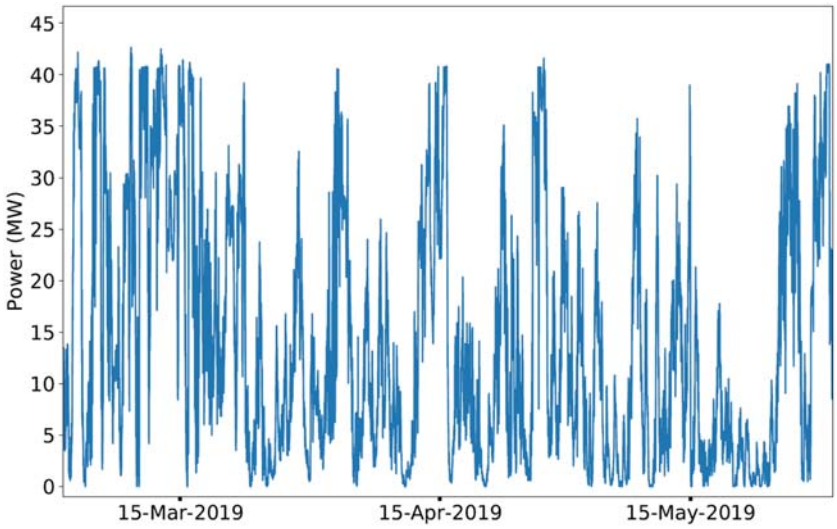

FIGURE 33.1 Wind power data from an Irish wind farm (10-minute resolution).

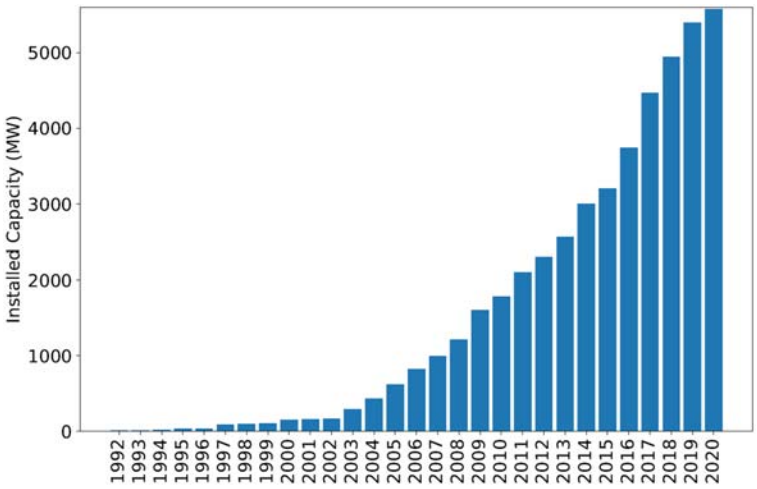

FIGURE 33.2 Installed wind power capacity in Ireland.

The installed wind power capacity has increased dramatically over the last few years, especially in countries with a great wind resource as Ireland (Fig. 33.2). This region is particularly representative of benchmark WPF models, as the electrical grid of the island is only connected to Great Britain by the Moyle Interconnector and the East-West Interconnector. Due to this limited interconnection, maintaining the stability of the grid becomes a challenge not found in the highly interconnected grid of Continental Europe or other regions of the world. On the other hand, a brand and ambitious new electricity market arrangement was set in both Ireland and Northern Ireland, known as I-SEM (Integrated Single Electricity Market) to harmonize the existing markets on the whole island and further integrate electricity markets across the European Union. Additional challenges are found in this electricity market, such as the operation with two different currencies.

The importance of WPF has led to an ample amount of research on WPF has been carried out to this day (Table 33.1). The progressive development and publication of wind speed forecasting (WSF) and WPF approaches have required a recurrent update of the state-of-the-art wind energy forecasting, reflected in the continuous (yet necessary) reviews published over time [2,3].

Studying the uncertainty of WPFs is one of the main areas of research, and aims to build more complex and complete forecasting models. Zhang et al. [4] address the impact of WPFs on electricity prices and presents optimal bidding

TABLE 33.1 Examples of review papers on wind power forecasting.

Publication	Year	No. of references	Review focus
Giebel et al. [2]	2011	381	State-of-the-art WPF (deliverable for the ANEMOS project)
Foley et al. [3]	2012	68	Research on WSF and WPF
Zhang et al. [4]	2014	116	Probabilistic methodologies for WPF
Yan et al. [5]	2015	76	Evaluation of uncertainty analysis of WPFs
Marugán et al. [6]	2018	189	Application of ANNs to wind energy applications
Liu and Chen [7]	2019	128	Data processing strategies for wind energy forecasting
Qian et al. [8]	2019	133	Data decomposition strategies for wind energy forecasting
Roungkvist and Enevoldsen [9]	2020	56	Time scale classifications proposed for wind energy forecasting
González-Sopeña et al. [10]	2021	92	Metrics for short-term statistical WPF

strategies for energy markets, whereas influential factors with respect to forecasting uncertainty are addressed by Yan et al. [5], such as the uncertainty on numerical weather prediction data, the power curve, and the forecasting algorithms themselves. In both reviews, the authors analyze the existing categorizations of WPF uncertainty: (1) probabilistic forecasting, (2) risk index, and (3) scenario forecasting.

WPF modeling is another key area of research. Different aspects of WPF modeling have been analyzed in the literature, for instance, the categorization of certain architectures to build WPF models such as artificial neural networks (ANNs) [6], the classification of WPF models in terms of prediction horizon [9], or the classification of metrics to evaluate statistical WPF models [10].

The third main area of research is the use of data processing strategies. Liu and Chen [7] present a review of data processing strategies for wind energy forecasting. Seven categories are identified: data decomposition, feature selection, feature extraction, denoising, residual error modeling, outlier detection, and filter-based correction. Some of these strategies are further discussed by other authors, such as the application of data decomposition strategies for wind energy forecasting [8].

33.3 Downtime detection

Downtime is the period of time between stopping and restarting an operation of a given nonfunctional unit. Most of the O&M cost of wind farms is produced by unscheduled maintenance, leading to downtime and therefore a loss of revenue. Downtime detection can be achieved by continuous monitoring of wind turbines, thus being part of predictive maintenance strategies [11].

SCADA data can be leveraged for downtime detection. These data must be (1) carefully processed to remove duplicates and missing values generated by issues in the acquisition of SCADA data and (2) alarm logs must be categorized taking into consideration those events which can potentially lead to downtime. Fig. 33.3 shows a snapshot correlating some of these events (fault, lack of wind, maintenance, or other) with wind power generation.

In addition, this information is not only useful to reduce the O&M cost of wind farms by detecting downtime but can be used as an additional input to generate improved WPFs.

33.4 Data preprocessing

Among the data processing strategies listed by Liu and Chen [7], data decomposition is one of the most applied approaches for wind forecasting [8]. As wind power time series is such complex data, affected by meteorological conditions and activities performed in a wind farm, this strategy aims to find the main components of these data to build a group of more accurate forecasting models. The components are reconstructed at a later stage to obtain the final WPF estimate.

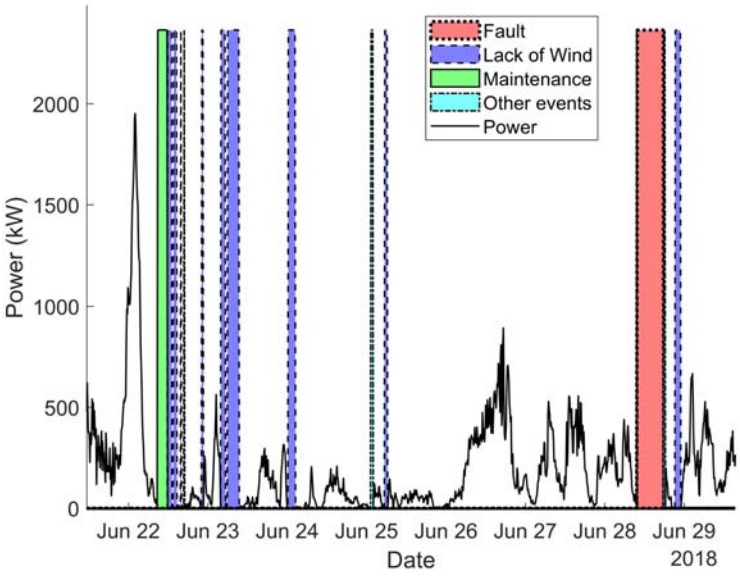

FIGURE 33.3 Visualization of events in a wind farm data.

TABLE 33.2 Examples of publications applying decomposition algorithms in the WPF literature.

Reference	WT	EMD	VMD	SSA
Osório et al. [22]	X			
Abdoos [23]			X	
Safari et al. [24]				X
Naik et al. [25]		X		
Abedinia et al. [26]		X		
Wang et al. [27]				X
Dong et al. [28]	X			
Liu et al. [29]		X		
Yildiz et al. [30]			X	
Duan et al. [31]			X	

The components vary depending on the decomposition algorithm. Wavelet transform extracts the approximation components, which contain the trend existing in the original data, and the detail components, which represent the higher-frequency ones.

Empirical mode decomposition (EMD) and variational mode decomposition (VMD) define these components as amplitude modulated−frequency modulated (AM−FM) signals called intrinsic mode functions (IMFs):

$$u_k(t) = A_k(t)\cos\phi_k(t) \text{ where } A_k(t), \quad \phi_k{}' > 0 \tag{33.1}$$

where the variation of A_k and $\phi_k{}'$ is less than the variation of ϕ_k, so the IMF $u_k(t)$ is a harmonic function of amplitude A_k and frequency $\phi_k{}'$ for a given interval $[t-\delta, t+\delta]$.

Another type of decomposition is performed by another algorithm called singular spectrum analysis (SSA), identifying the trend, periodic/quasi-periodic, and noise components by a two-stage process (Table 33.2).

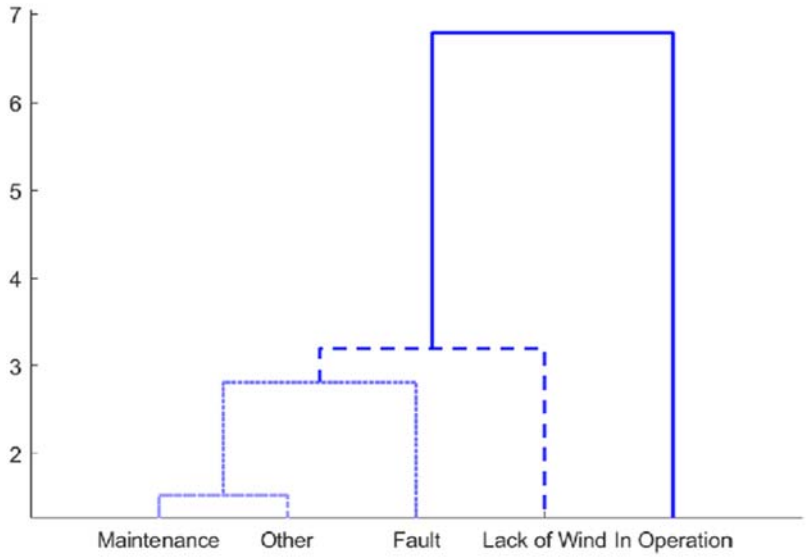

FIGURE 33.4 Example of a dendrogram considering five possible classification outcomes.

33.5 Understanding classification

Previous studies using Irish data have shown that three metrics are useful as classification features for anomaly detection [11]. The first metric is called Recursive Mahalanobis Distance (RMD):

$$m_d(k) = \sqrt{(x_k - M_k)C_k^{-1}(x_k - M_k)} \tag{33.2}$$

where x_k, M_k, and C_k are respectively the sample vector, mean vector, and covariance matrix of the data at step k. RMD is defined as the deviation of each sample from the mean of the data along its principal components. Those samples concurrent with stoppages are more likely to have a value close to zero.

The other two features are known as Recursive Residual Errors (RREs). The first one can be calculated as follows:

$$\chi_{rr_1} = X_k^* - V_k^{1^T} X_k^{*^2}; \;\; X_k^* = V_{k-1}^1 V_k^{1^T} X_k \tag{33.3}$$

where V_{k-1}^1 is the concatenation of the collection of eigenvectors explaining more than 95% of the variance of this dataset. It considers variations in the eigenspace between $k-1$ and k, providing information about the changes across two samples, and therefore is able to encapsulate timely changes. On the other hand, the second RRE determines the difference between a given sample vector and its projection X_k^*:

$$\chi_{rr_2} = X_k^* - X_k{}^2 \tag{33.4}$$

The resulting features are posteriorly fed to a classifier together with alarm labels to achieve the desired classification, identifying anomalies such as maintenance operations or lack of wind events (Fig. 33.4).

33.6 Statistical wind power forecasting modeling for short-term forecasting

Many statistical methodologies have been applied in the literature to model short-term estimates of WPFs. The major categorizations of WPF models and estimates are shown in Fig. 33.5. In particular, time series analysis and artificial intelligence-based models are the most commonly used frameworks for this purpose, but other methodologies such as Gaussian Processes [12] and Markov models have been proposed as well in the literature [13].

WPF models can produce either point estimates, or additionally, estimate the uncertainty of such forecasts. In the second case, this uncertainty can be represented in several manners, usually in the form of probabilistic estimates. They can be represented as:

1. Predictive densities indicate the future probability distribution.
2. Quantile forecasts to predict the future probability distribution at a predetermined set of quantiles.
3. Prediction intervals by estimating the upper and lower boundaries of an interval where the future observations will fall.

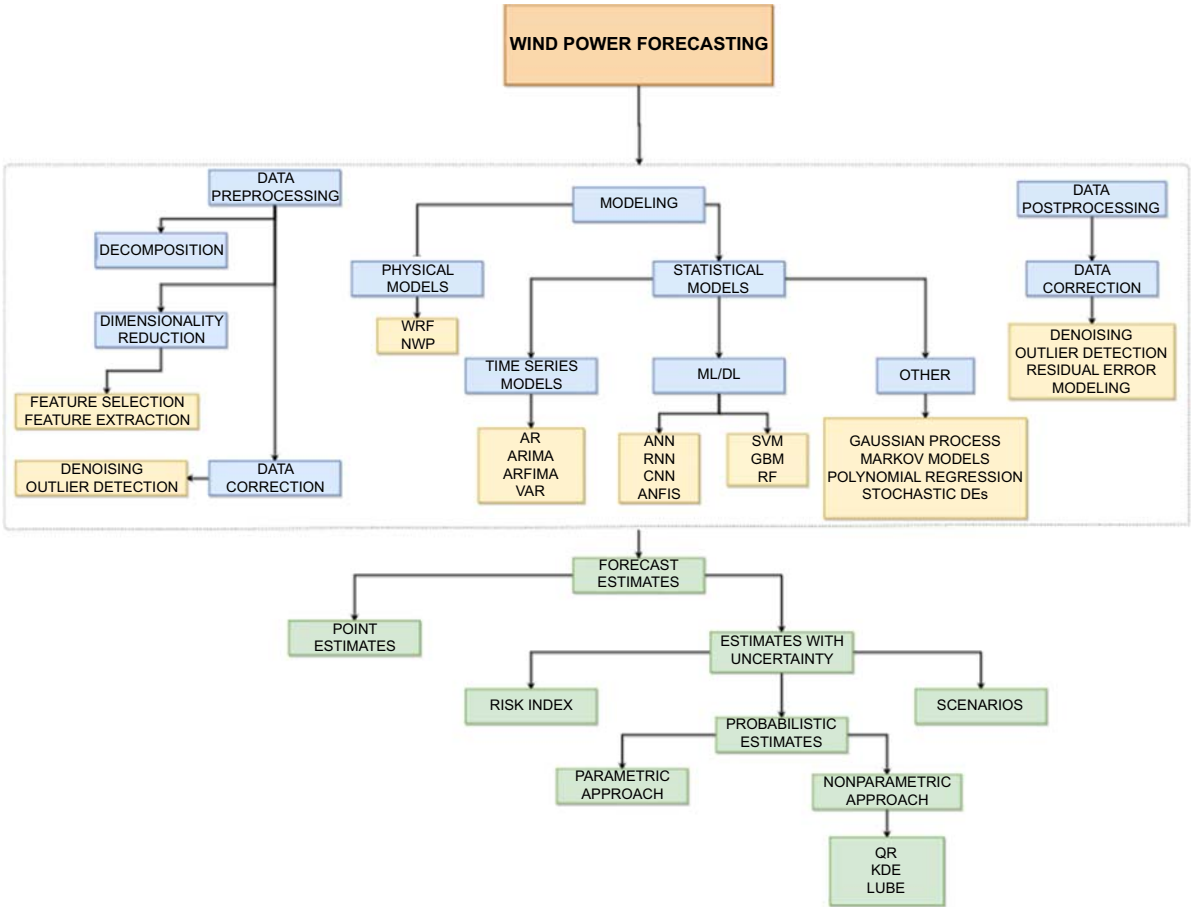

FIGURE 33.5 Main categorizations of WPF models.

Prediction intervals are easier to understand compared to the other representations, so are usually the preferred way to calculate probabilistic estimates.

33.6.1 Time series analysis models

The basic elements of time series analysis, based models are autoregressive (AR) and moving average (MA) processes [14,15]. AR terms take into consideration the values of previous observations to estimate future outputs, and MA terms are formed by previous forecast errors in the same fashion as a regression model. More complex models can be set using AR and MA terms. Vector autoregression (VAR) is the type of time series model, which has gained more traction in the most recent literature, as WPFs of several wind farms can be calculated at the same time, while taking into consideration the Spatio-temporal dependencies of such farms. For instance, Messner and Pinson [16] apply a VAR-based forecasting model to predict improved WPFs of 172 farms located in Western France (with 10-minute resolution data) and 100 wind farms in Denmark (15-minute resolution data).

33.6.2 Artificial intelligence models

ANNs are the core artificial intelligence architecture to build WPF models. Fig. 33.6 shows the structure of a simple feedforward neural network, characterized by the flow of information only in a forward direction: the data arrive at the input layer and pass through the network on a layer-by-layer basis till the output is computed. Usually, more complex ANNs are applied to wind power data to model Spatio-temporal relations.

Temporal dependencies can be captured by adding some sort of memory to the neurons, such as in the case of long short-term memory (LSTM) or gated recurrent unit (GRU) architectures. LSTM networks regulate the flow of information using three gates (namely forget, input, and output gates), and a reservoir of long-term memory known as cell state in order to determine the hidden state of the network, which corresponds to the output computed every time step. GRUs

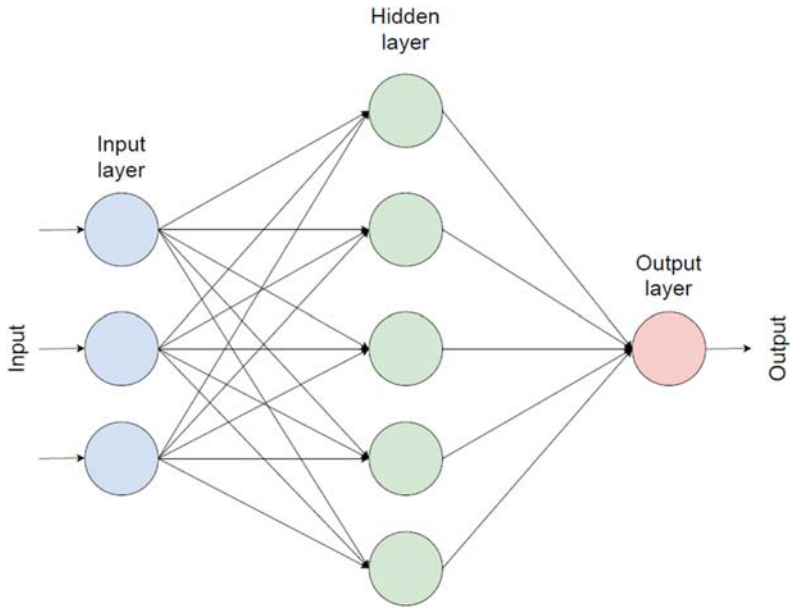

FIGURE 33.6 Structure of a simple feedforward neural network.

control the flow of information using two gates instead of three as LSTM networks: the update gate, which passes relevant previous information to the current state, and the reset gate, which acts as a filter to erase unnecessary information.

On another note, convolutional neural networks are a type of neural network architecture in which at least one of the layers perform a convolution to find features invariant across spatial dimensions [17]. Mathematically, a convolution is defined as follows:

$$(f \times g)(t) = \int_{-\infty}^{\infty} f(\tau)g(t-\tau)d\tau \tag{33.5}$$

where $(f \times g)(t)$ indicates the convolution between the functions f and g, in which the function f can be considered as a *filter* or *kernel* and g as the input data. On the right-hand side, $g(t-\tau)$ indicates that the input data g is reversed and shifted to a certain time t. In the context of CNNs, the convolutional layer is formed by a certain number of filters which are convoluted with the input data to detect any existing hidden features.

33.6.3 Other models

Modeling of WPFs is not limited to time series analysis or artificial intelligence-based architectures. An alternative is provided by Gaussian Processes, used for authors such as Yan et al. [18], where this model is tailored to capture time-varying features existing in wind power data. Other well-known methodologies are Markov models [19] and stochastic differential equations [20].

33.7 Downtime detection and classification

SCADA data must be carefully cleaned to correct any errors produced during the acquisition of such data. Mucchiell et al. [11] applied the process shown in Fig. 33.7 to classify any possible anomalies detected in a wind turbine.

In particular, the alarms logs were divided into five categories depending on the state of the turbine:

1. In operation: logs do not indicate the occurrence of any anomalous event.
2. Fault: logs show that the turbine was halted due to a fault.
3. Lack of wind: The turbine is shut down when the wind speed is below the cut-off speed of the wind turbine.
4. Maintenance: the turbine is stopped to perform scheduled maintenance activities.
5. Other: the turbine is stopped for any other type of events.

Using real-time Eigen-perturbation [21] and the classifiers mentioned above, such anomalies can be detected with a great degree of accuracy (Fig. 33.8).

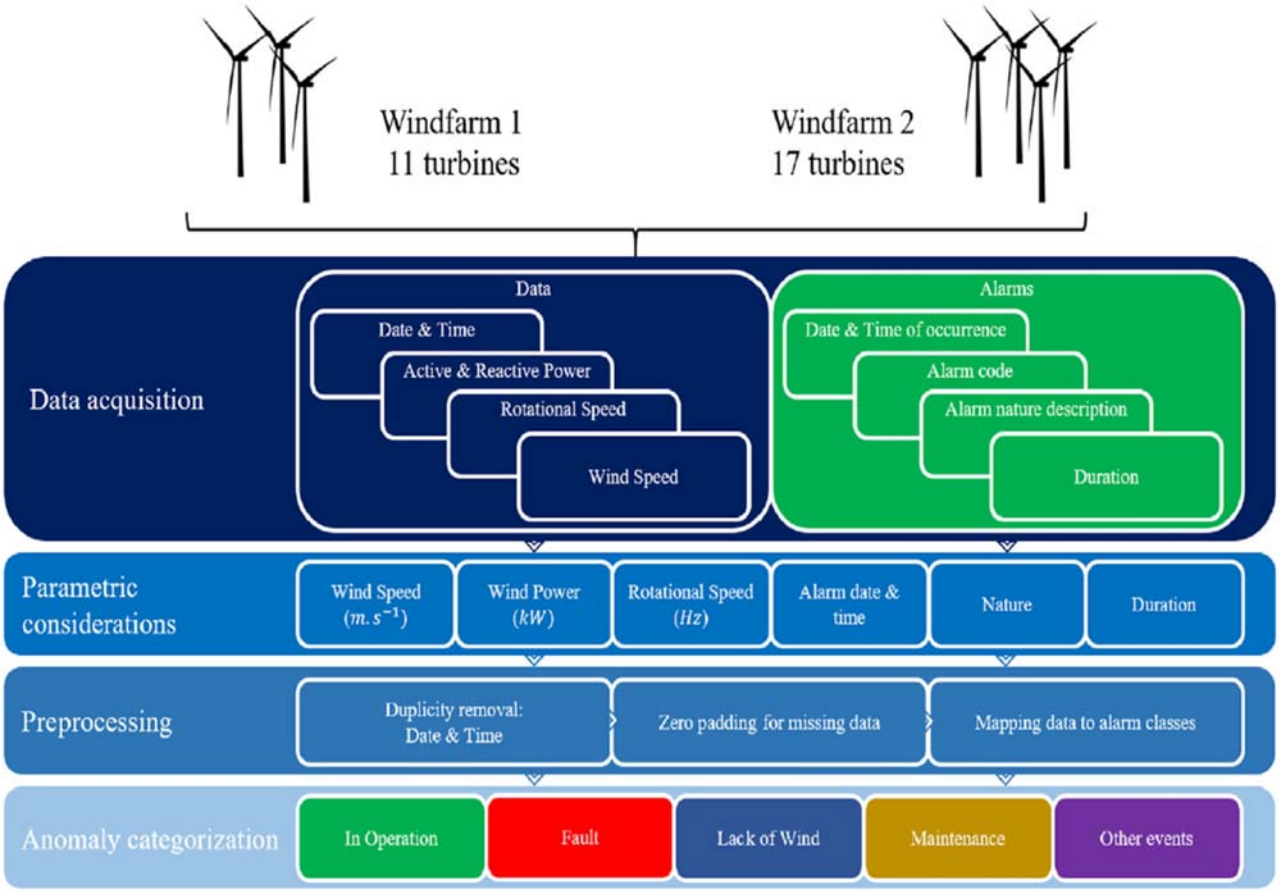

FIGURE 33.7 Flowchart representing the proposed approach in the extraction, processing, and categorization of data.

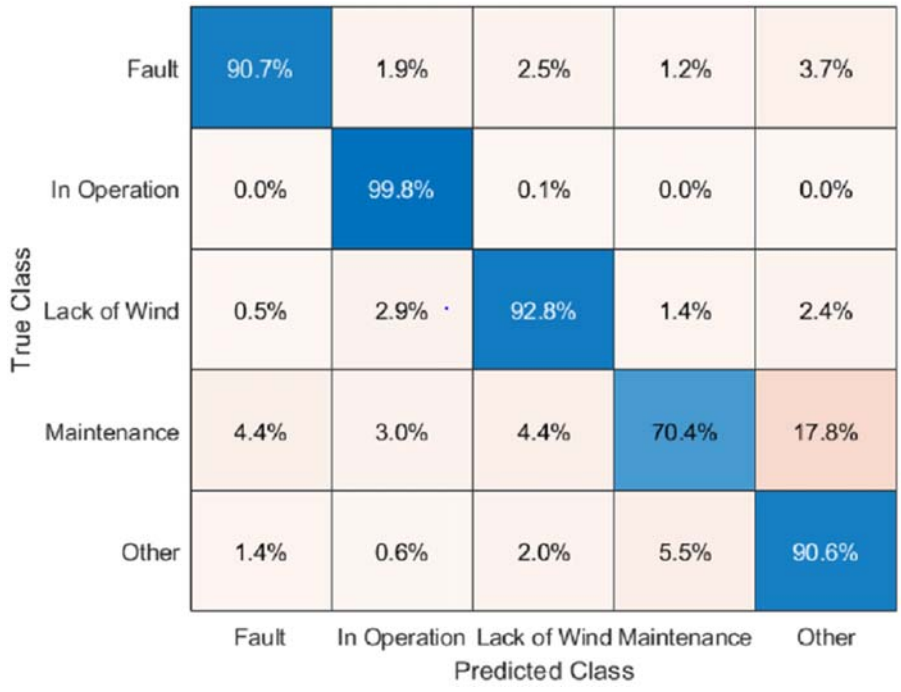

FIGURE 33.8 Example of a confusion matrix for a five-class classification problem.

33.8 Conclusions

Real-time detection of downtime and its classification remains a significant possibility, but its performance will be dependent on the quality and the variety of data available. Benchmarks for such classification are thus required for multiple farms and this can lead to consistent features that can be extracted, calibrated, and compared. Artificial Intelligence can play a key role here. Data over geographical regions can thus be integrated in this manner. This chapter focuses on how time series analysis and Eigen perturbative methods can be useful in this. A wide range of approaches and related literature are discussed and such approaches are also aligned well to continued engagement with data collection, preprocessing, analysis and interpretation. Data from Irish wind farms are used to illustrate these methods and a range of literature is presented in this regard. With time, short-term WPF is expected to continue to be a core challenge, while a significantly wide range of scenarios must be analyzed and calibrated from real wind farm data to create consistent markers of detection, which will also be aided well by machine learning and deep learning approaches. Overall, these approaches will continue to de-risk the wind energy sector and make it more competitive over time. Eventually, it is expected that there will be pathways toward standardizing the use and interpretation of these methods through robust guidelines and recommendations.

References

[1] International Energy Agency. World energy outlook 2021; 2021. <https://www.iea.org/reports/world-energy-outlook-2021> [accessed 5.05.22].

[2] Giebel G., Draxl C., Brownsword R., Kariniotakis G., Denhard M. The state-of-the-art in short-term prediction of wind power. A literature overview; 2011.

[3] Foley AM, Leahy PG, Marvuglia A, McKeogh EJ. Current methods and advances in forecasting of wind power generation. Renew Energy 2012;37(1):1–8.

[4] Zhang Y, Wang J, Wang X. Review on probabilistic forecasting of wind power generation. Renew Sustain Energy Rev 2014;32:255–70.

[5] Yan J, Liu Y, Han S, Wang Y, Feng S. Reviews on uncertainty analysis of wind power forecasting. Renew Sustain Energy Rev 2015; 52:1322–30.

[6] Marugán AP, Márquez FPG, Perez JMP, Ruiz-Hernández D. A survey of artificial neural network in wind energy systems. Appl Energy 2018;228:1822–36.

[7] Liu H, Chen C. Data processing strategies in wind energy forecasting models and applications: a comprehensive review. Appl Energy 2019;249:392–408.

[8] Qian Z, Pei Y, Zareipour H, Chen N. A review and discussion of decomposition-based hybrid models for wind energy forecasting applications. Appl Energy 2019;235:939–53.

[9] Roungkvist JS, Enevoldsen P. Timescale classification in wind forecasting: a review of the state-of-the-art. J Forecast 2020;39(5):757–68.

[10] González-Sopeña JM, Pakrashi V, Ghosh B. An overview of performance evaluation metrics for short-term statistical wind power forecasting. Renew Sustain Energy Rev 2021;138:110515.

[11] Mucchielli P, Bhowmik B, Ghosh B, Pakrashi V. Real-time accurate detection of wind turbine downtime-an Irish perspective. Renew Energy 2021;179:1969–89.

[12] Srbinovski B, Temko A, Leahy P, Pakrashi V, Popovici E. Gaussian Mixture Models for Site-Specific Wind Turbine Power Curves. Proc Inst Mech Eng A J Power Energy 2020; 0957650920931729.

[13] Otter A, Murphy J, Pakrashi V, Robertson A, Desmond C. A review of modelling techniques for Floating Offshore Wind Turbines. Wind Energy 2021;25(5):831–57.

[14] Box George EP, Gwilym MJenkins, Gregory CReinsel, Greta MLjung. Time Series Analysis: Forecasting and Control. John Wiley & Sons; 2015.

[15] Kantz H, Schreiber T. Nonlinear Time Series Analysis. Cambridge University Press; 2004.

[16] Messner JW, Pinson P. Online adaptive lasso estimation in vector autoregressive models for high dimensional wind power forecasting. Int J Forecast 2019;35(4):1485–98.

[17] Goodfellow I, Bengio Y, Courville A. Deep Learning. MIT Press; 2016.

[18] Yan J, Li K, Bai EW, Deng J, Foley AM. Hybrid probabilistic wind power forecasting using temporally local Gaussian process. IEEE Trans Sustain Energy 2015;7(1):87–95.

[19] Xie W, Zhang P, Chen R, Zhou Z. A nonparametric Bayesian framework for short-term wind power probabilistic forecast. IEEE Trans Power Syst 2018;34(1):371–9.

[20] Iversen EB, Morales JM, Møller JK, Trombe PJ, Madsen H. Leveraging stochastic differential equations for probabilistic forecasting of wind power using a dynamic power curve. Wind Energy 2017;20(1):33–44.

[21] Mucchielli P, Bhowmik B, Hazra B, Pakrashi V. Higher-order stabilized perturbation for recursive eigen-decomposition estimation. J Vib Acoust 2020;142(6).

[22] Osório GJ, Matias JCO, Catalão JPS. Short-term wind power forecasting using adaptive neuro-fuzzy inference system combined with evolutionary particle swarm optimization, wavelet transform and mutual information. Renew Energy 2015;75:301–7.

[23] Abdoos AA. A new intelligent method based on combination of VMD and ELM for short term wind power forecasting. Neurocomputing 2016;203:111−20.
[24] Safari N, Chung CY, Price GCD. Novel multi-step short-term wind power prediction framework based on chaotic time series analysis and singular spectrum analysis. IEEE Trans Power Syst 2017;33(1):590−601.
[25] Naik J, Satapathy P, Dash PK. Short-term wind speed and wind power prediction using hybrid empirical mode decomposition and kernel ridge regression. Appl Soft Comput 2018;70:1167−88.
[26] Abedinia O, Lotfi M, Bagheri M, Sobhani B, Shafie-Khah M, Catalão JP. Improved EMD-based complex prediction model for wind power forecasting. IEEE Trans Sustain Energy 2020;11(4):2790−802.
[27] Wang C, Zhang H, Ma P. Wind power forecasting based on singular spectrum analysis and a new hybrid Laguerre neural network. Appl Energy 2020;259:114139.
[28] Dong Y, Zhang H, Wang C, Zhou X. Wind power forecasting based on stacking ensemble model, decomposition and intelligent optimization algorithm. Neurocomputing 2021;462:169−84.
[29] Liu X, Yang L, Zhang Z. Short-term multi-step ahead wind power predictions based on a novel deep convolutional recurrent network method. IEEE Trans Sustain Energy 2021;12(3):1820−33.
[30] Yildiz C, Acikgoz H, Korkmaz D, Budak U. An improved residual-based convolutional neural network for very short-term wind power forecasting. Energy Convers Manag 2021;228:113731.
[31] Duan J, Wang P, Ma W, Fang S, Hou Z. A novel hybrid model based on nonlinear weighted combination for short-term wind power forecasting. Int J Electr Power Energy Syst 2022;134:107452.

Section F

Economics of wind energy and certification issues

This page intentionally left blank

Chapter 34

Levelized cost of energy (UK offshore wind power) drivers, challenges, opportunities and practice 2010–20

Lovemore Machiridza[1] and Subhamoy Bhattacharya[2]
[1]Buckinghamshire, United Kingdom, [2]University of Surrey, Guildford, London, United Kingdom

34.1 Offshore wind power and climate change

The pursuit of renewable green energy and Net-zero by 2050 are key factors that influenced the metrics of progress in offshore wind power in the United Kingdom.

Uncontrolled costs along the value chain from design, manufacture, transportation, installation, operation, and decommissioning all add to the pressure on the cost per megawatt of offshore wind energy. These costs fall into the broad baskets of capital, operating, and decommissioning costs of offshore wind turbines, accounting for 70%, 28%, and 2% of offshore wind farm (OWF) levelized cost of energy (LCOE), respectively [1].

The measure for the cost of offshore wind energy is the LCOE, defined as the present value revenue required to earn a rate of return on investment equal to the discount rate [also referred to as the weighted average cost of capital (WACC)], over the life of the wind farm. Tax and inflation are excluded. In other words, it is the lifetime average cost for a unit of energy produced, quoted in today's prices.

Implementation of the much researched and recommended cost efficiency programs along the offshore wind energy value chain is evaluated by paying attention to the interplay of opportunities, threats, strengths, and weaknesses that have interplayed in the OWF industry and are expressed in the observed trends of LCOE, as highlighted by selected case studies.

34.2 Levelized cost of energy

LCOE is a term that refers to leveling the terms of comparison of energy projects. The Office of Indian Energy (see [2]) explains LCOE as "Critical to making an informed decision to proceed with development of a facility, community or commercial-scale project."

The Department of Business Energy and Industrial Strategy (United Kingdom) (2020) (see reference) refers to LCOE as the discounted lifetime cost of building and operating a generating asset, expressed as a cost per unit of electricity generated (£/MWh). It covers all relevant costs faced by the generator, including predevelopment, capital, operating, fuel, and financing costs. This is sometimes called a life-cycle cost, which emphasizes the "cradle to grave" aspect of the definition.

Smart (in [3]) gives a break-even angle view of LCOE by stating that LCOE is the £/MWh, the generator must earn for each megawatt hour produced over the full life of the assets, to cover its capital and operating costs and its cost of capital. LCOE combines costs and energy production into one metric, rather than comparing cost and energy production separately.

LCOE is a comparator metric between businesses, allowing projects of different lifetimes and cash flow patterns to be fairly compared.

While LCOE has become a "universal" metric, it has its limitations that need to be considered in order to derive the best value out of its application. Shah (see Shah, 2020) [4] notes that while LCOE is simple, easy to understand and

Wind Energy Engineering. DOI: https://doi.org/10.1016/B978-0-323-99353-1.00029-3

relate to and widely used, it is best used for comparing similar systems in similar contexts (e.g., one natural gas plant vs. another of a similar type). When comparing producers across different national jurisdictions, LCOE may mask national peculiarities like legislative requirements that may impose out-of-market risks. LCOE is cost-based and analysts of it point out that it ignores revenue and other benefit streams accruing to a project and which need to be considered together with the LCOE "gate" metric. Its sensitivity to interest rates (cost of capital) has been highlighted, to possibly favor short-term projects against long-term projects, especially in unstable interest rate regimes [2].

All factors considered, pros, cons and caveats, lower LCOE as an indicator of lower lifetime business costs, which should translate to lower costs of electricity for the consumer (and taxpayers if any subsidy is paid to generators).

Factors affecting LCOE are wide and numerous and a systems theory is proposed here to describe and understand the factors influencing trends in LCOE in the decade to 2020. A systems theory approach brings to the fore, threats, and opportunities to the outcome of interest.

34.3 Levelized cost of energy and the systems theory of management

Successful organizations, exemplified by OWFs, are like living organisms, one of whose hallmarks is to successfully ride the operating challenges that come from the environment in which they operate and those that arise from within the organization itself. They successfully interact with the environment around them and within them to meet their objectives and goals. They evolve with time, making sufficient changes, often to react to and or influence events and people within their internal and external environments in the furtherance of organizational goals.

The environment or Supra-System that organizations operate in throws political, regulatory, economic, social-cultural, technological, economic, legal challenges, often summed up as PEST or PESTEL [5], at them. Like living organisms, organizations react to these challenges or manage them.

A successful organization interacts with its environment by taking inputs from it, manipulating them through internal production processes in its subsystems and generating outputs into the environment. An organization takes raw materials of information, man, money, knowledge and machines from the environment, and uses its internal interrelated but independent strategic, organizational, social, information and management subsystems to process these in designing and construction of OWFs, bridges, motorways and similar for output and usage into and in the environment.

In these open systems, organizations visit the external and internal impacts and contingent on these, organizational decisions are made to address any threats and or take advantage of opportunities for the survival of the organismic organization through the systems or contingency theory of management, Fig. 34.1 [6].

In the context of an OWF as illustrated in Fig. 34.1, the Supra-System is the social, political, regulatory, market, geography, industry, etc., that they operate in, and from this environment, there are PEST impacts or inputs into OWF in the form of political or regulatory (laws, business standards), economic (interest rates, investment climate, competitor climate, consumer, procurement), social (social attitudes, environment) and technological (technical constraints and requirements, information, components, processes) aspects.

Using internal transformational processes, the organization converts these inputs into a functional OWF, operates and maintains it, and then decommissions it. Operations result in a vital output to the supra-system, in the form of electrical energy, and in the process, the business needs of shareholder returns and capital growth are satisfied. The business measures its performance with selected metrics and uses these to improve itself (Fig. 34.1).

For OWF, electricity is their output to the environment (its customers) and an index of this output is LCOE. It is thus important to understand the relationship between LCOE and the supra-system, the push-pull relationship between the offshore wind industry, and the environment around it. It shows a commensal relationship.

Systems theory clarifies the setting of changes, factors, and events that impacted changes in offshore wind energy as measured by the statistic LCOE, in the decade leading to 2020.

34.4 Trends in levelized cost of energy trends 2010–20

The Office of Energy Efficiency and Renewable Energy (2018) in the Department of Energy (USA) reported a global trend of decreasing LCOE from offshore wind (Fig. 34.2) showing that the decline of LCOE started well before 2010 and is projected to continue into the future. Meißner's research (see Meißner [7]) unsurprisingly confirms the global picture (Fig. 34.3).

With this decline in LCOE, corresponding and exponential growth in offshore wind energy has been witnessed to the extent that offshore wind's share of annual UK generation increased from 0.8% in 2010 to 6.2% in 2017 and is

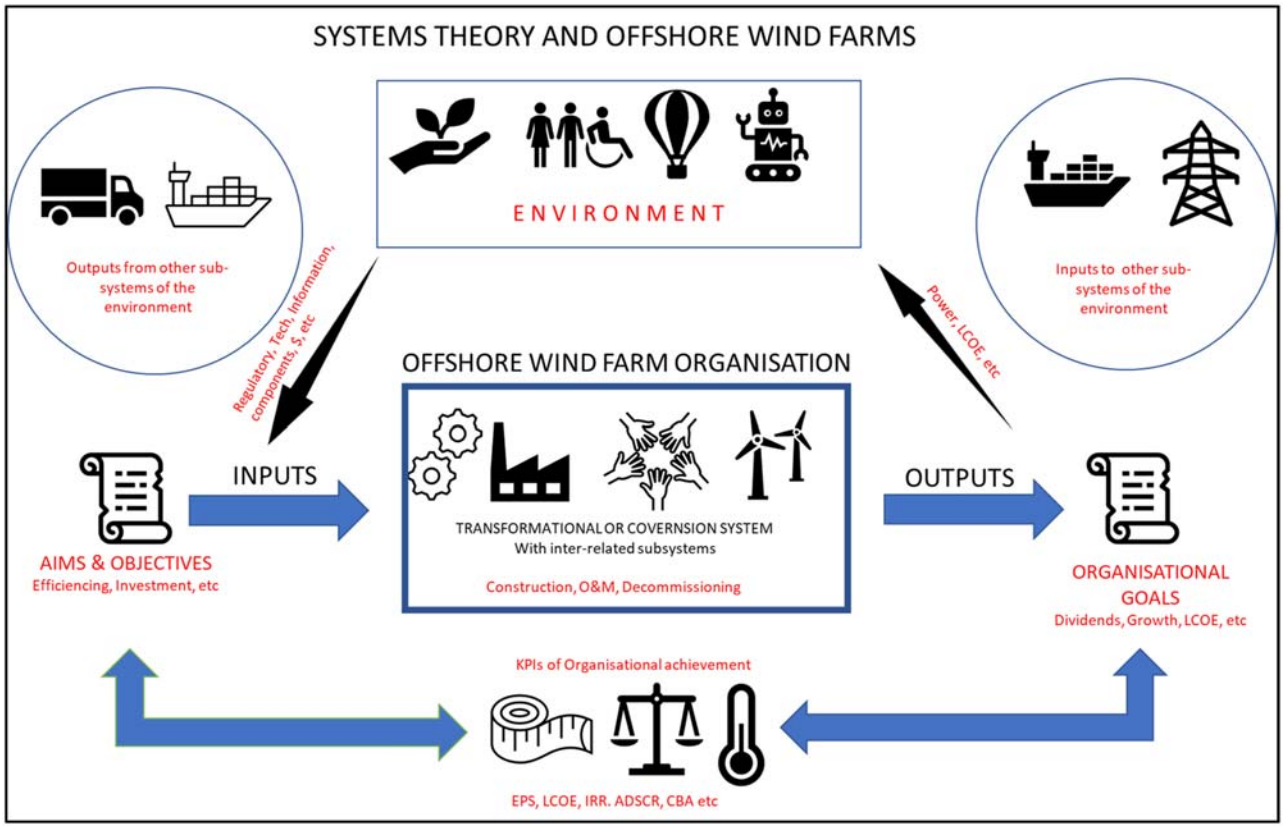

FIGURE 34.1 The open systems model of organization. Conceptualised after Gordon, J. Systems theory of management - explained. Retrieved from The Business Professor: <https://thebusinessprofessor.com/en_US/management-leadership-organizational-behavior/systems-theory-of-management#-what-are-the-components-of-an-organizational-system-2>; 2022.

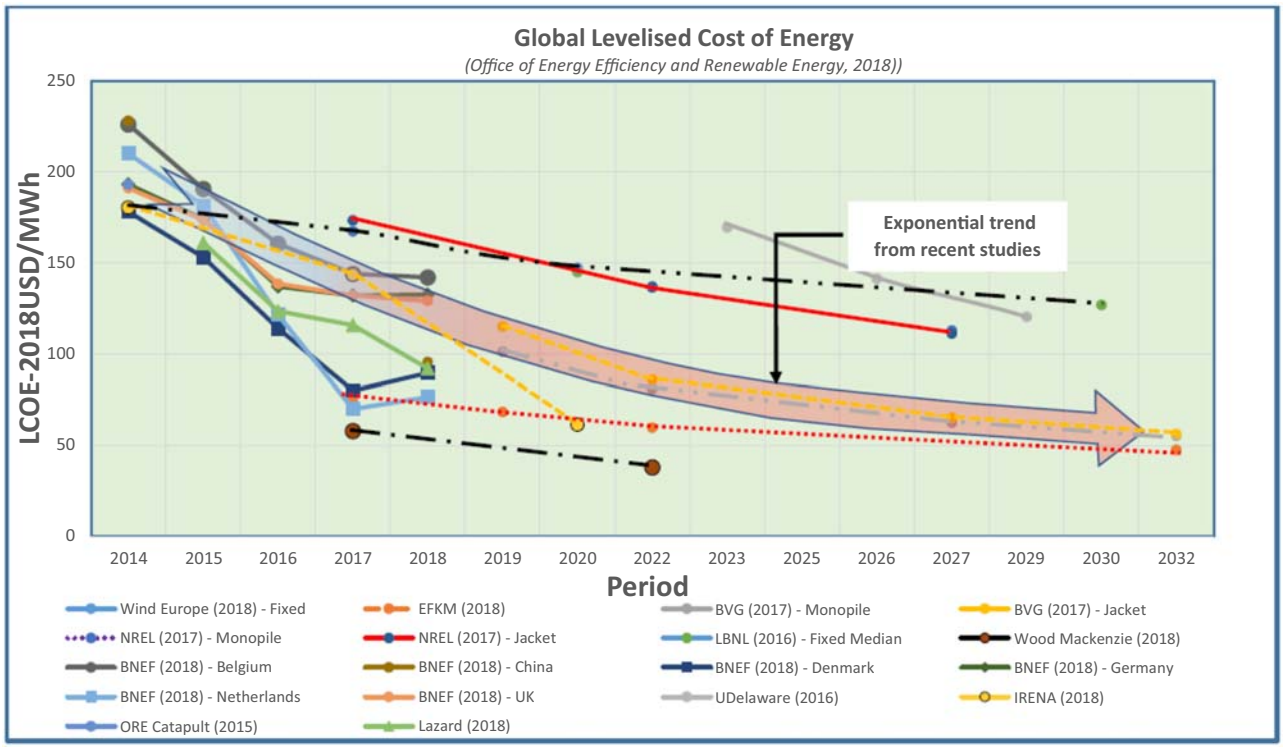

FIGURE 34.2 Global trends in LCOE [8]. *Modified after Office of Energy Efficiency and Renewable Energy. Top trends in offshore wind, <https://www.energy.gov/eere/wind/articles/top-trends-offshore-wind>; 2019 [accessed 13.11.20].*

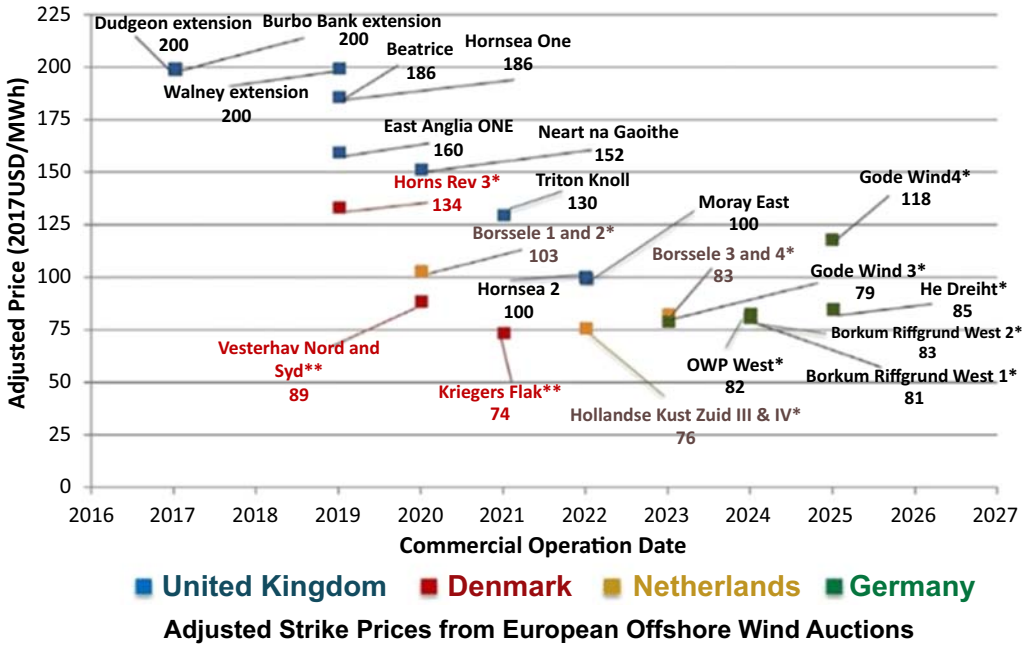

FIGURE 34.3 LCOE reduction pathway. *After Meißner, M. Offshore wind turbine cost scaling - A critical assessment and theoretical investigation. Retrieved from ResearchGate: <https://www.researchgate.net/publication/348356086_Offshore_Wind_Turbine_cost_scaling_-A_critical_Assessment_and_theoretical_Investigation>; 2020*

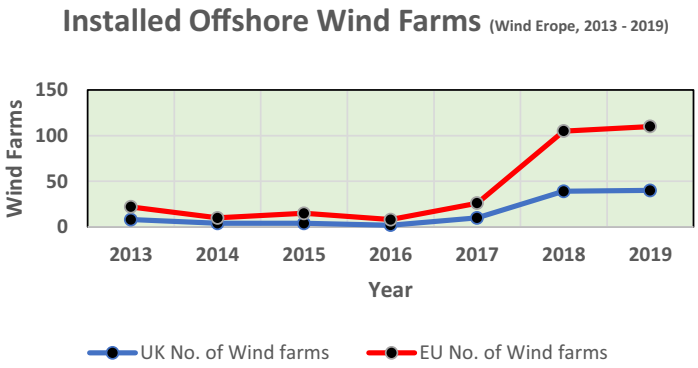

FIGURE 34.4 Installed OFW.

expected to reach around 10% by 2020 [9]. The threats to LCOE are insignificant and the opportunities are quite significant.

At global and national level, LCOE has seen a downward trend in the decade under review and is forecast to continue the same trend into the future as the Supra-System governs the offshore wind power industry, as explained in the following paragraphs. Opportunities are bound to increase and strengthen as the Supra-System continues to evolve, with OWF tapping into this enabling and regulatory environment.

While LCOE was trending down, OWF installations were going up as did the installed power generation [10–16], as can be seen in Fig. 34.4, Fig. 34.5, and Fig. 34.6.

It is interesting to note that the aspect of economies of scale was an important factor in the decline of LCOE, with wind farms increasing in number and similarly the generated power. Even more interesting is the apparent slow or no growth in turbine numbers over the same period, a trend that seems to point to improving the efficiency of production, that is, the same number of turbines but increased power output. This efficiency is driven by many Supra-System factors like improving investment climate (political and economic) and improving technology (importantly foundation designs) that increases output while reducing input variables. These changes in the Supra-System will be discussed in the following paragraphs.

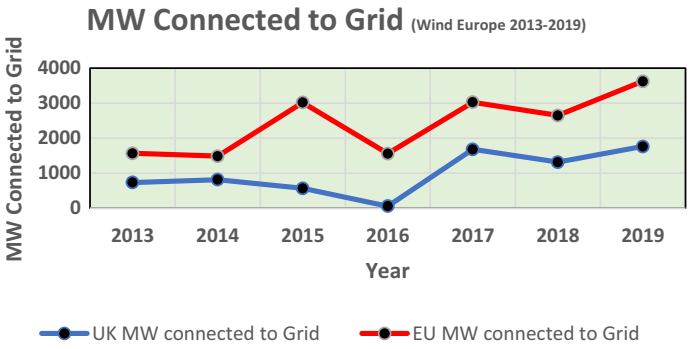

FIGURE 34.5 MW connected to grid.

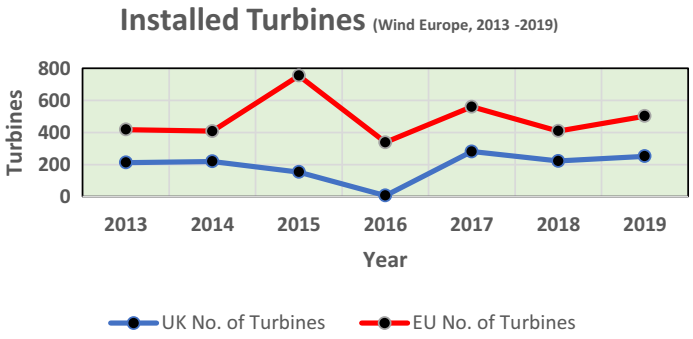

FIGURE 34.6 Installed turbines.

34.5 The supra-system

The Supra-System is the environment within which OWFs operate. This is the environment from which OWF draw supply chain inputs and the market to which OFWs provide services and goods. These inputs into OWFs are actually the outputs from other systems that are subsystems of the supra-system, like political, economic, legal, manpower, contractual, and financial subsystems that are regulatory or direct production inputs. Measurable outputs are green energy and organizational goals and OFW's green energy reputation as an intangible output.

34.5.1 Enabling environment legal

The most significant indicator of government policy and commitment to the success of the desired policy is found in its statutes. Acts of parliament enact government policies into laws that define such policies and grant authority for the enforcement of promulgated laws that shape the policies. These laws define the conducive legal environment that enables the implementation of the policy. They define the opportunities to be advanced and threats to be limited. The motivation for these acts may lie in domestic policies and or international treaties.

These policies and treaties in general serve to promote desired and beneficial outcomes and discourage and even punish undesirable outcomes for the domestic populace or party nations. The United Kingdom is a party to international treaties and conventions on climate change. She is a signatory to the United Nations Convention on the Law of the Sea, the United Nations Framework Convention on Climate Change, and the various protocols emanating from it, for example, Kyoto Protocol and the several Conferences of Parties (COP), to name but a few. The Kyoto Protocol (COP 1) covered the period before 2020 and the Paris Agreement (COP 21), a legally binding pact to build a global strategy for the fight against climate change, covers the post-2020 period in tackling climate change [17]. In the quest for "bet zero by 2050," the European Green Deal states that "no person and no place left behind" lending emphasis to the catch phrases of "Building back better," "Building back Greener," "Levelling up," and "Building back Fairer" that have found fertile context and meaning in the climate-conscious world. These international treaties and conventions placed obligations on the government to put in place strategies to tackle climate change through various stages of cutting carbon emissions to carbon neutrality by 2050 [18,19]. They define the opportunities for the development of offshore wind energy and by corollary, the threats to be addressed and minimized.

In the case of renewable energy, Her Majesty's government has since before the end of the last century recognized the importance of renewable energy, especially offshore wind energy. This enabling legal environment was and is crucial in the increased development of offshore wind energy by regulating and promoting the development of the industry.

A well-regulated industry allows for security, stability, and planning in business. The benefits of this stability can be seen in the security and stability of supply and prices of goods and services for the benefit of the consumers. Electricity is one such service.

In the decade up to 2020, several acts of parliament were passed to promote and regulate the renewable energy industry in line with international conventions and treaties on climate change, and to recognize the increasing importance of green energy in the UK economy, then and in the future. These acts are the Energy Act 2008, 2011, 2013, 2015, 2016, and 2019. These are briefly noted in the following paragraphs as the drivers and opportunities for improved LCOE and by their nature, mitigators of threats to the decline of LCOE. Fuller accounts of these legal factors are given in Ref. [20].

34.5.2 The Energy Act 2008

The Energy Act 2008 was an act interalia "...to stimulate growth of electricity generation from renewable sources; to make provision relating to electricity transmission; to make provision about payments to small-scale generators of low carbon electricity..." By the Energy Act 2008, Her Majesty's government stated its commitment to ensuring that renewable energy generation played an increasing role in the UK's energy mix, through affirmed politico-legal will.

34.5.3 The Energy Act 2011

An overview of the Energy Act 2011 outlines that the Act was aimed at "...energy efficiency. Improving energy efficiency by tackling barriers to investment in energy efficiency through the Green Deal and measures to maximize its uptake...conferring powers to require cheapest tariff information to be included on energy bills." Both sides of the supply and demand equation were being empowered to drive supply, efficiency, and affordability.

34.5.4 Electricity market reform

In 2012, the Department of Energy and Climate Change (DECC) announced the Electricity Market Reform (ERM) policy, an energy policy that was the bedrock of Energy Bill (2012) and the subsequent Energy Act (2013). The policy had three objectives, "to keep the lights on, to keep energy bills affordable, and to decarbonize energy generation" [21].

In ERM, it was crucial to address both security of supply and climate change challenges, while maximizing the benefits and minimizing the costs for consumers and other potential negative impacts. EMR is graphically illustrated in Fig. 34.7, outlining the motivations, assumptions, goals, and forecast timelines. Costs were a threat to the EMR's success and needed to be mitigated.

DECC further outlined the guiding drivers and obligations for EMR as follows.

34.5.5 2012–20

The United Kingdom had a legally binding EU target for 15% of the UK's energy to come from renewable sources by 2020. To meet this target, DECC expected that around 30% of UK electricity would need to come from renewable generation by the end of the decade, and switching from coal to gas-fired generation was also likely to deliver emission reductions in this decade.

34.5.6 2020–30

Further deep cuts in emissions from the power sector were necessary to keep the UK on a cost-effective path to meeting its 2050 commitments. Reducing emissions from the power sector would become increasingly important to help her decarbonize other sectors. Large-scale opportunities for new low-carbon energy needed to be exploited in 2010–20 in order to meet 2050 commitments.

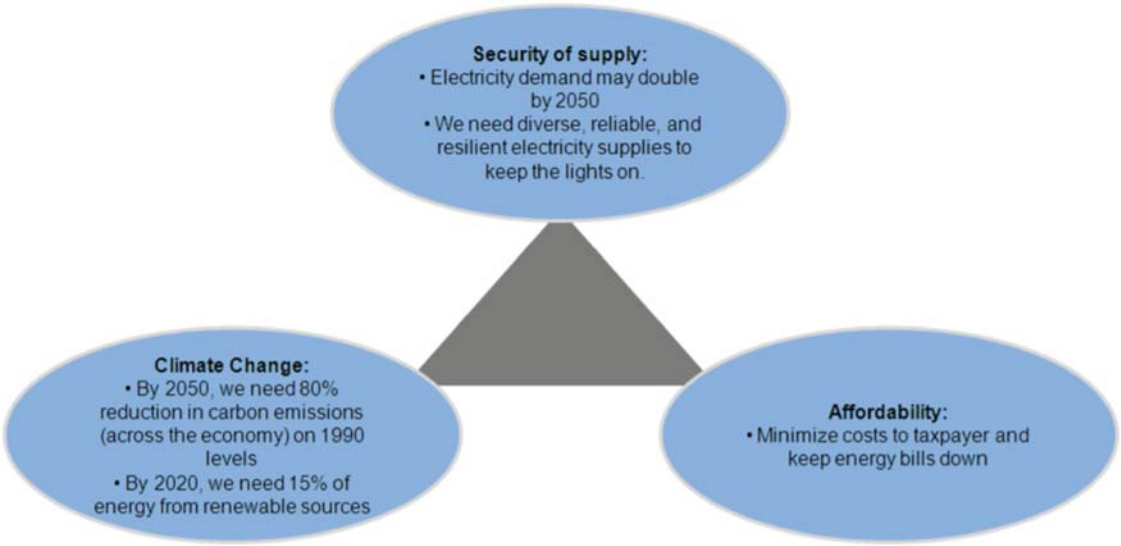

FIGURE 34.7 The pillars of ERM. *After DECC (2012) [22].*

34.5.7 2030–50

Forecasts [23] showed that by 2050, as industrial and domestic heating, transport and industry become increasingly electrified, the demand for electricity generation would increase and DECC forecasts showed that electricity demand was likely to increase by between 30% and 100% by 2050.

For the United Kingdom to meet her legally binding 2050 carbon emission reduction target, she should expect that her power would be generated largely from renewables, nuclear, and fossil fuel stations fitted with CCS technology, although the mix would be for the market to decide. In tandem with this projection, technologies with the lowest costs would win the biggest market share as opportunities to drive LCOE further down.

34.5.8 The Energy Act 2013

The Energy Act (2013) has been described as an Act to make provision for the setting of a decarbonization target range and duties in relation to decarbonization [24]. The act aimed interalia to:

1. reform the electricity market for purposes of encouraging low-carbon electricity generation or ensuring the security of supply

34.5.9 The Energy Act 2016

The Energy Act 2016 [25] streamlined decision-making for onshore oil and gas energy by formally establishing the Oil and Gas Authority as an independent regulator and this took the form of a Government company that had some of the Secretary of State's powers and was charged with (interalia) the asset stewardship and regulation of domestic oil and gas recovery in line with Maximizing Economic Recovery for the UK (MER UK).

Although MER UK largely aimed at the oil and gas sector, the business friendliness it embodies toward this sector can certainly be expected to have spilled over to other publicly promoted sectors of the British economy. The same parliament that superintended over the oil and gas sectors was responsible for the offshore wind sector.

34.5.10 Policy instruments

34.5.10.1 Electricity market reform

The impact of EMR can be summed in the three pillars in Fig. 34.7, as creating an environment conducive to:

1. Honoring international obligations on carbon emission goals;
2. Focus on the security of supply of low carbon energy to meet increasing demands over time;

3. Promote the development of affordable electricity for both generator and customer.

EMR dedicated itself to meeting international obligations through the successful development of customer affordable and sustainable low carbon renewable electricity. These are reassuring goals and opportunities for the market, investors in design, development, construction, and delivery of commercial products. EMR promoted competitive business development and competitively priced product and services. Low carbon renewable energy was the prime beneficiary of this policy and it is expected that the policy contributed to a decline in LCOE as a measure of the *development of affordable electricity for both generator and customer.*

34.5.11 Maximizing economic recovery strategy for the United Kingdom

MER UK was developed pursuant to the Petroleum Act 1998, as amended by the Infrastructure Act 2015 [26]. The role played by MER UK in creating a less bureaucratic system by decentralizing power to those immediately affected by industrial developments, went a long way to creating an enabling environment for industry, an environment that laid foundations to reduce setup costs. The benefits of such an environment were not limited to the oil and gas sector only [20].

Noonan (see [6]) reports that ". . .the UK Government and offshore wind industry agreed a Sector Deal, securing offshore wind's position at the heart of the future UK energy mix as a large-scale, low-carbon form of electricity." The offshore wind industry is the "Clean Growth" pillar in the Grand Challenges subsector of the 2017 Industrial Strategy. Within the industrial strategy, BEIS announced sector deals as a way for the government to directly support productivity growth in specific industries [6] and offshore wind energy is one of such industries.

The sector deal secured offshore wind's position at the heart of the future UK energy mix as a large-scale, low-carbon form of electricity. The *Industrial Strategy Offshore Wind Sector Deal* [9] served to strengthen the offshore wind energy sector with long-term view of a sustainable government support. The direct spin-off of this was better business planning for both contractor and investor, leading to better matching of product supply and demand of all inputs and outputs in the industry. One important metric of the success of the sector deals is the reduction of LCOE, riding on the back of maximizing of opportunities and minimizing threats.

34.5.12 Legal instruments

By their nature, acts of parliament regulate society, interbusiness, business-customer, and business-environment relationships. The desired product of this regulation is an affordable and sustainable product with minimum harm to the physical and operational environment. Statutes encourage and reward, discourage and punish business practices that violate the statutes. Statutes aim to render, cultivate, and promote fair business practices where no participant should come off worse as other participants get better, building back fairer.

The spirit of the statutes outlined in the foregoing passages captures the need to meet international obligations while promoting the development of sustainable low-carbon energy, from pre-2010 till 2020 and beyond. Each act aimed to improve the business environment, define performance parameters, and ensure the delivery of sustainable and affordable low-carbon energy for specific energy sectors. These inputs from the Supra-System were the opportunities and minimized threats for and to LCOE [20].

Table 34.1 summarizes the policies, acts, and impacts of the legal framework aimed at the goal of sustainable development of competitive and affordable low-carbon energy. Electrical energy is the ultimate beneficiary.

34.5.13 Political intent

The development and growth of offshore wind energy have benefited from this enabling, political-legal-commercial environment and the metric for this is LCOE. The political intent (which seems to be similar across the floor of the Palace of Westminster, is captured in the statement by Prime Minister Johnson at his party conference "As Saudi Arabia is to oil, the United Kingdom is to wind—a place of almost limitless resource, but in the case of wind without the carbon emissions, without the damage to the environment" [28].

Moreover, the president of the United States of America recently announced that "We have to ensure that the benefits of growth are shared broadly and equitably, not just by a few," (The Whitehouse, 2021) [29], further underlining the political intent for economic growth across nations, ensuring that the benefits accrue to all citizenry, that is, building back better, building back greener, and building back fairer.

TABLE 34.1 Summary of policies, statutes, and their impacts.

Legal instrument/ policy	Year	Key points	Impact
Energy Act 2008	2008	• To make provision in relation to electricity generated from renewable sources. • To make provisions relating to electricity transmission; • To make provision about payments to small-scale generators of low carbon electricity	• Stimulation of the growth of electricity generation from renewable sources
Energy Act 2011	2011	• Improving energy efficiency • Tackling barriers to investment in energy efficiency through the Green Deal • Measures to maximize uptake of low carbon energy	• Stimulating investment in low carbon energy
ERM	2012	• Secure energy • Sustainable low carbon future • Action on climate change at home and abroad	• Security of supply • Climate change challenges, • Maximizing the benefits and minimizing costs
Energy Act 2013	2013	• Decarbonization targets • Reforming the electricity market • Establishing Office for Nuclear regulations	• Development of low carbon electricity • Ensuring security of supply • Honor climate change commitments
Energy Act 2016	2016	• Maximizing UK offshore oil and gas recovery and its regulation • The creation of a new arm's length regulatory body charged with effective stewardship and regulation of petroleum recovery.	• Establishment of the Oil and Gas Authority as an independent regulatory authority • The Act makes changes so that local authorities decide whether to approve planning applications for new onshore wind farms
MER	2016	• Promoting a strong business approach to oil and gas industry	• Reduce permitting red tape for onshore wind farms

34.5.14 Procurement environment and its changes

Offshore wind energy is an industry that is on the path to being the "new kid on the block" of the renewable energy sector as the world of opportunities unfolds in the years. It is an evolving industry that is picking up a lot of interest amongst politicians and investors. By its nature, it is located in the deep seas where the best wind is available and often seas deeper than 60 m. The environment poses its own risk for the investor and the construction engineer and the management of the perceived risks drives procurement strategies that give the best return for the interested parties. It is an evolving industry which means it is not a standard industry with many precedents and many subsectors of it are First of a Kind that demand unique solutions [20].

Harling et al. [30] noted that each component of an offshore wind project [such as the turbine and foundation/anchoring system, subsea connection, and grid connection (both offshore and onshore)] has different requirements. For example:

1. The foundation system of a wind turbine presents a substantial engineering challenge.
2. Installation requires specialist vessels and specialist marine engineering skills and knowledge.
3. Particular attention is needed in relation to the allocation of risk at the interfaces, especially where the risk is impacted by a hostile and changing site.

34.5.15 Engineering procurement and construction contract

Repairing a wind turbine at sea is very different from doing so onshore. On account of the special nature and risk profile and site specificity of offshore wind projects, a true EPC turnkey solution is not always a wholesale solution. [30] as early as then, noted that parties had adopted a multicontracting approach, with those members of the project team

involved in design, manufacture, installation, commissioning, and operation each taking the risks with which they are most familiar.

Risk is thus managed by those best placed to control it and their costs will correspondingly be managed. While the aggregation of these multicontracts solves one problem, they introduce another (a threat), interface risks for the sponsor as they must manage the interface between the multicontracts. Some challenges arise at the interface between any two contracts on one project, let alone the multiplicity of contracts on an OWF [20].

EPC contracts typically pass all design development and construction risks to the contractor. The developer acquires a "bankable" turnkey project at a premium for the assumption of risk by the contractor. EPC is the traditional procurement where procurement risks are low because of proven technology; understood low geotechnical and natural risks; project processes that are similar and have low risk; few or one contractor is involved like in motorway, hospitals or airports. Rewards tend to be higher than the risks undertaken by the contractor.

Developing OWF projects on an EPC basis was always going to be difficult for reasons associated with an evolving and emerging industry [31], emerging technology not fully tried, novel geotechnical risks in deep seas, weather, turbines risks form manufacturers who do not regard offshore contracting as part of their core business, competition from onshore wind farms where risks are lower. OWF faced competition, putting pressure on OWF EPC procurement.

34.5.16 Multicontracting

OWF procurement needed to evolve with the industry and it saw the emergence of multicontracting as a more realistic model of contracting which considered both the underlying commercial realities and the growing sophistication and maturity of the offshore wind market.

Multicontracting had the following components, that is:

1. The Developer took ultimate contractual responsibility for project-specific and interface risks as they were the party best placed to manage these risks in the evolving environment.
2. Direct and separate contracting of the turbine supplier from civil and electrical contractors, typically on a target cost model.
3. Putting in place “over-lay” arrangements to wrap the “multicontracts” with mutual alliance obligations to drive better management of technical interfaces, construction schedules, and construction risks on a project-wide basis.

Even though more complicated than EPC [31], multicontracting had the benefits such as:

1. Cheaper contracts
2. Presented a pragmatic way forward
3. Eliminate unmanageable and disproportionate risks from the supply chain
4. Offered attractive options to suppliers and contractors and hence promote greater competition for projects and the market.

34.5.17 New engineering contract

In this multicontracting environment, there are several forms of contract that are available to the construction engineer, Federation Internationale Des Ingenieurs-Conseils where there are international contractors or NEC4 Alliance contracting (ALC). Partners (client or promoter and all key members of the supply chain) in the ALC are engaged under a single contract and have an equal voice and share in the performance of the alliance as a whole as opposed to their own individual performance [32], in a spirit of trust and cooperation. The study [20] expands on details is now very popular form of contract in the construction industry, in the United Kingdom and abroad, with special reference to OWF as a sub-system of the Supra-System.

The trend toward NEC4 ALC form of collaborative contract with its spirit of mutual trust and cooperation for win-win outcomes, improved risk management, and related costs, leading to lower contract costs and therefore unit product price is easily understandable as an opportunity, especially for LCOE.

34.5.18 Developments in project financing

Project financing is a key component in project development. Project financing involves the availability of investment and the terms of that investment. These two key aspects reflect the level of perceived project risks from investors. The higher the risk, the lower the appetite for investment and the stricter the terms of investment or cost of project debt.

The opposite is also true. For the end user, this level of investment risk is reflected in the cost of the product or service and for OWF energy, LCOE is a direct measure of this risk. Any mitigation of project finance risk will be reflected in the level of LCOE and a Supra-System that acts to lower investment risks will directly impact LCOE. It is thus expected that the Supra-System parameters highlighted in the foregoing paragraphs, whose intended outcome was an OWF-friendly environment, impacted developments in project finance, ultimately lowering project finance risks.

Key components of project finance are Contracts for Differences (CfD) and Power Purchase Agreements (PPA). These are considered key areas that provide government assurance for the supply of OWF energy and for commerce to provide assurance for the assured demand of OWF energy. The study [20] gives comprehensive accounts and impacts of these aspects of project finance and how they impacted trends in LCOE.

Once the supply and demand ends of the equation of economics are ascertained, industry risk is lowered and investor capital flows into the industry easier than otherwise.

34.5.19 Power purchase agreements

PPA are a type of offtake contract [33] used for projects generating electricity. Offtake contracts are common across the industry, mining companies are known to enter into similar agreements with smelters, refineries, or product users. Agricultural companies can similarly enter into offtake agreements with enterprises that process farm produce.

PPAs are unique to power generation and provide a generator/developer constructing a power station, in this case, an OWF with agreed technical and performance characteristics of:

1. output in MW
2. delivery date
3. delivery profile (amounts and durations)

The generated power is sold to the offtaker who may be a public entity, private transmission, and distribution company or direct end-user of the power. The agreement also stipulates penalties for failure to meet contractual commitments. The offtaker requires assurance that the generator and its sponsors or shareholders have the requisite technical skills and financial wherewithal to construct, operate and deliver the contracted power without exposing the offtaker to undue risk [33].

Management of financial risk is key in PPAs and these can range up to 25 years from commercial production and are renewable. Their value in OWF project development is underlined by the fact that they are a condition to any equity and debt financing of the project [34] especially with the government being the offtaker of last resort (OLR) as per EMR, underlining the government's drive to see the success of OWF energy and the reduction of financial risk in the project set up.

OLR is designed to reduce the risk of market failure at the outset of the CfD, and therefore reduce the cost of investment in renewable electricity generation. It boosts competition and lowers costs to consumers. At its simplest form, the OLR achieves this by providing renewable CfD generators with a guaranteed, "backstop" route to market for their power: a Backstop PPA (BPPA) (DECC, 2014) [35]. Competition is guaranteed by the government by providing eligible generators with a guaranteed BPPA route-to-market at a specified discount to the market price. The discount would be set to be larger (more expensive) than discounts expected to be available in the market, ensuring that it is a genuine "last resort," (BEIS, 2015) [36].

PPAs assure a project developer that there will be a market for their product and the conditions of that market for example, price, time (duration). The market is also assured that there will be a certainty of supply of the goods or service, price and duration included. Business certainty is reflected in the lower cost of business as measured by LCOE for example see [20].

34.5.20 Contract for difference

One of the pillars of EMR (Fig. 34.7) was/is to promote the development of affordable electricity for both generator and customer. As part of MER and to meet this objective, the contract for difference was introduced, replacing renewable obligation certificates for new larger-scale projects as the principal mechanism for subsidizing renewable generation [37].

The CfD scheme is the government's main mechanism for supporting low-carbon electricity generation. CfDs incentivize investment in renewable energy by providing developers of projects with high upfront costs and long lifetimes with direct protection from volatile wholesale prices, and they protect consumers from paying increased support costs when electricity prices are high (BEIS, 2020)[38].

CfDs work together with PPAs to the extent that the OWF is required to negotiate a PPA and [37] explain that under CfDs, a generator (OWF) is required to enter into a contract for the sale of its actual power output (a route to market power purchase agreement, "PPA"), and is paid for that power according to the commercial deal that it negotiates PPA. The mechanics of CfDs is explained in [20] and illustrated in Fig. 34.8.

CfDs have the benefit of stabilizing returns for OWF at a fixed level, throughout the contract. This removes the OWF's long-term exposure to electricity price volatility, substantially reducing the commercial risks they face. As commercial risks are lower under the CfD, this lowers the cost of raising finance, and, ultimately, encourages investment in low-carbon generation at the least cost to consumers (DECC, 2012). Ultimately LCOE is lowered by CfDs.

34.5.21 Strike price

CfDs are a key mechanism of EMR and under EMR, the government divided renewable energy technologies into pots or groups as follows (BEIS, 2015) [36]

1. Pot 1 (established technologies, such as onshore wind and solar)
2. Pot 2 (less established technologies, such as offshore wind and biomass)
3. Pot 3 (biomass conversion)

To these pots, the government allocates a budget and from this budget, administrative maximum strike prices or costs of renewable energy are determined to support energy generators in each pot. Not always is there enough money to support all intending generators and the allocation becomes subject to an auction run by the Delivery Body, National Grid. This is a sealed bid auction process, which is based on the strike price established by the auction for a specific delivery year and rewards the least expensive projects with CfDs. The projects which bid for a higher strike price than that set by the auction do not receive a CfD [37]. This competition for CfDs via the strike price has been a major factor in the decline of LCOE and [39] outlines the decline in strike price in Figure 34.9, mirroring the decline in LCOE in Fig. 34.2.

34.5.22 Technological developments

Technological developments in any industry aim to improve the efficiency of the application of 4 M resources of money, man, machine, and minute (time). Efficiency results in more or better-quality output per input resource. Efficiency results in achieving more with less. This has been the quest of the industry since the Industrial Revolution. The current catch phrase is to "build back better." A vast array of technological changes has impacted the decline of LCOE and a few key ones will be discussed.

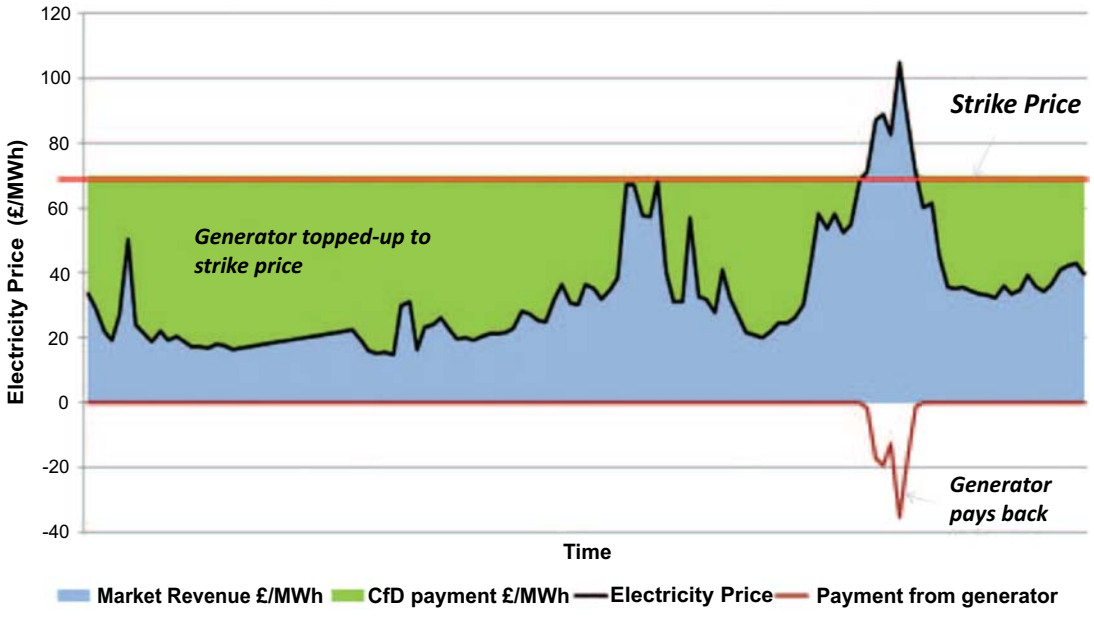

FIGURE 34.8 Illustration of the operation of a Feed-in Tariff with contracts for difference. *After DECC (2012).*

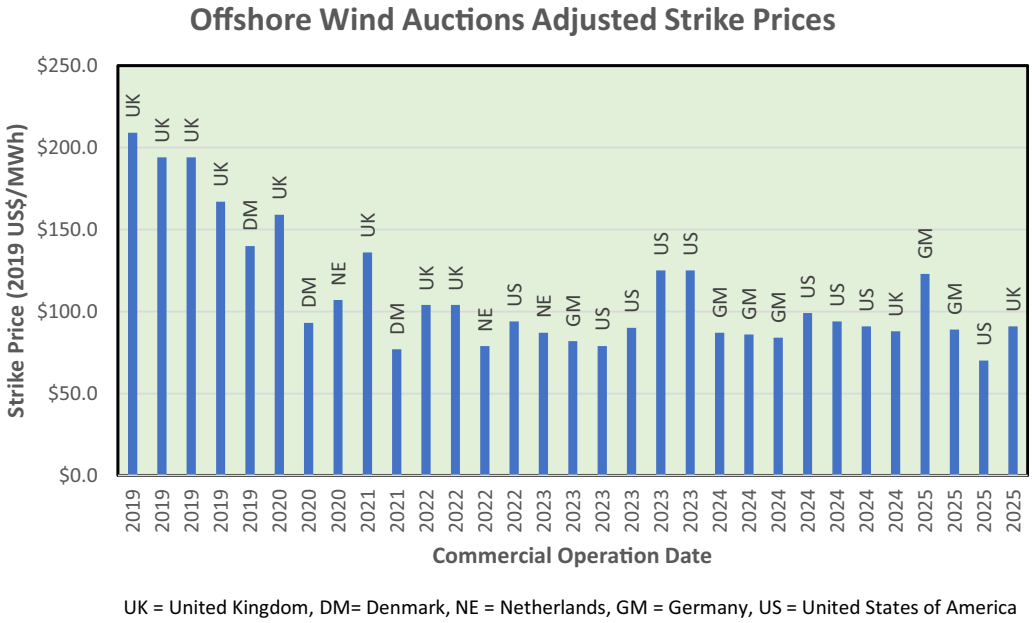

FIGURE 34.9 Decline of global strike price (https://www.nrel.gov/docs/fy21osti/77411_data_tables.xlsx, 2019).

34.5.23 Changes in rotor blades

Comparatively more space will be devoted to this subtopic because of the importance of blades in power generation.

The wind has powered man through civilization, Arab dhows, and windmills in agriculture. The designs that were used especially for windmills were typically large, heavy, and inefficient, and gradually they fell into disuse and were replaced with new technology of steam, coal, and oil. These technological advances were complimented by an improved understanding of aerodynamics and advances in materials, particularly polymers and methods in the design and construction of blades or rotors that capture wind energy.

Efficient rotors capture high levels of energy from the wind blowing against them and the energy (P) in a moving mass of wind is given in Eq. (34.1) [40,41].

$$P = \frac{1}{2} Cp\rho AV^3 \tag{34.1}$$

where Cp, power coefficient, ρ, density of air, A, Swept area, V, velocity of moving wind

The amount of energy (P) captured by a rotor is dependent on the reduction of air speed as the wind moves over the turbine and this reduced speed can never be zero or 100% extraction as this will mean no air movement. The maximum extraction also called the power coefficient (Cp) or Betz limit is 59.3% and is independent of design [41]. The Betz limit theory assumes constant linear velocity.

As a result, any rotational forces such as wake rotation turbulence caused by drag or vortex shedding, or tip losses will further reduce the maximum efficiency from 59.3%. The study [41] reports that efficiency losses are generally reduced by:

1. Avoiding low tip speed ratios which increase wake rotation
2. Selecting aerofoils that have a high lift-to-drag ratio
3. Specialized tip geometries

These three ways of improving rotor efficiency have been at the center of rotor improvement strategies across the industry, to ensure that more energy is captured, or electricity is generated at marginal increases in associated costs and therefore lowering LCOE.

While Cp is independent of design, according to [41], there is a fundamental design parameter around which all other optimum rotor dimensions are calculated, Tip Speed Ratio. Tip Speed Ratio (λ) is the relationship between rotor blade velocity and relative wind velocity, as can be observed in Eq. (34.2).

$$\lambda = \frac{\Omega r}{Vw} \tag{34.2}$$

where Ω, Rotational velocity (rad/s), r, Rotor radius, Vw, Wind speed

Tip Speed Ratio is directly proportional to rotor radius and this has been reflected in the change in turbine sizes over time in the offshore wind sectors. [40] adds that given Eq. (34.1), for a given wind speed and air density, there are two ways to increase the output power, that is:

1. Increasing Power coefficient (Cp)
2. Increasing Swept Area (A) (increasing blade radius and therefore swept area A)

Eq. (34.1) and Eq. (34.2) form the theoretical basis for the increase in turbine sizes, as shown in Fig. 34.11. This is easier to understand given that turbine power increases with the square of the radius swept by its blades, as can be seen in Eq. (34.1). A turbine with blades twice as long would, theoretically, be four times as powerful. It is thus more convenient to increase blade size rather invest in more efficient blade design [40].

But the expansion of the area swept by the rotor puts great strain on the entire assembly, and because blade mass should *(simplistically looking at volume being Length cubed)* increase as a cube of blade length, larger designs should be extraordinarily heavy and pose many challenges like taller towers, larger nacelles, and components. This is a potential threat to continually decreasing LCOE. Designs using lightweight synthetic materials and balsa can keep the actual exponent to as little as 2.3 [42]. Most rotor blades are made of glass fiber reinforced plastic and for some manufactures, their materials are a closely guarded secret. The Haliade 150−6 MW wind turbine is air-cooled and pressurized. Construction materials and protection treatments are specifically designed for offshore environments. Heat exchangers and pressuring units to prevent salty air from entering while dehumidifiers prevent corrosion of components inside the wind turbine [43].

34.5.24 Operation and maintenance—subsea

Maintenance and service costs can contribute as much as 19% of LCOE [1]. These costs go toward planned and unplanned maintenance of wind turbines and associated balance of plant including associated transmission assets, ensuring their continuous operational integrity. Turbines and towers are easier to access than the subsea balance of plant assets. Specialized helicopters and sea-craft permit access to the turbines and tower but subsea assets present unique challenges of access, installation, inspection, and maintenance. With operation and maintenance costs contributing up to 28% toward LCOE, it is no wonder that there has been considerable focus in the industry on optimizing maintenance and service activities to reduce OPEX.

As late as 2020, subsea inspection methods were time-consuming, expensive, and imprecise, requiring large crews, expensive and highly labor-intensive processes, and careful analysis of thousands of hours of videos [44]. Automation of this very important step of assessment was a key technological gap whose bridging would save as much as 80% of the cost of subsea inspections.

34.5.25 Developments in turbine design

Turbines are the powerhouse of an OWF. All the infrastructure at an OWF is to structurally and functionally support the turbine. Turbines are the powerhouse, their blades capture wind energy, and transmission and drive trains transfer captured energy to the generators that convert it into electrical energy in the nacelle. All this assembly is structurally supported by a tower.

Figs. 34.4, 34.5, and 34.6 have pointed to a situation of increasing business efficiency where there is growth in wind farms and installed generating capacity while there is no sympathetic growth in turbines installed, showing that the same number of turbines installed in each year produced more power than the year before. Turbines were becoming more efficient with time.

For the British offshore wind industry, BEIS (2020) [38] data confirms the growth in OWF power generation, showing increasing power generation over the decade and, a continuing positive trend (Fig. 34.10).

The inference made in Section 3b is further supported by global data from the [8], Fig. 34.11, showing a trend of increasing turbine size and rating (nameplate capacity) over the decade under review. The increase in turbine size is matched by the increase in power generation, showing that the capacity per turbine was increasing over the decade; a situation of technological efficiency of turbines.

Larger blades and therefore larger turbines have greater power output, and capital costs do not increase proportionally when building larger turbines. These economies of scale have reduced the unit costs of building a wind farm, as farms consisting of fewer (Fig. 34.6) but larger turbines lead to savings the costs of foundations, electrical cables, and

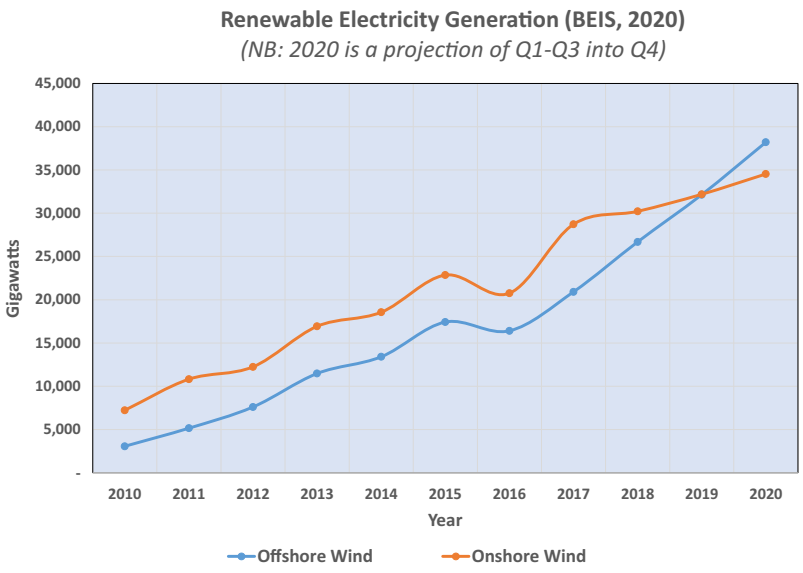

FIGURE 34.10 Renewable electricity generation. *After BEIS (2013). [45].*

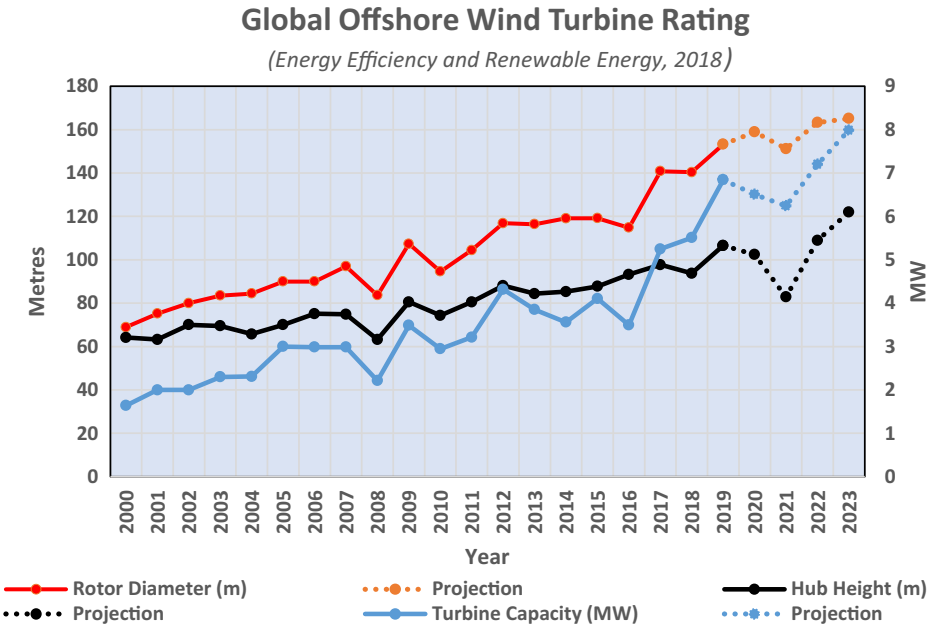

FIGURE 34.11 Global offshore wind turbine rating, hub height, and diameter. *After Office of Energy Efficiency and Renewable Energy, 2018.*

installation. It is estimated that an increase in capacity from 4 MW to between 6 and 8 MW can reduce the levelized cost of electricity by up to 10% [46].

In tandem with these technological developments in turbine design, is the increase in the capacity factor (CF) of the turbines. The CF compares how much energy was generated against the maximum that could have been produced at the continuous full-power operation during a specific period. This is a metric of machine efficiency and the higher the better. Offshore CFs have increased from 34% (for projects completed in 2016–17) to 38% (in 2019–20) and are projected to exceed 50% in 2022–23. Onshore CFs have more than doubled since 1990 [46].

34.5.26 Developments in generator design

Generators convert wind energy to electrical energy and are linked to rotors via a gearbox or drive train. International Renewable Energy Agency [47] estimated that for a 5 MW turbine, generators and gearbox can cost up to 16% of a

wind turbine capital cost budget. It is not beyond imagination that this can nearly triple for a 14 MW turbine. Historically, gearbox failures have been major challenges to the operation of wind farms, resulting in substantial O&M costs over the life of the project. This is especially true for offshore wind turbines which are situated in harsh and less-accessible environments. On account of this, direct drive systems have increasingly been desirable in new wind turbine systems [48].

In 2014, Greenspur (an offshore renewable energy company) began work on its direct drive permanent magnet (DD-PMG) design in cooperation subsequently with the University of Warwick where Ridge, Ademi, McMahon, and Kelly (2018) [49] researched to validate a novel axial flux direct-drive permanent magnet generator. The technology pointed to significant LCOE reductions via capital expenditure and operating expense savings. Although the ferrite DD-PMG generator design is still in the testing phase, researchers believe that the generator will help the market reach the point of "subsidy free" [50,51].

34.5.27 Sympathetic industries

Running in parallel, sympathetic and elastic growth and support were registered in other sectors of industry and technological growth. These can be regarded as push-pull factors from the Supra-system, pushing inputs and pulling outputs from OWF in elastic response to growth in offshore wind energy and industry at large. Opportunities created by offshore wind energy were push factors responded to by these sympathetic industries in a commensal relationship of industrial growth. The study [20] outlines these sympathetic industries and highlights their impact on LCOE. These are the mining industry, power storage systems, pump storage industries, compressed air storage systems, battery energy storage systems, vehicle to grid systems, and hydrogen from OWFs.

34.5.28 Foundations and changes in foundation designs

Foundations typically cost 15%−35% of an OWF [40], a significant contribution to LCOE. OWF by their nature are in challenging settings and their foundations need to be well designed and installed as the costs of reworking (corrections and maintenance) can be enormous. For this reason, the following paragraphs will outline pertinent details of foundations and insight into the importance of foundations in OWFs and developments that contributed to a decline in LCOE.

34.5.29 Offshore wind farm foundations

The purpose of foundations in any infrastructure is to safely transfer infrastructure loads into the soil or ground on which the asset rests [40] and do so without exceeding the load-bearing capacity of the ground. Infrastructure loads may consist of static vertical loads from the asset weight or cyclic/dynamic loads from the asset itself or from the environment surrounding the asset, for example, wind, earthquakes, and sea waves.

[40] gives a comprehensive account of OWF foundations, as summed up in Fig. 34.12.

Wang et al. (2017) [52] summarize the physico-commercial characteristics of OWF foundations in Table 34.2.

From Table 34.2, a broad OWF seabed depth and foundation cost matrix can be drawn (Table 34.3), which are drawing attention to the relationship between foundation type, foundation location relative to seabed depth, and all other selection factors highlighted in this section held constant. With the increase in water depth and the quest for good quality wind, the relationship broadly leans away from GBS, Tripod, and jacket foundations in a bid to reduce OWF life cycle costs, in other words, LCOE. This relationship influences technological developments in the race for deeper waters with more reliable winds and lower unit costs.

In real life, the relationship alluded to above is tampered with considerations highlighted earlier, geology, loads (static, cyclic, seismic, wind, wave, and current), and economics, driving the concept of building back better and/or building back greener.

Fig. 34.13 is a trend over time of OWFs being located in deeper waters further away from shore, a trend aligned to decreased use of gravity-based foundations in favor of the other types, and more significantly, the incoming of floating foundations.

Reviews of trends in OWT capacity and sea depths are shown in Fig. 34.14, reinforcing Sores-Ramos (2020) [53], more importantly, that future wind turbine foundations will be designed for deep seabeds of 100 m and deeper.

Resulting from the foregoing are the following characteristics: physical features, location, and support services for offshore wind turbines, and these are supported by developments in foundations, given the impact of foundations on WTG costs.

1. Larger RNA, tower, substructure, and foundation

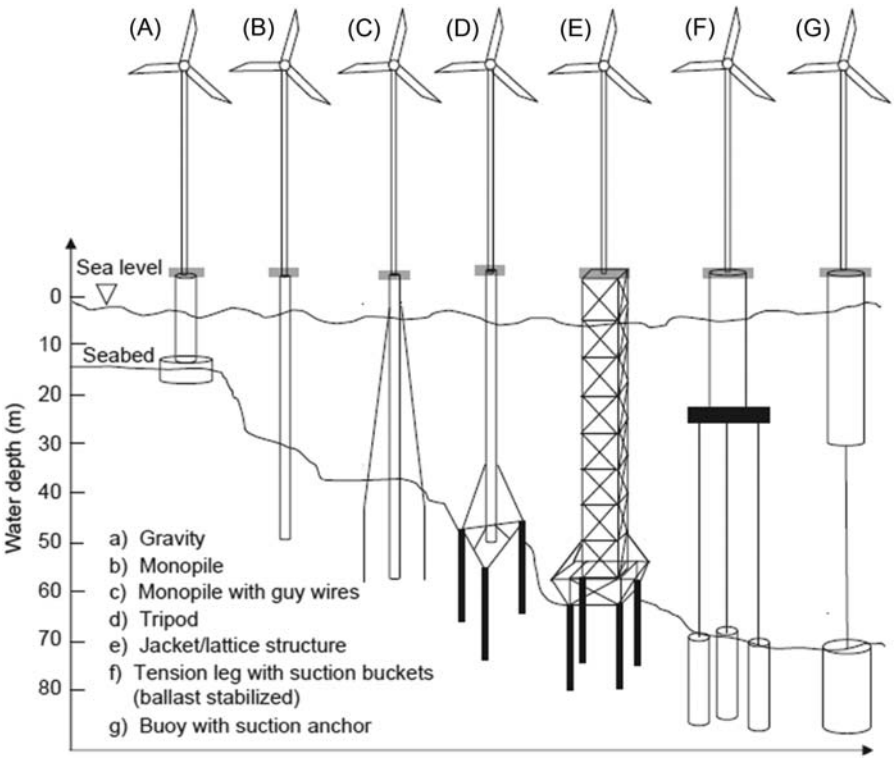

FIGURE 34.12 OWF foundations and seabed depths. *After O'Kelly BC, Arshad M. Offshore wind turbine foundations—analysis and design. In: Owen C, editor. Offshore wind farms: technologies, design and operation. Ducford: Elsevier; 2016. p. 589–610.*

TABLE 34.2 Characteristics of OWF foundations.

Foundation	Priorities/(attributes[a])	Limitations
Suction bucket	Adaptable to larger water depth (up to 60 m); easy transportation and installation; low cost; no seabed preparation	No industrialization
Monopile	Simplest technical solution; low cost; industrialization (widely used[a])	Limitation of water depth; scour effect
Gravity	Simple technical solution; used at locations where piles cannot be driven. Higher total cost than monopile	Limitation of water depth; seabed preparation is necessary
Tripod	Larger bearing capacity; adapt to larger water depth (up to 50 m).	More difficult installation. Higher cost
Jacket	Adaptable to larger water depths (up to 80 m)	Higher cost in construction and installation
Floating	Largest adaptable water depth; flexibility. (Cheap to maintain and in decommissioning[b])	Large movement during operation

[a] *Author's addition*
[b] *[40] Red text = author's own emphasis*
Modified after Wang et al. (2017) [52].

2. Location in deeper waters
3. Unique transport and logistical infrastructure

Bar the last characteristic, the other characteristics mean more asset weight leading to challenging soil-structure interaction and foundation requirements. It is no wonder that wind turbines are getting taller to capture faster and more consistent winds above sea level. Blades are getting longer for reasons stated earlier (Fig. 34.15).

Many considerations must be made in selecting a suitable foundation for a particular site. Some of these aspects are as follows:

1. Easy installation under most weather conditions

TABLE 34.3 OWF foundation seabed—cost matrix

Offshore wind farm foundation seabed depth—cost matrix			
		Cost	
		Low	High
Seabed depth	<30 m	1. Suction bucket 2. Monopile	1. Gravity based system
	30–60 m	1. Suction bucket	1. Tripod 2. Jacket
	>60 m	1. Suction bucket 2. Floating	

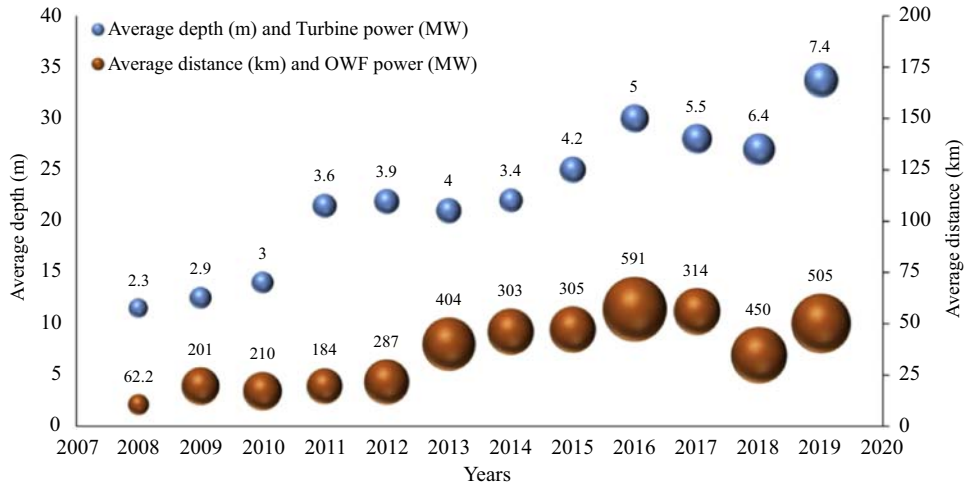

FIGURE 34.13 Trends in location of OWF. *After Soares-Ramos et al. (2020) [53].*

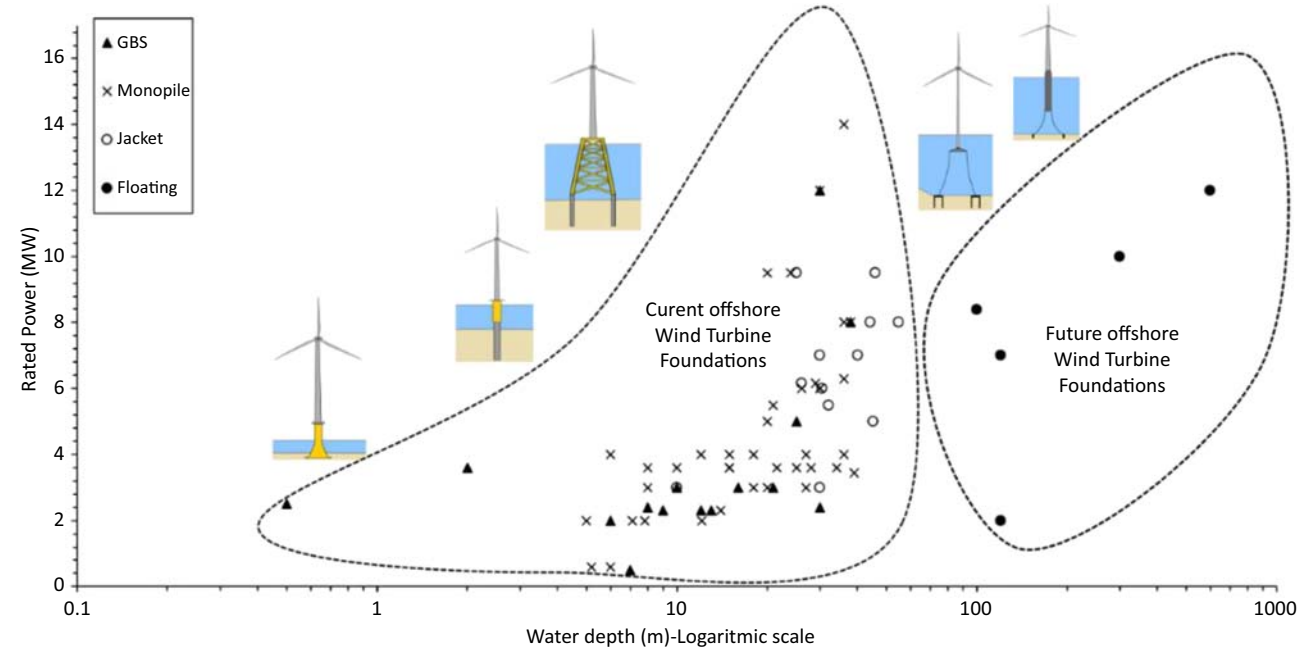

FIGURE 34.14 Trends in OWT power output and seabed depths. *After Bhattacharya S, et al. Physical modelling of offshore wind turbine foundations for trl (technology readiness level) studies. J Mar Sci Eng 2021;9:589.*

Offshore wind turbines have increased in size over the years, in line with advancements in turbine technology and construction.

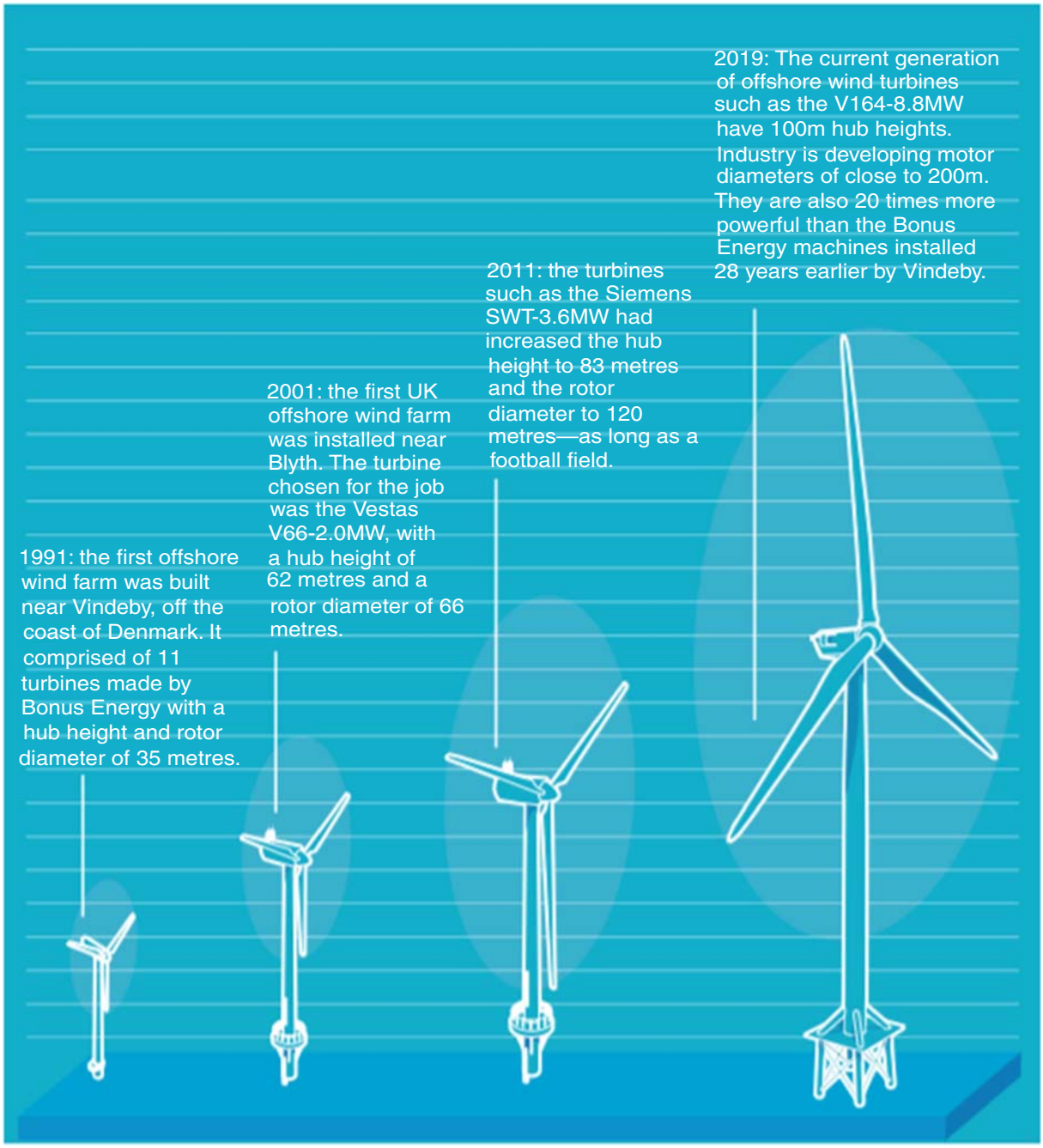

FIGURE 34.15 Changes in offshore wind turbine sizes. *After Smith M, Backwell B, Medic N. Offshore wind energy powering the UK since 2000, https://events.renewableuk.com/images/Images/2019/GOW19/HAYNES-OFFSHORE-WEBSITE-VERSION.pdf; 2019 [accessed 13.03.21]*

2. Seabed conditions
3. Aspects of installation including installation of vessels and equipment
4. Local regulatory controls, for example, for the environment or archeology

Ideal foundations should embody the following points [40].

1. Be "rated power" specific and not turbine manufacturer specific. Turbines can be replaced easier than foundations

2. Installation is not weather dependent to save on project times
3. Be low maintenance type to save on maintenance costs, for example, an inspection of weld joints on jacket foundations or similar.
4. Amenable to automated fabrication and maintenance.
5. Easily transported and installed, for example, using the Vibro method of installation.
6. Light and effective (saves on fabrication, transport, and installation costs) gravity-based foundations are cheaper but heavy and require large cranes and vessels for transport.

34.5.30 Offshore wind farm foundations and installations

Once manufactured, OWT components of foundations, substructure, tower, and rotor-nacelle assembly (RNA) need to be put together and installed at the chosen sites out at sea. This requires specialized ocean craft to transport and install and even maintain the components. These specialized crafts are costly and require a lot of planning to ensure that no time is lost "waiting" for precedent events or bad weather. Installation costs can cost up to 30% of project budgets over the lifetime of a wind farm [54,55].

These installations and O&M costs can be minimized by matching task to boat and form of the charter so that costs are correctly applied by matching the right tool with the right job for the right charter contract. It is noteworthy that in this context, floating foundations can be transported to the site with smaller vessels than other foundations. Detailed explanations of forms of the charter can be found in [20].

34.5.31 Offshore wind farm foundations and loads

This is a subject that has been researched in detail by various workers, and key researches among them are Refs. [40,56–58].

The suitability of different foundations for different settings (structure, environment, and purpose) are key considerations with considerable impact on asset life cycle costs. The ultimate measure of the successful design, construction, operations and maintenance, and decommissioning of an OFW asset is LCOE. The role of foundations cannot be overstated, and the work of the above workers goes into detail about the types of foundations, loads affecting them, and how successful OFW assets are indeed founded on good foundations.

34.5.32 Case studies in offshore wind energy

This section highlights a case study of British OWF. It will have a deliberate bias toward how the Supra-System influenced OWFs and how OWFs responded, the objectives and outcomes of their responses in the context of LCOE. The highlights will be confined to aspects pertinent to the context of the research topic. More case studies can be found in Ref. [20].

34.5.33 Dogger bank wind farm

The Dogger Bank wind farm is located 130 km off the northeast coast of England and consisted of three projects, Creyke Beck A, Creyke Beck B, and Teesside A that were developed by Dogger Bank Wind Farm Limited as Dogger Bank A, B, and C, respectively, since 2017 (Fig. 34.16). This project is a 50:50 Joint Venture between SSE Renewables and Equinor, with SSE Renewables leading the construction phase [59]. Construction started in 2020 for A and B and commissioning is expected in 2023. Dogger Bank C will come into operation in 2026. A and B will deliver a combined 2.4 GW power from 190 Heliade turbines or 13 MW/turbine in seas up to 35 m depth.

34.5.34 Foundations

Dogger Bank wind turbines will be constructed on monopile foundations installed using the jack-up vessel Voltaire.

34.5.35 Contract for difference

The project was granted consent as a Nationally Significant Infrastructure Project in 2015 and successfully secured 15-year contracts (CfDs) for 3.6 GW of new offshore wind energy in the UK Government's round three auctions for low carbon power in 2019.

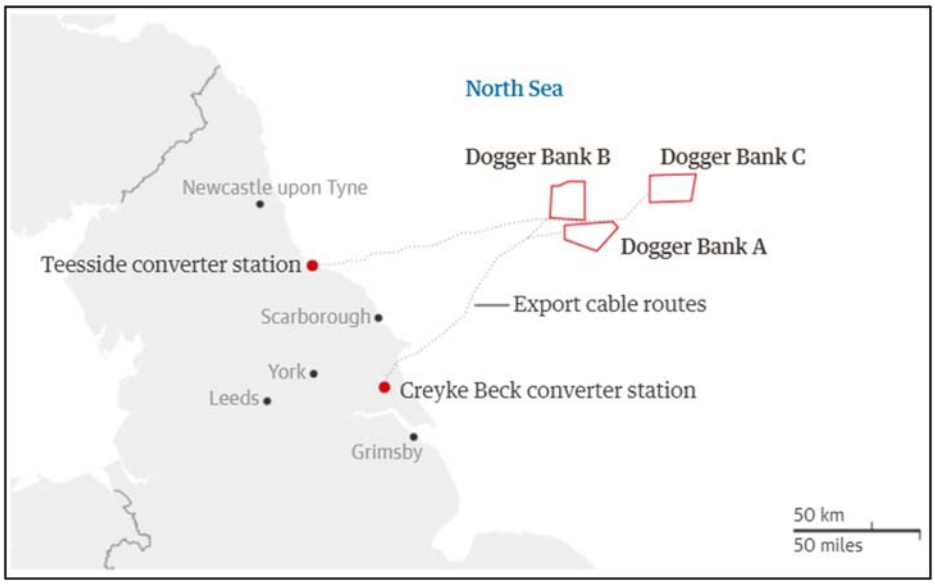

FIGURE 34.16 Dogger bank offshore wind farm. *After SSE Renewables. Power purchase agreements signed for dogger bank A and B, <https://dogger-bank.com/project-news/power-purchase-agreements-signed-for-dogger-bank-a-and-b/>; 2020 [accessed 8.03.21].*

The clearing or strike prices for the projects were £ 39.65 per MWh for Dogger Bank A and £41.61 per MWh for the Dogger Bank B and Dogger Bank C projects (all in 2012 real prices)

The strike prices reflected the continued cost reductions and technological developments and the increasing competitiveness of offshore wind. The contracts offered a fixed price for the first 15 years of operation, providing the projects with a long-term predictable revenue stream [60]. This was in line with the government's underlying objective for CfDs in securing sustainable, competitive, and affordable energy supplies.

The import of CfDs in project finance and its impact on LCOE has been explained in the foregoing paragraphs, market certainty in supply and demand and therefore pricing, LCOE. CfDs are a crucial input from the Supra-System for the success of OWFs like Dogger Bank.

34.5.36 Power purchase agreement

The following is an abridged extract from a press release by [61], briefly outlining the Dogger Bank PPA and its terms.

> **24 November 2020**: SSE Renewables and Equinor, the joint venture partners co-developing the 3.6 GW Dogger Bank Wind Farm in the North Sea, have announced today that 15-year offtake Power Purchase Agreements (PPAs) have been signed for the first two phases of the world's largest offshore wind farm.
>
> Separate PPAs for a total of 2.4 GW across both Dogger Bank Wind Farm A and B have been concluded with external offtakers Ørsted (40% share) and Shell Energy Europe Limited (20% share), and with sponsor offtakers Danske Commodities (20% share) on behalf of Equinor and SSE Energy Supply Limited (20% share) on behalf of SSE Renewables. The agreements are subject to Financial Close on Dogger Bank A and Dogger Bank B, which is expected shortly.
>
> The deals to buy the power generated by the first two phases of the wind farm follow the conclusion of a competitive bidding process. Taken together they represent the largest set of PPAs completed to date in a tender process for a renewable energy project in the UK energy market.
>
> Ørsted will have trading and balancing responsibility for 960 MW while Shell Energy Europe, SSE Energy Supply and Danske Commodities will have responsibility for 480 MW each of installed generation capacity across Dogger Bank A and B.

The PPA, a Supra-System input, assures Dogger Bank that there will be a market for the power they generate, and this lowers project risk and it is ultimately reflected in LCOE.

34.5.37 Dogger bank and technology

The following technological highlights are notable at Dogger Bank (Dogger [61]), enabling Dogger Bank's pressure on LCOE.

The Haliade-X turbine that GE Renewable Energy and Ore Catapult cooperated on saw its first commercial use at Dogger Bank A and B where the 13 MW Haliade-X turbines powered the two phases of the project. It was the first time the turbine was installed in the world. The capacity and efficiency of the Haliade-X turbine have been highlighted in the foregoing passages and Dogger Bank took advantage of this technology in the war against LCOE.

34.5.38 Dogger bank and levelized cost of energy

The foregoing passages highlighting Dogger Bank show how Dogger Bank OWF has been influenced by and has taken advantage of the Supra-System conditions and used them as inputs in their organizational transformational system to meet their organizational goals and other outputs to the Supra-System. In their own words, "We have an important role to play in the UK's offshore wind ambitions and in delivering further carbon emission reductions. Our Haliade-X technology is helping our customers to make offshore wind a more competitive source of clean and renewable energy by reducing the LCOE," [62]. The impact of the outlined factors on LCOE for Dogger Bank cannot be overstated.

34.6 Discussion

LCOE is the major metric with which we can track the cost-effectiveness of the delivery of low-carbon offshore electricity.

The factors that influenced trends in LCOE have been contextualized in systems management theory wherein the offshore wind industry is viewed as an entity or organism in a Supra-System environment. From this environment, the organism takes inputs, and manipulates them in its black box or transformational system to generate outputs into the environment and to meet the organism's own internal goals. For OWF, electricity is the output of interest into the environment and corporate goals are the OWF's internal goals that it uses to measure and improve its performance. Fig. 34.1 summarizes this paragraph and LCOE is used to track the impact of various aspects of the Supra-System on the cost of the product of interest from OWF electricity. The inputs themselves are subsystems of the Supra-System as well, whose outputs are the inputs into OWFs.

34.6.1 The legal environment

By far the most important, overriding, and overarching influence on the trends of LCOE has been the climate change commitments and objectives of the government of the United Kingdom. These commitments are enshrined in the international treaties and conventions that the UK government is part of, and which placed legal obligations on the UK government. A brief mention of these has been made above. These obligations were translated into UK law, enforced by the UK government, and actionable by UK society and industry.

With respect to the energy industry, the emission of greenhouse gases was in the cross hairs of government action in order to reduce global warming, and the Paris Agreement (COP 21), once ratified, it sets an ambitious goal to keep global atmospheric temperature increases well below 2°C, pursue efforts to limit the temperature increase to 1.5°C and achieving net-zero emissions in the second half of the 22nd century [18,19]. The use of fossil fuels in power generation would see consistent reduction over time, with sympathetic growth in nuclear and renewable energy. The Fukushima accident in 2011 however swung preference, and social and industry attitudes toward wind energy from nuclear energy. The commitment by the government of Germany not to build any more nuclear power stations is a milestone in this shift of attitude in favor of renewable energy.

Ratification by the UK government of COP 21 or being party to other climate change conventions showed that the United Kingdom was morally and or legally bound by international law to act consistently with the new global level aims of limiting global warming [18,19].

The legal and policy framework highlighted above describes an enabling environment where the development of renewable energy was a political intent enshrined in law and policy. The Supra-System environment for offshore wind energy was beneficial for the growth of the organism of offshore wind energy. Literary no stone was left unturned for the development of inputs into and for the growth of offshore wind energy. The investment climate, social attitudes, research and development, procurement climate, and many other aspects at the two ends of the renewable energy supply and development continuum were set up for the success of this sector over the 2010–20 decade and beyond. The trend in LCOE as an index of the health of the offshore wind energy industry as outlined above is seen to parallel the improving climate in the legal and policy environment, also outlined above. The commitment to build back better, build back fairer and greener was enshrined in law.

34.6.2 The commercial environment

Having set up the enabling legal and political environment, the commercial aspects of the business could develop and nourish the business. The offshore wind energy sector drew nourishment from the Supra-System in many ways including the commercial inputs. The developments in the commercial sector that promoted the healthy development of offshore wind energy are shown by the declining LCOE over time, with the industry driving to meet government policies and national statutes and ultimately international conventions and treaties, (Figs. 34.2 and 34.9). The positive impact of the various forms of contract and their evolution, CfD and PPA and their impact on the sustainable development, and supply of affordable green energy have been discussed above. These were key drivers in the decline of LCOE.

34.6.3 The technological environment

In the PESTEL setting, some of the technological developments and their impact on the trends in LCOE have been outlined, noting that LCOE is a barometer of industry health and compliance with national policy. Technology, through research, development, and implementation aims to produce more with less, better but cheaper or more affordable equipment. This was one of the tenets of ERM and MER UK. Efficiency was and is key in technological development.

Innovative research and development through principles of technology readiness levels have led to cost-saving technology and with respect to foundations, has had a significant impact on turbine life cycle costs while increasing turbine power generation capacity.

By virtue of the cost impact of foundations in OWT, foundation innovation has led to positively impacting LCOE through changes in design, ease of installation, operational effectiveness, maintenance, and decommissioning (even though not much decommissioning has happened yet).

34.6.4 The transformational unit in the supra-system

A study shown in Mullins [5] and Gordon [6] also refer to this as the transformational or conversion unit known elsewhere in the literature as the Black Box, a subsystem of the Supra-System. Examples have been given in [20] of four OWFs in a time sequence in the 2010−20 decade so that a time-related evolution of the industry is portrayed to capture this in a time parallel to changes in LCOE.

Each case study has outlined a selected Supra-System input or inputs that the project exploited to its benefit and thus impact changes in LCOE. Project basic statistics have also been outlined again with a view to portraying these in a time evolution in parallel to make changes in LCOE. Strike price has been used as a proxy for LCOE, in the context of CfD. Table 34.4 summarizes the basic facts of the case study of OWFs.

Graphs in Figs. 34.4, 34.5, and 34.6 show increasing numbers of OWF, installed capacity, and the number of installed turbines, respectively. While growth has been registered in the number of farms and installed capacity, the number of installed turbines has marginally increased in the decade, a sign that the transformational unit is increasing in efficiency, doing more with less or better, building back better.

Table 34.4 is graphically depicted in Fig. 34.17, showing the decay of strike price and therefore LCOE and the increase in turbine efficiency. The exponential growth in turbine size as measured by rotor diameter reflects the growth and health of the industry.

TABLE 34.4 Offshore wind farms, basic facts.

Project	Commissioned	Foundation	Turbines	Capacity (MW)	MW/ turbine	Strike price (£)	Rotor diameter (m)
Hywind Scotland	2017	Floating	5	30	6	205	154
Beatrice	2019	Piled Jacket	84	588	7	140	154
Triton Knoll	2022	Monopile	90	857	10	74.75	164
Dogger Bank	2023	Monopile	190	2400	13	40.63	220

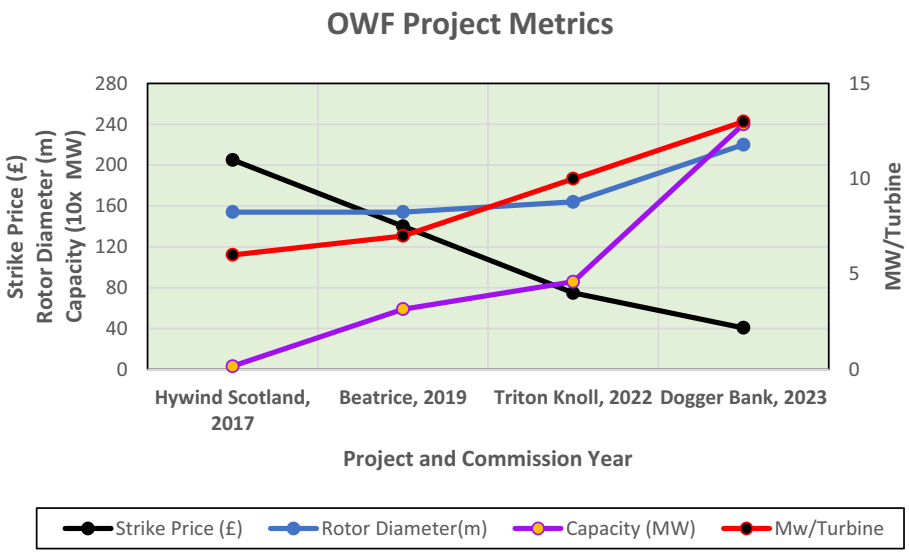

FIGURE 34.17 Case study of OWF, basic facts (NB Capacity is scaled down by 10x).

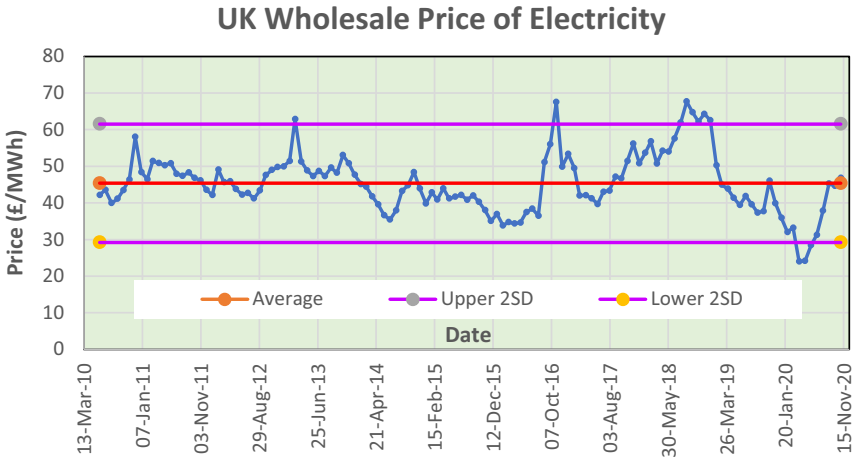

FIGURE 34.18 Wholesale price of electricity [63].

Considered holistically with trends in LCOE (Fig. 34.2) and the improving Supra-System, Fig. 34.17 shows that the case study of OWFs did respond positively to changes in the Supra-system, took these inputs into their Transformational units, generated renewable energy in a manner aligned to the Supra-System requirements (regulatory and sympathetic/supportive). There was positive elasticity.

The improving health and growth of the industry are captured by the indices shown in Fig. 34.17, showing the real-life impact of changes in the UK economy and society on OWFs. The showcased OWFs are a small window of the industry at large and they sum up the drivers of the changes in LCOE as a metric of OWF development in the decade to 2020.

Although OWFs have not been the only source of electricity in the decade to 2020, they have been a major and growing sector that has impacted the stability of supply and prices of electricity to the consumer, which is reflected in the wholesale price of electricity in the same period. Fig. 34.18 reflects data from [63], showing that although prices have fluctuated, they have done so in two standard deviation ranges of £16/MWh around an average of £43/MWh, assuring the consumer of sustainable and affordable electricity supply, with a growing OWF green energy component, making building back greener and fairer.

References

[1] BVG Associates. Catapult offshore renewable energy, wind farm costs, <https://guidetoanoffshorewindfarm.com/wind-farm-costs>; 2019 [accessed 25.09.20].

[2] Office of Indian Energy. Levelized cost of energy (LCOE), <https://www.energy.gov/sites/prod/files/2017/12/f46/levelized-cost.pdf>; 2017 [accessed 12.08.20].
[3] Smart G. Offshore Wind Cost Reduction Recent and Future Trends in the UK and Europe. London: Catapult Offshore Renewable Energy; 2016.
[4] Shah. S. Energy For Growth Hub; LCOE and its Limitations.Available from: https://www.energyforgrowth.org/wp-content/uploads/2020/01/LCOE-and-its-Limitations.pdf; 2020 [accessed 25.09.20].
[5] Mullins LJ. Management and Organisational Behaviour. 11th ed. London: Pearson Education Limited; 2016. s.l.
[6] Gordon, J. Systems theory of management - explained. Retrieved from The Business Professor: <https://thebusinessprofessor.com/en_US/management-leadership-organizational-behavior/systems-theory-of-management#what-are-the-components-of-an-organizational-system-2>; 2022.
[7] Meißner, M. Offshore wind turbine cost scaling -A critical assessment and theoretical investigation. Retrieved from ResearchGate: <https://www.researchgate.net/publication/348356086_Offshore_Wind_Turbine_cost_scaling_-A_critical_Assessment_and_theoretical_Investigation>; 2020.
[8] Office of Energy Efficiency and Renewable Energy. Top trends in offshore wind, <https://www.energy.gov/eere/wind/articles/top-trends-offshore-wind>; 2019 [accessed 13.11.20].
[9] HM Government. Industrial Stratergy Offshore Wind Sector Deal. London: BEIS; 2019.
[10] Wind Europe. Offshore Wind in Europe Key Trends and Statistics 2018. Brussels: Wind Europe; 2018.
[11] Wind Europe. Offshore Wind in Europe Key Trends and Statistics 2019. Brussels: Wind Europe; 2019.
[12] Wind Europe. Offshore Wind in Europe Key Trends and Statistics 2013. Brussels: Wind Europe; 2013.
[13] Wind Europe. Offshore Wind in Europe Key Trends and Statistics 2014. Brussels: Wind Europe; 2014.
[14] Wind Europe. Offshore Wind in Europe Key Trends and Statistics 2015. Brusssels: Wind Europe; 2015.
[15] Wind Europe. Offshore Wind in Europe Key Trends and Statistics 2016. Brussels: Wind Europe; 2016.
[16] Wind Europe. Offshore Wind in Europe Key Trends and Statistics 2017. Brussels: Wind Eurpoe; 2017.
[17] UK Parliament. The history of global climate change negotiations, <https://commonslibrary.parliament.uk/the-history-of-global-climate-change-negotiations/>; 2020 [accessed 18.03.021].
[18] Gov.uk. Explantory Memorandum on the Paris Agreement, <https://assets.publishing.service.gov.uk/government/uploads/system/uploads/attachment_data/file/558185/EM_Paris_Ag.pdf> [accessed 18.03.21].
[19] Gov.uk. Microsoft Word—CFD round 2 allocation round outcome FINAL.docx, <https://assets.publishing.service.gov.uk/government/uploads/system/uploads/attachment_data/file/643560/CFD_allocation_round_2_outcome_FINAL.pdf> [accessed 14.03.21].
[20] Machiridza L. Levelised cost of energy (UK offshore wind power) drivers, challenges, opportunities and practice 2010 to 2020. University of Surrey, Guildford, UK. Unpublished M.Sc.Thesis, 2021.
[21] Department of Energy and Climate Change. Electricity Market Reform: Policy Overview. London: The Stationery Office Limited; 2012.
[22] DECC:. Electricity Market Reform: policy overview. Available from: https://assets.publishing.service.gov.uk/government/uploads/system/uploads/attachment_data/file/65634/7090-electricity-market-reform-policy-overview-.pdf. ; 2012 [accessed 18.12.20].
[23] Gov.uk. Guidance 2050 pathways, <https://www.gov.uk/guidance/2050-pathways-analysis>; 2013 [accessed 12.01.21].
[24] HM Government. The Energy Act 2013, <https://www.legislation.gov.uk/ukpga/2013/32/pdfs/ukpga_20130032_en.pdf>; 2013 [accessed 18.12.20].
[25] HM Government. Explanatory Notes Energy Act 2016 Chapter 20, <https://www.legislation.gov.uk/ukpga/2016/20/pdfs/ukpgaen_20160020_en.pdf>; 2016 [accessed 17.12.20].
[26] Oil and Gas Authority. The Maximising Economic Recovery Stratergy for the UK. London: Oil and Gas Authority; 2015.
[27] Noonan M. UK Offshore Wind: Realising the Sector Deal Opportunity. London: Catapult Offshore Renewable Energy; 2019.
[28] Johnson B. Read the Prime Minister's keynote speech in full, <https://www.conservatives.com/news/boris-johnson-read-the-prime-ministers-keynote-speech-in-full>; 2020 [accessed 23.12.21].
[29] The Whitehouse:. Remarks by President Biden at the 2021 Virtual Munich Security ConferenceAvailable from: https://www.whitehouse.gov/briefing-room/speeches; 2021 [accessed 19.02.21].
[30] Harling, Gard, James, Salmon. Future trends in procurement strategy: the influence of new nuclear and offshore energy projects, <https://uk.practicallaw.thomsonreuters.com/3-549-1845?transitionType = Default&contextData = (sc.Default)&firstPage = true>; 2013 [accessed 3.11.20].
[31] Hartley K. Mondaq Pinsent Masons UK: the winds of change—EPC contracts for offshore wind farms, <https://www.mondaq.com/uk/industry-updates-analysis/39948/the-winds-of-change-epc-contracts-for-offshore-wind-farms>; 2006 [accessed 13.12.20].
[32] NEC. Introducing the new NEC4 Alliance Contract, <https://www.neccontract.com/About-NEC/News-and-Media/Introducing-the-new-NEC4-Alliance-Contract>; 2018 [accessed 4.03.21].
[33] Yescombe ER. Principles of Project Finance. 2nd ed. Oxford: Elsevier Inc; 2014.
[34] Daniels L. Chapter 13: power purchase agreement, <https://www.windustry.org/community_wind_toolbox_13_power_purchase_agreement>; 2007 [accessed 14.02.21].
[35] DECC:. Implementing the Offtaker of Last Resort, London: Department of Energy and Climate Change.Available from: https://assets.publishing.service.gov.uk/government/uploads/system/uploads/attachment_data/file/324227/OLR_Consultation_Final_27_June.pdf ; 2014 [accessed 22.09.20].
[36] BEIS:. The CFD contractAvailable from: https://www.gov.uk/government/collections/electricity-market-reform-contracts-for-difference#the-cfd-contract. ; 2015 [accessed 07.03.21].
[37] Clifford Chance. Contracts for Difference: An EMR CfD. London: Clifford Chance; 2015.
[38] BEIS:. Policy Paper Contracts for DifferenceAvailable from: https://www.gov.uk/government/publications/contracts-for-difference/contract-for-difference; 2020 [accessed 29.01.21].

[39] NREL. (2019). 2019 Offshore Wind Technology Data - NREL. Retrieved from 2019 Offshore Wind Technology Data Update: <https://www.nrel.gov/docs/fy21osti/77411_data_tables.xlsx>.

[40] Bhattacharya S. Design of Foundations for Offshore Wind Turbines. 1st ed. Hoboken: John Wiley & Sons Ltd; 2019.

[41] Schubel P, Crossley RJ. Wind turbine blade design. Energies 2012;5(6):3425–49 September.

[42] Smil V. Wind turbines just keep getting bigger, but there's a limit, <https://spectrum.ieee.org/energy/renewables/wind-turbines-just-keep-getting-bigger-but-theres-a-limit>; 2019 [accessed 13.03.21].

[43] GE Renewable Energy. GE's Haliade* 150-6MW High yield offshore wind turbine, <https://www.ge.com/renewableenergy/sites/default/files/2020-01/wind-offshore-haliade-wind-turbine.pdf>; 2015 [accessed 13.03.21].

[44] Catapult. ROVCO, <https://ore.catapult.org.uk/stories/rovco/>; 2020 [accessed 18.01.21].

[45] BEIS:. National Statistics Energy Trends: UK renewablesAvailable from: https://www.gov.uk/government/statistics/energy-trends-section-6-renewables; 2013 [accessed 13.01.21].

[46] Postnote. Developments in Wind Power. London: Houses of Parliament. Parliamentary Office of Science and Technology; 2019.

[47] IRENA. Renewable Energy Technologies: Cost Analysis Series—Wind Power. Abu Dhabi: International Renewable Energy Agency; 2012.

[48] Wenping C. X. Ying. T. Zheng. Advances in Wind Power (Wind Turbine Generator Technologies). 1st, (Rupp Carriveau) ed. London: IntechOpen, 2012.

[49] Ridge A, Ademi S, McMahon A R, Kelly H. Ferrite-based axial flux permanent magnet generator for wind turbines. The Journal of Engineering 2019;3942–6 Submitted for publication.

[50] Wind Energy Network. Wind energy network, Issue 36, <http://www.windenergynetwork.co.uk/wp-content/uploads/2017/02/wen36-spreads-1.pdf>, 2017. [accessed 8.03.21].

[51] O'Kelly BC, Arshad M. Offshore wind turbine foundations—analysis and design. In: Owen C, editor. *Offshore Wind Farms: Technologies, Design and Operation*. Ducford: Elsevier; 2016. p. 589–610.

[52] Wang X, Zeng X, Li J, Yang X, Wang H. A Review on Recent Advancements of Substructures for Offshore Wind TurbinesAvailable from: https://pdf.sciencedirectassets.com/271098/1-s2.0-S0196890417X00241/1-s2.0-S019689041731213X/am_s0.pdf?X-Amz-Security-Token = IQoJb3JpZ2luX2VjEM%2F%2F%2F%2F%2F%2F%2F%2F%2F%2F%2F%2FwEaCXVzLWVhc3QtMSJGMEQCIBMRbK3VXrdAkZ3zqZjGF87W7PqU63opqSdxqe6Z6gnmAiB8EqC17DjBq%2BvxR8V6lQXxT4e1PsTQFPyM71V3O0xpGSrVBAiY%2F%2F%2F%2F%2F%2F%2F%2F%2F%2F%2F8BEAUaDDA1OTAwMzU0Njg2NSIMdLwlIFiKe0XBuhEvKqkEoEDWG0poLkLaExZzDogXC%2BypXEhTIz9YCuUhDBzuVSOGEiEUmtazpnDgjxrPumqpY1wXyLp5GQFbtj1Jct%2BklKeVHoWCh%2BEEjwrPJl6YGlOAHhfdHeXxE0rhXehog38OFQuAsy1KerwJHbVMo4CoECY880iv4PMQlefdV1CO33bPgZNxTjVR86EHUYz0Qb0O2N1YTYM6d4ggsbDTjhiEbsQvDpXqJjb2jaSDpoEVoolVaQKn6ATQaSOKU%2Bh0A3PIgQmIFwJhrGaUWAPvqooXQUvt5FiLKqXMb6G7L%2FuJLdKHC%2ByREJgFIU4tCeXVUb63fkPfwauhtVu%2BXbniQiuDw8sVWRlWTuemkIR5F4wrs0M3CmCx8TeqELoM4IbA%2BQmPJ%2Fjp6%2FJr5MJ8mcZ2%2FPmkROTu1%2B1TOQo4aizW3bB8XnGmgbHutdYGXP7JEnVx1%2Ff2pleTS%2F5JM6aCrRtqlJwTh%2FZ3oHhdRD%2Fa07lO21G6GxxtndR5Py2JBxE1h85C4ywYshrpUtSBcEaT9PL0Ul4hdfWtyrs5PpNjJoIcLa9DJ%2F2L19sFaGtLbufMo0lQcbc9Kmgq3HocJaOzhkamvUsHGs5cB1YsLof08unNMvC3sAHBO1YJCVEx9%2BB%2F2o%2B1YYINzELLjp43XCNPNLL0m11F4PAGCEjyjvZx0bSQb4V%2BmxuUcnneP9Z48i8bfDWKAVVmig9vVVcrfSS1GnR%2FhsJZBSn3qWJI%2FB2rBTCcgJ2aBjqqASNnLBFYFLR0ac%2F0DkebfJgyWiV2SXdUKjpW3fcdPYtRlcCe3LMx7bv3SZhro4e%2F%2B3zfZQOxrbvRAj%2BORWzWp9OcElYXehfYr4ZuF%2BuavlT%2BSWQAR44T27Ney92GXLMPHrMkUTS5ylCi7WjrVln61BaYgxIW4bpGxYS0dhEjz59fYgdoc4eALKpOj5%2FjUt13XFNpcPgs9bAuUBEuHpllP3HPc5J0x9%2BBOz2v&X-Amz-Algorithm = AWS4-HMAC-SHA256&X-Amz-Date = 20221012T234856Z&X-Amz-SignedHeaders = host&X-Amz-Expires = 300&X-Amz-Credential = ASIAQ3PHCVTYUNX34IVH%2F20221012%2Fus-east-1%2Fs3%2Faws4_request&X-Amz-Signature = 2947c89ab96ebb3fc64c2ebdbdcfb4dba1db9ac27a1df8d6498d9cee824dd92e&hash = 4a19809f76f34bc418e27accf391daab2f4584f119ddbe193231cdf8db7f5f75&host = 68042c943591013ac2b2430a89b270f6af2c76d8dfd086a07176afe7c76c2c61&pii = S019689041731213X&tid = pdf-039552d2-7382-4c1d-a2a2-c1a5daf060a3&sid = a80e86192aecc848c5697b454e2d621e3723gxrqa&type = client. ; 2017 [accessed 13.01.21].

[53] Soares-Ramos P. E, Oliveira-Assis L, Sarrias-Mena R, Fernández-Ramírez, M. L. Current status and future trends of offshore wind power in Europe. Energy 2020;202 Submitted for publication.

[54] Smith M. Backwell B. Medic N. 2019. Offshore wind energy powering the UK since 2000, https://events.renewableuk.com/images/Images/2019/GOW19/HAYNES-OFFSHORE-WEBSITE-VERSION.pdf. [accessed 13.03.21].

[55] Paterson J, et al. Offshore wind installation vessels—a comparative assessment for UK offshore rounds 1 and 2. Ocean Eng 2018;148(15):637–49 January.

[56] Bhattacharya S, et al. Physical modelling of offshore wind turbine foundations for trl (technology readiness level) studies. J Mar Sci Eng 2021;9:589.

[57] Jalbia S, Nikitasa G, Bhattacharya S, Alexander N. Dynamic design considerations for offshore wind turbine jackets supported on multiple foundations. Mar Struct 2019;67.

[58] Nikitasa G, Nathan J, Vimalan, Bhattacharya S. An innovative cyclic loading device to study long term performance of offshore wind turbines. Soil Dyn Earthq Eng 2016;82:154–60.

[59] SSE Renewbles. Dogger bank wind farm, <https://www.sserenewables.com/offshore-wind/projects/dogger-bank/>; 2019 [accessed 8.03.21].

[60] Equinor. Hywind Scotland, <https://www.equinor.com/en/what-we-do/floating-wind/hywind-scotland.html>; 2019 [accessed 17.03.21].

[61] SSE Renewables. Power purchase agreements signed for Dogger Bank A and B, <https://doggerbank.com/project-news/power-purchase-agreements-signed-for-dogger-bank-a-and-b/>; 2020 [accessed 8.03.21].

[62] NS Energy. Beatrice offshore wind farm, Scotland, <https://www.nsenergybusiness.com/projects/beatrice-offshore-wind-farm-scotland/>; 2019 [accessed 13.03.21].

[63] OFGEM. Wholesale market indicators, <https://www.ofgem.gov.uk/data-portal/wholesale-market-indicators#thumbchart-c6009892667643726-n98510>; 2021 [accessed 27.03.21].

Chapter 35

Certification of new foundations for offshore wind turbines

Muhammad Aleem[1], Subhamoy Bhattacharya[1,2], Jorge Mendoza[1] and Ganga Prakhya[3]
[1]University of Surrey, Guildford, London, United Kingdom, [2]OWF-PRA, London, United Kingdom, [3]Sir Robert McAlpine, London, United Kingdom

35.1 Need for new types of foundations for offshore wind farm development

Offshore wind turbines are relatively new structures and differ considerably from their offshore oil and gas counterpart [1]. From a design perspective, one of the most important distinctions is that offshore wind turbines are extremely sensitive to dynamic loads arising from wind, waves, and earthquakes. Furthermore, they have stringent serviceability limit state (SLS) criteria compared to other structures due to vibration-sensitive components. Therefore, research and development are crucial to significantly reducing the levelized cost of energy (LCOE) and cutting the subsidies on which offshore wind projects rely.

One of the research endeavors is to reduce LCOE through cost-effective foundation design, as foundations typically cost 16%−34% of the overall project. Fig. 35.1 plots the different types of foundations for bottom fixed offshore wind farms based on rated power and water depths. The data for the table is provided in Appendix 35.A. Fig. 35.1 shows that if the water depth is more than 40 m, jacket type of structures is used. Concrete gravity-based foundations are often used for structures in water depths of less than 40 m.

There are typically two types of foundations to support grounded systems: piles (deep foundation) and shallow foundations for which codes of practice and best practice guides exist. In offshore, installation time is a critical component, and therefore, many innovations are aimed at reducing the cost from a holistic point of view: minimizing the material use, robustness in installation and maintenance, and ease of decommissioning.

Fig. 35.2 shows a range of innovations conceptualized to cater for challenging offshore seabed, ease and robustness of installation and environmental conditions (i.e., tropical cyclones, seabed liquefaction), etc. In some cases, research is carried out to support larger turbines in deeper waters and to retrofit or for repowering purposes. Among the concepts presented in

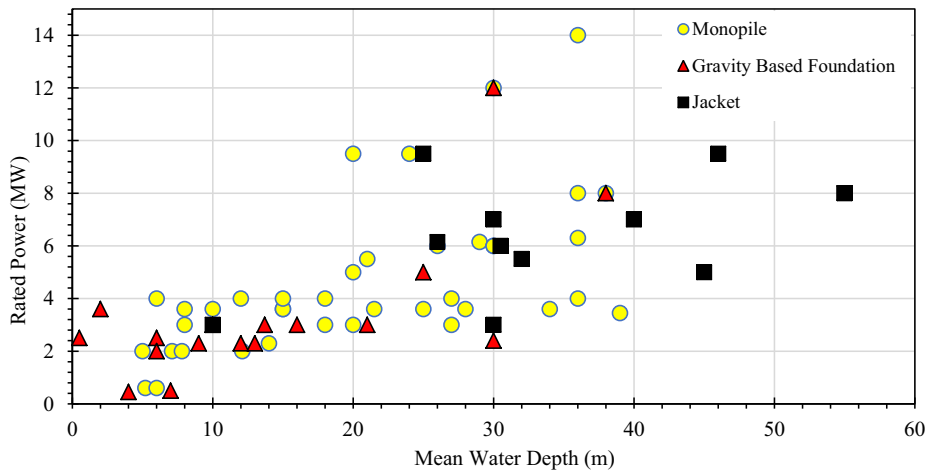

FIGURE 35.1 Foundation for grounded system with different water depth.

Wind Energy Engineering. DOI: https://doi.org/10.1016/B978-0-323-99353-1.00034-7

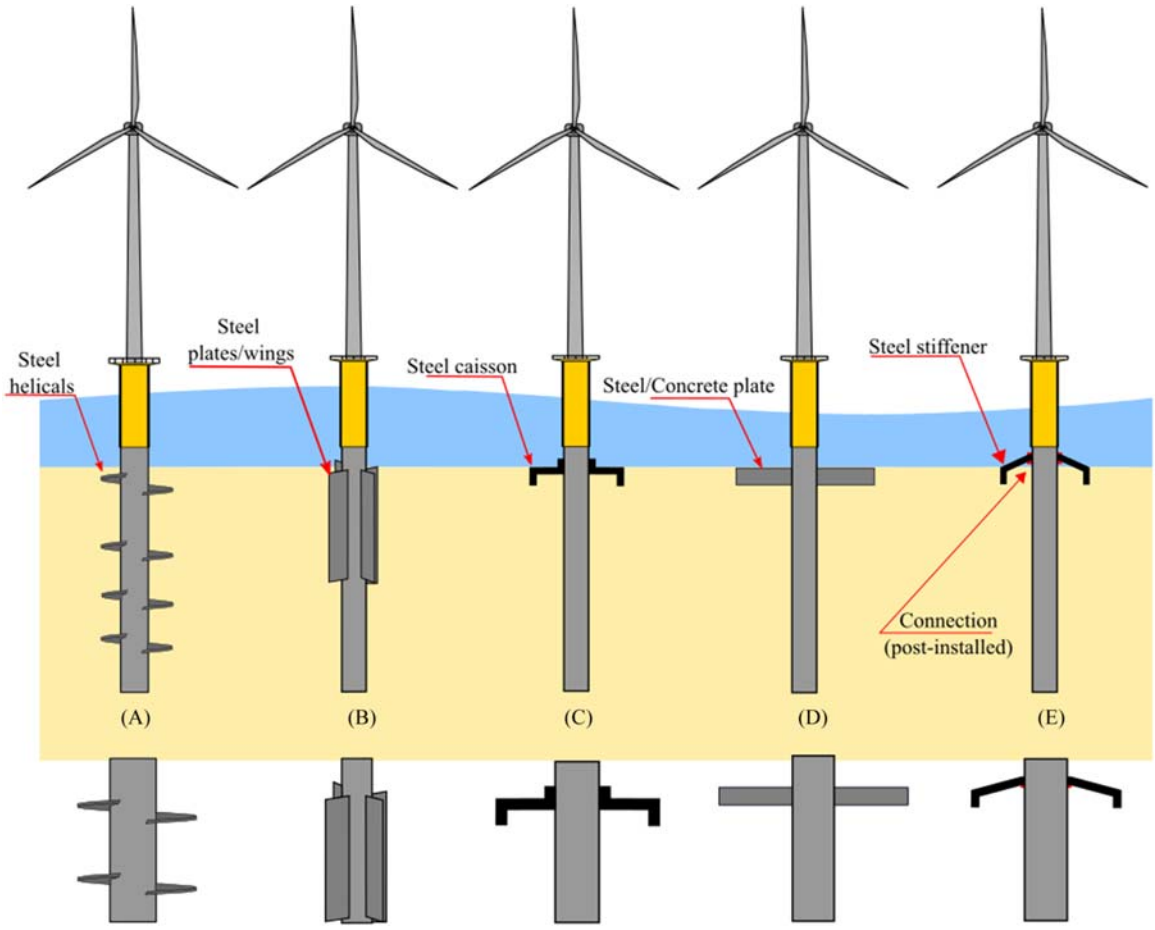

FIGURE 35.2 New innovative foundations for which codes do not exist, helical monopiles; winged piles, collared monopile (caisson + monopile); hybrid monopile with plate; stiffened monopole.

Fig. 35.2C–E is a form of hybrid foundation. By hybrid, we mean the characteristics of the foundation that will have features of both shallow and deep foundations. There are no guidelines for designing hybrid foundations, and therefore studies are needed for quality assurance, validation and de-risking purposes. Essentially, it is necessary to verify different design aspects and the failure modes. In practical terms, they are:

1. Modes of failure of the foundation that will satisfy the ultimate limit state (ULS). It will be later shown that this can be quantified through the load utilization (LU) framework, where the capacity of the foundation can be compared with the applied loads. This is akin to the principles of the Eurocode, where the resistance is compared to the actions. The readers are referred to [2] Aleem et al. (2022) for further details on LU methodology (see Fig. 35.3).
2. Modes of vibration of the whole system which is related to SLS) and fatigue limit state, see Fig. 35.4.
3. To understand the deformations of foundations under various design situations and limit states which are also long-term performance, see Fig. 35.5.

35.2 De-risking of foundation based on technology readiness level

As mentioned before, a thorough technology review needs to be carried out before any new type of foundations can be deployed for real offshore wind farm projects. Moreover, validation of new foundation types through testing requires certifications. European Commission defines this process through the so-called technology readiness level (TRL), and the steps are briefly summarized in Table 35.1, and the readers are referred to reference [4] Bhattacharya et al. (2021).

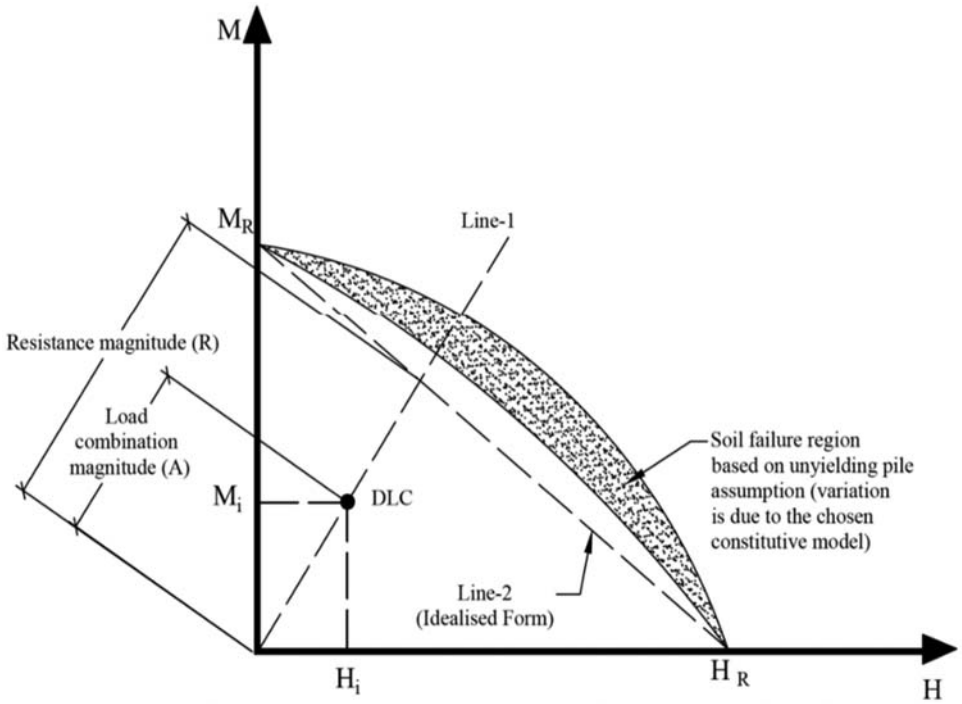

FIGURE 35.3 ULS framework [3].

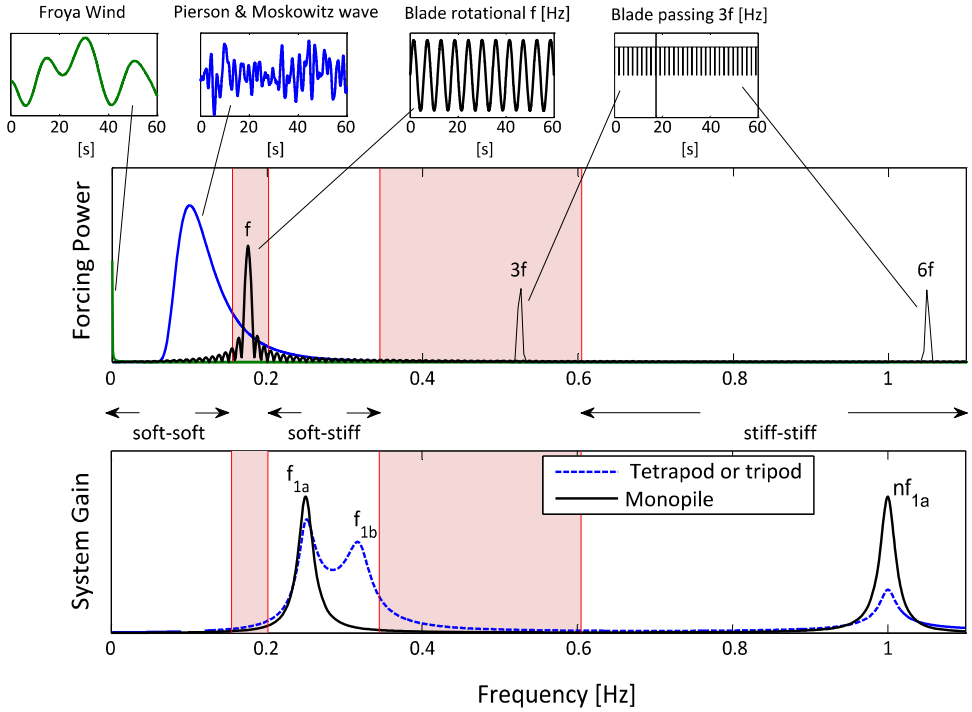

FIGURE 35.4 Modes of vibration.

One of the early studies that need to be carried out is technology validation in the laboratory environment (TRL 3 and 4). In this context, it means carrying out the tests to verify the possible failure mechanism, modes of vibration and long-term performance of the foundations under the action of complex and repetitive loads. It must be realized that it is very expensive and operationally challenging to validate the new technology in a relevant environment, and therefore laboratory-based testing may offer a more economical solution that is robust enough to justify the next stages of investment.

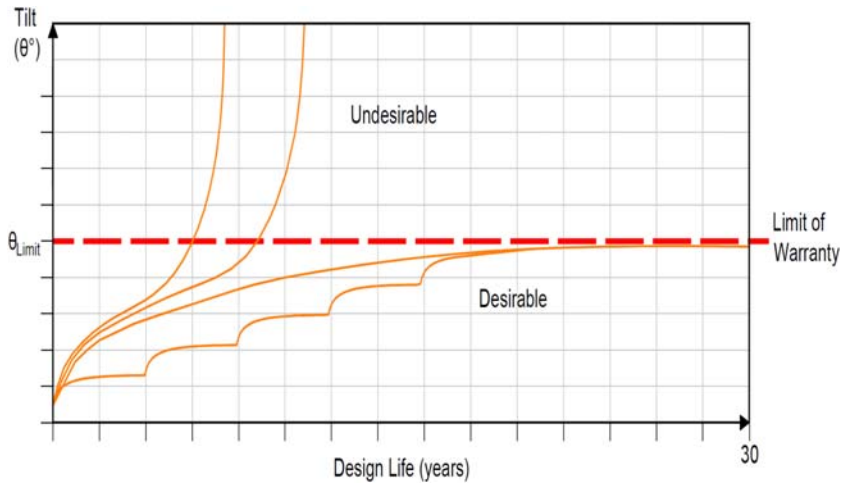

FIGURE 35.5 SLS framework.

TABLE 35.1 TRL (technology readiness level).

TRL level as European Commission	Interpretation of the terminology and remarks
TRL-1: Basic principles verified	It is necessary to verify that the governing mechanics' principles are obeyed. For example, in the case of foundations, it must be checked whether the whole system is in equilibrium under the action of environmental loads.
TRL-2: Technology concept formulated	It is necessary to assess the whole technology starting from fabrication to methods of installation and finally, operation, maintenance (O&M), and decommissioning. In this step, it is expected that method statements will be developed.
TRL-3: Experimental proof of concept	Small-scale models need to be tested to verify TRL 1 and TRL 2. In terms of foundation, this would correspond to checking the modes of failure in ULS (Ultimate Limit State) and identifying the modes of vibration.
TRL-4: Technology validated in lab	Once TRL 3 is satisfied and the business decision is taken to go ahead with the development/design, it is necessary to assess the proposed technology is sound under the most likely scenarios encountered during the wind turbine operation. This may include long-term performance under millions of cycles of loading and evaluate the dynamic performance over the lifetime in relation to Serviceability Limit State (SLS) and Fatigue Limit State.
TRL-5: Technology validated in a relevant environment	Validation in a relevant environment may require further numerical simulation where models are calibrated based on the results from the small-scale model tests and element tests. In the context of foundation, this step may use advanced soil constitutive models to verify the performance under extreme loading.
TRL-6: Technology demonstrated in the relevant environment	To demonstrate the technology in the relevant environment, a prototype foundation may need to be constructed and tested in the offshore environment representative of the real site conditions.
TRL-7: System prototype demonstration in an operational environment	The foundation is subjected to operational loads, and the performance is monitored.
TRL-8: System complete and qualified	Based on TRL 7, the system can be classified as qualified or not qualified, or changes are required.
TRL-9: Actual system is proven in the operational environment	Technology may be used in energy generation with contingency plans.

35.3 What does technology readiness level 3 and 4 constitute in the context of foundation design

35.3.1 Requirements of foundation testing for offshore wind turbine foundations

The turbine manufacturer's design and performance specifications are based on projected future performance. One of the main objectives is to be economically efficient and maximize the energy output over the lifetime of the wind turbine. For foundation design, the main issues are as follows:

1. Load transfer from the superstructure to the supporting ground in the case of extreme load events accounts for the supporting soil yielding;
2. Modes of vibration of the adopted structural system, that is, rigid rocking modes, flexible modes, or combinations;
3. Long-term change in dynamic characteristics, that is, change in natural frequency and damping due to repetitive cyclic loads or extreme dynamic loads associated with natural hazards such as typhoons and earthquakes;
4. Long-term deformation does not violate stringent SLS requirements, such as a limit to maximum rotation.

The SLS requirements are dictated by the intended system performance criteria, and it is necessary to discuss these criteria. For a fixed wind turbine operating in a nonseismic area, the excitations due to the rotation of blades govern the design. For such a turbine, the foundation is often allowed to rotate 0.5−0.75 degrees at the mudline. Table 35.2 shows the criteria of allowable tilt for floating and deep foundations.

35.4 Steps in the design of physical modeling

Bhattacharya et al. (2021) reviewed the steps necessary for physical modeling [5]. The design and interpretation of the test carried out on a small-scale model require the assessment of a set of laws of similitude that relate the model to the prototype structure. These can be derived from dimensional analysis from the assumptions that every physical process can be expressed in terms of nondimensional groups, and the fundamental aspects of physics must be preserved in the design of model tests. The necessary steps associated with designing such a model can be stated as follows:

Step 1: What are the potential failure mechanisms or processes that are likely to occur? Care needs to be taken for the particular ones that would dictate the behavior of potential interest in the prototype.

Step 2: Deduction of the relevant nondimensional groups for the identified mechanisms or processes in Step 1. This step can be carried out in many ways. One of the ways is to write the governing equation and use dimensional analysis and Buckingham Pi theorem to derive the underlying dimensionless groups

Step 3: Ensure that the set of crucial scaling laws (which are essential) are simultaneously conserved between model and prototype through pertinent similitude relationships.

Step 4: Identify scaling laws that are approximately satisfied and those which are violated, and which therefore require special consideration.

TABLE 35.2 SLS criteria for allowable rotation.

Foundation type	Allowable rotation
Fixed foundations (nonseismic area)	0.5−0.75 degrees at the mudline
Floating foundation (nonseismic area)	a. The combined pitch and roll should be within 7−10 degrees. b. The nacelle contains critical components such as gearbox, bearings, and acceleration sensitive to acceleration. The common acceleration adopted for the design is 20%−30% of g. c. Translational displacement, also referred to as excursion, must be kept within 20% of water depth.
Turbines in seismic areas	In addition to the requirements discussed above, the following conditions need to be considered: a. Possible liquefaction of loose to medium-dense sand deposits may induce permanent tilting to bottom-fixed foundations or loss of uplift capacity to anchors of floating systems. b. Excessive vibrations due to resonance effects when the earthquake's predominant frequency comes close to one of the fundamental frequencies of the structure.

Once the nondimensional groups are identified, scaled tests need to be designed to check the nonlinearity amongst those groups and compare with numerical results where applicable. These nondimensional groups can later be used to develop design charts. Bhattacharya et al. [4,5] summarize the do's and don'ts in physical modeling:

Do's

1. Try to replicate the mechanisms (for example, failure mechanism) in small-scale tests. Examples include verifying ULS design, see the example of the failure of anchor foundation for floating wind turbines.
2. Repeat the tests in few scales (at least 3), such as 1:200, 1:100, and 1:50 (modeling of models) to remove artifacts (if any) and to establish reliability. Nonlinearity is defined by amplitude and this step helps to identify it.
3. Identify or clarify physical mechanisms or processes (essentially the laws of physics) that governs the observation or control the behavior of interest. This can guide SLS.
4. If possible, write the governing equation and by using mathematical techniques, find the nondimensional groups.
5. Check nonlinearity of the nondimensional groups.

Don'ts

Unless a very simple problem, do not scale the numerical values of the observations to predict the prototype consequences.

35.5 A novel test set-up for technology readiness level studies

This section discusses a novel apparatus that can carry out TRL studies. The apparatus is scalable and, therefore can be used in a variety of scenarios. Fig. 35.6 shows a time history of the overturning moment at the foundation level caused by wind and wave loads. The wind and wave provide the largest overturning moment on the foundation, which is typically three orders of magnitude higher than that induced by the blade rotation through 1 P and 3 P frequencies, where P is the number of revolutions taken per second. As a result, effects due to blade rotation may be neglected (in most cases) when designing scaled model tests for ULS testing. Before the apparatus is discussed, it is important to discuss specific features of the loading and overall system:

1. Load is a combination of two cyclic loads: wind and wave. The apparatus should be able to apply both the loads comprising different magnitudes, frequencies, and number of cycles.
2. The apparatus needs to apply millions of loading cycles of load and ideally can be left unmanned for a good duration.
3. Offshore wind turbine (OWT) is sensitive to dynamics in the sense that the natural frequency is relatively close to the forcing frequencies which must be preserved.
4. Soil−structure interaction must also be maintained.

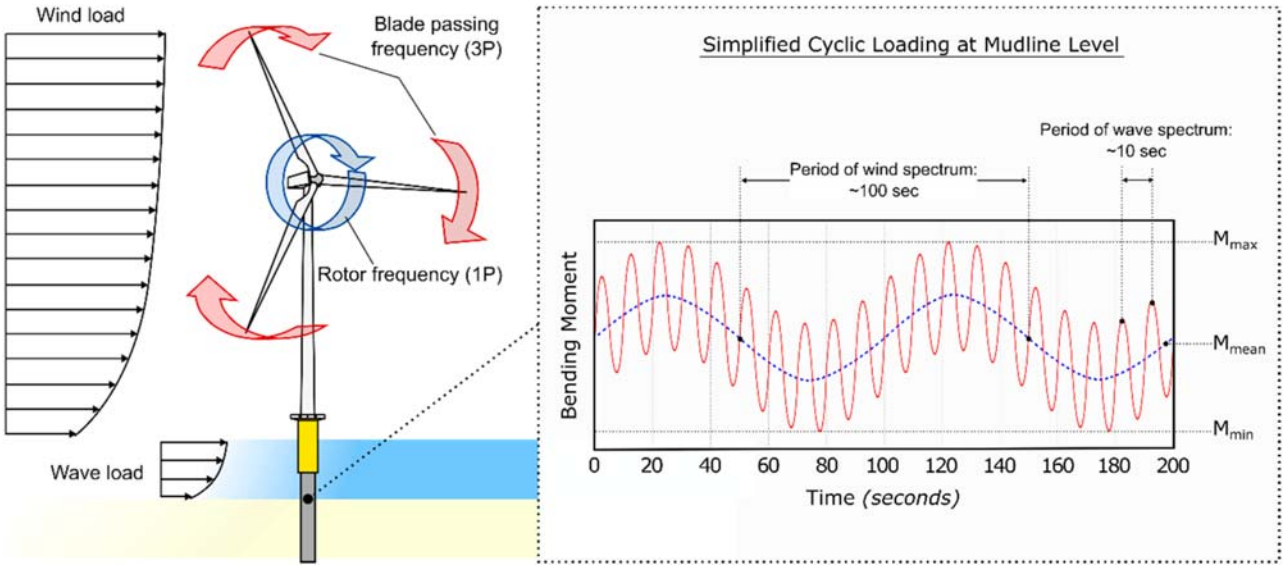

FIGURE 35.6 Simplified loading pattern.

FIGURE 35.7 Photo of test setup from GBS and Jacket testing.

The similitude relationships between the prototype and model OWTs are needed to interpret and scale up the experimental results (by multiplying the model observations by a scaling factor) to predict the behavior of the prototypes. This process is expressed as nondimensional groups, relying on the parameters that control these processes. It, therefore, follows that the derivation of the correct scaling laws relevant to the experiment is the starting point of any study. The readers are referred to similitude relation papers [6–8] for the monopile structure.

Model testing can be performed to determine the capacity of a foundation, that is, the different combinations of lateral load and moment that will cause the foundation to fail, and a failure envelope can be created, such as the one shown in Fig. 35.10. The setup in Fig. 35.9 can be used to find the ultimate lateral load and moment carrying capacity. Before investigating the cyclic behavior, a benchmarking static test is recommended.

35.5.1 To characterizing the dynamics features of the system (modes of vibration)

Modes of vibration of the structures can be investigated and carried out through free vibration/perturbation tests or white noise testing. This is an important part of the validation process as modes of vibration can strongly influence the foundation design, fatigue life, and wear and tear of the mechanical components in the rotor nacelle assembly.

35.6 Long-term serviceability limit state tests

Foundations for offshore wind turbines are subjected to hundreds of millions of loading cycles, which can be cyclic or dynamic in nature. The set-up in Figs. 35.7 and 35.8 can be used to study: (1) change in dynamic characteristics (natural frequency & damping) in long term; (2) long-term tilt.

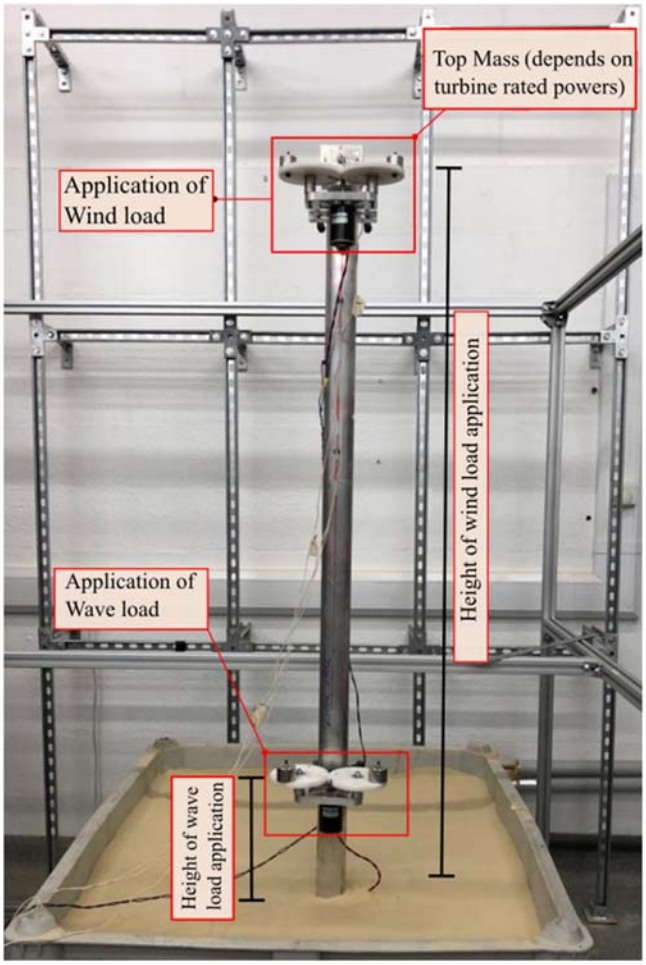

FIGURE 35.8 Photo of the test setup.

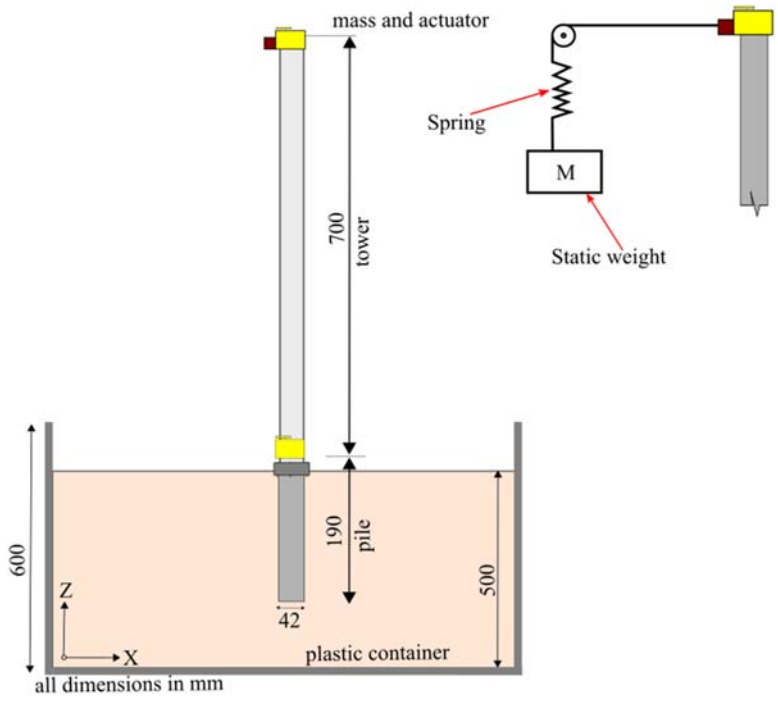

FIGURE 35.9 Schematics of ULS testing.

FIGURE 35.10 Typical moment–horizontal force interaction curve [2].

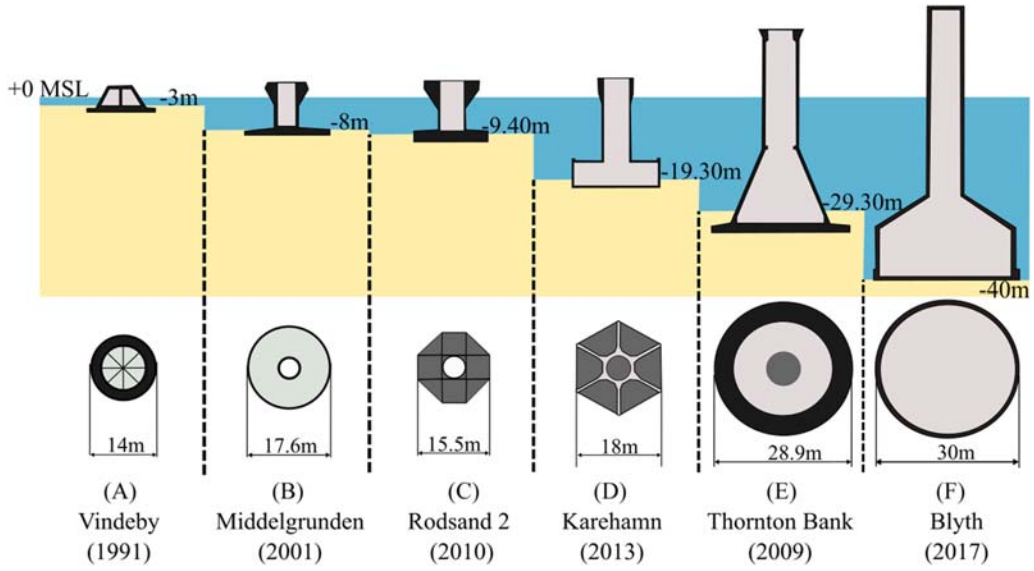

FIGURE 35.11 Development of GBS.

35.7 Technology readiness level example from gravity based structures

A concrete GBS system is being planned for upcoming offshore wind farms, and the shapes of GBS can be rectangular, square, circular, or polygonal in plan, see Fig. 35.11. Table 35.3 shows GBS used around the world, and Fig. 35.12A,B show two examples from GBS.

35.7.1 Technology readiness level testing

Laboratory testing was conducted for three scaled models, see Figs. 35.13 and 35.14. The loading was based on the understanding shown in Fig. 35.15. Using the test setup shown in Fig. 35.9, M_r and H_R curves were generated as this can be named as capacity curve as shown in Fig. 35.16 [2]. Different scenarios were investigated, such as the effects of diameter (scale size) and the role of ballast. In the same graph, the design load cases can also be visualized. Using the LU framework developed in Aleem et al. [2], one can evaluate the effects. Fig. 35.17 shows the results from SLS testing, where the behavior of three scaled models can be observed.

35.8 Technology readiness level example from monopile

Fig. 35.18 shows a similar example from monopile testing generated from the test set-up. The results from ULS and SLS testing are plotted in the same graph. The yield value and yield line are the capacity line similar to H_R–M_r. On the other hand, SLS testing was conducted whereby millions of loading cycles were applied, and the final rotation is given in the figure. It is important to note that the closer the foundation is to the yield line, the higher the final residual rotation.

TABLE 35.3 List of GBS used around the world.

Project	Water depth (m)	Rated power (MW)	Hub height (m)	Distance to shore (km)
Vindeby (Denmark)	2–4	0.45	35	2.5
Tuno Knob (Denmark)	3–7	0.5	45	5.5
Middelgrunden (Denmark)	3–6	2	–	–
Nysted-I (Rodsand I) (Denmark)	6–9	2.3	69	10.7
Rodsan II (Nysted II) (Denmark)	6–12	2.3	68.5	9
Lillgrund (Sweden)	4–13	2.3	68	10
Breitling (Germany)	0.5	3	80	0.3
Karehamn (Sweden)	21	3	80	7
Vindpark Vanern (Sweden)	10	3	90	10.1
Sprogo (Denmark)	6–16	3	70	10.6
Avedore Holme (Denmark)	2	3.6	–	0.5
Thornton Bank Phase 1 (Belgium)	25	5	94	27
Blyth Demonstrator (United Kingdom)	38	8	–	–
Tromp Binnen (Netherlands)	25.5	5	89	65
Asa Branca 22 (Brazil)	14∼21	5	–	35.7
Asa Branca 23 (Brazil)	12∼24	5	–	36.9
Kemi Ajos I (Finland)	1–7	3	88	2.6
Kemi Ajos II (Finland)	1–7	3	88	2.6
Pori I (Finland)	16–19	2	80	6.6
Calvados (France)	19–22	5		11
Oriel Wind Farm (Ireland)	17–27	6	-	7.8
Poweo (France)	19–22	5.7	90	11

35.9 Technology readiness level example for hybrid foundation

Hybrid foundations can be of many types, and they can support wind turbines in the transition water depth, see Fig. 35.19. A plate is attached to the monopile at the mudline level in this example. The efficacy of hybrid can be evaluated through ULS and SLS testing and is shown in Fig. 35.20. The study compares the capacity of monopile and hybrid foundations. As expected, with the increase in plate diameter, the capacity increases. The main purpose is to show the application of testing for TRL studies.

35.9.1 Prototype response

The next step is to predict the prototype behavior and numerical modeling can be used for such purposes whereby the fundamental mechanics' principles are preserved. Fig. 35.21 shows the monopile foundation for the wind farm (Barrow-II), and a numerical model can be used to generate the capacity curve for LU understanding. The readers are referred to Aleem et al. [2] for details on the numerical modeling.

(A)

(B)

FIGURE 35.12 Photos of GBS (A) Thornton Bank (B) Karehamn https://www.rsb.info/en/project/karehamn-sweden/.

FIGURE 35.13 Lab models of GBS.

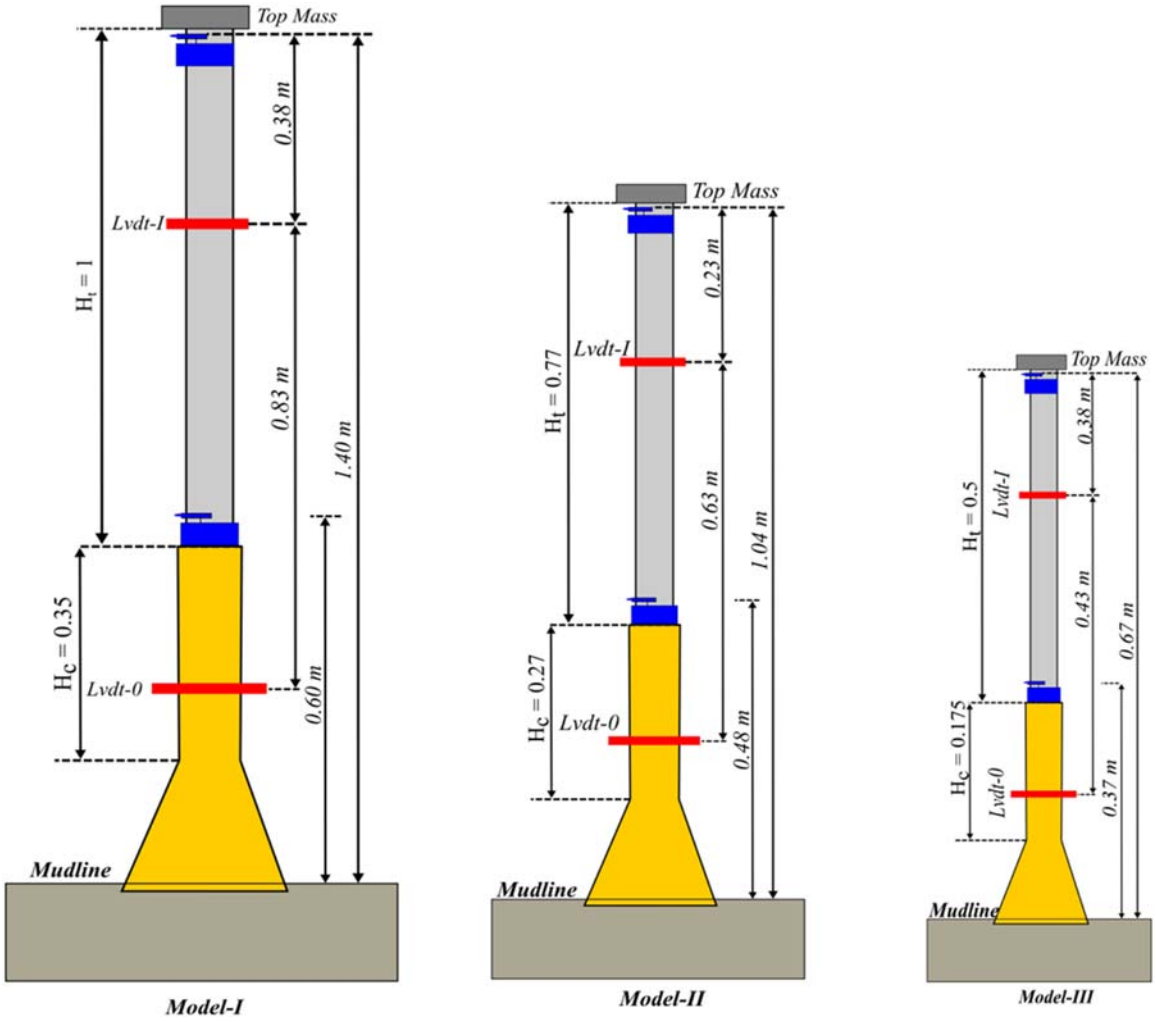

FIGURE 35.14 Studied models.

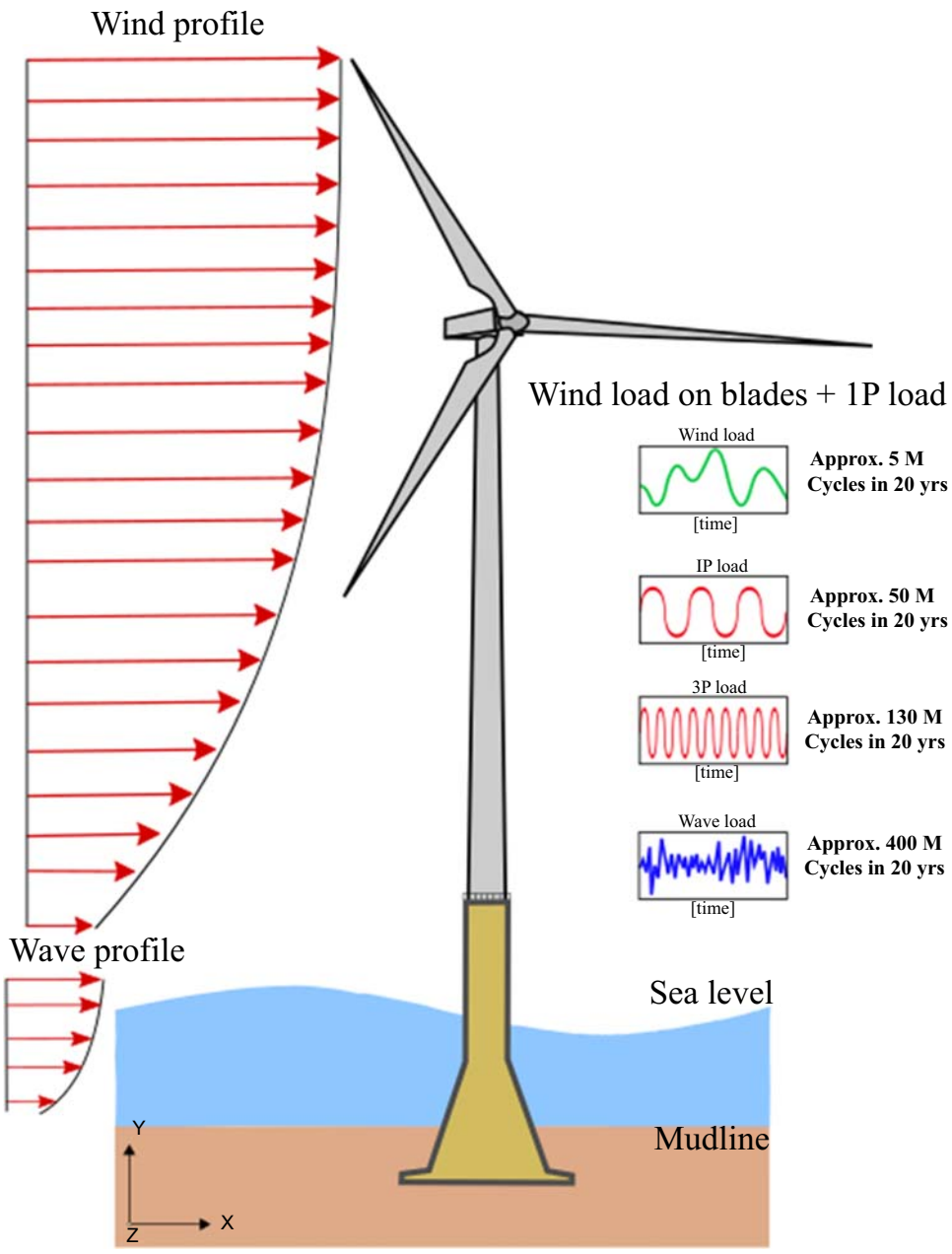

FIGURE 35.15 Load complexity with an approximate number of cycles for 20–25 years assumed lifetime.

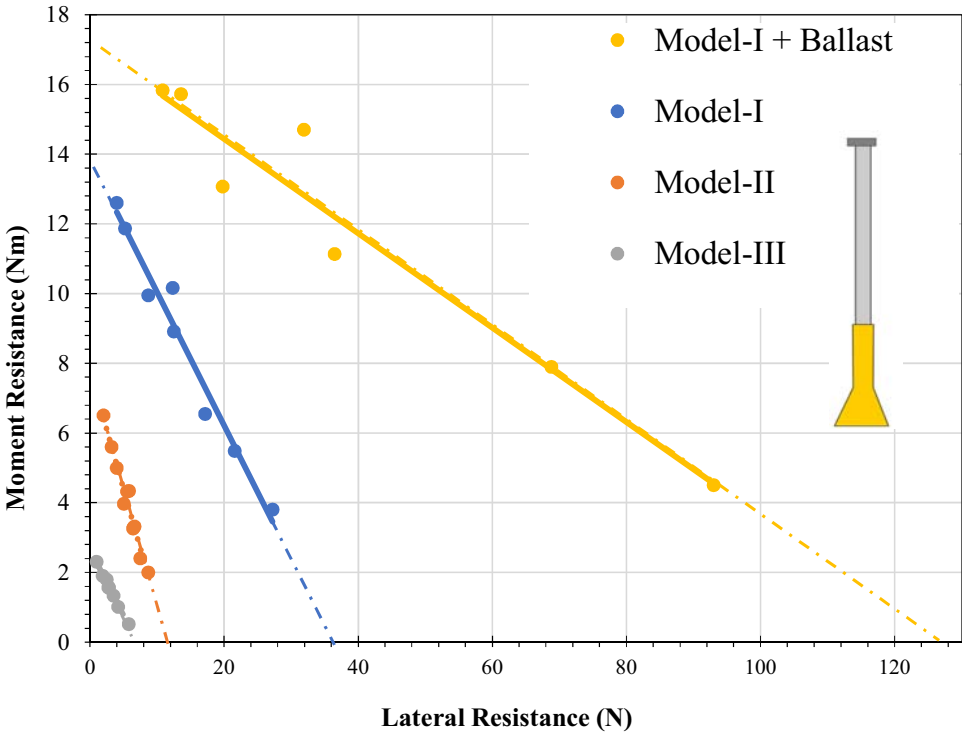

FIGURE 35.16 ULS framework for the gravity-based foundation.

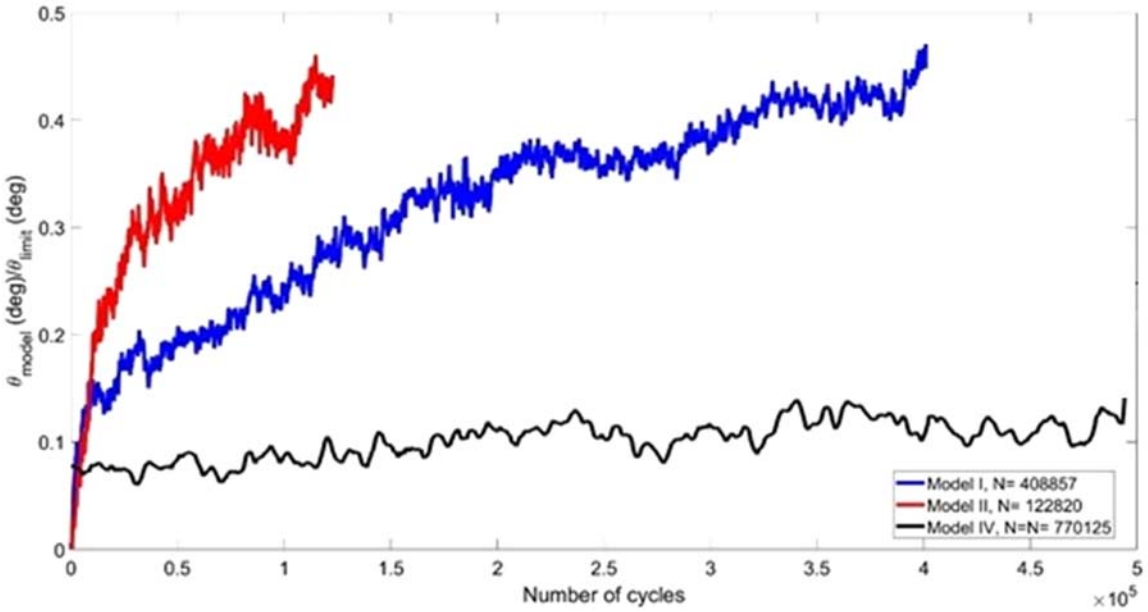

FIGURE 35.17 SLS framework.

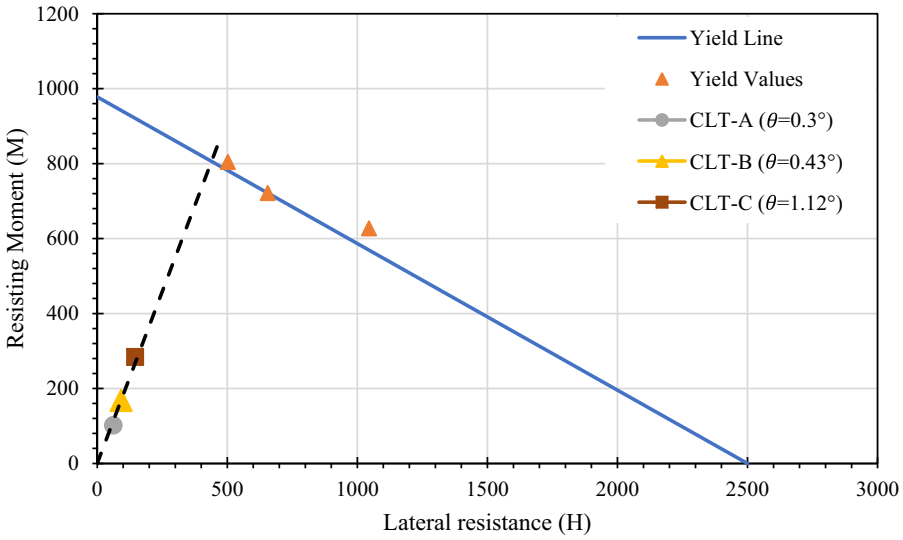

FIGURE 35.18 Interaction curve for monopile foundation.

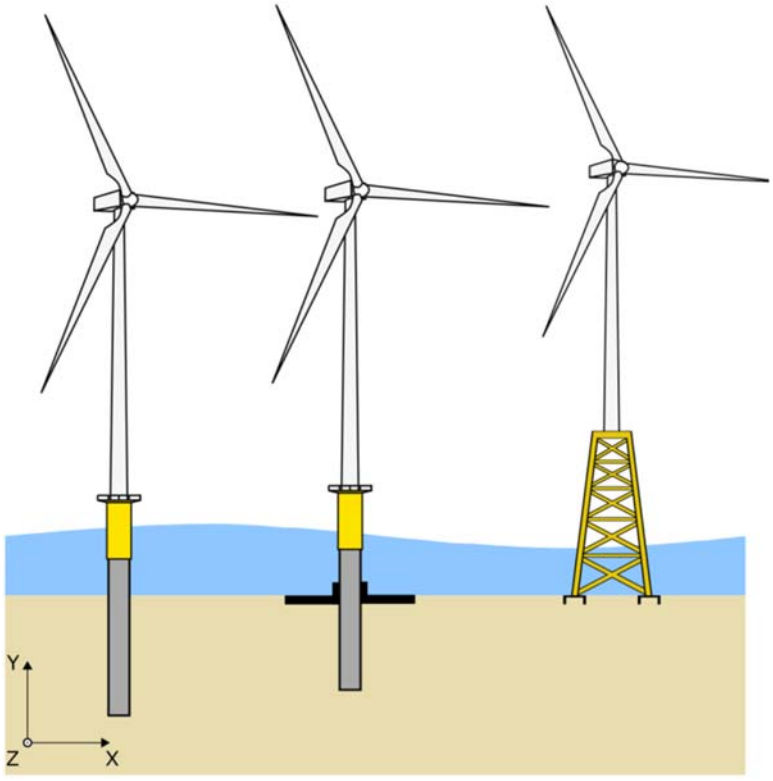

FIGURE 35.19 Comparison of hybrid foundation with a jacket and typical monopole.

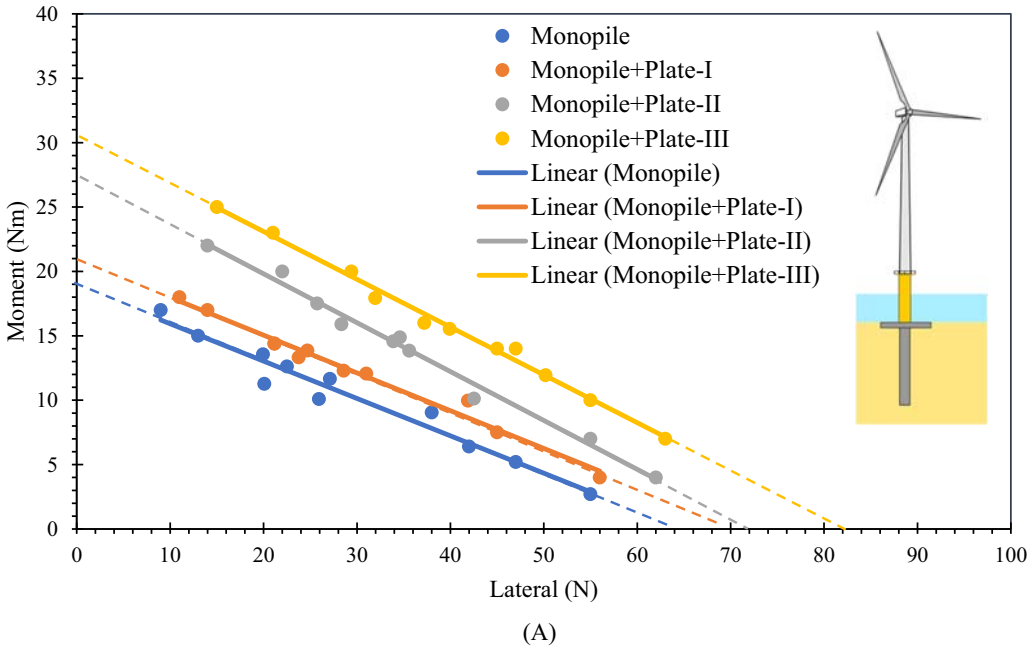

(A)

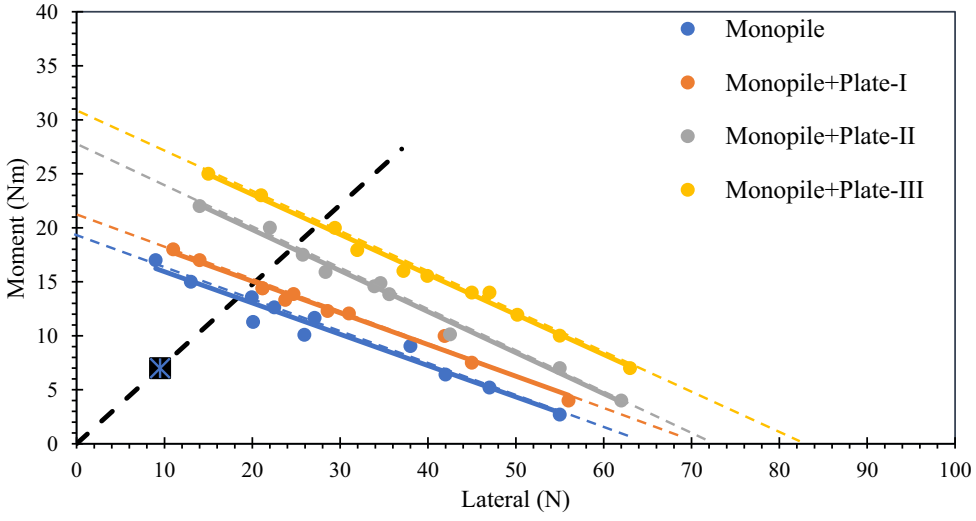

(B)

FIGURE 35.20 (A) ULS framework for hybrid type foundation (B) ULS framework for a hybrid with the assumed Design Load Case (DLC).

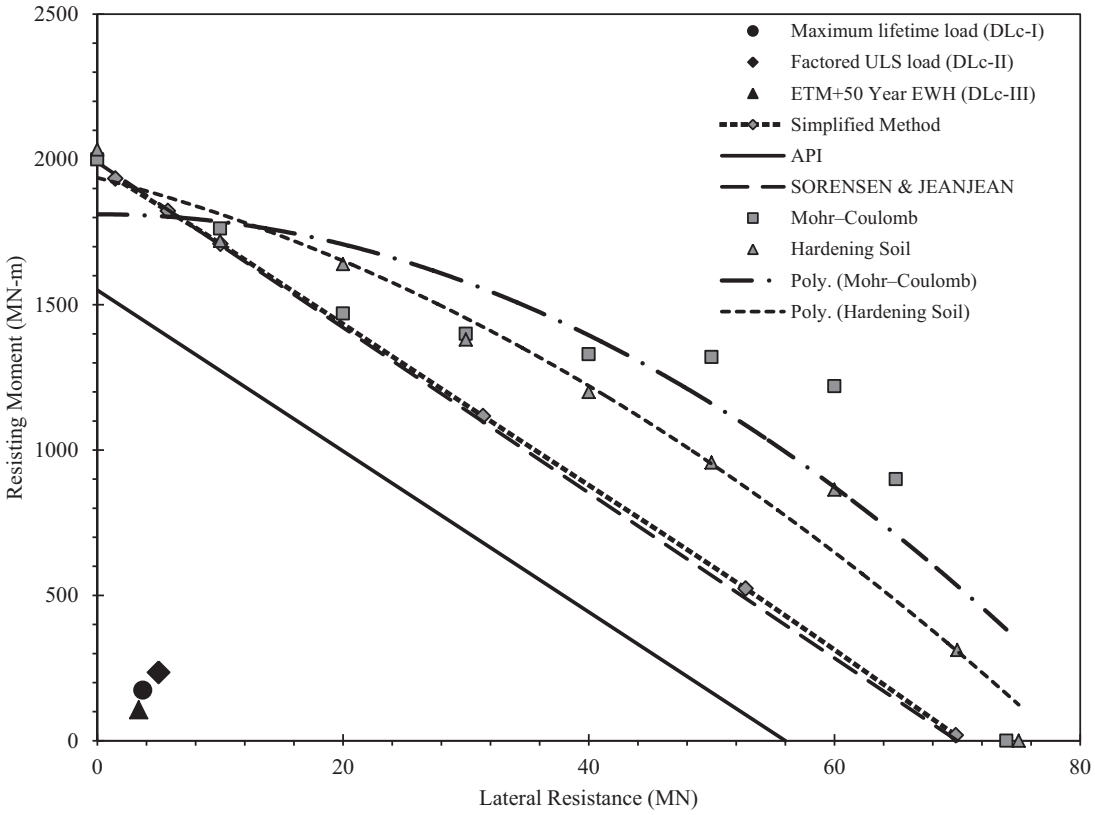

FIGURE 35.21 Interaction curve for Barrow-II.

35.10 Concluding remarks

The aim of the chapter is to focus on the important aspects of the certification of new foundations for a given set of performance criteria. The principles of certification focusing on various limit states are discussed. A setup that can be used to study various aspects of the foundation is described, and illustrative data is presented for a few types of foundations: GBS, monopile, and hybrid foundation.

Often it is necessary to design a prototype foundation for which no guidelines exist, and the only understanding is the observations from scaled model tests. For a hybrid foundation, the scaled model tests showed that adding a plate enhanced the load-carrying capacity of the whole foundation.

Appendix-A List of projects

Table 35.A1–35.A3

TABLE A35.1 Monopiles.

Project	Mean water depth (m)	Rated Power (MW)	Foundation type
Lely A2	12.1	2	Monopile
Lely A3	7.1	2	Monopile
Irene Vorrink	5.2	0.6	Monopile
Irene Vorrink	6	0.6	Monopile
Blyth	7.8	2	Monopile
Kentish I	8	3	Monopile
Barrow II	18	3	Monopile
Thanet III	27	3	Monopile
Belwind IV	20	3	Monopile
Burbo Bank	8	3.6	Monopile
Walney I	21.5	3.6	Monopile
Gunfleet Sands	15	3.6	Monopile
Horns rev	14	2.3	Monopile
London Array 1	25	3.6	Monopile
London Array 2	10	3.6	Monopile
Rampion	39	3.45	Monopile
Sofia	36	14	Monopile
Triton knoll	24	9.5	Monopile
Rhyl Flats	15	3.6	Monopile
Greater Gabbard	34	3.6	Monopile
Gwynt y Mor	28	3.6	Monopile
Gemini WF	36	4	Monopile
Gode Wind 1 and 2	30	6	Monopile
Race Bank WF	26	6	Monopile
Formosa WF1	30	6	Monopile
Spic Binhai	18	4	Monopile
Huaneng Rudong	20	5	Monopile
Laothing	27	4	Monopile
Guodian	15	4	Monopile
Dongtai	6	4	Monopile
Skipjack	30	12	Monopile
South forrk	36	8	Monopile
Zuhai Jinwan	21	5.5	Monopile
Jiangsu Xiangshui	12	4	Monopile
Akita Yurihonjo	20	9.5	Monopile
Yunlin	38	8	Monopile
Kamisu	5	2	Monopile
Nordsee One	29	6.15	Monopile
Galloper	36	6.3	Monopile

TABLE A35.2 Jacket.

Project	Mean water depth (m)	Rated Power (MW)	Foundation type
Tamara	10	3	Jacket
Zhong Neng	25	9.5	Jacket
Changhua 1	55	8	Jacket
Southwest	30	3	Jacket
Changfang	46	9.5	Jacket
Nordsee Ost	26	6.15	Jacket
Hornsea 1	30	7	Jacket
East Anglia ONE	40	7	Jacket
Beatrice WF	45	5	Jacket
Formosa WF2	55	8	Jacket
CGN Yangjiang Nanpeng Island	32	5.5	Jacket
Block Island	30.5	6	Jacket
Nordsee Ost	26	6.15	Jacket

TABLE A35.3 Gravity-based foundation.

Project	Mean water depth (m)	Rated Power (MW)	Foundation type
Thornton Bank	25	5	GBS
Karenhamn	21	3	GBS
Korean	13.7	3	GBS
Chinese	6	2.5	GBS
Vindpark Vanern	10	3	GBS
Avedore Holme	2	3.6	GBS
Rodsan II (Nysted II)	12	2.3	GBS
Sprogo	16	3	GBS
Lillgrund	13	2.3	GBS
Breitling	0.5	2.5	GBS
Nysted I (Rodsan I)	9	2.3	GBS
Middelgrunden	6	2	GBS
Tuno Knob	7	0.5	GBS
Vindeby (dismantled)	4	0.45	GBS
Blyth Demonstrator	38	8	GBS
Empire Wind	30	12	GBS
Choshi (Taiwan)	30	2.4	GBS

References

[1] Bhattacharya S. Design of Foundations for Offshore Wind Turbines. 1st ed. Chichester: John Wiley & Sons Ltd; 2019.

[2] Aleem M, et al. Load utilisation (LU) ratio of monopiles supporting offshore wind turbines: formulation and examples from European Wind Farms. Ocean Eng 2022;248:110798. Available from: https://doi.org/10.1016/J.OCEANENG.2022.110798.

[3] Aleem M, Demirci HE, Bhattacharya S. 'Lateral and moment resisting capacity of monopiles in layered soils'. Proc ICEESEN Kayseri-Turkey 2020;19–21.

[4] Bhattacharya S, et al. Physical modelling of offshore wind turbine foundations for TRL (Technology readiness level) studies. J Mar Sci Eng 2021;9(6). Available from: https://doi.org/10.3390/jmse9060589.

[5] Bhattacharya S, Demirci HE, Nikitas G, Prakhya GKV, Lombardi D, Alexander NA, et al. Physical modelling of interaction problems in geotechnical engineering. Model Geotech Eng 2021;205–56.

[6] Bhattacharya S, Lombardi D, Wood DM. Similitude relationships for physical modelling of monopile-supported offshore wind turbines. Int J Phys Model Geotech 2011;11(2):58–68. Available from: https://doi.org/10.1680/ijpmg.2011.11.2.58.

[7] Bhattacharya S, et al. Dynamics of offshore wind turbines supported on two foundations. Proc Inst Civ Eng: Geotech Eng 2013;166(2):159–69. Available from: https://doi.org/10.1680/geng.11.00015.

[8] Lombardi D, Bhattacharya S, Muir Wood D. Dynamic soil-structure interaction of monopile supported wind turbines in cohesive soil. Soil Dyn Earthq Eng 2013;49:165–80. Available from: https://doi.org/10.1016/j.soildyn.2013.01.015.

This page intentionally left blank

Index

Note: Page numbers followed by "*f*" and "*t*" refer to figures and tables, respectively.

C

D

E

F

G

H

I

J

K

L

M

N

O

P

Q

R

S

T

X

Y

Z

WIND ENERGY ENGINEERING
A HANDBOOK FOR ONSHORE AND OFFSHORE WIND TURBINES

EDITED BY TREVOR M. LETCHER **SECOND EDITION**

This book covers a wide spectrum of topics in the field of wind turbines (offshore and onshore), written by world authorities, all experts in their own fields.

Key Features

- Offers an all-round understanding of links between resources worldwide, wind turbine technology, electricity and environmental issues, and economics
- Provides information on the latest research and development related to wind power in the chapters
- Includes extensive sets of references in each chapter, giving readers the latest thinking and information on each topic to become aware of the challenges

With this fully revised Second Edition, *Wind Energy Engineering: A Handbook for Onshore and Offshore Wind Turbines* continues to be the most advanced, up-to-date, and research-focused text on all aspects of wind energy engineering. Covering a wider spectrum of topics in the field of wind turbines (offshore and onshore), this new edition includes new intelligent turbine designs and optimization, current challenges and efficiencies, remote sensing and smart monitoring, and key areas or advancement such as floating wind turbines.

Each chapter includes a research overview with a detailed analysis and new case studies looking at how recent research developments can be applied. Written by some of the most forward-thinking professionals in the field and giving a complete examination of one of the most promising and efficient sources of renewable energy, this book is an invaluable reference for readers approaching this cross-disciplinary field.

About the Editor

Professor Trevor M. Letcher was a professor of chemistry, and head of department in South Africa (University of the Witwatersrand, Rhodes University, and Natal) (1969–2004). He has published over 300 papers on chemical thermodynamic topics in peer-reviewed journals and 100 papers in popular science and education journals. He has edited and written 32 books such as *Future Energy Climate Change*, *Storing Energy*, *Wind Energy*, *Solar Energy*, *Managing Global Warming*, and *Unraveling Environmental Disasters*. He has been awarded gold medals by the South African Institute of Chemistry and the South African Association for the Advancement of Science. He is currently an emeritus professor at the University of KwaZulu-Natal, South Africa and resides in the United Kingdom.

ELSEVIER

ACADEMIC PRESS
An imprint of Elsevier
elsevier.com/books-and-journals

ISBN 978-0-323-99353-1